

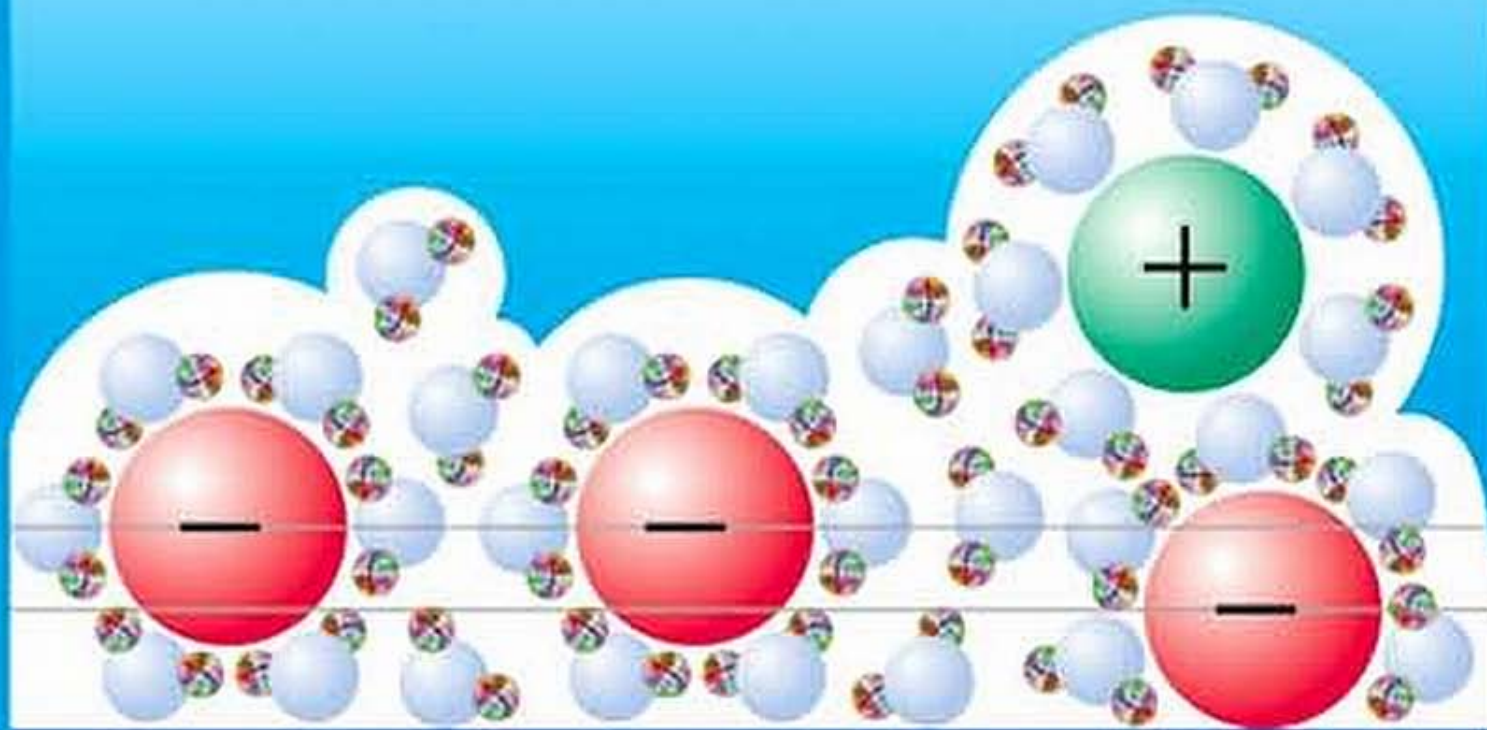
Bard–Stratmann

Encyclopedia of Electrochemistry

Volume 7b

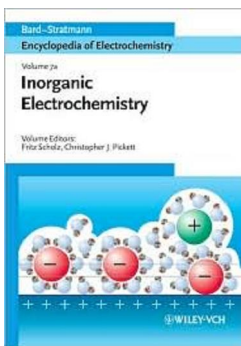
Inorganic Electrochemistry

Volume Editors:
Fritz Scholz, Christopher J. Pickett



++ + + + + + + + + + + +

 WILEY-VCH



Encyclopedia of Electrochemistry, Inorganic Chemistry, Vol. 7b

by Allen J. Bard (Editor), Fritz Scholz (Editor), Martin Stratmann (Editor), Christopher J. Pickett (Editor)

Product Details

Pub. Date: May 2006
Publisher: Wiley, John & Sons,
Incorporated
Format: Hardcover , 537pp

Series: Encyclopedia of Electrochemistry
ISBN-13: 9783527317004
ISBN: 3527317007
Edition Description: 1ST

Synopsis

Electrochemical processes play an increasingly large role in our daily lives; whether in producing or saving energy, rust protection or nerve stimuli in our bodies. This 11-volume encyclopedia provides both an easy introduction to all topics related to modern electrochemistry as well as comprehensive overview of the subject.

Unrivalled in its breadth and depth, this first-class reference work has been created and written by renowned scientists, covering everything from fundamental research to areas of application.

Biography

Series Editors:

Prof. Allen J. Bard: Born December 18, 1933, Prof. Bard received his early education in the public schools of New York City and attended The City College of NY (B.Sc., 1955). He did his graduate work at Harvard Univ. with J.J. Lingane (MA, 1956; PhD, 1958) in electroanalytical chemistry. In 1958 he joined the faculty of The Univ. of Texas at Austin where he currently holds the Norman Hackerman/Welch Regents' Chair in Chemistry. His research interests have been in the application of electrochemical methods to the study of chemical problems and include investigations in electro-organic chemistry, photoelectrochemistry, electrogenerated chemiluminescence, and electroanalytical chemistry. He has published three books (Electrochemical Methods, with Larry Faulkner, Integrated Chemical Systems, and Chemical Equilibrium) and over 600 papers and chapters while editing the series Electroanalytical Chemistry (21 volumes) and the Encyclopedia of the Electrochemistry of the Elements (16 volumes) plus co-editing the monograph, Standard Potentials in Aqueous Solution. He is currently editor-in-chief of the Journal of the American Chem. Society. The ISI listing of the "50 most cited chemists from 1981-1997" ranks Prof. Bard at number 13 (taken from a total of 627,871 chemists surveyed).

Prof. Martin Stratmann: Born 20 April 1954, studied chemistry at the Ruhr Univ. Bochum and received his diploma in 1980. He finished his PhD in 1982 at the Max Planck Inst. (MPI) für Eisenforschung in Düsseldorf. His professorship in physical chemistry followed in 1992 at the Univ. of Düsseldorf with electrochemical studies on metal surfaces covered with ultrathin electrolyte layers. In 1994 he took over the Chair in Corrosion Sci. and Surface Engin. at the Univ. of Erlangen and since 2000 has been a scientific member of the MPI and director at the MPI für Eisenforschung Düsseldorf, heading a department of interface chemistry and surface engineering. His research interests concentrate on corrosion related electrochemistry, in particular with emphasis on microscopic aspects and in-situ spectroscopy, electrochemistry at buried metal/polymer interfaces - an area where he pioneered novel electrochemical techniques - atmospheric corrosion, adhesion and surface chemistry of reactive metal substrates. He has published more than 150 papers and is co-editor of Steel Research and Materials and Corrosion.

Volume Editors:

Prof. Christopher J. Pickett: Professor Pickett gained both his BSc and his PhD at Southampton University, in 1972 and 1975 respectively. He began his career as Higher Scientific Officer at the Unit of Nitrogen Fixation, where he progressed to Principal Scientific Officer in 1980. He became an honorary professor at the University of East Anglia in 2000 and is currently Associate Head of the Department of Biological Chemistry at the John Innes Centre in Norwich, UK. His research areas are artificial hydrogenases, bioelectropolymers and the chemistry of biological nitrogen fixation. Chris Pickett was a Professeur at the Universit Occidentale in 1992 and a Wilsmore Fellow of the University of Melbourne in 1998. He is the holder of a Royal Society of Chemistry Medal for Chemistry and Electrochemistry of the Transition Metals, as well as a Joint Research Councils' Individual Merit Promotion.

Prof. Fritz Scholz: Fritz Scholz was born in 1955, and studied chemistry at Humboldt Univ., Berlin, where he received a Diploma in 1978, a Dr. rer nat in 1982, and a Dr. sc. nat (habilitation) in 1987. He held the position of Professor in Berlin from 1993-1998. Since 1998 he is Professor at the Univ. of Greifswald. In 1987-1988 he worked with Alan M. Bond in Australia. Beside various contributions to electronanalysis, he developed a new kind of mercury flow-through electrodes (bubble electrodes) and established the voltammetry of immobilized particles as a technique to study the electrochemistry of solid compounds. He published more than 200 papers and 2 books, and he has founded the Journal of Solid State Electrochemistry.

Table of Contents

- 20. A Few Selected Aspects of Electrode-induced Reactions at Monoand Dinuclear Molybdenum-sulfur Centers
(Francois Y. Pétillon, Philippe Schollhammer, and Jean Talarmin)
- 21. Aspects of Metallo-sulfur Clusters' Electrochemistry (Frédéric Barrière)
- 22. Electrochemistry of Isopoly and Heteropoly Oxometalates (Bineta Keita and Louis Nadjo)
- 23. Electrochemistry of Polycyanometalates (Fritz Scholz and Heike Kahlert)
- 24. Electrochemistry of Zinc, Cadmium, Lead, Gold, Silver, Mercury, and Copper
 - Part A: Electrochemistry of Zinc, Cadmium, and Lead (Jadwiga Stroka, Krzysztof Maksymiuk, and Zbigniew Galus)
 - Part B: Electrochemistry of Gold, Silver, and Mercury (Marek Orlik and Zbigniew Galus)
 - Part C: Electrochemistry of Copper (David B. Rorabacher and Ronald R. Schroeder)
- 25. The Actinides (Michael E. Stoll)
- Volume Index.

20

A Few Selected Aspects of Electrode-induced Reactions at Mono- and Dinuclear Molybdenum-sulfur Centers

Dedicated to the memory of Alain Talarmin

Francois Y. Pétillon, Philippe Schollhammer, and Jean Talarmin
Université de Bretagne Occidentale, 29283 Brest Cedex 3, France

20.1	Introduction	567
20.2	Mononuclear Mo-S Centers	567
20.2.1	Electron Transfer-induced Structure Change	567
20.2.2	Electrochemically Induced Metal-ligand Bonds Cleavage	568
20.2.3	Electrochemical Transformation of Ligands	571
20.3	Dinuclear Thiolate-bridged Molybdenum Complexes	573
20.3.1	Electron Transfer-induced Structure Changes	573
20.3.2	Electron Transfer-induced and Electron Transfer-catalyzed Ligand Substitution	576
20.3.3	Electrochemically Induced Metal-Ligand Bonds Cleavage	577
20.3.4	Electrochemical Deprotection of a Substrate-binding Site	581
20.3.5	Electrochemical Transformations of Bound Substrate	582
20.4	Conclusion	588
	Acknowledgments	589
	References	589

20.1 Introduction

A large number of studies devoted to metal–sulfur centers are motivated by the occurrence of such arrangements at the active site of various metalloenzymes [1–13]. Mononuclear complexes with Mo=O function(s) and possessing sulfur ligands in their coordination sphere have been extensively investigated since they can be seen as models of the active site of enzymes such as nitrate- and DMSO reductases or sulfite- and xanthine oxidases [1–4]. On the other hand, a large variety of mono-, di-, and polynuclear Mo–S centers have been synthesized in order to produce functional models of the Mo–nitrogenase since the exact nature (mono-, di- or polynuclear) of the metal center, where N₂ interacts within the iron–molybdenum cofactor (FeMo–co) of the enzyme is still unknown [4–8].

Although many studies of Mo–S complexes make use of electrochemical techniques, and particularly of cyclic voltammetry (CV), this is often restricted to measurements of redox potentials, and to discussions of their variation with structure or of their relationships with spectroscopic properties. Such examples can be found in the above-mentioned reviews. In this article, we will comment

on a few studies where chemical reactions such as structural changes, metal–ligand bond(s) cleavage, substitution, transformations of ligands, were induced or catalyzed by electron transfer step(s). This will be illustrated, in the case of mononuclear Mo–S centers, by complexes in which the sulfur ligands are supplied by a tetrathioether macrocycle, by dithiocarbamates, or by ligands providing a mixed thiolate/thioether donor set. In the case of binuclear complexes, we will focus on compounds where thiolate bridges link the metal centers, although examples of compounds containing sulfide or thioether groups will be briefly mentioned.

20.2 Mononuclear Mo–S Centers

20.2.1 Electron Transfer-induced Structure Change

The occurrence of structure changes as a result of electron transfer steps is well-documented [14–16]. Such a reaction has been observed for a molybdenum complex of the macrocyclic tetrathioether Me₈[16]aneS₄ (Me₈[16]aneS₄ = 3,3,7,7,11,11,15,15-octamethyl-1,5,9,13-tetrathiacyclohexadecane) [17–20], which is among the

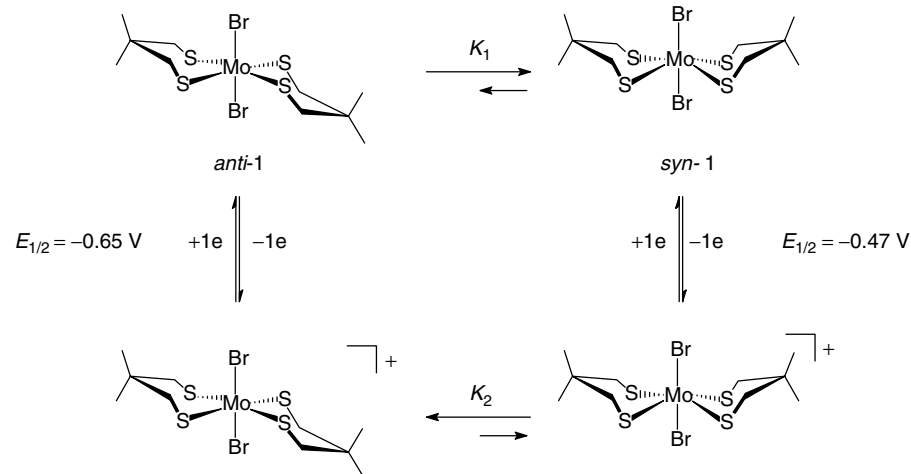
rare [21] Mo–S site able to bind N₂ [18]. The electrochemical behavior of the Mo(II) precursor of the bis-N₂ complex, namely *trans*-[MoX₂(Me₈[16]aneS₄)] **1** (X = Cl, Br), has been investigated in order to compare with the phosphorus-ligated analog, *trans*-[MoX₂(dppe)₂] (X = Cl, Br) [22]. The oxidation of **1** (X = Br) [20] at room temperature appeared as an uncomplicated, reversible, diffusion-controlled one-electron step with $E_{1/2}^{ox} = -0.52$ V/Fc (Fc = ferrocene). However, the CV recorded at -55°C in dichloromethane showed two partially reversible oxidation processes, at -0.65 V and -0.47 V. The temperature-dependence of the oxidation of **1** was assigned to the occurrence of dynamic equilibria involving two different conformers of the neutral and cationic complexes, differing by the “all-up” (*syn*) or “up-up-down-down” (*anti*) conformation of the carbon ring atoms of the crown thioether (Sch. 1) [20].

This assignment is supported by the X-ray crystal structures of **1** and **1⁺** ($X = \text{Br}$), which show the different arrangements adopted by the macrocyclic ligand in the

neutral Mo(II) complex (*syn*) and in the Mo(III) cation (*anti*) [20]. The fluxional behavior of the complexes was rationalized in terms of electronic effects, since the *anti* conformation favored at the Mo(III) level would maximize net charge donation by the sulfur ligands and compensate for the decrease of the electron density at the metal center resulting from the one-electron oxidation. It is also interesting to note that the two axial sites are not equivalent for the *syn* conformation of the macrocycle [19]. Therefore, the one-electron oxidation of 1 might induce a different reactivity of the complex, not only because of the change in the metal oxidation state but also, possibly, because of different geometric/steric requirements.

20.2.2 Electrochemically Induced Metal–ligand Bonds Cleavage

The electrochemical behavior of the seven-coordinate complexes $[\text{MoOX}_2(\text{dtc})_2] \cdot 2$ (X = Cl, Br; dtc = S_2CNEt_2), $[\text{MoO}(\text{cat})]$



Scheme 1 Carbon ring atoms at the front and at the back were omitted for clarity; potentials are relative to Fc^+/Fc .

$(dtc)_2$] **3**, and $[MoO(dtCl)_3]^+$ **4⁺** has been investigated in order to evaluate the role of the metal environment on the electron transfer processes [23]. The reduction of **2-4⁺** was shown to result in metal-ligand bonds cleavage, according to mechanisms that depend on the nature of the ligands present in the coordination sphere.

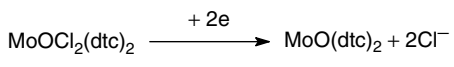
The CV of $[MoOX_2(dtCl)_2]$ **2** in MeCN showed that the complex reduces in an irreversible two-electron step, with the elimination of both halide ligands (Sch. 2). The metal product of the electrochemical reduction, $[MoO(dtCl)_2]$, detected by CV through its reduction and oxidation systems, was obtained by controlled-potential reduction of **2** (2 F mol^{-1} **2**).

The process in Sch. 2 is chemically reversible since controlled potential oxidation of $[MoO(dtCl)_2]$ in the presence of an excess chloride regenerated **2** after the transfer of ca. 2 F mol^{-1} $[MoO(dtCl)_2]$. The detailed mechanism represented in Sch. 3

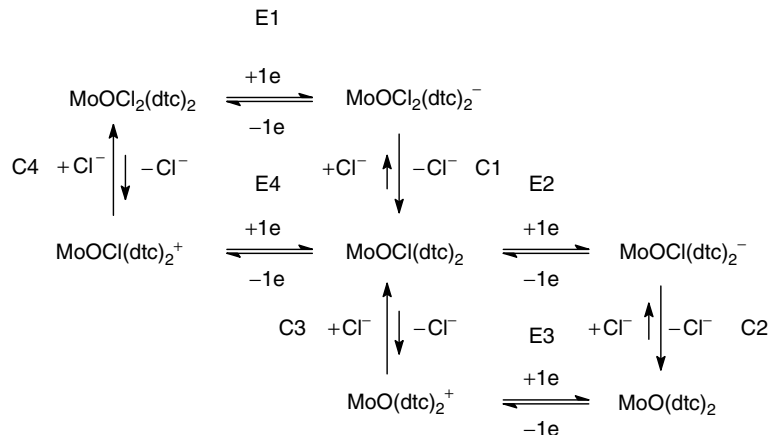
was confirmed by investigations of the individual steps.

The loss of a halide from **2** (step C4) was shown to be a reversible reaction, which was more shifted toward the monohalide cation for $X = \text{Br}$ than for $X = \text{Cl}$. The electrochemical steps E2 and E4 were studied using the Mo(V) complex $[MoOCl(dtCl)_2]$. The reduction of **2** follows the E1-C1-E2-C2 pathway and the oxidation of $[MoO(dtCl)_2]$ the E3-C3-E4-C4 pathway [23].

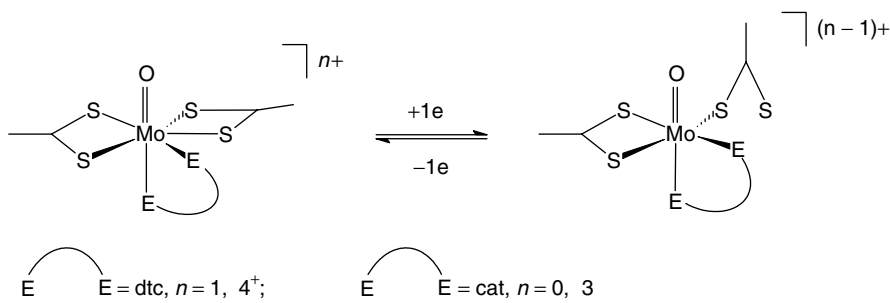
The two-electron reduction of both **3** and **4⁺** resulted in the elimination of a dtc^- ligand [23]. For these compounds, the two-electron reduction could be resolved in two separate one-electron steps. The first electron transfer for both **3** and **4⁺** led to partial dissociation of a dtc ligand; nevertheless this step was quasi-reversible, as evidenced by the scan rate dependence of the peak-to-peak separation (ΔE_p) [24] (Sch. 4). This was assigned to the fact that the decoordination sulfur atom



Scheme 2



Scheme 3



Scheme 4

remained at proximity of the metal center, thus allowing the reverse reaction to take place [24].

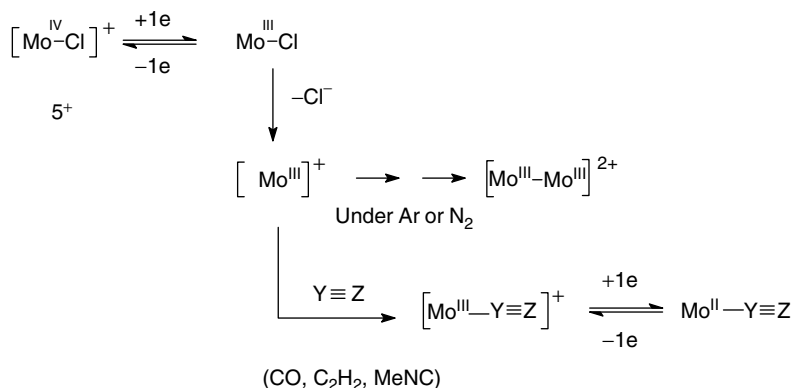
The apparent rate constant of the heterogeneous electron transfer (k_s^{app}) was about 100 times larger for 4^+ than for 3 [24]. Furthermore, k_s^{app} for 3 was dependent on the nature of the catecholate ligand (Cl_4cat , NO_2cat , cat , DTBcat) [24]. This indicated that the activation barrier contains a substantial contribution from the catecholate ligand and that the Gibbs free energy of activation for the process in Sch. 4 accounts for reorganization of the entire coordination sphere.

The cleavage of one equatorial Mo–X or Mo–S bond upon one-electron reduction of 2 , 3 , and 4^+ was assigned to unfavorable electrostatic interactions between the lobes of the half-filled Mo $4d_{xy}$ antibonding orbital and the five equatorial metal–ligand bonding electron pairs [23]. This interpretation was confirmed by the fact that the Mo(VI)/Mo(V) reduction of six-coordinate complexes (i.e. with four equatorial ligands) was found fully reversible, as expected [25].

In the following example, the electrochemical cleavage of the Mo–Cl bond of the seven-coordinate complex $[\text{MoCl}(\text{dtc})_2(\text{dppe})]^+$ ($\text{dtc} = S_2\text{CNR}_2$; $R = \text{Me}$ or Et ; $\text{dppe} = \text{Ph}_2\text{PCH}_2\text{CH}_2\text{PPh}_2$)

generated a vacant site that binds nitrogenase substrates (C_2H_2 , MeNC) or inhibitor (CO). The first reduction of $[\text{MoCl}(\text{dtc})_2(\text{dppe})]^+$ ($[\text{Mo}-\text{Cl}]^+$) 5^+ in MeCN under argon occurred according to an EC process [26]. The chemical reactions following the one-electron transfer step, which were responsible for complicated CV curves, could be suppressed at fast scan rates. Under these conditions, reduction of 5^+ appeared as a partially reversible couple. Controlled potential electrolysis under argon at the potential of the first reduction afforded a $[\text{Mo}^{\text{III}}-\text{Mo}^{\text{III}}]^{2+}$ dimer after transfer of $1 \text{ F mol}^{-1} 5^+$ (Sch. 5). Whereas the CV under N_2 was the same as under argon, the presence of other $\text{Y}\equiv\text{Z}$ substrates (CO , C_2H_2 , MeNC) resulted in a simplification of the cyclic voltammograms, since a single two-electron (ECE) reduction was observed. This clearly indicated binding of $\text{Y}\equiv\text{Z}$ to the Mo(III) intermediate generated by the EC process (Sch. 5). However, only the carbonyl derivative $[\text{Mo}(\text{CO})(\text{dtc})_2(\text{dppe})]$ could be obtained by controlled potential electrolysis ($2 \text{ F mol}^{-1} 5^+$). Electrolyses performed in the presence of acetylene afforded the dimer $[\text{Mo}^{\text{III}}-\text{Mo}^{\text{III}}]^{2+}$ after the transfer of $1 \text{ F mol}^{-1} 5^+$.

These experiments demonstrated that, although C_2H_2 and MeNC bind at the electrogenerated Mo(III) site (Sch. 5), these

**Scheme 5**

substrates, but not CO, were lost after one-electron reduction of the $\{\text{Mo}^{\text{III}}-\text{Y} \equiv \text{Z}\}$ complex [26].

Complexes with thiolate/thioether ligands such as dttd [$\text{dttd} = 1,2\text{-bis}(2\text{-mercaptoethylthio})ethane$] have been extensively investigated [7] as they provide a coordination sphere similar to that found at the active site of various metalloenzymes [1–4]. $[\text{Mo}(\text{NO})\text{Cl}(\text{dttd})]$ **6** showed a rich electrode-induced reactivity [27]. **6** undergoes two diffusion-controlled reduction steps, the first one ($E_{1/2}^{\text{red}1} = -0.70 \text{ V/Fc}$) was reversible at room temperature, while the second ($E_{1/2}^{\text{red}2} = -2.20 \text{ V/Fc}$) showed some reversibility only at low temperature. Whereas controlled potential reduction at the first step afforded the stable monoanion, electrolysis at the potential of the second process was found to generate the highly reduced species $[\text{Mo}(\text{NO})(1,2\text{-C}_6\text{H}_4\text{S}_2)_2]^{3-}$ 7^{3-} , in an overall 4e transfer (Sch. 6). Thus, the 4e-reduction of **6** caused the cleavage of the Mo—Cl bond, as well as the cleavage of two C—S bonds, the latter resulting in the extrusion of ethylene from the ligand backbone.

Gas chromatographic analyses during the electrolysis showed that C_2H_4 release

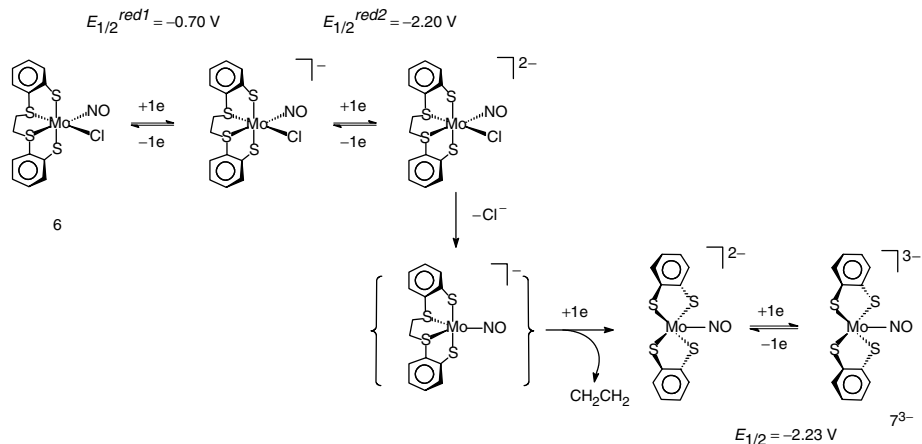
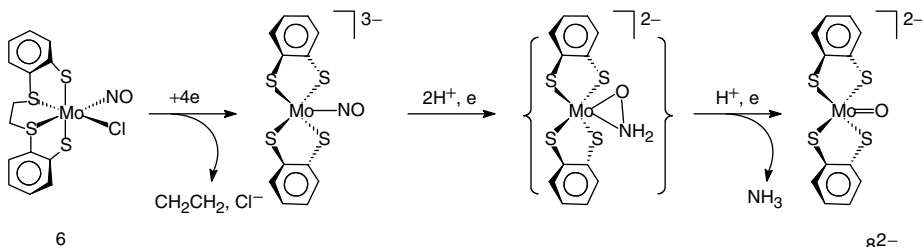
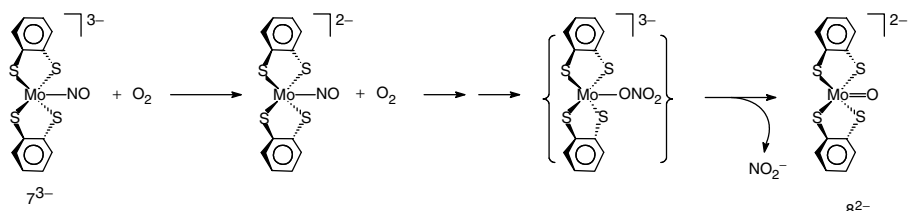
started after 2 F mol^{-1} **6** had passed, Sch. 6 [27].

20.2.3

Electrochemical Transformation of Ligands

A particularly interesting aspect of electrochemistry is that it may allow transformations of bound substrates, by coupling proton(s) and electron(s) transfers. This makes possible to mimic certain steps of the reactions driven by metalloenzymes. For example, the nitrosyl ligand in 7^{3-} (Sch. 6) is activated toward protic attack. Controlled potential reduction of **6** at the potential of the second process in the presence of PhOH (5–10 equiv) as a proton source consumed 6 F mol^{-1} **6** and afforded the molybdenum oxide $[\text{MoO}(1,2\text{-C}_6\text{H}_4\text{S}_2)_2]^{2-}$ 8^{2-} and ammonia. The reductive cleavage of the N—O bond was proposed to involve a hydroxylamide intermediate, Sch. 7 [27]. Relevant to this is the fact that the chemical reduction of $[\text{Mo}(\text{NO})_2(\text{dttd})]$ by sodium borohydride or hydrazine in methanol produced $[\text{Mo}(\text{NO})(\text{NH}_2\text{O})(\text{dttd})]$ with a side-on hydroxylaminyl ligand [28].

The nitrosyl ligand in 7^{3-} is also activated toward attack by molecular oxygen.

**Scheme 6** Species in braces is a postulated intermediate.**Scheme 7** Species in braces is a postulated intermediate.**Scheme 8** Species in braces is a postulated intermediate.

The first step of the mechanism leading to the formation of 8^{2-} and free nitrite from the reaction of 7^{3-} with O_2 probably involved a single electron transfer. Subsequent radical–radical coupling of the products, to afford a molybdenum-bound nitrate, followed by N–O bond cleavage would eventually lead to the observed products (Sch. 8) [27].

The electrochemical study of the seven-coordinate complex $[\text{Mo}(\text{N}_2\text{RR}')(\text{dtc})_3]^{+}\text{9}^{+}$ ($\text{R}, \text{R}' = \text{alkyl or aryl, dtc} = \text{S}_2\text{CNMe}_2$) provided an example of electrode-induced activation of a hydrazido(2–) ligand. Complex 9^{+} was shown to reduce in two separate diffusion-controlled one-electron steps, with the first one reversible on the CV timescale at room temperature and

moderate scan rate ($v > 0.3 \text{ V s}^{-1}$) [29]. On longer timescale at room temperature, the one-electron reduced complex **9** was not stable and was involved in chemical reactions so that the reduction of **9⁺** at the potential of the first step occurred according to an ECE-type process. Controlled potential reduction at the first or at the second step afforded the same product **10**, after the transfer of 2 F mol⁻¹ **9⁺**. Product **10** could not be characterized, but it was shown to retain an organodinitrogen moiety. The electronic strain resulting from the two-electron reduction of **9⁺** was proposed to be relieved either by partial dissociation of one of the dtc ligands (see Sch. 4) or by bending of the hydrazido(2-) group followed by protonation at N α (Sch. 9). The latter possibility is entirely consistent with the observed release of the substituted hydrazine H₂NNRR' upon treatment of **10** with HCl [29].

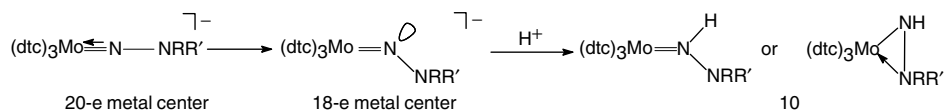
20.3 Dinuclear Thiolate-bridged Molybdenum Complexes

20.3.1 Electron Transfer-induced Structure Changes

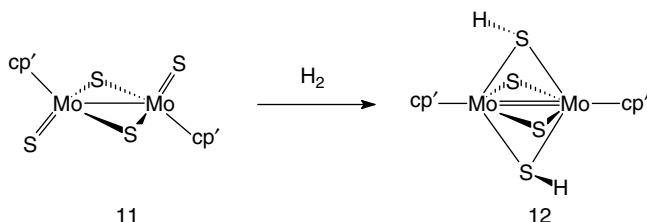
Electron transfers may lead to modifications of the metal–sulfur core of binuclear sulfur-bridged complexes. The CV of [M₂S₂(cp')₂(μ -S)₂] **11** (M = Mo or W, cp' = η -C₅H_{5-n}Me_n) [30] showed that the first reduction was a one-electron process,

whose reversibility was dependent on the nature of the metal centers. Whereas the reduction of the tungsten complex was reversible on the CV timescale, that of the Mo analog (cp' = cp* = η -C₅Me₅) was not. This was assigned to an isomerization of the core, from the bis-bridged [M₂S₂(μ -S)₂] structure of **11** to the more compact [M₂(μ -S)₄] core of **12**, which would be easier for the Mo complex than for the W one [30]. Although the product of the one-electron reduction of **11** was not isolated, the reductively induced structure change could be compared to that resulting from the reaction of **11** with dihydrogen (Sch. 10) [31]. The structure change is best illustrated by the shortening of the Mo–Mo distance from 2.905 Å in **11** (cp' = cp*) to 2.582 Å in an analog of **12** (cp' = Me–cp, SR = SMe instead of SH) [31].

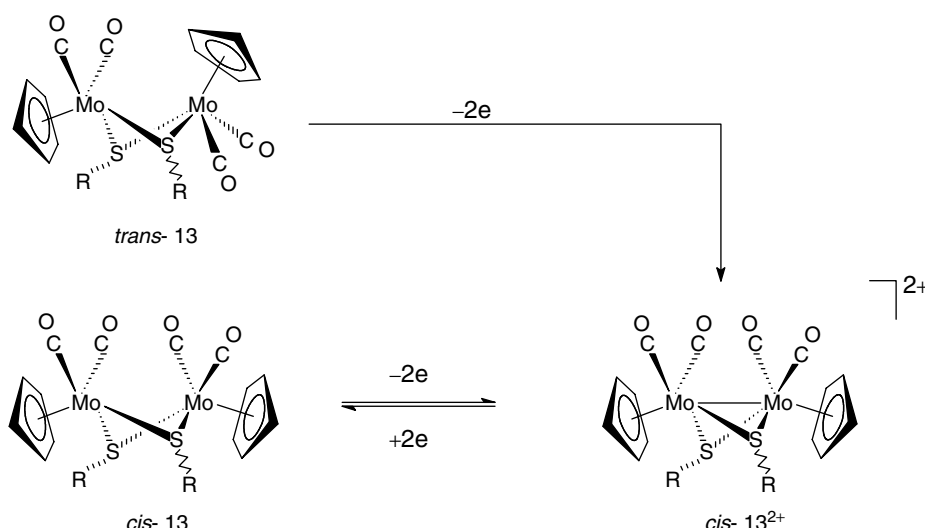
Other examples of electron transfer-induced modifications of metal-sulfur cores have been reported. In the case of *trans*-[M₂(cp)₂(μ -SR)₂(CO)₄] (*trans*-**13**: M = Mo, R = Me, ^tBu, Ph; *trans*-**14**: M = W, R = Me; cp = η -C₅H₅), the electrochemical oxidation is an irreversible two-electron process, which led to the dication with the *cis* arrangement of the CO ligands (Sch. 11). The presence of an M–M single bond in *cis*-**13²⁺** was evidenced by the X-ray crystal structure of the dication (R = ^tBu) [32]. The other isomer, *cis*-[M₂(cp)₂(μ -SR)₂(CO)₄] (*cis*-**13**: M = Mo, R = Me, ^tBu, Ph; *cis*-**14**: M = W, R = Me) was shown to oxidize in a reversible, “single step” two-electron transfer (Sch. 11).



Scheme 9



Scheme 10



Scheme 11

Although there are no crystal structures of corresponding couples of $\text{cis}[\text{M}_2(\text{cp})_2(\mu\text{-SR})_2(\text{CO})_4]^{0/2+}$ complexes, the metal–metal separations in cis-13^{2+} [$\text{R} = {'}\text{Bu}$, $d(\text{Mo–Mo}) = 3.008 \text{ \AA}$] [32] and in an analog of cis-14 , namely $\text{cis-}[W_2(\text{cp})_2(\mu\text{-SiPr})_2(\text{CO})_4]$ [$d(W \dots W) = 3.835 \text{ \AA}$] [33], have been reported. It is thus likely that the reversible two-electron process leads to substantial changes in the M_2S_2 core dimensions ($\text{M} \dots \text{M}$ distance, M–S–M and S–M–S bond angles). The peak-to-peak separation of the reversible, “single step” two-electron transfer ($\text{M} = \text{Mo}$, $\Delta E_p = 40 \text{ mV}$ in thf ; 35 mV in CH_3CN ; $\text{M} = \text{W}$, $\Delta E_p = 60 \text{ mV}$ in thf ; 35 mV in

CH_3CN ; $v = 0.2 \text{ V s}^{-1}$) indicated that the electrode process was not a Nernstian two-electron transfer but involved two successive one-electron steps, with the second thermodynamically more favorable than the first one [32]. Therefore, the reversible, overall two-electron process in Sch. 11 is better represented by two successive, reversible, one-electron steps involving a thermodynamically unstable and undetected cation intermediate (see Sch. 13; EE process, or ECE process, where the chemical step C is a fast, reversible deformation of the M_2S_2 core). In agreement with this, it should be noted that the oxidation of $\text{cis-}[\text{Mo}_2(\text{cp}^*)_2(\mu\text{-SMe})_2(\text{CO})_4] \text{ cis-13}^*$ also

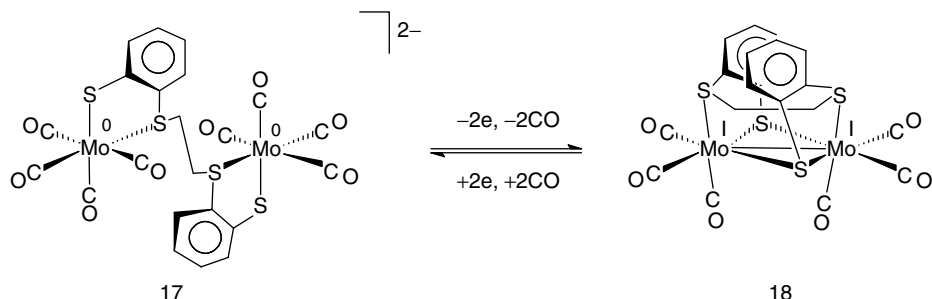
occurred in a single step, reversible two-electron transfer with $\Delta E_p = 40$ mV in thf ($\Delta E_p = 35$ mV in CH_3CN), whereas two separate ($\Delta E_{1/2} = 70$ mV), reversible one-electron couples (ΔE_p ca. 60 mV) were observed in CH_2Cl_2 [34]. This illustrates the effect of the solvent on the separation of successive electron transfer processes [35–37]; in the present case, it resulted from a better solvation of the dication by solvents such as MeCN and thf as compared to dichloromethane [34].

Similarly, the $[\text{M}_2(\mu\text{-SR})_2(\text{CO})_8]^{0/2^-}$ complexes ($\text{M} = \text{Mo}$, **15/15**²⁻; $\text{M} = \text{W}$, **16/16**²⁻; $\text{R} = \text{Ph}$, ^tBu, Bz) are related by a reversible, overall two-electron process [38–41]. As for *cis*- $[\text{M}_2(\text{cp})_2(\mu\text{-SR})_2(\text{CO})_4]$, the 2e process causes important structural changes of the M_2S_2 core, with the formation of an M–M single bond resulting in the decrease of $d(\text{M}\dots\text{M})$ by ca. 1 Å upon oxidation [42–46]. Detailed investigations and simulations of the electrochemical process for $[\text{W}_2(\mu\text{-SBz})_2(\text{CO})_8]^{2-}$ led to the conclusion that the oxidation consisted of two successive reversible one-electron steps, with $\Delta E^{\circ'} \approx 0$ V [41].

The fact that the electrochemical oxidation of *cis*- $[\text{M}_2(\text{cp})_2(\mu\text{-SR})_2(\text{CO})_4]$ and of $[\text{M}_2(\mu\text{-SR})_2(\text{CO})_8]^{2-}$ is reversible despite the amount of structural reorganization involved suggests that these changes require low activation energy. Extended Hückel Molecular Orbital (EHMO) calculations on the model complex *cis*-**13**²⁺ ($\text{R} = \text{H}$) indicated that the Lowest Unoccupied Molecular Orbital (LUMO) was the $\sigma^*_{\text{Mo-Mo}}$ level [47]. Weakening of the Mo–Mo bond by adding one electron into this orbital might cause an increase in the metal–metal separation. This would result in the stabilization of the semi-occupied orbital, as shown by the Walsh diagram associated with the variations of the Mo_2S_2

core dimensions, which in turn would trigger the transfer of the second electron at the same potential as the first one [48]. Therefore, “the nuclear displacements that occur along the two-electron reaction coordinate serve to favor the thermodynamics of the second charge transfer” (quotation from Ref. 41).

However, the occurrence of major structural changes, including the formation of an M–M bond, upon reduction or oxidation of a complex with an M_2E_2 core does not necessarily result in an overall two-electron transfer. Indeed, although the first oxidation of the iron complex $[\text{Fe}_2(\text{cp})_2(\mu\text{-SMe})_2(\text{CO})_2]$ causes a shortening of the $\text{Fe}\dots\text{Fe}$ distance by ca. 0.5 Å, the formation of the dication occurs in two well-separated reversible one-electron steps [48, 49]. EHMO calculations indicated that the LUMO of the dication possesses metal–metal antibonding character and the Walsh diagram associated with the Fe_2S_2 core deformations showed similar stabilization of this orbital as in the case of *cis*-**13**²⁺, so that an overall two-electron transfer might have been expected [48]. Investigations of the electrochemical oxidation of $[\text{Fe}_2(\text{cp})_2(\mu\text{-SMe})_2(\text{CO})_2]$, $[\text{Fe}_2(\text{cp})_2(\mu\text{-PPh}_2)_2(\text{CO})_2]$, and $[\text{Mo}_2(\text{cp})_2(\mu\text{-SMe})_4]$ demonstrated [49] that the standard heterogeneous electron transfer rate constant, k_s , was about the same for the iron compounds (both of which undergo important structure change upon oxidation) as for the molybdenum complex whose structure is little affected by oxidation [50]. The reasons why the heterogeneous electron transfers are fast for complexes **13–16** and for the above iron compounds despite the structural changes involved, which is in apparent contradiction with the Marcus–Husch theory [51, 52], are still unclear [41, 48, 49]. Also, the reasons why



Scheme 12

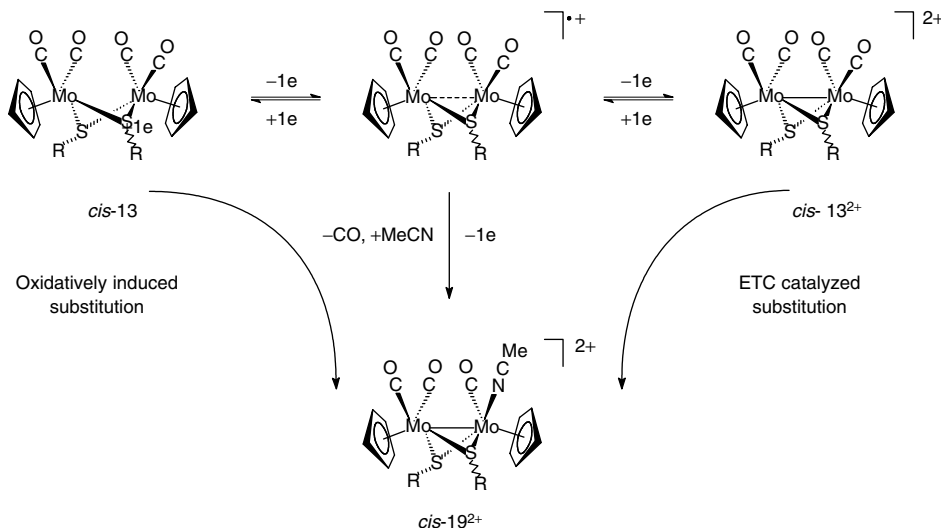
$[\text{Fe}_2(\text{cp})_2(\mu\text{-SMe})_2(\text{CO})_2]$ and $[\text{Fe}_2(\text{cp})_2(\mu\text{-PPh}_2)_2(\text{CO})_2]$ undergo two discrete one-electron oxidation steps while complexes **13**, **14**, **15**²⁻, and **16**²⁻ oxidize in an overall two-electron process are not well understood [41, 48, 49].

Although the redox reactions in Sch. 12 have not been achieved electrochemically, they illustrate another type of redox-induced structural change in a dimolybdenum compound with a sulfur-rich coordination sphere. In this case, $\text{Mo}_2(\mu\text{-S})_2$ ring opening in **18** (cleavage of Mo–Mo and Mo–S bonds) is associated with the exposure of vacant coordination sites, and the uptake of two carbonyl ligands in **17** [7, 53].

20.3.2 Electron Transfer-induced and Electron Transfer-catalyzed Ligand Substitution

Controlled potential oxidation of **13** (*cis* and *trans* isomers) in a MeCN electrolyte at room temperature produced variable amounts of the acetonitrile substituted derivative *cis*- $[\text{Mo}_2(\text{cp}')_2(\mu\text{-SR})_2(\text{CO})_3(\text{MeCN})]^{2+}$ **cis-19**²⁺ ($\text{R} = \text{Me}$, Ph; $\text{cp}' = \text{cp}$ or cp^*) along with *cis-13*²⁺ [34, 54]. However, *cis-19*²⁺ was the major product when the electrolysis was performed at 40–45 °C. Interestingly, the electrochemical reduction of *cis-13*²⁺ under similar

conditions also produced *cis-19*²⁺, with a low charge consumption, according to an Electron Transfer Chain (ETC) catalyzed reaction. The catalytic role of electrons was evidenced by initiating the substitution reaction by passage of a small amount of charge (typically 0.05–0.1 F mol⁻¹ *cis-13*²⁺), and by monitoring the formation of *cis-19*²⁺ by CV after the electrolysis was stopped. Since neither **13** nor *cis-13*²⁺ reacted with MeCN on the electrolysis timescale, the formation of *cis-19*²⁺ from both the electrochemical oxidation of **13** and the electrochemical reduction of *cis-13*²⁺ involved a cation intermediate (Sch. 13) [34, 54]. The formation of the substituted complex with a *cis* geometry (as evidenced by the X-ray crystal structure of *cis-19*²⁺, $\text{R} = \text{Ph}$; $\text{cp}' = \text{cp}$) from both the *cis* and *trans* isomers of **13** ($\text{R} = \text{Me}$) suggested that the substitutionally labile intermediate cation might have a singly SR-bridged structure [54]. In the case where $\text{cp}' = \text{cp}$, controlled potential electrolyses (oxidation of **13** and reduction of *cis-13*²⁺) performed in the presence of ^tBuNC afforded the isocyanide singly substituted analog of *cis-19*²⁺ [54]. Doubly substituted ^tBuNC complexes could be obtained by electrochemical reduction of the singly substituted precursor in the presence of an excess ligand, according to an ETC process [54].



Scheme 13

Complexes 15^{2-} and 16^{2-} were also shown to undergo oxidatively induced substitution of MeCN for CO. In this case, however, doubly substituted derivatives were obtained via the singly substituted species, which could not be isolated, but was detected by CV [40].

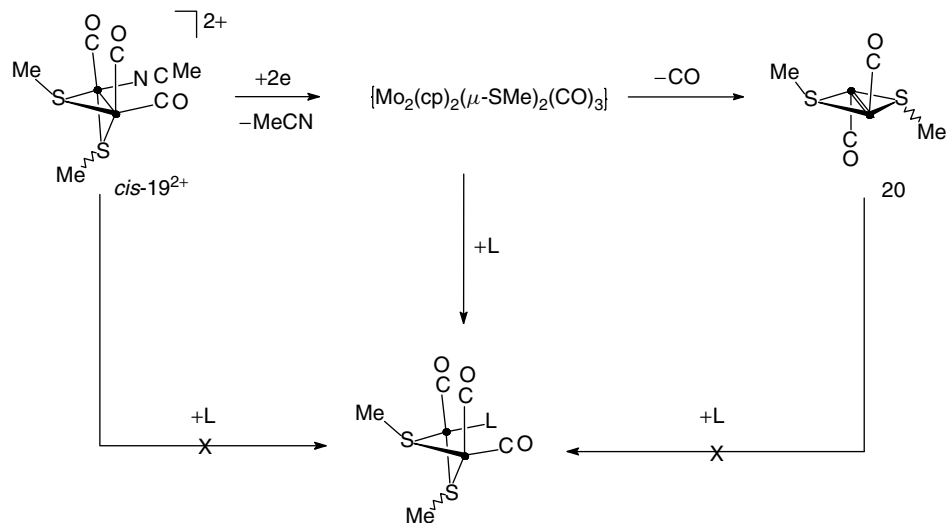
20.3.3 Electrochemically Induced Metal–Ligand Bonds Cleavage

Electrochemical cleavage of metal–ligand bond(s) is a convenient way of generating vacant coordination sites at a metal center (see Sch. 5). The eliminated ligand can be neutral (L) or anionic (X).

Cleavage of a Mo–L bond. The electrochemical reduction of the acetonitrile complex $cis\text{-}19^{2+}$ is an overall two-electron process leading to the cleavage of the Mo–NCMe bond. The CV of $cis\text{-}[Mo_2(cp')_2(\mu\text{-SR})_2(CO)_3(MeCN)]^{2+}$ appeared to be strongly dependent upon the nature of the sulfur substituents and of the

cp' ring [34, 55]. When R = Me and cp' = cp, the CV under N₂ or Ar showed an irreversible two-electron reduction, and the redox systems of the electrogenerated $trans\text{-}[Mo_2(cp)_2(\mu\text{-SMe})_2(CO)_2]$, 20, (Sch. 14), which was produced by controlled potential electrolysis. However, the phenyl analog was also obtained by controlled potential reduction of $cis\text{-}19^{2+}$ (R = Ph), along with $trans\text{-}[Mo_2(cp)_2(\mu\text{-SPh})_2(CO)_4]$. This is consistent with the fact that the kinetic product of the electrochemical two-electron reduction of $cis\text{-}19^{2+}$ (R = Ph), detected by CV, was not $trans\text{-}[Mo_2(cp)_2(\mu\text{-SPh})_2(CO)_2]$. The kinetic product was assigned as a tricarbonyl intermediate [55]. Although the methyl analog was not detected by CV ($v \leq 1 \text{ V s}^{-1}$), its transient formation was evidenced by trapping experiments. Indeed, the CV of $cis\text{-}19^{2+}$ (R = Me) in the presence of a substrate L (L = CO or ^tBuNC) showed the formation of $cis\text{-}[Mo_2(cp)_2(\mu\text{-SMe})_2(CO)_3(L)]$ (Sch. 14).

The electrochemistry of $cis\text{-}[Mo_2(cp')_2(\mu\text{-SMe})_2(CO)_3(MeCN)]^{2+}$ was also affected

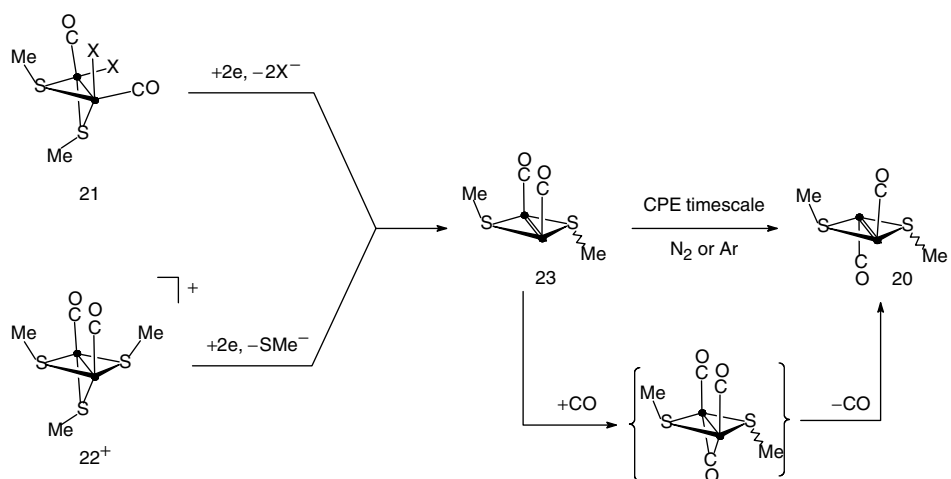


Scheme 14 • = Mo-*cp'*; the product in braces was not detected.

by the nature of the *cp'* rings. In addition to the effect on the redox potentials, the substitution of *cp** for *cp* resulted in the stabilization of the Mo-NCMe bond. Instead of the irreversible two-electron reduction of the *cp* analog, that of the *cp** complex **cis-19*²⁺** occurred in two successive one-electron steps, both reversible at low temperature (inert atmosphere, MeCN, thf or CH₂Cl₂ electrolyte) [34]. The reduction of **cis-19*²⁺** under CO in thf at 40 °C (or in CH₂Cl₂) was an irreversible two-electron (ECE) process affording **cis-13***. In contrast, two one-electron steps were still observed under CO in a MeCN electrolyte. Although the first reduction remained reversible at moderate scan rate ($v = 0.2 \text{ V s}^{-1}$) under these conditions, the occurrence of an ECE-type mechanism, where the chemical step consisted in the reversible decoordination of MeCN from the radical cation, could be evidenced [34]. The product formed at the first reduction was **cis-13***, whereas **trans-13*** was obtained after the second (irreversible) reduction had been traversed.

This suggested that two tricarbonyl species with *cis* and *trans* arrangements of the *cp** ligands were formed transiently. These experiments illustrate the effects of “spectator” ligands on the mechanism and products of electrochemical processes. Therefore, the differences in the electrochemical behavior of **cis-[Mo₂(cp')₂(μ-SMe)₂(CO)₃(MeCN)]²⁺** for *cp'* = *cp* or *cp** were assigned to a stronger Mo-NCMe bond for *cp'* = *cp**, and to the longer lifetimes of **cis-19*ⁿ⁺** ($n = 0, 1$) and of the *cp** tricarbonyl intermediates as compared to their *cp* analogs [34].

Cleavage of Mo-X bonds. An example of the reductive cleavage of Mo-S(R) bonds is shown in Schs. 4 and 12. Similarly, the electrochemical two-electron reduction of **[Mo₂(cp)₂(μ-SMe)₂(CO)₂(X)₂]** **21**, (X = Cl, Br) and of **[Mo₂(cp')₂(μ-SMe)₃(CO)₂]⁺**, **22⁺** (*cp'* = *cp* or *cp**) afforded a reactive site, assigned as the transient *cis*-**[Mo₂(cp)₂(μ-SMe)₂(CO)₂]** **23**, by cleavage of two M-X bonds [56]. Complex **23** rearranged to the stable *trans* isomer **20** on the electrolysis timescale (Sch. 15).



Scheme 15 • = Mo–cp; the nature of the product in braces was not demonstrated.

The *cis* dicarbonyl intermediate **23** could not be isolated, although it was longer lived when $\text{cp}' = \text{cp}^*$ [57] than when $\text{cp}' = \text{cp}$. The *cis* \rightarrow *trans* isomerization of the dicarbonyl complex is catalyzed by CO, presumably via an unstable CO-bridged intermediate, which would decay to the *trans* isomer and carbon monoxide (Sch. 15) [56].

EHMO calculations performed on the reactants, products, and possible intermediates of the reactions shown in Sch. 15 supported the proposed mechanism [58]. Thus, steric and electronic factors combine to make **23** a good substrate-binding site: it has an uncongested Mo_2S_2 face and a low-lying LUMO available to hold an incoming nucleophile. The proposed mechanism remains valid if the CO substrate is replaced by other two-electron donor ligands such as isocyanide [56] or cyanide [59].

$[\text{Mo}_2(\text{cp})_2(\mu\text{-SMe})_3(\text{CO})_2]^+$ derives from **13²⁺** by substitution of two carbonyl ligands by a methylthiolate anion. Similarly, $[\text{Mo}_2(\mu\text{-SPh})_3(\text{CO})_6]^-$ is derived from **15** by replacement of two COs by a SPh bridge.

It should be noted that the reduction of $[\text{Mo}_2(\mu\text{-SPh})_3(\text{CO})_6]^-$, as that of **15**, occurred in a single, reversible two-electron step [46]. In contrast, the reduction of $[\text{Mo}_2(\text{cp})_2(\mu\text{-SMe})_3(\text{CO})_2]^+$ was an essentially irreversible (ECE) process leading to the cleavage of two Mo–S bonds (Sch. 15). The difference might be partly due to the fact that, in $[\text{Mo}_2(\mu\text{-SPh})_3(\text{CO})_6]^-$, the excess charge resulting from the reduction can be dissipated by the six CO ligands.

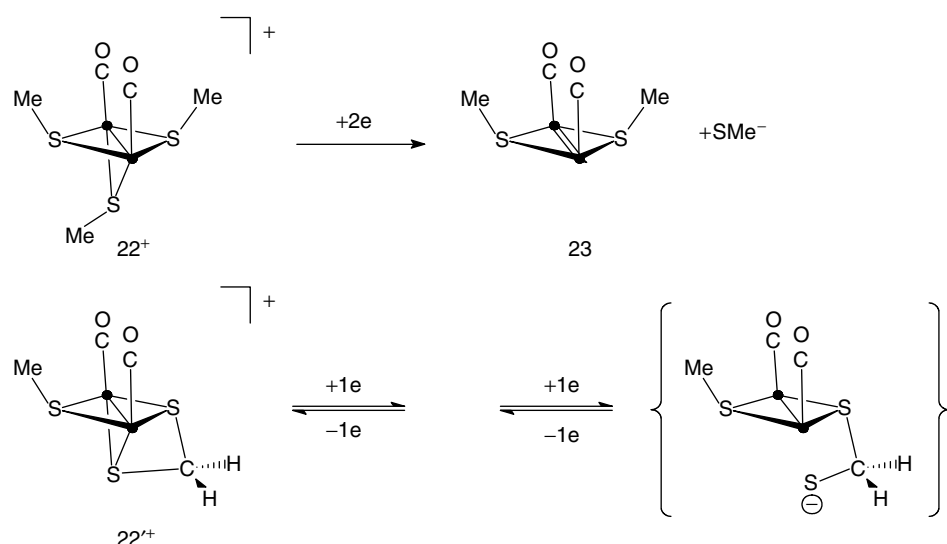
An analog of **22⁺**, $[\text{Mo}_2(\text{cp})_2(\mu\text{-S}_2\text{CH}_2)(\mu\text{-SMe})(\text{CO})_2]^+$ **22⁺** has been synthesized by Rakowski DuBois [60]. **22⁺** undergoes a reversible, “single step” two-electron reduction ($E_{1/2}^{\text{red}} = -1.41 \text{ V/Fc}$; $\Delta E_p = 35 \text{ mV}$ for $v = 0.04 \text{ V s}^{-1}$) in MeCN, whereas two overlapping reversible one-electron reductions were observed in THF ($E_{1/2}^{\text{red}1} = -1.43 \text{ V/Fc}$, $\Delta E_p^{\text{red}1} \approx 80 \text{ mV}$; $E_{1/2}^{\text{red}2} = -1.52 \text{ V/Fc}$, $\Delta E_p^{\text{red}2} \approx 100 \text{ mV}$ for $v = 0.2 \text{ V s}^{-1}$) [61]. Although the redox system(s) of **22⁺** (in MeCN and in THF) were not fully reversible ($i_p^a/i_p^c < 1$), the reduction of **22⁺** appears much more reversible than that of **22⁺** on the basis of the

measured anodic-to-cathodic peak current ratios. Therefore, the substitution of two methylthiolate bridges by one 1,1-dithiolate bridge, which has a limited influence on the redox potentials of these complexes ($22^+ : E_{1/2}^{red} = -1.47$ V/Fc in MeCN [56]), has a pronounced effect on the reversibility of the electrode process. The nature of the chemical reaction coupled to the reduction of 22^+ was not determined. However, the fact that the reduction of 22^+ is more reversible than that of 22^+ could be due to the (initial) bidentate coordination of the S_2CH_2 fragment in 22^+ . If the reduction of 22^+ (like that of 22^+) resulted in the cleavage of the two Mo–S bonds trans to the carbonyl ligands, the de-coordinated S atom would remain in the metal's coordination sphere, making the reverse reactions possible (Sch. 16). Such an example has been reported in the case of mononuclear complexes (see Sch. 4).

Although *trans*-[Mo₂(cp)₂(μ-SMe)₂(CO)₂] **20** shows an interesting reactivity with substrates such as isocyanides

and cyanide [59], it can be seen as arising from the deactivation of electrogenerated sites, namely {[Mo₂(cp)₂(μ-SMe)₂(CO)₃] (Sch. 14) and *cis*-[Mo₂(cp)₂(μ-SMe)₂(CO)₂] **23** (Sch. 15). It is clear that such a reaction could prevent the formation of the desired (site-substrate) complex, and the subsequent metal-assisted reduction of the substrate, if the substrate-binding step is slow or reversible, as it could be when dinitrogen is involved.

The problem raised by the deactivation of vacant site could be solved by the design of a protective device such as a *redox-switchable hemilabile ligand*, RHL [62]. Ideally, the protective device should (1) be activated by an electronic (redox) or chemical (pH) instruction, (2) open the binding site only in the presence of the substrate, (3) function reversibly so that the site is protected back when the bound substrate is lost (due to reversibility of the binding step or due to decoordination during subsequent steps). An example of an electrochemically



Scheme 16 • = Mo–cp; the nature of the product in braces was not demonstrated.

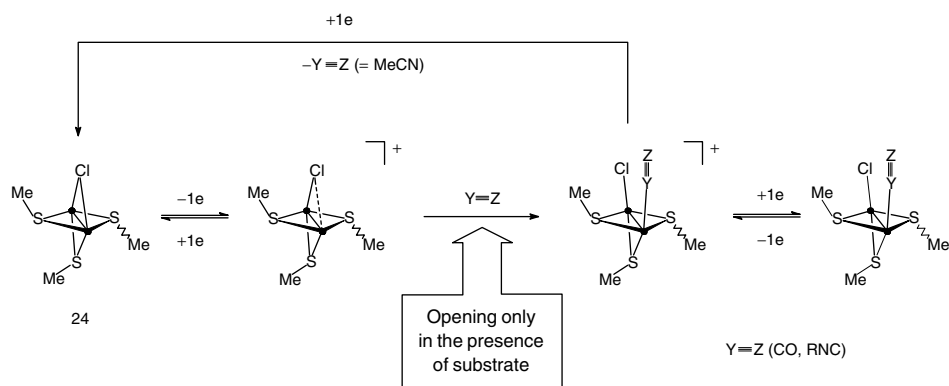
activated protecting group is provided in the following.

20.3.4 Electrochemical Deprotection of a Substrate-binding Site

The chloride-bridged complex $[\text{Mo}_2(\text{cp})_2(\mu\text{-SMe})_3(\mu\text{-Cl})]$ 24 [63] is unreactive toward $\text{Y}\equiv\text{Z}$ molecules such as CO, MeCN, or RNC; in contrast, 24^+ was shown to react with these substrates [64]. 24 undergoes two successive quasi-reversible one-electron oxidations in a THF- (or dichloromethane) $[\text{NBu}_4]\text{PF}_6$ electrolyte. Controlled potential electrolysis at the potential of the first step in THF or CH_2Cl_2 afforded the paramagnetic cation after the passage of ca. 1 F mol⁻¹ 24. That the oxidized complex retained the quadruply bridged structure of its neutral precursor was indicated by the EPR spectrum of 24^+ (-50°C , CH_2Cl_2), showing hyperfine coupling consistent with delocalization of the unpaired electron over two equivalent molybdenum nuclei (Class III complex [65]). In contrast, the first oxidation occurred according to an EC process in MeCN. In this solvent, the one-electron oxidation of 24 led

to the opening of the chloride bridge and to the binding of MeCN at the exposed metal site [64]. The EPR spectrum of $[\text{Mo}_2(\text{cp})_2(\mu\text{-SMe})_3(\text{Cl})(\text{NCMe})]^+$ was consistent with the localization of the unpaired electron on one Mo center (Class I complex [65]). Similar spectra were obtained for analogous substituted complexes where the bound substrate was CO or an isocyanide molecule [64]. These reactions are illustrated in Sch. 17.

Since 24 does not react with $\text{Y}\equiv\text{Z}$ (CO, MeCN, RNC), the one-electron oxidation can be seen as “unlocking” the access to a coordination site. However, in the absence of $\text{Y}\equiv\text{Z}$, the chloride ligand remains in a bridging position, thus preventing the premature opening of the site. Furthermore, when the bound substrate is lost, which is the case for the MeCN ligand upon one-electron reduction of $[\text{Mo}_2(\text{cp})_2(\mu\text{-SMe})_3(\text{Cl})(\text{NCMe})]^+$, the chloride ligand moves back in the bridging position, thus preventing decomposition of the complex (Sch. 17). Therefore, the $\mu\text{-Cl}$ atom in 24 appears as an effective protective device, which possesses the desired properties (1)–(4) mentioned earlier.



Scheme 17 • = Mo—cp.

Modifications at the Mo_2S_3 core affect the electron transfer-induced reactivity of the chloride bridge. A complex closely related to **24**, namely $[\text{Mo}_2(\text{cp})_2(\mu\text{-S}_2\text{CH}_2)(\mu\text{-SMe})(\mu\text{-Cl})]$ **24'**, has been reported [60]. Comparison of the redox potentials of both species indicates that the $\{\text{Mo}_2(\mu\text{-SMe})_3\}$ core is slightly more electron-rich than $\{\text{Mo}_2(\mu\text{-S}_2\text{CH}_2)(\mu\text{-SMe})\}$ and that substitution of two SMe bridges by a bridging 1,1-dithiolate has a more pronounced effect for **24/24'** (**24**: $E_{1/2}^{\text{ox}1} = -0.40 \text{ V/Fc}$; $E_{1/2}^{\text{ox}2} = 0.34 \text{ V/Fc}$, $\text{thf}-[\text{NBu}_4][\text{PF}_6]$ [64]; **24'**: $E_{1/2}^{\text{ox}1} = -0.29 \text{ V/Fc}$; $E_{1/2}^{\text{ox}2} = 0.37 \text{ V/Fc}$, $\text{MeCN}-[\text{NBu}_4][\text{BF}_4]$ [60]) than for $(\mathbf{22}^+)/(\mathbf{22}^+)$ (as seen earlier). In addition to producing this electronic effect, the substitution affects the reactivity of the complexes. Indeed, the first oxidation of **24'** is reversible on the CV timescale in MeCN [60]. Therefore, **24'** is missing the oxidatively induced reactivity of **24** (cf. Sch. 17). Examination of the electrochemical behavior of an other analog of **24**, $[\text{Mo}_2(\text{cp})_2(\mu\text{-SMe})_2(\mu\text{-PPh}_2)(\mu\text{-Cl})]$ **24''**, confirms the influence of the Mo_2E_3 core on the reactivity at the chloride bridge. Although the first oxidation of **24''** looks quasi-reversible in $\text{MeCN}-[\text{NBu}_4][\text{BF}_4]$, the reactivity of **24''** can be described by a mechanism similar to that in Sch. 17, with the substrate-binding step being a dynamic equilibrium, however [66].

20.3.5

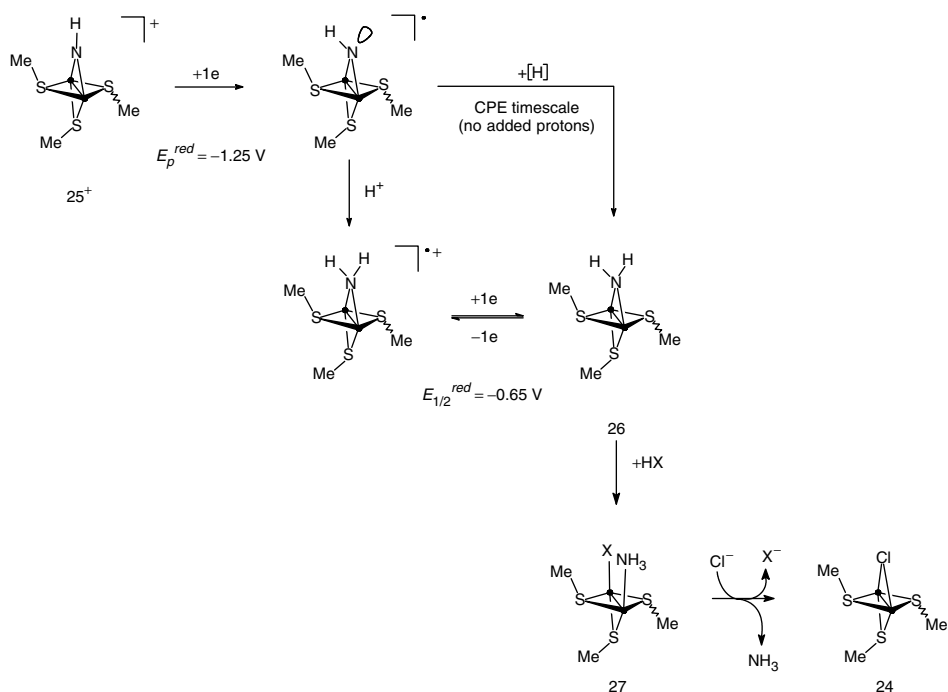
Electrochemical Transformations of Bound Substrate

A large part of the research involving metal–sulfur complexes (metal = molybdenum or iron) is aimed at designing functional models of the active site of nitrogenase, the iron–molybdenum cofactor, FeMo–co [4–8, 12, 13]. Only a very

limited number of dinitrogen complexes containing sulfur in the metal coordination sphere have been obtained [21]. However, a not so limited number of mono- or binuclear metal–sulfur sites react with nitrogenous molecules or ions to afford complexes containing {N} or {N–N} fragments bound to the metal center(s). Studies of the latter may give new insights in the mechanism of the enzyme-driven reactions.

In the family of compounds with the $\{\text{Mo}_2(\text{cp})_2(\mu\text{-SMe})_3\}$ core, complexes with ammine (NH_3) [67, 68], amido (NH_2^-) [67–69], imido (NH^{2-}) [68, 70], substituted diazene ($\text{R}-\text{N}=\text{N}-\text{H}$) or isodiazene/hydrazido(2–) [$\text{R}(\text{H})\text{N}=\text{N}/\text{R}(\text{H})\text{N}-\text{N}^{2-}$], and diazenido ($\text{R}-\text{N}=\text{N}^-$) [68, 71, 72] ligands have been isolated and characterized. Among them, the amido/imido complexes are related by a reduction step. Also, cleavage of the N=N bond of diazene or isodiazene/hydrazido(2–) ligands, to produce imido or amido derivatives, requires several $\{\text{H}^+/\text{e}\}$ transfer steps.

The imido complex $[\text{Mo}_2(\text{cp})_2(\mu\text{-SMe})_3(\mu\text{-NH})]^+$ **25⁺** undergoes an irreversible one-electron (EC) reduction [70]. Controlled potential electrolysis afforded the amido analog $[\text{Mo}_2(\text{cp})_2(\mu\text{-SMe})_3(\mu\text{-NH}_2)]$ **26** almost quantitatively after the transfer of 1F mol^{-1} **25⁺**. The amido complex was not the primary reduction product; the latter was assigned as a rearranged imide radical (Sch. 18), which is able to abstract a H-atom from the environment (supporting electrolyte, solvent, or adventitious water) on the electrolysis timescale. In the presence of protons, the reduction of **25⁺** became a two-electron (ECE) process. This is consistent with the protonation at the nitrogen lone pair of the primary reduction product, followed by reduction of the resulting amido cation



Scheme 18 • = Mo–cp; X = TsO.

(Sch. 18). It must be noted that 25^+ can be protonated by $\text{HBF}_4/\text{Et}_2\text{O}$ (or by HTsO) in MeCN . The protonation step producing $[\text{Mo}_2(\text{cp})_2(\mu\text{-SMe})_3(\mu\text{-NH}_2)]^{2+}$ 26^{2+} allowed the formation of the μ -amido to take place (CE process) at a potential about 600 mV less negative than the reduction of the imide cation 25^+ [70].

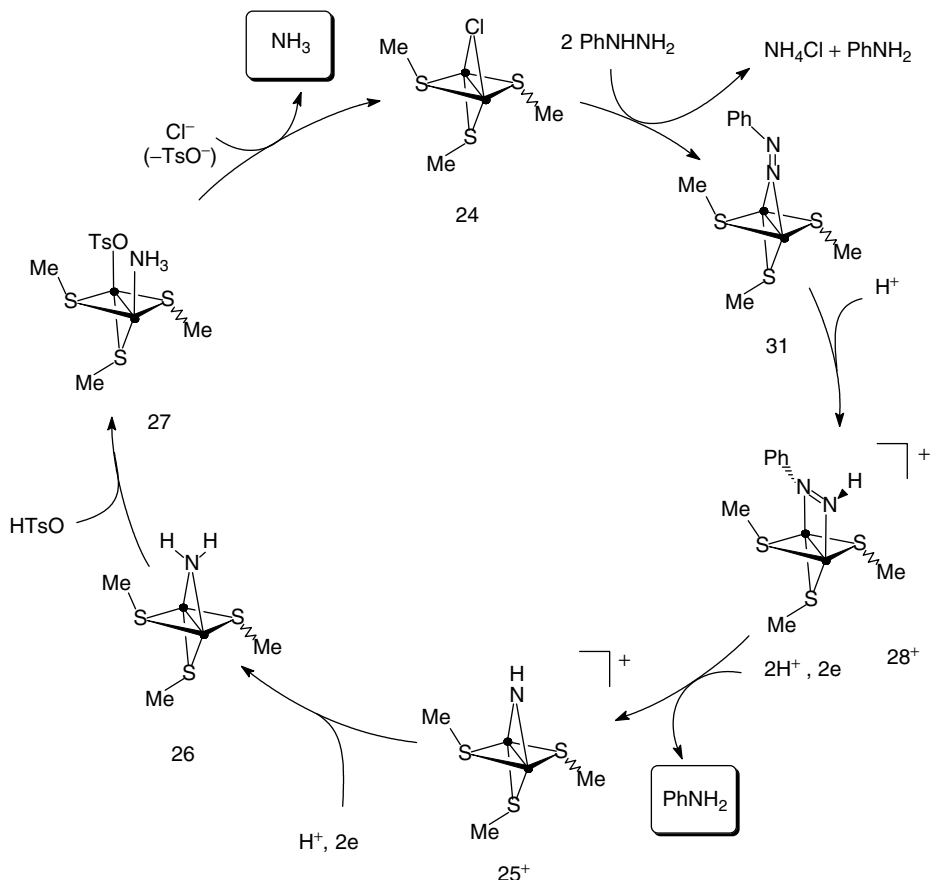
Controlled potential reduction of 25^+ in the presence of 3 equiv acid and 2–2.5 equiv $[\text{NEt}_4]\text{Cl}$ in a THF electrolyte produced $[\text{Mo}_2(\text{cp})_2(\mu\text{-SMe})_3(\mu\text{-Cl})]^{2+}$ 24 (>95%) and $[\text{NH}_4]\text{Cl}$ (ca. 70% mol $[\text{NH}_4]^+$ per mol of 25^+), after the transfer of 2 F mol $^{-1}$ 25^+ . This demonstrated that an imide group bridging two molybdenum atoms in a sulfur environment can be reduced to ammonia via amide (26) and ammine (27) intermediates [70].

The electrochemical reductions of complexes with an organodiazene ligand $[\text{Mo}_2(\text{cp})_2(\mu\text{-SMe})_3(\mu\text{-}\eta^1\text{-H}-\text{N}=\text{N}-\text{R})]^+$ 28^+ ($\text{R} = \text{Me, Ph}$) and with a methylhydrazido(2-) (or isodiazene) ligand $[\text{Mo}_2(\text{cp})_2(\mu\text{-SMe})_3(\mu\text{-}\eta^1\text{-NN(H)-Me})]^+$ 29^+ have been investigated [73]. Compounds 28^+ and 29^+ were obtained by protonation of the diazenido precursors $[\text{Mo}_2(\text{cp})_2(\mu\text{-SMe})_3(\mu\text{-}\mu\text{-}\eta^1\text{-N}=\text{N}-\text{R})]$ 30 , or $[\text{Mo}_2(\text{cp})_2(\mu\text{-SMe})_3(\mu\text{-}\eta^1\text{-NNR})]$ 31 ($\text{R} = \text{Me or Ph}$). Complex 28^+ ($\text{R} = \text{Ph}$) undergoes a reversible one-electron reduction, which is followed by a chemical step (EC process). In the presence of acid, the reduction became irreversible with a substantial increase of the corresponding peak current (almost doubled at $v = 1\text{ V s}^{-1}$), indicative of the occurrence of a rapid ECE mechanism. At lower scan rates ($v \leq 0.4\text{ V s}^{-1}$),

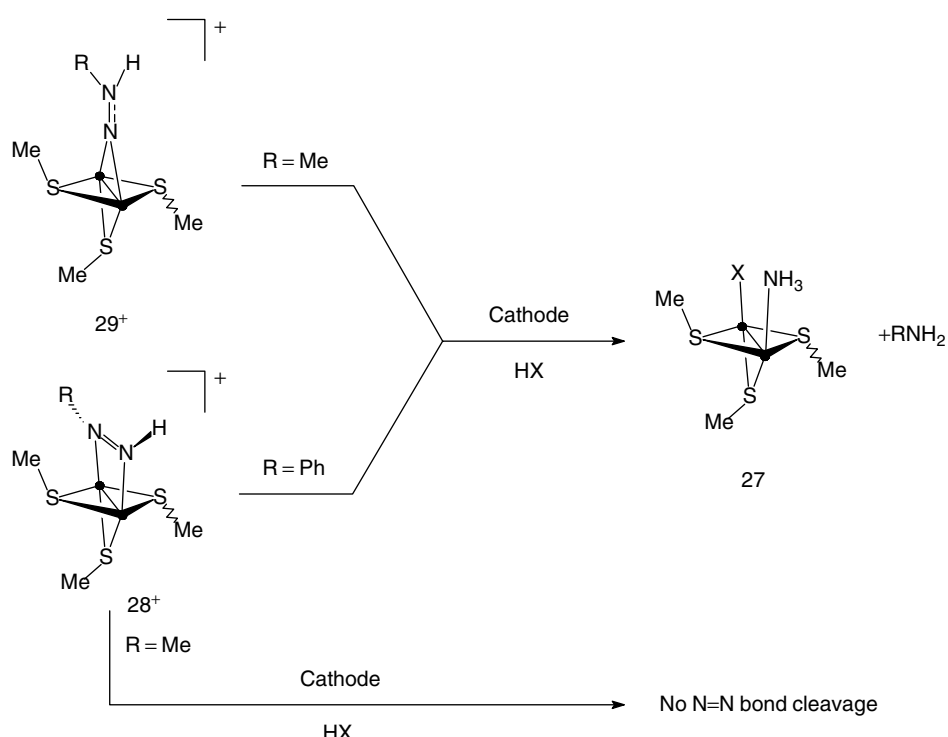
the plot of the current function ($i_p^{red}/v^{1/2}$) versus scan rate deviates markedly from linearity thus showing that more electrons were transferred on a longer timescale. In agreement with this, controlled potential reduction of $\mathbf{28}^+$ ($R = Ph$) in the presence of an excess acid HX (4–6 equiv $HX = HTsO$ or CF_3CO_2H ; $thf-[NBu_4][PF_6]$ electrolyte) was completed after 4 to 6 F mol $^{-1}$ $\mathbf{28}^+$ (depending on the amount of acid) have been consumed. The electrolysis afforded either $[Mo_2(cp)_2(\mu-SMe)_3(\mu-NH_2)]$ $\mathbf{26}$ or $[Mo_2(cp)_2(\mu-SMe)_3(NH_3)(X)]$ $\mathbf{27}$ (depending on the amount of acid) and aniline. The dependence of the charge

passed on the amount of added acid suggested that H_2 might also be produced [73]. The formation of $\mathbf{26}$ (or $\mathbf{27}$) and of $PhNH_2$ demonstrated that the N=N bond of the $Ph-N=N-H$ ligand had been reductively cleaved. This allowed the construction of the cycle shown in Sch. 19 [68].

In contrast, no N=N bond rupture was observed in the case of the methyldiazene ligand (Sch. 20). However, electrochemical reduction of the hydrazido(2-) /isodiazene isomer $[Mo_2(cp)_2(\mu-SMe)_3(\mu-\eta^1-NN(H)Me)]^+$ $\mathbf{29}^+$ in the presence of acid also afforded $\mathbf{26}$ and methylamine, showing that the N=N bond had been cleaved



Scheme 19 • = Mo—cp.



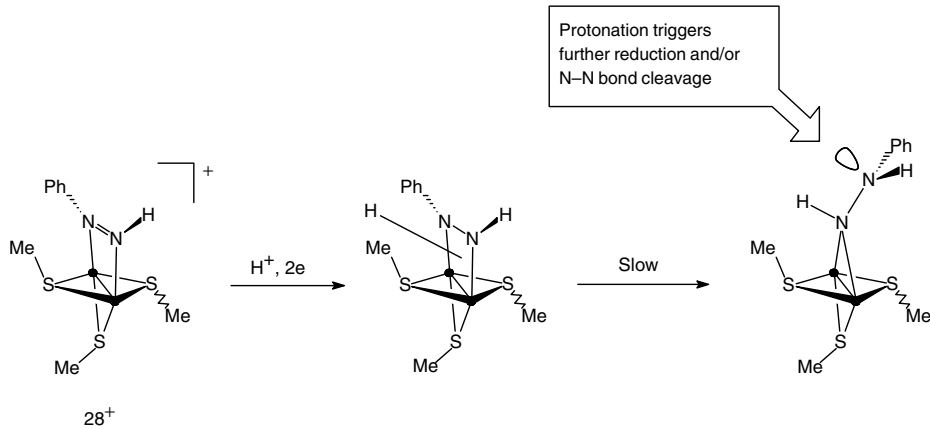
Scheme 20 • = Mo–cp; X = TsO or CF₃CO₂.

(Sch. 20) [73]. In this case also, it is likely that dihydrogen was a coproduct of the electrolysis.

The behavior of **28⁺** in terms of reductive cleavage of the N=N bond was thus different depending on whether R = Me or Ph. This was assigned to the electronic effect of the R substituent on the strength of the Mo–N(R) bond: whereas electron withdrawing R (R = Ph) would allow the release of the N(R) end of the ligand from the metal and a $\mu\text{-}\eta^1:\eta^1 \rightarrow \mu\text{-}\eta^1$ rearrangement, probably at the hydrazido(1-) stage of the reduction process (Sch. 21), the electron-releasing Me substituent would not [73]. When R = Ph, protonation at the lone pair of the distant N atom would either cause the N=N bond cleavage in the resulting

cation, or allow further reduction of the latter and eventually N–N bond cleavage (Sch. 21). The fact that the metal product arising from the N–N bond rupture, respectively a bent imide cation or radical, was shown to reduce to **26** (or **27**) in the presence of acid, at a potential about 1 V less negative than the reduction of **28⁺** (R = Ph), is consistent with the proposed mechanism [70, 73].

From the effect of the R substituent on the mechanism and products of the reduction of **28⁺** (R = Me or Ph), it was concluded that reductive cleavage of the N=N bond of a $\mu\text{-}\eta^1:\eta^1$ coordinated organodiazene might occur only in particular cases. Therefore, this type of coordination might be a dead-end as far as the N=N bond cleavage is



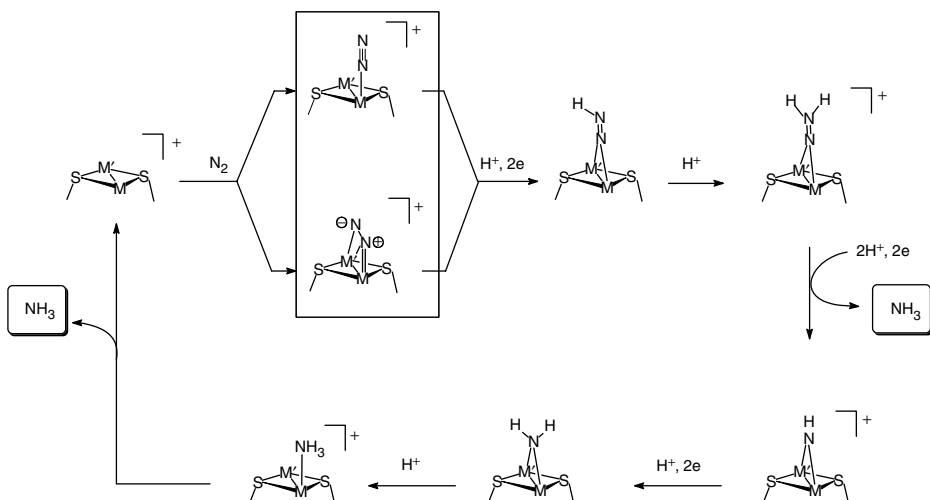
Scheme 21 • = Mo-cp.

concerned, at least at the $\{\text{Mo}_2(\text{cp})_2(\mu-\text{SMe})_3\}$ core [73].

In the earlier examples, the binuclear complexes with a $\{\text{Mo}_2\text{S}_3\}$ core clearly cannot be seen as modeling the metal sites in FeMo-co since it is known to contain a single molybdenum center [74]. However, what is suggested by these studies is that several steps (if not all) of the reduction of dinitrogen to ammonia by Mo-nitrogenase could take place at a

bimetallic-sulfur site. The different steps in Sch. 22 (M and M' could be similar or different) were proposed on the bases of the chemistry and electrochemistry involving the $\{\text{Mo}_2(\text{cp})_2(\mu-\text{SMe})_3\}$ core, except for the key N_2 -binding step (boxed in Sch. 22), which has not been observed yet [73].

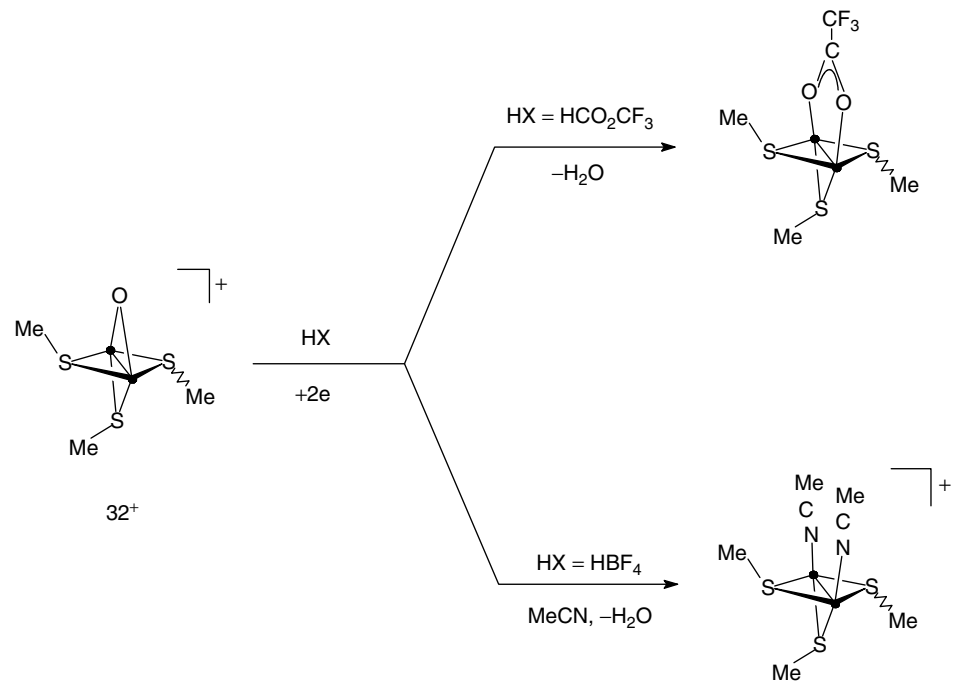
The electrochemical study of the μ -oxo complex $[\text{Mo}_2(\text{cp})_2(\mu-\text{SMe})_3(\mu-\text{O})]^{+} 32^{+}$ [75], which is isoelectronic with the

Scheme 22 Proposed cycle for the reduction of N_2 at a bimetallic-sulfur site.

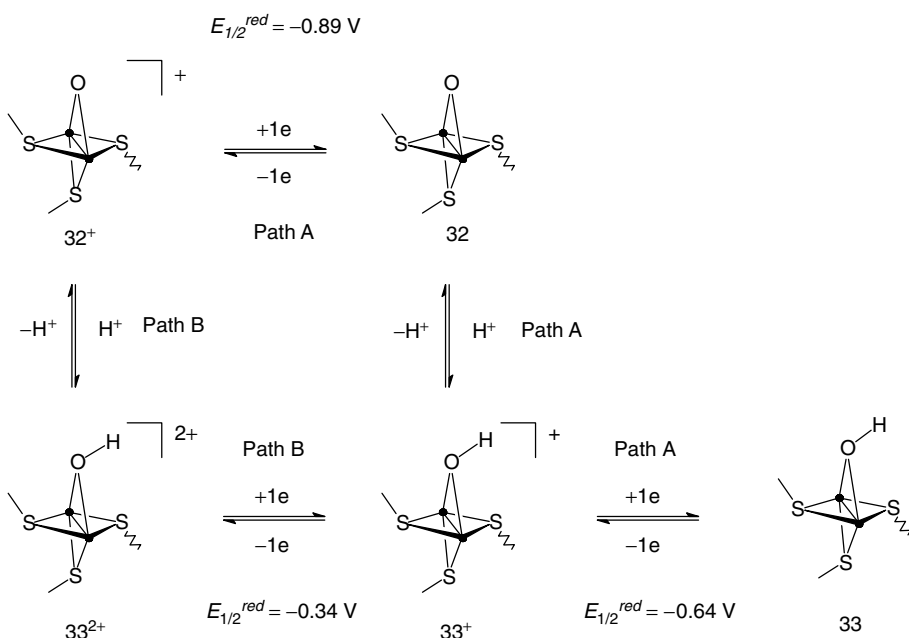
imido derivative **25⁺**, is another example of electrochemically induced transformation of a ligand (the oxo bridge) and of the electrochemical generation of substrate-binding sites. In this study, it was shown that the controlled potential reduction of **32⁺** in the presence of acid resulted in the protonation of the oxo bridge, which was eventually released as a water molecule, after transfer of ca. 2F mol⁻¹ **32⁺**, when a coordinating anion or solvent was present (Sch. 23).

The detailed investigation of the reduction mechanism by CV in thf-[NBu₄][PF₆] showed that the first steps of the reduction of **32⁺** in the presence of acid occurred according to an EC_{rev}E mechanism in which the intervening chemical reaction is a protonation equilibrium (Sch. 24, Path A). Therefore, in the presence of 1 equiv acid, the diffusion-controlled, one-electron

reduction of **32⁺** ($E_{1/2}^{red} = -0.89$ V/Fc) is replaced by a pseudo reversible two-electron system observed at $E_{1/2}^{red} \sim -0.7$ V/Fc ($\Delta E_p \sim 120$ mV) that is at a potential intermediate between those of **32⁺** and of the hydroxo-bridged complex **33⁺** ($E_{1/2}^{red} = -0.64$ V/Fc). As its imido analog **25⁺** (as seen earlier), **32⁺** could also be protonated by HBF₄/H₂O in thf-[NBu₄][PF₆]. Therefore, reduction of **32⁺** can take place according to a CE process (Sch. 24, Path B), at a potential by ca. 0.4 V less negative than in the absence of this protonation step ($E_{1/2}^{red} \sim -0.7$ V/Fc), via the hydroxo dication **33²⁺**. This kind of mechanism where protonation of a ligand substantially facilitates the reduction of a metal center might be relevant to biological processes involving redox enzymes, due to the restricted potential range accessible to natural reductants.



Scheme 23 • = Mo—cp.



Scheme 24 • = Mo—cp.

The square scheme in Sch. 24 allowed estimating the effect of the reduction of the complexes on the basicity of the oxo bridge, in the $33^{2+}/32^+$ and $33^+/32$ couples. The ΔpK_a was found to be ca. 9 units in thf-[NBu₄][PF₆] ($E_{1/2}^{red}$ ($33^{2+}/33^+$) = -0.34 V/Fc) and 11 units in MeCN-[NBu₄][PF₆] ($E_{1/2}^{red}$ ($33^{2+}/33^+$) = -0.24 V/Fc). Although these values are only approximate due to the quasi-reversible character of the $33^{2+}/33^+$ couple, they illustrate the substantial effect of the reduction of 32^+ on the basicity of the oxo bridge.

20.4 Conclusion

Electrochemistry is a powerful analytical and synthetic tool. The few examples described earlier illustrate that control of the electron transfers by controlling

the electrode potential allows selective transformations of complexes or those of bound substrates, which would be difficult, or impossible, to accomplish chemically.

Beyond thermodynamic information, CV gives access to reaction mechanisms, which is one of the fundamental challenges of molecular electrochemistry, through the detection of intermediates, and to the kinetics of chemical steps coupled to the electron transfer events. In this way, useful chemical information is also provided. The use of electrochemical techniques can help understand mechanisms (or part of them) of biological processes, involving {H⁺/e} transfer steps, catalyzed by metalloenzymes, through the investigations of much less complicated model compounds. In the field of biomimetic chemistry, detailed investigations of the effect of a redox step on the acid/base properties of a ligand, and conversely,

examinations of the consequences of protonating an even weakly basic ligand on the reduction potential and mechanism of the metal center(s) of synthetic models are particularly needed.

Acknowledgments

Part of the studies described in this contribution comes from the authors' laboratory. We are thankful to our coworkers and students who took an active part in these studies, and whose names can be found in the references.

References

- R. H. Holm, *Coord. Chem. Rev.* **1990**, *100*, 183–221; R. H. Holm, *Chem. Rev.* **1987**, *87*, 1401–1449, and references therein.
- C. D. Garner, S. Bristow, in *Molybdenum Enzymes, Metal Ions in Biology*, Vol. 7 (Ed.: T. G. Spiro), Wiley, New York, 1985, pp. 343–410, Chapter 7, and references therein.
- R. S. Pilato, E. I. Stiefel, in *Bioinorganic Catalysis*, 2nd ed. (Eds.: J. Reedijk, E. Bouwman), Marcel Dekker, New York, 1999, pp. 81–152, Chapter 6, and references therein.
- R. H. Holm, P. Kennepohl, E. I. Solomon, *Chem. Rev.* **1996**, *96*, 2239–2314, and references therein.
- R. H. Holm, E. D. Simhon, in *Molybdenum Enzymes, Metal Ions in Biology*, Vol. 7 (Ed.: T. G. Spiro), Wiley, New York, 1985, pp. 1–87, Chapter 1, and references therein.
- D. Coucouvanis, in *Molybdenum Enzymes, Cofactors, and Model Systems, ACS Symposium Series 535* (Eds.: E. I. Stiefel, D. Coucouvanis, W. E. Newton), American Chemical Society, Washington, DC, 1993, pp. 304–331, Chapter 20, and references therein.
- D. Sellmann, in *Molybdenum Enzymes, Cofactors, and Model Systems, ACS Symposium Series 535* (Eds.: E. I. Stiefel, D. Coucouvanis, W. E. Newton), American Chemical Society, Washington, DC, 1993, pp. 332–345, Chapter 20, and references therein.
- M. Hidai, Y. Mizobe, *Chem. Rev.* **1995**, *95*, 1115–1133, and references therein.
- M. Rakowski DuBois, *J. Clust. Sci.* **1996**, *7*, 293–315; M. Rakowski DuBois, *Chem. Rev.* **1989**, *89*, 1–9, and references therein.
- P. Zanello, *Coord. Chem. Rev.* **1988**, *83*, 199–275, and references therein.
- H.-B. Kraatz, P. M. Boorman, *Coord. Chem. Rev.* **1995**, *143*, 35–69, and references therein.
- F. Y. Pétillon, P. Schollhammer, J. Talarmin et al., *Coord. Chem. Rev.* **1998**, *178–180*, 203–247, and references therein.
- J. R. Dilworth, N. Weatherley, *Coord. Chem. Rev.* **2000**, *199*, 89–158, and references therein.
- W. E. Geiger, *Prog. Inorg. Chem.* **1985**, *33*, 275–352, and references therein.
- D. H. Evans, K. M. O'Connell, in *Electroanalytical Chemistry* (Ed.: A. J. Bard), Marcel Dekker, New York, 1986, pp. 113–207, Vol. 14, and references therein.
- A. J. L. Pombeiro, M. F. Guedes da Silva, M. A. N. D. A. Lemos, *Coord. Chem. Rev.* **2001**, *219–221*, 53–80, and references therein.
- T. Yoshida, T. Adachi, T. Ueda et al., *Angew. Chem., Int. Ed. Engl.* **1987**, *26*, 1171–1172; T. Yoshida, T. Adachi, T. Ueda et al., *Angew. Chem., Int. Ed. Engl.* **1989**, *28*, 1040–1042; T. Adachi, N. Sasaki, T. Ueda et al., *J. Chem. Soc., Chem. Commun.* **1989**, 1320–1322.
- T. Yoshida, T. Adachi, M. Kaminaka et al., *J. Am. Chem. Soc.* **1988**, *110*, 4872–4873.
- T. Yoshida, T. Adachi, K. Kawazu et al., *Angew. Chem., Int. Ed. Engl.* **1991**, *30*, 982–984.
- T. Adachi, M. D. Durrant, D. L. Hughes et al., *J. Chem. Soc., Chem. Commun.* **1992**, 1464–1467.
- D. Sellmann, B. Hautsch, A. Rössler et al., *Angew. Chem., Int. Ed. Engl.* **2001**, *40*, 1505–1507.
- T. I. Al Salih, C. J. Pickett, *J. Chem. Soc., Dalton Trans.* **1985**, 1255–1264.
- J. R. Bradbury, F. A. Schultz, *Inorg. Chem.* **1986**, *25*, 4408–4416.
- F. A. Schultz, *J. Electroanal. Chem.* **1986**, *273*, 169–174.
- J. U. Mondal, F. A. Schultz, *Inorg. Chim. Acta* **1989**, *157*, 5–7.
- J. R. Dilworth, B. D. Neaves, C. J. Pickett et al., *Inorg. Chem.* **1983**, *22*, 3524–3529.
- S. K. Ibrahim, C. J. Pickett, *J. Chem. Soc., Chem. Commun.* **1991**, 246–249.

28. D. Sellmann, B. Seubert, F. Knoch et al., *Z. Naturforsch* **1991**, *46b*, 1449–1458.
29. B. L. Crichton, J. R. Dilworth, C. J. Pickett et al., *J. Chem. Soc., Dalton Trans.* **1981**, 419–424.
30. O. A. Rajan, M. McKenna, J. Noordik et al., *Organometallics* **1984**, *3*, 831–840.
31. M. Rakowski DuBois, D. L. DuBois, M. C. VanDerveer et al., *Inorg. Chem.* **1981**, *20*, 3064–3071.
32. J. Courtot-Coupez, M. Guéguen, J. E. Guerchais et al., *J. Organomet. Chem.* **1986**, *312*, 81–95.
33. A. Shaver, B. Soo Lum, P. Bird et al., *Inorg. Chem.* **1990**, *29*, 1832–1835.
34. F. Y. Pétillon, S. Poder-Guillou, P. Schollhammer et al., *New J. Chem.* **1997**, *21*, 477–494.
35. E. Ahlberg, O. Hammerich, V. D. Parker, *J. Am. Chem. Soc.* **1981**, *103*, 844–849.
36. R. G. Finke, R. H. Voegeli, E. D. Lagakis et al., *Organometallics* **1983**, *2*, 347–350.
37. D. T. Pierce, W. E. Geiger, *J. Am. Chem. Soc.* **1992**, *114*, 6063–6073.
38. B. Zhuang, J. W. McDonald, F. A. Schultz et al., *Organometallics* **1984**, *3*, 943–945.
39. B. Zhuang, J. W. McDonald, F. A. Schultz et al., *Inorg. Chim. Acta* **1985**, *99*, L29–L31.
40. D. A. Smith, B. Zhuang, W. E. Newton et al., *Inorg. Chem.* **1987**, *26*, 2524–2531.
41. J. B. Fernandes, L. Qun Zhang, F. A. Schultz, *J. Electroanal. Chem.* **1991**, *297*, 145–161.
42. D. J. Dahrenbourg, K. M. Sanchez, J. Reibenspies, *Inorg. Chem.* **1988**, *27*, 3636–3643.
43. B. Zhuang, L. R. Huang, L. J. He et al., *Acta Chim. Sin.* **1986**, *4*, 294–300.
44. B. Zhuang, L. Huang, Y. Yang et al., *J. Struct. Chem.* **1985**, *4*, 103–106.
45. B. Zhuang, L. Huang, L. He et al., *Inorg. Chim. Acta* **1989**, *157*, 85–90.
46. B. Zhuang, H. Sun, G. Pan et al., *J. Organomet. Chem.* **2001**, *640*, 127–139.
47. M. El Khalifa, F. Y. Pétillon, J.-Y. Saillard et al., *Inorg. Chem.* **1989**, *28*, 3849–3855.
48. P. Madec, K. W. Muir, F. Y. Pétillon et al., *J. Chem. Soc., Dalton Trans.* **1999**, 2371–2383.
49. T. E. Gennett, W. E. Geiger, B. Willett et al., *J. Electroanal. Chem.* **1987**, *222*, 151–160.
50. N. G. Connelly, L. F. Dahl, *J. Am. Chem. Soc.* **1970**, *92*, 7470–7472.
51. R. A. Marcus, *J. Chem. Phys.* **1965**, *43*, 679.
52. N. S. Hush, *Electrochim. Acta* **1968**, *13*, 1005.
53. D. Sellmann, G. Binker, J. Schwarz et al., *J. Organomet. Chem.* **1987**, *323*, 323–338.
54. M. Guéguen, J. E. Guerchais, F. Y. Pétillon et al., *J. Chem. Soc., Chem. Commun.* **1987**, 557–559; M. El Khalifa, M. Guéguen, R. Mercier et al., *Organometallics* **1989**, *8*, 140–148.
55. M. Guéguen, F. Y. Pétillon, J. Talarmin, *Organometallics* **1989**, *8*, 148–154.
56. F. Gloaguen, C. Le Floch, F. Y. Pétillon et al., *Organometallics* **1991**, *10*, 2004–2011.
57. F. Y. Pétillon, P. Schollhammer, J. Talarmin unpublished results.
58. M. El Khalifa, J.-Y. Saillard, F. Gloaguen et al., *New J. Chem.* **1992**, *16*, 847–854.
59. M.-L. Abasq, D. L. Hughes, F. Y. Pétillon et al., *J. Chem. Soc., Dalton Trans.* **1997**, 2279–2291.
60. D. S. Tucker, S. Dietz, K. G. Parker et al., *Organometallics* **1995**, *14*, 4325–4333.
61. M. Rakowski DuBois, J. Talarmin, unpublished results.
62. A. M. Allgeier, C. A. Mirkin, *Angew. Chem., Int. Ed. Engl.* **1998**, *37*, 894–908, and references therein.
63. M. B. Gomes de Lima, J. E. Guerchais, R. Mercier et al., *Organometallics* **1986**, *5*, 1952–1964.
64. F. Barrière, Y. Le Mest, F. Y. Pétillon et al., *J. Chem. Soc., Dalton Trans.* **1996**, 3967–3976.
65. M. B. Robin, P. Day, *Adv. Inorg. Chem. Radiochem.* **1967**, *10*, 247.
66. C. Le Roy, F. Y. Pétillon, K. W. Muir et al., submitted for publication.
67. F. Y. Pétillon, P. Schollhammer, J. Talarmin, *J. Chem. Soc., Dalton Trans.* **1997**, 4019–4024.
68. F. Y. Pétillon, P. Schollhammer, J. Talarmin et al., *Inorg. Chem.* **1999**, *38*, 1954–1955.
69. P. Schollhammer, F. Y. Pétillon, S. Poder-Guillou et al., *Chem. Commun.* **1996**, 2633–2634.
70. J.-Y. Cabon, C. Le Roy, K. W. Muir et al., *Chem. Eur. J.* **2000**, *6*, 3033–3042.
71. P. Schollhammer, E. Guénin, F. Y. Pétillon et al., *Organometallics* **1998**, *17*, 1922–1924.
72. P. Schollhammer, B. Didier, N. Le Grand et al., *Eur. J. Inorg. Chem.* **2002**, 658–663.
73. N. Le Grand, K. W. Muir, F. Y. Pétillon et al., *Chem. Eur. J.* **2002**, *8*, 3115–3127.
74. J. S. Kim, D. C. Rees, *Science* **1992**, *257*, 1677–1682; O. Einsle, F. A. Teczan, S. L. A. Andrade et al., *Science* **2002**, *297*, 1696–1700.
75. M. Le Hénaff, C. Leroy, K. W. Muir et al., *Eur. J. Inorg. Chem.* **2004**, 1687–1700.

21

Aspects of Metallo-sulfur Clusters' Electrochemistry

*Frédéric Barrière
Université de Rennes, Rennes, France*

21.1	Introduction	593
21.2	Abiological Iron–Sulfur Clusters' Electrochemistry: The Black Roussinates as an Example	594
21.3	Models of Iron–Sulfur Centers in Protein	595
21.3.1	Models of Fe(SR) ₄ Sites	595
21.3.2	Models of Fe ₂ S ₂ (SR) ₄ Sites	596
21.3.3	Models of Linear Fe ₃ S ₄ (SR) ₄ or Cuboidal Fe ₃ S ₄ (SR) ₃ Sites	596
21.3.4	Models of Fe ₄ S ₄ (SR) ₄ Sites, The Iron-protein of Nitrogenase as an Example	597
21.4	Bridged Iron–Sulfur Molecular Assemblies	599
21.4.1	Nitrogenases	599
21.4.1.1	Introduction	599
21.4.1.2	Electrochemistry of the Fe ₈ S ₇ P Cluster and Models	601
21.4.1.3	Electrochemistry of the MoFe ₇ S ₉ FeMo Cofactor and Models	602
21.4.2	Hydrogenases	603
21.5	Conclusions	604
	References	605

21.1 Introduction

Iron–sulfur cluster synthesis in the laboratory and the subsequent study of their electrochemical properties has been driven and stimulated by the occurrence and characterization of such centers in many redox enzymes. The reason for the ubiquitous occurrence of these clusters in the biological world may rest on the abundance and wide availability of these two elements on earth. However, the chemical properties of iron and sulfur also seem well suited to meet the needs of some proteins in terms of electron transfer and catalysis. Indeed, iron electrochemical properties (discussed in Chapter 16) bring some latitude in spin and oxidation states for these centers. Here again, iron oxidation state two and three are overwhelmingly dominant, especially because of the moderate oxidizing and reducing potentials available in biology. Sulfur fills the coordination sphere of iron, yielding pseudotetrahedral centers. Two types of sulfur ligands are found: thiolate and sulfide. The thiolate itself is in fact cysteinate, from the natural cysteine amino acid, and provides an anchor between the active inorganic center and the protein within? it is buried. Cysteinate may coordinate in a terminal fashion or in a bridging fashion between two iron

centers. Sulfide ligands are found bridging two or three centers usually, but in some instances also up to six iron atoms as in one of the characterized structures of a nitrogenase metal–sulfur site (the P cluster, *vide infra*). Sulfur being in the third row of the periodical classification of the elements, its diffuse orbitals and low-lying empty d orbitals are likely to participate in strong hydrogen bonds or even in a reaction leading to protonation of the ligand to hydrosulfide. This combination of individual atomic properties, together with the assembly of biological iron–sulfur clusters ranging from one to as many as seven iron centers, which may also accommodate other metals, give these chemical assemblies a large modularity as elementary pieces of the complex living world [1]. Of course, in trying to mimic and understand these biological inorganic centers, chemists have produced an immense array of original, abiological clusters, interesting in their own right, and by nature electrochemically active, which also contribute to the understanding of the properties of this family of compounds, whether they are biological or not [2]. It is only fair and right to recall that iron–sulfur chemistry perhaps started with the synthesis of $[Fe_4S_3(NO)_7]^-$ and related species by Roussin in 1858 [3]. This example shows that terminal coordination at iron is not

restricted to thiolate (NO here), especially in synthetic species, and many other terminal ligands may be found. Even in biology, some unexpected ligands may occur as we shall discuss later for hydrogenase (see also Sect. 16.2.2.4).

This section is organized as follows: we first start with a discussion of the electrochemical behavior of the Roussin-type synthetic iron–sulfur clusters for their historic importance and as an interesting introduction to poly iron–sulfur centers' redox chemistry. Then we review iron–sulfur centers in proteins and artificial models in the order of increasing iron content. Finally, biological iron–sulfur centers and artificial models directly linked to other inorganic centers, the so-called bridged molecular assemblies, are considered,

with a focus on nitrogenases and hydrogenases.

21.2 Abiological Iron–Sulfur Clusters' Electrochemistry: The Black Roussinate as an Example

A recent review on abiological iron–sulfur clusters should be the primary entry reference to anyone wishing to gain information on this wide field [2]. Indeed, Ogin et al. provide a comprehensive source of data, of synthetic, structural, spectroscopic, and electrochemical nature, on many synthetic iron–sulfur clusters. The electrochemical properties of Roussin's black anion [3] have been investigated

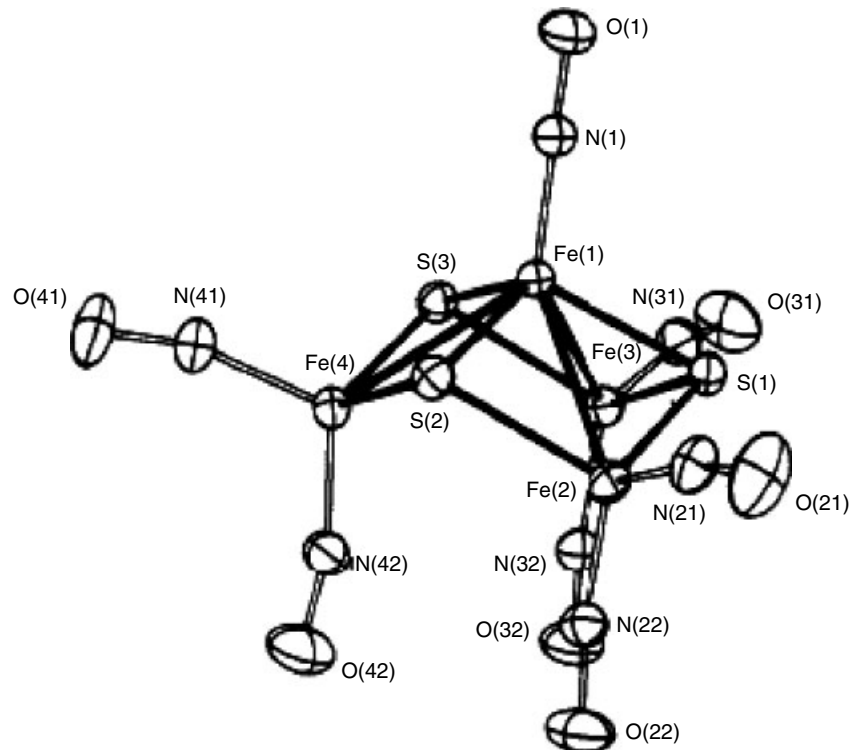


Fig. 1 Structure of $[(NO)Fe(\mu_3-S)_3Fe_3(NO)_6]^-$ (from Ref. 4).

[4]. The $[(NO)Fe(\mu_3\text{-}S)_3Fe_3(NO)_6]^-$ anion (cf Fig. 1) is best described as a trigonal pyramid of iron with each of its face being capped by a triply bridging sulfur atom. The apical iron atom capping the pyramid has one terminal nitrosyl ligand and shares metal–metal bonds with all three iron atoms of the pyramid base. These iron atoms do not themselves share metal–metal bonds and have two nitrosyl ligands each: one axial and one equatorial. The idealized point group symmetry of the cluster is C_{3v} . NO is a strong π -acceptor ligand, so that it is expected to stabilize electron-rich metal centers. The black Roussiniate monoanion is indeed sequentially and reversibly reducible in three consecutive monoelectronic steps to three more reduced states, at the rather negative potentials of -0.68 , -1.26 , and -1.75 V versus saturated calomel electrode (SCE) in acetonitrile. The paramagnetic dianion has been generated in tetrahydrofuran by sodium naphthalenide reduction, and then crystallized. The structure of the dianion confirmed that there is no major structural change upon reduction, as was suggested by the chemical and electrochemical reversibility of the reduction. When the crystal structures of the mono- and dianion with the same counteraction (Et_4N^+) are compared, the very good π -acceptor nature of the nitrosyl ligand is noticeable in a significantly shorter average N–O bond

length in the reduced state (1.646 versus 1.667 Å) and longer Fe–N distance (1.176 versus 1.161 Å). Because all three redox processes are reversible, it is anticipated that the cluster does not experience major structural change upon reduction. The trianion could only be studied and generated in solution by sodium reduction in hexamethylphosphoramide.

21.3

Models of Iron–Sulfur Centers in Protein

The synthesis, structures, and properties of analogs of iron–sulfur protein active sites has been recently reviewed by Venkateswara Rao and Holm [5]. In the order of increasing iron content, these sites are of $\text{Fe}(\text{SR})_4$, $\text{Fe}_2\text{S}_2(\text{SR})_4$, $\text{Fe}_3\text{S}_4(\text{SR})_4$, or $\text{Fe}_3\text{S}_4(\text{SR})_3$, and $\text{Fe}_4\text{S}_4(\text{SR})_4$ stoichiometry (cf. Fig. 2) and are now briefly treated.

21.3.1

Models of $\text{Fe}(\text{SR})_4$ Sites

Although not a metallic cluster, the simplest iron–sulfur center of proteins and its synthetic analogs are discussed here. $[\text{Fe}(\text{SR})_4]^-$ synthetic species are generally reversibly reduced to $[\text{Fe}(\text{SR})_4]^{2-}$ in aprotic solvents at potentials controlled, or tuned, by the nature of R. For example, $E_{1/2} = -1.11$ V versus SCE for $[\text{Fe}(\text{SPri})_4]^{1-/2-}$

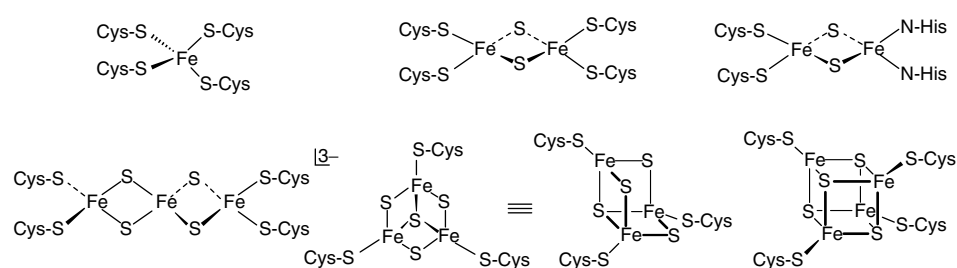


Fig. 2 Structures of simple iron–sulfur centers in proteins (from Ref. 5.).

and -0.52 V for $[\text{Fe}(\text{SPh})_4]^{1-/2-}$. Functionalization of the phenyl ring allows for alteration of the Fe (III/II) redox potential via specific N–H···S hydrogen bonds, an effect that is of relevance to biological sites. For example, a positive shift of 250 mV is obtained with respect to $[\text{Fe}(\text{SPh})_4]^{1-/2-}$ when R = 2-(MeCONH)C₆H₄ in acetonitrile. Water soluble derivatives like $[\text{Fe}(\text{SCH}_2\text{CH}_2\text{OH})_4]^{1-/2-}$ ($E_{1/2} = -0.35$ V) are more biologically relevant because of the solvent and associated hydrogen-bonding properties. However, specific interactions from the protein cannot be fully reproduced. Indeed, the redox potential of $[\text{Fe}(\text{SCH}_2\text{CH}_2\text{OH})_4]^{1-/2-}$ in water is close to the lower limit of FeS₄ sites in rubredoxin proteins (-0.1 to $+0.1$ V versus standard hydrogen electrode (SHE)).

21.3.2

Models of Fe₂S₂(SR)₄ Sites

The synthetic $[\text{Fe}_2\text{S}_2(\text{SPh})_4]^{2-}$ complex has been shown to undergo two reductions in acetonitrile or dimethylformamide (DMF) at $E_{1/2} = -1.13$ and -1.41 V versus SCE. Again, N–H···S hydrogen bonds with functionalized phenyl groups shift this redox potential toward positive values. The first reduction product, $[\text{Fe}_2\text{S}_2(\text{SR})_4]^{3-}$, has some instability as it tends to dimerize to the more stable cubane-type cluster $[\text{Fe}_4\text{S}_4(\text{SR})_4]^{2-}$, with concomitant release of two equivalents of thiolate and one equivalent of disulfide. The biologically relevant cluster oxidation states involve the $[\text{Fe}_2\text{S}_2(\text{SR})_4]^{2-/3-}$ couple. Heteroligated biological site exists in Rieske protein where one of the iron centers is ligated to the polypeptide backbone via two histidine residues instead of cysteine. Accurate models for this site are not available although it is possible to get N₂S₂ terminal coordination by ligand

substitution reaction of $[\text{Fe}_2\text{S}_2\text{Cl}_4]^{2-}$ with bidentate chelating ligands. The very air-sensitive all-ferrous state ($[\text{Fe}_2\text{S}_2]^0$ core) of a Rieske protein has been generated and characterized, with E^0 for the $[\text{Fe}_2\text{S}_2]^{1+/0}$ couple being -0.73 V versus SHE at pH 7, that is, 1 V more negative than for $[\text{Fe}_2\text{S}_2]^{2+/1+}$ [6]. The $[\text{Fe}_2\text{S}_2]^0$ core is stabilized by protonation of one of the bridging sulfides at pH > 9.8. The basic nature of the bridging sulfide in iron–sulfur clusters is an important property that has been studied extensively [7].

21.3.3

Models of Linear Fe₃S₄(SR)₄ or Cuboidal Fe₃S₄(SR)₃ Sites

Linear Fe₃S₄(SR)₄ clusters have been found in partially unfolded proteins, but are not known to exist as functional centers to date. Synthetic analogs comprise the all-ferric $[\text{Fe}_3\text{S}_4(\text{SPh})_4]^{3-}$ species (a $[\text{Fe}_3\text{S}_4]^{1+}$ core) that may be reduced to the corresponding $[\text{Fe}_3\text{S}_4]^0$ core at -1.35 V versus SCE in acetonitrile (-1.66 V for the ethylthiolate derivative).

The cuboidal Fe₃S₄(SR)₃ sites have the Fe₄S₄ cubane-type structure of which one iron corner is missing. This open structure can accommodate a fourth metal ion, as in the aconitase enzyme that binds Fe²⁺ after one-electron reduction of the $[\text{Fe}_3\text{S}_4(\text{SCys})_3]^{2-}$ center. The enzyme then becomes active, and catalyzes the isomerization of citrate to isocitrate at the fourth iron site. The first synthetic analog of the “open-cube” Fe₃S₄(SR)₃ sites has only been obtained recently [8]. It involves the uses of a tridentate thiolate ligand (LS₃) that acts as a cavitand for the Fe₃S₄ open-cube core. A whole new chemistry is being developed from this structure with binding of a fourth site-differentiated iron center or other metal fragments. The model

cluster exhibits two-electron-transfer processes involving the $[\text{Fe}_3\text{S}_4(\text{LS}_3)]^{2-/3-}$ and $[\text{Fe}_3\text{S}_4(\text{LS}_3)]^{3-/4-}$ of which only the first one is of biological relevance (redox potentials are -0.79 and -1.72 V respectively, versus SCE in acetonitrile).

21.3.4

Models of $\text{Fe}_4\text{S}_4(\text{SR})_4$ Sites, The Iron-protein of Nitrogenase as an Example

Fe_4S_4 clusters with cysteinate ligation at iron, in their $[\text{Fe}_4\text{S}_4]^{1+/2+/3+}$ redox states, are of pervasive occurrence in iron–sulfur proteins, functioning mostly as electron transfer relays as in ferredoxins ($1+/2+$, -0.3 to -0.8 V range versus normal hydrogen electrode (NHE)) and high potential iron-proteins ($2+/3+$, $+0.1$ to $+0.5$ V range versus NHE). Examples are also known where they are implied in catalysis [1, 5]. Mo-nitrogenase [9] is an enzyme responsible for the reduction of atmospheric nitrogen to ammonia. It comprises two proteins: the iron-protein and the molybdenum-protein. The Fe-protein specifically reduces the MoFe-protein with its Fe_4S_4 cluster cycling between the $[\text{Fe}_4\text{S}_4]^{1+}$ and $[\text{Fe}_4\text{S}_4]^{2+}$ redox states at a potential of -0.31 V versus NHE, that is lowered by about 0.1 V upon nucleotide binding. The Fe_4S_4 cluster is symmetrically bridged between the α -subunits of the iron-protein and is accessible to solvent molecules (H_2O). Vicinal amino-acid residues provide NH–S hydrogen bonds from amide groups to the iron–sulfur center. The $[\text{Fe}_4\text{S}_4]^0$ state can be artificially generated as a stable center within the iron-protein of nitrogenase (-0.79 V versus NHE); however, it is not known if this state is biologically relevant [10].

The iron–sulfur cluster of the iron-protein in its $[\text{Fe}_4\text{S}_4]^{1+}$ redox state exists in a mixture of spin states of similar energy

in frozen solution ($S = 3/2$ and $S = 1/2$). However, proton nuclear magnetic resonance (NMR) analysis suggests that in standard conditions, only one spin state is populated ($S = 1/2$). Proton NMR spectroscopy is useful for the analysis of paramagnetic iron–sulfur clusters (those with the $[\text{Fe}_4\text{S}_4]^{1+}$ and $[\text{Fe}_4\text{S}_4]^{3+}$ core). Indeed, significant low or high field hyperfine isotropic shifts for the resonance of the protons bound at the carbon β to an iron center greatly simplify the analysis of the chemical environment of each iron center of the protein even if the signal is usually broad. ^{57}Fe Mössbauer spectroscopy is a method of choice to assign the overall core oxidation state of a native or synthetic iron–sulfur cluster. There exists an empirical linear relationship between the ^{57}Fe Mössbauer spectroscopy isomer shift (i.s.) and the oxidation state (or mean oxidation state) of an iron center (or a cluster of iron centers) in a pseudotetrahedral sulfur environment [5].

Synthetic structural models for the Fe_4S_4 clusters have been known for three decades now [5]. They are readily prepared by self-assembly from ferric or ferrous chloride, a source of reduced sulfur and thiolates, acting as ligands to the iron sites (Fig. 2). Ligand substitution reactions at the iron centers allow the tuning over a large window of their redox potential that is linearly linked to the electron donor/acceptor properties of the ligands, usually an alkyl or phenyl thiolate, or a halide. Crystal structures of model Fe_4S_4 clusters with thiolate ligands are available for all $[\text{Fe}_4\text{S}_4]^{1+/2+/3+}$ redox states, the $[\text{Fe}_4\text{S}_4]^0$ state being only transiently generated in solution.

It has been shown that the Fe_4S_4 cluster of the Fe-protein can be further reduced with nonbiological reductants from the

$[\text{Fe}_4\text{S}_4]^{1+}$ to the $[\text{Fe}_4\text{S}_4]^0$ (all-ferrous) redox state, which suggests that the Fe-protein could transfer two electrons per reduction cycle to the MoFe-protein [10]. Although there is no precedence for a functional $[\text{Fe}_4\text{S}_4]^0$ state in biology, this is an attractive proposal considering (1) that substrates of nitrogenase can be reduced by multiple of two electrons, (2) that the dicubane structure of both the P cluster and the FeMo cofactor (vide infra) is perhaps tailored to accept two electrons at once, and (3) the homodimeric structure of the Fe-protein that may bind two donor molecules at a time [9, 10]. Moreover, the redox potential originally reported for the $[\text{Fe}_4\text{S}_4]^{1+/0}$ redox couple (-0.46 V versus NHE) was well within physiological range and only 150 mV negative to that of the $[\text{Fe}_4\text{S}_4]^{2+/1+}$ redox couple. The biological relevance of the $[\text{Fe}_4\text{S}_4]^0$ oxidation state, however, is contentious. In synthetic models with thiolate ligands, the all-ferrous redox state ($[\text{Fe}_4\text{S}_4]^0$) can be detected transiently in some instances at the cyclic voltammetry timescale, and has been first generated, but not isolated, as a persistent species in solution in the case of $\text{Fe}_4\text{S}_4(\text{PR}_3)_4$ bearing less biologically relevant phosphine ligands known to stabilize reduced oxidation states of metal complexes. Recently [11], the first Fe_4S_4 cluster in the zero oxidation state has been synthesized and characterized. Each iron atom has terminal cyanide ligands that allow the stabilization of such a reduced core. Indeed, compared to other clusters with terminal thiolate ligands, the redox potential of $[\text{Fe}_4\text{S}_4(\text{CN})_4]^{0/1+}$ is shifted positive by about 0.3 V. In acetonitrile, the $[\text{Fe}_4\text{S}_4(\text{CN})_4]^{0/1+}$ couple is detected at -1.42 V versus SCE and the $[\text{Fe}_4\text{S}_4(\text{CN})_4]^{1+/2+}$ at -0.44 V.

Such a narrow potential separation ($\Delta E = 0.15$ V) between the $2+/1+$ and

$1+/0$ redox couples of the iron-protein Fe_4S_4 cluster, was hard to reconcile with redox potentials of synthetic models. Indeed, a range of models with ligands differing by their charge, structure, and electron-withdrawing properties, has been studied electrochemically in dipolar aprotic organic solvent electrolytes (MeCN, DMF, dimethylsulfoxide (DMSO)) in order to assess the effect of the direct environment of the cluster core on its redox potentials [12]. The measured ΔE between the $2+/1+$ and $1+/0$ redox potentials of model clusters with thiolate ligands remains consistently in the range ca 0.70 ± 0.05 V in organic solvent electrolytes, and ca 0.40 ± 0.02 V in water. The reported absolute potential for the one-electron reduction of $[\text{Fe}_4\text{S}_4]^{1+}$ in nitrogenase was also too high compared to model system values generally reported to be in the range -1.50 to -1.85 V (SCE) in organic solvent electrolytes and ca -1.2 V (SCE) in water. Recently, the redox potential for the $[\text{Fe}_4\text{S}_4]^{1+/0}$ couple of the iron-protein has been measured at -0.79 V (NHE; i.e. ca -1.03 V SCE), corresponding to a ΔE of 0.48 V between the two redox couples, more in line with experimental and theoretical redox potential and associated ΔE in model clusters [12, 13].

The polypeptide environment of the iron-protein Fe_4S_4 cluster appreciably stabilizes the $[\text{Fe}_4\text{S}_4]^0$ state compared to corresponding model clusters. This can be assigned to the network of hydrogen bonds between the protein residues and the cluster sulfide groups, and, to some extent, to the accessibility of water molecules to the cluster. However, the iron–protein iron–sulfur cluster in its $[\text{Fe}_4\text{S}_4]^{1+}$ state does not appear to be reducible *in vivo* by known physiological electron donors, unless a currently unknown mechanism, such as a protein conformation change,

stabilizes the $[\text{Fe}_4\text{S}_4]^0$ state even more. Accurate synthetic models have helped to understand the structural, spectroscopic, and electronic properties of the Fe_4S_4 cluster, particularly that of the iron-protein of nitrogenase. Whether or not the $[\text{Fe}_4\text{S}_4]^0$ state is implied in the physiological electron-transfer chain in nitrogenase remains to be proven. However, the sole fact that this latter state can be generated as a stable center within the protein encourages the quest for stable synthetic models in the all-ferrous state and bearing terminal thiolate ligands. These future models might bear a ligand scaffold mimicking the immediate stabilizing protein environment of the native cluster. In particular, it would be interesting to study the effect in terms of structure and associated electronic properties (electron transfer) of specific hydrogen bonds to the bridging sulfides as a function of the oxidation state of the cluster core. The modeling of a dielectric medium similar to the polarity and Lewis acidity experienced by iron–sulfur centers within proteins might be imposed by ligands sharing both covalent and noncovalent bonds to the cluster core.

More complex iron–sulfur centers in the MoFe-protein of Mo-nitrogenase are discussed next.

21.4 Bridged Iron–Sulfur Molecular Assemblies

More complex assemblies of iron and sulfur, sometimes extended to other metals like nickel, molybdenum, vanadium, or other iron centers are found in some enzymes, that catalyze the transformation of small molecules [1, 14]. Among these centers, we will focus next on the P cluster and the FeMo cofactor of nitrogenase and on the H cluster of the iron-only hydrogenase.

21.4.1 Nitrogenases

21.4.1.1 Introduction

The most extensively studied nitrogenase enzyme contains two kinds of transition metals, namely, iron and molybdenum, and is called *molybdenum nitrogenase* [9]. In growth conditions where molybdenum concentration is low, a nitrogenase dependent on iron and vanadium is expressed [15]. When both molybdenum and vanadium are unavailable, a third type of nitrogenase is expressed that contains iron as the only transition metal [16]. The vanadium-nitrogenase and iron-only nitrogenases, also known as *alternative nitrogenases*, are related to the molybdenum nitrogenase but are all genetically distinct. A fourth and completely different “nonconventional” type of nitrogenase is known; it also contains iron and molybdenum, but couples dinitrogen reduction to the oxidation of superoxide and carbon monoxide [17].

Mo-nitrogenase is the only one for which both detailed structural and mechanistic data are available [9, 18]. The enzymatic complex comprises two proteins: the iron-protein and the molybdenum-iron-protein. The Fe-protein is an α_2 -homodimer with a Fe_4S_4 cluster (*vide supra*) bridging the two α -subunits via four iron-cysteinate ligations. Each α -monomer of the iron-protein possesses a nucleotide-binding site (ATP or ADP). The Fe-protein is a specific reductant of the MoFe-protein, an event that depends on, and is coupled to, the hydrolysis of MgATP. The MoFe-protein is an $\alpha_2\beta_2$ tetramer and contains two types of metal–sulfur centers: the so-called P cluster of Fe_8S_7 stoichiometry that is located at the interface of each homologous $\alpha-\beta$ subunit, and the FeMo cofactor (MoFe_7S_9) found in each α -subunit.

Two different structures are known for the P cluster (cf. Fig. 3) and are assigned to different cluster core oxidation states. In the reduced or P^N (native) state, the Fe_8S_7 cluster can be described as two Fe_4S_4 cubes sharing one common hexacoordinate sulfur atom, the iron atoms being linked to the protein by cysteinate ligands, two of them bridging the subcubes. In the P^{OX} state, oxidized by two electrons relative to P^N , the central sulfur atom loses two bonds with two iron atoms in one of the subcubes, thus becoming more open. The tetrahedral coordination of these two iron atoms is then completed by extra ligations from neighboring cysteine and serine residues.

The FeMo-cofactor structure can be viewed as the assembly of two incomplete

$Fe_4(\mu_3-S)_3$ and $MoFe_3(\mu_3-S)_3$ subcubes, linked together by three central μ_2 -S bridging sulfide ligands (cf. Fig.4). The six central iron atoms form an approximate trigonal prism centered on a light atom "Y" that has only been structurally recognized recently [18b]. The identity of the light atom has been proposed to be either nitrogen, carbon, or oxygen. Recently, the possibility of "Y" being a nitrogen atom seems to have been excluded [18d]. The pseudo-octahedral coordination of molybdenum is completed by the exogenous bidentate (*R*)-homocitrate ligand and by imidazole from a neighboring histidine residue. A cysteine residue, covalently bound to the tetrahedral apical iron atom, provides the cofactor with its other protein ligation.

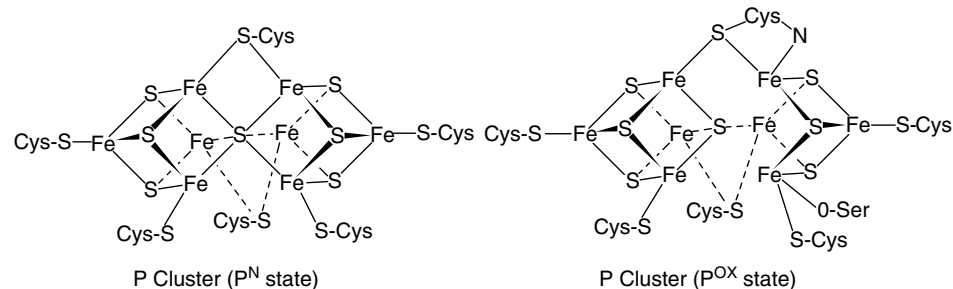


Fig. 3 Known structures of the P cluster of nitrogenase in two oxidation states.

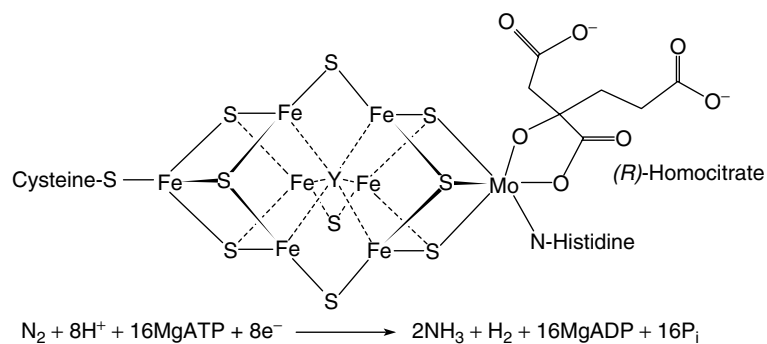


Fig. 4 Structures of the FeMo cofactor of nitrogenase (Y is C, N, or O) and limiting stoichiometry of the catalyzed reaction.

The electrons transferred from the Fe₄S₄ cluster of the iron-protein to the molybdenum-iron-protein are believed to shuttle through the P cluster before eventually reaching FeMo-co where N₂ binding, reduction, and protonation occurs.

The limiting stoichiometry for the reduction of one equivalent of dinitrogen by Mo-nitrogenase to two equivalents of ammonia involves the hydrolysis of 16 MgATP and the production of one molecule of dihydrogen, as outlined in Fig. 4. The three metal clusters found in Mo-nitrogenase belong to the diverse class of iron–sulfur prosthetic centers largely distributed in all living organisms. However, while the Fe₄S₄ center is a common cluster found in many other iron–sulfur proteins (*vide supra*), the P cluster and the FeMo cofactor represent unique structures in biology to date.

21.4.1.2 Electrochemistry of the Fe₈S₇ P Cluster and Models

The Fe₈S₇ inorganic core of the P cluster has been synthesized from tetramethylthiourea, 2,4,6-triisopropylbenzenethiol, elemental sulfur, and iron(II)bis(ditrimethylsilylamine) in toluene, in the respective 3/12/7/8 ratio [19]. The differences between the model and the native P cluster lie within the nature of the ligands to the iron–sulfur sites, the iron atoms' oxidation states and the shorter bond distances in the model around the central hexacoordinated sulfur. While the iron atoms are terminated or bridged by cysteinate ligands in the P cluster, different ligations are involved in the model. Indeed, the two opposite apical iron sites of the synthetic cluster have a terminal bis-amide ligation; thiourea completes the tetrahedral coordination of two opposite central iron atoms, and the two remaining pairs of opposite iron centers are linked by a bis-amide bridge. The tighter amide

bridge of the model compared to the cysteinate bridge found in the MoFe-protein explains the shorter μ_6 S–Fe bonds and shorter distance between opposite central iron atoms in the model. ⁵⁷Fe Mössbauer spectroscopy of the model compound distinguishes two iron sites in a 3/1 ratio: each quadrupole doublet's isomer shift and quadrupole splitting are consistent respectively with six Fe(II) and two Fe(III), the former assigned to the six central iron atoms and the latter assigned to the two opposite apical iron centers. The oxidation state of the model (six ferrous/two ferric) is therefore directly related to that of the P cluster in the P^{OX} state. Nevertheless, the structure of the Fe₈S₇ core of the model resembles closely that of the P^N state, which is likely because the bridging amide prevents a more open structure similar to that of P^{OX}.

The model cluster has been reported to be very sensitive to oxygen and heat. This is consistent with the known instability of the P cluster toward extraction from the MoFe-protein. It is perhaps for this reason that no redox potentials were reported for the model.

In the as-isolated state [9], the diamagnetic P cluster can be oxidized to the P¹⁺ and P²⁺ (P^{OX}) states at a midpoint potential of -0.309 V (NHE at pH 8). The identical midpotential for both the P^N/P¹⁺ and P¹⁺/P²⁺ couples may be accounted for by a model in which both halves of the P cluster may be oxidized separately, and by the structural change observed between P^N and P^{OX}. The P²⁺ state (P^{OX}) may be further oxidized to P³⁺ (PSUPEROX) at $E_m = 0.09$ V. With $E_m = -0.309$ V for P^N/P^{OX}, the P cluster seems well positioned for electron transfer from the MgATP bound iron–protein ($E_m = -0.600$ V). In a complex between

the iron–protein and the molybdenum–iron–protein, the P^N/P^{OX} E_m value is shifted negative to -0.390 V while that of the Fe_4S_4 cluster in the Fe-protein is -0.620 V. This may be required for the P cluster to be a better reductant of the FeMo cofactor. The additional cysteine and serine residues' ligation to the P cluster in the P^{OX} state have been proposed to serve as proton donor. Indeed, the E_m value for the P^{1+}/P^{2+} couple varies linearly with pH in the range pH 6.0 to 8.4 (-53 mV per pH unit). Despite these electrochemical data on the P-cluster redox potential and oxidation state, it is not yet clear as to which ones are relevant to the biological process, how this center reduces the FeMo cofactor, and whether it is the only specific iron–sulfur structure capable of sustaining nitrogenase reactivity [9c].

21.4.1.3 Electrochemistry of the $MoFe_7S_9$ FeMo Cofactor and Models

The FeMo cofactor (or M center) in the MoFe-protein is in the native paramagnetic M^N state. Reduction of the MoFe-protein by the Fe-protein results in the reduction of FeMo-co from the M^N state to the M^R state at a potential estimated to be less than -0.465 V (NHE). The electron paramagnetic resonance (EPR) silent M^R state is only transiently produced during catalysis, and relaxes to the M^N state when catalysis stops. The intimate consequences of the M^N state reduction are not precisely known. A more oxidized diamagnetic state may also be generated (M^{OX}) at -0.042 V but its biological relevance is unclear [9].

The electrochemistry of the extracted FeMo cofactor has also been studied in depth [20]. Extracted N -methyl formamide (NMF) solutions of FeMo-co contain the intact cluster, probably with retention of the exogenous homocitrate ligand. Protein ligation are replaced with NMF ligands at

Mo and apical Fe. The as-isolated FeMo-co in reducing conditions (dithionite) is in the EPR active ($S = 3/2$) so-called “semireduced” state. $FeMo\text{-}co^{semired}$ may be oxidized to $FeMo\text{-}co^{ox}$ at -0.32 V (NHE), a process that is complicated by a redox-linked isomerization of mono- to bidentate coordination mode of the $MeNHCHO^-$ anion at the apical iron atom. Addition of thiophenolate to the solution simplifies the redox process by ligand substitution at this iron site. A partially reversible one-electron reduction step, corresponding to $FeMo\text{-}co^{semired/red}$ is observed at about -1 V, followed by an irreversible process at some 150 mV more negative. The $ox/semireduced/reduced$ triad is proposed to be associated with the cluster core reduction while the last process would be more localized at the molybdenum center. Interaction of extracted FeMo-co with substrates or inhibitors like proton, carbon monoxide or cyanide is informative given that (1) no interaction between dinitrogen and FeMo-co has been shown, (2) nitrogenase is also a hydrogenase, (3) CO binds to FeMo-co in the MoFe-protein. Details of these interactions may be found in Ref. 20. In short, the semireduced state of extracted FeMo-co catalyzes H_2 evolution at high acidity (-0.28 V) in the presence of thiophenol (both an acid and ligand for the apical iron site). At low acidity, H_2 evolution occurs at the reduced FeMo-co state. CO binding to the iron–sulfur core involves a two-electron reduction of the semireduced FeMo-co. Upon CO release, the semireduced state is recovered via oxidation by protons. The third-electron-transfer process (reduced/super reduced) is associated with a second CO binding site, probably at Mo. Accurate models of the FeMo cofactor are not available but are being actively pursued [21].

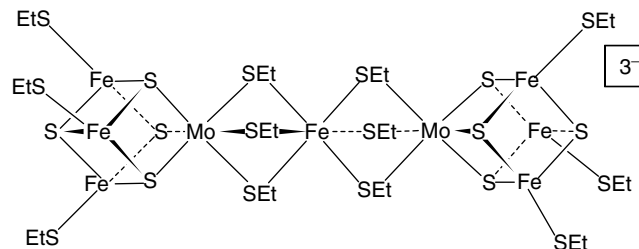


Fig. 5 The double cubane $[Mo_2Fe_7S_8(SEt)_{12}]^{3-}$ cluster.

The fragment of FeMo-co that has been most accurately modeled by synthetic clusters is its molybdenum cap. Indeed, cubane-like $MoFe_3S_4$ clusters reproduce very well the first and second coordination sphere of molybdenum in nitrogenase. $MoFe_3S_4$ clusters are usually synthesized from the double cubane $[Mo_2Fe_7S_8(SEt)_{12}]^{3-}$ (Fig. 5) whose central iron bridge can be cleaved to yield independent $MoFe_3S_4$ monocubes [22, 23]. The $[Mo_2Fe_7S_8(SEt)_{12}]^{3-}$ double cubane has an interesting electrochemistry. The first reduction is associated with the central low-spin iron(III) center. The monoelectronic reduction to iron(II) is associated with a spin state change, confirmed by Mössbauer spectroscopy, and by an increase of the Fe–S bond length by an average of 0.2 Å. Electrochemically, these structural and spin state changes translate into a quasi-reversible reduction (slow electron transfer) as shown by an increase of the ΔE_p at low temperature (ΔE_p increase from 80 to 270 mV between 293 and 243 K). The two other redox-active sites in this cluster are the equivalent $MoFe_3S_4$ cubes that undergo a monoelectronic reduction at very close potentials (about 90 mV apart). Only under low temperature conditions are the two redox processes fully reversible. At room temperature, the cubane reductions are associated with a reversible opening of some of the

thiolate bridges to the central iron center. The cubane reduction potentials are consistent with the $[MoFe_3S_4]^{2+/3+}$ core oxidation state. The inherent lability of the central iron bridge in $[Mo_2Fe_7S_8(SEt)_{12}]^{3-}$ allows synthesis of independent $MoFe_3S_4$ cubes that are good structural models of the molybdenum center of nitrogenase. In isolated monocubane, three redox processes may be observed electrochemically, involving the $[MoFe_3S_4]^{1+/2+}$, $[MoFe_3S_4]^{2+/3+}$, and $[MoFe_3S_4]^{3+/4+}$ couples. Direct synthesis of $MoFe_3S_4$ or VFe_3S_4 clusters is also possible from $TpMoS(S_4)$, $FeCl_2$ and $NaSEt/PPh_3$ (Tp is hydro(trispyrazolyl)borate(1-)) [23c].

21.4.2 Hydrogenases

The iron-only hydrogenase is a nice example of an electron-transfer path paved with different iron–sulfur clusters within a protein. The [Fe]-hydrogenase from *Clostridium pastorianum* and *Desulfovibrio desulfuricans* consists of one Fe_2S_2 and three Fe_4S_4 centers, ending at the H cluster that comprises a Fe_4S_4 center bridged via a cysteine residue to a dinuclear iron site [24a]. The structure of the H cluster and hydrogen evolution by dinuclear models of its di-iron subsite have already been discussed in Sect. 16.2.2.4. Recently, a synthetic model of the whole

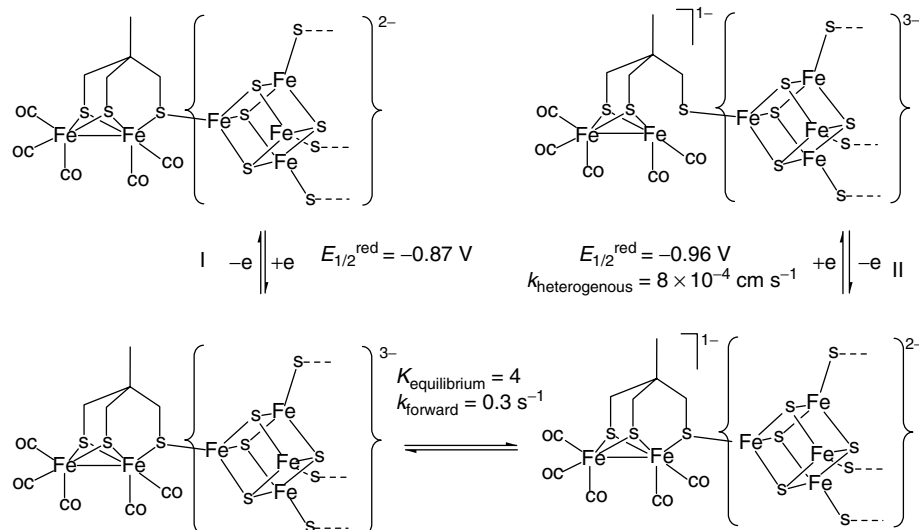


Fig. 6 Reduction of the H-cluster analog and interconversion of redox processes (from Ref. 24b).

structure of the H cluster has been published [24]. The key to the synthesis of the model cluster rests on the use of the tridentate thiolate cavitand ligand, already discussed in Sect. 21.3.3, that prevents expansion of the Fe_4S_4 cluster. The electrochemical reduction of the H-cluster model at -0.87 V versus Ag/AgCl (process I, Fig. 6) is associated with the reversible decoordination from the di-iron site of the bridging thiolate. The decoordination corresponds to a formal intramolecular electron transfer from the reduced cubane to the di-iron site (process II, Fig. 6). The reoxidized cubane then undergoes a reduction at -0.96 V . The interconverting redox processes I and II have been satisfactorily simulated. The accurate structural analog of the H cluster is also a good functional model as it catalyzes H_2 evolution in the presence of acid (4,6-dimethyl pyridinium in MeCN). The catalytic current potential is shifted some 200 mV positive in the presence of the catalyst ($E_p = -1.13 \text{ V}$) but the current

remains within some 5% of the current in the absence of the catalyst.

21.5 Conclusions

The association of sulfur and iron into simple to more complex molecular assemblies allows a great flexibility of electron transfer relays and catalysis in metalloproteins. Indeed, the array of different structures, the interactions with amino-acid residues and solvent and their effect on redox potential and spectroscopic signatures is both inspiring for chemists and electrochemists, and of paramount importance for the study of these centers in native conditions. Most of the simpler natural clusters have been synthesized and studied in the laboratory. Particularly, the multiple redox and spin states can be studied on pure synthetic samples with electrochemical and spectroscopic techniques such as EPR or ^{57}Fe Mössbauer spectroscopy. More complex assemblies still resist structural

and functional modeling by artificially synthesized complexes, with the notable exception of the H cluster of hydrogenase. The FeMo cofactor of nitrogenase combines both a difficult structure to be synthesized and an extremely difficult reaction to catalyze under ambient condition. This and other challenges are partly driving the development of more rational iron–sulfur chemistry and electrochemistry that extend well beyond the present restricted number of iron–sulfur sites of biological relevance.

References

1. H. Beinert, R. H. Holm, E. Münck, *Science* **1997**, *277*, 653–659.
2. H. Ogino, S. Inomata, H. Tobita, *Chem. Rev.* **1998**, *98*, 2093–2121.
3. M. L. Roussin, *Ann. Chim. Phys.* **1858**, *52*, 285.
4. S. D'Addario, F. Demartin, L. Grossi et al., *Inorg. Chem.* **1993**, *32*, 1153–1160.
5. P. Venkateswara Rao, R. H. Holm, *Chem. Rev.* **2004**, *104*, 527–559.
6. E. J. Leggate, E. Bill, T. Essigke et al., *Proc. Natl. Acad. Sci. U.S.A.* **2004**, *101*, 10913–10918.
7. R. A. Henderson, *Chem. Rev.* **2005**, *105*, 2365–2438.
8. (a) J. Zhou, R. H. Holm, *J. Am. Chem. Soc.* **1995**, *117*, 11353. (b) J. Zhou, Z. Hu, E. Münck et al., *J. Am. Chem. Soc.* **1996**, *118*, 1966.
9. (a) B. K. Burgess, D. J. Lowe, *Chem. Rev.* **1996**, *96*, 2983–3010. (b) R. Y. Igarashi, L. C. Seefeldt, The mechanism of Mo-dependent nitrogenase: thermodynamics and kinetics in *Nitrogenase and Chemical Models*. (Eds.: B. E. Smith, R. L. Richards, W. E. Newton), Kluwer, Amsterdam, 2004, pp. 97–140, chapter 5. (c) Y. Hu, M. C. Corbett, A. W. Fay et al., *Proc. Natl. Acad. Sci. U.S.A.* **2005**, *102*, 13825–13830.
10. (a) G. D. Watt, K. R. N. Reddy, *J. Inorg. Biochem.* **1994**, *53*, 281–294. (b) M. Guao, F. Sulc, M. W. Ribbe et al., *J. Am. Chem. Soc.* **2002**, *124*, 12100–12101.
11. (a) T. A. Scott, H.-C. Zhou, *Angew. Chem., Int. Ed. Engl.* **2004**, *43*, 5628–5631. (b) T. A. Scott, C. P. Berlinguette, R. H. Holm et al., *Proc. Natl. Acad. Sci. U.S.A.* **2005**, *102*, 9741–9744.
12. C. Zhou, J. W. Raebiger, B. M. Segal et al., *Inorg. Chim. Acta* **2000**, *300*–*302*, 892–902.
13. R. A. Torres, T. Lovell, L. Noddleman et al., *J. Am. Chem. Soc.* **2003**, *125*, 1923–1936.
14. (a) R. H. Holm, *Pure Appl. Chem.* **1995**, *67*, 217–224. (b) C. L. Drennan, J. W. Peters, *Curr. Opin. Struct. Biol.* **2003**, *13*, 220–226.
15. (a) R. R. Eady, *Coord. Chem. Rev.* **2003**, *237*, 23–30. (b) B. J. Hales, Vanadium nitrogenase in *Nitrogenase and Chemical Models*. (Eds.: B. E. Smith, R. L. Richards, W. E. Newton), Kluwer, Amsterdam, 2004, pp. 255–279, chapter 10.
16. K. Schneider, A. Müller, Iron-only nitrogenase:exceptional catalytic, structural and spectroscopic features in *Nitrogenase and Chemical Models*. (Eds.: B. E. Smith, R. L. Richards, W. E. Newton), Kluwer, Amsterdam, 2004, pp. 281–307, chapter 11.
17. (a) M. Ribbe, D. Gadkari, O. Meyer, *J. Biol. Chem.* **1997**, *272*, 26627–26633. (b) D. Gadkari, Superoxide dependant nitrogenase in *Nitrogenase and Chemical Models*. (Eds.: B. E. Smith, R. L. Richards, W. E. Newton), Kluwer, Amsterdam, 2004, pp. 309–332, chapter 12.
18. (a) J. B. Howard, D. C. Rees, *Chem. Rev.* **1996**, *96*, 2965–2982. (b) O. Einsle, F. A. Tezcan, S. L. A. Andrade et al., *Science* **2002**, *297*, 1696–1700. (c) F. A. Tezcan, J. T. Kaiser, D. Mustaphi et al., *Science* **2005**, *309*, 1377–1380. (d) T.-C. Yang, N. K. Maeser, M. Laryukhin et al., *J. Am. Chem. Soc.* **2005**, *127*, 12804–12805.
19. Y. Ohki, Y. Sunada, M. Honda et al., *J. Am. Chem. Soc.* **2003**, *125*, 4052–4053.
20. (a) C. J. Pickett, K. A. Vincent, S. K. Ibrahim et al., *Chem. – Eur. J.* **2003**, *9*, 76–87. (b) F. Barrière, M. C. Durrant, C. J. Pickett, Chemical Models, Theoretical calculations, and the reactivity of isolated Iron-Molybdenum cofactor. in *Nitrogenase and Chemical Models*. (Eds.: B. E. Smith, R. L. Richards, W. E. Newton), Kluwer, Amsterdam, 2004, chapter 7, pp. 161–199.
21. S. C. Lee, R. H. Holm, *Proc. Natl. Acad. Sci. U.S.A.* **2003**, *100*, 3595–3600.
22. R. H. Holm, E. D. Simhon, Molybdenum-Tungsten-Iron-Sulfur chemistry: Current status and relevance to the Native Cluster

- of Nitrogenase in *Molybdenum Enzymes*. (Ed.: T. G. Spiro), Wiley, New York, 1985, pp. 1–87. (b) R. H. Holm, *Adv. Inorg. Chem.* **1992**, *38*, 1–71. (c) D. Coucouvanis, S. M. Malinak, *Prog. Inorg. Chem.* **2001**, *49*, 599–662.
23. R. E. Palermo, R. Singh, J. K. Bashkin et al., *J. Am. Chem. Soc.* **1984**, *106*, 2600–2612. (b) F. Barrière, D. J. Evans, D. L. Hughes et al., *J. Chem. Soc., Dalton Trans.* **1999**, 957–964. (c) D. V. Fomitchev, C. C. McLaughlan, R. H. Holm, *Inorg. Chem.* **2002**, *41*, 958–966.
24. (a) R. Cammack, *Nature* **1999**, *397*, 214–215. (b) C. Tard, X. Liu, S. K. Ibrahim et al., *Nature* **2005**, *433*, 610–613.

22

Electrochemistry of Isopoly and Heteropoly Oxometalates

*Bineta Keita and Louis Nadjo
Laboratoire de Chimie Physique, Université Paris-Sud, Orsay Cedex,
France*

22.1	Introduction	611
22.1.1	Definitions	611
22.1.2	General Properties, Literature, and Topics Covered	611
22.2	A simplified Overview of the Formation of POMs	614
22.3	Fundamental Redox Mechanisms of POMs at Electrodes	615
22.3.1	Electrochemical Reductions of Selected Plenary POMs: α -[SiW ₁₂ O ₄₀] ⁴⁻ , α -[PW ₁₂ O ₄₀] ³⁻ , α -[P ₂ W ₁₈ O ₆₂] ⁶⁻ , and α -[H ₂ W ₁₂ O ₄₀] ⁶⁻	616
22.3.1.1	Aqueous Media	616
22.3.1.2	Nonaqueous and Mixed Solvents	619
22.3.2	Quinone/hydroquinone-like Behaviors in the First Several Reduction Waves of POMs	623
22.4	Selected Achievements that Illustrate the Basic Behaviors of Plenary POMs at Electrodes	625
22.4.1	Heterogeneous One-electron Exchange of α -[SiW ₁₂ O ₄₀] ⁴⁻ in Dimethylformamide	625
22.4.2	The Reduction Potential of the One-electron Wave and the Role of the Central Heteroatom	626
22.4.3	Isomerization upon Reduction	626
22.4.4	POM-solvent Interactions as Probed by the Redox Potentials of Two POMs	627
22.4.5	Structure of Electrolyte Solutions As Probed by the Electrochemical Behaviors of POMs	629
22.4.6	Cation and Pressure Effects on the Electrochemistry of 12-Tungstocobaltate and 12-Tungstophosphate Ions in Acidic Aqueous Solution	630

22.5	Mixed Addenda and Other Substituted POMs	632
22.5.1	Comparison of Valence Trapping in Uniform and Mixed Addenda Plenary POMs	632
22.5.2	Lacunary and Transition Metal–substituted POMs	635
22.5.2.1	Lacunary POMs	635
22.5.2.2	Transition Metal–monosubstituted POMs	637
22.5.2.3	An Interesting Case of Mixing up of Substituent and Tungsten Waves: α_1 - and α_2 -[Fe ^{III} (OH) ₂ P ₂ W ₁₇ O ₆₁] ⁷⁻	646
22.5.3	Sandwich-type POMs	649
22.5.3.1	Electron Transfer Behaviors of Multi-iron Sandwich-type POMs	649
	Ion-pairing:	653
	pH Effects:	654
	Diferric and Triferric Sandwich-type Complexes:	655
	Mixed-Metal Sandwich-type Complexes:	656
22.5.3.2	Electrochemical Probing of Siderophoric Behavior in Sandwich-type Multi-iron Wells–Dawson Heteropolytungstates	658
22.6	Recent Developments	660
22.6.1	Electrochemistry of a New Family of Wells–Dawson Anions: Semivacant Tungstophosphates and Arsenates [H ₄ XW ₁₈ O ₆₂] ⁷⁻ (X = P or As)	660
22.6.1.1	Evidence for an Influence of the Dissymmetry on the Voltammetric Behavior of PW ₁₈ : Comparison with P ₂ W ₁₈	660
22.6.2	Recent Achievements in Apparently Direct Multiple Electron Transfers on the First Waves of POMs	662
22.6.2.1	Electrochemistry of the Multi-nickel Polyoxoanions [Ni ₆ As ₃ W ₂₄ O ₉₄ (H ₂ O) ₂] ¹⁷⁻ , [Ni ₃ Na(H ₂ O) ₂ (AsW ₉ O ₃₄) ₂] ¹¹⁻ , and [Ni ₄ Mn ₂ P ₃ W ₂₄ O ₉₄ (H ₂ O) ₂] ¹⁷⁻	664
22.6.2.2	Electrochemistry of the Iron(III)-substituted Keggin Dimer, [Fe ₆ (OH) ₃ (A- α -GeW ₉ O ₃₄ (OH) ₃) ₂] ¹¹⁻	667
22.6.3	Theoretical Approaches	667
22.6.3.1	Electronic Structures of POMs Explain their Redox Behaviors and the Relative Stability of Reduced Forms	667
22.6.3.2	An Extended Hückel Calculations Approach to a Qualitative Understanding of the Initial Electron Transfer Site in Dawson-type POMs	668
22.7	Electrocatalysis	672
22.7.1	Basic Concepts of Homogeneous Catalysis of Electrode Reactions	672
22.7.2	Selected Electrocatalysis in Homogeneous Solution	673
22.7.2.1	Electrocatalytic Reductions	674
22.7.2.1.1	Electrocatalytic reduction of nitrite and nitrate	675
	Studies with [{Cu ^{II} (H ₂ O)} ₂ Cu ^{II} ₂ (X ₂ W ₁₅ O ₅₆) ₂] ¹⁶⁻ (abbreviated in the following as Cu ₄ X ₄ W ₃₀ with X = P or As)	675

Cooperative effect of Mn- and Fe-centers within $Mn_2Fe_2P_4W_{30}$ in the electrocatalytic reduction of nitrite	676
Evaluation of the behaviors of $Ni_3P_2W_{18}$, $Ni_4Mn_2P_3W_{24}$, $Ni_6As_3W_{24}$, and $Fe_6Ge_2W_{18}$ in the electrocatalytic reduction of nitrate and nitrite	678
22.7.2.1.2 Electrocatalytic Reduction of Dioxygen and Hydrogen Peroxide	680
Electrocatalytic reduction of dioxygen in the presence of α_2 - $P_2W_{15}Mo_2Cu$	680
Reduction of dioxygen and hydrogen peroxide by $Cu_4X_4W_{30}$ (X = P or As)	684
Electrocatalytic reduction of dioxygen and hydrogen peroxide in the presence of $Mn_2Fe_2X_4$ (X = P or As)	685
22.7.2.2 Electrocatalytic Oxidations	687
22.7.2.2.1 $[Ru^{III}(H_2O)PW_{11}O_{39}]^{4-}$ and $[Ru^{III}(H_2O)SiW_{11}O_{39}]^{5-}$ as an Electrochemical Oxygen Transfer Catalysts	687
22.7.2.2.2 α - $[Cr^{III}(H_2O)PW_{11}O_{39}]^{4-}$ and α_2 - $[Cr^{III}(OH_2)P_2W_{17}O_{61}]^{7-}$ as Oxygen Transfer Catalysts in Electrochemistry	687
22.7.2.2.3 A Detailed Study of $K_n[Mn^{II}(OH_2)SiW_{11}O_{39}]^{(6-n)-}$ as Oxidation Electrocatalyst	689
22.7.2.2.4 Catalytic Oxidation of NAD(P)H: A Continuously Improved Selection of Suitable POMs	690
22.8 Conclusion	695
Acknowledgment	695
References	695

22.1 Introduction

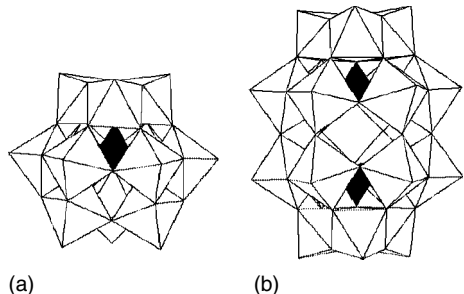
22.1.1 Definitions

Polyoxometalates (POMs for convenience) constitute a unique class of molecular metal-oxygen clusters, remarkable in several respects: the multitude of their properties based on their sizes, shapes, charge densities, and reversible redox potentials, and their enormous diversity of structures. Even though there are metal oxide clusters that are neutral or cationic, the present text will adopt the simplified view that most POMs are anionic structures constituted of early transition-metal elements in their highest oxidation state, hence their usual designation as early transition-metal-oxygen-anion clusters. These atoms in positive oxidation state constitute the so-called addenda atoms. Condensation of MO_6 octahedra, mostly with $M^{z+} = \text{W}^{6+}$, Mo^{6+} and V^{5+} , gives isopolyanions or isopoly compounds. Heteropolanions are obtained when a large number of MO_6 octahedra are condensed with a much smaller proportion of another atom in positive oxidation state (the so-called heteroatom). In the following text, POM will be kept as the general term, but these other designations might also be used

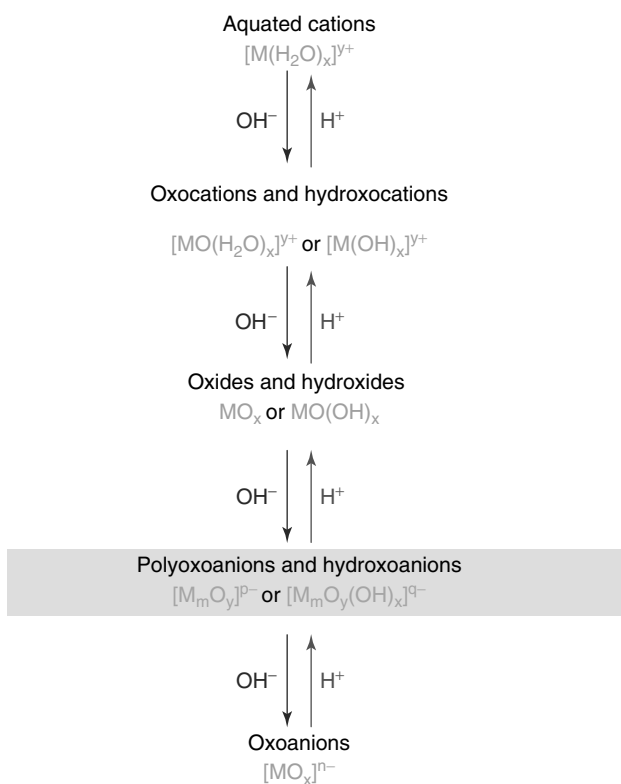
occasionally. The structures of the vast majority of POMs studied in electrochemistry are primarily derived from the Keggin structure and the Dawson structure. These two basic precursor structures are sketched in Sch. 1. POMs of these groups are characterized by the M/X ratio, where M designates the addenda atom and X the heteroatom. The Keggin structure belongs to the 12/1 series and the Dawson structure to the 18/2 series.

22.1.2 General Properties, Literature, and Topics Covered

The interest in the redox, catalytic, and electrocatalytic properties of unsubstituted and substituted polyoxometalates arouses much attention [2–15] because they are a versatile family of molecular metal-oxide clusters with applications in catalysis as well as in medicine and material science. Such versatility must be traced to at least two main characteristics. First, the size and mass of these unique molecular oxides place their solution chemistry in an intermediate position between small molecule solution chemistry and infinite lattice solid-state chemistry. Second, their redox behaviors may be very flexible and finely tuned on purpose, by changing smoothly their composition, with a



Scheme 1a Polyhedral representations of prototypical (A) Keggin ($\alpha\text{-XW}_{12}\text{O}_{40}^{n-}$) and (B) Wells–Dawson ($\alpha\text{-X}_2\text{W}_{18}\text{O}_{62}^{n-}$) anions (taken from Ref. 1).



Scheme 1b Formal sequence of hydrolysis reactions linking metal cations, oxyions, and polymeric oxides (adapted from Ref. 4).

tremendously diverse variety of structures [6].

Keeping first with unsubstituted POMs, their oxidized forms may only accept electrons; in contrast, their reduced forms,

owing to their electron and proton transfer and/or storage abilities, may behave as donors or acceptors of several electrons while maintaining their structure. In this series, most POMs may be considered

as close mimics of mixed-metal oxides and therefore, be studied as their soluble analogs, at least as regards their catalytic properties in photochemistry and electrochemistry. As a consequence, extensive attention was exercised to their acidity and redox capabilities as oxidation catalysts in heterogeneous vapor phase catalysis, and more recently, in homogeneous phase catalysis [7]. An enlightening example is the comparative study of POMs and semiconductor metal oxides as catalysts in the photochemical oxidative degradation of thioethers that demonstrates that POMs remain active even under anaerobic conditions [16].

Turning now to the ability of unsubstituted POMs to generate lacunary species and then metal cation-substituted derivatives, it appears that a virtually enormous family of compounds might result. The impetus for their study was triggered by the seminal remark of Baker [17] that mono-substituted POMs can be considered as the analogs of metalated porphyrins and used in catalytic processes with the advantage, relative to their organic counterparts, of thermal stability, robustness, and inertness toward oxidizing environments.

The foregoing remarks suggest strongly that electrochemistry should be an invaluable technique to study several aspects of POMs properties. Following the pioneering work of Souchay who demonstrated that polarography is suitable for the study of oxometalate solutions, electrochemical techniques are now extensively used in diverse directions: distinguish between isopoly and heteropoly anions and even between two isomers by establishing appropriate fingerprints; follow the kinetics of transformation of most of these compounds or establish potential-pH diagrams; establish reaction mechanisms; study electron transfer processes, catalytic

and electrocatalytic pathways, and so on. Among remarkable results, electrochemical reduction avoids secondary reactions like the exchange of some elements of the oxometalate with those of the reducing agent. For instance, in the reduction of molybdic species by SnCl_2 , substitution of Mo by Sn was observed [18]. Electrochemistry allows sequential additions of electrons and allows to demonstrate that the reduced species, most of which, but by no means all, are intensely blue (and henceforth named *heteropolyblues*, HBP), are stable in a larger pH domain than the oxidized forms and that this domain extends toward more alkaline pH values as the number of added electrons increases [19–23].

In short, most work on POMs address primarily their pH of formation, the stability of the various complexes with emphasis on their analytical properties, homogeneous catalysis, radiochemical, and photochemical behaviors. All these properties have been described in a series of excellent reviews, which usually include short developments on their electrochemistry and redox catalysis properties [2–9, 24–28]. The reader is referred to these reviews for general descriptions of POMs synthesis, structures, and reactivity. Among these reviews, particular attention is drawn to those few containing substantial developments on electron transfer behaviors and the electrochemistry of POMs [2, 4, 5, 7–9, 24–28].

In the present chapter devoted to the electrochemistry of POMs, our purpose is not to provide an exhaustive review of all the papers in which some electrochemical aspects of POMs intervene, but rather to emphasize the fundamental principles that govern the vast majority, if not all, of the electron transfer behaviors of these chemicals at electrodes and help to explain their electrocatalytic properties. As

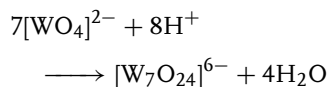
a consequence, illustrative examples will be selected. Details not necessary to establish the mechanisms will be omitted or not commented and can be found in the original papers. The reader is referred to exhaustive reviews and to the current literature for these particular details. Therefore, in addition of seminal papers, particular attention is exercised toward the literature covering the period from 1996 to 2004 to provide a satisfactory overlap with the two following reviews: (1) a 1998 review [8] devoted to the properties of POMs as electrocatalysts; (2) a development in Volume 10 of the present series that considers the electrocatalysis with POMs attached to electrode surfaces [9]. Therefore, the examples selected in the following text will highlight the molecular aspects of the electrochemistry of POMs in solution.

22.2 A simplified Overview of the Formation of POMs

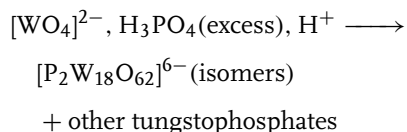
Although POMs have been known for about 200 years [6d,e,f] a large number of novel polyoxoanions with unexpected shapes and sizes are still being discovered. However, despite this diversity that precludes from complete rational and systematic design of synthesis for all POMs, a few guidelines can be retained. For specific details, the reader is referred to books, reviews, and original papers [3–7, 27]. Primarily, the evolution of aquated metal cations in aqueous solution depends on the pH of the medium, going from the hydrated cation $[M(H_2O)_x]^{n+}$, viable in very acidic medium, to the oxoanion $[MO_x]^{n-}$ obtained in very basic solution (see Sch. 1b). The route between these two extremes is populated by a series of more or less stable oxocations and hydroxocations,

oxides and hydroxides, and finally polyoxoanions and hydroxoanions, which are the focus of our study.

More specifically, acidification of $[MO_x]^{n-}$ oxoanion-containing solutions in appropriate experimental conditions (pH, concentration, temperature...) results in polycondensation of these oxoanions to build up large and eventually giant anionic species, the so-called Polyoxoanions or Polyanions (POMs). Such assemblies are known with transition metals in high oxidation states, among which the d° states of vanadium, molybdenum, and tungsten are the most common ones. Polycondensation of the same oxoanion gives an Isopolyoxoanion $[M_mO_y]^{p-}$. The structures can be viewed as the association of tetrahedral $[MO_4]$ (mainly vanadium) and/or octahedral $[MO_6]$ groups sharing corners, edges, and/or faces. As an example, paratungstate $[W_7O_{24}]^{6-}$ is synthesized by acidification of tungstate solutions according to the stoichiometry:



When polycondensation of these “ad-denda atoms” is carried out in the presence of another oxoanion containing an “heteroatom” X, an Heteropolyanion is obtained, formulated as $[X_xM_mO_y]^{q-}$. X belongs usually to the main group elements (B, Si, Ge, P, As, ...) but can also be a metal.



The two foregoing examples illustrate the variability of experimental conditions and suggest the necessity of further

specific conditions for isolation of a pure sample of the desired POM.

Usually, addition of an appropriate counterion, commonly an alkali metal, ammonium, or tetraalkylammonium permits the isolation of the polyanion. Lithium and sodium salts are generally more water-soluble than those of the larger cations. In contrast, salts of alkylammonium and similar cations are insoluble in water but can be recrystallized from several nonaqueous solvents.

POMs can be viewed as assemblies of discrete fragments of oxides with definite sizes and shapes. These assemblies represent usually thermodynamically stable arrangements, even though their formation, especially in the case of polytungstates, is rather under kinetic control [3]. Most of them keep their identity in aqueous and nonaqueous solutions.

In short, the mechanism of formation of POMs is far from well understood and commonly proposed descriptions as self-assembly are rather elusive. Only syntheses in aqueous solutions are briefly outlined. Actually, successful POM formations in nonaqueous media were also described, without any deeper insight into the reaction pathways. Therefore, attempts at rationalization of the hitherto mysterious equilibria that generate polyoxometalates are necessary so that, eventually, straightforward syntheses of novel species might be designed. In contrast, a better knowledge exists as regards the transformation mechanisms of a POM into another one or the partial degradation pathways of a POM. As a matter of fact, rational stereospecific methods of synthesis of substituted POMs were developed starting from appropriate lacunary species [3, 4, 6a,b].

Finally, a survey of the literature confirms the evolution of such systems to be controlled by numerous, apparently

insignificant, parameters. For instance, the sequence of adding reagents might be important [4]. It was also shown that the concentration of a counterion like Na^+ plays an important role in the evolution of a system apparently as "simple" as the hydrolysis of molybdate in aqueous medium [5].

The above considerations show that the rational synthesis and structural characterization of new POMs remain a challenge. Nevertheless, the potentially attractive catalytic properties of such species are a strong motivation to undergo this kind of research.

22.3

Fundamental Redox Mechanisms of POMs at Electrodes

The possibilities of POMs compositions and structures are virtually enormous, and the number of these molecules actually prepared and characterized continues to grow unabated. However, examination of their short electrochemical studies, which are becoming a usual part of their characterization, shows that a limited selection of representative groups of POMs is sufficient for a description of the main electrochemical behaviors of this class of chemicals. Therefore, α -Keggin- and Dawson-type heteropolyanions of phosphotungstate, silicotungstate, phosphomolybdate, and silicomolybdate; mixed addenda heteropolyanions, and transition-metal substituted heteropolyanions including sandwich-type derivatives were selected for the present article.

Unless otherwise stated, most studies were performed by cyclic voltammetry with freshly polished glassy carbon working electrode (GC) and a saturated calomel reference electrode (SCE).

22.3.1

Electrochemical Reductions of Selected Plenary POMs: $\alpha\text{-[SiW}_{12}\text{O}_{40}]^{4-}$, $\alpha\text{-[PW}_{12}\text{O}_{40}]^{3-}$, $\alpha\text{-[P}_2\text{W}_{18}\text{O}_{62}]^{6-}$, and $\alpha\text{-[H}_2\text{W}_{12}\text{O}_{40}]^{6-}$

When no confusion is possible, these POMs will be abbreviated as SiW₁₂, PW₁₂, P₂W₁₈, and H₂W₁₂ respectively

22.3.1.1 Aqueous Media

A first point of concern is the knowledge of the pH domain where the molecule under scrutiny is stable. For these classical POMs, such domains were determined and found to be shifted to more alkaline pH values as the number of added electrons increases [19–23]. H₄SiW₁₂O₄₀, H₃PW₁₂O₄₀, and H₆P₂W₁₈O₆₂ are known as *strong acids in aqueous solutions*, presumably with a uniform acidity [29]. In addition, each reduction step increases the negative charge density on the

POMs and hence, their basicity. Therefore, the electrochemical observations are anticipated to depend on the acidity functions of the various classical mineral acids, HClO₄, H₂SO₄, and HCl, used as supporting electrolytes.

In their usual pH domains of stability, starting from low to high pH values, the electrochemistry of the three heteropolyanions, SiW₁₂, PW₁₂, P₂W₁₈, shows at least two successive one-electron waves followed eventually by multielectron waves [4, 30]. This observation is consistent with the very strong acidity of these POMs [29], even in the solid state as demonstrated for H₄SiW₁₂O₄₀ and H₃PW₁₂O₄₀ [31]. Even though a two-electron reduction on the first wave of H₄SiW₁₂O in solutions more concentrated than 5 M HCl was occasionally mentioned [32], only recently was this possibility of apparently direct two-electron reductions on the first waves of these POMs generalized and

Tab. 1 Reduction peak potentials (E_{pc}) vs. SCE and anodic-to-cathodic peak separations (ΔE_p) for 10⁻³ M $\alpha\text{-K}_6\text{P}_2\text{W}_{18}\text{O}_{62}$ with various hydrochloric acid concentrations in water^a (taken from Ref. 33c)

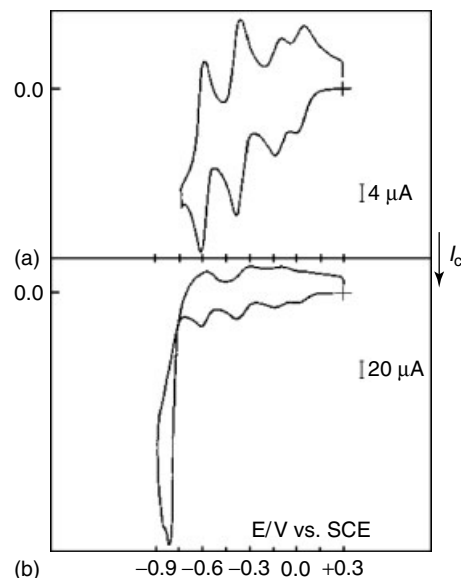
Medium	$n_{app.}^b$ ($n_{corr.}$)	$-E_{pc_1}^c$ [mV]	ΔE_{p_1} [mV]	$-E_{pc_2}$ [mV]	ΔE_{p_2} [mV]	$-E_{pc_3}$ [mV]	ΔE_{p_3} [mV]	$-E_{pc_4}$ [mV]	ΔE_{p_4} [mV]	$-E_{pc_5}$ [mV]
1 M HCl	1 (1.0)	−5	55	135	50	380	30	610	25	805
2 M HCl	1.06 (1.08)	−5	55	125	50	365	30	595	25	~800
3 M HCl	~ −5			115		345	30	565	20	~780
4 M HCl	~ −5			90		330	30	550	20	
Medium	$n_{app.}^b$ ($n_{corr.}$)	$-E_{pc_1}^c$ [mV]		ΔE_{p_1} [mV]	$-E_{pc_2}$ [mV]	ΔE_{p_2} [mV]	$-E_{pc_3}$ [mV]	ΔE_{p_3} [mV]	$-E_{pc_4}$ [mV]	
6 M HCl	1.40 (1.54)	65		100		290	25	515	20	~750
8 M HCl	1.50 (1.73)	35		60		275	25	495	20	~725
12.4 M HCl	1.54 (1.96)	−5		30		240	25	460	20	650

^aMissing values correspond to very ill-defined patterns. The potential sweep rate is 100 mV s^{−1}.

^b $n_{app.}$ is the apparent electron number for the first voltammetric wave, $n_{corr.}$ is the same value corrected for viscosity effects.

^cWhen the two first waves are merged, the new numbering of waves is obvious.

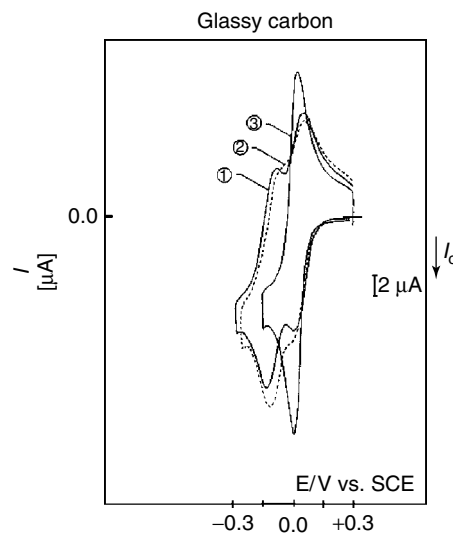
Fig. 1 Cyclic voltammetry pattern at a glassy carbon electrode (GC Tokai, Japan) with 10^{-3} M α -K₆P₂W₁₈O₆₂ in 1 M HCl supporting electrolyte. Sweep rate: 100 mV s⁻¹; electrode surface area: 0.07 cm²; (a) voltammetric pattern restricted to the four first waves of [P₂W₁₈O₆₂]⁶⁻; (b) the whole voltammetric pattern showing ill-defined reoxidation peaks on potential reversal (taken from Ref. 33c).



studied systematically [33b,c]. The results for P₂W₁₈ are the most complete because, among the three POMs, this molecule turned out to be the most soluble up to the highest acid concentrations. Table 1 summarizes the quantitative parameters associated with the cyclic voltammograms of 10^{-3} M P₂W₁₈ dissolved in various HCl concentrations in water. Figures 1 through 3 illustrate the main evolutions of these CVs. Figure 1(a) shows the CV obtained in 1 M HCl. Four waves appear, with electrons numbers being 1:1:2:2. It was demonstrated previously that six electrons could be added to P₂W₁₈ and reversibly removed [33, 34].

Figure 1(b) shows that scanning the potential up to the fifth wave complicates the voltammetric pattern. In the following, the pattern is restricted to a potential domain in which no undesirable derivatization of the electrode surface was observed [28]. For this acid concentration and

Fig. 2 Evolution of the cyclic voltammetry pattern with hydrochloric acid concentration in water with 10^{-3} M α -K₆P₂W₁₈O₆₂. The figure is restricted to the merging process of the first two waves. Curve 1: 1 M HCl; Curve 2: 3 M HCl; Curve 3: 12.4 M HCl. Sweep rate: 100 mV s⁻¹; electrode surface area: 0.07 cm² (taken from Ref. 33c).



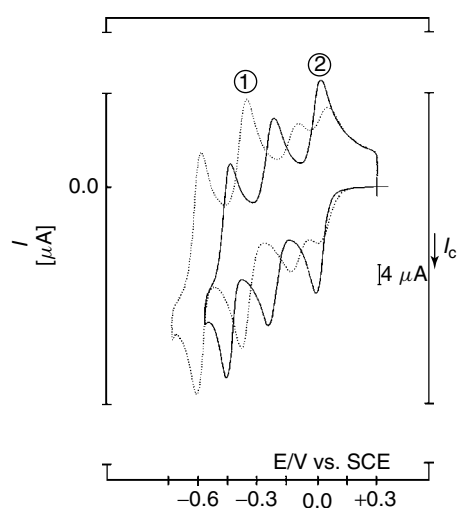


Fig. 3 Final voltammetric pattern obtained with 10^{-3} M α -K₆P₂W₁₈O₆₂ in 12.4 M HCl (Curve 2) from the set of four waves (Curve 1) observed in 1 M HCl. Sweep rate: 100 mV s⁻¹; electrode surface area: 0.07 cm² (taken from Ref. 33c).

with a potential scan rate of 100 mV s⁻¹, the anodic-to-cathodic peak separations quoted in Table 1 fit the 1:1:2:2 electron numbers. The corresponding waves may feature diffusion-controlled processes. This conclusion was checked to be true for the first reduction process. The evolution of the voltammetric pattern when the hydrochloric acid concentration increases is described by Table 1 and sketched in Fig. 2. Already at 2 M HCl, all the waves move in the positive potential direction, except for the first one that remains at its initial potential location. This evolution continues with increasing concentrations of HCl until the first and the second waves are practically merged into a broad composite wave at 6 M HCl for potential scan rates between 20 mV s⁻¹ and 500 mV s⁻¹. For the sake of simplicity and continuity, this combined wave is renumbered 1 as it is clear from Table 1. In more and more acidic solutions, the peak current intensity of this composite wave grows larger and larger, while its reduction peak potential becomes less negative and the anodic-to-cathodic peak potential

difference decreases down to 30 mV in 12.4 M HCl. The final voltammetric pattern appears also on Fig. 2. At such high concentration of hydrochloric acid, the change in viscosity of the solution [33a] must be taken into account to demonstrate consistently that the wave has now the characteristics of an overall, apparently direct, two-electron transfer process. Figure 3 shows the final pattern of three waves in 12.4 M HCl, from the set of four initial waves in 1 M HCl of Fig. 1. The chemical reversibility of these two-electron waves is reminiscent of the electrochemical behaviors of quinone/hydroquinone systems in molecular electrochemistry and suggests the use of this unifying analogy, which is developed in the following.

The same kind of experiments was carried out with HClO₄. The observations in the two media parallel each other. At the same concentration of 4 M, HClO₄ is much stronger an acid than HCl, as the first two waves of P₂W₁₈ are already merged in the former medium while they are not in the latter. Concentrations of HClO₄ higher than 7 M could not be used, due to the very poor solubility of P₂W₁₈ in these media.

SiW₁₂ behaves in much the same way as P₂W₁₈ in perchloric acid. The final unique two-electron wave obtained in strongly acid solution from the initial set of two one-electron waves in 1 M HClO₄ is built-up by the same mechanism as observed for P₂W₁₈, which is the gradual positive potential shift of the second wave. It is also noted that the merging of the first

two waves of P_2W_{18} is complete at 4 M $HClO_4$ while it only begins for SiW_{12} . This observation supports the idea that the two-electron reduction product of P_2W_{18} is more basic than that of SiW_{12} . Results for other acids can be found in the original papers [33b,c,d].

PW_{12} turns out to be sparingly soluble in concentrated acid solutions. The first three waves feature 1:1:2 electron processes. On varying the perchloric acid concentration from 1 M to 4 M, the first two waves move to more negative potentials while the third one moves in the positive direction. The first wave goes from a value corresponding to one electron to 0.95 electron. This last value was corrected to 1.0 electron when taking into account the change in viscosity of the various media. The anodic-to-cathodic peak potential separation remains constant throughout. Higher concentrations of $HClO_4$ are precluded by the poor solubility of PW_{12} in these media. A concentration as high as 6 M has been possible for HCl. Much the same phenomena are observed as in $HClO_4$. In particular, the height of the first wave, corrected for viscosity effects, corresponds to one electron whatever the medium.

It thus appeared that coalescence of the first waves of P_2W_{18} or SiW_{12} could be achieved only in very high acidity media. A complete simulation of all these processes over the entire acidity range would require the input of a large number of parameters [35]. The merging of the third and fourth waves of P_2W_{18} upon increasing the acidity of the supporting electrolyte could only be simulated [35].

In contrast with the examples of P_2W_{18} and SiW_{12} , much more ordinary pH media were sufficient to obtain the coalescence of the first two one-electron waves of H_2W_{12} [35]. As a matter of fact, at pH above 4.0, the initial reduction processes of H_2W_{12}

involve two successive one-electron waves with their potentials independent of pH. Figure 4 shows the voltammetric behavior of 10^{-3} M H_2W_{12} solutions in the pH range 2–7 in aqueous NaCl (0.5 M). When the pH decreases below 4.0, the second wave diminishes in intensity while the first one increases. The evolution of the voltammetric pattern appears in Fig. 4.

Typically, a single wave is observed at pH = 3.4. This gradually sharpens and below pH 3.2 begins to move to more positive potentials as the pH is decreased. At pH 1.1, the anodic-to-cathodic peak potential separation is 55 mV, consistent with a chemically reversible two-electron process comprising two unresolved one-electron events. The whole evolution could be simulated, on the basis of the following scheme and on an established program (DIGISIM V 2.0 and partly 2.1, Bioanalytical Systems, West Lafayette, IN) in which unknown parameters are adjusted. The relevant parameters are gathered in Table 2 and the corresponding voltammograms are represented by dots in Fig. 4. The hypotheses and adjustments necessary to achieve a satisfactory simulation of the case of H_2W_{12} indicate the difficulty of the task in more sophisticated media. Nonetheless, the achievement is important as a quantitative support of the more general classical nine-member box scheme that summarizes the possible intermediates for all two-electron two-proton reactions such as the quinone/hydroquinone systems. This general scheme that applies in a wide variety of experimental conditions will be discussed after examination of electron transfer behaviors of the same plenary POMs in other solvents and mixed solvents.

23.3.1.2 Nonaqueous and Mixed Solvents

Nonaqueous solvents and their mixtures with various amounts of water are

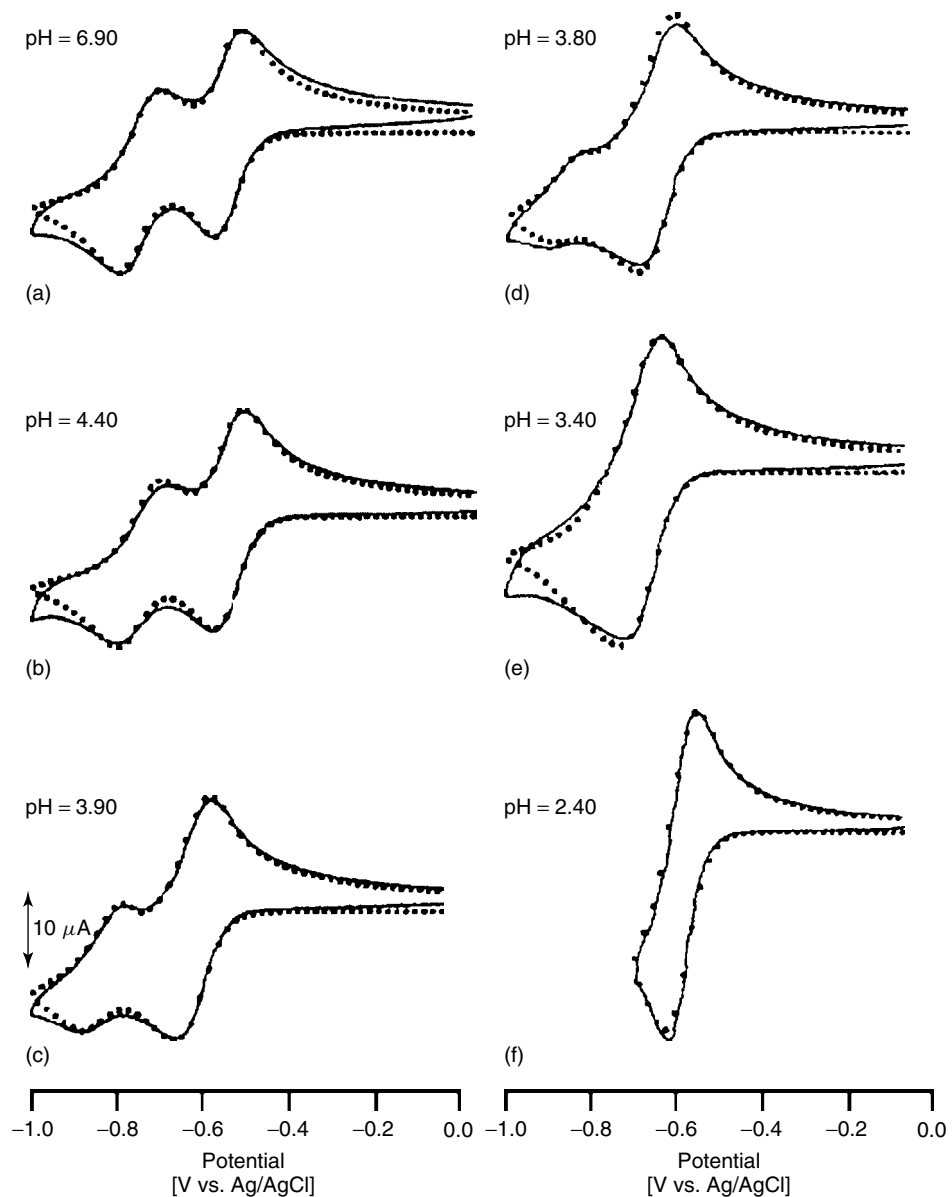


Fig. 4 Cyclic voltammograms of solutions of $(\text{NH}_4)_6[\text{H}_2\text{W}_{12}\text{O}_{40}]$ (1 mM) in aqueous NaCl (0.5 M); $v = 100 \text{ mV s}^{-1}$; full line: experiment; dotted line: simulation (taken from Ref. 35).

interesting because they may promote ion-pairing of oxidized and/or reduced forms of POMs with small cations such as H⁺, Li⁺, and Na⁺, and thus orient

the reduction pathways observed for these molecules. These behaviors must be traced both to the basicity of these solvents and also to their permittivity [33, 36–39].

Tab. 2 Parameters for simulation of cyclic voltammetry of 1 mM solution of $[H_2W_{12}O_{40}]^{6-}$ in aqueous NaCl (0.5M)

	$[H_2W_{12}O_{40}]^{6-}$		
Couple	$0'/1'$	$1'/2'$	$1'h/2'h$
$E'_{1/2}$, mV	-555	-755	-585
ΔE_p , mV	72	101	
Protonic equil.	$K_{1'h}$ 2.8×10^3	$K_{2'h}$ 2.4×10^6	$K_{2'h_2}$ 3.0×10^3
Dispropn equil.	$21' \rightleftharpoons 0' + 2'$	$1' + 1'h \rightleftharpoons 0' + 2'h$	$21'h \rightleftharpoons 0' + 2'h_2$
Equil. const	4×10^{-4}	0.35	
Diffusion coeff.	D_{anion} $10^6 \text{ cm}^2 \text{s}^{-1}$	D_{H^+} 2.0	19

The action of H^+ from perchloric acid on the reduction of SiW_{12} , P_2W_{18} , and PW_{12} in DMF in the presence of 0.1 M lithium perchlorate is studied as a representative example [33b,33c]. Perchloric acid is known to be strong in DMF [36]. The evolution of the voltammetric pattern of 10^{-3} M $K_4SiW_{12}O_{40}$ (abbreviated as K_4SiW_{12}) is shown in Fig. 5. For clarity, the pattern in this figure is restricted to the evolution of the first one-electron wave of this salt in DMF + 0.1 M $LiClO_4$, upon stepwise addition of $HClO_4$. With the acid, a new wave appears, more positive than the previous one and grows at its expense when the acid concentration is raised. The evolution ends up in the formation of a two-electron wave.

Table 3 gives in more detail the evolution of the whole voltammetric pattern. The

first waves in the absence of acid are in electron ratios 1:1:2. Their smooth evolution upon perchloric acid addition ends up in a set of three new waves in electron ratios 2:2:4, the last value varying with the acid concentrations. Completely similar trends are obtained with 10^{-3} M $K_6P_2W_{18}O_{62}$ in DMF. Here again, a new wave appears on addition of acid, albeit at a smaller acid to POM ratio, underscoring the higher basicity and/or ion-pairing ability of P_2W_{18} compared with SiW_{12} . Again, PW_{12} behaves differently and the experiments could be started directly with

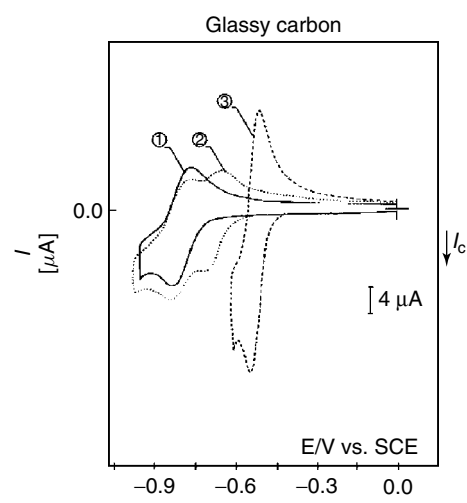


Fig. 5 Voltammetric pattern obtained with 10^{-3} M α - $K_4SiW_{12}O_{40}$ in DMF + 0.1 M $LiClO_4$ solution – Curve 1: in the absence of acid; Curve 2: with 2×10^{-3} M perchloric acid; curve 3: with 5×10^{-1} M $HClO_4$. The pattern is restricted to the evolution of the first wave observed in the absence of acid. Sweep rate: 100 mV s^{-1} ; GC electrode surface area: 0.07 cm^2 (taken from Ref. 33c).

Tab. 3 Reduction peak potentials (E_{pc}) versus SCE and anodic-to-cathodic peak separations (ΔE_p) for 10^{-3} M α -K₄SiW₁₂O₄₀ in dimethylformamide with various perchloric acid concentrations^a (taken from Ref. 33c)

[HClO ₄] mM	$n_{app.}^b$			$-E_{pc1}^c$ [mV]	ΔE_{p_1} [mV]	$-E_{pc2}$ [mV]	ΔE_{p_2} [mV]	$-E_{pc3}$ [mV]
0	1			840	75	1060	115	1320
[HClO ₄] mM	$n_{app.}^b$	$-E_{pc1}^c$ [mV]	ΔE_{p_1} [mV]	$-E_{pc2}$ [mV]	ΔE_{p_2} [mV]	$-E_{pc3}$ [mV]	ΔE_{p_3} [mV]	$-E_{pc4}$ [mV]
2	~0.90	720	60	845	70	~1030		1315
4	1.34	715	75	~850		~1030		~1250
5	1.56	705	75	~850		~1030		~1200
6	1.63	700	75	~855	~75	~1040		~1175
8	1.69	680	65	~855	~90	~1070		
10	1.74	670	60	~835	~80	~1070		
20	1.81	645	50	775	60	~1040		~1170
40	1.85	615	45	735	50	~1000		~1170
100	1.85	595	45	705	45	~1000		
500	1.79	545	35	655	40	~920		
1000	1.72	525	30	650	30	900	30	~1050

^aThe solvent contains 0.1 M LiClO₄ for all the solutions. The potential sweep rate is 100 mV s⁻¹; missing values correspond to very ill-defined patterns.

^b $n_{app.}$ is the apparent electron number for the first voltammetric wave.

^cWhen a new wave appears, the renumbering of waves is obvious.

its acidic form. Up to 4 M HClO₄, the first two one-electron waves of PW₁₂ remain monoelectronic throughout.

Such effect of small cations on the voltammetric behaviors of α -[SiMo₁₂O₄₀]⁴⁻ and α -[PMo₁₂O₄₀]³⁻ in acetone and acetonitrile was investigated recently [37]. For the α -[SiMo₁₂O₄₀]⁴⁻ complex, the presence of Li⁺ or Na⁺ caused the one-electron wave to be converted into a two-electron wave at ca. 0.3 V more positive than the first one-electron wave. In the presence of Li⁺ or Na⁺, the α -[PMo₁₂O₄₀]³⁻ complex underwent a two-electron reduction at the same potential as the original first one-electron wave in CH₃COCH₃, whereas it exhibited only successive

one-electron waves in CH₃CN. The addition of a trace amount of H⁺ produced new two-electron waves at more positive potentials. These observations were rationalized by considering both the greater basicity of CH₃COCH₃ compared to that of CH₃CN (Donor Number DN: CH₃CN, 14.1; CH₃COCH₃, 17.1) [38] on the one hand and the greater relative permittivity of CH₃CN ($\epsilon_r = 35.9$) than CH₃COCH₃ ($\epsilon_r = 20.7$) [39]. An even more striking solvent and small cations effect could be demonstrated for the 18-molybdodiphosphate complex [(P₂O₇)Mo₁₈O₅₄]⁴⁻ that contains [P₂O₇]⁴⁻ as heteroion [40]. Unlike the usual Dawson complexes that consist of two A-type XM₉ units (X = S, P, As),

the $[(\text{P}_2\text{O}_7)\text{Mo}_{18}\text{O}_{54}]^{4-}$ complex has a structure based on two B-type PMo_9 fragments. For this molecule, the presence of small cations such as H^+ , Li^+ , and Na^+ caused one-electron wave to be converted into four- and two-electron waves in a complex manner. With the addition of a trace amount of H^+ , a four-electron reduction wave was obtained in solvents of weaker basicity like acetone, acetonitrile, or propylene carbonate; the relative permittivity does not affect the appearance of the four-electron wave. Two-electron waves were obtained in solvents of stronger basicity like *N,N*-dimethylformamide (DMF), *N,N*-dimethylacetamide (DMA), and *N*-methylpyrrolidinone (NMP). With the addition of Li^+ or Na^+ , the one-electron waves were converted into two-electron waves only in acetone, indicating that the conversion can occur in solvents of both weak basicity and low relative permittivity. The interaction of Li^+ toward the reduced forms of the Dawson $[\text{S}_2\text{Mo}_{18}\text{O}_{62}]^{4-}$ polyoxometalate anion was interpreted in the same framework by considering this cation as a moderately strong Lewis acid [41]. In the 95:5 $\text{CH}_3\text{CN} + \text{H}_2\text{O}$ solvent mixture (0.1 M NBu_4ClO_4), the voltammetric behavior obtained upon

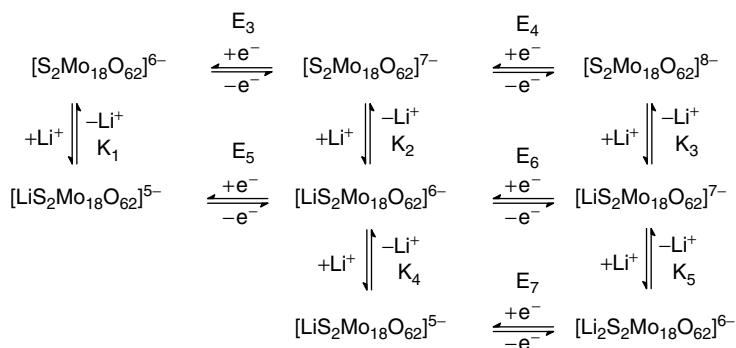
stepwise addition of Li^+ is analogous to that observed upon addition of HClO_4 [41b], except that Li^+ appears to act as a weaker acid than H^+ . Following experimental observations, it is assumed that $[\text{S}_2\text{Mo}_{18}\text{O}_{62}]^{4-}$ and its one-electron reduced species do not interact with Li^+ . Then, the various possibilities sketched in Sch. 2 involving an extensive series of reversible potentials and equilibrium constants could be simulated. Parameters used to simulate cyclic voltammograms are gathered in Table 4.

Phenomenologically, the reactions between reduced forms of $[\text{S}_2\text{Mo}_{18}\text{O}_{62}]^{4-}$ and Li^+ are analogous to those with H^+ , with acidity strength being in the order $\text{HClO}_4 > \text{LiClO}_4 > \text{H}_2\text{O}$. However, as this simulation involves a significant number of unknown parameters, the coherent set of data obtained cannot be assumed to be unique.

22.3.2

Quinone/hydroquinone-like Behaviors in the First Several Reduction Waves of POMs

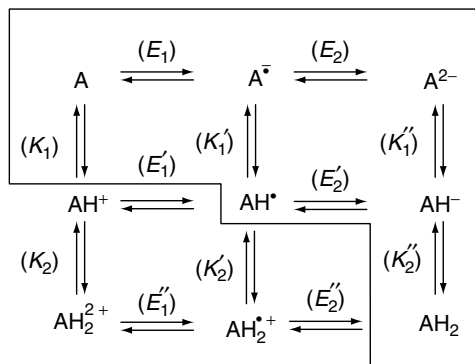
Whatever the solvent and the salt used as supporting electrolyte, it appears that the first several waves of POMs could be



Scheme 2 General scheme for the interaction of lithium cation with the reduced forms of $[\text{S}_2\text{Mo}_{18}\text{O}_{62}]^{6-}$ (Ref. 41a).

Tab. 4 (a) See Ref. 41a. (b) Diffusion coefficient used in the simulation was $1.4 \times 10^{-5} \text{ cm}^2 \text{ s}^{-1}$ for Li^+ and $6.4 \times 10^{-6} \text{ cm}^2 \text{ s}^{-1}$ for all polyoxo anions. (c) Reversible charge transfer process simulated by use of value of $10^{-4} \text{ cm s}^{-1}$ for the heterogeneous charge transfer rate constant (k_s) and 0.5 for the charge transfer (α). (d) Reversible conditions achieved by making the rate constant for both forward (k_f) and reverse (k_b) reaction of homogeneous chemical reactions extremely fast

Charge transfer reactions ^c	$E_{1/2} [\text{V}]$
$[\text{S}_2\text{Mo}_{18}\text{O}_{62}]^{4-} + \text{e}^- \rightleftharpoons [\text{S}_2\text{Mo}_{18}\text{O}_{62}]^{5-}$	-0.12
$[\text{S}_2\text{Mo}_{18}\text{O}_{62}]^{5-} + \text{e}^- \rightleftharpoons [\text{S}_2\text{Mo}_{18}\text{O}_{62}]^{6-}$	-0.11
$[\text{S}_2\text{Mo}_{18}\text{O}_{62}]^{6-} + \text{e}^- \rightleftharpoons [\text{S}_2\text{Mo}_{18}\text{O}_{62}]^{7-}$	-0.73
$[\text{S}_2\text{Mo}_{18}\text{O}_{62}]^{7-} + \text{e}^- \rightleftharpoons [\text{S}_2\text{Mo}_{18}\text{O}_{62}]^{8-}$	-0.91
$[\text{LiS}_2\text{Mo}_{18}\text{O}_{62}]^{5-} + \text{e}^- \rightleftharpoons [\text{LiS}_2\text{Mo}_{18}\text{O}_{62}]^{6-}$	-0.56
$[\text{LiS}_2\text{Mo}_{18}\text{O}_{62}]^{6-} + \text{e}^- \rightleftharpoons [\text{LiS}_2\text{Mo}_{18}\text{O}_{62}]^{7-}$	-0.67
$[\text{Li}_2\text{S}_2\text{Mo}_{18}\text{O}_{62}]^{5-} + \text{e}^- \rightleftharpoons [\text{Li}_2\text{S}_2\text{Mo}_{18}\text{O}_{62}]^{6-}$	-0.60
Chemical reactions ^d	K/M^{-1}
$[\text{S}_2\text{Mo}_{18}\text{O}_{62}]^{6-} + \text{Li}^+ \rightleftharpoons [\text{LiS}_2\text{Mo}_{18}\text{O}_{62}]^{5-}$	$10^1 (K_1)$
$[\text{S}_2\text{Mo}_{18}\text{O}_{62}]^{7-} + \text{Li}^+ \rightleftharpoons [\text{LiS}_2\text{Mo}_{18}\text{O}_{62}]^{6-}$	$5 \times 10^2 (K_2)$
$[\text{S}_2\text{Mo}_{18}\text{O}_{62}]^{8-} + \text{Li}^+ \rightleftharpoons [\text{LiS}_2\text{Mo}_{18}\text{O}_{62}]^{7-}$	$10^6 (K_3)$
$[\text{LiS}_2\text{Mo}_{18}\text{O}_{62}]^{6-} + \text{Li}^+ \rightleftharpoons [\text{Li}_2\text{S}_2\text{Mo}_{18}\text{O}_{62}]^{5-}$	$10^3 (K_4)$
$[\text{LiS}_2\text{Mo}_{18}\text{O}_{62}]^{7-} + \text{Li}^+ \rightleftharpoons [\text{Li}_2\text{S}_2\text{Mo}_{18}\text{O}_{62}]^{6-}$	$8 \times 10^3 (K_5)$



Scheme 3 Nine-member box scheme summarizing the possible intermediates for all two-electron, two-proton reactions (taken from Ref. 2).

considered to follow the same mechanistic scheme as quinones. As a representative example, H^+ will be selected as the active cation in the supporting electrolyte (Sch. 3).

$E_1, E_2, E'_1, E'_2, E''_1, E''_2$ are the normal potentials of the various redox couples

and $K_1, K_2, K'_1, K'_2, K''_1, K''_2$ are the acid dissociation constants.

It is assumed that $E_1 > E_2$. Then the actual reaction mechanism depends on the relative rates of proton and electron transfers [42–44]. The whole set of experimental results suggests clearly two main

reaction pathways, depending on the solvent. Taking SiW_{12} in water as an example, its second wave was found to shift to less negative potentials, the peak potential of its first wave remaining unchanged when the perchloric acid concentration was varied in the range 1–4 M. From 5–7 M perchloric acid concentration, this phenomenon continues, while the first wave now grows at the expense of the second one, conceivably due to the very close proximity of the redox potentials of the two couples [45–47]. Obviously, the behavior in water is consistent with a reaction mechanism in which the second electron transfer is followed by a protonation shifting in the positive potential direction of this step. This mechanism leads to the formation of an overall, apparently direct two-electron process. In the present case, an Electrochemical-Electrochemical-Chemical (EEC) pathway is followed. Nuances of this mechanism and/or thermodynamically equivalent pathways can be found and were described previously [42, 48].

In DMF, the appearance, upon addition of acid, of a new wave located at a more positive potential than the former first wave in the absence of acid suggests strongly that the preferred reaction pathway should feature a Chemical-Electrochemical-Electrochemical-Chemical pathway (CEEC) or Chemical-Electrochemical-Chemical-Electrochemical pathway (CECE). The foregoing considerations indicate, however, that determination of the kinetic parameters of the reaction, in water as well as in DMF, is a formidable task that, up to now, could be carried out only in selected experimental conditions.

All these considerations apply also to heteropolytungstates, with the general remark that they are more easily reduced than heteropolytungstates and that the

media where they are stable must be carefully selected.

22.4

Selected Achievements that Illustrate the Basic Behaviors of Plenary POMs at Electrodes

22.4.1

Heterogeneous One-electron Exchange of $\alpha\text{-}[\text{SiW}_{12}\text{O}_{40}]^{4-}$ in Dimethylformamide

The one electron exchange of $\alpha\text{-}[\text{SiW}_{12}\text{O}_{40}]^{4-}$ in dimethylformamide was studied with the aim to obtain a deeper insight into the formal analogy between quinones and POMs as regards their respective electron transfer kinetics [49]. In particular, it was of interest to check whether the simpler treatments of Marcus [50], commonly applied to quinoidic compounds [51], can be also applied to POMs to evaluate quantitative parameters of electron transfer kinetics. Cyclic voltammetry was used for this purpose. Important experimental details can be found in the original paper. Great care was exercised to collect experimental data without ohmic drop and without adsorption effects. Table 5 gathers the values of diffusion coefficients, heterogeneous rate constants k_s , collision number Z_{het} , free enthalpy of activation ΔG_T^\neq and standard free enthalpy of activation ΔG_{298}^\neq for the reduction of 10^{-3} M $\text{K}_4\text{SiW}_{12}\text{O}_{40}$ in DMF containing 0.1 M LiClO_4 . Several approximations were discussed in detail and have permitted to evaluate a theoretical value of $\Delta G_{\text{th}}^\neq$ between 0.22 and 0.43 eV, in fairly acceptable agreement with the experimental value, considering the very crude approximations used in the estimation of $\Delta G_{\text{th}}^\neq$. It appears that the

Tab. 5 Diffusion coefficient, heterogeneous rate constant k_s , collision number Z_{het} , free enthalpy of activation DG^{\neq}_T and standard free enthalpy of activation DG^{\neq}_{298} for the reduction of 10^{-3} M $\alpha\text{-K}_4\text{SiW}_{12}\text{O}_{40}$ in DMF containing 0.1 M LiClO₄ (taken from Ref. 49)

T/°C	$10^6 D \text{ cm}^{-2} \text{ s}^{-1}$	$10^3 k_s \text{ cm}^{-2} \text{ s}^{-1}$	$Z_{\text{het}} \text{ cm}^{-1} \text{s}^{-1}$	DG_T^{\neq}/eV	$DG_{298}^{\neq}/\text{eV}$
25	3.12	9.19	1171	0.302	0.302
10	2.39	5.16	1141	0.300	0.302
0	2.24	3.57	1120	0.298	0.301
-10	1.88	2.26	1100	0.297	0.301
-30	1.19	0.895	1057	0.293	0.299

bulkiness and structure of this POM, resulting on a very small surface charge, are the main parameters favoring its straightforward comparison with organic compounds like quinones.

22.4.2

The Reduction Potential of the One-electron Wave and the Role of the Central Heteroatom

Detailed studies of this problem were performed for Keggin-type heteropolytungstates and heteropolymolybdates. It came out that the reducibility increases in the sequence α -, β - and γ -isomers according to the number of M_3O_{13} rotated groups [4, 52, 53]. A related question of interest concerns the influence or fate of the central heteroatom during the reduction of heteropolyanions. It was shown that the reductions of $\alpha\text{-[PW}_{12}\text{O}_{40}]^{3-}$, $\alpha\text{-[SiW}_{12}\text{O}_{40}]^{4-}$, $\alpha\text{-[Fe}^{\text{III}}\text{W}_{12}\text{O}_{40}]^{5-}$, $\alpha\text{-[Co}^{\text{II}}\text{W}_{12}\text{O}_{40}]^{6-}$, and $\alpha\text{-[H}_2\text{W}_{12}\text{O}_{40}]^{6-}$ in 1 M H₂SO₄, electrons can be added without protonation until the charge of the reduced species is -6 [30a]. Further reduction is always accompanied by protonation keeping the overall ionic charge at -6. In the case of $\alpha\text{-[Fe}^{\text{III}}\text{W}_{12}\text{O}_{40}]^{5-}$ and $\alpha\text{-[Co}^{\text{II}}\text{W}_{12}\text{O}_{40}]^{6-}$ where the central heteroatom might be reduced, the reduction takes place only

on the tungsten atoms and no Fe(II) and Co(I) species were observed. In the absence of protonation in aqueous solutions, the reduction of $\alpha\text{-[XW}_{12}\text{O}_{40}]^n^-$ ($X = \text{P(V), Si(IV), Ge(IV), Fe(III), B(III), Co(II), H}_2, \text{Cu(I)}$) is featured by two one-electron processes. Their potentials are linearly dependent on the ionic charge by -0.18 V per unit charge [Chapter 6 in Ref. 4, 54a,b,c as sketched in Fig. 6]. The same trend is also reported in organic solvents [54d].

In short, the central heteroatom was admitted to intervene in the reduction of these POMs essentially by the overall ionic charge it imposes to the molecule. Recently, however, the Si center was shown, by XPS, FTIR, and ESR, to be partly reduced in the one-electron reduction species of $\alpha\text{-[SiMo}_{12}\text{O}_{40}]^{4-}$ [55].

22.4.3

Isomerization upon Reduction

Possibilities of isomerization of POMs, during their reduction processes, were reported [56]. For example, the one-electron reduction of the γ^* -isomer of $[\text{S}_2\text{W}_{18}\text{O}_{62}]^{4-}$ leads to isolation of the α -isomer and this transformation is associated with the $[\text{S}_2\text{W}_{18}\text{O}_{62}]^{4-}/[\text{S}_2\text{W}_{18}\text{O}_{62}]^{5-}$ [56]. However, the transformation could not be detected on the timescale of

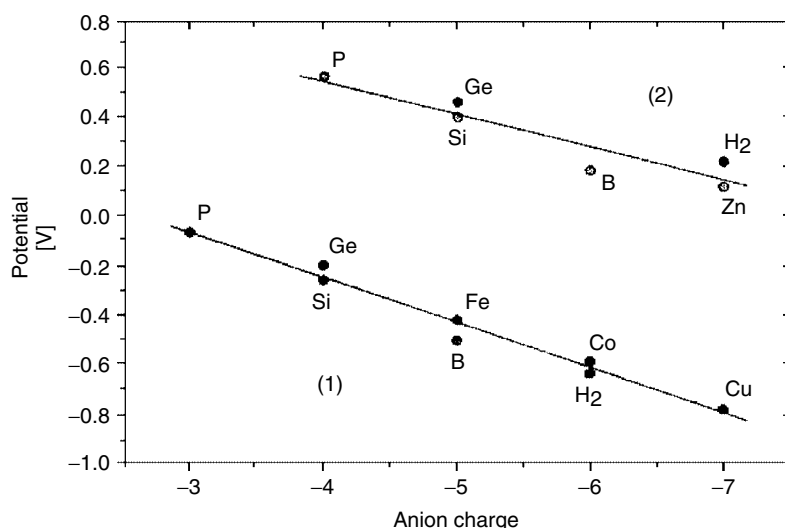


Fig. 6 Dependence of the first one-electron reduction potentials (in V vs. SCE) on the negative charge: (1) $XW_{12}O_{40}^{n-}$, X = P, Si, Ge, Fe, B, Co, H₂, Cu; and (2) $XW_{11}VO_{40}^{n-}$, X = P, Si, Ge, B, H₂, Zn (taken from Ref. 8).

cyclic voltammetry up to a scan rate of 10 V s^{-1} and was solved by X-ray crystallography. The available data suggest that either (1) the $\gamma^*-\alpha$ equilibrium favors one of the isomers in solution for both redox states or (2) the isomerization is slow on the cyclic voltammetry timescale but the difference in $E_{1/2}$ for the $\alpha\text{-}[S_2W_{18}O_{62}]^{4-}/\alpha\text{-}[S_2W_{18}O_{62}]^{5-}$ and $\gamma\text{-}[S_2W_{18}O_{62}]^{4-}/\gamma\text{-}[S_2W_{18}O_{62}]^{5-}$ couples cannot be resolved by cyclic voltammetry.

22.4.4

POM-solvent Interactions as Probed by the Redox Potentials of Two POMs

$\alpha\text{-K}_4SiW_{12}O_{40}$ (SiW₁₂) and $\alpha\text{-K}_6P_2W_{18}O_{62}$ (P₂W₁₈) were selected as representative examples to enlarge the current knowledge of ion-solvent interactions [34]. In related studies, cations have received considerable attention [57], but anions suitable for work in nonaqueous media are scarce [57a, 58]. The best representative examples are

hexacyanoferrate(III)/hexacyanoferrate(II) and hexacyanomanganate(III)/hexacyanomanganate(II) redox couples that contain cyano groups. Therefore, the high nominal negative charge of SiW₁₂ and P₂W₁₈ as well as the lack of cyano groups were anticipated to be of interest.

The following discussion is based on the study of the first voltammetric waves of SiW₁₂ and P₂W₁₈ respectively, in the various media, with 0.1 M LiClO₄ as supporting electrolyte except in water where HClO₄ was used [34]. The reference system was ferrocene-ferricinium. These waves were checked to be one-electron chemically reversible processes in all the solvents used in the following. The main results are gathered in Table 6.

They show that the electron transfer is reversible or quasi-reversible, the deviation from reversibility remaining quite modest for scan rates from 10 mV s^{-1} to 100 mV s^{-1} . Although the reversibility of the ferrocene-ferricinium in all the

Tab. 6 Cyclic voltammetry data for the reduction of 10^{-3} M solution of $\alpha\text{-K}_4\text{SiW}_{12}\text{O}_{40}$ or $\alpha\text{-K}_6\text{P}_2\text{W}_{18}\text{O}_{62}$ in various solvents. $T = 25^\circ\text{C}$; working electrode: glassy carbon disk. Sweep rate: 100 mV s^{-1} (taken from Ref. 34)

Solvent	$\text{SiW}_{12}\text{O}_{40}\text{K}_4$		$\text{P}_2\text{W}_{18}\text{O}_{62}\text{K}_6$	
	$-E_{pc}$ [mV]	ΔE_p [mV]	$-E_{pc}$ [mV]	ΔE_p [mV]
<i>N,N</i> -dimethylformamide (DMF)	1297	75	1087	75
Dimethylsulfoxide (DMSO)	1130	60–65	910	63
<i>N</i> -methylformamide (NMF)	756	57	485	63
Formamide (FA)	574	60	295	55
Water (H_2O) + 1 M HClO_4	340	55	95	55

E_{pc} : reduction peak potential measured versus the reduction peak potential of ferricinium in the same medium.

ΔE_p : anodic-to-cathodic peak potential difference. The supporting electrolyte is 0.1 M LiClO_4 .

solvents was verified, only the reduction peak potentials are quoted in Table 6, instead of standard potentials, taking the reduction peak potential of ferricinium in the relevant medium as a reference. This procedure was shown to be useful in an attempt to extend the correlation to water in the series of solvents [34]. The reduction peak potentials of SiW_{12} and P_2W_{18} depend strongly on the nature

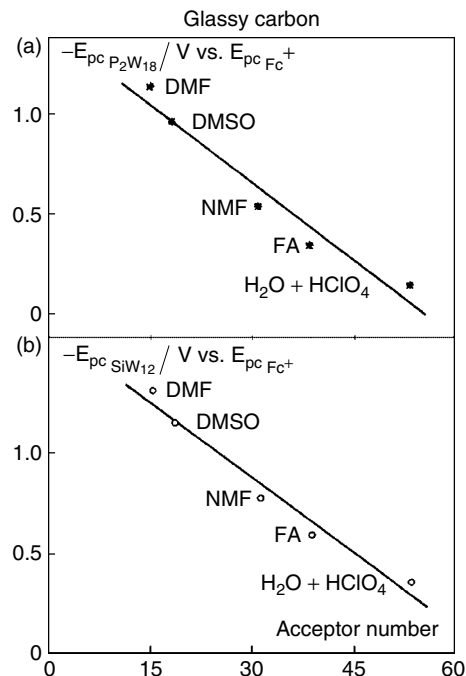
of the solvent. On the assumption that preferential solvation of the molecules by residual water was not prevalent, the following conclusions emerge from the discussion based on the bulk properties of the solvents, gathered in Table 7; (1) the dielectric continuum model of Born is not successful in correlating solvent effects with redox potentials of POMs [34, 57b, 57c, 58], a conclusion also reached for

Tab. 7 Solvent parameters [dielectric constant (ϵ), dipole moment (μ), acceptor number (AN) and free enthalpy of transfer (ΔG_{tr}°) of the chloride ion from *N,N*-dimethylformamide as reference solvent (taken from Ref. 34)

Solvent	ϵ	μ^a Debye	AN	$-\Delta G_{tr}(\text{Cl}^-)$ kJ mol^{-1}
<i>N,N</i> -dimethylformamide (DMF)	36.7	3.82	16.0	0
Dimethylsulfoxide (DMSO)	46.7	3.96	19.3	+6
<i>N</i> -methylformamide (NMF)	182.4	3.83	32.1	+25
Formamide (FA)	109.5	3.73	39.8	+33
Water (H_2O)	78.5	1.87	54.8	+46

^a1 Debye = 3.3356×10^{-30} c.m.

Fig. 7 Relationship between the reduction peak potential, E_{pc} , of $\alpha\text{-K}_6\text{P}_2\text{W}_{18}\text{O}_{62}$ or $\alpha\text{-K}_4\text{SiW}_{12}\text{O}_{40}$ versus the reduction peak potential, $E_{pc\text{Fc}^+}$, of ferricinium and the acceptor number of studied solvents. Abbreviations are the same as in Tables 6 and 7. The solid line is the best linear regression fit to all the experimental points, including water as a solvent. (a) $\alpha\text{-K}_6\text{P}_2\text{W}_{18}\text{O}_{62}$: correlation coefficient for the solid line: 0.974. The correlation coefficient for the best fit to “nonaqueous solvents” only is 0.994. (b) $\alpha\text{-K}_4\text{SiW}_{12}\text{O}_{40}$: correlation coefficient for the solid line: 0.983. The correlation coefficient for the best fit to “nonaqueous solvents” only is 0.995 (taken from Ref. 34).



cyano complexes of iron and manganese; (2) in contrast, the Lewis-type concept that proved satisfactory for ion-solvent interactions [57, 58] was successful here also.

The Gutmann acceptor number is one quantitative expression of this solvent parameter. Figure 7 shows that the reduction peak potentials of SiW_{12} and P_2W_{18} respectively correlate satisfactorily with the acceptor numbers of the corresponding solvents. The correlation coefficient is above 0.99 for the line including only “nonaqueous” solvents, and is still larger than 0.97 when the $\text{H}_2\text{O}/\text{HClO}_4$ was included as a solvent. Alternatively, the free enthalpies (ΔG_{tr}^0) of transfer of the chloride ion express also quantitatively the electron-pair acceptor properties of solvents. Figure 8 shows good correlations for SiW_{12} and P_2W_{18} reduction peak potentials with this parameter, with correlation coefficients as high as 0.999. As such

strikingly good correlation coefficients were obtained also for hexacyano complexes [58], it can be concluded that any specific interaction between the solvents and anions in this work are small, absent or smoothly parallel each other. Furthermore, a plot of the reduction peak potentials data for SiW_{12} versus those for P_2W_{18} gives a straight line with a slope close to unity, thus indicating that solvent effects must be very similar for both systems.

22.4.5

Structure of Electrolyte Solutions As Probed by the Electrochemical Behaviors of POMs

Sizes, shapes, diffusion coefficients, redox behaviors, and spectroscopic properties of oxidized and reduced forms of POMs make these species eminently suitable for a variety of physicochemical studies [4, 18, 19, 22, 23, 30a–d]. Owing to the minimal

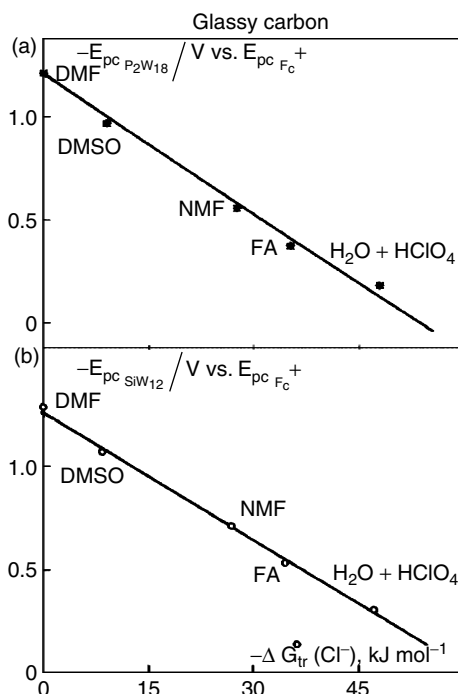


Fig. 8 Relationship between the reduction peak potential, E_{pc} , of $\alpha\text{-K}_6\text{P}_2\text{W}_{18}\text{O}_{62}$ or $\alpha\text{-K}_4\text{SiW}_{12}\text{O}_{40}$ versus the reduction peak potential, $E_{pc F_c^+}$, of ferricinium and the free enthalpy of transfer of the chloride ion, $\Delta G_{tr}^\circ(\text{Cl}^-)$, taking DMF as the reference solvent. Abbreviations are the same as in Tables 6 and 7. The solid line is the best linear regression fit to all the experimental points, including water as a solvent. (a) $\alpha\text{-K}_6\text{P}_2\text{W}_{18}\text{O}_{62}$: correlation coefficient for the solid line: 0.996. The correlation coefficient for the best fit to “nonaqueous solvents” only is 0.999. (b) $\alpha\text{-K}_4\text{SiW}_{12}\text{O}_{40}$: correlation coefficient for the solid line: 0.999. The correlation coefficient for the best fit to “nonaqueous solvents” only is also 0.999 (taken from Ref. 34).

solvation and ion-pairing of SiW_{12} and PW_{12} in concentrated aqueous solutions of alkali-metal salts, these species were used to probe the structure of electrolyte solutions [33a,b]. Ion-water interactions in highly concentrated solutions are currently a matter of interest that has benefited from the modern developments of various spectroscopies, including NMR, X-ray scattering, and IR studies. A classification of commonly used ions has resulted, among which Li^+ , Na^+ , H_3O^+ ... are net-structure making ions, while K^+ , Cl^- , ClO_4^- are net-structure breaking ions [59]. In contrast, other IR results would suggest that Li^+ , Na^+ , and K^+ are net-structure breaking species at high concentrations. It was anticipated that the electrochemical behaviors of SiW_{12} might allow a cross-check of this classification. Electrochemical measurements were supplemented

by UV-visible spectroscopy and viscosity measurements. In the absence of any salt added to acid, it was easy to obtain the following order of structure breaking ability for anions: $\text{ClO}_4^- > \text{Cl}^- > \text{SO}_4^{2-}$, HSO_4^- [33a]. For cations, the structure-making abilities were in the order $\text{Li}^+ > \text{Na}^+ >> \text{K}^+$. With special attention paid to the case of K^+ , electrochemical data suggest unambiguously a small net-structure making ability for K_2SO_4 .

22.4.6

Cation and Pressure Effects on the Electrochemistry of 12-Tungstocobaltate and 12-Tungstophosphate Ions in Acidic Aqueous Solution

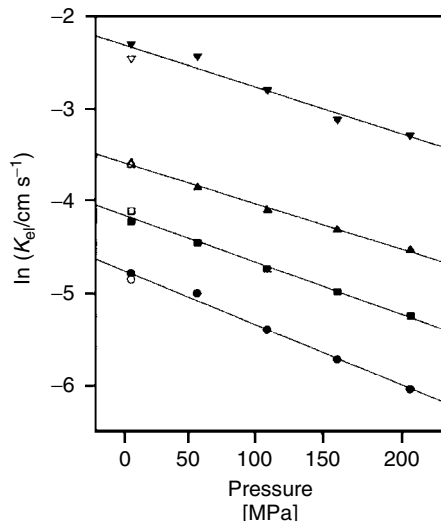
Also, cation and pressure effects were studied on two selected POMs, $\text{CoW}_{12}\text{O}_{40}^{5-/6-}$ (CoW_{12}) and $\text{PW}_{12}\text{O}_{40}^{3-/4-}$

($\text{PW}_{12}^{3-/4-}$) and $\text{PW}_{12}\text{O}_{40}^{4-/5-}$ ($\text{PW}_{12}^{4-/5-}$), with the aim to extend investigations on electron transfer chemistry of anions at electrodes to couples other than cyanometalates that could arguably represent special cases because of the “softness” conferred by the π -acceptor action of the cyano ligands [60]. Indeed, marked cation effects have been reported on the reduction potentials of heteropolyoxometalates in aqueous [33a,d, 61a], organic [37, 40], and aqueous organic media [61b,c,d] and also on the rates of self-exchange [62] and of net redox reactions [25], [61a, 63] although it has not always been clear whether the effects observed are cation specific or arise in a general way from ionic strength. The study as a function of pressure has permitted to clarify the role of various cations in the reduction process. The half-wave potentials for the CoW_{12} couple become moderately more positive with increasing electrolyte concentration and cationic charge and also in the sequences $\text{Li}^+ \approx \text{Na}^+ < \text{NH}_4^+ \leq \text{H}^+ < \text{K}^+ < \text{Rb}^+ < \text{Cs}^+$ and $\text{Na}^+ < \text{Mg}^{2+} < \text{Ca}^{2+} < \text{Eu}^{3+}$. The mean diffusion coefficients for CoW_{12}

with the 1:1 electrolytes are independent of electrolyte concentration and rise only slightly from Li^+ to Cs^+ , averaging $(2.4 \pm 0.3) \times 10^{-6} \text{ cm}^2 \text{ s}^{-1}$. It was found [60] that $E_{1/2}$, $\ln D$ and $\ln k_{\text{el}}$ are linear functions of the pressure, the slopes of which therefore gave, respectively, mean values of the reaction volume relative to $\text{Ag}/\text{AgCl}/\text{NaCl}(\text{satd})\Delta V_{\text{Ag}/\text{AgCl}} (= -F(\delta E_{1/2}/\delta P)_T)$, the volume of activation for diffusion $\Delta V_{\text{diff}}^\ddagger (= -RT(\delta \ln D/\delta P)_T)$ and the volume of activation $\Delta V_{\text{el}}^\ddagger (= -RT(\delta \ln k_{\text{el}}/\delta P)_T)$ of the electrode reaction for the aqueous $\text{CoW}_{12}\text{O}_{40}^{5-/6-}$ couple, over the pressure range 0–204 MPa.

Figure 9 illustrates the results for k_{el} . Neither the volume of activation for diffusion $\Delta V_{\text{diff}}^\ddagger$ (average $-0.9 \pm 1.1 \text{ cm}^3 \text{ mol}^{-1}$) nor the electrochemical cell reaction volumes $\Delta V_{\text{Ag}/\text{AgCl}}$ average $(-22 \pm 2 \text{ cm}^3 \text{ mol}^{-1})$ for the CoW_{12} couple show significant dependence on electrolyte identity or concentration. For the $\text{PW}_{12}^{3-/4-}$ and $\text{PW}_{12}^{4-/5-}$ couples $\Delta V_{\text{Ag}/\text{AgCl}} = -14$ and $-26 \text{ cm}^3 \text{ mol}^{-1}$, respectively, suggesting a dependence on $\Delta(z^2)$ (z = ionic

Fig. 9 Pressure and supporting electrolyte concentration dependences of rate constants k_{el} for the $\text{CoW}_{12}\text{O}_{40}^{5-/6-}$ electrode reaction in aqueous KCl at 25.0 C, $[\text{KCl}] = 0.10$ (●), 0.20 (■), 0.50 (▲), and 1.00 (▼) mol L^{-1} ; hollow symbols represent return to low pressure after the pressure cycle. $[\text{K}_6\text{CoW}_{12}\text{O}_{40}] = 1.0 \text{ mmol L}^{-1}$ (taken from Ref. 60).



charge number), which would fit the Born-Drude-Nernst theory of electrostriction of solvent in the form $\Delta V_{\text{Ag}/\text{AgCl}} = \Delta V_{\text{ref}} + B\Delta(z^2/r)$ in the one-electron reduction of an electroactive species with an effective radius r , and B being a positive constant at a given pressure. Actually, comparison of these $\Delta V_{\text{Ag}/\text{AgCl}}$ with those for CoW_{12} and other anion–anion couples shows that the Born-Drude-Nernst approach fails in this context. For aqueous electrode reactions of CoW_{12} as for other anionic couples such as cyanometalates, the standard rate constants k_{el} show specific cation catalysis ($\text{Na}^+ < \text{K}^+ < \text{Rb}^+ < \text{Cs}^+$), and $\Delta V_{\text{el}}^\ddagger$ is invariably positive, in the presence of supporting electrolytes. For the heavier group 1 cations, $\Delta V_{\text{el}}^\ddagger$ is particularly large ($10\text{--}15 \text{ cm}^3 \text{ mol}^{-1}$), consistent with a partial dehydration of the cation to facilitate catalysis if the electron transfer process. The positive values of $\Delta V_{\text{el}}^\ddagger$ for the CoW_{12} couple cannot be attributed to rate control by solvent dynamics, which would lead to $\Delta V_{\text{el}}^\ddagger \leq \Delta V_{\text{diff}}^\ddagger$, that is, to negative or zero $\Delta V_{\text{el}}^\ddagger$ values. These results stand in sharp contrast to those for aqueous cationic couples, for which k_{el} shows relatively little influence of the nature of the counterion and $\Delta V_{\text{el}}^\ddagger$ is always negative.

22.5 Mixed Addenda and Other Substituted POMs

22.5.1 Comparison of Valence Trapping in Uniform and Mixed Addenda Plenary POMs

As far as the first electron fixation site on plenary POMs is concerned, a distinction must be made between those containing a single addenda ion like W(VI), Mo(VI), or V(V) and those in which at least two

different addenda ions are present. As a consequence of such substitution, the electrochemical character of these POMs can be widely modulated [54c].

Symmetries in the structures of the POMs result in the equivalence of several metal centers detectable, for example, by NMR on fully oxidized species, and by EPR and/or NMR on their reduced analogs [30f, 64–69]. In agreement with the complete structural equivalence of the twelve tungsten atoms of the α -Keggin anions, EPR experiments show that the “blue” electron is delocalized over all the tungsten centers in the one-electron reduced species, for instance in $\alpha\text{-}[\text{PW}_{12}\text{O}_{40}]^{4-}$ [30f]. Ample confirmation by EPR and also NMR of this pioneering work exists in the literature for this compound and several others and even on two-electron reduced Keggin derivatives [65]. In contrast, the electron is localized on the more reducible atom at room temperature in the one-electron-reduced mixed addenda POMs. In short, substitution of one or several W atom(s) by Mo or V atom(s), reveals that the added electrons can be trapped according to various timescales, over certain atoms in the case of monosubstitution and/or regions for multisubstituted derivatives [30f, 66, 67, 69–71]. The following order of decreasing oxidizing ability is found: $\text{V(V)} > \text{Mo(VI)} > \text{W(VI)}$.

Such equivalence raises the following question in the molecular electrochemistry of these compounds: in the absence of other possible mechanistic complications, related usually to pH or ion-pairing of the countercations, can it be expected that symmetry equivalent metal centers will be reduced simultaneously or will the interactions between adjacent metal centers induce a stepwise reduction. (The problem of pure electron transfer reactions to and from molecules containing at least

two identical redox centers has received appropriate attention in several studies. Two main classes are described: The first class of compounds gathers those cases in which noninteracting redox centers are present and for which successive electron transfers are expected to follow simple statistics, in the absence of coupled chemical steps. For example, see [71a–c]. The second group includes molecules in which various phenomena (including conjugation, ion-pairing, solvation changes, and structural variations) induce or reveal interactions between the sites, and correspondingly, differences between their half-reaction potentials. These constitute the majority of published examples. For example, see [71d–h] [72].

Despite the structural equivalence of the twelve metal centers in the α -PW₁₂O₄₀³⁻ Keggin anion, a stepwise reduction of the tungsten centers is observed [30f]. EPR experiments on this species show that the added electron is delocalized (type II in the scheme proposed by Robin and Day) [4]. Over all 12 tungsten centers suggesting that there is communication

between the metal centers. (The delocalized electron undergoes localization at low temperatures, otherwise the mixed valence compound is classified as type III under the scheme of Robin and Day.) In general, complete delocalization of the added electrons over all 12 metal centers appears to be the rule for all unsubstituted, highly symmetrical α -Keggin anions. Introduction of lower symmetry results in a variation in the degree of valence trapping [66, 67, 69].

Unlike the spherical α -Keggin anion, the Wells–Dawson structure is shaped like a prolate ellipsoid [73], consisting of six “cap” tungsten centers and twelve “belt” tungsten centers. The nonequivalence of the “cap” and “belt” tungsten sites raises the issue of the initial site of the electron transfer. Various lines of experimental evidence all converge to support that the added electrons are first introduced into the “belt” tungsten sites [54a, 65–70, 74–77]. As will be elaborated in the following, extended Hückel calculations provide a qualitative understanding of the initial electron transfer site in these compounds [78]. Tables 8 through 11

Tab. 8 Half-wave potential for the various complexes at pH = 4.7. The values in this table are essentially those from Ref. 79, but the same measurements were also carried out in Refs. 14, 83, with small numerical variations that have no consequence on the interpretations. The numbering of the substituent(s) follows the IUPAC recommendations

Compound	$E_{1/2}$ (V vs. SCE) (number of electrons)	References
P ₂ W ₁₈	+0.04 (1)	14, 79, 83
(4)-P ₂ MoW ₁₇ (α_1)	+0.39 (1)	14, 79, 83
(1)-P ₂ MoW ₁₇ (α_2)	+0.23 (1)	14, 79, 83
(1,2,3)-P ₂ Mo ₃ W ₁₅	+0.26 (1)	14, 79, 83
(4, 9, 10, 15)-P ₂ Mo ₄ W ₁₄	+0.48 (2)	79
(1,4, 9, 10, 16)-P ₂ W ₁₃ Mo ₅	+0.46 (1)	79
(1, 4, 9, 10, 15)-P ₂ W ₁₃ Mo ₅	+0.47 (2)	79
(1, 4, 9, 10, 15, 16)-P ₂ W ₁₂ Mo ₆	+0.45 (2)	79
P ₂ Mo ₁₈	+0.32 (2)	79, 83

Tab. 9 Half-wave potential for the various complexes. The values in this table are taken from Ref. 80. The numbering of the substituent(s) follows the IUPAC recommendations

Compound	pH	$E_{1/2}$ (V vs. SCE) (number of electrons)
α -As ₂ W ₁₈	1	+0.08 (1)
(4)-As ₂ W ₁₇ (α_1)	4,6	-0.47 (2)
(1)-As ₂ W ₁₇ (α_2)	4,6	-0.44 (2)
(1, 2)-As ₂ W ₁₅ Mo ₂	4,6	-0.42 (2)
(1)-As ₂ W ₁₇ Mo (α_2)	1	+0.28 (1)
(4)-As ₂ W ₁₇ Mo (α_1)	1	+0.45 (1)
(1,2) – As ₂ W ₁₆ Mo ₂	1	+0.29 (1)
(1,2,3)-As ₂ W ₁₅ Mo ₃	1	+0.31 (1)
(1)-As ₂ W ₁₇ V (α_2)	1	+0.46 (1)
(1,2)-As ₂ W ₁₆ V ₂	1	+0.42 (2)
(1,2,3)-As ₂ W ₁₅ V ₃	1	+0.32 (3)

Tab. 10 Half-wave potential for various V-substituted complexes. The numbering of the substituent(s) follows the IUPAC recommendations

Compound	pH	$E_{1/2}$ (V vs. SCE) (number of electrons)	References
(4)-P ₂ W ₁₇ V (α_1)	5.5 (Li ⁺)	+0.48 (1)	81
(1)-P ₂ W ₁₇ V (α_2)	5.5 (Li ⁺)	+0.39 (1)	81
(1,2)-P ₂ W ₁₆ V ₂	5.5 (Li ⁺)	+0.27 (1)	81
(1,2,3)-P ₂ W ₁₅ V ₃	5.5 (Li ⁺)	+0.23 (1)	81
(1,2,3)-P ₂ W ₁₅ V ₃	7.0 (Li ⁺)	+0.11 (1)	81
(4)-P ₂ W ₁₇ V (α_1)	4.7(Na ⁺)	+0.51 (1)	74, 81
(1)-P ₂ W ₁₇ V (α_2)	4.7(Na ⁺)	+0.41 (1)	74, 81
(4)-P ₂ W ₁₇ V (α_1)	7	+0.48 (1)	82
(1)-P ₂ W ₁₇ V (α_2)	7	+0.39 (1)	82
(1,2)-P ₂ W ₁₆ V ₂	7	+0.28 (2)	82

gather the reduction half-wave potentials or peak potentials of selected Dawson-type POMs [14, 15, 74–82].

In the formulae of these anions, oxygen atoms and charges were omitted. Experimental evidence proved that the first waves observed for Mo(VI)- and V(V)-substituted derivatives are restricted to the reduction of these cations. The interpretations are based on the comparisons of the reduction potentials of the same element within

α_1 and α_2 -substituted Dawson anions and also with those of the corresponding unsubstituted derivatives. Specifically, it appears that α_1 -P₂MoW₁₇, which contains the Mo atom in an equatorial position, is more easily reduced than P₂Mo₁₈ [79]. In contrast, α_2 -P₂MoW₁₇ in which the Mo atom is in one cap is less reducible than P₂Mo₁₈. This observation is in agreement with the proposal that P₂W₁₈ is initially reduced at one of the twelve equatorial

Tab. 11 Half-wave potential for variously substituted complexes at pH = 1. The values are culled from Ref. 83. The numbering of the substituent(s) follows the IUPAC recommendations

Compound	$E_{1/2}$ (V vs. SCE) (number of electrons)
P ₂ W ₁₈	+0.04 (1)
(1,2)-P ₂ W ₁₆ Mo ₂	+0.27 (1)
(1,2,3)-P ₂ W ₁₅ Mo ₂ V	+0.46 (1) (V ^V /V ^{IV})
(1,2,3)-P ₂ W ₁₅ MoV ₂	+0.37 (2) (V ^V /V ^{IV})
(1,2,3)-P ₂ W ₁₅ V ₃	+0.42 (1) (V ^V /V ^{IV})
(1,2)-P ₂ W ₁₆ V ₂	+0.36 (2)
(4)-P ₂ W ₁₇ V (α_1)	+0.49 (1)
(1)-P ₂ W ₁₇ V (α_2)	+0.41 (1)

tungsten atoms. This conclusion can be extended to P₂Mo₁₈ itself, as suggested by the results in Tables 8–11. In short and in complete analogy with the Keggin model, a stepwise reduction of the equivalent metal centers is also seen in the Wells–Dawson POMs, with various degrees of valence trapping observed upon the introduction of other addenda atom substituents.

22.5.2 Lacunary and Transition Metal–substituted POMs

This section is separated from the former one, even though mixed addenda POMs are mostly, if not exclusively, synthesized from the appropriate lacunary precursors and can be viewed normally as substituted POMs. At least two reasons can be invoked to justify such dichotomy: first, a substitutionally labile position is available on the transition metal substituted into the POMs framework, which is not the case with mixed addenda compounds; second, these transition metal centers are usually the active sites for catalytic and electrocatalytic reactions and might deserve special attention.

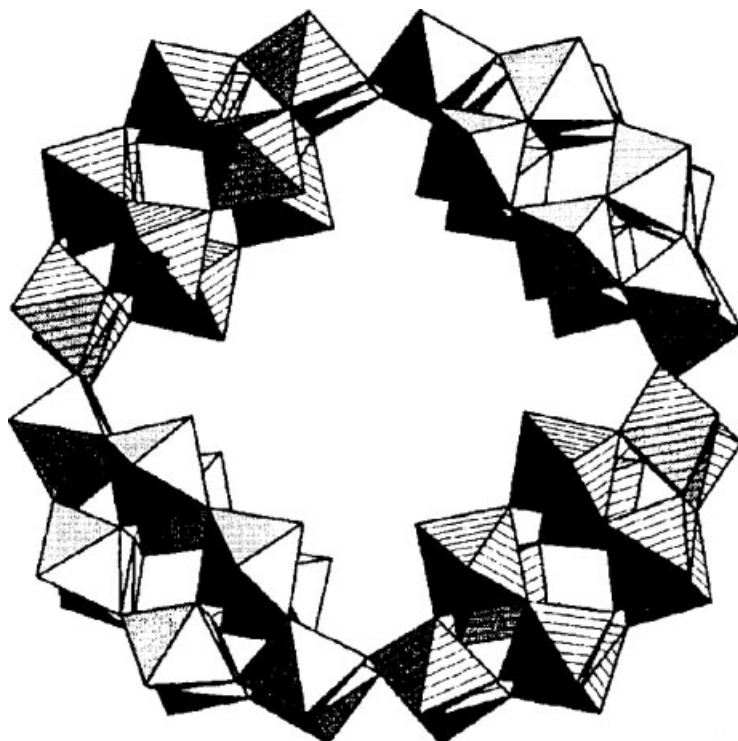
The so-called mono “lacunary” POMs are derived from plenary Keggin, (XM₁₂O₄₀), or Dawson, (P₂W₁₈O₆₂), anions by the removal of one MO unit to yield (XM₁₁O₃₉) or (P₂W₁₇O₆₁) respectively. (Note that charges are omitted for convenience.) Trivacant species, XW₉O₃₄ and X₂W₁₅O₅₆ and even hexavacant species like X₂W₁₂O₄₈ are the precursors of new families of POMs, some of which will also be studied briefly in the following text. In most, but not all cases, the free lacunary polyanions are independently stable. Metal ion binding occurs at the octahedral vacant site(s). In addition of being interesting in its own right, the electrochemistry of lacunary POMs is useful for comparison with the redox processes of the framework in the corresponding plenary compounds and in the transition metal–substituted derivatives.

22.5.2.1 Lacunary POMs

Various lines of experimental evidence confirm the very low surface charge density, at least for symmetrical plenary Keggin- and Dawson-type POMs [33a,d, 84]. For example, a simple linear variation

of the first reduction potentials of α -[XW₁₂O₄₀]ⁿ⁻ with the anion charge is observed under conditions without protonation [4, 54]. Extension of these remarks to the corresponding lacunary species and to their first transition metal ion-substituted derivatives do not seem straightforward, possibly owing to the change of symmetry in the charge distribution in the molecules, in conjunction with the increase of the overall negative charge. As a matter of fact, the lacunary POMs are known to exhibit “a donor set of hard oxide ions while the adjacent d° (Mo^{VI}, W^{VI}) atoms provide acceptor orbitals” [85]. As a consequence, the first framework reduction wave in the cyclic voltammogram of these lacunary derivatives appears usually

as a reversible two-electron process, in pH media where the corresponding plenary complexes still undergo a reversible one-electron reduction. In this context, the cyclic voltammetric behavior of selected Keggin- and Dawson-type POMs was studied as a function of electrolyte composition [86a]. The buffer capacity of the electrolyte appeared as an important parameter that can be used to reveal the symmetry or dissymmetry in charge distribution within each oxometalate. A fully symmetrical POM like [P₂W₁₈O₆₂]⁶⁻ exhibits a uniform protonability, while its α_1 and α_2 lacunary derivatives present stepwise acid–base equilibria, owing to their charge dissymmetry. The behavior of these sites is revealed readily in unbuffered or



Scheme 4 Structure of the anion [P₈W₄₈O₁₈₄]⁴⁰⁻. The four building blocks are easily identified (taken from Ref. 86b).

poorly buffered media at pH = 3. In short, it is shown [86a] that cations other than the proton, even in very high excess, fail to give rise to the classical voltammograms of lacunary POMs. The same behavior was observed also for $\alpha_2[P_2Mo_2W_{15}O_{61}]^{10-}$, $\alpha[PW_{11}O_{39}]^{7-}$, $\alpha[SiW_{11}O_{39}]^{8-}$, but to a lesser extent in $\alpha_2[Ni(OH_2)P_2W_{17}O_{61}]^{8-}$ and $\alpha_2[Zn(OH_2)P_2W_{17}O_{61}]^{8-}$ [86a]. The phenomenon was very severe with $[H_2P_2W_{12}O_{48}]^{12-}$ [86a] and was also studied in some detail on its remarkably stable and inert cyclic tetramer $K_{28}Li_5H_7P_8W_{48}O_{184}\cdot 92H_2O$ (P_8W_{48} for convenience) [86b]. The structure of this crown POM is sketched in Sch. 4.

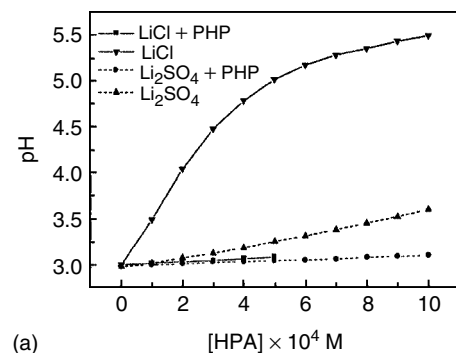
A constant pH = 3 value, was selected to start the experiments. It was made up with H_2SO_4 without or with potassium hydrogenophthalate (PHP) and the appropriate concentration of Li_2SO_4 or $LiCl$ to maintain the total concentration of Li^+ constant. First pH measurements illustrated by Fig. 10 give some insight into the acid–base equilibria of the oxidized form of the crown complex. Proton consumption occurs even with the smallest concentration of POM used in that work. The results are easily explained by taking into account the buffer capacity of the various media. A fast increase of the pH is observed in chloride medium as a consequence of the absence of any buffer capacity. In pure sulfate solution, the hydrogen sulfate anion $[HSO_4]^-$ confers some

buffer capacity to the medium. Finally, the mixture $Li_2SO_4 + PHP$ is slightly more efficient than $LiCl + PHP$, as the former contains two-proton donors. The cyclic voltammograms in Fig. 11 shows the behaviors observed during the redox processes of P_8W_{48} . The voltammetric patterns speak by themselves. In particular, the increase in Li^+ concentration does not compensate for the lack of buffer capacity of the supporting electrolyte, an observation that underscores again the essential role of proton sources in the electrochemistry of lacunary POMs.

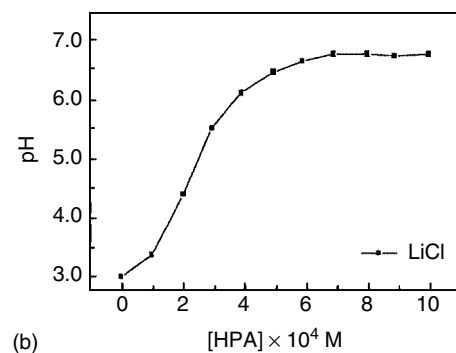
22.5.2.2 Transition

Metal–monosubstituted POMs

In addition to structural studies, one of the main incentives to synthesize and characterize these transition metal–substituted complexes is the remark that they might



(a)



(b)

Fig. 10 Evolution of the pH of an initially pH 3 solution as a function of the concentration of the relevant heteropolyanion. The compositions of the four starting pH 3 electrolytes were respectively: ($H_2SO_4 + 1M LiCl$); ($H_2SO_4 + 0.5M Li_2SO_4$); ($H_2SO_4 + 1M LiCl + 0.069M PHP$); ($H_2SO_4 + 0.5M Li_2SO_4 + 0.069M PHP$). (a) P_8W_{48} ; (b) P_2W_{12} . For further details, see text (taken from Ref. 86b).

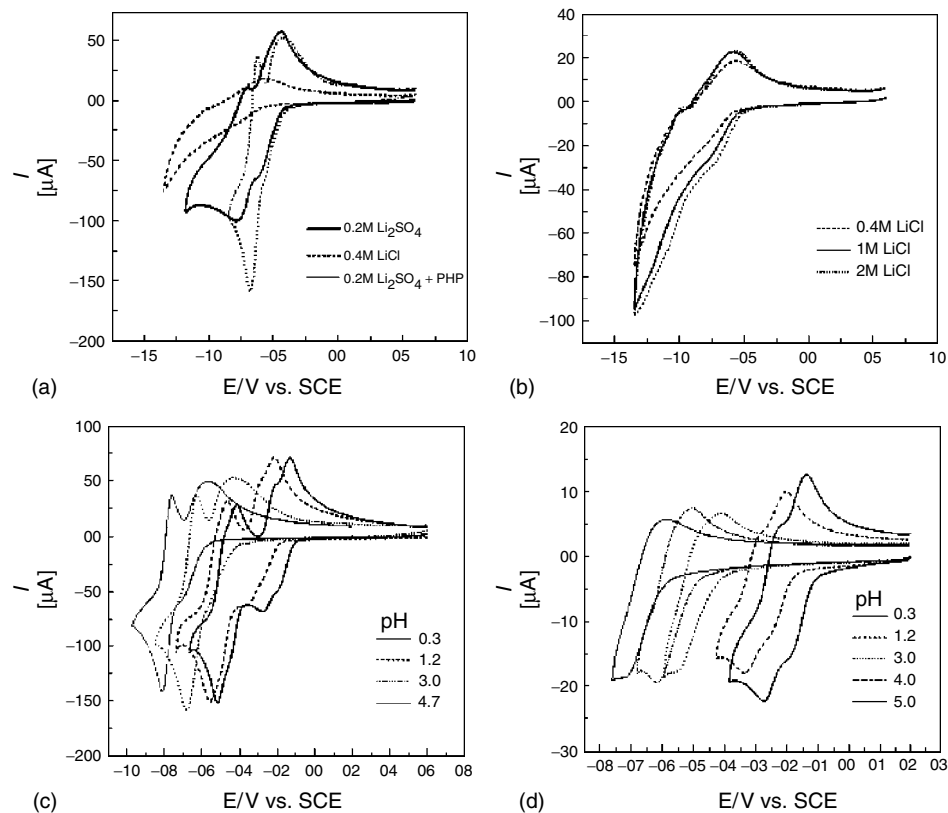
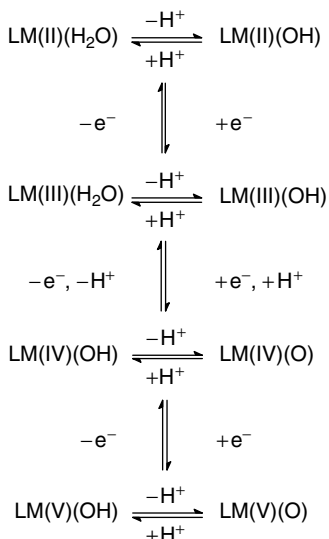


Fig. 11 Evolution of the cyclic voltammograms of P_8W_{48} as a function of the composition of the supporting electrolyte. Scan rate: 10 mV s^{-1} . (a) $5 \times 10^{-4} \text{ M}$ P_8W_{48} in several pH 3 solutions: $(\text{H}_2\text{SO}_4 + 0.4 \text{ M LiCl})$; $(\text{H}_2\text{SO}_4 + 0.2 \text{ M Li}_2\text{SO}_4)$; $(\text{H}_2\text{SO}_4 + 0.2 \text{ M Li}_2\text{SO}_4 + 0.069 \text{ M PHP})$. (b) $5 \times 10^{-4} \text{ M}$ P_8W_{48} in several pH 3 solutions: $(\text{H}_2\text{SO}_4 + 0.4 \text{ M LiCl})$; $(\text{H}_2\text{SO}_4 + 1 \text{ M LiCl})$; $(\text{H}_2\text{SO}_4 + 2 \text{ M LiCl})$. (c) $5 \times 10^{-4} \text{ M}$ P_8W_{48} in various pH solutions: pH = 4.7: ($0.1 \text{ M CH}_3\text{COOLi}/\text{CH}_3\text{COOH} + 1 \text{ M LiCl})$; pH = 3: ($\text{H}_2\text{SO}_4 + 0.069 \text{ M PHP} + 0.5 \text{ M Li}_2\text{SO}_4$). (d) 10^{-4} M P_8W_{48} in various pH solutions; the study is restricted to the first wave obtained at pH 5 and to its evolution for lower pH values; pH = 4 and pH = 5: ($0.1 \text{ M CH}_3\text{COOLi}/\text{CH}_3\text{COOH} + 1 \text{ M LiCl})$; pH = 3: ($\text{H}_2\text{SO}_4 + 0.069 \text{ M PHP} + 0.5 \text{ M Li}_2\text{SO}_4$); pH = 1.2: ($\text{H}_2\text{SO}_4 + 0.5 \text{ M Li}_2\text{SO}_4$); pH = 0.3: ($0.5 \text{ M H}_2\text{SO}_4$). For further details, see text (taken from Ref. 86b).

($\text{H}_2\text{SO}_4 + 0.069 \text{ M PHP} + 0.5 \text{ M Li}_2\text{SO}_4$); pH = 1.2: ($\text{H}_2\text{SO}_4 + 0.5 \text{ M Li}_2\text{SO}_4$); pH = 0.3: ($0.5 \text{ M H}_2\text{SO}_4$). (d) 10^{-4} M P_8W_{48} in various pH solutions; the study is restricted to the first wave obtained at pH 5 and to its evolution for lower pH values; pH = 4 and pH = 5: ($0.1 \text{ M CH}_3\text{COOLi}/\text{CH}_3\text{COOH} + 1 \text{ M LiCl}$); pH = 3: ($\text{H}_2\text{SO}_4 + 0.069 \text{ M PHP} + 0.5 \text{ M Li}_2\text{SO}_4$); pH = 1.2: ($\text{H}_2\text{SO}_4 + 0.5 \text{ M Li}_2\text{SO}_4$); pH = 0.3: ($0.5 \text{ M H}_2\text{SO}_4$). For further details, see text (taken from Ref. 86b).

serve as catalysts and electrocatalysts [17]. With the lacunary POM functioning as a ligand, two global stoichiometries were observed: 1 : 1 metal-ligand and 1 : 2 metal-ligand complexes. In the 1 : 1 complexes formed predominantly with “octahedral” metal ions, the POM is a pentadentate ligand, whereas the metal can be viewed

as 8-coordinate in 1 : 2 complexes. The number of such complexes is virtually enormous and very numerous examples were reported. The sixth coordination site on the substituent metal in the 1 : 1 complexes may be occupied by a variety of ligands, usually a water molecule as most syntheses are carried out in that medium.



Scheme 5 General electrochemical behavior of transition metal–substituted POMs (taken from Ref. 8).

The formal potentials of substituent metals are modulated by numerous influences among which those of the central heteroion and the addenda ions must be highlighted, in addition of the effects of pH, counterions, additives, solvents, and so on. For example, the redox potential of the Mn(III/II) couple was found to increase with X = B < Zn < Si < Ge < P [88]. In aqueous solutions, the pH of the supporting electrolyte might induce deprotonation of the aquametal or hydroxymetal, thus changing its redox potential. The labile water molecule on the sixth site of the substituent metal can be substituted by a large variety of other ligands, including other solvents, with an expected consequence on the redox potential. In addition to these general trends, more specific insights can be obtained by detailed descriptions of selected experiments. Among complementary issues of interest in electrochemical studies, particular attention should be drawn to questions including, but not exhaustively: the redox activity of the transition metal centers within the POMs, when that is visible; the influence on their location on the framework of the molecule and eventually, the number and mutual influences of these centers in the molecules; the redox activity of the POM framework and the appropriate comparison with a precursor, and so on. These points are studied in the literature [13, 15, 30f, 74, 79, 81, 85, 88, 89]. The electrochemistry of metal ion complexes derived from α_1 - and α_2 -[P₂W₁₇O₆₁]¹⁰⁻ illustrates most of the features of interest [15]. The complexes substituted by Ca(II), V(V), Mn(II), Fe(III), Co(II), Ni(II), Cu(II), and Zn(II) were synthesized in the α_1 and in the α_2 series. Complexes with V(V)

The POM ligands in these complexes undergo, at least one, but generally two reversible two-electron reductions, with the addition of between two and three protons in acidic solutions. Eventually, the two-electron reductions split into two-one-electron reductions when the pH of the electrolyte is raised. These behaviors are the same as observed with the plain precursor lacunary complexes, albeit at a different potential location as will be shown in the following. We consider the metal centers in their role of active oxidation sites. A behavior that can be viewed as general is sketched in Sch. 5 [8].

Usually, the aquametal(III) is reducible to aquametal(II) and oxidizable to the corresponding oxometal(IV), hydroxometal(IV) and oxometal(V) derivatives depending on the character of the incorporated metals. Further oxidations to oxometal(VI) and –(VII) are possible in the cases of metals like rhenium [87]. The interest of hydroxometal and oxometal species as oxidation catalysts in synthetic applications must be stressed.

and Mo(VI) were also added for the sake of comparison. As a matter of fact, an interesting issue concerns the choice of

the more appropriate precursor to which to compare the cyclic voltammograms of metal ion-substituted POMs. For this

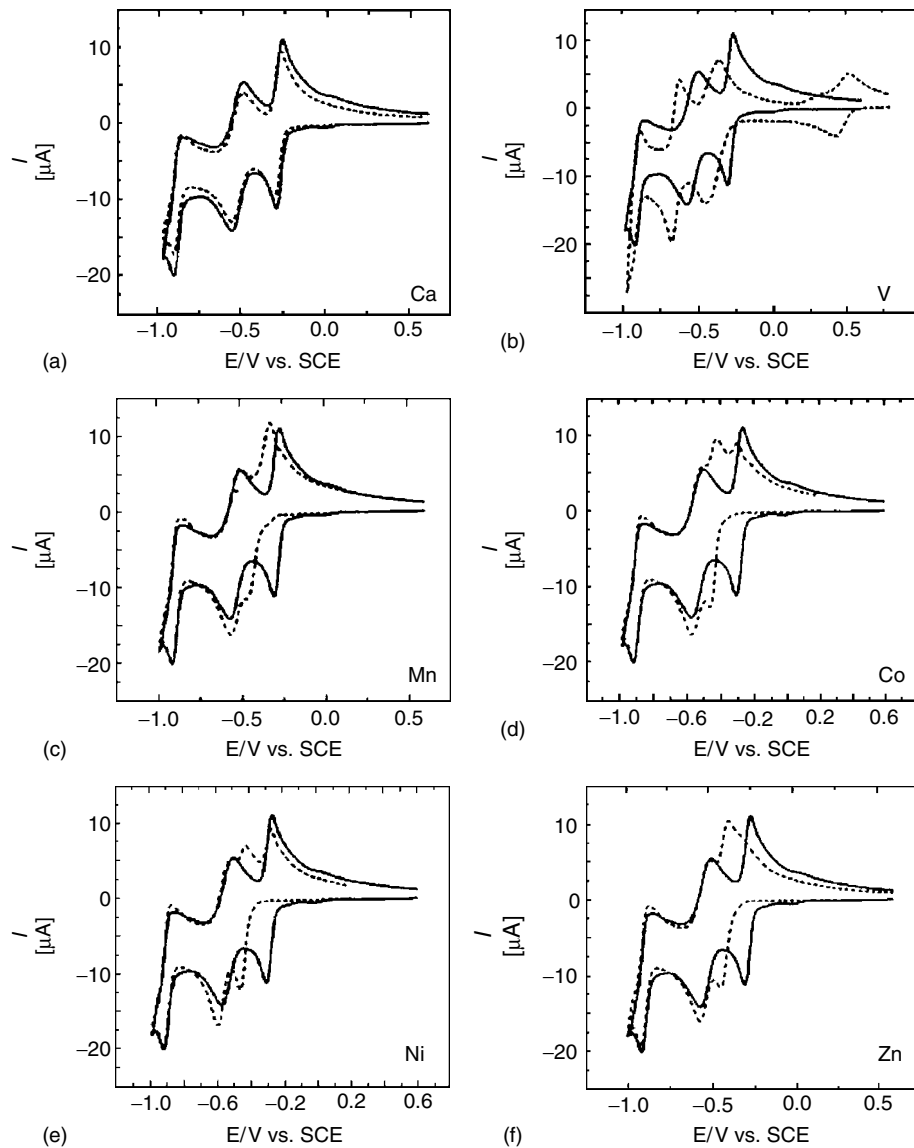


Fig. 12 Comparison of the cyclic voltammograms of $\alpha_1\text{-P}_2\text{W}_{17}$ with those of its substituted complexes in 0.2 M $\text{Na}_2\text{SO}_4 + \text{H}_2\text{SO}_4$ (pH 3) medium. Scan rate: 10 mV s⁻¹. Concentration $c_0 = 2.5 \cdot 10^{-4}$ M for

each complex. The substituent cation is indicated on each curve. The full line corresponds to the lacunary species. For further details, see text (taken from Ref. 15).

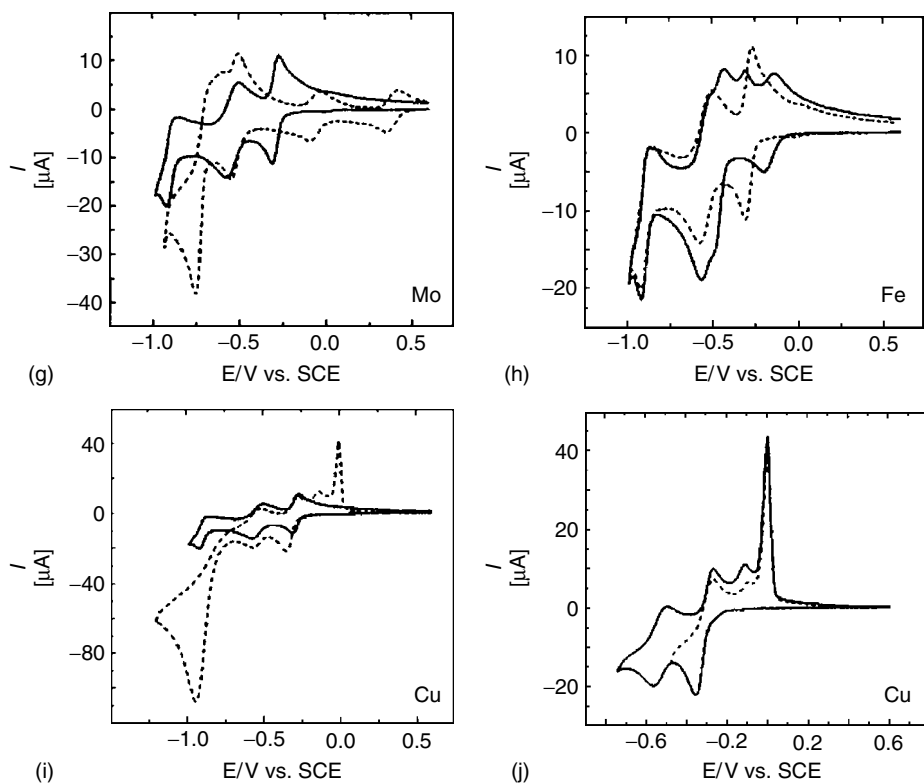


Fig. 12 (Continued).

purpose, the substituted compounds are symbolized by $(P_2W_{17})(ZL)$, where Z is the substituent metal cation and L the terminal ligand [4, 14, 89]. This formula permits to take also into account mixed addenda complexes, and two groups of POMs can be distinguished: the first group is constituted by those complexes in which $Z = W^{6+}$, Mo^{6+} , V^{5+} or V^{4+} and $L = O^{2-}$ and the second group gathers complexes with $Z = M^{n+}$ and $L = H_2O$ where M^{n+} is the metal cation. The complexes of the first group, which encompasses plenary and mixed addenda POMs, can be considered as really “saturated” compounds while the others are not. As a matter of fact, these two groups behave differently in electrochemistry [14, 15, 89], and the

voltammetry of the second group is better considered as deriving from that of the precursor lacunary species.

For convenience, two groups are distinguished among these substituted compounds, depending on whether the potential location of the redox activity of the substituent heterometal cation, in cases when it is visible on cyclic voltammograms is far or close to that of the tungsten framework. A pH = 3 medium (0.2 M $Na_2SO_4 + H_2SO_4$) was selected for this study.

In the α_1 series, Fig. 12(a–f) gather the cyclic voltammograms of those complexes in which the redox activity of the transition metal cation, when visible, occurs far from the potential locations of the waves

associated with the tungsten framework. In each case, the cyclic voltammogram of the α_1 lacunary complex was superimposed for direct comparison. Among these figures, the voltammogram of the Ca(II)-substituted complex is remarkable because it is close to that of the lacunary species. In the pH = 3 medium, $\alpha\text{P}_2\text{W}_{18}$ was observed to grow during the decomposition of the calcium-substituted derivative. Also traces of $[\text{H}_2\text{P}_2\text{W}_{12}\text{O}_{48}]^{12-}$ were detected on the voltammograms. This compound is known to be formed concurrently with $\alpha_1\text{-}[\text{P}_2\text{W}_{17}\text{O}_{61}]^{10-}$ upon degradation of $\alpha\text{P}_2\text{W}_{18}$. Here its presence can be attributed to the formation of $\alpha_1\text{-}[\text{P}_2\text{W}_{17}\text{O}_{61}]^{10-}$ as an intermediate in the Ca(II)-substituted complex transformation at pH 3. Further details on this transformation can be found in the original paper [15]. For the whole series of complexes, it could have been expected, on a purely electrostatic basis, that the addition of a substituent metal cation should just lower the negative charge on the precursor lacunary species and thus facilitate the electron transfer. Such a reasoning would not take into account any specific modification like acid–base properties brought about by each substituent cation. Parameters like the size of each ion, its electronic configuration, its favorite geometry in complexes, the possibility and extent of Jahn-Teller effect, should contribute to the specificity. Throughout the series of compounds, the interplay of these characteristics results in the fact that the first tungsten wave in the substituted complexes appears at a more negative potential location than in the precursor species. Furthermore, in the cases of V(V) and Mn(II), Fig. 12(b) and (c), respectively, this wave tends to split up, which can be attributed to a lowering in basicity of the intermediate reduction species. Another general trend

is the tendency to the appearance of a small second wave associated with the first reduction step, in-line with the composite nature of this first reduction step.

Redox behaviors of the incorporated metal cations are diverse. In the potential domains explored, no electrochemical activity was detected for Ni(II) or Zn(II). The Co(II) center can be oxidized to Co(III). A well-behaved, reversible one-electron wave is observed for the oxidation of V(IV) to V(V) and the subsequent reduction of V(V) to V(IV). The case of Mn(II) is more striking, as at least two fairly stable states are obtained, featuring the Mn(II)/Mn(III) and Mn(III)/Mn(IV) steps.

Figure 12(g–j) illustrates the cases in which the substituent metal cations are reduced in the potential vicinity of the tungsten framework. This situation is encountered with Mo(VI), Fe(III), and Cu(II) cations. The cyclic voltammogram of $\alpha_1\text{P}_2\text{MoW}_{17}$ begins with two well-behaved, largely separated one-electron waves, followed by a two-electron wave. The first one features the reduction of the molybdenum center, the other two are associated with the redox activity of the tungsten framework. The observation of two successive one-electron waves is unique in the series under examination and is rationalized as already explained previously. The molybdenum-substituted compound must be considered as a really “saturated or plenary” species. Therefore, the appropriate comparison must be made with another “plenary” POM like $\alpha\text{P}_2\text{W}_{18}$ or $[\text{P}_2\text{Mo}_{18}\text{O}_{62}]^{6-}$. The better reducibility of the molybdenum over the tungsten atom must also be taken into account. The observed order of potentials in cyclic voltammetry ensues. A relatively detailed account of the study of the Fe(III)-substituted POM will be given in the following as an interesting

example of mixing up of iron and tungsten waves in appropriate pH conditions. It is just worth stressing here the obvious

difference between the cyclic voltammogram of the Fe(III)-complex and the precursor lacunary species in Fig. 12(h–j)

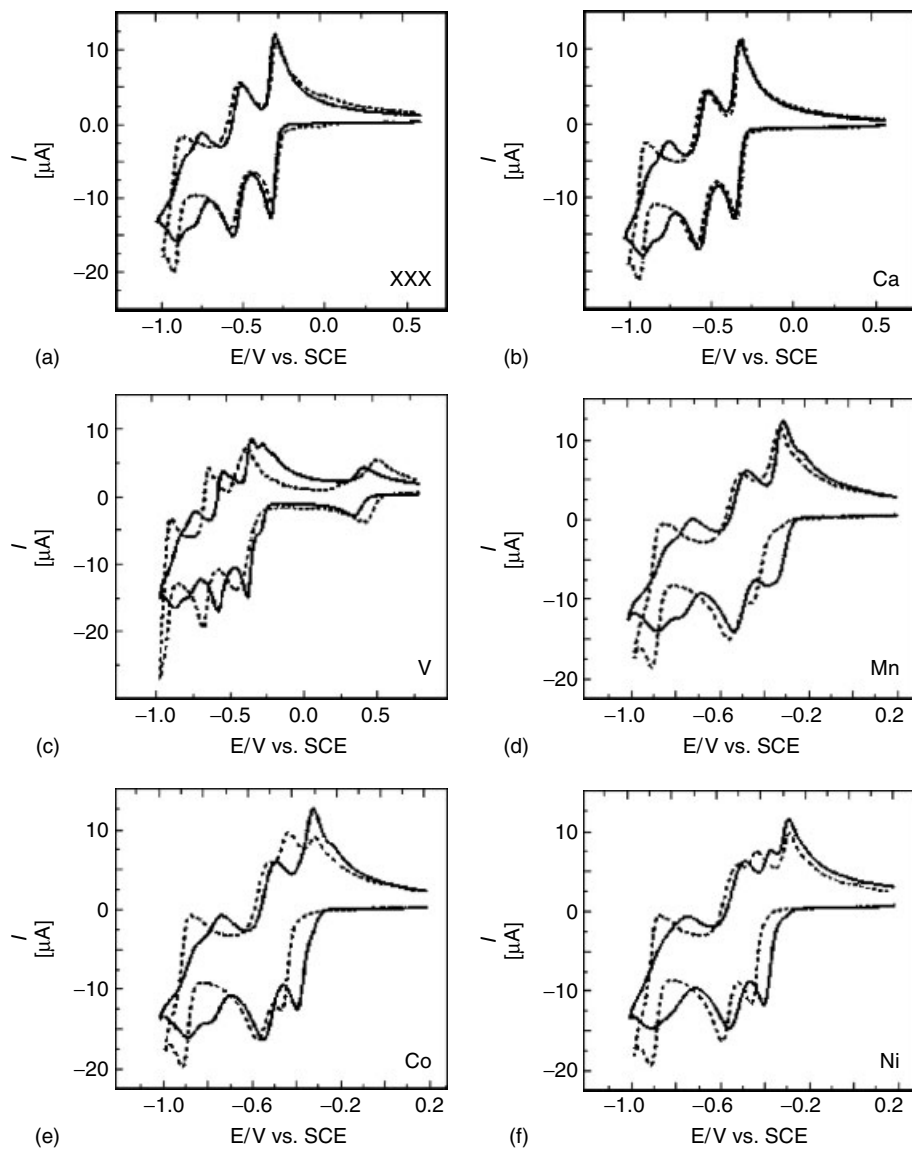


Fig. 13 Comparison of the cyclic voltammograms of α_1 and α_2 - $P_2\Box W_{17}$ and comparison of their metal cation-substituted derivatives in 0.2 M $Na_2SO_4 + H_2SO_4$ (pH 3) medium. Scan rate: 10 mV s⁻¹. Concentration

$c_0 = 2.5 \cdot 10^{-4}$ M for each complex. The substituent cation is indicated on each curve. The full line corresponds to the α_2 species. For further details, see text (taken from Ref. 15).

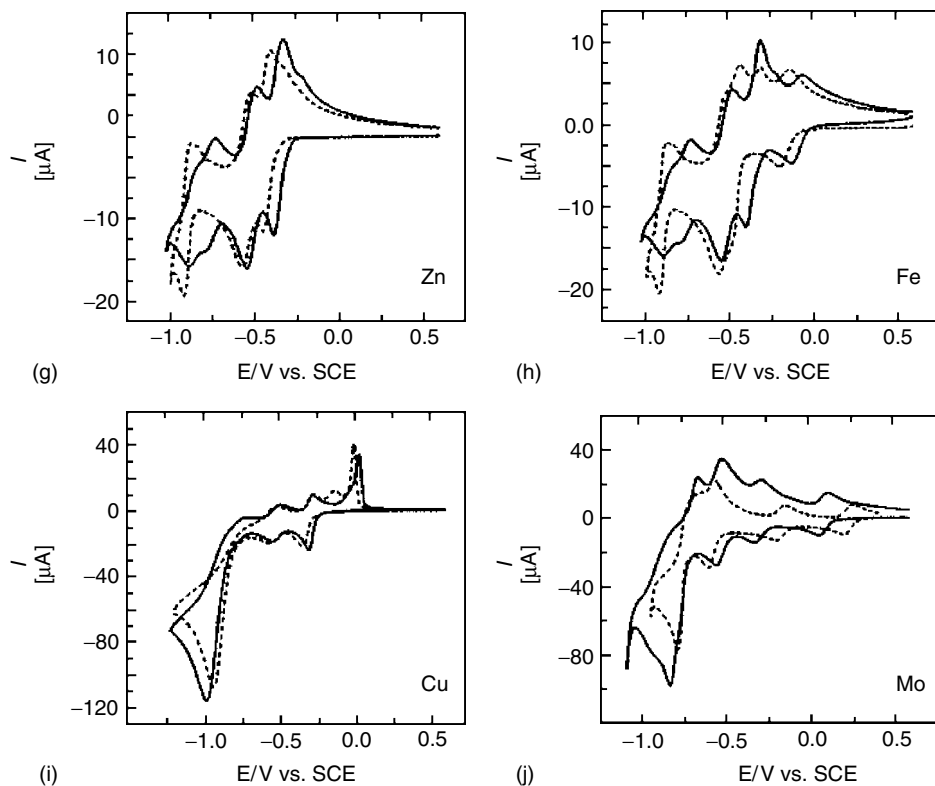


Fig. 13 (Continued).

illustrates the voltammetric behavior of the Cu(II)-substituted POM. The current intensity of the first slightly composite wave is obviously larger than that of the precursor lacunary species at the same concentration, thus signaling at least a partial merging of the copper and tungsten waves in this pH medium. Coulometry on this wave gives four electrons per molecule [90]. The two less negative oxidation waves are attributed to the oxidation of copper (Fig. 12j). One of them is clearly a desorptive oxidation process and its shape indicates that the deposition of copper has occurred during the negative potential directed scan. The large current intensity and chemically irreversible wave in the cyclic voltammogram of the copper

complex reflects the interference of the hydrogen evolution reaction.

Coming to the comparison of the α_1 and α_2 series, the possibilities of isomerization and/or decomposition of the precursor lacunary complexes and, presumably, of their metal ion-substituted derivatives, make it necessary to insure first that no fast conversion occurs, in particular from the α_1 structure to the α_2 one. Figure 13(a) compares the cyclic voltammograms of the two lacunary complexes in the pH 3 medium. The main difference appears on the “third” redox system: a single two-electron, reversible wave is obtained for the α_1 complex; in contrast, the corresponding system for the α_2 isomer is clearly constituted by two,

closely spaced, presumably one-electron waves. This observation is taken as a good distinctive fingerprint of the α_2 complex. In Fig. 13(b–j), the distinction between most compounds of the two groups is obtained readily, owing to the particular fingerprint of the α_2 series. In addition to the special fingerprint in Fig. 13(a–g), at least two other general trends appear: they concern the first redox system associated with the tungsten framework. First, it is split into two unequal steps, the preponderance of one step over the next being a function of the particular substituent metal cation. Second, on average, the cathodic peak potential is more negative in the α_1 than

in the α_2 series. These observations are quantified in Table 12.

This behavior can be understood on the following basis. It was inferred from the comparison of the stability constants of the complexes that they reflect steric effects and that the vacancy in the α_2 position is more prone to deformation than that in the α_1 position [91, 92]. Then the abilities of these two kinds of sites to accommodate various metal cations being different and in favor of the α_2 position, it is obvious that the reduction potentials should become less negative as the negative charge on the anion decreases. Furthermore, it has been proposed [30f, 74] and experimental evidence [79] and

Tab. 12 Reduction peak potentials versus SCE for the first tungsten wave in the various complexes and comparison with the first peak potential of the appropriate lacunary species; electrolyte: 0.2 M Na₂SO₄ + H₂SO₄ (pH = 3) medium (taken from Ref. 15)

Substituent in the complex	α_1 series		α_2 series	
	− E_p [mV] for the 1 st W-wave	ΔE_p [mV]	− E_p [mV] for the 1 st W-wave	ΔE_p [mV]
□	306	0	320	0
Ca	318	12	334	14
V	446	140	(280) 372	52
Mn	(330) 468	162	(358) 394	74
Fe	500	194	(340) 402	82
Co	462	156	(330) 392	72
Ni	460	154	(325) 406	86
Cu	(254) 350	44	306	−14
Zn	450	144	(300) 386	66
Mo	88	−218	236	−84

^aScan rate: 10 mV s^{−1}. The numbers in brackets correspond to the first part of composite waves and are not considered for the calculation of ΔE_p values. For further details, see text.

$\Delta E_p = (E_{p,\text{lacunary}} - E_{p,\text{substituted}})^{\text{1st W-wave}}$.

theoretical approach support [78] that α P₂W₁₈ is initially reduced at one of the twelve equivalent tungsten atoms. Then introduction of electrons in any α_1 position should markedly influence the reduction processes of the tungsten atoms, and, in particular, drive their potentials in the negative direction in comparison of the α_2 derivatives. This situation is indeed observed throughout.

22.5.2.3 An Interesting Case of Mixing up of Substituent and Tungsten Waves: α_1 - and α_2 -[Fe^{III}(OH₂)P₂W₁₇O₆₁]⁷⁻

It is usual that the first reduction wave of commonly studied POMs be monoelectronic or, at the utmost, bielectronic [89]. As a consequence, energetically favorable catalytic processes that require larger numbers of electrons can only be accomplished at fairly negative potentials where the necessary number of charges is accumulated and delivered by the POM framework; hence the search for strategic parameters that could favor apparently multiple electron uptake on the first wave of POMs. The present case deserves emphasis as a simple illustrative example that proved to be very beneficial in the electrocatalytic reduction of nitrite.

In the preceding section, the electrochemistry of copper-substituted derivatives shows an example of mixing up of the substituent metal cation and tungsten waves, but this process was accompanied by the deposition of Cu⁰. Analogous merging was studied in detail in the case of α_1 - and α_2 -[Fe^{III}(OH₂)P₂W₁₇O₆₁]⁷⁻, where this complicating feature was absent [89].

In a pH = 2 medium, the main differences in the cyclic voltammograms of α_1 - and α_2 -[Fe^{III}(OH₂)P₂W₁₇O₆₁]⁷⁻ appear in Fig. 14 and can be summarized as follows: (1) a Fe³⁺ cation filling the vacancy in the

α_2 position introduces nearly no influence in the cyclic voltammogram in which, except for the one-electron “Fe” wave, all the others correspond strictly to those of α_2 -[P₂W₁₇O₆₁]¹⁰⁻; (2) the presence of the iron substituent in the α_1 position modifies substantially the electron transfer pattern associated with the first two waves of α_1 -[P₂W₁₇O₆₁]¹⁰⁻. The “Fe” wave peak intensity is larger and its potential location more negative than the corresponding parameters of α_2 -[Fe^{III}(OH₂)P₂W₁₇O₆₁]⁷⁻. A rationale for this observation was proposed by considering the symmetry of the PO₄ tetrahedron in each of the compounds of the series [89, 93]: its symmetry is C_{3v} in α P₂W₁₈; it turns to T_d, very close to C_{3v}, in the PO₄ tetrahedron belonging to the half lacunary moiety of α_2 -[P₂W₁₇O₆₁]¹⁰⁻. In this case, little perturbation is to be expected from the addition of a heteroatom in the α_2 position, which is actually observed. In contrast, the corresponding PO₄ tetrahedron in α_1 -[P₂W₁₇O₆₁]¹⁰⁻ assumes a C_s symmetry, which would favor a stronger coupling of the heterometal with the tungsten atoms in the “belt” of the Dawson POM.

Gradual lowering of the solution pH down to pH = 0.16 shows the steady increase of the “iron” wave intensity, which reaches finally a current corresponding to the consumption of 3.0 electrons per molecule, a value confirmed by coulometry. Following literature result that whatever the pH dependence of the “iron” wave in classical POMs [94] it involves only one electron, the reasonable assumption is that the observed three-electron wave should feature the merging of the one-electron process of Fe³⁺ with a two-electron process of tungsten. Noteworthy is the reversibility of the pH effect. Upon gradual addition of NaOH in the pH = 0.16 solution up to the pH = 2, the cyclic

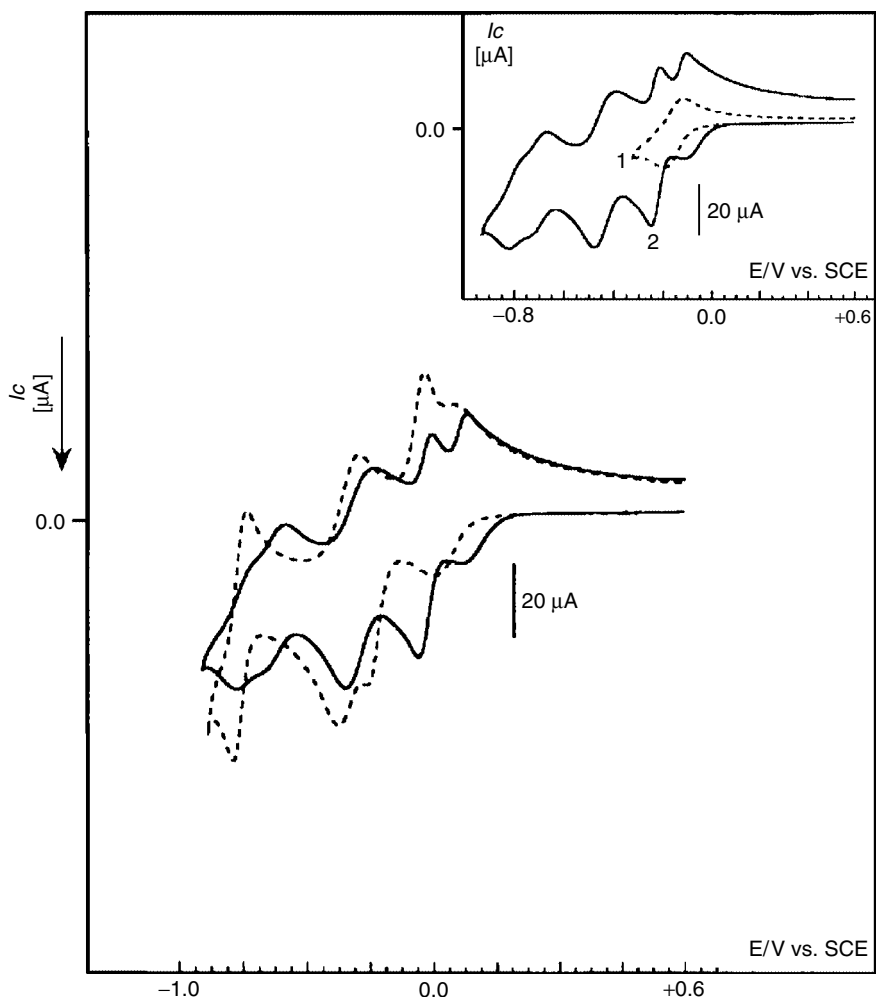


Fig. 14 Comparison of the cyclic voltammograms observed in a pH = 2 medium (0.2 M $\text{Na}_2\text{SO}_4 + \text{H}_2\text{SO}_4$) for 5×10^{-4} M solution of the substituted POM $\alpha_1\text{FeP}_2\text{W}_{17}$ (Curve 1) and $\alpha_2\text{FeP}_2\text{W}_{17}$ (Curve 2). Inset: comparison of the first wave of $\alpha_1\text{FeP}_2\text{W}_{17}$ (Curve 1) with that of $\alpha_2\text{FeP}_2\text{W}_{17}$ (Curve 2). Scan rate: 100 mV s⁻¹ (taken from Ref. 89).

voltammogram goes back exactly through the same situations obtained when the pH was made to decrease by addition of H_2SO_4 . Coulometry and spectroelectrochemistry experiments were carried out with the aim to confirm the preceding observations. Figure 15 gathers spectroelectrochemistry results obtained, essentially at pH = 2. For clarity and simplicity,

shown here are the spectra corresponding to exhaustive reduction of the relevant POM. For each POM, the electrolysis potential was fixed at the reversal potential of the first wave on the cyclic voltammogram. Fig. 15(a) pertains to the reduced form of $\alpha_1\text{-}[\text{P}_2\text{W}_{17}\text{O}_{61}]^{10-}$ which was checked previously to be stable in the pH = 2 medium. The spectra of $\alpha_1\text{-}[\text{Fe}^{\text{III}}(\text{OH}_2)\text{P}_2\text{W}_{17}\text{O}_{61}]^{7-}$

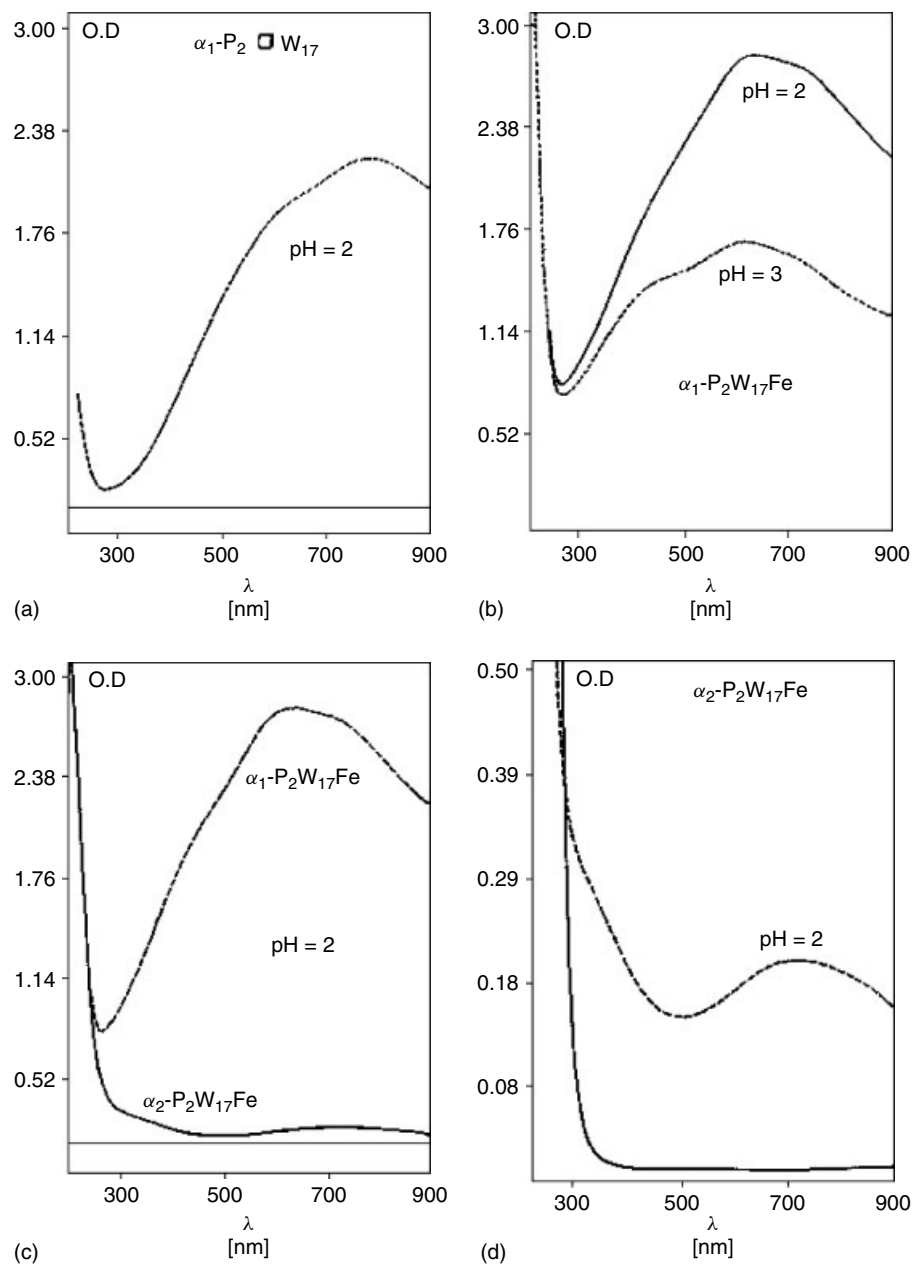


Fig. 15 Final UV-visible spectra run at the end of spectroelectrochemistry experiments. The concentration of POM is 10^{-3} M throughout, except for the spectrum A for which the concentration is $2.8 \cdot 10^{-4}$ M (taken from Ref. 89).

at pH = 2 and pH = 3 are shown in Fig. 15(b). Exactly the same concentration of the POM was used. Following analogous assignments [22, 85, 95–97], the d-d band for Fe(II) appears around 525 nm and the broad band extending into the near-infrared region is assigned to “metal” to “ligand” charge transfers, specifically Fe(II) → W(VI) charge transfer up to the coexistence of Fe(II) and W(V) [96]. In this case, the chromophore W(V) can be expected to contribute the most to the absorption, owing to the more delocalized character of a “tungstic” electron in this environment. The intensities of absorption bands in Fig. 15(b) are in agreement with this line of reasoning and also with the number of electrons consumed in coulometry at each pH (1.08 at pH = 3 and 1.80 at pH = 2). Finally, it was observed that the blue color observed for reduced α_1 -[Fe^{III}(OH₂)P₂W₁₇O₆₁]⁷⁻ became deeper and deeper as the pH of the medium was made more and more acidic. It was checked that the increase in optical density observed in Fig. 15(b) cannot be attributed mainly to a variation in extinction coefficient of the reduced species as described for other POMs [22, 97]. The observations for α_1 - and α_2 -[Fe^{III}(OH₂)P₂W₁₇O₆₁]⁷⁻ are contrasted in Fig. 15(c). They underscore and confirm the differences obtained in cyclic voltammetry and coulometry. Fig. 15(d) shows the spectrum of α_2 -[Fe^{III}(OH₂)P₂W₁₇O₆₁]⁷⁻ (solid line) and that of its reduced form on a magnified scale. The d-d band of Fe(II) appears now around 440 nm and the Fe(II) → W(VI) charge transfer band is small, in agreement with electrochemistry conclusions. The smaller extinction coefficient of reduced α_2 -[Fe^{III}(OH₂)P₂W₁₇O₆₁]⁷⁻ compared to that of reduced α_1 -[Fe^{III}(OH₂)P₂W₁₇O₆₁]⁷⁻ may be attributed to a stronger trapping

of the electron on the Fe center when it occupies an α_2 position.

Thus, in this example, combination of pH effects and spectroelectrochemistry proves very beneficial in the detailed study of merging of POM waves.

22.5.3

Sandwich-type POMs

Transition metal–substituted POMs (TMSPs) can be considered as the largest subclass of polyanions [6]. Within the class of TMSPs, the sandwich-type compounds represent the largest family. In short, sandwich-type POMs are formed by the fusion of two trivacant α -XW₉O₃₄ⁿ⁻ (X = P(V), As (V), Si(IV), Fe(III), Co(II), Cu(II), or Zn(II)), α -XW₉O₃₃ⁿ⁻ (X = As(III), Sb(III), Bi(III), Se(IV), or Te(IV)), or α -X₂W₁₅O₅₆ⁿ⁻ (X = P(V) or As(V)) units via two or more d-electron centers and now constitute one of the largest classes of transition metal–substituted heteropolytungstates. To date, the Hervé-[98], Weakley-[99], Krebs-[100], and Knoth-[101] type sandwich polyanions can be distinguished. The synthesis of fundamentally novel, discrete polyanions is among the most interesting, but also the most difficult challenges in POM chemistry. Transition metal–substituted, sandwich-type polyanions are of particular interest, because of their highly tunable nature, coupled with their chemical robustness. This unique combination of properties is of interest for applications in several areas, including catalysis, electrocatalysis, medicine, and material science [102].

22.5.3.1 Electron Transfer Behaviors of Multi-iron Sandwich-type POMs

In parallel with the explosion of sandwich-type POMs synthesis and characterization, their electrochemistry is studied, both on

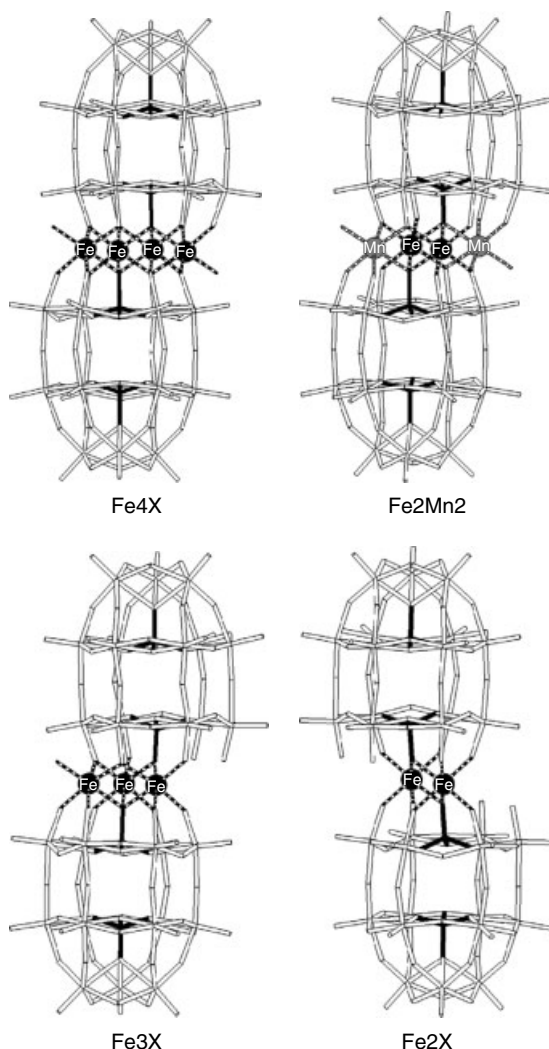
their own interest and also to find out the effects of accumulation of transition metal centers on catalytic and electrocatalytic properties. The same general trends encountered in the preceding section with POMs monosubstituted with a transition metal cation are also observed with sandwich-type species. Electrochemical studies [1, 103–121] indicate the existence of two groups of substituents: (1) the metal cations showing a redox activity within these complexes, with an expected pH dependence of the electrochemistry of the centers bearing a water molecule; (2) the metal cations electrochemically silent in the sandwich complexes; in that case, only a slight modification of the peak potential locations of the ligand waves is observed in comparison with those of the precursor lacunary species. Ni(II)- and Zn(II)-substituted derivatives belong to this group [103, 104, 113, 114].

Some specific behaviors are encountered. As expected, Cu(II)-containing complexes [103, 115, 121] show a deposition of copper upon reduction, and the redox behaviors of Mn(II) within Mn(II)-sandwich complexes were also studied [109, 110, 112, 119]. Electron transfer behaviors of multi-iron sandwich-type oxometalates reveal several illustrative features and these POMs are selected for a detailed electrochemical description [1]. Eight several recently reported multi-iron Wells–Dawson sandwich-type POMs (including **Fe4As4**, **Fe4P4**, $\alpha\alpha\alpha\alpha$ -Na₁₆(NaOH₂)₂(Fe^{III})₂(X₂W₁₅O₅₆)₂ (X = As(V) (**Fe2As4**) or P(V) (**Fe2P4**)), $\alpha\alpha\beta\alpha$ -Na₁₄(NaOH₂)(Fe^{III}OH₂)(Fe^{III})₂(X₂W₁₅O₅₆)₂ (X = As(V) (**Fe3As4**) or P(V) (**Fe3P4**)) and the mixed-metal complexes, $\alpha\beta\beta\alpha$ -Na₁₄(Mn^{II}OH₂)₂(Fe^{III})₂(X₂W₁₅O₅₆)₂ (X = As(V) (**Fe2Mn2As4**) or As(V) (**Fe2Mn2P4**)), (see Sch. 6 for structures)

are used to identify and quantify the interactions between adjacent Fe(III) (or Mn(II)) centers, and electrochemical measurements illustrate how ion-pairing, pH, and electrolyte compositions affect the redox properties of the complexes.

In addition, these results show also how the redox properties of the sandwich-type POMs are affected by the metal population of the central unit. All of these compounds are stable, at least in the timescale of these voltammetric studies, in the pH = 5 buffer (1 M CH₃COOLi and CH₃COOH) medium selected for their studies. The electrochemistry of the lacunary species (α -P₂W₁₅O₅₆¹²⁻ and α -As₂W₁₅O₅₆¹²⁻) were previously described [80, 103, 117]. In contrast with the voltammograms of α -As₂W₁₅O₅₆¹²⁻ and α -P₂W₁₅O₅₆¹²⁻, those of **Fe4As4** and **Fe4P4** show four new waves in the potential domain +0.2 through –0.5 V. Figure 16(a) compares the CVs of α -P₂W₁₅O₅₆¹²⁻ and **Fe4P4**. The four new waves are attributed to the reduction of the four Fe(III) centers within the sandwich complex. At pH 3 (2 M NaCl + HCl), the formal potentials for the Fe(III)/Fe(II) redox couples are: 0.227, 0.124, –0.016, and –0.093 V (vs. SCE), respectively. These locations are distinctly positive of the first W-wave of α -P₂W₁₅O₅₆¹²⁻ and **Fe4P4** (Fig. 16a). This is consistent with the fact that Fe(III) is known to be more easily reduced than W(VI) centers within substituted heteropolytungstates [89]. Corresponding data for the other complexes can be found in the original paper [1]. The reduction of W(VI) centers is also influenced by the presence of the Fe(III) centers in the sandwich molecule. The first wave of α -P₂W₁₅O₅₆¹²⁻, which is slightly composite, is now split into two waves in **Fe4P4**. This behavior is related to differences in the acid–base properties of the two POMs. In analogy with the CVs of α -As₂W₁₅O₅₆¹²⁻

Scheme 6 Combination wireframe/ball-and-stick representations of the eight multi-iron Wells–Dawson sandwich-type complexes studied in this section (taken from Ref. 1).



and $\alpha\text{-P}_2\text{W}_{15}\text{O}_{56}^{12-}$, those of **Fe4As4** and **Fe4P4** are also very similar to each other. The presence of the arsenic heteroatom facilitates the reduction of both the Fe(III) and W(VI) centers (Fig. 16b). The number of W(VI)-waves observed for **Fe4As4** or **Fe4P4**, and hence, the electron number for each wave, depends on the pH of the electrolyte. Rather classical electrochemical behaviors were observed for the W(VI) centers in these complexes. Therefore,

the focus of these studies remains exclusively with the Fe(III) centers. Fig. 16(c) shows the stepwise reduction of the Fe(III) centers in **Fe4P4**, with the domain restricted to the Fe(III) redox processes. The X-ray crystal structures of **Fe4As4** and **Fe4P4** suggest that there are two types of symmetry-equivalent Fe(III) centers [99d, 111a]. There are two “external” Fe(III) sites which share two oxygen atoms with one $\alpha\text{-X}_2\text{W}_{15}\text{O}_{56}^{12-}$ unit and three oxygen

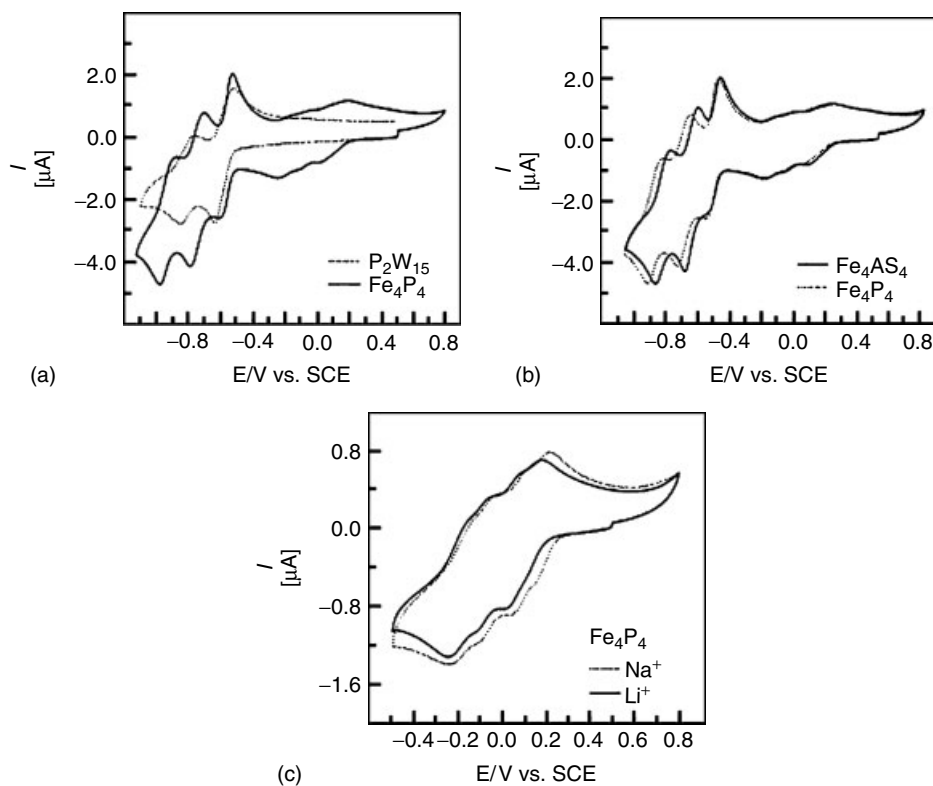


Fig. 16 Cyclic voltammograms of Fe_4As_4 and Fe_4P_4 ($2 \cdot 10^{-4}$ M). The scan rate was 10 mV s^{-1} , the working electrode was glassy carbon, and the reference electrode was SCE. All measurements were performed in a $1\text{ M }CH_3COOLi + 1\text{ M }$

CH_3COOH (pH = 5) buffer solution except in (c), where the dotted line represents a measurement taken in a $0.5\text{ M }Na_2SO_4 + NaOH$ (pH = 5) buffer solution (taken from Ref. 1).

atoms with the other $\alpha\text{-}X_2W_{15}O_{56}^{12-}$ unit. The sixth vertex of the octahedra is composed of a water molecule. The sixth vertex of the two “internal” Fe(III) sites is composed of an additional oxygen atom from one of the two $\alpha\text{-}X_2W_{15}O_{56}^{12-}$ units (rather than a water ligand). The structural data alone would suggest that there would be two groups of redox processes rather than four. The complete splitting into four distinct one-electron reduction processes suggests that there is some type of electronic communication involving the Fe(III) centers. This possibility deserves

careful consideration because it might compete with others (Although coupling between the Fe-centers is invoked as an explanation for the separation (or lack thereof) of the various reduction waves, the behavior for reduction of these centers (whether clearly sequential or not) may also depend simply on the effect of the extra negative charge the POM takes on each time a Fe(III) center is reduced to Fe(II). Literature has solved the case of the first reduction potentials of several Keggin species under conditions of no protonation. The correlation line has a

slope of -0.18 V/unit charge (see Refs. 4 and 54a). The same correlation was also suggested for select examples of second reduction potentials (see Ref. 30a). In the latter case, only highly symmetrical POMs with little or no ion-pairing were addressed and the reduced centers were all W-based. In the multi-iron compounds we address here, electrons are localized essentially in the Fe₄ central unit where ion-pairing is extensively operative and in competition with protonation. In addition, we have to consider the Wells–Dawson trivacant species as the precursors in the synthesis of the present sandwich complexes. Therefore, only a semiquantitative evaluation of this phenomenon can be made at best. However, the observation of a broad, single large cathodic current featuring the combined series of one-electron reduction processes of the four Fe-centers made on $[\text{Fe}_4(\text{OH}_2)_{10}(\beta\text{-XW}_9\text{O}_{33})_2]^{n-}$ ($n = 6$, X = As^{III}, Sb^{III}; $n = 4$, X = Se^{IV}, Te^{IV}) in which Fe centers are not directly connected (Ref. 107a) supports the idea of electronic communication between Fe centers. It can therefore be concluded that the stepwise addition of electrons required in molecular electrochemistry and the subsequent stepwise increase in the overall negative charge of the POM are not sufficient to split the waves measurably in a case where direct influence between structurally equivalent centers does not exist.). This interaction must generate and/or reinforce inequivalence among the sites, especially in the reduced state, and it is also consistent with the magnetic measurements. Finally, it is worth noting that all of the voltammetric patterns of Fe4As4 and Fe4P4 are perfectly well defined and well behaved at pH = 5. This observation is in contrast with the report that Fe4P4 shows ill-defined waves with very small intensity in media of pH > 4 [118]. These differences

may be due to differences in the media used to collect these measurements. This point was checked by running the CV in the same electrolyte (0.5 M Na₂SO₄ and NaOH, pH = 5) as that used in Ref. 118. The results in Fig. 4(c) show that the waves remain perfectly well-defined (dotted line curve) with no current decrease observed compared to the curve recorded in acetate medium (solid line curve). The lesson from these comparisons is that the most severe attention must be paid to the challenging problem of the synthesis and characterization of sandwich-type POMs.

Ion-pairing: Although ion-pairing, pH effects, and ionic strength effects all exist simultaneously and act in competition, the data presented in Fig. 16(c) allows the opportunity to discuss the first of these phenomena. In this system, an overall positive shift is observed for the Fe(III) centers when a Na₂SO₄-based medium is used instead of CH₃COOLi. Since the two systems have the same ionic strength and pH (even though the buffer capacity is greater for CH₃COOLi), this positive shift must be due in part to the nature of the cation. It was previously shown that Na⁺ engages in more intimate ion-pairing with POMs than Li⁺ since the hydrodynamic radius of Li⁺ is greater than Na⁺ [61c,d] (Ref. 94a) have also shown that reduced forms of Fe(III)-monosubstituted Keggin anions engage in ion-pairing with alkali-metal cations.). The positive shift of the Fe(III) centers increases with increased ion-pairing (i.e. K⁺ > Na⁺ > Li⁺). For example, with both the pH and ionic strength kept constant, the formal potential measured for the Fe(III)/Fe(II) couple in Ge(FeOH₂)W₁₁O₃₉⁵⁻ is more positive with a Na⁺ countercation than Li⁺. Complexes Fe4As4 and Fe4P4, however,

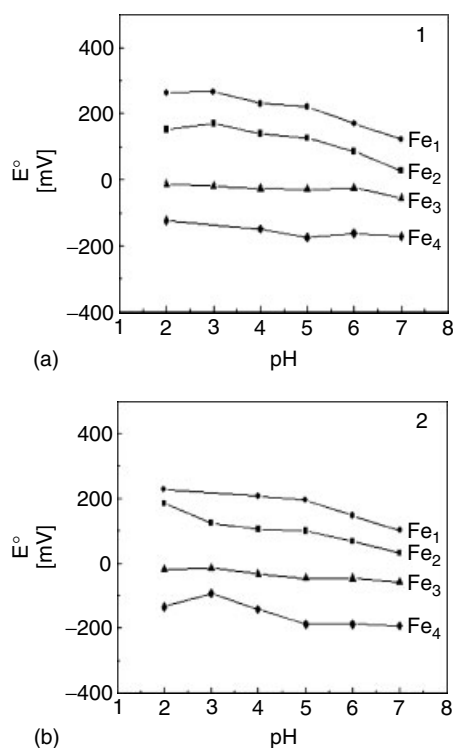
contain four Fe(III) centers and could display more complex ion-pairing behavior. In addition, the two Fe(III) sites with ionizable terminal water ligands add further complexity since ion-pairing and protonation can compete [94]. Figure 16(c) illustrates this complexity by showing that cation influences differ from one wave to the next. For example, the second and fourth redox couples (which are better behaved) experience a 35 mV shift and a negligibly small shift, respectively, with the change of Na^+ to Li^+ medium. The shift due to cation effects is larger for the first two redox couples. To further illustrate the competition between ion-pairing and protonation of the terminal water ligands, the pH of the system was lowered from five to three, prepared with 0.5 M Li_2SO_4 and H_2SO_4 or 0.5 M Na_2SO_4 and H_2SO_4 . The results suggest that protonation supersedes ion-pairing with decreasing pH. These general trends are in good agreement with the apparent pK_a values measured previously. Complex **Fe4As4** gave results similar to **Fe4P4** under the same experimental conditions. The nature of the cation of the supporting electrolyte has a similar effect on W(VI) waves as described previously for monosubstituted Keggin derivatives [94]. For the remaining electrochemical studies, Na^+ is the countercation used since most of the POMs studied here were originally synthesized as Na^+ salts.

pH Effects: The behaviors of the W(VI) waves within POMs as a function of pH were the subject of several previous investigations [3, 4, 28, 89, 94, 103, 107, 122]. The same types of variations were roughly observed within the present multi-iron sandwich-type derivatives, but these were not the focus of this particular study. For the present purpose, pH effects (from pH = 2 to pH = 7) were studied by adding

an appropriate amount of concentrated mineral acid or base to a 2 M solution of NaCl. The high concentration of NaCl is intended to minimize any effect induced by small ionic strength variations. The observation of interest is to determine how changes in pH affect the formal potentials of the Fe(III) waves. Provisionally, it is worth noting that changes in pH might induce the merging of two or more of these waves, although that phenomenon was not observed in these studies.

Figure 17 represents the formal potential variations between pH 2 and pH 7 for each of the Fe(III) centers in **Fe4As4** and **Fe4P4**. The four Fe(III) centers are numbered according to their formal potentials from the least negative (Fe_1) to the most negative (Fe_4). The formal potentials of the Fe(III)/Fe(II) redox couples do not vary smoothly with pH. Analogous intricate pH dependence was previously described in the case of a single Fe(III) center within monosubstituted Keggin derivatives [94]. Electronic communication between Fe(III) centers in the sandwich-type derivatives might render their formal potential variations pH interdependent, and possibly, might also render them more complex. Nevertheless, some new trends do appear in Fig. 17. Focusing first on **Fe4As4**, Fe_1 and Fe_2 centers show almost parallel formal potential variations, with a small domain of quasi-independence from pH 2 to 3 and then again from pH 4 to 5. The variation is roughly linear above pH 5, with a slope of 55 mV/pH. In contrast, the formal potential for Fe_3 is nearly independent for pH values up to 6, and then it begins to vary slightly above this value. For Fe_4 , a linear variation is obtained from pH 3 to 5 with a slope of 26 mV/pH. Then it is fairly pH independent for higher pH values. Even though the present observations specifically concern the Fe(III)/Fe(II)

Fig. 17 Plot of the formal potentials of **Fe4As4** (a) and **Fe4P4** (b) as function of pH for the four one-electron Fe(III)-centered redox processes. The Fe(III) centers are labeled Fe X (with $X = 1, 2, 3$, or 4) from the most positive to the least positive reduction potential. The pH 2–3 solutions are composed of 2 M NaCl + HCl, the pH 4–5 solutions are composed of 2 M NaCl + 0.1 M CH₃COONa + 0.1 M CH₃COOH, and the pH 6–7 solutions are composed of 2 M NaCl + 0.05 M NaH₂PO₄ + 0.05 M NaOH (taken from Ref. 1).



redox couples and not solely the Fe(III) redox states, the formal potential variations follow the trends expected from the knowledge of apparent pK_a values. In particular, the zones of pH independence are consistent with the possibility that ion-pairing supersedes protonation. Furthermore, the formal potentials of the two internal Fe(III) centers are not expected to depend directly on pH. The observed dependence must therefore be traced back to the electronic communication between all of the Fe(III) centers. The same trends were observed for **Fe4P4** as well, albeit with only small differences, presumably linked to differences induced by the different heteroatoms (As vs. P) within these complexes. Finally, ion-pairing and pH effects converge during the reduction processes to suggest that external Fe(III) centers are reduced first.

This is consistent with Pope's report on $(\text{MnOH}_2)_2(\text{Mn})_2(\text{PW}_9\text{O}_{34})_2^{10-}$, in which it was discovered that oxidation first occurs at the aquated Mn centers [112]. However, due to the low intensity of the observed effects and to the fact that oxidation and reduction might involve different molecular orbitals, support or invalidation for the present hypothesis should be sought through complementary theoretical calculations.

Diferric and Triferric Sandwich-type Complexes: Figure 18 shows, in superposition, the voltammograms of **Fe4As4**, **Fe3As4**, and **Fe2As4**, restricted to the waves attributed to the reductions of the Fe(III) centers only. Several conclusions emerge from these patterns. For each CV, the number of waves corresponds to the

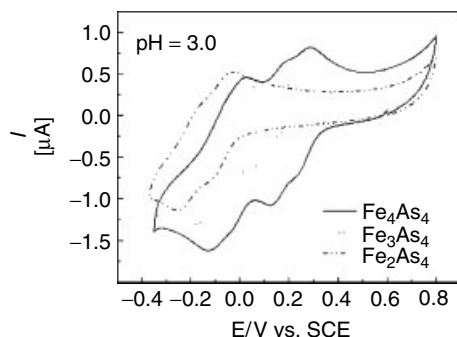


Fig. 18 Cyclic voltammograms of **Fe₄As₄**, **Fe₃As₄**, and **Fe₂As₄** in $2 \cdot 10^{-4}$ M, pH = 3 (2M NaCl + HCl) buffer solution. The scan rate was 10 mV s^{-1} , the working electrode was glassy carbon, and the reference electrode was SCE (taken from Ref. 1).

number of Fe(III) atoms in each complex. These observations suggest there are sufficiently strong interactions between the Fe(III) centers in each of the complexes to induce complete splitting of their redox processes into separate steps. Magnetization measurements were used to identify and quantify the antiferromagnetic interactions between the edge-sharing Fe^{III} units, in complete agreement with electrochemical conclusions [1]. Qualitatively, the overall current intensities are also consistent with the number of Fe(III) atoms in each complex. The number of Fe(III) centers was also checked by controlled potential coulometry measurements, which give three electrons per molecule for **Fe₃As₄** and **Fe₃P₄** and two electrons per molecule for **Fe₂As₄** and **Fe₂P₄** for the exhaustive reduction of these centers. At pH 3, the following values were determined: 3.95 ± 0.05 electrons per molecule for **Fe₄As₄** and **Fe₄P₄** at -0.250 V (vs. SCE); 2.95 ± 0.06 electrons per molecule for **Fe₃As₄** and **Fe₃P₄** with the potential set at -0.300 V (vs. SCE); 1.95 ± 0.07 electrons per molecule for **Fe₂As₄** and **Fe₂P₄** at -0.360 V (vs. SCE). The CV patterns shift in the negative potential direction with a decrease in the number of Fe(III) atoms. This is most likely related to the overall increase in the negative charge of the POM due to the decrease in the

number of Fe(III) atoms. It is probably also related to pK_a differences in the reduced forms. The formal potentials measured from the CVs of the Fe(III)-only complexes can be found in the original paper.

The relative potential shifts of the waves also seem to support the distinction between the external Fe^{III}O₅(OH₂) centers and the internal Fe^{III}O₆ centers within the present complexes. Previously, we concluded that the external Fe^{III}O₅(OH₂) centers are likely reduced before the internal Fe^{III}O₆ ones. Indeed, the CVs of **Fe₃As₄** and **Fe₃P₄** show the disappearance of a wave attributable to an external Fe^{III}O₅(OH₂) center in **Fe₄As₄** and **Fe₄P₄**. The CVs of **Fe₂As₄** and **Fe₂P₄**, which have no external Fe^{III}O₅(OH₂) centers, also agree with this hypothesis since only two waves attributable to internal Fe^{III}O₆ centers are observed. These conclusions are also supported by the apparent pK_a values.

Mixed-Metal Sandwich-type Complexes: Characterization of the mixed-metal multi-iron sandwich complexes indicated that they are stable from pH 0 to 7. This thoroughly-checked observation is in contrast with the instability of several mixed-metal sandwich-type complexes claimed in Ref. 120. In **Fe₂Mn₂P₄**,

the presence of Mn(II) modifies the characteristics of the Fe(III) and W(VI) waves that are observed at slightly more positive potentials than in compound **Fe2P4**. Figure 19 compares the Fe(III)-based redox processes of complexes **Fe2P4** and **Fe2Mn2P4**. Controlled potential coulometry confirms that exhaustive reduction of these centers consumes 2.00 ± 0.05 electrons per molecule. Examination of Fig. 19(a) shows that the

first wave of **Fe2P4** is larger than that of **Fe2Mn2P4** and it has a tendency to merge with the second wave. Thus, an ECE- or EEC-type process seems to be favored in the former complex. This observation leads to the conclusion that the reduced form of **Fe2Mn2P4** is less basic than the corresponding form of **Fe2P4**. Support for the important influence of basicity is illustrated in Fig. 19(b). At pH 5, the two Fe(III)-based

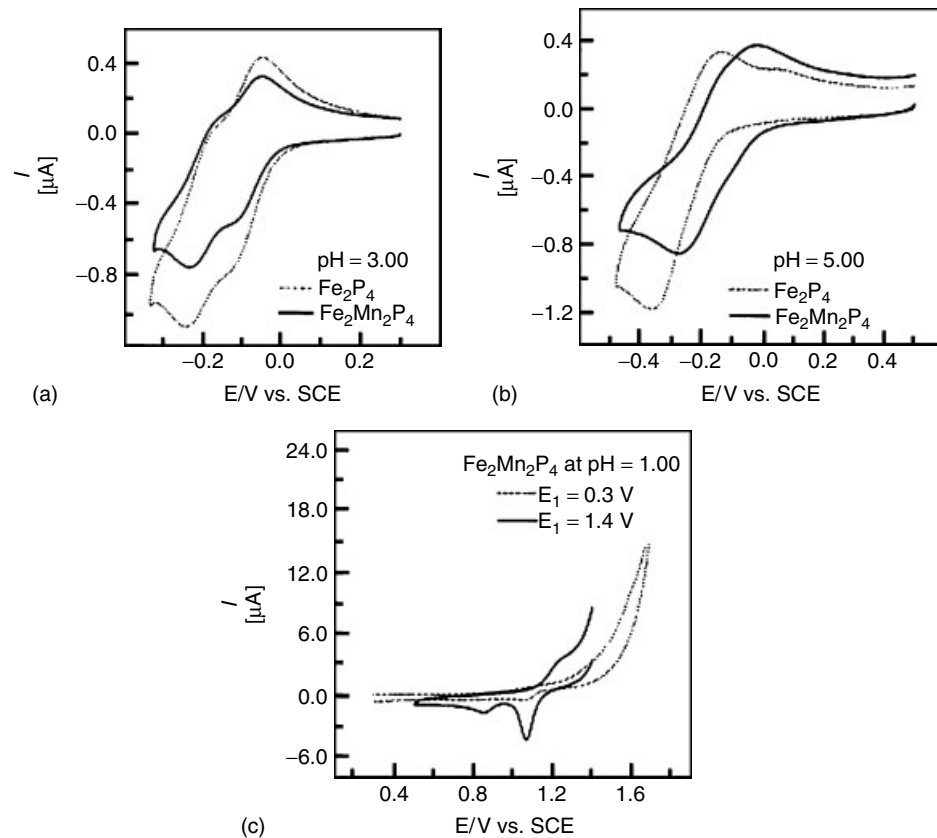


Fig. 19 Cyclic voltammograms of **Fe2P4** and **Fe2Mn2P4** in different buffer solutions. The concentration of the POM was 2×10^{-4} M in all the solutions. The scan rate was 10 mV s^{-1} , the working electrode was glassy carbon, and the reference electrode was SCE. (a) Comparison of **Fe2P4** and **Fe2Mn2P4** in a pH = 3 buffer (0.5 M $\text{Na}_2\text{SO}_4 + \text{H}_2\text{SO}_4$); (b) Comparison of **Fe2P4** and **Fe2Mn2P4** in a pH = 5 medium (1 M $\text{CH}_3\text{COOLi} + 1 \text{ M CH}_3\text{COOH}$); (c) Study of the Mn(II) centers in **Fe2Mn2P4** in a pH = 1 medium (0.5 M $\text{Na}_2\text{SO}_4 + \text{H}_2\text{SO}_4$). E_i = initial potential. See the text for more details (taken from Ref. 1).

waves merge in both complexes with coalescence being somewhat incomplete for **Fe2Mn2P4**, which shows a slightly composite wave. Such differences in the pK_a values of the two complexes might be explained by considering that **Fe2Mn2P4** should behave much like a saturated complex while **Fe2P4** is more lacunary in nature. The differences in behavior of the arsenic analogs (complexes **Fe2As4** and **Fe2Mn2As4**) are less clear than those of the corresponding phosphorus analogs. The results suggest a clear influence of the central heteroatom, P or As, that consists (at pH 3) of an overall positive shift of the Fe(III) waves without a current increase when P is replaced by As. A tentative explanation for this lack of current variation is that the relevant pK_a values in the reduced forms of the As derivatives are very close from one complex to another.

A detailed study of the Mn(II) wave in complex **Fe2Mn2P4** reveals, as expected, that the oxidation process becomes more difficult (i.e. moves toward more positive potentials) when the pH of the supporting electrolyte decreases. This point is illustrated for pH = 1 in Fig. 19(c) where this process is kinetically sluggish. However, pretreating the electrode surface by pausing its potential at +1.4 V for a short time (120 s) prior to scanning the potential in the negative direction clearly reveals the presence of Mn(II). Under these conditions, two reduction waves were observed, accompanied on potential reversal by a fairly well-behaved oxidation wave for the Mn(II) centers. This result is also shown in Fig. 19(c). Separation of the reduction into two steps is less pronounced in a pH 3 medium, where only a shoulder is observed. Examination of all these results together suggests that, for the two pH values

we have explored (pH 3 and 5), the oxidation of Mn(II) to Mn(IV) is followed on potential reversal by the stepwise reduction of Mn(IV). In addition, holding the potential at a selected positive value activates the electrode surface faster than continuous potential cycling. Continuous potential cycling of the electrode through the domain in which the oxidation of interest is expected constitutes another nuance of the activation of the glassy carbon surface electrode in the study of POM-based Mn(II) centers. Steckhan and Sadakane found that this procedure gradually revealed the presence of the two waves of $\alpha\text{-Si}(\text{MnOH}_2)\text{W}_{11}\text{O}_{39}^{6-}$ in a pH 6 phosphate buffer [123]. In contrast, it was shown previously that the merging of the two redox systems of Mn(II) in $\alpha_2\text{-P}_2(\text{MnOH}_2)\text{Mo}_2\text{W}_{15}\text{O}_{61}^{8-}$ results in a composite broad wave while cycling in a pH 6 phosphate medium (with concomitant deposition of an electroactive film on the electrode surface) [14].

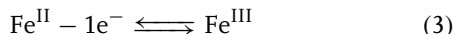
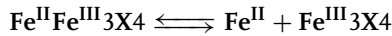
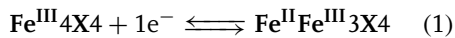
22.5.3.2 Electrochemical Probing of Siderophoric Behavior in Sandwich-type Multi-iron Wells–Dawson Heteropolytungstates

The formation of sandwich-type POMs from solutions of metal cations and trivalent heteropolytungstate species may alternatively be viewed as means to sequester cations from solution [116]. The question then arises if reversible dissociation of the metal cations from the multidentate ligands is possible as well. The sequestration and subsequent release of metal cations under appropriate conditions is of considerable interest in waste decontamination technology as well as in medicine [124]. Following these ideas, the demetallation process of ten multi-iron Wells–Dawson polyoxometalates is studied by cyclic

voltammetry and controlled potential coulometry. Eight sandwich-type complexes ($\alpha\alpha\alpha\alpha\text{-Na}_{16}(\text{NaOH}_2)_2(\text{Fe}^{\text{III}})_2(\text{X}_2\text{W}_{15}\text{O}_{56})_2$, $\alpha\alpha\beta\alpha\text{-Na}_{14}(\text{NaOH}_2)\text{-}(\text{Fe}^{\text{III}}\text{OH}_2)(\text{Fe}^{\text{III}})_2(\text{X}_2\text{W}_{15}\text{O}_{56})_2$, $\alpha\beta\beta\alpha\text{-Na}_{12}(\text{Fe}^{\text{III}}\text{OH}_2)_2(\text{Fe}^{\text{III}})_2(\text{X}_2\text{W}_{15}\text{O}_{56})_2$, and $\alpha\beta\beta\alpha\text{-Na}_{14}(\text{Mn}^{\text{II}}\text{OH}_2)_2(\text{Fe}^{\text{III}})_2(\text{X}_2\text{W}_{15}\text{O}_{56})_2$ (where $\text{X} = \text{P(V)} \text{ or } \text{As(V)}$) and two monomeric complexes ($\alpha\text{-Na}_{11}(\text{P}_2(\text{Fe}^{\text{III}}\text{Cl})_2(\text{Fe}^{\text{III}}\text{OH}_2)\text{W}_{15}\text{O}_{59})$ and $\alpha\text{-Na}_{11}(\text{As}_2(\text{Fe}^{\text{III}}\text{Cl})_2\text{Fe}^{\text{III}}\text{OH}_2)\text{W}_{15}\text{O}_{59})$) were selected for this study.

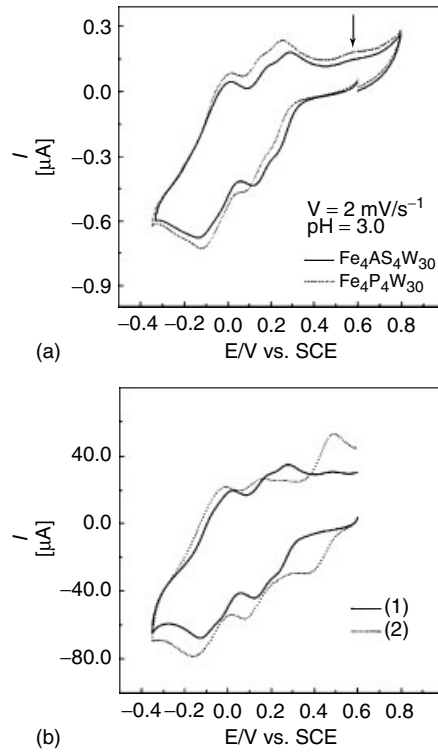
Specifically, Fig. 20 shows representative slow potential scan rate cyclic voltammograms of Fe_4P_4 and Fe_4As_4 in a $\text{pH} = 3$ solution and also as a function of ionic strength for this last complex. A demetallation process of the reduced POMs was detected as appears on this figure. Detailed study of the whole process

was performed as a function of several parameters including the pH, the ionic strength, and the composition of the electrolyte. The observations lead to the conclusion that the following reaction pattern applies, in which Eq. (4) may be only partially operable on the timescale of cyclic voltammetry:



In short, all ten complexes considered here show $\text{Fe}(\text{III})$ waves that are well separated from the redox activity of the

Fig. 20 Cyclic voltammograms of complexes Fe_4P_4 and Fe_4As_4 (2×10^{-4} M). The scan rate was 2 mV s^{-1} and the reference electrode was SCE. All measurements were performed in a $2 \text{ M NaCl} + \text{HCl}$ (pH 3) buffer solution.
(a) The working electrode was glassy carbon (3 mm diameter). The arrow indicates the oxidation of free $\text{Fe}(\text{II})$; (b) The working electrode was a glassy carbon plate (4 cm^2) that was used for the exhaustive controlled potential reduction of the $\text{Fe}(\text{III})$ centers within Fe_4As_4 , followed by an attempt at their regeneration. The cyclic voltammogram before electrolysis is marked “1” while the cyclic voltammogram after the forward and backward electrolyses is indicated by a “2.” See the text for more details (taken from Ref. 116).



W(VI) centers. At room temperature and under mild conditions, iron release from the complexes is observed upon reduction of the Fe(III) centers. This release is controlled by the ionic strength of the medium, the nature and concentration of the anions present in the supporting electrolyte, and by the pH of the solution. This behavior parallels those described for most siderophores that depend on the same parameters.

It is noteworthy that the analogous ejection of Fe(II) was observed previously upon reduction of the single Fe(III) center within $\alpha_2\text{-}[\text{Fe(OH}_2\text{)} \text{P}_2\text{W}_{17}\text{O}_{61}]^{7-}$ [89] and $\alpha\text{-}[\text{Fe(OH}_2\text{)} \text{ZnW}_{11}\text{O}_{39}]^{7-}$ [122].

22.6 Recent Developments

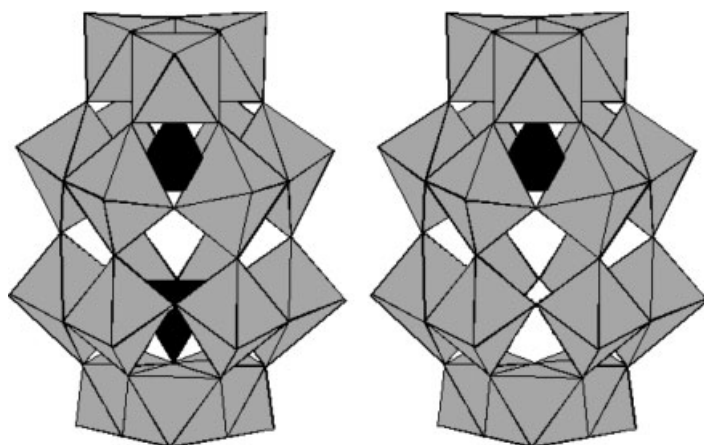
22.6.1 Electrochemistry of a New Family of Wells–Dawson Anions: Semivacant Tungstophosphates and Arsenates [$\text{H}_4\text{XW}_{18}\text{O}_{62}]^{7-}$ ($\text{X} = \text{P or As}$)

Following the pioneering synthesis of $[\text{H}_4\text{PW}_{18}\text{O}_{62}]^{7-}$ (PW₁₈ for convenience)

[187], the general possibility of establishing a novel Dawson-type family structures with two different central heteroatoms was demonstrated with the syntheses of $[\text{H}_4\text{XW}_{18}\text{O}_{62}]^{7-}$ ($\text{X} = \text{P or As}$), their monolacunary species and their first transition metal ion derivatives [103, 125, 126]. The new structure is sketched in Sch. 7 and was confirmed very recently by direct X-ray crystallography determination [127, 128].

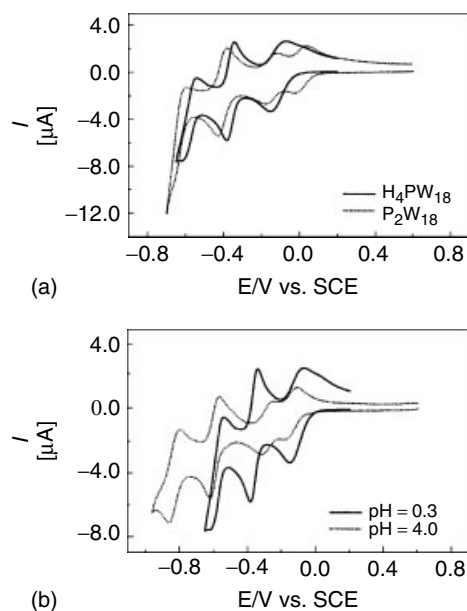
22.6.1.1 Evidence for an Influence of the Dissymmetry on the Voltammetric Behavior of PW₁₈: Comparison with P₂W₁₈

The comparison of the voltammetric characteristics of PW₁₈ and P₂W₁₈ is useful to highlight the peculiarities of the former complex. Figure 21 shows in superimposition the cyclic voltammograms (CVs) of the two complexes in a pH 0.3 sulfate medium. The potential domain was selected to avoid any deleterious derivatization of the electrode surface [28]. Furthermore, such domain is the most useful for elucidation of electrocatalytic processes. Here, the voltammetric pattern is restricted to the first three waves observed for PW₁₈ in this medium. In



Scheme 7 Schematic representations of the Dawson-type tungstodiphosphate and tungstomonophosphate (taken from Ref. 125).

Fig. 21 Cyclic voltammograms (CVs) run on 5×10^{-4} M solutions of the relevant polyoxometalates; scan rate: 10 mV s^{-1} ; working electrode: glassy carbon; reference electrode: SCE. (a) comparison of the CVs observed in a pH 3 medium (0.2 M $\text{Na}_2\text{SO}_4 + \text{H}_2\text{SO}_4$) for the two unsubstituted tungstophosphates: PW_{18} and P_2W_{18} ; (b) pH effect on the CV of PW_{18} . For further details, see text (taken from Ref. 125).



the same conditions, the voltammetry of P_2W_{18} is known [29] and is constituted by two one-electron waves followed by two two-electron waves. These waves feature reversible diffusion-controlled processes. The comparison of the CVs of the two POMs is shown in Fig. 21(a) and is enlightening. The first wave of PW_{18} represents unambiguously a two-electron chemically reversible process. This point was checked by controlled potential coulometry. The two subsequent waves also feature two-electron processes. In short, the pattern for PW_{18} is constituted by a set of three reversible diffusion-controlled waves. This observation was expanded by a brief study of the pattern as a function of pH. Figure 21(b) illustrates this point and shows, in superimposition, the CVs of PW_{18} at pH 0.3 and 4. With the increase in pH, the formerly two-electron wave splits into two supposedly one-electron processes. No attempt was made to ascertain quantitatively that the

splitting was complete at pH 4. Turning more specifically to the comparison of the voltammetric behaviors of the two POMs, all the observations point to the higher basicity of the reduced forms of PW_{18} compared to those of P_2W_{18} . The results fit in the following scheme that could have been forecast from the structures. Formally, PW_{18} is constituted by two A-type half-anions that can be formulated H_4W_9 and PW_9 respectively. A loose analogy might induce one to point out the similarity between the hydrogenated fragment of PW_{18} and $[\text{H}_2\text{W}_{12}\text{O}_{40}]^{6-}$ (H_2W_{12}). This analogy should be expressed in terms of compared basicity between PW_{18} and P_2W_{18} , with reference to the known basicity influence in the reduction of H_2W_{12} compared to those of the corresponding species of classical Keggin-type POMs [33c, 129, 130]. As a matter of fact, polarograms (and voltammograms) of H_2W_{12} at pH < 3.5, show three waves of 2, 2, and ca. 10 electrons each [35, 129, 130], in conditions in which

the first two reductions of its analogs $[PW_{12}O_{40}]^{3-}$ and $[SiW_{12}O_{40}]^{4-}$ and even the Dawson-type P_2W_{18} , are one-electron pH-independent processes. Therefore, the pH-dependent voltammetric behavior observed for PW_{18} in comparison with that of P_2W_{18} can be paralleled with that of H_2W_{12} vis à vis $[PW_{12}O_{40}]^{3-}$ and $[SiW_{12}O_{40}]^{4-}$. It must be concluded that PW_{18} and its first several reduced species show larger basicity compared to the corresponding species of P_2W_{18} . Provisionally, it is worth mentioning, in contrast, that roughly 6 M HCl solution was necessary to make the first two waves of P_2W_{18} merge [33c]; the concentration of acid reaches 7–8 M HCl in the case of $[SiW_{12}O_{40}]^{4-}$. Such merging could not be achieved for $[PW_{12}O_{40}]^{3-}$ in solution [33c] and was only realized inside polymer matrices [130]. This observation is rewarding and constitutes a good step in the continuous search for means to accumulate electrons on the first or the first several waves of POMs in mild conditions. To our knowledge, this series of compounds represent the first example in which a two-electron W-wave in a saturated species is found to appear at relatively less negative potential and mild acidity than generally obtained in classical Dawson HPAs in aqueous media. This constitutes one of the favorable conditions for eventual electrocatalytic processes.

Following the synthesis of pure $[H_4PW_{18}O_{62}]^{7-}$ (PW_{18}), its derivatives monosubstituted by M (M \equiv Mo^{VI}, V^{IV}, V^V, Mn^{II}, Fe^{III}, Co^{II}, Ni^{II}, Cu^{II}, and Zn^{II}) were obtained. Their cyclic voltammetry behaviors were studied as a function of pH and systematically compared with those of their analogs derived from the symmetrical $[P_2W_{18}O_{62}]^{6-}$ (P_2W_{18}). The fingerprint observed for α_2 - $P_2W_{17}M$ derivatives in pH 3 media consisted in the splitting of the

third W-redox system into two one-electron closely spaced waves, in contrast with the same system in α_1 - $P_2W_{17}M$. This peculiarity was also obtained for several of the present α_2 - $PW_{17}M$ in pH 3 medium and confirmed that α_2 -substituted derivatives were indeed prepared. The disappearance of this peculiar behavior in some other derivatives is consistent with smooth variations of acid–base properties from one derivative to the next.

Comparison with the electrochemistry of $[H_4AsW_{18}O_{62}]^{7-}$ with that of the P analog reveals only small differences between the two plenary species. In contrast, a remarkable difference in stability was observed for the lacunary derivatives. Unlike its phosphorus analog, the defect species of $[H_4AsW_{18}O_{62}]^{7-}$ was sufficiently stable for a few voltammetric runs. For the two series, several lines of experimental evidence converge to indicate that the substitution occurs in the α_2 position. As a consequence, in the case of $[H_4AsW_{18}O_{62}]^{7-}$ substituted derivatives, the cyclic voltammetry properties of substituted compounds could be studied as a function of pH and systematically compared with those of the lacunary precursor rather than with those of their analogs derived from the symmetrical species $[As_2W_{18}O_{62}]^{6-}$.

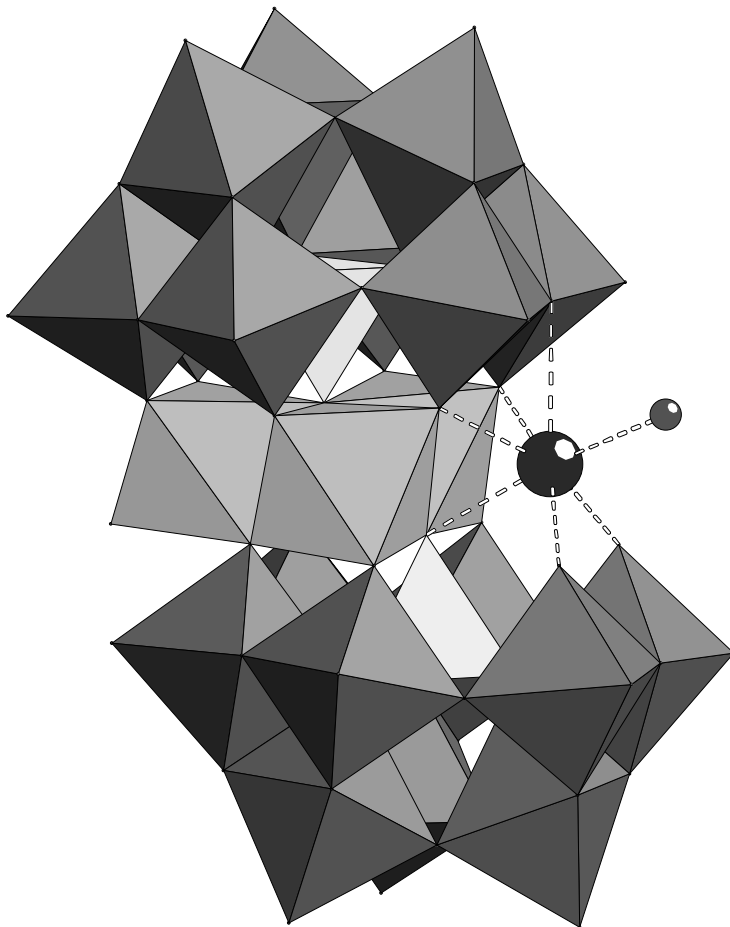
22.6.2

Recent Achievements in Apparently Direct Multiple Electron Transfers on the First Waves of POMs

An issue that is being considered with attention concerns the possibility to achieve multiple electron transfers on the first wave of POMs. The aim is twofold: (1) save energy by favoring those electrocatalytic processes that necessitate several electron to be performed; (2) avoid the

derivatization of the electrode surface. In this context and with particular regard to the electrochemistry and correlatively the use of these POMs in electrocatalysis, three factors were identified recently that promote their multielectron transfer reactions: first, the pH [2] of the solution that also determines the stability domain of the POM; second, a “substituent effect” was identified in which one or more of the skeletal d⁰ (usually W^{VI} or Mo^{VI}) centers

of the POM structure are replaced by other d⁰ centers and/or by d-electron containing transition metal cations [11, 13–15, 103, 111, 113, 125]; of particular interest for the present purpose, it was found that accumulation of such substituted centers is more favorable for electrocatalytic processes compared to the results observed with the corresponding mono-substituted derivatives [103, 111]; third, the nature of the central heteroatom was



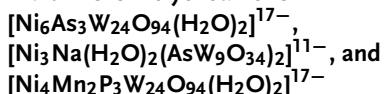
Scheme 8 Combined polyhedral/ball-and-stick representation of $[Ni_3Na(H_2O)_2(AsW_9O_{34})_2]^{11-}$. The AsO₄, WO₆, and NiO₆ polyhedra are shown in yellow, red, and green, respectively. The sodium atom is shown as a blue ball and its terminal water molecule as a red ball (taken from Ref. 106).

found to influence the potential locations of the first several waves [111b]. A comparison of a series of monosubstituted Wells–Dawson tungstodiphosphates and tungstodiarsenates revealed that the presence of the As heteroatom drives the first several voltammetric waves in the positive potential direction [111b]. As illustration of these lines, several POMs which engage in multiple electron transfer in the potential domain of their first redox wave were synthesized and studied. However, before going into descriptions of the results, it is worth emphasizing both the difficulty of the syntheses and the necessity for these POMs to be stable in the

media in which they are studied. In the following, the selection is restricted to stable POMs, even though several others were synthesized with larger numbers of metallic centers.

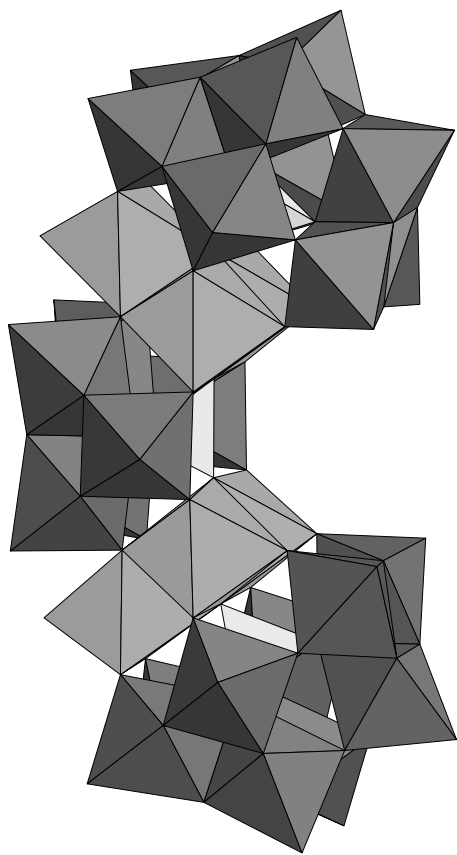
22.6.2.1 Electrochemistry of the

Multi-nickel Polyoxoanions



The structures of these new POMs are sketched in Schs. 8 and 9 [108].

$[Ni_4Mn_2P_3W_{24}O_{94}(H_2O)_2]^{17-}$ ($Ni_4Mn_2P_3W_{24}$). Figure 22(a) compares, in a pH 3 medium, the cyclic voltammograms of $Ni_4Mn_2P_3W_{24}$ and of the original precursor used for its synthesis, $Ni_3P_2W_{18}$ [106]. In the negative potential domain, only the first two redox couples located just before proton reduction are represented. The CVs of the two complexes are very similar in shape, with the pattern for $Ni_4Mn_2P_3W_{24}$ located slightly more negatively in potential. This observation might be traced to the difference in the overall negative charges of the complexes. As a matter of fact, with the assumption that all other factors act practically in the same way, it is expected that $Ni_4Mn_2P_3W_{24}$ with 17 negative charges should be more difficult to reduce than $Ni_3P_2W_{18}$ with only 12 negative charges [4, 54a,b,c]. It must be noted, however, that the magnitude of this difference might be modulated by acido-basic properties of the reduced forms of the complexes. As observed previously for $Ni_3P_2W_{18}$, these two waves are attributed to redox processes of W^{VI} centers. In the positive potential domain, only $Ni_4Mn_2P_3W_{24}$ shows a wave



Scheme 9 Polyhedral representation of $[Ni_6As_3W_{24}O_{94}(H_2O)_2]^{17-}$. The AsO_4 , WO_6 , and NiO_6 polyhedra are shown in yellow, red, and green, respectively (taken from Ref. 108).

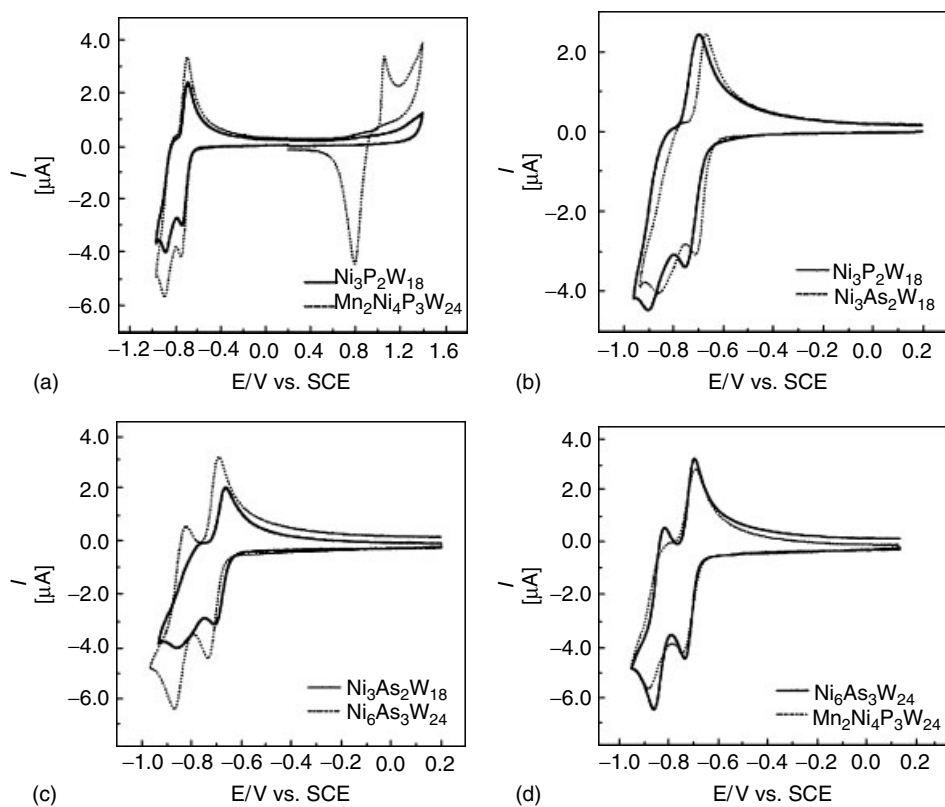


Fig. 22 (a) Comparison of the cyclic voltammograms of $2 \cdot 10^{-4} \text{ M } \text{Ni}_3\text{P}_2\text{W}_{18}$ and $\text{Mn}_2\text{Ni}_4\text{P}_3\text{W}_{24}$, respectively, at pH 3 (0.2 M $\text{Na}_2\text{SO}_4 + \text{H}_2\text{SO}_4$). Scan rate: 10 mV s^{-1} ; working electrode: polished glassy carbon; reference electrode: SCE. For further details, see text. (b) Comparison of the cyclic voltammograms of $2 \cdot 10^{-4} \text{ M } \text{Ni}_3\text{P}_2\text{W}_{18}$ and $\text{Ni}_3\text{As}_2\text{W}_{18}$, respectively, at pH 3 (0.2 M $\text{Na}_2\text{SO}_4 + \text{H}_2\text{SO}_4$). Scan rate: 10 mV s^{-1} ; working electrode: polished glassy carbon; reference electrode: SCE. For further details, see text. (c) Comparison of the cyclic

voltammograms of $2 \cdot 10^{-4} \text{ M } \text{Ni}_3\text{As}_2\text{W}_{18}$ and $\text{Ni}_6\text{As}_3\text{W}_{24}$, respectively, at pH 3 (0.2 M $\text{Na}_2\text{SO}_4 + \text{H}_2\text{SO}_4$). Scan rate: 10 mV s^{-1} ; working electrode: polished glassy carbon; reference electrode: SCE. For further details, see text. (d) Comparison of the cyclic voltammograms of $2 \cdot 10^{-4} \text{ M } \text{Ni}_6\text{As}_3\text{W}_{24}$ and $\text{Mn}_2\text{Ni}_4\text{P}_3\text{W}_{24}$, respectively, at pH 3 (0.2 M $\text{Na}_2\text{SO}_4 + \text{H}_2\text{SO}_4$). Scan rate: 10 mV s^{-1} ; working electrode: polished glassy carbon; reference electrode: SCE. For further details, see text (taken from Ref. 108).

with a peak located at $+1.058 \text{ V}$, featuring the oxidation of Mn^{II} centers.

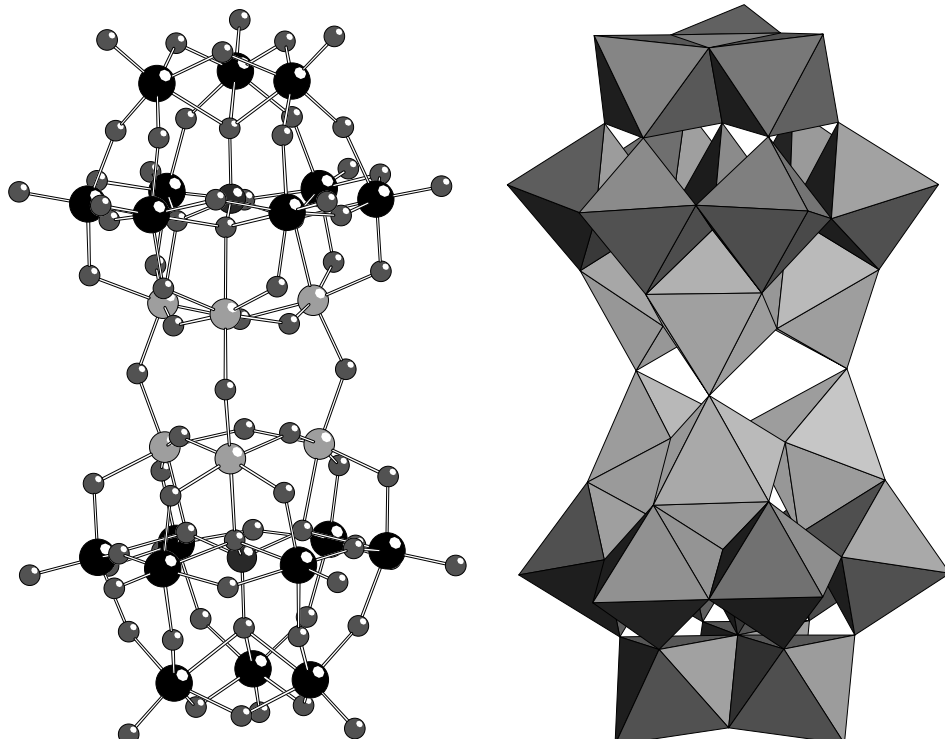
$[\text{Ni}_6\text{As}_3\text{W}_{24}\text{O}_{94}(\text{H}_2\text{O})_2]^{17-}(\text{Ni}_6\text{As}_3\text{W}_{24})$ and $[\text{Ni}_3\text{Na}(\text{H}_2\text{O})_2(\text{AsW}_9\text{O}_{34})_2]^{11-}(\text{Ni}_3\text{As}_2\text{W}_{18})$. The CV of $\text{Ni}_3\text{As}_2\text{W}_{18}$ is also constituted by two reversible waves, which are located in a more positive potential

domain than that of its P analog $\text{Ni}_3\text{P}_2\text{W}_{18}$ as shown in Fig. 22(b). This observation is in agreement with results on other heteropolyanions for which the presence of As instead of P as the central heteroatom facilitates the reduction process [111b]. In analogy to the case of $\text{Ni}_3\text{P}_2\text{W}_{18}$, the

second wave is followed by the reduction of protons. Furthermore, controlled potential coulometric determination at -0.730 V in a pH 3 medium confirms that four electrons are consumed per molecule in the first wave, as already observed previously for the P analog [106]. In short, the electrochemical and IR characterizations as well as elemental analysis converge to confirm that $\text{Ni}_3\text{As}_2\text{W}_{18}$ and $\text{Ni}_3\text{P}_2\text{W}_{18}$ have the same structure.

On the basis of CV it is possible to clearly distinguish $\text{Ni}_6\text{As}_3\text{W}_{24}$ and $\text{Ni}_3\text{As}_2\text{W}_{18}$ as shown in Fig. 22(c). In agreement with the difference in charges of the two polyanions, the more heavily negative one, $\text{Ni}_6\text{As}_3\text{W}_{24}$, is slightly more

difficult to reduce than $\text{Ni}_3\text{As}_2\text{W}_{18}$. As the two molecules are not expected to have the same diffusion coefficient, the simple comparison of the peak current intensities of the respective CVs of $\text{Ni}_6\text{As}_3\text{W}_{24}$ and $\text{Ni}_3\text{As}_2\text{W}_{18}$ cannot be used for an accurate determination of the number of electrons on the latter species. Nevertheless, it can be easily concluded that this number of electrons is larger for $\text{Ni}_6\text{As}_3\text{W}_{24}$. Figure 22(d) compares the CVs of $\text{Ni}_6\text{As}_3\text{W}_{24}$ and $\text{Ni}_4\text{Mn}_2\text{P}_3\text{W}_{24}$ and as expected the compound with P as the heteroatom is more difficult to reduce than its As-analog [111b]. These two polyanions are likely to have fairly similar diffusion coefficients;



Scheme 10 Ball and stick (left) and polyhedral (right) representations of $[\text{Fe}_6(\text{OH})_3(\text{A}-\alpha\text{-GeW}_9\text{O}_{34}(\text{OH})_3)_2]^{11-}$ (**1**). The color code is as follows: iron (green), tungsten (black), germanium (blue) and oxygen (red) (taken from Ref. 107b).

therefore, their CVs can be compared straightforwardly and correspond to the same number of electrons, albeit for the potential locations. Controlled potential coulometry performed at pH 3 on the first W-wave of these two compounds indicates that these waves correspond to six-electron processes for each polyanion.

22.6.2.2 Electrochemistry of the Iron(III)-substituted Keggin Dimer, $[\text{Fe}_6(\text{OH})_3(\text{A}-\alpha\text{-GeW}_9\text{O}_{34}(\text{OH})_3)_2]^{11-}$

The complex $\text{Fe}_6\text{Ge}_2\text{W}_{18}$ (Sch. 10) was found to be stable between pH = 3 and pH = 7 [107].

Figure 23 shows the cyclic voltammogram of $\text{Fe}_6\text{Ge}_2\text{W}_{18}$ obtained at a scan rate of 10 mV s⁻¹, in a pH 3 sulfate medium (0.2 M Na₂SO₄ + H₂SO₄). The pattern is restricted to the two waves that feature respectively the reduction of Fe³⁺ centers and the first W-wave. In the following text, attention is focused on the reduction of Fe³⁺ centers. Its reduction peak potential is observed at $E_{pc} = -0.248$ V vs. SCE. A loose comparison with the corresponding E_{pc} values for free Fe³⁺ ($E_{pc} = 0.074$ V vs. SCE) and $[\text{Fe}_4(\text{H}_2\text{O})_{10}(\beta\text{-AsW}_9\text{O}_{33})_2]^{6-}$ ($E_{pc} = -0.126$ V vs. SCE) in the same electrolyte [107a], supports the usual expectation that the order of peak potentials should follow the overall negative charges of the complexes, under the

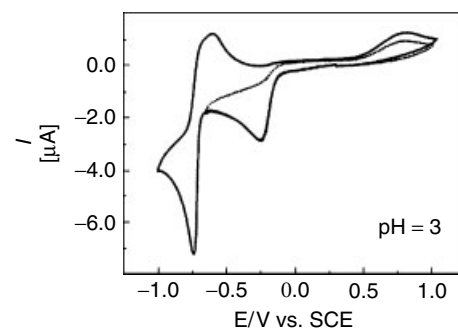
complementary assumption of otherwise identical influences. Whatever the scan rate from 1000 mV s⁻¹ down to 2 mV s⁻¹, no splitting of the single Fe-wave of $\text{Fe}_6\text{Ge}_2\text{W}_{18}$ was observed. Controlled potential coulometry with the potential set at -0.400 V vs. SCE indicates the consumption of 6.08 ± 0.05 electrons per molecule, thus confirming the simultaneous one-electron reduction of each of the six Fe-centers. As a good piece of evidence that the tungsten-oxo framework was not reduced, the electrolysis did not give the characteristic blue color. Exchange of a relatively high number of electrons in polyoxometalate electrochemistry was described previously. In cases when such exchanges are associated with proton consumption, the buffer capacity of the supporting electrolyte might influence the shape and potential location of the voltammetric waves [86a,b]. This point was also studied in the paper.

22.6.3 Theoretical Approaches

22.6.3.1 Electronic Structures of POMs Explain their Redox Behaviors and the Relative Stability of Reduced Forms

As a consequence of the high number of heavy atoms in POMs in addition to the complexity of the problems

Fig. 23 Cyclic voltammograms in a 2×10^{-4} M solution of $\text{Fe}_6\text{Ge}_2\text{W}_{18}$ complex in pH = 3 media; working electrode: glassy carbon; reference electrode: SCE. pH = 3 sulfate medium (0.2 M Na₂SO₄ + H₂SO₄); superposition of the CVs restricted to the Fe-wave and to the Fe-wave and the first W-redox processes; scan rate: 10 mV s⁻¹ (taken from Ref. 107b).



of interest, attempts at direct theoretical rationalization of observations and/or prediction of behaviors are rather limited. A remarkable characteristic, however, is that different issues were tackled as directly as possible, whatever the available theoretical tools at hand at the moment. Even the earliest theoretical works on polyoxometalates using the simple semiempirical extended Hückel approach are devoted to problems as complicated as the comparison of the catalytic and structural properties of heteropolycompounds [131], or the behaviors of polyoxometalates as models of oxide catalysts [132]. Other achievements include the Molecular Orbital Theory treatment of the photodimerization of cyclohexene and methane by decatungstate anions [133] or the oxidative dehydrogenation of methanol by metal oxide surfaces [134]. Progressively, more sophisticated ab initio or DFT methods are being introduced [135–150]. Their ability to tackle problems as diverse as the acidity and basicity of polyoxometalates [142, 143], the localization or delocalization of metal electrons in reduced species [140, 141, 144, 147, 150] is receiving increasing attention. Among several very interesting examples, a recent DFT study [150] focuses on the relative stability, upon reduction, of the five isomers of $[PW_{12}O_{40}]^{3-}$. In the oxidized form, the energy grows as follows $\alpha < \beta < \gamma < \delta < \varepsilon$ and fits the experimental findings. The reduced clusters behave differently as long as the β form becomes the most stable isomer after the second reduction. The γ isomer also gains stability upon reduction, but not enough to be competitive with β . For the fourfold reduced $[PW_{12}O_{40}]^{3-}$ cluster, the energy difference computed between β and γ in solution is 11 kcal mol⁻¹. This large difference proves that the $\beta \rightarrow \gamma$ isomerization is not favored upon simple reduction. The other isomers, d and e, are

much more unstable than a or b in any reduction state.

22.6.3.2 An Extended Hückel Calculations Approach to a Qualitative Understanding of the Initial Electron Transfer Site in Dawson-type POMs

The nonequivalence of the “cap” and “equatorial” atoms in Well–Dawson anions raises the problem of the initial site of electron transfer in such structures. In a pioneering work [30f], a striking similarity of magnetic and ESR properties in $[WO_5]^{2-}$ complexes and Keggin and Dawson one-electron blues was pointed out. Comparisons of the widths of the spectra and, especially, observation of the distinctly longer relaxation times in reduced 2:18 anions than in the other anions guide Pope et al. to the following statement: “This may mean that it is the ‘equatorial’ (non-Keggin-like) tungsten atoms which are reduced first in 2:18 anions” [30f]. Since then, various lines of experimental evidence, culled from the results of different techniques, converge to support the fact that the added electrons should first be introduced into the equatorial atoms [54a, 65–71, 74–77]. Yet, a direct theoretical proof was lacking and was sought through extended Hückel calculations [78].

The nonequivalence of the “cap” (α_2 positions) and the “belt” (α_1 positions) metal atoms in $P_2W_{18}O_{62}^{6-}$ is reflected by the composition of metal-centered vacant orbitals (Fig. 24). It is worth noting that the lowest unoccupied molecular orbital (LUMO) (a''_1) is almost entirely developed on the α_1 positions (96%), with equal weights on each of the twelve metal atoms. With the reasonable assumption that the initial electron transfer involves the LUMO of the starting species, the shape of

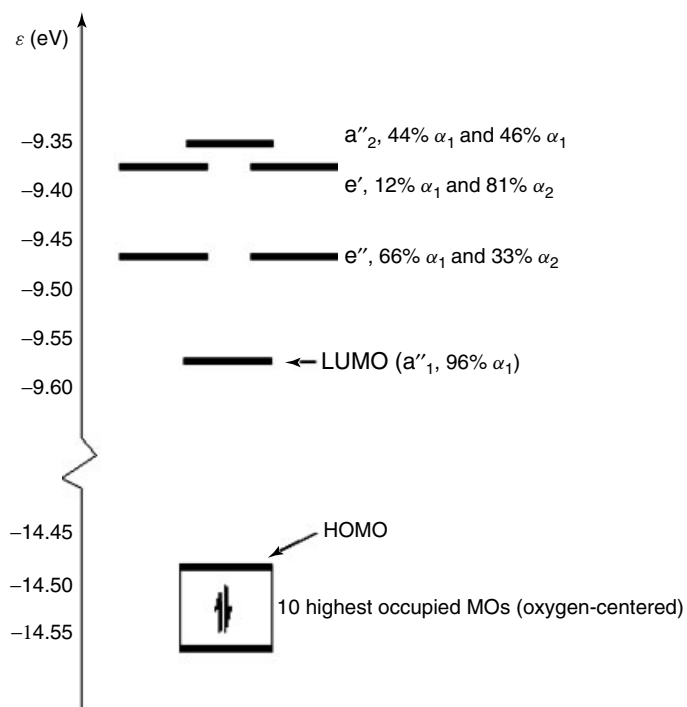


Fig. 24 Selected frontier orbitals of the $P_2W_{18}O_{62}^{6-}$ heteropolyanion (EH calculations). The symmetry and the contributions of the α_1 and α_2 positions to the six lowest vacant MOs are given (taken from Ref. 78).

this molecular orbital nicely rationalizes the experimental evidence that the added electrons should first be introduced into the equatorial atoms. Interestingly, the composition of the vacant orbitals located above the LUMO is very different. For instance, in the first set of degenerate MOs, of e'' symmetry, the orbitals are spread out over both the α_1 (61%) and the α_2 (33%) positions in such a way that almost equal weights are found for the eighteen metal centers (12 and 6 in the α_1 and the α_2 positions, respectively). In the second set of degenerate MOs (e'), the orbitals are mainly located on the α_2 positions (81% instead of only 12% for the twelve α_1 positions). Finally, the sixth low-lying vacant orbital (a''_2) is developed on both the α_1 (44%) and the α_2 (46%) positions.

The shape and the energies of the metal-centered vacant molecular orbitals are sensitive to the substitution of W atom(s) by more electronegative metal atom(s) (Mo for instance). Assuming the geometry of the substituted $P_2W_{18-x}Mo_xO_{62}^{6-}$ heteropolyanions is identical to that of the unsubstituted species, the electronegativity perturbation can be accounted for, in the first approximation, by the lowering of the atomic orbital energies on the substituted metal center(s) [151]. Any substitution in the α_1 (“belt”) position(s) leads to a LUMO of lower energy, still developed on the α_1 positions, but mainly centered on the α_1 -Mo center(s). For instance, with a single α_1 -Mo atom, the LUMO is lowered by 0.08 eV and remains located on the “belt” (93%). However, instead of an

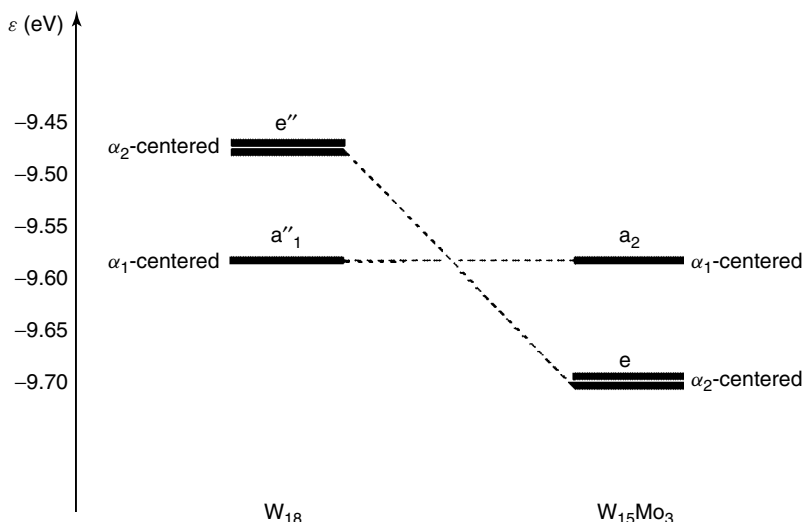


Fig. 25 Energy crossing between the lowest unoccupied MOs of the $\text{P}_2\text{W}_{18}\text{O}_{62}^{6-}$ heteropolyanion upon substitution by three molybdenum centers in a “cap” (α_2 positions) (EH calculations) (taken from Ref. 78).

equal weight of about 8% on each metal atom, 45% of the LUMO is now concentrated on the single α_1 -Mo center. Note that such a localization of the LUMO upon substitution was also reported by Poblet and colleagues for α -Keggin anions (DFT orbitals) [148]. The same conclusions apply for compounds with several α_1 substituted centers. On the contrary, substitution at the α_2 position(s) lets this α_1 -centered vacant orbital unchanged but stabilizes the MOs developed on the α_2 sites. Therefore, a dramatic change in the localization of the LUMO can occur with respect to the unsubstituted compound, as it is illustrated in Fig. 25 for the (1, 2, 3)- $\text{P}_2\text{Mo}_3\text{W}_{15}\text{O}_{62}^{6-}$ complex with three Mo centers in one cap. In this compound, a set of two degenerate LUMOs of the symmetry (C_{3v}), centered on the three α_2 -Mo positions (86%), are now located 0.10 eV below the α_1 -centered (94%) vacant orbital that has been left unchanged by the

substitution. Even for a single substitution, the LUMO is located at 80% on the α_2 -Mo center and its energy is 0.06 eV below that of the belt-centered vacant orbital. In the “mixed” face-substituted complex, with four α_1 -Mo and two α_2 -Mo centers, the LUMO remains located on the four substituted α_1 positions (82%) while the vacant MO just above is mainly developed on the two substituted α_2 positions (77%). Finally, in the fully substituted Mo_{18} compound, the situation is identical to that found in the starting W_{18} species, with a LUMO entirely developed on the twelve α_1 centers. A nice correlation is thus found between the localization of the LUMO (either α_1 - or α_2 -centered) and the nature of the first reduction site in the substituted $\text{P}_2\text{W}_{18-x}\text{Mo}_x\text{O}_{62}^{6-}$ heteropolyanions deduced from the experimental evidences recalled earlier.

Finally, the HOMO–LUMO energy gap depends on the substitution pattern

since the HOMO level (oxygen-centered) remains unchanged while the LUMO level (metal-centered) is lowered when

more electronegative metal centers are introduced. It is illustrated in Fig. 26 for the $\text{P}_2\text{W}_{18}\text{O}_{62}^{6-}$ heteropolyanion and

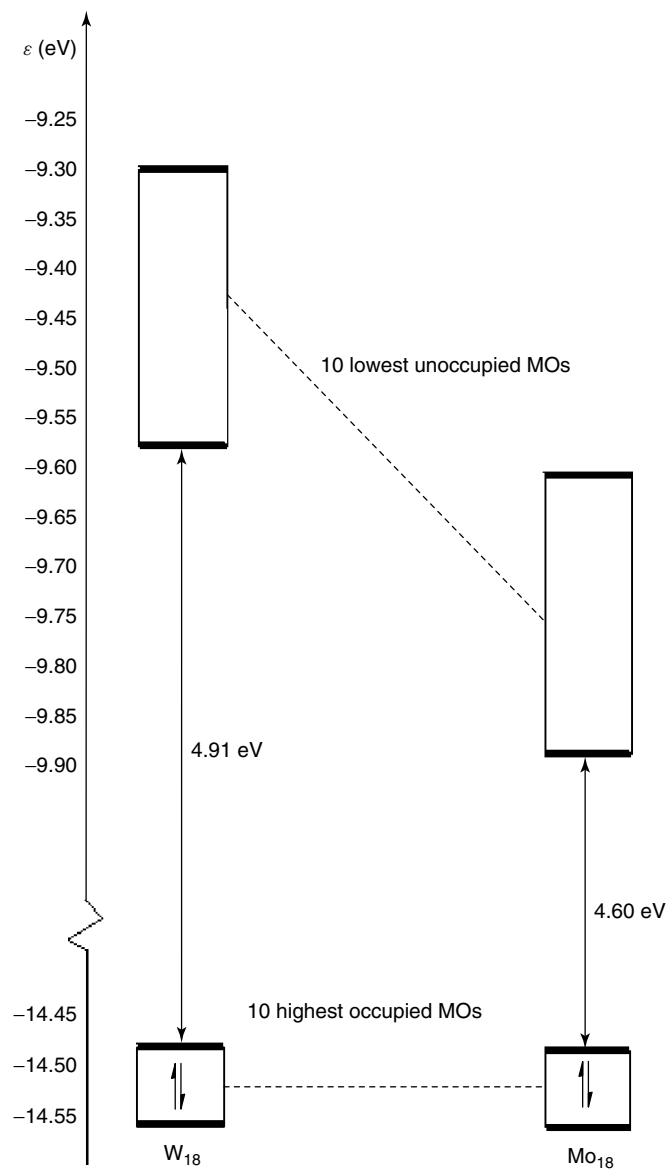


Fig. 26 Energy change of the ten highest occupied (oxygen-centered) and the ten lowest unoccupied (metal-centered) MOs in going from the $\text{P}_2\text{W}_{18}\text{O}_{62}^{6-}$ heteropolyanion to its molybdenum analog $\text{P}_2\text{Mo}_{18}\text{O}_{62}^{6-}$ (EH calculations) (taken from Ref. 78).

its fully substituted analog $\text{P}_2\text{Mo}_{18}\text{O}_{62}^{6-}$. The HOMO energy level is -14.48 eV in both complexes but the LUMO energy level is lower by 0.31 eV in the Mo_{18} species (-9.88 instead of -9.57 eV in the tungsten analog). Such a lowering of the LUMO level upon substitution can be correlated with the easier reduction of the Mo substituted species (Table 8).

In conclusion, it was shown that the experimental evidence for an initial electron transfer site in an equatorial position (α_1) of the unsubstituted Dawson-type $\text{P}_2\text{W}_{18}\text{O}_{62}^{6-}$ heteropolyanion can be rationalized by the “belt”-centered character of the LUMO. The change of the reduction site ($\alpha_1 \rightarrow \alpha_2$) upon substitution in the “cap” region (α_2 site) by a more electronegative metal center (Mo for instance) is also consistent with the localization of the LUMO on the substituted center(s).

22.7 Electrocatalysis

Possibilities of electrocatalysis of reactions at electrodes are among the powerful incentives for the electrochemical study of POMs. Interesting results were obtained both in electrocatalytic reductions and oxidations, provided the appropriate form of the POM is used. Two recent reviews devoted to the electrochemical properties of polyoxometalates as electrocatalysts are available [8, 9]. The second one focuses more specifically on electrocatalysis on modified electrodes. In the present text, attention will be drawn specially to the basic principles that could be considered to govern most of solution processes. The principles will be illustrated by several recent experimental results, even though earlier achievements will also be described briefly.

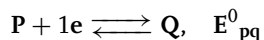
Strictly speaking, electrocatalysis applies to the “dependence of the electrode reaction rate on the nature of the electrode material” [152]. In the following, this term will be used in a broader sense and will be admitted to include the possibility that the catalyst be homogeneously dissolved in the electrolyte solution as well as the case where the catalyst is attached to the electrode surface. A short chapter on the electrocatalysis of inorganic chemicals by chemically modified electrodes can also be found in Vol. 10 of this Encyclopedia [9].

22.7.1

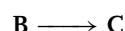
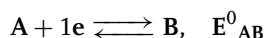
Basic Concepts of Homogeneous Catalysis of Electrode Reactions

The first observations of catalytic phenomena in electrochemistry in the early 1930s were followed by attempts at modelization on the example of hydrogen peroxide reduction in the 1940s. A general framework was expressed, in which electron exchange occurred in solution between the reduced catalyst and the substrate, thus regenerating the catalyst and explaining the observed catalytic effect. In short, electron transfers to or from a molecule must be viewed as a succession of elementary electrochemical and chemical reaction steps. Such simplified reaction schemes served as the basis for theoretical analysis of catalytic phenomena. In molecular electrochemistry, electrochemical reductions can therefore be sketched by the following reaction schemes:

For the catalyst (P) :



For the substrate (A) :



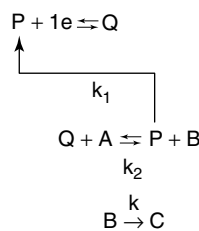
The catalytic effect is reflected in the interaction of Q with A, resulting in the regeneration of P.



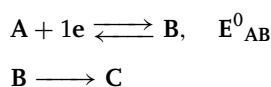
The only thermodynamic condition then required for this reaction to be driven from left to right is that the standard molar free enthalpy of the reaction be negative, that is, the following inequality must hold: $E^0_{PQ} < E^0_{AC}$, where E^0_{AC} represents the standard redox potential of the A/C couple.

However, this overall scheme might feature two types of successive reaction steps. The first one considers the possibility of solution electron transfers; the second one goes through the formation of an adduct.

The first scheme is simple and reads as follows:

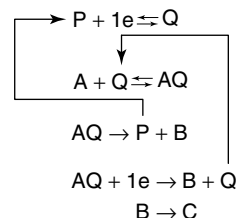


It is worth reminding that the direct reduction of the substrate is realized according to the following pathways:



The catalyst constitutes an electron shuttle between the electrode and the solution, where it is engaged in a direct redox electron transfer with the substrate. This type of catalysis is termed *redox catalysis*.

The second reaction scheme reads:



In this case, the reduced form of the catalyst builds up with the substrate a relatively unstable adduct AQ, which then decomposes, eventually after further reduction at the electrode surface or in solution. Finally, either the oxidized form P of the catalyst or its reduced form Q is regenerated. As regards the substrate, its reduction follows the aforementioned E.C. (Electrochemical Chemical) mechanism. This type of catalysis is termed *chemical catalysis*. Finally, it must be pointed out that the clear-cut distinction between redox catalysis and chemical catalysis might be difficult, but amounts ultimately to a detailed study of the nature of the redox reaction.

22.7.2 Selected Electrocatalysis in Homogeneous Solution

In principle, the choice of a specific electrochemical technique is not crucial in the study of electrocatalytic processes. However, from a practical and qualitative point of view, cyclic voltammetry is, in most cases, suited for a rapid assessment of an electrocatalytic process triggered by POMs. The interest stems from the following general behavior: most POMs undergo a series of reversible one- and two-electron reductions and these reduced forms act usually as the active species, inducing an increase of the corresponding

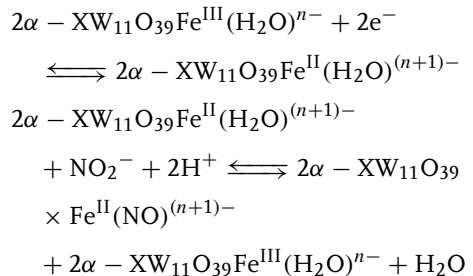
cathodic current and a concomitant loss of its reversibility.

22.7.2.1 Electrocatalytic Reductions

Table 13 gathers the main electrocatalytic processes triggered by POMs dissolved in solution. The electrocatalytic reductions of dioxygen, hydrogen peroxide and of several NO_x including nitrite, nitric oxide, and nitrate are selected for a more detailed description.

Electrocatalysis of the reduction of HNO_2 and NO was demonstrated in the late 1980s independently by Anson et al. [153d] and by Keita et al. [157, 158]. Since then, this reaction has been selected and is being used worldwide as a classical test of the electrocatalytic properties of the POMs. Consideration of $[\text{Fe}(\text{H}_2\text{O})\text{SiW}_{11}\text{O}_{39}]^{6-}$ (**SiW₁₁Fe**) for

short), one of the electrocatalysts proposed by Anson [153d], is particularly enlightening: a Fe-nitrosyl complex is formed upon reduction of the Fe center and the actual catalytic process to obtain ammoniac occurs at more negative potentials where the necessary number of charges is accumulated and delivered by the W-framework. The overall mechanism up to the Fe-nitrosyl formation involves the following steps [153d]:



Tab. 13 Electrocatalytic reductions by homogeneously dissolved heteropolyanions

Catalyst	Reduction	condition	References
$\text{SiW}_{12}\text{O}_{40}^{4-}$	h.e.r.	Acidic solution	33b,c
	Nitrite reduction	Buffer	153a
	O_2 reduction	Triflate buffer (pH 2)	154
$\text{SiMo}_{12}\text{O}_{40}^{4-}$	Chlorate reduction	50% (v/v) dioxane-water (0.5 M H_2SO_4)	153b
	Nitrite reduction	50% (v/v) dioxane-water (0.5 M H_2SO_4)	155
$\text{PMo}_{12}\text{O}_{40}^{3-}$	Chlorate reduction	50% (v/v) dioxane-water (0.5 M H_2SO_4)	153b
	Nitrite reduction	Buffer	153c
$\text{P}_2\text{W}_{18}\text{O}_{62}^{6-}$ $\text{XW}_{11}\text{O}_{39}\text{Fe}^{\text{III}}(\text{H}_2\text{O})^{n-}$ ($\text{X} = \text{P}$, As, Si, Ge)	Nitrite reduction	Buffer	156
	Nitrite reduction	Buffer	153c
$\text{SiW}_{11}\text{O}_{39}\text{Fe}^{\text{III}}(\text{H}_2\text{O})^{5-}$ $\text{P}_2\text{W}_{17}\text{O}_{61}\text{Fe}^{\text{III}}(\text{H}_2\text{O})^{8-}$	H_2O_2 reduction	Buffer	94b
	H_2O_2 reduction	Sulfate buffer (pH 3)	94b
$\text{PW}_{11}\text{O}_{39}\text{Ru}^{\text{III}}(\text{H}_2\text{O})^{4-}$	Nitrite reduction	Acetate buffer (pH 5)	
	DMSO reduction	Sulfate buffer (pH 2)	85
$\text{K}_{17}[\text{Ln}(\text{As}_2\text{W}_{17}\text{O}_{61})_2]$ ($\text{Ln} = \text{La}$, Pr, Sm, Eu, Gd, Dy, Tm)	h.e.r.		
	Nitrite reduction	Acetate buffer (pH 5.5)	153e
$\text{Nd}(\text{SiMo}_7\text{W}_4\text{O}_{39})_2^{13-}$	Bromate reduction	Buffer	153f

$X = \text{Si, Ge, n} = 5; X = \text{P, As, n} = 4$

Nitrous acid was shown to be the reactive intermediate depending on the pH domain explored. As a matter of fact, the following sequence is known: $\text{HNO}_2 \rightleftharpoons \text{H}^+ + \text{NO}_2^-$ $pK_a = 3.3$ at 18°C and HNO_2 disproportionates in fairly acidic solution: $3\text{HNO}_2 \rightleftharpoons \text{HNO}_3 + 2\text{NO} + \text{H}_2\text{O}$. The rate of this reaction is known to be low.

However, a loss in selectivity and a low yield ensue [153d] from electrode derivatization [28]. Recently, to avoid the shortcomings encountered with SiW_{11}Fe , several alternative POMs were proposed [8, 10, 157–159]. Among all of these potentially acceptable candidates, N_2O was obtained with a quantitative yield of 100% with molybdic and molybdo-tungstic POMs [10]. A supramolecular compound like $[\text{P}_8\text{W}_{48}\text{O}_{184}]^{40-}$, with only W-centers, can also be used to reduce NO efficiently without derivatization of the electrode surface [86b]. Finally, mixed addenda POMs and also sandwich-type complexes have the advantage of accumulating metal centers known for their catalytic behaviors in the reduction of NO_x , or alternatively in the reductions of dioxygen and hydrogen peroxide; in cases they are electroactive within the POM, they permit generally a substantial positive shift of the potential because these metal centers are easier to reduce than the W-centers of the polytungstic framework [1, 103, 115]. Specifically, Cu, Ni, and Fe-centers were the most efficient among metal ion substituents. In addition, their efficiency was enhanced by the presence of Mo atoms [159, 160]. A cooperative effect was also noted between Mn- and Fe-centers as will be shown in the following text.

The electrocatalytic reduction of nitrate by reduced POMs was demonstrated for the first time [160a]. Following general

conclusions emerge from recent achievements in NO_x reductions. In $\text{pH} < 4$ media, most POMs are active for the reduction of nitrite (which is actually a mixture of HNO_2 and NO). In contrast, for $\text{pH} > 4$ media where nitrite itself is the main species in solution, few examples of electrocatalysis exist and Cu-substituted POMs are the most efficient. For the reduction of nitrate, Cu- and Ni-containing POMs show a good efficiency. In addition, $\text{Ni}_4\text{Mn}_2\text{P}_3\text{W}_{24}$, $\text{Ni}_6\text{As}_3\text{W}_{24}$, and $\text{Fe}_6\text{Ge}_2\text{W}_{18}$ with their six-electron first waves proved remarkably efficient in the electrocatalytic reduction of nitrate. These observations are taken into account for the selection of following examples.

22.7.2.1.1 Electrocatalytic reduction of nitrite and nitrate

Studies with $[(\text{Cu}^{\text{II}}(\text{H}_2\text{O}))_2\text{Cu}^{\text{II}}_2(\text{X}_2\text{W}_{15}\text{O}_{56})_2]^{16-}$ (abbreviated in the following as $\text{Cu}_4\text{X}_4\text{W}_{30}$ with $\text{X} = \text{P or As}$) This example is selected to compare nitrate reduction with the more classical nitrite reduction [115]. Correlatively, the study of the possible intermediate or final product in this reaction, namely nitrite, was also to be considered. All the experiments were carried out at $\text{pH} = 5$.

The oxidized forms of these two sandwich-type POMs are stable from $\text{pH} 3$ to at least $\text{pH} 7$. Their characterization by cyclic voltammetry revealed the stepwise reduction of the Cu^{2+} centers within the POMs, before Cu° deposition on the glassy carbon electrode surface [115]. Phenomena are described mainly for the P-derivative and are the same for the As-analog.

The cyclic voltammograms in Fig. 27 sketch the main observations with $\text{Cu}_4\text{P}_4\text{W}_{30}$ as a catalyst; they were run at the same scan rate as a function of the excess parameter γ ($\gamma = C^\circ \text{NO}_3^- / C^\circ \text{POM}$). Starting from $\gamma = 0$, it is seen that addition of even

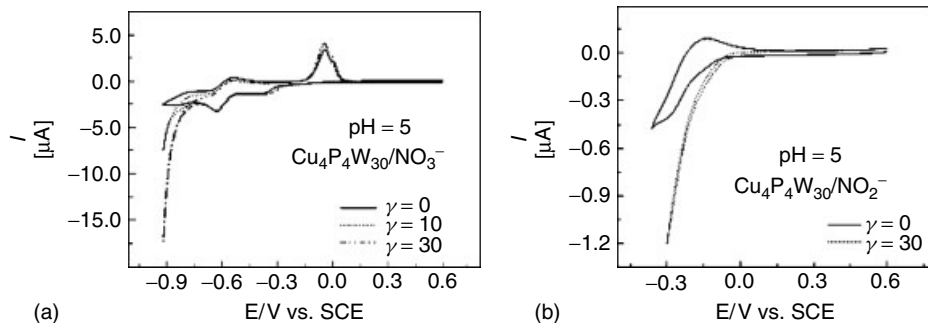


Fig. 27 Electrocatalysis of NO_x reduction in the presence of 2 10⁻⁴ M Cu₄P₄W₃₀ in a pH 5 medium. The scan rate was 2 mV s⁻¹, the working electrode was glassy carbon and the reference electrode was SCE. (a) Nitrate (b) nitrite. For more detailed information, see text (taken from Ref. 115).

a small amount of nitrate to the solution induces a large cathodic current increase just negative of the peak potential location of the first W-wave. Concomitantly, the reversibility of the second W-wave is suppressed even for small γ values. These observations indicate an efficient reduction of nitrate anions by reduced species of Cu₄P₄W₃₀. The catalytic efficiencies CAT (defined as CAT = 100 × [I_(POM+NO₃) − I_(POM)]/I_(POM)) where I_(POM+NO₃) represents the reduction peak current observed for the POM in the presence of nitrate and I_(POM) is the corresponding reduction peak current for the POM alone) varies from 194 to 580% when γ increases from γ = 10 to γ = 30. The corresponding CAT values for Cu₄As₄W₃₀ are 203 and 607% for γ = 10 and γ = 30 respectively. It is likely from these values that the nature of the central heteroatom (P or As) does not influence significantly the catalytic process. It is worth pointing out that no direct reduction of nitrate anions on glassy carbon electrode is observed in the potential domain explored here in the absence of heteropolyanion [160a].

In addition to these experiments, we have checked that the probable

intermediates in the reduction of nitrate, namely NO and NO₂⁻, are also efficiently reduced by the reduced Cu₄X₄W₃₀ at a less negative potential than necessary for nitrate itself. As an example, Fig. 27(b) shows the reduction of NO₂⁻ by Cu₄P₄W₃₀. It comes out that Cu²⁺ retain its catalytic properties upon complexation with an heteropolyanion, accompanied by supplementary advantages; these advantages include the possibility to accumulate Cu²⁺ active centers and also the possibility to fabricate highly reduced species with the electrons accumulated in the reduced W-framework of the heteropolyanion.

As a whole, it was found that the electrocatalytic reduction of nitrate, nitrite, and nitric oxide proceeds efficiently from pH 3 to 7.

Cooperative effect of Mn- and Fe-centers within Mn₂Fe₂P₄W₃₀ in the electrocatalytic reduction of nitrite In the preceding sections, it was well established that Fe(III)-substituted POMs catalyze the reduction of NO and/or NO₂⁻ [1]. The first step in this process is the formation of a complex with the Fe(II) form of the POM and nitrogen oxide.

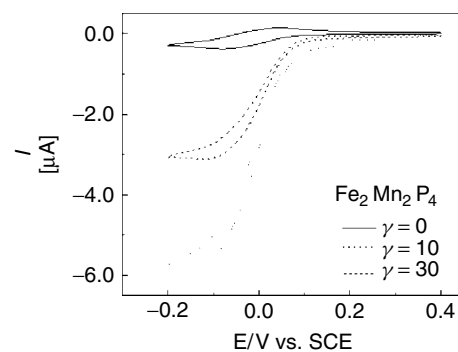
The actual catalytic step takes place with remarkable enhancement of the current intensity, and it occurs at more negative potentials in the reduction domain, where the W(VI) centers accumulate a suitable number of electrons within the complex framework for subsequent delivery. With the goal of saving energy by moving the electron reservoir closer to the Fe(III)-reduction potential, several Wells–Dawson-type monosubstituted derivatives were previously synthesized, including α_1 -(FeOH₂) P₂W₁₇O₆₁⁷⁻ and α_2 -(FeOH₂)P₂Mo₂W₁₅O₆₁⁷⁻ in which the Fe- and W-waves or Fe- and Mo-waves merge in appropriate pH media [14, 159]. This strategy turns out to be favorable, and the entire catalytic process shows up at the reduction potential of the Fe(III) center, which is now observed concomitantly with the Mo(VI) or W(VI) reduction waves. The same phenomenon is observed here.

These results are illustrated briefly with **Fe2Mn2P4** in Fig. 28, with NaNO₂ as the starting substrate. An important current intensity increase is observed with increasing γ values (γ is the excess parameter defined as $\gamma = C^\circ (\text{NO}_x)/C^\circ (\text{POM})$) at the reduction potential of the Fe(III) centers in a pH 1 solution in which a mixture of HNO₂ and NO must be considered. In this potential

domain, no reduction is observed for NO or HNO₂ present in the solution. Figure 28 shows unambiguously that the catalytic process begins simultaneously with the reduction of the Fe(III) centers. Furthermore, it is worth noting the high efficiency of the electrocatalysis, even though modest γ values were used. Finally, in the timescale of cyclic voltammetry, **Fe2P4** shows the same phenomenon as **Fe2Mn2P4** concerning the electrocatalytic reduction of NO and NO₂⁻. However, the latter complex might be a better choice for this catalytic process due to the improved stability of its Fe(II) forms [109]. Under the same experimental conditions, **Fe2Mn2As4** also shows good catalytic efficiency for the reduction of nitrite. In addition, its activity at 0 V is 25% higher than that of **Fe2Mn2P4** due to the slight positive potential shift of the Fe(III) waves in the former complex compared with the latter due to the different heteroatoms (i.e. As vs. P).

However, in a pH = 5 medium, the catalytic process (obtained with NaNO₂ as the starting substrate) is no longer observed in the iron reduction–potential domain, but is relegated to the reduction potential of the first W-wave. This observation is in full agreement with the expected absence of NO and HNO₂ in this medium.

Fig. 28 Cyclic voltammetry study of the electrocatalytic reduction of nitrite with a 2×10^{-4} M solution of **Fe2Mn2P4** in a pH = 1 medium (0.5 M Na₂SO₄ + H₂SO₄). The scan rate was 2 mV s⁻¹, the working electrode was glassy carbon, and the reference electrode was SCE (taken from Ref. 1).



In contrast, experiments with pure NO [10, 155] at pH = 5 show that the catalytic process starts directly in the iron reduction–potential domain. We have also checked the catalytic reduction of NO at pH = 1. All these results converge to designate NO as the species electrocatalytically reduced by the present complexes throughout the pH domain evaluated.

Evaluation of the behaviors of $\text{Ni}_3\text{P}_2\text{W}_{18}$, $\text{Ni}_4\text{Mn}_2\text{P}_3\text{W}_{24}$, $\text{Ni}_6\text{As}_3\text{W}_{24}$, and $\text{Fe}_6\text{Ge}_2\text{W}_{18}$ in the electrocatalytic reduction of nitrate and nitrite A few general conclusions can be drawn from literature results before going into specific details [107b, 113]. These POMs, specifically those exhibiting six-electron first waves, constitute unique examples of multielectron catalysts active in the electrocatalytic reduction of nitrate without derivatization of the electrode surface. In addition, highly reduced products were obtained, because nitrite is reduced at a less negative potential than nitrate whatever the pH from acidic to neutral media. With the examples of $\text{Ni}_4\text{Mn}_2\text{P}_3\text{W}_{24}$ and $\text{Ni}_6\text{As}_3\text{W}_{24}$, it was demonstrated that the availability of large number of electrons is not a sufficient condition for an efficient catalysis of nitrate reduction. As a matter of fact, the crown POM P_8W_{48} does not perform such a catalysis, despite the eight electrons available in its first reduction step. Finally, Fe-centers within POMs are usually poor catalysts for the reduction of nitrate. Therefore, it is remarkable that they turned out to be efficient in the particular structure of $\text{Fe}_6\text{Ge}_2\text{W}_{18}$.

Coming to details, cyclic voltammetry was used to evaluate the activity of $\text{Ni}_3\text{P}_2\text{W}_{18}$ and $\text{Mn}_2\text{Ni}_4\text{P}_3\text{W}_{24}$ in the electrocatalytic reduction of nitrate. The choice of the substrate is tricky, as nitrate is difficult to reduce. Other few examples

where POMs have proven to be useful in this system have been described recently [13, 103, 160]. For this purpose, the excess parameter is an operational parameter defined as $\gamma = C^{\circ}\text{NO}_3^- / C^{\circ}\text{POM}$. The electrocatalysis is characterized by the catalytic efficiency CAT, defined as follows: $CAT = 100 \times [I_{(\text{POM}+\text{NO}_3^-)} - I^d_{(\text{POM})}] / I^d_{(\text{POM})}$ where $I_{(\text{POM}+\text{NO}_3^-)}$ is the peak current for reduction of the heteropolyanion (POM) in the presence of NO_3^- and $I^d_{(\text{HPA})}$ is the corresponding diffusion peak current for the HPA alone. CAT values are sufficient to compare the efficiencies for a given electrocatalytic process either for one compound as a function of pH or for two compounds at the same experimental conditions. However, it must be recognized that a more detailed comparison would necessitate determination of the nature and yields of the final products, which was considered beyond the scope of this work. As a first example, CAT values were measured in the presence of $\text{Ni}_3\text{P}_2\text{W}_{18}$ for the electrocatalytic reduction of nitrate in a pH 2 sulfate medium. CAT was measured at -0.840 V and varies from 2098 to 2733 for $\gamma = 500$ and $\gamma = 1000$ respectively. These values indicate an efficient electrocatalysis of the reduction of nitrate by $\text{Ni}_3\text{P}_2\text{W}_{18}$ at pH 2. Furthermore, several tests with NO_2^- and/or with NO under the aforementioned conditions confirm that these species are easily reduced electrocatalytically at substantially less negative potentials than nitrate [10]. Insofar as nitrite and NO are known to appear as intermediates in the reduction of nitrate on various metals, the present results would suggest that highly reduced species should be obtained in the electrocatalytic reduction of nitrate in the presence of $\text{Ni}_3\text{P}_2\text{W}_{18}$. Also, the number of accumulated electrons in the polyoxoanion framework at the potential where the transformation of

nitrate takes place is large enough for a complete reduction, which constitutes a complementary circumstance supporting the preceding assumption.

The media of pH 3 and 5, respectively, were selected to compare the efficiencies of $\text{Ni}_3\text{P}_2\text{W}_{18}$ and $\text{Mn}_2\text{Ni}_4\text{P}_3\text{W}_{24}$ in the electrocatalytic reduction of nitrate, because the latter complex is not very stable at pH 2. Whatever the pH, $\text{Mn}_2\text{Ni}_4\text{P}_3\text{W}_{24}$ was found to be the more efficient of the two complexes: its CAT values were four and seven times larger, at pH 3 and 5 respectively, than those measured for $\text{Ni}_3\text{P}_2\text{W}_{18}$ under the same conditions.

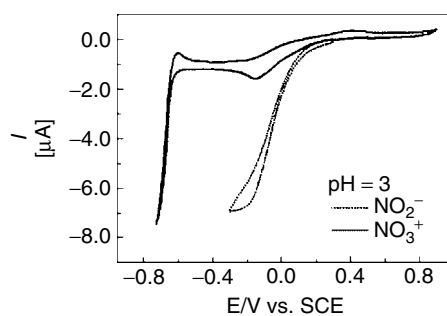
The results for these two complexes were compared with the efficiencies obtained with $\text{Ni}_4\text{P}_2\text{W}_{18}$ and $\text{NiPW}_{11}([\text{Ni}(\text{OH}_2)\text{PW}_{11}\text{O}_{39}]^{5-})$ in the pH 5 medium where all these complexes are stable. The efficiencies for $\text{Ni}_3\text{P}_2\text{W}_{18}$ and $\text{Ni}_4\text{P}_2\text{W}_{18}$ turned out to be comparable. In contrast, NiPW_{11} shows a negligibly small activity toward the electrocatalytic reduction of nitrate in this medium.

Finally, comparisons of the efficiencies of several Ni-substituted tungstophosphates vis-à-vis the catalytic electroreduction of nitrate suggest that an increase of the Ni centers incorporated in stable sandwich-type polyoxoanions has a very beneficial effect.

The electrocatalytic behavior of $\text{Fe}_6\text{Ge}_2\text{W}_{18}$ toward the reduction of nitrite

and nitrate was tested at pH = 3. In the absence of either of the two NO_x , the voltammetric pattern is that of Fig. 29. Upon addition of even modest amounts of nitrite, a large cathodic current enhancement was observed, starting in a potential domain positive to the Fe-wave. This observation must be linked with the beneficial accumulation of electrons in the POM framework. It was checked that NO is also electrocatalytically reduced in the same potential domain. Concerning nitrate, it is worth reminding that a comparative study of several metal ion-substituted heteropolyanions including α_1 - and α_2 - $\text{P}_2\text{W}_{17}\text{M}$ and $\alpha_2\text{-P}_2\text{W}_{15}\text{Mo}_2\text{M}$ where $\text{M} \equiv \text{V}^{\text{IV}}$, Mn^{II} , Fe^{III} , Co^{II} , Ni^{II} , Cu^{II} , Zn^{II} and \Rightarrow (where \Rightarrow indicates the absence of M) most heteropolyanions, except those substituted by Cu or Ni do not show any important electrocatalytic ability toward its reduction [160a]. Specifically, Fe^{III} -substituted heteropolyanions are not efficient in the electrocatalytic reduction of nitrate [160a]. Such observation complies with literature where Epstein et al. had shown that efficient oxidation of Fe^{II} by nitrate necessitates a catalyst [160b]. In contrast, the electrocatalytic reduction of nitrate was observed here when the first W-reduction processes were reached. Furthermore, the potential domain where this electrocatalysis was obtained is comparable with those of the best

Fig. 29 Cyclic voltammograms in a 2×10^{-4} M solution of $\text{Fe}_6\text{Ge}_2\text{W}_{18}$ complex in pH = 3 acetate medium ($0.4 \text{ M } \text{CH}_3\text{COONa} + \text{ClCH}_2\text{COOH}$); superposition of the CVs run in the presence of 6×10^{-3} M of nitrite and of 2×10^{-1} M of nitrate; scan rate: 2 mV s^{-1} (taken from Ref. 107b).



HPA-based electrocatalysts [113]. Owing to the slightly positive location of the W-wave of $\text{Fe}_6\text{Ge}_2\text{W}_{18}$ relative, for example, to that of $[\text{Ni}_4\text{Mn}_2\text{P}_3\text{W}_{24}\text{O}_{94}]^{17-}$ [113] the electrocatalytic reduction of nitrate at pH 3 begins roughly 100 mV positive in the case of the former complex. Comparison of the nitrite and nitrate electrocatalysis patterns is enlightening: insofar as nitrite and NO are known to appear as intermediates in the reduction of nitrate on various metals, the potential locations of the corresponding waves would suggest that highly reduced species should be obtained in the electrocatalytic reduction of nitrate in the presence of $\text{Fe}_6\text{Ge}_2\text{W}_{18}$. Provisionally, the remarkable activity of $\text{Fe}_6\text{Ge}_2\text{W}_{18}$ in the electrocatalytic reduction of nitrate is worth emphasizing as it constitutes the first example, to our knowledge, in which such an efficiency is demonstrated for a Fe-containing POM. Finally and in agreement with expectations, it was noted that $\text{Fe}_6\text{Ge}_2\text{W}_{18}$ catalyses also the electroreductions of dioxygen and hydrogen peroxide.

22.7.2.1.2 Electrocatalytic Reduction of Dioxygen and Hydrogen Peroxide These two processes must be emphasized because reduction of dioxygen, and eventually hydrogen peroxide, features the usually claimed pathway for reoxidation of reduced POMs after the participation of the latter in oxidation processes. As a consequence, electrocatalysis of dioxygen and hydrogen peroxide reduction is a valuable catalytic test with most new POMs [154, 156, 161].

In aqueous solution, the catalytic reduction of hydrogen peroxide was observed on the wave corresponding to the reduction of Fe(III) to Fe(II) within $\alpha\text{-}[\text{Fe}(\text{OH}_2)\text{SiW}_{11}\text{O}_{39}]^{5-}$ and $\alpha\text{-}[\text{Fe}(\text{OH}_2)\text{P}_2\text{W}_{17}\text{O}_{61}]^{8-}$ [156]. The rate constants for the process triggered by the

Fe(II) forms were evaluated at 9×10^2 and $1.16 \times 10^4 \text{ M}^{-1} \text{ s}^{-1}$ for the two complexes respectively. The mechanism involves complicated competing reactions including Fe(II), Fe(III), Fe(IV), and Fe(V) complexes, species that are usually invoked in metalloporphyrin chemistry.

Two examples are selected to describe and discuss the electrocatalytic reduction of dioxygen, the first one with a TMSP [161] and the second one with a sandwich-type complex [162]. The discussion reflects the questions encountered also with usual plenary POMs.

Electrocatalytic reduction of dioxygen in the presence of $\alpha_2\text{-P}_2\text{W}_{15}\text{Mo}_2\text{Cu}$ The main features of the dioxygen electrocatalytic reduction in the presence of $\alpha_2\text{-P}_2\text{W}_{15}\text{Mo}_2\text{Cu}$, in a pH = 3 medium, are illustrated in Fig. 30(b) by a selection of cyclic voltammograms. The direct reduction of dioxygen on the glassy carbon surface is observed at a fairly negative potential. In contrast, its electrocatalysis occurs readily in the potential domain that was demonstrated previously to correspond mainly to the reduction of Mo centers. It is worth emphasizing that the voltammetric pattern indicates no obvious deposition of copper in this domain. Qualitatively, the efficiency of the catalysis is already revealed even for an excess parameter ($\gamma = C^\circ_{\text{O}_2}/C^\circ_{\text{POM}}$) as low as $\gamma = 2$. The catalytic efficiency CAT is a useful parameter and is defined as follows: $CAT = 100 \times [I_{(\text{POM}+\text{O}_2)} - I_{(\text{POM})}^d]/I_{(\text{POM})}^d$ where $I_{(\text{POM}+\text{O}_2)}$ is the peak current for reduction of the heteropolyanion (POM) in the presence of O_2 and $I_{(\text{POM})}^d$ is the corresponding diffusion peak current for the HPA alone. For $\gamma = 10$, CAT calculated at -0.060V is 2.5 times larger than for $\gamma = 2$. Whatever

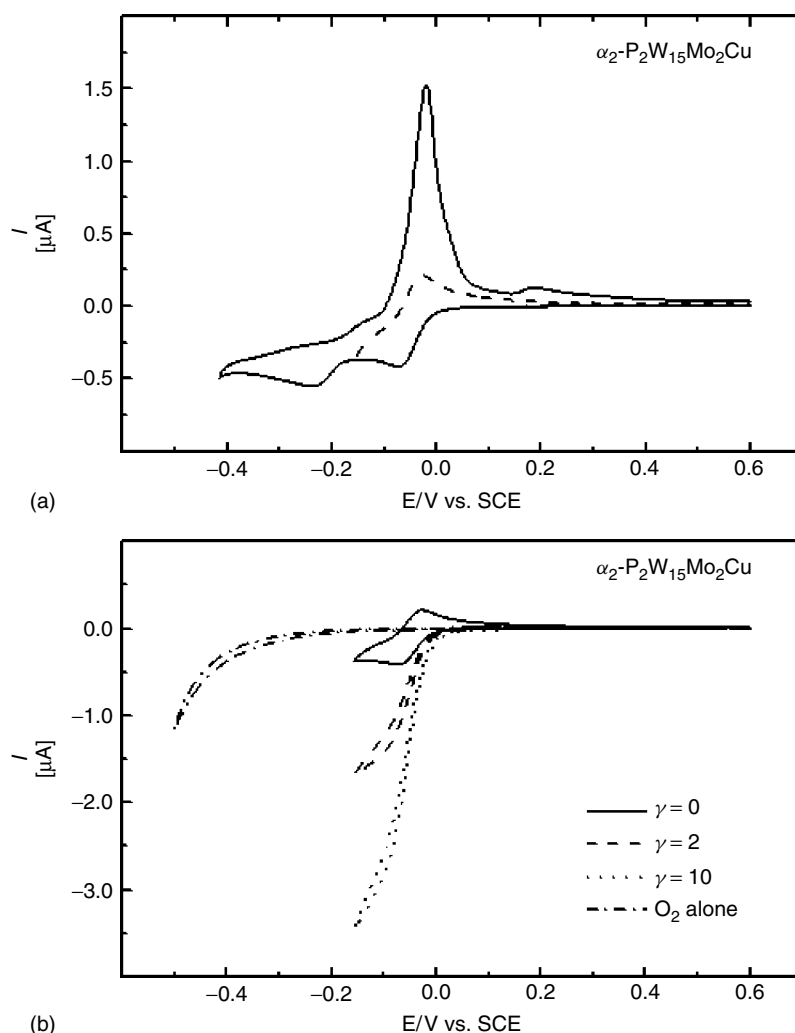


Fig. 30 Cyclic voltammograms (scan rate: 2 mV s^{-1}) observed in 0.2 M $\text{Na}_2\text{SO}_4 + \text{H}_2\text{SO}_4$ (pH 3); the working electrode was glassy carbon and the reference electrode was SCE. (a) 10^{-4} M $\alpha_2\text{-P}_2\text{W}_{15}\text{Mo}_2\text{Cu}$. The choice of the reversal potentials help to distinguish the various steps. (b) dioxygen alone and 10^{-4} M $\alpha_2\text{-P}_2\text{W}_{15}\text{Mo}_2\text{Cu}$ in the presence of different concentrations of dioxygen. For further details, see text (taken from Ref. 161).

the value of γ , the polarogram shape of the cyclic voltammogram at low scan rates must be noted. Also worthy of notice is the observation that the plateau current for these polarograms at fixed γ value does not depend on the scan

rate. These details facilitate the evaluation of the overall rate constant of the catalytic process [163] which is found to be: $k = 2.110^3 \text{ M}^{-1} \text{ s}^{-1}$. After completion of the dioxygen reduction experiments, the initial voltammogram under argon was

routinely restored by bubbling the inert gas through the solution. This result is an indication that no irreversible complex was formed between dioxygen and the oxidized POM. At slow scan rate, the electrocatalytic activity is also observed on the other waves beyond the first one. A correct comparison with the activity of a solution of pure copper sulfate is plagued or, at least, made difficult by several parameters: the difference in diffusion coefficient between the POM and Cu²⁺; some deposition of copper modifying the electrode surface area; the potential at which the catalysis begins, and so on. Nonetheless, even ignoring these shortcomings, the catalytic efficiency of the POM was found to remain better than that of Cu²⁺ alone. A remarkable example of additivity and/or cooperativity of the influences of Mo and Cu centers was found in this study.

The closeness of the reduction potentials of Mo and Cu centers within the molecule of $\alpha_2\text{-P}_2\text{W}_{15}\text{Mo}_2\text{Cu}$ at most pH values, where the catalysis occurs, raises the question of the actual role of each particular atom in the electrocatalytic reduction of dioxygen. Various parameters of the system were studied to clarify the situation. The lacunary heteropolyanion $\alpha_2\text{-P}_2\text{W}_{15}\text{Mo}_2$ develops no dioxygen reduction catalysis in the potential domain of reduction of Mo moieties, even though the Mo centers are reduced at the same potential in both the lacunary and the Cu-substituted complexes. Indeed, a catalytic effect is seen to start at the substantially more negative potential corresponding to the first reduction wave of W-centers. Provisionally, it is worth noting that such catalysis of the dioxygen reduction on the W waves is encountered in most of the heteropolyanions studied to-date. Keeping specifically with the Mo atom, it was found also that the first wave of $\alpha_2\text{-P}_2\text{W}_{15}\text{Mo}_3$

does not show any catalytic activity toward dioxygen, even though sufficiently energetic electrons are available. It must be concluded, at the very least, that the Mo centers alone within $\alpha_2\text{-P}_2\text{W}_{15}\text{Mo}_2\text{Cu}$ are not the loci of the observed catalysis process.

$\alpha_2\text{-P}_2\text{W}_{17}\text{Cu}$ was selected to test and compare the catalytic ability of another closely related Cu-containing heteropolyanion in the dioxygen electrocatalytic reduction. Its electrochemistry at pH 3 was studied previously [90]. Its first wave was observed at a more negative potential than the Mo wave of $\alpha_2\text{-P}_2\text{W}_{15}\text{Mo}_2\text{Cu}$. Copper deposition during the first reduction wave of $\alpha_2\text{-P}_2\text{W}_{17}\text{Cu}$ was revealed by the characteristic stripping oxidation wave on potential reversal [90]. In this compound, the first W-wave was shown to overlap partly with the copper wave. Spectroelectrochemistry studies indicated, however, that the two-electron reduction of Cu²⁺ is complete before any significant reduction of W moieties.

In this work, the electrocatalytic dioxygen reduction by reduced $\alpha_2\text{-P}_2\text{W}_{17}\text{Cu}$ is indeed observed. In contrast with the case of $\alpha_2\text{-P}_2\text{W}_{15}\text{Mo}_2\text{Cu}$, the catalytic wave current intensity depends on the scan rate. The characteristic stripping oxidation wave of the copper deposited during the cathodic processes diminishes drastically upon increase of the γ values. All these observations together point to a prominent role of the copper center within $\alpha_2\text{-P}_2\text{W}_{17}\text{Cu}$ in the catalytic reduction of dioxygen, albeit at a substantially more negative potential than observed with $\alpha_2\text{-P}_2\text{W}_{15}\text{Mo}_2\text{Cu}$.

Figure 31 compares the currents of the catalytic waves obtained in identical experimental conditions with $\alpha_2\text{-P}_2\text{W}_{15}\text{Mo}_2\text{Cu}$ and $\alpha_2\text{-P}_2\text{W}_{17}\text{Cu}$ respectively. The electrocatalytic process is less favorable with the latter complex,

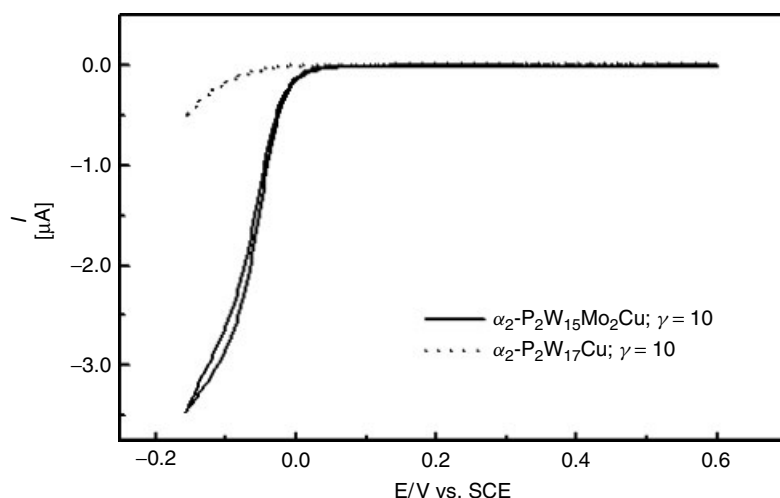


Fig. 31 Cyclic voltammograms (scan rate: 2 mV s^{-1}) observed in $0.2 \text{ M Na}_2\text{SO}_4 + \text{H}_2\text{SO}_4$ (pH 3); the working electrode was glassy carbon and the reference electrode was SCE. Comparison of the behaviors of $10^{-4} \text{ M } \alpha_2\text{-P}_2\text{W}_{17}\text{Cu}$ and $10^{-4} \text{ M } \alpha_2\text{-P}_2\text{W}_{15}\text{Mo}_2\text{Cu}$ in the presence of dioxygen. For further details, see text (taken from Ref. 161).

in which the catalysis can be admitted to be triggered essentially by the Cu center. In other words, no synergism could be observed between the W and Cu influences in the explored potential domain. In contrast, this result, associated with the lack of “intrinsic” activity of Mo centers, highlights the cooperativity between Mo and Cu centers within $\alpha_2\text{-P}_2\text{W}_{15}\text{Mo}_2\text{Cu}$ in the electrocatalytic dioxygen reduction.

The question arises as to the actual sequence of events that end up in the reduction of dioxygen into water. Even though complementary investigation is needed before a complete answer could be proposed, several observations are worth mentioning provisionally. The reoxidation of reduced heteropolyanions by dioxygen after the catalytic processes in which they participate is a popular practice. Its mechanism was generally and indistinctly explained to go through an intermediate adduct formation accompanied by inner sphere electron transfers [164].

Recently a clarification by Duncan and Hill [165] established clearly that simple outer sphere electron transfer might be the actual pathway in the case of unsubstituted POMs; in the case of vanadium-substituted derivatives, the conclusion was less clear-cut. The present results should be considered in the framework of metal ion–substituted complexes. In other words, the reasoning parallels those used in the dioxygen electroreduction by copper-containing organometallic complexes. In these examples, “ $\text{Cu(I)}-\text{O}_2$ ” constitutes the favorite intermediate [166]. Here, the proximity of the reduction potentials of Mo and Cu^{2+} centers within $\alpha_2\text{-P}_2\text{W}_{15}\text{Mo}_2\text{Cu}$ at appropriately selected pH values suggests strongly that such a mechanism could be operative. Furthermore, the efficiency of the catalysis would indicate that the reduction potential of the adduct is very close to or even more positive than that of Mo centers. Tentatively, mixed acceptor orbitals containing both Mo and

Cu contributions can be suggested to exist.

Finally, the possibility that a specificity of the Mo/Cu association exists to favor the observed cooperativity should be considered. Even though the present work is performed in homogeneous conditions, a parallel was, tentatively, made with the case of catalytic solid electrodes prepared for the reduction of dioxygen into water: specifically, $(\text{Ru}_{1-x}\text{Mo}_x)_y\text{SeO}_z$ layers containing very small amounts of Mo realize the four-electron reduction of dioxygen in acidic media [167]. The presence of Mo was demonstrated to be required to favor the catalytic process. The mechanistic assumption that guided to the synthesis and study of such layers is that oxygen is adsorbed by Mo due to its higher interaction energy among the surface atoms, but the electrocatalysis must occur at the ruthenium. Such cooperativity can be considered as a successful operational hypothesis.

Reduction of dioxygen and hydrogen peroxide by $\text{Cu}_4\text{X}_4\text{W}_{30}$ ($\text{X} = \text{P}$ or As)

Direct dioxygen reduction occurs at fairly negative potential on glassy carbon electrode [115]. In the presence of the sandwich-type complexes of this work, this reduction is observed readily on the first Cu^{2+} reduction wave as shown in Fig. 32. For $\gamma = 10$, the catalytic efficiency, CAT, reaches values as high as 615 and 722% for $\text{Cu}_4\text{P}_4\text{W}_{30}$ and $\text{Cu}_4\text{As}_4\text{W}_{30}$ respectively. The small difference between the two CAT values result from the fact that Cu^{2+} is slightly more easily reduced in the As-containing complex. Analogous results were obtained recently with Mn-sandwich complexes [110].

The possible final products are hydrogen peroxide and water. Electrolyses were performed at the peak potential location E_{pc1} of the first Cu^{2+} reduction wave to try and determine the identity of the final product. In each experiment, enough charge was passed through the solution to generate 13 mM to 27 mM H_2O_2 if this substance were the final product. At the end of each electrolysis, the amount of generated H_2O_2 was tested by the spectrophotometry, using

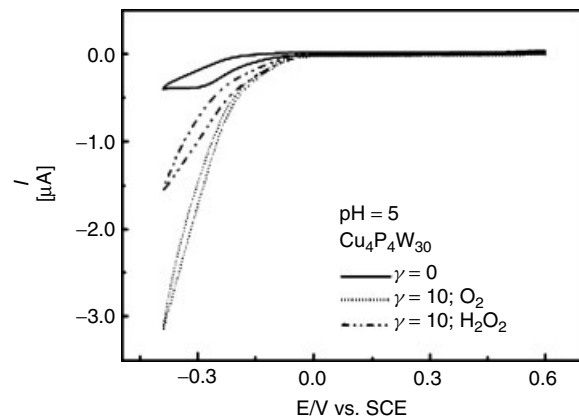


Fig. 32 Electrocatalysis of O_2 and H_2O_2 reductions in the presence of 10^{-4} M $\text{Cu}_4\text{P}_4\text{W}_{30}$ in a pH 5 medium. The scan rate was 2 mV s^{-1} , the working electrode was glassy carbon and the reference electrode was SCE. For more detailed information see text (taken from Ref. 115).

the sensitive $\text{Ti}(\text{SO}_4)_2$ as reagent [168]. In all batches, only traces of H_2O_2 were detected. This observation indicates that the final product of the reduction of dioxygen by the present sandwich complexes is essentially water. The intermediacy of H_2O_2 can be suspected, as traces of this substance are detected. However, Fig. 32 confirms that H_2O_2 is also efficiently reduced in the presence of $\text{Cu}_4\text{P}_4\text{W}_{30}$, for example. Finally, it must be concluded that the electrocatalytic reduction of dioxygen features an overall four-electron process.

Finally, it is worth noting that much the same results as obtained here in the reduction of nitrate, nitrite, dioxygen, and hydrogen peroxide with $\text{Cu}_4\text{As}_4\text{W}_{30}$ are observed also with the semivacant analog $\text{H}_8\text{Cu}_4\text{As}_2\text{W}_{30}$ ($[\alpha\beta\beta\alpha-(\text{Cu}^{\text{II}}\text{OH}_2)_2(\text{Cu}^{\text{II}})_2(\text{AsW}_{15}(\text{OH})_3(\text{OH})\text{O}_{52})_2]^{12-}$).

Electrocatalytic reduction of dioxygen and hydrogen peroxide in the presence of $\text{Mn}_2\text{Fe}_2\text{X}_4$ ($\text{X} = \text{P}$ or As) In this example selected from recent work [162], the studies of the electrocatalytic reductions of O_2 and H_2O_2 were performed in a $\text{pH} = 5$ medium. The efficiency of the catalysis is again evaluated by an excess parameter γ , which is defined as $C^\circ(\text{O}_2)/C^\circ(\text{POM})$ for dioxygen and $C^\circ(\text{H}_2\text{O}_2)/C^\circ(\text{POM})$ for hydrogen peroxide (C° = concentration of the relevant species indicated in parentheses). The catalytic efficiency (CAT) is defined as follows: $\text{CAT} = 100 \times [I(\text{POM} + \text{O}_2 \text{ or } \text{H}_2\text{O}_2) - I^\text{d}(\text{POM})]/I^\text{d}(\text{POM})$, where $I(\text{POM} + \text{O}_2 \text{ or } \text{H}_2\text{O}_2)$ is the current for the reduction of the POM in the presence of O_2 or H_2O_2 and $I^\text{d}(\text{POM})$ is the corresponding diffusion current for the POM alone. Selected values of cat-

Tab. 14 Selected values of catalytic efficiencies measured at $E = -420 \text{ mV vs. SCE}$ in a pH 5 medium (1 M $\text{CH}_3\text{COOLi} + \text{CH}_3\text{COOH}$) for O_2 and H_2O_2 reductions with various electrocatalysts^a

Complex	CAT	
	O_2	H_2O_2
$\text{Zn}_2\text{Fe}_2\text{As}_4$	680	334
$\text{Zn}_2\text{Fe}_2\text{P}_4$	817	222
$\text{Mn}_2\text{Fe}_2\text{As}_4$	944	464
$\text{Mn}_2\text{Fe}_2\text{P}_4$	1055	380

^aThe scan rate was 2 mV s^{-1} . The catalytic efficiency (CAT) is defined as follows:
 $\text{CAT} = 100 \times [I(\text{POM} + \text{O}_2 \text{ or } \text{H}_2\text{O}_2) - I^\text{d}(\text{POM})]/I^\text{d}(\text{POM})$, where $I(\text{POM} + \text{O}_2 \text{ or } \text{H}_2\text{O}_2)$ is the current for the reduction of the POM in the presence of O_2 or H_2O_2 and $I^\text{d}(\text{POM})$ is the corresponding diffusion current for the POM alone.

alytic efficiencies (CAT) for the reduction of dioxygen and hydrogen peroxide are included in Table 14. CAT values were measured at -420 mV vs. SCE , in the potential domain of the $\text{Fe}(\text{III})$ -reduction waves.

Corresponding CAT values for $\text{Mn}_2\text{Fe}_2\text{X}_4$ ($\text{X} = \text{P}$ or As) were also measured and included for comparison. Under the same experimental conditions, the phosphorus-containing complexes, $\text{M}_2\text{Fe}_2\text{P}_4$ ($\text{M} = \text{Zn}(\text{II})$ or $\text{Mn}(\text{II})$), are more efficient than their arsenic analogs, $\text{M}_2\text{Fe}_2\text{As}_4$ ($\text{M} = \text{Zn}(\text{II})$ or $\text{Mn}(\text{II})$), for dioxygen reduction, while the opposite is true for hydrogen peroxide reduction. This observation underscores the difficulty for anticipating which electrocatalyst would be more efficient when an inner sphere pathway is operative. The electrocatalytic

processes observed here remain efficient in other media, and they establish the utility of the Fe(III) centers within these mixed-metal sandwich complexes even in media of low proton availability. There is still ample room for optimization of the selected media for efficient electrocatalytic processes within these compounds.

Examination of the dioxygen and hydrogen peroxide electrocatalytic processes discussed here may also shed some light on possible reaction pathways. Dioxygen does not coordinate to Fe(III) but it does coordinate to Fe(II). Then, the presence of another reduced Fe center could drive the catalytic process to completion by carrying out immediate further reduction of the Fe–O₂ adduct. In-line with these observations, the

measured catalytic efficiencies decrease when the number of F''-centers decrease [111a, 1]. Also noteworthy is that the synthesis of M₂Fe₂X₄ (M = Zn(II) or Mn(II); X = P or As) from Fe₂X₄ (X = P or As) diminishes the overall negative charge of the POM, rendering its reduction more facile, and ultimately, saving energy during the electrocatalytic process.

Indeed, other electrocatalytic processes were studied, including the pioneering work on chlorate reduction by the six-electron reduction product of 12-molybdophosphate in water-dioxane solutions [169]. This process, extended to bromate, has become a classical test of the electrocatalytic abilities of several POMs [see Table 13].

Tab. 15 Electrochemical oxidations catalyzed by heteropolyanions

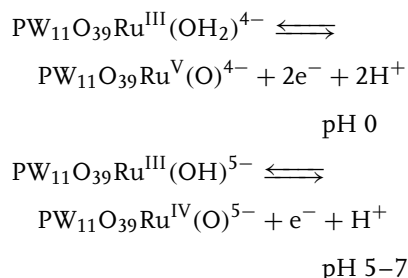
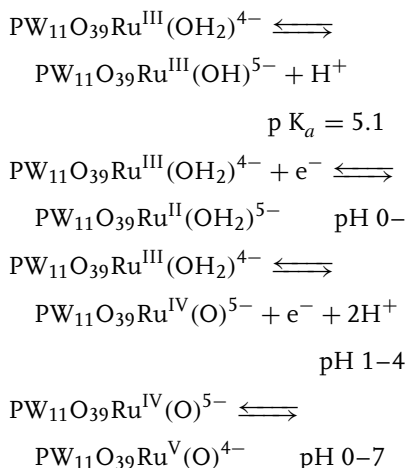
Catalyst	Substrate	Products	Conditions	References
$\alpha\text{-PW}_{11}\text{O}_{39}\text{Ru}(\text{H}_2\text{O})^{4-}$	Me ₂ SO	Me ₂ SO ₂	Electrolysis, sulfate buffer (pH 1) 1.1 V vs. SCE, divided cell, room temperature	85
	Alcohols	carbonyl compounds	acetate buffer, room temperature	169
$\alpha\text{-Q}_5\text{SiW}_{11}\text{O}_{39}\text{Ru}^{\text{a}}$	Olefins	aldehydes	double-mediator electrolysis CH ₂ Cl ₂ -H ₂ O, NaIO ₃ , undivided cell, 50° C, PbO ₂ anode, Pt cathode	170
$\alpha\text{-PW}_{11}\text{O}_{39}\text{Cr}(\text{H}_2\text{O})^{4-}$	Alcohols	carbonyl compounds	Sulfate buffer (pH 1), room temperature	171
$\text{P}_2\text{W}_{17}\text{O}_{61}\text{Cr}(\text{H}_2\text{O})^{7-}$				
$\alpha\text{-SiW}_{11}\text{O}_{39}\text{Mn}(\text{H}_2\text{O})^{6-}$	Alcohols	carbonyl compounds	Electrolysis, phosphate buffer (1U1pH 6) 1.25 V vs. Ag/AgCl, divided cell, room temperature, C anode, Pt cathode	153g + h
$\alpha_2\text{-P}_2\text{W}_{17}\text{O}_{62}\text{V}^{8-}$	NADH	NAD ⁺	Phosphate buffer (pH 7), room temperature	82, 172–174
$\alpha_1\text{-P}_2\text{W}_{17}\text{O}_{62}\text{V}^{8-}$				
$\alpha_1\text{-P}_2\text{W}_{17}\text{MoO}_{62}^{6-}$				

^aQ = tetrabutylammonium.

22.7.2.2 Electrocatalytic Oxidations

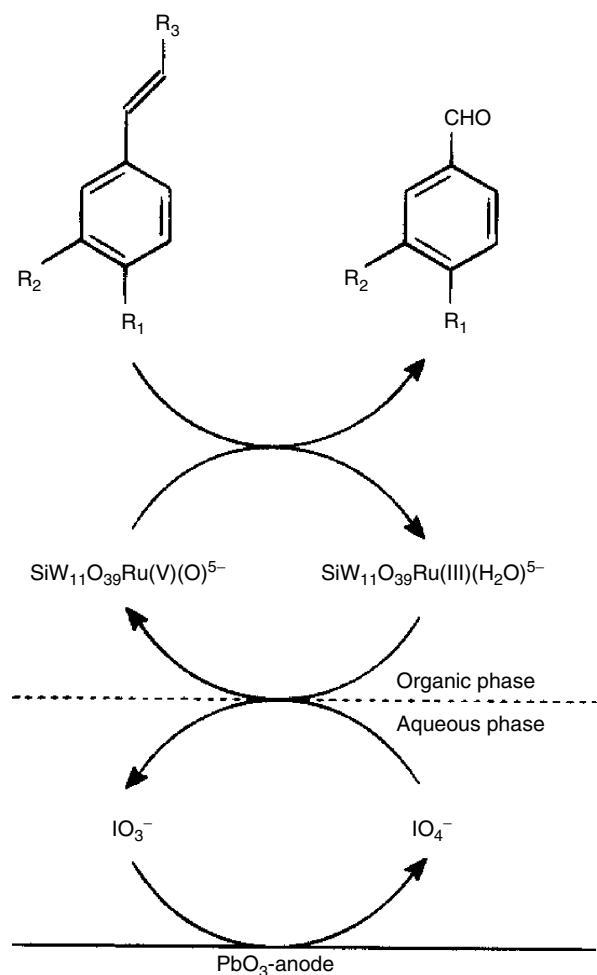
Table 15 gathers the main electrocatalytic processes triggered by POMs dissolved in solution. Most of these examples highlight the prominent role of the metal substituted into the POM framework. The catalyst can be considered as soluble POM-supported catalytic centers, with the advantage, relative to their organic counterparts, of thermal stability, robustness, and inertness toward oxidizing environments of the ligand. With this view, most electrochemically-assisted catalytic oxidation reactions described in the literature were designed to parallel analogous known effective processes in organometallic chemistry.

22.7.2.2.1 $[\text{Ru}^{\text{III}}(\text{H}_2\text{O})\text{PW}_{11}\text{O}_{39}]^{4-}$ and $[\text{Ru}^{\text{III}}(\text{H}_2\text{O})\text{SiW}_{11}\text{O}_{39}]^{5-}$ as an Electrochemical Oxygen Transfer Catalysts Depending on the pH domain studied in acidic solution, $[\text{Ru}^{\text{III}}(\text{H}_2\text{O})\text{PW}_{11}\text{O}_{39}]^{4-}$ ($\text{PW}_{11}\text{O}_{39}\text{Ru}^{\text{III}}(\text{H}_2\text{O})$ for short) was demonstrated to exhibit three reversible redox couples corresponding to the Ru center processes [85]. These redox couples can be assigned to the aquaruthenium (II), oxoruthenium (IV), and oxoruthenium (V) as sketched in the following equations:

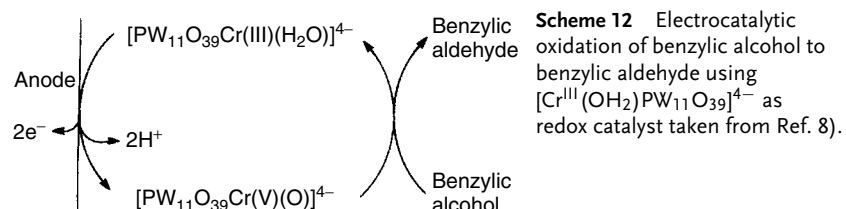


The two-electron oxidation to generate the oxoruthenium(V) constitutes the basis of an electrocatalytic oxidation of Dimethylsulfoxide to dimethylsulfone with >90% current efficiency and a modest total turnover of 40 for the catalyst. Substitution of π -acids to the water molecule stabilizes the Ru(II) form and shifts all the redox potentials in the positive direction, so that the Ru(IV/III) and Ru(V/III) couples are no longer seen on the voltammograms, owing to the absence of an aqua ligand [175]. The oxoruthenium (V) species were also shown to oxidize alcohols. The quaternary ammonium salt of the tungstosilicate analog, $\text{SiW}_{11}\text{O}_{39}\text{Ru}^{\text{III}}(\text{OH}_2)^{5-}$ was used to catalyze the periodate-mediated oxidative cleavage of olefins [170, 176]. However, electrochemical investigation and direct electrochemical oxidation of this compound failed, as also the electrochemical regeneration of the active oxoruthenium(V) species. Yet, Steckhan and Kandzia [177] found an elegant two-phase double-mediator system based on this complex. In this system sketched in Sch. 11, the IO_4^- was regenerated at the PbO_2 anode in the aqueous phase and various olefins were converted to the corresponding aldehydes in the organic phase.

22.7.2.2.2 $\alpha_1\text{-}[\text{Cr}^{\text{III}}(\text{H}_2\text{O})\text{PW}_{11}\text{O}_{39}]^{4-}$ and $\alpha_2\text{-}[\text{Cr}^{\text{III}}(\text{OH}_2)\text{P}_2\text{W}_{17}\text{O}_{61}]^{7-}$ as Oxygen Transfer Catalysts in Electrochemistry Following the intensive study of the oxygen

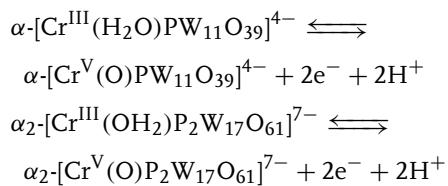


Scheme 11 Indirect electrochemical oxidation cleavage of alkenes using a double-mediator system consisting of IO_4^- and ruthenium tungstosilicate (taken from Ref. 8).



Scheme 12 Electrocatalytic oxidation of benzylic alcohol to benzylic aldehyde using $[\text{Cr}^{\text{III}}(\text{OH}_2)\text{PW}_{11}\text{O}_{39}]^{4-}$ as redox catalyst taken from Ref. 8).

transfer abilities of these POMs by the groups of Pope [171] and Hill [178], Rong and Anson evaluated the possibility to use them as electrocatalysts in water [179]. The reduction of Cr(III) to Cr(II) could not be observed by cyclic voltammetry at pH = 1. The following steps were demonstrated:



The electrochemically generated Cr^V=O complexes are able to oxidize alcohols to carbonyl compounds according to the following catalytic cycle, sketched in Sch. 12.

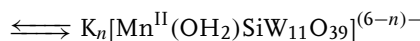
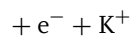
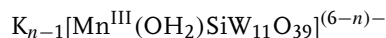
22.7.2.2.3 A Detailed Study of K_n[Mn^{II}(OH₂)SiW₁₁O₃₉]⁽⁶⁻ⁿ⁾⁻ as Oxidation Electrocatalyst

Pope and coworkers [112] were the first to identify that the chemical or electrochemical oxidation of Mn(II) center within K_n[Mn^{II}(OH₂)SiW₁₁O₃₉]⁽⁶⁻ⁿ⁾⁻ yields a Mn^{IV}(OH) complex rather than a Mn^V(O) complex. An electrochemical confirmation of the formation of the complex

K_{n-1}[Mn^{IV}(OH)SiW₁₁O₃₉]⁽⁶⁻ⁿ⁾⁻ was obtained in cyclic voltammetry by observing the average redox potential when pH and potassium concentration were changed in the electrolyte [153g,h]. Reproducible cyclic voltammograms could be run only either after pretreatment of the electrode by continuous cycling between 1.3 and 0 V vs. Ag/AgCl or by starting the CV from 1.3 V where the manganese was oxidized to Mn(IV). The following overall steps are in agreement with observations.

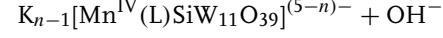
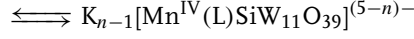
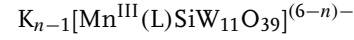
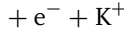
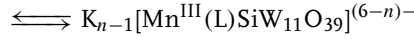
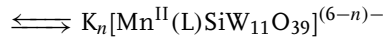


(E_{1/2} = 0.99 V vs. Ag/AgCl at pH = 6.0)

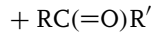
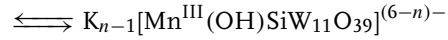
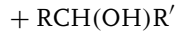
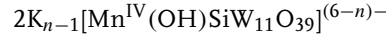


(E_{1/2} = 0.53 V vs. Ag/AgCl at pH = 6.0)

These steps were explained in more detail by the following sequence of events, by taking into account the competition between a water molecule and a counterion L in the electrolyte (L = H₂PO₄⁻ or HPO₄²⁻ in phosphate buffer) to occupy the sixth site on the Mn atom.



The complex K_{n-1}[Mn^{IV}(L)SiW₁₁O₃₉]⁽⁶⁻ⁿ⁾⁻ was shown to be efficient in the oxidation of different alcohols via hydride ion transfer.



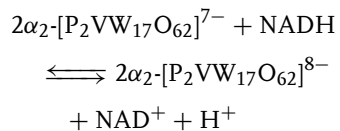
22.7.2.2.4 Catalytic Oxidation of NAD(P)H:

A Continuously Improved Selection of Suitable POMs This research is triggered by at least two reasons: (1) the importance of NAD(P)H/NAD(P)⁺ redox couples in biological systems is known, as is known the dependence of oxidation mechanisms on the oxidants [14, 82, 172–174]; (2) the possibility of developing amperometric biosensors for NAD(P)⁺-dependent dehydrogenases. As a consequence, much attention is devoted to the regeneration of these coenzymes in their reduced or oxidized forms for their application in biosensors or in enzymatic synthesis [180]. Here, we are concerned with electrochemical regeneration [181].

However, the oxidation of NAD(P)H to NAD(P)⁺ at practical rates on most electrode materials proceeds only at high overpotentials [182] and often fouling of the electrode surface has been observed. This situation induces the search for suitable mediators or electrode modification processes to accelerate the highly irreversible oxidation of NAD(P)H. The stability of the reaction products in the presence of each other is also a necessary condition for usefulness.

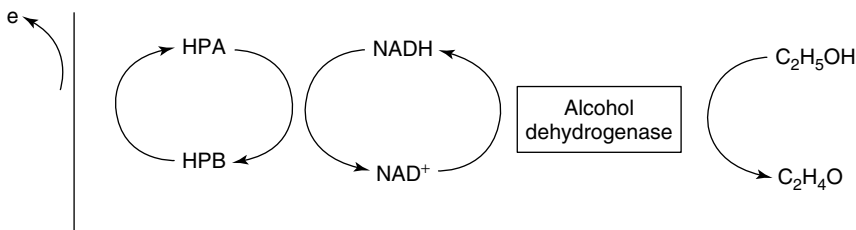
The first studies were devoted to NADH. The challenge was to select POMs likely to meet all these criteria and be stable in neutral alkaline media. As a matter of fact, quantitative studies in fairly acidic

solutions are precluded by the known rapid hydration of NADH below pH = 6. Nadjo and Keita demonstrated an efficient oxidation of NADH by several vanado-tungsto phosphoric heteropolyanions, stable at pH = 7 [14, 82, 172–174]. The correct stoichiometry of NADH to POM was found, by spectrophotometry and coulometry, to be 1:2, thus indicating that the POM acts as a one-electron oxidant. The stability of the mixtures was established. In addition, complete regeneration of NADH was obtained from NAD⁺ in the mixtures with the heteropolyblue (HPB) in the presence of alcohol dehydrogenase (ADH) and ethanol. Thus, the catalytic process sketched in Sch. 13 is fully established.



The kinetics of NADH oxidation by three vanado-tungstodiphosphoric species were studied at pH = 7 by the stopped flow technique [82], giving values in complete agreement with electrochemistry results to be discussed in the following.

Figure 33 shows a representative example of the oxidation of NADH by POMs using cyclic voltammetry at a scan rate of 5 mV s⁻¹. Other examples can be found in the original papers. Typically, the system $\alpha_1\text{-[P}_2\text{VW}_{17}\text{O}_{62}\text{]}^{7-}$ /NADH is shown. The



Scheme 13 General catalytic redox process of NADH triggered by POMs (taken from Ref. 174).

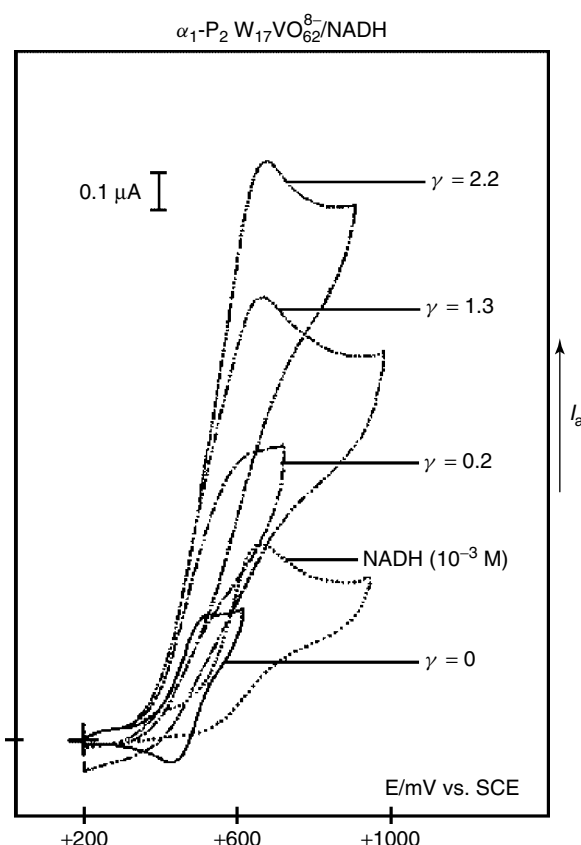


Fig. 33 Cyclic voltammograms obtained for the system $\alpha_1\text{P}_2\text{W}_{17}\text{VO}_{62}^{8-}/\text{NADH}$. Electrolyte pH 7 phosphate buffer. Reference electrode SCE; working electrode: 1 mm diameter Pt disk. The solutions contain $10^{-3} \text{ M } \alpha_1\text{P}_2\text{W}_{17}\text{VO}_{62}^{8-} + 10^{-3} \gamma \text{ M }$ NADH, except for the one containing 10^{-3} M NADH alone. Scan rate $v = 5 \text{ mV s}^{-1}$ (taken from Ref. 174).

excess parameter ($\gamma = C^\circ_{\text{NADH}}/C^\circ_{\text{POM}}$) values appear on each curve. It is worth noting, in Fig. 33, the cyclic voltammogram associated with the first redox system of the POM and corresponding to a one-electron diffusion-controlled process ($\gamma = 0$). Also, the cyclic voltammogram featuring the direct oxidation of NADH on the electrode surface in the same medium is shown. The other curves in this figure show the evolution of the CV of the POM upon addition of various amounts

of NADH. For $\gamma \neq 0$, it is observed that the anodic current component of the one-electron system of the HPB increases substantially and the corresponding reduction process is suppressed at the scan rate used for these CVs. The evolution of the CVs is easily understood on the basis of a fast oxidation of NADH by the oxidized form of the POM.

Determinations of rate constants for the catalytic process were carried out by double potential step chronocoulometry

Tab. 16 Standard potential for the first redox system of each POM and second-order rate constant k derived from DPSC experiments on HPB/NADH systems at pH = 7. Each value of k is the average of at least five experiments. The values of γ are not necessary, but have been added to give a better idea of the experimental conditions (taken from Ref. 174)

HPB	$\alpha_1\text{-P}_2\text{W}_{17}\text{VO}_{62}^{8-}$	$\alpha_1\text{-P}_2\text{W}_{17}\text{MoO}_{62}^{7-}$	$\alpha_2\text{-P}_2\text{W}_{17}\text{VO}_{62}^{8-}$	$\text{P}_2\text{W}_{16}\text{V}_2\text{O}_{62}^{9-}$	$\alpha_2\text{-P}_2\text{W}_{17}\text{MoO}_{62}^{7-}$
E° (mV vs. SCE)	477.5	395.5	392.5	277.5	225
γ	10	10	10	10	20
K ($M^{-1} \times s^{-1}$)	1.5×10^4	6.9×10^2	6.4×10^2	7.1	1.2

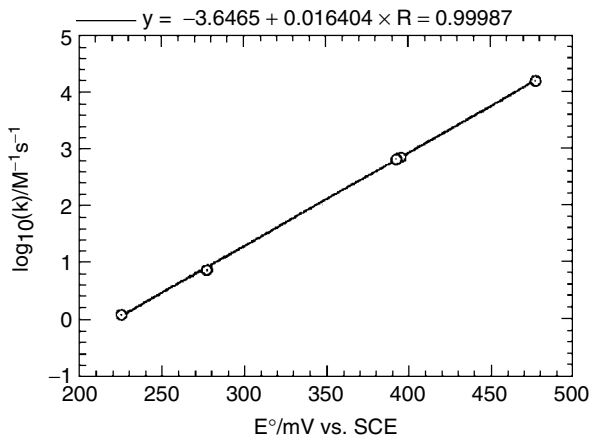


Fig. 34 Plot of $\log k$ versus the one-electron redox potentials E of the POMs (taken from Ref. 174).

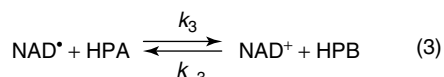
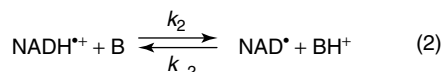
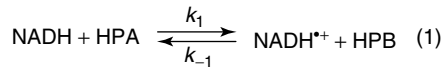
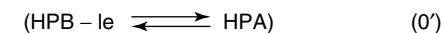
[183]. The experiments were performed under pseudo first order rate conditions. The results are gathered in Table 16, which also gives the standard potential for the first redox system of each POM. Figure 34 shows the plot of $\log_{10}k$ as a function of the one-electron redox potentials of the POMs. A straight line is obtained with a slope of 16.4 V^{-1} .

A detailed mechanistic pathway could be written (Sch. 14) and discussed.

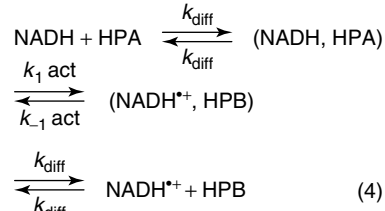
It is shown first that hydride transfer is not a likely reaction pathway. The rate-limiting step is established to be the initial one-electron transfer by using rate constants obtained by independent

measurements. Then to go deeper into the mechanism, the initial one-electron rate-limiting step was developed into three successive steps in Sch. 15 in which (NADH, HPA) and (NADH $^+$, HPB) represent the reactants in their reaction sites, whereas NADH + HPA and NADH $^+$ + HPB represent the reactants and products beyond the average distance of diffusion; k_{diff} is the diffusion-limited rate constant, $k_{1\text{act}}$ and $k_{-1\text{act}}$ are the activation-controlled rate constants. Each of these steps could be, in principle, rate-limiting [184]. However, the experimental results in Fig. 34 indicate that the diffusional separation of the HPB/NADH $^+$ pair is rate limiting without

Scheme 14 Detailed mechanistic NADH oxidation pathway suggested by the experiments with POMs (taken from Ref. 174).



Scheme 15 The initial one-electron rate-limiting step in the oxidation of NADH by the POMs studied in this work (taken from Ref. 174).



any tendency to observe a rate-limiting electron hop. A value of $E^\circ = +0.80$ V was determined for the NADH/NADH⁺ couple at pH = 7.

However, a pH of 8 or 9 is more favorable to shift the overall equilibrium toward the oxidized product. Taking this remark into account, Keita and Nadjo showed recently that efficient POMs exist that meet these conditions [185]. A preliminary work is being published. The series of V-substituted derivatives selected in this work contain several POMs stable in their oxidized and reduced forms in alkaline media, thus guaranteeing the stability of the species generated during the catalytic process. The preliminary study is devoted to the electrocatalytic oxidation of NADPH, a substrate closely related to NADH, with the same importance *in vivo* and *in vitro*.

Figure 35(a) shows the current enhancements accompanying the addition of increasing amounts of NADPH to a pH 8 solution of P₂V₂W₁₆. The current intensity increase is observed readily at the

reduction potential of the first V center. It is worth noting the high efficiency of the electrocatalysis, even though modest γ values were used (γ is the excess parameter defined here as $\gamma = C^\circ(\text{NADPH})/C^\circ(\text{POM})$). To characterize the process itself, the catalytic efficiency (CAT) is defined as follows: $CAT = 100 \times [I(\text{POM} + \text{NADPH}) - I^d(\text{POM})]/I^d(\text{POM})$, where $I(\text{POM} + \text{NADPH})$ is the current for the reduction of the POM in the presence of NADPH and I^d is the corresponding diffusion current for the POM alone. In the present experiments, CAT values of 403 and 730% were calculated for $\gamma = 10$ and $\gamma = 20$ respectively at +308 mV vs. SCE. Figure 35(b) shows the direct NADPH oxidation wave on the glassy carbon electrode surface and the rising section of the catalytic wave for $\gamma = 20$ in the same pH 8 medium. It is clear from this figure that no direct oxidation of NADPH is observed in this potential domain explored in Fig. 35(a). Furthermore, the substantial improvement in potential brought about

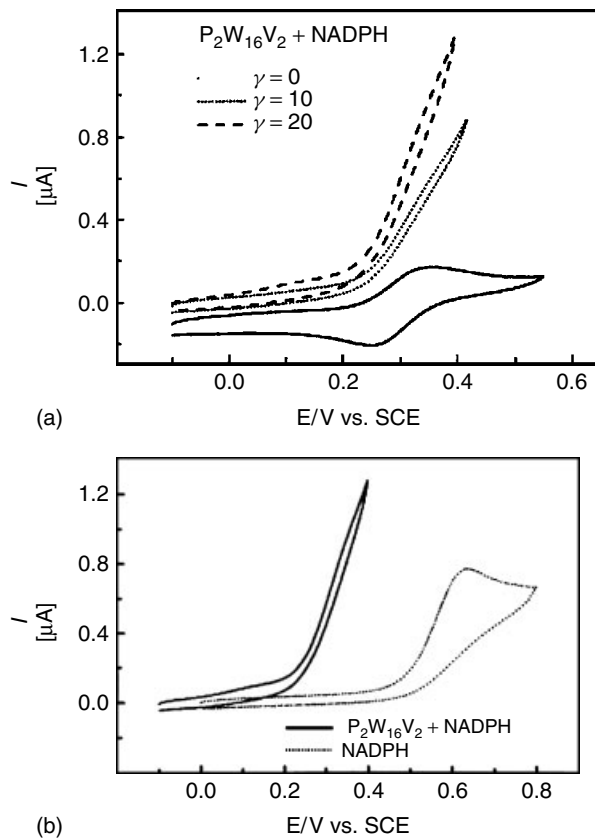


Fig. 35 Cyclic voltammograms for the electrocatalytic oxidation of NADPH by 2×10^{-4} M $\text{P}_2\text{W}_{16}\text{V}_2$, in pH 8 buffer (50 mM TRIS + 0.5 M Na_2SO_4 + H_2SO_4); the scan rate was 2 mV s $^{-1}$, the working electrode was glassy carbon (3 mm diameter disk), the reference electrode was SCE. (a) The excess parameter values for NADPH were $\gamma = 10$ and $\gamma = 20$ respectively; (b) Comparison of the catalytic process ($\gamma = 20$) by $\text{P}_2\text{W}_{16}\text{V}_2$ with the direct oxidation of NADPH on the glassy carbon electrode (taken from Ref. 185).

by the catalysis for the oxidation of NADPH is obvious. Double potential step chronocoulometry experiments [172] performed between 0 and +400 mV vs. SCE had allowed the value of the second-order rate constant to be evaluated: $k = 3.5 \times 10^3$ M $^{-1}$ s $^{-1}$. The present experiments were performed in deaerated solution. However, it has been checked that an inert

atmosphere was not necessary, because the V^{V} and V^{IV} forms of $\text{P}_2\text{V}_2\text{W}_{16}$ are insensitive to the presence of dioxygen. This remark is important as that it opens the way for working in conditions close to those of biological environments, in contrast with most mediators, especially quinonoid mediators proposed in the literature [186].

22.8 Conclusion

This chapter describes most of the significant electrochemical behaviors of POMs. The variety of these behaviors justifies that these molecular oxides are studied in almost every domain of chemistry from synthesis, physical chemistry, catalysis through material science, and even medicine. Yet, the widespread applicability of these molecules necessitates that the interest in their study, which is growing unabated during these recent several years, result in substantial breakthrough in several directions, including the following possibilities: the possibility to finely tune the properties by varying the POM compositions and structures on purpose; find out new structures in which substituent metal cations remain electroactive and electrocatalytic; improve the stability of the POMs; improve the kinetics of reactions that are already demonstrated to be the equivalent of several processes known with organometallic species, and so on. In electrochemistry, several domains deserve further attention. Studies in nonaqueous media are scarce and the electrocatalytic processes that can be triggered by POMs in such media should be of interest. The first attempts at use of POMs in bioelectrochemistry are very promising. Continuous efforts must aim at obtaining new POMs stable in alkaline media, which could be useful in the redox processes of coenzymes and proteins in general.

In short, much work remains to be done but the perspectives might be rather bright.

Acknowledgment

We thank all our colleagues and coworkers who have participated in the work on

Polyoxometalates. As regards the synthesis and characterization of some POMs, special thanks are addressed to Dr. R. Contant (Université Paris VI), Professor C.L. Hill, Dr. T.M. Anderson and Professor I.K. Hardcastle (Emory University, Atlanta), Professor U. Kortz (International University of Bremen), Professor M.T. Pope (University of Washington), Dr. I.M. Mbomekalle and Dr. Y.W. Lu (Université Paris XI).

References

1. B. Keita, I. M. Mbomekalle, Y. W. Lu et al., *Eur. J. Inorg. Chem.* **2004**, 3462.
2. B. Keita, L. Nadjo, *Curr. Top. Electrochem.* **1993**, 2, 77.
3. C. L. Hill (Guest Ed.), *Chem. Rev.* **1998**, 98, 1–389.
4. M. T. Pope, *Heteropoly and Isopoly Oxometalates*, Springer-Verlag, Berlin, 1983.
5. M. T. Pope, A. Müller, (Eds.), *Polyoxometalates: From Platonic Solids to Antiretroviral Activity*, Kluwer Academic Publications, Dordrecht, 1994.
6. (a) M. T. Pope, Polyoxo anions: synthesis and structure in *Comprehensive Coordination Chemistry II: Transition Metal Groups 3–6* (Ed.: A. G. Wedd), Elsevier Science, New York, 2004, pp. 635–678, Vol. 4, Chapter 4.10; (b) R. Contant, G. Hervé, *Rev. Inorg. Chem.* **2002**, 22, 63; (c) J. J. Cruywagen, *Adv. Inorg. Chem.* **2000**, 49, 127; (d) J. Berzelius, *Pogg. Ann.* **1826**, 6, 369–380; (e) L. Svanberg, H. Struve, *J. Prakt. Chem.* **1848**, 44, 257–291; (f) C. Marignac, *C. R. Acad. Sci.* **1862**, 55, 888.
7. C. L. Hill, Polyoxometalates: reactivity in *Comprehensive Coordination Chemistry II: Transition Metal Groups 3–6* (Ed.: A. G. Wedd), Elsevier Science, New York, 2004, pp. 679–759, Vol. 4, Chapter 4.11.
8. M. Sadakane, E. Steckhan, *Chem. Rev.* **1998**, 98, 219.
9. B. Keita, L. Nadjo, *Electrocatalysis by Chemically Modified Electrodes of the Main Inorganic Chemicals, Encyclopedia of Electrochemistry*, Vol. 10 (Eds.: A. J. Bard, M. Stratmann), Wiley-VCH, Weinheim, 2003.

10. A. Belhouari, B. Keita, L. Nadjo et al., *New J. Chem.* **1998**, 83.
11. R. Contant, M. Abbessi, J. Canny et al., *Inorg. Chem.* **1997**, 36, 4961.
12. B. Keita, L. Nadjo, R. Contant, *J. Electroanal. Chem.* **1998**, 443, 168–174.
13. (a) R. Contant, M. Abbessi, J. Canny, et al., *Eur. J. Inorg. Chem.* **2000**, 567; (b) R. Belgħiche, R. Contant, Y. W. Lu et al., *Eur. J. Inorg. Chem.* **2002**, 1410.
14. B. Keita, Y. W. Lu, L. Nadjo et al., *J. Electroanal. Chem.* **1999**, 477, 146–157.
15. B. Keita, F. Girard, L. Nadjo et al., *J. Electroanal. Chem.* **1999**, 478, 76–82.
16. R. C. Chambers, C. L. Hill, *Inorg. Chem.* **1991**, 30, 2776.
17. L. C. Baker, *Plenary Lecture Proceedings of XV Internation Conference on Coordination Chemistry 15th*, Moscow, 1973.
18. M. Fournier, Contribution à l'étude des hétéropolyanions molybdiques et des ions mixtes qui en dérivent, Thesis, Université Paris VI, 1976.
19. (a) G. Hervé, *Ann. Chim. Paris* **1971**, 6, 219; (b) G. Hervé, *Ann. Chim. Paris* **1971**, 6, 287; (c) G. Hervé, *Ann. Chim. Paris* **1971**, 6, 337.
20. G. Hervé, Contribution à l'étude des hétéropolyanions tungstiques, Thesis, Université Paris VI, 1970.
21. J. P. Launay, Contribution à l'étude de la réduction électrochimique de l'ion métatungstique et des complexes chlorés de W(VI). Propriétés des produits obtenus, Thesis, Université Paris VI, 1974.
22. J. P. Ciabrini, Contribution à l'étude ses 18-tungsto-2-phosphates et de leurs dérivés lacunaires, Thesis, Université Paris VI, 1982.
23. M. Abbessi, Synthèse et propriétés d'hétéropolyanions vanado-molybdo-tungsto-phosphoriques en vue d'une application en catalyse d'oxydation, Thesis, Université Paris VI, 1989.
24. G. A. Tsirlina, V. Yu. Kotov, *Rossiiskii Khim. Z.* **1998**, 42, 96–102.
25. I. A. Weinstock, *Chem. Rev.* **1998**, 98, 113–170.
26. M. T. Pope, *Introduction to Polyoxometalate Chemistry*, NATO Science Series, II: Mathematics, Physics and Chemistry, Vol. 98. (Polyoxometalate Molecular Science), Kluwer Academic Publishers, Dordrecht, Boston, London, 2003, pp. 3–31.
27. L. E. Briand, G. T. Baronetti, H. J. Thomas, *Appl. Catal., A: Gen.* **2003**, 256, 37–50.
28. B. Keita, L. Nadjo, *Mater. Chem. Phys.* **1989**, 22, 77.
29. (a) L. P. Maslov, N. A. Tsvetkov, *Chem. Abstr.* **79 1973**, 58, 263k; (b) *Chem. Abstr.* **85 1976**, 149, 794z.
30. (a) M. T. Pope, G. M. Varga, *Inorg. Chem.* **1966**, 5, 1249; (b) T. J. R. Weakley in *Structure and Bonding* (Ed.: J. O. Dunitz), Springer, Berlin, p. 131, Vol 18; (c) P. Stonehart, J. G. Koren, J. S. Brinen, *Anal. Chim. Acta* **1968**, 40, 65; (d) J. P. Launay, R. Massart, P. Souchay, *J. Less-Common Met.* **1974**, 36, 139; (e) M. T. Pope, E. Papaconstantinou, *Inorg. Chem.* **1967**, 6, 1147; (f) G. M. Varga Jr., E. Papaconstantinou, M. T. Pope, *Inorg. Chem.* **1970**, 9, 662; (g) E. Papaconstantinou, M. T. Pope, *Inorg. Chem.* **1967**, 6, 1152.
31. M. Otake, T. Onodo, *J. Catal.* **1975**, 38, 494.
32. P. Souchay, R. Massart, G. Hervé, *Rev. Polarography (Japan)* **1967**, 14, 723.
33. (a) B. Keita, T. Lucas, L. Nadjo, *J. Electroanal. Chem.* **1986**, 208, 343; (b) B. Keita, L. Nadjo, *J. Electroanal. Chem.* **1987**, 217, 287; (c) B. Keita, L. Nadjo, *J. Electroanal. Chem.* **1987**, 227, 77; (d) B. Keita, L. Nadjo, *J. Electroanal. Chem.* **1987**, 230, 267.
34. B. Keita, D. Bouaziz, L. Nadjo, *J. Electrochem. Soc.* **1988**, 135, 87.
35. P. D. Prenzler, C. Boskovic, A. M. Bond, et al., *Anal. Chem.* **1999**, 71, 3650–3656.
36. T. Fujinaga, I. Sakamoto, *J. Electroanal. Chem.* **1977**, 85, 185.
37. S. Himeno, M. Takamoto, T. Ueda, *J. Electroanal. Chem.* **2000**, 485, 49–54.
38. C. Reichardt, *Solvent Effects in Organic Chemistry*, VCH, New York, 1990.
39. J. A. Riddick, W. B. Bunger, T. K. Sakano in *Techniques in Chemistry, Organic Solvents*, Vol. II (Ed.: A. Weissberger), Wiley, New York, 1986.
40. S. Himeno, M. Takamoto, *J. Electroanal. Chem.* **2000**, 492, 63–69.
41. (a) A. M. Bond, T. Vu, A. G. Wedd, *J. Electroanal. Chem.* **2000**, 494, 96–104; (b) D. M. Way, J. B. Cooper, M. Sadek et al., *Inorg. Chem.* **1997**, 36, 4227.
42. M. Mastragostino, L. Nadjo, J. M. Saveant, *Electrochim. Acta* **1968**, 13, 721.
43. (a) E. Laviron, *J. Electroanal. Chem.* **1984**, 164, 213; (b) *J. Electroanal. Chem.* **1984**, 169, 23.

44. D. O. Wipf, K. F. Wehmeyer, R. M. Wightman, *J. Org. Chem.* **1986**, *51*, 4760.
45. D. S. Polcyn, I. Shain, *Anal. Chem.* **1966**, *38*, 370.
46. R. L. Myers, I. Shain, *Anal. Chem.* **1969**, *41*, 980.
47. C. P. Andrieux, L. Nadjo, J. M. Saveant, *J. Electroanal. Chem.* **1973**, *41*, 137.
48. C. Amatore, M. Gareil, J. M. Saveant, *J. Electroanal. Chem.* **1983**, *147*, 1.
49. B. Keita, L. Nadjo, *J. Electroanal. Chem.* **1987**, *219*, 355.
50. (a) R. A. Marcus, *Can. J. Chem.* **1959**, *37*, 155; (b) R. A. Marcus, *J. Chem. Phys.* **1965**, *43*, 679; *J. Chem. Phys.* **1956**, *24*, 966; (c) R. A. Marcus in *Dahlem Workshop on the Nature of Seawater* (Ed.: E. D. Goldberg), Verlag Chemie, Weinheim, Berlin, 1975, p. 477.
51. (a) R. Samuelsson, M. Sharp, *Electrochim. Acta* **1978**, *23*, 315; (b) T. W. Rosanske, D. H. Evans, *J. Electroanal. Chem.* **1976**, *72*, 277; (c) A. Capon, R. Parsons, *J. Electroanal. Chem.* **1973**, *46*, 215; (d) C. Rüssel, W. Jaenicke, *J. Electroanal. Chem.* **1986**, *200*, 249; (e) A. Kapturkiewicz, *J. Electroanal. Chem.* **1986**, *201*, 205.
52. (a) Y. Izumi, K. Urabe, M. Onaka, *Zeolite, Clay and Heteropoly Acid in Organic Reactions*, Kodansha, Tokyo, 1992, Chapter 3; (b) M. T. Pope, A. Müller, *Angew. Chem., Int. Ed. Engl.* **1991**, *30*, 34; (c) T. Okuhara, M. Misuno, *J. Synth. Org. Chem. Jpn* **1993**, *51*, 128.
53. A. Tézé, J. Canny, L. Gurban et al., *Inorg. Chem.* **1996**, *33*, 1001.
54. (a) J. J. Altenau, M. T. Pope, R. A. Prados et al., *Inorg. Chem.* **1975**, *14*, 417; (b) T. Okuhara, N. Misuno, M. Misuno, *Adv. Catal.* **1996**, *41*, 113; (c) C. L. Hill, C. M. Prosser-McCartha, *Coord. Chem. Rev.* **1995**, *143*, 407; (d) K. Maeda, H. Katano, T. Osakai, et al., *J. Electroanal. Chem.* **1995**, *389*, 167.
55. M. Nakayama, T. Ii, H. Komatsu et al., *Chem. Commun.* **2004**, 1098.
56. P. J. S. Richardt, J. M. White, P. A. Tregloan et al., *Can. J. Chem.* **2001**, *79*, 613.
57. (a) V. Gutmann, *The Donor-Acceptor Approach to Molecular Interactions*, Plenum Press, New York, 1978, p. 29; (b) G. Gritzner, *J. Phys. Chem.* **1986**, *90*, 5478; (c) P. C. Maria, J. F. Gal, *J. Phys. Chem.* **1985**, *89*, 1926.
58. (a) G. Gritzner, K. Danksagmuller, V. Gutmann, *J. Electroanal. Chem.* **1976**, *72*, 177; (b) G. Gritzner, K. Danksagmuller, V. Gutmann, *J. Electroanal. Chem.* **1978**, *90*, 203; (c) A. Messina, G. Gritzner, *J. Electroanal. Chem.* **1979**, *101*, 201; (d) G. Gritzner, *J. Electroanal. Chem.* **1983**, *144*, 259.
59. (a) J. L. Kavanau, *Water and Solute-Water Interactions*, Holden Day, San Francisco, London, Amsterdam, 1964; (b) J. Broadhead, P. J. Elving, *J. Electrochem. Soc.* **1971**, *118*, 63; (c) P. G. Wolynes, *Ann. Rev. Phys. Chem.* **1980**, *31*, 345; (d) H. L. Friedman, *Ann. Rev. Phys. Chem.* **1981**, *32*, 179; F. Franks, (Ed.), *Water, a Comprehensive Treatise*, Plenum Press, New York, London, 1972–1975, Vols. 1–5.
60. M. Matsumoto, N. I. Neuman, T. W. Swaddle, *Inorg. Chem.* **2004**, *43*, 1153.
61. (a) L. Eberson, *J. Am. Chem. Soc.* **1983**, *105*, 3192; (b) P. Carloni, L. Eberson, *Acta Chem. Scand.* **1991**, *45*, 373; (c) V. A. Grigoriev, D. Cheng, C. L. Hill, et al., *J. Am. Chem. Soc.* **2001**, *123*, 5292; (d) V. A. Grigoriev, C. L. Hill, I. A. Weinstock, *J. Am. Chem. Soc.* **2000**, *122*, 3544.
62. (a) P. G. Rasmussen, C. H. Brubaker Jr., *Inorg. Chem.* **1964**, *3*, 977; (b) J. F. Kirby, C. L. W. Baker, *Inorg. Chem.* **1998**, *37*, 5537.
63. S. K. Saha, M. Ali, P. Banerjee, *Coord. Chem. Rev.* **1993**, *122*, 41; (b) L. Eberson, M. Ekström, *Acta Chem. Scand. B* **1988**, *42*, 101.
64. J. F. Keggin, *Proc. Roy. Soc.* **1934**, A144, 75.
65. C. Sanchez, J. Livage, J. P. Launay et al., *J. Am. Chem. Soc.* **1983**, *105*, 6817.
66. M. Kozik, C. F. Hammer, L. C. W. Baker, *J. Am. Chem. Soc.* **1986**, *108*, 2748.
67. M. Kozik, C. F. Hammer, L. C. W. Baker, *J. Am. Chem. Soc.* **1986**, *108*, 7627.
68. M. Kozik, L. C. W. Baker, *J. Am. Chem. Soc.* **1990**, *112*, 7604.
69. N. Casañ-Pastor, L. C. W. Baker, *J. Am. Chem. Soc.* **1992**, *114*, 10384.
70. R. A. Prados, M. T. Pope, *Inorg. Chem.* **1976**, *15*, 2547.
71. S. P. Harmalker, M. T. Pope, *J. Am. Chem. Soc.* **1981**, *103*, 7381.
72. (a) F. Ammar, J. M. Savéant, *J. Electroanal. Chem.* **1973**, *47*, 115; (b) F. Ammar, J. M. Savéant, *J. Electroanal. Chem.* **1973**, *47*, 215; (c) J. B. Flanagan, S. Margel, A. J. Bard et al., *J. Am. Chem. Soc.* **1978**, *100*, 4248;

- (d) A. J. Bard, *Pure Appl. Chem.* **1971**, *25*, 379; (e) A. J. Bard, J. Phelps, *J. Electroanal. Chem.* **1970**, *25*, A2–A5; (f) J. M. Fritsch, H. Weingarten, *J. Am. Chem. Soc.* **1968**, *90*, 793; (g) C. P. Andrieux, J. M. Savéant, *J. Electroanal. Chem.* **1970**, *28*, 339–348; (h) V. D. Parker, K. Nyberg, L. Eberson, *J. Electroanal. Chem.* **1969**, *22*, 150.
73. (a) B. Dawson, *Acta Crystallogr.* **1953**, *6*, 113; (b) H. D'Amour, *Acta Crystallogr.* **1976**, *B32*, 729.
74. R. Acerete, S. Harmalker, C. F. Hammer et al., *J. Chem. Soc., Chem. Commun.* **1979**, 777.
75. L. Kazansky, M. Fedotov, *J. Chem. Soc., Chem. Commun.* **1980**, 644.
76. A. Chemseddine, C. Sanchez, J. Livage et al., *Inorg. Chem.* **1984**, *23*, 2609.
77. J. N. Barrows, M. T. Pope, *Inorg. Chim. Acta* **1993**, *213*, 91.
78. B. Keita, Y. Jean, B. Levy et al., *New J. Chem.* **2002**, *26*, 1314–1319.
79. J. P. Ciabruni, R. Contant, J. M. Fruchart, *Polyhedron* **1983**, *2*, 1229.
80. R. Contant, R. Thouvenot, *Can. J. Chem.* **1991**, *69*, 1498.
81. S. P. Harmalker, M. A. Leparulo, M. T. Pope, *J. Am. Chem. Soc.* **1983**, *105*, 4286.
82. B. Keita, K. Essaadi, L. Nadjo et al., *Chem. Phys. Lett.* **1995**, *237*, 411.
83. M. Abbessi, R. Contant, R. Thouvenot et al., *Inorg. Chem.* **1991**, *30*, 1695.
84. (a) L. Barcza, M. T. Pope, *J. Phys. Chem.* **1973**, *77*, 1795; (b) L. Barcza, M. T. Pope, *J. Phys. Chem.* **1975**, *79*, 92.
85. C. Rong, M. T. Pope, *J. Am. Chem. Soc.* **1992**, *114*, 2932.
86. (a) B. Keita, Y. W. Lu, L. Nadjo et al., *Eur. J. Inorg. Chem.* **2000**, *2463*; (b) B. Keita, Y. W. Lu, L. Nadjo et al., *Electrochim. Commun.* **2000**, *2*, 720.
87. (a) F. Ortega, M. T. Pope, *Inorg. Chem.* **1984**, *23*, 3292; (b) F. Ortega, M. T. Pope, H. T. Evans, *Inorg. Chem.* **1997**, *36*, 2166.
88. C. M. Tourné, G. F. Tourné, A. Malik et al., *J. Inorg. Nucl. Chem.* **1970**, *32*, 3875.
89. B. Keita, A. Belhouari, L. Nadjo et al., *J. Electroanal. Chem.* **1998**, *442*, 49.
90. B. Keita, E. Abdeljalil, L. Nadjo et al., *Electrochim. Commun.* **2000**, *2*, 145.
91. R. Contant, J. P. Ciabruni, *J. Chem. Res.* **1977**, *S*, 222; *M*, 2601.
92. J. Bartis, Y. Kunina, M. Blumenstein et al., *Inorg. Chem.* **1996**, *35*, 1497.
93. C. Rocchiccioli-Deltcheff, R. Thouvenot, *Spectrosc. Lett.* **1979**, *12*, 127.
94. (a) J. E. Toth, F. C. Anson, *J. Electroanal. Chem.* **1989**, *256*, 361; (b) S. Dong, M. Liu, *J. Electroanal. Chem.* **1994**, *372*, 95.
95. R. D. Peacock, T. J. R. Weakley, *J. Chem. Soc. A* **1971**, 1937.
96. J.-M. Fruchart, G. Hervé, J. P. Launay et al., *J. Inorg. Nucl. Chem.* **1976**, *18*, 1627.
97. R. Contant, Thesis, Université Paris VI, 1972.
98. (a) M. Bösing, A. Nöh, I. Loose et al., *J. Am. Chem. Soc.* **1998**, *120*, 7252; (b) U. Kortz, N. K. Al-Kassem, M. G. Savelieff et al., *Inorg. Chem.* **2001**, *40*, 4742; (c) U. Kortz, S. Nellutla, A. C. Stowe et al., *Inorg. Chem.* **2004**, *43*, 144.
99. (a) T. J. R. Weakley, H. T. Evans, J. S. Showell et al., *J. Chem. Soc., Chem. Commun.* **1973**, 139; (b) T. J. R. Weakley, R. G. Finke, *Inorg. Chem.* **1990**, *29*, 1235; (c) N. Casañ-Pastor, J. Bas-Serra, E. Coronado, et al., *J. Am. Chem. Soc.* **1992**, *114*, 10380; (d) X. Zhang, Q. Chen, D. C. Duncan et al., *Inorg. Chem.* **1997**, *36*, 4208; (e) J. M. Clemente-Juan, E. Coronado, J. R. Galán-Mascarós, et al., *Inorg. Chem.* **1999**, *38*, 55; (f) L.-H. Bi, E.-B. Wang, J. Peng et al., *Inorg. Chem.* **2000**, *39*, 671; (g) U. Kortz, S. Nellutla, A. C. Stowe et al., *Inorg. Chem.* **2004**, *43*, 2308.
100. (a) I. Loose, E. Droste, M. Bösing et al., *Inorg. Chem.* **1999**, *38*, 2688; (b) B. Krebs, E. Droste, M. Piepenbrink et al., *C. R. Acad. Sci. Paris, Ser. IIc* **2000**, *3*, 205; (c) U. Kortz, M. G. Savelieff, B. S. Bassil et al., *Inorg. Chem.* **2002**, *41*, 783.
101. (a) W. H. Knoth, P. J. Domaille, R. D. Farlee, *Organometallics* **1985**, *4*, 62; (b) W. H. Knoth, P. J. Domaille, R. L. Harlow, *Inorg. Chem.* **1986**, *25*, 1577; (c) R. G. Finke, B. Rapko, T. J. R. Weakley, *Inorg. Chem.* **1989**, *28*, 1573; (d) F. B. Xin, M. T. Pope, *J. Am. Chem. Soc.* **1996**, *118*, 7731; (e) N. Laronze, J. Marrot, G. Hervé, *Inorg. Chem.* **2003**, *42*, 5857.
102. (a) J. M. Clemente-Juan, H. Andres, J. J. Borras-Almenar et al., *J. Am. Chem. Soc.* **1999**, *121*, 10021; (b) D. Sloboda-Rozner, P. Witte, P. L. Alsters et al., *Adv. Synth. Catal.* **2004**, *346*, 339.
103. B. Keita, I. M. Mbomekalle, L. Nadjo et al., *Electrochim. Commun.* **2001**, *3*, 267.

104. L. H. Bi, E. B. Wang, J. Peng et al., *Inorg. Chem.* **2000**, *39*, 671.
105. (a) L. H. Bi, J. Y. Liu, Y. Shen et al., *Gaodeng Xuexiao Huaxue Xuebao* **2002**, *23*, 472; (b) L. Bi, J. Liu, Y. Shen et al., *New J. Chem.* **2003**, *27*, 756.
106. U. Kortz, I. M. Mbomekalle, B. Keita et al., *Inorg. Chem.* **2002**, *41*, 6412.
107. (a) U. Kortz, M. G. Savelleff, B. S. Bassil et al., *Inorg. Chem.* **2002**, *41*, 783; (b) L.-H. Bi, U. Kortz, S. Nellutla et al., *Inorg. Chem.* **2005**, *44*, 896; (c) L. H. Bi, M. Reicke, U. Kortz et al., *Inorg. Chem.* **2004**, *43*, 3915; (d) L. H. Bi, U. Kortz, B. Keita et al., *Inorg. Chem.* **2004**, *43*, 8367.
108. I. M. Mbomekalle, B. Keita, M. Nierlich et al., *Inorg. Chem.* **2003**, *42*, 5143.
109. I. M. Mbomekalle, B. Keita, L. Nadjo et al., *Eur. J. Inorg. Chem.* **2003**, 3924.
110. I. M. Mbomekalle, B. Keita, L. Nadjo et al., *Dalton Trans.* **2003**, *13*, 2646.
111. (a) I. M. Mbomekalle, B. Keita, L. Nadjo et al., *Inorg. Chem.* **2003**, *42*, 1163; (b) B. Keita, I. M. Mbomekalle, L. Nadjo, et al., *Eur. J. Inorg. Chem.* **2002**, 473.
112. X. Zhang, G. B. Jameson, C. J. O'Connor et al., *Polyhedron* **1996**, *15*, 917.
113. D. Jabbour, B. Keita, I. M. Mbomekalle et al., *Eur. J. Inorg. Chem.* **2004**, 2036.
114. I. M. Mbomekalle, B. Keita, L. Nadjo et al., *Inorg. Chem. Commun.* **2003**, *6*, 435.
115. B. Keita, I. M. Mbomekalle, L. Nadjo, *Electrochim. Commun.* **2003**, *5*, 830.
116. B. Keita, I. M. Mbomekalle, L. Nadjo et al., *Inorg. Chem.* **2004**, *43*, 3257.
117. W. Song, X. Wang, Y. Liu et al., *J. Electroanal. Chem.* **1999**, *476*, 85.
118. L. Ruhlmann, L. Nadjo, J. Cannet et al., *Eur. J. Inorg. Chem.* **2002**, 975.
119. L. Ruhlmann, J. Cannet, J. Vaissermann et al., *J. Chem. Soc., Dalton Trans.* **2004**, 794.
120. L. Ruhlmann, J. Cannet, R. Contant et al., *Inorg. Chem.* **2002**, *41*, 3811.
121. J. A. F. Gamelas, M. S. Balula, H. M. Carapuça et al., *Electrochim. Commun.* **2003**, *5*, 378.
122. L. Cheng, H. Sun, B. Liu et al., *Electrochim. Commun.* **1999**, *1*, 155.
123. M. Sadakane, E. Steckhan, *J. Mol. Catal. A: Chem.* **1996**, *114*, 221.
124. S. M. Cohen, S. Petoud, K. N. Raymond, *Chem. – Eur. J.* **2001**, *7*, 272.
125. I. M. Mbomekalle, B. Keita, Y. W. Lu et al., *Eur. J. Inorg. Chem.* **2004**, 276.
126. I. M. Mbomekalle, B. Keita, Y. W. Lu et al., *Eur. J. Inorg. Chem.* **2004**, 4132.
127. I. M. Mbomekalle, B. Keita, L. Nadjo et al., *J. Chem. Soc., Dalton Trans.* **2004**, 4094.
128. N. Belai, M. H. Dickman, M. T. Pope et al., *Inorg. Chem.* **2005**, *44*, 169.
129. B. Keita, A. Belhouari, L. Nadjo, *J. Electroanal. Chem.* **1993**, *355*, 235.
130. A. Mahmoud, B. Keita, L. Nadjo et al., *J. Electroanal. Chem.* **1999**, *463*, 129.
131. J. B. Moffat, *J. Mol. Catal.* **1984**, *26*, 385.
132. D. Masure, P. Chaquin, C. Louis et al., *J. Catal.* **1989**, *119*, 415.
133. M. K. Awad, A. B. Anderson, *J. Am. Chem. Soc.* **1990**, *112*, 1603.
134. R. S. Weber, *J. Phys. Chem.* **1994**, *98*, 2999.
135. H. Taketa, S. Katsuki, K. Eguchi et al., *J. Phys. Chem.* **1986**, *90*, 2959.
136. K. Eguchi, T. Seiyama, N. Yamazoe et al., *J. Catal.* **1988**, *111*, 336.
137. J. Y. Kempf, M.-M. Rohmer, J.-M. Poblet et al., *J. Am. Chem. Soc.* **1992**, *114*, 1136.
138. M. Bénard, M.-M. Rohmer, *J. Am. Chem. Soc.* **1994**, *116*, 6959.
139. M.-M. Rohmer, J. Devémy, R. Wiest et al., *J. Am. Chem. Soc.* **1996**, *118*, 13007.
140. J. M. Maestre, J. M. Poblet, C. Bo et al., *Inorg. Chem.* **1998**, *37*, 3444.
141. H. Duclusaud, S. A. Borshch, *Chem. Phys. Lett.* **1998**, *290*, 526.
142. J. M. Maestre, J. P. Sarasua, C. Bo et al., *Inorg. Chem.* **1998**, *37*, 3071.
143. B. B. Bardin, S. V. Bordawekar, M. Neurock et al., *J. Phys. Chem.* **1998**, *102*, 10817.
144. M.-M. Rohmer, M. Bénard, J.-P. Blaudeau et al., *Coord. Chem. Rev.* **1998**, *178–180*, 1019.
145. H. Duclusaud, S. A. Borshch, *Inorg. Chem.* **1999**, *38*, 3489.
146. H. Duclusaud, S. A. Borshch, *J. Am. Chem. Soc.* **2001**, *123*, 2825.
147. X. Lopez, J. M. Maestre, C. Bo et al., *J. Am. Chem. Soc.* **2001**, *123*, 9571.
148. J. M. Maestre, X. Lopez, C. Bo et al., *J. Am. Chem. Soc.* **2001**, *123*, 3749.
149. X. López, C. Bo, J. M. Poblet, *J. Am. Chem. Soc.* **2002**, *124*, 12574.
150. X. López, J. M. Poblet, *Inorg. Chem.* **2004**, *43*, 6863.
151. T. A. Albright, J. K. Burdett, M. H. Whangbo, *Orbital Interactions in Chemistry*, John Wiley & Sons, New York, 1985, pp. 82–86.

152. W. Kutner, J. Wang, M. L'Her et al., *Pure Appl. Chem.* **1998**, *70*, 1301.
153. (a) S. Dong, X. Xi, M. Tian, *J. Electroanal. Chem.* **1995**, *385*, 227; (b) K. Unoura, A. Iwashita, E. Itabashi et al., *Bull. Chem. Soc. Jpn.* **1984**, *57*, 597; (c) X. Xi, S. Dong, *J. Mol. Catal. A: Chem.* **1996**, *114*, 257; (d) J. E. Toth, F. C. Anson, *J. Am. Chem. Soc.* **1989**, *111*, 2444–2451; (e) X. Xi, G. Wang, S. Dong, *Electrochim. Acta* **1995**, *40*, 1025; (f) L. Cheng, X. Zhang, X. Xi et al., *J. Electroanal. Chem.* **1996**, *407*, 97; (g) M. Sadakane, E. Steckhan, *J. Mol. Catal. A: Chem.* **1996**, *114*, 221; (h) E. Steckhan, G. Hilt, E. Kempf et al., *Organic Synthesis via Organometallics* (Ed.: G. Helmchem), OSM5, Heidelberg, 1997.
154. B. Keita, L. Nadjo, J. P. Haeussler, *J. Electroanal. Chem.* **1988**, *243*, 481.
155. B. Keita, A. Belhouari, L. Nadjo et al., *J. Electroanal. Chem.* **1995**, *381*, 243.
156. J. E. Toth, J. D. Melton, D. Cabelli et al., *Inorg. Chem.* **1990**, *29*, 1952.
157. B. Keita, L. Nadjo, R. Contant et al., Process for the selective catalytic reduction of nitrogen compounds and catalysts used. (CNRS) French Patent 89/1,728, 1989.
158. B. Keita, L. Nadjo, R. Contant et al., Process for the selective catalytic reduction of nitrogen compounds and catalysts used. (CNRS) Europe Patent Applied EP 382,644, 1990; *Chem. Abst.* **1991**, *114*, 191882u.
159. B. Keita, F. Girard, L. Nadjo et al., *J. Electroanal. Chem.* **2001**, *508*, 70.
160. (a) B. Keita, E. Abdeljalil, L. Nadjo et al., *Electrochim. Commun.* **2001**, *3*, 56; (b) I. R. Epstein, K. Kustin, L. J. Warshaw, *J. Am. Chem. Soc.* **1980**, *102*, 3751.
161. B. Keita, M. Benaissa, L. Nadjo et al., *Electrochim. Commun.* **2002**, *4*, 663.
162. I. M. Mbomekalle, R. Cao, K. I. Hardcastle et al., *C. R. Acad. Sci. Paris* **2005**, Special Issue, *8*, 1077.
163. R. Greef, R. Peat, L. M. Peter et al., *Instrumental Methods in Electrochemistry*, Ellis Horwood, Chichester, England, 1985, Chapter 6.
164. A. Hiskia, E. Papaconstantinou, *Inorg. Chem.* **1992**, *31*, 163.
165. D. C. Duncan, C. L. Hill, *J. Am. Chem. Soc.* **1997**, *119*, 243.
166. J. Zhang, F. C. Anson, *J. Electroanal. Chem.* **1992**, *341*, 323.
167. N. Alonso-Vante, H. Tributsch, O. Solorza-Feria, *Electrochim. Acta* **1995**, *40*, 567.
168. A. I. Vogel, *Quantitative Inorganic Analysis*, Longmans, London, 1960.
169. K. Inoura, A. Iwashita, E. Itabashi et al., *Bull. Chem. Soc. Jpn.* **1984**, *57*, 597.
170. R. Neuman, C. Abu-Gnim, *J. Chem. Soc., Chem. Commun.* **1989**, 1324.
171. D. E. Katsoulis, M. T. Pope, *J. Chem. Soc., Chem. Commun.* **1986**, 1186.
172. K. Essaadi, B. Keita, L. Nadjo et al., *J. Electroanal. Chem.* **1994**, *367*, 275.
173. B. Keita, K. Essaadi, L. Nadjo et al., *J. Electroanal. Chem.* **1996**, *404*, 271.
174. B. Keita, K. Essaadi, A. Belhouari et al., *C. R. Acad. Sci. Paris, Sér. IIc* **1998**, 343.
175. J. C. Bart, F. C. Anson, *J. Electroanal. Chem.* **1995**, *390*, 11.
176. R. Neuman, C. Abu-Gnim, *J. Am. Chem. Soc.* **1990**, *112*, 6025.
177. E. Steckhan, C. Kandzia, *Synlett* **1992**, 139.
178. A. M. Khenkin, C. L. Hill, *J. Am. Chem. Soc.* **1993**, *115*, 8178.
179. C. Rong, F. C. Anson, *Inorg. Chem.* **1994**, *33*, 1064.
180. K. Drauz, H. Waldmann, *Enzyme Catalysis on Organic Synthesis-A Comprehensive Handbooks*, VCH, Weinheim, 1995, Vol. 2.
181. E. Steckhan, *Top. Curr. Chem.* **1994**, *170*, 83.
182. (a) H. Jaegfeldt, *J. Electroanal. Chem.* **1980**, *110*, 295; (b) W. G. Kuhr, V. L. Barrett, M. R. Gagnon et al., *Anal. Chem.* **1993**, *65*, 617.
183. (a) J. H. Christie, *J. Electroanal. Chem.* **1967**, *13*, 79; (b) J. H. Christie, R. A. Osteryoung, F. C. Anson, *J. Electroanal. Chem.* **1967**, *13*, 236; (c) F. C. Anson, J. H. Christie, R. A. Osteryoung, *J. Electroanal. Chem.* **1967**, *13*, 343; (d) P. J. Lingane, J. H. Christie, *J. Electroanal. Chem.* **1967**, *13*, 227.
184. (a) R. A. Marcus, *J. Phys. Chem.* **1968**, *72*, 891; (b) C. P. Andrieux, C. Blocman, J. M. Dumas-Bouchiat et al., *J. Am. Chem. Soc.* **1979**, *101*, 3431.
185. B. Keita, I.-M. Mbomekalle, L. Nadjo et al., *C. R. Acad. Sci. Paris* **2005**, Special Issue, *8*, 1057.
186. L. Gorton, E. Dominguez, *Rev. Mol. Biotechnol.* **2002**, *82*, 371.
187. R. Contant, S. Piro-Sellem, J. Canny et al., *C. R. Acad. Sci. Ser. IIc Chim.* **2000**, *3*, 157.

23

Electrochemistry of Polycyanometalates

Fritz Scholz and Heike Kahlert
University of Greifswald, Greifswald, Germany

23.1	Introduction	703
23.2	The Structure of Polycyanometalates	703
23.3	The Electrochemistry of Polycyanometalates	708
23.3.1	General Features	708
23.3.2	Correlations between the Structures of PCMs and the Thermodynamics of their Electrochemical Reactions	710
23.3.3	Special Features	712
23.3.3.1	Metal Hexacyanoferrates	712
23.3.3.2	Hexacyanocobaltates, Hexacyanomanganates, Hexacyanochromates, Hexacyanoruthenates	715
23.3.3.3	Octacyanomolybdates, Octacyanotungstates	716
23.3.3.4	Pentacyanonitrosyl Metalates	716
23.4	Preparation of Electrodes Modified by Polycyanometalates and their Applications	716
23.4.1	Preparation of Polycyanometalate Modified Electrodes	716
23.4.2	Applications of PCM Modified Electrodes	717
	References	718

23.1 Introduction

The cyanide ion is one of the strongest ligands. It is isoelectronic with carbon monoxide and in the spectrochemical series, it is comparable with carbon monoxide. Cyanide ions act as monodentate ligands for almost all d-block elements and several f-block elements. In these complexes, it is carbon that bonds to the metal ions. The metal–cyano group M–C≡N is linear or almost so in stable cyano complexes. Cyanide is also a bidentate ligand that is capable of forming a large number of sparingly soluble polymer metal polycyanometalates (PCMs). Mostly they are hexacyanometalates, as, for example, hexacyanoferrates; however, there are also octacyanometalates, for example, octacyanotungstates, octacyanomolybdates, and there are a few tetracyanometalates, for example, tetracyanoplatinates. Copper(I) cyanide is in fact a copper(II) dicyanocuprate(I), and in the polymeric silver(I) cyanide, the cyanide ligand is also bidentate.

The electrochemistry of dissolved cyanide complexes of metal ions is very well documented [1] and there is no need to discuss these compounds here. However, the electrochemistry of

the polymeric metal PCMs has seen tremendous development in the last few decades. This chapter is aimed at giving a conscious overview on the state of the art in this field of research.

23.2 The Structure of Polycyanometalates

1. Hexacyanometalates: Polymeric hexacyanometalates are by far the most important and best-studied group of metal PCMs. Prussian blue is the archetype of these compounds. The general formula of the family members of Prussian blue type compounds is $\text{Me}^{(i)}\{\text{Me}^{(N)}[\text{Me}^{(C)}(\text{CN})_6]\}$ with (i), (N) and (C) indicating the position in the crystal lattice, where (i) means interstitial sites, (N) means metal ions coordinated by the nitrogen of the cyanides, and (C) means metal ions coordinated by the carbon of the cyanides. The braces {} include all ions that form the rigid framework of the PCMs, and the square brackets [] include the complex metal cyanide anions. From Mössbauer spectroscopy, it is known that Prussian blue and Turnbull's blue are both iron(III) hexacyanoferrate(II) with high-spin Fe(III) and low-spin Fe(II). Very early, Keggin [2] proposed a simple cubic structure for Prussian blue with $-\text{Fe}^{\text{II}}-\text{C}-\text{N}-\text{Fe}^{\text{III}}-\text{N}-\text{C}-\text{Fe}^{\text{II}}$

chains along all three crystallographic directions. In many cases, for charge compensation, additional cations must be located at interstitial positions. The idealized structure is given in Fig. 1.

The most important compounds for electrochemistry possess the d-block elements Fe, Co, Cr, Ru, and V on position $M^{(C)}$ (carbon-bonded metal ions). Position $M^{(N)}$ can be occupied by almost all d-block elements and several f-block elements. Position $M^{(i)}$ can be occupied either by alkali metal ions or by other metal ions. Metal hexacyanometalates exhibit a great variety of compositions and the real structures depend very much on the method of preparation. Most of the compounds belonging to the Prussian blue family, like metal hexacyanocobaltates and hexacyanochromates, with alkali cations on the interstitial positions, crystallize with a high symmetry and belong to the space group $Fm\bar{3}m$. Some metal hexacyanometalates, for example, hexacyanoferrates with zinc ions, silver ions, and f-block elements in position $M^{(N)}$ crystallize with hexagonal symmetry. Typical examples are given in Table 1.

Metal hexacyanoruthenates possess a lower symmetry. Several compounds have highly disordered structures, especially when no alkali cations are present for charge compensation. Such a complex defect structure has been found for a completely potassium free Prussian blue precipitated very slowly from a solution in concentrated hydrochloric acid [25, 26]. Here, the structure still remains cubic face-centered; however, one-third of the $[M^{(C)}(CN)_6]$ is vacant, randomly distributed and that space is filled with water molecules. The coordination sphere of the remaining $M^{(C)}$ ions is maintained unchanged; however, the mean coordination sphere of the $M^{(N)}$ ions is decreased ($M^{(N)}(NC)_{4.5}(H_2O)_{1.5}$). No iron ions occupy interstitial positions, that is, only two types of iron environments exist. Since that special kind of Prussian blue has been the first and hitherto only Prussian blue that could be obtained as sufficiently large crystals to perform a single crystal structure analysis, practically all textbooks, and later publications present that defect structure as the “real structure” of Prussian blue, completely forgetting that this defect structure is an extreme that forms

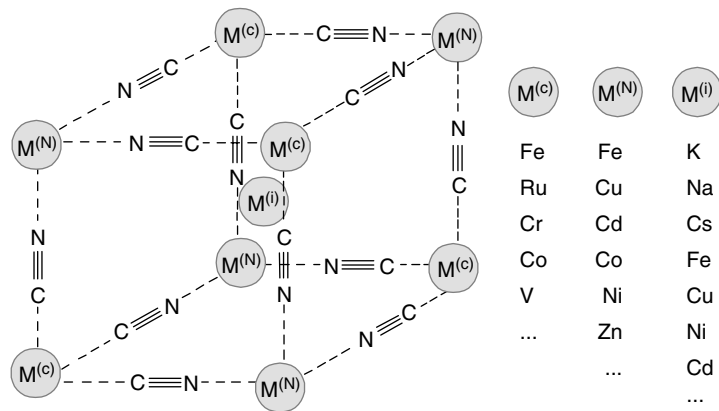


Fig. 1 Idealized structure of metal hexacyanometalates $Me^{(i)}\{Me^{(N)}[Me^{(C)}(CN)_6]\}$.

Tab. 1 Space groups of some metal hexacyanometalates. The chemical formulae indicate the coordination of the metal ions by using the notation $\text{Me}^{(i)}\{\text{Me}^{(N)}[\text{Me}^{(C)}(\text{CN})_6]\}$ (cf. Fig. 1)

Compound	Space group	Reference
$\text{Zn}\{\text{Zn}_2[\text{Co}(\text{CN})_6]_2\}\cdot 12\text{H}_2\text{O}$	$F\bar{4}3m$ (216)	3
$\text{K}\{\text{Cu}[\text{Co}(\text{CN})_6]\}$	$Fm\bar{3}m$ (225)	4, 5
$\text{K}\{\text{Ni}[\text{Co}(\text{CN})_6]\}$	$Fm\bar{3}m$ (225)	4
$\text{K}\{\text{Co}[\text{Co}(\text{CN})_6]\}$	$Fm\bar{3}m$ (225)	4
$\text{K}\{\text{Co}[\text{Fe}(\text{CN})_6]\}$	$Fm\bar{3}m$ (225)	4
$\text{K}\{\text{La}[\text{Fe}(\text{CN})_6]\}\cdot 4\text{H}_2\text{O}$	$P6_3/m$ (176)	6
$\{\text{La}[\text{Fe}(\text{CN})_6]\}\cdot 5\text{H}_2\text{O}$	$P6_3/m$ (176)	7
$\text{Na}_{0.26}\text{Ni}_{0.8}\{\text{Ni}[\text{Fe}(\text{CN})_6]\}$	$Fm\bar{3}m$ (225)	8
$\{\text{Zn}_3[\text{Fe}(\text{CN})_6]_2\}\cdot n\text{H}_2\text{O}$	$Fm\bar{3}m$ (225)	9
$\{\text{Sm}[\text{Fe}(\text{CN})_6]\}\cdot 4\text{H}_2\text{O}$	$Cmcm$ (63)	10
$\text{Fe}\{\text{Fe}_2[\text{Rh}(\text{CN})_6]_2\}\cdot 12\text{H}_2\text{O}$	$F\bar{4}3m$ (216)	11
$\{\text{Pb}_2[\text{Fe}(\text{CN})_6]\}$	$P\bar{3}$ (147)	12
$\text{K}\{\text{Ln}[\text{Fe}(\text{CN})_6]\}\cdot n\text{H}_2\text{O}$ ($\text{Ln} = \text{La-Lu}$)	$Cmcm$ (63)	13
$\text{Na}_2\{\text{Cu}[\text{Fe}(\text{CN})_6]\}\cdot 10\text{H}_2\text{O}$	$P2_1/m$ (10)	14
$\{\text{Cd}_2[\text{Fe}(\text{CN})_6]\}\cdot 8\text{H}_2\text{O}$	$P2_1/c$ (14)	15
$\text{Cd}\{\text{Cd}_2[\text{Fe}(\text{CN})_6]\}$	$Fm\bar{3}m$ (225)	16
$\{\text{Mn}_2[\text{Ru}(\text{CN})_6]\}\cdot 8\text{H}_2\text{O}$	$P2_1/c$ (14)	17
$\text{K}\{\text{La}[\text{Ru}(\text{CN})_6]\}\cdot 4\text{H}_2\text{O}$	$P6_3/m$ (176)	18
$\{\text{Cd}_2[\text{Ru}(\text{CN})_6]\}\cdot 8\text{H}_2\text{O}$	$P2_1/c$ (14)	15
$\{\text{Cd}_2[\text{Os}(\text{CN})_6]\}\cdot 8\text{H}_2\text{O}$	$P2_1/c$ (14)	15
$\{\text{Mn}_2[\text{Os}(\text{CN})_6]\}\cdot 8\text{H}_2\text{O}$	$P2_1/c$ (14)	19
$\{\text{Mn}_3[\text{Co}(\text{CN})_6]_2\}\cdot 12\text{H}_2\text{O}$	$Fm\bar{3}m$ (225)	20, 21
$\{\text{Cd}_3[\text{Co}(\text{CN})_6]_2\}\cdot 12\text{H}_2\text{O}$	$Fm\bar{3}m$ (225)	21
$\{\text{Co}_3[\text{Co}(\text{CN})_6]_2\}\cdot 12\text{H}_2\text{O}$	$Fm\bar{3}m$ (225)	22
$\{\text{Ag}_3[\text{Co}(\text{CN})_6]\}$	$P\bar{3}1m$ (162)	23
$\{\text{Sm}[\text{Co}(\text{CN})_6]\}\cdot 4\text{H}_2\text{O}$	$Cmcm$ (63)	24

as a result of the complete absence of cations that could stabilize the Keggin structure. Recent attempts to prepare a potassium ion stabilized Prussian blue of a crystallinity that allows a Rietveld refinement, unambiguously show that the Keggin structure is the structure that Prussian blue assumes under the usual precipitation conditions, that is, when stabilizing potassium ions are available, just as Keggin and Miles stated long ago [27].

The most important feature of all polymeric metal hexacyanometalates is that they possess channels and holes, the size of which is mostly determined by the

large cyanide ions. The large cyanide ions also determine the unit cell dimension (ranging from 0.1 to 0.109 pm).

Since many metal hexacyanometalates have very similar structures, the formation of solid solutions is possible. The positions $\text{M}^{(C)}$, $\text{M}^{(N)}$, and $\text{M}^{(i)}$ can be occupied not only by one kind of ion, but by a variety of similar ions, allowing the existence of substitutional solid solutions with a random distribution of the different ions on their specific positions. Table 2 gives an overview of the types of solid solutions that can be formed and some examples.

Very complex mixed crystals with mixed occupation of all metal positions by

Tab. 2 Types of solid solutions of metal hexacyanometalates

Type and stability	General formula	Examples	References
Type I Very stable	$\text{Me}^{(i)}\{\text{Me}^{(N)}[\text{Me}_x^{(C)'} \text{Me}_{1-x}^{(C)''} (\text{CN})_6]\}$	$\text{K}[\text{Cu}[\text{Fe}_{x\text{Co}_{1-x}}(\text{CN})_6]]$	28
Type Ia	$\text{Me}^{(i)}\{\text{Me}^{(N)}[\text{Me}_x^{(C)'} \text{Me}_{1-x}^{(C)''} (\text{CN})_6]\}$ with $\text{Me}^{(C)'} = \text{Me}^{(C)''}$; however, in different oxidation states		
Type II Relatively stable	$\text{Me}^{(i)}\{\text{Me}_x^{(N)'} \text{Me}_{1-x}^{(N)''} [\text{Me}^{(C)} (\text{CN})_6]\}$	$\text{K}[\text{Ni}_x\text{Co}_{1-x}[\text{Fe}(\text{CN})_6]]$ $\text{K}[\text{Ni}_x\text{Fe}_{1-x}[\text{Fe}(\text{CN})_6]]$ $\text{K}[\text{Cu}_x\text{Co}_{1-x}[\text{Fe}(\text{CN})_6]]$ $\text{K}[\text{Ni}_x\text{Pd}_{1-x}[\text{Fe}(\text{CN})_6]]$	29 30 31 32
Type IIa	$\text{Me}^{(i)}\{\text{Me}_x^{(N)'} \text{Me}_{1-x}^{(N)''} [\text{Me}^{(C)} (\text{CN})_6]\}$ with $\text{Me}^{(N)'} = \text{Me}^{(N)''}$; however, in different oxidation states		
Type III Not stable	$\text{Me}_x^{(i)'} \text{Me}_{1-x}^{(i)''} \{\text{Me}^{(N)}[\text{Me}^{(C)} (\text{CN})_6]\}$		
Type IV Combination of types I (or Ia) and II (or IIa) Relatively stable	$\text{Me}^{(i)}\{\text{Me}_x^{(N)'} \text{Me}_{1-x}^{(N)''}$ $[\text{Me}_y^{(C)} \text{Me}_{1-y}^{(C)} (\text{CN})_6]\}$	$\text{K}[\text{Cu}_{0.5}\text{Ni}_{0.5}$ $[\text{Fe}_{x\text{Co}_{1-x}}(\text{CN})_6]]$	28
Type V Combination of types II and III Not stable with respect to III	$\text{Me}_x^{(i)'} \text{Me}_{1-x}^{(i)''} \{\text{Me}_y^{(N)'} \text{Me}_{1-y}^{(N)''}$ $[\text{Me}^{(C)} (\text{CN})_6]\}$		
Type VI Combination of types I and III Not stable with respect to III	$\text{Me}_x^{(i)'} \text{Me}_{1-x}^{(i)''} \{\text{Me}_y^{(N)'} [\text{Me}_y^{(C)'} \text{Me}_{1-y}^{(C)''} (\text{CN})_6]\}$		
Type VII Combination of all types Not stable with respect to III	$\text{Me}_x^{(i)'} \text{Me}_{1-x}^{(i)''} \{\text{Me}_y^{(N)'} \text{Me}_{1-y}^{(N)''}$ $[\text{Me}_z^{(C)'} \text{Me}_{1-z}^{(C)''} (\text{CN})_6]\}$		

Fe(II), Fe(III), Cd(II), and K⁺ have been described [33].

Generally, only the interstitial metal ions M⁽ⁱ⁾ can diffuse through the solid polymer compounds. So far, the other metal ions have not been shown to diffuse, although very slow processes of diffusion, especially

in the structures with a high concentration of vacancies, cannot be excluded.

Mixed crystals of type I are very stable and can be used for electrochemical investigations. Recently, it has been shown that such solid solutions maintain the regular cubic structure and only a single

phase exists rather than a mixture of the phases $\text{Me}^{(\text{i})}\{\text{Me}^{(\text{N})}[\text{Me}^{(\text{C}')}\text{(CN)}_6]\}$ and $\text{Me}^{(\text{i})}\{\text{Me}^{(\text{N})}[\text{Me}^{(\text{C}'')}\text{(CN)}_6]\}$ [28]. The lattice parameters obey the Vegard rule, that is, the lattice constants vary linearly with the composition of the solid solution (cf. Fig. 2).

An interesting fact is that in the case of $\text{K}\{\text{Cu}[\text{Fe}_{1-x}\text{Co}_x(\text{CN})_6]\}$, the potassium ions occupy statistically one-half of the eight cubes of one unit cell, but with a high value of the isotropic temperature factor indicating a smudgy position of the potassium ions. In the compound $\text{K}\{\text{Ni}[\text{Fe}_{1-x}\text{Co}_x(\text{CN})_6]\}$, an eccentric position of potassium ions was found. Such an eccentric position of the counterocation was also described by Bocarsly et al. for sodium-containing nickel hexacyanoferrate(II) [34].

The situation is more complex in the case of $\text{Me}^{(\text{C}')}= \text{Fe}^{\text{II}}$ and $\text{Me}^{(\text{C}'')}= \text{Cr}^{\text{III}}$. Obviously, the incorporation of the hexacyanoferrate ions is preferred. The content of hexacyanochromate in the precipitated solid compound is less than in the solution used for precipitation [35].

Mixed crystals of type II have been used in the form of thin films on electrodes as well as in the form of chemically synthesized powders immobilized on electrodes. Depending on the radii of the ions involved in the synthesis, solid solutions can also be formed as single phases. In the case of $\text{K}\{\text{CuCo}[\text{Fe}(\text{CN})_6]\}$ films, XRD results indicated that a single phase with a cubic face-centered symmetry was formed [31]. The situation is more complex in the case of $\text{K}\{\text{NiPd}[\text{Fe}(\text{CN})_6]\}$ deposited as a thin film on electrodes [32]. Kulesza et al. have pointed out that there is a critical concentration of Pd^{2+} below which Pd^{2+} was taken as the countercation at interstitial position, while above that value a solid solution is formed in which both Ni^{2+} and Pd^{2+} are nitrogen coordinated.

Mixed crystals of type III, V, VI, and VII are not stable, because the interstitial counterions can be easily exchanged.

Mixed crystals of type IV are very stable. One example of such mixed crystal series is $\text{K}\{\text{Ni}_{0.5}\text{Cu}_{0.5}[\text{Fe}_{1-x}\text{Co}_x(\text{CN})_6]\}$ [28]. Also, in that case only a single phase with a cubic phase centered

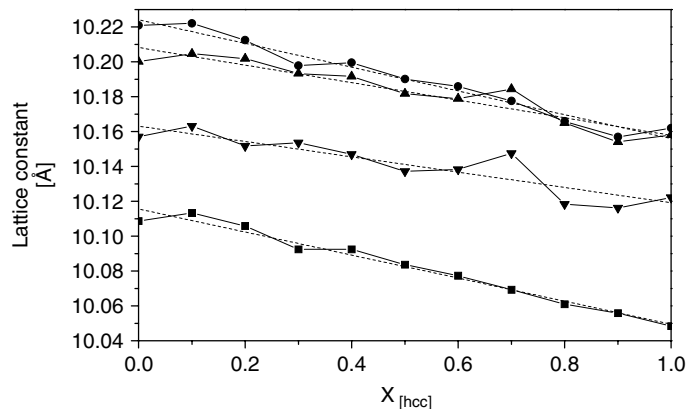


Fig. 2 Lattice constants of (●) $\text{K}\{\text{Ni}[\text{Fe}_{1-x}\text{Co}_x(\text{CN})_6]\}$, (▲) $\{\text{Fe}[\text{Fe}_{1-x}\text{Co}_x(\text{CN})_6]\}$, (■) $\text{K}\{\text{Cu}[\text{Fe}_{1-x}\text{Co}_x(\text{CN})_6]\}$, and (▼) $\text{K}\{\text{Ni}_{0.5}\text{Cu}_{0.5}[\text{Fe}_{1-x}\text{Co}_x(\text{CN})_6]\}$ dependent on the molar ratio of cobalt. The dashed lines result from a linear fitting.

symmetry could be indexed. The lattice constants obey the Vegard rule (cf. Fig. 2). Recently [36], the structure of $K_{0.4}\{Cu_{0.65}Zn_{0.65}[Fe_{0.45}Co_{0.55}(CN)_6]\}$ has been described. Whereas the structure of $K\{Cu[Co(CN)_6]\}$ is cubic face-centered and that of $K\{Zn[Fe(CN)_6]\}$ is hexagonal, the X-ray powder analysis indicates that the structure of the solid solution is of cubic face-centered symmetry.

2. Tetracyanometalates: Solid metal tetracyanometalates with nickel(II), platinum(II), and palladium(II) ions as carbon coordinated metals are known. In such compounds, Ni, Pt, or Pd are bridged with other metal ions (e.g., Er, Tl, Nd, Eu, Co) through the cyano groups. This arrangement defines a square planar coordination environment for Ni, Pt, or Pd. The compounds contain a large amount of crystal water. Examples are: $Co(H_2O)[Ni(CN)_4]$ [37], $Cr_2[Ni(CN)_4]_3 \cdot 10H_2O$ [38], $Cd(H_2O)_2[Ni(CN)_4] \cdot 4H_2O$ [39], $Er_2[Pt(CN)_4]_3 \cdot 21H_2O$ [40], $Tl_2[Pt(CN)_4]$ [41], $Nd_2[Pd(CN)_4]_3 \cdot 12H_2O$ [42], $Eu_2[Pd(CN)_4]_3 \cdot H_2O$ [43].

3. Dicyanometalates: Dicyanometalates of silver and gold are known. Abrahams et al. [44] have described a cobalt dicyanoaurate. In these compounds, gold ions are carbon coordinated and form linear structures. Cobalt ions are coordinated by four nitrogen atoms of the cyanide group. The unit cell has a hexagonal symmetry.

23.3

The Electrochemistry of Polycyanometalates

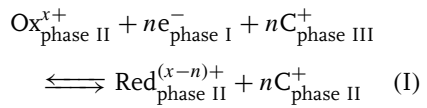
23.3.1

General Features

1. The insertion electrochemistry of PCMs:

Most of the PCMs possess two characteristic properties, they have redox-active metal centers and they have an open

structure that allows small cations to enter the solid crystals and to diffuse inside the materials. Therefore, they are prone to undergo insertion electrochemical reactions [45]. Insertion electrochemistry means that two coupled electrochemical processes proceed across two different interfaces: (1) an electron transfer across the interface of the metal PCM with the electron conductor (metal, carbon, or, rarely, a semiconductor), and (2) an ion transfer across the interface of the PCM with an electrolyte solution. These two reactions are of truly electrochemical nature because they involve the transfer of charged particles across interfaces. Although, from time to time, reports appeared in the literature that anions could enter solid PCMs, no proof of this has ever been given. Since particles that enter the channels and holes of PCMs will see practically only the cyanide anions, it is hard to believe that anions can be forced to enter these locations. Analytical data that have indicated the presence of anions like chloride, and so on are most probably the results of contaminations since the compounds usually have a very low crystallinity and very large inner surface areas ready for absorption of various ions. In numerous studies, it has been proven that small cations are able to be housed in the PCMs, and thus another argument against the anion transfer is that in chemistry there is never a case in which anions and cations are interchangeable on the same places in a given structure. The two electrochemical reactions of PCMs can be written in one equation:



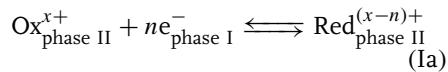
$Ox_{\text{phase II}}^{x+}$ and $Red_{\text{phase II}}^{(x-n)+}$ denote the oxidized and reduced metal ions in the

PCM and C^+ are the cations exchanged between the PCM and the electrolyte solution. In Eq. (I), three different phases are indicated, phase I being the metal that conducts the electrons to or away from the PCM, phase II being the solid PCM, and phase III being the electrolyte solution. The three phases constitute the essential feature of a so-called three-phase electrode as it is schematically depicted in Fig. 3.

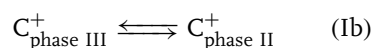
The Nernst equation corresponding to that overall chemical equation is:

$$E = E_{\text{Ox}/\text{Red/C}}^\theta + \frac{RT}{nF} \ln \frac{a_{\text{Ox}^{x+}_{\text{phase II}}} a_{C^+_{\text{phase III}}}^n}{a_{\text{Red}^{(x-n)+}_{\text{phase II}}} a_{C^+_{\text{phase II}}}^n} \quad (1)$$

This equation can be divided into two equilibria, one involving the transfer of electrons



and one involving the transfer of ions



with the following Nernst equations

$$E_{\text{I/II}} = E_{\text{Ox/Red}}^\theta + \frac{RT}{nF} \ln \frac{a_{\text{Ox}^{x+}_{\text{phase II}}}}{a_{\text{Red}^{(x-n)+}_{\text{phase II}}}} \quad (2)$$

$$E_{\text{II/III}} = E_C^\theta + \frac{RT}{F} \ln \frac{a_{C^+_{\text{phase III}}}}{a_{C^+_{\text{phase II}}}} \quad (3)$$

The standard potentials for the electron-and ion-transfer reactions are interrelated by the following equation:

$$E_{\text{Ox/Red/C}}^\theta = E_{\text{Ox/Red}}^\theta + E_C^\theta \quad (4)$$

An important prerequisite for reaction (I) to proceed is that both the electrons and the ions have the chance to be conducted within the PCM. For ions, it is sufficient that a system of channels exists in the solid material and that these channels need to have a sufficiently wide diameter for ions to diffuse through. For the electrons, there are two pathways that depend on the electronic structure of the PCM. Provided the PCM is a semiconductor and the conduction band is accessible at room temperature, this conduction band can support the electron conduction. When the redox centers, that is, the metal ions interact less strongly so that the band structure of a

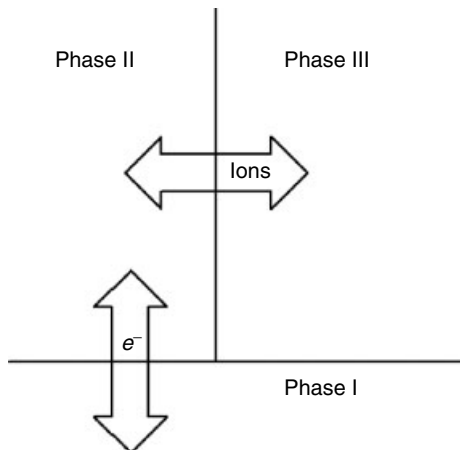


Fig. 3 Situation at a three-phase electrode where a phase II possessing redox center is in close contact with phase I that can provide or take away electrons, and with phase III that can exchange ions with phase II.

semiconductor is not built up, an electron exchange is still possible by a hopping mechanism. It seems that both pathways can be observed in PCMs, sometimes even both for one and the same PCM, but in different oxidation states. Of course, the oxidation state of the metal cations decides about the electronic structure, and hence the electronic properties of PCMs can be varied just by that parameter. Unfortunately, no conclusive and exhaustive studies of this conduction mechanism for PCMs in different oxidation states have been performed so far. An electrochemical impedance study of the reactions of copper (II) hexacyanoferrate has shown that the dependence of the charge transfer and the Warburg coefficients have a pronounced minimum at the formal potential of the redox system [46]. This indicates that the bimolecular electron hopping mechanism is operative. It was concluded in that study that the electron transport from the electrode to the reaction front inside the PCM goes via the conduction band of the semiconducting PCM, whereas the electron transport in the reaction zone proceeds via hopping.

For the case in which phase II in Fig. 3 is a solid, it is not yet clear how the activities of the species Ox, Red, and C⁺ in the solid have to be defined on a strict thermodynamic basis, and how they could be determined. No experiments are known that would lead to a separation of the free energies of the equilibria Ia and Ib in the case of solids. When phase II is a solution phase, the activities of Ox, Red, and C⁺ are in principle accessible; however, in that case also, it remains the problem that an extrathermodynamic assumption is necessary for quantifying the free energy of ion transfer between the liquid phases II and III.

2. Complex mechanisms of electrochemical reactions of PCMs: Frequently it can

be observed that the “simple” insertion electrochemical reactions of PCMs are associated with complex chemical reorganizations, as, for example, bond isomerization or metal ion substitution reactions. An early example of an isomerization reaction prompted by an electrochemical reaction was the transformation of iron(II) hexacyanochromate(III) to chromium(III) hexacyanoferate(II) [47]. This reaction proceeds because a reduction of chromium(III) ions to chromium(II) leads to the well-known labilization of ligands that allows the cyanide ions to turn into the thermodynamically more favorable position with the carbon coordinated toward the iron ions and the nitrogen toward the chromium ions. A similar example was observed when iron hexacyanomanganates are subjected to electrochemical redox reactions. The electrochemical behavior is very similar to the chemical isomerizations [48].

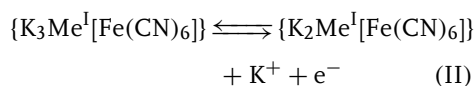
Examples of electrochemically initiated metal ion substitution reactions have been described for the case of substitution of high-spin iron by cadmium ions [49, 50], high-spin iron by nickel, and silver by nickel [51] and high-spin iron ions [52]. The reasons for the proceeding of these electrochemically initiated substitution reactions have been ascribed as well to the labilization of the cyanide ions in certain oxidation states of the metal ions of the involved PCMs.

23.3.2

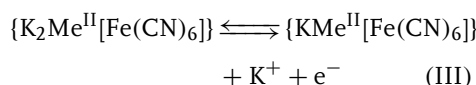
Correlations between the Structures of PCMs and the Thermodynamics of their Electrochemical Reactions

The electrochemical properties of PCMs can be tuned in certain limits by variation of the metal ions constituting the framework of these compounds. Only for the

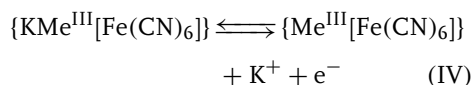
hexacyanometalates, and especially for the hexacyanoferrates, both theoretical and experimental studies have been performed so far to rationalize the dependencies between the thermodynamic electrochemical data and the structures of the compounds. Figure 4 shows a plot of the formal potentials of the following reactions versus the ion potentials of the metal ions Me^+ , Me^{2+} , and Me^{3+} [53]:



($\text{Me}^{\text{I}} = \text{Ag}$)



($\text{Me}^{\text{II}} = \text{Cd}, \text{Zn}, \text{Pb}, \text{Mn}, \text{Ni}, \text{Co}$)



($\text{Me}^{\text{III}} = \text{Ga}, \text{In}, \text{Al}, \text{Fe}, \text{Cr}, \text{Co}$).

These reactions are solid-state insertion electrochemical processes with coupled electron and ion transfers. Figure 4 includes the standard potential of hexacyanoferrate in aqueous solution. It is rather surprising that the data for the solid-state insertion electrochemistry and

that of the dissolved hexacyanoferrate in water are all situated on one and the same straight line. Obviously, this plot shows that the factor controlling the magnitude of the formal potentials is in the solid compounds and in the solution the same, that is, the ion potential of the nearest neighbor of the nitrogen end of the cyanide ions. These nearest neighbors are the metal ions Me^{I} , Me^{II} , and Me^{III} in the solid PCMs, and the proton of water in the aqueous solution! On the basis of simple thermodynamic considerations it has been shown that the following equation holds [54, 55]:

$$E_A^{\theta'} = -\frac{\kappa}{zF} + \frac{\xi}{zF} \frac{a}{r_{\text{Me}}} \quad (5)$$

(κ and ξ are constants, a is the charge of the nitrogen coordinated metal ions $\text{Me}^{(\text{I}),(\text{II}),(\text{III})}$ and r_{Me} is their radius.)

The differences in formal potentials of different metal hexacyanometalates is the basis of tuning the redox properties of PCMs by synthesis of mixed solutions, as far as that is possible due to the ion radii. Examples for a continuous tuning of the hexacyanoferrate redox potential are mixed nickel/iron hexacyanoferrates [30], mixed copper/iron hexacyanoferrates [56], and mixed cadmium/iron hexacyanoferrates [33].

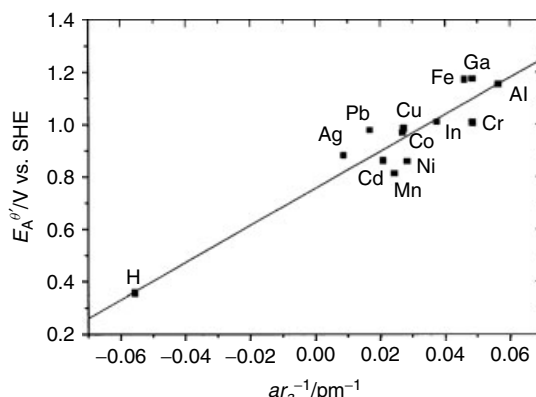


Fig. 4 Correlation between the formal potentials of the hexacyanoferrate units of the solid hexacyanoferrates and the ion potential (charge/radius) of the nitrogen coordinated metal ions [53, 55].

The formal potential of the hexacyanoferrate systems also shift by inserting different metal ions into the channels [57]. With the help of Born–Haber cycles, the following equation has been derived [55]:

$$E_A^{\Phi'} \approx -\frac{\text{const}_3}{zF} - \frac{\Phi}{zF} \frac{b_I}{r_I} \quad (6)$$

(const_3 and Φ are constants, b_I is the charge of the inserting metal ions Me^I and r_I is its radius).

Figure 5 gives the experimental proof of the validity of Eq. 6. However, some hexacyanoferrates exhibit a different affinity for the alkali metal ions. An example is samarium hexacyanoferrate [58]. The reasons for the different behavior are not yet known.

The formal potentials of solid hexacyanometalates can also be correlated with the lattice constants, that is, with a parameter that depends mainly on the radii of the two metal ions forming the framework of the compounds. This theoretically derived dependence can be verified when the nitrogen coordinated metal ion and the inserting metal ions are kept constant and the carbon coordinated metal ions are varied, for example, when hexacyanoferrate, hexacyanocobaltate, hexacyanomanganate, and so on are compared [53, 55]. The equation

that has been derived is:

$$E_A^{\Phi'} \approx -\frac{2\Psi}{zF} \left[\frac{b_C - b_B}{L} \right] - \frac{\omega_I}{zF} \quad (7)$$

(Ψ and ω_I are constants, $(b_C - b_B)$ is the difference of charges of the oxidized and reduced forms of the hexacyanometalate unit, that is, it is 1, and L is the lattice constant of the solid hexacyanometalate).

Figure 6 shows the experimental data that obviously follow Eq. (7).

The experimental data verifying the dependencies of the formal potentials on ion parameters, as shown in Figs 4, 5, and 6 have been accessible only by application of voltammetry of immobilized particles [59], since that method is the only one that allows the study of different compounds that have been chemically synthesized and completely characterized to be measured under the very same conditions. This is not, or only to some extent possible with electrochemically prepared thin films on electrodes.

23.3.3 Special Features

23.3.3.1 Metal Hexacyanoferrates

1. *Metal hexacyanoferrates possessing only one kind of redox-active metal ions:* Most of the metal hexacyanoferrates show only

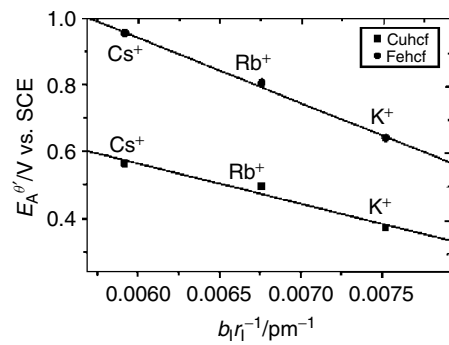


Fig. 5 Correlation between the formal potentials of the hexacyanoferrate units of the solid hexacyanoferrates and the ion potential (charge/radius) of the inserting metal ions [53, 55].

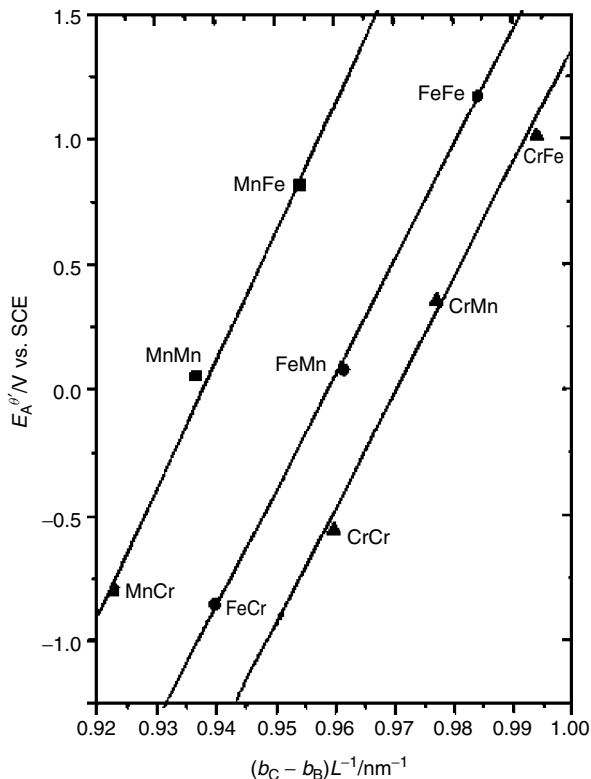


Fig. 6 Correlation between the formal potentials of the hexacyanometalate units of the solid hexacyanometalates and the inverse lattice constant L of the solid compounds [53, 55].

one electrochemically active system, that is, the hexacyanoferrate unit. This is the case for the following compounds: Cu^{2+} , Ni^{2+} , Co^{2+} , Cd^{2+} , Zn^{2+} , and other metal hexacyanoferrates. This is surprising because most of these ions are themselves electroactive in aqueous solutions. A formal reasoning is that the solubility products of these salts are so small that the reduction of the metal ions is simply shifted to inaccessible values, because even a reductive decomposition of the hexacyanometalates is not possible using aqueous electrolytes. This is not true for silver hexacyanoferrates that can be easily decomposed by reduction to metallic

silver and dissolved hexacyanoferrate ions. To this group of hexacyanoferrates belongs also vanadium hexacyanoferrate, which was described first by Shaojun [60], and studied in detail by Carpenter et al. [61], who have proved that vanadium is not active in these films, although two overlapping redox systems are present in the cyclic voltammograms. It can be supposed that different vanadium hexacyanoferrate phases may be responsible for the two systems (cf. cobalt hexacyanoferrate, although in that case cobalt is also active).

2. Metal hexacyanoferrates possessing two kinds of redox-active metal ions: Here we consider those hexacyanoferrates that

possess two redox systems that support insertion electrochemical reactions. The most prominent member of this group is the archetype of metal hexacyanoferates, Prussian blue. About no other PCM so many papers have been published as on Prussian blue. Inevitably, there are contradictory and inconsistent reports among them. One reason is certainly the great variety of Prussian blues resulting from the ability to (1) house different amounts and kinds of cations in the interstitial cavities (e.g. different alkali metal ions and also high-spin Fe ions), and (2) the formation of defect structures with a considerable number of hexacyanoferate vacancies. The latter effect is especially pronounced when no suitable cations are available during the synthesis, as in the case of the famous Ludi experiment where Prussian blue was slowly crystallized from concentrated hydrochloric acid in the absence of potassium ions [25].

Prussian blue shows two distinct redox systems, one at rather positive potentials

(around 0.8 V vs. SCE) and one at considerably more negative potentials (around 0.2 V vs. SCE) (cf. Fig. 7). Itaya et al. [62] have shown by *in situ* Mössbauer spectroscopy that the more negative system is caused by the nitrogen coordinated high-spin iron ions, and the other system is caused by the carbon coordinated low-spin iron ions of the hexacyanoferate. It is a very peculiar property of Prussian blue that a cyclic electrochemical oxidation and reduction involving both redox systems, in some electrolyte solutions leads to the blocking of the low-spin iron system, that is, that voltammetric response vanishes [63]. This happens always when Tl^+ , Rb^+ , or NH_4^+ [64] ions are present in the electrolyte solution. The reason for that behavior are the small lattice constant differences between the three oxidation states of Prussian blue and the ion radii of the three earlier-mentioned cations. Both lead to a trapping of these cations in the Prussian blue that blocks ion diffusion for the interconversion of Prussian blue and

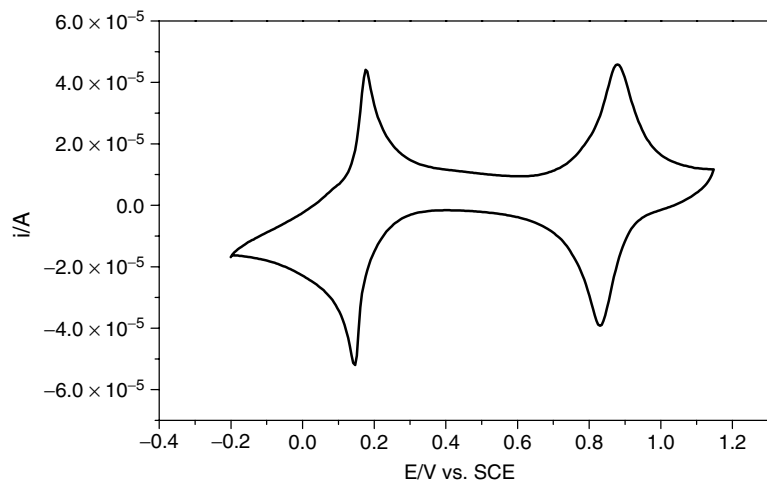


Fig. 7 Cyclic voltammogram of Prussian blue immobilized on a graphite electrode and using an electrolyte solution containing 0.1 mol L^{-1} KCl. Scan rate: 0.01 V s^{-1} .

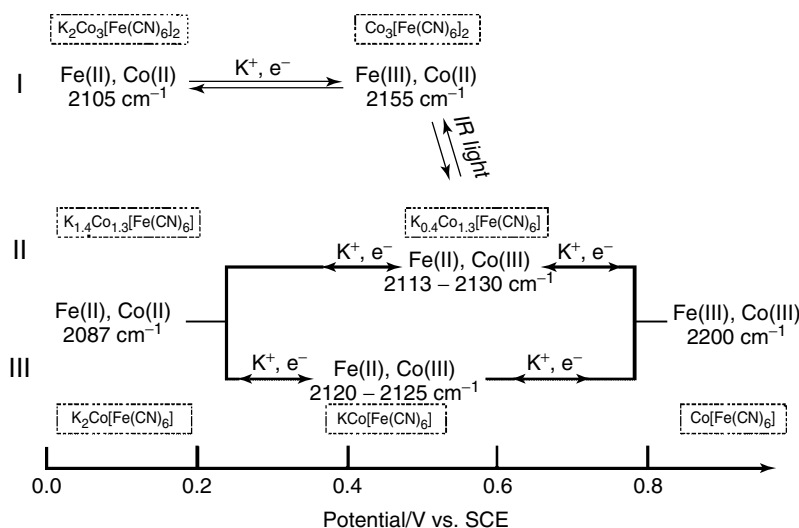


Fig. 8 Scheme of the electrochemical and photochemical conversions involved in the electrochemistry of cobalt hexacyanoferate films according to Ref. 65.

Prussian yellow. This irreversible binding of thallium(I) ions is probably related to the well-known use of Prussian blue to bind thallium ions following poisoning.

Cobalt(II) hexacyanoferate, formally similar to Prussian blue, exhibits a far more complex electrochemistry. Only recently, Lezna et al. [65] succeeded in elucidating this system by a combination of *in situ* infrared spectroscopy and electrochemistry, and *ex situ* X-ray photoelectron spectroscopy. Figure 8 shows the pathways of the three different phases involved in the electrochemistry, and their interconversion by electrochemical redox reactions and photochemical reactions.

23.3.3.2 Hexacyanocobaltates, Hexacyanomanganates, Hexacyanochromates, Hexacyanoruthenates

Hexacyanocobaltate(III) is not reducible and hence, most metal hexacyanocobaltates are not electrochemically active. A very interesting exception is copper(II) hexacyanocobaltate(III) that can

be reduced both chemically and electrochemically to copper(I) hexacyanocobaltate(III) coupled to a transfer of charge compensating potassium ions [28]. Hexacyanocobaltate(III) ions can be used to prepare solid solutions with hexacyanoferate ions. In the case of mixed solid solutions of copper(II) hexacyanoferate/hexacyanocobaltate, this causes small shifts of the formal potential of the hexacyanoferate system, and also of the copper(II)/copper(I) system. The latter is only visible for an excess of hexacyanocobaltate [28]. Iron hexacyanoferate is not stable in electrochemical experiments, but isomerizes to chromium hexacyanoferate [47]. Hexacyanomanganates exhibit two redox systems, corresponding to the redox states Mn(III)/Mn(II), and Mn(II)/Mn(I) respectively. Whereas chromium(II) and iron(II) hexacyanomanganate are stable in cyclic voltammetry, the manganese(II) hexacyanomanganate(III) decomposes rapidly when the potential is cycled between 0 and -1.5 V vs. Ag/AgCl.

The latter compound, however, is completely stable when the potential is cycled only between -0.7 and -1.5 V vs. Ag/AgCl, where only the Mn(II)/Mn(I) system is active [66].

23.3.3.3 Octacyanomolybdates, Octacyanotungstates

Octacyanomolybdates and octacyanotungstates exhibit an insertion electrochemistry, which is rather similar to that of the hexacyanoferrates, [67] and the compounds show a pronounced electrochromic effect [68].

23.3.3.4 Pentacyanonitrosyl Metalates

Metal pentacyanonitrosyl metalates show an electrochemical behavior similar to that of hexacyanometalates. The compounds show electrocatalytic properties [69].

23.4

Preparation of Electrodes Modified by Polycyanometalates and their Applications

23.4.1

Preparation of Polycyanometalate Modified Electrodes

For choosing the right way of preparation of PCM modified electrodes, the decisive question is the intention of preparation. There are two principally different goals: (1) The electrodes ought to be applied for electrocatalysis, for electrochromic devices and the like, and (2) modified electrodes are prepared to study the electrochemistry of the compounds. For the first goal, there are two principally different approaches: (a) the preparation of films on electrode surfaces, and (b) the incorporation of the PCM into a matrix, for example, a mixture of graphite and a binder, leading to composite electrodes.

1. The preparation of film electrodes: Prussian blue films are usually prepared by cycling an electrode in a freshly prepared solution containing iron(III) and hexacyanoferrate(III) ions [70–72]. As substrate, mostly platinum is used, sometimes glassy carbon [73] is used, and very frequently ITO electrodes [74] are used because the latter are very useful for electrochromism studies. Similar procedures using solutions containing metal ions and hexacyanoferrate(III) have been used to deposit cobalt hexacyanoferrate [75] and chromium hexacyanoferrate [76, 77]. Crumbliss et al. reported a plasma deposition of iron species from a plasma containing iron pentacarbonyl and ethane, followed by electrochemical derivatization of the deposited iron sites with the help of hexacyanoferrate solutions [78].

To prepare metal hexacyanoferrate films, very frequently the following procedure was followed: first a film of the respective metal, for example, cadmium [79], copper [80], silver [81], or nickel [82, 83] was electrochemically plated on the surface of a platinum electrode, and that was followed by chemical oxidation of the metal film in a solution of $K_3[Fe(CN)_6]$, leading to the formation of the metal hexacyanoferrates. The same method has been used to produce films of nickel hexacyanoruthenate and hexacyanomanganate using the appropriate anions [83]. It is also possible to perform the oxidation of the deposited metals in solutions containing hexacyanoferrate(II) by cyclic oxidation/reduction of the latter. In a similar way, films of copper heptacyanonitrosylferrate have been deposited [84].

Sauter and Wittstock [85] have described a method for local deposition of cobalt and nickel hexacyanoferrates using the technique of electrochemical scanning

microscopy and sacrificial electrodes from cobalt and nickel.

2. The preparation of electrodes with immobilized PCM: If the purpose of modifying an electrode is the study of the electrochemistry of PCMs, of course, the best choice is to use those compounds that have been synthesized in larger amounts, and that have been characterized by all available analytical techniques, as, for example, X-ray diffraction, infrared spectroscopy, elemental analysis, and so on. (This is usually rather difficult if not impossible with the thin films precipitated on electrode surface by the techniques discussed previously.) Such well-defined samples can be very advantageously investigated by immobilizing microparticles on suitable electrodes [59], mostly on graphite electrodes. The technique of mechanical immobilization has been described in detail [59, 86–89], and it may suffice here to say that, usually, a very tiny amount (around 1 mg) of the powder sample is placed on a glass plate or tile and a graphite electrode is gently rubbed on the sample spot to press some of the microparticles into the electrode surface. This technique proved to be highly useful in systematic studies of the PCMs (see [28, 47, 50, 53, 54]). The technique of immobilizing microparticles on electrodes has also been utilized for *in situ* calorimetric studies of the insertion electrochemical reactions of PCMs [90, 91]. In this case, very small gold and graphite electrodes had been used and the immobilization technique was slightly different from the procedure described earlier.

23.4.2

Applications of PCM Modified Electrodes

1. Electrochromic devices: The strong differences in the spectra of the PCMs in their various oxidation states, the ease

with which the insertion electrochemical reactions can be performed, their rather good reversibility, and the low price of the PCMs has led to serious expectations for an exploitation in electrochromic windows and displays [92]. Prussian blue is still the compound exhibiting the most pronounced absorption differences, and many attempts have been made to codeposit Prussian blue with other PCMs [93] or with organic conducting polymers to get improved electrochromic properties.

2. Electrocatalysts for electroanalysis: Since PCMs contain transition metal ions that can easily undergo electron exchange reactions, they can act as effective mediators in electron transfer reactions, and thus as catalysts to bring about otherwise strongly inhibited electrode reactions. Mattos and Gorton [94] have recently reviewed the vast literature on electrocatalytic applications of metal hexacyanoferrate films. Although many examples are known, no commercial devices are known that utilize such compounds. PCMs can also be used in biosensors in combination with enzymes. A first-generation biosensor consisting of glucose oxidase immobilized onto a thin film Prussian blue electrode with a Nafion membrane was introduced by Karyakin et al. [95]. Wang et al. [96] have suggested screen printed electrodes containing cupric hexacyanoferrate and glucose oxidase. The dispersed cupric hexacyanoferrate catalyst offers the detection of glucose substrate at very low potentials (the overvoltage for the reduction of the enzymatically liberated hydrogen peroxide is decreased to around 0.1 V at physiological pH).

3. Ion Sensitive electrodes: Metal hexacyanoferrate film electrodes as well as metal hexacyanoferrate particles incorporated in solid composite electrodes have been used for the quantitative analysis of the ions

that are exchanged between the metal hexacyanoferrate and the aqueous solution. Ion selective electrodes for potentiometric sensing of intercalating ions have been described on the basis of nickel hexacyanoferrate [82, 97, 98] and copper hexacyanoferrate [99, 100]. These electrodes display a quasi Nernstian response toward cesium and potassium ions. Rotating disk electrodes modified with cobalt hexacyanoferrate or nickel hexacyanoferrate can be used as ion selective electrodes in the case of Na^+ or K^+ , respectively [101]. Nickel or cupric hexacyanoferrate film electrodes have been also used for amperometric detection of intercalating ions in a flow-injection system (K^+ and NH_4^+ in urine and K^+ in blood samples) [102]. Composite electrodes with different metal hexacyanoferrates incorporated into a graphite/paraffin matrix were used for the voltammetric determination of potassium [103]. A graphite silver hexacyanoferrate composite electrode can be used for the determination of iron(III) ions in solution [52]. Here, the silver ions are reduced to silver(0) and the liberated hexacyanoferrate anions can react with iron(III) ions to give Prussian blue. Following that preconcentration step, the iron(III) ions can be electrochemically determined by evaluating the characteristic signals of Prussian blue. Thallium ions can be determined by preconcentration in Prussian blue and using anodic stripping voltammetry, that is, the thallium ions are reduced to thallium(0), which is subsequently oxidized to give the anodic stripping signal [104]. Prussian blue immobilized in a composite electrode can also be used to determine the concentration of NH_4^+ by evaluating the decrease of the peak system of the carbon coordinated iron ion in cyclic voltammetric measurements [64].

4. Corrosion protection: Metal hexacyanoferrate films also attracted interest as corrosion protective layers on metals, especially as additives to conducting polymers [105, 106]. Kulesza et al. [107] reported the coating of steel with an organic anion exchanger (poly(4-vinylpyridine)) incorporating hexacyanoferrate ions that lead to the formation of a Prussian blue layer on the metal, providing surprisingly good corrosion resistance in strongly acidic solutions. This film seems to have even better properties than polyaniline/Prussian blue/hexacyanoferrate films [108].

5. Batteries: Metal PCMs should be useful for making rocking chair batteries because one and the same metal ions, for example, potassium ions could be shuttled between the anode and the cathode when suitable compounds are used. The published results indicate that such rocking chair batteries indeed work [109–113]; however, their properties are insufficient to be real competitors on the battery market. Despite the rather low voltages, it is also the presence of as-yet unidentified side reactions that reduces the cycleability of the batteries. Further problems are due to the bad adherence of the PCMs to the current collectors. However, it still cannot be excluded that technical developments may improve the performance of such batteries so that applications are possible.

References

1. A. G. Sharpe, *The Chemistry of Cyano Complexes of the Transition Metals*, Academic Press, London, New York, San Francisco, 1976.
2. J. F. Keggin, F. D. Miles, *Nature* **1936**, 137, 577.
3. A. Ferrari, M. E. Tani, G. Manano, *Gazz. Chim. Ital.* **1959**, 89, 2512.
4. A. Ratuszna, G. Małecki, *Mater. Sci. Forum* **2000**, 321, 947.

5. S. Ayrault, B. Jimenez, E. Garnier et al., *J. Solid State Chem.* **1998**, *141*, 475.
6. G. W. Beall, D. F. Mullica, W. O. Milligan, *Acta Crystallogr., Sect. B* **1978**, *34*, 1446.
7. W. E. Bailey, R. J. Williams, W. O. Milligan, *Acta Crystallogr., Sect. B* **1973**, *29*, 1365.
8. M. V. Zil'berman, V. G. Kuznetsov, V. V. Vol'khin, *Zh. Neorg. Khim.* **1974**, *19*, 1838.
9. P. Gravereau, E. Garnier, *Acta Crystallogr., Sect. C* **1984**, *40*, 1306.
10. W. Petter, V. Gramlich, F. Hulliger, *J. Solid State Chem.* **1989**, *82*, 161.
11. A. Ferrari, M. E. Tani, *Gazz. Chim. Ital.* **1960**, *90*, 1565.
12. V. G. Zubkov, A. P. Tyutyunik, I. F. Berger et al., *Solid State Sci.* **2001**, *2*, 361.
13. F. Goubard, A. Tabuteau, *J. Solid State Chem.* **2002**, *167*, 34.
14. S. Ayrault, C. Loos-Neskovic, M. Fedoroff et al., *Talanta* **1995**, *42*, 1581.
15. A. Gomez, E. Reguera, *Int. J. Inorg. Mat.* **2001**, *3*, 1045.
16. H. B. Weiser, W. O. Milligan, J. B. Bates, *J. Phys. Chem.* **1942**, *46*, 99.
17. M. Rueegg, A. Ludi, K. Rieder, *Inorg. Chem.* **1971**, *10*, 1775.
18. D. F. Mullica, P. K. Hayward, E. L. Sappenfield, *Inorg. Chim. Acta* **1996**, *244*, 273.
19. A. Gomez, V. H. Lara, P. Bosch et al., *Powder Differ.* **2002**, *17*, 144.
20. A. Ludi, H. U. Guedel, N. Rueegg, *Inorg. Chem.* **1970**, *9*, 2224.
21. G. W. Beall, W. O. Milligan, J. D. Korp et al., *Inorg. Chem.* **1977**, *16*, 2715.
22. A. Ludi, H. U. Guedel, *Helv. Chim. Acta* **1968**, *51*, 2006.
23. (a) A. Ludi, H. U. Guedel, *Helv. Chim. Acta* **1968**, *51*, 1762; (b) A. Ludi, H. U. Guedel, *Helv. Chim. Acta* **1967**, *50*, 2035.
24. D. F. Mullica, E. L. Sappenfield, *J. Solid State Chem.* **1989**, *82*, 168.
25. A. Ludi, H. U. Güdel, *Struct. Bonding (Berlin)* **1973**, *14*, 1.
26. H. J. Buser, D. Schwarzenbach, W. Petter et al., *Inorg. Chem.* **1977**, *16*, 2704.
27. H. Kahlert, F. Scholz, H. Wulff, unpublished.
28. A. Widmann, H. Kahlert, I. Petrovic-Preljevic et al., *Inorg. Chem.* **2002**, *42*, 5706.
29. P. J. Kulesza, M. A. Malik, J. Skorek et al., *J. Electroanal. Chem.* **1999**, *461*, 3757.
30. S. J. Reddy, A. Dostal, F. Scholz, *J. Electroanal. Chem.* **1996**, *403*, 209.
31. X. Ciu, L. Hong, X. Lin, *J. Electroanal. Chem.* **2002**, *526*, 115.
32. P. J. Kulesza, M. A. Malik, R. Schmidt et al., *J. Electroanal. Chem.* **2000**, *487*, 57.
33. N. F. Zakharchuk, N. Naumov, R. Stösser et al., *J. Solid State Electrochem.* **1999**, *3*, 264.
34. M. T. Kelly, G. A. Arbuckle-Keil, L. A. Johnson et al., *J. Electroanal. Chem.* **2001**, *500*, 311.
35. A. Widmann, *Insertionselektrochemie Von Festen Metallhexacyanometalaten*, Ph.D. Thesis, Universität Greifswald, 2003.
36. A. Widmann, H. Kahlert, H. Wulff et al., *J. Solid State Electrochem.* **2005**, *9*, 380.
37. T. Niu, G. Crisci, J. Lu et al., *Acta Crystallogr., Sect. C* **1998**, *54*, 565.
38. A. Ratuszna, S. Juszczak, G. Małecki, *Powder Differ.* **1996**, *11*, 318.
39. W. K. Ham, T. J. R. Weakley, C. J. Page, *J. Solid State Chem.* **1993**, *107*, 101.
40. A. Loosli, M. Wermuth, H. U. Guedel et al., *Inorg. Chem.* **2000**, *39*, 2289.
41. J. K. Nagle, A. L. Balch, M. M. Olmstead, *J. Am. Chem. Soc.* **1988**, *110*, 319.
42. U. Klement, *Z. Kristallogr.* **1993**, *208*, 285.
43. U. Klement, *Z. Kristallogr.* **1993**, *208*, 288.
44. S. C. Abrahams, L. E. Zyontz, J. L. Bernstein, *J. Chem. Phys.* **1982**, *76*, 5458.
45. R. Schöllhorn, *Angew. Chem.* **1980**, *92*, 1015.
46. H. Kahlert, U. Retter, H. Lohse et al., *J. Phys. Chem.* **1998**, *102*, 8757.
47. A. Dostal, U. Schröder, F. Scholz, *Inorg. Chem.* **1995**, *34*, 1711.
48. E. Reguera, J. F. Bertrán, L. Nuñez, *Polyhedron* **1994**, *13*, 1619.
49. A. Dostal, B. Meyer, F. Scholz et al., *J. Phys. Chem.* **1995**, *99*, 2096.
50. M. Hermes, M. Lovrić, M. Hartl et al., *J. Electroanal. Chem.* **2001**, *501*, 193.
51. A. Dostal, M. Hermes, F. Scholz, *J. Electroanal. Chem.* **1996**, *415*, 133; *J. Electroanal. Chem.* **1997**, *422*, 205.
52. H. Kahlert, F. Scholz, *Electroanalysis* **1997**, *9*, 922.
53. F. Scholz, A. Dostal, *Angew. Chem.* **1995**, *107*, 2876; *Angew. Chem., Int. Ed. Engl.* **1995**, *34*, 2685.
54. M. Bárcena Soto, *Thermodynamische Untersuchungen zur Insertionselektrochemie*

- von Metallhexacyanoferraten, Ph.D. Thesis, Humboldt-Universität, Berlin, 2000.
55. M. Bárcena Soto, F. Scholz, *J. Electroanal. Chem.* **2002**, *521*, 183.
 56. D. Schwudke, R. Stößer, F. Scholz, *Electrochim. Commun.* **2000**, *2*, 301.
 57. A. Crumbliss, P. S. Lugg, N. Morosoff, *Inorg. Chem.* **1984**, *23*, 4701.
 58. P. Wu, C. Cai, *J. Solid State Electrochem.* **2004**, *8*, 538.
 59. F. Scholz, U. Schröder, R. Gulaboski, *Electrochemistry of Immobilized Particles and Droplets*, Springer, Berlin, 2005.
 60. D. Shaojun, L. Fengbin, *J. Electroanal. Chem.* **1986**, *210*, 31.
 61. M. K. Carpenter, R. S. Conell, S. J. Simko, *Inorg. Chem.* **1990**, *29*, 845.
 62. K. Itaya, T. Ataka, S. Toshima et al., *J. Phys. Chem.* **1982**, *86*, 2415.
 63. A. Dostal, G. Kauschka, S. J. Reddy et al., *J. Electroanal. Chem.* **1996**, *406*, 155.
 64. M. Hermes, F. Scholz, *J. Solid State Electrochem.* **1997**, *3*, 215.
 65. R. O. Lezna, R. Romagnoli, N. R. de Tacconi et al., *J. Phys. Chem. B* **2002**, *106*, 3612.
 66. A. Dostal, *Festkörperreaktionen an Metallhexacyanometalat-Modifizierten Elektroden*, Ph.D. Thesis, Humboldt University, Berlin, 1997.
 67. U. Schröder, F. Scholz, *Inorg. Chem.* **2000**, *39*, 1006.
 68. U. Schröder, B. Meyer, F. Scholz, *Fresenius' J. Anal. Chem.* **1996**, *356*, 295.
 69. H. Razmi, M. Agazadeh, B. Habibi-A., *J. Electroanal. Chem.* **2003**, *547*, 25.
 70. V. D. Neff, *J. Electrochem. Soc.* **1978**, *125*, 886.
 71. D. Ellis, M. Eckhoff, V. D. Neff, *J. Phys. Chem.* **1981**, *85*, 1225.
 72. K. Itaya, I. Uchida, V. D. Neff, *Acc. Chem. Res.* **1986**, *19*, 162.
 73. C. Kuhnhardt, *J. Electroanal. Chem.* **1994**, *369*, 71.
 74. A. Roig, J. Navarro, R. Tamarit et al., *J. Electroanal. Chem.* **1993**, *360*, 55.
 75. P. J. Kulesza, M. A. Malik, S. Zamponi et al., *J. Electroanal. Chem.* **1995**, *397*, 287.
 76. M. Jiang, X. Zhou, Z. Zhao, *J. Electroanal. Chem.* **1990**, *287*, 389.
 77. Z. Gao, *J. Electroanal. Chem.* **1994**, *370*, 95.
 78. A. L. Crumbliss, P. S. Lugg, D. L. Patel et al., *Inorg. Chem.* **1983**, *22*, 3541.
 79. C. H. Luangdilok, D. J. Arent, A. B. Bocarsly, *Langmuir* **1992**, *8*, 650.
 80. L. M. Siperko, T. Kuwana, *J. Electrochem. Soc.* **1983**, *130*, 396.
 81. S. Moon, J. D. Moon, *Bull. Korean Chem. Soc.* **1994**, *15*, 1042.
 82. L. F. Schneemeyer, S. E. Sprengler, D. W. Murphy, *Inorg. Chem.* **1985**, *24*, 3044.
 83. S. Sinha, B. D. Humphrey, A. B. Bocarsly, *Inorg. Chem.* **1984**, *23*, 203.
 84. Z. Gao, Y. Zhang, M. Tian et al., *J. Electroanal. Chem.* **1993**, *358*, 161.
 85. S. Sauter, G. Wittstock, *J. Solid State Electrochem.* **2001**, *5*, 205.
 86. F. Scholz, B. Lange, *Trends Anal. Chem.* **1992**, *11*, 359.
 87. F. Scholz, B. Meyer, *Chem. Soc. Rev.* **1994**, *23*, 341.
 88. F. Scholz, B. Meyer, Voltammetry of solid microparticles immobilized on electrode surfaces in *Electroanalytical Chemistry, A Series of Advances* (Eds.: A. J. Bard, I. Rubinstein), Marcel Dekker, New York, 1998, p. 1, Vol. 20.
 89. D. A. Fiedler, F. Scholz, Electrochemical studies of solid compounds and materials in *Electroanalytical Methods - Guide to Experiments and Applications* (Ed.: F. Scholz), Springer, Berlin, p. 331.
 90. M. Bárcena Soto, G. Kubisch, F. Scholz, *J. Electroanal. Chem.* **2002**, *528*, 18.
 91. M. Bárcena Soto, F. Scholz, *J. Electroanal. Chem.* **2002**, *528*, 27.
 92. P. M. S. Monk, R. J. Mortimer, D. R. Rosseinsky, *Electrochromism: Fundamentals and Applications*, VCH, Weinheim, 1995.
 93. L.-C. Chen, Y.-H. Huang, K.-C. Ho, *J. Solid State Electrochem.* **2002**, *7*, 6.
 94. I. L. de Mattos, L. Gorton, *Quim. Nova* **2001**, *24*, 200.
 95. A. A. Karyakin, O. V. Gitelmacher, E. E. Karyakina, *Anal. Chem.* **1995**, *67*, 2419.
 96. J. Wang, X. Zhang, *Anal. Lett.* **1999**, *32*, 1739.
 97. M. Giorgetti, E. Scavetta, M. Berrettoni et al., *Analyst* **2001**, *126*, 2168.
 98. L. J. Amos, A. Duggal, E. J. Mirsky et al., *Anal. Chem.* **1988**, *60*, 245.
 99. D. Engel, E. W. Grabner, *Ber. Bunsen-Ges. Phys. Chem.* **1985**, *89*, 982.
 100. Y. Tani, H. Eun, Y. Umezawa, *Electrochim. Acta* **1998**, *43*, 3431.
 101. L. Muresan, I. C. Popescu, L. Oniciu, *Stud. Univ. Babes-Bolyai, Chem.* **1995**, *40*, 161.
 102. K. N. Thomsen, R. P. Baldwin, *Electroanalysis* **1990**, *2*, 263.

103. H. Düssel, A. Dostal, F. Scholz, *Fresenius' J. Anal. Chem.* **1996**, *355*, 21.
104. H. Kahlert, Š. Komorsky-Lovrić, M. Hermes et al., *Fresenius' J. Anal. Chem.* **1996**, *356*, 204.
105. D. E. Tallman, G. Spinks, A. Dominis et al., *J. Solid State Electrochem.* **2002**, *6*, 73.
106. G. Spinks, A. Dominis, G. G. Wallace et al., *J. Solid State Electrochem.* **2002**, *6*, 85.
107. M. T. Galkowski, P. J. Kulesza, K. Miecznikowski et al., *J. Solid State Electrochem.* **2004**, *8*, 430.
108. M. Galkowski, M. A. Malik, P. J. Kulesza et al., *J. Electrochem. Soc.* **2003**, *150*, B249.
109. V. D. Neff, *J. Electrochem. Soc.* **1985**, *132*, 1382.
110. E. W. Grabner, S. Kalwellis-Mohn, *J. Appl. Electrochem.* **1987**, *17*, 653.
111. K. Kuwabara, J. Nunome, K. Sugiyama, *Solid State Ionics* **1991**, *48*, 303.
112. M. Jayalakshmi, F. Scholz, *J. Power Sources* **2000**, *87*, 212.
113. M. Jayalakshmi, F. Scholz, *J. Power Sources* **2000**, *91*, 217.

24
**Electrochemistry of Zinc,
Cadmium, Lead, Gold, Silver,
Mercury, and Copper**

Part A:	Electrochemistry of Zinc, Cadmium and Lead	725
	<i>Jadwiga Stroka, Krzysztof Maksymiuk, and Zbigniew Galus</i>	
24.1	Electrochemistry of Zinc	725
24.2	Electrochemistry of Cadmium	767
24.3	Electrochemistry of Lead	804
Part B:	Electrochemistry of Gold, Silver, and Mercury	839
	<i>Marek Orlik and Zbigniew Galus</i>	
24.4	Electrochemistry of Gold	839
24.5	Electrochemistry of Silver	913
24.6	Electrochemistry of Mercury	958
Part C:	Electrochemistry of Copper	992
	<i>David B. Rorabacher and Ronald R. Schroeder</i>	
24.7	Electrochemistry of Copper	992

Part A:
Electrochemistry of Zinc, Cadmium, and Lead*

*Jadwiga Stroka, Krzysztof Maksymiuk, and Zbigniew Galus
Department of Chemistry, University of Warsaw, Warsaw,
Poland*

**Dedicated to the memory of Professor Robert A. Osteryoung, prominent
electrochemist and analyst*

24.1
Electrochemistry of Zinc

24.1.1	Double-layer Properties of Zinc Electrodes	726
24.1.1.1	Pc-Zinc in Aqueous Solutions	726
24.1.1.2	Zn Single Crystals in Aqueous Solutions	727
24.1.2	Electrochemical Properties and Kinetics of the Zn(II)/Zn(Hg) and Zn(II)/Zn Systems	727
24.1.2.1	Electrochemistry in Aqueous Solutions	727
24.1.2.2	Electrochemistry in Water-organic Solvent Mixtures	731
24.1.2.3	Electrochemistry in Nonaqueous Solvents	733
24.1.2.4	The Influence of Organic Compounds on the Electrode Processes . .	734
24.1.2.5	The Electrochemical Properties of the Zinc Complexes	736
24.1.2.6	Properties of Zinc Oxide Electrode	737
24.1.2.7	Electrode Processes in Molten Salts	738
24.1.3	Deposition and Underpotential Deposition of Zn on Solid Electrodes	740
24.1.3.1	Underpotential Deposition of Zinc	740
24.1.3.1.1	Zn UPD on Pt	740
24.1.3.1.2	Zn UPD on Au	741
24.1.3.2	Zinc Electrodeposition on Solid Electrodes	742
24.1.3.2.1	Electrodeposition on Zn Electrodes	742
24.1.3.2.2	Electrodeposition on Other Electrodes	744
24.1.4	Passivation and Corrosion of Zinc	745
24.1.4.1	Anodic Dissolution and Passivation of Zinc	745
24.1.4.2	Corrosion	747

24.1.5	Applied Electrochemistry	748
24.1.5.1	Batteries	748
24.1.5.1.1	Ni-Zn Cells	748
24.1.5.1.2	Zn-Air Batteries	749
24.1.5.1.3	Zn-MnO ₂ Batteries	749
24.1.5.1.4	Zn-Ag Batteries	750
24.1.5.1.5	Other Cells	751
24.1.5.2	Electrowinning	751
24.1.5.3	Zinc Electroplating	753
24.1.5.4	Zinc Alloys Electroplating	753
24.1.5.5	Electrochemical Sensors and Modified Electrodes	754
24.1.5.5.1	Potentiometric Sensors	754
24.1.5.5.2	Voltammetric/Amperometric Sensors	755
24.1.5.5.3	Modified Electrodes	755
	References	756

This chapter is a supplement to the issue of *Encyclopedia of Electrochemistry of the Elements*. Owing to limited space, not all relevant work could even be briefly discussed. In this review, mainly the recent papers published in the last 10 years have been presented, with some relation to earlier works published after 1977, when the chapters on lead, cadmium, and zinc electrochemistry appeared.

24.1.1 Double-layer Properties of Zinc Electrodes

Electrical double-layer (edl) properties of solid polycrystalline zinc (pc-Zn) electrodes and single-crystal zinc electrodes in aqueous solution were studied in many works, which are reviewed in Refs 1, 2.

24.1.1.1 Pc-Zinc in Aqueous Solutions

The pc-Zn electrode was found to be nearly ideally polarizable at sufficiently wide negative polarization range [3–8]. The differential capacitance of zinc electrode was

studied in aqueous electrolytes: KCl (pH 7) [6], Na₂SO₄ [7], NaClO₄, KCl, KNO₃, and Na₂SO₄ (pH 6.6–7) [9]. Minima on the differential capacitance (*C*-*E*) curves on the pc-Zn electrodes were observed. In 0.01 M KCl aqueous solutions, the minimum was broader.

For pc-Zn/H₂O, the value of zero charge potential (*E*_{pzc}) was found to be equal to about -1.15 V (versus saturated calomel electrode (SCE)) [10, 11]. The same values of *E*_{pzc} were obtained by a scrape method in a neutral NaClO₄ aqueous solution [12].

In the presence of tetrabutylammonium iodide (TBAI) in its adsorption region on the pc-Zn electrode, the *edl* capacitance decreased with increasing TBAI concentration and the capacity minimum shifted to more negative potentials [13]. At still more negative potentials, a well-defined adsorption-desorption peak was observed. Splitting of this peak was explained by the presence of different faces on the surface of pc-Zn electrode.

24.1.1.2 Zn Single Crystals in Aqueous Solutions

Zinc crystallizes in a hexagonal close-packed system; its basal face (0001) was prepared by cleavage of single crystal at the temperature of liquid nitrogen, and the prismatic face (1010) and the face (1120) were prepared by polishing in nitric acid [2].

The first attempt to determine zero charge potential for single-crystal sp metal was described for zinc [3, 6] from $C-E$ capacitance curves in dilute solutions. E_{pzc} for the face of Zn(0001) was about 80 mV more positive than that for Zn(1010). Later, it was pointed out [6, 10] that the determination of E_{pzc} directly from $C-E$ dependencies was not possible for zinc because the potential is close to the reversible standard potential of zinc in aqueous solution.

Therefore, E_{pzc} was determined using the indirect methods valid for single-crystals electrodes and pc-Zn electrodes [1, 2, 14, 15]: (1) salting-out of organic compounds from surface inactive electrolyte solutions, (2) from the potential corresponding to maximum on $C-E$ curves for organic compounds with high attractive interaction constant a , and (3) from the dependence of the capacitance minimum on thiourea (TU) concentration. The obtained values of zero charge potentials were in good agreement with other results [7, 8]. For various faces of Zn single-crystal electrode, the maximum difference between E_{pzc} was about 90–100 mV [2, 15, 16].

Most investigations on edl of zinc single-crystal faces were made in solutions containing organic compounds: tetraethylammonium cations [7], hexanol [17–19], tetrabutylammonium cations [13, 14, 18, 19], camphor [18–20], cyclohexanol [14, 21], and TU [22, 23]. For these substances, dependence of adsorption properties on

crystal face was observed. The potential of adsorption–desorption peak on $C-E$ curves shifts to more negative potentials in the order Zn(0001) < Zn(1010) < Zn(1120), and this sequence was explained by increasing the negative values of E_{pzc} .

The adsorption–desorption peaks on the single-crystal faces were narrower and higher than the peaks on the polycrystalline electrodes.

The adsorption of some neutral organic compounds on the individual faces of zinc single-crystal electrodes was described by the Frumkin-Damaskin theory with the use of two parallel capacitors model [14]. For pc-Zn electrode, a departure from the two parallel capacitors model due to the energetic inhomogeneity of the surface was observed.

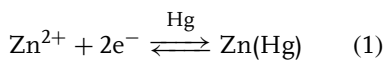
The edl parameters and adsorption parameters for various electrodes are presented by Lust et al. [24].

24.1.2

Electrochemical Properties and Kinetics of the Zn(II)/Zn(Hg) and Zn(II)/Zn Systems

24.1.2.1 Electrochemistry in Aqueous Solutions

The electroreduction of Zn(II) at a mercury electrode has been studied in aqueous media [25–38]. In noncomplexing media, this reaction can be described as



Two different mechanisms have been proposed to explain Zn(II) electroreduction in aqueous solutions, either a simple two-electron transfer in one step [28–30, 32, 33, 35, 37] or two successive one-electron transfer processes [25–27, 30] with Zn(I) as an intermediate.

From the galvanostatic and chronopotentiometric polarization measurements

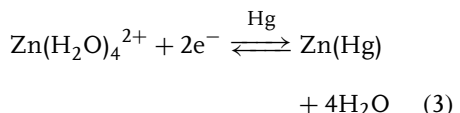
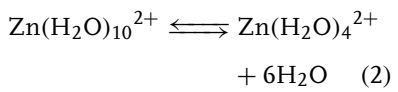
in both directions of the Zn(Hg)/Zn(II) electrode process at 25°C in 1 M chloride solutions ($1 \text{ M Cl}^- = c(\text{ZnCl}_2) + c(\text{MgCl}_2) + c(\text{HCl})$) of pH 3, Hurlen and Eriksrud [25] have found that the charge transfer occurs in two consecutive steps and that both steps are essentially symmetric. For both steps the quantitative kinetic data were presented and discussed.

Eriksrud [26] has also studied the Zn(II)/Zn(Hg) system in $x \text{ M KI} + (1-x) \text{ M KCl}$, 1 M KBr, and 1 M MeCl ($\text{Me} = \text{Li, Na, K, and Cs}$) solutions of pH 3. The substitution of chloride by bromide or iodide ions increases the rate of the Zn(I)/Zn(Hg) step more significantly than that of the Zn(II)/Zn(I) step. At iodide concentrations higher than 0.1 M, the rate of the Zn(I)/Zn(Hg) step is too high for the used experimental methods to be measured. Contrary to the Zn(I)/Zn(II) system, the rate of charge transfer for Zn(I)/Zn(Hg) step is practically independent of the kind of alkali metal cation supporting electrolyte. It can be explained by the change of Zn(II) activity in dependence on a type of cation of the supporting electrolyte.

In work [27], the Zn(II)/Zn(Hg) electrode process was investigated in 0.5 M MgSO_4 solutions at 25°C by ac and faradic rectification polarography. The Zn(II)/Zn(Hg) electrode reaction was considered as a two-step process. The kinetic parameters of both steps were evaluated.

Jindal et al. [28] have determined the kinetic parameters of Zn(II) reduction on the dropping mercury electrode (DME) in concentrated NaNO_3 , LiNO_3 , NH_4NO_3 , $\text{Mg}(\text{NO}_3)_2$, $\text{Ca}(\text{NO}_3)_2$, and NaClO_4 as supporting electrolytes, using the square-wave polarographic method. Diffusion coefficient of Zn(II) decreases with increasing concentration of supporting electrolyte caused by the change of solution viscosity.

The reversible half wave potential ($E_{1/2}$) values became higher with the increase of the concentration of supporting electrolyte, but the α values were practically constant. The rate parameters decreased with increase of radius and charge of the cation of supporting electrolyte at the same ionic strength. The number of water molecules associated with zinc ions in the solutions and with reactant, which directly takes part in the charge-transfer process, was estimated and the following reaction scheme was proposed.



The electrode reaction of Zn(II) on the DME was also studied in aqueous solutions of $(\text{NH}_4)_2\text{SO}_4$ and the kinetic parameters were determined [29].

The double-layer influence on the electrode reaction of Zn(II)/Zn(Hg) on DME in NaNO_3 solutions was studied in the concentration range from 0.01 to 1 M, using dc and ac polarography [30]. The apparent rate constants of the Zn(II)/Zn(Hg) system increase with dilution of the NaNO_3 supporting electrolyte. However, after the Frumkin correction, the rate constant was virtually independent of the supporting electrolyte concentration.

Go and Osteryoung [31] presented the alternative interpretation of the data for electroreduction of Zn(II) on the mercury electrode. They have found that in non-complexing media, zinc electroreduction may be represented by a single step with transfer of both electrons.

Osteryoung and coworkers [32, 33] optimized the square-wave voltammetry and

rapid-scan voltammetry to determine the kinetic parameters of the Zn(II)/Zn(Hg) system in 1 M NaNO₃ [32] and KNO₃ solutions with different concentrations [33].

Sluyters and coworkers [34] have studied the mechanism of Zn(II) reduction on DME in NaClO₄ solutions at different water activity (a_w) using faradaic impedance method. D_{Ox} and $E'_{1/2}$ were determined from dc polarographic curves. Hydration numbers of Zn(II) ion were estimated from the dependence of $E'_{1/2}$ on $\ln a_w$. The obtained standard rate constant was changing with a NaClO₄ concentration and the slope of the dependence of $\ln k_f$ on potential was changing with potential (see Fig. 1). Therefore, the following mechanisms were proposed:

1. Fast partial dehydration of electroactive species Zn(H₂O)_{19.6}²⁺, which loses in average 9.3 water molecules.

2. Fast transport of reactant from solution into diffusion layer.
3. Slow transfer of first electron with $\alpha_{e1} = 0.4$.
4. Fast loss of the remaining 10.3 water molecules.
5. Slow transfer of the second electron with $\alpha_{e2} = 0.4$.

In 7 M NaClO₄ solution, the hydration number of Zn(II) decreased to about 8.6.

The authors believe that the reaction plane is situated at a greater distance from the electrode surface than the Helmholtz outer plane.

The kinetic parameters of Zn(II)/Zn(Hg) electrode reaction in aqueous solution containing perchlorate, nitrate, chloride, and bromide ions were measured at different temperatures (5–50°C) [35]. The Arrhenius activation energy and thermodynamic parameters for the Zn(II)/Zn(Hg) system

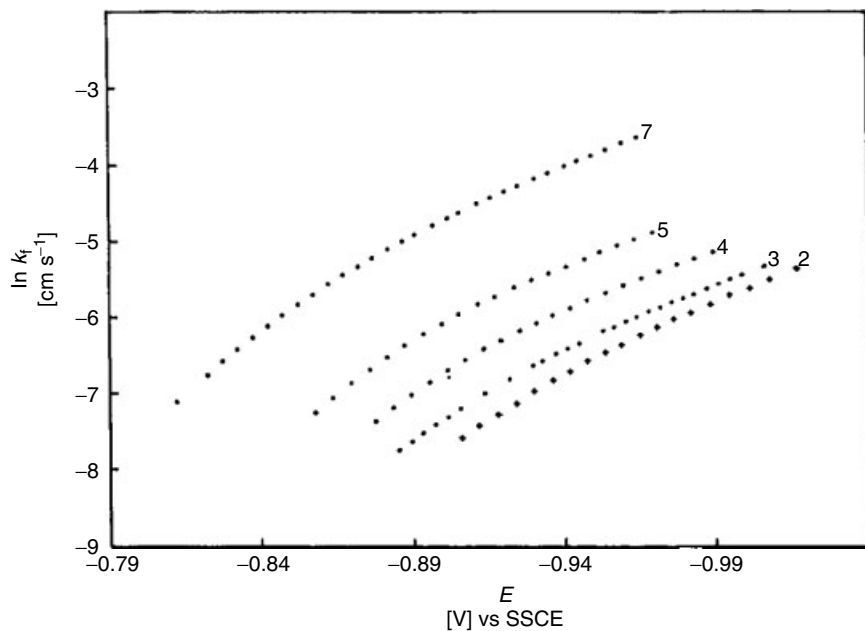
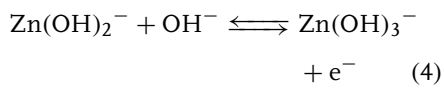


Fig. 1 Plots of $\ln k_f$ versus potential for the Zn(II) reduction in concentrated NaClO₄ supporting electrolytes. The molarity of NaClO₄ is indicated at each curve [34].

were determined from the temperature dependence of the rate constant and equilibrium potential, respectively. Empirical correlations between some pairs of kinetic and thermodynamic quantities were observed.

Hendrikx et al. [36] investigated the reaction kinetics and mechanism of zinc and amalgamated zinc electrode in KOH solutions in the concentration range 1.5–10 M using galvanostatic methods. On the basis of Tafel slopes and reaction orders for OH^- , the following rate determining step (rds) in anodic and cathodic processes was postulated:



The obtained results are in agreement with the mechanism suggested by Bockris and Nagy [37].

Sluyters and coworkers [38] have studied the catalytic influence of adsorbed iodide ions on the electroreduction of Zn(II) on the mercury electrode. It was found that the charge-transfer process proceeds through two consecutive one-electron transfer steps. Logarithms of the rate constant of both steps are linearly dependent on the amount of adsorbed iodides (Fig. 2). The experimental data were compared with the existing theoretical anion-binding model used to describe the observed results.

The Zn(II)/Zn(Hg) was also studied at dropping mercury microelectrodes.

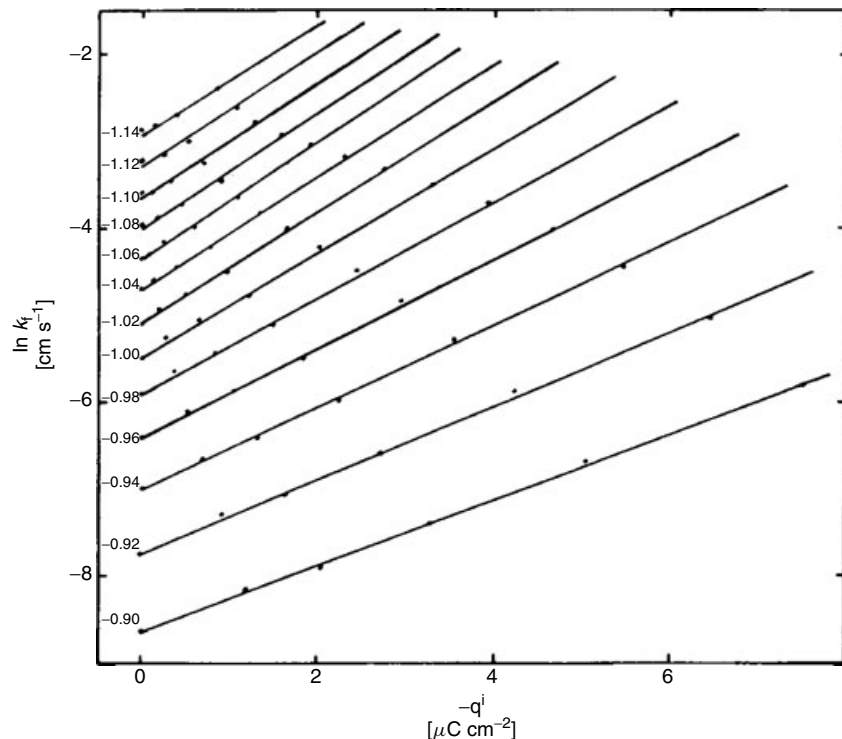


Fig. 2 The relationship between the electroreduction rate constant of Zn(II) and the amount of specifically adsorbed anion obtained at constant potentials in x M NaI + $(1-x)$ M NaClO₄ electrolyte [38]. The potentials are indicated at each curve.

Kinetic parameters were found similar to those obtained with classical mercury electrodes [39].

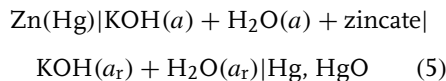
Using the dropping zinc amalgam microelectrode, detailed kinetic data were obtained [40], and the two consecutive electron transfers followed by a chemical reaction (EEC) mechanism of Zn(II) reduction could be revealed.

Dropping indium and thallium amalgam electrodes [41] were used to determine kinetic parameters of Zn(II) reduction as a function of the amalgam composition. The formal potentials were shifted to more negative values with increasing thallium and indium amalgam concentrations.

The reduction of Zn(II) from 1 M NaClO₄ in the presence of 1 mM HClO₄ was studied at the dropping gallium and mercury electrodes [42]. Zn(II)/Zn(Ga) waves were obtained after subtraction of the H₃O⁺ reduction current recorded in the absence of Zn(II)/Zn(Ga) couple.

Reduction of Zn(II) on the above mentioned electrodes [40–42] proceeds via the same two-step electron transfer mechanism that was established earlier at mercury [34].

The redox equilibria of the amalgamated zinc electrode in unsaturated and saturated zincates solutions were studied in the cell [43]



where a is the activity of species in the working compartment and a_r is the activity of species in the reference compartment solutions. It was found that the equilibrium potential of the amalgamated zinc electrode first increases and then decreases with increase of zincates concentration in the solutions. The influence of zincates concentration and its activity coefficient

on the equilibrium potential of the amalgamated zinc electrode were discussed.

Temperature effect on the electrodeposition of zinc on the static mercury drop electrode (SMDE) and glassy carbon (GC) electrode was studied in acetate solutions [44]. From the obtained kinetic parameters, the activation energies of Zn(II)/Zn(Hg) process were determined.

Quantum chemical calculations concerning reduction of the Zn(II) aqua complexes on metal electrodes were also presented [45].

24.1.2.2 Electrochemistry in Water-organic Solvent Mixtures

Kinetic parameters of zinc electrode processes in water-organic mixtures depend strongly on the composition of the surface layer, which is modified by the adsorption of organic solvent on the electrode and also on reactant solvation [46], which is changing with a solvent composition.

The electrode behavior of the Zn(II)/Zn(Hg) system was investigated in mixtures of water with several organic solvents – *N,N*-dimethylformamide (DMF) [47], dimethylsulfoxide (DMSO) [48–50], hexamethylphosphoramide (HMPA) [51, 52], 1,3-dimethyl-3,4,5,6-tetrahydro-2(1*H*)-pyrimidinone (DMPU) [53], ethylene glycol [54], and 1,2-propanediol [55]. The obtained values of Gibbs energies of transfer (ΔG_{tr}) of Zn(II) ion from water to water-organic mixtures are negative in the case of mixtures with DMF [47], DMSO [48], DMPU [53], and HMPA [51]. This suggests that Zn(II) ions are preferentially solvated by the organic components of these mixtures.

In the mixtures of water with solvents that are characterized by donor numbers (DN) higher than that of water, such as DMF, DMPU, DMSO, and HMPA, the rate of the electrode process

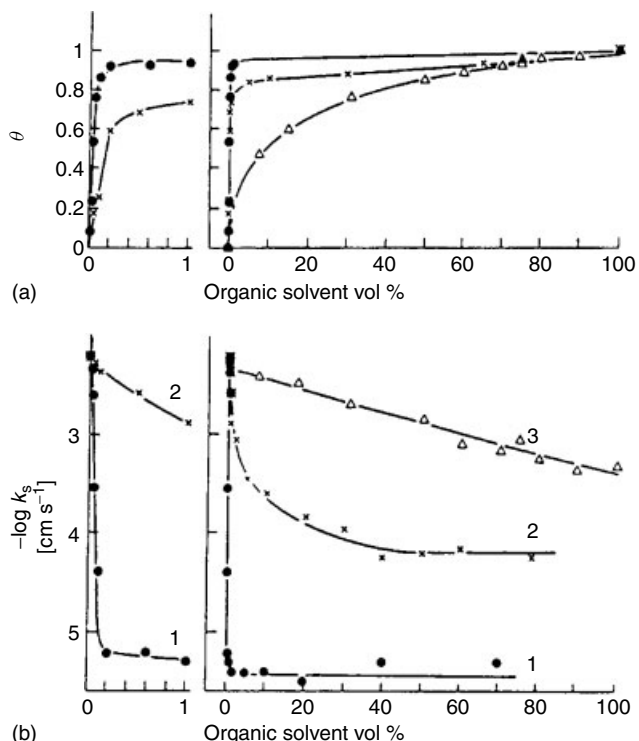


Fig. 3 (a) Adsorption isotherms of organic solvents on the mercury electrode at the formal potential of the Zn(II)/Zn(Hg) system: (1-●) HMPA, (2-x) DMPU, (3-Δ) DMSO. (b) Dependence of the standard rate constant of the Zn(II)/Zn(Hg) system on the mixed solvent composition: (1) HMPA + water, (2) DMPU + water, (3) DMSO + water mixtures [53].

of the Zn(II)/Zn(Hg) system decreased at concentrations corresponding to the rising part of adsorption isotherm of the organic component of the mixture on the mercury electrode (see Fig. 3) [53]. In these mixtures the following equation was obeyed

$$k_s = k_w(1 - \theta)^a + k_{\text{sol}}\theta^b \quad (6)$$

where k_s , k_w , and k_{sol} denote the standard rate constants in mixtures, water, and organic solvent respectively, and a and b denote the number of molecules of water and organic solvents, respectively, that interact with one reactant ion when it is penetrating the surface layer.

In the mixtures of water with organic solvents of lower than water donicity such as water-methanol [56, 57] and water-ethanol [58], the rate constant of the Zn(II)/Zn(Hg) system changes nonmonotonically with solvent composition and exhibits a minimum for such concentration of organic component in the mixture, at which the Zn(II) ions are solvated by water molecules but the electrode is already solvated by the organic solvent. The influence of the composition of such mixtures on the rate of the Zn(II)/Zn(Hg) electrode processes was described by the equation [56, 57, 59]

$$c^s = c^b \exp[-\Delta G_{\text{tr}}/RT] = c^b P \quad (7)$$

where c^s and c^b are the reactant concentrations in the surface and bulk phase respectively, and P is the partition coefficient of the reactant between bulk and surface phase.

The influence of concentration and type of supporting electrolyte [49, 52] and also temperature [50] on the Zn(II) electroreduction was investigated in water–DMSO and water–HMPA mixtures. The change of kinetic parameters under the influence of these factors was similar to that observed in pure aqueous solutions.

The influence of TU on the electroreduction of Zn(II) at the mercury electrode has been investigated in several water–organic solvent mixtures. It was found that in water–DMSO 1 M NaClO₄ solutions [60–63], the presence of TU in the solutions accelerated the rate of Zn(II) electroreduction. This accelerating effect was lower at higher DMSO content in the mixture. The acceleration of the Zn(II)/Zn(Hg) electrode process is connected with the structure of the primary solvation shell of Zn(II) ions [61]. The kinetics of Zn(II) electroreduction in water–DMSO mixtures containing 1 M NaClO₄ and TU was also investigated as a function of temperature [62]. The diffusion coefficients, formal potentials, standard rate constants, and the real activation energy of the electrode reaction were determined. The presence of TU decreased the values of real energy of activation in all investigated solutions.

The influence of TU on Zn(II) electroreduction at the mercury electrode was also investigated in mixtures of water with DMF [63, 64], methanol [62, 63, 65], ethanol, and acetone [66, 67] with NaClO₄ as a supporting electrolyte. In all these mixtures, the rate of Zn(II)/Zn(Hg) process was accelerated by adsorbed TU molecules. It was postulated that the composition

of the activated complex formed on the electrode plays the dominant role in the acceleration of the electrode processes.

The kinetics of Zn(II) electroreduction in water–methanol mixtures containing 1 M NaClO₄ and TU was also investigated as a function of temperature [62]. The values of activation energy of Zn(II) electroreduction in these mixtures reached a maximum in the solution with 20 vol % of methanol. The apparent and true rate constants of the first and second electron charge transfer of Zn(II) electroreduction on Hg electrode in aqueous solution, and in the mixtures of water with methanol 91 vol %, DMSO 70 vol %, and DMF 90 vol % containing TU were estimated [63]. The data have shown acceleration of Zn(II) electroreduction in examined solutions. Very high catalytic influence of TU was observed in the mixtures in which Zn(II) ions were specifically hydrated.

The influence of *p*-toluidine [68], 1,5-diaminonaphthalene (DAN), and *N,N'*-diphenylthiourea (DFTU) [69] in water–organic mixtures on the two-step electroreduction of Zn(II) was also examined. The presence of *p*-toluidine accelerated the first electron transfer in water –90 vol % DMF and water –91 vol % methanol [68]. DAN and DFTU had no effect on Zn(II) electroreduction in aqueous solutions but they also catalyzed this process in water–methanol mixtures [69].

24.1.2.3 Electrochemistry in Nonaqueous Solvents

The behavior of the Zn(II)/Zn(Hg) system in nonaqueous solvents containing tetraalkylammonium perchlorate ions was presented in works [70–73]. The data show that the standard rate constant, k_s , in DMF and DMSO [70] solutions changes with size of the electrolyte cation in the order k_s (TPA⁺) > k_s (TBA⁺) > k_s (TEA⁺); k_s

values also become lower with increasing concentration of the electrolyte [70, 71]. The rate of the reaction for a given supporting electrolyte is always lower in DMSO than in DMF. It is connected with a stronger solvation of Zn(II) ions by DMSO than by DMF. In DMSO solutions [71] the dependence of the logarithm of the rate constant on the electrode potential indicated a two-step process. The possible mechanisms were discussed, namely, (1) two one-electron reduction processes and (2) cation transfer through the double layer.

The electrochemical rate constants of the Zn(II)/Zn(Hg) system obtained in propylene carbonate (PC), acetonitrile (AN), and HMPA with different concentrations of tetraethylammonium perchlorate (TEAP) decreased with increasing concentration of the electrolyte and were always lower in AN than in PC solution [72]. The mechanism of Zn(II) electroreduction was proposed; in PC and AN the electroreduction process proceeds in one step. In HMPA, the Zn(II) electroreduction on the mercury electrode is very slow and proceeds according to the mechanism in which a chemical reaction was followed by charge transfer in two steps (CEE). The linear dependence of logarithm of heterogeneous standard rate constant on solvent DN was observed only for values corrected for the double-layer effect.

The electrode kinetics of the Zn(II)/Zn(Hg) system was investigated in PC + DMSO mixtures [73] containing 0.1 M TEAP. It was found that the $\log k_{s,\text{corr}}$ varies linearly with the Gibbs energy of transfer of the Zn(II) ion.

Anastopoulos [74–76] has investigated the inhibition of the Zn(II) electroreduction in organic solvents. The electroreduction of Zn(II) on the mercury electrode was inhibited by the adsorbed molecules

of triphenylphosphine oxide (TPO) in PC and AN [74, 76] and formamide [75, 76] solutions. The reaction rate decreased with increasing electrode coverage, θ , by TPO molecules. The dependences of $\ln k_f$ on $\ln (1 - \theta)$ at constant potential were linear [74] with different slopes, $r \neq$. The size parameter, $r \neq$, of the activated complex was changing from 3.0 to 5.5. It was concluded that the most probable mechanism for electroreduction Zn(II) on the mercury electrode in AN, PC, and formamide solutions is the ion transfer–adsorption mechanism.

24.1.2.4 The Influence of Organic Compounds on the Electrode Processes

The organic substances adsorbed on the mercury electrodes exert either inhibiting or catalytic influence on the process of Zn(II)/Zn(Hg) system. The inhibiting influence was observed in the presence of butyl acetate [77] and was dependent on the electrolyte concentration probably owing to the “salting-out” effect.

The catalytic influence of several organic substances on the electrode process of the system Zn(II)/Zn(Hg) was investigated intensively. In the presence of anthranilic and thiosalicylic acids [78], the rate constant of the first electron transfer k_{s1} increased with increasing surface concentration of acids, while the rate constant of the second electron transfer decreased. The catalytic effect of thiosalicylic acid is higher than that of anthranilic acid.

In the presence of TU [79, 80], the rate constant of Zn(II) electroreduction changes nonmonotonically with surface concentration of TU and a maximum was observed for $\Gamma_{\text{TU}} = 3 \times 10^{-7} \text{ mol m}^{-2}$. The accelerating effect of TU was larger at more negative potentials. The adsorbed TU molecules accelerated the first and second electron transfer. The activation enthalpies

of both steps were determined from the measurements at different temperatures.

The catalytic effect of *N,N'*-dialkylthioureas on Zn(II) electroreduction was also observed by Dalmata [81]. In this case, the rate constant of the first electron transfer increased with increasing concentration of *N,N'*-dialkylthioureas, whereas the rate constant of the second electron transfer was largely dependent on the double-layer effect.

The studies on catalytic influence of diaminotoluene isomers on zinc reaction have shown the highest accelerating effect for 3,4-diaminotoluene [82–85]. The difference in catalytic activity of these isomers resulted from the difference in complex formation with Zn(II) ions because the adsorption properties of these isomers on the mercury electrode are similar [82, 84]. Two steps of Zn(II) electroreduction were postulated in the presence of diaminotoluene isomers, with the first electron transfer as a rate-determining step. The influence of diaminotoluene isomers and pH on this electrode process was studied in acetate buffers [86].

The influence of mixed adsorption layer on the Zn(II) electroreduction was also

studied [87–90]. *n*-Butanol (BU) is an inhibitor of the Zn(II)/Zn(Hg) electrode process, whereas TU accelerates this process [87]. With the increase of TU concentration, the standard rate constant values increased to the maximum value of 0.1 cm s^{-1} , which is reached at the concentration of 0.33 M TU. When BU was added to TU solutions, the rate of the Zn(II)/Zn(Hg) process decreased. For the molar concentration ratio $[\text{BU}]/[\text{TU}] \approx 12$, the inhibition was compensated by the accelerating effect.

A similar influence was observed for mixed adsorption layers of BU/toluidine isomers [88, 89].

The obtained values of true standard rate constants of transfer of the first electron, $k'_{s,1}$, and second electron step, $k'_{s,2}$, show that the charge transfer in the first step is stronger accelerated by toluidine than the second one [89]. Greater catalytic activity of *p*-toluidine compared with *m*-toluidine was observed (see Fig. 4).

In the presence of poly(ethyleneglycols) (PEG)–TU layers [90], the Zn(II)/Zn(Hg) process could be accelerated by TU, inhibited by PEG, or the compensation of these effects could occur depending on

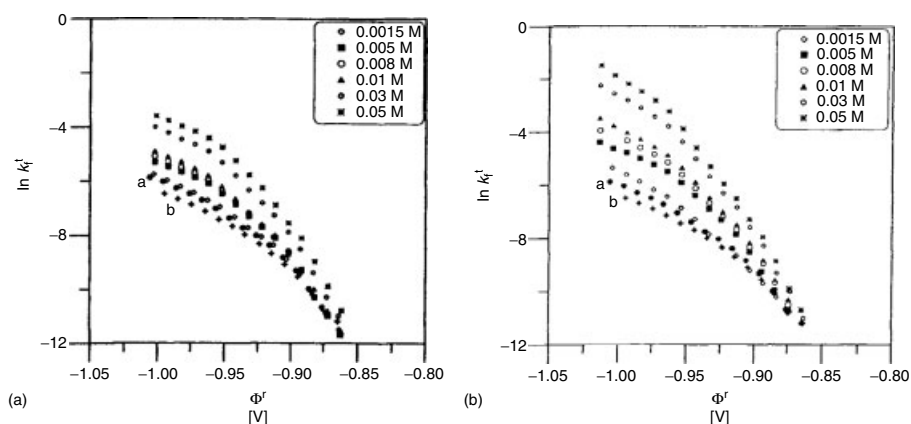


Fig. 4 Natural logarithms of corrected rate constant versus Φ' for the Zn(II)/Zn(Hg) system in 1 M NaClO₄ + 0.11 M *n*-butanol and various concentration of (a) *m*-toluidine, (b) *p*-toluidine [89].

the ratio of the molar concentrations of PEG to TU.

The quasi-reversible electroreduction processes of Zn(II) in the absence and in the presence of *N,N'*-dimethylthiourea (DMTU) were quantitatively compared by Sanecki [91]. It has been shown that in the presence of DMTU enhanced response of cyclic voltammetry and normal pulse polarography was complex and could be resolved into its regular reduction part and a part caused by the catalytic influence of adsorption of organic substance.

24.1.2.5 The Electrochemical Properties of the Zinc Complexes

The early electrochemical studies of Zn(II) complexes with inorganic ligands were reviewed in Volume 5 of the Encyclopedia [92]. In this part, only the later studies are covered.

Kinetics and mechanism of electroreduction of Zn(II) ammonia and hydroxy-ammonia complexes on the DME were investigated by Kravtsov and coworkers [93]. The reduction of Zn(II) on DME in solution of pH 9.2–12 and $[\text{NH}_3] = 0.05\text{--}2 \text{ M}$ occurred in one irreversible diffusion-limited cathodic wave. In dilute supporting electrolyte, the maximum on the polarographic waves was observed, which is connected with accumulation of insoluble reduction product on the electrode surface. The apparent rate constant for cathodic reduction process of ammonia complexes of Zn(II) was obtained.

The equilibrium potentials of saturated zinc amalgam were determined [94] as a function of concentration of free ethylenediamine in the solutions of pH 9.5, 10.5, and 11.5. The stability constants of complexes with different compositions, which were formed, have been estimated.

The effect of ligands on the character and degree of the inner-sphere reorganization during electroreduction of aqua-, aquahydroxy-, hydroxy-, and ethylenediamine tetraacetic acid (EDTA) complexes of Zn(II) [95] and electrochemical process of Zn(II) complexed by different ligands – glycinate [96], ethanol amine [97], azinyl methyl ketoximes [98], aspartame [99], glutathione [100, 101] and several cephalosporin antibiotics [102] – were studied at mercury electrodes in aqueous solutions.

The polarographic method has been used to determine the stability constants and kinetic parameters of ternary complexes of Zn(II) with L-lysine, L-ornithine, L-serine, L-phenylglycine, L-phenylalanine, L-glutamic acid, and L-aspartic acid as primary ligands and picoline as secondary ligand at pH 8.5 [103] and also of zinc complexation by extracellular polymers extracted from activated sludge [104].

Zn(II) complexes with glycine, *N*-acetyl, and *N*-benzoyl glycine were investigated in DMSO, CH₃CN, and DMF solutions [105]. Voltammetric study of the redox chemistry of 2,3-dihydroxy-quinoxaline and its zinc complexes in nonaqueous medium was also presented [106].

Metal ions, especially Zn(II), play an important role in many enzyme-catalyzed reactions involving nucleic acids, such as DNA cleavage by zinc nuclease. Therefore, the binding of Zn(II) to a 19-mer double-stranded oligodeoxyribonucleotide was investigated to understand the role of zinc in DNA cleavage catalyzed by mung bean nuclease [107].

Also, the electrochemical behavior of copper–zinc superoxide dismutase (Cu₂Zn₂SOD) [108] and porcine superoxide dismutase (PESOD) [109] were studied on the mercury electrode.

Metallothioneins (MT), low molar mass proteins, have been studied electrochemically alone and in the presence of Cd(II) and Zn(II) ions [110–115]. The electrochemical behavior of zinc MTs from rabbit liver, with respect to solution pH, as well as the influence of the addition of zinc [116] and also zinc MT from rat liver, was investigated [117] using electroanalytical techniques. Studies of complexing properties of the alpha-MT with Zn(II) were carried out using differential pulse polarography [118].

The Zn(II) complexes with acetylacetone – Zn(acac)₂, Zn(OEt)₂(acac)₂, Zn(OBu)₂(acac)₂, and also Zn(OR)₂ [119] as well as binuclear bis{1-phenylglyoxal bis(3-piperidylthiosemicarbazone)} Zn(II)}, [Zn(C₂₀H₂₆N₆S₂)]₂, complexes [120] were synthesized electrochemically using zinc metal as an anode.

The series of Zn(II) complexes with 1-amidino-3-aryl-substituted-thioureas [121], acetamidomalondihydroxymate [122], benzilbisthiosemicarbazone [123], novel fluorene-substituted terpyridine [124], perfluoroalkoxy-substituted phthalocyanine [125], and 3-carboxylacetonehydroxamic acid [126] were synthesized. The behavior of these complexes was investigated by spectroscopic and electrochemical methods.

The preparation of a novel pentadentate ligand, 2-hydroxy-5-methylisophthalaldehyde bis(*p*-methoxy thiobenzoylhydrazone), was described together with the chloro-bridged Zn(II) complexes [127]. Synthesis and electrochemical properties of some long-chain 1,4,8,11,15,18,22,25-octa-alkylated metal-free and zinc phthalocyanines were presented by Swarts et al. [128]. The zinc derivatives show higher liquid crystalline behavior than the free-metal compounds.

In the last three decades, the complexes formed with macrocyclic ligands were intensively studied. The thermodynamic data of Zn(II)-macrocyclic complexes were collected and presented by Izatt et al. [129–131]. Examples of studies of Zn(II) complexes with macrocyclic ligands were described ([132–137] and works cited therein).

Macrocyclic ligands of biological importance as thiophenolate-containing Schiff-base macrocycles and their amine analogs (see review [138]) and new helical complexes with bis(bidentate) Schiff-base ligand [139] were also described.

The metalloporphyrins were very intensively studied and their properties are presented in monographs [140–142]. The synthesis and properties of Zn(II)-porphyrin complexes are presented in selected works [143–154].

24.1.2.6 Properties of Zinc Oxide Electrode

A number of works are devoted to the electrochemical preparation of ZnO, which may have application in photocatalysis, ceramics, piezoelectric transducers, chemical sensors, photovoltaics, and others. ZnO has the same band-gap energy as TiO₂, and the oxygenation capacities for both compounds should be similar. Yamaguchi et al. [155] prepared photoactive zinc oxide films by anodizing a zinc plate. Such films could decompose gaseous acetaldehyde with the aid of black lights.

Izaki [156] has developed the two-step electrolysis technique in order to prepare a transparent and conductive ZnO film.

Pauporte and Lincot [157, 158] have developed the preparation of zinc oxide thin films by cathodic deposition at 70°C from chloride aqueous solutions with dissolved zinc(II) chloride and hydrogen peroxide.

Potential modulation method in electrodeposition of ZnO on indium tin oxide

(ITO) electrode was used by Lee and Tak, [159]. Zinc oxide with strong photoluminescence at room temperature was prepared by electrolyzing a zinc plate in ethanol solution [160]. The particles of ZnO were initially suspended in the solution and later deposited on the Pt cathode by electrophoresis. A similar method was used by Tang et al. [161]

ZnO thin films doped with In or Al were electrodeposited at a constant potential at 80°C from aqueous solutions of $\text{Zn}(\text{NO}_3)_2$ with InCl_3 or $\text{Al}(\text{NO}_3)_3$ [162].

ZnO-based organic (eosin) inorganic hybrid semiconductor compounds have been grown heteroepitaxially in one step at low temperature by a simple electrochemical method from an oxygenated zinc chloride aqueous solution [163].

Karappuchamy et al. [164] have described cathodic electrodeposition of porous ZnO thin film modified with the dye in an aqueous solution of zinc nitrate and riboflavin 5'-phosphate.

The surface morphology of films was dependent on the dye concentration, suggesting its strong interaction with the growing surface of ZnO.

Recently, the mechanism of cathodic electrodeposition of ZnO thin films from aqueous $\text{Zn}(\text{NO}_3)_2$ baths has been studied using a rotating disc electrode [165]. Non-electrochemical methods of preparation of ZnO were also described, but they are not covered in this review.

Photocurrent generation was observed after illumination of the cell with ZnO electrode; see for instance, Refs 166–169.

24.1.2.7 Electrode Processes in Molten Salts

The combination of quaternary ammonium chloride salt, such as 1-ethyl-3-methylimidazolium chloride (EMIC), with

anhydrous metal chlorides generally produces molten salts that exhibit a melting point much lower than that of the conventional inorganic molten salt systems [170, 171]. The low melting temperatures of such molten salt systems make them easier to handle, and these molten salts can be very useful for the electrodeposition of pure metals and alloys. Studies on electrodeposition of zinc have been carried out in acidic AlCl_3 -EMIC melt [172] and in acidic AlBr_3 -dimethylethylphenylammonium bromide (DMEPB) melt [173]. While good zinc deposits could be obtained from the acidic AlCl_3 -EMIC melt [172], aluminum was codeposited with zinc from the AlBr_3 -DMEPB melt [173].

The electrodeposition of zinc on polycrystalline Au, Pt, and tungsten electrodes was preceded by underpotential deposition (UPD) [172]. The formal potential of $\text{Zn}(\text{II})/\text{Zn}(0)$ couple and diffusion coefficient of Zn(II) were also determined [172].

The mixtures of ZnCl_2 -EMIC also exhibit a lower melting temperature than the conventional inorganic molten salts. The Lewis acidity of ZnCl_2 -EMIC ionic liquid can be adjusted by varying the molar ratio of ZnCl_2 to EMIC [174]. The ionic liquids that have a ZnCl_2 mole fraction higher than 33 mol % are acidic because there are not enough chloride ions to fully coordinate with Zn(II). The melts containing less than 33 mol % ZnCl_2 are basic. In such liquids, the major zinc species is probably ZnCl_4^{2-} . Underpotential deposition of zinc was observed on Pt and Ni electrodes in acidic liquids.

The electrodeposition of zinc on GC, nickel, and tungsten electrodes was investigated in ZnCl_2 -EMIC, and AlCl_3 -EMIC [175, 176]. The nucleation on GC required a larger overpotential than on the other used electrodes. The addition of

PC [175] or benzene [176] as a cosolvent in the plating solution hinders the zinc nucleation.

The zinc electrodeposition on Au(111) from molten salts containing 58–42 mol % AlCl_3 –1-methyl-3-butylimidazolium chloride (MBIC) and 1 mM Zn(II) was investigated also using scanning tunneling microscopy (STM) [177]. In the underpotential range, three successive Zn monolayers were resolved, and the thickness of the Zn layers in the UPD range had a value of 2.4 ± 0.2 Å.

The influence of ethylene glycol and water content on the zinc electrodeposition from ZnBr_2 –1-ethyl-3-methylimidazolium bromide (EMIB) was investigated [178]. The structure of the deposits was dependent on the mole ratio of ZnBr_2 to EMIB, water concentration, and presence of ethylene glycol.

The zinc electroreduction investigated [179] in urea-chlorides melts was found to be reversible with two-electron transfer.

In ZnCl_2 –EMIC (1:1) melt containing Cu(I), the electrodeposition of Cu–Zn alloys on tungsten and nickel electrodes was carried out [180]. The composition of the Cu–Zn deposit was changed by deposition potential, temperature, and Cu(I) concentration in a plating bath.

Zinc telluride was obtained by deposition on the nickel electrode from 40 to 60 mol % ZnCl_2 –EMIC melt containing Te(IV) and PC [181]. The composition of the Zn–Te deposits was dependent on the deposition potential and Te(IV) concentration in the plating solution.

Electrodeposition of Zn–Co alloys on Ni, W, and GC electrodes from 40 to 60 mol % ZnCl_2 –EMIC melt containing Co(II) was investigated [182]. X-ray measurements indicated that Zn–Co alloy deposits with low zinc content are amorphous and the crystalline nature of Zn–Co alloys

increases as the zinc content in deposits rises.

The Zn–Cd alloys were obtained from ZnCl_2 –EMIC melt containing Cd(II), during reduction on Pt, Ni, or W electrodes at the potentials sufficient to reduce Zn(II) to metal [183]. The composition of Zn–Cd alloys was dependent on the deposition potential, temperature, and Cd(II) concentration.

The same researchers [184] studied electrodeposition of Zn–Sn alloys on tungsten and GC electrodes from ZnCl_2 –EMIC ionic liquid containing Sn(II). The Zn–Sn codeposits consist of two-phase mixtures of Zn and Sn.

Also, the Pt–Zn electrodeposition on tungsten electrode was studied in ZnCl_2 –EMIC melts containing Pt(II) [185]. The morphology of Pt–Zn alloys is dependent on the deposition potential and Pt(II) concentration in the plating solution. Pt–Zn alloys were also obtained on the electrode surface when Zn(II) was reduced on Pt electrode.

For Zn–Mg alloys in ZnBr_2 –EMIB–ethylene glycol melts [186] and ZnBr_2 –EMIB–glycerin containing Mg(II) [187], the grayish metallic colored electrodeposits were obtained. The Mg content in Zn–Mg electrodeposits varied from 12 to 25 mol % [187].

Zn–Fe alloys were deposited and studied on the nickel electrode in ZnCl_2 –EMIC melts [188]. The composition of Zn–Fe alloy was also dependent on the deposition potential and Fe(II) concentration in the plating solution.

The electrolysis of a mixture of ZnCl_2 with alkaline chlorides and the effect of different elements were investigated as a method to extract zinc from ores and industrial wastes. The studies on electrolysis of ZnCl_2 in molten ZnCl_2 – KCl – NaCl

chlorides at 450°C have shown ohmic limitations [189]. The energy consumption is to a large extent determined by the anodic process of chlorine evolution.

24.1.3 Deposition and Underpotential Deposition of Zn on Solid Electrodes

24.1.3.1 Underpotential Deposition of Zinc

There was significant interest in zinc UPD, since zinc plays a major role in plating technology. Underpotential deposition of zinc in acidic solutions on polycrystalline Pt electrode was shown by using cyclic voltammetry [190]. Later, Zn UPD was also demonstrated on Au and Pd electrodes in acidic and alkaline solutions [191, 192].

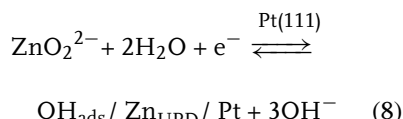
In recent years, there have been a number of works on Zn UPD on single-crystal electrodes.

UPD of various metal ions is accompanied by the adsorption of anions. Evidently, such additional adsorption makes stoichiometric calculations based on the determined charge value misleading.

24.1.3.1.1 Zn UPD on Pt Underpotential deposition of zinc was observed on Pt(111) in alkaline solution as a sharp cyclic voltammetric (CV) peak, in contrast to the behavior on polycrystalline Pt, when several broad UPD peaks were observed [193]. The changes of the peak potential with concentration of ZnO_2^{2-} were equal to 60 mV/ $\log [\text{ZnO}_2^{2-}]$ and led to the apparent electron transfer number $n_a = 1$.

This value is discussed in terms of two-electron transfer when Zn^{2+} is reduced to free zinc on Pt(111) surface with a true electron transfer number of $n = 2$. Also, induced adsorption of OH^- ions takes place to give OH_{ads} in an oxidative process.

Therefore, the overall UPD process may be represented by the reaction



to give the apparent electron transfer number $n_a = 1$.

The UPD of Zn on Pt(111) electrode in phosphate solutions (pH 4.6 or 3.0) was studied by Aramata and coworkers [194] in the presence of adsorbed anions. In phosphate solutions, the Zn UPD obeyed the Langmuir adsorption mechanism. On the addition of 10^{-3} M Br^- ions, the Zn^{2+} ion UPD potential shifts 120 mV to more negative values. The desorption of specifically adsorbed anions is suggested to trigger the UPD of Zn.

The effect of adsorbed anions on Zn UPD has been studied using CV [195] in 0.1 M KH_2PO_4 of pH 4.4 with and in the absence of halide ions. The charge transfer to Zn^{2+} was initiated near the desorption potential of adsorbed anions. The Zn UPD potentials moved to more negative values following the order of the anion adsorption strength $\text{H}_2\text{PO}_4^- < \text{Cl}^- < \text{Br}^- < \text{I}^-$. In the presence of Br^- and I^- ions, the CV peaks were narrower than in the presence of Cl^- or H_2PO_4^- anions. The number of transferred electrons to one Zn^{2+} ion was estimated to be about two by correlating with the number of electrons for the anion discharge with and without Br^- ions.

The specific adsorption of H_2PO_4^- ions that accompany the UPD of Zn^{2+} ions on Pt (platinized electrodes obtained by Pt electrodeposition on the gold-plated plastic foil) electrodes was studied by using a radiotracer method with ^{32}P phosphate species in the presence of a great excess of ClO_4^- ions [196]. It was found that the specific adsorption of species induced

by Zn adatoms depends on the pH value and at constant potential on Zn^{2+} concentration.

The same authors [197] have studied the specific adsorption of other anions, which accompany the Zn UPD on Pt electrodes. Again, radiotracer technique with ^{35}S -labeled sulfate and ^{36}Cl -labeled chloride ions has been used. It was found that sulfate ions adsorb on the top of Zn adatoms, and the adsorption strength of Cl^- ions on the Zn adlayer is significantly lower than that of HSO_4^- (SO_4^{2-}) ions.

Comparative studies of Zn UPD on Pt(111) and Au(111) electrodes were carried out with consideration of the anion adsorption/desorption process [198].

In the case of Zn UPD, the number of electrons transferred, n , was two, which implies that adsorbed anions are desorbed in the UPD region and readsorbed on the UPD metal in a similar amount.

Underpotential codeposition of Cu^{2+} and Zn^{2+} at Pt(111) was examined using voltammetry [199]. In phosphate solutions of $pH = 4.5$, the codeposition of Cu^{2+} and Zn^{2+} was found to occur when Cu^{2+} concentration was lower than that of Zn^{2+} ions.

24.1.3.1.2 Zn UPD on Au In the case of Au(111) [198], specifically adsorbed anions are not present in the UPD region, and the value n_a equal to one was explained by the anion adsorption on the UPD Zn by the oxidative process.

The UPD of Zn^{2+} on Au(111), Au(100), and Au(110) was studied in phosphate buffer with addition of $NaClO_4$ and $NaCl$ [200]. The apparent number of electrons transferred in the UPD process was nearly one, irrespective of the single-crystal face. Although UPD shift potential ΔE_p was independent of the kind of solutions, the CV characteristics were altered in different solutions. In $NaCl$ solutions, two UPD peaks appeared in contrast to the case of phosphate and perchlorate solutions.

The influence of anion adsorption on Zn UPD on Au(111) was further studied in the presence of halide ions [201]. The order of the adsorption strength of the anions on Zn UPD was found to be different from that of specific adsorption on a substrate Au electrode $ClO_4^- < SO_4^{2-} \leq PO_4^{3-} < Cl^- < Br^- < I^-$. In phosphate solutions, chloride and bromide ions did not influence the Zn UPD, and iodide ions inhibited this process (see Fig. 5).

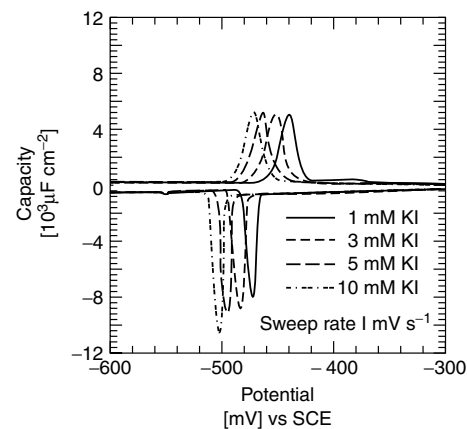


Fig. 5 Cyclic voltammograms of the $Zn^{(II)}/Zn$ system obtained at 1 mV s^{-1} on Au(111) in the solutions with $0.1\text{ M }K_2H_2PO_4$, $1\text{ mM }Zn^{(II)}$, and various KI concentrations [201].

The UPD of zinc on Au(111) in phosphate solutions at pH 4.6 was also studied using the STM method [202]. It was shown that the oxidative adsorption of phosphates occurs on the UPD Zn at Au(111) by the UPD-induced adsorption.

24.1.3.2 Zinc Electrodeposition on Solid Electrodes

Various processes are generally involved in metals electrodepositions – ion transport, ion adsorption, nucleation and growth from adions, and multistep charge transfer [203–206]. The electrodeposition process can be perturbed by the presence of inhibiting species adsorbed at the electrode. The impedance spectroscopy was used for elaboration of the reaction models accounting for the experimental data obtained during electrodeposition from various electrolytes. In alkaline solutions, the discharge of zincate ions takes place in multisteps [36, 37, 207, 208]. In acidic solutions, the electroreduction of Zn(II) ions proceeds in several steps with the participation of the intermediate adions Zn^{+}_{ad} [25]. Usually, small amounts of organic additives improve the homogeneity and the surface state of the zinc deposit.

24.1.3.2.1 Electrodeposition on Zn

Electrodes Rezaite and Vishomirskis [209, 210] have investigated the effect of potassium cyanide on the electrodeposition of zinc from zincate solutions on the Zn electrode. It is known that cyanide added to the zincate solution led to high-quality zinc coatings. The presence of KCN decreased the limiting current of Zn(II).

The behavior of zinc and zinc oxide electrode in 5.3 M KOH in the presence of alkaline earth oxides, SnO , $Ni(OH)_2$ and $Co(OH)_2$, was examined using cyclic voltammetry by Renuka et al. [211].

The aging behavior of the porous zinc electrode in 6 M KOH in the presence of different electrolyte additives such as ZnO , $LiOH$, and KF has been studied using cyclic voltammetry by Shivkumar et al. [212]. The mechanism of the electrode reaction in all these electrolytes was investigated.

Wang et al. [213] investigated the effect of bismuth ion and tetrabutylammonium bromide (TBAB) on the dendritic growth of zinc in alkaline zincate solution on Zn electrode. It was found that this growth is inhibited by the synergistic effect of Bi(III) and TBAB at higher overpotentials. The zinc electrodeposits

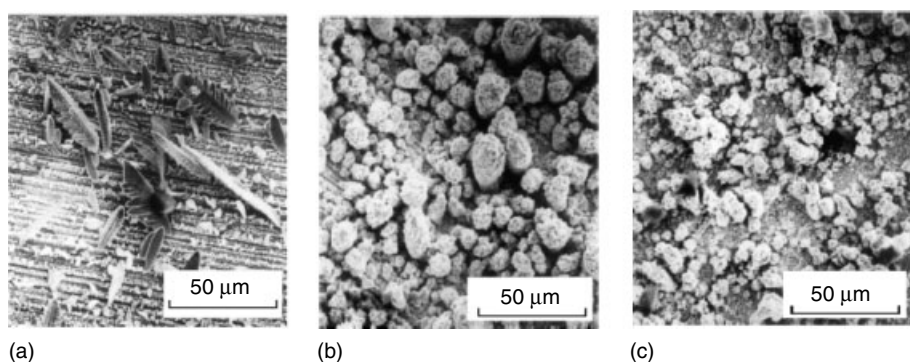


Fig. 6 Zinc electrodeposits at $\eta = -0.200$ V (a) from the alkaline solutions, (b) from the alkaline solutions containing 0.1 g l^{-1} Bi(III) [213], (c) as in b but with addition of 0.02 g l^{-1} TBAB.

obtained at the cathodic overpotential equal to -200 mV in alkaline solutions with and without additives are presented in Fig. 6.

Using the rotating disk electrode, Selivanov et al. [214] have investigated the zinc electrodeposition from zincate electrolyte containing polyethylene polyamine. The limiting current density of $[\text{Zn}(\text{OH})_4]^{2-}$ ion diffusion through a film of zinc oxides and hydroxides is shown to be responsible for the formation of dark zinc deposits in the potential range from -1.33 to -1.47 V.

The thermal phenomena – heat flux, heat quantity, and temperature gradient – occurring at the zinc electrode during the electrolysis from aqueous solutions containing zinc salt were investigated [215].

Zinc electrodeposition on zinc electrode with rough surface exhibited potential oscillations accompanied by fern-leaf-shaped deposits, contrary to the case

of zinc electrode with a smooth surface. A new autocatalytic mechanism was proposed [216] to explain these phenomena systematically.

The influence of Pb^{2+} ions on the kinetics of zinc electrodeposition on Zn electrode in acidic sulfate electrolyte was discussed [217] in terms of a reaction model involving hydrogen adsorption and evolution, a multistep mechanism for zinc deposition and the overall reaction for zinc dissolution. The strongly adsorbed Pb_{ads} inhibited all the reactions taking place on the zinc electrode.

The kinetics of zinc deposition on Zn electrode from a concentrated $\text{ZnCl}_2 + \text{KCl}$ electrolyte containing commercial long-chain polymer additives was investigated using impedance spectroscopy [218]. The additive modifies the deposit morphology by changing some specific rates of the electrode reaction surface steps (see Fig. 7).

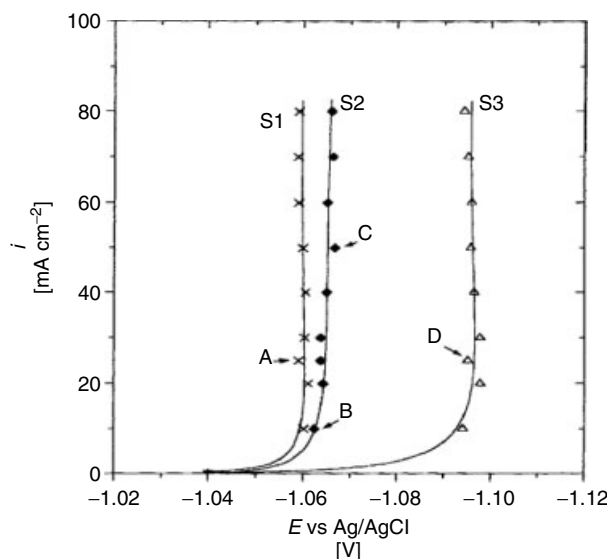


Fig. 7 Experimental steady state polarization curves of $\text{Zn}(\text{II})$ electroreduction for various electrolytes: (S1) additive-free bath ($1.6 \text{ M } \text{ZnCl}_2 + 5.3 \text{ M KCl}$); (S2) industrial bath ($1.6 \text{ M } \text{ZnCl}_2 + 5.3 \text{ M KCl} + \text{long-chain polymer} + \text{pH buffer of pH 4.7}$); solution (S3) ($1.6 \text{ M } \text{ZnCl}_2 + 5.3 \text{ M KCl} + \text{long-chain polymer}$ with the same additive at the concentration of 10^{-3} M in volume) [218]; $t = 62^\circ\text{C}$.

Zhu et al. [219] have also investigated the influence of surfactants on the electrochemical behavior of zinc electrodes in alkaline solutions. In the presence of surfactants, the dendrite growth is reduced and the zinc deposit is more uniform and compact. Therefore, perfluorosurfactants can be used for decreasing the corrosion of zinc batteries.

The influence of the nonionic surfactant Forafac F1110 on the kinetics of zinc deposition in sulfate or chloride solutions was investigated using voltammetry and impedance spectroscopy [220]. The additive slightly modifies the rate of the reactions corresponding to the adsorption and evolution of hydrogen on the zinc electrode, thus affecting very little the current efficiency of zinc deposition. The additives (1) inhibit different steps of charge transfer leading to the zinc deposit and (2) modify the kinetic parameters of the slow reactions involved in the formation and destruction of the active sites for zinc deposition.

The electrochemical properties of secondary zinc electrodes after La addition (by the solid-phase diffusion method) have been investigated by Yang et al. [221]. The results showed that the La addition to the zinc electrode significantly improved the life cycle. After 80 cycles at 100 mA g^{-1} , the zinc electrode with 0.5 atom % La addition showed the best cyclic behavior. La addition significantly suppressed the corrosion behavior of secondary zinc electrodes, and the growth of zinc dendrites was effectively inhibited and the formation of zinc deposition was changed. On the Zn electrode surface, $\text{La}_2\text{O}_3/\text{La(OH)}_3$ was formed and this prevented the discharge products of zinc electrodes from dissolving in the alkaline electrolyte and suppressed the dendrite growth during charging.

Similar results were obtained by Zhu et al. [222], who have investigated the influence of lanthanum and neodymium hydroxides on the properties of secondary alkaline zinc electrode.

The kinetics of cathodic deposition and anodic dissolution of zinc on Zn or Pt electrodes in DMSO, DMF, and AN solution was investigated by Białozór and Bandura [223].

24.1.3.2.2 Electrodeposition on Other

Electrodes Trejo et al. [224] have investigated the influence of the zinc chloride concentration on the zinc nucleation process on GC electrode in KCl solutions under conditions close to those employed in commercial acid deposition baths for zinc. The results show that the nucleation process and the density number of sites are dependent on ZnCl_2 concentration. The deposits are homogeneous and compact, although a change in morphology is observed as a function of ZnCl_2 concentration.

Trejo et al. [225, 226] have also investigated the influence of several ethoxylated additives (ethyleneglycol and PEG polymers of different molecular weights) on the nucleation, growth mechanism, and morphology of zinc electrodeposited on GC from an acidic chloride bath. Results have shown that the presence of additives modifies the nucleation process and determines the properties of the deposits.

Chronoamperometric experiments on zinc electroreduction on GC from acetate solutions showed that the nucleation density increases with increase of temperature [44]. Moreover, the nucleation rate constant is always very large, equal to $1.41 \times 10^9 \text{ s}^{-1}$. This indicates that the mechanism of zinc electrodeposition on the GC electrode follows a three-dimensional instantaneous nucleation and growth model within the controlled temperature range.

The same mechanism of zinc electrodeposition on the GC electrode was observed in sulfate, chloride, and acetate ion solutions [227]. The anions mainly affected the nucleation densities during zinc deposition, which resulted in a different surface morphology. The nucleation rate constant was the same in the chloride and sulfate solutions and was equal to $1.22 \times 10^9 \text{ s}^{-1}$. In the presence of acetate and chloride ions, the deposited zinc film tends to grow in a multilayered pattern, while in sulfate solution, the zinc deposition forms irregular grains. A new approach to the estimation of zinc electrocrystallization parameters on the GC electrode from acetate solutions was described by Yu et al. [228].

The influence of convection, pH, and Zn(II) of solution on electrodeposition on GC electrode of zinc–cobalt alloys was studied by Gómez and Vallés [229]. The presence of zinc in the bath always decreases the rate of the cobalt deposition.

The influence of quaternary aliphatic polyamine (QAA) on zinc electrodeposition from an alkaline non-cyanide bath was investigated [230]. In the presence of QAA, the exchange current density decreased and zinc deposit had a smaller grain size.

The electrodeposition of Zn on highly oriented pyrolytic graphite from $\text{ZnSO}_4 + \text{Na}_2\text{SO}_4$ solution was analyzed in the presence and absence of gelatin [231]. The morphology of the Zn-formed crystals was affected by the gelatin adsorption and the nucleation rate was decreased.

An experimental study of zinc electrodeposition on copper wire from 0.1 M zincate solution in 1.0 M KOH was presented by Simić et al. [232]. A possible mechanism of the formation of spongy zinc deposits was considered. Also, it was shown that in the case of a square-wave pulsating overpotential regime, the deposit was less

agglomerated than the one obtained in the case of direct overpotential regime.

The Zn electrodeposition [233] on gold electrode was investigated in a solution of $\text{H}_3\text{BO}_3 + \text{NH}_4\text{Cl} + \text{Na}_2\text{SO}_4$ at pH 4.4 using electrochemical impedance spectroscopy and electrochemical quartz crystal microbalance (EQCM).

Also, the influence of benzylideneacetone on the mechanism of zinc electrodeposition on Pt electrode in a chloride acidic bath was studied [234].

Rodríguez-Torres et al. [235] have used ammonia-containing baths for Zn–Ni alloy electrodeposition on Pt. Zinc and nickel species exist in the form of $[\text{Zn}(\text{NH}_3)_4]^{2+}$ and $[\text{Ni}(\text{NH}_3)_6]^{2+}$ complexes in such solutions. The deposition at pH 10 was investigated and compared with deposition from ammonium chloride baths at pH 5. The Ni content in the alloys was found to be 40–60% higher from the ammonia-containing bath than from the acidic baths. The deposition mechanism was found to be affected by complexation of the metal cations by ammonia.

Raeissi et al. [236, 237] showed that temperature, pH, and current density affected the morphology and texture, as well as the nucleation mechanism of the zinc deposits on carbon steel electrode.

Zn_3N_2 reversibly reacts with lithium in electrochemical conversion reaction to give LiZn and a matrix of $\beta\text{-Li}_3\text{N}$ [238]. Upon oxidation, LiZn transformed into metallic Zn, while $\beta\text{-Li}_3\text{N}$ contributed to the transformation into LiZnN .

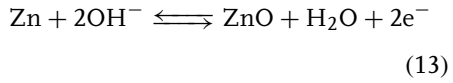
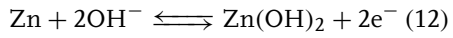
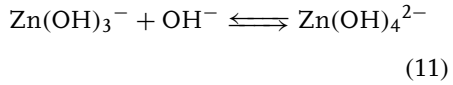
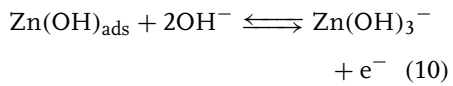
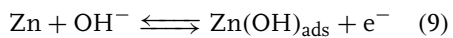
24.1.4

Passivation and Corrosion of Zinc

24.1.4.1 Anodic Dissolution and Passivation of Zinc

The electrochemical behavior of zinc anode was intensively investigated. A survey

of the literature data indicates that the nature and mechanism of the zinc passivation in alkaline solutions is the subject of debate. Various mechanisms involving several intermediate species have been proposed for passivation of Zn in alkaline solutions [36, 37, 92, 207, 208, 239–246]. In some works, $\text{Zn}(\text{OH})_2$ has been proposed to be the passivating species [243, 244], while other authors assume that this role is played by ZnO [240, 245]. Moreover, in certain cases, the passive film consists of a dual layer, composed of ZnO and $\text{Zn}(\text{OH})_2$ [243, 247, 248] or of two types of ZnO [240, 243, 247, 248]. The oxide growth on the zinc electrode under prevailing experimental conditions could be explained on the basis of the following reactions [249, 250]:



The thickness of the passive layer formed on Zn electrode in alkaline solutions changes with operating conditions and reaches about 50 nm [244, 251]. Recently, it was found that the rate of oxide growth in the passive region increases with decreasing concentration of borate and increases with the imposed current density [252].

Influence of pH, solvent composition, type of anions and surfactants on zinc electrochemical dissolution, and passivation was studied intensively. The nature

of the passive state on zinc was investigated in alkaline [253–256] and borate solutions [253, 257]. It was found that the metal is covered by a duplex film comprising a highly defective ZnO barrier layer covered by a precipitated outer layer of ZnO or $\text{Zn}(\text{OH})_2$. The formation of the latter can be inhibited by optimal solution composition.

Zinc dissolution was also investigated in phosphate solutions over a wide pH range of 4.5–11.7 [258], in aerated neutral perchlorate [259], and in sulfate solutions [260, 261]. In the phosphate solutions [258], zinc phosphates were present in a passive layer of zinc electrode, while for sulfate solutions a kinetic model of spontaneous zinc passivation was proposed [261].

The anodic dissolution of bulk zinc [262] and zinc-coated steel sheet [263] in aerated sulfate media was studied. During this process, a compact nonstoichiometric zinc oxide layer was formed on the surface of zinc.

The anodic dissolution of zinc [233, 264] was investigated in solution $\text{H}_3\text{BO}_3 + \text{NH}_4\text{Cl} + \text{Na}_2\text{SO}_4$ at pH 4.4 using electrochemical impedance spectroscopy and EQCM. In the same solution, zinc anodic dissolution of different galvanized steel sheets of zinc [265] was studied. The postulated [41, 266] mechanism of Zn oxidation in acidic solution corresponds to two consecutive monoelectronic transfers.

The anions such as halogenides stimulate the active dissolution of zinc and tend to break down the passive film. Therefore, the effect of halogenide anions [267–270], thiocyanate [271], and sulfur-containing anions [272–274] in different media was studied. There are also anions that inhibit active dissolution and pitting corrosion, and this effect decreases in the

order $\text{Cr}_2\text{O}_7^{2-} > \text{CrO}_4^{2-} > \text{WO}_4^{2-} > \text{MoO}_4^{2-}$ [274].

Addition of sodium dodecyl benzene sulfonate to dilute alkaline electrolyte depresses the passivation of zinc surface [275]. Owing to the dodecyl benzene sulfonate adsorption, the passive layer on zinc has a loose and porous structure. Zinc electrodissolution was inhibited by the presence of sodium metasilicate [276] and some acridines [277]. The protection effect was described by a two-parameter equation.

The anodic dissolution experiments of zinc rotating disk electrode were carried out in alkaline electrolyte [278] and in solution at pH 5.5 containing NH_4Cl and $\text{NH}_4\text{Cl} + \text{ZnCl}_2$ [279], $\text{NH}_4\text{Cl} + \text{NiCl}_2$, and $\text{NH}_4\text{Cl} + \text{NiCl}_2 + \text{ZnCl}_2$ [280, 281]. The zinc electrode was covered by a porous film composed of a mixture of metallic zinc and zinc hydroxide [279]. In Ni-containing solutions, the passivation of Zn was a result of Zn–Ni alloy formation and $\text{Zn}(\text{OH})_2$ precipitation [280].

The influence of illumination [255, 282] and magnetic field [256] on the passive layer behavior and anodic current oscillations was also studied.

24.1.4.2 Corrosion

Zinc and zinc-coated products corrode rapidly in moisture present in the atmosphere. The corrosion process and its mechanism were studied in different media, nitrate [283], perchlorate [259], chloride ions [284], and in simulated acid rain [285]. This process was also investigated in alkaline solutions with various iron oxides or iron hydroxides [286] and in sulfuric acid with oxygen and Fe(III) ions [287]. In the solution with benzothiazole (BTAH) [287], the protective layer of BTAH that formed on the electrode surface inhibited the Zn corrosion.

Youssef et al. [288] studied the corrosion of nanocrystalline zinc produced from chloride electrolyte with polyacrylamide and TU as additives.

The influence of several anions such as perchlorate [259], halogenide [267–270], sulfate ions [272, 273], and their concentration on breakdown of the passive layer and pitting corrosion was also analyzed.

A great research interest concerns zinc corrosion inhibition. Chromate solutions were used [289–293] for the inhibition of zinc corrosion. The surface film contained a mixture of zinc oxide and hydroxide of chromium(III). Different behaviors of the passivated zinc electrode was observed depending on the cation of the used chromate [293].

Because Cr(VI) is very toxic, the chromate ions were replaced by other solutions or reagents in corrosion protection. Therefore, a chromate-free, self-healing protective film was prepared on a zinc electrode using as inhibitors $\text{Ce}(\text{NO}_3)_3$ and sodium phosphate Na_3PO_4 . [294–299]. The film was composed of an inner layer of Ce_2O_3 with small amounts of Ce^{4+} and an outer layer of Na_3PO_4 containing CePO_4 . The formed layer suppressed the cathodic process. The anodic process was inhibited by coverage of surface with precipitates of $\text{Zn}(\text{OH})_2$, $\text{Zn}_3(\text{PO}_4)_2 \cdot 4 \text{ H}_2\text{O}$, and CePO_4 .

The corrosion of zinc was also inhibited by Al^{3+} , La^{3+} , Ce^{3+} , and Ce^{4+} cations [300].

An important group of zinc corrosion inhibitors are compounds that are adsorbed on the metal surface and/or that form precipitate with Zn(II) on the zinc surface together with zinc hydroxide and oxide [301–307].

Synergistic influence of Ce(III) ions and sodium silicate $\text{Na}_2\text{Si}_2\text{O}_5$, [308] and

octylthiopropionate [302] was also discussed.

Some ligands chelating Zn(II) ions were also found to be effective corrosion inhibitors [309, 310] owing to the growth of an organometallic layer strongly attached to the metal surface, which prevent the formation of porous corrosion products.

The corrosion behavior of zinc-coated steel electrodes electrochemically modified by polypyrrole [311] and zinc electrode in solution containing reducing polymer (Polyox WSR-301) [312] was investigated.

Photocorrosion of zinc [282, 313] and zinc alloys [314–316] was studied in NaCl solution.

The spatial distribution of Zn(II) during galvanic corrosion of a Zn/steel couple in 0.01 M NaCl was studied by Tada et al. [317].

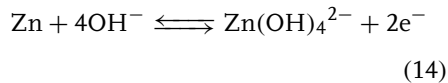
Park and Szpunar [318] have shown that the texture, surface morphology, alloy composition, and phase composition of zinc-based coatings strongly influence corrosion resistance.

24.1.5 Applied Electrochemistry

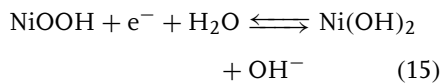
24.1.5.1 Batteries

There is significant interest in the development of batteries, which have zinc as one of the electrodes. General information about such devices is given in the book of Vincent and Scrosati [319]. In recent years, several types of batteries, which use zinc, were developed and/or improved.

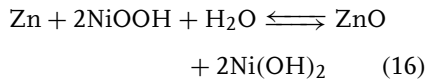
24.1.5.1.1 Ni-Zn Cells These alkaline storage batteries exhibit good performance. They are based on the following electrochemical processes:



and



and the overall reaction is



In a rechargeable battery, the initial material is the ZnO powder, which is dissolved in KOH to form $\text{Zn}(\text{OH})_4^{2-}$. Zincate is reduced to Zn during the charging process.

The progress in sealed-type Ni-Zn cells has been reviewed by Jindra [320, 321]. In the first paper, the period 1991–1995 and in the second paper the period 1996–1998 was covered. One may find here the novelties in the development of this type of batteries.

Later, a polymerized zinc electrode was developed [322] using wetting polymer and plastically shaping polymer materials, which improved the performance of batteries for many cycles.

There were also studied processes that cause passivation of the zinc electrode in many cycling operations of Ni-Zn batteries [323]. Positive effect for increasing the reaction reversibility was found when zinc-ion additives were introduced to the positive electrode [324].

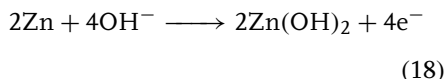
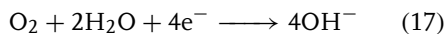
The same group have also studied [325] a mechanism of zinc(II) transfer from the negative to positive electrode of a Ni-Zn battery.

The influence of zinc intercalation on processes in nickel oxide electrode and on the long life of Ni-Zn batteries was also studied.

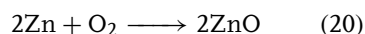
Also, an improved method for the fabrication of zinc electrodes was presented [326], which consists of electrolytic

deposition of active zinc material on very thin microfibrous copper substrates. Such zinc electrodes with various additives were examined and tested for performance. A new structure of electrode design was employed.

24.1.5.1.2 Zn–Air Batteries The reactions occurring in these batteries may be represented by the following equations:



Overall reaction is



with the theoretical voltage 1.65 V.

For good performance of the battery, both reactions, oxygen reduction (positive electrode) and zinc oxidation (negative electrode), should be fast. It is known that the oxygen electroreduction reaction is quite complex and relatively slow. Therefore, the acceleration of the rate of this reaction in the Zn–air battery is important for the good performance of the battery. For this purpose, Wang et al. [327] prepared a perovskite-type $\text{La}_{0.6}\text{Ca}_{0.4}\text{CoO}_3$ compound as a catalyst, which improves such properties as discharge capacity.

Earlier, such catalyst was used for the preparation of a 100 W rechargeable bipolar zinc–oxygen battery [328]. Also, nanostructured MnO_2 combined with mesocarbon microbeads was prepared and used [329] in such batteries as a catalyst for oxygen reduction, which has a very good electrocatalytic activity with respect to oxygen, and in comparison with electrolytic MnO_2 . Prepared with this material, the all solid-state zinc–air cell

has good discharge characteristics at room temperature.

For the development of a long-lived, electrically rechargeable zinc–air battery, the structure and wettability of pasted zinc electrodes (with 1–10% cellulose) were optimized [330]. It was found that the addition of 10 wt % cellulose to the pasted zinc electrode, improved the life cycle and peak power drain capacity of the battery substantially.

The zinc electrode in such batteries was also modified by making porous zinc anodes from a mixture of zinc and graphite powder using gelatinized agar solution [331] as a binding agent. In the cell design, a thin agar layer was introduced between the electrode-gelled electrolyte interfaces, which resulted in substantial improvement of a cell discharge performance.

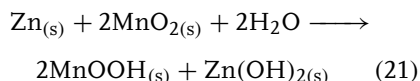
Such thin KOH-treated gelatinized agar electrolyte was also applied between the electrode-gelled electrolyte interfaces [332].

The agar layer improved the interface and simultaneously served as the electrolyte reservoir to both electrodes.

Modeling of rechargeable alkaline Zn–air batteries was also described [333], useful for optimizing zinc cell designs for specific applications.

24.1.5.1.3 Zn– MnO_2 Batteries Though this classical type with the Leclanché electrolyte has now decreasing importance, its improved modifications based on Zn (anode) and MnO_2 (cathode) as basic materials are in wide use.

The reaction of such a cell with alkaline electrolyte may be represented by the following reaction:



The nature of reactions that occur in the Leclanché cell [334] and $\text{ZnO}-\text{MnO}_2$ alkaline cell [335] have been studied and discussed.

Such alkaline cells have become the standard by which primary cells are judged in North America, Europe, and Japan. Approximately 12 billion cells were produced worldwide in 2001 [336].

The zinc powder has new alloying elements such as bismuth and indium to control zinc corrosion and reduce hydrogen evolution and leakage [337, 338]. Kumar and Sampath [339] have prepared a gel-polymer electrolyte based on a zinc salt for applications in a rechargeable solid-state zinc battery. The charge-discharge behavior of the cells with such zinc electrode and MnO_2 showed no significant changes during 70 cycles.

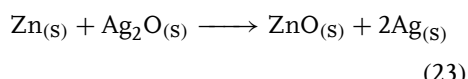
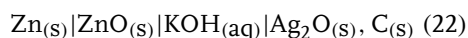
The same authors [340] have proposed another polymer gel electrolyte for $\text{Zn}-\text{MnO}_2$ cells.

Also, a new composite consisting of a mixture of zinc and hydrated ammonium zinc sulfate has been elaborated and studied [341] as anode material for all solid-state protonic cells. $\text{Zn}-\text{MnO}_2$ cells with this composite have a relatively high specific capacity.

An application of thick-film printing technology for the fabrication of a $\text{Zn}-\text{MnO}_2$ alkaline batteries [342] was also described. The mechanism of the capacity fade of rechargeable alkaline zinc–manganese cell was studied and discussed [343]. Zinc electrode with addition of several oxides (HgO , Sb_2O_3) for alkaline $\text{Zn}-\text{MnO}_2$ cells [344] was also studied.

Czerwiński and coworkers [345] reviewed the electrochemical applications of reticulated vitreous carbon (RVC). Special attention was paid to the use of RVC as an electrode support in zinc–manganese and zinc–halogen batteries.

24.1.5.1.4 Zn–Ag Batteries The cell may be represented by the scheme



The electromotive force (EMF) of this cell calculated from the potentials of the half-cells is equal to 1.593 V. Basic information about this cell are given by Vincent and Scrosati [319].

Though these alkaline silver–zinc batteries are quite expensive, they are frequently used in aerospace and military applications because they have high specific and volumetric energy density. These batteries may be kept in a dry state for several years and may be activated by introducing the electrolyte into the cells. Their status of technology and applications was presented by Karpinski et al. [346].

Various problems related to the construction and performances of these batteries, such as changes in materials of membranes and additives both to the electrode materials and to the electrolyte, were studied in recent years. Some instability of the silver electrode during such storage period and the ways of avoiding these difficulties were studied and discussed [347]. Reserve activated silver oxide–zinc cells were constructed [348] with synthetic Ag_2O and Pb-treated zinc electrodes were produced by a nonelectrolytic process. The cells were tested before and after thermally accelerated aging.

The study on the characterization of alkaline silver–zinc cells and composite electrodes for such cells was carried out [349, 350]. The improved silver–zinc battery with new developments in additives (Bi_2O_3) to the negative electrode and separator coatings for underwater

applications was also described [351]. A micromachined battery based on liquid electrolyte with gold as the positive electrode and zinc as the negative electrode was described [352].

24.1.5.1.5 Other Cells Several other cells with zinc as an active material have been studied in recent years. The zinc-containing compounds were used as anodes in lithium-ion batteries [353–355]. One such compound is nanocrystalline $ZnFe_2O_4$ and $Ag_xZnFe_2O_4$ ($x = 0.16, 0.37$, and 0.50) [355], which have been prepared as thin films, by reactive pulsed laser deposition. Especially good performance in the battery of the $Ag_{0.37}ZnFe_2O_4$ film electrode has been shown.

ZnO displays similar redox and alloying chemistry to the tin oxides on Li insertion [353]. Therefore, it may be an interesting network modifier for tin oxides. Also, $ZnSnO_3$ was proposed as a new anode material for lithium-ion batteries [354]. It was prepared as the amorphous product by pyrolysis of $ZnSn(OH)_6$. The reversible capacity of the $ZnSnO_3$ electrode was found to be more than 0.8 Ah/g . Zhao and Cao [356] studied antimony–zinc alloy as a potential material for such batteries. Also, zinc-graphite composite was investigated [357] as a candidate for an electrode in lithium-ion batteries. Zinc particles were deposited mainly onto graphite surfaces. Also, zinc–polyaniline batteries were developed [358]. The authors examined the parameters that affect the life cycle of such batteries. They found that Zn passivation is the main factor of the life cycle of zinc-polyaniline batteries. In recent times [359], zinc-poly(aniline-co-*o*-aminophenol) rechargeable battery was also studied. Other types of batteries based on zinc were of some interest [360].

24.1.5.2 Electrowinning The earlier works on electrowinning of zinc from ore or waste are well described [92].

The electrowinning process is connected with higher power consumption; but, on the other hand, the electrolytically produced zinc has higher purity. Therefore, further investigations are in progress. The main factors that must be considered in electrowinning process are (1) the electrochemical properties of the cathode materials, (2) the effect of ionic impurities in the electrolyte, and (3) the cohesion strength between the deposited metal and its substrate.

Metallic impurities complicated zinc electrowinning [361–368] from acidic sulfate solutions and can adversely affect the cathodic current efficiency, cell potential, power consumption, deposit quality, and the overall polarization behavior of the cathode.

This effect was mainly studied for cadmium, iron, copper [369], nickel [370, 371], antimony [372–378], manganese [371, 379], and iron impurities [376]. Electrowinning of zinc from acidified zinc chloride solutions was investigated [380]. The deposits having lesser surface defects, which act as the active sites of hydrogen adsorption, exhibited higher current efficiency. The presence of gelatin inhibited the H_2 evolution and significantly improved the current efficiency (see Fig. 8).

The organic additives have been employed to counteract the harmful effects of different metallic impurities. Such additives act by increasing the induction period, by complexing the harmful impurities, or by suppressing the hydrogen evolution reaction. The additives also increase the current efficiency, reduce the power consumption, and improve the surface morphology.

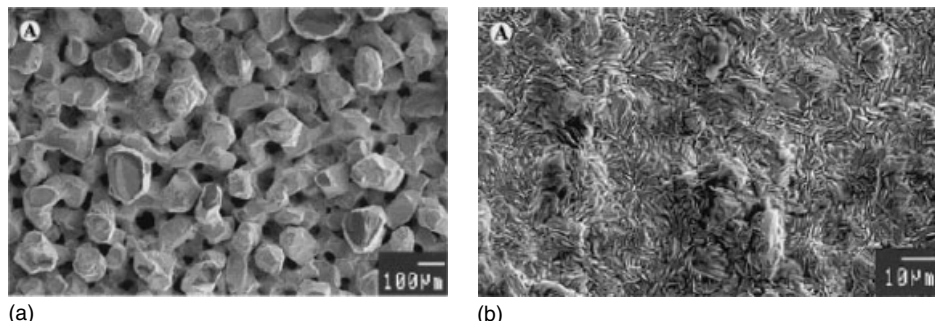


Fig. 8 Surface morphology of zinc deposits from (a) the gelatin-free solution 0.5 M $\text{ZnCl}_2 + 2 \text{ M HCl}$ and (b) gelatin-containing solution 0.75 M $\text{ZnCl}_2 + 1.5 \text{ M HCl}$ [380].

Traditionally, glues [362, 381–383] and arabic gum [384] were used as organic additives in the electrowinning of zinc. Hosny [385] and Karavasteva et al. [386, 387] used surfactants to improve the deposit morphology and current efficiency.

The influence of a number of organic additives—2-butyne-1,4-diol [388], 2-picoline [389], sodium lauryl sulfate [372], 4-ethylpyridine, 2-cyanopyridine [373], hydroxyethylated-butyne-2-diol-1,4 [376, 377, 379]—on the zinc electrowinning was studied. This influence is also presented and discussed in a review paper [390].

MacKinnon and coworkers [391–393] have studied a number of organic compounds as additives and have shown that tetrabutylammonium chloride improves surface morphology and current efficiency during zinc electrowinning from acidic chloride solutions. A similar influence was observed using other tetraalkylammonium compounds as additives [371, 374, 375, 394].

The applications of commercially available perfluorinated compounds have been reported in a number of recent publications [395–397]. In the presence of perfluorocarboxylic acids, the current efficiency increased, and surface morphology

of zinc was better during its electrowinning from acidic sulfate solutions [378]. The perfluorocarboxylic acids were found to be better additives for zinc electrodeposition when Sb(III) was absent from the zinc electrolyte.

Fluorinated organic compounds have also been used as suppressant of hydrogen evolution on zinc [395, 398].

The influence of orthophenylene diamine and sodium lignin sulfonate on zinc electrowinning from industrial zinc electrolyte was studied [399]. A very negative effect of orthophenylene diamine on current efficiency was found.

The effect of antimony, germanium, and nickel ions, and the organic additives on the zinc electrowinning from sulfuric acid electrolytes was also studied by Ivanov [400].

Also, the influence of aluminum sulfate, animal glue, and an extract of horse-chestnut nuts on zinc electrowinning from a weak acidic sulfate electrolyte prepared from an industrial waste product was investigated [401]. The use of additives mixture has a beneficial effect on zinc electrowinning and results in smooth, slightly bright zinc deposits.

Synthetic and pure zinc(II) solutions produced from laboratory leached,

oxidized zinc ores, under controlled temperature and pH were subjected to continuous electrowinning operations [402, 403]. Copper and iron additives were found to decrease the current efficiency and worsen the quality of the deposited zinc, while manganese and silica slightly influenced the properties of the deposit. Organic additives, gelatin, and TU have good leveling effects on the cathode deposits.

Lead–cobalt anodes used for electrowinning of zinc from sulfate solutions were investigated by Rashkov et al. [404].

The zinc electrowinning was also studied in alkaline solutions [405–407].

24.1.5.3 Zinc Electroplating

The deposits of zinc on different metals, especially on steel, have special relevance because of their anticorrosive properties by the formation of passive layers on contact with air, and in aqueous medium.

Mechanism of zinc electrodeposition on steel in acidic solution of zinc chloride was investigated [408] as a function of pH, grain-refining additives, and current density.

The effects of organic additives, such as benzoic acid (BA) and PEGs, on the initial stage of the zinc electrodeposition on iron have been investigated [409, 410] in an acidic zinc chloride solution. Benzoic acid molecules control the deposition rate at the dendritic sites by blocking the active surface through adsorption. PEGs are adsorbed with a well-ordered structure on the iron surface and appear to desorb in the underpotential deposition region of zinc, which helps to inhibit proton reduction by effective blocking of the electrode surface.

Effects of other additives such as *o*-vanilline [411], Triton X-10, sodium methylene bis(naphthalene sulfonate),

phenylbenzylketone, and a CH-1 brightener [412] on the electrodeposition of zinc were studied. It was found that the electrocrystallization mechanisms of zinc and microstructure of deposits are sensitive to the identity of organic additives.

Zinc electrodeposition was studied using three-dimensional electrodes [413, 414] or rotating disc electrodes (Cu, Al, and stainless steel) [415].

The effect of potential on the cathodic efficiency of a zinc electrodeposition in a cyanide-free alkaline bath was also investigated [416].

Chandran et al. have intensively studied electrodeposition of zinc on steel from noncyanide plating bath [417] and bromide electrolytes [418, 419].

The details of zinc plating from an acetate-based electrolyte were also presented [420].

24.1.5.4 Zinc Alloys Electroplating

The earlier papers on zinc alloys plating were described by Brodd and Leger [92]. In the last 10 years, the electrodeposition of the new Zn–Me alloys and ternary alloys was studied. The influence of plating conditions and different additives for deposition of alloys of Zn with iron group metals was studied in detail.

Electrochemical behaviors of Zn–Fe alloy and Zn–Fe–TiO₂ composite electrodeposition were studied in alkaline zincate solutions [421]. From the results, it can be concluded that Zn shows underpotential deposition. The content of Fe in the Zn–Fe coating changes with the composition of the electrolyte.

Electrodeposition of Zn–Ni alloys attracted considerable attention. The influence of electrolyte composition [422–428] hydrodynamic conditions [424] and the electrochemical polarization mode [424, 426, 428] on the properties of Zn–Ni

deposit were studied. The composition, morphology, and structure of the Zn–Ni alloys coatings, cathode current efficiency, and corrosion resistance were determined. Corrosion resistance of compositionally modulated multilayered Zn–Ni alloys deposit from a single bath was investigated [427]. Thermal stability of Zn–Ni alloys [425] and also their structures using X-ray diffraction [422] were studied.

Relative contributions of Ni(II) and Zn(II) reduction to anomalous electrodeposition of Zn–Ni alloys from solutions containing and not containing organic additives were reported [429].

In the presence of organic additives such as benzyl triethanol ammonium bromide [430], the smooth and uniform deposits that exhibited superior corrosion resistance were obtained.

The composition, surface morphology, and appearance of Zn–Co alloy deposits were studied as a function of experimental conditions [431–435]. These alloys were also found to be more corrosion resistant than zinc but less resistant than cobalt [432].

The influence of benzylidene acetone on the electrodeposition mechanism of Zn–Co alloy was investigated [436]. A relationship between corrosion resistance, microstructure, and cobalt content in Zn–Co alloys was investigated [437] using X-ray photoelectron spectroscopy (XPS) and Auger spectroscopy [438]. The role of vitreous carbon, copper, and nickel substrates in Zn–Co deposition from chloride bath was analyzed [439].

The electrodeposition of Zn–Sn alloys was studied using the EQCM method [440]. The influence of electrolyte composition on the Zn–Sn alloys properties was investigated and discussed [440–442].

The electrodeposition of zinc and iron group metal alloys (Zn–Co, Zn–Ni, Zn–Fe) on Cu electrode was also studied in methanol bath [443].

In addition, other zinc binary Zn–Te [444, 445] and ternary alloys such as Zn–Co–Cu [446], Zn–Ni–Co [447], Zn–Cu–Sn [448], Zn–Co–TiO₂ [435], and Ni–Zn–P [449] were also investigated.

24.1.5.5 Electrochemical Sensors and Modified Electrodes

24.1.5.5.1 Potentiometric Sensors The ion-selective electrodes have seen spectacular achievements in the last decade. Selective complexation of ligands and Zn(II) was used in the construction of chemical sensors, using different excluder and solvent mediators.

Using a typical poly(vinyl chloride) (PVC)-based membrane with different ionophores – Zn-bis(2,4,4-trimethylpentyl) dithiophosphinic acid complex [450], protoporphyrin IX dimethyl ester [451], porphyrin derivative [452] and hematoporphyrin IX [453], tetra(2-aminophenyl) porphyrin [454], cryptands [455, 456], 12-crown-4 [457], benzo-substituted macrocyclic diamide [458], 5,6,14,15-dibenzo-1,4-dioxa-8,12, diazacyclopentadecane-5,14-diene [459], and (*N*-[(ethyl-1-pyrrolidinyl-2-methyl)] methoxy-2-sulfamoyl-5-benzamide [460] – the sensors for zinc ions were prepared and investigated. The armed macrocycle, 5,7,7,12,14,14-hexamethyl-1,4,8,11-tetraazacyclo tetradeca-4,11-diene dihydrogen perchlorate was used for the preparation of polystyrene-based Zn(II)-sensitive electrode [461].

Dumkiewicz et al. [462, 463] have investigated the ion-selective electrode with a chelating pseudo-liquid membrane for zinc determination.

These electrodes exhibit a working concentration range from 1.0×10^{-5} to 1.0×10^{-1} M with a Nernstian slope of 29 ± 1 mV per decade activity and a fast response time (10–30 s). In some cases, the slope was lower [455, 456, 459].

The tetraphenylborate ion-doped poly-pyrrole electrode was sensitive to zinc ions [464, 465], and its sensitivity was dependent on the polymer macrostructure.

Zinc-selective electrodes based on a solid solution of $\text{Na}_{2-x}\text{Zn}_x\text{V}_{12}\text{O}_{30}$ ($x = 0.4$ or 0.6) [466] as well as sensor containing highly lipophilic $[(\text{CH}_3)_3\text{N}(\text{C}_{43}\text{H}_{79}\text{O}_3)]_2\text{Zn}(\text{SCN})_4$ ion exchanger [467] were examined. A zinc-selective electrode with low detection limit was used for the determination of Zn(II) in environmental samples [467].

The ion-selective electrodes based on different types of zinc-Schiff's bases were used for the determination of SO_4^{2-} [468] and thiocyanate ions concentration [469].

Zirconia solid electrolyte and zinc oxide sensing electrodes were used as a high-temperature NO_x sensor [470, 471]. The response of the electrode potential was linear for the logarithm of NO_x (NO) concentration from 40 to 450 ppm.

A solid-state potassium-selective electrode based on potassium zinc hexacyanoferrates, $\text{K}_2\text{Zn}_3[\text{Fe}(\text{CN})_6]_2$, ion exchanger is described [472]. The sensor can be used in the determination of K^+ ion in concentration range 10^{-4} –1 M KCl.

24.1.5.2 Voltammetric/Ampereometric Sensors

Thick-film carbon-containing screen-printed electrodes modified with formazan [473] were used for zinc determination.

The electrochemical properties of immobilized copper, zinc superoxide dismutase, and their interaction with super oxide radicals were investigated [474].

The modified Zn/polytetrafluoroethylene electrode can be used at high negative potentials (to -2.5 V versus Ag/AgCl) without significant hydrogen evolution [475]. Such electrode was used to detect organochloride compounds in water-AN mixtures.

Zinc hexacyanoferrate was supported on the surface of Ti(IV) oxide grafted on a silica gel [476]. Electrochemical behavior of this electrode was dependent on alkaline metal cations and acetate anion concentrations.

24.1.5.3 Modified Electrodes A carbon paste electrode modified with zinc diethyldithiocarbamate was used for selective accumulation and stripping analysis of mercury(II) [477].

Electrochemical and electrocatalytic behavior of zinc hexacyanoferrate directly formed on Zn electrode [478] and on carbon substrates [479] were studied.

Also, the catalytic ability of Zn electrode modified by Pt-doped nickel hexacyanoferrate for methanol electrooxidation was investigated [480].

Preparation, electrochemical, and spectroscopic properties of zinc-porphyrins and anthraquinone-based polymers [481] and also conducting polymers with Zn(II)-5-vinyl-10,15,20-triphenylporphyrin [482] coated electrodes were described.

Electropolymerized thin films of Zn(II)-4,9,16,23-tetraaminophthalocyanine immersed in a solution of relatively high pH have been studied using electrochemistry and spectroelectrochemistry [483].

The ZnO/eosinY hybrid films were prepared by cathodic electrodeposition from a hydrogen peroxide oxygen precursor in chloride medium [484,] and the role of reduced eosin bound to ZnO in the electrocatalysis was discussed.

The electrochemical formation of zinc selenide from acidic solutions [485] and electrodeposition of zinc telluride thin films, its properties, and photoelectrochemical applications were presented and discussed by Mahalingam et al. [486, 487].

References

- S. Trasatti, E. Lust, in *Modern Aspects of Electrochemistry* (Eds.: R. E. White, B. E. Conway, J. O. M. Bockris), Kluwer Academic/Plenum Publisher, New York and London, 1999, p. 1, Vol. 33.
- A. Hamelin, T. Vitanov, E. Sevastyanov et al., *J. Electroanal. Chem.* **1983**, *145*, 225–264.
- V. L. Heyfets, B. S. Krasikov, *Dokl. Akad. Nauk SSSR* **1956**, *109*, 586–588.
- A. Marshall, N. A. Hampson, *J. Electroanal. Chem.* **1974**, *53*, 133–144.
- V. V. Batrakov, A. I. Sidnin, *Elektrokhimiya* **1972**, *8*, 122–125.
- B. S. Krasikov, V. Sisoeva, *Dokl. Akad. Nauk SSSR* **1957**, *114*, 826–828.
- T. Chuan-Sin, Z. A. Iofa, *Dokl. Akad. Nauk SSSR* **1960**, *131*, 137–140.
- P. Caswell, N. A. Hampson, *J. Electroanal. Chem.* **1969**, *20*, 335–338.
- D. S. Brown, J. P. G. Farr, N. A. Hampson et al., *J. Electroanal. Chem.* **1968**, *17*, 421–424.
- V. Ya. Bartenev, E. S. Sevastyanov, D. I. Leikis, *Elektrokhimiya* **1970**, *6*, 1868–1870.
- A. I. Damilov, V. V. Batrakov, V. A. Safonov, *Elektrokhimiya* **1980**, *16*, 100–104.
- T. N. Anderson, J. L. Anderson, H. Eyring, *J. Phys. Chem.* **1969**, *73*, 3562–3570.
- A. N. Frumkin, V. V. Batrakov, A. I. Sidnin, *J. Electroanal. Chem.* **1972**, *39*, 225–228.
- V. V. Batrakov, B. B. Damaskin, *J. Electroanal. Chem.* **1975**, *65*, 361–372.
- Yu. P. Ipatov, V. V. Batrakov, V. V. Salaginov, *Elektrokhimiya* **1976**, *12*, 286–290.
- E. J. Lust, K. K. Lust, A. A. J. Jänes, *Elektrokhimiya* **1990**, *26*, 1627–1632.
- V. V. Batrakov, A. I. Sidnin, *Elektrokhimiya* **1972**, *8*, 743–747.
- V. V. Batrakov, A. N. Frumkin, A. I. Sidnin, *Elektrokhimiya* **1974**, *10*, 216–222.
- V. V. Batrakov, A. I. Sidnin, *Elektrokhimiya* **1974**, *10*, 1757–1761.
- V. V. Batrakov, B. B. Damaskin, Yu. P. Ipatov, *Elektrokhimiya* **1974**, *10*, 144–148.
- Yu. P. Ipatov, V. V. Batrakov, *Elektrokhimiya* **1975**, *11*, 1717–1720.
- Yu. P. Ipatov, V. V. Batrakov, *Elektrokhimiya* **1980**, *16*, 624–630.
- Yu. P. Ipatov, V. V. Batrakov, *Elektrokhimiya* **1980**, *16*, 630–638.
- E. J. Lust, A. Jänes, K. Lust et al., *J. Electroanal. Chem.* **1997**, *431*, 183–201.
- T. Hurlen, E. Eriksrud, *J. Electroanal. Chem.* **1973**, *45*, 405–410.
- E. Eriksrud, *J. Electroanal. Chem.* **1977**, *76*, 27–49.
- F. van der Pol, M. Sluyters-Rehbach, J. H. Sluyters, *J. Electroanal. Chem.* **1975**, *58*, 177–188.
- H. L. Jindal, K. Matsuda, R. Tamamushi, *J. Electroanal. Chem.* **1978**, *90*, 185–196.
- H. L. Jindal, K. Matsuda, R. Tamamushi, *J. Electroanal. Chem.* **1978**, *90*, 197–201.
- S. Vavřička, J. Kuta, L. Pospišil, *J. Electroanal. Chem.* **1982**, *133*, 299–305.
- W. S. Go, J. Osteryoung, *J. Electroanal. Chem.* **1987**, *233*, 275–281.
- J. J. O'Dea, J. Osteryoung, R. A. Osteryoung, *J. Phys. Chem.* **1983**, *87*, 3911–3918.
- W. S. Go, J. J. O'Dea, J. Osteryoung, *J. Electroanal. Chem.* **1988**, *255*, 21–44.
- R. Andreu, M. Sluyters-Rehbach, A. G. Remijnse et al., *J. Electroanal. Chem.* **1982**, *134*, 101–115.
- S. Kang, K. Matsuda, R. Tamamushi, *Collect. Czech. Chem. Commun.* **1982**, *47*, 1433–1443.
- J. Hendrikx, A. van der Putten, W. Visscher et al., *Electrochim. Acta* **1984**, *29*, 81–89.
- J. O. M. Bockris, Z. Nagy, A. Dajmanovic, *J. Electrochem. Soc.* **1972**, *119*, 285–295.
- R. Andreu, M. Sluyters-Rehbach, J. H. Sluyters, *J. Electroanal. Chem.* **1984**, *171*, 139–155.
- A. Baars, M. Sluyters-Rehbach, J. H. Sluyters, *J. Electroanal. Chem.* **1994**, *364*, 189–197.
- M. Pérez, A. Baars, S. J. M. Zevenhuizen et al., *J. Electroanal. Chem.* **1995**, *397*, 87–92.
- L. Koene, M. Sluyters-Rehbach, J. H. Sluyters, *J. Electroanal. Chem.* **1996**, *402*, 57–72.

42. T. G. J. van Venrooij, M. Sluyters-Rehbach, J. H. Sluyters, *J. Electroanal. Chem.* **1996**, *419*, 61–70.
43. C. Zhang, J. M. Wang, L. Zhang et al., *J. Electrochem. Soc.* **2001**, *148*, E310–E312.
44. J. X. Yu, L. Wang, L. Su et al., *J. Electrochem. Soc.* **2003**, *150*, C19–C23.
45. R. R. Nazmutdinov, W. Schmickler, A. M. Kuznetsov, *Chem. Phys.* **2005**, *310*, 257–268.
46. Y. Marcus, *Ion Solvation*, Wiley, Chichester, 1985.
47. J. Taraszewska, A. Wałęga, *J. Electroanal. Chem.* **1986**, *200*, 261–277.
48. J. Taraszewska, A. Wałęga, *J. Electroanal. Chem.* **1984**, *171*, 243–256.
49. J. Taraszewska, A. Wałęga, *J. Electroanal. Chem.* **1985**, *185*, 3–13.
50. J. Taraszewska, J. Śledzik, *J. Electroanal. Chem.* **1986**, *215*, 287–291.
51. J. Stroka, K. Maksymiuk, Z. Galus, *J. Electroanal. Chem.* **1984**, *167*, 211–226.
52. K. Maksymiuk, J. Stroka, Z. Galus, *Pol. J. Chem.* **1987**, *61*, 529–536.
53. J. Stroka, W. Górski, H. Schneider, *J. Electroanal. Chem.* **1990**, *288*, 143–152.
54. R. M. Rodriguez, E. Brillas, J. A. Garrido et al., *Can. J. Chem.* **1986**, *64*, 891–896.
55. E. Brillas, J. A. Garrido, R. M. Rodriguez et al., *Electrochim. Acta* **1993**, *38*, 2459–2465.
56. J. Taraszewska, A. Broda, *J. Electroanal. Chem.* **1983**, *153*, 243–254.
57. B. Behr, J. Taraszewska, J. Stroka, *J. Electroanal. Chem.* **1975**, *58*, 71–80.
58. B. Marczevska, *Collect. Czech. Chem. Commun.* **1994**, *59*, 1545–1550.
59. Z. Galus, in *Advances in Electrochemical Science and Engineering* (Eds.: H. Gerischer, Ch. Tobias), VCH Publishers, Weinheim, 1995, p. 217.
60. B. Marczevska, *Pol. J. Chem.* **1993**, *67*, 2205–2211.
61. B. Marczevska, *Collect. Czech. Chem. Commun.* **1997**, *62*, 843–848.
62. B. Marczevska, J. Włoszek, U. Kozłowska, *Electroanalysis* **1999**, *11*, 243–248.
63. B. Marczevska, *Electroanalysis* **1998**, *10*, 50–53.
64. B. Marczevska, *Gazz. Chim. Ital.* **1996**, *126*, 259–263.
65. B. Marczevska, *Monatsh. Chem.* **1996**, *127*, 859–866.
66. B. Marczevska, *J. Electroanal. Chem.* **1994**, *374*, 251–254.
67. B. Marczevska, *Indian J. Chem. A* **1997**, *36*, 440–445.
68. B. Marczevska, *Collect. Czech. Chem. Commun.* **1999**, *64*, 585–594.
69. B. Marczevska, *Electroanalysis* **1999**, *11*, 1101–1107.
70. W. R. Fawcett, A. Lasia, *J. Electroanal. Chem.* **1990**, *279*, 243–256.
71. A. Lasia, M. Bouderbala, *J. Electroanal. Chem.* **1990**, *288*, 153–164.
72. M. Manzini, A. Lasia, *Can. J. Chem.* **1994**, *72*, 1691–1698.
73. C. Cronnelly, K. Ch. Pillai, W. E. Waghorne, *J. Electroanal. Chem.* **1986**, *207*, 177–187.
74. A. G. Anastopoulos, *Electrochim. Acta* **1998**, *43*, 2273–2279.
75. A. G. Anastopoulos, *J. Electroanal. Chem.* **1997**, *424*, 179–183.
76. A. G. Anastopoulos, G. N. Nikolaidis, *J. Electroanal. Chem.* **2004**, *571*, 309–317.
77. D. Gugała, D. Sieńko, J. Saba, *Collect. Czech. Chem. Commun.* **2001**, *66*, 411–422.
78. G. Dalmata, *J. Electroanal. Chem.* **1997**, *431*, 67–75.
79. J. Saba, K. Sykut, G. Dalmata et al., *Monatsh. Chem.* **1999**, *130*, 1453–1459.
80. B. Marczevska, A. Persona, T. Gęca, *J. Electroanal. Chem.* **2004**, *562*, 267–271.
81. G. Dalmata, *Collect. Czech. Chem. Commun.* **1998**, *63*, 749–760.
82. G. Dalmata, *Croat. Chem. Acta* **1996**, *69*, 85–94.
83. G. Dalmata, *Gazz. Chim. Ital.* **1997**, *127*, 419–424.
84. G. Dalmata, *Electrochim. Acta* **1997**, *42*, 1307–1314.
85. K. Sykut, G. Dalmata, B. Marczevska et al., *Pol. J. Chem.* **2004**, *78*, 1583–1596.
86. G. Dalmata, A. Nosal-Wiercińska, T. Zięcina, *Collect. Czech. Chem. Commun.* **2004**, *69*, 267–278.
87. J. Saba, *Electrochim. Acta* **1994**, *39*, 711–717.
88. J. Saba, *Collect. Czech. Chem. Commun.* **1995**, *60*, 1457–1468.
89. J. Saba, J. Nieszporek, D. Gugała et al., *Electroanalysis* **2003**, *15*, 33–39.
90. J. Saba, *Electrochim. Acta* **1996**, *41*, 297–306.
91. P. Sanecki, *Electrochim. Commun.* **2004**, *6*, 753–756.
92. B. J. Brood, V. E. Leger, in *Encyclopedia of Electrochemistry of the Elements* (Ed.: A. J. Bard), Marcel Dekker, New York, 1976, Vol. 5, Chapter 1.

93. V. I. Kravtsov, E. G. Tsventarnyi, O. Yu. Kurtova et al., *Russ. J. Electrochem.* **2001**, *37*, 559–568.
94. O. Yu. Kurtova, V. I. Kravtsov, E. G. Tsventarnyi, *Russ. J. Electrochem.* **2004**, *40*, 893–897.
95. R. R. Nazmutdinov, M. S. Shapnik, E. E. Starodubets et al., *Russ. J. Electrochem.* **2002**, *38*, 1339–1345.
96. N. B. Berezin, K. A. Sagdeev, N. V. Gudin et al., *Russ. J. Electrochem.* **2005**, *41*, 203–205.
97. C. S. Kumar, V. S. Muralidharan, S. S. Begum et al., *Indian J. Chem. Technol.* **2000**, *7*, 202–204.
98. R. Cibulka, I. Císařová, J. Ondráček et al., *Collect. Czech. Chem. Commun.* **2001**, *66*, 170–184.
99. S. Çakır, E. Coskun, E. Biçer et al., *Carbohydr. Res.* **2003**, *338*, 1217–1222.
100. M. S. Díaz-Cruz, J. Mendieta, A. Monjonell et al., *J. Inorg. Biochem.* **1998**, *70*, 91–98.
101. M. S. Díaz-Cruz, J. M. Díaz-Cruz, J. Mendieta et al., *Anal. Biochem.* **2000**, *279*, 189–201.
102. N. Abo El-Maali, A. H. Osman, A. A. M. Aly et al., *Bioelectrochem. Bioenerg.* **2005**, *65*, 95–104.
103. S. Vajhallya, F. Khan, *J. Indian Chem. Soc.* **1999**, *76*, 292–295.
104. G. Guibaud, N. Tixier, A. Bouju et al., *Process Biochem.* **2004**, *39*, 833–839.
105. R. Andreoli, L. Benedetti, G. Grandi et al., *Electrochim. Acta* **1984**, *29*, 227–231.
106. M. E. Bodini, M. A. del Valle, G. E. Copia et al., *Polyhedron* **1998**, *17*, 2109–2114.
107. C. S. Pires de Castro, J. R. SouzaDe, C. B. Júnior, *Biophys. Chem.* **2004**, *112*, 59–67.
108. A. Gartner, U. Weser, in *Molecular and Functional Aspects of Superoxide Dismutases* (Eds.: F. Vögtle, E. Weber), Springer, Berlin, 1986, p. 1.
109. Z. L. Wang, W. Qian, Q. H. Luo et al., *J. Electroanal. Chem.* **2000**, *482*, 87–91.
110. A. Muñoz, A. R. Rodriguez, *Electroanalysis* **1995**, *7*, 674–680.
111. J. Mendieta, A. R. Rodriguez, *Electroanalysis* **1996**, *8*, 473–479.
112. O. Nieto, A. R. Rodriguez, *Bioelectrochem. Bioenerg.* **1996**, *40*, 215–222.
113. C. Harlyk, G. Bordini, O. Nieto et al., *J. Electroanal. Chem.* **1998**, *446*, 139–150.
114. C. Harlyk, O. Nieto, G. Bordini et al., *J. Electroanal. Chem.* **1998**, *451*, 267–272.
115. C. Harlyk, O. Nieto, G. Bordini et al., *J. Electroanal. Chem.* **1998**, *458*, 199–208.
116. M. Dabrio, A. R. Rodriguez, *Anal. Chim. Acta* **1999**, *385*, 295–306.
117. M. Dabrio, A. R. Rodriguez, *Electroanalysis* **2000**, *12*, 1026–1033.
118. M. Dabrio, A. R. Rodriguez, *Anal. Chim. Acta* **2000**, *424*, 77–90.
119. X. F. Zhou, A. J. Han, D. B. Chu et al., *Acta Chim. Sin.* **2002**, *60*, 2064–2068.
120. M. L. Duran, A. Sousa, J. Romero et al., *Inorg. Chim. Acta* **1999**, *294*, 79–82.
121. C. P. Joshua, M. Avaudeen, A. George, *J. Indian Chem. Soc.* **2003**, *80*, 171–173.
122. F. Yilmaz, V. T. Yilmaz, S. Topcu, *J. Coord. Chem.* **2004**, *57*, 525–534.
123. E. Lopez-Torres, M. A. Mendiola, J. Rodriguez-Procopio et al., *Inorg. Chim. Acta* **2001**, *323*, 130–138.
124. K. R. J. Thomas, J. T. Lin, C. P. Chang et al., *J. Chin. Chem. Soc.* **2002**, *49*, 833–840.
125. T. Sugimori, S.-I. Horike, M. Handa et al., *Inorg. Chim. Acta* **1998**, *278*, 253–255.
126. F. Yilmaz, V. T. Yilmaz, S. Topcu et al., *J. Coord. Chem.* **2003**, *56*, 903–911.
127. A. Naik, S. Annigeri, U. Gangadharmath et al., *Bull. Chem. Soc. Jpn.* **2002**, *75*, 2161–2167.
128. J. C. Swarts, E. H. G. Langner, N. Krokeide-Hove et al., *J. Mater. Chem.* **2001**, *11*, 434–443.
129. R. M. Izatt, J. S. Bradshaw, S. A. Nielsen et al., *Chem. Rev.* **1985**, *85*, 271–339.
130. R. M. Izatt, K. Pawlak, J. S. Bradshaw et al., *Chem. Rev.* **1991**, *91*, 1721–2085.
131. R. M. Izatt, K. Pawlak, J. S. Bradshaw et al., *Chem. Rev.* **1995**, *95*, 2529–2586.
132. V. W. W. Yam, Y. L. Pui, K. K. Cheung et al., *New J. Chem.* **2002**, *26*, 536–542.
133. M. Peters, L. Siegfried, T. A. Kaden, *J. Chem. Soc., Dalton Trans.* **2000**, *24*, 4664–4668.
134. K. M. Kadish, J. G. Shao, Z. P. Ou et al., *J. Porphyr. Phthalocya.* **2000**, *4*, 639–648.
135. V. B. Arion, E. Bill, M. T. Reetz et al., *Inorg. Chim. Acta* **1998**, *282*, 61–70.
136. M. Raidt, M. Neuburger, T. A. Kaden, *Dalton Trans.* **2003**, *7*, 1292–1298.
137. J. Costamagna, G. Ferraudi, B. Matsuhiro et al., *Coord. Chem. Rev.* **2000**, *196*, 125–164.
138. S. Brooker, *Coord. Chem. Rev.* **2001**, *222*, 33–56.

139. M. Vazquez, M. R. Bermejo, M. Fondo et al., *Eur. J. Inorg. Chem.* **2002**, 2, 465–472.
140. K. M. Kadish, K. M. Smith, R. Guilard, (Eds.), *The Porphyrin Handbook*, Academic Press, 2000.
141. R. A. Sheldon, *Metalloporphyrins in Catalytic Oxidations*, Marcel Dekker, New York, 1994.
142. F. Montanari, L. Casella, *Metalloporphyrins in Catalyzed Oxidations*, Kluwer, Academic Publishers, Dordrecht, 1994.
143. Y. Terazono, B. O. Patrick, D. H. Dolphin, *Inorg. Chem.* **2002**, 41, 6703–6710.
144. Y. X. Zhou, Z. X. Wang, D. K. Wang et al., *J. Porphyr. Phthalocya.* **2001**, 5, 523–527.
145. A. Giraudeau, S. Lobstein, L. Ruhlmann et al., *J. Porphyr. Phthalocya.* **2001**, 5, 793–797.
146. C. Y. Lin, Y. C. Hung, C. M. Liu et al., *Dalton Trans.* **2005**, 2, 396–401.
147. J. Bley-Escrich, S. Prikhodovski, C. D. Brandt et al., *J. Porphyr. Phthalocya.* **2003**, 7, 220–226.
148. J. G. Goll, K. T. Morre, A. Ghosh et al., *J. Am. Chem. Soc.* **1996**, 118, 8344–8354.
149. K. Ozette, P. Leduc, M. Palacio et al., *J. Am. Chem. Soc.* **1997**, 119, 6442–6443.
150. E. K. Woller, S. G. DiMagno, *J. Org. Chem.* **1997**, 62, 1588–1593.
151. Y. Amao, T. Kamachi, I. Okura, *Inorg. Chim. Acta* **1998**, 267, 257–263.
152. J. T. Fletcher, M. J. Therien, *J. Am. Chem. Soc.* **2002**, 124, 4298–4311.
153. N. Armaroli, F. Diederich, L. Echegoyen et al., *New J. Chem.* **1999**, 23, 77–83.
154. C.-L. Lin, M.-Y. Fang, S.-H. Cheng, *J. Electroanal. Chem.* **2002**, 531, 155–162.
155. Y. Yamaguchi, M. Yamazaki, S. Yoshihara et al., *J. Electroanal. Chem.* **1998**, 442, 1–3.
156. M. Izaki, *J. Electrochem. Soc.* **1999**, 146, 4517–4521.
157. Th. Pauporte, D. Lincot, *J. Electroanal. Chem.* **2001**, 517, 54–62.
158. Th. Pauporte, D. Lincot, *J. Electrochem. Soc.* **2001**, 148, C310–C314.
159. J. Lee, Y. Tak, *Electrochem. Solid State Lett.* **2001**, 4, C63–C65.
160. H. X. Li, R. H. Wang, C. H. Guo et al., *Mater. Sci. Eng., B* **2003**, 103, 285–288.
161. F. Q. Tang, Y. Sakka, T. Uchikoshi, *Mater. Res. Bull.* **2003**, 38, 207–212.
162. M. Kemell, F. Dartigues, M. Ritala et al., *Thin Solid Films* **2003**, 434, 20–23.
163. T. Pauporte, T. Yoshida, R. Cortes et al., *J. Phys. Chem. B* **2003**, 107, 10077–10082.
164. S. Karappuchamy, T. Yoshida, T. Sugiura et al., *Thin Solid Films* **2001**, 397, 63–69.
165. T. Yoshida, D. Komatsu, N. Shimokawa et al., *Thin Solid Films* **2004**, 451–452, 166–169.
166. J. Katayama, M. Izaki, *J. Appl. Electrochem.* **2000**, 30, 855–858.
167. T. N. Rao, L. Bahadur, *J. Electrochem. Soc.* **1997**, 144, 179–185.
168. T. Hirano, H. Kozuka, *J. Mater. Sci.* **2003**, 38, 4203–4210.
169. N. G. Park, M. G. Kang, K. M. Kim et al., *Langmuir* **2004**, 20, 4246–4253.
170. S. P. Wiceliński, R. J. Gale, J. S. Wilkes, *J. Electrochem. Soc.* **1987**, 134, 262–263.
171. M. K. Carpenter, M. W. Verbrugge, *J. Mater. Res.* **1994**, 9, 2584–2591.
172. W. R. Pitner, C. L. Hussey, *J. Electrochem. Soc.* **1997**, 144, 3095–3103.
173. L. Simanavicius, A. Stakenas, A. Sarkis, *Electrochim. Acta* **1997**, 42, 1581–1586.
174. S. I. Hsiu, J. F. Huang, I. W. Sun et al., *Electrochim. Acta* **2002**, 47, 4367–4372.
175. Y. F. Lin, I. W. Sun, *Electrochim. Acta* **1999**, 44, 2771–2777.
176. Y. F. Lin, I. W. Sun, *J. Electrochem. Soc.* **1999**, 146, 1054–1059.
177. J. Dogel, W. Freyland, *Phys. Chem. Chem. Phys.* **2003**, 5, 2484–2487.
178. T. Iwagishi, H. Yamamoto, K. Koyama et al., *Electrochemistry* **2002**, 70, 671–674.
179. P. Liu, Q. Q. Yang, G. K. Liu, *Trans. Nonferrous Metal. Soc. China* **1996**, 6, 41.
180. P. Y. Chen, M. C. Lin, I. W. Sun, *J. Electrochem. Soc.* **2000**, 147, 3350–3355.
181. M. C. Lin, P. Y. Chen, I. W. Sun, *J. Electrochem. Soc.* **2001**, 148, C653–C658.
182. P. Y. Chen, I. W. Sun, *Electrochim. Acta* **2001**, 46, 1169–1177.
183. J. F. Huang, I. W. Sun, *J. Electrochem. Soc.* **2002**, 149, E348–E355.
184. J. F. Huang, I. W. Sun, *J. Electrochem. Soc.* **2003**, 150, E299–E306.
185. J. F. Huang, I. W. Sun, *Electrochim. Acta* **2004**, 49, 3251–3258.
186. T. Iwagishi, K. Sawada, H. Yamamoto et al., *Electrochemistry* **2003**, 71, 318–321.
187. T. Iwagishi, T. Nakamura, H. Yamamoto et al., *Electrochemistry* **2004**, 72, 618–623.
188. J. F. Huang, I. W. Sun, *J. Electrochem. Soc.* **2004**, 151, C8–C14.

189. S. C. Lans, A. van Sandwijk, M. A. Reuter, *J. Appl. Electrochem.* **2004**, *34*, 1021–1027.
190. A. Aramata, M. A. Quaiyyum, W. A. Balais et al., *J. Electroanal. Chem.* **1992**, *338*, 367–372.
191. M. A. Quaiyyum, A. Aramata, S. Taguchi et al., *Denki Kagaku Oyobi Kogyo Butsuri Kagaku* **1993**, *61*, 847–848.
192. M. A. Quaiyyum, A. Aramata, S. Moniwa et al., *J. Electroanal. Chem.* **1994**, *373*, 61–66.
193. K. Igarashi, A. Aramata, S. Taguchi, *Electrochim. Acta* **2001**, *46*, 1773–1781.
194. S. Taguchi, T. Fukuda, A. Aramata, *J. Electroanal. Chem.* **1997**, *435*, 55–61.
195. S. Taguchi, A. Aramata, *J. Electroanal. Chem.* **1995**, *396*, 131–137.
196. G. Horányi, A. Aramata, *J. Electroanal. Chem.* **1997**, *437*, 259–262.
197. G. Horányi, A. Aramata, *J. Electroanal. Chem.* **1997**, *434*, 201–207.
198. A. Aramata, S. Taguchi, T. Fukuda et al., *Electrochim. Acta* **1998**, *44*, 999–1007.
199. S. A. Abd El-Maksoud, S. Taguchi, T. Fukuda et al., *Electrochim. Acta* **1996**, *41*, 1947–1952.
200. S. Moniwa, A. Aramata, *J. Electroanal. Chem.* **1994**, *376*, 203–206.
201. S. Takahashi, K. Hasebe, A. Aramata, *Electrochim. Commun.* **1999**, *1*, 301–304.
202. M. Nakamura, A. Aramata, A. Yamagishi et al., *J. Electroanal. Chem.* **1998**, *446*, 227–231.
203. J. O. M. Bockris, G. A. Razumney, *Fundamental Aspect of Electrocristallization*, Plenum Press, New York, 1967.
204. A. R., Despic, in *Comprehensive Treatise of Electrochemistry*, (Eds.: B. E. Conway, J. O. M. Bockris et al.) Plenum Press, New York, 1983, p. 399, Vol. 7.
205. J. H. Lindsay, T. J. O'Keefe, in *Modern Aspects of Electrochemistry* (Ed.: B. E. Conway, J. O'M. Bockris, R. E. White), Plenum Press, New York, 1994, p. 165, Vol. 26.
206. E. Budevski, G. Stoikov, W. J. Lorenz, *Electrochemical Phase Formation and Growth*, VCH Publishers, Weinheim/New York, 1996.
207. Y. C. Chang, G. Prentice, *J. Electrochem. Soc.* **1984**, *131*, 1465–1476.
208. Y. C. Chang, G. Prentice, *J. Electrochem. Soc.* **1985**, *132*, 375–381.
209. V. Rezaite, R. Vishomirskis, *Prot. Met.* **2001**, *37*, 25–30.
210. V. Rezaite, R. Vishomirskis, *Prot. Met.* **2001**, *37*, 310–313.
211. R. Renuka, L. Srinivasan, S. Ramamurthy et al., *J. Appl. Electrochem.* **2001**, *31*, 655–661.
212. R. Shrivkumar, P. Manikandan, G. P. Kalaignan et al., *Bull. Electrochem.* **1998**, *14*, 204–210.
213. J. M. Wang, L. Zhang, C. Zhang et al., *J. Power Sources* **2001**, *102*, 139–143.
214. V. N. Selivanov, I. G. Bobrikova, S. V. Molchanov et al., *Russ. J. Electrochem.* **1997**, *33*, 166–169.
215. Y. Y. Tevtul, *Russ. J. Electrochem.* **1996**, *32*, 535–540.
216. S. Nakanishi, K. Fukami, S. Sakai et al., *Chem. Lett.* **2002**, *6*, 636–637.
217. R. Ichino, C. Cachet, R. Wiart, *Electrochim. Acta* **1996**, *41*, 1031–1039.
218. F. Ganne, C. Cachet, G. Maurin et al., *J. Appl. Electrochem.* **2000**, *30*, 665–673.
219. J. L. Zhu, Y. H. Zhou, C. Q. Gao, *J. Power Sources* **1998**, *72*, 231–235.
220. C. Cachet, R. Wiart, *Electrochim. Acta* **1999**, *44*, 4743–4751.
221. H. B. Yang, X. L. Meng, E. D. Yang et al., *J. Electrochem. Soc.* **2004**, *151*, A389–A393.
222. J. Zhu, Y. H. Zhou, H. X. Yang, *J. Power Sources* **1997**, *69*, 169–173.
223. S. Biallozór, E. T. Bandura, *Electrochim. Acta* **1987**, *32*, 891–894.
224. G. Trejo, R. Ortega, Y. Meas et al., *J. Electrochem. Soc.* **1998**, *145*, 4090–4097.
225. G. Trejo, H. Ruiz, R. Ortega Borges et al., *J. Appl. Electrochem.* **2001**, *31*, 685–692.
226. G. Trejo, R. Ortega, Y. Meas, *Plat. Surf. Finish.* **2002**, *89*, 84–87.
227. J. X. Yu, H. X. Yang, X. P. Ai et al., *Russ. J. Electrochem.* **2002**, *38*, 321–325.
228. J. X. Yu, H. Q. Cao, Y. Y. Chen et al., *J. Electroanal. Chem.* **1999**, *474*, 69–73.
229. E. Gómez, E. Vallés, *J. Electroanal. Chem.* **1995**, *397*, 177–184.
230. V. Zuniga, R. Ortega, Y. Meas et al., *Plat. Surf. Finish.* **2004**, *91*, 46–51.
231. A. E. Alvarez, D. R. Salinas, *J. Electroanal. Chem.* **2004**, *566*, 393–400.
232. M. V. Simičić, K. I. Popov, N. V. Krstajić, *J. Electroanal. Chem.* **2000**, *484*, 18–23.
233. D. Giménez-Romero, J. J. García-Jareño, F. Vicente, *J. Electroanal. Chem.* **2003**, *558*, 25–33.
234. P. Díaz-Arista, Y. Meas, R. Ortega et al., *J. Appl. Electrochem.* **2005**, *35*, 217–227.

235. I. Rodriguez-Torres, G. Valentín, F. Lapicque, *J. Appl. Electrochem.* **1999**, *29*, 1035–1044.
236. K. Raeissi, A. Saatchi, M. A. Golozar, *J. Appl. Electrochem.* **2003**, *33*, 635–642.
237. K. Raeissi, A. Saatchi, M. A. Golozar, *J. Appl. Electrochem.* **2004**, *34*, 1249–1258.
238. N. Pereira, L. C. Klein, G. G. Amatucci, *J. Electrochem. Soc.* **2002**, *149*, A262–A271.
239. P. L. Cabot, M. Cortes, F. A. Centellas et al., *J. Electroanal. Chem.* **1986**, *201*, 85–100.
240. R. W. Powers, M. W. Breiter, *J. Electrochem. Soc.* **1969**, *116*, 719–729.
241. N. A. Hampson, G. A. Herdman, R. Taylor, *J. Electroanal. Chem.* **1970**, *25*, 9–18.
242. D. A. Payne, A. J. Bard, *J. Electrochem. Soc.* **1972**, *119*, 1665–1674.
243. M. C. H. McKubre, D. D. Macdonald, *J. Electrochem. Soc.* **1981**, *128*, 524–530.
244. X. Shan, P. Scholl, G. Prentice et al., *J. Electrochem. Soc.* **1989**, *136*, 3594–3599.
245. S. B. Saidman, J. R. Vilche, A. J. Arvia, *Electrochim. Acta* **1994**, *39*, 1401–1407.
246. G. Prentice, Y. C. Chang, X. Shan, *J. Electrochem. Soc.* **1991**, *138*, 890–895.
247. N. A. Hampson, M. J. Tarbox, *J. Electrochem. Soc.* **1963**, *110*, 95–103.
248. R. D. Armstrong, M. F. Bell, *J. Electroanal. Chem.* **1974**, *55*, 201–211.
249. G. Zhang, *Corrosion and Electrochemistry of Zinc*, Plenum Press, New York, 1996.
250. W. Fürbeth, M. Stratmann, *Corros. Sci.* **2001**, *43*, 207–227.
251. P. Scholl, X. Shanb, D. Bonham et al., *J. Electrochem. Soc.* **1991**, *138*, 895–900.
252. E. E. Abd El Aal, *Corrosion* **1999**, *55*, 582–589.
253. D. D. Macdonald, K. M. Ismail, E. Sikora, *J. Electrochem. Soc.* **1998**, *145*, 3141–3149.
254. M. Cai, S. M. Park, *J. Electrochem. Soc.* **1996**, *143*, 2125–2131; 3895–3902.
255. A. L. Rudd, C. B. Breslin, *Electrochim. Acta* **2000**, *45*, 1571–1579.
256. I. Mogi, H. Kikuya, K. Watanabe et al., *Chem. Lett.* **1996**, *8*, 673–674.
257. C. V. Dalkaine, M. N. Boucherit, *J. Electrochem. Soc.* **1997**, *144*, 3331–3336.
258. L. P. Podgornova, Y. I. Kuznetsov, S. V. Gavrilova, *Prot. Met.* **2003**, *39*, 217–221.
259. H. H. Hassan, *Appl. Surf. Sci.* **2001**, *174*, 201–209.
260. N. Ibriş, J. C. Mirza-Rosca, A. Santana et al., *J. Solid State Electrochem.* **2002**, *6*, 119–125.
261. L. Sziráki, Á. Cziráki, I. Geröcs et al., *Electrochim. Acta* **1998**, *43*, 175–186.
262. C. Cachet, F. Ganne, G. Maurin et al., *Electrochim. Acta* **2001**, *47*, 509–518.
263. C. Cachet, F. Ganne, S. Joiret et al., *Electrochim. Acta* **2002**, *47*, 3409–3422.
264. D. Giménez-Romero, J. J. García-Jareño, F. Vicente, *Electrochim. Commun.* **2003**, *5*, 722–727.
265. D. Giménez-Romero, J. J. García-Jareño, F. Vicente, *Electrochim. Commun.* **2004**, *6*, 148–152.
266. R. Wiart, *Electrochim. Acta* **1990**, *35*, 1587–1593.
267. S. S. Abd El Rehim, S. M. Abd El Wahab, E. E. Fouad et al., *Mater. Corros.* **1995**, *46*, 633–638.
268. E. E. Abd El Aal, *Corros. Sci.* **2000**, *42*, 1–16.
269. E. E. Abd El Aal, *Corros. Sci.* **2004**, *46*, 37–49.
270. F. H. Assaf, S. S. Abd El-Rehiem, A. M. Zaky, *Mater. Chem. Phys.* **1999**, *58*, 58–63.
271. S. S. Abd El Rehim, E. E. Foad El-Sherbini, M. A. Amin, *J. Electroanal. Chem.* **2003**, *560*, 175–182.
272. S. S. Abd El Rehim, E. E. Fouad, S. M. Abd El Wahab et al., *J. Electroanal. Chem.* **1996**, *401*, 113–118.
273. E. E. Abd El Aal, *Corros. Sci.* **2002**, *44*, 2041–2053.
274. E. E. F. El Sherbini, S. S. Abd El Rehim, *Corros. Sci.* **2000**, *42*, 785–798.
275. H. X. Yang, Y. L. Cao, X. P. Ai et al., *J. Power Sources* **2004**, *128*, 97–101.
276. Y. C. Chang, G. Prentice, *J. Chinese Inst. Chem. Eng.* **1996**, *27*, 17–24.
277. V. V. Ekilik, A. G. Berezhnaya, M. N. Svyataya, *Prot. Met.* **2001**, *37*, 525–528.
278. S. C. Barton, A. C. West, *J. Electrochem. Soc.* **2001**, *148*, A490–A495.
279. A. B. Velichenko, J. Portillo, M. Sarret et al., *J. Appl. Electrochem.* **1999**, *29*, 1119–1123.
280. A. B. Velichenko, J. Portillo, M. Sarret et al., *Electrochim. Acta* **1999**, *44*, 3377–3387.
281. A. B. Velichenko, J. Portillo, M. Sarret et al., *Appl. Surf. Sci.* **1999**, *148*, 17–23.
282. E. Juzeliūnas, P. Kalinauskas, P. Mieciškės, *J. Electrochem. Soc.* **1996**, *143*, 1525–1531.
283. F. Roubani-Kalantzopoulou, G. Paternarakis, K. Karayianni, *Anti-Corros. Methods Mater.* **1998**, *45*, 84.
284. S. C. Chung, J. R. Cheng, S. D. Chiou et al., *Corros. Sci.* **2000**, *42*, 1249–1268.

285. S. Magaino, M. Soga, K. Sobue et al., *Electrochim. Acta* **1999**, *44*, 4307–4312.
286. V. Alonzo, A. Darchen, D. Hauchard et al., *Electrochim. Acta* **2003**, *48*, 951–955.
287. P. Jinturkar, Y. C. Guan, K. N. Han, *Corrosion* **1998**, *54*, 106–114.
288. Kh. M. S. Youssef, C. C. Koch, P. S. Fedkiw, *Corros. Sci.* **2004**, *46*, 51–64.
289. I. M. Baghni, S. B. Lyon, B. Ding, *Surf. Coat. Technol.* **2004**, *185*, 194–198.
290. R. Sarmaitis, V. Dikinis, V. Rezaite, *Prot. Met.* **2003**, *39*, 316–324.
291. A. I. Marshakov, T. I. Sokolova, Y. N. Mikhailovskii, *Prot. Met.* **1997**, *33*, 29–36.
292. S. F. L. Mertens, E. Temmerman, *Corros. Sci.* **2001**, *43*, 301–316.
293. E. Frąckowiak, J. M. Skowroński, *J. Power Sources* **1998**, *73*, 175–181.
294. K. Aramaki, *Corros. Sci.* **2002**, *44*, 2621–2634.
295. K. Aramaki, *Corros. Sci.* **2003**, *45*, 199–210.
296. K. Aramaki, *Corros. Sci.* **2003**, *45*, 451–464.
297. K. Aramaki, *Corros. Sci.* **2003**, *45*, 1085–1101.
298. K. Aramaki, *Corros. Sci.* **2004**, *46*, 1565–1579.
299. K. Aramaki, *Corros. Sci.* **2003**, *45*, 2361–2376.
300. K. Aramaki, *Corros. Sci.* **2001**, *43*, 1573–1588.
301. K. Aramaki, *Corros. Sci.* **2002**, *44*, 1375–1389.
302. K. Aramaki, *Corros. Sci.* **2002**, *44*, 1361–1374.
303. K. Aramaki, *Corros. Sci.* **2001**, *43*, 1985–2000.
304. K. Wang, H. W. Pickering, K. G. Weil, *J. Electrochem. Soc.* **2003**, *150*, B176–B180.
305. C. Huang, W. Zhang, X. Cao, *J. Appl. Electrochem.* **1997**, *27*, 695–698.
306. R. T. Vashi, V. A. Champaneri, *Indian J. Chem. Technol.* **1997**, *4*, 180–184.
307. T. I. Devyatkina, Y. L. Gun'ko, M. G. Mikhaleko, *Russ. J. Appl. Chem.* **2001**, *74*, 1122–1125.
308. K. Aramaki, *Corros. Sci.* **2002**, *44*, 871–886.
309. S. Manov, A. M. Lamozouere, L. Aries, *Corros. Sci.* **2000**, *42*, 1235–1248.
310. S. Manov, F. Noli, A. M. Lamazouere et al., *J. Appl. Electrochem.* **1999**, *29*, 995–1003.
311. J. I. Martins, T. C. Reis, M. Bazzououi et al., *Corros. Sci.* **2004**, *46*, 2361–2381.
312. R. R. Zahran, G. H. Sedahmed, *Mater. Lett.* **1997**, *31*, 29–33.
313. P. Kalinauskas, I. Valsiūnas, M. Samulevičienė et al., *Corros. Sci.* **2001**, *43*, 2083–2092.
314. X. G. Zang, *J. Electrochem. Soc.* **1996**, *143*, 1472–1484.
315. I. Milosev, A. Minovic, *Ann. Chim. Rome.* **2001**, *91*, 343–354.
316. M. A. Pech-Canul, R. Ramanauskas, L. Maldonado, *Electrochim. Acta* **1997**, *42*, 255–260.
317. E. Tada, S. Satoh, H. Kaneko, *Electrochim. Acta* **2004**, *49*, 2279–2285.
318. H. Park, J. A. Szpunar, *Corros. Sci.* **1998**, *40*, 525–545.
319. C. A. Vincent, B. Scrosati, *Modern Batteries. An Introduction to Electrochemical Power Sources*, Arnold, London, 1997.
320. J. Jindra, *J. Power Sources* **1997**, *66*, 15–25.
321. J. Jindra, *J. Power Sources* **2000**, *88*, 202–205.
322. M. Geng, D. O. Northwood, *Int. J. Hydrogen Energy* **2003**, *28*, 633–636.
323. M. E. Alekseeva, Z. P. Arkhangel'skaya, R. P. Ivanova et al., *Russ. J. Appl. Chem.* **1998**, *71*, 1759–1761.
324. H. K. Liu, B. Bright, C. Y. Wang et al., *J. New Mater. Electrochem. Syst.* **2002**, *5*, 47–52.
325. Z. P. Arkhangel'skaya, R. P. Ivanova, T. B. Kas'yan et al., *Russ. J. Appl. Chem.* **2001**, *74*, 607–610.
326. W. H. Zhu, M. E. Flanzer, B. J. Tatarchuk, *J. Power Sources* **2002**, *112*, 353–366.
327. X. Y. Wang, P. J. Sebastian, M. A. Smit et al., *J. Power Sources* **2003**, *124*, 278–284.
328. S. Muller, O. Hass, C. Schlatter et al., *J. Appl. Electrochem.* **1998**, *28*, 305–310.
329. G. Q. Zhang, X. G. Zhang, *Electrochim. Acta* **2004**, *49*, 873–877.
330. S. Muller, F. Holzer, O. Hass, *J. Appl. Electrochem.* **1998**, *28*, 895–898.
331. R. Othman, A. H. Yahaya, A. K. Arof, *J. Appl. Electrochem.* **2002**, *32*, 1347–1353.
332. R. Othman, A. H. Yahaya, A. K. Arof, *J. New Mater. Electrochem. Syst.* **2002**, *5*, 177–182.
333. E. Deiss, F. Holzer, O. Hass, *Electrochim. Acta* **2002**, *47*, 3995–4010.
334. J. Larkin, W. C. Maskell, F. L. Tye, *Electrochim. Acta* **1997**, *42*, 2649–2658.
335. Q. C. Horn, Y. Shao-Horn, *J. Electrochem. Soc.* **2003**, *150*, A652–A658.
336. R. J. Brodd, K. R. Bullock, R. A. Leising et al., *J. Electrochem. Soc.* **2004**, *151*, K1–K11.

337. W. Glaeser, *ITE Lett.* **1999**, *1*, 59.
338. W. Glaeser, S. Kunzel-Keune, P. Merkel, *ITE Lett.* **1999**, *1*, 91.
339. G. G. Kumar, S. Sampath, *J. Electrochem. Soc.* **2003**, *150*, A608–A615.
340. G. G. Kumar, S. Sampath, *Solid State Ionics* **2003**, *160*, 289–300.
341. L. Telli, A. Hammouche, B. Brahimi et al., *J. Power Sources* **2002**, *103*, 201–206.
342. G. A. Ghurcan, C. C. Liu, A. Webber et al., *J. Electrochem. Soc.* **2003**, *150*, A922–A927.
343. Y. W. Shen, K. Kordes, *J. Power Sources* **2000**, *87*, 162–166.
344. R. Shivkumar, G. P. Kalaignan, T. Vasudevan, *J. Power Sources* **1998**, *75*, 90–100.
345. Z. Rogulski, W. Lewdorowicz, W. Tokarz et al., *Pol. J. Chem.* **2004**, *78*, 1357–1370.
346. A. P. Karpinski, B. Makovetski, S. J. Russell et al., *J. Power Sources* **1999**, *80*, 53–60.
347. D. F. Smith, C. Brown, *J. Power Sources* **2001**, *96*, 121–127.
348. D. F. Smith, J. A. Gucinski, *J. Power Sources* **1999**, *80*, 66–71.
349. B. Hariprakash, S. K. Martha, A. K. Shukla, *J. Power Sources* **2003**, *117*, 242–248.
350. E. P. Koval'chuk, O. R. Artymyshyn, O. V. Reshetnyak et al., *Pol. J. Chem.* **1998**, *72*, 1089–1095.
351. J. Skelton, R. Serenyi, *J. Power Sources* **1997**, *65*, 39–45.
352. K. B. Lee, L. W. Lin, *J. Microelectromech. Syst.* **1997**, *12*, 840–847.
353. F. Belliard, J. T. S. Irvine, *J. Power Sources* **2001**, *97*–*98*, 219–222.
354. Z. Y. Yuan, F. Huang, J. T. Sun et al., *Chem. Lett.* **2002**, *3*, 408–409.
355. Y. N. Nuli, Y. Q. Chu, Q. Z. Qin, *J. Electrochem. Soc.* **2004**, *151*, A1077–A1083.
356. X. B. Zhao, G. S. Cao, *Electrochim. Acta* **2001**, *46*, 891–896.
357. A. Dailly, J. Ghanbaja, P. Willmann et al., *J. Appl. Electrochem.* **2004**, *34*, 885–890.
358. M. S. Rahmanifar, M. F. Mousavi, M. Shamsipur et al., *J. Power Sources* **2004**, *132*, 296–301.
359. S. L. Mu, *Synth. Met.* **2004**, *143*, 269–275.
360. W. Kautek, A. Conradi, M. Sahre et al., *J. Electrochem. Soc.* **1999**, *146*, 3211–3216.
361. C. L. Mantell, *Electrochemical Engineering*, 4th ed., McGraw-Hill, New York, 1980, p. 210.
362. D. J. Robinson, T. J. O'Keefe, *J. Appl. Electrochem.* **1976**, *6*, 1–7.
363. D. R. Fosnacht, T. J. O'Keefe, *Met. Trans. (B)* **1983**, *14*, 645–655.
364. P. A. Adcock, A. R. Ault, O. M. G. Newmann, *J. Appl. Electrochem.* **1985**, *15*, 865–878.
365. D. J. MacKinnon, R. M. Morrison, J. M. Brannen, *J. Appl. Electrochem.* **1986**, *16*, 53–61.
366. M. Karavasteva, E. Maahn, *Hydrometallurgy* **1993**, *34*, 255–261.
367. A. R. Ault, E. J. Frazer, *J. Appl. Electrochem.* **1988**, *18*, 583–589.
368. E. J. Frazer, *J. Electrochem. Soc.* **1988**, *135*, 2465–2471.
369. L. Muresan, G. Maurin, L. Oniciu et al., *Hydrometallurgy* **1996**, *43*, 345–354.
370. C. Cachet, R. Wiart, *J. Electrochem. Soc.* **1994**, *141*, 131–139.
371. Y. Stefanov, I. Ivanov, *Hydrometallurgy* **2002**, *64*, 193–203.
372. B. C. Tripathy, S. C. Das, G. T. Hefter et al., *J. Appl. Electrochem.* **1997**, *27*, 673–678.
373. S. C. Das, P. Singh, G. T. Hefter, *J. Appl. Electrochem.* **1997**, *27*, 738–744.
374. B. C. Tripathy, S. C. Das, G. T. Hefter et al., *J. Appl. Electrochem.* **1998**, *28*, 915–920.
375. B. C. Tripathy, S. C. Das, P. Singh et al., *J. Appl. Electrochem.* **1999**, *29*, 1229–1235.
376. Y. Stefanov, I. Ivanov, S. Rashkov, *Hydrometallurgy* **1997**, *44*, 71–81.
377. I. Ivanov, Y. Stefanov, *Hydrometallurgy* **2002**, *64*, 111–117.
378. B. C. Tripathy, S. C. Das, P. Singh et al., *J. Electroanal. Chem.* **2004**, *565*, 49–56.
379. I. Ivanov, Y. Stefanov, *Hydrometallurgy* **2002**, *64*, 181–186.
380. D. S. Baik, D. J. Fray, *J. Appl. Electrochem.* **2001**, *31*, 1141–1147.
381. D. J. MacKinnon, J. M. Brannen, *J. Appl. Electrochem.* **1977**, *7*, 451–459.
382. D. J. MacKinnon, J. M. Brannen, P. L. Fenn, *J. Appl. Electrochem.* **1987**, *17*, 1129–1143.
383. D. J. MacKinnon, R. M. Morrison, J. E. Mouland et al., *J. Appl. Electrochem.* **1990**, *20*, 728–736.
384. R. Sato, *J. Electrochem. Soc.* **1959**, *106*, 206–211.
385. A. Hosny, *Hydrometallurgy* **1993**, *32*, 261–269.
386. M. Karavasteva, St. Karaivanov, *J. Appl. Electrochem.* **1993**, *23*, 763–765.
387. M. Karavasteva, *Hydrometallurgy* **1994**, *35*, 391–396.

388. M. Sider, D. L. Piron, *J. Appl. Electrochem.* **1988**, *18*, 54–61.
389. S. C. Das, P. Singh, G. T. Heftner, *J. Appl. Electrochem.* **1996**, *26*, 1245–1252.
390. B. C. Tripathy, I. N. Bhattachary, P. G. Krishna et al., *Trans. Indian Inst. Met.* **1998**, *51*, 303–310.
391. D. J. MacKinnon, J. M. Brannen, R. M. Morrison, *J. Appl. Electrochem.* **1988**, *18*, 252–256.
392. D. J. MacKinnon, J. M. Brannen, *J. Appl. Electrochem.* **1982**, *12*, 21–31.
393. D. J. MacKinnon, J. M. Brannen, R. M. Morrison, *J. Appl. Electrochem.* **1983**, *13*, 39–53.
394. B. C. Tripathy, S. C. Das, P. Singh et al., *Bull. Electrochem.* **1998**, *14*, 436–438.
395. G. Juvel, B. Beden, C. Lamy et al., *Electrochim. Acta* **1990**, *35*, 479–481.
396. C. Cachet, Z. Charni, R. Wiart, *Electrochim. Acta* **1987**, *32*, 465–474.
397. C. Cachet, B. Saidani, R. Wiart, *J. Electrochem. Soc.* **1991**, *138*, 678–687.
398. M. Naja, N. Penazzi, G. Farnia et al., *Electrochim. Acta* **1993**, *38*, 1453–1459.
399. A. M. Alfantazi, D. B. Dreisinger, *Hydrometallurgy* **2003**, *69*, 99–107.
400. I. Ivanov, *Hydrometallurgy* **2004**, *72*, 73–78.
401. L. Muresan, G. Maurin, L. Oniciu et al., *Hydrometallurgy* **1996**, *40*, 335–342.
402. A. E. Elshierief, A. S. Saba, *Trans. Indian Inst. Met.* **1996**, *49*, 769–779.
403. A. S. Saba, A. E. Elshierief, *Hydrometallurgy* **2000**, *54*, 91–106.
404. St. Rashkov, Ts. Dobrev, Z. Noncheva et al., *Hydrometallurgy* **1999**, *52*, 223–230.
405. J. St. Pierre, D. L. Piron, *J. Appl. Electrochem.* **1986**, *16*, 447–456.
406. J. St. Pierre, D. L. Piron, *J. Appl. Electrochem.* **1990**, *20*, 163–165.
407. Z. Youcui, R. Stanforth, *J. Hazard. Mater. B* **2000**, *80*, 223–240.
408. J. R. Park, H. T. Kim, *Plat. Surf. Finish.* **1999**, *86*, 108–112.
409. J. Y. Lee, J. W. Kim, M. K. Lee et al., *J. Electrochem. Soc.* **2004**, *151*, C25–C31.
410. J. W. Kim, J. Y. Lee, S. M. Park, *Langmuir* **2004**, *20*, 459–466.
411. S. J. Kim, H. T. Kim, S. M. Park, *J. Electrochem. Soc.* **2004**, *151*, C850–C854.
412. J. X. Yu, Y. Y. Chen, H. X. Yang et al., *J. Electrochem. Soc.* **1999**, *146*, 1789–1793.
413. M. Wery, J. C. Catonné, V. Ligier et al., *J. Appl. Electrochem.* **1999**, *29*, 729–739.
414. M. Wery, J. C. Catonné, J. Y. Hihn, *J. Appl. Electrochem.* **2000**, *30*, 165–172.
415. V. S. Kolsnitsyn, O. A. Yapryntseva, *Russ. J. Appl. Chem.* **2004**, *77*, 222–225.
416. J. A. Diez, C. Muller, H. Grande, *Rev. Metal. Madrid* **2004**, *40*, 182–187.
417. M. Chandran, R. L. Sarma, R. M. Krishnan, *Trans. Inst. Met. Finish.* **2003**, *81*, 207–209.
418. M. Chandran, R. L. Sarma, R. M. Krishnan, *Bull. Electrochem.* **1999**, *15*, 242–247.
419. M. Chandran, R. L. Sharma, R. M. Krishnan, *Plat. Surf. Finish.* **2001**, *88*, 74–77.
420. R. Sekar, S. Sriveeraraghavan, R. M. Krishnan, *Bull. Electrochem.* **1999**, *15*, 219–222.
421. Y. Y. Wang, W. J. Peng, L. Y. Chai et al., *J. Cent. South. Univ. Technol.* **2003**, *10*, 183–189.
422. Z. Wu, L. Fedrizzi, P. L. Bonora, *Surf. Coat. Technol.* **1996**, *85*, 170–174.
423. Y. S. Jin, T. Y. Kim, K. Y. Kim, *Surf. Coat. Technol.* **1998**, *106*, 220–227.
424. E. Beltowska-Lehman, P. Ozga, Z. Swiatek et al., *Surf. Coat. Technol.* **2002**, *151*–*152*, 444–448.
425. C. Bories, J.-P. Bonino, A. Rousset, *J. Appl. Electrochem.* **1999**, *29*, 1045–1051.
426. G. Roventi, R. Fratesi, R. A. Della Guardia et al., *J. Appl. Electrochem.* **2000**, *30*, 173–179.
427. I. Ivanov, I. Kirilova, *J. Appl. Electrochem.* **2003**, *33*, 239–244.
428. J. B. Bajat, M. D. Maksimovic, G. R. Radovic, *J. Serb. Chem. Soc.* **2002**, *67*, 625–634.
429. B. Y. Chang, S. M. Park, *J. Electrochem. Soc.* **2004**, *151*, C786–C788.
430. Z. A. Hamid, *Anti-Corros. Methods Mater.* **1998**, *45*, 31.
431. R. Fratesi, G. Roventi, G. Giuliani et al., *J. Appl. Electrochem.* **1997**, *27*, 1088–1094.
432. I. Kirilova, I. Ivanov, S. Rashkov, *J. Appl. Electrochem.* **1997**, *27*, 1380–1384.
433. C. R. Tomachuk, C. M. D. Freire, M. Ballester et al., *Surf. Coat. Technol.* **1999**, *122*, 6–9.
434. K. Hayashi, Z. Tanaka, K. Kondo, *J. Iron Steel Inst. Jpn.* **1999**, *85*, 314–318.
435. Z. A. Hamid, *Anti-Corros. Methods Mater.* **2001**, *48*, 235–240.
436. G. Trejo, R. Ortega, Y. Meas et al., *J. Appl. Electrochem.* **2003**, *33*, 373–379.

437. A. Cunha, S. D. Carpenter, J. Z. Ferreira et al., *Corros. Eng. Sci. Technol.* **2003**, *38*, 313–316.
438. D. E. O. S. Carpenter, M. Ashworth, J. P. G. Farr, *Trans. Inst. Met. Finish.* **2003**, *81*, 177–181.
439. E. Gómez, X. Alcobe, E. Vallés, *J. Electroanal. Chem.* **2001**, *505*, 54–61.
440. K. Wang, H. W. Pickering, K. G. Weil, *Electrochim. Acta* **2001**, *46*, 3835–3840.
441. E. Guaus, J. Torrent-Burgués, *J. Electroanal. Chem.* **2005**, *575*, 301–309.
442. E. Guaus, J. Torrent-Burgués, *J. Electroanal. Chem.* **2003**, *549*, 25–36.
443. T. Tsuru, S. Kobayashi, T. Aktiyama et al., *J. Appl. Electrochem.* **1997**, *27*, 209–214.
444. A. E. Rakhshani, B. Pradeep, *Appl. Phys. Mater. Sci. Process.* **2004**, *79*, 2021–2025.
445. A. E. Rakhshani, *Semicond. Sci. Technol.* **2004**, *19*, 543–547.
446. S. M. Rashwan, *Mater. Chem. Phys.* **2005**, *89*, 192–204.
447. M. M. Younan, *J. Appl. Electrochem.* **2000**, *30*, 55–60.
448. W. S. Miú, J. Ross, F. Lau et al., *Trans. Inst. Mater Met. Finish.* **1997**, *73*, 137–139.
449. M. Bouanani, F. Cherkaoui, M. Cherkaoui et al., *J. Appl. Electrochem.* **1999**, *29*, 1171–1176.
450. V. K. Gupta, A. K. Jain, L. P. Sing et al., *Electrochim. Acta* **1998**, *43*, 2047–2052.
451. V. K. Gupta, A. Kumar, R. Mangla, *Sens. Actuators, B* **2001**, *76*, 617–623.
452. V. K. Gupta, D. K. Chauhan, V. K. Saini et al., *Sensors* **2003**, *3*, 223–235.
453. A. K. Jain, S. M. Sondhi, S. Rajvanshi, *Electroanalysis* **2002**, *14*, 293–296.
454. A. R. Fakhari, M. Shamsipur, K. Ghanbari, *Anal. Chim. Acta* **2002**, *460*, 177–183.
455. S. K. Srivastava, V. K. Gupta, S. Jain, *Anal. Chem.* **1996**, *68*, 1272–1275.
456. H. R. Pouretedal, M. Shamsipur, *Fresenius' J. Anal. Chem.* **1998**, *362*, 415–418.
457. V. K. Gupta, *Sens. Actuators, B* **1999**, *55*, 195–200.
458. M. Shamsipur, S. Rouhani, M. R. Ganjali et al., *Sens. Actuators, B* **1999**, *59*, 30–34.
459. A. R. Fakhari, M. Alaghemand, M. Shamsipur, *Anal. Lett.* **2000**, *33*, 2169–2181.
460. M. B. Saleh, A. A. Abdel Gaber, *Electroanalysis* **2001**, *13*, 104–108.
461. A. K. Singh, G. Bhattacharjee, M. Singh et al., *Electroanalysis* **1997**, *9*, 1005–1008.
462. R. Dumkiewicz, C. Wardak, S. Zaręba, *Analyst* **2000**, *125*, 527–530.
463. R. Dumkiewicz, C. Wardak, J. Lenik et al., *Chem. Anal. (Warsaw)* **2002**, *47*, 257–265.
464. P. C. Pandey, G. Singh, *Sens. Actuators, B* **2002**, *85*, 256–262.
465. P. C. Pandey, G. Singh, P. K. Srivastava, *Electroanalysis* **2002**, *14*, 427–432.
466. O. I. Gyrdasova, V. L. Volkov, *J. Anal. Chem.* **1998**, *53*, 535–538.
467. E. M. Rakham'ko, V. V. Egorov, M. Ya. Tarazevich et al., *J. Anal. Chem.* **2003**, *58*, 691–697.
468. M. R. Ganjali, M. Rezapour, M. R. Pourjavid et al., *Anal. Lett.* **2003**, *36*, 881–894.
469. P. Buhlmann, L. Yahya, R. Enderes, *Electroanalysis* **2004**, *16*, 973–978.
470. S. Zhuiykov, T. Ono, N. Yamazoe et al., *Solid State Ionics* **2002**, *152*, 801–807.
471. N. Miura, K. Akisada, J. Wang et al., *Ionics* **2004**, *10*, 1–9.
472. H. A. Arida, R. F. Aglan, *Anal. Lett.* **2003**, *36*, 895–907.
473. N. Y. Stozhko, G. N. Lipunova, T. I. Maslakova et al., *J. Anal. Chem.* **2004**, *59*, 179–184.
474. B. Ge, F. W. Scheller, F. Lisdat, *Biosens. Bioelectron.* **2003**, *18*, 295–302.
475. W. Wiyaratn, M. Somasundrum, W. Surareungchai, *Electroanalysis* **2003**, *15*, 1719–1722.
476. D. R. do Carmo, D. W. Franco, U. P. Rodrigues et al., *J. Coord. Chem.* **2001**, *54*, 455–468.
477. S. B. Khoo, Q. T. Cai, *Electroanalysis* **1996**, *8*, 549–556.
478. A. Eftekhari, *J. Electroanal. Chem.* **2002**, *537*, 59–66.
479. J. Joseph, H. Gomathi, G. P. Rao, *J. Electroanal. Chem.* **1997**, *431*, 231–235.
480. M. H. Pournaghi-Azar, H. Nahalparvari, *J. Solid State Electrochem.* **2004**, *8*, 550–557.
481. N. Allietta, R. Pansu, C. Bied-Charreton et al., *Synth. Met.* **1996**, *81*, 205–210.
482. S. N. Kuester, M. M. McGuire, S. M. Drew, *J. Electroanal. Chem.* **1998**, *452*, 13–18.
483. K. L. Brown, J. Shaw, M. Ambrose et al., *Microchem. J.* **2002**, *72*, 285–298.
484. T. Pauporte, T. Yoshida, A. Goux et al., *J. Electroanal. Chem.* **2002**, *534*, 55–64.
485. M. Bouroushian, T. Kosanovic, Z. Loizos et al., *J. Solid State Electrochem.* **2002**, *6*, 272–278.

486. T. Mahalingam, V. S. John, P. J. Sebastian, *J. Phys.: Condens. Matter* **2002**, *14*, 5367–5375.
487. T. Mahalingam, V. S. John, S. Rajendran et al., *Semicond. Sci. Technol.* **2002**, *17*, 465–470.

24.2**Electrochemistry of Cadmium**

24.2.1	Double-layer Properties of Cadmium Electrodes	768
24.2.2	Electrochemical Properties and Kinetics of the Cd(II)/Cd(Hg) Systems	770
24.2.2.1	Electrochemistry in Aqueous Solutions	770
24.2.2.1.1	Kinetics of Simple Ions	770
24.2.2.1.2	Influence of a Catalyst	771
24.2.2.1.3	Influence of Inhibitors	773
24.2.2.2	Electrochemistry in Mixed and Nonaqueous Solvents	774
24.2.2.3	Electrochemical Properties of the Cadmium Complexes	775
24.2.2.3.1	Determination of Stability Constants	777
24.2.2.3.2	Electrochemical Preparation of Cadmium Complexes	778
24.2.2.4	Preparation and Electrochemical Properties of Cadmium Chalcogenides	779
24.2.2.4.1	CdS	779
24.2.2.4.2	CdSe	780
24.2.2.4.3	CdTe	781
24.2.2.5	Properties of Cadmium Intermetallic Compounds	782
24.2.3	Cadmium Underpotential Deposition and Electrodeposition on Solid Electrodes	782
24.2.3.1	Deposition of Cd on Cadmium Electrode	782
24.2.3.2	Electrodeposition of Cd on Other Solid Substrates	783
24.2.3.2.1	Gold	783
24.2.3.2.2	Platinum	786
24.2.3.2.3	Silver	787
24.2.3.2.4	Copper	787
24.2.3.2.5	Silicon	788
24.2.3.2.6	Other Substrates	788
24.2.4	Passivation and Corrosion of Cadmium	789
24.2.4.1	Passivation of Cadmium Electrode	789
24.2.4.2	Corrosion of Cadmium	789
24.2.5	Applied Electrochemistry	790
24.2.5.1	Batteries	790
24.2.5.1.1	Cadmium–Mercuric Oxide Primary Cells	790

24.2.5.1.2	Cadmium–Nickel Oxide (Ni–Cd) Secondary Cells	790
24.2.5.1.3	Cadmium–Silver Oxide Secondary Cells	791
24.2.5.2	Application in Electrochemical Sensors	792
24.2.5.2.1	Potentiometric Sensors	792
24.2.5.2.2	Amperometric-voltammetric Sensors	793
	References	794

24.2.1 **Double-layer Properties of Cadmium Electrodes**

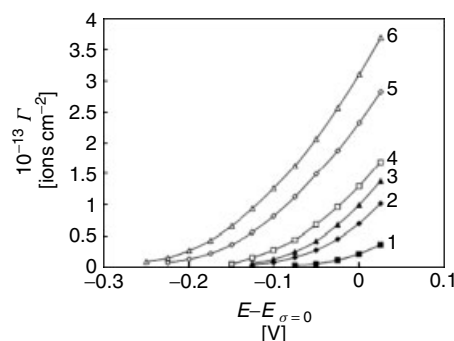
The electrical double-layer (edl) properties pose a fundamental problem for electrochemistry because the rate and mechanism of electrochemical reactions depend on the structure of the metal–electrolyte interface. The theoretical analysis of edl structures of the solid metal electrodes is more complicated in comparison with that of liquid metal and alloys. One of the reasons is the difference in the properties of the individual faces of the metal and the influence of various defects of the surface [1]. Electrical double-layer properties of solid polycrystalline cadmium (pc-Cd) electrodes have been studied for several decades. The dependence of these properties on temperature and electrode roughness, and the adsorption of ions and organic molecules on Cd, which were studied in aqueous and organic solvents and described in many works, were reviewed by Trasatti and Lust [2].

In recent years, similar studies have been carried out for Cd single crystal electrode. Korotkov et al. [3] showed that the zero charge potential (E_{pzc}) of a Cd(11 $\bar{2}$ 0) in surface inactive electrolytes, NaF and Na₂SO₄, was shifted slightly in the negative direction in comparison with E_{pzc} of pc-Cd.

Naneva and Popov et al. [4, 5] have studied Cd(0001) grown electrolytically in a Teflon capillary in NaF aqueous solution. A value of E_{pzc} equal to –0.99 V (versus saturated calomel electrode (SCE)) was evaluated from minimum potential (E_{min}) on the differential capacity $C-E$ curves obtained in dilute electrolyte. The zero charge potential was found to be practically independent of the crystallographic orientation. The E_{pzc} and the inner layer capacity of Cd(0001) single crystals were determined in KF solution as a function of temperature [5]. The positive values of $\Delta E_{\text{pzc}}/\Delta T$ indicated that the water dipoles in the inner part of the double layer were orientated with their negative part to the electrode surface. It was found that the hydrophilicity of the electrodes was increasing in the order Cd(0001) < Ag(100) < Ag(111).

The capacitance-potential dependences of Cd(0001) in dilute solutions of ClO₄[–], NO₂[–], and NO₃[–] were also studied [6]. A weak specific adsorption of anions increasing in the order ClO₄[–] < NO₂[–] < NO₃[–] was observed. The adsorption of halides on the Cd(0001) single crystal electrode was studied [7], and was found to increase in the sequence Cl[–] < Br[–] < I[–] [8]. Analysis of the impedance data does not point to the specific adsorption of Cl[–] ions, and shows that the surface excess (Γ) of halide ions changes with potential and increases from Br[–] to I[–] (Fig. 1) [7]

Fig. 1 Surface concentration of adsorbed ions versus rational electrode potential curves for the Cd(0001) electrode in aqueous solution with constant ionic strength $0.1x\text{ M}$ $\text{KA}^* + 0.1(1-x)\text{ M KF}$, where A^* is the surface-active halide ion (Br^- curves 1–3) and (I^- curves 4–6), and x is its mole fractions. $x = 0.1$ (curves 1, 4); $x = 0.5$ (curves 2, 5); and $x = 1.0$ (curves 3, 6) [7].



in accordance with the hydration energy of the anions. To describe adsorption of halide ions, the cluster model and quantum chemical calculations were used.

The double-layer structure at the electrochemically polished and chemically treated Cd(0001), Cd(1010), Cd(11̄20), Cd(1011), and Cd(11̄21) surface electrodes was studied using cyclic voltammetry, impedance spectroscopy, and chronocoulometry [9, 10]. The limits of ideal polarizability, E_{pzc} , and capacity of the inner layer were established in the aqueous surface inactive solutions. The values of E_{pzc} decrease, and the capacity of the inner layer increases, if the superficial density of atoms decreases. The capacity of metal was established using various theoretical approximations. The effective thickness of the thin metal layer increases in the sequence of planes $\text{Cd}(11\bar{2}0) < \text{Cd}(10\bar{1}0) < \text{Cd}(0001)$. It was also found that the surface activity of ClO_4^- was higher than that of F^- anions [10].

The experimental data concerning capacitance of edl at the selected faces of Bi, Sb, and Cd single crystals in solutions of surface inactive electrolytes in water and organic solvent were analyzed in terms of various models [11]. From these data, it follows that the interface electrode/electrolyte properties depend both on the crystallographic and electronic characteristics of the metal and on the nature of the solvent.

Lust et al. have also investigated the adsorption of cyclohexanol [12] and various organic compounds [13, 14] on several cadmium single crystal electrodes. It was also found that the zero charge potential depended on the crystallographic structure (plane) of the electrode surface and on the nature of the solvent studied [12]. The Gibbs energy of metal–water interaction depends weakly on the chemical nature of the metal and aliphatic organic compound [13]. The edl properties of cadmium electrode were studied [15, 16] in terms of the Debye length dependent roughness theory recently developed by Daikhin et al. [17, 18]. This theory was used for the interpretation of capacitance data for cadmium electrode with various surface roughness and energetic inhomogeneity.

Structural aspects of electrochemical adsorption of inorganic ions and neutral organic molecules and water dipoles on quasi-perfect cadmium electrode were also studied [19].

The edl structure of a Cd–Ga (0.3 atom % Cd) liquid electrode in aqueous [20, 21], methanol, and propylene carbonate (PC) [21, 22] solutions with inactive electrolyte (LiClO_4 , LiBF_4) was investigated. The double layer at the liquid Cd–Ga alloy differs from that of a Ga electrode, and was virtually identical with edl at the Cd electrode.

24.2.2

Electrochemical Properties and Kinetics of the Cd(II)/Cd(Hg) Systems**24.2.2.1 Electrochemistry in Aqueous Solutions**

24.2.2.1.1 Kinetics of Simple Ions The electroreduction of Cd(II) ions to its amalgam was investigated in aqueous 1 M KF [23] and 1 M (KF + KCl) mixed electrolyte solutions at dropping mercury electrode (DME) using the faradaic impedance method [24]. From the analysis of the impedance data, it follows that the electrode process is described by mechanism with chemical step followed by two one-electron transfers (CEE). The kinetic parameters of both steps are reported and discussed. The rate constant of the chemical step increases rapidly with chloride concentration.

In mixed $(0.8 - x)$ M NaClO₄ + x M NaF supporting electrolyte the electroreduction of Cd(II) was also studied by Saakes et al. [25]. The kinetic parameters were analyzed using CEE mechanism. The obtained chemical rate constants $k_{s,0}^c$ at both steps, $k_{s,1}$ and $k_{s,2}$, decreased with increasing NaF concentration. The data were corrected for nonspecific double-layer effect (Frumkin correction). The interpretation of CEE mechanism with parallel pathways connected with coexisting cadmium complexes was presented.

The mechanism of the reduction of cadmium ions at DME in NaClO₄ solutions with varied water activity was also studied [26]. In these solutions, the electrode process of the Cd(II)/Cd(Hg) system was described by the mechanism that includes: (1) fast loss of 12.5 water molecules in a preceding equilibrium, (2) a slow “chemical” step, which is not a desolvation, (3) slow transfer of the first electron,

$k_{s,1}$, (4) fast loss of four water molecules, (5) slow transfer of the second electron $k_{s,2}$, and (6) fast loss of the remaining nine water molecules. The $k_{s,1}$ and $k_{s,2}$ values increase with decreasing water activity.

The reduction of Cd(II) ions on DME was also investigated in 1 M perchlorate, fluoride and chloride solutions using dc, ac admittance, and demodulation methods [27]. It was found that in the perchlorate supporting electrolyte, the reduction mechanism is also CEE, and that the rate constant of the chemical step is quite close to the value characteristic for fluoride solutions. The theories available at present could not be applied to the Cd(II) reduction in chloride solution because of the inapplicability of the Randles equivalent circuit.

The combination of three transient techniques – coulostatic, modified coulostatic, and galvanostatic methods was applied for the study of the electrode reaction Cd(II)/Cd(Hg) in aqueous solution of 1 M Na₂SO₄, pH 4 [28].

Recently, Darowicki [29, 30] has presented a new mode of electrochemical impedance measurements. This method employed a short time Fourier transformation to impedance evaluation. The digital harmonic analysis of cadmium-ion reduction on mercury electrode was presented [31]. A modern concept in nonstationary electrochemical impedance spectroscopy theory and experimental approach was described [32]. The new investigation method allows determination of the dependence of complex impedance versus potential [32] and time [33]. The reduction of cadmium on DME was chosen to present the possibility of these techniques. Figure 2 illustrates the change of impedance for the Cd(II) reduction on the hanging drop mercury electrode obtained for the scan rate 10 mV s⁻¹.

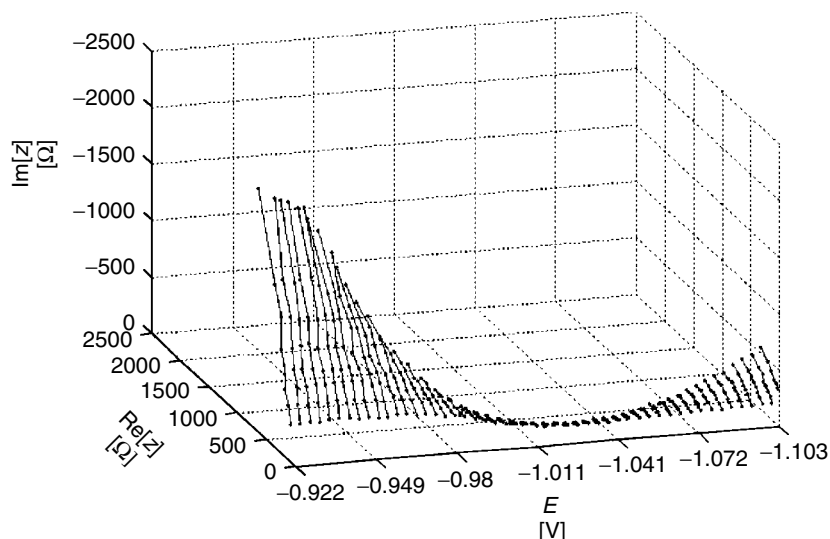


Fig. 2 Changes of impedance during reduction of 2 mM Cd(II) in 0.5 M Na_2SO_4 on HDME. Potential scan rate 10 mV s^{-1} [32].

A uniform approach to trace the analysis and evaluation of electrode kinetics of the Cd(II)/Cd(Hg) system with fast Fourier transform electrochemical instrumentation was presented by Schiewe et al. [34].

The principles of thin-layer anodic stripping voltammetry were discussed, and a model for the stripping stage was developed for anodization by a linear potential ramp [35]. The experimental test of the theories was carried out for cadmium and lead amalgams.

The convolution–deconvolution voltammetry, combined with digital simulation techniques, was applied [36] to determine the electrochemical and chemical parameters for the Cd(II)/Cd(Hg) system in aqueous NaNO_3 solution. The agreement between experimental and theoretical data indicated that the reduction mechanism at the mercury electrode proceeds via consisting in chemical step (C) followed by charge transfer step (E)-so-called CE mechanism [37].

The dropping mercury microelectrode (DM_μE) technique was used for the mechanistic study of Cd(II) reduction in aqueous KF [38] and 0.5 M Na_2SO_4 [39] solutions.

24.2.2.1.2 Influence of a Catalyst From the data obtained with impedance and de-modulation voltammetry for a solution of x M KCl + $(1-x)$ M KF [40], it follows that chloride ions catalyze the Cd(II)/Cd(Hg) process (Fig. 3); the cadmium reduction proceeds according to several chemical (C) and charge transfer (E) steps, so-called CE-CEC mechanism. The catalyst accelerates specifically the first chemical and the first electrochemical step.

The adsorption of reactant in the system Cd(II) + 1 M KBr/Cd(Hg) was investigated by using chronocoulometry [41]. The values of the reactant surface excess were calculated. The authors proposed the adsorption isotherm, which allows the adsorption of the reactant and ligand to

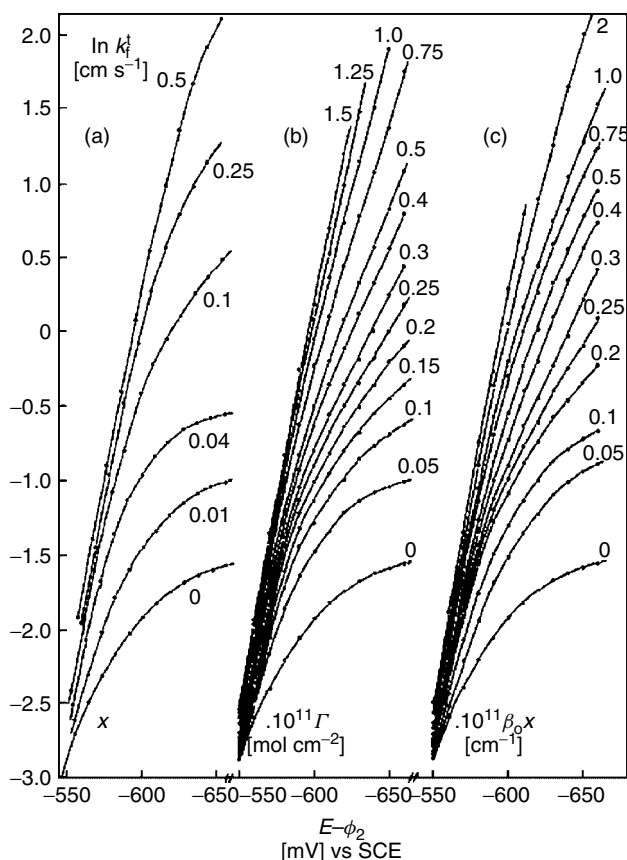


Fig. 3 The natural logarithms of “true” rate constants of Cd(II)/Cd(Hg) system versus $E - \phi_2$, depending on: (a) Cl^- concentration – (x); (b) surface excess of Cl^- ions – (Γ_{Cl^-}) and (C) $\beta_0 x$ values at each curve [40].

be correlated. A statistical thermodynamic approach to the study of anion-induced adsorption of Cd(II) from halide solutions was also presented by Guaus et al. [42]. The simultaneous adsorption of metal complex and ligand was introduced in the isotherms by considering two possible mechanisms (1) competitive adsorption of metal complex and (2) surface complexation. These isotherms were tested for the Cd(II)-KBr system at several ionic strengths. It was found that CdBr_3^- and CdBr_4^{2-} are the adsorbed species.

This approach was also applied for the investigation of anion-induced adsorption in the Cd(II)-KI system at several ionic strengths [43].

The adsorption of reactant in the Cd(II)-I⁻ system [44], and the influence of electrolyte concentration (1–6 M NaClO₄) on the parameters of the Frumkin isotherm system were investigated [45]. The obtained data indicated that the maximum surface concentration of CdI_2 ($\Gamma_{\text{max}} = 1 \times 10^{-10}$ to $(2.2 \pm 0.2) \times 10^{-10}$ mol cm⁻²), adsorption constant ($\beta = 3.1 \times 10^5$ to

$(1.55 \pm 0.35) \times 10^7 \text{ l mol}^{-1}$

and Frumkin coefficient ($a = 0$ to 0.5 ± 0.1) all increase with increasing electrolyte concentration.

The catalytic effect of thiourea on the electrochemical reduction of Cd(II) ions at the DME from aqueous 1 M KF solutions was investigated [46] and described by the equation $k_f^t = k_f^{t,0} (1 + B\Gamma_{Tu})$, where B is a proportionality constant, Γ_{Tu} is the surface excess of thiourea, while k_f^t and $k_f^{t,0}$ denote the true rate constant determined at certain potential in the presence and absence of thiourea, respectively. Because of the stepwise reaction mechanism, an explanation in terms of the bridging or the surface reaction model fails. A possible alternative interpretation of the effect was given.

The formalism developed to describe current-potential characteristics for the Cd(II)/Cd(Hg) multistep electrode reaction [47] was used for the investigation of catalytic and inhibiting influence connected with variation of electrolyte composition.

A theoretical model of square-wave voltammetry (SWV) combined with adsorptive accumulation of reactant was presented [48].

24.2.2.1.3 Influence of Inhibitors The Cd(II) reduction at the mercury electrode from aqueous 1 M NaClO₄ in the presence of sucrose was described [49] by CEE mechanism. An attempt was made to correlate the individual standard rate constants that became lower with increasing concentration of sucrose, with (1) the surface coverage by sucrose, and (2) the viscosity of the solution layer adjacent to the electrode surface.

Catalysis and inhibition of the electroreduction of cadmium ions at a partially blocked DM _{μ} E by 1-butanol was

studied [50]. The rate constant showed nonlinear dependence on the coverage; it was enhanced by the adsorption of 1-butanol at potentials $E < -0.85$ V versus SCE, whereas it was inhibited at $E > -0.75$ V. A statistical model interpreting both the catalytic and the inhibiting influence was proposed.

The mechanism of Cd(II) discharge and cadmium amalgam dissolution in the absence and presence of adsorbed aliphatic alcohols and acids [51], and also the inhibiting influence of the adsorbed aliphatic alcohols and acids on the kinetics of the Cd(II)/Cd(Hg) system was studied [52, 53]. The role of the steric factors on the electrode reaction occurring in the presence of adsorbed inhibitors was investigated.

The behavior of the Cd(II)/Cd(Hg) system in the absence and presence of *n*-pentanol in noncomplexing media was analyzed using reciprocal derivative and double derivative chronoamperometry with programmed current (RDCP and RDDCP respectively) [54]. The RDCP and RDDCP are very versatile in the determination of kinetic parameters of electrode processes.

Marczewska [55] has found that the Cd(II) electroreduction in water-*N,N*-dimethylformamide (DMF) + NaClO₄ solutions was inhibited in the presence of thiourea.

The inhibiting influence of cyclodextrins on the Cd(II)/Cd(Hg) electrode processes was studied [56]. It was found that the inhibition coefficient increases in the series α -cyclodextrin < γ -cyclodextrin < β -cyclodextrin. It was observed [57] that the reduction current of Cd(II) ions was affected by the condensed film of α -cyclodextrin formed on the mercury electrode.

In the presence of methylated β -cyclodextrin [58,] the reaction rate of

the Cd(II)/Cd(Hg) system decreases in the order *per*-(2,3-di-*O*-methyl)- β -cyclodextrin > *per*-(2,3,6-tri-*O*-methyl)- β -cyclodextrin > *per*-(6-amino-2,3-di-*O*-methyl)- β -cyclodextrin.

24.2.2.2 Electrochemistry in Mixed and Nonaqueous Solvents

For the rapid electron transfer process, which follows a reversible chemical step (CE), a procedure is presented for the determination of chemical and electrochemical kinetic parameters. It is based on convolution electrochemistry and was applied for cyclic voltammetry with digital simulation [59] and chronoamperometric curves [60]. The analysis was applied to both simulated and experimental data. As an experimental example, the electroreduction of Cd(II) on HMDE electrode in dimethylsulphoxide (DMSO) [59] and DMF [60] with 0.5 M tetraethylammonium perchlorate (TEAP) was investigated.

The electrode process of the Cd(II)/Cd(Hg) system was investigated in water–DMSO [61] and hexamethylphosphoramide (HMPA) solutions [62]. The formal potentials, charge-transfer rate constant, and diffusion coefficients were determined. In the presence of adsorbed HMPA molecules, the rate constant was found to be dependent only on the surface phase composition.

It was concluded that the change in the kinetics of the Cd(II)/Cd(Hg) system with mixed solvent composition may be described by different model equations in water–DMSO [61], and water–HMPA solvents [62].

Generally, the influence of solvent adsorption and reactant solvation on electrochemical rate constants of the Cd(II)/Cd(Hg), Zn(II)/Zn(Hg), and Pb(II)/Pb(Hg) systems in mixed solvents

was theoretically described and compared with experimental data [63].

The kinetics of the Cd(II)/Cd(Hg) reaction was also studied in organic solvents [64–66]. The double-layer effect on electroreduction of Cd(II) ions at mercury electrode was investigated in DMF solution with various concentrations of tetraalkylammonium salts [64]. The standard rate constant decreased with increasing concentration of TEAP, tetrapropylammonium perchlorate (TPAP), and tetrabutylammonium perchlorate (TBAP), while the diffusion coefficient and cathodic transfer coefficient of the cadmium electrode process changed only slightly. At constant concentration of the electrolyte, the standard rate constant decreased with increase in the size of the supporting electrolyte cation in the order $k_s(\text{TEA}^+) > k_s(\text{TPA}^+) > k_s(\text{TBA}^+)$. The change of the kinetic parameters with the nature of the base electrolyte was discussed in terms of double-layer effect and nature of the rate-determining step. The low values of the transfer coefficients were explained, assuming slow transfer of the reactant across the inner layer.

In DMSO solution, the standard rate constant and cathodic transfer coefficient of the Cd(II)/Cd(Hg) system decreased with increasing concentration of TEAP [65]. It was found that a chemical reaction, probably partial desolvation of the reactant, precedes the electron transfer, and Cd(II) is reduced according to the CEE mechanism. The kinetic parameters of this process were determined.

The standard rate constants of the Cd(II)/Cd(Hg) system measured in several solvents [66] corrected for the double-layer effect, decrease in the order $k_{s,a}(\text{AN}) > k_{s,a}(\text{PC}) > k_{s,a}(\text{formamide}) > k_{s,a}(\text{DMF}) > k_{s,a}(\text{DMSO}) > k_{s,a}(\text{HMPA})$ (see Fig. 4). Solvent

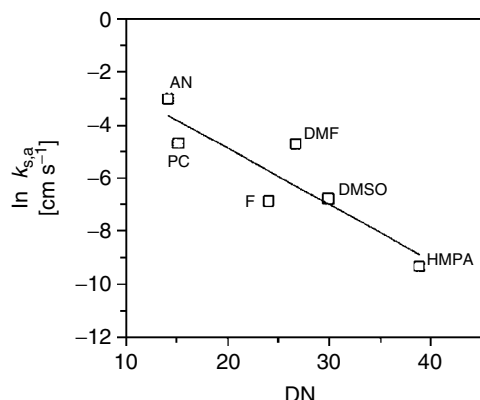


Fig. 4 Dependence of the logarithm of standard rate constant corrected for the double-layer effect of the Cd(II)/Cd(Hg) system on donor number of the solvents [66].

effects were analyzed in terms of the solvation parameters of the cation and dynamic properties of the solvent.

The double-layer effect in the electrode kinetics of the amalgam formation reactions was discussed [67]. The dependences on the potential of two reduction (EE) mechanisms of divalent cations at mercury electrode, and ion transfer–adsorption (IA) were compared. It was suggested that a study of temperature dependence of the course of these reactions would be helpful to differentiate these two mechanisms.

The half-wave potentials of Cd(II), Zn(II), and Pb(II) ions electroreduction in 22 nonaqueous solvents were used in the analysis of solvent effect on electrode potential [68].

The literature data on the kinetics of Cd(II), Zn(II), and Pb(II) electrodeposition on mercury electrode in different organic solvents were also analyzed [69].

The solvation number of reactants and reaction orders of the electrode processes of Cd(II)/Cd(Hg), Zn(II)/Zn(Hg), and Pb(II)/Pb(Hg) systems were evaluated in nonaqueous media [70].

The mechanism of Cd(II) transfer in methanol across saturated organic compounds monolayers adsorbed on the mercury electrode was also studied [71].

24.2.2.3 Electrochemical Properties of the Cadmium Complexes

The electrochemical properties of Cd(II) complexes with inorganic ligand presented in early papers were discussed by Hampson and Latham [72]. Later, electrochemical investigations of cadmium complexes were oriented on the mechanism of complex formation, determination of stoichiometry and stability constants, mechanisms of reduction on the electrodes, and evaluation of kinetic parameters of these processes. The influence of ligands and solvents on stability and kinetic parameters of electroreduction was also studied.

Electroreduction of Cd(II)–nitrilotriacetic acid and Cd(II)–aspartic acid systems was studied on DME using SWV [73]. The CE mechanism in which the chemical reaction precedes a reversible electron transfer was established. Also, the rate constants of dissociation of the complexes were determined. Esteban and coworkers also studied the cadmium complexes with nitrilotriacetic acid [74, 75] and fulvic acid [76]. The complexation reaction of cadmium by glycine was investigated by different electrochemical methods using HMDE and mercury microelectrode [77, 78].

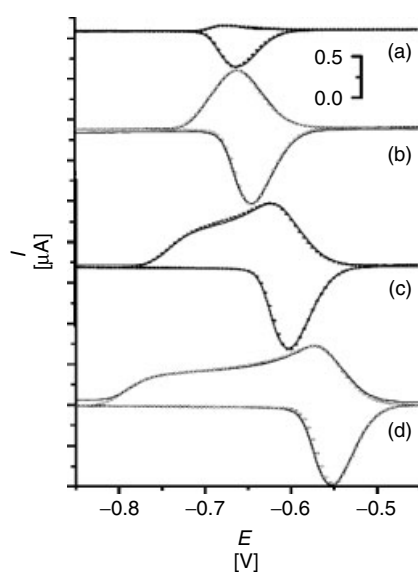


Fig. 5 Experimental (—) and calculated (symbols) square-wave voltammograms (SWV) for 3.9×10^{-7} M $\text{Cd}(\text{NO}_3)_2 + 1.35 \times 10^{-5}$ M oxine in 0.1 M buffer solution pH 6.7 $E_A = -0.1$ V. The SWV were obtained for frequency $-f = 300$ Hz, step height $-dE = 5$ mV and varied E_{sw} : (a) 8; (b) 35; (c) 80; and (d) 130 mV [84].

The reduction of the $\text{Cd}(2,2,2)^{2+}$ complex on mercury electrodes was studied in aqueous solutions free and saturated with *n*-pentanol and *n*-octanol [86] and also in acetonitrile [87]. The corresponding reduction mechanism was established and the kinetic parameters were calculated.

The synthesis, structure, and complexing properties of new triazacoronands with respect to Cd(II), were presented [88].

The Cd(II)/Cd(Hg) system was investigated in the presence of 2-mercaptoacetic acid as a function of pH [89]. The bidentate complexes of Cd(II) with 2-mercaptoacetic acid are stable and undergo a reversible two-electron reduction on the mercury electrode.

The effect of the solvent properties on the polarographic behavior of Cd(II) complexes with glycine, *N*-acetyl, and *N*-benzoylglycine was studied in DMSO, acetonitrile (AN), and DMF solutions [90]. The stability constants were found to depend linearly on the acceptor numbers of the solvents.

Synthesis, photophysical, and electrochemical properties of dinuclear Cd(II) diimine complexes with bridging chalcogenolate ligands were described [91].

The reduction mechanism of Cd(II)-ferrocene complexes accumulated on static mercury electrode was studied using square wave voltammetry (SWV) [92]. The electrochemical behavior of Cd(II) complexes with cysteine and folic acid was investigated. Folic acid forms adducts

The electrode reaction of Cd(II) complexes with acetylacetone (acac) was investigated on the mercury electrode in the absence and in the presence of *n*-pentanol and *n*-octanol [79]. The kinetics parameters were evaluated, and the ionophoretic effect of acac was postulated on the basis of the interaction of the reactant with the adsorbed surface layer.

The electrochemical behavior of Cd-oxine complexes was analyzed by square-wave stripping voltammetry [80] from the mechanistic point of view, applying the theoretical model developed previously [81–83]. Influence of ligand and reactant adsorption, and the ligand concentration on the Cd-oxine electroreduction were also examined [84] using SWV. Typical curves recorded and calculated for several E_{sw} are shown in Fig. 5.

The reduction of Cd(II) on mercury electrode was used to study the interaction of Cd(II) ions with β -cyclodextrin. It was found that $[\text{Cd}(\beta\text{-cyclodextrin})(\text{OH})_2]^{2-}$ complex is formed in alkaline solutions [85].

with cysteine thiolate at the electrode surface, which influence the process of electroreduction of Cd(II)–cysteine complex [93]. The kinetics of cadmium binding by surface groups of chlorella marina cells [94, 95] was studied, and stability constants were determined.

An important mechanism of metal-detoxification involves intercellular thiol-containing compounds, such as glutathione (γ -glutamyl-cysteinyl glycine, denoted as GSH) and phytochelatins. Therefore, different electrochemical techniques and multivariate curve resolutions were used by Esteban with coworkers [96–103] for the investigation of Cd(II) complexes with such ligands. Complexes of Cd(II) with GSH [96–98], were studied and used as a model for coordination of Cd(II) by thiol-containing peptides [97]. Two complexes, $\text{Cd}(\text{GSH})_2$ and $\text{Cd}_2(\text{GSH})_2$ were formed in this system. The complexation of Cd(II) by GSH fragments [99], phytochelatine (γ -Glu-Cys)₃Gly [100, 101], and C-terminal hexapeptide of mouse metallothionein [102, 103], were also investigated.

The polarographic characteristics of Cd(II) and Zn(II) complexes with phytochelatin extracted from marine alga phaeodactylum tricornutum [104] were presented.

The peptide fragments of metallothioneins Lys-Cys-Thr-Cys-Cys-Ala [56–61] (FT) were studied by different electrochemical techniques. The cyclic voltammetric behavior of the peptide fragment in the presence of Cd(II) indicated two reversible electrochemical processes due to the oxidation of the mercury electrode in the presence of CdFT and reduction of CdFT complex, both from the dissolved and adsorbed state [105]. The influence of the experimental conditions on electroreduction of Cd–metallothioneins

complexes was also studied [106–111]. The cadmium(II) complexes with two different metallothioneins from rabbit liver were investigated by cyclic voltammetry [112].

24.2.2.3.1 Determination of Stability

Constants For the determination of the complexing ability of Cd(II) ions, the potentiometric and different polarographic methods were used [113–116]. The composition and the stability constants of Cd(II) complexes with phthalic acid [113], some benzene polycarboxylic acids [114], glycinamide [115] and crystal structure of Cd(II) phthalate hydrate were determined. The influence of basicity of ligand on the stability of Cd(I) mixed ligand complexes with glycine, alpha-alanine, L-valine, L-leucine, L-asparagine, and L-glutamine as the primary ligands and vitamin B₆ as secondary ligand was studied [116].

A polarographic study of the composition and stability constant of 2-aminoquinoxaline complex with Cd(II) in methanol–water mixtures was published by Pratihar [117].

The polarographic experimental and calculated curves of complex formation with the following ligands: *N*, *N'*-bis(2-pyridyl methyl)-1,2-diaminoethane [118], picolinic acid [119], *N*-(2-hydroxyethyl)ethylenediamine [120], 1-hydroxyethylenediphosphonic acid [121], and *N*-(2-hydroxyethyl)imidodiacetic acid [122] was used for modeling the Cd(II)–ligand systems. The stoichiometry and stability constants of formed complexes were evaluated. The same method was used for determinations of stability constants of Cd(II) complexes with monoaza-12-crown-4 ether in aqueous solution in the presence of an excess of sodium ions [123].

A polarographic study of Cd(II) complexes with macrocyclic ligands 18-crown-6, 1,10-diaza-18-crown-6 and cryptand (222) [124] and 18-crown-6 [125], dicyclohexano-18-crown-6 [126] in water-organic mixtures and aza-18-crown-6 and dibenzopyridino-18-crown-6 in nonaqueous solvents [127] was presented and stability constants were evaluated.

The cadmium complexes were also investigated potentiometrically. Using this method, the complexes of cadmium with asparagine [128], taurine [129], *N*-(6-amino-3-methyl-5-nitroso-4-oxo-3,4-dihydropyrimidin-2-yl)glycine [130], succinate and malate [131], acetate at different temperatures [132], pyridine oxime ligands [133], 2-hydroxypropene-1,3-diamine-*N,N,N',N'*-tetraacetic acid [134] were studied. The stoichiometry and stability constants of these complexes were determined.

The stability constants of the formed chloro-cadmium complexes in aqueous solution [135] and water-2-butanone mixtures [136] were also determined, using potentiometric measurements. The influence of hydrogen bonding of the solvent on the stability of Cd(II)-ethylenediamine complexes in water-DMSO mixtures was analyzed using pH and calorimetric measurement [137]. In five water-acetonitrile mixtures, the stability constants of Cd(II) and Zn(II) cyanide complexes were determined [138].

The complexation of Cd(II) with polymethacrylic acid, and humic acid [139] was studied potentiometrically using the Cd(II) ion-selective electrode.

In the last three decades, the complexes of many metal ions including Cd(II) with macrocyclic ligands were studied intensively. The thermodynamic data of Cd(II)-macrocyclic complexes were presented by Izatt et al. ([140–142] and literature cited therein).

24.2.2.3.2 Electrochemical Preparation of Cadmium Complexes

The application of electrochemical procedures for the preparation of cadmium complexes was studied intensively. In these syntheses, the cadmium metal or its amalgam was anodically oxidized in the presence of a ligand in an appropriate solution. Electrochemical synthesis of cadmium with 4-methyl-6-trifluoromethylpyrimidine-2-thione [143], 6-*tert*-butyldimethylsilylpyridine-2-thionate [144], 2,6-bis(1-salicyloylhydrazonoethyl)pyridine [145], and pentadentate ligand 1,6-bis{1-[2-(tosylamino)phenylimino]ethyl}pyridine [146] were carried out. Using the same method, the cadmium complexes with *N*-[(2-hydroxyphenyl) methylidine]-*N'*-tosylbenzene-1,2-diamine were obtained. When 1,10-phenanthroline or 2,2'-bipyridine was added to the cell, mixed ligand complexes were formed [147].

Pedrido et al. [148] also described the electrochemical synthesis and characterization of new neutral Zn(II), Cd(II), and Pb(II) complexes with bis(4-*N*-methylthiosemicarbazone)-2,6-diacylpyridine. The properties and crystal structure of the obtained complexes were studied.

Electrochemical oxidation of cadmium in a solution of [(4-methylphenyl)sulfonyl]-2-pyridylamine] (*HL*) in acetonitrile/di chloromethane mixtures resulted in CdL₂ complex formation [149]. The electrochemical oxidation of cadmium amalgam in nonaqueous solvents CH₂Cl₂, 1,2-C₂H₄Cl₂, and PC was also used for the preparation of cadmium complexes with 18-membered macrocyclic ligands, 18-O₆, 18-S₆, 18-N₂O₄, and 18-N₆ [150]. The stoichiometry and stability of resulted complexes were determined. The same method was used to examine the complexation of Cd(II) cation with 12-crown-4 ether, azacrown ether 1,4,8,11-tetraazacyclotetradecane, and thiaazacrown

ether 1,4,6,11-tetrathiacyclotetradecane in dichloromethane [151].

The electrochemical synthesis of cadmium and zinc thiolate complexes and their properties were reviewed in addition to other metal ion complexes [152].

24.2.2.4 Preparation and Electrochemical Properties of Cadmium Chalcogenides

24.2.2.4.1 CdS CdS is a typical example of semiconductor material; its properties and applications were presented in a review by Koval and Howard [153].

Cadmium chalcogenides CdS, CdSe, and CdTe (CdX) are important in a variety of applications ranging from solar cells to chemical/biological sensors. Thin films of these materials can be prepared by using many methods (e.g. vacuum evaporation, chemical bath deposition, and electrodeposition). Three types of electrochemical methods were used for growing thin films of CdX : (1) anodic oxidation of cadmium in a chalcogenide-containing electrolyte, (2) cathodic coreduction of $\text{Cd}(\text{II})$ and a chalcogenide oxyanion on an inert substrate, and (3) cathodic reduction of $\text{Cd}(\text{II})$ ions in nonaqueous solvent containing chalcogen in elemental form [154–156]. An alternative two-step method is based on initial electrochemical modification of the

substrate, usually polycrystalline gold, with the chalcogen. Then voltammetric stripping of the chalcogen (X) in an aqueous solution containing $\text{Cd}(\text{II})$ ions generates the CdX compound *in situ* on the electrode surface. This approach was used for CdS and CdSe formation [157–159].

The two-step synthesis of CdS on sulfur or thiol modified polycrystalline gold electrode was described [160]. The morphologies of CdS formed in both cases and the electrochemical behavior of these compounds were compared.

An electrochemical scanning probe microscopy and Raman spectroscopy investigation of thin CdS films grown by electrochemical atomic layer epitaxy (ECALE) aimed at understanding the role played by the order of deposition on film quality were reported [161].

Using the ECALE method, thin films of CdS were deposited on Ag (111). The deposit and its morphology were characterized [162].

Synthesis and characterization of nearly monodispersed CdX semiconductor nano crystallites were studied [163].

The hybrid electrochemical/chemical synthesis of epitaxially oriented CdS nanocrystallites-size selectively on graphite surface was described by Anderson et al. [164]. A schematic diagram of such synthesis is presented in Fig. 6.

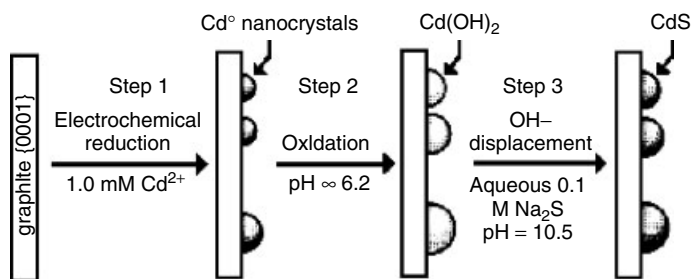


Fig. 6 Schematic diagram illustrating the three-step electrochemical/chemical epitaxial synthesis of CdS nanocrystals [164].

Synthesis and characterization of CdS nanoparticles embedded in a polymethylmethacrylate matrix was presented [165]. The assembly of CdS semiconductor nanoparticle monolayer on Au electrode was obtained, and its structural properties and photoelectrochemical applications were studied [166].

Rapid formation of CdS thin films by microwave-assisted chemical bath deposition and electrical properties of the films were studied [167].

Uniform thin films of CdS were prepared by template-assisted electrochemical deposition on Au electrodes covered with Langmuir-Blodgett (LB) films of cadmium arachidate [168]. It was found that different CdS films could be produced depending on the type of LB film used.

CdS thin films were also prepared on indium tin oxide (ITO)-covered glass by successive ionic layer adsorption and reaction (SILAR) techniques [169]. The thickness of the CdS film increased with the number of SILAR cycles. The surface roughness increased with the growth of CdS films. To increase the film thickness and to reduce roughness, the chelating agent was added to the solution. The effect of the chelating reagents, triethanolamine and cysteine, on the layer by layer CdS film formation in the electroless and electrochemical deposition process was studied [170, 171].

Thin films of CdS were also prepared by the SILAR method on the (100)GaAs [172–174], ITO [174], and glass [175, 176] substrates.

The electrodeposition of CdS films on conductive substrates from aqueous solutions is a low-cost process, which is well suited for the preparation of film solar cells. Polycrystalline CdS films of good quality were obtained by electrolysis with rectangular voltages on indium

tin oxide/glass substrate from low concentration CdSO₄ and Na₂S₂O₃ aqueous solutions [177].

CdS thin films were prepared by electrodeposition from an aqueous solution containing Cd(II) and Na₂S₂O₃ in the presence of colloidal sulfur [178].

The electrodeposition of cadmium sulfide thin films was carried out by the electroreduction of the aqueous thiocyanate complex of Cd(II). Formation of CdS is supposed to proceed by metal-catalyzed ligand reduction [179].

Studies of the kinetics and photoelectrochemistry of nanocrystalline composite films of CdS/Ni in aqueous sulfite [180] and thin film CdS/electrolyte interface were carried out [181].

Thiols were adsorbed on a CdS surface and used to control the growth of CdS particles [182].

The Cd/CdS electrode was also prepared in solutions containing cadmium sulfate and sodium thiosulfate using the potentiodynamic method [183]. The electrochemical behavior of such electrodes in electrolytes containing sulfide ions was studied.

24.2.2.4.2 CdSe

CdSe was deposited on different substrates. The two-step method of the electrosynthesis of CdSe films, based on the initial chemical modification of polycrystalline gold surface with selenium overlayer was described [157]. In the second step, this overlayer was cathodically stripped as a Se²⁻ in a Se(IV)-free electrolyte medium that was dosed with the requisite amounts of Cd(II) ions.

The electrochemical preparation of CdSe nanoparticles at gold electrodes modified with molecular templates was reported [159]. The molecular templates were obtained by arranging thiolated

β -cyclodextrin self-assembled monolayers on gold electrodes.

The ECALE method was used for the growth of CdSe on Ag(111) electrode [184].

The thermodynamic analysis of Se(IV) electroreduction and CdSe electrolytic formation on Ni, Ti, and Pt cathodes in acidic aqueous solution were presented [185].

Semiconducting thin films of CdSe were electrochemically deposited on Ti substrates [186, 187]. The film electrodes were characterized with photoelectrochemical imaging, optical microscopy, and scanning electron microscopy (SEM)/energy-dispersive X-ray analysis.

The CdSe was used as a photoelectrode in photoelectrochemical cells. The CdSe film doped with Zn, has favorable states in band gap and enhances charge-transfer kinetics at the interface.

CdSe thin films and CdSe nanocrystal layers were electrodeposited on Ti or ITO substrates in solutions containing CdSO₄ and H₂SeO₃ at pH 2.5 [188, 189]. The influence of different deposition potentials on the surface morphology and crystal structure of CdSe films was studied.

Under potentiostatic conditions, CdSe films were deposited on titanium substrate from a bath containing sodium selenosulfite, cadmium sulfate, and sodium citrate [190].

CdSe films of variable composition were prepared using electrochemical codeposition under potentiostatic control [191,] and the photoelectrochemical behavior of such films was investigated.

The structure, morphology, and photoelectrochemical properties of CdSe and CdSe_xTe_{1-x} semiconductor thin films prepared by cathodic electrodeposition on Ni and Ti electrodes from acidic solution containing CdSO₄, SeO₂, and TiO₂ were investigated [192].

In sulfuric acid solution containing selenous acid and uncomplexed Cu(II) and Cd(II) ions, the formation of ternary Cu–Cd–Se thin film layers on a polycrystalline Pt electrode during the voltammetric scanning was studied [193].

24.2.2.4.3 CdTe The mechanism of CdTe electrodeposition was studied intensively [194–197]. Electrodeposition of CdTe semiconductor thin films was carried out in acidic aqueous solutions at pH 1–3 [195–197]. To prevent accumulation of tellurium in CdTe film, the concentration of Te(IV) ions in acidic electrolyte must be much lower than the concentration of Cd(II).

The electrochemical aspects of CdTe growth on Ag(111) by ECALE were studied [198].

The electrodeposition of CdTe films from various ammonia-alkaline solutions at low cathodic overpotential [199, 200] was also studied, and the mechanism of CdTe formation was discussed [201, 202]. The properties of films were electrochemically characterized.

The nucleation and growth mechanism of CdTe thin films at polycrystalline gold surface [203] and on the rough face side of a Si(100) were studied as a function of different potential steps. Schematic representation of CdTe formation is shown in [204].

CdTe was also obtained using rotating disc electrode; the kinetics of tellurium deposition process on solid tellurium electrode was analyzed, and the kinetic parameters were calculated [205].

Electrodeposition and stripping of tellurium and CdTe in sulfate electrolyte was studied by voltammetric and electrogravimetric experiments [206].

Cathodic electrodeposition of CdTe in acidic solutions with higher tellurium

concentrations was studied [207]. The effects of the deposition potential and the hydrodynamic regime were investigated.

Voltammetry at a glassy carbon (GC) electrode was used to study of the electrochemical deposition of CdTe from the Lewis basic 1-ethyl-3-methylimidazolium chloride/tetrafluoroborate room temperature ionic liquid [208].

Electrochemistry and electrogenerated chemiluminescence of CdTe nanoparticles was also studied [209].

Electrodeposition of $\text{Cd}_x\text{Hg}_{1-x}\text{Te}$ films on a titanium [210] and stainless steel substrates [211] from a bath containing CdSO_4 and TeO_2 and HgCl_2 was investigated. Film composition and band-gap energy were evaluated.

24.2.2.5 Properties of Cadmium Intermetallic Compounds

The mechanism of the formation of intermetallic compounds between cadmium and nickel during the storage of charged cadmium electrodes and the kinetics and mechanism of anodic dissolution of $\text{Cd}_{21}\text{Ni}_5$ in alkaline solutions were investigated [212]. This study helped to eliminate the negative effect of $\text{Cd}_{21}\text{Ni}_5$ on the discharge characteristics of nickel–cadmium batteries.

The structural and electrochemical characteristics of cadmium electrodes with nickel introduced in metallic state into the active material of the electrode by electroless plating were studied [213]. The specific role played by hetero phase interactions between nickel and cadmium in the mechanism of the Cd electrode activation was substantiated experimentally.

The identification of intermetallic compounds in electrodeposition of copper–cadmium alloys by electrochemical techniques was described [214].

The mechanism of anodic dissolution of the intermetallic compound CdSb was studied in concentrated KOH solutions [215].

The properties of Cd species formed by the dissolution of cadmium metal in molten cadmium halides and at electrode interface were investigated [216].

24.2.3

Cadmium Underpotential Deposition and Electrodeposition on Solid Electrodes

24.2.3.1 Deposition of Cd on Cadmium Electrode

The cadmium electrodeposition on the solid cadmium electrode from the sulfate medium was investigated [217]. The following kinetic parameters were obtained: cathodic transfer coefficient $\alpha = 0.65$, exchange current density $I_0 = 3.41 \text{ mA cm}^{-2}$, and standard rate constant $k_s = 8.98 \times 10^{-5} \text{ cm s}^{-1}$. The electrochemical deposition of cadmium is a complex process due to the coexistence of the adsorption and nucleation process involving Cd(II) species in the adsorbed state.

Surfaces of cadmium with various morphological properties were electro-formed on the Cd electrode from sulfate solutions by varying current densities, temperature, and pulse electrolysis conditions [218]. The surface properties were defined by the values of slopes of quasi-steady state E versus logarithm current density dependencies and exchange current densities in 0.5 M $\text{CdSO}_4 + 0.15 \text{ M H}_2\text{SO}_4$ solution. The dependence of the slope values on surface properties was explained in terms of the influence of crystallization overpotential.

Thermal phenomena at the Cd electrode during the electrolysis of aqueous solutions of Cd(II) were investigated [219]. The determination of heat flux, heat quantity, and temperature gradient at the

Cd/solution interface under galvanostatic conditions was carried out.

The blocking effect of benzyl and substituted benzyl alcohol additives on the electrodeposition of cadmium [220] and stabilization of cadmium electrode properties [221] were studied voltammetrically.

The cadmium electrodeposition on the cadmium electrode from water–ethanol [222, 223], water–DMSO [224], and water–acetonitrile mixtures [225–229] was studied intensively. It was found that promotion of Cd(II) electrodeposition [222] was caused by the formation of unstable solvates of Cd(II) ions with adsorbed alcohol molecules or by interaction with adsorbed perchlorate anions. In the presence of I[−] anions, the formation of activated Cd(II)–I[−] complex in adsorbed layer accelerated the electrode reaction [223].

In water–DMSO mixtures in the presence of ClO₄[−] and I[−] anions, the electroreduction of Cd(II) ions was influenced by competitive adsorption of DMSO molecules and anions [224] and the rate of the Cd(II)/Cd process changed nonmonotonically with solvent composition. In water-rich mixtures, the electrode process was accelerated by the formation of activated complex Cd(II)–anion (ClO₄[−], I[−]). At higher DMSO concentration, the rate of the Cd(II)/Cd process was found to decrease and reach minimum at DMSO concentration equal to 9 M. At c_{DMSO} > 9 M, the rate of the process increased again.

The effect of perchlorate ions on cadmium electrodeposition was investigated in water–AN mixtures [227, 228]. The formation of ionic associates in the surface layer inhibited cadmium electrodeposition, and promoted the formation of higher quality coatings.

It was found that the competitive adsorption of I[−] and AN molecules on the Cd electrode affected the kinetics of the Cd(II) electroreduction [226]. The physicochemical properties of coatings and effects of organic additives on cadmium deposition from iodide–water–AN mixtures were also studied by Kuznetsov et al. [225].

The same authors have found that the inhibition effect of crown ethers [230] and crown esters [229] on cadmium electrodeposition from water–AN mixtures was caused by the competitive adsorption of macrocycles and organic solvents molecules. The effect of structure and concentration of crown ethers on the cadmium electrodeposition from aqueous sulfate solutions was also studied [231].

The solution composition and the nature of particles adsorbed and reduced on the electrode, as well as ϵ -caprolactam additive, affected the electroreduction of cadmium ions [232, 233].

The experimental data for the rate of stationary two-dimensional nucleation in electrocrystallization of cadmium on the surface of the Cd(0001) crystal face in 2.5 M CdSO₄ aqueous solution at 45 °C were presented [234]. The overpotential dependence of the nucleus size was determined.

A method was proposed for electrolytic cadmium refining in molten CdCl₂ using electrolyzer with bipolar cadmium electrode [235]. The results demonstrated that high-purity Cd could be obtained in a single electrolysis cycle.

24.2.3.2 Electrodeposition of Cd on Other Solid Substrates

24.2.3.2.1 Gold Electrodeposition of Cd on gold was studied by many scientists (early papers [72, 236–239]). A considerable effort was made to study and

understand the underpotential deposition (UPD) processes, both on single crystal and polycrystalline gold surfaces [240]. The influence of Cd–Au alloy formation on gold electrodes was underlined [241–245], and details were studied on the basis of electrochemical and electrochemical quartz crystal microbalance (EQCM) results [246]. The two-step process of fast turnover reaction – replacement of surface atoms and slow solid-state diffusion was postulated. The influence of anions on UPD process of polycrystalline electrodes was analyzed on the basis of voltammetric and EQCM data [247].

The UPD process was studied most intensively on Au(111) plane, where scanning tunneling microscopy (STM) measurements revealed a series of linear structures [248, 249]. The influence of coadsorbed anions on deposit morphology based on electrochemical and STM data, was also discussed [250, 251]. In the presence of chloride ions, nanostructures such as “nanowires” were observed by STM, the surface alloy structure following the morphology of Au(111) reconstruction [252]. The UPD process was affected not only by the applied potential and electrolyte, but also by its concentration, as shown for H₂SO₄ solutions using specular X-ray reflectivity measurements [253]. The mechanism of the process has been described in other papers. These works [254–259] also point to UPD process on reconstructed Au(111) surface and its relation with lifting the reconstruction. The early stages of Cd–Au alloy growth accompanying UPD were studied recently by del Barrio et al. [260] and Schmuki with coworkers [257–259]. Atomic size clusters start to nucleate at a relatively high underpotential, close to 0.35 V. Two-dimensional islands can grow and coalesce with the formation of new two-dimensional islands on top of

the partially formed first monolayer [260]. Alternatively, the growing clusters arrange linearly until overgrowth takes place and a complete layer is formed at underpotential close to 80 mV [257]. Atomic resolution images revealed a hexagonal structure with an interatomic distance of 0.29 nm [260]. Owing to alloying, the UPD layer contains both Cd and Au atoms. Dissolution of the Cd layer is coupled with dealloying and formation of mono- or 2–3 atomic holes resulting in surface roughening [259, 260]. Figure 7 presents STM images of Cd nanoclusters, produced at different potentials, and their anodic dissolution, confirming the presence of the interfacial dealloying process. Higher deposition potentials result in smaller and less stable clusters. The site selective mechanism of early-stage Cd clusters nucleation at the elbow sites of the Au (111) herringbone reconstruction was also postulated [258]. This process can result in self-organized patterning consisting of Cd nano-islands on the surface. Cd UPD process was also studied in organic solvents such as PC, tetrahydrofuran, and dimethoxyethane [261, 262]. The observed differences, compared to aqueous solutions, were ascribed to differences in anion adsorption and the influence of solvent on metal–substrate interactions, resulting from the partial discharge state of Cd adatoms. Electrocatalytic influence of Cd UPD on nitrate reduction [251, 263] or glucose oxidation [264] was described.

UPD Cd can also be used to obtain cadmium sulfide, an important semiconductor for electronics. Electrochemical epitaxial growth of organized CdS structures, involving underpotentially deposited Cd on Au(111) was thus reported [161, 265].

The atomic structures corresponding to Cd UPD on Au (100) plane were revealed using electrochemical atomic force microscopy (AFM) technique [241, 266].

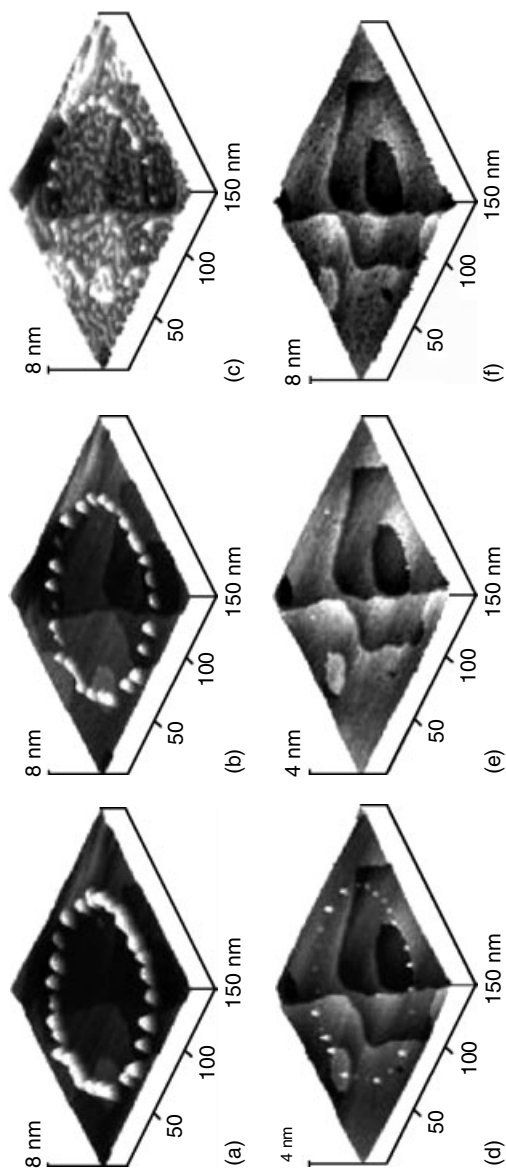


Fig. 7 Anodic dissolution of STM-tip-induced Cd nanoclusters on $\text{Au}(111)$. The first row (a–c) shows clusters obtained at potential of 50 mV, at (a) 50; (b) 300; (c) 1000 mV. Second row (d–f) shows clusters obtained at potential of 100 mV, at (d) 100; (e) 200; (f) 200 mV [259].

Within the potential range from -0.3 to -0.45 V, a quick surface-alloying process occurs, with dynamics depending on polarization conditions [266]. A turnover mechanism was proposed for the surface-alloying process, while for long polarization times, the surface alloy formation process was determined by solid-state diffusion of Cd or Au atoms across the alloy phase [242, 267]. In sulfuric acid solutions, the diffusion coefficients corresponding to the fast process occurring within two monolayers is approximately 10^{-16} cm 2 s $^{-1}$, while the second slow solid diffusion process is characterized by diffusion coefficient in the range 10^{-18} [243] or 10^{-19} cm 2 s $^{-1}$ [245]. The alloying process was also studied using EQCM and X-ray diffractometry techniques [268]. On the basis of temperature dependence of the inward diffusion rate, activation energies of the surface and bulk solid-state processes were estimated [268]. In the presence of chloride ions in solution, the inward diffusion of Cd to the Au(100) phase is promoted [269]. Electrochemical atomic force microscopy (EC-AFM) observations for the Cd stripping process confirmed that the removing of Cd from the alloy phase resulted in surface roughening [266].

Cadmium bulk deposition was found to occur according to Stranski-Krastanov mechanism, with the Cd(0001) plane parallel to Au(100) [241, 266].

Cd UPD process on Au(100) and Au(110) was also studied in the presence of Te, leading to CdTe formation [270–272].

For Au (111) coated by self-assembling monolayers of alkanethiols, the Cd UPD process occurs if the alkyl chain of the thiol is shorter than eight carbon atoms [273].

The electrochemical deposition of metal (Cd, Zn, Pb) from Me(II)-ethylenediaminetetraacetic acid (EDTA) complexes

studied by quartz crystal microgravimetry [274] may be important for the development of environmental cleanup processes.

24.2.3.2.2 Platinum Electrodeposition of Cd on platinum has been described in early papers [for example [72, 239, 275]. Considerable attention has also been paid to UPD processes. This process occurring on Pt(111) was studied using electrochemical and radiotracer methods [276]. Bisulfate ions adsorption promotes the formation of a Cd adlayer, at potentials much lower than those typical for the bare Pt(111) surface. This effect was explained by lower work function for Cd, compared to Pt. Voltammetric and charge displacement (Cd displaced by anions and CO) studies of Gómez and Feliu pointed out the deposition of two UPD layers before the onset of the bulk deposition process [277]. The first layer was found open (surface coverage degree near 0.31), probably due to Cd–Cd repulsion, while the second layer was found more compact. Due to strong attractive interactions with adsorbing Br $^-$ or Cl $^-$ anions, voltammetric peaks are very sharp.

The process of Cd UPD on polycrystalline Pt was investigated by Machado et al. [278–280], and adsorption electrovalence of Cd adions was found to be close to 0.5 [280]. The detailed mechanism was also studied, using electrochemical and EQCM measurements [281, 282]. The formal partial charge number was found to vary between 1 and 2, for higher and lower potentials, respectively. A mechanism involving two adsorption sites and the presence of Cd $^{+}$ adsorbed ions was proposed.

The influence of surface roughness, surface diffusion of metal atoms, and exchange current density of the Cd(II)/Cd

couple on the early stages of cadmium deposition was analyzed [283]. Studies of the Cd UPD process from ionic liquid: acidic zinc chloride-1-ethyl-3-methylimidazolium chloride were also reported [284].

24.2.3.2.3 Silver Early descriptions of Cd deposition process on Ag can be found in Ref. 285. Cadmium UPD studies were carried out on Ag(111) and Ag(100) single crystals. For Ag(111) at high underpotentials (up to 0.3 V), the process is characterized by a quasi-reversible adsorption/desorption of Cd, while at lower underpotentials (below 50 mV), Ag–Cd alloy formation occurs [286]. The influence of different anions (sulfate, perchlorate, citrate) was also studied [287]. In the presence of adsorbed chloride ions, the Cd UPD occurs by replacement of Cl adatoms (not desorption), which remain adsorbed and discharged on top of Cd layer [288]. The first combined electrochemical and STM studies revealed some details of the UPD process [289]. It starts with a formation of an expanded adlayer, which at lower underpotentials transforms to a condensed close-packed Cd monolayer. This monolayer is not quite stable, because it slowly transforms with place exchange between Cd and Ag surface atoms. A formation of a second monolayer and a significant Ag–Cd surface alloying occurs at underpotentials lower than 50 mV. The anodic process is connected with dealloying resulting in the appearance of 2D islands and monoatomically deep pits, quickly disappearing at higher underpotentials, pointing to high surface mobility of Ag atoms. Cd UPD process was also studied in organic solvents such as PC, tetrahydrofuran, and dimethoksyethane [261, 262]. Similarly, as for Au(111), the observed differences, compared to aqueous solutions,

were ascribed to difference in anion adsorption and influence of solvent on metal–substrate interactions, resulting from the partial discharge state of Cd adatoms. Electrochemical epitaxial growth of organized CdS structures involving UPD Cd on Ag(111) was described [290]. Electrocatalytic influence of Cd UPD on nitrate ions reduction was revealed, as for Au(111) [263].

For Ag(100) crystals, a similar electrochemical behavior was observed with quasi-reversible adsorption/desorption of Cd and surface alloying, faster than for Ag(111) [286]. Electrochemical and AFM experiments have shown that the alloying process consisted of two steps: a very fast reaction occurring within a few atomic layers, and a much slower one, represented by a solid-state diffusion process [244].

UPD process and surface Cd–Ag alloying were also studied on polycrystalline Ag electrode [285, 286]. The surface alloy formation rate was similar to that for Ag(100) [286]. The dynamics of surface alloying promoted by Cd UPD was studied on irregular Ag substrates, dendritic, and columnar Ag deposits [291].

24.2.3.2.4 Copper Early studies of electrochemical deposition of Cd have been described in Refs 236, 239. These studies were also carried out on single crystal Cu(111), Cu(110), and Cu(100) planes. On Cu(111) different structures were proposed. The bulk deposited cadmium forms a close-packed hexagonal lattice in perchlorate solutions, growing according to modified Stranski-Krastanov mechanism [292]. UPD of Cd has been described in a few papers. Ge and Gewirth [292], using voltammetric methods and AFM, found the interatomic distance 0.343 nm for UPD Cd(4×4) structure, with a slightly open structure due to retained partial

charge of Cd adatoms, while Stuhlmann et al., using voltammetry and ultrahigh vacuum (UHV) based spectroscopy, reported 0.371 nm for $(\sqrt{19} \times \sqrt{19}) R23.4^\circ$ structure [293]. In both cases, this distance is higher than that for bulk Cd. In situ STM studies confirmed the $(\sqrt{19} \times \sqrt{19}) R23.4^\circ$ structure [294]. The reduction process is characterized by two pairs of UPD peaks, where the peak at lower potential, close to reversible Nernstian potential, corresponds to Cd–Au alloying [295]. The role of adsorbed chloride ions was discussed, pointing to stabilization of open Cd structure [293] and surface site exchange between Cl^- ions and Cd^{2+} cations [294, 295]. The influence of potential on Cd UPD structure studied by STM and comparison of results with predictions of hard sphere model (Cd–Cd distance 0.38 nm) was recently discussed [296]. Deposition of CuCd alloys was also studied [297, 298].

For Cu(100) in the presence of chloride ions, the structure of UPD Cd is dependent on the deposition rate [296]. For high deposition rate, nearly defect-free films were obtained with domains as large as Cu(100) terraces previously coated by chloride ions. For low deposition rate, Cd films with a high density of domain boundaries can be obtained.

The Cd UPD behavior on Cu(110) was found similar to that for Cu(111), with more pronounced alloying, resulting in irreversible changes of the original (110) surface of copper [295].

Electrodeposition of Cd on polycrystalline copper was analyzed from the point of view of oxide influence [299], and a comparison of electrochemical data with results of numerical calculations was presented.

24.2.3.2.5 Silicon

The Cd deposition process was studied on H-terminated

n -Si(111) plane [300]. Because the redox potential of the Cd^{2+}/Cd couple is much lower than the flat band potential of Si substrate, the surface electron concentration is sufficiently high. Thus the process occurs similarly as on a metal surface at relatively low cathodic overpotentials. The initial stages of Cd deposition were explained by progressive nucleation and cluster growth controlled by hemispherical diffusion. CdTe deposition on Si was also studied due to interest in application in IR radiation detectors. Mechanisms of this process on different planes of n -Si(100) was also discussed ([203, 301, 302] and references given therein).

24.2.3.2.6 Other Substrates Deposition of cadmium was also studied on Bi, Sn and Pb [303], Ni [304], reticulated vitreous carbon [305], Ti [306], and indium tin oxide [307]. UPD of Cd on tellurium results in CdTe formation [270, 308]. Electrodes coated with conducting polymers were also used to deposit cadmium electrochemically. In the case of polyaniline, the metal reduction potential corresponds to the neutral (nonconducting) state of the polymer, therefore cadmium was found to deposit on the substrate–glassy carbon electrode surface, in the open pores of the polymer film [309, 310].

The electrowinning of cadmium from dilute sulfate solution was studied using rotating GC and spiral wound steel electrodes [311].

The electrochemistry of Cd(II) was investigated at different electrodes (GC, polycrystalline tungsten, Pt, Ni) in a basic 1-ethyl-3-methylimidazolium chloride/tetrafluoroborate, at room temperature molten salt [312], and in acidic zinc chloride-1-ethyl-3-methylimidazolium [284].

24.2.4

Passivation and Corrosion of Cadmium

24.2.4.1 Passivation of Cadmium Electrode

The electrochemical behavior of the cadmium electrodes in alkaline solutions was intensively studied [313–318]. It was suggested [314–318] that during anodic dissolution of the Cd electrode in alkaline solutions, a passive layer consisting of $\text{Cd}(\text{OH})_2$ and CdO is formed, and $\text{Cd}(\text{II})$ soluble species are also generated. The composition of the anodically formed layer on cadmium in alkaline solution was dependent on the electrolyte cation [319]. In 1 M NaOH and KOH solutions, both $\beta\text{-Cd}(\text{OH})_2$ and $\gamma\text{-Cd}(\text{OH})_2$ were formed, while in 1 M LiOH, $\beta\text{-Cd}(\text{OH})_2$ was the only product.

The electrochemical behavior of Cd electrode in 1 M NaOH solutions was studied in detail [320]. It was found that the passive film formed on Cd electrode was composed of two layers: a barrier layer CdO and/or $\text{Cd}(\text{OH})_2$ covered with porous layers of $\text{Cd}(\text{OH})_2$.

The influence of concentration of KOH and separator materials on the soluble cadmium compounds, for example, cadmium hydroxyl complexes formed near the Cd electrode during the anodic process was also studied [321, 322].

The passivating layer formed on Cd electrode in alkaline solution in the presence of Na_2S was studied voltammetrically [323]. At low Na_2S concentrations, CdO , $\text{Cd}(\text{OH})_2$, and CdS layer were produced during the anodic oxidation of the Cd electrode. At higher Na_2S content, a few monolayers of thick CdS film were formed.

24.2.4.2 Corrosion of Cadmium

From the point of view of environmental stability, cadmium represents an

intermediate case between noble and base metals. It is relatively corrosion-resistant. However, dangerous environmental pollution by cadmium required studies concerning the corrosion behavior of this metal. The influence of solution pH on cadmium corrosion was studied using classical electrochemical methods, as well as electrochemical impedance spectroscopy, X-ray photoelectron spectroscopy, and SEM observations [324–327]. In acidic solutions, continuous corrosion takes place, while in neutral and alkaline solutions, the passivation process occurs, and is enhanced by higher oxygen concentration. Polycrystalline cadmium undergoes crystallographic etching after breakdown of the passive layer in NaCl solutions alkalinized to $\text{pH} = 11$ [328]. In alkaline solutions, the inhibiting influence of aliphatic alcohols (methanol, ethanol, propanol) was studied [329]. The inhibiting influence was ascribed to alcohol molecules adsorption on the cadmium surface, increasing with growing chain length. In borate solutions, in the absence and presence of Cl^- ions, the pitting corrosion of Cd electrode was studied. The corrosion potential was a linear function of logarithm of chloride concentration; the inhibiting influence of fatty acid sulfonate was also investigated [330].

In acidic solutions, the corrosion rate is relatively high. Studies on cadmium monocrystals and polycrystals in acidic chloride solutions revealed anodic dissolution independent of the crystallographic orientation; the dissolution rate was controlled by the mass transport of CdCl^+ ions [331]. The inhibitive influence of adsorbed organic substances, for example, alcohols [332], phenotiazine [333], and some polymers (e.g. poly(vinyl alcohol), poly(acrylic acid), sodium polyacrylate,

poly(ethylene glycol), etc.) [334] on the corrosion process in acidic solutions was studied.

A protective influence of commercial coatings [335] and chromates [335, 336] as well as surface coating formation in water-acetonitrile mixed solvents [227] was analyzed.

Corrosion studies on cadmium alloys, for example, [337–339], also from the point of view of stress corrosion cracking [340, 341] have been described recently.

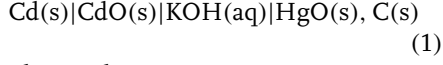
24.2.5

Applied Electrochemistry

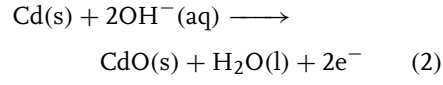
24.2.5.1 Batteries

24.2.5.1.1 Cadmium–Mercuric Oxide Primary Cells

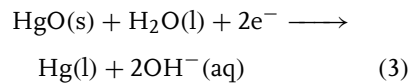
The scheme of the cell is:



The anode reaction is:



and the cathode reaction is:



The electrolyte is usually 40% KOH aqueous solution. The open-circuit voltage of this system is 0.90 V. The battery can be used and stored in a wide range of temperatures, from –55 to 80 °C, due to low solubility of cadmium oxide in concentrated KOH solutions [342].

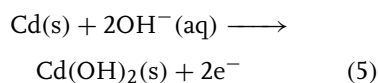
The kinetics of electrode processes on Cd electrode of an alkaline accumulator in dependence on changes in concentration of cadmium species in near-electrode layer of electrolyte was studied [343].

24.2.5.1.2 Cadmium–Nickel Oxide

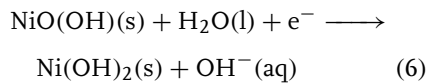
(Ni–Cd) Secondary Cells Besides lead-acid batteries, cadmium–nickel oxide cells represent the most popular type of rechargeable batteries [344]. The scheme of the cell is:



The discharge of the negative electrode is described by equation:



while the discharge of the positive electrode is:



The open-circuit voltage of the charged cell is 1.30 V.

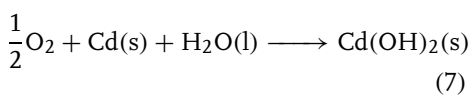
The electrolyte is usually 20–28% aqueous solution of KOH. Solid-state compositions of KOH aqueous electrolyte obtained by addition of poly(ethylene oxide) [345] or polymer based electrolyte (based on polyacrylates) were also proposed [346]. For low temperature applications, higher concentrations of KOH were used, while for higher temperatures, sodium hydroxide was sometimes applied. The influence of the temperature from 0 to 200 °C, pressure and electrolyte concentration on the thermodynamic parameters of the cells, was studied in detail [347].

The active material of the negative electrode consists of metallic cadmium. Addition of iron (up to 25%), nickel, and graphite, prevents agglomeration [348]. Cadmium does not undergo corrosion, since the equilibrium potential is higher than that of hydrogen in the same solution.

However, it can undergo self-reductive dissolution (loss of active material) accompanied by oxygen evolution [349]. The active material of the positive electrode (in pocket plate cells) consists of nickel hydroxide mixed with small additions of cobalt and barium hydroxides to improve the capacity and charging/discharging performance and graphite to improve conductivity [348].

The sintered electrode constructions are gradually replaced with structures of higher capacity as, for example, felted nickel fibril or foam structures [350–352]. An open nickel foam structure can be obtained by vapor deposition of nickel from nickel carbonyl into a bed of urethane foam and then burning off the polymer. The porosity increases from 80% typical for sinter electrodes and reaches 90–95% for felted or foam structures. Application of polymer bonded cadmium electrodes significantly reduces environmentally dangerous dusting during cell production [350].

In sealed cells, which are the most important kind of Ni–Cd batteries, the gas (H_2 and O_2) evolution accompanying discharge should be minimized. This can be achieved by incorporation of “antipolar mass” – cadmium hydroxide in the positive electrode. In this case overdischarge results in reduction of $Cd(OH)_2$ to Cd, instead of hydrogen evolution [348]. On the other hand, oxygen evolved on the positive electrode during overcharging can react with cadmium [348]:



The negative electrode is thus designed to be larger than the positive one to avoid full charging of the negative electrode [351].

The state of charging, mainly of sealed cells, can be studied using galvanostatic methods [353] and electrochemical impedance spectroscopy [354–356] (see reviews [357, 358]). The battery behavior was analyzed using electronic network modeling [359, 360].

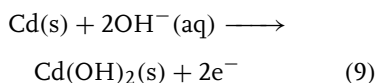
The cadmium–nickel oxide cell is the most robust secondary cell which can deliver a high charge in a short time, withstand overcharge, over discharge, and operate at temperatures as low as $-40^\circ C$ [350]. The vented Ni–Cd cells dominate in commercial jet-aircraft applications [350]. Ni–Cd batteries are gradually replaced by nickel–metal hydride and lithium-ion cells, especially in consumer electronics devices, due to higher energy storage capability and low weight. However, they are still useful for applications that require low temperatures and high-rate capability [361, 362].

24.2.5.1.3 Cadmium–Silver Oxide Secondary Cells

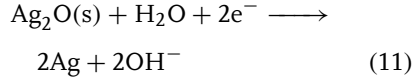
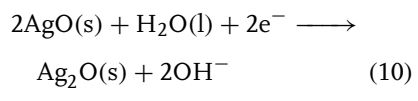
The scheme of the cell is:



The discharge of the negative electrode is described by equation:



while the discharge of the positive electrode is a two-step process:



The positive electrodes are usually fabricated by sintering of silver powders and

slurry pasting [348]. The negative electrode and electrolyte are similar as in Ni–Cd batteries, but the energy density is about 30% higher. The open-circuit voltage is 1.2–1.4 V, depending on the reaction at the positive electrode. Applications are practically limited to small button cells [348].

24.2.5.2 Application in Electrochemical Sensors

24.2.5.2.1 Potentiometric Sensors The determination of cadmium is important due to its toxic nature [363]. It comes to water and soil through wastewater from metal plating industries, nickel–cadmium batteries and alloys.

Crown ethers [364] have proved to be an excellent choice as ionophores for the fabrication of ion sensors because of their ability to complex selectively a particular ion. The cadmium selective sensors have been fabricated from poly(vinyl chloride) (PVC) matrix membranes containing macrocyclic ionophores: benzo-15-crown-5 [365], monoaza-18-crown-6 [366], dibenzo-24-crown-8 [367], dicyclohexano-18-crown-6 [368], 3,4:11,12-dibenzo-1,6,9,14-tetraazacyclohexadecane [369], and polystyrene based membrane of 3,4:12,13-dibenzo-2,5,11,14-tetraoxo-1,6,10,15-tetraazacyclooctadecane [370]. Javanabakht et al. [371] have investigated Cd(II)-selective PVC membranes based on the synthesized tetrol compound. These membranes give a linear potential response in the concentration range 1.6×10^{-6} to 1.0×10^{-1} M with a Nernstian slope 28 ± 3 mV per decade of Cd(II) concentration. The cadmium ion-selective electrode based on tetrathia-12-crown-4 [372] is very sensitive, and exhibits Nernstian response for Cd(II) ions in the concentration range 4.0×10^{-7} to 1.0×10^{-1} M with a slope of 29 ± 1 mV per decade.

Gupta and D'Arc [373] have prepared the Cd(II) ion-selective electrode based on cyanocopolymer using 8-hydroxyquinoline as an electroactive ionophore. The effect of concentration of ion exchanger, plasticizer, and molecular weight of cyanocopolymers on selectivity and sensitivity of Cd(II) ion-selective electrode was also investigated [374].

Prodi et al. [375] have characterized a 5-chloro-8-methoxyquinoline appended diaza-18-crown-6 as a chemosensor for cadmium ions.

New PVC membrane sensors for Cd(II) ions based on 2-(3',4'-dihydroxyphenylazo-1')-1,3,4-thiadiazole [376] and 3-(2',4'-dihydroxyphenylazo-1')-1,2,4-triazol [377] were prepared. Their basic analytical parameters were established.

Selectivity of liquid membrane cadmium microelectrode based on the ionophore *N,N,N',N'*-tetrabutyl-3,6-dioxaoctanedithioamide was characterized by Pineros et al. [378].

The electrochemical flow sensor for *in situ* monitoring of total cadmium concentration in the presence of EDTA and nitrilotriacetic acid (NTA) ligands has been described [379].

The octamethyl-1,1'-di(2-pyridyl)ferrocene, redox-active ligand was used as an electrochemical sensor for Cd(II) and Zn(II) ions in acetonitrile [380].

The PVC membrane electrode based on new Schiff base complexes of 2,2-[(1,3-dimethyl-1,3-propanediylidene)dinitrilo]bis-benzenethiolato with Cd(II) [381] and cadmium-salen (*N,N'*-bis-salicylidene-1,2-ethylenediamine) complex [382] were used as the selective electrodes for tiocyanate ions.

The preparation and investigation of a stable, long lived, and highly selective fast-response novel solid-state cadmium-ion electrode, based on the ion pairing

compounds of the tetraiodocadmite and tetrabromocadmite anions with cetylpyridinium cations has been described by Abbas and Zahran [383]. The two sensors exhibit near Nernstian slopes independently of pH over a wide range with very fast-response time.

A number of Cd(II) sensors based mainly on the $\text{Ag}_2\text{S}/\text{CdS}$ mixtures [384, 385] and cadmium chelates [386] were described. Ito et al. [387] used an $\text{Ag}_2\text{S}/\text{CdS}$ ion-selective electrode for determination of cadmium ion in industrial wastewater by titration method.

Solid-state cadmium sensors based on chalcogenide thin film layer were prepared [388]. The electrochemical behavior of the sensor in terms of ionic sensitivity, detection limit, Nernstian response interval and effect of pH was evaluated.

Recent research in the field of polymer membrane ion-selective electrodes [389–391], has revealed that their selectivities [392–396] and limits of detections [394–397] could be improved by several orders of magnitude. The review of Bakker and Pretsch [398] summarized recent progress in the development and application of potentiometric sensors with low detection limit in the range 10^{-8} – 10^{-11} M.

Potentiometric Cd(II)-selective electrode with detection limit in ppt range has

been described [399]. The selectivity behavior was determined for two membranes based on the ionophore N, N, N', N' -tetradodecyl-3, 6-dioxaoctanedithioamide, having different concentrations of ionophore and ion exchanger. The detection of 10^{-10} M Cd(II) was achieved at pH 7 with an ionic background of 10^{-4} M NaNO_3 (see Fig. 8).

24.2.5.2.2 Amperometric-voltammetric Sensors

Thick-film screen-printed carbon containing electrodes modified with formazan were used for determination of Pb(II), Zn(II), and Cd(II) concentration [400].

A 1-(pyridylazo)-2-naphthol modified glassy carbon electrode was investigated as a voltammetric sensor for the Cd(II) ions [401], its detection limit was 5×10^{-10} M Cd(II).

The concentration of Cd(II) was determined using a carbon paste electrode modified with organofunctionalized amorphous silica with 2-benzothiazolethiol [402] or diacetyl dioxime [403] and differential pulse anodic stripping voltammetry. The same method was used for determination of Cd(II) ion using GC electrode modified by antraquinone improved Na-montmorillonite nanoparticles [404].

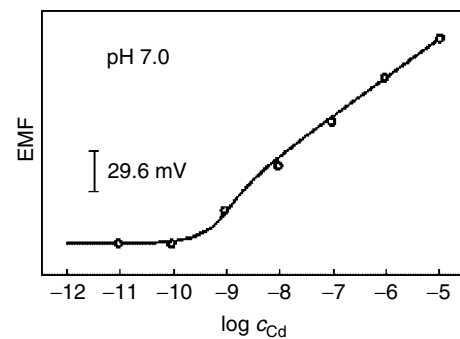


Fig. 8 The dependence of the electromotive force (EMF) of Cd(II) ion-selective electrode on logarithm of Cd(II) concentration in 10^{-4} M NaNO_3 at pH 7. Solid lines, calculated response curves on the basis of Eq. (7) in Ref. 399.

Voltammetric behavior in trace determination of cadmium at a calixarene modified screen-printed carbon paste electrode was investigated [405].

The GC electrode modified by dithizone was used for determination of Cd(II) and Pb(II) concentration using anodic stripping voltammetry [406].

Chow et al. have described [407] the electrochemical sensor for cadmium ions with gold electrode modified by 3-mercaptopropionic acid followed by covalently coupling the cadmium selective hexapeptide His-Ser-Gln-Lys-Val-Phe.

Roa et al. reported [408] the determination of Pb(II) and Cd(II) ions concentration using a polycyclodextrin-modified carbon paste electrode with anodic stripping voltammetry.

The electrodes modified by hexacyanoferrates compounds were also used as voltammetric sensors [409–412]. The cadmium hexacyanoferrate-based composite ion-sensitive electrode for voltammetry was explored by Scholz and coworkers [409]. The potential of such electrode depends linearly on the logarithm of concentration of alkali and alkaline-earth metals ions in the solutions. Bo and Lin have studied [410] Prussian blue (PB)/Pt modified electrode in CdCl₂ electrolyte by cyclic voltammetry and in situ Fourier transform IR spectroscopy (FTIR) spectroelectrochemistry. Cadmium hexacyanoferrates were formed on a PB film.

The solid-state electrochemical formation of bilayer electrode structures of different hexacyanoferrates was studied, and a theoretical model was proposed for cyclic voltammetric behavior of the transformation of PB into cadmium hexacyanoferrates [411].

Solid-state electrochemistry of mixed iron(III)–Cd(II) hexacyanoferrates was also developed [412].

References

1. A. Hamelin, T. Vitanov, E. Sevastyanov et al., *J. Electroanal. Chem.* **1983**, *145*, 225–264.
2. S. Trasatti, E. Lust, in *Modern Aspects of Electrochemistry*, (Eds.: R. E. White, B. E. Conway, J. O. M. Bockris), Kluwer Academic/Plenum Publisher, New York and London, 1999, p. 1, Vol. 33.
3. A. Korotkov, E. Bezlepkin, B. B. Damaskin et al., *Elektrokhimiya* **1985**, *22*, 1298–1304.
4. R. Naneva, V. Bostanov, A. Popov et al., *J. Electroanal. Chem.* **1989**, *274*, 179–183.
5. A. Popov, N. Dimitrov, R. Naneva et al., *J. Electroanal. Chem.* **1994**, *376*, 97–100.
6. R. Naneva, T. Vitanov, N. Dimitrov et al., *J. Electroanal. Chem.* **1992**, *328*, 287–293.
7. R. R. Nazmutdinov, T. T. Zinkicheva, M. Probst et al., *J. Electroanal. Chem.* **2005**, *577*, 112–126.
8. R. Naneva, N. Dimitrov, A. Popov et al., *J. Electroanal. Chem.* **1993**, *362*, 281–286.
9. E. Lust, K. Lust, A. Jänes, *Russ. J. Electrochim.* **1995**, *31*, 807–821.
10. E. Lust, K. Lust, A. Jänes, *J. Electroanal. Chem.* **1996**, *413*, 111–121.
11. E. Lust, A. Jänes, K. Lust et al., *Russ. J. Electrochim.* **1996**, *32*, 552–564.
12. E. Lust, A. Jänes, K. Lust et al., *Electrochim. Acta* **1997**, *42*, 771–783.
13. E. Lust, A. Jänes, K. Lust et al., *J. Electroanal. Chem.* **1997**, *431*, 183–201.
14. E. Lust, A. Jänes, K. Lust et al., *Electrochim. Acta* **1997**, *42*, 2861–2879.
15. E. Lust, A. Jänes, V. Sammelselg et al., *Electrochim. Acta* **1998**, *44*, 373–383.
16. E. Lust, A. Jänes, V. Sammelselg et al., *Electrochim. Acta* **2000**, *46*, 185–191.
17. L. I. Daikhin, A. A. Kornyshev, M. Urbakh, *Electrochim. Acta* **1997**, *42*, 2853–2860.
18. L. I. Daikhin, A. A. Kornyshev, M. Urbakh, *Phys. Rev. E* **1996**, *53*, 6192–6199.
19. A. Popov, *Electrochim. Acta* **1995**, *40*, 551–559.
20. V. V. Emets, B. B. Damaskin, I. A. Bogotskaya et al., *Russ. J. Electrochim.* **2000**, *36*, 661–667.
21. V. V. Emets, B. B. Damaskin, *J. Electroanal. Chem.* **2000**, *491*, 30–38.
22. V. V. Emets, B. B. Damaskin, I. A. Bogotskaya, *Russ. J. Electrochim.* **2001**, *37*, 88–94.

23. C. P. M. Bongenaar, A. G. Remijnse, M. Sluyters-Rehbach et al., *J. Electroanal. Chem.* **1980**, *111*, 139–153.
24. C. P. M. Bongenaar, A. G. Remijnse, E. Temmerman et al., *J. Electroanal. Chem.* **1980**, *111*, 155–162.
25. M. Saakes, M. Sluyters-Rehbach, R. M. Souto et al., *J. Electroanal. Chem.* **1989**, *264*, 217–234.
26. M. Saakes, M. Sluyters-Rehbach, J. H. Sluyters, *J. Electroanal. Chem.* **1989**, *259*, 265–284.
27. J. Struijs, M. Sluyters-Rehbach, J. H. Sluyters, *J. Electroanal. Chem.* **1984**, *171*, 177–193.
28. E. Kirowa-Eisner, A. Kaplevatsky, Ch. Yarnitzky et al., *J. Electroanal. Chem.* **1995**, *394*, 127–139.
29. K. Darowicki, *J. Electroanal. Chem.* **2000**, *486*, 101–105.
30. K. Darowicki, J. Orlikowski, G. Lentka, *J. Electroanal. Chem.* **2000**, *486*, 106–110.
31. K. Darowicki, A. Krakowiak, *Russ. J. Electrochem.* **2003**, *39*, 134–140.
32. K. Darowicki, P. Ślepski, *J. Electroanal. Chem.* **2003**, *547*, 1–8.
33. K. Darowicki, P. Ślepski, *Electrochim. Acta* **2004**, *49*, 763–772.
34. J. Schiewe, J. Hazi, V. A. Vicente-Beckett et al., *J. Electroanal. Chem.* **1998**, *451*, 129–138.
35. J. Schiewe, K. B. Oldham, J. C. Myland et al., *Anal. Chem.* **1997**, *69*, 2673–2681.
36. I. S. El-Hallag, M. M. Ghoneim, E. Hammam, *Anal. Chim. Acta* **2000**, *414*, 173–180.
37. I. S. El-Hallag, *Anal. Chim. (Rome)* **1994**, *84*, 443.
38. A. Baars, F. J. C. Bijl, M. Sluyters-Rehbach et al., *J. Electroanal. Chem.* **1996**, *404*, 149–152.
39. F. J. C. Bije, M. Sluyters-Rehbach, J. H. Sluyters, *J. Electroanal. Chem.* **1997**, *435*, 137–147.
40. R. M. Souto, M. Saakes, M. Sluyters-Rehbach et al., *J. Electroanal. Chem.* **1988**, *245*, 167–189.
41. E. Guaus, F. Sanz, M. Sluyters-Rehbach et al., *J. Electroanal. Chem.* **1994**, *368*, 307–314.
42. E. Guaus, F. Sanz, M. Sluyters-Rehbach et al., *J. Electroanal. Chem.* **1995**, *385*, 121–134.
43. E. Guaus, F. Sanz, *Electroanalysis* **1999**, *11*, 424–431.
44. M. Zelić, I. Pizeta, *Electroanalysis* **1997**, *9*, 155–160.
45. M. Zelić, M. Lovrić, *J. Electroanal. Chem.* **2003**, *541*, 67–76.
46. R. M. Souto, M. Sluyters-Rehbach, J. H. Sluyters, *J. Electroanal. Chem.* **1986**, *201*, 33–45.
47. M. Sluyters-Rehbach, J. H. Sluyters, *Electrochim. Acta* **1988**, *33*, 983–989.
48. M. Lovrić, *Electroanalysis* **2002**, *14*, 405–414.
49. M. Saakes, M. Sluyters-Rehbach, J. H. Sluyters, *J. Electroanal. Chem.* **1990**, *282*, 161–174.
50. A. Baars, K. Aoki, Y. Numata, *J. Electroanal. Chem.* **1997**, *436*, 133–140.
51. M. L. Kisova, M. Golędzinowski, J. Lipkowski, *J. Electroanal. Chem.* **1979**, *95*, 29–42.
52. M. Golędzinowski, L. Kisova, J. Lipkowski et al., *J. Electroanal. Chem.* **1979**, *95*, 43–57.
53. G. Pezzatini, M. L. Foresti, R. Guidelli, *J. Electroanal. Chem.* **1982**, *138*, 139–153.
54. A. Molina, J. Gonzalez, M. M. Moreno, *Electroanalysis* **2002**, *14*, 281–291.
55. B. Marczevska, *Gazz. Chim. Ital.* **1996**, *126*, 259–263.
56. M. Golędzinowski, *J. Electroanal. Chem.* **1989**, *267*, 171–189.
57. M. Hromadova, R. de Levie, *J. Electroanal. Chem.* **1999**, *465*, 51–62.
58. D. Trzciński, W. Kośnik, J. Stroka et al., *Pol. J. Chem.* **2004**, *78*, 1149–1163.
59. Y. I. Moharram, *Anal. Chim. (Rome)* **1999**, *89*, 309.
60. Y. I. Moharram, *J. Electroanal. Chem.* **2004**, *563*, 283–290.
61. J. Taraszevska, A. Wałęga, *J. Electroanal. Chem.* **1984**, *171*, 243–256.
62. J. Stroka, K. Maksymiuk, A. Mital, *J. Electroanal. Chem.* **1989**, *272*, 145–160.
63. K. Maksymiuk, J. Stroka, Z. Galus, *J. Electroanal. Chem.* **1988**, *248*, 35–53.
64. W. R. Fawcett, A. Lasia, *J. Phys. Chem.* **1985**, *89*, 5695–5698.
65. G. M. Brisard, A. Lasia, *J. Electroanal. Chem.* **1987**, *221*, 129–141.
66. G. M. Brisard, A. Lasia, *J. Electroanal. Chem.* **1991**, *314*, 103–116.
67. W. R. Fawcett, *J. Electroanal. Chem.* **1991**, *302*, 13–29.
68. G. Gritzner, *J. Phys. Chem.* **1986**, *90*, 5478–5485.

69. J. Broda, Z. Galus, *J. Electroanal. Chem.* **1986**, *198*, 233–244.
70. K. Maksymiuk, J. Stroka, Z. Galus, *J. Electroanal. Chem.* **1990**, *279*, 1–18.
71. A. Anastopoulos, I. Mountzis, *Electrochim. Acta* **1990**, *35*, 1805–1808.
72. N. A. Hampson, R. S. Latham, in *Encyclopedia of Electrochemistry of the Elements*, (Ed.: A. J. Bard), Marcel Dekker, New York, 1973, p. 156, Vol. 1.
73. M. M. Correia dos Santos, M. L. Simões Gonçalves, J. C. Romão, *J. Electroanal. Chem.* **1996**, *413*, 97–103.
74. M. Torres, J. M. Diaz-Cruz, C. Ariño et al., *Anal. Chim. Acta* **1998**, *371*, 23–37.
75. M. Torres, J. M. Diaz-Cruz, C. Ariño et al., *Electroanalysis* **1999**, *11*, 93–100.
76. M. M. Antunes, J. E. Simao, A. C. Duarte et al., *Anal. Chim. Acta* **2002**, *459*, 291–304.
77. M. M. Correia dos Santos, M. L. Simões Gonçalves, S. Capelo, *Electroanalysis* **1996**, *8*, 178–182.
78. M. Fernandez, C. Ariño, J. M. Diaz-Cruz et al., *J. Electroanal. Chem.* **2001**, *505*, 44–53.
79. R. Schmidt, J. Stroka, Z. Galus, *J. Electroanal. Chem.* **1998**, *456*, 131–137.
80. F. Garay, V. Solis, *J. Electroanal. Chem.* **1999**, *476*, 165–170.
81. M. Lovrič, I. Pižeta, Š. Komorsky-Lovrič, *Electroanalysis* **1992**, *4*, 327–337.
82. M. Lovrič, *Russ. J. Electrochem.* **1996**, *32*, 988–995.
83. M. Lovrič, Š. Komorsky-Lovrič, *J. Electroanal. Chem.* **1988**, *248*, 239–253.
84. F. Garay, V. Solis, *J. Electroanal. Chem.* **2001**, *505*, 109–117.
85. E. Norkus, G. Grinciene, T. Vuorinen et al., *Int. J. Biol. Macromol.* **2003**, *33*, 251–254.
86. M. Łobacz, J. Stroka, Z. Galus, *Chem. Anal. (Warsaw)* **2002**, *47*, 347–359.
87. J. Stroka, B. G. Cox, H. Schneider, *J. Electroanal. Chem.* **1989**, *266*, 337–348.
88. A. Nikonorowicz, P. Grzegorzewski, M. Palys et al., *Polish. J. Chem.* **2004**, *78*, 1785–1793.
89. I. Turyn, D. Mandler, *Electrochim. Acta* **1995**, *40*, 1093–1100.
90. R. Andreoli, L. Benedetti, G. Grandi et al., *Electrochim. Acta* **1984**, *29*, 227–231.
91. V. W. W. Yam, Y. L. Pui, K. K. Cheung, *New J. Chem.* **1999**, *23*, 1163–1169.
92. F. Garay, V. Solis, *Electroanalysis* **2004**, *16*, 450–457.
93. S. Cakir, E. Bicer, O. Cakir, *J. Inorg. Biochem.* **1999**, *77*, 249–255.
94. M. C. E. Rollemburg, M. L. S. Simões Gonçalves, A. M. A. Mota et al., *Anal. Chim. Acta* **1999**, *384*, 17–26.
95. M. C. Rollemburg, M. S. L. Simões Gonçalves, *Bioelectrochem.* **2000**, *52*, 57–62.
96. J. Mendieta, M. S. Diaz-Cruz, R. Tauler et al., *Anal. Biochem.* **1996**, *240*, 134–141.
97. M. S. Diaz-Cruz, J. Mendieta, R. Tauler et al., *J. Inorg. Biochem.* **1997**, *66*, 29–36.
98. M. S. Diaz-Cruz, J. Mendieta, R. Tauler et al., *Anal. Chem.* **1999**, *71*, 4629–4636.
99. B. H. Cruz-Vasquez, J. M. Diaz-Cruz, C. Arino et al., *Analyst* **2002**, *127*, 401–406.
100. B. H. Cruz, J. M. Diaz-Cruz, I. Šestáková et al., *J. Electroanal. Chem.* **2002**, *520*, 111–118.
101. B. H. Cruz, J. M. Diaz-Cruz, C. Arino et al., *Environ. Sci. Technol.* **2005**, *39*, 778–786.
102. M. Esteban, C. Harlyk, A. R. Rodriguez, *J. Electroanal. Chem.* **1999**, *468*, 202–212.
103. J. Mendieta, M. S. Diaz-Cruz, A. Monjonell et al., *Anal. Chim. Acta* **1999**, *390*, 15–25.
104. G. Scarano, E. Morelli, *Electroanalysis* **1998**, *10*, 39–43.
105. C. Harlyk, G. Bordin, O. Nieto et al., *Electroanalysis* **1997**, *9*, 608–613.
106. C. Harlyk, G. Bordin, O. Nieto et al., *J. Electroanal. Chem.* **1998**, *446*, 139–150.
107. M. Erk, B. Raspor, *J. Electroanal. Chem.* **1999**, *466*, 75–81.
108. M. Erk, B. Raspor, *Anal. Chim. Acta* **2001**, *442*, 165–170.
109. M. Erk, B. Raspor, *J. Electroanal. Chem.* **2001**, *502*, 174–179.
110. O. Nieto, A. R. Rodriguez, *Electroanalysis* **1999**, *11*, 175–182.
111. I. Sestakova, M. Kopanica, L. Havran et al., *Electroanalysis* **2000**, *12*, 100–104.
112. C. Harlyk, O. Nieto, G. Bordin et al., *J. Electroanal. Chem.* **1998**, *458*, 199–208.
113. J. L. L. Vaz, G. Duc, M. Petit-Ramel et al., *Can. J. Chem.-Rev. Can. Chim.* **1996**, *74*, 359–364.
114. A. Assabbane, M. Belmouden, A. Albourine et al., *Bull. Electrochem.* **2000**, *16*, 497–499.
115. J. M. Zhang, Z. W. Wang, Q. Z. Shi, *Chinese J. Inorg. Chem.* **2004**, *20*, 324–330.
116. P. L. Sahu, F. Khan, *Bull. Electrochem.* **2000**, *16*, 449–452.
117. P. L. Pratihar, *Asian J. Chem.* **2000**, *12*, 1146–1158.
118. I. Cukrowski, *Analyst* **1997**, *122*, 827–833.

119. I. Cukrowski, S. A. Loader, *Electroanalysis* **1998**, *10*, 877–885.
120. I. Cukrowski, *Electroanalysis* **1997**, *9*, 1167–1173.
121. I. Cukrowski, J. R. Zeevaart, N. V. Jarvis, *Anal. Chim. Acta* **1999**, *379*, 217–226.
122. I. Cukrowski, N. Maseko, *Electroanalysis* **2003**, *15*, 1377–1388.
123. E. Cukrowska, I. Cukrowski, *Talanta* **1998**, *47*, 1175–1189.
124. H. Parham, M. Shamsipur, *J. Electroanal. Chem.* **1991**, *314*, 71–80.
125. G. Rounaghi, M. Chamsaz, A. Nezhadali, *J. Incl. Phenom. Macrocyclic Chem.* **2000**, *38*, 153–161.
126. G. Rounaghi, A. S. Yazdi, Z. Monsef, *J. Incl. Phenom. Macrocycl. Chem.* **2002**, *43*, 231–237.
127. Z. Monsef, G. Rounaghi, A. Sarafraza, *J. Incl. Phenom. Macrocycl. Chem.* **2001**, *39*, 321–325.
128. E. Bottari, M. R. Festa, *Chem. Spec. Bioavailab.* **1996**, *8*, 75–83.
129. E. Bottari, M. R. Festa, *Talanta* **1998**, *46*, 91–99.
130. P. Arranz-Mascarós, R. López-Garzón, M. L. Godino-Salino et al., *Transition Met. Chem.* **1998**, *23*, 501–505.
131. M. Filella, R. M. Town, M. G. Bugarin, *J. Chem. Eng. Data* **1999**, *44*, 1009–1019.
132. P. Benezech, D. A. Palmer, *Chem. Geol.* **2000**, *167*, 11–24.
133. M. Salonen, H. Saarinen, M. Orama, *J. Coord. Chem.* **2003**, *56*, 1041–1047.
134. V. P. Vasil'ev, S. N. Gridchin, L. A. Kochergina et al., *J. Anal. Chem.* **2003**, *58*, 47–49.
135. R. Tomas, M. Visic, I. Tominic et al., *Croat. Chem. Acta* **2001**, *74*, 91–101.
136. R. Tomas, I. Tominic, V. Sokol et al., *Croat. Chem. Acta* **2004**, *77*, 519–527.
137. S. F. Ledénkov, V. A. Sharmin, G. V. Chistyakova, *Russ. Chem. Bull.* **2004**, *53*, 758–765.
138. K. Kurnia, D. E. Giles, P. M. May et al., *J. Coord. Chem.* **1996**, *38*, 183–197.
139. R. Serra, F. Mas, J. M. Diaz-Cruz et al., *Electroanalysis* **2000**, *12*, 60–65.
140. R. M. Izatt, J. S. Bradshaw, S. A. Nielsen et al., *Chem. Rev.* **1985**, *85*, 271–339.
141. R. M. Izatt, K. Pawlak, J. S. Bradshaw et al., *Chem. Rev.* **1991**, *91*, 1721–2085.
142. R. M. Izatt, K. Pawlak, J. S. Bradshaw et al., *Chem. Rev.* **1995**, *95*, 2529–2586.
143. J. A. Castro, J. Romero, J. A. Garcia-Vázquez et al., *Polyhedron* **1996**, *15*, 2741–2745.
144. P. Perez-Lourido, J. A. Garcia-Vazquez, J. Romero et al., *Inorg. Chim. Acta* **1998**, *271*, 1–8.
145. M. Fondo, A. Sousa, M. R. Bermejo et al., *Eur. J. Inorg. Chem.* **2002**, *3*, 703–710.
146. R. Pedrido, M. R. Bermejo, A. M. Garcia-Deibe et al., *Eur. J. Inorg. Chem.* **2003**, *17*, 3193–3200.
147. M. Bernal, J. A. Garcia-Vázquez, J. Romero et al., *Inorg. Chim. Acta* **1999**, *295*, 39–47.
148. R. Pedrido, M. R. Bermejo, M. J. Romero et al., *Dalton Trans.* **2005**, *3*, 572–579.
149. S. Cabaleiro, E. Vázquez-Lopez, J. Castro et al., *Inorg. Chim. Acta* **1999**, *294*, 87–94.
150. C. Boudon, J. P. Gisselbrecht, M. Gross, *Electroanalysis* **1992**, *4*, 19–26.
151. A. Bobrowski, A. M. Bond, S. R. Ellis, *Inorg. Chim. Acta* **1999**, *293*, 223–228.
152. A. José, J. A. Garcia-Vázquez, J. Romero et al., *Coord. Chem. Rev.* **1999**, *193–195*, 691–745.
153. C. A. Koval, J. N. Howard, *Chem. Rev.* **1992**, *92*, 411–433.
154. K. Rajeshwar, *Adv. Mater.* **1992**, *4*, 23–29.
155. G. Hodes, in *Physical Electrochemistry* (Ed.: I. Rubinstein), Marcel Dekker, New York, 1995, p. 515.
156. R. K. Pandey, S. N. Sahu, S. Cahndra, *Handbook of Semiconductor Electrodepositon*, Marcel Dekker, New York, 1996.
157. N. Myung, N. R. de Tacconi, K. Rajeshwar, *Electrochim. Commun.* **1999**, *1*, 42–45.
158. N. Myung, S. Kim, D. Lincot et al., *Electrochim. Acta* **2000**, *45*, 3749–3756.
159. S. J. Choi, D. H. Woo, N. S. Myung et al., *J. Electrochim. Soc.* **2001**, *148*, C569–C573.
160. N. Myung, S. Ham, B. Choi et al., *J. Electroanal. Chem.* **2005**, *574*, 367–373.
161. A. Gichuhi, B. E. Boone, U. Demir et al., *J. Phys. Chem. B* **1998**, *102*, 6499–6506.
162. M. Innocenti, S. Cattarin, M. Cavallini et al., *J. Electroanal. Chem.* **2002**, *532*, 219–225.
163. C. B. Murray, D. J. Norris, M. G. Bawendi, *J. Am. Chem. Soc.* **1993**, *115*, 8706–8715.
164. M. A. Anderson, S. Gorer, R. M. Penner, *J. Phys. Chem. B* **1997**, *101*, 5895–5899.
165. L. Pedone, E. Caponetti, M. Leone et al., *J. Colloid Interface Sci.* **2005**, *284*, 495–500.
166. E. Granot, F. Patolsky, I. Willner, *J. Phys. Chem. B* **2004**, *108*, 5875–5881.

167. R. Zhai, S. B. Wang, H. Y. Xu et al., *Mater. Lett.* **2005**, *59*, 1497–1501.
168. X. Xu, J. Cesarano, E. Burch et al., *Thin Solid Films* **1997**, *305*, 95–102.
169. M. Sasagawa, J. Nishino, Y. Nosaka, *Electrochim. Acta* **1999**, *67*, 1237–1239.
170. M. Sasagawa, Y. Nosaka, *J. Electroanal. Chem.* **2002**, *536*, 141–144.
171. M. Sasagawa, Y. Nosaka, *Electrochim. Acta* **2003**, *48*, 483–488.
172. S. Tamulevicius, M. P. Valkonen, G. Laukaitis et al., *Thin Solid Films* **1999**, *356*, 430–434.
173. G. Laukaitis, M. Lindroos, S. Tamulevicius et al., *Appl. Surf. Sci.* **2001**, *185*, 134–139.
174. M. P. Valkonen, T. Kannainen, S. Lindroos et al., *Appl. Surf. Sci.* **1997**, *115*, 386–392.
175. B. R. Sankapal, R. S. Mane, C. D. Lokhande, *Mater. Res. Bull.* **2000**, *35*, 177–184.
176. C. D. Lokhande, B. R. Sankapal, H. M. Pathan et al., *Appl. Surf. Sci.* **2001**, *181*, 277–282.
177. J. Nishino, S. Chatani, Y. Uotani et al., *J. Electroanal. Chem.* **1999**, *473*, 217–222.
178. M. Takahashi, S. Hasegawa, M. Watanabe et al., *J. Appl. Electrochem.* **2002**, *32*, 359–367.
179. T. Yoshida, K. Yamaguchi, T. Kazitani et al., *J. Electroanal. Chem.* **1999**, *473*, 209–216.
180. N. R. de Tacconi, H. Wenren, K. Rajeshwar, *J. Electrochem. Soc.* **1997**, *144*, 3159–3163.
181. S. K. Haram, A. J. Bard, *J. Phys. Chem. B* **2001**, *105*, 8192–8195.
182. Y. Nosaka, N. Ohta, T. Fukuyama et al., *J. Colloid Interface Sci.* **1993**, *155*, 23–29.
183. N. N. Gudeleva, F. S. Bekmukhametova, Z. P. Salaeva et al., *Russ. J. Gen. Chem.* **1999**, *69*, 1548–1552.
184. F. Loglio, M. Innocenti, F. D'Acapito et al., *J. Electroanal. Chem.* **2005**, *575*, 161–167.
185. M. Bouroushian, T. Kosanovic, Z. Loizos et al., *Electrochim. Commun.* **2000**, *2*, 281–285.
186. S. Eriksson, T. Gruszecki, P. Carlsson et al., *Thin Solid Films* **1995**, *269*, 14–17.
187. M. Ramrakhiani, *Mater. Sci. Eng., B* **1995**, *35*, 493–496.
188. C. M. Shen, X. G. Zhang, H. L. Li, *Appl. Surf. Sci.* **2005**, *240*, 34–41.
189. C. M. Shen, X. G. Zhang, H. L. Li, *Mater. Sci. Eng., B* **2001**, *84*, 265–270.
190. C. D. Lokhande, E. H. Lee, K. D. Jung et al., *Mater. Chem. Phys.* **2005**, *91*, 399–403.
191. M. D. R. Tanveer, *Bull. Electrochem.* **2000**, *16*, 370–375.
192. M. Bouroushian, J. Charoud-Got, Z. Loizos et al., *Thin Solid Films* **2001**, *381*, 39–47.
193. N. Dukstiene, *Russ. J. Electrochem.* **2003**, *39*, 1331–1337.
194. A. Saraby-Rentjes, L. M. Peter, M. E. Ozsan et al., *J. Electrochem. Soc.* **1993**, *140*, 2880–2888.
195. R. D. Engelken, T. P. Van Doren, *J. Electrochem. Soc.* **1985**, *132*, 2910–2919.
196. M. W. Verbrugge, C. W. Tobias, *J. Electrochem. Soc.* **1987**, *134*, 3104–3109.
197. E. A. Meulenkamp, L. M. Peter, *J. Chem. Soc., Faraday Trans.* **1996**, *92*, 4077–4082.
198. F. Forni, M. Innocenti, G. Pezzatini et al., *Electrochim. Acta* **2000**, *45*, 3225–3231.
199. K. Murase, H. Uchida, T. Hirato et al., *J. Electrochem. Soc.* **1999**, *146*, 531–536.
200. M. B. Dergacheva, V. N. Statsyuk, L. A. Fogel, *J. Electroanal. Chem.* **2005**, *579*, 43–49.
201. K. Murase, H. Watanabe, T. Hirato et al., *J. Electrochem. Soc.* **1999**, *146*, 1798–1803.
202. K. Murase, H. Watanabe, S. Mori et al., *J. Electrochem. Soc.* **1999**, *146*, 4477–4484.
203. H. Gómez, R. Henríquez, R. Schrebler et al., *Electrochim. Acta* **2001**, *46*, 821–827.
204. H. Gómez, R. Henríquez, R. Schrebler et al., *Electrochim. Acta* **2005**, *50*, 1299–1305.
205. T. Montiel-Santillán, O. Solorza-Feria, H. Sánchez-Soriano, *Int. J. Hydrogen Energy* **2002**, *27*, 461–464.
206. J. G. N. Matias, J. F. Juliao, D. M. Soares et al., *J. Electroanal. Chem.* **1997**, *431*, 163–169.
207. C. Lepiller, D. Lincot, *J. Electrochem. Soc.* **2004**, *151*, C348–C357.
208. S. I. Hsiu, I. W. Sun, *J. Appl. Electrochem.* **2004**, *34*, 1057–1063.
209. Y. Bae, N. Myung, A. J. Bard, *Nano Lett.* **2004**, *4*, 1153–1161.
210. M. B. Dergacheva, V. N. Statsyuk, L. A. Fogel et al., *Russ. J. Appl. Chem.* **1998**, *71*, 634–636.
211. A. E. Rakhshani, *Phys. Status Solidi A-Appl. Res.* **2002**, *191*, 179–187.
212. I. A. Kazarinov, A. N. Stepanov, N. N. Kutnaeva et al., *Russ. J. Electrochem.* **1998**, *34*, 1282–1289.
213. I. A. Kazarinov, M. M. Burashnikova, A. N. Stepanov, *Russ. J. Appl. Chem.* **2001**, *74*, 430–433.

214. V. D. Jović, A. R. Despić, J. S. Stevanović et al., *Electrochim. Acta* **1989**, *34*, 1093–1102.
215. I. A. Kazarinov, N. N. Kutnaeva, E. L. Vlasova, *Russ. J. Electrochem.* **1999**, *35*, 463–466.
216. B. Borresen, G. A. Voyatzis, G. N. Papatheodorou, *Phys. Chem. Chem. Phys.* **1999**, *1*, 3309–3314.
217. T. Montiel, O. Solorza, H. Sanchez, *J. Electrochem. Soc.* **2000**, *147*, 1031–1037.
218. E. Juzeliūnas, M. Samulevičiene, *Surf. Coat. Technol.* **1996**, *80*, 293–294.
219. Y. Y. Tevtul, *Russ. J. Electrochem.* **1996**, *32*, 535–540.
220. T. C. Franklin, T. S. N. S. Narayanan, *J. Electrochem. Soc.* **1996**, *143*, 2759–2764.
221. M. E. Alekseeva, F. K. Mansurov, V. A. Nikolskii, *Russ. J. Appl. Chem.* **1995**, *68*, 1753–1755.
222. V. V. Kuznetsov, L. M. Skibina, A. I. Sokolenko, *Prot. Met.* **2004**, *40*, 77–81.
223. V. V. Kuznetsov, L. M. Skibina, I. N. Loskutnikova et al., *Prot. Met.* **2004**, *40*, 331–336.
224. V. V. Kuznetsov, O. V. Fedorova, O. A. Gulidova, *Russ. J. Electrochem.* **1995**, *31*, 1252–1258.
225. V. V. Kuznetsov, L. M. Skibina, I. N. Loskutnikova, *Prot. Met.* **1998**, *34*, 363–367.
226. V. V. Kuznetsov, L. M. Skibina, I. N. Loskutnikova et al., *Prot. Met.* **1998**, *34*, 465–469.
227. V. V. Kuznetsov, L. M. Skibina, I. N. Loskutnikova, *Prot. Met.* **2000**, *36*, 565–570.
228. V. V. Kuznetsov, L. M. Skibina, I. N. Loskutnikova, *Prot. Met.* **2000**, *36*, 571–574.
229. V. V. Kuznetsov, L. M. Skibina, I. N. Loskutnikova et al., *Prot. Met.* **2001**, *37*, 31–34.
230. V. V. Kuznetsov, L. M. Skibina, I. N. Loskutnikova, *Prot. Met.* **2002**, *38*, 37–44.
231. V. V. Kuznetsov, L. M. Skibina, R. A. Levochkin et al., *Prot. Met.* **2003**, *39*, 154–159.
232. V. V. Kuznetsov, L. M. Skibina, I. N. Loskutnikova et al., *Prot. Met.* **2003**, *39*, 81–86.
233. V. V. Kuznetsov, L. M. Skibina, A. I. Sokolenko et al., *Prot. Met.* **2004**, *40*, 310–315.
234. V. Bostanov, E. Mladenova, D. Kashchiev, *J. Electroanal. Chem.* **2000**, *481*, 7–12.
235. V. F. Kozin, A. A. Omel'chuk, *Inorg. Mater.* **2002**, *38*, 207–211.
236. D. M. Kolb, M. Przasnyski, H. Gerischer, *J. Electroanal. Chem.* **1974**, *54*, 25–38.
237. J. W. Schultze, F. D. Koppitz, M. M. Lohren-gel, *Ber. Bunsen-Ges. Phys. Chem.* **1974**, *78*, 693–701.
238. F. M. Romeo, R. I. Tucceri, D. Posadas, *Surf. Sci.* **1988**, *203*, 186–200.
239. B. W. Gregory, M. L. Norton, J. L. Stickney, *J. Electroanal. Chem.* **1990**, *293*, 85–101.
240. E. Herrero, L. J. Buller, H. D. Abruna, *Chem. Rev.* **2001**, *101*, 1897–1930. and the references given therein.
241. R. Vidu, S. Hara, *Scripta Mater.* **1999**, *41*, 617–624.
242. R. Vidu, S. Hara, *J. Electroanal. Chem.* **1999**, *475*, 171–180.
243. R. Vidu, S. Hara, *Surf. Sci.* **2000**, *452*, 229–238.
244. G. Horanyi, *J. Solid State Electrochem.* **2000**, *4*, 177–180.
245. R. Vidu, N. Hirai, S. Hara, *Phys. Chem. Chem. Phys.* **2001**, *3*, 3320–3324.
246. G. Inzelt, G. Horanyi, *J. Electroanal. Chem.* **2000**, *491*, 111–116.
247. M. C. Santos, D. W. Miwa, S. A. S. Machado et al., *Quim. Nova* **2001**, *24*, 465–472.
248. A. A. Gewirth, B. K. Niece, *Chem. Rev.* **1997**, *97*, 1129–1162. and the references given therein.
249. J. C. Bondos, A. A. Gewirth, R. G. Nuzzo, *J. Phys. Chem.* **1996**, *100*, 8617–8620.
250. B. K. Niece, A. A. Gewirth, *Langmuir* **1997**, *13*, 6302–6309.
251. S.-J. Hsieh, A. A. Gewirth, *Langmuir* **2000**, *16*, 9501–9512.
252. M. D. Lay, J. L. Stickney, *J. Am. Chem. Soc.* **2003**, *125*, 1352–1355.
253. H. Kawamura, M. Takahasi, J. Mizuki, *J. Electrochim. Soc.* **2002**, *149*, C586–C591.
254. B. Pettinger, A. Friedrich, C. Shannon, *Electrochim. Acta* **1991**, *36*, 1829–1833.
255. D. Lee, T. Raymond, *Electrochim. Commun.* **2002**, *4*, 832–837.
256. M. D. Lay, K. Varazo, N. Srivastava et al., *J. Electroanal. Chem.* **2003**, *554*–555, 221–231.
257. S. Maupai, Y. Zhang, P. Schmuki, *Surf. Sci.* **2003**, *527*, L165–L170.
258. S. Maupai, Y. Zhang, P. Schmuki, *Electrochim. Solid State Lett.* **2003**, *6*, C63–C65.
259. Y. Zhang, S. Maupai, P. Schmuki, *Surf. Sci.* **2004**, *551*, L33–L39.
260. M. C. del Barrio, S. G. Garcia, D. R. Salinas, *Electrochim. Commun.* **2004**, *6*, 762–766.

261. X. Xing, P. Abel, R. McIntyre et al., *J. Electroanal. Chem.* **1987**, *216*, 261–271.
262. X. Xing, I. Tae Bae, D. A. Scherson, *Electrochim. Acta* **1995**, *40*, 29–36.
263. X. Xing, D. A. Scherson, C. Mak, *J. Electrochem. Soc.* **1990**, *137*, 2166–2175.
264. S. B. Aoun, Z. Dursun, T. Koga et al., *J. Electroanal. Chem.* **2004**, *567*, 175–183.
265. U. Demir, C. Shannon, *Langmuir* **1996**, *12*, 6091–6097.
266. R. Vidu, S. Hara, *J. Vac. Sci. Technol., B* **1999**, *17*, 2423–2430.
267. R. Vidu, S. Hara, *Electrochem.* **1999**, *67*, 1240–1242.
268. T. Tanaka, K. Kubo, N. Hirai et al., *Mater. Trans.* **2003**, *44*, 688–691.
269. K. Kubo, N. Hirai, S. Hara, *J. Jpn. Inst. Met.* **2002**, *66*, 881–884.
270. D. W. Suggs, J. L. Stickney, *Surf. Sci.* **1993**, *290*, 362–374.
271. B. W. Gregory, D. W. Suggs, J. L. Stickney, *J. Electrochem. Soc.* **1991**, *138*, 1279–1284.
272. D. W. Suggs, J. L. Stickney, *Surf. Sci.* **1993**, *290*, 375–387.
273. D. Oyamatsu, S. Kuwabata, H. Yoneyama, *J. Electroanal. Chem.* **1999**, *473*, 59–67.
274. E. Juzeliunas, H. W. Pickering, K. G. Weil, *J. Electrochem. Soc.* **2000**, *147*, 1088–1095.
275. R. R. Adžić, D. N. Simić, D. M. Dražić et al., *J. Electroanal. Chem.* **1975**, *61*, 117–120.
276. K. Varga, P. Zelenay, G. Horanyi et al., *J. Electroanal. Chem.* **1992**, *327*, 291–306.
277. R. Gómez, J. M. Feliu, *J. Electroanal. Chem.* **2003**, *554*–555, 145–156.
278. S. A. S. Machado, A. A. Tanaka, E. R. Gonzalez, *Electrochim. Acta* **1992**, *37*, 2559–2564.
279. M. C. dos Santos, S. A. S. Machado, *J. Brazil. Chem. Soc.* **1998**, *9*, 211–218.
280. M. C. Santos, S. A. S. Machado, L. A. Avaca et al., *Quim. Nova* **2000**, *23*, 392–400.
281. V. Daujotis, R. Randonis, *J. Electroanal. Chem.* **1992**, *326*, 253–275.
282. V. Daujotis, *Pol. J. Chem.* **1998**, *72*, 2432–2439.
283. M. E. Martins, R. C. Salvarezza, A. J. Arvia, *Electrochim. Acta* **1996**, *41*, 2441–2449.
284. J. F. Huang, I. W. Sun, *J. Electrochem. Soc.* **2002**, *149*, E348–E355.
285. E. Schmidt, M. Christen, P. Beyeler, *J. Electroanal. Chem.* **1973**, *42*, 275–289.
286. H. Bort, K. Jüttner, W. J. Lorenz et al., *Electrochim. Acta* **1983**, *28*, 993–1001.
287. V. D. Jović, B. M. Jović, A. R. Despić, *J. Electroanal. Chem.* **1990**, *288*, 229–243.
288. V. D. Jović, B. M. Jović, *Electrochim. Acta* **2002**, *47*, 1777–1785.
289. S. G. Garcia, D. R. Salinas, G. Staikov, *Surf. Sci.* **2005**, *576*, 9–18.
290. M. L. Foresti, G. Pezzatini, M. Cavallini et al., *J. Phys. Chem. B* **1998**, *102*, 7413–7420.
291. M. E. Martins, A. Hernández-Creus, R. C. Salvarezza et al., *J. Electroanal. Chem.* **1994**, *375*, 141–155.
292. M. Ge, A. A. Gewirth, *Surf. Sci.* **1995**, *324*, 140–148.
293. C. Stuhlmann, Z. Park, C. Bach et al., *Electrochim. Acta* **1998**, *44*, 993–998.
294. J. Hommrich, S. Hümann, K. Wandelt, *Faraday Discuss.* **2002**, *121*, 129–138.
295. V. D. Jović, B. M. Jović, *J. Serb. Chem. Soc.* **2001**, *66*, 345–357.
296. S. Hümann, J. Hommrich, K. Wandelt, *Thin Solid Films* **2003**, *428*, 76–82.
297. A. Budniok, *J. Electroanal. Chem.* **1981**, *123*, 365–372.
298. A. Budniok, *Thin Solid Films* **1981**, *81*, 289–299.
299. M. A. Lovell, D. Roy, *Electrochim. Acta* **1998**, *43*, 2117–2130.
300. R. Krumm, B. Guel, C. Schmitz et al., *Electrochim. Acta* **2000**, *45*, 3255–3262.
301. Y. Sugimoto, L. M. Peter, *J. Electroanal. Chem.* **1995**, *381*, 251–255.
302. Y. Sugimoto, L. M. Peter, *J. Electroanal. Chem.* **1995**, *386*, 183–188.
303. E. Schmidt, H. R. Gygax, *J. Electroanal. Chem.* **1966**, *12*, 300–319.
304. G. E. Badea, T. Badea, *Rev. Roum. Chim.* **2003**, *48*, 843–848.
305. J. Tramontina, D. S. Azambuja, C. M. S. Piatnicki, *J. Brazil. Chem. Soc.* **2002**, *13*, 469–473.
306. H. D. Shih, F. Jona, D. W. Jepsen et al., *Phys. Rev. B* **1977**, *15*, 5550–5560; 5561–5666.
307. F. Kadirgan, S. Kutun, S. Suzer, *Ann. Chim.* **1998**, *88*, 705–718.
308. E. A. Streletsov, N. P. Osipovich, *Dokl. Akad. Nauk Belarus.*, **1998**, *42*, 58–63.
309. V. D. Jović, T. Trišović, B. M. Jović et al., *J. Electroanal. Chem.* **1996**, *408*, 149–155.
310. V. D. Jović, B. M. Jović, E. R. Stojilković et al., *J. Serb. Chem. Soc.* **1999**, *64*, 265–273.
311. A. E. Elshерief, *Electrochim. Acta* **2003**, *48*, 2667–2673.

312. P. Y. Chen, I. W. Sun, *Electrochim. Acta* **2000**, *45*, 3163–3170.
313. R. Barnard, *J. Appl. Electrochem.* **1981**, *11*, 217–237.
314. S. B. Saidman, J. R. Vilche, A. J. Arvia, *Electrochim. Acta* **1987**, *32*, 395–409.
315. J. O. Zerbino, S. B. Saidman, J. R. Vilche et al., *Electrochim. Acta* **1989**, *34*, 1167–1167.
316. J. O. Zerbino, S. B. Saidman, J. R. Vilche et al., *Electrochim. Acta* **1990**, *35*, 605–612.
317. Y. Duhirel, B. Beden, J. M. Léger et al., *Electrochim. Acta* **1992**, *37*, 665–671.
318. J. I. De Urraza, C. A. Gervasi, S. B. Saidman et al., *J. Appl. Electrochem.* **1993**, *23*, 1207–1213.
319. N. Simic, A. Ahlberg, *J. Electroanal. Chem.* **1998**, *451*, 237–247.
320. K. M. Ismail, *J. Appl. Electrochem.* **2001**, *31*, 1333–1338.
321. T. G. Dmitrienko, E. A. Khomskaya, N. F. Buranova et al., *Russ. J. Electrochem.* **1997**, *33*, 910–914.
322. T. G. Dmitrienko, E. A. Khomskaya, N. F. Buranova et al., *Russ. J. Electrochem.* **1998**, *34*, 423–428.
323. S. B. Saidman, J. R. Vilche, A. J. Arvia, *Electrochim. Acta* **1987**, *32*, 1153–1157.
324. W. A. Badawy, F. M. Al-Kharafi, E. Y. Al-Hassan, *Corros. Prevent Contr.* **1998**, *45*, 95–108.
325. W. A. Badawy, F. M. Al-Kharafi, E. Y. Al-Hassan, *Mater. Sci. Forum* **1998**, *289–2*, 849–859.
326. W. A. Badawy, F. M. Al-Kharafi, E. Y. Al-Hassan, *Bull. Electrochem.* **1998**, *14*, 449–455.
327. W. A. Badawy, F. M. Al-Kharafi, E. Y. Al-Hassan, *Corros. Prevent Contr.* **1999**, *46*, 51–62.
328. M. G. Alvarez, J. R. Galvele, *J. Electrochem. Soc.* **1980**, *127*, 1235–1241.
329. W. A. Badawy, F. M. Al-Kharafi, *Bull. Electrochem.* **2000**, *16*, 155–160.
330. M. Abdullah, *Bull. Electrochem.* **1997**, *13*, 149–155.
331. D. Tromans, B. Foster, F. Weinberg, *Corros. Sci.* **1997**, *39*, 1291–1305.
332. W. A. Badawy, F. M. Al-Kharafi, E. Y. Al-Hassan, *Corros. Prevent Contr.* **1998**, *45*, 145–155.
333. A. El-Sayed, *J. Appl. Electrochem.* **1997**, *27*, 193–200.
334. K. S. Khairou, A. El-Sayed, *J. Appl. Polym. Sci.* **2003**, *88*, 866–871.
335. L. A. S. Silva, L. Sathler, *Plat. Surf. Finish.* **2003**, *90*, 38–42.
336. T. Dobrev, M. Monev, I. Krastev et al., *Trans. Inst. Metal Finish.* **1996**, *74*, 45–50.
337. A. Durairajan, B. S. Haran, R. E. White et al., *J. Electrochem. Soc.* **2000**, *147*, 1781–1786.
338. P. W. Haberecht, B. R. W. Hinton, *Trans. Inst. Met. Finish.* **2000**, *78*, 17–22.
339. H. S. Kim, B. N. Popov, K. S. Chen, *Corros. Sci.* **2003**, *45*, 1505–1521.
340. J. R. Galvele, *Electrochim. Acta* **2000**, *45*, 3537–3541.
341. M. L. Montoto, G. S. Duffó, J. R. Galvele, *Corros. Sci.* **2001**, *43*, 755–764.
342. M. Lazzari, C. A. Vincent, in *Modern Batteries* (Eds.: C. A. Vincent, B. Scrosati), Arnold, London, 1997, p. 65.
343. V. V. Tenkovtsev, L. S. Nadezhina, B. A. Borisov et al., *Russ. J. Appl. Chem.* **1995**, *68*, 980–984.
344. J. McBreen, in *Handbook of Battery Materials* (Ed.: J. O. Besenhard), Wiley-VCH, New York, 1999, p. 135.
345. S. Guinot, E. Salmon, J. F. Penneau et al., *Electrochim. Acta* **1998**, *43*, 1163–1170.
346. X. Zhu, H. Yang, Y. Cao et al., *Electrochim. Acta* **2004**, *49*, 2533–2539.
347. S. N. Lvov, D. D. Macdonald, *J. Power Sources* **1998**, *72*, 136–145.
348. F. Bonino, C. A. Vincent, in *Modern Batteries*, (Eds.: C. A. Vincent, B. Scrosati), Arnold, London, 1997, p. 162.
349. G. P. Kalaignan, C. Umaprakatheevaran, B. Muralidharan et al., *J. Power Sources* **1996**, *58*, 29–34.
350. R. J. Brodd, K. R. Bullock, R. A. Leising et al., *J. Electrochem. Soc.* **2004**, *151*, K1–K11.
351. Y. Morioka, S. Narukawa, T. Itou, *J. Power Sources* **2001**, *100*, 107–116.
352. D. Ohms, M. Kohlhase, G. Benczúr-Ürmössy et al., *J. Power Sources* **2002**, *105*, 127–133.
353. X. Y. Xiong, H. Van der Porten, M. Crappe, *Electrochim. Acta* **1996**, *41*, 1267–1275.
354. J. P. Diard, B. Le Gorrec, C. Montella et al., *Electrochim. Acta* **1997**, *42*, 3417–3420.
355. J. P. Diard, B. Le Gorrec, C. Montella, *J. Power Sources* **1998**, *70*, 78–84.
356. A. Hammouche, E. Karden, R. W. De Doncker, *J. Power Sources* **2004**, *127*, 105–111.
357. F. Huet, *J. Power Sources* **1998**, *70*, 59–69.

358. S. Rodrigues, N. Munichandraiah, A. K. Shukla, *J. Power Sources* **2000**, *87*, 12–20.
359. W. S. Kruijt, H. J. Bergveld, P. H. L. Notten, *J. Electrochem. Soc.* **1998**, *145*, 3764–3773.
360. P. H. L. Notten, W. S. Kruijt, H. J. Bergveld, *J. Electrochem. Soc.* **1998**, *145*, 3774–3783.
361. M. Winter, R. J. Brodd, *Chem. Rev.* **2004**, *104*, 4245–4269.
362. U. Köhler, C. Antonius, P. Bäuerlein, *J. Power Sources* **2004**, *127*, 45–52.
363. J. K. Dunnick, B. A. Flower, in *Cadmium in Handbook on Toxicity of Inorganic Compounds*, (Eds.: H. G. Seiler, H. Sipel, M. Dekker), New York, 1988, Chapter 14.
364. H. Tsukube, *Talanta* **1993**, *40*, 1313–1324.
365. S. K. Srivastava, V. K. Gupta, S. Jain, *Electroanalysis* **1996**, *8*, 938–940.
366. V. K. Gupta, P. Kumar, R. Mangla, *Electroanalysis* **2000**, *12*, 752–756.
367. V. K. Gupta, P. Kumar, *Anal. Chim. Acta* **1999**, *389*, 205–212.
368. V. K. Gupta, S. Chandra, R. Mangla, *Electrochim. Acta* **2002**, *47*, 1579–1586.
369. A. K. Singh, P. Saxena, R. Singh, *Anal. Sci.* **2005**, *21*, 179–181.
370. A. Panwar, S. Baniwal, C. L. Sharma et al., *Fresenius' J. Anal. Chem.* **2000**, *368*, 768–772.
371. M. Javanbakht, A. Shabani-Kia, M. R. Darvich et al., *Anal. Chim. Acta* **2000**, *408*, 75–81.
372. M. Shamsipur, M. H. Mashhadizadeh, *Talanta* **2001**, *53*, 1065–1071.
373. K. C. Gupta, M. J. D'Arc, *Electroanalysis* **2000**, *12*, 1408–1413.
374. K. C. Gupta, M. J. D'Arc, *Talanta* **2000**, *52*, 1087–1103.
375. L. Prodi, M. Montalti, N. Zaccheroni et al., *Tetrahedron Lett.* **2001**, *42*, 2941–2944.
376. C. Wardak, B. Marczevska, *Chem. Anal. (Warsaw)* **2004**, *49*, 497–508.
377. C. Wardak, B. Marczevska, J. Lenik, *Desalination* **2004**, *163*, 69–75.
378. M. A. Pineros, J. E. Shaff, L. V. Kochian et al., *Electroanalysis* **1998**, *10*, 937–941.
379. J. Wang, B. M. Tian, J. Y. Wang, *Anal. Commun.* **1998**, *35*, 241–243.
380. U. Siemeling, B. Neumann, H. G. Stammeler et al., *Z. Anorg. Allg. Chem.* **2002**, *628*, 2315–2320.
381. M. M. Ardakani, M. Salvati-Niassari, A. Sadeghi, *New J. Chem.* **2004**, *28*, 595–599.
382. M. R. Ganjali, T. Pouršaber, F. Basiripour et al., *Fresenius' J. Anal. Chem.* **2001**, *370*, 1091–1095.
383. M. N. Abbas, E. Zahran, *J. Electroanal. Chem.* **2005**, *576*, 205–213.
384. Y. G. Vlasov, E. A. Bychkov, A. D. Safarov et al., *Zh. Anal. Khim.* **1985**, *40*, 1438–1446.
385. R. D. Tsingarelli, I. P. Nikolenko, A. F. Radchenko et al., *Zh. Anal. Khim.* **1986**, *41*, 449–452.
386. O. P. Ryabushko, A. T. Pilipenko, Yu. S. Savin, L. A. Batkovskaya, *Ukr. Khim. Zh.* **1990**, *56*, 263–267.
387. S. Ito, Y. Asano, H. Wada, *Talanta* **1997**, *44*, 697–704.
388. Y. G. Mourzina, M. J. Schöning, J. Schubert et al., *Anal. Chim. Acta* **2001**, *433*, 103–110.
389. Y. Umezawa, *Handbook of Ion-Selective Electrodes: Selectivity Coefficients*, CRC Press, Boca Raton, 1990.
390. P. Bühlmann, E. Pretsch, E. Bakker, *Chem. Rev.* **1998**, *98*, 1593–1687.
391. E. Bakker, P. Bühlmann, E. Pretsch, *Electroanalysis* **1999**, *11*, 915–933.
392. E. Bakker, *J. Electrochem. Soc.* **1996**, *143*, L83–L85.
393. E. Bakker, *Anal. Chem.* **1997**, *69*, 1061–1069.
394. T. Sokalski, A. Ceresa, T. Zwickl et al., *J. Am. Chem. Soc.* **1997**, *119*, 11347–11348.
395. T. Sokalski, A. Ceresa, M. Fibbioli et al., *Anal. Chem.* **1999**, *71*, 1210–1214.
396. W. Qin, T. Zwickl, E. Pretsch, *Anal. Chem.* **2000**, *72*, 3236–3240.
397. S. Mathison, E. Bakker, *Anal. Chem.* **1998**, *70*, 303–309.
398. E. Bakker, E. Pretsch, *Trends Anal. Chem.* **2005**, *24*, 199–207.
399. A. C. Ion, E. Bakker, E. Pretsch, *Anal. Chim. Acta* **2001**, *440*, 71–79.
400. Y. Stozhko, G. N. Lipunova, T. I. Maslakova et al., *J. Anal. Chem.* **2004**, *59*, 179–184.
401. S. S. Hu, K. B. Wu, H. C. Yi et al., *Fresenius' J. Anal. Chem.* **2001**, *370*, 101–103.
402. G. Marino, M. F. Bergamini, M. F. S. Teixeira et al., *Talanta* **2003**, *59*, 1021–1028.
403. C. G. Hu, K. B. Wu, X. Dai et al., *Talanta* **2003**, *60*, 17–24.
404. S. Yuan, W. H. Chen, S. H. Hu, *Talanta* **2004**, *64*, 922–928.
405. K. C. Honeychurch, J. P. Hart, D. C. Cowell et al., *Electroanalysis* **2002**, *14*, 177–185.
406. W. S. Huang, C. H. Yang, S. H. Zhang, *Chinese J. Anal. Chem.* **2002**, *30*, 1367–1370.

407. E. Chow, D. B. Hibbert, J. J. Gooding, *Electrochem. Commun.* **2005**, 7, 101–106.
408. G. Roa, M. T. Ramirez-Silva, M. A. Romero-Romo et al., *Anal. Bioanal. Chem.* **2003**, 377, 763–769.
409. H. Düssel, A. Dostal, F. Scholz, *Fresenius' J. Anal. Chem.* **1996**, 355, 21–28.
410. A. L. Bo, X. Q. Lin, *Chinese J. Anal. Chem.* **1999**, 27, 392–397.
411. M. Hermes, M. Lovrić, M. Hartl et al., *J. Electroanal. Chem.* **2001**, 501, 193–204.
412. N. F. Zakharchuk, N. Naumov, R. Stösser et al., *J. Solid State Electrochem.* **1999**, 3, 264–276.

**24.3
Electrochemistry of Lead**

24.3.1	Double-layer Properties of Pb Electrodes	805
24.3.1.1	Properties of Solid Electrodes	805
24.3.1.2	Properties of Liquid Electrodes	805
24.3.1.3	Adsorption on Solid Electrodes	806
24.3.2	Electrochemical Properties and Kinetics of Lead and Lead Compounds	806
24.3.2.1	Pb(II)/Pb(Hg) System	806
24.3.2.1.1	Studies in the Presence of Inhibitors and Organic Solvents	806
24.3.2.1.2	Other Phenomena	807
24.3.2.2	Complexes of Pb(II) and Related Phenomena	808
24.3.2.3	Electrochemical Processes of Liquid Lead in Molten Salts	808
24.3.2.4	Voltammetric Behavior of Lead	808
24.3.2.4.1	Sulfuric Acid Solutions	808
24.3.2.4.2	Nitric Acid Solutions	812
24.3.2.4.3	Phosphoric Acid Solutions	812
24.3.2.4.4	Sodium Hydroxide Solutions	812
24.3.2.4.5	Different Salt Solutions	814
24.3.2.5	Voltammetric Behavior of Several Lead Compounds	815
24.3.2.5.1	PbO	815
24.3.2.5.2	PbO ₂	816
24.3.2.5.3	Pb chalcogenides	816
24.3.3	Electrodeposition and Underpotential Deposition of Lead on Solid Substrates	817
24.3.3.1	Platinum	817
24.3.3.2	Gold	818
24.3.3.3	Silver	820
24.3.3.4	Copper	821
24.3.3.5	Carbon	821
24.3.3.6	Silicon	822
24.3.3.7	Germanium	822
24.3.3.8	Other Materials	822
24.3.4	Corrosion and Passivation	823

24.3.5	Applied Electrochemistry	825
24.3.5.1	Lead-acid Batteries	825
24.3.5.2	Electrocatalytic Properties	826
24.3.5.2.1	Pb	826
24.3.5.2.2	PbO ₂	827
24.3.5.3	Electrochemical Sensors	828
24.3.5.3.1	Potentiometric Sensors	828
24.3.5.3.2	Amperometric/Voltammetric Sensors	828
	References	829

24.3.1

Double-layer Properties of Pb Electrodes

24.3.1.1 Properties of Solid Electrodes

The main properties of the double layer of solid lead electrodes have been already described in the Encyclopedia [1]. New achievements in this field have been the subject of reviews [for example [2–6]. Some of the new results relate to impedance of polycrystalline Pb electrodes in aqueous [7–9] and nonaqueous solvents (references in [3, 6]). Special attention has been paid to chemically and electrochemically polished polycrystalline electrodes, mainly in aqueous [10–12] and methanolic [13] fluoride solutions.

The influence of the single crystal face of the Pb electrode on zero charge potential has been analyzed. The difference between these potentials is within the range of 60 mV [8] and the potential value increases with lowering atomic density [11]. The increase of the inner layer capacitance at zero charge in the sequence Pb(100) \leq Pb(110) \leq Pb(112) < polycrystalline Pb < Pb(111) has been explained by increasing hydrophilicity of the surface [6, 11].

A solid drop Pb electrode with additionally remelted surface has been studied in KF and NaClO₄ solutions; the

minimum capacitance versus potential curve is practically independent of the electrolyte solution concentration [6].

24.3.1.2 Properties of Liquid Electrodes

Double-layer properties as capacitance and potential of zero charge obtained for both single crystal and polycrystalline Pb electrodes differ significantly, depending also on the pretreatment procedure [6]. Therefore, some studies concern liquid electrodes containing lead. Liquid lead in molten NaX–KX (X = Cl, Br, I) eutectic mixtures has been studied using electrochemical impedance spectroscopy [14]. The double-layer capacitance at the rest potential is of the order of 0.9, 0.6, and 0.2 μ F cm⁻², for Cl⁻, Br⁻, and I⁻ melts, respectively. These values are much lower than those obtained previously, in the sixties of the twentieth century, because of the improvement of experimental technique and detailed studies on the influence of frequency on the measured parameters. The measured capacitance is affected by reduction of alkali metal cations to alloy with Pb (at negative potentials), substitution of metal cations by anions for more positive potentials, and also anodic dissolution of lead at highly positive potentials. An influence of possible spontaneous dissolution

of lead electrode in molten alkali metal halides has also been considered.

Double-layer properties in aqueous, propylene carbonate and formamide solutions have been studied at room temperature for liquid Ga–Pb alloy (0.06 atom % of Pb) [15], as a model of Pb electrode with renewable surface. The electrode behaves as an ideally polarizable electrode in a wide potential range, and its capacitance is intermediate between that of Ga and Hg electrodes and is independent of the solvent. This electrode is much less lipophilic than Ga. Adsorption of anions on this electrode increases in the sequence $-BF_4^- = SO_4^{2-} < Cl^- < Br^- < I^-$.

24.3.1.3 Adsorption on Solid Electrodes

Adsorption studies in $(C_4H_9)_4NI$ solution, showing splitting of adsorption–desorption peaks, point to energetic inhomogeneity of the surface [6]. This inhomogeneity has been analyzed using the concept of constant phase element affecting the impedance spectra [9]. It has been found that incomplete reduction of the Pb surface lowers the double-layer capacitance and increases the surface inhomogeneity [6]. Compact layer capacity has been found to be in quantitative agreement with that for Hg at negative charges.

The influence of organic additives on the properties of lead electrodes has been studied from the viewpoint of application in lead-acid batteries, to improve the properties of the negative electrode. These materials can be classified into two types [16]: inhibitors and expanders. Inhibitors increase the overpotential for the hydrogen evolution reaction and lower the self-discharge of the negative plate. Expanders are used to restrain the surface area shrinkage of electrode active material during cycling and to inhibit the passivation of the negative plate. The inhibitor

and expander role of different surfactants in H_2SO_4 solutions has been studied – of the cationic type (cetyltrimethyl ammonium bromide), anionic type (sodium dodecyl benzenesulfonate, sodium dodecyl sulfate, sodium lignosulfonate, amine perfluoroalkylsulfonates), and some nonionic surfactants [16–20]. The influence of adsorbed lignin, an important additive for the negative electrode in lead-acid batteries, has been studied using the electrochemical atomic force microscopy (AFM) method [21, 22]. The presence of surfactants usually moves the hydrogen evolution potential to more negative values; however, some perfluorinated substances exert an opposite or negligible effect [16]. On the other hand, only nonionic surfactants can raise the discharge capacity of the negative electrode of lead-acid batteries [16]. Perfluorinated surfactants are more resistant to oxidation.

Specifically adsorbed inorganic ions as halide anions [23] and organic substances can inhibit corrosion (see e.g. [24]).

24.3.2 Electrochemical Properties and Kinetics of Lead and Lead Compounds

24.3.2.1 Pb(II)/Pb(Hg) System

This system with lead amalgam is especially suitable to determine thermodynamic and electrochemical kinetic data related to Pb(II) owing to renewability of the mercury electrode surface.

24.3.2.1.1 Studies in the Presence of Inhibitors and Organic Solvents The charge-transfer rate constant for the Pb(II)/Pb(Hg) couple in aqueous solution is very high [1]; therefore, the kinetics of electrode processes of this system has been

studied in the presence of inhibitors adsorbed on the electrode surface – aliphatic alcohols [25, 26], amines [27], or complexes with organic ligands [28]. In the case of full surface coverage by an inhibitor, the logarithm of standard rate constant is linearly dependent on the logarithm of bulk inhibitor concentration with the slope determined by the so-called steric factor, which represents the ratio of surface area occupied by the activated complex and inhibitor molecules, both for noncomplexed ions [29] and Pb(II) complexes [30]. This relation also discloses stereochemical information, concerning orientation of adsorbed molecules, as confirmed on the basis of quantum chemical calculations [31].

Studies in nonaqueous and aqueous organic mixed solvents have shown the influence of two factors on charge-transfer kinetics – adsorption of the organic component of the mixture and solvation of reactant ions [32–34]. Adsorption of the organic solvent on the electrode surface decreases the electrode reaction rate in a similar manner as in the case of adsorbed inhibitors, as discussed above. On the other hand, stronger solvation of metal cations results in lower charge-transfer rate. Both the solvation and activation energy of electrodeposition reactions in pure solvents, rise with increasing basicity of the solvent, expressed, for example, by donor number. A separate influence of adsorption and solvation on the electrode kinetics of the Pb(II)/Pb(Hg) couple has been shown for water–hexamethylphosphoramide mixed solvents [34]. Moreover, on the basis of formal potential values and electrochemical rate constants in mixed solvents, solvation numbers and reaction orders with respect to the organic solvent have been determined [35]. Half-wave potentials of

the Pb(II)/Pb(Hg) in numerous organic solvents have been presented [36].

Diffusion coefficients of Pb(II) determined in organic solvents – dimethylsulfoxide and hexamethylphosphoramide – are about 1 order of magnitude lower than in aqueous solutions [33, 34, 37].

24.3.2.1.2 Other Phenomena Interaction of metallic Pb in the mercury phase [38] and amalgam decomposition in alkaline medium [39] have also been discussed. Formation of anodic monolayer PbCO_3 or $\text{Pb}_3(\text{CO}_3)_2(\text{OH})_2$ on Pb(Hg), depending on pH, in carbonate or bicarbonate solutions, has been detected using electrochemical methods (chronoamperometry and linear sweep voltammetry) and powder X-ray diffractometry [40].

The Pb(II)/Pb(Hg) electrode process has been analyzed using digital simulation and the results have been compared with experiments carried out in aqueous sodium nitrate solutions applying convolution/deconvolution voltammetry to determine charge-transfer rate constants and transfer coefficients [41]. Principles of thin-layer anodic stripping voltammetry have been discussed and a model for the stripping step has been proposed. This model has been tested experimentally for amalgams of Cd and Pb [42]. Fast Fourier transform instrumentation has been shown to be advantageous, both in the analytical and kinetic applications of voltammetry, for example, on Cd and Pb redox systems [43]. Active/pассив transition for the Pb(Hg)/ PbCl_2 system has been studied using digital simulation [44].

Pb(Hg) electrode in the presence of PbSO_4 and H_2SO_4 has been used in thermodynamic studies and equilibrium potential determination [45].

The Pb(II)/Pb(Hg) system has been studied under high-pressure conditions

([46] and the references given therein). Pb dissolution process has not been found to be favored by increased pressure.

Surface tension of Pb amalgams in relation to the electronic structure of the metal and adsorption properties has been discussed [47].

24.3.2.2 Complexes of Pb(II) and Related Phenomena

Complexation equilibria and complexation processes have been studied mainly on mercury electrodes (see book [48]), for Pb(II) with, for example, oxalates, maleates, tartrates, citrates [49], phytochelatin [50], amino acids [51–57], carboxylic acids [53], cyclodextrins and their derivatives [58, 59], ferrocene derivatives [60], picolinic acid [61], sulfonic acids derivatives [62], fulvic like organic ligands/acids [63, 64], ligands involving cephalosporins [65], phthalocyanines [66], organic ligands giving pentagonal symmetry [67], or cryptands and other macrocyclic ligands (see reviews [68–70] and [71–77]). Complexation by other systems as dissolved organic matter from an estuarine sample [78], components of oxic and sulfidic waters [79] as well as red wines [80] have also been studied. The role of ligand adsorption in stripping voltammetry has been reviewed [81]. The Pb(II)/Pb(Hg) has been used as a redox probe to study complexation processes between macrocyclic ligands and several cations competing with Pb²⁺ ions (e.g. [82]).

Electrochemical formation of Pb(II) complexes by anodic dissolution of lead [83–89] and studies on electrochemical properties of Pb(IV) complexes as well as organo-lead compounds have been reported [90, 91]. Electrogenerated chemiluminescence of Pb(II)-bromide complexes has been described [92]. Reduction of lead to Zintl ions, such as Pb₉⁴⁻, has been

observed in liquid ammonia, accompanied by intermetallic phase formation, as a result of alkali metal incorporation into lead [93, 94].

Complexation of Pb(II) by cyclic thioethers facilitates reversible interfacial transfer in ion-transfer voltammetry for the water–nitrobenzene and water–1,2-dichloroethane systems [95, 96].

24.3.2.3 Electrochemical Processes of Liquid Lead in Molten Salts

The oxidation/reduction processes of Pb(II) with formation of liquid Pb(0) have been studied in molten halides ([97, 98] and references given therein). Most authors have concluded that Pb(II) species are reduced to the metal in the course of the single two-electron process. PbO₂ has been found unstable because of the reduction by Cl⁻ ions to Pb(II). On the other hand, in the presence of Zn(II), lead(II) oxide, PbO, transforms to Pb(II) with ZnO formation. In ZnCl₂–2NaCl melts, using a tungsten electrode, kinetic parameters of the charge-transfer reaction for the couple Pb(II)/Pb(0) at 450 °C have been determined, log k_s⁰ and α values are equal to -4.3 ± 0.1 and 0.48 ± 0.06 , respectively [98]. The diffusion coefficient value for Pb(II) is $(7.5 \pm 0.7) 10^{-6} \text{ cm}^2 \text{ s}^{-1}$ [98]. The influence of electrolyte cation [99] and anion [100] on the kinetics of lead in molten halides has been studied.

24.3.2.4 Voltammetric Behavior of Lead

24.3.2.4.1 Sulfuric Acid Solutions

Voltammetric properties of pure lead electrodes have been studied in different media, but owing to obvious applications in lead-acid batteries, most data relate to sulfuric acid solutions. Typically, voltammetric curves of lead, limited by hydrogen

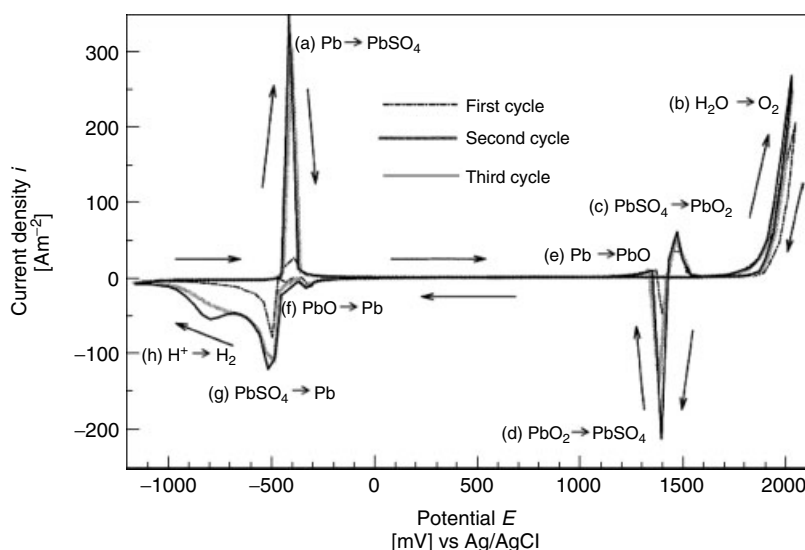


Fig. 1 Cyclic voltammetric curves of Pb electrode in 4.5 M H_2SO_4 solution [103].

and oxygen evolution processes, exhibit several peaks, for example [101, 102]. An example is presented in Fig. 1 [103] with four anodic peaks:

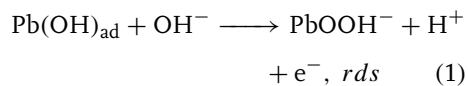
- (a) oxidation of Pb to PbSO_4 ,
- (b) oxygen evolution,
- (c) oxidation of PbSO_4 to PbO_2 (usually β form),
- (e) oxidation of Pb to PbO ;
- and with four cathodic peaks:
- (d) reduction of PbO_2 to PbSO_4 ,
- (f) reduction of PbO to Pb,
- (g) reduction of PbSO_4 to Pb, and
- (h) hydrogen evolution.

The inner PbO layer is formed because of the impermeability of PbSO_4 layer for SO_4^{2-} ions; only Pb^{2+} , OH^- , and H^+ ions can transfer across this film. Thus, in the course of anodic scan, H^+ ions can flow from the reaction site into solution, resulting in alkaline medium formation near the electrode surface. With increasing H_2SO_4 concentration, the lead sulfate layer is more compact and electrolyte ions

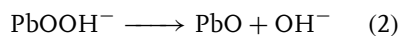
access to the inside layer is hindered [104, 105]. A characteristic, and not quite a clear feature, is the presence of a small anodic peak (*anodic excursion* peak [101, 106, 107]) recorded in the course of the cathodic scan, if the electrode potential is cycled in a potential range limited by hydrogen and oxygen evolutions. This peak is located either before [107, 108] or after [101, 106] the reduction peak (d), in low or high H_2SO_4 concentration in solution, respectively [102, 109, 110]. The presence of *anodic excursion* peak has been explained in different ways (see literature review [110]). The most probable explanation is based on the large increase of molar volume accompanying reduction peak (d) – from $25 \text{ cm}^3 \text{ mol}^{-1}$ for $\beta\text{-PbO}_2$ to $48 \text{ cm}^3 \text{ mol}^{-1}$ for PbSO_4 [101], resulting in cracks on the electrode surface. Thus, the metallic lead surface, which can be oxidized by sulfuric acid, is exposed. Water oxidation by Pb(III) , generated during surface reduction of PbO_2 has also been postulated [106, 107]. The electrochemical

properties of Pb in sulfuric acid solutions have been studied and described mainly by Pavlov (see e.g. [111, 112] and references given therein), some mathematical models concerning nucleation and growth of solid phases have been proposed, for example [113].

However, the process of Pb oxidation/reduction is more complicated because of the presence of different Pb oxides (as e.g. $3\text{PbO}\cdot\text{H}_2\text{O}$, $\alpha\text{-PbO}_2$, and also non-stoichiometric oxides) on the surface [111, 114] as electrochemical impedance spectroscopy [115], photocurrent [116], or grazing incidence X-ray diffraction studies [117] show. Soluble Pb(II) and Pb(IV) species have also been revealed on the basis of measurements obtained with the use of rotating ring-disk electrode [118]. The size and amount of PbSO_4 crystals [104, 105] and the charge-transfer rate [119] is dependent on acid concentration. Current transient experiments have pointed to two-dimensional nucleation and growth of PbSO_4 , electrodissolution of lead electrode in the zones not covered by PbSO_4 as well as passive layer growth due to lead electrodissolution, and Pb(II) transport across the PbSO_4 layer [120, 121]. Proposed mechanism of PbO formation points to intermediate $\text{Pb}(\text{OH})_{\text{ad}}$ oxidation to PbOOH^-



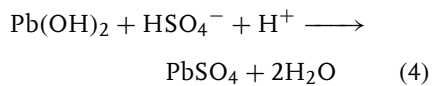
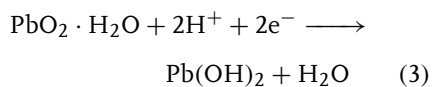
and then the final product is obtained [115]:



Diffusion of O^{2-} ions has also been taken into account as rate determining step (rds) and the value of their solid phase diffusion coefficient has been determined as $2.4 \times 10^{-15} \text{ cm}^2 \text{ s}^{-1}$ [122].

Current transient studies have also demonstrated instantaneous nucleation and two-dimensional growth mechanism of $\beta\text{-PbO}_2$ [123] and a higher rate of reduction of small PbSO_4 crystals, compared to greater ones [124].

On the basis of electrochemical results, scanning electron microscopy (SEM) images and X-ray diffraction analysis, Pavlov et al. have discussed the influence of sulfuric acid concentration on the mechanism and rate of $\text{Pb-PbSO}_4-\text{PbO}_2$ transformations [125]. Three acid concentration ranges have been distinguished. The first is active H_2SO_4 concentration range (from 0.5 to 5 M), where the concentration of HSO_4^- is the highest and $\beta\text{-PbO}_2$ phase is formed. This phase is reached in hydrated gel areas ($\text{PbO}(\text{OH})_2$), which are ionically (H^+) and electronically conductive, necessary for the electrochemical process to occur, for example, for hydrated PbO_2 reduction:



Concentrations higher than 5 M correspond to a passive high concentration region, where $\alpha\text{-PbO}_2$ crystals are formed. In passive, low concentration region (H_2SO_4 concentration lower than 0.5 M), the content of $\alpha\text{-PbO}_2$ is also high. In both passive regions, the amount of gel zones is low, resulting in low electroactivity. For very low H_2SO_4 concentrations (not buffered), the changes in the potential can result in the formation of a diffusion layer at the PbO_2 surface with different pH, which can considerably affect the formation of complexes.

Formation of $3\text{PbO}\cdot\text{PbSO}_4\cdot\text{H}_2\text{O}$ depends on the properties of PbSO_4 passivation layer. When the anodic film is passivated significantly, the diffusion of ions across the PbSO_4 becomes a rate-determining step [126]. After reactivation of the passive layer, the rate is controlled by diffusion-limited nucleation and growth. The process is promoted by decreasing acid concentration and by the presence of small amounts of Sb in alloy with Pb.

The hydrogen and oxygen evolution processes on Pb are affected by other metal additions to Pb, for example, addition of bismuth enhances both the hydrogen and oxygen evolution [127], while addition of silver inhibits hydrogen ions reduction [128].

In the presence of Pb(II) ions in sulfuric acid, potential oscillations have been observed for galvanostatic oxidation of hydrogen on platinum electrode [129]. This behavior has been attributed to adsorption/oxidation/desorption processes of lead on the platinum surface. Lead at high values of coverage is oxidized to insoluble PbSO_4 , which blocks the Pt surface.

Oxidation/reduction of Pb electrode has been studied using in situ spectroscopic techniques – Raman [114, 130–132], fourier transform infrared (FTIR) [133–135], Auger [136], and photocurrent spectroscopy [131, 137–141]. Ellipsometric studies underlined nonuniform PbSO_4 film growth; a dissolution–precipitation mechanism with nucleation and three-dimensional growth has been proposed as a result of large oversaturation of Pb(II) ionic species [142]

and formation of thin and flat PbO_2 layers [143]. In situ studies using electrochemical quartz crystal microbalance (EQCM) under galvanostatic conditions have confirmed the oxidation of Pb to PbSO_4 at low current densities and transformation of PbSO_4 to PbO_2 at higher current densities [103]. AFM studies, coupled with X-ray photoelectron spectroscopy (XPS) and X-ray diffraction (XRD) measurements give better insight into the PbSO_4 and PbO_2 structure details and have pointed to dissolution–precipitation mechanism of PbSO_4 formation [144]. Figure 2 presents AFM images of Pb electrode held at reduction or oxidation

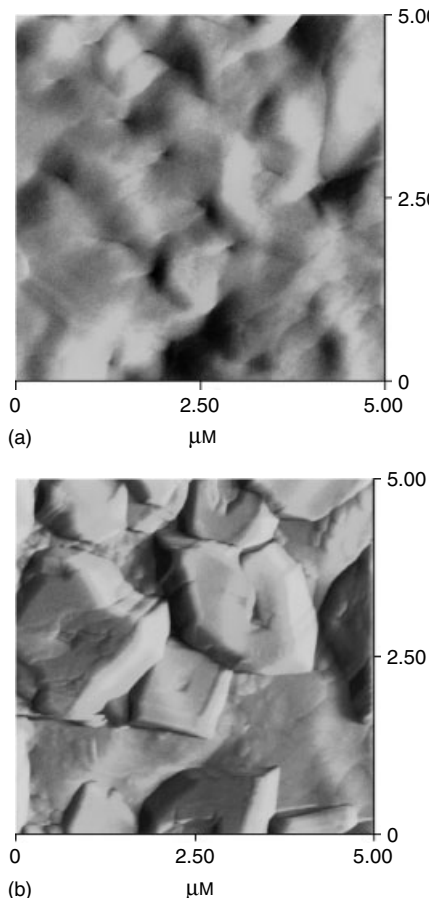


Fig. 2 AFM images of lead surface in sulfuric acid (density: 1.25 g cm^{-3}) after holding: (a) for 2 min at reducing potential -1050 mV , (b) for 6 min at oxidizing potential -1035 mV versus $\text{Hg}/\text{Hg}_2\text{SO}_4$ [145].

potential, showing the structure of metallic lead or PbSO_4 , respectively [145]. On the basis of AFM studies under potentiostatic conditions, a new mechanism of “sulfation” reaction has also been proposed [145]. It has been shown that the lead surface is covered with a lead oxide film and the lead sulfate crystals grow up on the surface. Lead sulfate crystals formed by electrochemical reaction have been found rougher than those obtained by a chemical reaction and thus, chemically more active. Therefore, during longer standing, lead sulfate recrystallizes and a new, chemically obtained PbSO_4 is formed of lower activity. This results in lower charge storage ability in lead-acid batteries. An electrochemical method to reactivate the “sulfated” lead electrode has been proposed [102].

Voltammetric experiments have revealed that lead oxidation is a fast reaction and thus, PbSO_4 deposition occurs by nucleation in supersaturated solution of Pb^{2+} , followed by the growth process. The reduction process is slower because of the slow dissolution of PbSO_4 . The crystal size becomes smaller when the potential scan rate is fast or the electrolyte concentration is high [146]. Other AFM experiments have been described elsewhere [21, 22]. Electrochemical atomic force microscopy (EC-AFM) potentiostatic studies have also been carried out at $\text{Pb}(100)$ and $\text{Pb}(111)$ single crystals in 0.05 M H_2SO_4 solutions [147]. The top faces of PbSO_4 crystals formed on $\text{Pb}(100)$ and $\text{Pb}(111)$ have been found to be $\text{PbSO}_4(001)$ and $\text{PbSO}_4(100)$, respectively. The comparison of voltammetric curves for $\text{Pb}(100)$ and $\text{Pb}(111)$ and AFM image is presented in Fig. 3 [147].

The effect of immobilizing the electrolyte using sodium silicate as thixotropic agent on electrochemical properties of lead in sulfuric acid has been described [148].

24.3.2.4.2 Nitric Acid Solutions The voltammogram of Pb in nitric acid shows two well-defined anodic peaks (first peak – PbO and lead nitrate formation, and second peak – PbO_2 deposition) in the course of the positive scan [149]. In the reverse scan, either a wide plateau followed by a cathodic peak at very negative potentials or two cathodic peaks have been observed [150]. The inhibition of Pb dissolution process in more concentrated HNO_3 results from the presence of a protective PbO_2 layer [149]. Successive cycling results in increasing current due to increasing electrode surface area by deposited PbO_2 [150].

24.3.2.4.3 Phosphoric Acid Solutions In phosphoric acid (pure liquid or concentrated aqueous solution, 12 and 6 M), a pair of peaks has been recorded corresponding to the redox couple PbHPO_4/Pb as confirmed by XRD studies and SEM photographs [151]. The presence of chloride or bromide ions also results in precipitation of $\text{Pb}_5(\text{PO}_4)_3\text{Cl}$ and $\text{Pb}_5(\text{PO}_4)_3\text{Br}$, respectively, while in the presence of iodide ions PbI_2 is formed. Addition of H_3PO_4 to H_2SO_4 , changes the voltammetric behavior (references in [151] and [152]). The lead phosphate formation blocks the lead surface oxidation to PbO_2 . For higher H_3PO_4 concentration (5 M), the *anodic excursion* peak is visible on voltammograms as in H_2SO_4 solutions, located after PbO_2 reduction peak [152].

24.3.2.4.4 Sodium Hydroxide Solutions In NaOH solutions, two main lead anodic peaks owing to the formation of PbO and PbO_2 have been recorded, followed by oxygen evolution ([153–156] and the references given therein). In the step preceding PbO production, the formation of

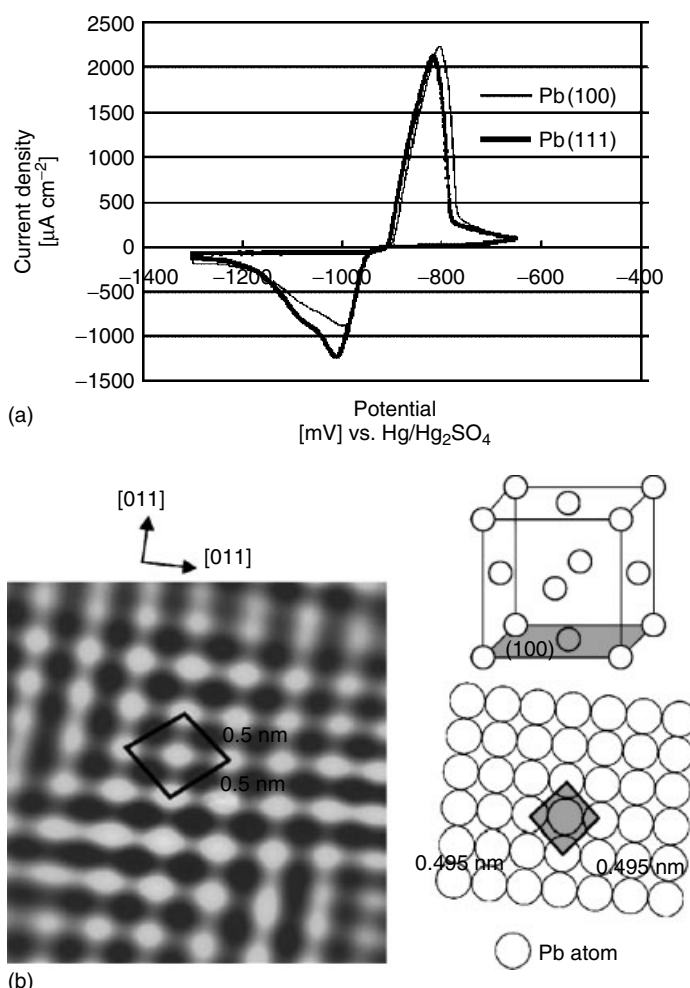


Fig. 3 (a) Cyclic voltammetric curves of Pb(100) and Pb(111) in 50 mM H_2SO_4 solution, scan rate: 1 mV s^{-1} . (b) EC-AFM high resolution image ($3 \text{ nm} \times 3 \text{ nm}$) on Pb(100) in 50 mM H_2SO_4 solution at -1040 mV versus $\text{Hg}/\text{Hg}_2\text{SO}_4$ and schematic illustration of the image [147].

adsorbed PbOH or $\text{Pb}(\text{OH})_2$ can occur, while PbO_2 formation has been assumed to be preceded by Pb_3O_4 production; however, this has not been unequivocally confirmed. The electrochemical processes are accompanied by partial dissolution of PbO and PbO_2 to HPbO_2^- and PbO_3^{2-} , respectively. A longer conditioning of PbO film results in slow dissolution to HPbO_2^- .

Addition of anions to NaOH solution affects the anodic film formation kinetics and morphology. These films are mainly $\alpha\text{-PbO}$, with the exception of chloride ions solution, where $\beta\text{-PbO}$ is formed [157]. Anodic oxidation of Pb electrode in hot alkaline solution (containing NaOH) facilitates selective growth of $\alpha\text{-PbO}$, $\beta\text{-PbO}$, and PbO_{2-x} ($x = 0\text{--}1$) phases, depending

on the applied potential, as confirmed by XPS spectroscopy [158].

24.3.2.4.5 Different Salt Solutions In alkaline Na_2HPO_4 solutions, anodization of lead results in the formation of several peaks observed at a potential lower than that of oxygen evolution, Fig. 4 [159]. On the basis of cyclic voltammetry and X-rays surface analysis, the shoulder A

and peak A have been assigned to Pb oxidation to $\text{Pb}(\text{OH})_2$ (accompanied by possible dehydration to PbO). At higher anodic potentials, two-dimensional nucleation and spreading of PbO (peak B) followed by three-dimensional nucleation and growth of PbO (region C) and then PbO_2 formation (D) occurs. Figure 4 also presents a schematic illustration of the anodic process.

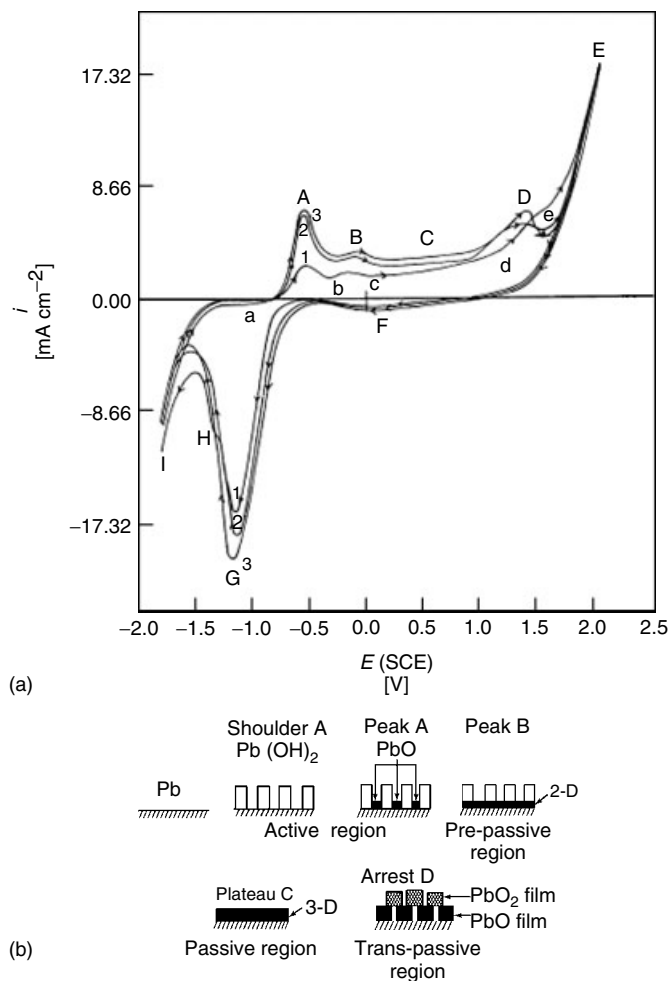


Fig. 4 Three successive sweeps of Pb electrode in 0.10 M Na_2HPO_4 solutions at scan rate of 25 mV s^{-1} (a). Schematic simplified illustration of films formation on Pb in Na_2HPO_4 solution (b) [159].

In the cathodic scan, reduction of PbO_2 (peak F), reduction of PbO (peak G), and reduction of $\text{Pb}(\text{OH})_2$ (shoulder H) can be observed on the voltammetric curve.

A more complicated pattern is recorded in Na_2SO_4 solutions [160, 161], where a behavior, typical for H_2SO_4 can also be observed. Additionally, some phenomena that are typical for alkaline solutions are visible as presence of soluble species HPbO_2^- [160, 162]. The voltammetric anodic oxidation is characterized by peaks of PbSO_4 , PbO , PbO_2 , and by the transformation of PbSO_4 to PbO_2 , as well as by the formation of intermediate oxides in the second and following scans. During reverse cathodic scan, peaks are formed, corresponding to the reduction of PbO_2 to PbSO_4 , PbO_2 to PbO and PbO with PbSO_4 to Pb , and finally PbH_2 formation is observed just before hydrogen evolution. In sulfuric acid solution containing sodium sulfate, an additional oxidation process has been recorded owing to the higher conductivity of lead sulfate in the presence of sodium ions [163].

Voltammetric characteristics of lead electrodes have also been studied in sodium borate solutions [164], where formation/dissolution of lead oxides can be accompanied by lead borate precipitation on the electrode.

24.3.2.5 Voltammetric Behavior of Several Lead Compounds

24.3.2.5.1 PbO PbO exists in two polymorphic forms – tetragonal $\alpha\text{-PbO}$ and orthorhombic $\beta\text{-PbO}$; they are photosensitive substances. Basic electrochemical properties of PbO have been studied in acidic [105, 111], neutral [165,] and alkaline [153] media. In acidic solutions, the $\beta\text{-PbO}$ formation is followed by transformation to $\alpha\text{-PbO}$ [166, 167]. In sulfuric acidic

solution, the $\alpha\text{-PbO}$ formation/dissolution is accompanied by processes involving lead sulfate. PbO growth rate has been found to be dependent on the migration of Pb^{2+} and OH^- ions into the oxide layer, as well as of H^+ ions into the PbSO_4 layer [104, 105]. PbO reduction process to Pb has been postulated to occur according to progressive nucleation and growth path [132, 168, 169], assisted with OH^- ion diffusion through the PbSO_4 layer [104]. With decreasing concentration of sulfuric acid, the structure of PbSO_4 layer becomes looser, facilitating mass transfer of H^+ and SO_4^{2-} ions. Therefore, in the cathodic voltammetric scan, the transformation of a part of $\alpha\text{-PbO}$ into basic lead sulfate or lead sulfate occurs [105], followed then by lead deposition. The reduction rate can be controlled by the nucleation and growth of metallic lead and OH^- ions diffusion across the PbSO_4 layer [105]. With decreasing sulfuric acid concentration, the reduction of tetragonal PbO to Pb changes from two- to three-dimensional progressive nucleation and growth [105]. A solid-state mechanism related to migration of O^{2-} anions has also been postulated [170]. Oxidation of lead-tin alloy results in PbO of increased conductivity compared to pure PbO [171].

PbO is more stable in alkaline solutions. Anodic oxidation of Pb leads to the selective growth of $\beta\text{-PbO}$, which transforms into $\alpha\text{-PbO}$ in the course of prolonged polarization, as supported by X-ray diffraction studies and photoelectrochemical experiments [172]. In the presence of sulfate ions, simultaneous formation of basic lead sulfate with PbO has been observed, until the formation of $4\text{PbO}\cdot\text{PbSO}_4$. At higher potentials, the oxide film in sulfate ions solution has a strong (110) orientation with microporous structure. X-ray diffractometry and photocurrent measurements have confirmed the presence of

highly oriented (110) α -PbO phase, obtained in 0.05–0.5 M NaOH solutions, while the films obtained at higher NaOH concentrations exhibit submicrocrystalline or amorphous nature [155, 173]. In dilute solutions (0.01 M NaOH), the presence of β -PbO has also been detected. In neutral KCl solutions, X-ray diffraction [165] and AFM studies [174] show that the α -PbO reduction to Pb is an epitactic solid-state reaction occurring with conservation of the initial crystal orientation on the electrode surface. Dissolution of PbO in molten carbonates has been studied, from the point of view of materials stability in molten carbonate fuel cells [175].

24.3.2.5.2 PbO₂ PbO₂ has two crystallographic forms – orthorhombic α -PbO₂ and tetragonal β -PbO₂. PbO₂ has been electrochemically obtained on different substrates – platinum [176–178], gold [177, 179–181], nickel [182], glassy carbon [183, 184], vitreous carbon [185], titanium [180, 186–188], tin or indium-tin oxide [189, 190], stainless steel [188], titanium oxides [191], polystyrene templates enabling macroporous PbO₂ formation [189], and in acetonitrile solutions [192]. Nanostructured PbO₂ obtained by hydrolysis of Pb(CH₃COO)₄ has been found to exhibit high electrochemical activity [193]. The preparation and properties of lead dioxide electrodes have been reviewed [194–196]. α -PbO₂ has a more compact structure, is more stable mechanically, and can be obtained electrochemically in alkaline solutions, while β -PbO₂, which is thermodynamically stable, is obtained in acidic solutions and is more porous [177, 183, 197]. The morphology of PbO₂ depends on temperature, solution composition (e.g. [182, 186, 198]), and applied current density. Lower current density leads to β -PbO₂ deposition [182].

The mechanism of nucleation and growth of PbO₂ in H₂SO₄ has been described in Ref. 199 and references cited there. In sulfuric acid solutions, the phase composition (α - and β -PbO₂ content, determined on the basis of X-ray diffraction) and structure depend on many factors [196, 200, 201], as well as on the time duration of continuous cycling. The amount of β -PbO₂ phase increases in the cycling process [201, 202]. Properties of PbO₂ have also been studied in perchlorate [179, 202] and HNO₃ solutions (e.g. [150, 178]). The lead dioxide that is obtained is a non-stoichiometric compound, for example, PbO_{2- δ} · nH₂O [203], and more complex formulae have also been proposed. Influence on PbO₂ properties by doping with Bi [204], Fe [205], and Co [206] has been analyzed.

EC-AFM studies have shown that the two-step reduction process of lead dioxide is the dissolution process of PbO₂ and the deposition process of PbSO₄ crystals after saturation of the electrolyte with lead ions [207]. Two reduction peaks of PbO₂ can be ascribed to the partial reduction of larger and smaller crystals of electrodeposited PbO₂ [196]. Other mechanisms such as “hydrogen loss” [208] or “proton–electron mechanism” in gel zones of PbO₂ in all-solid-state systems [209] have also been discussed. Cathodic reduction of PbO₂ in alkaline media has been postulated to proceed with the formation of soluble PbO₃²⁻ and then HPbO₂⁻ [154].

24.3.2.5.3 Pb chalcogenides PbS is an important semiconductor material, which can find application in photovoltaic devices owing to its low-band gap energy, depending on the size of PbS particles (0.41 eV for bulk PbS). Methods of PbS synthesis have been summarized

in, for example [210], and electrochemical deposition of PbS has been described in Refs 211–215. Using electrochemical atomic layer epitaxy, underpotential deposition (UPD) growth of each element (Pb and S) follows layer-by-layer, forming a cubic rock salt crystal structure with (200) plane parallel to the Au(111) substrate surface [210]. The obtained PbS film shows anodic photocurrents. Nanocrystals of PbS have also been obtained using electrochemical methods [214, 216]. Electrochemical properties of synthesized and natural PbS have been studied in aqueous solutions using electrochemical methods [217–220], FTIR-spectroelectrochemical methods [221–225], and synchrotron radiation excited photoelectron spectroscopy [226]. One of the main products of PbS oxidation, involving holes, has been found to be $\text{Pb}(\text{OH})_2$ [221]. Analytical applications of PbS nanoparticles as oligonucleotides labels for electrochemical stripping detection of DNA hybridization have been reported [227].

Electrochemical deposition and electrochemical properties of other Pb chalcogenides – PbSe [228–233], PbTe [234, 235], and mixed $\text{PbSe}_{1-x}\text{Te}_x$ [236–238] have also been studied.

24.3.3 Electrodeposition and Underpotential Deposition of Lead on Solid Substrates

Studies on lead electrodeposition on conducting solid substrates are related mainly to electrocatalysis, searching for alternative collectors/grids for lead-acid batteries, as well as for removing Pb(II) ions from aqueous solutions and stripping for analytical purposes.

An important group of works relates to problems of UPD. Processes of lead

electrodeposition are presented systematically depending on the substrate material.

24.3.3.1 Platinum

Voltammetric behavior of UPD of Pb has been studied on polycrystalline Pt electrodes and on defined Pt faces [239–241]. Earlier works have pointed to irreversible adsorption of lead and anionic species on Pt(111) [242, 243]. Ex situ XPS studies have revealed adsorption of Pb and Pb^{2+} on Pt(111) surface [244], and thermal properties of emersed adlayers have been studied [245]. UPD on Pt(111), using rotating ring-disk electrode in perchloric acid solutions [246], has pointed to two-step process of Pb deposition in the presence of adsorbed OH^- ions and desorption of adsorbed OH^- concurrent with Pb deposition. Similar studies in the presence of bromide ions have shown competitive influence of anion adsorption [247], since deposition of Pb adatoms is associated with desorption of bromide ions. Pb UPD process on Pt(111) in mixed solutions of perchloric and sulfuric acid has shown a large influence of sulfuric acid addition, and adsorption of Pb has been found on the surface already covered by HSO_4^- or SO_4^{2-} anions [248]. The influence of CO adsorption on Pb UPD process has also been studied [249]. On Pt(100) face, in perchloric acid, deposition of Pb adatoms is accompanied by displacement of adsorbed OH^- anions [250], and in the presence of bromide ions, these anions are desorbed by Pb adatoms. Thus, the potential range of a closely packed monolayer is shifted to lower values [250]. Scanning tunneling microscopy (STM) studies on Pt(001) face have shown Pb islands covering the entire Pt surface [251] but with no long range order in the surface plane, as confirmed by in situ X-ray diffraction studies [252]. The presence of strongly adsorbed Br at

step edges on the Pt(001) surface and the competitive nature of Pb–Br interactions result in a rapid exchange of Pb and Br on the Pt terraces. Thus, Pb forms a strongly bonded $c(2 \times 2)$ adlayer. The role of electrode smoothness and potential scan rate at early stages of electrodeposition have been analyzed from the point of view of the deposit structure (presence of Pb–Pb and Pb–Pt domains) and its accompanying rearrangement/equilibration by surface diffusion of metal atoms [253].

24.3.3.2 Gold

Pb UPD on Au electrodes has been studied by numerous authors, using various classical electrochemical and optical methods (e.g. Refs 254–260 and references given therein), as well as using AFM [261] and STM techniques [262, 263]. Voltammetric depositions on Au single crystals have revealed complex peaks, which have been ascribed to different structures observed by low-energy electron diffraction (LEED) experiments [257]. A range of lead layer structures, changing with surface coverage of lead, with possible formation of AuPb_2 , has also been detected by LEED and Auger spectroscopy [264]. Pb UPD has been intensively studied on polycrystalline gold and defined $\text{Au}(h, k, l)$ planes [255–258], and comparison of voltammetric curves recorded on different planes has been discussed in [256]. Pb UPD process on different $\text{Au}(h, k, l)$ planes has been reviewed by Herrero et al. [265]. Owing to a large difference in the atomic sizes of gold and lead (lead atom is ca. 20% larger than gold), formation of incommensurate adlayers is favored (see [265] and references given therein). Alloy formation is not unequivocally confirmed [265]; its formation is suggested to occur only at edges and on defect sites.

The UPD process has been studied mainly on Au(111) plane [261, 262, 266–268]. Voltammetric curves exhibit a pair of peaks (splitting in two) and a series of irreversible peaks at higher underpotentials [265]. Splitting results from kinetics of the process, growth of lead deposited islands (at higher underpotentials), and coalescence process (at lower underpotentials) [263, 265]. The initial step of Pb UPD on Au(111) is a decoration of monoatomic steps. At higher coverages, the uncompleted Pb monolayer is relatively unstable owing to surface alloy formation. Then, two-dimensional Pb islands of hcp structure are observed. Stability of two-dimensional islands on Au(111) has been recently confirmed by atom dynamics simulation studies [269]. At high surface coverages *in situ* STM and AFM images point to compressed and rotated hcp structures of Pb [270]. An overview of processes occurring on Au(111) surface is presented in Table 1 [268].

Stability of lead monolayers [271] and a dependence of the Pb UPD layer structure on surface coverage have also been studied on Au(100) face [272]. A phase transition from an expanded Pb overlayer to compressed hcp structure has been considered [270]. A coupled process of gold and Pb UPD oxidation process on single crystal Au(110) has been studied using XPS method [273].

The process of Pb deposition depends on the presence of adsorbed species. On polycrystalline gold, in HClO_4 acid solutions, a combined quartz crystal microbalance and probe beam deflection methods have pointed to three stages of the process – (1) water molecules release from gold surface, (2) metal UPD associated with adsorbed OH^- ions replacement, followed by (3) water formation [274]. In the presence of adsorbed anions or organic

Tab. 1 Phenomena accompanying Pb UPD on Au(111) substrate [268]

<i>Scan direction</i>	<i>Potential range [ΔE/mV]</i>	<i>Description</i>
Cathodic	220–255	Growth at existing step edges
	235–250	First nuclei form, some unstable
	210–230	Stable nuclei and other islands grow and join
	195–215	Most rapid visible change
	170–190	Continued slow filling of plane
Anodic	190–225	Small islands shrink and disappear
	210–240	Terrace edges recede
	220–245	Appearance and growth of pits
	240–250	Most rapid visible change
	245–275	Slight continued shrinking of remaining islands

molecules, competition with Pb adatoms can occur [275–277]. Using EQCM, XPS, and time of flight secondary ion mass spectrometry [275, 276] the presence of adsorbed anions has been demonstrated. The deposition process involves reduction of both adsorbed lead complex with anions and lead(II) present in the electrolyte bulk. The PbCl_4^{2-} complex has been found to be adsorbed before the potential of its reduction to Pb. On the basis of voltammetric experiments, carried out at different temperatures, standard entropies of Pb adatoms have been evaluated [278]. These data point to surface mobility of Pb adatoms, significantly dependent on the solvent, where the deposition process occurs. Frumkin isotherm of Pb adsorption has been used to explain the shape of voltammetric peaks [279].

Spontaneously adsorbed monolayers possessing sulfonate terminal groups on gold electrodes can enhance the lead UPD current, for example [280], see also Chapter Electrochemistry of Gold (24.4) in the present book.

Surface stress measurements also reveal useful data concerning surface processes.

Changes in surface stress of Au(111) electrode during Pb UPD have been measured using the bending beam method [281, 282]. A maximal surface stress appears at the onset of UPD, corresponding to the formation of a completed incommensurate monolayer. The shape of surface stress versus cathodic charge for UPD has been explained by change in rotation angle of hexagonal close packed Pb layer. Coadsorption of chloride ions promotes the structural changes of the UPD lead. Studies on Pb deposition on gold colloids have pointed to similarity of the deposition process to that on bulk electrode [283].

In the oxide region of gold electrodes, residual lead can be present, resulting from irreversible adsorption, and presence of hydroxide species has been postulated [265]. Pb UPD on Au(111) has also been studied in selected organic solvents, mainly propylene carbonate [284]. Results similar to those in aqueous solutions have been obtained. Deposition of Pb on Au electrodes coated by silver has also been studied [285]. Depending on the silver layer thickness, results typical for Pb deposited on Au or Ag have been obtained.

24.3.3.3 Silver

Pb UPD on Ag(111) and Ag(100) has been studied using X-ray diffraction method, electrochemical impedance spectroscopy, and in situ scanning probe microscopy [272, 286–288]. This process has been reviewed in [265, 270], see Table 2. Both structure and voltammetric behavior are dependent on the Ag(h, k, l) plane [265, 289].

On Ag(111) in perchloric acid solutions, three pairs of voltammetric peaks have been observed, prior to bulk deposition [265]. The first and third peaks have been ascribed to adsorption at defect sites, the middle (the highest) peak represents the major deposition process, and it appears owing to the first-order phase transition. In the presence of adsorbing anions, owing to blocking effects, only a single peak representing deposition/stripping is observed. The deposited zero-valent lead layer has been found incommensurate with the silver substrate. Extended polarization of the electrode

induces transformation of the lead overlayer, also represented by changes of the voltammetric curves. STM studies have revealed the presence of hcp, which can change under the influence of extended polarization [290]. The influence of adsorbed Cl⁻ ions results in narrowing of potential ranges corresponding to Pb adsorption [288]. Pb nanostructures have been observed using STM method [291]. Pb UPD on Ag(111) has also been studied in selected organic solvents [284]. Results similar to those observed in aqueous solutions have been obtained.

For Ag(100), the voltammetric curve exhibits two main pairs of peaks and a pair of smaller peaks at lower potentials [265]. The first peak has been ascribed to adsorption, while the second to filling of the remaining sites to a closely packed monolayer and a phase transition. Under conditions of extended polarization, a transformation occurs, similar to that in Ag(111). However, in contrast to Ag(111), this transformation relates to

Tab. 2 Phenomena accompanying Pb UPD on silver substrates [270]

Ag plane	Potential range [ΔE/mV]	Description
Ag(111)	150–250	Step decoration and formation of expanded 2D Pb _{ads} phase at terraces
	120–150	Formation of a condensed 2D hcp Pb _{ads} phase from an expanded 2D Pb _{ads} phase via first-order phase transition starting at steps
	0–120	Completion and compression of 2D hcp Pb _{ads} phase at terraces
Ag(100)	140–250	Step decoration and formation of expanded Ag(100)-c(2 × 2) Pb _{ads} structure at terraces
	100–140	Formation of a condensed 2D hcp Pb _{ads} phase from an expanded 2D Pb _{ads} phase via first-order phase transition starting at steps
	100–120	Formation and limited growth of 2D Pb _{ads} clusters on top of the first Pb _{ads} monolayer
	0–100	Completion and compression of the 2D hcp Pb _{ads} phase at terraces

the adsorption layer or the competitive adsorption of anions. A dependence of the Pb UPD layer structure on surface coverage has been studied on the Ag(100) face [272].

On Ag(110), three voltammetric peaks have also been observed [265], owing to adsorption, phase transformation, and deposition on the previously formed monolayer.

Frumkin isotherm of Pb adsorption has been used to explain the shape of voltammetric peaks on polycrystalline electrodes and on the polycrystalline gold surface [279].

Comparison of electrochemical data with Monte Carlo simulation of Pb UPD on Ag(111) has enabled discussion on mechanism details [292].

UPD process has also been studied on screen-printed silver electrodes using voltammetric techniques and scanning electron microscope analysis [293]. The relative occurrence of UPD and bulk Pb process has been dependent on the scan rate, with increasing role of UPD process in higher rates. Studies on Pb deposition on silver colloids have pointed to its similarity to bulk electrode [283].

The effect of adsorbed albumin on Pb UPD has been recently studied using Ag rotating disk electrode [294].

24.3.3.4 Copper

Good adhesion of electrodeposited lead to copper substrates has been reported [295–299]. Voltammetric curves of Pb deposition on Cu in alkaline solution with glycerol [299] are characterized by two peaks, corresponding to film and mass transfer-controlled bulk deposition, respectively. SEM results have not confirmed the propagation of dendrites, even at very low deposition potentials. Lead film deposition occurs prior to lead bulk

process, explaining the adherence of the deposit. Pb UPD on Cu electrodes has been studied using voltammetric methods, rotating ring, and disk electrodes, as well as LEED, surface X-rays diffraction, and reflectivity measurements [297, 300–303]. Deposition occurs through a single process, the nucleation and growth of Pb islands. The Cu crystal face affects the deposit structure, it is hexagonally ordered on Cu(111) and disordered on Cu(100) surface [297, 301]. This difference has been ascribed to lower mobility of Pb adatoms in the latter case because of the greater atomic corrugation of the (100) surface [301]. Surface alloys can be formed, accompanied by a possible replacement of a pair of neighboring Cu atoms by two Pb atoms [302, 303]. Chloride anions significantly enhance the reduction rate of Pb^{2+} ions, probably because of the formation of Cl bridges between Cu support and reacting cations [300, 301]. The surface chloride anions also form a highly ordered structure, which can act as a template for Pb adatoms deposition [302].

24.3.3.5 Carbon

Properties of thin layers of lead electrodeposited on vitreous carbon have been found identical with that of metallic lead [304]. Therefore Pb and PbO_2 coated reticulated vitreous carbon (RVC) electrodes [185] can be applied as electrodes in lead-acid batteries, as reviewed in [305]. The deposition of lead on carbon is through the diffusion-controlled process with instantaneous or progressive nucleation, for high and low Pb^{2+} concentration, respectively, and three-dimensional growth mechanism. The number of nucleation sites increases with deposition overpotential, as shown for vitreous [306] and glassy carbon [307] electrodes. The concentration dependence of the nucleation

rate points to the incorporation of atoms to clusters directly from the bulk, and not through adsorbed intermediates [306]. This deposition process can be enhanced because of the creation of active sites by chloride ions adsorption [308, 309]. However, electrochemical pretreatment process accompanied by exposure to chloride or nitrate ions has resulted in the decrease of lead deposition efficiency. This is caused by smoother electrode surface and lower number of steps and grain edges, as shown by AFM images [310]. The greater efficiency of Pb deposition in chloride solutions has been ascribed to interactions between deposited lead and chloride ions.

On highly ordered pyrolytic graphite, HOPG(0001) electrodes, no UPD has been detected owing to weak carbon–lead interactions [311]. Deposition occurs by three-dimensional island growth according to Volmer–Weber mechanism. Initial steps are controlled by progressive nucleation on active sites and hemispherical diffusion.

Electrodeposition on boron-doped diamond has pointed to progressive growth mechanism, as confirmed by chronoamperometric transients and ex situ AFM images [312]. At lower concentrations, lead ions are deposited directly on the diamond substrate, while at higher concentrations, deposits overlap and further deposition occurs on lead. At higher temperatures, the size of the nuclei is bigger.

24.3.3.6 Silicon

Electrodeposition on semiconductor surfaces is useful from the point of view of application in metal/semiconductor–Schottky and ohmic contacts. Cyclic voltammetry, current transient methods, STM, and AFM techniques have been used to study Pb electrodeposition on *n*-Si(111) surface [311, 313–315]. Lead deposition on the H-terminated Si(111) is

reversible. Using Scharifker and Hills model [316] for three-dimensional growth under diffusion control, progressive [311] or instantaneous [314] nucleation behavior at early deposition steps has been postulated. This process occurs mainly at steps and other surface inhomogeneities. UPD has not been detected [311]. Surface X-rays diffraction studies have shown epitaxial growth of Pb clusters with Pb(111) plane predominantly aligned parallel to Si(111) plane [317]. In the case of rough silicon surfaces, this in-plane orientation is lost. Larger crystallites grow at the expense of smaller ones. The activation energy of exchange between Pb and Si atoms has been found to be 1.2 eV [318].

24.3.3.7 Germanium

In the case of *n*-Ge(111) substrates, surface states affect electrochemical deposition of Pb [319]. At high cathodic potentials, the deposition occurs by instantaneous nucleation and diffusion-controlled three-dimensional growth of lead clusters. Comparing H- and OH-terminated *n*-Ge(111) surfaces, the nucleation is more inhibited at *n*-Ge(111)-OH, which can be explained by the different densities of Ge surface free radicals, being nucleation sites. In this case, nucleation site density is about 1 order of magnitude lower than that for *n*-Ge(111)-H.

24.3.3.8 Other Materials

UPD of Pb on *n*-Se is induced by illumination [320]. The Pb adatoms modify the Se surface and form surface states in the band gap. In the dark, the Pb UPD occurs only on the Se surface where PbSe clusters have been deposited. The deposited Pb atoms interact irreversibly with surface Se atoms to form PbSe monolayer [320, 321]. The

UPD process is significantly enhanced by introducing lead into Se [322]. Pb UPD has also been studied on palladium [323], from the point of view of catalytic applications and on tellurium using electrochemical impedance spectroscopy [324]. The latter process has been found irreversible owing to the Pb–Te bonds formation. Periodic multilayer structures in Pb–Se–Te system have been studied using pulse potentiostatic methods [325].

Incorporation of Pb into nanoparticulate iridium oxide films has been realized by initial electrodeposition of Pb metal on Au substrate, followed by Ir metal coating [326].

Barium metaplumbate, being a good conductor, has been used as a substrate to deposit lead, for possible use in lead-acid batteries [327].

Electrodeposition on transparent material such as indium tin oxide (ITO) can be used for electrochromic applications [328]. Pb deposition on indium–tin oxide electrode occurs by three-dimensional nucleation with a diffusion-controlled growth step for instantaneous nucleation [329], and the electrode process has also been studied using electrochemical impedance spectroscopy [328].

24.3.4 Corrosion and Passivation

The corrosion of lead has been studied in various media, and this process has been found to be dependent on the properties of the water layer that is present on the metal surface, which is a medium for the dissolution of atmospheric gases, resulting in the formation of lead salts – chlorides, sulfates, and carbonates [24, 141, 167, 330]. Electrochemical AFM images reveal the structure of PbO and PbSO₄ on lead immersed in water or sulfuric

acid, respectively, Fig. 5 [145]. Application of different spectroscopic techniques for corrosion studies in sulfuric acid solutions has been reviewed by Bullock [131]. Influence of Pb alloy components as Ag, Sb, Bi, and Sn on passivation processes and corrosion resistance in sulfuric acid solutions has also been studied [128, 331–334].

In alkaline (NaOH) solutions [153], the role of Pb(OH)₂ and PbO is important for passivity phenomena, and the voltammetric curves represent active, passive, and transpassive regions [335]. The active region is displayed by a peak corresponding to Pb oxidation to PbO [153]. The passivity results from PbO film present on the surface. The transpassive region is represented by two peaks, ascribed to oxidation of PbO to Pb₃O₄ and PbO₂. Some anions can initiate pitting corrosion, for example, ClO₄[−], ClO₃[−], and NO₃[−] [335, 336]. The corrosion in carbonate solutions [24, 153, 337, 338] is connected with the oxidation of Pb (three voltammetric peaks) to PbCO₃ and PbO as well as PbO to PbO₂. The formation of PbO can be attributed to the oxidation of Pb within the pores of PbCO₃ and/or the transformation of PbCO₃ to the oxide. Pb dissolution is enhanced by perchlorate [339] and nitrate ions [337] causing pitting corrosion. In perchlorate ions solutions, the pitting corrosion extent, expressed by integrated anodic voltammetric charge, is linearly dependent on the logarithm of ClO₄[−] anions concentration. In the presence of nitrate ions, the pitting corrosion rate increases with rising NO₃[−] concentration and temperature. Chronoamperometric transients point to incubation time (needed for NO₃[−] ions to reach and initiate metal dissolution) before pit nucleation and instantaneous three-dimensional pit growth. The rate

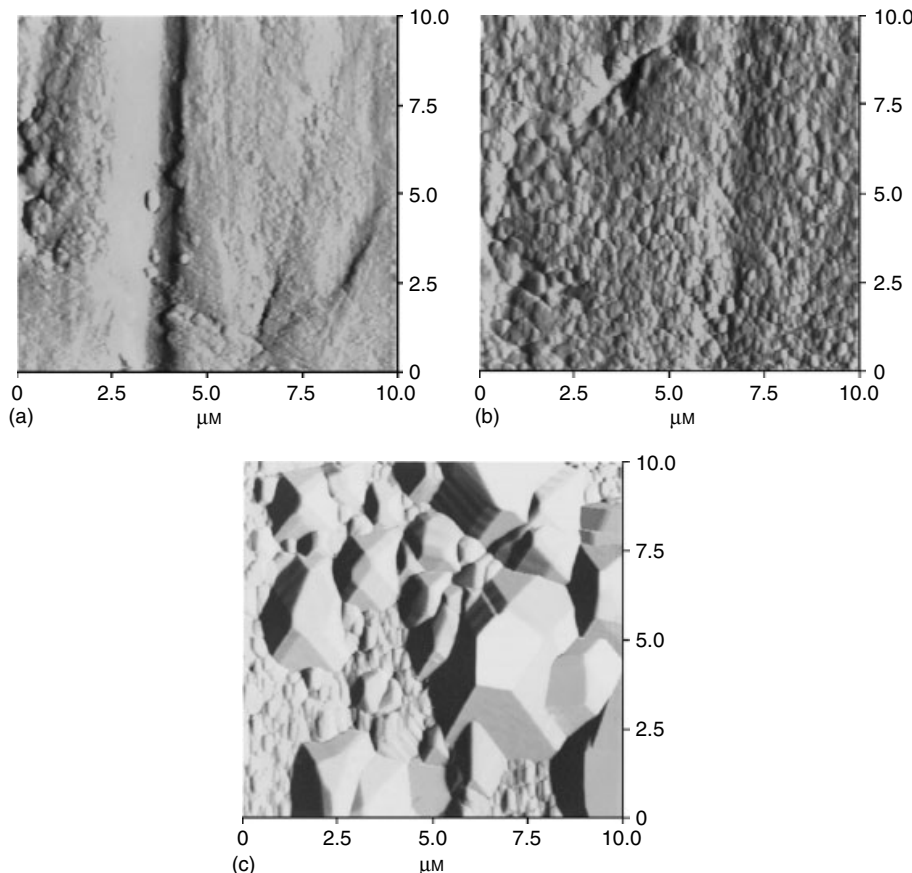


Fig. 5 AFM images of lead surface: (a) in air at room temperature, (b) in pure water after holding for 20 min at room temperature, (c) in 0.05 M sulfuric acid after holding for 60 min at room temperature [145].

of pit nucleation rises with increasing nitrate ions concentration, temperature, and applied anodic potential. In neutral nitrate solutions, the rate of metal dissolution is dependent on cation kind, and the dissolution rate is much slower in NaNO_3 than in NH_4NO_3 solutions [340]. XPS confirms formation of passive oxide layers containing a nitrogen compound (a product of nitrate reduction). The layer formed in NH_4NO_3 solution has been hydrolyzed and cracked, probably owing to locally acidified medium (from NH_4^+

acidic cation) at the oxide/solution interface, promoting hydrolysis of the oxide.

In carboxylic acid solutions, the corrosion rate increases with acid concentration (acetic, lactic); however, in oxalic and tartric acid solutions, the dissolution of metal is associated with the formation of passive lead salt layer [341].

The oxygen and oxidants (as $\text{Cr}_2\text{O}_7^{2-}$) affect the corrosion rate [342, 343]. A decrease in the corrosion resistance after longer time (3 h) in oxygen-rich solutions has been observed.

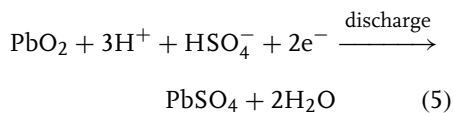
The corrosion process can be inhibited by the addition of phosphate or polyphosphate ions [344], inorganic inhibitors as, for example, chromate ions [336], adsorbed alcohols [345], adsorbed amines, competing with anions for adsorption sites [339,] as well as saturated linear aliphatic monocarboxylate anions, $\text{CH}_3(\text{CH}_2)_{n-2}\text{COO}^-$, $n = 7 - 11$, [24]. In the latter case, the formation of the passive layer requires Pb oxidation to Pb^{2+} by dissolved oxygen and then precipitation of hardly soluble lead carboxylate on the metal surface. The corrosion protection can also be related to the hydrophobic character of carboxylate anions, which reduce the wetting of the metal surface.

24.3.5 Applied Electrochemistry

24.3.5.1 Lead-acid Batteries

The most common applications of electrochemical processes of lead are lead-acid batteries, described in detail elsewhere ([1, 203, 346–349] and references given therein). Some detailed aspects of the electrochemistry of lead-acid batteries have already been described in the Sects 24.3.2.4 and 24.3.2.5. Therefore, only an overview of the main properties of this kind of power sources will be presented.

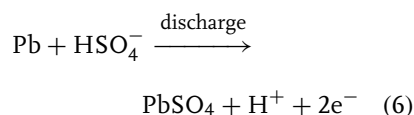
The discharge process at the positive electrode is



and the charging reaction proceeds in the opposite direction. In order to obtain high current densities, it is necessary to use the highly porous structure of PbO_2 in the β -form, which in contrast to $\alpha\text{-PbO}_2$ is not isomorphic with PbSO_4 .

Therefore, passivation of the positive electrode by poorly conducting PbSO_4 can be reduced [348]. The porosity is important because it enables the expansion during the solid phase volume increase, which accompanies the transformation of PbO_2 to PbSO_4 . In the most popular construction, the electrode paste material (mixture of metallic lead with lead oxides) is held in a framework composed of lead alloys with additions of tin, antimony, selenium, and calcium [348]. Antimony improves the mechanical stability; however, it increases the resistance and facilitates the self-discharge of the battery. Better results are obtained for low antimony content and/or for lead–calcium alloys [203]. Methods of positive electrodes improvement, from the point of view of lead oxide technology have been discussed [350]. Influence of different factors on life cycle, nature, and composition of the positive active mass has been studied by Pavlov with coworkers [200, 351, 352].

The discharge process at the negative electrode is



Negative electrodes are pasted plates using grids covered with perforated lead foil and the same paste as that used in positive electrode plates [203, 348]. Under specified conditions, the paste material is reduced to sponge lead of high porosity, assuring a high electrode surface area. Additions of expanders as surface-active substances (e.g. lignosulfonic acid) is useful to lower the surface energy of lead and thus to reduce large crystals formation. The crystal formation is also damped by the addition of fine BaSO_4 , isomorphic with PbSO_4 [348]. Influence of charge mode on

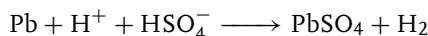
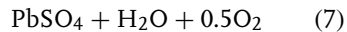
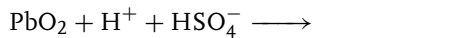
the capacity and cycle life of negative plates has been analyzed [353].

Separators used in lead-acid batteries are usually produced from synthetic polymers as sintered poly(vinylchloride) and extruded polyethylene, glass, or microglass fiber [203, 348, 354].

Properties of lead-acid cells, important from the practical point of view, related, for example, to charge/discharge process and its mechanism, conductivity, and so on are studied using different electrochemical techniques, the most powerful one being electrochemical impedance spectroscopy [355–358].

In recent years, a significant improvement of properties of the most popular automotive starting batteries has been obtained because of the technical modifications of the classical construction [349]: (1) application of thin-walled polypropylene cases, allowing more space for the plates, (2) through-the-wall intercell connections, lowering the internal resistance and also allowing more space for active elements, and (3) application of thinner polymeric separators. Also, lightweight plastic grids have been developed [359].

The stability of the charge that is stored is limited by the thermodynamically favored reactions connected with both hydrogen and oxygen evolution [348].



(8)

enhanced by impurities (e.g. Fe^{2+} ions) and presence of antimony.

These processes should be minimized, especially in maintenance free (MF) batteries because they lead to undesirable water losses. MF batteries have a grid

with reduced antimony amount, and other metals such as calcium, strontium, tin or aluminum are used [348, 360, 361]. Valve-regulated lead-acid (VRLA) batteries have been constructed to enhance the recombination of the oxygen at the negative electrode [362–364]. The oxygen transport and recombination in VRLA batteries have been discussed by Pavlov with coworkers [365, 366] and Guo with coworkers [367, 368]. Simulations and results of current-interrupt experiments for VRLA have been compared [369]. These batteries can be scaled from a few to several thousand amperes per hour and are suitable for almost all battery applications [349]. In VRLA batteries, the electrolyte amount is reduced, it is immobilized by gel formation [370] using silica or calcium sulfate, or by the incorporation of microporous glass separators [203, 348]. Leak-proof constructions with one-way vent – semisealed systems, exhibit significantly higher charge retention compared with conventional units [203, 348]. Properties of different size VRLA batteries have been studied and modeled using electrochemical impedance spectroscopy and fuzzy logic methodology of data analysis [371, 372].

A novel kind of flow lead-acid battery with no separator and single electrolyte, lead(II) in methanesulfonic acid has been proposed recently [373].

24.3.5.2 Electrocatalytic Properties

24.3.5.2.1 Pb Lead, and particularly underpotentially deposited Pb, exhibits electrocatalytic properties in numerous electrode processes. The model reaction can be oxygen reduction with slow step of peroxide reduction [374–376] or reduction of nitrobenzene and other nitrocompounds [377, 378]. In the case of

nitrocompounds, the catalytic effect observed at medium degrees of UPD adatom coverages has been interpreted in terms of strong adsorption of the nitro group with a bridged complex involving the substrate (Au) and adsorbate atom (Pb), favoring N–O bond cleavage. STM studies of Pb deposited on Au(111) suggest that the active sites are edges of the circular Pb islands [379, 380]. This activity can be reduced by the addition of adsorbing species.

Other model reactants are simple organic molecules, for example, formic acid [381, 382]. Pt(111) exerts lower catalytic influence on HCOOH oxidation than do Pt(100) and Pt(110) faces. However, in the presence of Pb adatoms on Pt(111) a strong catalytic influence has been observed [383]. The poisonous species production in HCOOH oxidation is then inhibited. Electrochemical reduction of CO₂ to glycolate/glyoxylate and oxalic acid has been studied [384]. Other products such as formic acid accompanied by CO and methane have also been detected [385]. In the latter case, the efficiency of the competing process of hydrogen evolution has been suppressed to less than 3.5%.

Other electrochemical processes of organic compounds on Pb electrodes or electrodes with UPD Pb have been studied – formaldehyde [323], oxalic acid [386], trichloro- and trifluoroethane [387], 1-phenylethylamine [388], 3-hydroxychiniclidine [388], dichlorodifluoromethane [389], polychlorobenzenes [390], 1-propanol [391], pyrrole polymerization [392], and inorganic compounds – phosphine [388] and sulfate(IV) ions [393]. Simultaneous catalytic or inhibiting influence of organic solvents – acetonitrile, dimethylsulfoxide, and Pb²⁺ presence on electro-oxidation of small organic molecules on Pt electrodes has been studied using on-line mass spectroscopy [394].

The influence of Pb alloy components on electrocatalytic processes has been discussed, for example, in Refs 386, 395.

24.3.5.2.2 PbO₂ Lead dioxide is an electrode material of relatively high electronic conductivity and high stability in acidic media, useful at high positive potentials. AFM studies have revealed the influence of PbO₂ structure on its electrocatalytic activity [150]. In model glucose oxidation process, the role of hydrated gel layer in the interaction between OH radicals and glucose, as well as coordination of the carbonyl atom to Pb(IV) center [150, 396, 397] has been analyzed.

The oxygen evolution overpotential on PbO₂ electrodes is high. The role of adsorbed intermediates in this process for both α - and β -forms of PbO₂ has been discussed [197]; Pavlov and Monahov proposed a mechanism of O₂ evolution with elementary reactions taking place at active centers in the hydrated zones of the electrode [398, 399]. The formation and properties of the hydrous layer can be affected by anions owing to the exchange reaction of OH[−] ions by these anions [400]. These adsorbed anions can inhibit both water electrode reactions and desorption of reaction intermediates. Low temperature inhibits the reaction by slowing down desorption of reaction intermediates [400]. The role of nonstoichiometry of PbO_{2-x} in oxygen evolution has been analyzed [401].

Another group of anodic reactions is connected with the electrogeneration of strong oxidants as ozone or persulfate, with efficiency decreasing with increasing efficiency of O₂ evolution (e.g. [191, 205, 400, 402–406]). Owing to high oxygen overpotential and high oxygen radicals formation efficiency, mainly OH radicals ([407] and references given therein), and lead dioxide electrodes are used as

anodes for the destruction of organic compounds because rates of such reactions are higher than on other traditional anodes ([408] and references given therein). Oxidation of different organics as, for example, glucose, acetic, oxalic [407] and 4-hydroxy-cinnamic acids [407, 409], phenol [204, 410, 411], 4-chlorophenols [412, 413], nitrocompounds [412–414], benzene and dimethylsulfoxide [204], 2-thiophene carboxylic acid [415], Mn(II) [415], and cyanides [188] has been reported to point to the role of the substrate molecules and intermediates adsorption. Conducting polymers – polypyrrole [416], polyani-line [417], polythiophene [418], poly(3-methylthiophene) [418,] as well as copolymers of aniline and thiophene [419] have been obtained by electropolymerization onto PbO₂ electrodes.

24.3.5.3 Electrochemical Sensors

The literature concerning electrochemical sensors, where lead electrochemistry can be applied, is extremely vast. Therefore, only some representative papers will be presented. More information can be found in recent reviews [420–423].

24.3.5.3.1 Potentiometric Sensors In the field of ion-selective electrodes, considerable progress has been achieved in the last few years. By buffering the primary ions concentration on a low level in the internal solution, ionic fluxes in the membrane are affected [424–426]. Thus, primary ion leakage into sample solution is hindered, resulting in a tremendous shift of detection limits to lower values; for Pb²⁺-selective electrodes, the detection limit up to 10⁻¹² M level has been achieved for internal solution electrodes [424, 427] and below 10⁻⁹ M for all-solid-state electrodes with conducting polymer solid

contact ([428, 429], see also recent review [423]). Efforts have been made to monitor ion fluxes in the membranes using electrochemical microscopy, potentiometric studies, and galvanostatic polarization [427, 430]. Both stability of Pb²⁺ complexes with several ionophores used in ion-selective membranes and selectivities have been discussed [431]. Recently, a new kind of Pb²⁺-selective electrode containing nonfunctionalized porous glassy carbon, loaded with ionophore/plasticizer/additive cocktail has been proposed [432]. Glassy carbon acts both as the support for the membrane and signal transducer. The reported detection limit is close to 10⁻¹¹ M.

24.3.5.3.2 Amperometric/Voltammetric

Sensors Amperometric sensors, based on lead accumulation by interaction with electrode components, for example, adsorbed ligand, forming products that can be stripped by anodic polarization [81] have been elaborated. Although mercury and mercury film electrodes are claimed to have the highest sensitivity for Pb²⁺ determination [433, 434], other electrode materials have also been tested: amalgams [435], silver [436–440], gold [439], gold–silver alloys [441], carbon [442–446], diamond [447, 448], mesoporous silica on carbon [449], Nafion on graphite [450], conducting polymers as polyani-line [451–454], polypyrrole [455, 456] or poly(1,8-diaminonaphthalene) [457], and microelectrodes [458–460]. Quartz crystal microgravimetry has been used to study Pb deposition from ethylenediamine tetraacetic acid (EDTA) complexes [461]. The multivariate calibration transfer method has been applied to routine polarographic determination of lead [462], and multisensor systems have been developed (e.g. [463]). There are numerous papers that reveal the very

promising areas related to stripping voltammetric and chronopotentiometric determination of lead using disposable screen-printed electrodes ([464–468] as also shown by review article [469]). Sono-electroanalytical methods have been also used to determine lead for example ([470–473] and review [474]).

References

- T. F. Sharpe, in *Encyclopedia of Electrochemistry of the Elements* (Ed.: A. J. Bard), Marcel Dekker, New York, 1973, p. 235, Vol. 1.
- A. Frumkin, *Zero Charge Potentials (in Russian)*, Nauka, Moscow, 1979.
- M. A. Vorotyntsev, in *Modern Aspects of Electrochemistry* (Eds.: J. O. M. Bockris, B. E. Conway, R. E. White), Plenum Press, New York, 1986, p. 131, Vol. 17.
- R. Parsons, *Chem. Rev.* **1990**, *90*, 813–826.
- A. Hamelin, T. Vitanov, E. Sevastyanov et al., *J. Electroanal. Chem.* **1983**, *145*, 225–264.
- S. Trasatti, E. Lust, in *Modern Aspects of Electrochemistry*, (Eds.: R. E. White, J. O. M. Bockris, B. E. Conway), Kluwer Academic/Plenum Publishers, New York, 1999, p. 1, Vol. 33.
- V. Y. Mishuk, E. A. Solomatin, V. V. Elkin, *Elektrokhimiya* **1978**, *14*, 1135–1135.
- L. P. Khmelevaya, B. B. Damaskin, A. I. Sidnin, *Elektrokhimiya* **1981**, *17*, 436–439.
- E. S. Sevastyanov, V. K. Chubarova, N. A. Morozova et al., *Elektrokhimiya* **1992**, *28*, 720–729.
- V. A. Safonov, B. B. Damaskin, M. A. Choba, *Elektrokhimiya* **1989**, *25*, 1432–1438.
- L. P. Khmelevaya, A. V. Chizhov, B. B. Damaskin et al., *Elektrokhimiya* **1980**, *16*, 257–260.
- K. V. Rybalka, D. I. Leikis, *Elektrokhimiya* **1967**, *3*, 383–386.
- Z. N. Ushakova, V. F. Ivanov, *Elektrokhimiya* **1976**, *12*, 485–487.
- A. Kisza, J. Kaźmierczak, B. Meissner, *Pol. J. Chem.* **2004**, *78*, 561–573.
- V. V. Emets, B. B. Damaskin, *J. Electroanal. Chem.* **2002**, *528*, 57–68.
- Z. Shi, Y.-H. Zhou, C.-S. Cha, *J. Power Sources* **1998**, *70*, 214–221.
- B. K. Mahato, *J. Electrochem. Soc.* **1981**, *128*, 1416–1422.
- Z. Shi, Y.-H. Zhou, C.-S. Cha, *J. Electroanal. Chem.* **1995**, *399*, 213–221.
- Z. Shi, H. Zhan, Y.-H. Zhou et al., *J. Power Sources* **1996**, *62*, 135–139.
- L. A. Beketayeva, V. I. Beklemyshev, I. I. Makhonin et al., *Russ. J. Electrochem.* **1997**, *33*, 1242–1245.
- I. Ban, Y. Yamaguchi, Y. Nakayama et al., *J. Power Sources* **2002**, *107*, 167–172.
- N. Hirai, D. Tabayashi, M. Shiota et al., *J. Power Sources* **2004**, *133*, 32–38.
- S. S. Mahmoud, G. A. El Mahdy, *Bull. Electrochem.* **1997**, *13*, 75–79.
- E. Rocca, J. Steinmetz, *Corros. Sci.* **2001**, *43*, 891–902.
- G. Pezzatini, M. L. Foresti, R. Guidelli, *J. Electroanal. Chem.* **1982**, *138*, 139–153.
- B. N. Afanasev, G. I. Merkulova, *Elektrokhimiya* **1985**, *21*, 739–746.
- J. Kúta, L. Pospišil, J. Smoler, *J. Electroanal. Chem.* **1977**, *75*, 407–420.
- V. I. Kravtsov, V. N. Statsyuk, *Russ. J. Electrochem.* **1997**, *33*, 377–384.
- J. Lipkowski, Z. Galus, *J. Electroanal. Chem.* **1979**, *98*, 91–104.
- E. Muszalska, W. Górska, Z. Galus, *J. Electroanal. Chem.* **1990**, *294*, 87–95.
- S. Romanowski, K. Maksymiuk, Z. Galus, *J. Electroanal. Chem.* **1995**, *385*, 95–103.
- G. J. Hills, L. M. Peter, *J. Electroanal. Chem.* **1974**, *50*, 175–185.
- A. Broda, J. Stroka, Z. Galus, *Electrochim. Acta* **1983**, *28*, 817–823.
- J. Stroka, K. Maksymiuk, Z. Galus, *J. Electroanal. Chem.* **1984**, *167*, 211–226.
- K. Maksymiuk, J. Stroka, Z. Galus, *J. Electroanal. Chem.* **1990**, *279*, 1–18.
- G. Gritzner, *J. Phys. Chem.* **1986**, *90*, 5478–5485.
- S. Kariuki, H. D. Dewald, *Electroanalysis* **1996**, *8*, 307–313.
- P. Paklepa, P. K. Wrona, *J. Electroanal. Chem.* **1998**, *453*, 205–210.
- E. F. Speranskaya, V. A. Speranskii, *Russ. J. Appl. Chem.* **1996**, *69*, 1319–1325.
- R. G. Barradas, T. J. Vandernoot, *J. Electroanal. Chem.* **1987**, *233*, 237–250.
- I. S. El-Hallag, *Bull. Electrochem.* **1998**, *14*, 44–47.
- J. Schiewe, K. B. Oldham, J. C. Myland et al., *Anal. Chem.* **1997**, *69*, 2673–2681.

43. J. Schiewe, J. Hazi, V. A. Vicente-Beckett et al., *J. Electroanal. Chem.* **1998**, *451*, 129–138.
44. R. G. Barradas, F. C. Benson, S. Fletcher, *J. Electroanal. Chem.* **1977**, *80*, 305–313.
45. P. Fusi, P. R. Mussini, *J. Solution Chem.* **1997**, *26*, 337–353.
46. D. Giovanelli, N. S. Lawrence, R. G. Compton, *Electroanalysis* **2004**, *16*, 789–810.
47. K. I. Ibragimov, V. S. Savvin, *Inorg. Mater.* **1996**, *32*, 963–970.
48. A. T. Kuhn, (Ed.), *The Electrochemistry of Lead*, Academic Press, New York, 1979.
49. R. J. Barrio Diez-Caballero, J. F. Arranz Valentin, A. Arranz Garcia et al., *J. Electroanal. Chem.* **1985**, *196*, 43–51.
50. G. Scarano, E. Morelli, *Electroanalysis* **1998**, *10*, 39–43.
51. M. M. Correia Dos Santos, M. L. S. Simões Gonçalves, *J. Electroanal. Chem.* **1986**, *208*, 137–152.
52. T. M. Borges Miquel, M. L. Sánchez, J. C. Macias et al., *Can. J. Chem.* **1996**, *74*, 2454–2459.
53. S. K. Singh, C. P. S. Chandel, *Asian J. Chem.* **2002**, *14*, 53–56.
54. S. K. Singh, C. P. S. Chandel, *Bull. Electrochem.* **2002**, *18*, 1–6.
55. S. K. Singh, C. P. S. Chandel, *Bull. Electrochem.* **2003**, *19*, 119–126.
56. J. C. Rodriguez Placeres, J. C. Macias, M. L. Sánchez et al., *Collect. Czech. Chem. Commun.* **2003**, *68*, 663–671.
57. E. Bottari, M. R. Festa, *Chem. Spec. Bioavailab.* **1996**, *8*, 75–83.
58. M. Ben Ali, R. Kalfat, H. Sfihli et al., *Mater. Sci. Eng., C* **1998**, *6*, 53–58.
59. G. Roya-Morales, L. Galicia, A. Rojas-Hernández et al., *Electrochim. Acta* **2005**, *50*, 1925–1930.
60. A. Ion, M. Buda, J. C. Moutet et al., *Eur. J. Inorg. Chem.* **2002**, *6*, 1357–1366.
61. I. Cukrowski, S. A. Loader, *Electroanalysis* **1998**, *10*, 877–885.
62. H. M. V. M. Soares, M. G. R. T. Barros, *Electroanalysis* **2001**, *13*, 325–331.
63. J. Buffle, A. M. Mota, M. L. S. Simões Gonçalves, *J. Electroanal. Chem.* **1987**, *223*, 235–262.
64. R. Mandal, M. S. A. Salam, C. L. Chakrabarti et al., *Electroanalysis* **2003**, *15*, 903–906.
65. A. A. A. Gaber, M. A. Ghadour, H. S. El-Said, *J. Indian Chem. Soc.* **2001**, *78*, 455–459.
66. Y. Z. Bian, L. Li, J. M. Dou et al., *Inorg. Chem.* **2004**, *43*, 7539–7544.
67. R. Pedrido, M. R. Bermejo, M. J. Romero et al., *Dalton Trans.* **2005**, *3*, 572–579.
68. R. M. Izatt, J. S. Bradshaw, S. A. Nielsen et al., *Chem. Rev.* **1985**, *85*, 271–339.
69. R. M. Izatt, K. Pawlak, J. S. Bradshaw et al., *Chem. Rev.* **1991**, *91*, 1721–2085.
70. R. M. Izatt, K. Pawlak, J. S. Bradshaw et al., *Chem. Rev.* **1995**, *95*, 2529–2586.
71. A. Lehmani, T. Cartailler, S. Rossy-Deluc et al., *J. Electroanal. Chem.* **1996**, *416*, 121–125.
72. G. Rounaghi, M. Chamsaz, A. Nezhadali, *J. Incl. Phenom. Macrocycl. Chem.* **2000**, *38*, 153–161.
73. G. Rounaghi, A. S. Yazdi, Z. Monsef, *J. Incl. Phenom. Macrocycl. Chem.* **2002**, *43*, 231–237.
74. Z. Monsef, G. Rounaghi, A. Sarafraza, *J. Incl. Phenom. Macrocycl. Chem.* **2001**, *39*, 321–325.
75. E. Cukrowska, I. Cukrowski, *Talanta* **1998**, *47*, 1175–1189.
76. R. Luckay, R. D. Hancock, I. Cukrowski et al., *Inorg. Chim. Acta* **1996**, *246*, 159–169.
77. C. Caltagirone, A. Bencini, F. Demartin et al., *Dalton Trans.* **2003**, *5*, 901–909.
78. M. C. Ezequiel Rollemburg, M. L. S. Simões Gonçalves, A. M. Almeida Mota et al., *Anal. Chim. Acta* **1999**, *384*, 17–26.
79. T. F. Rozan, G. W. Luther, D. Ridge et al., *Environ. Sci. Technol.* **2003**, *37*, 3845–3852.
80. M. T. Vasconcelos, M. Azehna, V. de Freitas, *Analyst* **2000**, *125*, 743–748.
81. O. Abollino, M. Aceto, C. Sarzanini et al., *Electroanalysis* **1999**, *11*, 870–878.
82. M. R. Ganjali, M. Shamsipur, *J. Inclusion Phenom.* **1995**, *23*, 41–51.
83. P. Perez-Lourido, J. Romero, J. A. García-Vázquez et al., *J. Chem. Soc., Dalton Trans.* **2000**, *5*, 769–774.
84. E. Labisbal, A. Sousa, A. Castineiras et al., *Polyhedron* **2000**, *19*, 1255–1262.
85. V. N. Kokozay, O. Y. Vassilyeva, P. Weinberger et al., *Rev. Inorg. Chem.* **2000**, *20*, 255–282.
86. G. M. Barnard, M. A. Brown, H. E. Mabrouk et al., *Inorg. Chim. Acta* **2003**, *349*, 142–148.
87. J. N. Liu, X. Q. Yu, Y. J. Dong et al., *Chin. J. Inorg. Chem.* **1999**, *15*, 680–684.
88. S. Kumar, D. Kishore, R. K. Mehta, *J. Indian Chem. Soc.* **2000**, *77*, 254–255.

89. A. Bobrowski, A. M. Bond, S. R. Ellis, *Inorg. Chim. Acta* **1999**, *293*, 223–228.
90. F. Marken, W. M. Leslie, R. G. Compton et al., *J. Electroanal. Chem.* **1997**, *424*, 25–34.
91. A. Morales-Pérez, M. Bernabe, G. Roa et al., *Electroanalysis* **2001**, *13*, 541–548.
92. P. Singh, M. M. Richter, *Inorg. Chim. Acta* **2004**, *357*, 1589–1592.
93. J. B. Chlistunoff, J. J. Lagowski, *J. Phys. Chem. B* **1997**, *101*, 2867–2873.
94. J. B. Chlistunoff, J. J. Lagowski, *J. Phys. Chem. B* **1998**, *102*, 5800–5809.
95. H. Katano, M. Senda, *Anal. Sci.* **1996**, *12*, 683–689.
96. G. Lagger, L. Tomaszewski, M. D. Osborne et al., *J. Electroanal. Chem.* **1998**, *451*, 29–37.
97. T. Store, G. M. Haarberg, R. Tunold, *J. Appl. Electrochem.* **2000**, *30*, 1351–1360.
98. Y. Castrillejo, S. Palmero, M. A. Garcia et al., *Electrochim. Acta* **1996**, *41*, 2461–2468.
99. V. P. Yurkinskii, D. V. Makarov, *Russ. J. Appl. Chem.* **1995**, *68*, 1285–1288.
100. D. V. Makarov, V. P. Yurkinskii, *Russ. J. Appl. Chem.* **1996**, *69*, 220–223.
101. R. L. Deutscher, S. Fletcher, J. A. Hamilton, *Electrochim. Acta* **1986**, *31*, 585–589.
102. Y. Yamamoto, M. Matsuoka, M. Kimoto et al., *Electrochim. Acta* **1996**, *41*, 439–444.
103. M. Taguchi, H. Sugita, *J. Power Sources* **2002**, *109*, 294–300.
104. Y. Guo, *J. Electrochem. Soc.* **1995**, *142*, 3378–3382.
105. Y. L. Guo, Z. Wei, S. Hua, *Electrochim. Acta* **1997**, *42*, 979–984.
106. S. Fletcher, D. B. Matthews, *J. Electroanal. Chem.* **1981**, *126*, 131–144.
107. J. G. Sunderland, *J. Electroanal. Chem.* **1976**, *71*, 341–345.
108. M. Metikoš-Huković, R. Babić, S. Omanić, *J. Electroanal. Chem.* **1994**, *374*, 199–206.
109. Y. Yamamoto, K. Fumino, T. Ueda et al., *Electrochim. Acta* **1992**, *37*, 199–203.
110. A. Czerwiński, M. Żelazowska, M. Grdeń et al., *J. Power Sources* **2000**, *85*, 49–55.
111. D. Pavlov, *Electrochim. Acta* **1978**, *23*, 845–854.
112. D. Pavlov, T. Rogachev, *Electrochim. Acta* **1978**, *23*, 1237–1242.
113. J. R. Vilche, F. E. Varela, *J. Power Sources* **1997**, *64*, 39–45.
114. K. R. Bullock, M. A. Butler, *J. Electrochem. Soc.* **1986**, *133*, 1085–1089.
115. M. Ma, C.-X. Yang, W.-B. Cai et al., *J. Electrochem. Soc.* **2003**, *150*, B325–B328.
116. Y.-Q. Wan, Q.-Z. Wang, H.-T. Liu et al., *J. Electroanal. Chem.* **1996**, *414*, 159–161.
117. G. E. Nauer, *Sci. Forum* **1996**, *228*, 387–392.
118. T. Laitinen, B. Monahov, K. Salmi et al., *Electrochim. Acta* **1991**, *36*, 953–963.
119. Z. Takehara, K. Kanamura, *J. Electrochem. Soc.* **1987**, *134*, 1604–1610.
120. F. E. Varela, M. E. Vela, J. R. Vilche et al., *Electrochim. Acta* **1993**, *38*, 1513–1520.
121. L. I. Espinoza-Ramos, C. Ramirez, J. M. Hallen-López et al., *J. Electrochem. Soc.* **2002**, *149*, B543–B550.
122. W.-B. Cai, H.-T. Liu, W.-F. Zhou, *J. Power Sources* **1996**, *63*, 131–135.
123. E. N. Codaro, J. R. Vilche, *Electrochim. Acta* **1997**, *42*, 549–555.
124. Y. L. Guo, L. Niu, S. Zhang et al., *J. Power Sources* **2000**, *85*, 38–43.
125. D. Pavlov, A. Kirchev, M. Stoycheva et al., *J. Power Sources* **2004**, *137*, 288–308.
126. Q. J. Sun, Y. L. Guo, *J. Electroanal. Chem.* **2000**, *493*, 123–129.
127. S. Zhong, J. Wang, H. K. Liu et al., *J. Power Sources* **1997**, *66*, 159–164.
128. S. Zhong, J. Wang, H. K. Liu et al., *J. Appl. Electrochem.* **1999**, *29*, 1–6.
129. E. Expósito, C. M. Sánchez-Sánchez, J. Solla-Gullón et al., *J. Power Sources* **2002**, *104*, 169–174.
130. P. Varma, C. A. Melendres, N. Yao, *J. Electrochem. Soc.* **1980**, *127*, 1416–1418.
131. K. R. Bullock, *J. Electroanal. Chem.* **1987**, *222*, 347–366.
132. Y. Guo, *J. Electrochem. Soc.* **1991**, *138*, 1222–1227.
133. G. L. J. Trettenhahn, G. E. Nauer, A. Neckel, *Ber. Bunsen-Ges. Phys. Chem.* **1993**, *97*, 422–426.
134. G. L. J. Trettenhahn, G. E. Nauer, A. Neckel, *J. Power Sources* **1993**, *42*, 137–144.
135. G. L. J. Trettenhahn, G. E. Nauer, A. Neckel, *Electrochim. Acta* **1996**, *41*, 1435–1441.
136. S.-J. Xia, W.-F. Zhou, *J. Appl. Electrochem.* **1994**, *24*, 894–899.
137. D. Pavlov, S. Zanova, G. Papazov, *J. Electrochem. Soc.* **1977**, *124*, 1522–1528.
138. J. S. Buchanan, L. M. Peter, *Electrochim. Acta* **1988**, *33*, 127–136.
139. Y. Yang, X. G. Chen, X. D. Zhuo et al., *J. Electroanal. Chem.* **1994**, *367*, 255–258.
140. J. Han, C. Pu, W.-F. Zhou, *J. Electroanal. Chem.* **1994**, *368*, 43–46.

141. R. Peat, P. T. Moseley, A. F. Hollenkamp et al., *J. Power Sources* **1993**, *42*, 119–135.
142. N. Stein, E. Rocca, R. Kleim et al., *Electrochim. Acta* **1998**, *44*, 445–454.
143. N. Stein, G. Bourguignon, L. Raboin et al., *Thin Solid Films* **2004**, *455*–456, 735–741.
144. K. Uosaki, K. Konishi, M. Koinuma, *Langmuir* **1997**, *13*, 3557–3562.
145. Y. Yamaguchi, M. Shiota, Y. Nakayama et al., *J. Power Sources* **2000**, *85*, 22–28.
146. Y. Yamaguchi, M. Shiota, Y. Nakayama et al., *J. Power Sources* **2001**, *93*, 104–111.
147. N. Hirai, K. Takeda, S. Hara et al., *J. Power Sources* **2003**, *113*, 329–334.
148. M. P. Vinod, A. B. Mandle, S. R. Sainkar et al., *J. Appl. Electrochem.* **1997**, *27*, 462–468.
149. M. M. El-Naggar, *Monatsh. Chem.* **2001**, *132*, 1189–1200.
150. M. E. Hyde, R. M. L. Jacobs, R. G. Compton, *J. Phys. Chem. B* **2004**, *108*, 6381–6390.
151. M. Chatelut, S. Chah-Bouzziri, O. Vittori et al., *J. Solid State Electrochem.* **2000**, *4*, 435–443.
152. I. Paleska, R. Pruszkowska-Drachal, J. Kotowski et al., *J. Power Sources* **2003**, *113*, 308–317.
153. V. I. Birrs, M. T. Shevalier, *J. Electrochem. Soc.* **1990**, *137*, 2643–2647.
154. B. Centeno, M. L. Tascón, M. D. Vázquez et al., *Electrochim. Acta* **1991**, *36*, 277–282.
155. A. A. Montaser, P. Veluchamy, H. Minoura, *J. Electroanal. Chem.* **1996**, *419*, 47–53.
156. S. S. Abd El Rehim, L. I. Ali, N. H. Amin et al., *Monatsh. Chem.* **1997**, *128*, 245–254.
157. P. Veluchamy, H. Minoura, *J. Electroanal. Chem.* **1997**, *440*, 41–49.
158. P. Veluchamy, H. Minoura, *Appl. Surf. Sci.* **1998**, *126*, 241–245.
159. M. M. El-Naggar, *J. Power Sources* **2004**, *126*, 207–213.
160. E. E. Abd El Aal, *J. Power Sources* **2001**, *102*, 233–241.
161. E. F. El-Sherbini, S. S. Abd El Rehim, *Mater. Chem. Phys.* **2004**, *88*, 17–22.
162. E. E. Abd El Aal, *J. Power Sources* **1998**, *75*, 36–43.
163. M. Shiota, T. Kameda, K. Matsui et al., *Electrochemistry* **2003**, *71*, 873–876.
164. J. S. Buchanan, N. P. Freestone, L. M. Peter, *J. Electroanal. Chem.* **1985**, *182*, 383–398.
165. B. Meyer, B. Ziemer, F. Scholz, *J. Electroanal. Chem.* **1995**, *392*, 79–83.
166. M. Dimitrov, K. Kochev, D. Pavlov, *J. Electroanal. Chem.* **1985**, *183*, 145–153.
167. K. R. Bullock, G. M. Trishan, R. G. Burrow, *J. Electrochem. Soc.* **1983**, *130*, 1283–1289.
168. R. G. Barradas, D. S. Nadezhdin, *Can. J. Chem.* **1984**, *62*, 596–600.
169. F. E. Varela, E. N. Codaro, J. R. Vilche, *Electrochim. Acta* **1995**, *40*, 1183–1189.
170. E. Rocca, J. Steinmetz, S. Weber, *J. Electrochem. Soc.* **1999**, *146*, 54–58.
171. I. Petersson, E. Ahlberg, *J. Power Sources* **2000**, *91*, 143–149.
172. P. Veluchamy, H. Minoura, *J. Electroanal. Chem.* **1995**, *396*, 211–217.
173. M. Sharon, I. Mukhopadhyay, S. Ghosh, *J. Solid State Electrochem.* **1999**, *3*, 141–147.
174. U. Hasse, F. Scholz, *Electrochim. Commun.* **2001**, *3*, 429–434.
175. Q. F. Li, F. Borup, I. Petrushina et al., *J. Electrochem. Soc.* **1999**, *146*, 2449–2454.
176. R. S. Robinson, *J. Power Sources* **1992**, *40*, 149–156.
177. M. E. Herron, D. Pletcher, F. C. Walsh, *J. Electroanal. Chem.* **1992**, *332*, 183–197.
178. A. B. Velichenko, R. Amadelli, A. Benedetti et al., *J. Electrochem. Soc.* **2002**, *149*, C445–C449.
179. A. B. Velichenko, D. V. Girenko, F. I. Danilov, *J. Electroanal. Chem.* **1996**, *405*, 127–132.
180. J. Lee, H. Varela, S. Uhm et al., *Electrochim. Commun.* **2000**, *2*, 646–652.
181. A. A. Vertegel, E. W. Bohannan, M. G. Shumsky et al., *J. Electrochem. Soc.* **2001**, *148*, C253–C256.
182. S. Tabat, A. Nowacki, B. Szczesniak, *J. Power Sources* **1990**, *31*, 339–348.
183. D. Velayutham, M. Noel, *Electrochim. Acta* **1991**, *36*, 2031–2035.
184. J. González-García, V. Sáez, J. Iniesta et al., *Electrochim. Commun.* **2002**, *4*, 370–373.
185. A. Czerwiński, M. Żelazowska, *J. Power Sources* **1997**, *64*, 29–34.
186. T. C. Wen, M. G. Wei, K. L. Lin, *J. Electrochem. Soc.* **1990**, *137*, 2700–2702.
187. M. Ueda, A. Watanabe, T. Kameyama et al., *J. Appl. Electrochem.* **1995**, *25*, 817–822.
188. G. Cifuentes, L. Cifuentes, R. Kammel et al., *Z. Metallkd.* **1998**, *89*, 363–367.
189. C. N. Ho, B. J. Hwang, *Electrochim. Acta* **1993**, *38*, 2749–2757.
190. P. N. Bartlett, T. Dunfod, M. A. Ghanem, *J. Mater. Chem.* **2002**, *12*, 3130–3135.

191. J. E. Graves, D. Pletcher, R. L. Clarke et al., *J. Appl. Electrochem.* **1992**, *22*, 200–203.
192. S. Abaci, K. Pekmez, T. Hokelek et al., *J. Power Sources* **2000**, *88*, 232–236.
193. J. Morales, G. Petkova, M. Cruz et al., *Electrochem. Solid State Lett.* **2004**, *7*, A75–A77.
194. J. P. Carr, N. A. Hampson, *Chem. Rev.* **1972**, *72*, 679–703.
195. J. P. Pohl, H. Rickert, in *Electrodes of Conductive Metallic Oxides* (Ed.: S. Trasatti), Elsevier, Amsterdam, 1980, Part A, Chapter 4.
196. D. Devilliers, M. T. Dinh Thi, E. Mahé et al., *J. Electroanal. Chem.* **2004**, *573*, 227–239.
197. J. C. K. Ho, G. T. Filho, R. Simpraga et al., *J. Electroanal. Chem.* **1994**, *366*, 147–162.
198. P. K. Shen, X. L. Wei, *Electrochim. Acta* **2003**, *48*, 1743–1747.
199. J.-R. Wang, G.-L. Wei, *J. Electroanal. Chem.* **1995**, *390*, 29–33.
200. B. Monahov, D. Pavlov, A. Kirchev et al., *J. Power Sources* **2003**, *113*, 281–292.
201. C.-H. Yeh, C.-C. Wan, J.-S. Chen, *J. Power Sources* **2001**, *101*, 219–225.
202. I. Petersson, E. Ahlberg, B. Berghult, *J. Power Sources* **1998**, *76*, 98–105.
203. H. Bode, *Lead-Acid Batteries*, Wiley, New York, 1977.
204. K. T. Kawagoe, D. C. Johnson, *J. Electrochem. Soc.* **1994**, *141*, 3404–3409.
205. A. B. Velichenko, R. Amadelli, G. L. Zucchini et al., *Electrochim. Acta* **2000**, *45*, 4341–4350.
206. A. B. Velichenko, R. Amadelli, E. A. Baranova et al., *J. Electroanal. Chem.* **2002**, *527*, 56–64.
207. M. Shiota, Y. Yamaguchi, Y. Nakayama et al., *J. Power Sources* **2001**, *95*, 203–208.
208. R. Fitas, L. Zerroual, N. Chelali et al., *J. Power Sources* **1997**, *64*, 57–60.
209. R. Fitas, N. Chelali, L. Zerroual et al., *Solid State Ionics* **2000**, *127*, 49–54.
210. T. Torimoto, S. Takabayashi, H. Mori et al., *J. Electroanal. Chem.* **2002**, *522*, 33–39.
211. M. Sharon, K. S. Ramaiah, M. Kumar et al., *J. Electroanal. Chem.* **1997**, *436*, 49–52.
212. H. Saloniemi, M. Ritala, M. Leskela et al., *J. Electrochem. Soc.* **1999**, *146*, 2522–2525.
213. A. A. Vertegel, M. G. Shumsky, J. A. Switzer, *Angew. Chem., Int. Ed. Engl.* **1999**, *38*, 3169–3171.
214. K. K. Nanda, S. N. Sahu, *Adv. Mater.* **2001**, *13*, 280.
215. H. Saloniemi, M. Kemell, M. Ritala et al., *Thin Solid Films* **2001**, *386*, 32–40.
216. Y. J. Yang, L. Y. He, Q. F. Zhang, *Electrochem. Commun.* **2005**, *7*, 361–364.
217. I. Cisneros-González, M. T. Oropesa-Guzmán, I. González, *Electrochim. Acta* **2000**, *45*, 2729–2741.
218. G. L. Pashkov, E. V. Mikhлина, A. G. Khomogorov et al., *Hydrometallurgy* **2002**, *63*, 171–179.
219. J. L. Nava, M. T. Oropesa, I. Gonzalez, *Electrochim. Acta* **2002**, *47*, 1513–1525.
220. Y. Mikhlin, A. Kuklinskiy, E. Mikhлина et al., *J. Appl. Electrochem.* **2004**, *34*, 37–46.
221. I. V. Chernyshova, *J. Phys. Chem. B* **2001**, *105*, 8178–8184.
222. I. V. Chernyshova, *J. Phys. Chem. B* **2001**, *105*, 8185–8191.
223. I. V. Chernyshova, *Russ. J. Electrochem.* **2001**, *37*, 579–584.
224. I. V. Chernyshova, *Langmuir* **2002**, *18*, 6962–6968.
225. I. V. Chernyshova, *J. Electroanal. Chem.* **2003**, *558*, 83–98.
226. I. Kartio, K. Laajalehto, T. Kaurila et al., *Appl. Surf. Sci.* **1996**, *93*, 167–177.
227. N. N. Zhu, A. P. Zhang, Q. J. Wang et al., *Electroanalysis* **2004**, *16*, 577–582.
228. E. A. Streltsov, N. P. Osipovich, L. S. Ivashkevich et al., *Electrochim. Acta* **1998**, *43*, 869–873.
229. H. Saloniemi, T. Kanniainen, M. Ritala et al., *J. Mater. Chem.* **1998**, *8*, 651–654.
230. E. A. Streltsov, N. P. Osipovich, L. S. Ivashkevich et al., *Electrochim. Acta* **1999**, *44*, 2645–2652.
231. H. Saloniemi, M. Kemell, M. Ritala et al., *J. Mater. Chem.* **2000**, *10*, 519–525.
232. D. K. Ivanov, C. K. Poznyak, N. P. Osipovich et al., *Russ. J. Electrochem.* **2004**, *40*, 1044–1051.
233. R. Vaideyanathan, J. L. Stickney, U. Happék, *Electrochim. Acta* **2004**, *49*, 1321–1326.
234. H. Saloniemi, T. Kanniainen, M. Ritala et al., *Thin Solid Films* **1998**, *326*, 78–82.
235. H. Saloniemi, M. Kemell, P. Ritala et al., *J. Electroanal. Chem.* **2000**, *482*, 139–148.
236. E. A. Strel'tsov, N. P. Osipovich, L. S. Ivashkevich et al., *Russ. J. Appl. Chem.* **1997**, *70*, 1651–1653.
237. E. A. Streltsov, N. P. Osipovich, L. S. Ivashkevich et al., *Electrochim. Acta* **1998**, *44*, 407–413.

238. E. A. Strel'tsov, N. P. Osipovich, L. S. Ivashkevich et al., *Russ. J. Appl. Chem.* **1998**, *71*, 1756–1758.
239. D. M. Kolb, R. Kotz, K. Yamamoto, *Surf. Sci.* **1980**, *101*, 490–498.
240. B. Beden, F. Kadirgan, C. Lamy et al., *J. Electroanal. Chem.* **1981**, *127*, 75–85.
241. J. M. Feliu, A. Fernández-Vega, J. M. Orts et al., *J. Chim. Phys.* **1991**, *88*, 1493–1518.
242. F. El. Omar, R. Durand, *J. Electroanal. Chem.* **1984**, *178*, 343–350.
243. J. Clavilier, J. M. Orts, J. M. Feliu et al., *J. Electroanal. Chem.* **1990**, *293*, 197–208.
244. R. L. Borup, D. E. Sauer, E. M. Stuve, *Surf. Sci.* **1993**, *293*, 10–26.
245. R. L. Borup, D. E. Sauer, E. M. Stuve, *Surf. Sci.* **1993**, *293*, 27–34.
246. B. N. Grgur, N. M. Marković, P. N. Ross, *Langmuir* **1997**, *13*, 6370–6374.
247. N. M. Marković, B. N. Grgur, C. A. Lucas et al., *J. Electroanal. Chem.* **1998**, *448*, 183–188.
248. C. Nishihara, K. Iwata, T. Tai et al., *Electrochim. Commun.* **1999**, *1*, 104–107.
249. N. Hoshi, I. Tae Bae, D. A. Scherson, *J. Phys. Chem. B* **2000**, *104*, 6049–6052.
250. N. M. Markovic, B. N. Grgur, C. A. Lucas et al., *J. Chem. Soc., Faraday Trans.* **1998**, *94*, 3373–3379.
251. R. R. Adzic, J. Wang, C. M. Vitus et al., *Surf. Sci.* **1993**, *293*, L876–L883.
252. C. A. Lucas, N. M. Markovic, P. N. Ross, *Langmuir* **1997**, *13*, 5517–5520.
253. M. E. Martins, R. C. Salvarezza, A. J. Arvia, *Electrochim. Acta* **1996**, *41*, 2441–2449.
254. R. Adzic, R. Yeager, B. D. Cahan, *J. Electrochem. Soc.* **1974**, *121*, 474–484.
255. J. Schultze, D. Dickermann, *Surf. Sci.* **1976**, *54*, 489–505.
256. K. Engelsmann, W. J. Lorenz, E. Schmidt, *J. Electroanal. Chem.* **1980**, *114*, 1–10.
257. K. Engelsmann, W. J. Lorenz, E. Schmidt, *J. Electroanal. Chem.* **1980**, *114*, 11–24.
258. A. Hamelin, J. Lipkowski, *J. Electroanal. Chem.* **1984**, *171*, 317–330.
259. D. M. Kolb, D. Leutloff, M. Przasnyski, *Surf. Sci.* **1975**, *47*, 622–634.
260. F. M. Romeo, R. I. Tucceri, D. Posadas, *Surf. Sci.* **1988**, *203*, 186–200.
261. C. Chen, N. Washburn, A. A. Gewirth, *J. Phys. Chem.* **1993**, *97*, 9754–9760.
262. M. Green, K. J. Hanson, *Surf. Sci.* **1991**, *259*, L743–L749.
263. N. J. Tao, J. Pan, Y. Li et al., *Surf. Sci.* **1992**, *271*, L338–L344.
264. J. Perdereau, J. P. Biberian, G. E. Rhead, *J. Phys. F: Met. Phys.* **1974**, *4*, 798–806.
265. E. Herrero, L. J. Buller, H. D. Abruña, *Chem. Rev.* **2001**, *101*, 1897–1930.
266. B. K. Niece, A. A. Gewirth, *J. Phys. Chem. B* **1998**, *102*, 818–823.
267. M. P. Green, K. J. Hanson, D. A. Scherson et al., *J. Phys. Chem.* **1989**, *93*, 2181–2184.
268. M. P. Green, K. J. Hanson, R. Carr et al., *J. Electrochem. Soc.* **1990**, *137*, 3493–3498.
269. M. Mariscal, W. Schmickler, *J. Electroanal. Chem.* **2005**, *582*, 64–68.
270. E. Budevski, G. Staikov, W. J. Lorenz, *Electrochemical Phase Formation and Growth*, VCH Publishers, Weinheim, 1996.
271. M. I. Rojas, *J. Electroanal. Chem.* **1996**, *405*, 33–38.
272. U. Schmidt, S. Vinzelberg, G. Staikov, *Surf. Sci.* **1996**, *348*, 261–279.
273. P. Hale, S. Thurgate, P. Wilkie, *Surf. Interface Anal.* **2003**, *35*, 842–851.
274. M. J. Henderson, E. Bitziou, A. R. Hillman et al., *J. Electrochem. Soc.* **2001**, *148*, E105–E111.
275. X. Q. Zeng, S. Bruckenstein, *J. Electrochem. Soc.* **1999**, *146*, 2549–2554.
276. X. Q. Zeng, S. Bruckenstein, *J. Electrochem. Soc.* **1999**, *146*, 2555–2561.
277. X. Q. Zeng, R. Hatton, *Electrochim. Acta* **2000**, *45*, 3629–3638.
278. B. E. Conway, J. C. Chacha, *J. New Mater. Electrochem. Syst.* **2004**, *7*, 231–240.
279. E. Kirowa-Eisner, Y. Bonfil, D. Tzur et al., *J. Electroanal. Chem.* **2003**, *552*, 171–183.
280. D. W. M. Arrigan, L. Le Bihan, M. J. Pickup, *Analyst* **1999**, *124*, 1797–1802.
281. T. A. Brunt, T. Rayment, S. J. O'Shea et al., *Langmuir* **1996**, *12*, 5942–5946.
282. M. Seo, M. Yamazaki, *J. Electrochem. Soc.* **2004**, *151*, E276–E281.
283. Y. V. Bokshits, N. P. Osipovich, E. A. Strel'tsov et al., *Colloids Surf. Physicochem. Eng. Aspects* **2004**, *242*, 79–83.
284. X. Xing, I. Tae Bae, D. A. Scherson, *Electrochim. Acta* **1995**, *40*, 29–36.
285. H. J. Pauling, K. Jüttner, *Electrochim. Acta* **1992**, *37*, 2237–2244.
286. K. J. Stevenson, D. W. Hatchett, H. S. White, *Langmuir* **1996**, *12*, 494–499.
287. J. Sackmann, A. Bunk, R. T. Pötzschke et al., *Electrochim. Acta* **1998**, *43*, 2863–2873.

288. R. Widmer, H. Siegenthaler, *J. Electrochem. Soc.* **2004**, *151*, E238–E245.
289. W. J. Lorenz, G. Staikov, *Surf. Sci.* **1995**, *335*, 32–43.
290. D. Carnal, P. I. Oden, U. Müller et al., *Electrochim. Acta* **1995**, *40*, 1223–1235.
291. R. Widmer, H. Siegenthaler, *Electrochim. Commun.* **2005**, *7*, 421–426.
292. W. Obretenov, N. Dimitrov, A. Popov, *J. Cryst. Growth* **1996**, *167*, 253–259.
293. J.-M. Zen, C.-C. Yang, A. S. Kumar, *Electrochim. Acta* **2001**, *47*, 899–904.
294. M. Hepel, *Electroanalysis* **2005**, *17*, 1401–1412.
295. L. Bonou, M. Eyraud, J. Crouxier, *J. Appl. Electrochem.* **1994**, *24*, 906–910.
296. J. Horkans, I. H. Chang, H. Deligianni et al., *J. Electrochem. Soc.* **1995**, *142*, 2244–2249.
297. Y. S. Chu, I. K. Robinson, A. A. Gewirth, *Phys. Rev. B* **1997**, *55*, 7945–7954.
298. K. I. Popov, M. G. Pavlović, E. R. Stojilković et al., *Hydrometallurgy* **1997**, *46*, 321–336.
299. I. A. Carlos, T. T. Matsuo, J. L. P. Siqueira et al., *J. Power Sources* **2004**, *132*, 261–265.
300. G. M. Brisard, E. Zenati, H. A. Gasteiger et al., *Langmuir* **1995**, *11*, 2221–2230.
301. G. M. Brisard, E. Zenati, H. A. Gasteiger et al., *Langmuir* **1997**, *13*, 2390–2397.
302. T. P. Moffat, *J. Phys. Chem. B* **1998**, *102*, 10020–10026.
303. H.-C. Wu, S.-L. Yau, *J. Phys. Chem. B* **2001**, *105*, 6965–6971.
304. A. Czerwiński, M. Żelazowska, *J. Electroanal. Chem.* **1996**, *410*, 55–60.
305. Z. Rogulski, W. Lewdorowicz, W. Tokarz et al., *Pol. J. Chem.* **2004**, *78*, 1357–1370.
306. J. Mostany, J. Mozota, B. R. Scharifker, *J. Electroanal. Chem.* **1984**, *177*, 25–37.
307. I. Petersson, E. Ahlberg, *J. Electroanal. Chem.* **2000**, *485*, 166–177.
308. J. Mostany, J. Parra, B. Scharifker, *J. Appl. Electrochem.* **1986**, *16*, 333–338.
309. G. Carreño, E. Sosa, I. González et al., *Electrochim. Acta* **1999**, *44*, 2633–2643.
310. E. Sosa, G. Carreño, C. Ponce de León et al., *Appl. Surf. Sci.* **2000**, *153*, 245–258.
311. B. Rashkova, B. Guel, R. T. Pötzschke et al., *Electrochim. Acta* **1998**, *43*, 3021–3028.
312. C. Prado, S. J. Wilkins, P. Gründler et al., *Electroanalysis* **2003**, *15*, 1011–1016.
313. J. C. Ziegler, G. E. Engelmann, D. M. Kolb, *Z. Phys. Chem.* **1999**, *208*, 151–166.
314. J. C. Ziegler, R. I. Wielgosz, D. M. Kolb, *Electrochim. Acta* **1999**, *45*, 827–833.
315. R. T. Pötzschke, G. Staikov, W. J. Lorenz et al., *J. Electrochem. Soc.* **1999**, *146*, 141–149.
316. B. Scharifker, G. Hills, *Electrochim. Acta* **1983**, *28*, 879–889.
317. J. C. Ziegler, G. Scherb, O. Bunk et al., *Surf. Sci.* **2000**, *452*, 150–160.
318. H. Hibino, T. Ogino, *Surf. Sci.* **1995**, *328*, L547–L552.
319. C. Elers, U. König, G. Staikov et al., *Electrochim. Acta* **2001**, *47*, 379–385.
320. E. A. Streletsov, S. K. Poznyak, N. P. Osipovich, *J. Electroanal. Chem.* **2002**, *518*, 103–114.
321. N. P. Osipovich, E. A. Streletsov, *Russ. J. Electrochem.* **2000**, *36*, 1–7.
322. D. K. Ivanov, N. P. Osipovich, S. K. Poznyak et al., *Surf. Sci.* **2003**, *532–535*, 1092–1097.
323. G. Ritzoulis, N. Georgolios, *J. Electroanal. Chem.* **1994**, *370*, 219–222.
324. G. A. Ragoisha, A. S. Bondarenko, N. P. Osipovich et al., *J. Electroanal. Chem.* **2004**, *565*, 227–234.
325. E. Streletsov, N. P. Osipovich, L. S. Ivashkevich et al., *Dokl. Akad. Nauk Belarus* **1997**, *41*, 62–65.
326. A. Piekarska, H. Elżanowska, V. I. Birss, *Pol. J. Chem.* **2004**, *78*, 1391–1412.
327. I. Paleska, R. Pruszkowska-Drachal, J. Kotowski et al., *J. Power Sources* **2004**, *129*, 326–329.
328. C. O. Avellaneda, M. A. Napolitano, E. K. Kaibara et al., *Electrochim. Acta* **2005**, *50*, 1317–1321.
329. L. O. Bulhões, L. H. Mascaro, *J. Solid State Electrochem.* **2004**, *8*, 238–243.
330. T. E. Graedel, *J. Electrochem. Soc.* **1994**, *141*, 922–927.
331. P. Mattesco, N. Bui, P. Simon et al., *J. Power Sources* **1997**, *64*, 21–27.
332. S. Zhong, J. Wang, H. K. Liu et al., *J. Power Sources* **1997**, *66*, 107–113.
333. S. Zhong, J. Wang, H. K. Liu et al., *J. Appl. Electrochem.* **1999**, *29*, 177–183.
334. E. Rocca, J. Steinmetz, *J. Electroanal. Chem.* **2003**, *543*, 153–160.
335. S. S. Abd El Rehim, N. F. Mohamed, *Corros. Sci.* **1998**, *40*, 1883–1896.
336. E. E. Abd El Aal, *Corrosion* **1992**, *48*, 482–488.
337. M. A. Amin, S. S. Abdel Rehim, *Electrochim. Acta* **2004**, *49*, 2415–2424.

338. S. S. El Egamy, W. A. Badawy, *Indian J. Chem. Technol.* **1996**, *3*, 37–43.
339. E. E. Abd El Aal, *Anti-Corros. Methods Mater.* **2001**, *48*, 116–125.
340. M. Uchida, A. Okuwaki, *Corros. Sci.* **1999**, *41*, 1977–1986.
341. S. S. Abd El Rehim, N. H. Amin, L. I. Ali et al., *J. Chem. Technol. Biotechnol.* **1998**, *72*, 197–201.
342. F. M. Al-Kharafi, W. A. Badawy, *Corros. Prev. Control* **1998**, *45*, 75–86.
343. W. A. Badawy, F. M. Al-Kharafi, *Bull. Electrochem.* **1998**, *14*, 1–9.
344. B. P. Boffardi, A. M. Sherbondy, *Corrosion* **1991**, *47*, 966–975.
345. S. Abd El Wanees, E. E. Abd El Aal, A. Abd El Aal, *Bull. Soc. Chim. Fr.* **1991**, (Nov.–Dec.) 889–893.
346. K. V. Kordesch, *Batteries*, Vol. 2, *Lead Acid Batteries and Electric Vehicles*, Marcel Dekker, New York, 1977.
347. D. Linden, *Handbook of Batteries*, McGraw-Hill, New York, 1995.
348. K. R. Bullock, C. A. Vincent, in *Modern Batteries* (Eds.: C. A. Vincent, B. Scrosati), Arnold, London, 1997, p. 142.
349. R. J. Brodd, K. R. Bullock, R. A. Leising et al., *J. Electrochem. Soc.* **2004**, *151*, K1–K11.
350. M. G. Mayer, D. A. J. Rand, *J. Power Sources* **1996**, *59*, 17–24.
351. T. Rogachev, D. Pavlov, *J. Power Sources* **1997**, *64*, 51–56.
352. D. Pavlov, G. Petkova, M. Dimitrov et al., *J. Power Sources* **2000**, *87*, 39–56.
353. G. Petkova, D. Pavlov, *J. Power Sources* **2003**, *113*, 355–362.
354. N. Clement, R. Kurian, *J. Power Sources* **2003**, *116*, 40–46.
355. J. P. Diard, B. Le Gorrec, C. Montella et al., *Electrochim. Acta* **1997**, *42*, 3417–3420.
356. G. Lindbergh, *Electrochim. Acta* **1997**, *42*, 1239–1246.
357. J. P. Diard, B. Le Gorrec, C. Montella, *J. Power Sources* **1998**, *70*, 78–84.
358. J. M. Skowroński, T. Doczekalski, *J. Power Sources* **2004**, *126*, 175–181.
359. B. Hariprakash, A. U. Mane, S. K. Martha et al., *Electrochem. Solid State Lett.* **2004**, *7*, A66–A69.
360. C. S. Lakshmi, J. E. Manders, D. M. Rice, *J. Power Sources* **1998**, *73*, 23–29.
361. Y. B. Zhou, H. T. Liu, W. B. Cai et al., *J. Electrochem. Soc.* **2004**, *151*, A978–A982.
362. A. Cooper, P. T. Moseley, *J. Power Sources* **2003**, *113*, 200–208.
363. D. Pavlov, V. Naidenov, S. Ruevski et al., *J. Power Sources* **2003**, *113*, 209–227.
364. R. J. Ball, R. Stevens, *J. Power Sources* **2003**, *113*, 228–232.
365. D. Pavlov, *J. Power Sources* **1997**, *64*, 131–137.
366. A. Kirchev, D. Pavlov, B. Monahov, *J. Power Sources* **2003**, *113*, 245–254.
367. Y. L. Guo, J. Y. Wu, L. K. Song et al., *J. Electrochem. Soc.* **2001**, *148*, A1287–A1293.
368. Z. H. Li, Y. L. Guo, L. Z. Wu et al., *J. Electrochem. Soc.* **2002**, *149*, A934–A938.
369. V. Srinivasan, G. Q. Wang, C. Y. Wang, *J. Electrochem. Soc.* **2003**, *150*, A316–A325.
370. M. P. Vinod, K. Vijayamohanan, *J. Power Sources* **2000**, *89*, 88–92.
371. A. Salkind, T. Atwater, P. Singh et al., *J. Power Sources* **2001**, *96*, 151–159.
372. A. J. Salkind, P. Singh, A. Cannone et al., *J. Power Sources* **2003**, *116*, 174–184.
373. A. Hazza, D. Pletcher, R. Wills, *Phys. Chem. Chem. Phys.* **2004**, *6*, 1773–1778.
374. G. Kokkinidis, D. Sazou, *J. Electroanal. Chem.* **1986**, *199*, 165–176.
375. K. Jüttner, *Electrochim. Acta* **1984**, *29*, 1597–1604.
376. K. Jüttner, *Electrochim. Acta* **1986**, *31*, 917–927.
377. G. Kokkinidis, A. Papoutsis, G. Papanastasiou, *J. Electroanal. Chem.* **1993**, *359*, 253–271.
378. A. Papoutsis, G. Kokkinidis, *J. Electroanal. Chem.* **1994**, *371*, 231–239.
379. S. J. Hsieh, A. A. Gewirth, *Surf. Sci.* **2002**, *498*, 147–160.
380. I. Oh, A. A. Gewirth, J. Kwak, *J. Catal.* **2003**, *213*, 17–22.
381. D. Pletcher, V. Solis, *J. Electroanal. Chem.* **1982**, *131*, 309–323.
382. X. H. Xia, T. Iwasita, *J. Electrochem. Soc.* **1993**, *140*, 2559–2565.
383. H.-W. Lei, H. Hattori, H. Kita, *Electrochim. Acta* **1996**, *41*, 1619–1628.
384. B. R. Eggins, C. Ennis, R. McConnell et al., *J. Appl. Electrochem.* **1997**, *27*, 706–712.
385. S. Kaneko, R. Iwao, K. Iiba et al., *Energy* **1998**, *23*, 1107–1112.
386. S. Q. Xia, S. P. Chen, S. G. Sun, *Acta Phys. Chem. Sin.* **2001**, *17*, 140–143.
387. P. L. Cabot, M. Centelles, L. Segarra et al., *J. Electrochem. Soc.* **1997**, *144*, 3749–3757.

388. I. M. Osadchenko, A. P. Tomilov, *Russ. J. Appl. Chem.* **1998**, *71*, 719–721.
389. N. Georgolios, G. Kyriacou, G. Ritzoulis, *J. Appl. Electrochem.* **2001**, *31*, 207–212.
390. S. T. Lin, R. Y. H. Chao, S. C. Lin et al., *J. Chin. Chem. Soc.* **2002**, *49*, 539–544.
391. B. F. Gianetti, C. M. V. B. Almeida, S. H. Bonilla et al., *Z. Phys. Chem.* **2003**, *217*, 35–44.
392. M. Bazzoui, E. A. Bazzoui, L. Martins et al., *Synth. Met.* **2002**, *130*, 73–83.
393. K. Wandachowicz, R. Dylewski, *Przem. Chem.* **1999**, *78*, 187–190.
394. S. Wasmus, W. Vielstich, *J. Electroanal. Chem.* **1993**, *359*, 175–191.
395. J. S. Ge, D. C. Johnson, *J. Electrochem. Soc.* **1996**, *143*, 2543–2548.
396. W. Gorski, R. T. Kennedy, *J. Electroanal. Chem.* **1997**, *424*, 43–48.
397. F. Bonfatti, S. Ferro, F. Lavezzo et al., *J. Electrochem. Soc.* **1999**, *146*, 2175–2179.
398. D. Pavlov, B. Monahov, *J. Electrochem. Soc.* **1996**, *143*, 3616–3629.
399. D. Pavlov, B. Monahov, *J. Electrochem. Soc.* **1998**, *145*, 70–77.
400. R. Amadelli, A. Maldotti, A. Molinari et al., *J. Electroanal. Chem.* **2002**, *534*, 1–12.
401. S. Abaci, K. Pekmez, A. Yildiz, *Electrochim. Commun.* **2005**, *7*, 328–332.
402. A. A. Babak, R. Amadelli, A. De Battisti et al., *Electrochim. Acta* **1994**, *39*, 1597–1602.
403. A. B. Velichenko, D. V. Girenko, S. V. Kovalyov et al., *J. Electroanal. Chem.* **1998**, *454*, 203–208.
404. C. N. Ho, B. J. Hwang, *J. Electroanal. Chem.* **1994**, *377*, 177–190.
405. R. Amadelli, L. Armelao, A. B. Velichenko et al., *Electrochim. Acta* **1999**, *45*, 713–720.
406. L. M. Da Silva, L. A. De Faria, J. F. C. Bootds, *Electrochim. Acta* **2003**, *48*, 699–709.
407. U. Schümann, P. Gründler, *Water Res.* **1998**, *39*, 2835–2842.
408. M. Panizza, G. Cerisola, *Electrochim. Acta* **2003**, *48*, 3491–3497.
409. R. Amadelli, A. De Battisti, D. V. Girenko et al., *Electrochim. Acta* **2000**, *46*, 341–347.
410. N. B. Tahar, A. Savall, *J. Appl. Electrochem.* **1999**, *29*, 277–283.
411. S. Abaci, U. Tamer, K. Pekmez et al., *Appl. Surf. Sci.* **2005**, *240*, 112–119.
412. C. Borrás, T. Laredo, J. Mostany et al., *Electrochim. Acta* **2004**, *49*, 641–648.
413. C. Borrás, T. Laredo, B. R. Scharifker, *Electrochim. Acta* **2003**, *48*, 2775–2780.
414. S. Abaci, U. Tamer, K. Pekmez et al., *J. Appl. Electrochem.* **2002**, *32*, 193–196.
415. I. H. Yeo, S. Kim, R. Jacobson et al., *J. Electrochem. Soc.* **1989**, *136*, 1395–1401.
416. B. J. Hwang, K. L. Lee, *Thin Solid Films* **1996**, *279*, 236–241.
417. S. Abaci, K. Pekmez, N. Pekmez et al., *J. Appl. Polym. Sci.* **2003**, *87*, 599–605.
418. S. Abaci, A. Yildiz, *J. Electroanal. Chem.* **2004**, *569*, 161–168.
419. S. Abaci, Y. Aslan, A. Yildiz, *J. Mater. Sci.* **2005**, *40*, 1163–1168.
420. P. Bühlmann, E. Pretsch, E. Bakker, *Chem. Rev.* **1998**, *98*, 1593–1687.
421. E. Bakker, M. Telting-Diaz, *Anal. Chem.* **2002**, *74*, 2781–2800.
422. E. Bakker, *Anal. Chem.* **2004**, *76*, 3285–3289.
423. E. Bakker, E. Pretsch, *Trends Anal. Chem.* **2005**, *24*, 199–207.
424. T. Sokalski, A. Ceresa, T. Zwickl et al., *J. Am. Chem. Soc.* **1997**, *119*, 11347–11348.
425. E. Bakker, E. Pretsch, *Trends Anal. Chem.* **2001**, *20*, 11–19.
426. E. Bakker, P. Bühlmann, E. Pretsch, *Electroanalysis* **1999**, *11*, 915–933.
427. É. Pergel, R. E. Gyurcsányi, K. Tóth et al., *Anal. Chem.* **2001**, *73*, 4249–4253.
428. J. Sutter, E. Lindner, R. E. Gyurcsányi et al., *Anal. Bioanal. Chem.* **2004**, *380*, 7–14.
429. J. Sutter, A. Radu, S. Peper et al., *Anal. Chim. Acta* **2004**, *523*, 53–59.
430. R. E. Gyurcsányi, É. Pergel, R. Nagy et al., *Anal. Chem.* **2001**, *73*, 2104–2111.
431. A. Ceresa, E. Pretsch, *Anal. Chim. Acta* **1999**, *395*, 41–52.
432. M. Foussaki, N. A. Chaniotakis, *Anal. Chem.* **2005**, *77*, 1780–1784.
433. N. P. R. Andersen, *Anal. Chim. Acta* **1998**, *368*, 191–196.
434. E. Fischer, C. M. G. van den Berg, *Anal. Chim. Acta* **1999**, *385*, 273–280.
435. O. Mikkelsen, K. H. Schroeder, *Electroanalysis* **2003**, *15*, 679–687.
436. M. Brand, I. Eshkenazi, E. Kirowa-Eisner, *Anal. Chem.* **1997**, *69*, 4660–4664.
437. O. Mikkelsen, K. H. Schroeder, *Electroanalysis* **2001**, *13*, 687–692.
438. Y. Bonfil, E. Kirowa-Eisner, *Anal. Chim. Acta* **2002**, *457*, 285–296.
439. Y. Bonfil, M. Brand, E. Kirowa-Eisner, *Anal. Chim. Acta* **2002**, *464*, 99–114.

440. B. Krasnodębska-Ostręga, J. Piekarska, *Electroanalysis* **2005**, *17*, 815–818.
441. Y. Bonfil, M. Brand, E. Kirowa-Eisner, *Electroanalysis* **2003**, *15*, 1369–1376.
442. P. N. Bartlett, G. Denault, M. F. B. Sousa, *Analyst* **2000**, *125*, 1135–1138.
443. J. M. Zen, H. H. Chung, G. Hangovan et al., *Analyst* **2000**, *125*, 1139–1146.
444. S. M. Silva, A. M. Bond, *Anal. Chim. Acta* **2003**, *500*, 307–321.
445. E. A. Osipova, V. E. Sladkov, A. I. Kamenev et al., *Anal. Chim. Acta* **2000**, *404*, 231–240.
446. M. A. Rahman, M. S. Won, Y. B. Shim, *Anal. Chem.* **2003**, *75*, 1123–1129.
447. C. Prado, S. J. Wilkins, F. Marken et al., *Electroanalysis* **2002**, *14*, 262–272.
448. R. I. Stefan, S. G. Bairu, *Talanta* **2004**, *63*, 605–608.
449. A. M. Bond, W. J. Miao, T. D. Smith et al., *Anal. Chim. Acta* **1999**, *396*, 203–213.
450. Z. Hu, C. J. Seliskar, W. R. Heineman, *Anal. Chim. Acta* **1998**, *369*, 93–101.
451. K. Wagner, J. W. Strojek, K. Koziel, *Anal. Chim. Acta* **2001**, *447*, 11–21.
452. K. Wagner, J. W. Strojek, K. Koziel, *Chem. Anal. (Warsaw)* **2002**, *47*, 385–397.
453. K. Wagner, J. W. Strojek, K. Koziel, *Anal. Chim. Acta* **2002**, *455*, 69–81.
454. A. M. Zimer, R. Bertholdo, M. T. Grassi et al., *Electrochim. Commun.* **2003**, *5*, 983–988.
455. M. Hepel, L. Dentrone, *Electroanalysis* **1996**, *8*, 996–1005.
456. A. Wanekaya, O. A. Sadik, *J. Electroanal. Chem.* **2002**, *537*, 135–143.
457. S. Majid, M. El Rhazi, A. Amine et al., *Microchim. Acta* **2003**, *143*, 195–204.
458. J. Wang, *Anal. Chem.* **1982**, *54*, 221–223.
459. P. R. M. Silva, M. A. El Khakani, B. Le Drogoff et al., *Sens. Actuators, B* **1999**, *60*, 161–167.
460. B. Le Drogoff, M. A. El Khakani, P. R. M. Silva et al., *Electroanalysis* **2001**, *13*, 1491–1496.
461. E. Juzeliunas, H. W. Pickering, K. G. Weil, *J. Electrochem. Soc.* **2000**, *147*, 1088–1095.
462. A. Herrero, M. C. Ortiz, *Anal. Chim. Acta* **1997**, *348*, 51–59.
463. Y. G. Mourzina, J. Schubert, W. Zander et al., *Electrochim. Acta* **2001**, *47*, 251–258.
464. G. S. Reeder, W. R. Heineman, *Sens. Actuators, B* **1998**, *52*, 58–64.
465. I. Palchetti, A. Cagnini, M. Mascini et al., *Mikrochim. Acta* **1999**, *131*, 65–73.
466. K. C. Honeychurch, J. P. Hart, D. C. Cowell, *Electroanalysis* **2000**, *12*, 171–177.
467. J. M. Zen, H. H. Chung, A. S. Kumar, *Anal. Chim. Acta* **2000**, *421*, 189–197.
468. N. Y. Stozhko, G. N. Lipunova, T. I. Maslakova et al., *J. Anal. Chem.* **2004**, *59*, 179–184.
469. I. Palchetti, G. Marazza, M. Mascini, *Anal. Lett.* **2001**, *34*, 813–824.
470. R. P. Akkermans, J. C. Ball, F. Marken et al., *Electroanalysis* **1998**, *10*, 26–32.
471. R. P. Akkermans, J. C. Ball, T. O. Rebbitt et al., *Electrochim. Acta* **1998**, *43*, 3443–3449.
472. A. N. Blythe, R. P. Akkermans, R. G. Compton, *Electroanalysis* **2000**, *12*, 16–20.
473. C. E. West, J. L. Hardcastle, R. G. Compton, *Electroanalysis* **2002**, *14*, 1470–1478.
474. C. E. Banks, R. G. Compton, *Electroanalysis* **2003**, *15*, 329–346.

Part B:
Electrochemistry of Gold, Silver, and Mercury*

*Marek Orlik and Zbigniew Galus
 Department of Chemistry, University of Warsaw, Warsaw, Poland*

**Dedicated to the memory of Professor Ralph N. Adams, a respected and unforgettable electrochemist and man*

**24.4
 Electrochemistry of Gold**

24.4.1	Preparation of Au Surfaces and Double-layer Properties	841
24.4.1.1	Polycrystalline (pc-Au) and Single-crystal Au/H ₂ O Interface	841
24.4.1.2	pc-Au and Single-crystal Au/Nonaqueous Solutions Interface	844
24.4.2	Adsorption of Inorganic Compounds on Gold Electrodes	845
24.4.2.1	Sulfate	845
24.4.2.2	Hydroxide	847
24.4.2.3	Nitrate	847
24.4.2.4	Chloride	847
24.4.2.5	Bromide	848
24.4.2.6	Iodide	849
24.4.2.7	Cyanide	851
24.4.2.8	Thiocyanate	852
24.4.2.9	Other Inorganic Species	852
24.4.3	Adsorption of Organic Compounds on Gold Electrodes	853
24.4.3.1	Adsorption of Sulfur-containing Compounds	853
24.4.3.1.1	Adsorption of Thiols	853
24.4.3.1.2	Adsorption of Modified Thiols	860
24.4.3.1.3	Adsorption of Thiourea	861
24.4.3.1.4	Adsorption of Disulfides and Related Compounds	861
24.4.3.1.5	Other Sulfur Compounds and Complex Adsorption Layers	863
24.4.3.2	Adsorption of Selenium-containing Compounds	866
24.4.3.3	Adsorption of Nitrogen-containing Compounds	866
24.4.3.3.1	Pyridine and its Derivatives	866
24.4.3.3.2	Pyrazine	870
24.4.3.3.3	Amines and Other Nitrogen-containing Compounds	870

24.4.3.4	Adsorption of Other Organic Compounds	870
24.4.3.4.1	Alcohols	870
24.4.3.4.2	Aminoacids	871
24.4.3.4.3	Other Organic Acids	872
24.4.3.4.4	Nucleic Bases and Other Biochemical Compounds	872
24.4.3.4.5	Other Compounds	875
24.4.4	Reconstruction of the Surface of Gold Electrodes	876
24.4.5	Formation of Oxides on Gold Electrodes	879
24.4.6	Underpotential Deposition of Various Metals on Au	883
24.4.6.1	Cu	883
24.4.6.2	Cd	886
24.4.6.3	Pd	888
24.4.6.4	S, Se, and Te	889
24.4.6.5	Sulfur	889
24.4.6.6	Selenium	889
24.4.6.7	Tellurium	890
24.4.6.8	Bi	890
24.4.6.9	Pt	892
24.4.6.10	Ni	892
24.4.6.11	Co	892
24.4.6.12	Sb	893
24.4.6.13	Sn	894
24.4.6.14	Al	894
24.4.6.15	Tl	894
24.4.6.16	Pb	895
24.4.6.17	Zn	895
24.4.6.18	Ge	895
24.4.6.19	Rh	896
24.4.6.20	Li	896
24.4.6.21	Fe	896
24.4.6.22	Ag	896
24.4.6.23	Hg	897
24.4.7	Electrochemistry of Coordination Compounds of Gold. Electrodissolution and Electrodeposition of Au	897
24.4.7.1	Au Electrodeposition	898
24.4.7.2	Au Electrodissolution	899
24.4.8	Gold Clusters	899
	References	900

In this chapter recent studies on electrochemistry of three noble metals, gold, silver, and mercury are presented.

In recent years, electrochemical studies of these metals and their compounds have been dominated by surface studies.

Three main groups of processes related to these metals have been intensively investigated:

1. underpotential deposition of different metals (ions),

2. specific adsorption of various neutral compounds and ions, and
3. self-assembling of various mostly sulfur-containing compounds on the surfaces of these noble metals.

In the study of solid metals, gold and silver single-crystal electrodes with well-defined surfaces were preferentially used.

A chapter on the electrochemistry of gold was published in the 4th volume of *Encyclopedia of Electrochemistry of the Elements* in 1975. At that time, mostly polycrystalline gold (pc-Au) electrodes were used, although already in the early sixties, the studies involving single-crystal electrodes had also been published. It appears from a review of the recent literature that polycrystalline gold electrodes are still in use; however, the following trends are emphasized the most:

1. wide use of single-crystal electrodes;
2. modification of gold electrode surfaces.

This review should, in principle, cover the literature on the electrochemistry of gold, which has been published over the last decade, though in some cases, the earlier literature also is discussed. However, a large number of papers on this subject make a comprehensive description difficult. Therefore, this chapter is focused only on the selected papers, which present the most representative trends and the most important results.

24.4.1 Preparation of Au Surfaces and Double-layer Properties

24.4.1.1 Polycrystalline (pc-Au) and Single-crystal Au/H₂O Interface

Detailed reviews on the properties of the pc-Au/H₂O interface have been published earlier by Frumkin [1], Hamelin [2], and

Vorotynsev [3], and more recently by Trasatti and Lust [4]. From the above papers, selected data have been taken and are presented below.

The potential corresponding to the minimum capacitance of the diffusion layer at the pc-Au|H₂O interface was found to be equal to -0.04 V (versus saturated calomel electrode, SCE), independently of the solution pH and NaF concentration studied. However, a slight negative shift of this potential with the increasing concentration of perchlorate ions was observed, thus suggesting a weak specific affinity of these anions to the gold surface. The role of surface contaminations could not be excluded as well. In spite of certain controversies, it seems that the GCSG theory is applicable to the description of the pc-Au|H₂O interface (taking into account the roughness factor), without any corrections for the crystallographic inhomogeneity of the metal surface [4–6]. This conclusion has become, however, also a subject of discussion since the crystalline Au faces of low indices, present on the pc-Au surface, have a characteristic size of 5–6 nm, which seems to be large enough to contribute to the surface inhomogeneity [4]. Noteworthy is the fact that the potential at the C₁ minimum is not equivalent to the zero charge potential [4].

In more recent studies, the double layer of a pc-Au electrode has been probed by atomic force microscopy (AFM) measurements [7]. The properties of the Au/solution interface were changed by variations in pH, salt concentration, and electrode potential.

Piela and Wrona [8] have employed impedance spectroscopy to study capacitance of the pc-Au electrode in 0.5 M H₂SO₄ in the double-layer potential region (-0.25 to 1.05 V versus SSCE) and

in the range corresponding to the formation of the oxide monolayer (1.05–1.4 V). In the latter case, it has been found that capacitance depends on the surface coverage with partially pure gold surface, MOH dipoles, oxide, or reconstructed gold surface. A simple equivalent circuit (without the constant phase element (CPE)) was found to be appropriate for the interpretation of the impedance data for both the pure gold surface and the surface covered with the oxide layer. The observed capacity versus electrode potential dependence, different from that for the mercury electrode, was attributed to the strong adsorption of (bi)sulfate ions. However, the roughness factor for the Au surface, both in the double layer and in the oxide formation region, was very low and comparable to that for the Hg electrode.

Hoogvliet et al. [9] have proposed a pulsed-potential pretreatment procedure, which allows one to decrease, in a reproducible manner, surface roughness of mechanically polished polycrystalline gold electrodes by a factor of 2.

Some methods of nanoscale preparation of gold surfaces have also been described. For instance, gold nanowell electrode arrays of a well depth of about 50 nm were prepared [10] by electrodeposition of Au through the pores of a porous alumina membrane. Nanoelectrode arrays were characterized using scanning tunneling microscopy (STM), AFM, scanning

electron microscopy, and electrochemical methods.

While considering single-crystal Au electrodes, attention should be drawn to the quite comprehensive review of the most recent achievements in the studies on the properties of these electrodes brought in contact with different solutions [4].

In electrochemical practice, mainly three types of gold surfaces, that is, Au(111), Au(110), and Au(100) are of the greatest importance, whereas other surfaces, as, for example, Au(210) are less frequently described in electrochemical papers.

The potentials of zero charge of single-crystal Au electrodes of various crystallographic orientations in contact with aqueous electrolyte solutions are given in Table 1.

It follows from the above data, similarly as for Ag, that the potential of zero charge increases with the surface density of atoms.

In Ref. 13, a new approach toward the preparation of Au(111) nanoisland-arrayed electrode based on fine colloidal nanolayer-directed seeding growth has been presented.

Chemically prepared colloidal gold nanoparticles were immobilized as a submonolayer on Au(111) surface modified with self-assembled monolayers (SAMs) of 4-aminothiophenol [14]. This submonolayer of Au nanoparticles was subsequently characterized using STM.

Tab. 1 Surface density of atoms, σ_{at} , and potentials of zero charge, E_{pzc} (versus SHE) for various crystal planes of Au electrodes [4, 11, 12]. Lattice constant $d = 0.2884 \text{ nm}$

Au crystal plane	$\sigma_{at}[\text{at.} \cdot \text{nm}^{-2}]$	$E_{pzc}[\text{V}](0.05\text{M NaF})$	$E_{pzc}[\text{V}](0.01\text{M HClO}_4)$
(111)	13.88	0.56 ± 0.01	0.52 ± 0.01
(100)	12.02	0.30 ± 0.01	0.29 ± 0.01
(110)	8.50	0.19 ± 0.01	0.19 ± 0.01

Dieluweit and Giesen [15] have presented STM studies on the dynamics of monolayer Au islands on Au(100) electrode surface in sulfuric acid solutions. The authors have given a quantitative description of the equilibrium shape of Au islands on Au(100) electrodes and of their thermal fluctuations around the equilibrium shape. Later, the same researchers [16] have applied STM to investigate a monolayer of Au islands on Au(100) electrode in H_2SO_4 solutions.

Bilger and Pettinger [17] have applied second-harmonic generation (SHG) method to study the anisotropy of Au(110) electrode in a wide potential range from -0.60 to 0.60 V, corresponding to the transition from the microfaceted to the unreconstructed surface.

Also, modulation resistometry of a gold electrode has been applied [18]. Mazine et al. [19] have used *in situ* reflectance anisotropy spectroscopy and *in situ* STM to characterize Au(100) surface in 0.1 M Na_2SO_4 solutions. Three ranges of the applied potential were distinguished: (1) negative potentials up to about -0.6 V (versus $\text{Ag}|\text{AgCl}$), for which clear (1×3) reconstruction is obtained, (2) positive potentials up to about $+0.6$ V, for which the surface remains unreconstructed, and (3) intermediate potential range corresponding to the mixed domains.

Au(111) and Au(210) electrodes have been investigated [20] using electrochemical impedance spectroscopy in aqueous solutions of HClO_4 and KF in the double-layer potential region, in order to identify and explain frequency dispersion of interfacial capacitance. At negative potentials, the behavior closest to the ideal dispersionless behavior has always been observed. In KF solutions, at positive potentials, dispersion on both electrodes may be attributed

to the adsorption of either OH^- or HF species.

Adsorption of some inorganic or organic compounds can facilitate formation of well-defined Au surfaces. Trevor et al. [21] have found that a roughened Au(111) surface undergoes “electrochemical annealing” associated with surface migration of Au atoms. It has also been observed that the step motion is significantly accelerated by the adsorbed chloride ions. Baumgärtel and coworkers [22, 23], using cyclic voltammetry (CV), capacitance measurements, *in situ* STM, and combined *in situ* IR and STM, have studied adsorption of tetramethylthiourea (TMTU) and adsorbate-induced etching of Au(111). It has been found that etching at sufficiently anodic potentials leads to the formation of Au-TMTU complexes soluble in the electrolyte solution. This soluble complex can be subsequently electrodeposited at more negative potentials. Etching and deposition processes are schematically depicted in Fig. 1 [23].

In a detailed discussion about the properties of single-crystal Au electrodes in contact with aqueous solutions, it is necessary to consider water molecules adjacent to the Au surface. Hydrophilic properties of single-crystal Au electrodes have been studied by determining the dependence of the Gibbs energy of adsorption of 2-ethylether on the electrode potential [24]. It has been found that water molecules particularly are strongly bound to Au(110) surfaces, accordingly to the sequence of the decreasing Gibbs energies of adsorption of 2-ethylether: Au(111) $>$ Au(100) $>$ Au(110). The structure of various Au surfaces has also been inferred from the studies on temperature coefficient of pzc (for a concise review, see Ref. 4). Finally, Ignaczak and Gomes

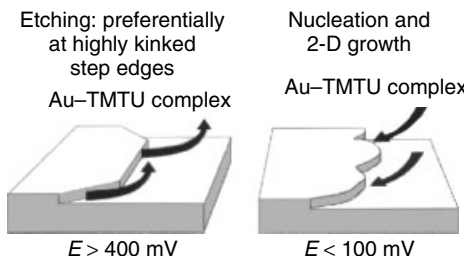


Fig. 1 The scheme of anisotropic surface etching and isotropic deposition of Au-TMTU complexes at step edges of the Au(111) surface in TMTU-containing electrolytes [23].

[25] have studied theoretically, an interaction of water molecule with Au(100), Ag(100), and Cu(100) surfaces, applying a cluster model approximation with Au-12, Ag-12, and Cu-12 clusters to mimic the (100) crystallographic plane. Two preferred conformations: bridge-perpendicular and top-tilted have been found indistinguishable in terms of adsorption energy. In both conformations, water molecule adsorbs via oxygen atom.

Under specific conditions, the potential of zero charge does not appear to be constant during electrochemical experiment, which makes the double-layer effect more complex. For example, the shift of the potential of zero charge during electroreduction of $S_2O_8^{2-}$, combined with the Frumkin-type double-layer effect, has been proposed [26] as an explanation for the oscillatory reduction of peroxodisulfate on Au(110) in diluted solutions of NaF.

24.4.1.2 pc-Au and Single-crystal Au/Nonaqueous Solutions Interface

Double layer at both pc-Au and single-crystal Au electrodes brought in contact with such nonaqueous solvents as dimethylsulfoxide (DMSO), dimethylformamide (DMF), acetonitrile, propylene carbonate (PC), and selected alcohols has also been studied. The experimental methods used involved CV and impedance measurements, except for butanol isomers, for which surface-enhanced

Raman spectroscopy (SERS) technique was also employed [27].

For example, Jarząbek and Borkowska [28] have found that the double-layer capacitance for the pc-Au|DMSO interface is significantly lower than for mercury (except for very negative charge densities). However, reproducibility of the results concerning double layer at pc-Au, as well as at single-crystal (111), (110), (100), and (210) Au electrodes, was limited, since the capacitance-potential relationships were time-dependent and, for instance, after about 1 h, a pseudostable C_d-E dependence was observed [4]. In consequence, conclusions could be drawn only for these pseudostable states. For DMSO solutions, the following sequence of the potentials of the capacitance minimum has been found: (111) \leq (100) $<$ pc-Au \leq (110) $<$ (210), whereas for aqueous solutions, this sequence is reversed [4]. Another conclusion from these studies was that Au-DMSO interactions are stronger than Au-H₂O interactions, the former ones also being more sensitive to the atomic structure of the Au surface [29].

More data regarding Au|nonaqueous solvent interfaces, including surface preparation problems, can be found elsewhere [4] and in references cited therein. Table 2 summarizes selected values of the potential of zero charge for the pc-Au electrodes in contact with some solvent-electrolyte systems.

Tab. 2 Potentials of zero charge (E_{pzc}) for pc-Au electrode in contact with selected nonaqueous solvent–electrolyte systems. The pzc for pc-Au|H₂O is equal to 0.20 V versus aqueous standard hydrogen electrode (SHE) and 0.85 V versus bis(biphenyl)chromium(I)/(0) redox couple (BBCr) [4]

Solvent–electrolyte system	E_{pzc} [V versus aqueous SHE]	E_{pzc} [V versus BBCr]	References
Dimethylsulfoxide + LiClO ₄	0.39	0.99	28
Acetonitrile + KPF ₆	0.90	1.49	30
Propylene carbonate + NaClO ₄	0.44	1.11	28, 31
N, N-Dimethylformamide + LiClO ₄	0.51	1.02	32
MeOH + 0.4M LiBr + 0.1M LiClO ₄	0.25	0.81	33

24.4.2 Adsorption of Inorganic Compounds on Gold Electrodes

The effect of the supporting electrolyte on the E_{pzc} of Au electrodes indicates specific affinity of either cations or anions of the dissolved salt to the given surface. For example, the studies performed by Hamelin [34] have shown the effect of the supporting electrolyte on the double-layer capacity – potential curves (see Table 3).

From these data, it follows that in aqueous solutions, sulfate ions exhibit relatively high affinity to the gold surface, which is reflected in the least positive value of E_{min} . In view of this important role of sulfate ions, their adsorption will be described below in more detail.

24.4.2.1 Sulfate

Adsorption of sulfate species at pc-Au electrode has been studied [35] in HF–KF buffer of pH = 2.8 applying Fourier transform infrared spectroscopy (FTIR). Adsorption of sulfate starts at 0.4 V versus Pd/H₂ (which is about 0.28 V more positive than the zero charge potential). Adsorption reaches a maximum at 1.2 V. At any potential applied, a band between 1165 and 1193 cm⁻¹ was observed. It was ascribed to the adsorbed SO₄²⁻. Adsorption

Tab. 3 The effect of the supporting electrolyte (in aqueous solution) on the potential (versus SHE) of the minimum of the double-layer capacitance [11, 34] of the Au(100) electrode surface

Electrolyte	E_{min} [V]
1 mM KPF ₆	+0.325 ± 0.005
10 mM LiClO ₄	+0.308 ± 0.01
10 mM NaF	+0.333 ± 0.01
2 mM H ₂ SO ₄	+0.242 ± 0.01
1 mM HClO ₄	+0.253 ± 0.005

of sulfate anions on Au(111) electrodes has been discussed later by Lipkowski and coworkers [36]. Quantitative characteristics of this process (together with the data for halide ions) are presented in Fig. 2.

Więckowski and coworkers [37] have reported adsorption of bisulfate anions on Au(111), Pt(111), and Rh(111) electrodes in sulfuric acid solution using electrochemical and several nonelectrochemical techniques. It was concluded from the low-energy electron-diffraction data that the structure of bisulfate on gold is different from that on Pt(111) and Rh(111). Adsorption of bisulfate on Au(111) is associated with a charge transfer from the electrode to the adsorbate. However, the formation of this particular bond does

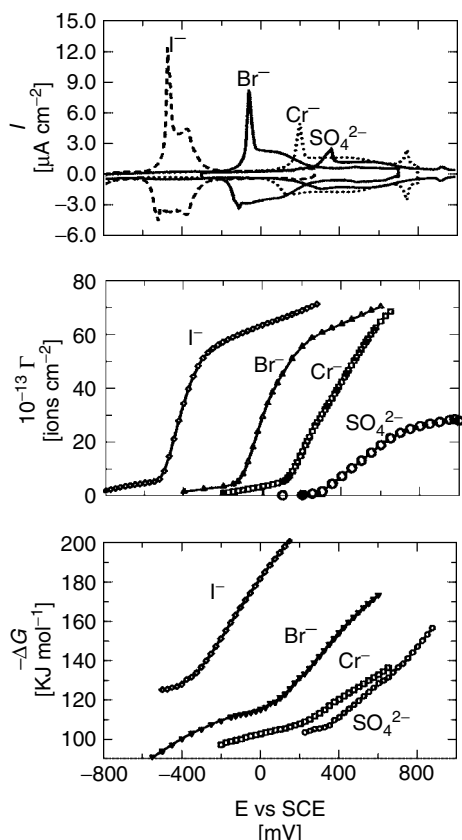


Fig. 2 Comparison of SO_4^{2-} , Cl^- , Br^- , and I^- adsorption at the Au(111) electrode surface from 0.1 M $\text{HClO}_4 + 10^{-3}$ M K_2SO_4 and 0.1 M $\text{KClO}_4 + 10^{-3}$ M KCl, KBr, and KI solutions. (a) Cyclic voltammograms at $v = 10 \text{ mV s}^{-1}$. (b) Gibbs surface excess versus potential. (c) Gibbs energy of adsorption versus potential. The standard state corresponds to the surface coverage $\Gamma = 1 \text{ ion per cm}^2$ and bulk concentration $c = 1 \text{ mol dm}^{-3}$ [36].

not significantly modify the band structure of the metal, which suggests that electrostatic forces mainly contribute to this bonding [38, 39]. Kolb and coworkers [40], using *in situ* STM, have observed an ordered adlayer of either sulfate or bisulfate ions at the unreconstructed Au(100) surface in 0.1 M H_2SO_4 . This adlayer is formed concomitantly with the lifting of the (hex)-reconstruction. In consequence, the newly generated layer consists of sulfate/bisulfate molecules ordered in rows that run parallel to the edges of the islands formed in the (hex) \rightarrow (1 \times 1) transition. Kolb and coworkers [41] have studied adsorption of sulfate anions (from 0.1 M H_2SO_4 and 0.1 M

Na_2SO_4), also in the presence of phosphates (from 0.1 M H_3PO_4 and 0.1 M $\text{KH}_2\text{PO}_4 + 0.1$ M K_2HPO_4), on Au(111) and Au(100) using *in situ* STM. Hirai et al. [42] have investigated the potential dependence of the decay of multilayered islands on Au(100) electrode in 0.05 M aqueous solution of H_2SO_4 , applying *in situ* AFM.

In all the above cases, surface distribution of anions was nonuniform. Apparently, this is a characteristic feature common to oxoanion adlayers because of their ability to form bridging hydrogen bonds via the lone electron pairs at their oxygen atoms. Since, in neutral solution, no ordered adsorption was

observed, one may deduce that coadsorption of hydronium ions is necessary to stabilize an ordered oxoanion lattice.

Recently, the change in the interfacial free energy and surface stress has been determined for Au(111) electrodes in electrolytes containing nonspecifically adsorbed F^- anions. This behavior was compared to that of specifically adsorbed SO_4^{2-} anions [43]. It was found that the surface stress is more sensitive to the changes in electrode potential than the interfacial free energy.

Some attention has also been paid to the simultaneous adsorption of sulfate anions and organic compounds. Futamata [44] has detected coadsorption of water molecules and sulfate species with uracil on polycrystalline gold electrode, applying attenuated total reflection-infrared spectroscopy. The adsorbed sulfate species appeared either as SO_4^{2-} or HSO_4^- , depending on the pH of the electrolyte solution. Skołuda [45] has presented a voltammetric study of the Au(100) electrode in the presence of alkyl sulfate. Dutkiewicz and Skołuda [46] have investigated adsorption of benzenesulfonate anions at the Au(111) electrode, using CV and differential capacity measurements.

24.4.2.2 Hydroxide

Hamelin [47] has shown that specific adsorption of OH^- ions increases in the following order: Au(111) < Au(100) < Au(311). Chen and Lipkowski [48] have applied chronocoulometry and subtractively normalized interfacial Fourier transform infrared spectroscopy to study adsorption of hydroxide ions on Au(111) electrode. This process proceeded in three steps. Bonding of OH^- with gold atoms that is quite polar at negatively charged surface becomes less polar at positively

charged electrode surface. Oxide formation starts at higher charge densities, when surface concentration of hydroxide ions exceeds one-third of a monolayer. Interfacial properties of pc-Au electrode in tetramethylammonium hydroxide solutions of concentrations ranging from 5×10^{-3} to 4.0 M have been studied using CV and impedance spectroscopy [49]. At highly negative potentials, the double-layer capacity has been found to depend on the kind of cations and to remain independent of their concentration. Strong adsorption of hydroxide anions was observed in wide concentration and potential ranges.

24.4.2.3 Nitrate

Marinkovic et al. [50] have used in situ IR reflection spectroscopy to study adsorption of nitrate ions on Au(111) electrodes. The ions were bonded to the gold surface via one of their oxygen atoms. Within the double-layer NO_3^- formed contact ion pairs with hydronium ions. The extent of this process depended on the applied potential.

24.4.2.4 Chloride

Więckowski and coworkers [51] have carried out electrochemical and radiochemical studies of Cl^- adsorption using radioactive ^{36}Cl . By combining radiochemical measurements with CV experiments, the potential dependence of adsorption and surface-bulk exchange processes has been studied.

Also, Cuesta and Kolb [52] have employed STM to investigate adsorption of chloride ions on Au(100) surfaces.

Shi and Lipkowski [53] have presented a thermodynamic analysis of charge density data. The study aimed at the description of adsorption of chloride on Au(111)

electrode surface and calculation of basic corresponding parameters. Chloride ions were attached to gold via chemisorption. Polarity of the formed bond strongly depended on the charge of the metal. Polarity decreased significantly when the charge attained positive values.

The role of chloride ions in the anodic dissolution of Au(111) in perchloric acid solutions has been studied in Ref. 54. The mechanism of anodic dissolution was discussed in relation to the structure of the chloride adlayer on the Au(111) electrode surface.

24.4.2.5 Bromide

Thermodynamic analysis of charge density resulted in the description of bromide adsorption on Au(111) electrode [55]. Bromide ions are chemisorbed at the gold surface and polarity of the formed bonds strongly depends on the metal charge. Polarity drops significantly when the surface charge changes from negative to positive values. The second-harmonic generation studies indicate that adsorption of bromide ions strongly affects electronic structure of the metal surface.

Bromide adsorption on Au(111) has also been studied, applying *in situ* surface X-ray scattering (SXS) and STM [56]. The potential-dependent adlayer density agreed well with the earlier published bromide surface excess densities, obtained in electrochemical measurements. At very positive potentials, a bromide-induced step-flow etching of Au occurred.

Ocko et al. [57, 58] have studied adsorption of bromide on Au(100) using *in situ* surface X-ray diffraction (SXD) in combination with electrochemical measurements. Low surface excess of bromide ions at Au(100)-(hex) caused a lifting of the

surface reconstruction. This process proceeded at high overpotentials via instantaneous nucleation and two-dimensional growth. Two ordered bromide adlayer phases were found at unreconstructed Au(100)-(1 × 1) surface.

These studies led to the detailed assignment of voltammetric features of bromide adsorption to the respective structural properties, stability, and transition kinetics.

Adsorption of Br⁻ on Au(111) has already been exemplified in Fig. 2, taken from Ref. 59. In Ref. 59, in turn, the dependence of phase transition on the electrode potential accompanying adsorption of Br⁻ on Au(100) has been investigated (see Figs 3 and 4).

Cuesta and Kolb [52] have studied bromide adsorption on Au(100) electrodes using *in situ* STM. Two quasi-hexagonal structures were found, which was in agreement with the previously published SXS data.

Wang and Rikvold [60] have applied ab initio total-energy density-functional methods in combination with supercell models to calculate the c(2 × 2) structure of bromide adsorbed on Au(100) and Ag(100) surfaces. The preferred bonding sites have been determined. The calculations have shown that bromide favorably binds the bridge site on the Au(100) surfaces. These results explain experimental observations that adsorption of bromide on the Au(100) and Ag(100) surfaces proceeds via different bonding configurations.

Lipkowski and coworkers [61] have analyzed the relationship between the changes in the bromide surface composition on Au(100) electrode and its specific behavior observed in CV.

Finally, Adzic and Wang [62], and Wang et al. [63] have studied the formation of thallium bromide on Au(111) electrode

Fig. 3 Linear sweep voltammogram ($v = 10 \text{ mV s}^{-1}$) for Au(100) in 0.05 M NaBr [59].

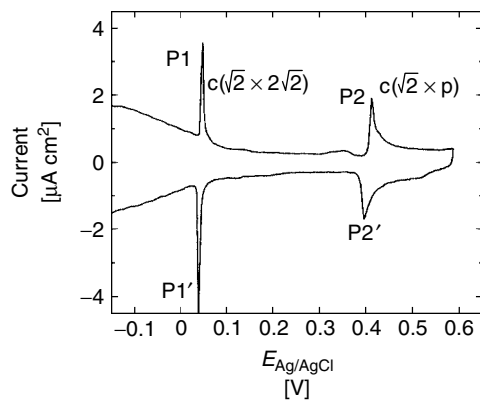
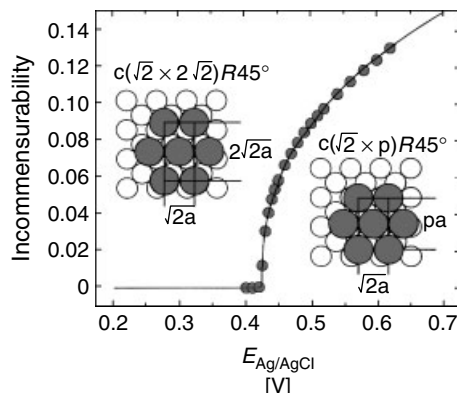


Fig. 4 The incommensurability versus electrode potential dependence for adsorption of Br^- on Au(100). Insets: atomic models of Br^- adlayers corresponding to the potentials below and above the critical point of phase transition [59].



induced by bromide adsorption. They have observed: (1) an underpotential shift for deposition of Tl on Au(111) in the presence of Br^- , (2) a formation of two mixed adlayers of two surface compounds TlBr_2^- and TlBr , and (3) a very complex structural behavior of this system. The above phenomena are related to underpotential deposition (UPD) that is reviewed in more detail in a later section.

Mitchell and Koper [64] have involved the density-functional theory to determine the parameters necessary for the construction of an off-lattice model with no freely adjustable parameters for Br^- electrodeposition on Au(100).

The simulation results were satisfactorily consistent with the experimental findings.

24.4.2.6 Iodide

Electrochemical quartz crystal microbalance (EQCM) has been used [65] to study adsorption/desorption of iodide on Au(111) electrodes. The coverages obtained at different potentials were quite close to those estimated from STM images and SXS measurements.

Iodine adlayers covering an Au(111) electrode have been characterized [66] and shown to be convenient substrates for the studies on adsorption of various organic molecules [66, 67].

Chen et al. [68] have performed chrono-coulometric studies of adsorption of iodide on Au(111) electrode and calculated the parameters describing this process quantitatively. As in the case of chloride and bromide adsorption, iodide also formed quite polar chemisorption bond at the negatively charged surface. However, the polarity dropped significantly when the charge of the electrode attained positive values. At high charge densities and coverages, the chemisorption bond had a predominantly covalent character. The strength of halide adsorption and covalent character of the bond increased progressively from chloride to iodide.

It has been found [69] that alkali metal cations coadsorb with iodide ions on Au(110) electrode at potentials more positive than the potential of Au(110) reconstruction and more negative than the potential of the formation of iodine monolayers. The coverages of both the cationic and anionic species in KI, NaI, and LiI solutions decrease with the increasing electrode potential.

Seo and Ueno [70] have used a piezoelectric technique to detect the changes in the surface energy of gold electrode in 1.0 M NaClO₄ solutions in the presence and absence of iodide ions. Additions of iodide moved the potential of zero charge to the negative direction, compared to the value determined from the piezoelectric signal curve, which points at the strong contact adsorption of iodide ions.

Chang et al. [71] have studied adsorption of iodine, iodo benzene, iodo heptane, and 1,4-dihydroxy-2-iodobenzene on Au(111) electrode from 0.1 M HClO₄ solutions using CV and STM. The results obtained indicate that organic iodide molecules are significantly decomposed upon their adsorption to give an iodine layer and alkyl

and aryl organic fragments dissolved in the solution.

A physical model and a theory have been proposed [72], which might be helpful in comparative studies on electrocompressive behavior of electrodeposited chloride, bromide, and iodide monolayers on the Au(111) electrode. The theoretical results were in good agreement with the experimental data, which evidence that the adatom–adatom interactions (especially repulsive ones) and electrosorption valency of halide anions determine the compressibility within halide adlayers. Also, Lipkowski et al. have discussed various aspects of adsorption of halide anions on Au(111) in a review paper [36]. From this paper, we have taken quantitative data concerning adsorption of halide anions on Au(111) (cf. Fig. 3).

Kerner and Pajkossy [73] have measured impedance spectra for Au(111) electrode in perchlorate solutions additionally containing SO₄²⁻, Cl⁻, Br⁻, and I⁻ at concentrations of about 10⁻⁴ M. Measurements were performed at adsorption potentials of these anions. Analysis of the impedance spectra led the authors to the conclusion that the adsorption rates of SO₄²⁻ and Cl⁻ are immeasurably high. For halide anions, the apparent rate coefficient changes in the order I⁻ < Br⁻ < Cl⁻ and decreases with the increasing electrode potential and coverage.

The SHG surface spectroscopy is another method useful in the studies on halide adsorption. Applicability of the SHG spectroscopy method to Au surface properties has been discovered by Pettinger, Kolb, and coworkers [74, 75]. It has also been shown that reconstruction of Au(111) and Au(100) electrodes remarkably affects SHG anisotropy [74]. For this reason, an interference second-harmonic generation anisotropy (ISHGA)

method has been recently applied to the analysis of structural changes of Au(110) surface and to study the effect of adsorption of halide ions on Au(111) (see Ref. 74 and references cited therein). In the light of these studies, it is interesting to note that Gao et al. [76] have performed surface reconstruction of Au(110) in 0.1 M HClO₄ solution as a function of electrode potential using atomic resolution STM.

24.4.2.7 Cyanide

Studies on adsorption of CN⁻ ions (and other pseudohalide ions) on both pc-Au and single-crystal electrodes are particularly important in view of their role in

metal etching and dissolution processes [77]. From potential-evolved differential frequency generation (DFG) measurements, it has been found that in the aqueous solution: 0.1 M NaClO₄ + 0.025 M KCN, adsorption of CN⁻ starts at -1.35 V (SCE) on Au(110), at -1.05 V on Au(100), and at -0.85 V on Au(111) [78]. The results of electrochemical measurements are concordant with these findings (see Fig. 5) and have been compared with earlier electrochemical studies using the pc-Au electrode [79].

Evidently, the CN⁻-Au interactions are the strongest at more open Au(110) surface, and this conclusion correlates well with the dependence of pzc on the type

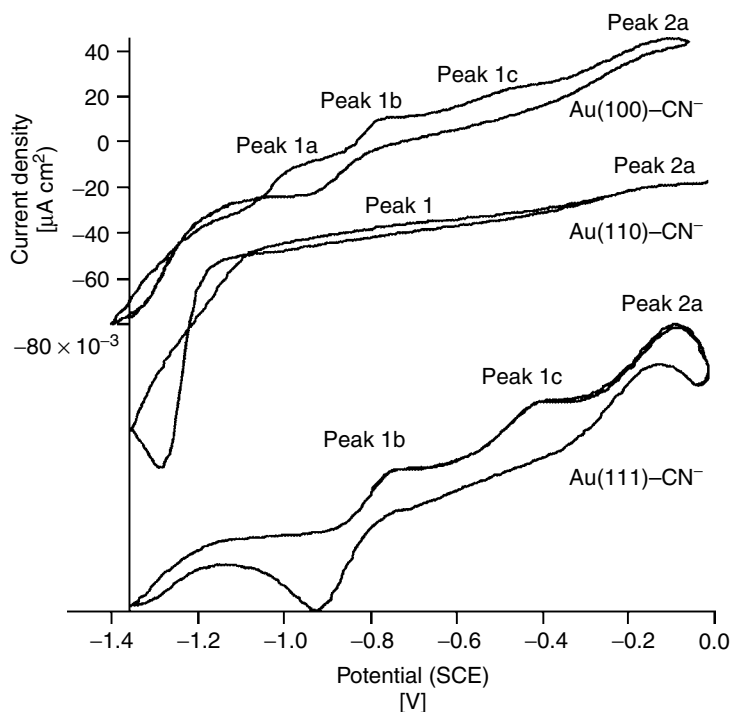
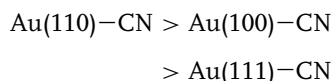


Fig. 5 Cyclic voltammograms of Au(110), Au(100), and Au(111) electrodes brought in contact with an aqueous solution of 0.1 M NaClO₄ and 0.025 M KCN; direction of polarization: from -1.35 to 0 V (versus SCE), sweep rate: 200 mV s⁻¹, CV after 10 cycles [77].

of Au surface (the pzc value in CN^- -free solutions attains the most negative value) [77, 80]. It has also been found that the rate of CN^- adsorption is roughly the same for all surface orientations, while the rate of CN^- desorption is the highest for Au(111), compared to Au(100) and Au(110) [77].

Adsorption of cyanide anions can be affected by adsorption of cations. In the solutions containing nonspecifically adsorbed anions, the nature of alkali metal cations was found to influence the measured value of the electrode capacitance at potentials more negative than -0.6 V (versus standard hydrogen electrode (SHE)). At $E < -1.0$ V adsorption of CN^- ions was enhanced in the presence of Li^+ and Na^+ cations, and inhibited in the presence of Cs^+ ions [81]. A combined SERS and density-functional theory has been applied to study cyanide adsorption at Au electrode [82]. The authors have arrived at the conclusion that the polarity of Au–CN bonds falls between that of Au–Cl and Au–Br surface bonds. The binding strength for three different gold surfaces decreased in the order:



and agreed with the order of bond ionicity.

24.4.2.8 Thiocyanate

Adsorption of thiocyanate ions on Au electrodes from alkaline solutions has been studied using *in situ* IR spectroscopy and SERS [83]. Even at negative potentials, adsorption of thiocyanate was observed, which occurred via Au–S interaction. At higher concentration of OH^- ions, the bond strength between the adsorbed SCN^- ion and the surface was decreased. At very positive potentials, both the oxidation of thiocyanate to cyanate and the

formation of a gold–thiocyanate complex were observed.

24.4.2.9 Other Inorganic Species

Jusys and Bruckenstein [84] have used electrochemical quartz crystal microbalance to study adsorption/desorption of perchlorate and perrhenate ions on a bare polycrystalline Au electrode. The change in the equivalent mass was undoubtedly assigned to the adsorption of both anions in the double-layer region of Au electrode.

Adsorption of ammonia on the Au(111) surface at $1/4$ and $1/2$ of the monolayer coverage has been theoretically modeled [85].

Hexacyanoferrates were immobilized on Au covered with SAM of 3,3'-thiodipropionic acid [86]. It has been found from voltammetric studies that the surface coverage of hexacyanoferrate is close to one monolayer and such an electrode exhibits very good surface redox behavior. Cheng et al. [87] have described the formation of an extremely thin multilayer film of polybasic lanthanide heteropolytungstate–molybdate complex and cationic polymer of quaternary poly(4-vinylpyridine), partially complexed with osmium bis(2,2'-bipyridine) on a gold electrode precoated with a cysteamine SAM. Consequently, adsorption of inorganic species might also be related to the properties of SAMs. This problem will be discussed in detail in a separate section later.

Oznuluer and Demir [88] have employed electrochemical atomic layer epitaxy (ALE) to the investigations of kinetics of structural changes occurring within initial monolayers of thin Bi_2S_3 films on Au(111).

Finally, adsorption of CO on Au(111) surface has been investigated under reduced pressure in the range from 10^{-3} to 10^3 Tr at the room temperature [89].

24.4.3 Adsorption of Organic Compounds on Gold Electrodes

24.4.3.1 Adsorption of Sulfur-containing Compounds

Evidently, adsorption of chemical compounds at gold surfaces via specific Au–S interactions has been very intensively studied for the last twenty years. In a recent review [90], Vericat et al. have described their own results of electrochemical, *in situ* STM, X-ray photoelectron spectroscopy (XPS), and SXD studies on adsorption of sulfur on Au(111). It has been stated that S–Au bonds determine the structure and adsorption/desorption kinetics for both S–Au(111) and alkanethiolate/Au(111) systems in NaOH.

Application of self-assembling has given a great impetus for the studies of Au surfaces modified with sulfur compounds. Such processes were already described a long-time ago [91], however, more intensive investigations have been initiated by seminal paper of Nuzzo and Allara [92], published in 1983. Self-assembling is very well suited to easily obtain well-ordered structures as very strong, specific adsorption of molecules with a sulfur atom in their terminal groups directs these molecules exactly to the gold surface.

Interest in these studies arises from fundamental research where monolayers serve as models of biomimetic systems, as well as from important applications of such systems in molecular and bioelectronic devices, in sensors constructions, corrosion/inhibition phenomena, and synthesis of nanostructures [93]. Although self-assembly processes of sulfur-containing compounds occur at the surfaces of many metals, especially the copper-group metals (Cu, Ag, Au), the most extensive studies have been

carried out on the modification of gold electrodes.

Even a very brief description of numerous papers published in the recent years was often beyond the scope of this work. Instead, a concise presentation of general properties of adsorption and desorption processes and electrochemical properties of such modified electrodes will be given.

24.4.3.1.1 Adsorption of Thiols Self-assembly of alkanethiols (RSH) on gold has especially been studied intensively. In this case, adsorption proceeds via formation of chemical bond between surface gold atoms and sulfur atoms of alkanethiols. Adsorption is further supported by hydrophobic interactions between the alkyl chains. The quality of self-assembled layers depends on a number of factors, such as morphology of the substrate [94], and temperature [95]. For successful deposition, it is very important to use highly purified solvent and reagents [96]. The electrode surface should also be thoroughly cleaned; however, some researchers claim that very careful cleaning is less important in view of the very strong interaction of sulfur with gold [97]. Concentration of the solution used for deposition and duration of deposition also play a key role in the preparation of the layers of good quality. The above factors are interrelated. The lower the thiol concentration, the longer the deposition time that is required to achieve a given surface coverage. In order to investigate the influence of these and other parameters on the quality of a monolayer, as well as the completeness of the surface coverage, the process of reductive desorption has been employed.

Modification of the gold surface in the self-assembly approach proceeds after dipping the gold electrode into the solution

containing the corresponding thiol [98]:



Porter and coworkers [98] who have used pc-Au electrodes and have examined monolayers of *n*-alkanethiols $\text{C}_n\text{H}_{2n+1}\text{SH}$ with $n = 3\text{--}10, 12, 16,$ and 18 , have found the surface coverage to be independent of n and equal to $9.3 (\pm 0.6) \times 10^{-10} \text{ mol cm}^{-2}$. Assuming that the real surface area of pc-Au electrode is 1.2 times larger than the geometric surface area, this is consistent with structures proposed on the basis of different experiments in which monolayers of various long-chain *n*-alkanethiols were found to form a $(\sqrt{3} \times \sqrt{3})R30^\circ$ overlayer structure on Au surfaces of predominantly (111) character. The charge associated with the reduction of monolayers of above-mentioned *n*-alkanethiols was found to be $(90 \pm 7) \mu\text{C cm}^{-2}$ and was independent of the chain length of the studied alkanethiols.

Taking into account the above-given surface coverage, the final result of Porter and coworkers [98] is written in the form of the reaction:



This 1e electrode reaction implies the loss of the thiol hydrogen and the oxidation of the S to a formal oxidation state of -1 upon adsorption of *n*-alkanethiol (RSH) at Au.

The results obtained on the double-layer properties show that the studied monolayers may be represented by a two-capacitors-in-series model. One capacitor corresponds to the thiol head-group region of the monolayer and the second to the hydrocarbon phase.

Porter and coworkers [98] have been the first to have performed electroreductive desorption of alkanethiols from the gold

surface. The charge, the shape, and the potential of the cathodic peak provided important information on the SAMs. Electroreduction was carried out in alkaline (KOH) solution. Desorption process was easily observable in cyclic voltammograms. Depending on the conditions, reductive desorption peak appeared between -0.7 and -1.4 V (versus SCE) [99–101]. The value of the peak potential depended on several parameters, including the length of the carbon chain in thiol molecule.

Formation of the thiol layer may occur also in the anodic process.

It is, however, noteworthy that despite quite intensive studies, the *detailed* mechanism of thiol adsorption is still not well known [102]. Even the most commonly accepted fact that the adsorbed species are thiolate anions (RS^-) is also questioned. In order to elucidate adsorption mechanism in more detail, Cohen-Atiya and Mandler [102] have studied potentiometrically, the effect of chain length of solvent molecules, end groups, and the nature of surface (Au, Ag, and Hg). The obtained results have confirmed again that thiol adsorption process is complex and is affected by the solvent, the nature of the surface, and also by the presence of additional functional groups in thiol molecules. When thiol was added to the electrolyte solution, a sudden shift of the potential to the negative range was noticed in the open-circuit potential experiment. This is indicative of the transfer of negative charge from the thiol group to the electrode surface during adsorption process and formation of the M–S bond. As a result, the H–S bond should be cleaved. In some cases, the authors have observed that negative potential shift is followed by a gradual shift to positive potentials, reflecting a discharge process, which probably might proceed via a reduction process.

The scheme in Fig. 6 illustrates the mechanism proposed by Cohen-Atiya and Mandler [102].

Cohen-Atiya and Mandler have also found that the extent of discharging process is significantly decreased in aprotic solutions and in the absence of oxygen. However, the influence of additional functional groups located at the other end of thiol molecules on the discharging process is still not fully understood. Possibly, such groups (e.g. carboxylic) affect accessibility of water to the electrode surface.

Brett et al. [103] have studied self-assembling of 1-decanethiol at the fixed positive potentials of pc-Au electrode in chronoamperometry and quartz crystal microgravimetry. The obtained layers appeared to have improved quality and were produced faster than in the open-circuit deposition. The factors possibly influencing the fine structure of monolayers observed in voltammetric reductive desorption and oxidative redeposition of long-chain alkane thiols, for example, hexadecanethiol (HT) and octadecanethiol on smooth Au electrodes have been discussed [104]. It has been shown that the local order of adlayer has a role to play in the formation of that fine structure.

There are also some papers in electrochemistry aimed at the estimation of

properties of generated monolayers. Since these papers are only loosely connected with the electrochemistry of gold, we refer to them very briefly. French and Creager [105] have found that oxidation of gold at the electrode surface and oxidation of $\text{Fe}(\text{CN})_6^{4-}$ is inhibited up to +1.6 V (versus Ag/AgCl electrode) when octanol-saturated solutions of pH 5 (buffer) and dodecanethiol monolayer-coated Au electrode are used. Octanol molecules fill in the defects in the monolayer and thus make the thickness of the barrier layer increase, causing inhibition of electrode reactions.

Passivating behavior of self-assembled octadecanethiol on pc-Au electrodes has been tested by CV using $\text{Ru}(\text{NH}_3)_6\text{Cl}_3$, $\text{K}_4\text{Fe}(\text{CN})_6$, and benzoquinone [106] as the redox probes. Inhibiting properties toward these reactants were found to be different.

Inhibiting properties may be influenced by the solvent molecules trapped within the monolayer during self-assembly of octadecanethiol molecules on gold electrodes [107].

Capacitance and charge-transfer rates of SAM of ω -(4'-methyl-biphenyl-4-yl)-alkanethiols ($\text{CH}_3-\text{C}_6\text{H}_4-\text{C}_6\text{H}_4-(\text{CH}_2)_n-\text{SH}$, $n = 0-6$) adsorbed on pc-Au have also been investigated. For $n = 1-6$, the reciprocal capacity exhibited a linear dependence on the alkane spacer

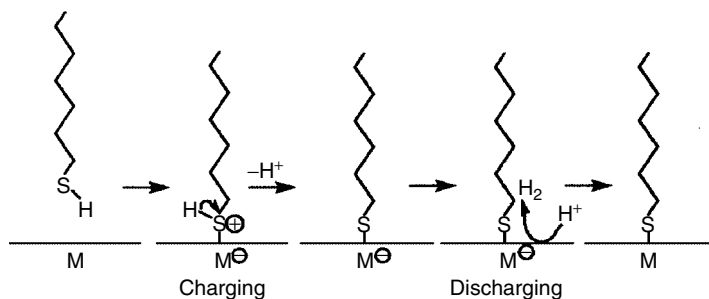


Fig. 6 Schematic representation of the mechanism of thiol adsorption on different metal surfaces [102].

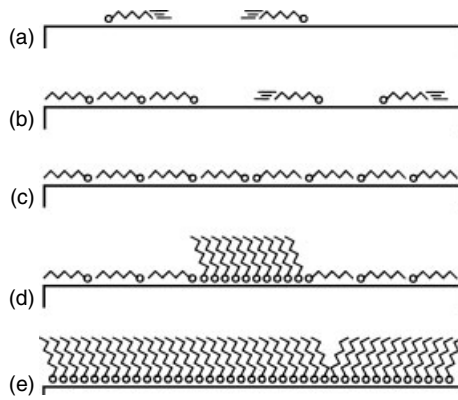


Fig. 7 Schematic of self-assembly mechanism for alkanethiols on Au(111).
 (a) Thiols adopt the highly mobile lattice-gas phase at very low coverage.
 (b) Above a critical value of surface coverage, striped-phase islands, characterized by surface-aligned molecular axes, nucleate heterogeneously, and grow in equilibrium with a constant pressure lattice gas. (c) Surface reaches saturation coverage of striped phase.
 (d) Surface undergoes lateral-pressure-induced solid–solid phase transition by nucleation of high-density islands at striped-phase domain boundaries. (e) High-density islands grow at the expense of the striped phase until the surface reaches saturation [110].

length. The incremental change of $0.054 \pm 0.0036 \text{ cm}^2 \mu\text{F}^{-1}$ per CH_2 group and the calculated dielectric permittivity of $\epsilon = 2.5$ agreed well with the data for *n*-alkanethiols [108].

For Hg–Au junctions containing bilayers of alkanethiols of different chain lengths, *I*–*E* curves were symmetrical with respect to the polarity of the voltage bias. Larger current was measured when a negative bias was applied to the metal modified with a monolayer of longer alkanethiol chains [109].

Au(111) electrodes. The schematic representation of the formation of the SAM of alkanethiols on Au(111) is shown in Fig. 7 [110].

Beardmore et al. [111] have presented a realistic empirical potential function to model the head-group interaction for SAMs of alkanethiols on Au(111). The main result of these calculations is that the barriers within the surface corrugation potential are too small to pin S atoms at any particular site.

It has been shown [112] that for low concentrations of thiols in the solution,

the kinetics of their self-assembly as a monolayer on Au(111) surface is limited by diffusion, and not by surface kinetics. When the coverage is low, alkanethiols are arranged on Au(111) in the striped structures and vacancy islands of the gold surface are created. At high coverages, the structure is $(\sqrt{3} \times \sqrt{3})R30^\circ$ and/or $c(4 \times 2)$ with a tilt angle of approximately 30° from the surface normal [113–115]. Alkanethiols are adsorbed on Au(111) in such a way that one sulfur atom corresponds to three gold atoms at the surface. STM studies have shown that the monolayers are seriously subjected to defects by missing rows and pits [116–118]. The missing-row defects arise from the orientational and translational domain boundaries. Density of the pits was found to be strongly dependent on the solvent [119] and the temperature [120] at which the self-assembly process was carried out. Wano and Uosaki [121] have studied electrochemical desorption process of hexanethiol from Au(111) surfaces in H_2SO_4 and KOH aqueous solutions. They have found that desorption begins at the defects

of monolayers. They have also found that desorbed thiolates form aggregates in H₂SO₄ solution. In CV experiments, after electroreduction, the electrode potential was scanned to positive values and a smaller anodic peak corresponding to the oxidative readsorption of some of the desorbed alkanethiolates was observed (see, for instance, Ref. 122). The anodic and cathodic peak potentials depended on the concentration of thiols [122]. Kolb and coworkers [123] have applied *in situ* STM and CV to study SAMs of ethanethiol on Au(111) electrodes. Electrochemical studies in 0.1 M H₂SO₄ have shown that at -0.31 V versus SCE, ethanethiol is reductively desorbed, while oxidative desorption of this thiol occurs at +1.15 V. Both processes were monitored in STM measurements. At potentials slightly negative of 0 V, the adlayer underwent structural transformation, which finally led to the formation of small pits and islands on the surface. In case of decanethiol on Au(111) and with an increasing concentration of decanethiol, both cathodic and anodic peaks were shifted to negative potentials by about 57 mV/decade, independently of the sweep rate (in the range 0.01 – 0.2 V s⁻¹). Assuming that the electrode reaction occurred according to Eq. (1) in both directions, and that the monolayer activity a_{Mon} was independent of the thiol concentration, one arrives at [122]:

$$E_{1/2} = E'_0 - 0.059 \log a_{\text{C10S}} - \text{constant} \quad (3)$$

where a_{C10S} is the activity of decanethiol. This equation is consistent with the experimental results [122] and confirms that oxidation and reduction proceeded as one-electron processes.

From electrochemical and STM experiments, as well as from density

functional theory (DFT) calculations, it can be concluded [124] that the difference between experimentally observed peak potentials for reductive desorption of a given alkanethiolate from Ag(111) and Au(111) surfaces is determined by the energy required to introduce an electron into the adsorbed alkanethiolate-metal species, by desorption energy of the alkanethiolate anion, and by the solvent/metal interaction energy. Moreover, the position of the peak depends on the alkyl chains. It has been found that the longer the alkyl chain, the more negative the reduction peak potential is, probably due to stronger attractive interaction between alkyl chains [98].

The measurement of the charge involved in the reductive desorption of layers prepared under various conditions provides very important information about the surface coverage and the nature of the oxidative adsorption. The influence of time and thiol concentration on both the potential and the charge of the reductive desorption has been investigated for decanethiol adsorbed on Au(111) [125] (see Fig. 8).

In these experiments, Au(111) electrode was immersed in 0.1 M KOH solutions with 10 µM, 100 µM and 1 mM C₁₀SH and kept at the constant potential of +0.1 V for a certain time. After that, the potential was scanned to more negative values in order to record the cathodic peak current. These and other experiments have proved that the saturated coverage is obtained after a sufficiently long holding time. The same applies to the cathodic peak potential also. Sumi and Uosaki [125] have found that the maximum reaction charge is equal to 103 (±5%) µC cm⁻². Two components contribute to the measured total charge: the first is produced in reaction (1), and the second is the capacitance charge

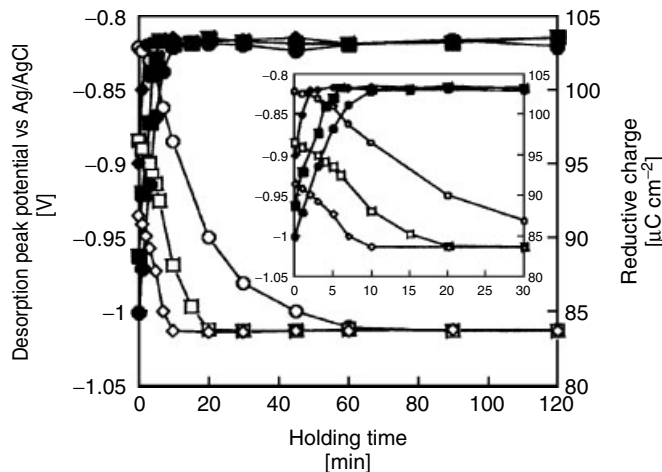


Fig. 8 Cathodic peak potential (empty symbols) and cathodic wave charge (filled symbols) as a function of holding time at +0.1 V in 0.1 M KOH ethanolic solutions containing 10 μM (\circ , \bullet), 100 μM (\square , \blacksquare), and 1 mM (\diamond , \blacklozenge) decanethiol. Inset shows the initial stage of the above relations. All data concerning reductive charge contain $\pm 5\%$ error [125].

arising from the difference in the double-layer capacity of the thiol-covered and bare surface. The value of 103 ($\pm 5\%$) $\mu\text{C cm}^{-2}$ agrees with the values reported for the reductive desorption of SAMs of other thiols with saturated coverage and a $(\sqrt{3} \times \sqrt{3})R30^\circ$ structure, which were formed in ethanol solutions containing only alkanethiol without the potential control [126–128]. The determined total charge equaled 103 ($\pm 10\%$) $\mu\text{C cm}^{-2}$ and comprised 73.3 $\mu\text{C cm}^{-2}$ of the Faradaic charge contribution due to reaction (1) and 30 $\mu\text{C cm}^{-2}$ of double-layer recharging contribution [126, 127, 129]. Also, the rate constant of the reductive desorption of decanethiol was determined from the peak potential versus scan rate relationship and equaled to 0.24 s^{-1} . A very close value was found for nonanethiol [125, 130].

In the formation of self-assembled layer, one can distinguish three steps [131, 132]. The first step lasts for several seconds and obeys chemisorption and formation

of Au–S bond. In this step, a coverage of about 80–90% is achieved. The second step consists of straightening of the alkyl chains. The third step is the slowest and obeys reorientation of terminal group. Reorientation is accompanied by some changes in the reduction peak potential, although the surface coverage remains practically unchanged. Reorganization may take several hours and has been monitored in contact angle, ellipsometry, and FTIR studies [93, 133–135].

In situ and ex situ STM studies of self-assembled butanethiol/Au(111) have been performed [136] in order to determine the ground-state configuration and long-term behavior of this system at room temperature. The results have shown that the most stable surface structure is a $c(4 \times 2)$ reconstruction of the basic $(\sqrt{3} \times \sqrt{3})R30^\circ$ adsorption site geometry containing four distinguishable molecules. This structure is extremely sensitive to the presence of defects in the substrate. Probably, the

limiting factor leading to the formation of $c(4 \times 2)$ domains is the preexistence of large atomically flat Au(111) terraces that cover evenly at least 200–400 nm² without any defects.

Yang and Morin [137] have presented vibrational studies of reorganization of the electrical double layer, following reduction of the self-assembled nonanethiol monolayer on Au(111). The absence of changes in the vibrational spectra recorded at potentials covering the double-layer range confirmed the stability of this monolayer over the range of 800 mV. Significant changes in the vibrational spectra of water molecules were observed when the applied potential was more negative than the reduction potential of the thiol monolayer. Interactions between water molecules and gold electrode support were modified by the electrode potential.

Poirier [138] has studied phase stability of decanethiol on the Au(111) surface.

In the voltammogram of Au(111) modified with binary SAM of 1-undecanethiol and 11-mercaptopoundecanoic acid, only one reductive desorption peak was formed for any value of mixing ratio of both thiols [139]. Such a response suggests that both thiols are well mixed in the SAM.

Arce et al. [140, 141] have studied the dynamics of 1-dodecanethiol and butanethiol SAMs on Au(111), applying ex situ and in situ STM. The potential of zero charge for the thiol-modified Au(111) electrode was determined for self-assembled monolayers of octadecanethiolate (−0.52 V), undecanethiolate (−0.49 V), propanethiolate (−0.3 V), and $1H,1H,2H,2H$ -perfluorodecanethiolate (1.04 V) [142]. The potentials (expressed versus Ag|AgCl|saturated KCl electrode) were determined from the measurements of the contact angle for a droplet of 0.1 M NaClO₄ aqueous solution.

Also, the potential dependence of ultrafast relaxation at electrochemical interfaces of 1-dodecanethiol- and 1-HT-modified Au(111) electrodes has been investigated in HClO₄ and H₂SO₄ solutions, applying transient reflectivity measurements [143]. The decay time constants found ranged from 100 to 300 fs and depended on the potential, interface modification, and the electrolyte used.

Hara et al. [144] have observed, in STM studies, an ordered nucleation of two-dimensional molecular islands at the initial growth stage.

It has been found [145] that the self-assembly of thiol molecules on Au(111) from ethanolic solution depends significantly on the electrode potential. Especially at cathodic potentials, chemisorption of thiol molecules and the development of a highly ordered structure are slowed down significantly.

Self-assembly of alkanethiols on Ag(1 × 1)-Au(111) obtained under conditions of UPD has been studied applying STM, Auger electron spectroscopy, and electrochemical techniques [146]. Even for the adsorbed short-chain alkanethiolates, the surface structure exhibited an incommensurable hexagonal lattice with the nearest-neighbor distances of approximately 0.48 nm that is usually found for long-chain alkanethiolates adsorbed on Ag(111).

Au(100) electrodes. Self-assembled thiol layers on Au(100) have also been studied. Kolb and coworkers [147] have investigated the potential-induced structure transitions in SAMs of ethanethiol in 0.1 M H₂SO₄ using STM. After modification, the STM images obtained in air exhibited a disordered thiol adlayer and Au islands of monoatomic height on about 25% of the surface. The islands originated from the lifting of the (hex) reconstruction during

thiol adsorption. In contrast to alkanethiol monolayers on Au(111), no vacancy islands were seen on the Au(100) surface.

Kolb and coworkers [148] have investigated SAMs of butanethiol applying CV and *in situ* STM. Adlayers comprised ordered domains of a striped structure, with the stripes running parallel to the main crystallographic axes of the substrate. Adsorption and desorption of butanethiol on Au(100)-(5 × 20) in ultrahigh vacuum have been studied using temperature-programmed desorption/reaction, low-energy electron diffraction, and Auger electron spectroscopy [149]. Physisorbed and chemisorbed states were shown to exist and desorb at quite different temperatures. Yamada and Uosaki [150] have presented structural investigations on decanethiol SAMs on the reconstructed and Au(100)-(1 × 1) surfaces using STM in air. Molecular arrangements of monolayers on both surfaces were similar to the c(2 × 8) structure with (1 × 4) gold row missing.

24.4.3.1.2 Adsorption of Modified Thiols
Amino-amido-thiol HS-(CH₂)₁₀-CO-NH-CH₂-NH₂ adsorbed on Au(111) has been studied by sum frequency generation and infrared reflection absorption spectroscopy (IRAS) in the CH₂ stretching vibration region [151].

Organized multilayers of ferrocene alkyl thiol have been self-assembled on Au(111) under conditions of controlled thiol concentration. Several methods, such as CV, ellipsometry, STM, AFM, and *in situ* FTIR spectroscopy have been applied in these studies in order to find out the differences between mono- and multilayers of the same compound [152]. Similar compounds, namely, short-chain alkyl thiols ($n = 3-10$) with ferrocene terminal group were allowed to form organized monolayers at Au(111) surfaces [153].

Applying subtractively normalized interfacial Fourier transform infrared spectroscopy, it has been found that electrooxidation of ferrocene groups is accompanied by rotation of these groups in such a manner that the plane of cyclopentadienyl rings turns to the position normal to the electrode surface. Also, biferrocenyl alkanethiols self-assembled on Au(111) surface and gold nanoclusters have been studied using various spectroscopic and electrochemical methods (CV) [154]. In the voltammogram, two reversible one-electron peaks were observed for both surfaces. Also, multilayered Au nanoclusters covered with mixed self-assembled alkanethiol monolayers containing methyl, ferrocene, or carboxylic terminal groups were obtained on Au(111) surface, and electrochemically characterized [155].

Gold electrodes covered with nonelectroactive alkanethiolate monolayers with amide bonds have been used to study the kinetics of long-range electron transfer, applying hexachloroiridate(IV) ion as the redox probe [156]. Ferrocene units were also attached [157] as terminal groups to alkanethiol molecules bonded via sulfur to the gold electrode support. These molecules were diluted with alkanethiol molecules without any reactive groups attached. Again, the rate of charge transfer between the ferrocene group and the electrode was calculated using voltammetry and chronoamperometry. Similarly, charge transfer occurring between the gold electrode and the ferrocene group attached to organic monolayer films with oligoglycine spacers has been studied [158].

Benzethiol adsorbs on Au(111) from the aqueous solution to form a well-ordered monolayer of a commensurate ($\sqrt{13} \times \sqrt{13}$)R13.9° symmetry [159]. It has been found that the ordered phase

is formed in 0.1 mM aqueous solution in several minutes. Further immersion results in the formation of multilayers.

Oxidative electrodeposition of three isomers of benzenedimethanethiol on Au(111) from alkaline aqueous solutions has been studied by Rifai and Morin [160]. All isomers were found to adsorb onto gold via sulfur and to form complete monolayers.

Kuwabata et al. [161] have prepared, via electrochemical polymerization on Au(111), SAMs comprising aminobenzenethiol and 3-aminophenethylthiol units. Polymerization of aminobenzenethiol required the use of ortho and meta isomers in the molar ratio of 1:1, whereas, in contrast, 3-amino-phenethylthiol was easily polymerized as a pure substance. The monolayers obtained exhibited electrochemical properties very similar to those of polyaniline and their derivatives.

24.4.3.1.3 Adsorption of Thiourea Earlier study of adsorption of thiourea on pc-Au electrode from aqueous solutions of KClO_4 and HClO_4 were carried out by Holze and Schomaker [162]. The adsorbed compound is perpendicularly oriented with sulfur atom interacting with the gold surface.

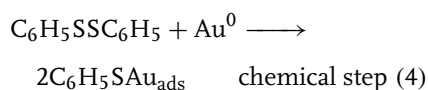
Azzaroni et al. [163] have used STM to study electrochemical reactivity of thiourea toward Au(111). Sequential STM imaging has shown that thiourea adsorbs as striped arrays that evolve to the hexagonal close-packed structure when surface charge density is decreased. The transient hcp structure undergoes electrooxidation to formamidine disulfide, which slowly yields adsorbed sulfur. Adsorption of thiourea on the pc-Au electrode from KClO_4 solutions has also been studied [164]. The film pressure and the Gibbs surface

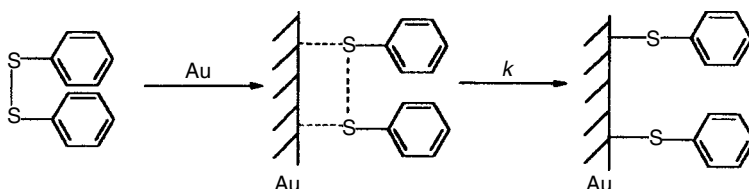
excess were determined as a function of potential applying CV differential capacity measurements and chronocoulometry.

Oxidation of thiourea adsorbed on Au(111) and pc-Au electrode in 0.1 M HClO_4 has been investigated using CV, in situ Fourier transform infrared spectroscopy, and differential electrochemical mass spectrometry [165]. Two reaction mechanisms were proposed for the oxidation of the adsorbed and nonadsorbed thiourea. For both types of Au electrodes, similar results were obtained.

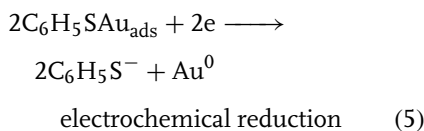
24.4.3.1.4 Adsorption of Disulfides and Related Compounds Adsorption and further electrode reactions of different disulfides at gold electrodes depend on chemical properties of the adsorbates. It has been evidenced in some papers that at least for some disulfides, adsorption process involves the cleavage of the S–S bond. Adsorption of diphenyl disulfide on a polycrystalline gold electrode has been studied in detail by Borsari et al. [166]. They have proposed the mechanism of adsorption shown in Scheme 1:

The gas–liquid chromatography with mass spectrometric detection (GLC-MS) analysis of the electrolyzed solution has shown that thiophenol is the only reduction product and the S–S bond cleavage is quantitative. Such a mechanism of bond breaking was confirmed by electrochemical studies. In cyclic voltammograms, anodic and cathodic peak potentials were the same for thiophenol and diphenyl disulfides; thus the same species were participating in these processes. Electrode reactions of diphenyl disulfide are given by the following equations [166]:

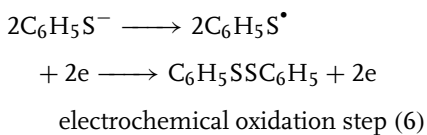




Scheme 1



and finally:



Similar behavior of other aromatic disulfides and thiols on gold electrodes has been described based on the SERS experiments [167]. Adsorption of benzenethiol, benzenemethanethiol, *p*-cyanobenzenemethanethiol, diphenyl sulfide, and dibenzyl sulfide was studied on the roughened gold electrode. All these species adsorb dissociatively as the corresponding thiolates. Monolayers formed from symmetric disulfides were exactly like those formed from the corresponding thiols. These monolayers were stable in a wide potential window: from +800 to −1000 mV (versus SCE), which was limited by the oxidation of the Au surface from the positive side and hydrogen evolution at −1000 to −1200 mV at the negative side.

Also, reductive desorption of SAMs of such asymmetrical disulfides as butyl hexadecyl disulfide and decyl-2(perifluoro-hexyl)ethyl disulfide has been studied on Au(111), using CV [168]. Peak potentials corresponding to electrochemical desorption waves of the adsorbed species were different from those obtained for monolayers

of the corresponding symmetrical disulfides (containing two identical chains). Possibly, these results reflect the process of mixing of the two constituent chains in the molecular scale.

Electrochemistry of disulfide unit present in cytochrome *c* (cyt *c*) molecules on gold electrodes has also been reported [169]. Disulfide unit in cytochrome *c* is strongly adsorbed on Au electrodes and this slows down the electron-transfer rate to the heme group. More recently, Krylov et al. [170] have immobilized cytochrome *c* by self-assembling on the surface-modified Au electrodes. CV was applied to study how denaturation and renaturation of cytochrome *c* depend on the solution composition.

Investigation of thiol- and disulfide-modified oligonucleotides with either 25 or 10 bases, or base pairs immobilized on polycrystalline and Au(111) electrodes has also been carried out [171]. In these studies, several techniques were employed, including X-ray photoelectron spectroscopy, cyclic and differential pulse voltammetry, interfacial capacitance data, and *in situ* STM.

Photoelectrochemical assemblies consisting of gold nanoparticles and a tris (2,2'-bipyridine)ruthenium(II)-viologen – disulfide derivative ($[\text{RuVS}]_2$) were obtained at gold electrodes by virtue of combination of the salting-out effect and self-assembly process [172].

The adsorbed state of heptyl viologen on the Au(111) electrode surface was

interrogated by *in situ* IRAS [173]. Both the dication HV^{2+} and the monocation HV^+ were detected. Complex spectral changes were observed when the electrode potential was varied. Recrystallization phenomena in bulk deposits of cation radical salts occurred more readily at Au(100) than Au(110) and Au(111) surfaces. Atomic arrangement of the gold electrode surface significantly affected the structure of adsorbed viologens.

Cysteine and cystine. Monolayers of L-cysteine and L-cystine assembled on Au(111) form highly ordered network-like clusters of a $(3\sqrt{3} \times 6)R30^\circ$ structure, as it has been shown in *in situ* STM and electrochemical studies [174]. Each cluster includes six molecules of cysteine or three molecules of cystine. One may assume that inter- and intramolecular hydrogen bonds between the adsorbed cysteine or cystine units are responsible for the observed structures, as they are not observed for 1-butanethiol adlayer under identical conditions. Adsorption of cysteine on Au(111) surface has been studied theoretically [175], involving periodic supercell density-functional theory calculations. Different adsorption modes were considered in these calculations. The strength of N–Au and S–Au adsorption bonds for amino-thiolate was estimated to be of the order of 6 and 47 kcal mol⁻¹, respectively. Hager and Brolo [176] have studied adsorption and desorption processes of the cysteine/cystine (thiol/disulfide) redox couple in neutral (0.1 M KClO₄) and basic (0.1 M NaOH) media on Au(111) electrodes. In 0.1 M KClO₄, adsorption peaks corresponding to cysteine and cystine were formed at 0.43 and 0.57 V (versus SCE), respectively. This difference in peak potentials reflects different adsorption properties of the thiol and disulfide species. Similar behavior was also

observed in 0.1 M NaOH. Disulfide was adsorbed when the applied potential was held at values more positive than +0.25 V in KClO₄ and -0.20 V in NaOH (versus SCE). The corresponding thiol (cysteine) was the only adsorbed species when the applied potentials were more negative than +0.25 V and -0.20 V in KClO₄ and NaOH, respectively. Thiol monolayers exhibited higher packing density than their disulfide counterparts.

24.4.3.1.5 Other Sulfur Compounds and Complex Adsorption Layers Adsorption of 5-(octyldithio)-2-nitrobenzoic acid on a gold electrode has been investigated using a quartz crystal microbalance [177]. This adsorption follows the Freundlich isotherm. AFM images of the films obtained in 10 mM ethanolic solution of the studied acid exhibited dramatically different morphologies, which were ascribed to the formation of multilayered aggregates.

Dijksma et al. [178] have described the formation of SAMs of thioctic acid on pc-Au electrodes in phosphate buffer of pH = 7.4. It has been found that potentiostatically formed monolayers of this acid have better characteristics than those generated under the open-circuit conditions. Also, a new strategy toward fast immobilization of thioctic SAM has been described [179]. It involved placing the known quantity of thioctic acid solution on a gold electrode surface. This way, one obtained modified electrodes that can be used in the preparation of sensors.

Yong and Beng [180] have deposited monolayers of 2-mercaptopbenzothiazole and 2-mercaptopbenzimidazole on Au surfaces from diluted ethanolic solutions and have studied their electrochemical behavior.

Che and Cabrera [181] have investigated molecular recognition based on

self-assembled (3-mercaptopropyl) trimethoxysilane monolayer on a gold surface.

Electrochemical dimerization of 2(2'-thienyl)pyridine adsorbed on Au(111) has been observed, applying *in situ* fluorescence [182]. The structure and electrochemical properties of 4,4'-dithiopyridine (PySSPy) on Au(111) have been investigated as well [183]. The S–S bond was broken during adsorption and the compound was attached to the Au surface via sulfur. Coadsorption of 2-mercaptopurimidine and 2,2'-bipyridine on Au(111) has been studied by STM [184]. 2,2'-Bipyridine molecule was adsorbed vertically via nitrogen. Mutual adsorbate–adsorbate interactions occurred as π -stacking. The behavior of 2-mercaptobenzimidazole SAM monolayer at the Au(111) electrode has been examined using CV and *in situ* FTIR spectroscopy [185]. The charge involved in reductive desorption was pH independent, while the oxidative partial redeposition charge increased with the decreasing pH. In alkaline and neutral media, 2-mercaptobenzimidazole desorbs as the thiolate anion, and in acidic solutions, as the neutral thiol [185].

CV investigations of 6-mercaptopurine and 8-mercatoquinoline SAMs on pc-Au electrodes have been presented by Madueno et al. [186] and He et al. [187], respectively. Several model electrode reactions involving various redox probes were studied using such modified electrodes. Baunach and Kolb et al. [188] have deposited copper on disordered benzyl mercaptan film on Au(111) surfaces. They have also studied the behavior of benzyl mercaptan SAM on Au(111) in H₂SO₄ solution using CV and STM. Structural and electrical properties of SAMs based on tetrathiafulvalene derivatives on Au(111) were investigated. These monolayers were disordered, or at least loosely

packed. Conduction through these molecular SAMs is remarkably high (due to the tetrathiafulvalene moiety).

Also, self-assembled layers of functionalized oligo(cyclohexylidene) molecules on Au(111) electrodes have been studied [189]. Their morphology has been investigated using STM and AFM. Dudek et al. [190] have studied electrochemical properties of SAMs comprising the mixture of ferrocene-terminated oligo(phenylenevinylene) methyl thiol and an alkanethiol diluent on gold electrodes. Szafrański et al. [191] have applied SERS to characterize monolayers of *p*-substituted benzenethiols and *p*-substituted benzenemethanethiols (substituents –F, Cl, Br) on gold electrodes. The studied compounds (six) existed on the surface as thiolate molecules of aromatic rings tilted with respect to the surface normal. They formed monolayers, which were stable at the surface in the potential range from +800 mV to –1000 mV (versus SCE) in neutral solutions.

It has been described [192] that the orientation of 2-mercaptomethylthiophene molecules adsorbed on Au(111) is almost vertical at the saturation coverage. At low coverage, in turn, the molecules form striped islands, within which the thiophene rings are tilted by $45 \pm 10^\circ$ with respect to the surface normal.

Mazur and Krysiński [193] have presented a comparative study of electrodeposition of poly(3-octylthiophene) films on gold electrodes – bare and modified with a dodecanethiol monomolecular layer. The polymer deposited on the thiol-coated electrode was more compact. There is also a significant interest in adsorption of organic compounds containing two functional groups in their molecules. Sulfur-containing group directly participates in the formation of bond with the gold surface, while another group, such as

$-\text{COOH}$, $-\text{NH}_2$, or $-\text{OH}$, participates in the interaction with other molecules in the solutions. We briefly present the selected papers on this topic below.

Adsorption of 2,3-dimercaptopropane sulfonate on Au(111) in alkaline solutions has been studied by Yang et al. [194]. STM studies have revealed that adsorption involves reorientation in the primarily formed adlayer and a slow lifting of the reconstruction. It has been shown that ω -mercaptohexanoic acid SAMs on pc-Au electrodes are stable and exhibit catalytic property toward redox reaction of chlorophylls [195]. Using SERS, it has been demonstrated that mercaptoethylamine is adsorbed on a gold electrode in the mixed trans and gauche conformations [196], initially at 0.0 V (versus Ag|AgCl). When the potential is changed anodically or cathodically over the range: +0.4 to -0.8 V, the population of adsorbate molecules switches mostly to the gauche conformation.

Zhang et al. [197] have studied adsorption of DL-homocysteine and L-homocysteine thiolactone on Au(111) electrode in 0.1 M HClO₄ using CV and STM. Both compounds formed highly ordered adlayer on Au(111). For both adlayers, structural models have been proposed.

Dopamine β -hydroxylase adsorbed on gold electrode has been investigated electrochemically and applying quartz crystal microbalance [198]. In the neutral phosphate buffer solution, the adsorbed layer was stable and did not desorb within the potential range of 0.6 to -0.7 V (versus Ag|AgCl – 1 M KCl). At potentials more positive than 0.8 V, the adsorbed compound was oxidized and, probably, residual tyrosine, tryptophan, and histidine participated in this process.

Nishizawa et al. [199] have analyzed electroreductive desorption of a mixed

self-assembled 3-mercaptopropionic acid (MPA) and HT monolayer in 0.5 M KOH on Au electrode. The monolayer prepared from 1 mM MPA and 0.2 mM HT gave two cathodic signals at different potentials, suggesting phase segregation within the mixed layer. Electrode behavior accompanying selective cathodic desorption of MPA was characteristic for an array of microelectrodes. This observation indicates that MPA domains are dispersed in the original mixed monolayer. Potential permeability of monolayers toward ionic species present in the solution has been investigated using mixed SAMs composed of MPA and poly(3-dodecylthiophene) adsorbed on gold electrodes [200]. Quartz crystal microgravimetric study of self-assembled thioglycollic acid on polycrystalline gold electrode in 0.5 M KOH has revealed formation of the monolayer. In 0.5 M HCl, in contrast, the frequency changes rather suggest the formation of a bi- or multilayer owing to the presence of hydrogen bonds.

Other studies on gold electrodes have been focused on various self-assembled reactants attached to Au via sulfur-containing groups. Some of these reactants may exhibit catalytic activity or participate in the electron transfer between the electrode and other reactants present in the solution (mediation). Thiol- or disulfide-modified gold electrodes are frequently used to attach other species to already modified surfaces, and form bilayers. Since such systems are very loosely connected with the electrochemistry of gold, only selected examples are given below. One among such compounds is metalloporphyrin deposited on a gold electrode modified with L-cysteine SAM [201]. A cupric-porphyrin-L-cysteine film exhibited good catalytic activity toward

reduction of H_2O_2 . Octabutylthiophthalocyaninato-cobalt(II) forming a SAM on gold electrodes has potential application as an electrochemical sensor in alkaline solutions [202], yet only in the potential range of -0.20 to $+0.55$ V (versus $\text{Ag}|\text{AgCl}$). Self-assembly of 4-ferrocene thiophenol immobilized on gold electrode modified with electroactive gold has been described as well [203]. Other immobilized compounds that have been studied include DNA and a C-reactive protein [204], DNA [205], fullerenes $\text{C}_{60}(\text{OH})_n$ [206], cytochrome *c* [170], bovin serum albumin [207], dipalmitoylphosphatidylcholine [208], J-aggregates of cyanine dyes [209], naphthoquinone [210], proteins [211], and α -cyclodextrin [212]. Other biologically or technically important compounds, for example, porphyrine [213] and metalloporphyrins [214], in combination with thiols or other sulfur-containing compounds have also been attached to gold electrodes. Iron(III) protoporphyrin IX and hematoporphyrin have been covalently bonded to dimercaptoalkane-modified gold electrodes [215]. Electrochemical reversibility of the attached complexes has been confirmed by CV. Heterogeneous rate constant of charge transfer between the iron protoporphyrin and the Au substrate has been found to decrease exponentially with the spacer length.

DNA has also been immobilized on Au electrode by its interaction with gemini surfactants [216]. Moreover, inclusion complexes of viologen-attached alkanethiols and α - and β -cyclodextrins that spontaneously assemble on Au electrodes have been studied [217, 218].

24.4.3.2 Adsorption of Selenium-containing Compounds

Only a few papers on the self-assembled organoselenol monolayers are available.

Samant et al. [219] have prepared a compact layer of docosaneselenol on Au(111). On the basis of X-ray scattering experiments, they have proposed a structure similar to that of thiol monolayers. Also, diphenyl diselenide forms a SAM on polycrystalline Au [220]. This compound is adsorbed even stronger than the corresponding sulfur analog [221]. Benzene-selenol chemisorbed on Au(111) forms initially only small islands, which develop later to large hexagonal-shaped facets, as it has been shown in STM studies [222]. Protsailo et al. [223] have studied adsorption of *n*-dodecaneselenol on Au(111) from ethanolic solutions. They have found that this process occurs in two steps; in the first step, lasting for several seconds, a monolayer is formed, and during the next few hours, a film is organized and self-ordering processes advance.

Employing STM, Monnell et al. [224] have characterized coexisting adsorbate phases in high-coverage decaneselenolate and dodecaneselenolate SAMs on Au(111). Two structure types have been distinguished: a densely packed distorted hexagonal lattice incommensurate to the underlying gold substrate, and a commensurate linear missing row. The differences between these structures and structurally analogous phases of alkanethiolate monolayers on Au(111) may be explained in terms of head group–head group and head group–substrate interactions guiding the self-assembly process.

24.4.3.3 Adsorption of Nitrogen-containing Compounds

24.4.3.3.1 Pyridine and its Derivatives

Adsorption of pyridine and its derivatives on different metal electrodes has been studied very intensively [11], both at polycrystalline Au surface and different

single-crystal Au surfaces. Using ellipsometry, Chao et al. [225] have detected that at positive potentials, pyridine molecules are oriented vertically on pc-Au, whereas they attain flat orientation at negative potentials. Lipkowski and coworkers, in a series of papers, have undertaken systematic studies on adsorption of pyridine from aqueous solutions at various gold electrodes. Adsorption of pyridine on polycrystalline Au electrodes has been studied first, using chronocoulometry [226]. In later studies, the results obtained from chronocoulometry and Raman spectra were compared to those from SERS [227] and radiochemical methods [228]. It has been shown that at a negatively charged surface, pyridine molecules adsorb in the flat orientation and the corresponding maximum surface concentration reaches 3×10^{-10} mol cm $^{-2}$ [226]. At positively charged surface, the adsorbed pyridine molecules reorient to a vertical position, presumably with nitrogen atoms facing the gold surface. Reorientation is accompanied with the increase in the limiting surface concentration up to 7×10^{-10} mol cm $^{-2}$. The change of orientation of Py molecules at the pzc is a two-dimensional phase transition. The standard Gibbs energy of adsorption equals to -38 kJ mol $^{-1}$. Also, a partial charge transfer has been found to be involved in the pyridine adsorption process [226]. Pyridine adsorption at single-crystal electrodes has been performed on Au(100) [229], Au(110) [230], Au(111) [231], Au(311) [232], and Au(210) [233]. The corresponding values of the standard Gibbs energy of adsorption (in kJ mol $^{-1}$) have been determined: -36 for Au(111) and Au(100), -42 for Au(311) and Au(110), and -47 for Au(210). According to these numbers, $\Delta G^\circ_{\text{ads}}$ decreases when densely packed surface layer is converted into the more

open one. Such an orientation is also typical of the Au lattice planes of high Miller indices. Reorientations of Py molecules on Au(100) are initially [229] analogous to those on pc-Au at negative and positive charges. Additionally, transitional orientation was suggested for the potentials close to the zero charge potential and intermediate surface concentrations. Later, however, Skołuda et al. [234] have shown that adsorption of pyridine on Au(100) is a more complex process than it appeared before, since at the unreconstructed Au(100) face, it is hampered by negative potential-induced reconstruction into the (111)-like structure. Therefore, in order to derive the adsorption isotherm for Py on unreconstructed Au(100), it is necessary to apply negative potential for the minimum time to reach the adsorption equilibrium. Consequently, Py molecules adsorbed on Au(100)-(1 \times 1) exhibit vertical orientation within the entire potential range studied. The studies of Au(110) [230] have revealed that Py molecules adsorb vertically also on this surface and are attached to the metal via the nonbonding orbital of the nitrogen atom. For Au(111), the dependence of the orientation of Py molecules on the surface charge has been found [231]. Several modern spectroscopies, for example, SHG [235, 236], DFG on Au(111) [237] and SERS on Au(210) [238], have been employed to determine the orientation of Py molecules at Au surfaces. At Au(210) and Au(311), the adsorbed Py molecules attain vertical N-bonded orientation. In general, the studies on different types of Au surfaces have shown that it is not always clear whether Py molecules desorb from the electrode or only change their orientation [11].

Arvia and coworkers [239] have investigated adsorption of pyridine on Au(111) in the potential range $0.15 \text{ V} < E < 0.55 \text{ V}$

(versus SHE) using *in situ* STM. At potentials higher than or equal to the pzc, both disordered and ordered domains were observed. For potentials lower than E_{pzc} , the ordered structure disappeared. In the ordered domain, pyridine molecules were adsorbed vertically and formed a (4 × 4) hexagonal lattice of the nearest-neighbor distance of 0.38 nm.

On a pc-Au electrode in 1 M NaF vertically oriented pyridine molecules have been observed at 0.7 V (versus Ag/AgCl), applying *in situ* IR. In contrast, they have not been detected at this potential in electrochemical method [240]. Considering the fact that adsorption of pyridine on gold electrodes is a replacement reaction and taking into account the results obtained from quartz crystal microbalance experiments, the conclusion has been made that adsorption of one pyridine molecule is accompanied by the removal of 10–12 water molecules [241].

Subtractively normalized interfacial FTIR has been employed [242] to study the changes in the surface coordination of pyridine molecules on Au(111). It has been deduced from the experiments that pyridine molecule is positioned upright at positive potentials and its plane rotates somewhat with respect to the electrode surface. *In situ* FTIR has also been used [243] to investigate adsorption of pyridine on Au(111), Au(100), and Au(110) electrodes. For the low-index electrodes, the behavior of band intensity located at 1309 cm^{-1} and corresponding to the total adsorbed pyridine, agreed with the surface excess results obtained earlier from chronocoulometry.

Hush and coworkers [244] have calculated theoretically, the binding energy and the dipole moment of isolated pyridine molecules adsorbed on Au(111) surfaces, and have determined the structure of this

system. Significant binding was found only for atop configurations, in which pyridine molecule is positioned directly above a single gold atom with its nitrogen atom bound to it.

Electrochemical and subtractively normalized interfacial FTIR studies of 4-cyanopyridine adsorption on Au(111) electrode [245] have shown that this compound is totally desorbed at potentials lower than -0.7 V versus SCE. At less negative potentials, the molecules were flatly oriented (π bonded) on the surface and reoriented to the vertical position, when potential approached 0 V. At potentials higher than 0.05 V, adsorption of 4-cyanopyridine becomes dissociative and the compound is partially hydrolyzed to isonicotinamide.

Electrochemical and SERS studies [246] have revealed strong adsorption of 4-phenylpyridine to pc-Au electrode in a wide potential range. The molecule was adsorbed via nitrogen in almost vertical orientation at electrode potentials $\leq 0 \text{ V}$ (versus Ag/AgCl), followed by the subsequent tilting of the molecular plane to adopt a more flat orientation. This reorientation resembled the behavior of 4-cyanopyridine on Au(111) [247].

Adsorption of three isomeric pyridine-carboxylic acids on pc-Au electrode in HClO_4 solutions has been investigated [248], applying *in situ* IRAS. When the potential was changed to more positive values, the adsorbed 3- and 4-picolinic acids were reoriented from the flat to the vertical configuration and thereafter bounded to the surface via lone electron pairs present at two oxygen atoms of the $-\text{COOH}$ group. No significant adsorption of the ortho isomer has been detected.

Using SERS, Brolo et al. [249] have studied the potential-dependent orientation of 2,2'-bipyridine molecules adsorbed on a

SERS-active Au(111) surface electrode. It has been found that at a positively charged surface, 2,2'-bipyridine adsorbs end-on via both nitrogen atoms. STM images have shown that [60]-fullerene-substituted 2,2'-bipyridine forms spontaneously, a SAM on Au(111) surface [250].

There is a class of compounds, known as promoters in redox reaction of horse cytochrome *c*, which increase the electron-transfer rate by several orders of magnitude [251]. Czerwiński et al. have studied electrochemically, using pc-Au electrodes, one of these compounds, 4,4'-bipyridyl (PyPy). It has been shown that adsorption of PyPy is governed by the Langmuir isotherm and is a one-center reaction involving the displacement of water molecules from the metal surface. In the adsorbed state, the PyPy molecules attain the perpendicular orientation toward the electrode surface. Later, Czerwiński et al. [252] have carried out CV studies of other compounds of that type, bis(4-pyridyl)disulfide (PySSPy) and 1,2-bis(4-pyridyl)ethylene (BPE). Adsorption of BPE has been found to be fast and increased with the adsorption time, whereas electrode coverage with PySSPy decreased with the adsorption time, suggesting that PySSPy molecules undergo a surface transformation.

Applying *in situ* infrared spectroscopy and STM, Cai et al. [253] have studied adsorption of pyridine on Au(111) electrodes from aqueous NaClO₄ solutions. It has been found that pyridine molecule is flatly adsorbed on the surface at negative potentials. Its molecular plane rises up as the applied potential and surface concentration increase. Moreover, orientation of pyridine molecule changed with the applied STM potential. Ikezawa et al. [243] have used *in situ* FTIR spectroscopy to investigate adsorption of pyridine on Au(111), Au(100),

and Au(110) electrodes in 0.1 M NaF solution containing 2 mM pyridine-*d*₅.

In situ subtractively normalized interfacial FTIR spectroscopy has been employed [254] to study adsorption of pyridine on the Au(110) electrode surface. The compound adsorbed via the nitrogen atom and the tilting angle decreased progressively with the increasing electrode potential, as it appeared from the IR data. At low charge density, the film of N-bonded pyridine molecules was less rigid and the molecules exhibited a waving motion.

Adsorption of pyridine on Au(110) electrodes was also studied using reflection anisotropy spectroscopy [255]. Reflection anisotropy of pyridine/Au(110) system has been attributed to *n*- π^* transitions, the band of which was shifted compared to their spectral position in the gas phase, due to the interaction of the lone electron pair orbitals at N atom with the gold surface.

Ikezawa and Kosugi [256] have studied 2-chloropyridine adsorbed on Au(111) and Au(110) electrodes in 0.1 M KClO₄ using *in situ* infrared spectroscopy and differential capacity measurements. Relative band intensity of N-bonded adsorbate for Au(110) was much stronger than for Au(111). Apparently, at Au(111), the adsorbed 2-chloropyridine molecules either exhibited flat configuration, or the tilting angle was large.

From electrochemical measurements, the dependence of adsorption of *N*-4-pyridinyl-hexadecanamide and *N*-pentadecyl-4-pyridinecarboxamide on the Au(111) electrode potential has been determined [257]. The results were compared to the behavior of 4-pentadecylpyridine described in the previous reports.

Neutron reflectometry (NR) has been employed to study the structure and

composition of thin films of 4-pentadecylpyridine at a Au(111) electrode surface [258]. At very negative potentials, the film was desorbed from the electrode surface. With the help of NR, it has been demonstrated that at these potentials, amphiphilic molecules remain in close proximity to the gold surface as a thick and water-rich film.

Using reflectometry, Barten et al. [259] have investigated adsorption of quaternized poly-2-vinyl pyridine, of a fixed charge per monomer, on a gold electrode. The total adsorbed amount of the compound decreased linearly with the double-layer potential of gold. Adsorption proceeded up to a relatively high double-layer potential and was accompanied by a relatively high contribution of nonelectrostatic interactions.

24.4.3.3.2 Pyrazine Adsorption of pyrazine on a pc-Au electrode has been studied [260]. The obtained relationships between the SERS intensity and the surface coverage, as well as the surface morphology have been analyzed. Later, adsorption of pyrazine on a pc-Au electrode has been investigated by Cai et al. [261], who have applied *in situ* surface-enhanced infrared absorption spectroscopy, chronocoulometry, and impedance spectroscopy. The infrared spectra have been compared to the earlier published SERS spectra [260] in order to get a better understanding of electrochemical interface. Pyrazine was adsorbed on the surface in a vertical end-on configuration via one N atom. Pyrazine adsorption has also been studied on single-crystal electrodes: Au(111), Au(100), and Au(110) using *in situ* FTIR [262]. It has been concluded that pyrazine molecules attain tilted orientation at negative potentials and undergo transition to the vertical position as the potential becomes more

positive. A new band at 1035 cm^{-1} observed for all the electrodes at positive potentials can be explained in terms of adsorption-related change in vertical orientation of the molecules. Earlier, Kolb and coworkers [263] have studied adsorption of pyrazine on Au(111) and Ag(111) electrodes using *ex situ* X-ray photoelectron spectroscopy. Ikezawa et al. [262] have investigated adsorption of pyrazine on Au(111), Au(100), and Au(110) electrodes in 0.1 M NaF, employing *in situ* infrared spectroscopy.

24.4.3.3.3 Amines and Other Nitrogen-containing Compounds Adsorption of *n*-octyloamine, *n*-dodecylamine, *n*-hexadecylamine, and octadecylamine from LiClO₄ methanolic solution on Au electrodes has been studied using capacitance measurements [264]. Also, adsorption of benzylamine from aqueous solutions of KClO₄ and HClO₄ on pc-Au electrodes [265] has been investigated, applying capacitance measurements and SERS.

Lipkowski and coworkers [266] have studied adsorption of benzonitrile on the Au(111) electrode using electrochemical and subtractively normalized interfacial FTIR.

Xiao and Sun [267] have investigated adsorption of *p*-nitrobenzoic acid at a gold electrode in 0.1 M HClO₄, using various methods. At potentials more positive than 0.3 V, the molecules tended to adsorb in a vertical orientation via their carboxylic group directed toward the Au surface.

24.4.3.4 Adsorption of Other Organic Compounds

24.4.3.4.1 Alcohols Richer and Lipkowski [268, 269] have performed extensive studies on adsorption of *tert*-pentanol

on single-crystal Au surfaces of low Miller indices. They have shown that adsorption characteristics of this compound are similar to those observed for the mercury electrode [11]. The lowest Gibbs adsorption energy found for Au(110) indicated the strongest binding of water molecules to the folded surface, compared to the smoother Au(111) and Au(100) surfaces. Adsorption of *n*-tetradecanol, *n*-hexadecanol, and *n*-octadecanol from LiClO₄ methanolic solutions has also been studied by capacitance measurements [270]. Yang and Bizzotto [271] have studied the influence of electrolyte concentration on adsorption of octadecanol on Au(111), applying electrochemical methods and elastically scattered light measurements. Electrolyte concentration most significantly influenced adsorption and desorption potentials, which opens up possibilities of investigating the dynamics of adsorption/desorption processes.

Lipkowski and coworkers [272] have studied adsorption of *n*-octadecanol monolayer on Au(111) electrode. Octadecanol molecules formed a two-dimensional film at any film pressures. At film pressures exceeding 12 mN m⁻¹, the film had low compressibility and the constituting molecules were slightly tilted with respect to the surface normal. At lower pressures, the film was compressed and the tilting angle increased with the decreasing surface pressure.

Sottomayor et al. [273] have investigated adsorption of *n*-hexanol on Au(111) electrode from 0.2 M NaClO₄ aqueous solution, applying chronocoulometry to measure dynamic capacitance and capacitive charge. They have found that in this case, adsorption may be described by the Frumkin isotherm and have determined the corresponding parameters. The obtained results were discussed and

compared to the literature data reported for adsorption of *n*-hexanol on Hg and single-crystal Ag electrodes.

Some conclusions pertaining to adsorption of 1-pentanol riboflavin and thioctic acid on Au electrode have been drawn from differential capacity-potential curves [274]. It has been found, for instance, that adsorption of these compounds obeys the Langmuir isotherm. Moreover, the free energies of adsorption have been determined.

It has also been evidenced [275] that octadenal and pyrenenonanol form a mixed monolayer during adsorption, yet they do not mix ideally.

24.4.3.4.2 Aminoacids

Adsorption of serine, tyrosine, and histidine [276], as well as asparagine [277] on a pc-Au electrode from 0.1 M LiClO₄ aqueous solutions has been investigated, applying ac-impedance measurements. For asparagine, Gibbs energy of adsorption (-47 kJ mol^{-1}) was calculated by fitting Henry's and Frumkin's isotherms to the experimental results. Electrochemical and IRAS results have revealed that asparagine interacts with Au surface via oxygen atoms of $-\text{COO}^-$ and amide carbonyl groups [277]. Adsorption strength of the studied amino acids on gold electrode was decreased in the sequence: tyrosine \geq histidine $>$ serine.

Li et al. [278] have studied adsorption of L-phenylalanine at Au(111) electrodes using electrochemical and subtractively normalized interfacial FTIR methods. It has been found that the adsorbed molecules change their orientation with the electrode potential. At a negatively charged surface, the compound was predominantly adsorbed in the neutral form of the amino acid. At potentials positive with respect to pzc, L-phenylalanine was adsorbed predominantly as zwitterion with $-\text{COO}^-$

group directed toward the surface and $-\text{NH}_3^+$ group facing the solution. At even more positive potentials, electrocatalytic oxidation of phenylalanine occurred, accompanied by the formation of CO_2 .

24.4.3.4.3 Other Organic Acids Adsorption of aliphatic acids on single-crystal Au electrodes has been studied by Dutkiewicz and coworkers [279, 280]. Specific adsorption of citrate from perchloric acid solutions at Au(111) electrodes has been investigated using *in situ* FTIR spectroscopy and CV [281]. The authors have discussed the models of surface coordination of citrate. Based on subtractively normalized interfacial FTIR spectra, Lipkowski and coworkers [282] have found that citric acid fully deprotonates during adsorption on Au(111) and the surface-bound carboxylate groups adopt a tilted orientation. They have also found that the limiting coverage is $3 \times 10^{-10} \text{ mol cm}^{-2}$. Employing *in situ* reflection-adsorption IR spectroscopy and CV, it has been shown [283] that 2-, 3-, and 4-fluorobenzoic acids adsorb at positive potentials on Au(100) from 0.1 M HClO_4 solutions. The adsorbate molecules were oriented vertically, with both oxygen atoms oriented toward the metal surface. Adsorption/desorption processes of 1-hydroxyethane-1,1-diphosphonic acid molecules on Au(111) surface have been investigated [284] in perchlorate solutions using CV and STM.

Adsorption of humic acid on Au(111) and pc-Au electrodes has been studied [285], employing several electrochemical techniques and electromicrogravimetry.

Zelenay et al. have applied CV and radiotracer technique to study adsorption of benzoic acid from 0.1 M HClO_4 solution on a pc-Au electrode prepared by electroplating [286]. Chemisorption occurred within the entire potential range

(0.05 to 1.75 V versus SHE); however, orientation of the adsorbed molecules was potential dependent, that is, at less positive potentials, flat orientation predominated, while at more positive potentials, vertical orientation was the most pronounced. It is noteworthy, that although desorption of benzoic acid to the pure supporting electrolyte solution was insignificant and extremely slow, its surface/bulk exchange was much faster. Later, Sobkowski et al. [287] have found that adsorption of benzoic acid on Au, Ag, and Cu electrodes from HClO_4 solution is reversible, whereas at Pt, it appears to be partly irreversible. For pc-Au, the following parameters of the Frumkin isotherm were found: $\Delta G^\circ_{\text{ads}} = -16.4 \text{ kJ mol}^{-1}$ (for the standard state defined as $c = 1 \text{ M}$, $\Gamma = 0.5\Gamma_\infty$, lateral interaction parameter $a = 0$), $\Gamma_\infty = 2.4 \times 10^{-14} \text{ molecules/cm}^2$, $a = 1.5$. Adsorption of benzoic acid on Au(111) and Au(110) electrodes in 0.1 M HClO_4 has been investigated, applying IRAS, voltammetry, and differential capacity measurements [288]. For both electrodes, the presence of vertically adsorbed anion at positive potentials has been confirmed by IRAS. Other orientations also occurred at negative potentials, as it followed from the IRA spectrum.

Finally, the structure of 3,4,8,10-perylene-tetracarboxylic-dianhydride grown on reconstructed and unreconstructed Au(100) has been investigated [289].

24.4.3.4.4 Nucleic Bases and Other Biochemical Compounds It has been found that cytosine is physisorbed at negative potentials and chemisorbed at positive potentials on Au electrodes from 0.1 M NaClO_4 and HClO_4 aqueous solutions [290]. In cyclic voltammogram

of cytosine, one pair of peaks was observed, which can be ascribed to the transition between the physisorbed and chemisorbed states. In both states, the molecules were oriented with N(3), C=O and NH₂ moieties toward the surface. Adsorption of uracil on Au(100) has been studied using *in situ* STM [291]. Depending on the Au electrode potential, uracil formed three highly ordered monolayers, which were imaged with a molecular resolution. Pronkin and Wandlowski [292] have studied adsorption and phase formation of uracil on massive Au[n(111)-(110)] single-crystal and Au(111–20 nm) film electrodes in 0.1 M H₂SO₄ using electrochemical measurements and attenuated total reflection (ATR) surface-enhanced infrared reflection/absorption spectroscopy. At $E < 0.15$ V, uracil molecules were disordered and planar oriented. Close to the zero charge potential, a 2D condensed physisorbed film of planar-oriented molecules, interconnected via directional hydrogen bonds, was formed. The formation of organic adlayers on single-crystal Au electrodes has been studied for such compounds as uracil, methyluracils, and uridine. Cyclic voltamograms of such compounds on, for example, Au(111) surface, typically exhibited broad peaks and sharp spikes, associated

with significant structural modifications of the interfacial region [293–297]. For the above-mentioned compounds, four such regions can be distinguished (see Fig. 9 as an example): (I) random adsorption and gradual desorption, (II) 2D condensed film, (III) charge-transfer process of physisorbed species (II) to the chemisorbed-like state (IV). As Roelfs and Baumgärtel [298] have shown, this CT process involves deprotonation of organic molecules, which makes the reaction pH dependent.

Adsorption and phase formation of uracil on massive Au[n(111)-(110)] single-crystal and Au(111–20 nm) film electrodes in 0.1 M H₂SO₄ has been studied in electrochemical measurements and applying ATR surface-enhanced infrared reflection absorption spectroscopy [299]. At $E < 0.15$ V (versus trapped hydrogen electrode), uracil molecules are disordered and planar oriented. Close to the pzc, a 2D condensed physisorbed film of planar-oriented molecules interconnected by directional hydrogen bonds, is formed.

Adsorption of adenine and coadsorption of adenine–thymine and uracil–thymine on Au(111) has been reported [300]. Adenine was chemisorbed in two different states. Mutual interaction between adenine and thymine was detectable only at

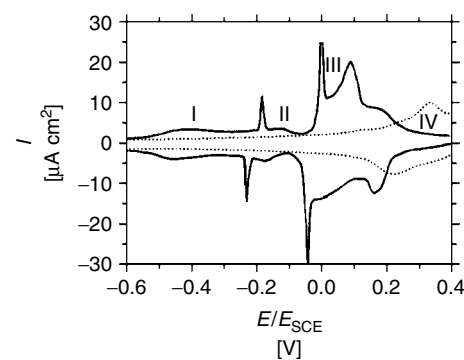


Fig. 9 Cyclic voltammograms recorded at Au(111) in the aqueous solution of 0.5 M NaF in the absence (.....) and the presence (—) of 12 mM uracil [297]. Temperature: 15 °C. See text for the description of the indicated regions.

negative potentials when both molecules had their planes oriented parallel to the surface.

Shen et al. [301] have used quartz crystal microbalance to study electrochemical behavior of guanine, guansine, and guansine phosphate at gold electrodes.

Hason and Vetterl [302] have studied adsorption of cytidine on Au(111) and mercury film electrodes.

Surface-enhanced near-infrared Raman spectroscopy has been utilized to study the behavior of nicotinamide adenine dinucleotide on a gold electrode [303]. It has been found that either adenine or nicotinamide moiety changes its adsorption states during potential scanning.

Adsorption of azurin – a copper-containing protein on Au electrodes under physiological conditions – has been monitored at the molecular level, applying STM [304].

It has been found that at Au electrode exposed to the solutions of human serum albumin and immunoglobulin in the phosphate buffer, the double-layer capacity is decreased, while charge-transfer resistance at the Au/solution interface increases [305, 306]. These changes were attributed to the formation of proteinaceous layer at the electrode.

Adsorption of putidaredoxin on gold electrodes has been studied using dynamic spectroscopic ellipsometry and differential capacitance measurements [307]. In Ref. 307, a method for the measurement of metal surface optical perturbation during protein adsorption at a constant potential has been described. The method is based on the concept that the charged transition layer develops between the electrode substrate and the adsorbate.

A simultaneous use of quartz crystal microgravimetry and fluorescence has

been proposed [308] to study adsorption/desorption and oxidation of vitamin B₆ at a pc-Au electrode in aqueous KOH solutions. Oxidation of vitamin was irreversible and was accompanied by strong electrogenerated fluorescence at the wavelength of 443 nm (excitation wavelength 360 nm).

Zerbino and Sustersic [309] have presented electrochemical and ellipsometric studies of dopamine adsorbed on gold electrodes in aqueous H₂SO₄ solutions of pH = 1.

Adsorption of glutathione on a gold electrode has been studied [310] using electrochemical quartz crystal impedance, electrochemical impedance spectroscopy, and CV.

Chronocoulometry and photon polarization modulation infrared reflection/absorption spectroscopy have been employed [311] to study the fusion of dimyristoylphosphatidylcholine vesicles onto an Au(111) electrode. The fusion was controlled either by the electrode potential, or charge. Film characteristics was also potential dependent. After removing the film from the electrode surface (negative potential), phospholipid molecules remained in its close proximity, in the ad-vesicle state. Several electrochemical and nonelectrochemical methods have been applied [312, 313] to investigate the spreading of small unilamellar vesicles onto Au(111) electrode. Vesicles fused onto the surface at $E > -0.5$ V (versus SSCE), to form defected bilayers in contact with the metal surface. At more negative potentials, the film was removed from the electrode surface, but it still remained in its close proximity.

A new approach to a directly controlled deposition of long DNA molecules on bare gold electrode array without any modification of gold electrodes and DNA

molecules has been described in Ref. 314. AFM studies have shown that DNA molecules are significantly less stable on bare gold surface than on the one modified with aminothiol.

24.4.3.4.5 Other Compounds Recently, low-temperature STM has been used [315] to characterize variously structured submonolayers and near monolayers of benzene on Au(111).

Adsorption of chlorobenzene on pc-Au electrode has been studied by Czerwiński and Sobkowski [316] as early as in 1980, using a ^{14}C radiotracer technique. The rate-determining step of this adsorption was diffusion of the reactant. Chlorobenzene was adsorbed in multilayers at sufficiently high bulk concentration. The adsorbed molecules were probably oriented vertically with respect to the Au surface and bounded to it via a Cl atom.

STM and CV have been applied [317] to investigate adsorption of three semi-crown ligands on Au(111) surface under conditions of potentiostatic control. Adsorption of alkanes on Au(111) surface was simulated by applying a simple computational scheme [318]. The calculated values of adsorption energies of 10 short-chain alkanes were reproducible with an average error below 1 kcal mol $^{-1}$. Adsorption of camphor on Au(111) and its effect on electroreduction of IO 4^- has been studied by Pettinger and coworkers [319]. Adsorption of camphor on Au(111) electrodes has also been investigated [320] by generating the second harmonic and applying CV. Also, Kolb and coworkers [321] have studied adsorption of camphor-10-sulfonic acid on reconstructed Au(111) electrode from perchlorate and sulfate solutions. In both solutions, the above compounds formed two-dimensional condensed phases. IR spectra have shown that urea molecule

is adsorbed on Au(100) with a molecular plane normal to the electrode surface. On Au(111) surface, in contrast, coordination of urea molecules was different [322]. Earlier, the adsorption of urea on pc-Au electrode from aqueous solutions of KClO $_4$ and HClO $_4$ has been studied by Holze and Schomaker [162]. The free energy of adsorption points toward strong adsorption of thiourea and less strong adsorption of urea in KClO $_4$ solutions. In acidic solutions, both compounds were not stable.

Structural differences between the monolayers of anthraquinone derivatives self-assembled on silver and gold electrodes have been investigated using CV and *in situ* SERS spectroscopy [323]. Neves et al. [324] have described Monte Carlo simulations of phenol adsorption on gold electrodes.

Potential-induced phase transition of trimesic acid on Au(111) electrode has been studied using *in situ* STM and CV [325]. In cyclic voltammograms, a pair of peaks was formed, which was ascribed to the structural transformation. On the basis of high-resolution STM images in 0.1 M HClO $_4$, it has been proposed that trimesic acid molecules assume flattening and vertical orientations at 0.25 V and 0.85 V, respectively. Both orientations coexisted at 0.65 V.

In situ STM has been applied [326] to study the potential-induced self-organization of α -cyclodextrin on Au(111) surfaces in NaClO $_4$ solutions. The adsorbed molecules formed an ordered array of a cylindrical structure in the potential range 0.20 to -0.15 V (versus SCE), while they were desorbed at potentials lower than -0.40 V.

Self-organized adlayer of calix[4]arene on Au(111) has been obtained by potential-controlled adsorption [327]. *In situ* STM

images have shown that the compound molecules are adsorbed as dimers.

Lipkowski and coworkers [328] have employed STM to study the spreading of 1,2-dimyristoyl-sn-glycero-3-phosphatidylcholine vesicles into the film at the Au(111) electrode surface. During the initial stage, phospholipid molecules were adsorbed flatly with the acyl chains oriented parallel to the surface and assembled into an ordered monolayer similar to that formed by alkanes. Later, the molecules reoriented and the monolayer was transformed into a hemimicellar film.

Brooksby and Fawcett [329] have studied adsorption of ethylene carbonate at Au(110) electrode from aqueous solutions of HClO_4 , NaClO_4 , and Mt_4NClO_4 , using *in situ* infrared spectroelectrochemical method.

Growth morphology, long-range ordering, and evolution of the valence bond electronic states of ultrathin films of copper phthalocyanine deposited on the Au(110)-(1 × 2) reconstructed surface have also been investigated as a function of organic molecule coverage [330]. Also, on Au(110)-(1 × 2) surface, growth morphology and electronic structure of 2D-ordered pentacene layers have been studied [331].

Lipkowski and coworkers [332] have applied several electrochemical techniques to study adsorption of *N*-dodecyl-*N*,*N*-dimethyl-3-ammonio-1-propanesulfonate, a model zwitterionic surfactant, on Au(111) electrode. Adsorption of this compound proceeded via a few states. The first two states were observed at potentials close to the zero charge potential. At low bulk concentrations, a nearly flat film of the adsorbed molecules was formed, which was converted into a hemimicellar state at higher concentrations. The second state at negative potentials corresponded to

the film of molecules oriented with their polar head directed toward the solution. Bizzotto and Lipkowski [333] have studied adsorption of insoluble surfactants on Au(111) in order to explain the mechanism of potential-induced adsorption and desorption of 12-(9-anthroxy) stearic acid, a surfactant dye. Applying electroreflectance spectroscopy and light scattering measurements, they have evidenced that desorbed surfactant molecules form micelles (flakes or vesicles) that are trapped under the electrode surface. The micelles spontaneously spread back on the electrode surface, when charge density at the metal approached zero.

Petri and Kolb [334] have studied the properties of sodium dodecyl sulfate adsorbed on Au(111) in H_2SO_4 solutions, using *in situ* STM.

24.4.4

Reconstruction of the Surface of Gold Electrodes

When using single-crystal electrodes, it is assumed that the structure of their surfaces reflects the structure of the bulk crystal. However, it appears that, frequently, the surface structure is different from that of the bulk due to their different atomic surroundings. In the bulk crystal, each metal atom is surrounded by identical atoms fixed within the well-defined structure. In contrast, the surface atoms participate in the interactions with metal atoms forming the crystal, and are involved as well in the interactions with the components of the solution at the solid/liquid interface. These asymmetrical interactions of the surface atoms may lead to the breakage of the old and formation of the new bonds, followed by the displacement of the surface atoms to the positions of the lower surface energy. The process of formation

of a new surface structure is known as *surface reconstruction*.

The process of reconstruction of gold electrode has already been mentioned in this chapter several times, for instance, in the discussion of adsorption of selected compounds, as these two processes may be coupled. We present a more systematic review of the papers devoted specifically to the problem of reconstruction of an Au surface below.

Reconstruction of all the three low-index faces of Au single crystal under elevated temperature has been described in several papers. This subject has been discussed in detail by Dakkouri and Kolb [335], as well as (also for other metals) by Kolb [336], and Gao et al. [337, 338]. A recent concise review of Au reconstruction, including experimental details of the surface preparation, has been published by Trasatti and Lust [4].

The studies under ultrahigh vacuum have shown that adsorption and surface charging influence the stability of the reconstructed surfaces. A similar influence has been observed for metal surfaces in contact with electrolyte solutions [336]. In this case, the separation of these two influences is not simple, since the surface charging and adsorption processes are interdependent. Generally, it has been concluded [4] that Au surface reconstruction occurs for negative electrode charges and disappears for positive surface charges. It is noteworthy that as early as in 1984, Kolb and coworkers [339, 340], who carried out systematic study on all three low-index faces Au electrodes, showed that the reconstructed surfaces can be stable in electrolyte solutions.

Reconstruction of Au(100) surface has been reported by Kolb and Schneider [341]. The Au(100) surface reconstructs to the hexagonal close-packed structure

(called *hex*) [342–345]. In *in situ* STM images, the hexagonal structure of surface atoms is easily observed. Model calculations have been performed [346, 347] to evidence that negative surface charge favors reconstruction, as arises from the comparison of the calculated surface energies for reconstructed and unreconstructed Au(100) [347].

Initial reconstruction caused by flame annealing is stopped when the surface is cooled in the atmosphere, though not in water. The rate of transition from unreconstructed to reconstructed surface is determined by the height of the activation barrier [348], especially at the room temperature. Reconstruction may be removed by adsorption of atoms and molecules [349], since unreconstructed, and thus, more open surface, interacts with the adsorbates stronger than does the densely packed surface. Therefore, the removal of reconstructed surface proceeds from the less to the more energetically favored state [348]. Reconstruction coupled with the formation of more dense surface structure may lead to quite a strong increase in the number of surface atoms. For instance, the Au(100)-(1 × 1) → Au(100)-(hex) reconstruction is accompanied by the increase in the number of surface atoms by 24%. In consequence, the reverse change connected with the expansion of the surface lattice leads to some surface roughening, owing to the formation of small, yet high monoatomic islands. This behavior for the Au(100) surface has been shown in STM images by Kolb and coworkers [350]. Also, Bohnen and Kolb [351] have calculated the surface energies γ of Au(100)-(1 × 1) and Au(111)-(1 × 1) as a function of the surface charge, applying ab initio local density-functional method. The obtained results suggest that the lifting of the Au(100) reconstruction in HClO₄ solution at +0.55 V

(versus SCE) is caused by specific adsorption of the anion, and not by a charge effect.

Since negative surface charge favors reconstruction of the gold surfaces, it occurs under the influence of the potential negative to the potential of zero charge [341, 352] Dakkouri and Kolb [335] have stressed that the immediate quenching after flame annealing is often advised to prevent the surface contamination, yet it leads to the rough and structurally ill-defined surfaces. In view of this fact, in STM studies of Au single-crystal electrodes, they were cooled down in a gentle stream of nitrogen [335]. Dakkouri [353], applying in situ STM, has determined the conditions required to preserve thermally induced reconstruction of Au(100) electrode surface both during and after the contact with the electrolyte. Structural changes of such electrode surface may occur in the potential range used in electrochemical experiments. The kinetics and a mechanistic model of structural transition have been briefly discussed.

Since specific adsorption of anions is harmful for the reconstructed surfaces, the immersion potential of the electrode should be negative to keep the surface free from the specifically adsorbed anions. In practice, it should be 0.5 to 0.6 V more negative than the zero charge potential. The influence of the anion adsorption on the potential of the reversed transition is shown in Fig. 10.

Transition potentials have been determined from cyclic voltammograms of Au(100)-(hex) in various solutions. For 0.05 M anion concentration, the (hex) \rightarrow (1 \times 1) transition for a freshly prepared reconstructed Au(100) surface occurs at -0.62, -0.23, +0.02, +0.2, +0.33, and +0.58 V (versus SCE), for I^- , Br^- , Cl^- , OH^- , HSO_4^- , and ClO_4^- , respectively. Obviously, the above sequence of potentials follows the sequence of the decreasing specific adsorption. Also, the adsorption of other adsorbates influences the stability potential of the reconstructed surfaces. Lipkowski and Stolberg [355], and Hamm

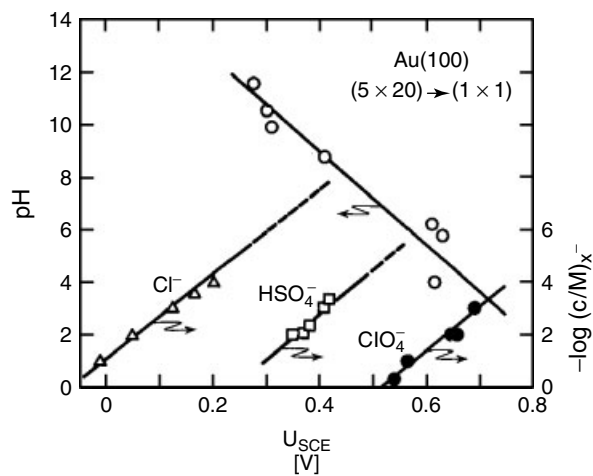
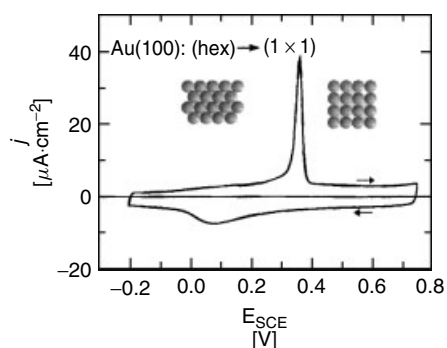


Fig. 10 Transition potential for Au(100): (5 \times 20) \rightarrow (1 \times 1) as a function of anion concentration and pH. Stability region of the (5 \times 20) structure is located to the left from the respective line (from Ref. 354).

Fig. 11 Cyclic current-potential curve for Au(100) in 0.1 M H₂SO₄ solution; beginning of polarization: -0.2 V (versus SCE) using a freshly prepared reconstructed surface. Scan rate: 50 mV s⁻¹. The peak formed in the positive scan corresponds to the lifting of the (hex) reconstruction. The subsequent scan in negative direction reflects electrochemical behavior of Au(100)-(1 × 1) [335].



and Kolb [356] have evidenced a significant influence of pyridine concentration on the potential of the (hex) → (1 × 1) transition.

Figure 11 exhibits the CV curve for Au(100) surface undergoing reconstruction.

Recently, the influence of γ -butyrolactone cyclohexanone [357] and propanal [358] on the stability range of the reconstructed Au(100) surface has been studied by CV.

A brief summary of reconstruction processes at other gold surfaces is given below. In order to obtain the reconstructed Au(110) surfaces after the flame annealing below the red heat, the cooling rate should be decreased [335]. Keefe et al. [359] have used the SHG method to study *in situ* potential-induced reconstruction of Au(110) electrode in 0.01 M HClO₄ aqueous solution. The influence of potential on the atomic structure of the ordered Au(110) in bromide solutions has been investigated, applying *in situ* STM [360]. A special attention has been paid to the adsorbate-induced nanoscale restructuring, which occurs at higher potentials. The observed behavior was compared to that of Au(110) surface in iodide solutions. Also, it has been found that clean Au(110) surface exhibits a (1 × 2) structure. However, after immersion into 0.01 M HClO₄ solution and under potentiostatic control in

the range 0.9–1.0 V (versus Ag|AgCl), it changes to the centered rectangular structure [361]. After the initial oxidation, this structure prevails up to the potentials of 1.2–1.3 V, whereupon oxidation occurs on a large scale and the surface structure becomes (1 × 1). After reduction of the oxide, these structures return to the (1 × 2) configuration.

Reconstruction of Au(111) is observed in STM images as double rows separated from each other by 6.3 nm [335]. Some model calculations have been performed [362] to show that the energy difference of the reconstructed and unreconstructed Au(111) is small. The effect of Triton X-100 on the reconstruction process of Au(111) surface has been studied in chloride media [363] applying CV and double potential-step chronocoulometry. It has been found that adsorption of Triton X-100 stabilizes the reconstructed face of Au(111). Hobara et al. [364] have used *in situ* STM to study reconstruction of Au(111), following reductive desorption of 2-mercaptopethanesulfonic acid SAMs.

24.4.5 Formation of Oxides on Gold Electrodes

Oxide layers on gold electrode surfaces are interesting, mainly due to their electrocatalytic properties.

A growth of a gold oxide on Au electrodes in aqueous H_2SO_4 and KOH solutions has been observed and investigated by many researchers (see, for instance, the reviews by Jerkiewicz [365] and Burke and Nugent [366]).

A detailed behavior of gold electrodes in 0.50 M H_2SO_4 and KOH aqueous solutions has been presented by Jerkiewicz and coworkers [367]. In CV experiments,

the upper oxidation potential limit was being changed from 1.30 to 1.90 V (RHE) in the forward scan to form the oxide. After that, the direction of polarization was reversed and a single peak corresponding to the reduction of the generated oxide was formed in the voltammogram, as shown in Fig. 12 [367].

In Fig. 12, it is shown that the oxide reduction current (and charge) increases

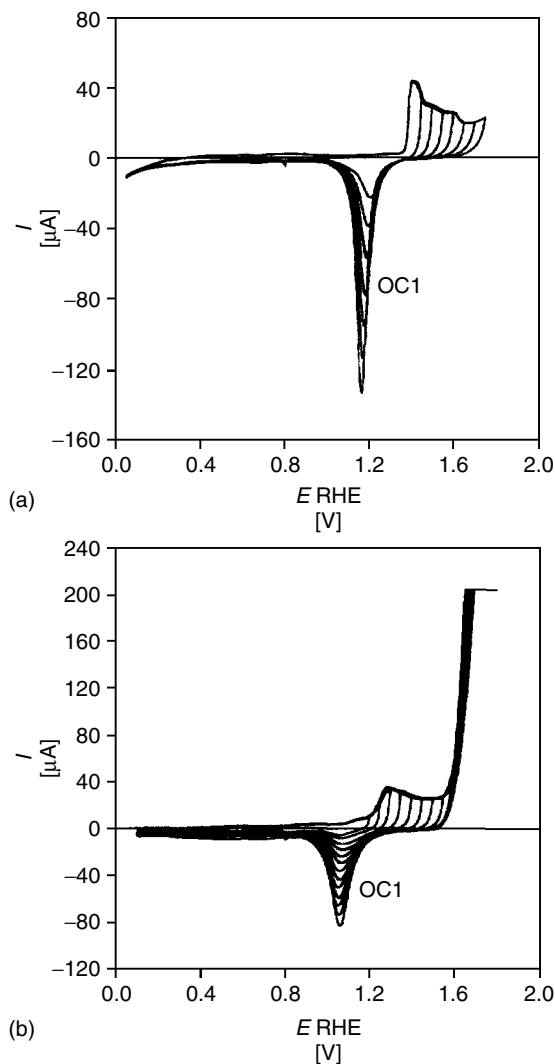


Fig. 12 (a) A series of CV profiles for Au electrode in 0.50 M aqueous H_2SO_4 solution: $T = 298 \text{ K}$, sweep rate $v = 50 \text{ mV s}^{-1}$, electrode surface area $A = 0.495 \text{ cm}^2$. The figure shows gradual development of the OC1 state and the changes in the oxide formation/reduction profiles upon the increase of the upper potential limit E_p . (b) A series of CV profiles for Au electrode in 0.5 M aqueous KOH solution: $T = 298 \text{ K}$, sweep rate $v = 50 \text{ mV s}^{-1}$, electrode surface area $A = 0.490 \text{ cm}^2$. The figure shows gradual development of the OC1 state and the changes in the oxide formation/reduction profiles upon the increase of the upper potential limit E_p (see text for the explanation of other symbols) [367].

as the upper oxidation potential limit is increased. In general, the higher the anodic polarization potential and the longer the polarization time, the thicker the oxide film that is obtained. Reduction of oxidation products occurs at potentials significantly less positive than oxidation potentials. It may point toward some transformations of the products of the electrooxidation reaction. In order to estimate the kinetics of the oxide growth, the $1/\rho_{\text{ox}}$ versus $\log t_p$ plots were constructed [367] (ρ_{ox} is the oxide reduction charge density, and t_p denotes polarization time). For electrode potentials of 2.05–2.20 V (RHE) in aqueous H_2SO_4 solution, such plots exhibit two linear regions of different slopes (indicating different mechanisms). The inflection point between these two linear ranges appears close to $1/\rho_{\text{ox}} = 0.10 \text{ mC}^{-1} \text{ cm}^2$. This agrees well with the fact that the oxide formation is preceded by chemisorption of OH, which competes with specifically adsorbed anions. However, the potential of OH/ H_2O couple is very positive (2.85 V versus SHE) and thus, adsorption of OH is rather limited. Instead, the formation of some type of polar covalently bonded $\text{Au}^{\delta+} \cdots \text{OH}^{\delta-}$ species is more probable [366].

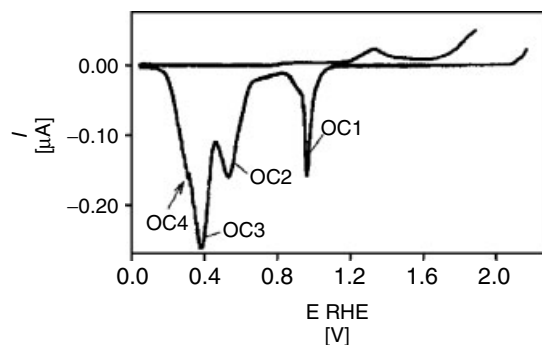
Cathodic behavior after the prolonged (up to 10^4 s) potentiostatic polarization in

the range 2.00–2.43 V is more complex. It is presented in Fig. 13 [367].

Apart from the cathodic peak observed in Fig. 12, there are three additional peaks, which correspond to new oxide states. The peak described as OC1 corresponds to either AuO or $\text{Au}(\text{OH})_2$ [367], depending on the pH of the solution. Other peaks denoted as OC2, OC3, and OC4 refer to either Au_2O_3 or $\text{Au}(\text{OH})_3$. Burke and Nugent [366] have described similar cathodic behavior. They have assumed that during oxidation at positive potentials, oxygen evolution, and production of oxides is accompanied by the formation of unstable gold peroxide species. In general, several cathodic peaks or steps observed during reduction of Au oxide may also result from the existence of several types of hydrous oxide species or several activity states of the produced gold atoms. It has been found by Jerkiewicz and coworkers [367] that the OC1 state grows to the limiting thicknesses of either three or one monolayer for AuO and $\text{Au}(\text{OH})_2$ in acidic and basic solutions, respectively. During the same time, other oxide states grow unlimitedly, even up to 100 equivalent monolayers of Au_2O_3 or $\text{Au}(\text{OH})_3$.

The combination of the electrochemical and ellipsometric data has led to the conclusion that Au oxides are composed of two layers: the inner film α and the outer

Fig. 13 Linear sweep voltammetry (LSV) oxide reduction profile for an Au electrode after polarization at $E_p = 2.23 \text{ V}$ (RHE) for $t_p = 900 \text{ s}$ in 0.50 M aqueous KOH solution; $T = 298 \text{ K}$, sweep rate $v = 50 \text{ mV s}^{-1}$, electrode surface area $A = 0.280 \text{ cm}^2$. The LSV profile reveals the OC1, OC2, and OC3 states; the onset of OC4 is marked with an arrow [367].



film β . From ellipsometry, it is known [367] that the α film thickness reaches 0.55 nm and 0.28 nm in acidic and basic solutions, respectively. α film is adjacent to the metallic substrate with a second film β growing on the top of α without any limit. It follows from the above that α film (AuO or Au(OH)_2) is sandwiched between the Au metal substrate and β film, composed most probably of a hydrous form of either Au_2O_3 or Au(OH)_3 .

In case of thicker layers, α -oxide is reduced as first [366] giving a peak at ca 1.0 V. Reduction potential depends on several factors, including oxide coverage and scan rate. Burke and Nugent [366] have assumed that the Au^{3+} transfer across α layer is quite slow. An α film passivates the surface to some extent with regard to the hydrous β oxide growth. However, the passivating layer does not form a barrier against electroreduction of β layer, especially in basic media.

According to the presented model of oxides formation on Au, the outer surface of the thick oxide film exposed to the solution is either Au_2O_3 or Au(OH)_3 . The type of oxide determines the surface electronic structure and electrocatalytic properties. Electrocatalytic properties of gold oxide-covered electrodes have been discussed by Burke and Nugent [366, 368].

Kolb and coworkers [369, 370] have studied and observed initial stages of anodic oxidation of Au(111) in H_2SO_4 solutions, oxide formation, and topography of the oxide layer. In these studies, apart from CV, STM and AFM methods have been employed.

The redox behavior of a polycrystalline gold electrode in 0.1 M $\text{NH}_3 + 0.1 \text{ M NaClO}_4$ solution has been investigated using electrochemical and spectrometric techniques [371]. Two gold compounds: AuO and AuNH_2 were distinguished at

the surface at +0.6 V (versus SCE) in amounts depending on the holding time at this potential. When the potential was held at +0.60 V for a longer time, other oxidized gold species might be formed at the surface.

Conway and coworkers [372] have studied anodic dissolution of gold coupled with anodic oxide formation in HClO_4 solutions with addition of bromide ions. It was observed that gold initially dissolves in a 3e oxidation process.

In recent years, Burke and coworkers have found [373] that severe cathodization of pc-Au in acid solution resulted in the appearance of faradaic responses in the double-layer region. Such anomalous behavior may be explained by the presence of active gold atoms on the electrode surface. These active atoms appear as a result of the pretreatment process, when the part of inserted energy into the gold sample is retained mostly by the surface atoms and atoms of the outer layers, in the form of various types of defects, for example, adatoms, vacancies, grain boundaries, and others.

Active low coordination, metastable state of the metal leads to anomalous electrochemical response in which hydrous (β) oxide species ($\text{Au}_2\text{O}_3 \cdot n\text{H}_2\text{O}$) are produced in a premonolayer oxidation. In contrast, conventional response yields a monolayer (α) oxide species (Au_2O_3). Since the activity of the active Au state is variable, the nature of the β oxide is also variable. Burke and Nugent [374] write about at least three forms of that oxide.

The authors [373] have studied the effect of prolonged cathodic polarization at negative potentials ($E \leq 0.00 \text{ V}$) using both gold wire and rotating disc electrodes. They have shown that Au electrode prepolarized at -0.60 V for 20 min reveals in

the anodic scan, a significant anodic current peak at $E_p = 0.42$ V. This peak was followed by the flow of a relatively large anodic current in the range 0.60–1.10 V. Finally, at about +1.4 V, the large second anodic peak was observed, which corresponded to the formation of a monolayer oxide film.

In the second sweep, the first anodic peak at about +0.50 V was observed, but it was much smaller. These unusual effects observed for Au electrodes were enhanced by raising the solution temperature.

In order to explain the observed phenomena, it is assumed that during prolonged cathodic polarization, there occurs an activation of the outer gold atom layers via hydrogen embrittlement.

The authors also discuss the electrocatalytic properties of gold active state at low potentials. There are no studies of such states by surface science techniques and the authors [373] claim that such active states would be very difficult to detect using such techniques.

The effect of severe thermal pretreatment of Au wire in an inert gas atmosphere [375] on the anodic behavior of gold was also considered. In some instances, premonolayer oxidation commenced at 0.25 V (SHE).

Also, in this case, such behavior was explained by the formation of a very active metastable state with low lattice stabilization energy.

The formation of the active surface states of gold was also found in an alkaline solution [376]. Both cathodic and thermal pretreatments were used. As a result, up to five distinct premonolayer oxidation responses in the range 0–1.0 V (SHE) were observed. In a separate paper, a study of gold electrodes in the metastable states in acid and base solutions was made. The active electrodes were prepared by

rapid thermal quenching [377]. When the gold electrode was cooled rapidly from the molten state, oxidation responses were observed for gold in base at $E < 0.0$ V.

One should add that the formation of such nonequilibrium surface states may be important for electrocatalytic properties.

Redox and electrocatalytic activity in base at unusually low premonolayer potentials were observed also for copper [378, 379].

24.4.6

Underpotential Deposition of Various Metals on Au

UPD of various metals on different gold surfaces is one of the most intensively studied subjects. Abruna and coworkers have reviewed [380] the UPD deposition at single-crystal surfaces of Au, Pt, Ag, and other materials. More recently, Magnussen [381] has described ordered anion adlayers on metal electrode surface, which can affect the UPD process.

24.4.6.1 **Cu**

As early as in 1987, Kolb and coworkers used Auger electron spectroscopy (AES) to study UPD of Cu on Au [382].

Zeng and Bruckenstein [383] have studied UPD of Cu at polycrystalline gold in 0.1 M NH₃ + 0.1 M NaClO₄ electrolyte using the rotating disk electrode, electrochemical quartz crystal microbalance, and time-of-flight secondary ion mass spectrometry (TOF-SIMS). The experiments have revealed that Cu(0) UPD occurs in the potential range -0.4 V $< E < 0.1$ V, at three different sites. The rate-determining step was the reduction of the dissolved copper ammonia complexes to Cu(0).

For single-crystal electrodes, an extended hexagon model, in which the adsorbate interactions are averaged, has

been applied [384] for Cu UPD on Au(111). Using this model, coupled adsorption isotherms for copper and sulfate ions were obtained and numerically solved. The isotherms obtained were in good agreement with the experimental dependences. Chabala and coworkers [385] have studied Cu UPD on Au(111). They have utilized X-ray diffraction *in situ* and in the real time. Both potentiodynamic and potential-step polarizations were applied and the adlayer spacing of Cu on Au(111) was determined as a function of several parameters, such as potential and time. Stimming and coworkers [386] have studied experimentally, Cu UPD on Au(100), applying *in situ* X-ray surface diffraction. The structure of the Cu UPD layer has been studied as a function of the applied potential and Cu(II) concentration in the solution. In another paper [387], the same group of researchers studied the influence of anions on Cu deposition on Au(100) using CV.

Xia et al. [388] have investigated the kinetics and phase transitions of Cu UPD on Au(111) using *in situ* STM.

It has been found that Cu electroreduction from perchloric acid solution on Au(100) exhibits the UPD properties [389]. X-ray surface diffraction measurements have shown that the Cu UPD layer has a primitive (1 × 1) structure and that the adsorbed Cu species are located in four-fold hollow sites, with a vertical distance between the Cu adlayer and the Au surface of 0.14 nm.

Early stages of copper electrodeposition and coadsorption of chloride on the Au(111) electrode surface have been studied by Wu et al. [390] applying electrochemical methods and *in situ* X-ray absorption measurements. The results indicate a large degree of static disorder and exclude the presence of high-symmetry structures. Krznaric and Goričnik [391]

have studied, applying CV, Cu UPD on Au(111) electrode in the presence of chloride ions at various concentrations ranging from trace amounts to 0.55 M. At NaCl concentrations exceeding 5×10^{-3} M, Cu(I) was stabilized by chloride and reduction of copper proceeded as the one-electron process at the Au(111) surface covered with Cu and chloride bilayer but not on Au(111) free from Cu.

Combined X-ray and electrochemical studies on Cu UPD at Au(111) in the presence of bromide have been carried out by Abruna and coworkers [392]. At the potentials more positive than +0.55 V (versus Ag/AgCl), bromide anions adsorbed at the electrode surface and formed an ordered and rotated hexagonal structure. Initial stages of Cu deposition were observed at ca +0.36 V. In the potential range of +0.32 to +0.20 V, two voltammetric signals were observed, associated with additional copper deposition and giving rise to the stoichiometric CuBr layer. At +0.147 V, a sharp voltammetric peak was formed, corresponding to the phase transition and formation of a (1 × 1) copper layer with a bromide (4 × 4) structure adsorbed on the Cu layer. At potentials less positive than +0.147 V, bulk copper deposition occurred. In another work, Abruna and coworkers [393] have compared the results of electrochemical and *in situ* SXS studies on Cu UPD at Au(111) and Pt(111) surfaces in the presence of bromide. The differences in the behavior of Cu UPD at these two electrodes were ascribed not to energetic reasons, but rather to geometric constraints imposed by the lattice structure of the metal on the deposited adlayer.

Initial stages of bulk Cu deposition onto Au(100) have been investigated, applying STM [394]. Many monolayers of Cu were deposited, with the first monolayer formed via UPD, growing pseudomorphic.

Later, Kolb and coworkers [395] have studied copper deposition on Au(100) using *in situ* STM and *in situ* SXS. At the potentials positive with respect to the reversible Nernstian potential in sulfuric acid solutions, pseudomorphic (1 × 1) copper monolayer was formed. In STM studies at negative potentials, it was observed that bulk copper nucleates at the surface defects, step edges, or island rims. STM images have shown that the copper film up to 10 layers has a pseudomorphic structure. On the other hand, SXS measurements allowed one to precisely measure the copper layer spacing ($1.45 \pm 0.02 \text{ \AA}$). The obtained number is in good agreement with the value determined from the copper–copper step height in STM measurements.

Sanchez and Leiva [396] have considered density functional in the investigations of Cu UPD on Au(111) and Au(100). The analysis of different energetic contributions to the underpotential shift has shown that deposition of Cu on these surfaces should occur at overpotentials. The authors have arrived at the conclusion that other factors, such as anion coadsorption, should be considered in order to explain their experimental observations.

UPD of Cu on Au(111) electrodes in the presence of sulfate anions has been particularly intensively studied, both experimentally and theoretically [397] (for the review covering the literature up to 1995, see Ref. 398). Sulfate ions are specifically coadsorbed with underpotentially deposited Cu at negative potentials. For this system, a very striking phenomenon is the appearance of two voltammetric peaks, separated by 50–150 mV, upon addition of Cu^{2+} ions to the H_2SO_4 solution [382, 397, 399–401]. For the potential range separating the peaks, the existence of adsorbate layer of the $(\sqrt{3} \times \sqrt{3})$ structure,

consisting in 2/3 of a copper monolayer and in 1/3 of sulfate ions monolayer, has been suggested [402]. Xu and Wang [403] have carried out the first-principles total-energy calculations to study the structure of Cu UPD on Au(111) in H_2SO_4 solutions. It has been evidenced that the proposed honeycomb structure comprising in 2/3 a copper monolayer is unstable without the coadsorbed sulfate, which bound to copper. Sulfate anions bind much more weakly to the clean Au(111) surface. Więckowski and coworkers [404] have presented the simulated dynamics of Cu UPD with sulfate ions present at the Au(111). Uchida et al. [405] have applied EQCM to study adsorption of anions (perchlorate, sulfate) on pc-Au electrodes with and without copper adatoms. It has been shown that the ratio of the number of Cu adatoms to the number of adsorbed anions is close to two when Cu coverage ranges from 0.2 to 0.5. Later, Uchida et al. [406] have studied adsorption of bisulfate and perchlorate on Au(111) electrodes, with and without Cu adatoms, applying electrochemical quartz crystal microbalance. Więckowski and coworkers [398] have applied combined computational statistical mechanics-based lattice-gas modeling, CV, coulometry, *ex situ* Auger electron spectroscopy, and low-energy electron diffraction to study Cu UPD on Au(111) electrodes in sulfate-containing electrolytes. Using group-theoretical ground-state calculations and Monte Carlo simulations, they have estimated effective electrovalencies and lateral adsorbate–adsorbate interactions, which cannot be calculated yet by the first-principles methods. Nakamura et al. [407] have applied *in situ* SXD to study the structure of coadsorbed copper bisulfate anion and hydration water molecule on Au(111) electrode in 0.5 M H_2SO_4 solution, in the potential range from 0.250 V

to 0.400 V. Two-thirds of the surface was occupied by Cu and 1/3 by the coadsorbed sulfate. On each Cu atom, one hydration water molecule was placed, forming a stable structure.

Recently, Kuzume et al. [408] have studied copper UPD at high-index single-crystal Au surfaces.

The mechanism of dissolution of the Cu UPD layer on Au(111) has been studied by Ataka et al. [409]. The monolayer comprised Cu in 2/3 and sulfate in 1/3 proportions. It has been found by applying time-resolved surface-enhanced infrared absorption spectroscopy and chronoamperometry that dissolution proceeds in two steps. In the first step, 1/3 Cu monolayer and all sulfate anions are removed via the Langmuir-type kinetics. In the second step, the rest of Cu is desorbed via nucleation and growth kinetics.

Copper was also deposited on gold electrodes modified by chemisorption with different substances. Nishizawa et al. [410] have studied Cu deposition on Au(111) electrode coated with a SAM of propanethiol in the potential region covering UPD. It has been found that the SAM remains at the electrode surface without significant changes in its amount and structure, even after repeating Cu deposition and stripping cycles. Similarly, Kolb and coworkers [411] have performed CV studies on the kinetics of Cu UPD from H₂SO₄ solutions on Au(111) modified with alkanethiol. They have found that Cu UPD proceeds on such surfaces, yet the UPD current peak is shifted to the overpotential region at typical scan rates. Also, in the underpotential region close to the Nernstian potential, the formation of the monolayer occurs, but it lasts for more than 1 h. Martinez-Ruiz et al. [412] have studied UPD of Cu on iodine-modified Au(111) using *in situ* STM and CV in

sulfuric acid solutions. In the UPD process, a (1 × 1) Cu monolayer was formed of a lattice parameter equal to that of Au(111). The results suggest that iodine adlayer is constantly present at the top layer during electrodeposition and stripping of Cu and no noticeable loss of iodine is observed. Kinetics of Cu UPD on iodine-modified Au(111) electrodes has also been studied by the same group of researchers [413] in 1 mM solution of CuSO₄ in 0.05 M H₂SO₄, applying CV and chronoamperometry. The presence of iodine adlayer slowed down the kinetics of Cu UPD compared to the iodine-free surface. The kinetics of deposition was described applying a model with three types of contributions.

Epitaxial electrodeposition has been applied to crystallize a 0.5-μm-thick Cu₂O film on Au(100) from an alkaline copper lactate solution [414].

Zhang et al. have studied the influence of bromine adsorption on copper electrodeposition on pc-Au electrodes modified with SAMs [415].

24.4.6.2 Cd

The formation and growth of thin alloy film at underpotentials during electrodeposition of Cd on Au(100) in 50 mM H₂SO₄ + 1 mM CdSO₄ solution has been studied using EC-AFM [416].

Santos et al. [417] have studied UPD of Cd on polycrystalline Au electrodes using voltammetry and microgravimetry.

Atomic structures of several adlayers of Cd deposited underpotentially on Au(111) surface in H₂SO₄ solution have been visualized applying *in situ* STM [418]. Three ordered adlattices have been observed, all of which had a long-range linear morphology and were rotated by 30° with respect to the substrate lattice directions. The same system has been studied later

[419] applying *in situ* and real-time surface differential diffraction. It has been found that at the initial stages of UPD, Cd atoms bind to the surface at the bridging sites. This was followed by the formation of an adlayer structure of Cd atoms adsorbed at the threefold hollow sites, before the Au–Cd intermixing took place.

Formation of the Au–Cd alloy during Cd UPD on Au(111) has been investigated by del Bario [420]. Apart from electrochemical methods, *in situ* STM has also been used. It appears from STM investigations that the alloy can be formed at relatively high underpotentials accompanied by the formation of 2D Cd islands. When appropriately large, these islands coalesce to form a new 2D island on the top of the partially formed first Cd monolayer. These islands exhibit hexagonal atomic structure of the interatomic distance of 0.29 ± 0.01 nm.

Kawamura et al. [421] have studied the effect of electrolytic conditions on the coverage of an Au(111) electrode with underpotentially deposited layer of Cd. The Cd atomic layer was located on the Au(111) surface similar to the reconstructed structure. Also, a layer of sulfate anions was positioned on the Cd atomic layer. Cd coverage was found to be dependent on the concentration of H_2SO_4 .

Schmuki and coworkers [422] have studied initial stages of Cd electrodeposition on the Au(111) surface from H_2SO_4 solutions. The results have shown that in such solutions (Cd(II) in H_2SO_4), the Au(111) surface starts to reconstruct at potentials around 850 mV versus bulk formal potential of cadmium electrode. Nucleation of Cd started in the potential range 350–300 mV as the formation of separated islands of monoatomic height. Further, cathodic polarization led to the formation of strings and finally to the cadmium layer

with the expected surface alloying. The same group of researchers [423] studied electrodeposition of Cd on a herringbone reconstructed Au(111) surface from the same solution as before, by also applying EC-STM. Distinct dots of monoatomic height were formed in the UPD region. At these potentials, nucleation proceeded exclusively at the elbow sites of the Au(111) herringbone reconstruction, leading to a self-organized surface patterning of nanoscale Cd islands.

Vidu et al. [424] have studied the kinetics of thin alloy film formation and growth during Cd electrodeposition on Au(100) and Ag(100) within the Cd UPD range from -0.3 to -0.45 V. Electrochemical and AFM experiments in 1 mM CdSO_4 and 0.05 M H_2SO_4 solutions have revealed that the overall alloying process comprises two processes: the first occurring relatively fast within a few atomic layers ($D \sim 10^{-16}$ $\text{cm}^2 \text{s}^{-1}$), and the second much slower ($D \sim 10^{-19}$ $\text{cm}^2 \text{s}^{-1}$), indicating a solid-state diffusion. In the later work [425], the process of inward diffusion of Cd UPD into an Au(100) substrate has been studied in the temperature range 295–333 K, applying voltammetry, microgravimetry, and X-ray diffractometry. Activation energy of the above-mentioned fast diffusion step is about 70 kJ mol^{-1} . It has been found that the amount of Cd UPD increases with the temperature. From X-ray diffraction studies, it was concluded that β -Au–Cd layer is formed on the sample after keeping the electrode in the UPD region at -1100 mV (versus $\text{Hg}|\text{Hg}_2\text{SO}_4$) for 1 h at 333 K. Vidu and Hara [426] have studied the kinetics of thin alloy film formation and growth on Au(100) from 1 mM CdSO_4 and 50 mM H_2SO_4 within the underpotential range of Cd electrodeposition. The distribution of Cd atoms on the Au electrode surface has

been estimated on the basis of the calculated diffusion coefficients of Cd. The mechanism of the surface alloying process in the UPD region has also been proposed.

Cd deposited underpotentially on Au(111) reaches a limiting coverage of 0.66 monolayer. Electrosorption valency corresponding to this coverage is equal to 0.5, which indicates that Cd adatoms are not fully discharged at the surface [427].

Surface alloy formation during Cd UPD on Au(110) in H_2SO_4 solutions has been investigated, applying long-time polarization experiments and *in situ* AFM [428]. The dynamics of this process depended on the polarization conditions. Moreover, alloying process competed with surface diffusion and further adsorption processes. Cd UPD on Au(111) from sulfate solutions has also been studied by Lay et al. [429], who have utilized electrochemical STM ultrahigh vacuum emersion techniques and quartz crystal microgravimetry. According to STM results, the Au(111)-(1 × 23) reconstruction is not lifted up by Cu UPD. Also, morphology of reconstruction indicates formation of the adlayer structure on the surface. EQCM studies suggest coadsorption of anions. Also, there are indications of a surface alloy formation.

24.4.6.3 Pd

In a series of papers, Kolb and coworkers have presented CV and *in situ* STM studies on palladium deposition on various gold single-crystal electrodes. They have found [430] that PdCl_4^{2-} is adsorbed on Au(111), forming a distorted hexagonal structure, which plays a crucial role in Pd deposition and dissolution. It has also been found that Pd deposition starts from the formation of a pseudomorphic layer in the underpotential region, followed by the formation of the second Pd monolayer at overpotentials. Pd nucleated

at monoatomic high steps and grows two dimensionally. Morphology of the overlayers changed with the increasing Pd coverage from the flat and well ordered for the first two monolayers to the increasingly rough and defect rich.

Electrochemical properties of Pd adlayers on Au(111) have also been compared to the behavior of massive Pd(111) [431]. Gradual transition to the bulk properties with increasing Pd coverage has been observed.

Similar to Pd UPD on Au(111), Pd deposition on unreconstructed Au(100) has also been studied applying CV and *in situ* STM by Kolb and coworkers [432]. They have investigated both an island-free surface and the surface covered with the islands originating from the lifting of the (hex)-reconstruction. It has been found that approximately one Pd monolayer accompanied with a distorted-hexagon chloride adlayer is formed in the UPD process. First Pd layers on Au(100) had different electrochemical behavior than large Pd(100) single crystals.

In another work from this series [433], deposition of Pd on the unreconstructed Au(110) has been studied. An ordered adlayer of PdCl_4^{2-} was imaged with atomic resolution. Pd deposition started at monoatomic high steps. From the coulometric data, it follows that approximately three monolayer equivalents are deposited in the UPD range, what may, in turn, be a result of the surface alloy formation.

Naohara et al. [434] have also studied electrodeposition of Pd from PdCl_4^{2-} complex on Au(100) electrode using *in situ* STM. Electrochemical deposition of Pd on Au(100) occurred at potentials more negative than 1.0 V. The first Pd layer was deposited not only on the terrace but also on gold islands, which were formed as a result of the lifting process

of the reconstructed Au(100). The bulk and surface structures of the deposited Pd layers were investigated by X-ray diffraction. The formation of a Pd(100) phase of a (1×1) surface structure has been confirmed.

Electrochemical behavior of ultrathin Pd epitaxial layers deposited electrochemically on Au(111) and Au(100) has been found to be strongly dependent on the surface structures and the thickness of the Pd thin films [435]. From the kinetic studies of Pd deposition on Au(111) electrode from K_2PdCl_4 in 0.1 M H_2SO_4 , it has been deduced [436] that this process proceeds via an instantaneous nucleation and two-dimensional (2D) growth. Initial stages of Pd deposition on Au(110) have also been studied by Robach et al. [437], who have applied STM, low-energy electron diffraction, and Auger electron spectroscopy for this purpose.

24.4.6.4 S, Se, and Te

Also, thin films of semiconducting compounds were formed on a gold electrode. To obtain them, a methodology called *electrochemical ALE* (electrochemical atomic layer epitaxy) has been developed. This procedure is based on the formation of individual atomic layers of particular elements, which may further form a compound. Accordingly, in each cycle, a controlled formation of a monolayer of the particular compound occurs. The advantage of this methodology is that three-dimensional growth of one-elemental deposit is inhibited.

The above method combined with UPD of atomic layers has been used for the preparation of such compounds as CdTe, CdSe, CdS, and others. A paper reviewing the formation process of such compounds has been published by Wade et al. [438]. Preparation of such compounds is usually

carried out on gold electrodes. In that case, the first atomic layer of the particular element is obtained via UPD at the gold surface.

We briefly present below the papers dealing with deposition of S, Se, and Te on Au electrodes and with the formation of semiconducting compounds at their surfaces.

24.4.6.5 Sulfur

Gichuhi et al. [439] have used Au(111) electrode covered with the initial underpotentially deposited Cd layer. When H_2S was electrolyzed at this surface, applying underpotential, an adlattice of the S–S interatomic spacing equal to 0.34 nm was obtained. The second monolayer of Cd and S had the same structure as the first CdS monolayer, showing that these two CdS monolayers were epitaxial. However, the third deposited monolayer of CdS exhibited interatomic spacing as observed for the bulk CdS. A direct fabrication of monodispersed, ultrasmall nanocrystals from the SAMs at Au(111) substrate has also been described [440]. Reconstruction of CdS monolayers has been studied by Demir and Shannon [441].

24.4.6.6 Selenium

Huang et al. have studied electrodeposition of selenium on Au(100) [442]. The structures of submonolayer coverages have been identified using ultrahigh vacuum electrochemical techniques, as well as STM. Selenium atomic layers were formed electrochemically by (1) direct electroreduction of $HSeO_3^-$, (2) anodic stripping of previously formed bulk Se. Alanyalioglu et al. [443] have investigated electroreduction of Se atomic layers on Au(111) from aqueous SeO_2 solutions. Two waves at the potentials more negative than that

expected for the Se(IV)/Se couple were observed. Therefore, Se deposition could not be accomplished via UPD. In addition, Ruach-Nir et al. [444] have analyzed structural effects in electrodeposition of CdSe quantum dots on mechanically strained gold.

24.4.6.7 Tellurium

Ikemiya et al. [445] have investigated both the atomic structure and growth of electrodeposited Te films on Au(100) and Au(111) with large lattice misfits. Deposition was performed in sulfuric acid solutions using *in situ* AFM. On both substrates, bulk-deposited Te films were formed according to the Stranski-Krastanov mechanism. Their atomic structures changed with the increasing film thickness.

It has been found [446] that *in situ* optical second-harmonic rotational anisotropy was significantly changed along with the first UPD of Te, and that bulk Te deposition attenuated the anisotropic character of the overall surface symmetry.

Later, Sorenson et al. [447] have studied electrochemical formation of tellurium atomic layers on Au(100) and phase transitions within these layers. They used voltammetry, *in situ* STM, and low-energy electron-diffraction methods. Two sub-monolayer reduction steps of HTeO_2^+ were observed. Three-dimensional nucleation progressed at potentials corresponding to the bulk Te deposition. The structures of electrodeposited atomic layers of Se and Te on Au(100) and Au(111) have been studied and compared [448]. At each surface, both elements formed a low-coverage structure, with atoms packed in high coordinate sites at distances just above their van der Waals diameters. When the coverage was increased, chalcogenide atoms formed either chains or rings. In

Ref. 448, a discussion concerning the appearance of triangular phase boundaries for both chalcogenide atoms on Au(111) is also presented.

Sorenson et al. [449] have carried out similar studies on electrodeposition of atomic Te layers on Au(111) surfaces from aqueous solutions. Similarly as in earlier works, in this study also, the following techniques were utilized: voltammetry, *in situ* STM, low-energy electron diffraction, and Auger electron spectroscopy. Prior to the deposition, tellurium oxide species coated the surface. Two steps were distinguished in the UPD process. Deposition process was kinetically slow.

Nicic et al. [450] have applied chronocoulometry and EQCM to perform UPD of Te monolayers on Au surfaces from HClO_4 solution.

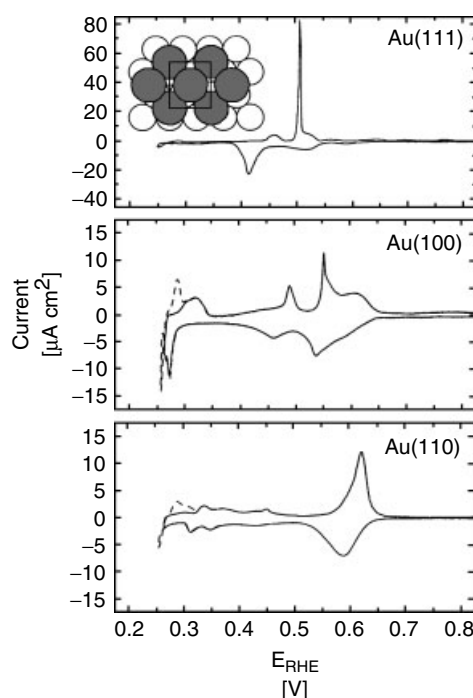
Auger electron spectroscopy, X-ray photoelectron spectroscopy, low-energy electron diffraction, and *in situ* STM have been employed to investigate two-step alternate electrodeposition of Cd and Te atomic layers, forming finally, CdTe monolayers (electrochemical ALE on Au(111)) [451]. STM images suggest that previously proposed hexagonal structures for CdTe may not be correct.

24.4.6.8 Bi

Wang et al. have compared UPD of Bi on different Au surfaces (see Fig. 14). It has been found that chemisorbed Bi adatoms bound preferably at more open surface.

From the CV data, the following charges associated with Bi^{3+} deposition have been estimated: 445, 472, and $357 \mu\text{C cm}^{-2}$ for Au(111), Au(100), and Au(110), respectively. The charges involved in the deposition of one Bi atom per one surface gold atom are 666, 576, and $408 \mu\text{C cm}^{-2}$, for the same sequence of the surface

Fig. 14 Linear sweep voltammograms for UPD of Bi on three low-index gold surfaces in 0.1 M HClO₄ containing 2.5 mM Bi₂O₃. Scan rate: 2 mV s⁻¹. Dashed line shows the onset of bulk deposition. Inset: atomic model of the close-packed 2Bi-($p \times \sqrt{3}$) monolayer on Au(111) (after Ref. 59).



types [59]. Hence, the following values of Bi coverage (with respect to monolayer) were calculated: 0.67 for Au(111), 0.82 for Au(100), and 0.88 for Au(110). These values are close to those determined from the SXS studies [59, 452]. It is noteworthy that Bi–Au bonding was found to be more non-metallic than those of Tl–Au and Pb–Au monolayers. Therefore, Bi monolayer differs substantially from the layers of the above-mentioned two elements [59].

Underpotential and overpotential deposition of Bi on Au(111) have been studied applying in situ STM [453]. It has been found that the adsorbed bismuth lifts the reconstruction of the Au(111) surface, leading to the formation of Au islands at potentials more cathodic than 0.170 V versus SCE. Atomic images of UPD Bi layer have shown the formation of a nearly rectangular unit cell of dimension $0.39 \pm 0.02 \times 0.43 \pm 0.02$ nm.

5–10-nm-diameter and 3–4 atomic layers deep nanometer-sized zero-dimensional (0D) cavities have been obtained at Au(111) surface applying short (80 ns) voltage pulses to the STM tip [454]. In these nanocavities, localized UPD of 0D bismuth dots has been observed applying in situ STM. The authors have discussed and compared the investigated system with the behavior of the Au(111)/Ag⁺,NO₃⁻ system.

Itaya and coworkers [455] have studied Bi UPD on Au(100) in HClO₄ solutions using in situ STM. It has been found that UPD occurs in three steps involving the formation of an A(3 × 3) structure and a square lattice has been found for the first layer.

Tamura et al. [456] have studied the kinetics of UPD of Bi monolayer on Au(111) applying simultaneously, electrochemical methods, current transients, and SXS.

Langmuir adsorption kinetics of Bi adsorption was observed for transients.

Du and Wang [457] have developed a method for bismuth determination, based on good electrochemical properties of gold electrode covered with underpotentially deposited Bi. In this method, Bi was preconcentrated at the Au surface and this step was followed by anodic stripping.

24.4.6.9 Pt

Electrochemical deposition of Pt on Au(111) electrode in acidic H_2PtCl_6 solutions has been studied [458] using STM and EQCM. The formation of the Pt(111) bulk phase and the surface structure of Pt(111)-(1 × 1) were confirmed by X-ray diffraction and UPD of copper and hydrogen, respectively.

Waibel et al. [459] have studied deposition of Pt on unreconstructed Au(111) and Au(100) applying CV and in situ STM. STM studies revealed that $PtCl_4^{2-}$ complex is adsorbed on both surfaces and Pt is further deposited at rather high overpotential. Nucleation of Pt started mainly at the defects, like step edges, at low deposition rates. Due to the high overpotential, some nuclei also appeared on terraces at the random sites.

Also, Nagahara et al. [460] have employed in situ STM to study molecular adlayers of haloplatinate complexes and electrochemically generated Pt monoparticles on Au(111). In atomic resolution STM images, pinwheel features of planar PtX_4^{2-} adsorbates ($X = Cl^-, Br^-, I^-$) were observed. Reduction potentials of these overlayers to metallic Pt decreased in the order $PtCl_4^{2-} > PtBr_4^{2-} > PtI_6^{2-}$. The Pt deposit existed in the form of nanoparticles of an average diameter of 3.0 nm and height of 0.46 nm. They were uniformly distributed on the Au(111) substrate.

24.4.6.10 Ni

Bubendorff et al. [461] have reported, on the basis of CV and STM studies, that it is possible to deposit, applying UPD, a Ni monolayer on Au (111) from a sulfamate solution. It has been found using high-resolution STM that the formation of Ni layer occurs via complexation of Ni(II) by sulfamate adlayer on the Au surface.

Moller et al. [462] have performed in situ STM observations of Ni electrodeposition on reconstructed Au(111) electrodes. Ni nucleation proceeded in three distinct potential-dependent steps. The same group of researchers [463] has studied electrodeposition and electrodissolution of Ni on Au(100) electrodes. Pronounced differences were observed for the nucleation and submonolayer growth on the reconstructed and unreconstructed surfaces. On perfectly reconstructed Au(100), the formation of Ni islands started at overpotentials significantly higher ($\eta \geq 100$ mV) than on unreconstructed surface ($\eta \geq 40$ mV), where Ni monolayer islands were formed. Dissolution of the Ni film exhibited better monolayer stability in comparison to the multilayer deposit.

Allongue et al. [464] have studied nucleation and growth mechanisms of Co and Ni on Au(111) using in situ STM and electrochemical methods.

Submonolayer of Ni deposited in the temperature range of 130–180 K on the missing-row reconstructed Au(110)-(1 × 2) surface has been analyzed using STM [465]. An order within the thin epitaxial AuNi film deposited on an Au(100) surface, accompanying temperature changes, has been investigated by applying X-ray diffraction [466].

24.4.6.11 Co

Repain et al. [467] studied a growth of cobalt on Au(111) vicinal surfaces in

the submonolayer range. The presence of surface reconstruction led to self-organized nanostructures, such as very regular arrays of clusters or nanowires. The obtained results may be useful in the development of the fabrication procedure of cobalt nanostructures or ultrathin films of unique magnetic properties.

Also, Kolb and coworkers [468] have studied initial stages of Co deposition on Au(111) and Au(100) using CV and STM. Depending on the crystallographic orientation of the substrate and electrochemical properties, either three- or two-dimensional growth has been observed. The influence of surface reconstruction on the nucleation and growth behavior has also been discussed.

Formation and stripping of a cobalt adlayer on/from a polycrystalline Au electrode have been studied [469] applying electrochemical methods under underpotential conditions. The kinetics of deposition fitted a model of a simultaneous adsorption and diffusion-controlled two-dimensional instantaneous nucleation of cobalt on the electrode surface.

Nucleation and growth of cobalt nuclei on a polycrystalline gold electrode have been studied by the same group of researchers [470] using electrochemical methods in 10^{-2} M CoCl_2 and 1 M NH_4Cl solutions of $\text{pH} = 9.5$. The authors have studied the transition accompanying the change of electrode potential from underpotential to overpotential deposition (OPD) region. The corresponding current-time transients were explained in terms of a kinetic mechanism involving three different contributions: (1) Langmuir-type adsorption process, (2) 2D diffusion-controlled instantaneous nucleation, and (3) mass transfer-limited 3D nucleation.

Stepanyuk et al. [471] have applied local approximation of the density-functional theory and the Korringa-Kohn-Rostoker (KKR) Green's function method to determine the energy of Co adatoms located at the ideal Au(100) surface. Total-energy calculations have shown that Co atoms and small Co clusters are preferably embedded inside the substrate.

24.4.6.12 Sb

Jung and Rhee [472] have reported voltammetric studies on the deposition of Sb on Au(111) and Au(100) electrodes. In the formation of the metallic Sb layer, two processes were involved. The first one was the reduction of the irreversibly adsorbed oxygenous Sb layer. The other was completing the full monolayer of Sb via UPD of oxygenous Sb species in the solution.

Later, Wu et al. [473] presented an *in situ* STM study of Sb electrodeposition on Au(111). The authors have studied irreversible adsorption of Sb and redox behavior of Sb(III) adspecies with and without the influence of UPD, and vice versa.

The process of irreversibly adsorbed Sb on Au(111) at the open-circuit potential (close to 0.2 V) has been investigated using *in situ* STM [474]. The oxygenated Sb adlayer was nucleated and grown on terraces and at step edges. The oxygenated Sb domains present on terraces were round-shaped islands of a diameter ranging between 3 and 6 nm.

Wang et al. [475] have proposed a similar analytical method as that for bismuth for antimony determination based on Sb UPD on gold electrode. In the proposed procedure, Sb was accumulated at the gold surface, and this step was followed by anodic stripping. A detection limit 2.1×10^{-9} M was reported for a 120 s electrochemical deposition.

Yan et al. [476] have presented *in situ* STM results of a structural transition of Sb on Au(100). Remarkable structural transition took place at the potential, sufficient to initiate UPD. Both the coverage and potential-dependent Sb–Au interactions were responsible for the structural transition. The formation of the surface compound AuSb_2 has been suggested.

24.4.6.13 Sn

UPD of Sn on Au(100) has been studied applying electrochemical methods and *in situ* STM [477]. Three stages of Sn UPD have been distinguished: (1) reversible submonolayer UPD, (2) surface alloying, and (3) bulk-extended alloying. Reversible UPD of a submonolayer proceeds in the form of 2 nm clusters at 0.04 V itself. The surface alloying took place at -0.04 V, and the bulk alloying at -0.3 V, which quickly changed the surface morphology.

Mao et al. [478] have applied *in situ* STM to study Sn UPD on reconstructed and unreconstructed Au(111) electrodes. On the unreconstructed Au(111), Sn formed size-confined two-dimensional clusters of 1–2 nm. At more negative potential, surface alloying was observed. On the reconstructed Au(111) surface, in turn, Sn preferably nucleated at face-centered cubic regions. The nuclei expanded toward the hexagonal close-packed regions to build up deposit domains.

24.4.6.14 Al

Aluminum underdeposited on gold electrodes from $\text{AlCl}_3 + \text{NaCl}$ melts at $200\text{--}300^\circ\text{C}$. The process has been studied [479] applying CV, potentiostatic deposition, and galvanostatic oxidation. The obtained deposits were characterized by electron microprobe analysis and glancing incidence by X-ray diffraction.

Formation of several successive layers of bulk intermetallic compounds has been shown. Also, Lee et al. [480] have detected, during Al UPD, the formation of two alloys on polycrystalline Au electrodes from acidic 1-ethyl-3-methylimidazolium chloroaluminate that melt at room temperature. Moreover, in the Al UPD region, fast phase transition between these two intermetallic compounds has been evidenced. Later, the same group of researchers [481] has performed EQCM studies on Al deposition and alloy formation on Au(111) in ambient temperature molten salts/benzene mixtures.

24.4.6.15 Tl

Thallium UPD on Au(111) has been studied, applying potential-step chronocoulometry and quartz crystal microbalance [482]. The UPD surface coverage increased with the increasing cathodic potential. At low coverage, the sublayer was not completely discharged, as it appeared from electrosorption valency.

Poškus and Agafonovas [483] have applied radioactive Tl-204 to study its UPD on a polycrystalline gold electrode in alkaline solutions. The potential dependence of the equilibrium surface concentration obtained from the radiometric method has been compared to that calculated from CV. Surface concentration of Tl decreased monotonically as the potential was changed from the more positive Nernstian values. This dependence exhibited a minimum without reaching zero. At more positive potentials (with respect to the minimum), adsorption of Tl^+ induced by specifically adsorbed hydroxyl anions occurred.

It has also been found that metal-halide coadsorption of Tl–Br and Tl–I proceeds on Au(111). This was a proof that UPD

of metals can be affected by specific adsorption of anions [59].

24.4.6.16 Pb

Pb UPD on polycrystalline Au electrode in 0.1 M perchloric acid solution has been studied by Henderson et al. [484]. In this study, CV, electrochemical quartz crystal microbalance (EQCM), and probe beam deflection methods have been used. It has been found that Pb UPD proceeds in three steps. The first step comprised water ejection from the gold surface. This step was followed by metal UPD accompanied by the removal of the adsorbed OH. Also, Zeng and Bruckenstein have studied UPD and adsorption of Pb on pc-Au electrodes, applying XPS and TOF-SIMS method in case of 0.1 M NaCl electrolyte [485], and EQCM in case of 0.1 M NaClO₄ and 0.1 M NaCl electrolytes [486]. In the presence of chloride anions, the adsorption of Pb–Cl[−] complex has been found.

A relation between the surface stress and the structural change within the Pb UPD layer on Au film electrode has been studied, applying a bending beam method [487]. A maximum in the surface stress versus potential dependence emerged at the onset of UPD, similarly as in electrocapillary curve.

Hale et al. [488] have studied Pb UPD on Au(110), applying XPS and ultrahigh vacuum apparatus with a chamber for electrochemical experiments. Lead was detected at the gold surface in the entire considered potential range: −0.5 to 1.5 V (versus Ag/AgCl). A large increase in the surface concentration of oxygen was found for lead-containing solutions.

Rojas [489] has investigated theoretically, the stability of either different submonolayers of Pb adsorbed on Au(100) or grown as the first monolayer. Calculations were performed using the atom

superposition and electron delocalization molecular orbital methodology in the cluster approximation.

Deposition of Pb has also been carried out at modified gold electrodes. The films of 3-mercaptopropane sulfonate on polycrystalline gold electrodes were prepared from an acidic solution. At such electrodes, UPD current corresponding to voltammetric reduction of lead(II) was enhanced, compared to the current observed at a clean polycrystalline gold electrode [490].

Also, epitaxial electrodeposition of Pb–Tl–O superlattices on single-crystal Au(100) has been carried out [491]. The films were formed at room temperature from aqueous solutions of 5×10^{-3} M TlNO₃ and 0.1 M Pb(NO₃)₂ in 5 M NaOH. Applying current density of 0.05 mA cm^{−2}, a bulk film of a composition of Pb_{0.46}Tl_{0.54}O_{1.7} was formed.

Finally, UPD of Pb on silver and gold colloids has been described by Bokshits et al. [492].

24.4.6.17 Zn

Takahashi et al. [493] have applied CV for UPD of Zn on an Au(111) electrode from phosphate solutions containing Cl[−], Br[−], and I[−].

24.4.6.18 Ge

Nanoscale electrodeposition of Ge on Au(111) from an ionic liquid has been studied [494] utilizing *in situ* STM. At underpotentials, a thin rough layer is formed. In turn, at overpotentials close to 250 mV, 50-nm-diameter nanoclusters of the initial height of several nanometers were grown. Interestingly, at overpotential of 50 mV, the deposits could be transformed within several hours into a layered structure, indicative of Ge(111) bilayers.

24.4.6.19 Rh

Kibler et al. [495] have studied electrochemical deposition of Rh on Au(111) using CV and in situ STM. Rhodium started to deposit irreversibly around 200 mV versus SCE. First, a Rh bilayer was grown, which exhibited electrochemical behavior similar to that of well-ordered Rh(111) surface.

24.4.6.20 Li

Li UPD on highly oriented Au(111) electrodes has been performed [496] from LiAsF₆ solutions in PC using quartz crystal microgravimetry, CV, and UV-visible reflectance spectroscopy simultaneously.

Saito and Uosaki [497] have studied the formation and morphological changes of the surface Li film on Au(111) electrode in 0.1 M LiClO₄ solution in PC applying STM. The surface film was observed at potentials more negative than 1.5 V (Li⁺/Li). Many nuclei appeared on the flat terrace of the electrode at potentials more negative than 0.9 V, where UPD of lithium on Au was started.

24.4.6.21 Fe

Kawagoe et al. [498] have investigated the growth of Fe submonolayer films on Au(001) in the temperature range of 300 to 500 K using STM. The STM images have shown that growth and morphology of the films markedly depend on the growth temperature. Fe islands of a monolayer-height nucleated and grew on Au(001) terraces at 300 K. At 353 and 393 K, Fe islands with double-layer height and small pinholes were observed on terraces. Step edges were decorated by Fe dendrites.

24.4.6.22 Ag

Więckowski and coworkers [499] have used AES to study UPD of Ag on the Au surface.

Chabala and Rayment [500] performed a time-resolved in situ and real-time X-ray diffraction study of Ag UPD on the Au(111) surface. Later, the same researchers [501] described an in situ surface differential diffraction and anomalous scattering of surface relaxation accompanying Ag UPD on Au(111). Time-resolved surface differential diffraction has been used [502] to study the mechanism and kinetics of Ag electrodeposition on Au(111). Also, the effect of the surface stress in the surface differential diffraction measurements has been investigated. Gimenez et al. [503] have performed Monte Carlo simulation of the formation and growth of low-dimension phases in Ag UPD on Au(111). From Monte Carlo simulations, it has also been found [504] that energetic atoms can promote nucleation and island growth at early stages of film growth and thus improve the smoothness of the film surface. Whelan et al. [505] have studied structural surface transitions induced by repetitive UPD of Ag on Au(111). More recently, Kondo et al. [506] have published the results concerning in situ structural study on Ag UPD on Au(111) electrode, applying SXS technique. In situ STM has been used to investigate electrodeposition of silver on Au(111) electrodes from H₂SO₄ solution [507]. STM images of Ag UPD have revealed a series of ordered adlayer structures of increasing coverage with decreasing potential.

Ag UPD onto gold substrates covered previously with SAMs of alkanethiols in order to induce penetration of silver between the monolayer and the gold substrate has been described by Oyamatsu et al. [508]

Wang et al. [509] have reported overpotential deposition of Ag monolayer and bilayer on Au(111) mediated by the Pb adlayer UPD/stripping cycles.

Brankovic et al. [510] have described the surfactant-mediated electrochemical deposition of Ag on Au(111). Also, Reyes-Cruz et al. [511] have studied electrochemical deposition of Ag and Au from cyanide leaching solutions.

24.4.6.23 Hg

Inukai et al. [512] have used STM to study Hg UPD on Au(111) in sulfuric and perchloric acid solutions. For sulfuric acid, the influence of adsorption of bisulfate was indicated. It has been found that after the formation of the first UPD adlayer, two different structures were simultaneously formed on the same terrace. For perchloric acid, only a single structure was found. These results reflected a significant influence of the supporting electrolyte anions on the UPD structure. Recently, Abaci et al. [513] have presented the temperature-dependent studies on the influence of counteranions on Hg UPD on Au(111).

Finally, we should mention the paper by Oyamatsu et al. [514] who have studied UPD of Tl, Pb, Ag, Cd, Cu, and Bi on an Au(111)/mica electrode coated with a SAM of alkanethiols, applying CV and STM. UPD proceeded for the alkyl chain length shorter than C8. It has also been suggested that the blocking effects of the SAM depend on the Stokes radius of metal ions. For a particular case of Ag deposition, the formation of islands of atomic monolayers on which octanethiol molecules were adsorbed hexagonally has been noticed.

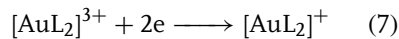
24.4.7

Electrochemistry of Coordination

Compounds of Gold. Electrodissolution and Electrodeposition of Au

For the general characteristics of complex compounds, it is useful to remember that both Au(I)/Au(0) and Au(III)/Au(I)

aqua complex systems have very positive potentials and thus exhibit strong oxidative properties. These potentials may be changed considerably when gold ions form complexes with different ligands, which stabilize both oxidation states [515–518]. Warren and Bennett [515] have prepared Au(III) complexes with diphos [*o*-phenylenebis(dimethylphosphine)] and its arsenic analog – diars. They were irreversibly reduced in acetonitrile at Pt electrode at the potentials of -0.45 and -0.17 V for diphos and diars complexes, respectively (versus Ag| 10^{-2} M AgClO₄ in CH₃CN).



Basil et al. [518] have studied theoretically and experimentally dinuclear phosphorus ylide complexes of Au(I) and Au(II). These compounds revealed irreversible redox behavior in CV experiments.

McArdle and Bossard [516] have performed a CV study on electrochemical properties of Au(I) and Au(III) complexes with four bis(diphenylphosphines) at a gold working electrode. Two-electron processes ($\text{Au}^{3+}/\text{Au}^+$) of these species were either reversible or quasi-reversible at moderate scan rates. Earlier papers were discussed in the 4th volume of *Encyclopedia of Electrochemistry*, published in 1975. More recently, Lagerge et al. [519], for example, have studied adsorption of potassium gold cyanide from water onto industrial activated carbon, widely used for the recovery of gold at pH = 6.0. In the applied concentration range, two distinct mechanisms of adsorption, either successive or overlapping, were experimentally proved to proceed at room temperature. At low concentrations, gold was reversibly adsorbed as $\text{Au}(\text{CN})_2^-$ anions.

Koelle and Laguna [520] have carried out a systematic study on gold complexes at both oxidation states with phosphine and tetrahydrothiophene as neutral ligands, halide ions, as well as C_6F_5 (C_6Cl_5) as anionic ligands. The prepared complexes (15) were investigated using CV at a Pt working electrode. CH_2Cl_2 or acetonitrile served as a solvent with tetrabutylammonium hexafluorophosphate as a supporting electrolyte. All complexes were irreversibly reduced and only voltammetric peak potentials were reported.

The results obtained allowed one to establish the sequence of electroreduction potentials for Au complexes with π -acceptor ligands.

Both electroreductions occur at potentials considerably more negative than those observed for halide or oxosystems. Obviously, phosphine ligands stabilize Au(I) more than, for instance, CN^- and, consequently, shift the respective potential to more negative values compared to the potential of $Au(CN)_2^-$. Even stronger effect is caused by C_6F_5 (C_6Cl_5) groups.

Bond and coworkers [521] have described Au(III) electroreduction and Au(0) oxidation stripping processes in dilute aqua regia utilizing platinum, rhodium, iridium, gold, and glassy carbon electrodes. Sorption of tetrachloroaureate ions on carbon paste electrode modified with montmorillonite has been performed as a preconcentration step in the determination of gold in pharmaceutical preparation [522].

Further review of the latest literature allows one to claim that the recent electrochemical studies on gold complexes involve mainly electrodissolution of gold in the complexing media and its further electrodeposition from the complexing solution. Obviously, a large number of such investigations is related to practical

applications, since gold is frequently used as a coating metal.

24.4.7.1 Au Electrodeposition

The influence of different metal ions on the kinetics of gold electrodeposition on gold from alkaline cyanide solutions has been studied by Bek and coworkers [523–527]. Au was also deposited on glassy carbon and Pt electrodes from Au(I) ammonium solutions [528]. Nucleation mechanism was temperature dependent. Also, Marquez et al. [529] have investigated, applying electrochemical and spectroscopic methods, deposition of Au, Ag, and Au–Ag alloys on glassy carbon, and silicon electrodes from alkaline cyanide electrolytes. Also, electroreduction of $AuCl_4^-$ at boron-doped diamond electrodes has been studied [530]. Boxley et al. [531] have carried out electrochemical deposition and reoxidation of Au on highly oriented pyrolytic graphite in 5 mM $AuCl_4^-$ and 6 M LiCl solution. It has been noticed from double potential-step chronocoulometry that electrodeposition is reversible. Au nanoparticles were preferentially deposited on the upper plane of the step edges. It has also been shown that Au(I)-thiourea aqueous baths are a promising alternative to cyanide solutions for electrodeposition of Au and its alloys [532]. Free thiourea molecules were found to be adsorbed on the electrode at cathodic potentials in a vertical configuration, interacting with the metal surface via amino groups. The same authors [533] have performed in situ spectroelectrochemical Raman investigations of Au deposition and electrodissolution in $KAu(CN)_2$ solutions at pH = 6.3. Under anodic conditions, enhanced formation of $Au(CN)_2^-$ and OCN^- was observed. Also, in situ SERS has been employed to study Au deposition from sulfite electrolytes [534] and in the presence of benzylidimethylphenylammonium

chloride [535]. In recent years, electrodeposition of gold from thiosulfate-sulfite baths has been investigated [536, 537]. Gold single crystals were prepared via periodic reverse current electrodeposition in organic ion-track membranes used as templates and in the presence of either $\text{KAu}(\text{CN})_2$ or $\text{Na}_3\text{Au}(\text{SO}_3)_2$ solution. Au single crystals were successfully grown only from the cyanide solutions. There is a large interest in deposition of gold on silicon (see, for instance, [538–540]) considering the applications in microelectronics. Electrodeposition of gold has been carried out on different n -GaAs crystal faces [541] at the water–1,2-dichloroethane interface [542] into three-dimensional polypyrrole film [543]. Electrodeposition of thin gold films on indium-tin oxide and platinum substrates from an aminosilicate-stabilized gold sol has been described [544]. The obtained films were conductive, semitransparent, and comprised 4–6 nm Au particles, each coated with a thin aminosilicate shell. Sih et al. [545] have electrodeposited and characterized conducting thin films of gold nanoparticles bridged with oligothiophene linkers. Electrochemical oxidation of these particles resulted in the deposition of thin films consisting of intact nanoparticles linked by oligothiophene moieties. Finally, Lasia and coworkers have studied nucleation and crystal growth accompanying soft [546] and hard gold deposition [547–550].

24.4.7.2 Au Electrodissolution

Dissolution of gold and silver from Au/Ag alloys in aerated cyanide solutions has been investigated using rotating disc electrodes [551]. Dissolution was partially controlled by transport of either oxygen or cyanide. Kinetics of anodic dissolution of gold in cyanide solutions containing different metal ions has been extensively

studied by Bek and coworkers [552–566] (see also [567]). Also, the effect of temperature on dissolution has been studied [79, 568]. Electrochemical studies on dissolution of gold in thiosulfate solution [569–571] and in ammonia solutions at temperatures above 100 °C have been carried out [572]. Anodic dissolution of gold and its associated elements, for example, silver, copper, nickel, and iron in alkaline thiourea solution has also been accomplished [573, 574]. Gold was passivated by elemental sulfur produced from irreversible decomposition of thiourea. Addition of Na_2SO_3 improved the stability of thiourea in alkaline media and decelerated selective dissolution of gold (see also [575]). In HClO_4 solutions containing chloride ions, it has been noticed, using EQCM, that Au(111) dissolves in the three-electron oxidation process [576] and no evidence for one-electron oxidation has been found. Oscillatory electrodissolution of Au in 2 M HCl solutions has been investigated in Raman spectroscopy studies [577]. The obtained results indicate that the transition between active and passive states of Au account for current oscillations in a very narrow potential range.

24.4.8

Gold Clusters

The color of the colloidal solutions of gold depends on the size of colloidal particles (clusters). Several methods have been used for the preparation of such clusters (for a review see [578]). Since the size of clusters may change from one to several hundred angstroms, their electronic structure may vary between that of single atoms and the solid metal.

Gold clusters are stabilized by the adsorption of surfactants. Alkanethiols play an important role in this stabilization,

since – as we discussed earlier – they are adsorbed strongly on gold surfaces. Therefore the synthesis of clusters is carried out frequently in the presence of thiols. The adsorption of surfactants on the surface of growing clusters is useful in controlling of their size. In the core of such clusters there are Au atoms, while on the surface Au^+ ions are present which interact with thiols as shown by XPS [579].

The energy of Au-S surface bond on a cluster is 490 kJ/mol and the surface coverage by sulfur atoms is high (30 percent), compared to Au(111) surface.

One may obtain a stabilized cluster having different terminal groups.

The protective layer of surfactants may be exchanged for another, more appropriate surfactants [580]. The kinetics of such substitution has been studied [580].

Such nanoparticles may be deposited on different surfaces also, either by electrodeposition or by interaction with the surface. Various methods were used to combine clusters with the surfaces of solid substrates [578]. Some of them are based on the interaction of terminal groups of protective thiols with surface atoms or compounds attached to the surface earlier. In the formation of the cluster monolayer on the surface of solid substrates, the electrostatic interaction of clusters, with surfactants having charged terminal groups with the surfaces modified with thiols, also with charged terminal groups ($-\text{NH}_3^+$, $-\text{COO}^-$) is very important (see for instance [581]). There are also modifications of solid substrates several layers thick [581] obtained with the use of linkers such as dithiols, which combine gold clusters with the gold support by the chemical Au-S bond.

Gold clusters were also attached to the Au electrode by dithiols with the reactive bipyridyl group (Bpy) incorporated into

their structure [582, 583]. The electrode reaction of Bpy was fast on gold electrode modified by such dithiol and also with attached Au clusters.

After application of a proper potential to the tip of STM, the oxidized form of Bpy was reduced. Such a system represents the electrochemical nanoswitch. For gold clusters tunneling of single electrons was also observed. This effect was observed for nanosystems separated from two electrodes by a tunneling layer, either using STM or electrochemical methods [584, 585].

The electron tunneling on Au clusters shows that the monolayer of alkanethiols has good insulating properties. The transfer of a single electron between a STM tip and cluster occurs if the charging energy $E = e^2/2C$ (C is the capacity of cluster and e the charge of electron) is higher than the thermal energy $E_T = kT$.

The transfer of single electrons is observed on the current-potential dependence as a sequence of steps. This shows that clusters behave as redox reactants. There are many applications of gold clusters in various fields, such as preparation of new materials, electronics, heterogeneous catalysis and electrocatalysis, biosensors and others.

In medicine and biology quantum dots (composed of several gold atoms) are used as markers of chemical substances.

We present gold clusters very briefly, because recently there an extensive review [578] on their preparation, properties and applications in various fields was published.

References

1. A. N. Frumkin, *Zero Charge Potentials*, Nauka, Moscow, 1979 (in Russian).

2. A. Hamelin, in *Modern Aspects of Electrochemistry* (Eds.: B. E. Conway, R. E. White, J. O. M. Bockris), Plenum Press, New York, 1985, p. 1, Vol. 16.
3. M. A. Vorotyntsev, in *Modern Aspects of Electrochemistry* (Eds.: J. O. M. Bockris, B. E. Conway, R. E. White), Plenum Press, New York, 1986, p. 131, Vol. 17.
4. S. Trasatti, E. Lust, in *Modern Aspects of Electrochemistry* (Eds.: R. E. White, J. O. M. Bockris, B. E. Conway), Plenum Press, New York, 1999, Vol. 33.
5. R. Yu. Beck, N. V. Makurin, A. G. Zelinsky, *Elektrokhimiya* **1975**, *11*, 1607.
6. A. G. Zelinsky, B. P. Tolochko, *Double Layer and Adsorption at Solid Electrodes*, VI, University of Tartu, 1981, p. 139.
7. D. Barten, J. M. Kleijn, J. Duval et al., *Langmuir* **2003**, *19*, 1133.
8. B. Piela, P. K. Wrona, *J. Electroanal. Chem.* **1995**, *388*, 69.
9. J. C. Hoogvliet, M. Dijksma, B. Kamp et al., *Anal. Chem.* **2000**, *72*, 2016.
10. M. S. Doescher, U. Evans, P. E. Colavita et al., *Electrochem. Solid State Lett.* **2003**, *6*, C112.
11. J. Sobkowski, M. Jurkiewicz-Herbich, *Wiad. Chem. (Poland)* **2004**, *58*, 449.
12. A. Hamelin, J. Lecour, *Surf. Sci.* **1976**, *57*, 771.
13. Y. D. Jin, S. J. Dong, *Chem. Commun.* **2002**, *16*, 1780.
14. Q. Peng, E. K. Wang, *Chin. J. Chem.* **2000**, *18*, 698.
15. S. Dieluweit, M. Giesen, *J. Phys.: Condens. Mat.* **2002**, *14*, 4211.
16. S. Dieluweit, M. Giesen, *J. Electroanal. Chem.* **2002**, *524*, 194.
17. C. Bilger, B. Pettinger, *J. Chem. Soc., Faraday Trans.* **1998**, *94*, 2795.
18. D. Bigeliene, G. Valincius, *Russ. J. Electrochem.* **2000**, *36*, 431.
19. V. Mazine, Y. Borensztein, L. Cagnon et al., *Phys. Status Solidi A* **1999**, *175*, 311.
20. A. Sadkowski, A. J. Motheo, R. S. Neves, *J. Electroanal. Chem.* **1998**, *455*, 107.
21. D. J. Trevor, C. E. D. Chidsey, D. N. Loiacono, *Phys. Rev. Lett.* **1989**, *62*, 929.
22. E. Bunge, R. J. Nichols, B. Roelfs et al., *Langmuir* **1996**, *12*, 3060.
23. E. Bunge, S. N. Port, B. Roelfs et al., *Langmuir* **1997**, *13*, 85.
24. J. Lipkowski, C. N. Van Huong, C. Hinnen et al., *J. Electroanal. Chem.* **1983**, *143*, 375.
25. A. Ignaczak, J. A. N. F. Gomes, *J. Electroanal. Chem.* **1997**, *420*, 209.
26. L. Treindl, K. Doblhofer, K. Krischer et al., *Electrochim. Acta* **1999**, *44*, 3963.
27. J. E. Pemberton, S. L. Joa, A. Shen et al., *J. Chem. Soc., Faraday Trans.* **1996**, *92*, 3683.
28. G. Jarzabek, Z. Borkowska, *J. Electroanal. Chem.* **1987**, *226*, 295.
29. Z. Borkowska, A. Hamelin, *J. Electroanal. Chem.* **1988**, *241*, 373.
30. A. Hamelin, L. Doubova, D. Wagner et al., *J. Electroanal. Chem.* **1987**, *220*, 155.
31. N. van Huong, *J. Electroanal. Chem.* **1985**, *194*, 131.
32. Z. Borkowska, W. R. Fawcett, *Elektrokhimiya* **1980**, *16*, 1092.
33. M. Brzostowska-Smolska, S. Minc, *Pol. J. Chem.* **1983**, *106*, 1005.
34. A. Hamelin, *J. Electroanal. Chem.* **1995**, *386*, 1.
35. M. Weber, F. C. Nart, *Langmuir* **1996**, *12*, 1895.
36. J. Lipkowski, Z. Shi, A. Chen et al., *Electrochim. Acta* **1998**, *43*, 2875.
37. S. Thomas, Y. E. Sung, A. Wieckowski, *Solid-Liquid Electrochem. Interfaces ACS Symp. Ser.* **1997**, *656*, 126.
38. Z. Shi, J. Lipkowski, S. Mirwald et al., *J. Electroanal. Chem.* **1995**, *396*, 115.
39. P. Paredes Olivera, M. Patrito, H. Sellers, Electronic structure calculations of polyatomic oxyanions adsorbed on metal surfaces in *Interfacial Electrochemistry. Theory, Experiment and Applications* (Ed.: A. Wieckowski), Marcel Dekker, New York-Basel, 1999, p. 63.
40. M. Kleinert, A. Cuesta, L. A. Kibler et al., *Surf. Sci.* **1999**, *430*, L521.
41. A. Cuesta, M. Kleinert, D. M. Kolb, *Phys. Chem. Chem. Phys.* **2000**, *2*, 5684.
42. N. Hirai, K. Watanabe, S. Hara, *Surf. Sci.* **2001**, *493*, 568.
43. N. Vasiljevic, T. Trimble, N. Dimitrov et al., *Langmuir* **2004**, *20*, 6639.
44. H. Futamata, *Chem. Phys. Lett.* **2000**, *317*, 304.
45. P. Skołuda, *J. Electroanal. Chem.* **1996**, *406*, 235.
46. E. Dutkiewicz, P. Skołuda, *J. Chem. Soc., Faraday Trans.* **1996**, *92*, 3763.
47. A. Hamelin, in *Trends in Interfacial Chemistry* (Ed.: A. F. Silva), Reidel, Dordrecht, 1986, p. 3.

48. A. C. Chen, J. Lipkowski, *J. Phys. Chem. B* **1999**, *103*, 682.
49. A. Tymosiak-Zielińska, Z. Borkowska, *Electrochim. Acta* **2000**, *45*, 3105.
50. N. S. Marinkovic, J. J. Calvente, A. Kloss et al., *J. Electroanal. Chem.* **1999**, *467*, 325.
51. A. Kolics, A. E. Thomas, A. Wieckowski, *J. Chem. Soc., Faraday Trans.* **1996**, *92*, 3727.
52. A. Cuesta, D. M. Kolb, *Surf. Sci.* **2000**, *465*, 310.
53. Z. C. Shi, J. Lipkowski, *J. Electroanal. Chem.* **1996**, *403*, 225.
54. S. Ye, C. Ishibashi, K. Shimazu et al., *Langmuir* **1999**, *15*, 807.
55. Z. C. Shi, J. Lipkowski, S. Mirwald et al., *J. Chem. Soc., Faraday Trans.* **1996**, *92*, 3746.
56. O. M. Magnussen, B. M. Ocko, J. X. Wang et al., *J. Phys. Chem.* **1996**, *100*, 5500.
57. B. M. Ocko, O. M. Magnussen, J. X. Wang et al., *Phys. Rev. B* **1996**, *53*, R7654.
58. T. Wandlowski, J. X. Wang, O. M. Magnussen et al., *J. Phys. Chem.* **1996**, *100*, 10277.
59. J. X. Wang, R. P. Adzic, B. M. Ocko, In situ surface X-ray scattering studies of electrosorption in *Interfacial Electrochemistry. Theory, Experiment and Applications* (Ed.: A. Więckowski), Marcel Dekker, New York-Basel, 1999, p. 175.
60. S. W. Wang, P. A. Rikvold, *Phys. Rev. B* **2002**, *65*, art. No. 155406.
61. F. Reniers, D. H. Fairbrother, S. Wu et al., *Surf. Sci.* **1999**, *435*, 12.
62. R. R. Adzic, J. X. Wang, *J. Phys. Chem. B* **1998**, *102*, 6305.
63. J. X. Wang, I. K. Robinson, R. R. Adzic, *Surf. Sci.* **1998**, *413*, 374.
64. S. J. Mitchell, M. T. M. Koper, *Surf. Sci.* **2004**, *563*, 169.
65. H. W. Lei, H. Uchida, M. Watanabe, *J. Electroanal. Chem.* **1996**, *413*, 131.
66. K. Itaya, N. Batina, M. Kunitake et al., *Solid-Liquid Electrochem. Interfaces, ACS Symp. Ser.* **1997**, *656*, 171.
67. O. Endo, Y. Fukushima, H. Ozaki et al., *Surf. Sci.* **2004**, *569*, 99.
68. A. C. Chen, Z. C. Shi, D. Bizzotto et al., *J. Electroanal. Chem.* **1999**, *467*, 342.
69. J. X. Wang, G. M. Watson, R. M. Ocko, *J. Phys. Chem.* **1996**, *100*, 6672.
70. M. Seo, K. Ueno, *J. Electrochem. Soc.* **1996**, *143*, 899.
71. C. C. Chang, S. L. Yau, J. W. Tu et al., *Surf. Sci.* **2003**, *523*, 59.
72. X. Q. Wang, R. Chen, Y. L. Wang et al., *J. Phys. Chem. B* **1998**, *102*, 7568.
73. Z. Kerner, T. Pajkossy, *Electrochim. Acta* **2002**, *47*, 2055.
74. B. Pettinger, C. Bilger, J. Lipkowski, Second harmonic generation anisotropy from single crystalline electrode surfaces in *Interfacial Electrochemistry. Theory, Experiment and Applications* (Ed.: A. Więckowski), Marcel Dekker, New York-Basel, 1999, p. 373.
75. A. Friedrich, B. Pettinger, D. M. Kolb et al., *Chem. Phys. Lett.* **1989**, *163*, 123.
76. X. Gao, A. Hamelin, M. J. Weaver, *Phys. Rev. B* **1991**, *44*, 10983.
77. A. Tadjeddine, A. Le Rille, Sum and difference frequency generation at electrode surfaces in *Interfacial Electrochemistry. Theory, Experiment and Applications* (Ed.: A. Więckowski), Marcel Dekker, New York-Basel, 1999, p. 317.
78. A. Le Rille, A. Tadjeddine, A. Peremans et al., *Chem. Phys. Lett.* **1997**, *271*, 95.
79. C. P. Thurgood, D. W. Kirk, F. R. Foulkes et al., *J. Electrochim. Soc.* **1981**, *128*, 1680.
80. S. Trasatti, *Surf. Sci.* **1995**, *335*, 1.
81. N. A. Rogozhnikov, N. M. Zakharova, *Russ. J. Electrochim.* **1997**, *33*, 131.
82. G. L. Beltramo, T. E. Szubina, S. J. Mitchell et al., *J. Electroanal. Chem.* **2004**, *563*, 111.
83. M. Bron, R. Holze, *Electrochim. Acta* **1999**, *45*, 1121.
84. Z. Jusys, S. Bruckenstein, *Electrochim. Commun.* **2000**, *2*, 412.
85. A. Bilic, J. R. Reimers, N. S. Hush et al., *J. Chem. Phys.* **2002**, *116*, 8981.
86. D. N. Upadhyay, V. Yegnaraman, G. P. Rao, *Langmuir* **1996**, *12*, 4249.
87. Z. L. Cheng, L. Cheng, S. J. Dong et al., *J. Electrochim. Soc.* **2001**, *148*, E227.
88. T. Oznuluer, U. Demir, *J. Electroanal. Chem.* **2002**, *529*, 34.
89. L. Piccolo, D. Loffreda, F. J. C. S. Aires et al., *Surf. Sci.* **2004**, *566*, 995.
90. C. Vericat, M. E. Vela, J. Gago et al., *Electrochim. Acta* **2004**, *49*, 3643.
91. W. G. Bigelow, D. L. Pickett, W. A. Zisman, *J. Colloid Sci.* **1946**, *513*, 1.
92. R. G. Nuzzo, D. Allara, *J. Am. Chem. Soc.* **1983**, *105*, 4481.
93. A. Ulman, *Chem. Rev.* **1996**, *96*, 1553.
94. G. G. Roberts, *Langmuir-Blodgett Film*, Plenum Press, New York, 1990

95. O. Cavalleri, A. Hirstein, J. P. Bucher et al., *Thin Solid Films* **1996**, *284–285*, 392.
96. C. J. Zhong, R. C. Brush, J. Anderegg et al., *Langmuir* **1999**, *15*, 518.
97. C. D. Bain, E. B. Troughton, Y. T. Tao et al., *J. Am. Chem. Soc.* **1989**, *111*, 321.
98. C. A. Widrig, C. Chung, M. D. Porter, *J. Electroanal. Chem.* **1991**, *310*, 335.
99. C. J. Zhong, M. D. Porter, *J. Electroanal. Chem.* **1997**, *425*, 147.
100. C. J. Zhong, J. Zak, M. D. Porter, *J. Electroanal. Chem.* **1997**, *421*, 9.
101. M. M. Walczak, D. D. Weisshaar, M. D. Porter, *Langmuir* **1993**, *9*, 323.
102. M. Cohen-Atiya, D. Mandler, *J. Electroanal. Chem.* **2003**, *550–551*, 267.
103. C. M. A. Brett, S. Kresak, T. Hianik et al., *Electroanalysis* **2003**, *15*, 557.
104. S. S. Wong, M. D. Porter, *J. Electroanal. Chem.* **2000**, *485*, 135.
105. M. French, S. E. Creager, *Langmuir* **1998**, *14*, 2129.
106. P. Krysiński, M. Brzostowska-Smolska, *J. Electroanal. Chem.* **1997**, *424*, 61.
107. A. Kudelski, P. Krysiński, *J. Electroanal. Chem.* **1998**, *443*, 5.
108. T. Felgenhauer, H. T. Rong, M. Buck, *J. Electroanal. Chem.* **2003**, *550–551*, 309.
109. M. Galperin, A. Nitzan, S. Sek et al., *J. Electroanal. Chem.* **2003**, *550–551*, 337.
110. G. E. Poirier, E. D. Pyland, *Science* **1996**, *272*, 1145.
111. K. M. Beardmore, J. D. Kress, N. Gronbech-Jensen et al., *Chem. Phys. Lett.* **1998**, *286*, 40.
112. N. Camillone, *Langmuir* **2004**, *20*, 1199.
113. R. Yamada, K. Uosaki, *Langmuir* **1997**, *13*, 5218.
114. R. Yamada, K. Uosaki, *Langmuir* **1998**, *14*, 855.
115. G. E. Poirier, *Chem. Rev.* **1997**, *97*, 1117.
116. C. Schönenberger, J. A. M. Sondag-Huet-horst, J. Jorritsma et al., *Langmuir* **1994**, *10*, 611.
117. J. A. M. Sondag-Huet-horst, L. G. J. Fokkink, *Langmuir* **1994**, *10*, 4380.
118. C. Schönenberger, J. Jorritsma, J. A. M. Sondag-Huet-horst et al., *J. Phys. Chem. B* **1995**, *99*, 3250.
119. R. Yamada, H. Sakai, K. Uosaki, *Chem. Lett.* **1999**, 667.
120. R. Yamada, H. Wano, K. Uosaki, *Langmuir* **2000**, *16*, 5523.
121. H. Wano, K. Uosaki, *Langmuir* **2001**, *17*, 8224.
122. T. Sumi, H. Wano, K. Uosaki, *J. Electroanal. Chem.* **2003**, *550–551*, 321.
123. H. Hagenstrom, M. A. Schneeweiss, D. M. Kolb, *Langmuir* **1999**, *15*, 2435.
124. O. Azzaroni, M. E. Vela, G. Andreasen et al., *J. Phys. Chem. B* **2002**, *106*, 12267.
125. T. Sumi, K. Uosaki, *J. Phys. Chem. B* **2004**, *108*, 6422.
126. D. F. Yang, C. P. Wilde, M. Morin, *Langmuir* **1996**, *12*, 6570.
127. D. F. Yang, C. P. Wilde, M. Morin, *Langmuir* **1997**, *13*, 243.
128. T. Kawaguchi, Y. Yasuda, K. Shimazu et al., *Langmuir* **2000**, *16*, 9830.
129. D. Qu, M. Morin, *J. Electroanal. Chem.* **2000**, *517*, 45.
130. I. A. Vinokurov, M. Morin, J. Kankare, *J. Phys. Chem. B* **2000**, *104*, 5790.
131. M. Himmelhaus, F. Eisert, M. Buck et al., *J. Phys. Chem. B* **2000**, *104*, 576.
132. F. Schreiber, *Prog. Surf. Sci.* **2000**, *65*, 151.
133. R. G. Nuzzo, L. H. Dubois, D. L. Allara, *J. Am. Chem. Soc.* **1990**, *112*, 558.
134. M. W. Walczak, C. Chung, S. M. Stole et al., *J. Am. Chem. Soc.* **1991**, *113*, 2370.
135. M. A. Bryant, J. E. Pemberton, *J. Am. Chem. Soc.* **1991**, *113*, 8284.
136. E. Paradis, P. Rowntree, *J. Electroanal. Chem.* **2003**, *550–551*, 175.
137. D. F. Yang, M. Morin, *Can. J. Chem.* **1997**, *75*, 1680.
138. G. E. Poirier, *Langmuir* **1999**, *15*, 3018.
139. T. Kakiuchi, M. Iida, N. Gon et al., *Langmuir* **2001**, *17*, 1599.
140. F. Teran Arce, M. E. Vela, R. C. Salvarezza et al., *Electrochim. Acta* **1998**, *44*, 1053.
141. F. Teran Arce, M. E. Vela, R. C. Salvarezza et al., *Langmuir* **1998**, *14*, 7203.
142. Y. Iwami, D. Hobara, M. Yamamoto et al., *J. Electroanal. Chem.* **2004**, *564*, 77.
143. T. Sugiyama, T. Ishioka, A. Harata, *Anal. Sci.* **2001**, *17*, S237.
144. M. Hara, H. Sasabe, W. Knoll, *Thin Solid Films* **1996**, *273*, 66.
145. M. Rohwerder, K. de Weldige, M. Stratmann, *J. Solid State Electrochem.* **1998**, *2*, 88.
146. M. Fonticelli, O. Azzaroni, G. Benitez et al., *J. Phys. Chem. B* **2004**, *108*, 1898.
147. M. Schweizer, H. Hagenstrom, D. M. Kolb, *Surf. Sci.* **2001**, *490*, L627.

148. F. Loglio, M. Schweizer, D. M. Kolb, *Langmuir* **2003**, *19*, 830.
149. V. Bondzie, S. J. Dion-Warren, Y. Yu et al., *Surf. Sci.* **1999**, *431*, 174.
150. R. Yamada, K. Uosaki, *Langmuir* **2001**, *17*, 4148.
151. A. M. Bittner, M. Epple, E. Kuhnke et al., *J. Electroanal. Chem.* **2003**, *550–551*, 113.
152. A. S. Viana, L. M. Abrantes, G. Jin et al., *Phys. Chem. Chem. Phys.* **2001**, *3*, 3411.
153. A. S. Viana, A. H. Jones, L. M. Abrantes et al., *J. Electroanal. Chem.* **2001**, *500*, 290.
154. T. Y. Dong, L. S. Chang, I. M. Tseng et al., *Langmuir* **2004**, *20*, 4471.
155. T. Kondo, M. Okamura, K. Uosaki, *Chem. Lett.* **2001**, 930.
156. S. Sek, R. Bilewicz, *J. Electroanal. Chem.* **2001**, *509*, 11.
157. S. Sek, A. Misicka, R. Bilewicz, *J. Phys. Chem. B* **2000**, *104*, 5399.
158. S. Sek, R. Moszynski, A. Sepiol et al., *J. Electroanal. Chem.* **2003**, *55*, 359.
159. L. J. Wan, M. Terashima, H. Noda et al., *J. Phys. Chem. B* **2000**, *104*, 3563.
160. S. Rifai, M. Morin, *J. Electroanal. Chem.* **2003**, *550–551*, 277.
161. S. Kuwabata, R. Fukuzaki, M. Nishizawa et al., *Langmuir* **1999**, *15*, 6807.
162. R. Holze, S. Schomaker, *Electrochim. Acta* **1990**, *35*, 613.
163. O. Azzaroni, G. Andreasen, B. Blum et al., *J. Phys. Chem. B* **2000**, *104*, 1395.
164. G. Garcia, V. A. Macagno, G. I. Lacconi, *Electrochim. Acta* **2003**, *48*, 1273.
165. G. Garcia, J. L. Rodriguez, G. I. Lacconi et al., *Langmuir* **2004**, *20*, 8773.
166. M. Borsari, M. Cannio, G. Gavioli, *Electroanalysis* **2003**, *15*, 1192.
167. C. A. Szafranski, W. Tanner, P. E. Laibinis et al., *Langmuir* **1998**, *14*, 3570.
168. H. Azebara, S. Yoshimoto, H. Hokari et al., *J. Electroanal. Chem.* **1999**, *473*, 68.
169. Y. X. Zhou, T. Nagaoka, G. Y. Zhu, *Biophys. Chem.* **1999**, *79*, 55.
170. A. V. Krylov, W. Pfeil, F. Lisdat, *J. Electroanal. Chem.* **2004**, *569*, 225.
171. H. Wackerbarth, R. Marie, M. Grubb et al., *J. Solid State Electrochem.* **2004**, *8*, 474.
172. T. Akiyama, K. Inoue, Y. Kuwahara et al., *J. Electroanal. Chem.* **2003**, *550–551*, 303.
173. K. Arihara, F. Kitamura, *J. Electroanal. Chem.* **2003**, *550–551*, 149.
174. J. D. Zhang, Q. J. Chi, J. U. Nielsen et al., *Langmuir* **2000**, *16*, 7229.
175. R. D. Felice, A. Selloni, *J. Chem. Phys.* **2004**, *120*, 4906.
176. G. Hager, A. G. Brolo, *J. Electroanal. Chem.* **2003**, *550–551*, 291.
177. M. Darder, E. Casero, D. J. Diaz et al., *Langmuir* **2000**, *16*, 9804.
178. M. Dijksma, B. Kamp, J. C. Hoogvliet et al., *Langmuir* **2000**, *16*, 3852.
179. M. Akram, M. C. Stuart, D. K. Y. Wong, *Anal. Chim. Acta* **2004**, *504*, 243.
180. Y. J. Yong, K. S. Beng, *Electrochem. Commun.* **2004**, *6*, 87.
181. G. Che, C. R. Cabrera, *J. Electroanal. Chem.* **1996**, *417*, 155.
182. E. Chung, J. L. Shepherd, D. Bizzotto et al., *Langmuir* **2004**, *20*, 8270.
183. W. P. Zhou, T. Baunach, V. Ivanova et al., *Langmuir* **2004**, *20*, 4590.
184. L. S. Pinheiro, M. L. A. Temperini, *Surf. Sci.* **1999**, *441*, 45.
185. T. Doneux, C. Buess-Herman, J. Lipkowski, *J. Electroanal. Chem.* **2004**, *564*, 65.
186. R. Madueno, J. M. Sevilla, T. Pineda et al., *J. Electroanal. Chem.* **2001**, *506*, 92.
187. L. Y. He, B. J. Xiang, Y. J. Yang, *Russ. J. Electrochem.* **2004**, *40*, 849.
188. T. Baunach, D. M. Kolb, *Anal. Bioanal. Chem.* **2002**, *373*, 743.
189. F. Reincke, S. G. Hickey, J. J. Kelly et al., *J. Electroanal. Chem.* **2002**, *522*, 2.
190. S. P. Dudek, H. D. Sikes, C. E. D. Chidsey, *J. Am. Chem. Soc.* **2001**, *123*, 8033.
191. C. A. Szafranski, W. Tanner, P. E. Laibinis et al., *Langmuir* **1998**, *14*, 3580.
192. H. Kondoh, T. Nakamura, F. Matsui et al., *Mol. Cryst. Liq. Cryst.* **2002**, *377*, 45.
193. M. Mazur, P. Krysiński, *Langmuir* **2000**, *16*, 7962.
194. Y. Yang, O. Valet, C. Donner et al., *Z. Phys. Chem.* **2003**, *217*, 493.
195. R. N. Gu, R. Sun, P. G. Cao et al., *Spectrosc. Spectr. Anal.* **1999**, *19*, 50.
196. L. S. Wong, V. L. Vilker, W. T. Yap et al., *Langmuir* **1995**, *11*, 4818.
197. H. M. Zhang, G. J. Su, D. Wang et al., *Electrochim. Acta* **2004**, *49*, 1629.
198. A. Ion, T. Ljones, F. G. Banica, *Collect. Czech. Chem. Commun.* **2004**, *69*, 759.
199. M. Nishizawa, T. Sunagawa, H. Yoneyama, *J. Electroanal. Chem.* **1997**, *436*, 213.
200. Z. Q. Gao, K. S. Siow, *Anal. Commun.* **1996**, *33*, 223.
201. S. Wang, D. Du, X. Xu, *J. Appl. Electrochem.* **2004**, *34*, 495.

202. K. Ozoemena, P. Westbroek, T. Nyokong, *J. Porphyrins Phthalocyanines* **2002**, 6, 98.
203. D. Li, J. H. Li, *Surf. Sci.* **2003**, 522, 105.
204. W. J. Miao, A. J. Bard, *Anal. Chem.* **2003**, 75, 5825.
205. C. W. Ge, J. H. Liao, W. Yu et al., *Biosens. Bioelectron.* **2003**, 18, 53.
206. A. H. Zhou, J. D. Zhong, Q. J. Xie et al., *Biomaterials* **2001**, 22, 2515.
207. Q. J. Xie, Y. Y. Zhang, M. C. Xu et al., *J. Electroanal. Chem.* **1999**, 478, 1.
208. M. Tarek, K. Tu, M. L. Klein et al., *Biophys. J.* **1999**, 77, 964.
209. M. Kawasaki, D. Yoshidome, T. Sato et al., *J. Electroanal. Chem.* **2001**, 543, 1.
210. T. Ohtsuka, M. Nagata, H. Komori et al., *Electrochemistry* **1999**, 67, 1184.
211. J. Zhang, Q. Chi, J. U. Nielsen et al., *Russ. J. Electrochem.* **2002**, 38, 68.
212. N. Nakashima, Y. Miyata, M. Tominaga, *Chem. Lett.* **1996**, 9, 731.
213. H. Imahori, H. Norieda, Y. Nishimura et al., *J. Phys. Chem. B* **2000**, 104, 1253.
214. X. Q. Li, B. Q. Lv, Z. H. Xue et al., *Anal. Lett.* **2002**, 35, 1811.
215. D. L. Pilloud, X. X. Chen, P. L. Dutton et al., *J. Phys. Chem. B* **2000**, 104, 2868.
216. F. Q. Zhao, L. J. Huang, B. Z. Zeng et al., *Electrochim. Commun.* **2004**, 6, 319.
217. J. C. Yan, S. J. Dong, *Electroanalysis* **1997**, 9, 1219.
218. J. C. Yan, S. J. Dong, J. H. Li et al., *J. Electrochem. Soc.* **1997**, 144, 3858.
219. M. G. Samant, C. A. Brown, J. G. Gordon II, *Langmuir* **1982**, 8, 1615.
220. K. Bandyopadhyay, K. Vijayamohanan, *Langmuir* **1998**, 14, 625.
221. F. K. Huang, R. C. Horton, D. C. Myles et al., *Langmuir* **1998**, 14, 4802.
222. M. H. Dishner, J. C. Hemminger, J. C. Feher, *Langmuir* **1997**, 13, 4788.
223. L. V. Protsailo, W. R. Fawcett, D. Russell et al., *Langmuir* **2002**, 18, 9342.
224. J. D. Monnell, J. J. Stapleton, J. J. Jackiw et al., *J. Phys. Chem. B* **2004**, 108, 9834.
225. F. Chao, M. Costa, A. Tadjeddine, *Bull. Soc. Chim. France* **1971**, 7, 5193.
226. L. Stolberg, J. Richer, J. Lipkowski, *J. Electroanal. Chem.* **1986**, 207, 213.
227. L. Stolberg, J. Lipkowski, D. E. Irish, *J. Electroanal. Chem.* **1991**, 300, 563.
228. J. Lipkowski, L. Stolberg, S. Morin et al., *J. Electroanal. Chem.* **1993**, 355, 147.
229. L. Stolberg, J. Lipkowski, D. E. Irish, *J. Electroanal. Chem.* **1987**, 238, 333.
230. L. Stolberg, J. Lipkowski, D. E. Irish, *J. Electroanal. Chem.* **1990**, 296, 171.
231. L. Stolberg, J. Lipkowski, D. E. Irish, *J. Electroanal. Chem.* **1991**, 307, 241.
232. L. Stolberg, J. Lipkowski, D. E. Irish, *J. Electroanal. Chem.* **1992**, 322, 357.
233. D. F. Yang, L. Stolberg, J. Lipkowski, *J. Electroanal. Chem.* **1992**, 329, 259.
234. P. Skołuda, M. Holze, J. Lipkowski et al., *J. Electroanal. Chem.* **1993**, 358, 343.
235. B. Pettinger, S. Mirwald, J. Lipkowski, *Ber. Bunsenges. Phys. Chem. Chem. Phys.* **1993**, 95, 395.
236. B. Pettinger, J. Lipkowski, S. Mirwald et al., *J. Electroanal. Chem.* **1992**, 329, 289.
237. P. Hebert, A. Le Rille, W. Q. Zeng et al., *J. Electroanal. Chem.* **1998**, 447, 5.
238. A. G. Brolo, D. E. Irish, J. Lipkowski, *J. Phys. Chem. B* **1997**, 101, 3906.
239. G. Andreassen, M. E. Vela, R. C. Salvarezza et al., *Langmuir* **1997**, 13, 6814.
240. Y. Ikezawa, T. Sawatari, T. Kitazume et al., *Electrochim. Acta* **1998**, 43, 3297.
241. G. Zilberman, V. Tsionsky, E. Gileadi, *Can. J. Chem.* **1997**, 75, 1646.
242. M. Hoon-Khosla, W. R. Fawcett, A. C. Chen et al., *Electrochim. Acta* **1999**, 45, 611.
243. Y. Ikezawa, T. Sawatari, H. Terashima, *Electrochim. Acta* **2001**, 46, 1333.
244. A. Bilic, J. R. Reimers, N. S. Hush, *J. Phys. Chem. B* **2002**, 106, 6740.
245. A. C. Chang, D. F. Yang, J. Lipkowski, *J. Electroanal. Chem.* **1999**, 475, 130.
246. M. Jurkiewicz-Herbich, R. Słojkowska, K. Zawada et al., *Electrochim. Acta* **2002**, 47, 2429.
247. O. Pluchery, A. Tajeddine, *J. Electroanal. Chem.* **2001**, 500, 379.
248. N. Nanbu, F. Kitamura, T. Ohsaka et al., *Electrochemistry* **1999**, 67, 1165.
249. A. G. Brolo, Z. Jiang, D. E. Irish, *J. Electroanal. Chem.* **2003**, 547, 163.
250. C. M. Xu, B. Xi, Y. L. Li et al., *New J. Chem.* **2001**, 25, 1191.
251. M. J. Eddowes, H. A. O. Hill, *J. Chem. Soc., Chem. Commun.* **1977**, 771.
252. A. Czerwiński, J. Sobkowski, S. Zamponi et al., *J. Electroanal. Chem.* **1990**, 288, 271.
253. W. B. Cai, L. J. Wan, H. Noda et al., *Langmuir* **1998**, 14, 6992.
254. N. H. Li, V. Zamlynny, J. Lipkowski et al., *J. Electroanal. Chem.* **2002**, 524, 43.

255. C. I. Smith, A. J. Maunder, C. A. Lucas et al., *J. Electrochem. Soc.* **2003**, *150*, E233.
256. Y. Ikezawa, T. Kosugi, *Electrochim. Acta* **2002**, *47*, 2921.
257. T. Sagara, K. Uematsu, K. Nagata, *J. Electroanal. Chem.* **2003**, *550–551*, 219.
258. I. Burgess, V. Zamlynny, G. Szymanski et al., *J. Electroanal. Chem.* **2003**, *550–551*, 187.
259. D. Barten, J. M. Kleijn, M. A. C. Stuart, *Phys. Chem. Chem. Phys.* **2003**, *5*, 4258.
260. A. G. Brolo, D. E. Irish, G. Szymanski et al., *Langmuir* **1998**, *14*, 517.
261. W. B. Cai, T. Amano, M. Osawa, *J. Electroanal. Chem.* **2001**, *500*, 147.
262. Y. Ikezawa, Y. Koda, M. Shibuya et al., *Electrochim. Acta* **2000**, *45*, 2075.
263. U. W. Hamm, V. Lazarescu, D. M. Kolb, *J. Chem. Soc., Faraday Trans.* **1996**, *92*, 3785.
264. M. Brzostowska-Smolska, P. Krysiński, *Pol. J. Chem.* **1997**, *71*, 1293.
265. T. Luczak, M. Beltowska-Brzezinska, M. Bron et al., *Vib. Spectrosc.* **1997**, *15*, 17.
266. A. C. Chen, J. Richer, S. G. Roscoe et al., *Langmuir* **1997**, *13*, 4737.
267. X. Y. Xiao, S. G. Sun, *Electrochim. Acta* **2000**, *45*, 2897.
268. J. Richer, J. Lipkowski, *Langmuir* **1986**, *2*, 630.
269. J. Richer, J. Lipkowski, *J. Electroanal. Chem.* **1988**, *251*, 217.
270. M. Brzostowska-Smolska, P. Krysiński, *Colloids Surf., A – Physicochem. Eng. Aspects* **1998**, *131*, 39.
271. Y. G. Yang, D. Bizzotto, *J. Electroanal. Chem.* **2001**, *500*, 408.
272. I. Zawissa, I. Burgess, G. Szymanski et al., *Electrochim. Acta* **2004**, *49*, 3651.
273. M. J. Sotomayor, V. Coelho, A. P. Ferreira et al., *Electrochim. Acta* **1999**, *45*, 775.
274. H. Sawamoto, S. Kashimori, *Bunseki Kagaku* **2002**, *51*, 1041.
275. D. Bizzotto, E. Wong, Y. G. Yang, *J. Electroanal. Chem.* **2000**, *480*, 233.
276. R. Słojkowska, M. Jurkiewicz-Herbich, *Colloids Surf.* **2001**, *178*, 325.
277. R. Słojkowska, B. Pałys, M. Jurkiewicz-Herbich, *Electrochim. Acta* **2004**, *49*, 4109.
278. H. Q. Li, A. C. Chen, S. G. Roscoe et al., *J. Electroanal. Chem.* **2001**, *500*, 299.
279. E. Dutkiewicz, P. Skołuda, A. Hamelin, *J. Electroanal. Chem.* **1988**, *240*, 291.
280. E. Dutkiewicz, P. Skołuda, A. Hamelin, *J. Electroanal. Chem.* **1988**, *248*, 209.
281. S. Floate, M. Hosseini, M. R. Arshadi et al., *J. Electroanal. Chem.* **2003**, *542*, 67.
282. R. J. Nichols, I. Burgess, K. L. Young et al., *J. Electroanal. Chem.* **2004**, *563*, 33.
283. Y. Ikezawa, A. Yoshida, R. Sekiguchi, *Electrochim. Acta* **2000**, *46*, 769.
284. E. Szocs, I. Felhosi, U. Schmidt et al., *Mater. Corros. – Werkstoffe Korrosion* **2002**, *53*, 631.
285. D. Krznaric, T. Gorlicnik, M. Vukovic et al., *Electroanalysis* **2001**, *13*, 109.
286. P. Zelenay, P. Waszcuk, K. Dobrowolska et al., *Electrochim. Acta* **1994**, *39*, 655.
287. J. Sobkowski, P. Waszcuk, P. Zelenay, *Russ. J. Electrochem.* **1995**, *31*, 850.
288. Y. Ikezawa, R. Sekiguchi, T. Kitazume, *Electrochim. Acta* **2000**, *46*, 731.
289. T. Schmitz-Hubsch, T. Fritz, R. Staub et al., *Surf. Sci.* **1999**, *437*, 163.
290. K. Ataka, M. Osawa, *J. Electroanal. Chem.* **1999**, *460*, 188.
291. T. Dretschkow, T. Wandlowski, *Electrochim. Acta* **1998**, *43*, 2991.
292. S. Pronkin, T. Wandlowski, *J. Electroanal. Chem.* **2003**, *550*, 131.
293. R. Roelfs, E. Bunge, C. Schröter et al., *J. Phys. Chem. B* **1997**, *101*, 754.
294. M. Scharfe, A. Hamelin, C. Buess-Herman, *Electrochim. Acta* **1995**, *40*, 61.
295. M. H. Hözlé, D. M. Kolb, D. Krznaric et al., *Ber. Bunsenges. Phys. Chem.* **1996**, *100*, 1779.
296. T. Wandlowski, M. H. Hözlé, *Langmuir* **1996**, *12*, 6604.
297. C. Buess-Herman, S. Baré, M. Poelman, Ordered organic adlayers at electrode surfaces in *Interfacial Electrochemistry. Theory, Experiment and Applications* (Ed.: A. Więckowski), Marcel Dekker, New York-Basel, 1999, p. 427.
298. R. Roelfs, H. Baumgärtel, *Ber. Bunsenges. Phys. Chem.* **1995**, *100*, 677.
299. S. Pronkin, Th. Wandlowski, *J. Electroanal. Chem.* **2003**, *550–551*, 131.
300. A. P. M. Camargo, H. Baumgärtel, C. Dinner, *PHYSCHEMCOM* **2002**, *151–152*.
301. H. B. Shen, J. F. Xia, Z. S. Wang et al., *Chem. J. Chinese Univ.–Chinese* **2001**, *22*, 962.
302. S. Hason, V. Vetterl, *Bioelectrochemistry* **2002**, *56*, 43.
303. Y. J. Xiao, T. Wang, X. Q. Wang et al., *J. Electroanal. Chem.* **1997**, *433*, 49.

304. J. J. Davis, C. M. Halliwell, H. A. O. Hill et al., *New J. Chem.* **1998**, *22*, 1119.
305. S. E. Moulton, J. N. Barisci, A. Bath et al., *Electrochim. Acta* **2004**, *49*, 4223.
306. E. P. Friis, J. E. T. Andersen, L. L. Madsen et al., *Electrochim. Acta* **1998**, *43*, 2889.
307. V. Reipa, A. K. Gaigalas, V. L. Vilker, *Langmuir* **1997**, *13*, 3508.
308. Z. J. Cao, Q. J. Xie, M. Li et al., *J. Electroanal. Chem.* **2004**, *568*, 343.
309. J. O. Zerbino, M. G. Sustersic, *Langmuir* **2000**, *16*, 7477.
310. A. H. Zhou, Q. J. Xie, Y. H. Wu et al., *J. Colloid Interface Sci.* **2000**, *229*, 12.
311. S. L. Horswell, V. Zamlynny, H. Q. Li et al., *Faraday Discuss.* **2002**, *121*, 405.
312. I. Zawissa, X. M. Bin, J. Lipkowski, *Bioelectrochemistry* **2004**, *63*, 137.
313. I. Zawissa, A. Lachenwitzer, V. Zamlynny et al., *Biophys. J.* **2003**, *85*, 4055.
314. Z. W. Xiao, M. X. Xu, T. Ohgi et al., *Physica E – Low Dimens. Syst. Nanostruct.* **2004**, *21*, 1098.
315. P. Han, B. A. Montooth, E. C. H. Sykes et al., *J. Am. Chem. Soc.* **2004**, *126*, 10787.
316. A. Czerwiński, J. Sobkowski, *Electrochim. Acta* **1980**, *25*, 1313.
317. G. B. Pan, H. J. Li, Q. H. Yuan et al., *Sci. China, Ser. B – Chem.* **2004**, *47*, 320.
318. R. J. Baxter, G. Teobaldi, F. Zerbetto, *Langmuir* **2003**, *19*, 7335.
319. M. Danckwerts, Y. J. Li, J. Oslonovitch et al., *J. Phys. Chem. B* **2004**, *108*, 14398.
320. B. Pettinger, M. Danckwerts, K. Krischer, *Faraday Discuss.* **2002**, *121*, 153.
321. H. Striegler, D. Krznaric, D. M. Kolb, *J. Electroanal. Chem.* **2002**, *532*, 227.
322. M. Nakamura, M. B. Song, M. Ito, *Surf. Sci.* **1999**, *428*, 167.
323. K. Nishiyama, S. Tahara, Y. Uchida et al., *J. Electroanal. Chem.* **1999**, *478*, 83.
324. R. S. Neves, A. J. Motheo, F. M. S. S. Fernandes et al., *J. Brazil. Chem. Soc.* **2004**, *15*, 224.
325. G. J. Su, H. M. Zhang, L. J. Wan et al., *J. Phys. Chem. B* **2004**, *108*, 1931.
326. A. Ohira, T. Ishizaki, M. Sakata et al., *J. Electroanal. Chem.* **1999**, *472*, 163.
327. T. Sakai, A. Ohira, M. Sakata et al., *Chem. Lett.* **2001**, *8*, 782.
328. S. Xu, G. Szymanski, J. Lipkowski, *J. Am. Chem. Soc.* **2004**, *126*, 12276.
329. P. A. Brooksby, W. R. Fawcett, *Electrochim. Acta* **2003**, *48*, 807.
330. F. Evangelista, A. Ruocco, V. Corradini et al., *Surf. Sci.* **2003**, *531*, 123.
331. V. Corradini, C. Menozzi, M. Cavallini et al., *Surf. Sci.* **2003**, *532*, 249.
332. E. Cholewa, I. Burgess, J. Kunze et al., *J. Solid State Electrochem.* **2004**, *8*, 693.
333. D. Bizzotto, J. Lipkowski, *Prog. Surf. Sci.* **1995**, *50*, 237.
334. M. Petri, D. M. Kolb, *Phys. Chem. Chem. Phys.* **2002**, *4*, 1211.
335. A. S. Dakkouri, D. M. Kolb, Reconstruction of gold surfaces in *Interfacial Electrochemistry. Theory, Experiment and Applications* (Ed.: A. Więckowski), Marcel Dekker, New York-Basel, 1999, p. 151.
336. D. M. Kolb, *Prog. Surf. Sci.* **1996**, *51*, 109.
337. X. Gao, A. Hamelin, M. J. Weaver, *Surf. Sci. Lett.* **1992**, *274*, L588.
338. X. Gao, G. J. Edens, A. Hamelin et al., *Surf. Sci.* **1993**, *296*, 333.
339. D. M. Kolb, G. Lehmpfuhl, M. S. Zei, *J. Electroanal. Chem.* **1984**, *179*, 289.
340. M. S. Zei, G. Lehmpfuhl, D. M. Kolb, *Surf. Sci.* **1984**, *221*, 23.
341. D. M. Kolb, J. Schneider, *Electrochim. Acta* **1986**, *31*, 929.
342. D. G. Fedak, N. A. Gjostein, *Surf. Sci.* **1967**, *8*, 77.
343. M. A. Van Hove, R. J. Koestner, P. C. Stair et al., *Surf. Sci.* **1981**, *103*, 189.
344. M. A. Van Hove, R. J. Koestner, P. C. Stair et al., *Surf. Sci.* **1981**, *103*, 218.
345. O. K. Binnig, H. Rohrer, Ch. Gerber et al., *Surf. Sci.* **1984**, *144*, 321.
346. K. M. Ho, K. P. Bohnen, *Phys. Rev. Lett.* **1987**, *59*, 1833.
347. C. L. Fu, K. M. Ho, *Phys. Rev. Lett.* **1989**, *63*, 1617.
348. G. Ertl, *Surf. Sci.* **1985**, *152–153*, 328.
349. G. A. Samorjai, M. A. Van Hove, *Prog. Surf. Sci.* **1989**, *30*, 201.
350. R. J. Nichols, O. M. Magnussen, J. Hotlos et al., *J. Electroanal. Chem.* **1990**, *290*, 21.
351. K. P. Bohnen, D. M. Kolb, *Surf. Sci.* **1998**, *407*, L629.
352. J. Schneider, D. M. Kolb, *Surf. Sci.* **1988**, *193*, 579.
353. A. S. Dakkouri, *Solid State Ionics* **1997**, *94*, 99.
354. D. M. Kolb, Surface reconstruction at metal-electrolyte interfaces in *Structure of Electrified Interfaces* (Eds.: J. Lipkowski, Ph. N. Ross), VCH, N.Y.-Weinheim-Cambridge, 1993, p. 65.

355. J. Lipkowski, L. Stolberg, Molecular adsorption at gold and silver electrodes in *Adsorption of Molecules at Metal Electrodes* (Eds.: J. Lipkowski, Ph. N. Ross), VCH, N.Y.-Weinheim-Cambridge, 1992, p. 171.
356. U. W. Hamm, D. M. Kolb, *J. Electroanal. Chem.* **1992**, *332*, 339.
357. P. Skołuda, *Electrochim. Commun.* **2003**, *5*, 142.
358. P. Skołuda, *Pol. J. Chem.* **2004**, *78*, 583.
359. C. D. Keefe, E. Revesz, M. Dionne et al., *Can. J. Chem.* **1997**, *75*, 449.
360. S. Z. Zou, X. P. Gao, M. J. Weaver, *Surf. Sci.* **2000**, *452*, 44.
361. P. Hale, S. Thurgate, P. Wilkie, *Surf. Interface Anal.* **2001**, *32*, 240.
362. S. Narasimhan, D. Vanderbilt, *Phys. Rev. Lett.* **1992**, *69*, 1564.
363. D. Krznaric, *Electroanalysis* **2002**, *14*, 657.
364. D. Hobara, M. Yamamoto, T. Kakiuchi, *Chem. Lett.* **2001**, *11*, 1200.
365. G. Jerkiewicz, Surface oxidation of noble metal electrodes in *Interfacial Electrochemistry. Theory, Experiment and Applications* (Ed.: A. Więckowski), Marcel Dekker, New York-Basel, 1999, p. 559.
366. L. D. Burke, P. F. Nugent, *Gold Bull.* **1997**, *30*, 43.
367. G. Tremiliosi-Filho, L. H. Dall'Antonia, G. Jerkiewicz, *J. Electroanal. Chem.* **1997**, *422*, 149.
368. L. D. Burke, P. F. Nugent, *Gold Bull.* **1998**, *31*, 39.
369. M. A. Schneeweiss, D. M. Kolb, D. Z. Liu et al., *Can. J. Chem.* **1997**, *75*, 1703.
370. M. A. Schneeweiss, D. M. Kolb, *Solid State Ionics* **1997**, *94*, 171.
371. X. Q. Zeng, S. Bruckenstein, *J. Electroanal. Chem.* **1999**, *461*, 131.
372. M. Tian, W. G. Pell, B. E. Conway, *J. Electroanal. Chem.* **2003**, *552*, 279.
373. L. D. Burke, A. P. O'Mullane, *J. Solid State Electrochem.* **2000**, *4*, 285.
374. L. D. Burke, P. F. Nugent, *J. Electroanal. Chem.* **1998**, *444*, 19.
375. L. D. Burke, L. M. Hurley, V. E. Lodge et al., *J. Solid State Electrochem.* **2001**, *5*, 250.
376. L. D. Burke, L. M. Hurley, *J. Solid State Electrochem.* **2002**, *6*, 101.
377. L. D. Burke, J. M. Moran, P. F. Nugent, *J. Solid State Electrochem.* **2003**, *7*, 529.
378. L. D. Burke, J. A. Collins, M. A. Murphy, *J. Solid State Electrochem.* **1999**, *4*, 34.
379. L. D. Burke, M. A. Murphy, *J. Solid State Electrochem.* **2001**, *5*, 43.
380. E. Herrero, L. J. Buller, H. D. Abruña, *Chem. Rev.* **2001**, *101*, 1897.
381. O. M. Magnussen, *Chem. Rev.* **2002**, *102*, 679.
382. M. S. Zei, G. Qiao, G. Lehmpfuhl et al., *Ber. Bunsenges. Phys. Chem.* **1987**, *91*, 349.
383. X. Q. Zeng, S. Bruckenstein, *J. Electroanal. Chem.* **1999**, *461*, 143.
384. M. Legault, L. Blum, D. A. Huckaby, *J. Electroanal. Chem.* **1996**, *409*, 79.
385. E. D. Chabala, J. Cairns, T. Rayment, *J. Electroanal. Chem.* **1996**, *412*, 77.
386. M. Cappadonia, K. M. Robinson, J. Schmidberger et al., *J. Electroanal. Chem.* **1997**, *436*, 73.
387. M. Cappadonia, U. Linke, K. M. Robinson et al., *J. Electroanal. Chem.* **1996**, *405*, 227.
388. X. H. Xia, L. Nagle, R. Schuster et al., *Phys. Chem. Chem. Phys.* **2000**, *2*, 4387.
389. M. Cappadonia, K. M. Robinson, J. Schmidberger et al., *Surf. Rev. Lett.* **1997**, *4*, 1173.
390. S. Wu, Z. Shi, J. Lipkowski et al., *J. Phys. Chem. B* **1997**, *101*, 10310.
391. D. Krznarić, T. Gorlicnik, *Langmuir* **2001**, *17*, 4347.
392. E. Herrero, S. Glazier, H. D. Abruña, *J. Phys. Chem. B* **1998**, *102*, 9825.
393. E. Herrero, S. Glazier, L. J. Buller et al., *J. Electroanal. Chem.* **1999**, *461*, 121.
394. R. Randler, M. Dietterle, D. M. Kolb, Z. Phys. Chem. – Int. J. Res. Phys. Chem. Chem. Phys. **1999**, *208*, 43.
395. R. J. Randler, D. M. Kolb, B. M. Ocko et al., *Surf. Sci.* **2000**, *447*, 187.
396. C. Sanchez, E. P. M. Leiva, *Electrochim. Acta* **1999**, *45*, 691.
397. G. Brown, P. A. Rikvold, S. J. Mitchell, Monte Carlo methods for equilibrium and nonequilibrium problems in interfacial electrochemistry in *Interfacial Electrochemistry. Theory, Experiment and Applications* (Ed.: A. Więckowski), Marcel Dekker, New York-Basel, 1999, p. 47.
398. J. Zhang, Y. E. Sung, P. A. Rikvold et al., *J. Chem. Phys.* **1996**, *104*, 5699.
399. J. W. Schultze, D. Dickertmann, *Surf. Sci.* **1976**, *54*, 489.
400. D. Dickertmann, F. D. Koppitz, J. W. Schultze, *Electrochim. Acta* **1976**, *21*, 967.
401. D. M. Kolb, Z. Phys. Chem. Neue Folge **1987**, *154*, 179.

402. D. A. Huckaby, L. Blum, *J. Electroanal. Chem.* **1991**, *315*, 255.
403. J. G. Xu, X. W. Wang, *Surf. Sci.* **1998**, *408*, 317.
404. G. Brown, P. A. Rikvold, M. A. Novotny et al., *J. Electrochem. Soc.* **1999**, *146*, 1035.
405. H. Uchida, N. Ikeda, M. Watanabe, *J. Electroanal. Chem.* **1997**, *424*, 5.
406. H. Uchida, M. Hiei, M. Watanabe, *J. Electroanal. Chem.* **1998**, *452*, 97.
407. M. Nakamura, O. Endo, T. Ohta et al., *Surf. Sci.* **2002**, *514*, 227.
408. A. Kuzume, E. Herrero, J. M. Feliu et al., *J. Electroanal. Chem.* **2004**, *570*, 157.
409. K. Ataka, G. Nishima, W. B. Cai et al., *Electrochim. Commun.* **2000**, *2*, 417.
410. M. Nishizawa, T. Sunagawa, H. Yoneyama, *Langmuir* **1997**, *13*, 5215.
411. H. Hagenstrom, M. A. Schneeweiss, D. M. Kolb, *Electrochim. Acta* **1999**, *45*, 1141.
412. A. Martinez-Ruiz, J. Valenzuela-Benavides, L. Morales de la Garza et al., *Surf. Sci.* **2001**, *476*, 139.
413. A. Martinez-Ruiz, M. Palomar-Pardave, J. Valenzuela-Benavides et al., *J. Phys. Chem. B* **2003**, *107*, 11660.
414. E. W. Bohannan, M. G. Shumsky, J. A. Switzer, *Chem. Mater.* **1999**, *11*, 2289.
415. X. G. Zhang, X. H. Li, H. L. Li, *J. Colloid Interface Sci.* **2001**, *234*, 68.
416. R. Vidu, S. Hara, *Electrochemistry* **1999**, *67*, 1240.
417. M. C. Santos, D. W. Miwa, S. A. S. Machado et al., *Quim. Nova* **2001**, *24*, 465.
418. J. C. Bondos, A. A. Gewirth, R. G. Nuzzo, *J. Phys. Chem.* **1996**, *100*, 8617.
419. D. Lee, T. Rayment, *Electrochim. Commun.* **2002**, *4*, 832.
420. M. C. del Barrio, S. G. Garcia, D. R. Salinas, *Electrochim. Commun.* **2004**, *6*, 762.
421. H. Kawamura, M. Takahashi, J. Mizuki, *J. Electrochem. Soc.* **2002**, *149*, C586.
422. S. Maupai, Y. Zhang, P. Schmuki, *Surf. Sci.* **2003**, *527*, L165.
423. S. Maupai, Y. Zhang, P. Schmuki, *Electrochim. Solid State Lett.* **2003**, *6*, C63.
424. R. Vidu, N. Hirai, S. Hara, *Phys. Chem. Chem. Phys.* **2001**, *3*, 3320.
425. T. Tanaka, K. Kubo, N. Hirai et al., *Mater. Trans.* **2003**, *44*, 688.
426. R. Vidu, S. Hara, *Surf. Sci.* **2000**, *452*, 229.
427. B. K. Niece, A. A. Gewirth, *Langmuir* **1997**, *13*, 6302.
428. R. Vidu, S. Hara, *J. Electroanal. Chem.* **1999**, *475*, 171.
429. M. D. Lay, K. Varazo, N. Srisook et al., *J. Electroanal. Chem.* **2003**, *554–555*, 221.
430. L. A. Kibler, M. Kleinert, R. Randler et al., *Surf. Sci.* **1999**, *443*, 19.
431. L. A. Kibler, A. M. El-Aziz, D. M. Kolb, *J. Mol. Catal. A – Chem.* **2003**, *199*, 57.
432. L. A. Kibler, M. Kleinert, D. M. Kolb, *Surf. Sci.* **2000**, *461*, 155.
433. L. A. Kibler, M. Kleinert, V. Lazarescu et al., *Surf. Sci.* **2002**, *498*, 175.
434. H. Naohara, S. Ye, K. Uosaki, *J. Electroanal. Chem.* **1999**, *473*, 2.
435. H. Naohara, S. Ye, K. Uosaki, *J. Electroanal. Chem.* **2001**, *500*, 435.
436. M. E. Quayum, S. Ye, K. Uosaki, *J. Electroanal. Chem.* **2002**, *520*, 126.
437. Y. Robach, M. Abel, L. Porte, *Surf. Sci.* **2003**, *526*, 248.
438. T. L. Wade, Th. A. Sorenson, J. L. Stickney, *Epitaxial compound electrodeposition in Interfacial Electrochemistry. Theory, Experiment and Applications* (Ed.: A. Więckowski), Marcel Dekker, New York-Basel, 1999, p. 757.
439. A. Gichuhi, B. E. Boone, U. Demir et al., *J. Phys. Chem. B* **1998**, *102*, 6499.
440. P. Jiang, Z. F. Liu, S. M. Cai, *J. Mater. Sci. Lett.* **2003**, *22*, 577.
441. U. Demir, C. Shannon, *Langmuir* **1996**, *12*, 594.
442. B. M. Huang, T. E. Lister, J. L. Stickney, *Surf. Sci.* **1997**, *392*, 27.
443. M. Alanyalioglu, U. Demir, C. Shannon, *J. Electroanal. Chem.* **2004**, *561*, 21.
444. I. Ruach-Nir, H. D. Wagner, I. Rubinstein et al., *Adv. Funct. Mater.* **2003**, *13*, 159.
445. N. Ikemiya, D. Iwai, K. Yamada et al., *Surf. Sci.* **1996**, *369*, 199.
446. I. Yagi, S. Nakabayashi, K. Uosaki, *J. Phys. Chem. B* **1998**, *102*, 2677.
447. T. A. Sorenson, D. W. Suggs, I. Nandhakumar et al., *J. Electroanal. Chem.* **1999**, *467*, 270.
448. T. A. Sorenson, T. E. Lister, B. M. Huang et al., *J. Electrochim. Soc.* **1999**, *146*, 1019.
449. T. A. Sorenson, K. Varazo, D. W. Suggs et al., *Surf. Sci.* **2001**, *470*, 197.
450. I. Nicic, J. Liang, V. Cammarata et al., *J. Phys. Chem. B* **2002**, *106*, 12247.
451. K. Verazo, M. D. Lay, T. A. Sorenson et al., *J. Electroanal. Chem.* **2002**, *522*, 104.

452. C. H. Chen, K. D. Keple, A. A. Gewirth et al., *J. Phys. Chem.* **1993**, *97*, 7290.
453. C. A. Jeffrey, D. A. Harrington, S. Morin, *Surf. Sci.* **2002**, *512*, L367.
454. T. Solomun, W. Kautek, *Electrochim. Acta* **2001**, *47*, 679.
455. M. Hara, Y. Nagahara, S. Yoshimoto et al., *J. Electrochem. Soc.* **2004**, *151*, E92.
456. K. Tamura, J. X. Wang, R. R. Adzic et al., *J. Phys. Chem. B* **2004**, *108*, 1992.
457. Y. L. Du, C. M. Wang, *Chinese J. Chem.* **2002**, *20*, 596.
458. K. Uosaki, Z. Ye, H. Naohara et al., *J. Phys. Chem. B* **1997**, *101*, 7566.
459. H. F. Waibel, M. Kleinert, L. A. Kibler et al., *Electrochim. Acta* **2002**, *47*, 1461.
460. Y. Nagahara, M. Hara, S. Yoshimoto et al., *J. Phys. Chem. B* **2004**, *108*, 3224.
461. J. L. Bubbendorff, L. Cagnon, V. Costakieling et al., *Surf. Sci.* **1997**, *384*, L836.
462. F. A. Moller, O. M. Magnussen, R. J. Behm, *Phys. Rev. Lett.* **1996**, *77*, 5249.
463. F. A. Moller, O. M. Magnussen, R. J. Behm, *Z. Phys. Chem. – Int. J. Res. Phys. Chem. Chem. Phys.* **1999**, *208*, 57.
464. T. Allongue, L. Cagnon, C. Gomes et al., *Surf. Sci.* **2004**, *557*, 41.
465. A. Hitzke, M. B. Hugenschmidt, R. J. Behm, *Surf. Sci.* **1997**, *389*, 8.
466. I. Schuster, G. Abadias, B. Gilles et al., *J. Phys. IV* **1998**, *8*, 231.
467. V. Repain, J. M. Berroir, S. Rousset et al., *Surf. Sci.* **2000**, *447*, L152.
468. M. Kleinert, H. F. Waibel, G. E. Engelmann et al., *Electrochim. Acta* **2001**, *46*, 3129.
469. L. H. Mendoza-Huizar, J. Robles, M. Palomar-Pardave, *J. Electroanal. Chem.* **2002**, *521*, 95.
470. L. H. Mendoza-Huizar, J. Robles, M. Palomar-Pardave, *J. Electroanal. Chem.* **2003**, *545*, 39.
471. V. S. Stepanyuk, W. Heigert, P. Rennert, *Comput. Mater. Sci.* **2000**, *17*, 309.
472. G. Jung, C. K. Rhee, *J. Electroanal. Chem.* **1997**, *436*, 277.
473. Q. Wu, W. H. Shang, J. W. Yan et al., *J. Mol. Catal. – A Chem.* **2003**, *199*, 49.
474. C. H. Jung, C. K. Rhee, *J. Electroanal. Chem.* **2004**, *566*, 1.
475. C. M. Wang, Y. L. Du, Z. L. Zhou, *Electroanalysis* **2002**, *14*, 849.
476. J. W. Yan, Q. Wu, W. H. Shang et al., *Electrochim. Commun.* **2004**, *6*, 843.
477. J. W. Yan, J. Tang, Y. Y. Yang et al., *Surf. Interface Anal.* **2001**, *32*, 49.
478. B. W. Mao, J. Tang, R. Randler, *Langmuir* **2002**, *18*, 5329.
479. B. S. Radovic, R. A. H. Edwards, J. N. Jovicevic, *J. Electroanal. Chem.* **1997**, *428*, 113.
480. J. J. Lee, I. T. Bae, D. A. Scherson et al., *J. Electrochem. Soc.* **2000**, *147*, 562.
481. J. J. Lee, Y. B. Mo, D. A. Scherson et al., *J. Electrochem. Soc.* **2001**, *148*, C799.
482. B. K. Niece, A. A. Gewirth, *J. Phys. Chem. B* **1998**, *102*, 818.
483. D. Poškus, G. Agafonovas, *J. Electroanal. Chem.* **2000**, *493*, 50.
484. M. J. Henderson, E. Bitziou, A. R. Hillmann et al., *J. Electrochem. Soc.* **2001**, *148*, E105.
485. X. Q. Zeng, S. Bruckenstein, *J. Electrochem. Soc.* **1999**, *146*, 2549.
486. X. Q. Zeng, S. Bruckenstein, *J. Electrochem. Soc.* **1999**, *146*, 2555.
487. M. Seo, M. Yamazaki, *J. Electrochem. Soc.* **2004**, *151*, E276.
488. P. Hale, S. Thurgate, P. Wilkie, *Surf. Interface Anal.* **2003**, *35*, 842.
489. M. I. Rojas, *J. Electroanal. Chem.* **1996**, *405*, 33.
490. D. W. M. Arrigan, L. Le Bihan, M. J. Pickup, *Analyst* **1999**, *124*, 1797.
491. H. M. Kothari, A. A. Vertegel, E. W. Bohannan et al., *Chem. Mater.* **2002**, *14*, 2750.
492. Y. V. Bokshits, N. P. Osipovich, E. A. Strel'tsov et al., *Colloids Surf. A* **2004**, *242*, 79.
493. S. Takahashi, K. Hasebe, A. Aramata, *Electrochim. Commun.* **1999**, *1*, 301.
494. F. Endres, S. Z. El Abedin, *Phys. Chem. Chem. Phys.* **2002**, *4*, 1640.
495. L. A. Kibler, M. Kleinert, D. M. Kolb, *J. Electroanal. Chem.* **1999**, *467*, 249.
496. Y. B. Mo, Y. Gofer, E. J. Hwang et al., *J. Electroanal. Chem.* **1996**, *409*, 87.
497. T. Saito, K. Uosaki, *J. Electrochem. Soc.* **2003**, *150*, A352.
498. T. Kawagoe, T. Kotaki, T. Shibasaki et al., *Surf. Sci.* **2000**, *468*, 1.
499. P. Mrozek, Y.-E. Sung, M. Han et al., *Electrochim. Acta* **1995**, *40*, 17.
500. E. D. Chabala, T. Rayment, *J. Electroanal. Chem.* **1996**, *401*, 257.
501. A. R. Ramadan, E. D. Chabala, T. Rayment, *Phys. Chem. Chem. Phys.* **1999**, *1*, 1591.

502. D. Lee, T. Rayment, *Phys. Chem. Chem. Phys.* **1999**, *1*, 4389.
503. M. C. Gimenez, M. G. Del Popolo, E. P. M. Leiva, *Electrochim. Acta* **1999**, *45*, 699.
504. Q. Y. Zhang, T. C. Ma, Z. Y. Pan et al., *Surf. Coat. Technol.* **2000**, *128*, 175.
505. C. M. Whelan, M. R. Smyth, C. J. Barnes et al., *J. Electroanal. Chem.* **1999**, *474*, 138.
506. T. Kondo, J. Morita, M. Okamura et al., *J. Electroanal. Chem.* **2002**, *532*, 201.
507. M. J. Esplandin, M. A. Schneeweis, D. M. Kolb, *Phys. Chem. Chem. Phys.* **1999**, *1*, 4847.
508. D. Oyamatsu, M. Nishizawa, S. Kuwabata et al., *Langmuir* **1998**, *14*, 3298.
509. J. X. Wang, B. M. Ocko, R. R. Adzic, *Surf. Sci.* **2003**, *540*, 230.
510. S. R. Brankovic, N. Dimitrov, K. Sieradzki, *Electrochem. Solid St.* **1999**, *2*, 443.
511. V. Reyes-Cruz, C. Ponce-de-Leon, I. Gonzalez et al., *Hydrometallurgy* **2002**, *65*, 187.
512. J. Inukai, S. Sugita, K. Itaya, *J. Electroanal. Chem.* **1996**, *403*, 159.
513. S. Abaci, L. S. Zhang, C. Shannon, *J. Electroanal. Chem.* **2004**, *571*, 169.
514. D. Omayatsu, S. Kuwabata, H. Yoneyama, *J. Electroanal. Chem.* **1999**, *473*, 59.
515. L. F. Warren, M. A. Bennett, *Inorg. Chem.* **1976**, *15*, 3126.
516. J. V. McArdle, G. E. Bossard, *J. Chem. Soc., Dalton Trans.* **1990**, 2219.
517. M. Bardaj, N. G. Connelly, M. C. Gimeno et al., *J. Chem. Soc., Dalton Trans.* **1994**, 1163.
518. J. D. Basil, H. H. Murray, J. P. Fackler Jr. et al., *J. Am. Chem. Soc.* **1985**, *107*, 6908.
519. S. Lagerge, J. Zajac, S. Partyka et al., *Langmuir* **1997**, *13*, 4683.
520. U. Koelle, A. Laguna, *Inorg. Chim. Acta* **1999**, *290*, 44.
521. A. M. Bond, S. Kratsis, S. Mitchell et al., *Analyst* **1997**, *122*, 1147.
522. P. Kula, Z. Navratilova, *Electroanalysis* **2001**, *13*, 795.
523. R. Y. Bek, N. A. Rogozhnikov, L. I. Shuraeva, *Russ. J. Electrochem.* **1996**, *32*, 1337.
524. R. Y. Bek, *Russ. J. Electrochem.* **2002**, *38*, 1237.
525. R. Y. Bek, L. I. Shuraeva, *Russ. J. Electrochem.* **2003**, *39*, 872.
526. R. Y. Bek, L. I. Shuraeva, *Russ. J. Electrochem.* **2003**, *39*, 229.
527. R. Y. Bek, L. I. Shuraeva, *Russ. J. Electrochem.* **2004**, *40*, 704.
528. G. Trejo, A. F. Gil, I. Gonzalez, *J. Appl. Electrochem.* **1996**, *26*, 1287.
529. K. Marquez, R. Ortiz, J. W. Schulze et al., *Electrochim. Acta* **2003**, *48*, 711.
530. K. B. Holt, G. Sabin, R. G. Compton et al., *Electroanalysis* **2002**, *14*, 797.
531. C. J. Boxley, H. S. White, T. E. Lister et al., *J. Phys. Chem. B* **2003**, *107*, 451.
532. A. Fanigliulo, C. Mele, B. Bozzini, *Trans. Inst. Met. Finish.* **2003**, *81*, 75.
533. B. Bozzini, A. Fanigliulo, *J. Appl. Electrochem.* **2002**, *32*, 1043.
534. A. Fanigliulo, B. Bozzini, *Trans. Inst. Met. Finish.* **2002**, *80*, 132.
535. A. Fanigliulo, B. Bozzini, *J. Electroanal. Chem.* **2002**, *530*, 53.
536. T. Osaka, A. Kodera, T. Misato et al., *J. Electrochem. Soc.* **1997**, *144*, 3462.
537. T. A. Green, M. J. Liew, S. Roy, *J. Electrochem. Soc.* **2003**, *150*, C104.
538. G. Oskam, P. C. Searson, *J. Electrochem. Soc.* **2000**, *147*, 2199.
539. K. Marquez, G. Staikov, J. W. Schulze, *Trans. Inst. Met. Finish.* **2002**, *80*, 73.
540. L. Magagnin, V. Bertani, P. L. Cavallotti et al., *Microelectron. Eng.* **2002**, *64*, 479.
541. L. M. Depestel, K. Strubbe, *J. Electroanal. Chem.* **2004**, *572*, 195.
542. Y. F. Cheng, D. J. Schiffri, *J. Chem. Soc., Faraday Trans.* **1996**, *92*, 3865.
543. B. J. Hwang, R. Santhanam, Y. L. Liu, *Electroanalysis* **2003**, *15*, 1667.
544. S. Bharathi, J. Joseph, O. Lev et al., *Electrochem. Solid State Lett.* **1999**, *2*, 284.
545. B. C. Sih, A. Teichert, M. O. Wolf, *Chem. Mater.* **2004**, *16*, 2712.
546. Y. G. Li, W. Chrzanowski, A. Lasia, *J. Appl. Electrochem.* **1996**, *26*, 843.
547. Y. G. Li, A. Lasia, *J. Appl. Electrochem.* **1996**, *26*, 853.
548. W. Chrzanowski, Y. G. Li, A. Lasia, *J. Appl. Electrochem.* **1996**, *26*, 385.
549. Y. G. Li, A. Lasia, *J. Appl. Electrochem.* **1997**, *27*, 643.
550. Y. G. Li, A. Lasia, *J. Electrochem. Soc.* **1997**, *144*, 1979.
551. X. W. Sun, Y. C. Guan, K. N. Han, *Metall. Mater. Trans. B – Process Metall. Mater. Process. Sci.* **1996**, *27*, 355.
552. R. Y. Bek, N. A. Rogozhnikov, G. V. Kosolapov, *Russ. J. Chem.* **1997**, *33*, 119.
553. Y. Bek, N. A. Rogozhnikov, G. V. Kosolapov et al., *Russ. J. Electrochem.* **1998**, *34*, 918.

554. R. Y. Bek, N. A. Rogozhnikov, G. V. Kosolapov, *Russ. J. Electrochem.* **1998**, *34*, 1162.
555. R. Y. Bek, N. A. Rogozhnikov, L. I. Shuraeva, *Russ. J. Electrochem.* **2000**, *36*, 726.
556. R. Y. Bek, *Russ. J. Electrochem.* **2000**, *36*, 721.
557. R. Y. Bek, *Russ. J. Electrochem.* **2001**, *37*, 250.
558. R. Y. Bek, G. V. Kosolapov, L. I. Shuraeva et al., *Russ. J. Electrochem.* **2001**, *37*, 244.
559. R. Y. Bek, *Russ. J. Electrochem.* **2001**, *37*, 387.
560. R. Y. Bek, *Russ. J. Electrochem.* **2001**, *37*, 723.
561. R. Y. Bek, *Russ. J. Electrochem.* **2002**, *38*, 407.
562. R. Y. Bek, *Russ. J. Electrochem.* **2002**, *38*, 398.
563. R. Y. Bek, L. I. Shuraeva, *Russ. J. Electrochem.* **2002**, *38*, 526.
564. R. Y. Bek, *Russ. J. Electrochem.* **2003**, *39*, 1036.
565. R. Y. Bek, *Russ. J. Electrochem.* **2004**, *40*, 130.
566. R. Y. Bek, A. G. Zelinskii, S. N. Ovchinnikova et al., *Russ. J. Electrochem.* **2004**, *40*, 123.
567. H. K. Lin, X. Chen, *Miner. Metall. Proc.* **2001**, *18*, 147.
568. R. Y. Bek, G. V. Kosolapov, L. I. Shuraeva, *Russ. J. Electrochem.* **2001**, *37*, 256.
569. S. C. Zhang, M. J. Nicol, *J. Appl. Electrochem.* **2005**, *35*, 339.
570. S. C. Zhang, M. J. Nicol, *J. Appl. Electrochem.* **2003**, *33*, 767.
571. I. Chandra, M. I. Jeffrey, *Hydrometallurgy* **2004**, *73*, 305.
572. Y. C. Guan, K. N. Han, *J. Electrochem. Soc.* **1996**, *143*, 1875.
573. L. Y. Chai, M. Okido, *Trans. Nonferr. Met. Soc. China* **1999**, *9*, 145.
574. L. Y. Chai, M. Okido, *Trans. Nonferr. Met. Soc. China* **1999**, *9*, 383.
575. R. Y. Beck, *Russ. J. Appl. Chem.* **1997**, *70*, 400.
576. S. Ye, C. Ishibashi, K. Shimazu et al., *J. Electrochem. Soc.* **1998**, *145*, 1614.
577. Z. L. Li, T. H. Wu, Z. J. Niu et al., *Electrochem. Commun.* **2004**, *6*, 44.
578. M.-C. Daniel, D. Astruc, *Chem. Rev.* **2004**, *104*, 293.
579. S. R. Johnson, S. D. Evans, S. W. Mahon et al., *Langmuir* **1997**, *13*, 51.
580. M. J. Hostetler, A. C. Templeton, R. W. Murray, *Langmuir* **1999**, *15*, 3782.
581. F. P. Zamborini, J. F. Hicks, R. W. Murray, *J. Am. Chem. Soc.* **2000**, *122*, 4514.
582. D. I. Gittins, D. Bethell, R. J. Nichols et al., *J. Mater. Chem.* **2000**, *10*, 79.
583. D. I. Gittins, D. Bethell, D. J. Schiffrin et al., *Nature* **2000**, *408*, 67.
584. S. Chen, R. S. Ingram, M. J. Hostetler et al., *Science* **1998**, *280*, 2098.
585. R. S. Ingram, M. J. Hostetler, R. W. Murray et al., *J. Am. Chem. Soc.* **1997**, *119*, 9279.

**24.5
Electrochemistry of Silver**

24.5.1	Properties of Ag Electrodes	915
24.5.1.1	Polycrystalline Ag Electrodes	915
24.5.1.1.1	Preparation	915
24.5.1.1.2	Surface and Double-layer Properties	915
24.5.1.2	Single-crystal Ag Electrodes	917
24.5.1.2.1	Preparation	917
24.5.1.2.2	Surface and Double-layer Properties	918
24.5.1.2.3	Surface Dynamics	919
24.5.1.2.4	Affinity of Water and Nonaqueous Solvent Molecules to Ag Surfaces	920
24.5.2	Adsorption of Inorganic Species on Ag Electrodes	921
24.5.2.1	Halide Ions	921
24.5.2.1.1	pc-Ag Electrodes	921
24.5.2.1.2	Single-crystal Ag Electrodes	922
24.5.2.2	Pseudohalide	924
24.5.2.3	Oxygen and its Compounds	925
24.5.2.4	Sulfur Compounds	925
24.5.2.5	Inorganic Carbon Compounds	926
24.5.2.6	Fullerenes	927
24.5.2.7	Other Inorganic Compounds	927
24.5.2.8	Metalocenes	928
24.5.3	Adsorption of Organic Species on Ag Electrodes	928
24.5.3.1	Hydrocarbons	928
24.5.3.2	Pyridine and Other Nitrogen Compounds	929
24.5.3.3	Carboxylic Acids	930
24.5.3.4	Alcohols	931
24.5.3.5	Sulfur Compounds	931
24.5.3.5.1	Thiourea (TU)	932
24.5.3.5.2	Alkanethiols and Self-assembled Monolayers	932
24.5.3.6	Biochemically Important Compounds	933
24.5.3.6.1	Adsorption on Modified Ag Electrodes	934
24.5.3.7	Other Organic Compounds	934

24.5.4	Electrode Processes with Participation of Silver Electrodes	935
24.5.4.1	Reactions Involving Oxidation of Ag Surface	935
24.5.4.1.1	Oxygen and its Compounds	935
24.5.4.1.2	Sulfur Compounds	937
24.5.4.1.3	Carbon Compounds	938
24.5.4.2	Electrode Reactions of Selected Organic Compounds, Adsorbed on Ag Electrodes	938
24.5.4.2.1	Biochemically Important Species	938
	Bare Ag electrodes	938
	Modified Ag electrodes	939
24.5.5	Underpotential Deposition Processes	940
24.5.5.1	Ag UPD on Ag	941
24.5.5.2	Ag UPD on Au and Pt	941
24.5.5.3	Pb	942
24.5.5.4	Tl	943
24.5.5.5	Ni	943
24.5.5.6	Chalcogenides	943
24.5.5.7	Other Elements and Compounds	944
24.5.6	Electrodeposition and Electrodissolution Processes of Ag	944
24.5.6.1	Electrodeposition Processes	944
24.5.6.2	Electrodissolution Processes	945
24.5.7	Silver Compounds at the Oxidation States Higher Than I	946
	References	948

The chapter on the electrochemistry of silver was published in 1978 as a part of the 8th volume of *Encyclopedia of Electrochemistry of the Elements*. At that time, most of the electrochemical properties of silver were limited to polycrystalline Ag (pc-Ag) surfaces, although the first studies with single-crystal electrodes were already described. Since the time that this chapter was published, one can indicate three main trends:

1. a continuous interest in pc-Ag electrodes;
2. a significant progress in the studies on single-crystal Ag electrodes; and
3. increasing applications of various surface spectroscopy techniques combined

with traditional electrochemical techniques in the studies of processes occurring both on polycrystalline and single-crystal Ag surfaces.

It is noteworthy that recent advances in the electrochemistry of silver are related more to the role of the surface of Ag electrodes, than to the investigations of Ag compounds in solutions.

The content of this chapter is essentially limited to physicochemical literature on the electrochemistry of silver published during the last decade. Since a large number of papers related to the chemistry of silver was published, it was not possible to include all of them in this review. Moreover, many of these publications seem to

be of interest to physicists rather than to chemists, and thus, it was not thought necessary to include them in the *Encyclopedia of Electrochemistry*. This review is, therefore, a selection of papers exemplifying representative trends in the recent studies of the properties of the silver electrode surfaces and in the electrochemical characteristics of the selected processes occurring at such electrodes. It also includes some analytical papers, but the readers particularly interested in analytical applications of various types of silver electrodes in voltammetric methods (including polycrystalline and single-crystal ones) are referred to, for example, a review by Gorokhovskii [1], covering the time period 1960–2000, and references cited therein.

24.5.1 Properties of Ag Electrodes

24.5.1.1 Polycrystalline Ag Electrodes

24.5.1.1.1 Preparation As compared to single-crystal Ag surfaces, the preparation of pc-Ag electrode may seem to be a relatively simple task. However, a pc-Ag surface, which ensures reproducibility and stability, also requires a special procedure. Ardizzone et al. [2] have described a method for the preparation of highly controlled pc-Ag electrode surface (characterized by electrochemical techniques and scanning electron microscopy (SEM)). Such electrodes, oriented toward electrocatalytic properties, were successfully tested in halide adsorption experiments, using parallelly, single-crystal and conventional pc-Ag rods as references.

24.5.1.1.2 Surface and Double-layer Properties An extensive, recent review on electrochemical properties of the (polycrystalline) pc-Ag/solution interface, together

with earlier works, is included in the paper by Trasatti and Lust [3]. Electrical double layer at the pc-Ag/aqueous solution interface was characterized with the diffuse layer minimum located on the $C_d - E$ curve at $E = -0.94$ to -0.96 V versus saturated calomel electrode (SCE). The roughness factor for pc-Ag was found as $f_{PZ} \geq 1.2$, applying the Parsons-Zobel method [4]. The potential of zero charge (PZC) found using the capacitance method was equal to -0.944 ± 0.015 V (SCE). Other experimental methods yielded this value ranging from -0.927 to -0.890 V for NaF , HClO_4 , and Na_2SO_4 solutions [3]. The effect of anions varied in the order: $\text{F}^- \geq \text{SO}_4^{2-} \geq \text{ClO}_4^-$. Ahern et al. [5] have observed four low-level redox responses within the double-layer region of pc-Ag in basic medium and hence suggested four different types of active surface state (or site) transitions. The correlation between the transition potentials and the onset/termination potentials of different electrocatalytic processes were found.

It is noteworthy that for investigating pc-Ag electrodes, various surface spectroscopic methods have been utilized recently. A majority of the relevant papers are focused on the Raman scattering phenomena, mainly on the surface-enhanced Raman scattering (SERS) and related methods. One should emphasize that silver was one of the few noble metals for which the SERS response was observed, provided that the surface was previously activated by electrochemical or other means [6] in order to roughen it. Kruszewski [7] has investigated light absorption at the SERS-active Ag electrode. The intensity of light reflected from the SERS-active electrode was measured as a function of the potential and time. It was concluded that the observed irreversible increase in the intensity of the reflected light was

caused by an irreversible decrease in light absorption, related to the irreversible decay of the number of “active sites”. Recently, Kruszewski [8] has analyzed the dependence of the SERS signal on the Ag surface roughness, which was changed by varying the parameters of oxidation–reduction procedure. The measurements of angular distribution of elastically scattered light, as well as scanning and transmission electron microscopy, were employed for the determination of roughness. The experimentally observed relationship between the roughness extent and the SERS signal was compared with the predictions of the classical electromagnetic enhancement model.

Another important technique is the second-harmonic generation (SHG) method [6]. Interestingly, ever since SHG

techniques in combination with SERS were introduced in the early 1980s to study electrode surfaces, silver surfaces have become the most investigated objects. Surface roughening supports activation of surface plasmons that cause a substantial increase of the electromagnetic field at the surface. Plasmon is a highly delocalized excitation state formed collectively via electrostatic interaction of weakly bound electrons. Since interfacial SHG depends on the fourth power of the surface electromagnetic field generated by the incident laser beam, the field enhancement at *rough* silver surfaces should also lead to the significant enhancement of SHG at these surfaces, as compared to SHG at the smooth surfaces. Since it has been found that the electrode potential significantly affects

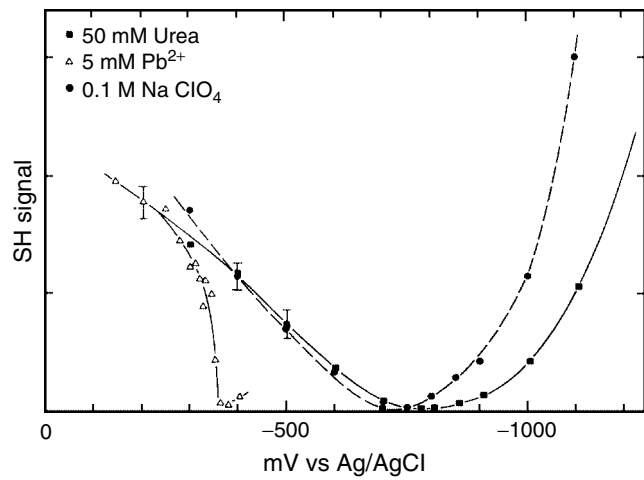


Fig. 1 Potential-dependent SHG response of a thin silver film (45 nm) in contact with a solution of 0.1 M NaClO_4 (solid circles), 0.1 M NaClO_4 + 50 mM urea (solid squares), and 0.1 M sodium acetate + 5 mM lead acetate (open triangles). Most of the crystallites of the pc-Ag film were oriented with the (111) face parallel to the surface. The minimum of the curve occurs at around -0.75 V , which is close to the PZC for $\text{Ag}(111)$ surface. Adsorption of urea causes a little shift in PZC and a significant decrease of the SHG intensity negative of PZC point, whereas the deposition of a monolayer of Pb causes a dramatic increase in the SHG intensity [6, 9].

the SHG response, this method appeared to be interesting also for electrochemical purposes [6]. Thus, potential-dependent adsorption of neutral molecules and ions, as well as deposition processes at the Ag surface, affect the SHG signal (see Fig. 1).

One of the early examples of the application of the SHG technique in electrochemistry, proving its high sensitivity, is the investigation of the sulfate monolayers adsorbed on pc-Ag electrodes [10]. Also, one should mention the paper by Campbell and Corn [11], who have evidenced that the SHG method is also applicable to studies in nonaqueous solutions, namely, to the investigations of hydrogen evolution in acetonitrile (ACN).

Apart from the methods based on Raman spectra and SHG, the Fourier transform coupled with infrared (IR) techniques (see e.g. Ref. 12), scanning tunneling microscopy (STM), and atomic force microscopy (AFM) have also been used.

Another relatively new technique is the infrared visible sum frequency generation (SFG) spectroscopy and the difference frequency generation (DFG) spectroscopy [13], both of which represent vibrational spectroscopic techniques sensitive only to the material located at interfaces.

Apart from the above techniques, the electromodulated reflectance spectroscopy combined with cyclic voltammetry has been utilized by Gaigalas et al. [14] in the investigations of electron transfer between the {2Fe–2S} protein putidaredoxin and either bare or bekamycin-modified Ag electrode. Of the two models considered, the free diffusion model, as compared to the adsorbed layer model, exhibited better concordance with the experimental data. After modification of the Ag electrode with bekamycin, it exhibited only a small increase in the observed redox reaction

rates. The measured rate constants were compared to the values predicted from the Marcus theory of electron transfer.

In addition to the application of roughened Ag electrodes in SERS measurements, one should add that Geddes et al. [15] have described the use of such Ag electrodes in metal-enhanced fluorescence studies also. The constant current flowing between two silver electrodes in pure water facilitated the growth of fractal-like structures on the cathode. The electrode was coated with a monolayer of human serum albumin protein labeled with Indocyanine Green. It was observed that the fluorescence intensity on the roughened electrode increased approximately the 50-fold, compared to the unroughened electrode.

Osuka and Iwasaki [16] have employed AFM method to observe the self-affine fractal structure of the electrochemically roughened Ag electrode surfaces [17]. Later, they have described the dynamic scaling in recrystallization of this electrode surface in water.

24.5.1.2 Single-crystal Ag Electrodes

24.5.1.2.1 Preparation A significant number of papers, which have appeared over the last decade, are focused on the studies of the Ag(*hkl*) surface in contact with various species. Our concise survey covers only those that are most relevant to electrochemists. In the electrochemical practice, the most intensively studied Ag surfaces include: Ag(111), Ag(100), Ag(110), and Ag(001), whereas the number of papers devoted to, for example, Ag(210) and Ag(410) is substantially smaller. Electrode surfaces can be prepared in various ways: electrolytic growth in a Teflon® capillary, electrolytic polishing of Ag single crystals, or chemical ($\text{CrO}_3 + \text{H}_2\text{O}$) polishing of Ag crystal

faces [3]. According to Hamelin et al. [18], during the oxidation–reduction potential cycle, surface oxide reduction and hydrogen evolution take place, and the surface roughness increases. It is also of practical importance to mention that thermal annealing, which is normally used for the preparation of an Au surface, in principle, can also be applied for single-crystal Ag electrodes; however, higher affinity of Ag to oxygen makes the experimental conditions more critical than they are for Au [3]. These difficulties in reproducible preparation of well-defined single-crystal Ag surfaces seem to limit the number of works, in which such electrodes were used.

24.5.1.2.2 Surface and Double-layer Properties

Valette [19] has analyzed earlier experimental data on the inner-layer capacity at PZC for Ag(111), Ag(100), and Ag(110) surfaces in order to estimate the surface area and capacitance contributions of superficial defects for real electrodes, as compared to ideal faces. Considering the application of surface spectroscopy techniques to single-crystal Ag electrodes, one should note that anisotropy of the SHG response for metal electrode allows one to analyze and correlate its pattern with interfacial symmetries and its variations by changing nonlinear susceptibility and the surface structure. Early studies on Ag(111) single-crystal electrodes have

been performed by Shannon et al. (cf. e.g. Ref. 20). In particular, one can monitor in situ, the reconstruction of the electrode surface (cf. e.g. Ref. 21). Also, recently, the interference second-harmonic generation anisotropy (ISHGA) technique has been applied to crystalline Ag and Au electrodes [6]. This advanced technique is expected to be an even better source of information on the geometric and electronic structure of the interface and its changes upon potential scanning and adsorption.

The differences between various Ag surfaces can be distinguished by comparing their surface morphology (generally, the surface of (110) crystal is more folded than that of (111)) and other properties, such as the surface density of atoms, the PZC, and double-layer capacitance. The double-layer properties of single-crystal Ag electrodes have been studied very intensively [3, 22–27]. Selected characteristics of various Ag surfaces are compared in Table 1, which shows that the higher the surface density of atoms, the more positive PZC becomes. Furthermore, Fig. 2 exemplifies differential capacity data of those Ag surfaces.

Zheng et al. [29] have compared surface properties of the assembled silver nanoparticle electrode/indium-tin oxide (AAgNP/ITO) and roughened silver electrode, using electrochemical

Tab. 1 Surface density of atoms (σ_{at}) measured at the potentials of zero charge (PZC), and double-layer capacitances of the *inner* part of the double layer (C_i) for different crystal planes of Ag (lattice constant $d = 0.2889 \text{ nm}$)

Ag plane	$\sigma_{\text{at}} [\text{at. nm}^{-2}]$	PZC [V] (versus SHE, 0.01 M KPF_6) [3]	$C_i [\mu\text{F cm}^{-2}]$ (KPF_6 solutions) [19]	$C_i [\mu\text{F cm}^{-2}]$ (LiClO_4 solutions) [28]
(111)	13.83	-0.445 ± 0.005	77 ± 2	40
(100)	11.98	-0.615 ± 0.005	92 ± 2	42
(110)	8.47	-0.725 ± 0.005	112 ± 2	70

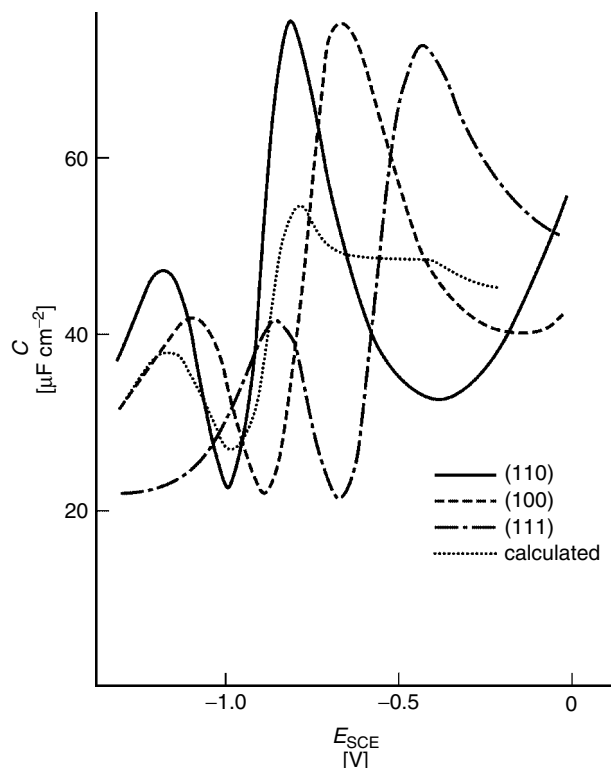


Fig. 2 Differential double-layer capacitances of Ag(111), Ag(100), and Ag(110) in 10 mM NaF determined applying an ac technique; $f = \omega/2\pi = 20$ Hz, scan rate $v = 5$ mV s $^{-1}$. The calculated curve corresponds to the model polycrystalline Ag electrode [24].

techniques and SERS, and methylviologen (MV) and *p*-aminothiophenol (PATP) as the probing molecules. MV molecules were strongly adsorbed on the roughened Ag electrode, but not on AAgNP/ITO. Also, since no SERS spectrum was observed for AAgNP/ITO, probably no active sites were present on the surface of the isolated Ag nanoparticles to participate in the interactions between the ring plane of MV and Ag nanoparticle.

24.5.1.2.3 Surface Dynamics Quass et al. [30] have studied diffusive transport of atoms along the step edges on Ag(111).

Baier, Giesen et al. have described the dynamics of step and island on Ag(111) and Cu(100) [31], as well as on Au(100) [32] electrodes in the electrolyte. Baier and Giesen [33] have determined the activation energies of mass transport processes on Ag(111) electrodes in the aqueous electrolyte. Haftel and Einstein [34] have studied the influence of the electrochemical potential on energy landscapes close to step-and island edges: Ag(111) and Ag(100). A model of the metal/solution interface involving hydrophilicity of Ag(111) and based on the capacitance analysis, has been published by Emets et al. [35]. Electron

confinement to the nanoscale Ag(111) islands on Ag(111) has been quantitatively studied by Li et al. [36]. Winkes et al. [37] have performed surface resistance measurements at the metal/electrolyte interface of Ag(110) and Ag(111) thin-film electrodes. An Ag(111)/water interface deserves special attention. The results of X-ray scattering studies [38] were consistent with the simulation results: it has been found that water is reorienting next to the charged surface and undergoes restructuring in the presence of the strong field [39]. Sun et al. [40] have described the structures of adatom clusters on Ag(111) surfaces, applying genetic algorithm. STM studies of bare Ag(100) electrode within the potential range 0.4 to -0.1 V did not reveal any potential-induced surface reconstruction (contrary to such reconstruction observed at Au(100) electrodes) [41]. Winkes et al. [37] have measured the surface resistance at the metal/electrolyte interface of Ag(100) and Ag(111) thin-film electrodes. Koga [42] has observed the diffusive motion of 2×2 adlayer formed on the Ag(100) nanoparticle facet induced by nitric acid adsorption. The adsorbates exhibited a profile image that was double-periodical to that of an Ag(100) surface along the [010] direction, and their collective diffusion was observed in the real time. A Monte Carlo simulation of submonolayer homoepitaxial growth on Ag(110) and Cu(110) has been performed by Mottet et al. [43]. Surface self-diffusion at intermediate temperatures for Ag(110) has been studied by Pedemonte et al. [44]. Substrate reconstruction and electronic surface states of Ag(001) have been studied by Savio et al. [45]. For the analysis of Ag(001) surface, Simpson and Furtak [46] have employed optical SHG spectroscopy with s-polarized excitation. The surface plasmon dispersion

on sputtered and nanostructured Ag(001) has been studied by Savio et al. [47].

24.5.1.2.4 Affinity of Water and Nonaqueous Solvent Molecules to Ag Surfaces

Hydrophilic properties of single-crystal Ag electrodes have been a subject of controversy [48]. Trasatti [49] has suggested the following series of the decreasing hydrophilicity: Ag(110) > Ag(100) > Ag(111), while Valette [50] has proposed the opposite order. Further studies, in which hydrophilicity of Ag was estimated from the adsorption energy of aliphatic alcohols [51–53], led to the following conclusion: since the adsorption energy is strongly dependent on the lattice plane of the electrode as well as on the size of the anion of the supporting electrolyte (through the salting-out effect of the adsorbate), it is not possible to indicate unambiguously the hydrophilicity series of lattice planes from electrochemical experiments [48]. Anyhow, the position of water molecules is the closest to the folded Ag(110) surface and the farthest – to the smooth Ag(111) surface [48]. As regards adsorption of anions, one should mention that the surface concentration of sulfate ions changes on particular Ag planes in the following order: Ag(111) > Ag(110) > Ag(100) (not concordant with the decreasing surface density of atoms). Such a sequence proves that for adsorption of ions, not only the electrode surface structure but also the structure of the adsorbed ions are important [54, 55]. A more detailed review of the problems of anions and water adsorption on different Ag surfaces is given in Ref. 3. Recently, Doubova et al. [56] have used ACN as either the adsorbate or the solvent to probe the crystal face specificity of Ag–water interaction at the electrode/solution interface. From the capacitance and voltammetric plots, it has been concluded that the

adsorption strength of ACN on Ag from the aqueous solution is weak and decreases in the following order: (111) > (100) > (110). It has also been suggested that ACN adsorption occurs in two alternative modes: (1) directly on the metal surface and (2) at the water layer adsorbed on the metal surface, which cause apparent inconsistencies of the adsorption parameters. Furthermore, the presence of variable amounts of water in ACN had an inhibiting effect on Ag surface oxidation. The diminution of the water content in ACN led to free anodic dissolution of the metal surface. Doubova and Trasatti [57] have investigated adsorption of isovaleronitrile versus ACN in 0.15 M NaClO₄ on Ag single-crystal face electrodes performing capacity measurements. The obtained data have shown that adsorption increases in the following sequence of crystal faces: (110) < (100) < (111) < Hg. In contrast with ACN adsorption, the mode of adsorption of isovaleronitrile is attributable to hydrophilic–hydrophobic interactions, resulting in a squeezing-out mechanism. Adsorption of neutral compounds depends on the crystallographic orientation of the metal surface, mainly because of the face specificity of metal–solvent interactions, the latter being stronger for more open surfaces (i.e. those of lower atomic density [22]). In the specific case of Ag single crystals, the following observations have been made. For linear aliphatic alcohols, the Gibbs energy of adsorption increases in the sequence: (110) < (100) < (111) [53, 58, 59], as expected from the concepts expressed above. For ACN [56, 60], in contrast, the adsorption order is: (111) < (100) < (110), although no interactions between the triple bond of the N group and the metal surface are possible.

Gu et al. [61] have studied the SERS response of Ag electrodes in ACN.

24.5.2

Adsorption of Inorganic Species on Ag Electrodes

24.5.2.1 Halide Ions

24.5.2.1.1 pc-Ag Electrodes Hecht and Strehblow [62] have utilized X-ray photoelectron spectroscopy (XPS) and ion scattering spectroscopy (ISS) in the examination of the electric double layer on Ag in NaCl solutions. It has been found that specific adsorption of Cl⁻ was accompanied by coadsorption of cations and water. A layered structure of the specifically adsorbed chloride anions and the coadsorbed cations was confirmed.

Adsorption of bromide ions on pc-Ag surface has been investigated in several alcohols: C_nH_{2n+1}OH (*n* = 1–5), including butanol isomers (see e.g. Refs 63–66), with supporting electrolytes LiClO₄ and LiBr (electrochemical methods were combined with surface spectroscopy techniques). The potential-dependent orientation of the alcohol molecules was driven by the interactions of nonbonding O electrons and the alkyl chain with the electrode, as well as by hydrogen bonding of OH groups with specifically adsorbed Br⁻ [3]. For a more detailed comprehensive review of the experimental procedure, the reader is referred to the original papers, cited above and summarized in Ref. 3. Later, Pemberton and Shen [67] utilized electrochemical and SERS techniques to study adsorption of bromide ions on Ag in a series of aliphatic alcohols (from methanol to pentanol, containing LiBr). An excellent correlation was observed between the SERS intensity and Br⁻ surface coverage determined from differential capacitance

Tab. 2 Maximum Br⁻ coverage and potentials of zero charge (PZC) values of Ag in alcohols with 0.4 M LiBr [67]

Solvent	$\Gamma \times 10^{11}$ [moles cm ⁻²]	PZC, V versus Ag/AgCl
Methanol	110	-0.7
Ethanol	110	-0.6
Propanol	90	-1.0
Butanol	135	-0.9
Pentanol	140	-0.6

data. The double-layer data are presented in Table 2.

Shi et al. [68] have studied iodine adsorption on Ag using atomic-resolution electrochemical scanning tunneling microscopy (ECSTM) method. Distinctly different iodine adlayer structures and surface diffusion behavior were observed on mechanically polished pc-Ag in comparison with those obtained on single-crystal electrodes.

24.5.2.1.2 Single-crystal Ag Electrodes
 Recently, Nazmutdinov and Zinkicheva [69] have studied adsorption of the fluoride ion from the gas phase on various single-crystal Ag surfaces, applying a density-functional method. Adsorption energy was found to increase in the series: Ag(100) < Ag(111) < Ag(311) < Ag(110). Sneddon and Gewirth [70] have published the in situ characterization of halide adsorption and Ag-halide growth on Ag(111) electrodes using AFM. The chemical bonding state of chlorine on Ag(100) has been studied by Chang and Lung, who applied angle-resolved secondary ion mass spectrometry [71]. It has been shown that chlorine dissociates at the surface to yield a bonding state of atomic form at room temperature and Cl adatom is chemisorbed highly above the topmost substrate layer of Ag

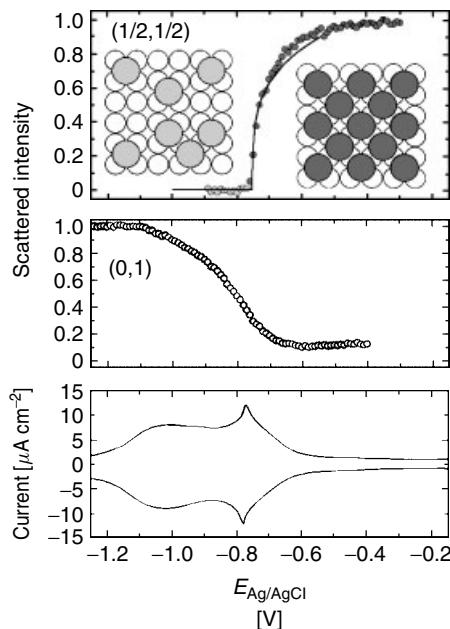
atoms. The Ag–Cl bond was oriented along the <100> azimuth with the adsorbate occupying a C-4 symmetry site. Andryushechkin et al. [72] have studied the epitaxial growth of AgCl layers on the Ag(100) surface. A potential-induced two-dimensional Ising order-disorder transition in bromide adsorbed on Ag(001) has been described by Ocko et al. [73]. In situ X-ray scattering studies have revealed that with the increasing potential, bromide undergoes a second-order phase transition from the lattice gas to the ordered c(2 × 2) structure. From a comparison of X-ray and electrochemical measurements, a significant lateral disorder at low coverage, decreasing with an increasing coverage, has been found. Endo et al. [74] have studied the structures of bromine adsorbed on the Ag(111) electrode at different applied potentials. They have employed for this purpose, in situ X-ray absorption fine-structure spectroscopy (XAFS). In the cyclic voltammogram, a characteristic peak was formed at 0.05 V (versus Ag/AgCl). In the region just before this peak, the Ag–Br bond length was estimated as 2.72 ± 0.05 Å, while after the peak, the spectra revealed the presence of two different Br–Ag bonds of 2.74 ± 0.05 and 2.80 ± 0.05 Å in lengths. These results were attributed to a drastic surface reconstruction taking place at the characteristic cyclic voltammetric peak potential without any changes in the surface Br density. Beltramo et al. [75] have investigated, applying SHG and impedance spectroscopy, the chloride and bromide layers adsorbed on single-crystal Ag electrodes. The SHG response at the incident wavelength of 1064 nm was measured and structural transitions in the adsorbed layer were detected. Beltramo and Santos [76] have studied further, specific adsorption of chloride and

bromide on Ag(111) surface, employing impedance spectroscopy. A physical model has been proposed to obtain different kinetic and mass transport parameters at low concentrations of halide ions. Moreover, the surface charge densities were calculated. In situ SHG studies of covered Ag(111) electrodes have also been published by Santos et al. [77]. XPS and STM studies of pseudo-AgX monolayers organized at Ag(111) and Au/Ag(111) have been published by Kawasaki et al. [78]. Recently, Jović and Jović [79] have combined differential capacitance measurements with the simulations of frequency curves for different equivalent circuits to study (111) in 0.01 M NaCl. The dependence of the capacitance on the frequency was investigated. It was suggested that in the equivalent circuit, the double-layer capacitance should be replaced with a constant phase element. The in situ X-ray adsorption studies of bromine on the Ag(100) electrode have been described by Endo et al. [80]. It was observed that the electron is transferred from the bromide anion to the silver substrate, and that the bond is partly covalent. The Br–Ag distance was determined to be 2.82 ± 0.05 Å, which is shorter than that of the bulk AgBr. The adsorption site appeared to be a fourfold hollow site. The authors have suggested that the bromide ionicity is reduced in the adsorbate phase at the electrode. Ab initio calculations for bromine adlayers on Ag(100) and Au(100) surfaces have

been performed by Wang and Rikvold [81]. Wandlowski et al. [82] have studied adsorption of bromide at the Ag(100) electrode surface. Under electrochemical conditions (similarly as in vacuum) an ordered $c(2 \times 2)$ structure was observed above a critical coverage, with halide ions located in the fourfold hollow sites of the underlying silver lattice. The difference found between Ag(100) and Au(100) is that for silver the packing arrangement is square, compared with the quasi-hexagonal structure detected for gold (Fig. 3) [83].

Hanewinkel et al. [84] have studied the change in the surface resistance of an Ag(100) electrode caused by the adsorbed bromide. It was suggested that bromide ions adsorbed in the double layer of the hollow sites do not exchange electron with the metal. Shimooka et al. [85] have studied the adlayer structures of Cl and Br, and a growth of bulk AgBr layers on Ag(100) electrodes using in situ

Fig. 3 The results of studies of electrosorption of bromide on the Ag(100) surface. The scattered intensities, after background subtraction, are shown at $(1/2, 1/2)$ and $(0, 1)$ versus the applied potential. The corresponding cyclic voltammogram (10 mV s^{-1}) is shown at the bottom [83].



STM and ex situ low-energy electron diffraction (LEED) in ultrahigh vacuum (UHV). It has been shown that the adsorbed Cl and Br monolayers possess a $c(2 \times 2)$ structure on Ag(100) in acidic solutions. At potentials corresponding to the formation of bulk AgBr, AgBr(100) layers grew epitaxially on Ag(100). On the Ag(100) surface, both Ag and Br ions in the topmost layer of the bulk AgBr were observed. LEED pattern revealed a $c(2 \times 2)$ crystallographic arrangement for the bulk AgBr(100) formed on Ag(100). Electrochemical studies and Monte Carlo simulations of electrosorption of Cl and Br on Ag(100) have been described by Rikvold, Abou Hamad et al. [86, 87], as well as by Mitchell et al. [88, 89].

Yamada et al. [90] have used *in situ* STM and ex situ LEED to monitor continuous variation of iodine adlattices on Ag(111) electrodes. Interestingly, contrary to the Ag(100) surface brought in contact with I^- ions, Ag(111), in the presence of I^- ions, exhibited, in cyclic voltammograms, small reversible peaks at potentials slightly negative to the bulk AgI formation. This phenomenon, in view of additional LEED and STM studies, was ascribed to the rotational phase transitions in the Ag(111)- I^- adlayer. The iodine atom adlayers on Ag(110) were studied, applying the energy band theory by Wang et al. [91]. A density-functional theory approach has been applied by Tang et al. [92] to investigate chemisorption of iodine. Ab initio pseudopotential density-functional study has been performed by Wang et al. [93] to analyze interactions of halogen atom with Ag(110). Teshima et al. [94], using *in situ* STM technique, have studied the effect of the adsorbed iodine on the deposition and dissolution reactions of Ag(100). It is noteworthy, in these studies, that clean Ag(100) surface was exposed

to the KI solution under potential control, since under open circuit conditions (OCP) the formation of bulk AgI and surface roughening were rather expected. Cyclic voltammetric studies have shown that Ag dissolution/deposition occurs reversibly at the same potential, regardless of the presence or absence of iodine at the Ag(100) surface. However, H_2 evolution process was shifted by ca -0.15 V when bare Ag(100) surface was replaced with the I-Ag(100) one (this is an example of the adsorbate-induced overpotential). One should add that the I-Ag(100) adlayer structure was found to be potential independent and emphasize the exceptional stability of I on Ag(100) [41]. In turn, it has appeared that the etching of Ag on I-Ag(100) is anisotropic: the etching rate along the [010] direction is faster than along the [001] direction. A model for the explanation of this phenomenon has been proposed [41].

24.5.2.2 Pseudohalide

Rogozhnikov [95] has analyzed the impedance response of an Ag electrode in cyanide solutions. The impedance spectra have shown time evolution of the surface blocking. Time evolution of the active Ag electrode area after immersion in CN^- containing solutions has been analyzed by Baltrunas et al. [96]. A time of 20–60 s was required for settling down the blocking (dependent also on CN^- concentration).

The SFG spectra of CN^- at Ag electrode at various potentials varying from -1.2 V (SCE) to the upper limit below Ag dissolution have been recorded by Tadjeddine and Le Rille [13]. Contrary to the IR spectra, in which four bands for this system were observed, SFG spectra exhibited a single band, providing direct spectroscopic information on the adsorbed species. According to the same authors, the

SFG method is also a powerful tool for a direct determination of the PZC. Tadjeddine et al. [97] have employed this method to determine the PZC of Ag(poly). The observed value was -0.95 V and -1.05 V (SCE) in the absence and in the presence of 25 mM CN^- , respectively, in the solution containing 100 mM NaClO_4 .

Vibrational properties of OCN^- adsorbed on a silver electrode from neutral solutions have been studied by Bowmaker et al. [98], applying *in situ* synchrotron far-infrared spectroscopy and visible-infrared SFG spectroscopy. As an example, the results of these studies are summarized below. In SFG spectra, two bands were formed; they were assigned to the antisymmetric stretching mode of OCN^- ions bound to the Ag surface: the first one in the region 2100 – 2130 cm^{-1} (for $E = -0.6$ to 0 V versus SCE, cyanate N bound to a bridging surface site), and the second in the region 2200 – 2240 cm^{-1} (for $E = 0$ – 4 V, cyanate in a terminal N-bonding mode). In the far-IR spectrum, the following were distinguished: (1) a broadband at about 360 cm^{-1} , at $E > 0$ V, which was assigned to the $\nu(\text{AgN})$ mode of terminally bound cyanate, in accordance with the assignment for the VIS-IR SFG band observed at these potentials, and (2) a sharper band at 90 cm^{-1} that might have arisen from a bending (or restricted rotation) of cyanate on the silver surface.

An *ab initio* study of the interaction of SCN^- with a silver electrode allowed Tielens et al. [99] to predict vibrational frequencies.

24.5.2.3 Oxygen and its Compounds

Lutzenkirchen-Hecht and Strehblow have investigated the electrochemical double layer on Ag electrodes in alkaline media [100] using *ex situ* XPS and ultraviolet photoelectron spectroscopy (UPS). An

evidence for specific adsorption of OH^- ions has been found. Noteworthy is the fact that adsorption of oxygen compounds was often coupled with the surface oxidation of Ag. The relevant papers are presented later in a separate chapter.

24.5.2.4 Sulfur Compounds

Innocenti et al. have studied the kinetics [101] of two-dimensional phase transitions of sulfide and halide ions, as well as electrosorption valency [102] of these ions adsorbed on Ag(111). The electrode potential was stepped up from the value negative enough to exclude anionic adsorption to the potential range providing stability of either the first or the second, more compressed, ordered overlayer of the anions. The kinetic behavior was interpreted in terms of a model that accounts for diffusion-controlled random adsorption of the anions, followed by the progressive polynucleation and growth. For the conditions under which a stable second overlayer is formed, the kinetic behavior was explained in terms of the transition from total desorption to the formation of the second overlayer occurring via the intermediate formation of the first monolayer [101]. Partial charge-transfer coefficients for the considered anions decreased in the order sulfide \cong iodide $>$ bromide $>$ chloride, that is, in the order of the increasing Pauling's electronegativity. Reaction of sulfur dioxide with oxygen adsorbed on Ag(110) has been studied by Alemozafar et al. [103], applying LEED, temperature programmed reaction spectroscopy (TPRS) and STM.

Theoretical calculations for the simplified systems have shown that on the Ag(110) surface, sulfate ions adsorb with the binding energy of 782 kJ mol^{-1} , whereas for carbonate ions, this energy is equal to 949 kJ mol^{-1} [104]. These

energies are higher than for Ag(111), since on the more open Ag(110) surface, the bond order between the surface metal atoms and other metal atoms is lower than in the case of closer surfaces; therefore, less coordinated surface atoms bind more strongly to the adsorbates [104]. Sobkowski et al. [105] have investigated adsorption of sulfate anions on various Ag electrodes. An effect of the surface structure on adsorption of sulfate ions on pc-Ag (and single-crystal Ag surfaces: (111), (110), and (100)) has been published by Smolinski et al. [55]. Radiometric and electrochemical methods were used in this study. On all the four studied surfaces, adsorption was reversible with respect to the potential and bulk concentration of sulfate. The pc-Ag surface exhibited intermediate adsorption properties, compared to the single-crystal surfaces, for which sulfate adsorption decreased in the sequence: $\text{Ag}(111) \geq \text{Ag}(110) > \text{Ag}(100)$ (with tetrahedral structure of the anion matching best the trigonal distribution pattern of the surface Ag atoms on (111) and (110) planes). Thermodynamic parameters of adsorption were fitted to the Frumkin isotherm. Also, Sobkowski et al. [106] have determined radiometrically, the adsorption isotherms, as well as the surface concentration/potential dependences, for various single-crystal Ag electrodes. The surface concentration sequence was found to change as follows: $\text{Ag}(111) \cong \text{Ag}(110) > \text{Ag}(100)$. Thermodynamic parameters of adsorption were calculated by fitting the experimental data to the virial, Frumkin's, and Henry's adsorption models. The sequence of the sulfate adsorption from 0.1 M NaClO_4 on three basal silver planes was quite different from that observed in acidic supporting electrolyte and agreed with the sequence of the zero-charge potentials for the investigated silver surfaces. Recently,

Schweizer and Kollb [107] have studied sulfate adsorption on Ag(111) and Ag(100) in 0.1 M H_2SO_4 , applying cyclic voltammetry and in situ STM. A new *surface preparation* method involving the inductive heating has been employed to eliminate oxygen during the annealing procedure. This method led to high quality Ag(111) and Ag(100) surfaces. An ordered adlayer of sulfate and bisulfate were found on the Ag(100) and (111) faces. An unusual $c(3 \times 3\sqrt{3})$ adlayer structure was found for Ag(111), while for Ag(100), an incommensurate (1.3×3) structure was observed. No ordered adlayer was found on Ag(110). These results constitute the first observation of ordered sulfate adlayers on single-crystal Ag electrodes. Marinkovic et al. [108] have performed the IR studies of sulfate adsorption on Ag(111) surface. Theoretical calculations have shown that at Ag(111) surface, sulfate ions have a binding energy of 159 kcal mol⁻¹, carbonate ions 183 kcal mol⁻¹, and tricoordinated bisulfate ions 58 kcal mol⁻¹ (calculated at the hollow sites of Ag(111)) [104].

Recently, S and O adsorption on pure and Ge-doped Ag(111) has been studied by Blomqvist et al. [109].

24.5.2.5 Inorganic Carbon Compounds

Quantitative determination of the local adsorption structure of carbonate on Ag(110) has been done by Kittel et al. [110]. They have found that the carbonate species is essentially planar and adsorbs almost parallel to the surface at the off-top site with respect to the outermost layer Ag atom. The C–Ag layer spacing was 0.264 ± 0.009 nm, with a well-defined azimuthal orientation. This geometry is understood best in terms of the added-row model proposed by Guo and Madix. This model assumes that additional Ag atoms lie adjacent to the carbonate, such that the

bonding involves at least one of the oxygen atoms. The distance between this oxygen atom and its nearest neighbor Ag adatom is 0.19 ± 0.04 nm. The C–O distances are in the range 1.26–1.30 Å.

24.5.2.6 Fullerenes

Morphology of C_{60} thin films grown on Ag(001) has been studied by Giudice et al. [111], applying UHV-STM. C_{60} molecules were arranged in a quasi-hexagonal $c(6 \times 4)$ structure, having the long axis positioned along the (110) direction of the Ag surface. Due to the presence of two equivalent directions, the C_{60} film presented different domains, separated by dislocation lines. The same research group [112] has continued the STM studies on C_{60} thin films on Ag(001). A peculiar irreversible transition, which led to the onset of brightness differences between the molecules in the same film, was observed at around 300 K. This effect was ascribed to electronic differences caused by nonequivalent orientation of C_{60} molecules on the surface. Goldoni and Paolucci [113] have studied the interaction of fullerene C_{60} with Ag(100) and indicated the occurrence of strong, predominantly ionic, bonding. Electronic structure and growth mode of the early stages of C_{60} adsorption at the Ag(001) surface [114], electronic structure of K-doped C_{60} monolayers on Ag(001), and coexisting inequivalent orientations of C_{60} on Ag(001) have been studied by Cepek et al. [115, 116]. Grobis et al. [117] have analyzed the local electronic properties of a molecular monolayer of C_{60} on Ag(001) using STM at $T = 7$ K. It has been confirmed that the appearance of bright and dim molecules originates from Ag surface reconstruction. Peculiar STM molecular contrast (“bright” and “dim”) in $C_{60}/\text{Ag}(100)$ has been observed by Pai et al. [118].

24.5.2.7 Other Inorganic Compounds

Valette [119] has used the dependence of the minimum of the double-layer capacitance on the concentration of the supporting electrolyte to find the adsorption sequence of anions on Ag(110) face: $\text{F}^- > \text{ClO}_4^- > \text{PF}_6^- = \text{BF}_4^-$. For the latter two ions, adsorption is practically negligible. This series shows that small ions undergo relatively strong adsorption since they can more easily penetrate the space between the silver atoms in the inner layer of the Ag(110) electrode than larger ions. It is known that the tendency of perchlorate to adsorb non-specifically is favored on metals of low work function [120], such as Ag(110) surface ($\phi = 2.3$ eV). For this reason, Stuve et al. [121, 122] have studied adsorption of perchloric acid and the reaction of adsorption products with coadsorbed H_2O . A model for tridentate adsorption of ClO_4^- on Ag(110) has been proposed [122]. It has been concluded that the chemisorbed perchlorate can be hydrated with the adsorbed H_2O under UHV conditions. Contrary to Ag(110), on Ag(100), perchlorate ions undergo stronger adsorption than F^- [123].

Niaura and Jakubenas [124] have studied the effect of alkali metal ions on the SERS spectra of phosphate anions adsorbed at Ag electrodes. The formation of ion pairs at the interface has been confirmed.

The bromide-induced adsorption of thallium complex on pc-Ag electrode has been studied using CV and chronocoulometry [125].

Electrochemical deposition of polyborate monolayers at Ag(111) electrodes has been studied by Stevenson et al. [126].

Coadsorption of ammonia and hydrogen fluoride with water on Ag(110) has been described by Krasnopoler et al. [127] as an example of hydrogen bonding and surface

interactions in protic solvents. Structural and morphological changes accompanying reaction of NH_3 with oxygen adsorbed on Ag(110) have been investigated by Guo and Madix [128].

Lee et al. [129] have studied adsorption configuration and local ordering of silicotungstate anions (STA) on Ag(100) electrode surfaces. Voltammetric studies have shown that STA passivates the Ag surface and thus slows down the electron transfer the dissolved redox species participate in. STA species is oriented with its fourfold axis perpendicular to the Ag(100) surface and the center of the STA molecule is located 4.90 Å above the top layer of the Ag substrate. From the analysis of bond lengths, it has been found that four terminal O atoms are located near the hollow sites and that an Ag—O bond length is 2.06 Å.

Jafarian et al. [130] have studied adsorption and absorption of hydrogen species on Ag electrodes in alkaline solution. Gurten et al. [131] have investigated the effect of alcohols: MeOH, EtOH, and PrOH on hydrogen evolution reaction on Ag electrode in contact with 0.01 M NaCl solution. It was observed that the presence of alcohols increased the hydrogen yield and decreased anodic overpotential (for the Pt anode).

24.5.2.8 Metalocenes

Welipitiya et al. [132] have studied adsorption and desorption of ferrocene on Ag(100), applying photoemission and thermal desorption. The initially adsorbed surface species closely resembled that of molecular ferrocene. The molecule was adsorbed with the cyclopentadienyl ring ligands parallel to the surface. Woodbridge et al. [133] have performed the high-resolution electron energy loss spectroscopy (HREELS) and XPS studies of ferrocene on Ag(100). Researchers from the

same group have also studied adsorption of other metalocenes. Langell et al. [134] have studied adsorption and decomposition of decamethylferrocene on Ag(100), while later, Pugmire et al. [135] have performed spectroscopic studies of adsorption and decomposition of nickelocene at the same surface. Also, Pugmire et al. [136] have investigated orientation of nickelocene molecules on Ag(100), following temperature-programmed desorption and applying HREELS. At relatively inert Ag(100) surface at 175 K, nickelocene was physisorbed molecularly to form a monolayer coverage. Its molecular axis was perpendicular to the surface plane. At 225 K nickelocene started to decompose to the adsorbed cyclopentadienyl and nickel. Molecular desorption was observed only for multilayer material, at 210 K, or for the first monolayer, when the adjacent surface sites were not available for decomposition.

24.5.3

Adsorption of Organic Species on Ag Electrodes

24.5.3.1 Hydrocarbons

IR reflection/absorption spectroscopic study of ethylene adsorption on Ag(110) and atomic oxygen precovered Ag(110) surfaces have been described by Akita et al. [137]. Interaction of ethylene with perfect and defective Ag(001) surfaces [138, 139], as well as coadsorption of ethylene and oxygen on Ag(001) [140], have been studied by Kokalj et al. It has been found that ethylene binds rather weakly to both clean and oxygen precovered Ag(001) surfaces, and that the molecular geometry is almost unchanged upon adsorption. The binding energy with Ag(001) increased considerably in the vicinity of steps and adatoms. Also, chemisorption energy

increased considerably in the presence of subsurface oxygen. Adsorption of ethylene on Ag(001) has also been studied by Vattuone et al. [141], who have employed vibrational excitation method to the description of the switching from the molecular to the dissociative adsorption of this compound. Later, Vattuone et al. [142] have studied ethylene adsorption on clean and oxygen-covered flat and stepped Ag(001). The final adsorption state depended on the translational and internal energies of the gas-phase molecules, as well as on the presence of defects. For instance, for low translational energy, ethylene was either physisorbed or very weakly chemisorbed at flat terrace sites. Kokalj et al. have studied adsorption of ethylene on the stepped Ag(n 10) surfaces [143] (with $n = 2, 3, 4$) using density-functional theory. It has been found that ethylene adsorbs preferably on the top sites of the step edge. The (100) terraces were found to behave similarly to the flat Ag(100) surface, which binds ethylene only weakly.

Pawela Crew and Madix [144] have investigated desorption of propylene and propane from Ag(110) with the emphasis put on the anomalous effects of weak chemisorption on desorption kinetics of alkenes. Molecular conformation of styrene on Ag(100) related to the catalytic epoxidation of terminal alkenes has been studied by Williams et al. [145]. IR studies of the adsorption structures of 1,3-butadiene at Ag(111) and Au(111) surfaces have been published by Osaka et al. [146].

The role of water in partial oxidation of propylene on the Ag(110) surface has been shown by Gland et al. [147].

Adsorption of benzene on Ag(110) has been investigated by Pascual, Kelly et al. [148–151].

24.5.3.2 Pyridine and Other Nitrogen Compounds

Adsorption of pyridine, a rigid molecule able to attain various orientations with respect to the metal surface, evidently remains the most studied process of adsorption of organic molecules at the electrodes. Pyridine replaces water molecules at the electrode surface; the number of removed H₂O molecules depends on the orientation of pyridine molecules with respect to the electrode surface. This process is associated with the partial charge transfer across the electrode surface. Using the SERS method, Ma and Wu have studied the pyridine–iodine charge-transfer complex at the Ag electrode [152]. Yang et al. [153] have analyzed the roughened Ag electrode with the adsorbed pyridine, employing two-dimensional surface-enhanced Raman imaging and comparing the result to the AFM images. Adsorption of pyridine on Ag (and Au) has been studied by Tsionky et al. [154], who applied the electrochemical quartz crystal microbalance (EQCM) method. The frequency shift caused by adsorption of pyridine depended strongly on the nature of the metal. Furthermore, the potential-related frequency shift was observed even in the absence of specific adsorption. Interaction of water with the Ag surface was found to be much weaker than with Au. Nicholson et al. [155] have analyzed speciation of pyridine at a rough Ag electrode surface during oxidation–reduction cycles and have determined the kinetic and spectroscopic profiles of three pyridine complexes.

The studies of pyridine adsorption on Ag(110) (as well as on Ag(311) and Ag(210) surfaces) have been performed by Hamelin et al. [156–158]. An increase in the electrode potential by only 10 mV appeared sufficient for pyridine molecules to change their surface concentration from

zero to the full coverage at the positively charged electrode. The C₅H₅N molecules were then oriented vertically and attached to the Ag surface via N atom. It is noteworthy that the adsorption energy of pyridine on single-crystal Ag electrodes is lower by 15–20 kJ mol⁻¹ than that for gold electrodes.

Ma and Wu [152] have carried out SERS studies on pyridine–iodine charge-transfer complex on pc-Ag electrode.

Shi et al. [159] have performed the time-resolved surface-enhanced Raman scattering (TR-SERS) investigations of adsorption and electroreduction of 4-cyanopyridine on Ag electrode. It has been shown that the nature of the adsorbed species and the reduction products depend on the solution concentration. The rate constants of the respective reaction steps were determined. Li et al. [160] have performed SERS and surface-enhanced hyper-Raman scattering (SEHRS) studies of pyrazine and pyridine adsorbed on Ag electrodes. Lopez-Tocon et al. [161] have performed SERS studied on photoinduced charge-transfer processes of 2,4,6-trimethylpyridine on Ag electrodes. Charge transfer in SERS, based on the spectra of 3,5-dimethylpyridine at an Ag electrode, has been discussed by Arenas et al. [162]. Bukowska et al. [163], using SERS and electrochemical techniques, have investigated adsorption of 4-phenylpyridine at the Ag/solution interface in a wide range of electrode potentials. 4-Phenylpyridine was adsorbed on Ag stronger than pyridine. For saturated solutions, it has been found that 4-PhPy molecules undergo reorientation from rather “flat” at potentials more positive than –0.7 V (SCE), to rather “perpendicular” at more negative potentials. Electrochemical reduction of pyrazine on Ag electrode has been studied by Brolo and Irish [164–167], applying SERS. The

complete analysis of the SERS response of pyrazine, based on a resonant charge-transfer mechanism, has been published by Arenas et al. [168]. Also Arenas et al. [169] have applied the charge-transfer mechanism to the explanation of the SERS spectra of 2,3-dimethylpyrazine adsorbed on Ag electrode. Kudelski and Bukowska [170] have employed SERS to analyze adsorption of piperidine on a silver electrode. For this process, relative SERS enhancement factors were determined as a function of the incident wavelength and the applied potential. The effect of charge transfer on the Raman intensity was estimated from these data. Cehn et al. [171] have studied the adsorption behavior of isoquinoline on Ag surface in HCl solution utilizing SERS spectra. Isoquinoline molecule was adsorbed on Ag via Ag–N interaction at the perpendicular orientation. As the applied voltage was shifted to –0.6 V, the strength of this bond declined and the molecule orientation was tilted.

Osaka et al. [172] have also studied the adsorption structures of acrylonitrile on Ag(111) and Ag(110) surfaces using IR reflection/absorption spectroscopy. Other nitrogen compounds are discussed in the section devoted to biochemically important compounds.

24.5.3.3 Carboxylic Acids

Waszcuk et al. [173] have performed radiometric and voltammetric studies of benzoic acid adsorption on a pc-Ag electrode in contact with 0.1 M HClO₄ solution. The electrodes were obtained by electroplating Ag black onto a vacuum-deposited silver substrate. Benzoic acid appeared to be surface active in the entire range of potentials available at Ag in aqueous solutions. Adsorption of benzoic acid increased as the potential became more positive and this surface process was

fully reversible, regardless of the potential range and solution concentration. Applying the Langmuir isotherm, the apparent Gibbs energy of adsorption was estimated and equaled to -31 kJ mol^{-1} . From the kinetic analysis, it has been concluded that the surface process, rather than diffusion, is a rate-determining step in benzoic acid adsorption. Parker et al. [174] have studied deprotonation of carboxylic acid on Ag(110) and Ag(111) surfaces.

24.5.3.4 Alcohols

Adsorption of *n*-hexanol on Ag(100) and Ag(110) from aqueous 0.05 M KClO₄ solutions has been studied by Foresti et al. [59], who performed capacitive charge measurements and compared the results with those obtained for Ag(111). The calculated adsorption free energy (at the potential of maximum adsorption) was $\Delta G_{\text{ads}}^0 = -17.7 \text{ kJ mol}^{-1}$ for Ag(100), compared to $-18.4 \text{ kJ mol}^{-1}$ for Ag(111). Adsorption parameters on Ag(100) surface have been compared to the molecular model by Guidelli and Foresti [175]. It has been concluded that *n*-hexanol molecules are adsorbed in a flat orientation, similarly as on Hg and Ag(111). On the Ag(110) surface, *n*-hexanol exhibited negligible adsorptivity. Based on ΔG^o_{ads} values, the following hydrophilicity sequence has been obtained: Hg << Ag(111) < Ag(100) < Ag(110), with the value for Ag(110) being anomalously low. Jurkiewicz-Herbich et al. [176] have studied adsorption of 1-butanol and 2-butanol on Ag(100) and Ag(110) surfaces in two different supporting electrolytes (NaF and LiClO₄). It has been found that for weak interactions between the alcohols and the metal, all interactions occurring in the inner-layer region at the electrode contribute to the free energy of adsorption; hence, the

latter depends on the adsorbate interactions with water and supporting electrolyte ions.

Wu et al. have studied adsorption and reaction of 2-iodoethanol [177] and acetaldehyde [178] on Ag(111). Doubova et al. [179] have studied adsorption of amyl alcohol on Ag(111) electrodes in 0.05 M KClO₄ solutions and explained the observed differences and inconsistencies in the light of the applied experimental technique (e.g. the role of ac frequency) and the electrode surface preparation procedure. Generally, amyl alcohol was adsorbed less on Ag(111) than on Hg. The electron-induced surface reactions of methyl formate [180] and methanol [181] on Ag(111) have been studied by Schwaner and White. Foresti et al. [182] have investigated electrochemically, adsorption of 1,5-pentanediol on the Ag(111) and Ag(110) faces.

24.5.3.5 Sulfur Compounds

Santos et al. [183] have performed electrochemical and SHG studies of the Ag(111) electrode surface covered with various organosulfur compounds. Li et al. [184] have studied adsorption of thiophenol, 4-aminothiophenol and 1,4-dithiobenzene on the roughened Ag electrode surface employing SERS technique. The substituent in the benzene ring affected the orientation of the molecules: thiophenol ring was tilted toward the normal of the electrode surface, 4-aminothiophenol adopted an upright orientation, 2,4-dithiobenzene lay flat on the electrode surface, resulting in a strong substrate- π ring interaction. All the molecules were adsorbed via the sulfur atom by forming the Ag-S bond. Correlation of electronic and local structures of 4-hydroxy-thiophenol on NaCl(100) and Ag(100) has been found by Tegenkamp and Pfnnur [185].

24.5.3.5.1 Thiourea (TU) Liu and Wu [186] have presented the results of SERS studies of thiourea (TU) adsorbed on Ag electrodes. Zhong et al. [187] have studied coadsorption of TU and various electrolyte anions. Łukomska and Sobkowski [188] have compared the results from electrochemical impedance spectroscopy and radiochemical methods concerning adsorption of TU on the pc-Ag electrode in neutral solution. Adsorption parameters, in terms of the Langmuir isotherm, were calculated. TU adsorption proceeded in the entire range of the applied potentials; it was reversible with respect to the electrode potential and bulk TU concentration (with small amount of TU being irreversibly adsorbed). Smoliński and Sobkowski [189] have investigated the influence of the Ag electrode surface structure on adsorption of TU in HClO_4 solution utilizing electrochemical and radiochemical methods. Adsorption of TU was reversible with respect to the bulk concentration and the applied potential in the range of ideal polarizability of the electrodes. The maximum surface concentration of TU followed the sequence: $\text{Ag}(111) > \text{Ag}(100) > \text{Ag}(110)$, in agreement with the atom surface density of the silver planes. For all planes, Gibbs energy of TU adsorption was similar: $25.5 \pm 1 \text{ kJ mol}^{-1}$ (in terms of the Langmuir isotherm). Yagi et al. [190] have used sulfur-K near-edge X-ray absorption fine structure (S K-edge XAFS) and XPS to study molecular adsorption of $(\text{CH}_3)_2\text{S}$ on Ag(111). The IR reflection/absorption spectroscopic studies of the adsorption structures of dimethyl sulfide and methyl ethyl sulfide on Ag(110) and Cu(110) have been published by Kasahara et al. [191].

24.5.3.5.2 Alkanethiols and Self-assembled Monolayers

The number of papers on self-assembled monolayers (SAM) on

silver surfaces is quite small compared to the papers concerning gold surfaces. This is probably because of the difficulties in preparing clean and well-ordered silver surfaces [192]. A large number of compounds contain sulfur atoms in their molecules that can interact with the Ag surface. Hatchett et al. [193, 194] have investigated electrochemical oxidative adsorption of ethanethiolate on Ag(111). Free energy of adsorption of *n*-alkanethiolates at Ag(111) was determined electrochemically [195].

Widrig et al. [196] have studied voltammetrically, the SAMs of several *n*-alkanethiols formed on pc-Ag electrodes. Analysis of data showed that during adsorption, the hydrogen of thiol group is lost and the sulfur is oxidized by one electron. Based on the charge required for the reductive desorption of the monolayer, the surface coverage was found to be $7.0 \times 10^{-10} \text{ mol cm}^{-2}$.

Further, Hatchett et al. [197] have described electrochemistry of sulfur adlayers on Ag(111) and found the evidence for the concentration- and potential-dependent surface phase transition. Electrochemical evidence for the adsorption of alkanethiols at two sites of the Ag(111) surface has been published by Mohtat et al. [198]. X-ray studies of the adsorbed monolayers of 1-octanethiol on Ag(111) and Cu(111) have been performed by Rieley et al. [199]. SAMs of 1,8-octanedithiol on Ag(111) have been investigated, applying electrochemical STM by Cavallini et al. [200]. Doomes et al. [201] have described anomalous X-ray absorption near edge structure (XANES) spectra of octadecanethiol adsorbed on Ag(111). Uibel et al. [202], utilizing electrochemical and SERS measurements, have determined the structure and free energy of adsorption of *n*-alkanethiolates at Ag(111). Lee

et al. [203] have studied nondissociative chemisorption of methanethiol on Ag(110) and compared it with adsorption on Cu(110) [204], discussing chemical aspects of the formation of SAMs. The structure and electrochemical behavior of ethanethiol SAMs on Ag(100) and Ag(111) in 0.1 M H₂SO₄ have been studied by Schweizer and Kolb [192], who have employed *in situ* STM and cyclic voltammetry for this purpose. Compared to the iso-electronic Au(111) and despite almost identical lattice constants, the structures of ethanethiols on Ag(111) were different and for thiols of longer chains, a distorted hexagonal structure (compared to the commensurate ($\sqrt{3} \times \sqrt{3}$) R30° structure for Au(111)) was observed. For Ag(100) and Ag(111), a double-layer capacity was equal to 4.4 and 3.4 μF cm⁻², respectively. These values are considerably lower than those obtained for ethanethiol-modified Au(100) and Au(111) (6.5 and 8 μF cm⁻², respectively) and probably reflect higher packing density of ethanethiol on silver surfaces. From the charges accompanying reductive desorption, assuming a one-electron process and subtracting the double-layer charge measured in 0.1 M NaOH, Schweizer and Kolb [192] have arrived at a coverage value equal to $\theta = 0.3$ (Ag(100)) and $\theta = 0.37$ (Ag(111)) for the monolayer. On Ag(100), an incommensurate structure of a next-neighbor distance of 0.44 nm was observed, while for Ag(111) a commensurate ($\sqrt{7} \times \sqrt{7}$) R19.1° structure with two different adsorption sites was found [192]. Reductive desorption of SAMs of alkanethiols on Ag(111) and Au(111) electrodes has been studied by Azzaroni et al. [205]. It has been concluded that the difference in peak potentials of that desorption is determined by the energy to introduce an electron into the

adsorbed alkanethiolate-metal species, the desorption energy of the alkanethiolate anion, and the solvent/metal interaction energy. Also, Hatchett et al. [194] have studied oxidative adsorption of ethanethiolate on Ag(111) in alkaline solutions, utilizing cyclic voltammetry and SERS methods. The structure of alkanethiols of different chain lengths (from 1 to 11 C atoms), adsorbed on Ag(111), has been studied by Heinz and Rabe [206], who used *ex situ* STM.

24.5.3.6 Biochemically Important Compounds

Vivoni et al. [207] have employed SERS to determine orientation of 6-mercaptopurine (6MP) molecules adsorbed on the roughened Ag electrode. It has been concluded that 6MP are attached head-on via N1 atom when the molecule is adsorbed onto a silver electrode surface.

Using the SERS method, Cunha et al. [208] have studied the potential dependence of thymine coordination on pc-Ag electrodes for potentials positive to PZC up to the end of the double-layer potential range. At less positive potentials, one of the ring oxygen atoms was involved in chemical bonding and the molecule assumed a tilted position. In contrast, at more positive potentials, one of the ring nitrogen atoms (possibly, the deprotonated one) established a new bond with the surface, making the molecule's axis closer to the surface normal. Wang et al. [209] have described the SERS studies of microperoxidase-11 on roughed Ag electrodes.

Li et al. have performed a comparative study on the surface-enhanced resonance hyper-Raman scattering and surface-enhanced resonance Raman scattering (SERRS) of dyes adsorbed on Ag electrode and Ag colloid [210].

Chen et al. [211] have studied the orientation of azathioprine adsorbed on the Ag electrode using SERS and ab initio calculations. Brolo et al. [212] have studied adsorption of L-cysteine on a polycrystalline silver electrode utilizing SERS and surface-enhanced second-harmonic generation (SESHG) methods. L-Cys was strongly adsorbed onto Ag and remained there up to the potential of -900 mV (versus Ag/AgCl). For potentials more positive than -650 mV, L-Cys adsorbed with the protonated amino group directed toward the Ag surface; at more negative potentials, reorientation occurred. SERS investigation of NAD(+) adsorbed on Ag electrode has been performed by Chen et al. [213]. Cao et al. have published the results of SERS investigation of the interaction of imidazole with a silver electrode in ACN solution [214]. These authors, also applying SERS, have investigated interfacial water at Ag electrodes in ACN solutions [215]. Carter et al. [216] have employed SERS to determine the orientation of 1- and 2-methylimidazole molecules at Ag electrodes. Milkowska and Jurkiewicz-Herbich [217] have investigated adsorption of tyrosine on Ag(110) and Ag(111) surfaces.

The effect of surface modifiers on electrode reactions and conformation of cytochrome *c*(3) adsorbed on Ag electrode has been investigated by Hobara et al. [218] using SERS and electroreflectance voltammetry. It has been shown that redox interactions of cytochrome *c*(3) are more reversible at Ag electrode modified with 11-mercaptopoundecanoic acid compared to bare metal surface. Using nonresonant SERS technique, Niaura et al. [219] have studied adsorption of cytochrome *c* on Ag electrode. The analysis performed by Wandlowski [220] has evidenced the intermediate position of silver in the series describing the stability of the condensed

physisorbed uracil phase: Hg < Ag(111) < Au(111). Guidelli et al. [221] have modeled short- and long-time behavior of two-dimensional phase transitions of chemisorbed uracil on Ag(111). Cavallini et al. [222] have performed *in situ* STM investigation of uracil on Ag(111).

24.5.3.6.1 Adsorption on Modified Ag Electrodes

Dick et al. [223] have described the SERS studies of cytochrome *c* bound to alkanethiols adsorbed on Ag electrodes. The studies were aimed at evidencing the distance and orientation dependence of heterogeneous charge transfer. Yang et al. [224] have presented *in situ* Raman spectra for the NAD⁺-modified Ag electrode at various potentials. The Ag surface was modified with a SAM. SERS studies have shown that NAD⁺ molecules undergo reorientation or desorption from the Ag electrode when potential is shifted from -0.5 to 0 V (SCE). Fang et al. [225] have studied the adsorption structure of RNA triple helix. Williams et al. [226] were the first who have observed the capping/uncapping by a ligand of Zn porphyrin adsorbed on Ag(100). Redox and conformational equilibria of cytochrome *c*(552) adsorbed on chemically modified Ag electrode probed by SERS have been further studied by Bernad et al. [227]

24.5.3.7 Other Organic Compounds

Grochala, Kudelski, and Bukowska [228] have described the anion-induced charge-transfer enhancement in SERS and SERRS spectra of rhodamine 6G on Ag electrode as a function of the electrode potential, upon addition of chloride and citrate anions. In a very recent paper, Brolo et al. [229] have discussed the ratio of the surface-enhanced anti-Stokes scattering to the surface-enhanced Stokes-Raman

scattering for molecules adsorbed on Ag electrode. For this purpose, SERS spectra for oxazine 720, rhodamine 6G, and pyridine adsorbed on a rough silver surface under controlled potential conditions were recorded. It has been concluded that the main features of the preferential enhancement of the anti-Stokes scattering for an adsorbed molecule on rough silver can be understood in the context of current SERS theories.

Electrochemical, SERS, and surface enhanced resonance Raman (SERR) studies of the reduction of methylene blue on silver electrode have been published by Nicolai et al. [230, 231]

Itaya et al. [232] have described *in situ* STM investigations of organic compounds adsorbed on iodine-modified Au(111), Ag(111), and Pt(111) electrodes.

Guo and Madix [233] have employed STM to study adsorption of acetylidyne on Ag(110). They have determined the number of metal atoms incorporated in such molecular intermediates, as, for example, imide, nitrate, and sulfite. Tautz et al. [234] have used HREELS to investigate the substrate influence on the ordering of organic submonolayers. They have also performed a comparative study of perylene-tetracarboxylic-dianhydride (PTCDA) on Ag(110) and Ag(111). The results of the studies of ultrathin films of PTCDA bear some importance in the context of organic epitaxy, which relies on the formation of highly ordered interfaces. Nowakowski et al. [235] have used STM and LEED for the analysis of the ordered structures of nonplanar derivative of perylene-tetracarboxylic-diimide (PTCDI) on Ag(110). The chosen adsorbate was perylene-3,4,9,10-tetra-carboxylic-diimide-di(2,6-isopropylphenyl), which is a derivative of organic semiconductor PTCDI. The adsorbate exhibited high

mobility on the Ag(110) surface at room temperature. In the submonolayer regime, well-ordered structures were observed. Moreover, two different structures were distinguished in the monolayer regime, depending on the preparation procedure. The first one was a random structure with the molecules lying nearly flat on the surface (relative to the perylene core). The second one was a closer-packed commensurate structure with the molecules of tilted perylene cores and forming stacks. For the second, more densely packed structure, flat-lying functional groups overlapped. The differences in submolecular image contrast between the two structures were considered to be a consequence of different tilting angles of the adsorbed molecules.

24.5.4

Electrode Processes with Participation of Silver Electrodes

24.5.4.1 Reactions Involving Oxidation of Ag Surface

24.5.4.1.1 Oxygen and its Compounds

Itagaki et al. [236] have studied electroreduction of oxygen at the oxidized Ag electrodes using channel-flow double electrode. The HO_2^- species was detected and the role of preoxidation of Ag electrode was discussed. Zabarnick et al. [237] have applied EQCM to study the silver surface corrosion and to detect sulfur. Using the TR-EQCM, Chen et al. [238, 239] have studied the mechanism of silver(I) oxide formation on a pc-Ag electrode in alkaline solution, in a series of potentiodynamic experiments. The first stage of the oxidation was unambiguously attributed to the formation of Ag_2O monolayer. In the second oxidation stage, a very small amount of Ag or its oxide was dissolved in the solution and the Ag_2O layer thickness was

gradually increased. Compact, Ag_2O layers were formed in the first two stages of the oxidation, while Ag_2O formed at more positive potential was porous. No species other than Ag_2O was detected. Anodic behavior of Ag electrode in KOH solutions has been studied by Bughiu et al. [240]. Nagle et al. [241] have investigated a growth of multi-layer oxide films on pc-Ag surface in basic media, under conditions of repetitive potential cycling. Depending on the lower potential limit of the oxide growth cycles, either Ag_2O or AgOH predominated. Savinova et al. [242] have studied the structure and reactivity relations for H_2O_2 reduction at Ag electrodes in NaF/NaOH electrolytes of various pH. Cyclic voltammetry and ac- impedance spectroscopy were used. OH^- chemisorption was observed in a wide potential range (between -1.1 and 0 V (SCE), depending upon pH). The occurrence of a slow chemical step in the overall reaction mechanism has been proved. Its rate was strongly affected by the oxidation of the surface submonolayer. The proposed reaction scheme involved the structure of the adsorbate layer at the electrode/electrolyte interface at various potentials. Flätgen et al. [243] have proposed autocatalytic mechanism of H_2O_2 reduction on Ag in acidic media, which may produce negative differential resistance and current oscillations. The proposed mechanism assumed the potential-dependent coverage of the Ag electrode with the activating adsorbate (OH_{ad}), which is formed in the course of H_2O_2 reduction as an unstable intermediate. Experiments, as well as model calculations, have been performed. Interaction of oxygen with $\text{Ag}(110)$ has been studied by Raukema et al. [244]. Adsorption of O_2 on $\text{Ag}(110)$ has been investigated by Bird and Gravil [245]. Formation of d-holes at the initial stages of the oxidation of $\text{Ag}(001)$ has been studied by Benedek

et al. [246] Cyprian et al. [247] have investigated adsorption of atomic oxygen on $\text{Ag}(001)$ using density-functional theory. Altieri et al. [248] have studied morphological change of a $\text{MgO}(001)$ monolayer deposited on $\text{Ag}(001)$ induced by the application of H_2O . Jovic et al. [249] have performed cyclic voltammetric studies on $\text{Ag}(111)$ and $\text{Ag}(100)$ faces in NaOH solutions. In situ Raman spectroscopy was used by Savinova et al. [250] to study the interface between $\text{Ag}(111)$ electrodes and alkaline NaF electrolytes at various pH. Submonolayer oxidation started much below the bulk silver oxide formation, namely, at the potential of ca -0.6 V versus Hg/HgO electrode at pH 11. In the Raman spectra, the bands attributed to $\text{Ag}-\text{OH}$ stretching and $\text{AgO}-\text{H}$ bending vibrations of electrochemisorbed hydroxide species were identified. Fluoride ions stabilized adsorption of hydroxide species. A multistep mechanism for the formation of hydroxide/oxide species at the Ag surface has been proposed. Using ex situ XPS, Savinova et al. [251, 252] have studied the interface between $\text{Ag}(111)$ and an alkaline electrolyte. In their earlier studies, Zemlyanov and Savinova et al. have observed OH groups incorporated in the $\text{Ag}(111)$ electrode [253]. More recently, Savinova et al. [254] have discussed the mechanism of $\text{Ag}(111)$ submonolayer oxidation, applying combined electrochemical, in situ SERS, ex situ XPS, and UPS. The potential-dependent formation of adsorbates was observed above the zero-charge point of the Ag electrode for OH groups ($\text{OH}_{\text{ads}}^{\gamma-}$) and oxide-like species ($\text{O}_{\text{ads}}^{\delta-}$). A mechanism of the oxidation of $\text{Ag}(111)$ submonolayer has been proposed on the basis of combined cyclic voltammetric, in situ SERS, ex situ XPS and UPS studies. Danckwerts et al. have published the results of electrochemical and SHG

studies of the Ag(111) surface [255] including coadsorption of fluoride and hydroxide ions in alkaline electrolytes, for pH ranging from 5.8 to 14 [256]. It has been found that OH^- adsorption at Ag(111)/alkaline electrolyte interface is the initial step leading to the formation of the surface oxide. A rapid transition from the F^- -dominated to the OH^- -dominated adsorption has been observed, as both species remained charged upon adsorption. At sufficiently positive potentials, yet below the reversible potential of the bulk oxide growth, OH was discharged, leading to the build up of the submonolayer oxide, whereas in acidic electrolyte, Ag was dissolved. At intermediate pH, the formation of a structured OH^-/F^- coadsorbed layer has been proposed. Shaikhutdinov [257] et al. have performed ex situ STM study of underpotential oxidation of Ag(111) electrode in alkaline ($\text{NaF} + \text{NaOH}$) electrolyte. The STM images have shown that the oxidation of the Ag(111) surface starts above the point of zero charge and proceeds according to the nucleation-growth mechanism. It started at the steps and extended to the terraces as the electrode potential was scanned in the positive direction. In the backward potential scan, the initial surface morphology was restored. Complex oxide structures formed during oxidation of Ag(111) and Ag(100) by hyperthermal atomic oxygen have been described by Li and Yang [258]. Carlisle et al. [259] have used STM for imaging the surface and the interface atoms of an oxide film on Ag(111). Recently, Kunze et al. [260] have performed an in situ STM study of the initial stages of electrochemical oxide formation at the Ag(111)/0.1 M NaOH interface. A comparative study of hydroxide adsorption from the mixed NaOH/NaF solutions, on Ag(111), Ag(110), and Ag(100) faces, using cyclic voltammetry, ex situ electron

diffraction, and in situ SHG has been recently published by Horswell et al. [261]. For all silver planes studied, two pairs of anodic and cathodic peaks were observed in cyclic voltammograms. They appeared in the potential range below the equilibrium $\text{Ag}_2\text{O}/\text{Ag}$ potential. These peaks were attributed to the specific adsorption of OH^- ions followed by submonolayer oxide formation. The differences between cyclic voltammograms for the (111), (110), and (100) planes were assigned to (1) different work functions; (2) surface atomic densities; and (3) corrugation potentials for these surfaces. Furthermore, ex situ LEED and reflection high-energy electron diffraction (RHEED) studies have shown that disordered adlayers are formed on Ag(111) and Ag(100), in contrast to Ag(110), where ordered structures are produced in the potential region corresponding to the first pair of voltammetric peaks. In the potential range of the second pair of peaks, LEED results indicated disordered oxide phases present on each crystal plane; RHEED results showed the presence of small islands of the $c(2 \times 2)$ structure at particular electrode potentials on (110) and (100). Also, isotropic (for (111), (110), and (100) planes) and anisotropic (for (110) and (111) planes) contributions to the measured SHG intensity were calculated. Recently, Kokalj et al. [262] have investigated adsorption of atomic oxygen and its inclusion into subsurface sites on Ag(210) and Ag(410) surfaces.

24.5.4.1.2 Sulfur Compounds

Electrochemical growth of Ag_2S on Ag(111) electrodes has been studied using XPS by Conyers and White [263].

Flätgen et al. [264, 265] have involved surface plasmon microscopy to study the formation of spatiotemporal potential

patterns at a silver electrode during reduction of peroxodisulfate.

24.5.4.1.3 Carbon Compounds Electrochemical behavior of pc-Ag electrodes in Na_2CO_3 solution and the effect of ClO_4^- ions have been studied by Ibrahim et al. [266] under potentiodynamic and potentiostatic conditions (the results were supplemented with X-ray diffraction (XRD) analysis). It has been found that the active/pассив transition (involving formation of Ag_2O and Ag_2CO_3 layers) occurs prior to oxygen evolution and that perchlorate ions stimulate active dissolution of Ag. These proceed in the passive region and lead to the pitting corrosion. Abd El Rehim et al. [267] have investigated further perchlorate pitting corrosion of a passivated silver electrode.

Constant et al. [268] have used HREELS to study the formation of carbonate on Ag(110). Also, Guo and Madix [269], using STM, have investigated the interaction of carbonate ions with Ag(110). Oxidation of CO by molecular oxygen adsorbed on Ag(110), as well as the influence of surface reconstructions on the CO oxidation reaction rate at the O/Ag(110) surface, has been investigated by Burghaus and Conrad [270, 271]. Later, Barth and Zambelli [272] have employed STM to the studies of CO oxidation by molecular oxygen at Ag(110) surface in the temperature range 60–110 K. At the lowest temperatures, CO remained weakly bound to Ag(110). Striped CO superstructures running along the [001] direction were observed at intermediate coverages, indicating weak anisotropic interactions between the molecules. Oxidation readily took place upon CO exposure, whereby single oxygen atoms were identified as an intermediate product, which could be further titrated

with CO molecules. More recently, CO oxidation on Ag(110) has also been analyzed by Burghaus et al. [273], who additionally discussed the surface reconstruction in relation to the subsurface oxygen problems. Transient CO_2 formation has been studied under “quasi-steady-state” conditions applying surface titrations. The reactivity of the surface toward CO oxidation was reduced in the course of the developing surface reconstruction and a possible influence of subsurface oxygen on CO_2 formation rates was excluded. Adsorption of oxygen and carbon dioxide on cesium-reconstructed Ag(110) surface has been studied by Guo and Madix [274].

24.5.4.2 Electrode Reactions of Selected Organic Compounds, Adsorbed on Ag Electrodes

Jones and Barteau [275] have studied the cyclization and related reactions of iodoethanol on Ag(110). The mechanism of diethyl ether formation on Ag(110) and its dependence on the coadsorbed oxygen species has been studied by Jones et al. [276].

Ab initio pseudopotential study of dehydrogenation of methanol on oxygen-modified Ag(110) surface has been described by Sun et al. [277].

24.5.4.2.1 Biochemically Important Species

Bare Ag electrodes. It is noteworthy that the recently studied electrode processes of organic compounds at pc-Ag electrodes involve mainly biochemically important species. For example, Zeng et al. [278] have investigated the voltammetric behavior of 2-mercaptopurine (MPD) and have found that at appropriate potentials, MPD adsorbs on and interacts with the electrode to form an insoluble silver salt at the surface. The first of two cathodic

peaks (-0.66 V) was ascribed to the reduction of this sparingly soluble silver MPD compound, whereas the second peak (-1.28 V) was attributed to the reduction of MPD to pyrimidine. Furthermore, Zeng and Purdy [279] have investigated the influence of cetyltrimethylammonium bromide (CTAB) on the voltammetric behavior of a series of thiopurines at Ag electrode. In the presence of CTAB, cathodic accumulation of thiopurines was greatly improved and made the stripping peaks increase. Adsorptive voltammetric behavior of resveratrol (a compound present in wine) at Ag electrode has been studied by Dong et al. [280]. The Langmuir-like adsorptive behavior was assumed and the free energy of adsorption was calculated as -46.21 kJ mol $^{-1}$ at 298 K. Ye and Zhou [281] have studied the redox behavior of tyrosinase, applying cyclic voltammetry and potential-step chronoamperometry. The investigated redox process involved two electrons and was quasi-reversible. The linear dependence of the measured current versus concentration makes the studied reaction analytically applicable. Ye and Zhou [282] have investigated the electrochemical behavior of hemoglobin at bare Ag electrode, also from the point of view of potential analytical applications of this process. A pair of redox peaks was observed at $+0.26$ V (oxidation) and $+0.01$ V (reduction), at a sweep rate of 20 mV s $^{-1}$. Cai et al. [283] have applied in situ SERS technique to study irreversible adsorption of hemin and/or its reduced counterpart on the roughened Ag electrodes, as a function of the applied potential in aqueous electrolytes. The standard redox potential was found to be -0.12 V (SCE). Fast preequilibrium between the electrochemically active (monomer) and inactive (μ -oxo dimer) forms of hemin has been proposed. Later, Zheng et al. [284] studied adsorption

of hemin on a roughened Ag electrode. Li et al. [285] have described the voltammetric response of nicotinamide coenzyme I at Ag electrode. This compound was directly oxidized at a bare Ag electrode at ca 0.23 V and the resulting species yielded a cathodic peak at ca 0.12 V. Raman studies of photochemical charge-transfer excitation of trans-4-stilbazole at a silver electrode have been reported by McMahon et al. [286]. Sanchez-Cortes and Garcia-Ramos [287] have analyzed the effect of charge-transfer mechanism on the SERS response of 1,5-dimethylcytosine adsorbed on Ag electrodes, as well as on different metal colloids. Li et al. have studied electroreduction of phenazine on silver electrodes, applying SEHRS and SERS [288].

Modified Ag electrodes. A significant number of papers have been devoted recently to electrode processes of biochemically important compounds at the *modified* Ag electrodes. Li, Chen, and Zhu have studied electrochemical behavior of cytochrome *c* at the imidazole-modified silver electrode [289] and electrochemical reduction of NAD $^{+}$ at the benzoimidazole-modified silver electrode [290]. Imidazole reacted with Ag and covered the metal to give a stable and long-lasting chemically modified electrode, suitable for the electrode process of cytochrome *c* (as similar to imidazole for NAD $^{+}$ reduction). The same electrode was utilized by Li et al. in the investigation of redox process of myoglobin [291]. Zhu et al. [292] have described the voltammetric response of myoglobin at a captopril-modified silver electrode. Furthermore, Li et al. [293] have performed electrochemical studies of hemoglobin at the L-cysteine-modified Ag electrode. The covalent binding of cysteine to Ag surface via sulfur atom allowed one to obtain very stable and long-lasting chemically

modified electrode, ensuring an excellent voltammetric response in the presence of hemoglobin. Zhang et al. [294] have investigated the electrochemical properties of hemoglobin at silver electrode modified with self-assembled lipoic acid monolayer. Lipoic acid molecules were strongly adsorbed at the Ag electrode surface through the cleavage of the S–H bond and formation of the Ag–S bond. Long et al. have described electrocatalytic oxidation of NAD(P)H [295] and electrochemical regeneration of coenzyme NADH [296] on a L-histidine-modified silver electrode. They have proposed its application to the flow detection of this compound. Tian et al. [297], using EQCM, have estimated kinetic parameters of adsorption of human serum albumin onto hydroxyapatite-modified Ag electrode. The voltammetric behavior of DNA at Ag electrode has also been studied by Trnkova [298]. In particular, the influence of electrochemical pretreatment of silver electrode surfaces, as well as the choice of the starting and switching potentials, on voltammetric signals of DNA

have been discussed. The conclusion was that elimination voltammetry with silver electrodes represents a promising alternative in the construction of a biosensor for nucleic acids.

24.5.5

Underpotential Deposition Processes

Discharge of H^+ ions reveals the role played by the structure of Ag surface in the underpotential deposition (UPD) of hydrogen. Figure 4 shows that in the acidic medium, the activity of the electrode surfaces toward H^+ discharge decreases in the series: $\text{Ag}(111) > \text{Ag}(\text{poli}) > \text{Ag}(100) > \text{Ag}(110)$, following the decrease in the surface density of atoms [48, 189].

The composition and the structure of electrodeposited metallic monolayers have always been a subject of intensive electrochemical investigations. However, the sources of information were limited by the number of available electrochemical methods. The UPD process on single-crystal surfaces (including Ag) has been summarized by Jüttner and Lorenz [299]

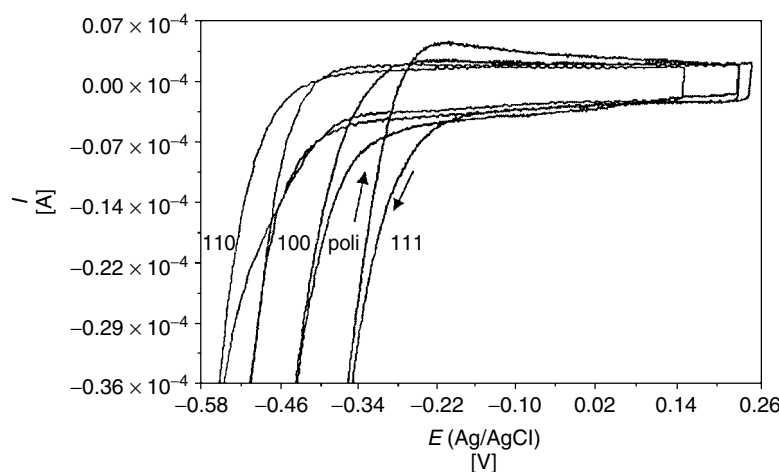


Fig. 4 Cyclic voltammograms recorded at single-crystal and polycrystalline Ag electrodes in 0.1 M HClO_4 . Scan rate: 0.1 V s^{-1} [189].

already in 1980. At that time, UPD was a relatively new field of investigation. Recently, owing to the development of such spectroscopic surface methods as Auger electron spectroscopy (AES), LEED, STM, XPS, and XRD (grazing angle X-ray diffraction), more complete analysis of the structure of metallic monolayers on single-crystal surfaces can be performed. It is clear now that for the anodic electrodissolution of metals, the important role is played by the adlayers of various species (e.g. iodine on Ag) [41]. A more recent review of UPD at single-crystal surfaces of Au, Pt, Ag, and other materials has been published by Herrero et al. [300].

The nature of bonding of the adsorbed species to the model cluster of metal surfaces can be analyzed in terms of the so-called constrained space orbital variation (CSOV) method. For halogen anions adsorbed on various silver surfaces, it has been found that Pauli repulsion, metal polarization, and charge transfer to the metal surface mainly contribute to the binding energy of the ions [104, 301].

24.5.5.1 Ag UPD on Ag

Garcia et al. [302] have performed an *in situ* STM study of electrocrystallization of Ag on Ag(111) and have shown that Ag deposition occurs preferentially at the step edges following a layer-by-layer growth mechanism.

24.5.5.2 Ag UPD on Au and Pt

A series of papers have been devoted to the silver deposition on single-crystal surfaces of other metals, mainly Au(111) and Au(100). Zell et al. [303] have performed electrochemical *in situ* STM, cyclic voltammetric, and potential-step studies of phase formation during Ag (and Al) electrodeposition from the room-temperature molten

salts on flame-annealed Au(111). Cyclic voltammograms of Ag on Au(111) were characterized by the adsorption-controlled UPD and diffusion-controlled overpotential deposition (OPD). In the UPD range, two-dimensional Ag islands were formed, which merged into a coherent Ag monolayer. Further reduction of the potential value was followed by the formation and growth of a second monolayer. In the OPD range, a diffusion-controlled layer-by-layer growth of Ag clusters occurred. Ag UPD on Au(111) and Au(100) has been investigated by Garcia et al. [304, 305], who employed *in situ* STM and electrochemical techniques for this purpose. Ag UPD was found to occur stepwise and similarly on both surfaces. On Au(111), the condensed Ag phase was preferentially generated in monoatomic steps, whereas on Au(100), a simultaneous 2D nucleation of Ag on flat terraces was observed. Deposition of Ag on the Au(100) surface has been studied experimentally by Ikemiya et al. [306] (*in situ* AFM measurements) and theoretically by Gimenez et al. [307, 308]. Also, Chabala, Ramadan et al. [309–311] have investigated Ag UPD on Au(111) using XRD techniques. Rooryck, Buess-Herman et al. [312] have performed Auger electron spectroscopic and LEED studies of the growth of Ag on Au(111), (311), and (554) single-crystal surfaces. It has been suggested that the growth mechanism depends partly on the atomic surface roughness. Rooryck et al. [313] have revisited later silver UPD on Au(111) and stepped Au(111) in sulfuric acid using cyclic voltammetry in combination with UHV-based methodologies. They have shown that the first step of silver UPD is strongly dependent on the superficial state of the substrate and on the formation of an Ag–Au surface alloy. In the absence of surface alloy, sharp and intense UPD peak at 0.53 V

(versus Ag/Ag⁺) was associated with the deposition of Ag on Au terraces. Potential cycling in the UPD region introduced some surface defects and gradually transformed the surface into the surface alloy phase, leading to the appearance of a silver UPD peak at 0.61 V. These findings constituted the basis for the discussion on voltammetric data from the previous studies on Au(111). Gimenez et al. [308] have performed theoretical (e.g. Monte Carlo) considerations of electrochemical phase formation for Ag deposited on Au(111) and Au(100). More recently, Kondo et al. [314] have employed X-ray scattering techniques for the *in situ* structural study of Ag UPD on Au(111) electrodes in sulfuric acid. They have found that Ag monolayer was formed in the potential range between the second and the third UPD peaks. Also, an Ag bilayer was formed in the potential range between the third UPD peak and bulk deposition potential. Recently, Cercellier et al. [315] have investigated epitaxial Ag ultrathin film grow on Au(111) using STM and angle-resolved photoemission spectroscopy (ARPES). Also, more complex deposition schemes were described. Watanabe et al. [316], using EQCM, have studied Cu and Ag adatoms at Au(111) in perchloric acid solutions. Takami et al. [317] have described the formation of a composite Ag–Cu monolayer on Au(111) applying sequential UPD. Wang et al. [318] have studied OPD of Ag monolayer and bilayer on Au(111) mediated by Pb adlayer UPD/stripping cycles.

UPD of Ag onto Au electrodes covered with SAM of alkanethiols has been described by Oyamatsu [319]. Hu et al. [320] have prepared nanoelectrode ensembles by assembling silver colloid and mercaptan on a gold electrode.

Finally, one has to mention an interesting study [321] of Ag electrodeposition onto

iodine-pretreated Pt(111). Spectroscopic studies (LEED, AES) have revealed that this deposition occurs in four steps: three subsequent underpotential processes are followed by the deposition of “bulk” Ag, while the iodine layer remains attached to the outermost layer, regardless of the number of Ag layers deposited.

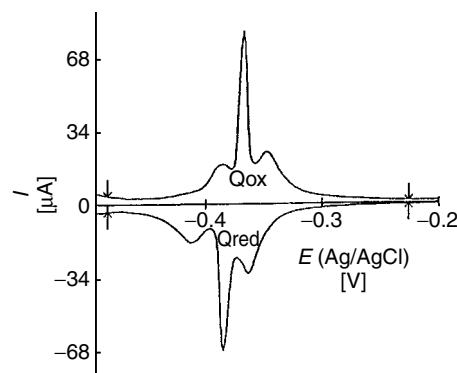
Ogura et al. [322] have studied hydrogen adsorption on Ag (and Au) monolayers grown on Pt(111).

24.5.5.3 Pb

Leiva and Schmickler [323] have employed the density-functional formalism to investigate the electronic properties of Pb monolayer deposited on Ag(111) electrode. They have predicted the enhancement of the signal observed in SHG spectroscopy. Stevenson et al. [324] have investigated the effect of the surface defect structure on the UPD deposition of Pb monolayers at Ag(111). Sackmann et al. [325] have studied Pb UPD on Ag(111) and Ag(100) using *in situ* scanning probe microscopy (SPM) combined with electrochemical impedance spectroscopy (EIS). Relatively simple conditions were found for Ag(111); formation of a condensed Pb monolayer, starting exclusively at monoatomic steps, was observed at low supersaturations with respect to the condensed 2D phase. The analysis of SPM and EIS data indicated that the lateral growth of the condensed Pb monolayer preferentially occurred via a direct transfer of Pb²⁺ from the electrolyte to the step edges. Smoliński and Sobkowski [189] have studied UPD of Pb on Ag(111) and have shown that the deposition/dissolution process is reversible in this sense that reduction and oxidation charges are practically equal (Fig. 5).

Widmer and Siegenthaler [326] have described STM investigation of Pb adsorption on Ag(111) surface in chloride electrolytes.

Fig. 5 Underpotential deposition of Pb on Ag(111) electrode from 0.1 M HClO_4 solution containing 1×10^{-3} M Pb^{2+} [189].



Obretenov et al. [327] have performed the Monte Carlo simulation of UPD in the $\text{Ag}(111)/\text{Pb}^{2+}$ system. Schmidt et al. [328], using *in situ* STM, have studied 2D phase formation accompanying Pb UPD on $\text{Ag}(100)$ and $\text{Au}(100)$. Sackmann et al. [325] have performed combined *in situ* SPM and EIS studies of Pb UPD on $\text{Ag}(100)$ and $\text{Ag}(111)$.

24.5.5.4 Tl

Waszczuk et al. [329] have carried out radiometric studies of UPD of thallium on single-crystal Ag electrode from perchloric acid solutions. Deposition of Tl on $\text{Ag}(100)$ to obtain monolayer, bilayer, and bulk crystallites has been studied by Wang et al. [330]. These studies have shown that apart from the substrate geometry, the nature of the substrate–adatom interactions also influence the structure of the UPD metal adlayers. This is because of the fact that, contrary to Au and Pt electrodes, Tl forms a well-ordered bilayer phase before bulk deposition on $\text{Ag}(100)$ surface occurs.

24.5.5.5 Ni

Morin et al. [331] have studied electrodeposition of Ni on $\text{Ag}(111)$ under the potential-controlled step flow conditions. Morin et al. [332], using *in situ* STM, have

investigated the formation of ultrathin Ni films on $\text{Ag}(111)$ and compared the obtained results with those of analogous studies with $\text{Au}(111)$. At multilayer coverages, atomically smooth Ni deposits were found of a lattice constant close to that observed for metallic Ni. More recently, Lachenwitzer et al. [333] from the same research group have performed the STM study of electrodeposition and anodic dissolution of Ni on $\text{Ag}(111)$. Sztyler and Budniok [334] have studied the initial stage of nickel electrocrystallization on the $\text{Ag}(111)$ substrate. Growth, structure, and epitaxy of ultrathin NiO films on $\text{Ag}(001)$ have been studied by Luches et al. [335]. The early stages of NiO growth on $\text{Ag}(001)$ have been studied by Caffio et al. [336], applying low-energy ion-scattering, XPS, and LEED.

24.5.5.6 Chalcogenides

Aloisi et al. [337] have performed *in situ* STM and electrochemical investigations of oxidative UPD of sulfur on $\text{Ag}(111)$. Electrodepositions of silver selenide [338], silver telluride thin films [339], and silver selenide nanowires [340] have also been described.

Innocenti et al. [341] have studied deposition of CdS and ZnS on $\text{Ag}(111)$, employing electrochemical atomic layer

epitaxy (ECALE). Thin films of CdS deposited on Ag(111) have been studied photometrically by Innocenti et al. [342], as well as electrochemically and microscopically (STM), by Foresti et al. [343]. Atomic structure of ultrathin CdS phase deposited on Ag(111) surface, applying ECALE, has been studied via X-ray photoelectron diffraction (XPD) by Cecconi et al. [344]. Pezzatini et al. [345] have investigated the formation of ZnSe on Ag(111) by ECALE. Cavallini et al. [346] have involved STM to the studies of Se electrodeposition on Ag(111).

24.5.5.7 Other Elements and Compounds

Electrodepositions of silver–cadmium alloys have also been described [347]. Underpotential and bulk depositions of Pb on the screen-printed Ag electrodes have been described by Zen et al. [348]. Del Popolo and Leiva [349] have studied Cu deposition on Ag(111) using embedded atom method. In situ STM study of the initial stages of Cu electrodeposition on Ag(100) has been published by Dietterle et al. [350]. A comparative kinetic study of Cd diffusion into Au(100) and Ag(100) during electrodeposition has been described by Vidu et al. [351]. The formation of a superficial alloy as a result of the initial growth, and the structure of Mn on Ag(100), have been investigated by Schieffer et al. [352]. Abt and Blugel [353] have reported the first-principles investigation of the formation of Mn/Ag(100) surface alloy. Elmouhssine et al. [354] have studied the growth and magnetic properties of Mn monolayer on Ag(100). Growth of Cr on Ag(001) has been investigated by Quinn et al. [355] using STM. Epitaxial growth of Cr on Ag(001) has been studied by Steadman et al. [356]. Two-dimensional Ising-type behavior of c(2 × 2) antiferromagnetic Mn and Cr

monolayers on Ag(001) has been studied by Hanf et al. [357]. Langelaar and Boerma [358] have studied the site exchange and mobility of Fe adatoms on Ag(100). Terreni et al. [359] have investigated the surfactant effect and dissolution of ultrathin Fe films on Ag(001). Step decoration of Co on Ag(001) has been studied by Dekoster, Degroote et al. [360, 361]. Supported magnetic Pd nanoclusters on Ag(001) have been described by Amitouche et al. [362]. Growth and temperature behavior of silicon thin films deposited on Ag(001) have been investigated by Leandri et al. [363]. Simulation of Cu growth on Ag(001) at experimental deposition rates has been published by Sprague et al. [364].

Sawaya et al. [365] have described the local density approximation studies of semiconductor metal adsorption characteristics: Ge/Ag(100).

24.5.6

Electrodeposition and Electrodissolution Processes of Ag

24.5.6.1 Electrodeposition Processes

Hasse et al. [366] have used in situ AFM for the detection of silver nucleation at the three-phase junction of the type: metal–silver halide–electrolyte solution. At this phase boundary, electrochemical reduction of submicrometer size silver halide crystals immobilized on the surface of gold and platinum electrodes took place. Following nucleation, the reaction advanced until the entire surface of the silver halide crystals was covered with 20 atomic layers of silver. Then, reduction was terminated. The obtained silver layer could be oxidized and the next layer of silver halide crystals became accessible for further reduction.

Also, single Ag₂S crystals immobilized on gold electrodes with edge lengths of

about 400 nm were electroreduced to silver [367]. In situ AFM images showed the start of the reaction at the three-phase junction Au–Ag₂S solution. The initial reduction product is a hump of silver atoms, which within minutes, recrystallize to a well-developed shape of a silver single crystal.

Initial stages of Ag electrocrystallization from silver thiosulfate complexes have been studied by Simons et al. [368] and Gonnissen et al. [369]. The formation of subcritical 2D silver clusters, preceding the formation of supercritical, stable 3D nuclei and their growth, has been suggested.

Dimitrov et al. [370] have investigated initial steps of silver deposition from nitrate solutions on silver and platinum substrates. Growth of independent large Ag grains was observed at lower overpotentials, while at higher overpotentials, dendrites were formed.

Employing in situ optical reflectivity and STM, Baltrunas et al. [371] have studied the surface roughness of an Ag electrode during electrocrystallization in cyanide electroplating bath. More recently, Baltrunas [372] has considered the role of the electrode surface inhomogeneity in the electrocrystallization mechanism in the silver/silver–cyanide system. The reaction order with respect to CN[−] was found to be close to 2, which suggests a direct participation of Ag(CN)₂[−] complex in the charge-transfer step. Daujotis et al. have studied the mechanism of electroreduction of silver–cyanide complexes in aqueous electrolyte using TR-EQCM [373] and SERS [374]. It has been shown that side by side with the electroreduction of silver–cyanide complexes, oxidation of (presumably) adsorbed cyanide ions occurs [373].

Saito et al. [375] have also studied the mechanism of silver electrodeposition from silver–cyanide complex solutions.

The kinetics of AgCl dissolution in aqueous solutions without supporting electrolyte have been studied utilizing well-defined and high mass transport properties of the scanning electrochemical microscope [376]. An ultramicroelectrode probe positioned close to the AgCl surface was used to induce and monitor dissolution of the salt via reduction of Ag⁺ from the initially saturated solution.

Scholz and Hasse [377] have shown that crystals of metallic silver can be grown at liquid/liquid interfaces (water with AgNO₃|*n*-octanol with ferrocene). Depending on the reactants concentrations in both phases, silver crystallized in the form of (1) wires (whiskers with radii from about 50 nm to 50 μm) growing into the organic phase; (2) Christmas tree-like deposits at the interface; and even (3) extremely smooth films of silver.

24.5.6.2 Electrodissolution Processes

Burke and coworkers [241] have studied the multilayer oxide films grown on silver in base during repetitive potential cycling. It was shown, on the basis of its reduction behavior, that the type of oxide obtained was dependent on the lower limit of the oxide growth cycles. Using limits of 1.03–2.60 V (SHE) the oxide film was assumed to be predominantly Ag₂O, while at limits 0.7–2.60 V, oxide deposit was assumed to be AgOH. Both types of silver oxides are assumed to be involved in premolecular oxidation and electrocatalysis at silver in base.

The mechanism of anodic dissolution of silver in cyanide solutions has been studied by Bek and coworkers [378–380]. For example, using [379] the rotating disc electrode and pulse potentiostatic method, it has been found that the limiting step involved the formation, at the electrode surface, of the adsorbed complex with two

CN⁻ ions. Anodic dissolution of silver electrode in cyanide solutions and also the behavior of Ag at potentials preceding dissolution have been studied applying electrode impedance measurements [381]. At potentials of anodic dissolution, the process was represented by the equivalent circuit with two parallel branches.

Sun et al. [382] have studied the dissolution behavior of gold and silver from Au–Ag alloys in aerated cyanide solutions using rotating disc electrodes.

Also, anodic dissolution of silver in ultrasonic field has been studied [383].

STM tip-induced local electrochemical dissolution of silver has been studied in the systems: Ag(111)/Ag⁺, ClO₄⁻ and Ag(111)/Ag⁺, SO₄²⁻ [384].

The inhibiting influence of sodium diisobutylthiophosphinate [385] and 2-mercaptopbenzothiazole [386] on silver dissolution in aqueous solutions of pH = 11 has also been investigated. Inhibition was caused by adsorption of both compounds, accompanied with the displacement of cyanides from the silver surface.

Dissolution of gold and silver from Au/Ag alloys in aerated cyanide solutions has been investigated, using rotating disc electrodes [387]. This process was partially controlled by transport of either oxygen or cyanide.

Structural changes of silver terrace domains during Ag electrodissolution in aqueous perchloric acid at constant anodic current density were followed by in situ STM sequential imaging [388].

Passivation of silver and current oscillations were observed [389] during anodic dissolution of silver in H₂SO₄ solutions. During dissolution of the electrode, silver powder was accumulated at the surface, which affected diffusion to the electrode and led to oscillations.

As regards other coordination compounds of silver, electrochemical synthesis of metallic (e.g. Ag and Cu) complexes of bidentate thiolates containing nitrogen as an additional donor atom has been described by Garcia-Vásquez et al. [390]. Also Marquez and Anacona [391] have prepared and electrochemically studied silver(I) complex of heptaaza quinquedentate macrocyclic ligand. It has been shown that the reversible one-electron oxidation wave at +0.75 V (versus Ag|AgBF₄) corresponds to the formation of a ligand-radical cation. Other applications of coordination silver compounds in electrochemistry include, for example, a reference electrode for aprotic media based on Ag(I) complex with cryptand 222, proposed by Lewandowski et al. [392]. Potential of this electrode was less sensitive to the impurities and the solvent than the conventional Ag/Ag⁺ electrode.

24.5.7

Silver Compounds at the Oxidation States Higher Than I

Compounds containing silver at the oxidation states higher than I were not reviewed in the earlier edition of *Encyclopedia of Electrochemistry*. Therefore, it seems reasonable to fill this gap with some fundamental information on the electrochemistry of such species and an account of recent achievements made therein.

One should emphasize that in neutral aqueous solutions can only complex compounds of Ag in such high oxidation states exist, as the uncomplexed ions of that type oxidize water to oxygen. For example, E^0 (Ag²⁺/Ag⁺) = +1.980 V (in 4 M HClO₄) is higher than E^0 for MnO₄⁻/Mn²⁺ [393]. Therefore, although Ag(II) ions can be, in principle, obtained by the oxidation of Ag(I) by ozone in strongly acidic solution,

the product is usually unstable. Ag(II) stability is increased in phosphoric acid media, possibly due to the complex formation between Ag(II) and phosphate anions [393]. Complex compounds of Ag(II) are, as a rule, square planar and paramagnetic ($\mu_B \sim 1.7\text{--}2.2$ BM) [393]. A variety of Ag(II) complexes with heterocyclic amines ($[\text{Ag}(\text{py})_4]^{2+}$, $[\text{Ag}(\text{bipy})_4]^{2+}$), with the accompanying nonreducing counteranions (NO_3^- , ClO_4^- , $\text{S}_2\text{O}_8^{2-}$), have been obtained by the oxidation of Ag(I) with $\text{S}_2\text{O}_8^{2-}$ [393]. Also, a violet $\text{Ba}[\text{AgF}_4]$ compound is known [393]. The importance of fluoride Ag compounds at various oxidation states is also related to their potential superconducting properties [394]. Stable Ag(II) coordination complexes can also exist in a gas phase [395].

Recently, Brückner [396] has collected the currently available data concerning compounds of silver at untypical oxidation states higher than 1. Reaction of elemental fluorine with finely powdered Ag produces $\text{Ag}^{\text{II}}\text{F}_2$, which can be further oxidized to the square-planar complex ion $[\text{Ag}^{\text{III}}\text{F}_4]^-$. By fluorinating the mixture of $\text{AgNO}_3 + \text{KCl}$ at 300°C , one obtains yellow, diamagnetic $\text{K}[\text{AgF}_4]$ compound, which is, however, unstable in contact with moist air and attacks glass [393]. Furthermore, using high-pressure fluorine in the presence of CsF, even $\text{Cs}_2[\text{Ag}^{\text{IV}}\text{F}_6]$ Ag(IV) complex can be obtained [396]. Oxidation of Ag_2O with $\text{S}_2\text{O}_8^{2-}$ at 90°C in strongly alkaline solutions generates the mixed-valence species $\text{Ag}^{\text{I}}\text{Ag}^{\text{III}}\text{O}_2$, sometimes oversimplified as “ $\text{Ag}^{\text{II}}\text{O}$ ”. Anodic oxidation of Ag in concentrated KOH solution gives a yellow $[\text{Ag}(\text{OH})_4]^-$ ion of a half-life of ~ 100 min in 1.2 M NaOH, which decomposes to AgO and O_2 [397]. Electrodeposition of Ag(II) oxide films has been described [398]. Complexes of Ag(III)

with various ligands and their reactions, including complexes with polypeptides and redox reaction of $[\text{Ag}(\text{OH})_4]^-$ with thiosulfate and arsenite, have been studied by Kirschenbaum et al. [399–402]. Eujen et al. have synthesized some di- and trifluoromethylated Ag(I) and Ag(III) complexes, and performed nuclear magnetic resonance (NMR) studies of their structures [403, 404].

Noteworthy is the fact that in spite of high oxidation potential of Ag(II) and Ag(III) ions, their complexes with various organic ligands are also known. The first known compounds of this type are: diamagnetic red ethylenedibiguanidine [393] and dibiguanidinium [396] complexes with Ag(III). Their stereochemical structures are, however, rather uncertain [396]. Later, Barefield and Mocella [405] described the synthesis of Ag(II) and Ag(III) complexes with macrocyclic tetraaza ligands. More recently, well-defined complexes of tetrapyrrolic-based ligands (porphyrin, carbaporphyrin, corrole) with Ag(II) and Ag(III) have been described (for representative examples, see e.g. Refs 406–410. The oxidation kinetics of thiosulfate ion by $[\text{Ag}(\text{cyclam})]^{2+}$, involving the inner-sphere mechanism, has been recently described by Ali et al. [411].

Redox equilibrium of Ag(II)–porphyrin /Ag(III) is characterized with $E^0 = 0.59$ V versus SCE [412]. Evidently, corroles and carbaporphyrins are able to stabilize the Ag(III) oxidation state, presumably due to the presence of π -electron donors, which reduce the formal oxidation state of the metal in such complex [396]. It is expected that such complexes have potential practical applications, for example, as the catalysts in the electron-transfer reactions.

Numerous papers devoted to Ag(II) and Ag(III) compounds represent coordination and analytical chemistry. Below, the

recently published papers of special relevance to electrochemists are discussed. Synthesis of aminomethylpiridine and its complex with Ag(III) (from AgNO_3) has been described by Kahani et al. [413] Naumann et al. [414] have described perfluoralkyl compounds of Ag(III). Li et al. have used the on-line electrogenerated Ag(II) as the oxidant in the flow-injection chemiluminescence determination of captopril [415] and sulfite [416]. Lehmani et al. have analyzed oxidation kinetics of water and organic compounds by silver(II), potentiometrically [417]. Electrochemistry and reaction kinetics of macrocyclic complexes of Ag(II) and substituted mercaptopyridines have been described by Hunting et al. [418] Sroczyński and Grzejdziak [419] have described Ag(I) and Ag(II) complexes with some tetraazamacrocyclic ligands in aqueous solutions. Electrodeposition of silver(II) oxide films has been described by Breyfogle et al. [398]. Panizza et al. [420] have reported electrochemical generation of silver(II) at boron-doped diamond electrodes. Silver(II) species served also as a mediator in electrochemical decomposition of hydrocarbons [421]. Graves et al. [422] have described electrochemical pretreatment and catalytic process for acrylonitrile-butadiene-styrene, utilizing silver(II) chemistry. Ravera et al. [423] have employed Ag(II) and peroxydisulfate reagents in the electrochemically mediated oxidation of polycyclic aromatic sulfonates. Kumar et al. [424] have analyzed the kinetics of oxidation of 3-aminopropan-1-ol and related compounds using Ag(III) species. Zilbermann et al. [425] have described electroprecipitation of Ag(II)/Ag(III) tetraphenylsulfonate porphyrin and electrocatalytic behavior of the obtained films. Also, an Ag(II) redox mediator has been used for electroassisted elimination of ruthenium from dissolved

$\text{RuO}_2 \times \text{H}_2\text{O}$ in nitric acid solution. This process has potential application in nuclear fuel reprocessing [426].

References

1. V. M. Gorokhovskii, *J. Anal. Chem.* **2003**, 58, 198.
2. S. Ardizzone, G. Capelletti, P. R. Mussini et al., *Russ. J. Electrochem.* **2003**, 39, 107.
3. S. Trasatti, E. Lust, in *Modern Aspects of Electrochemistry* (Eds.: R. E. White, J. O. M. Bockris, B. E. Conway), Plenum Press, New York, 1999, Vol. 33. and references cited therein.
4. D. I. Leikis, K. V. Rybalka, E. S. Sevastyanov, in *Double Layer and Adsorption at Solid Electrodes* (Eds.: A. N. Frumkin, B. B. Damaskin), Nauka, Moscow, 1972, p. 5.
5. A. J. Ahern, L. C. Nagle, L. D. Burke, *J. Solid State Electrochem.* **2002**, 6, 451.
6. B. Pettinger, C. Bilger, J. Lipkowski, Second harmonic generation anisotropy from single crystalline electrode surfaces in *Interfacial Electrochemistry. Theory, Experiment and Applications* (Eds.: A. Więckowski), Marcel Dekker, New York-Basel, 1999, p. 373.
7. S. Kruszewski, *J. Raman Spectrosc.* **1996**, 27, 513.
8. S. Kruszewski, *Surf. Interface Anal.* **2004**, 21, 830.
9. R. M. Corn, M. Romagnoli, M. D. Levenson et al., *Chem. Phys. Lett.* **1984**, 106, 30.
10. G. L. Richmond, *Surf. Sci.* **1984**, 147, 115.
11. D. J. Campbell, R. M. Corn, *J. Phys. Chem.* **1987**, 91, 5668.
12. H. Seki, *IBM J. Res. Develop.* **1993**, 37, 227, and references cited therein.
13. A. Tadjeddine, A. Le Rille, Sum and difference frequency generation at electrode surfaces, in *Interfacial Electrochemistry. Theory, Experiment and Applications*. (Eds.: A. Więckowski), Marcel Dekker, New York-Basel, 1999, p. 317.
14. A. K. Gaigalas, V. Reipa, V. L. Vilker et al., *Interf. Sci.* **1997**, 186, 339.
15. C. D. Geddes, A. Parfenov, D. Roll et al., *Spectrochim. Acta, Part A* **2004**, 60, 1977.
16. I. Otsuka, T. Iwasaki, *J. Vac. Sci. Technol. B* **1996**, 14, 1153.
17. I. Otsuka, T. Iwasaki, *Surf. Rev. Lett.* **1999**, 6, 923.

18. A. Hamelin, L. Doubova, L. Stoicoviciu et al., *J. Electroanal. Chem.* **1988**, *244*, 133.
19. G. Valette, *J. Electroanal. Chem.* **1987**, *224*, 285.
20. V. L. Shannon, D. A. Koos, G. L. Richmond, *J. Phys. Chem.* **1987**, *91*, 5548.
21. A. Friedrich, B. Pettinger, D. M. Kolb et al., *Chem. Phys. Lett.* **1989**, *163*, 123.
22. S. Trasatti, L. M. Doubova, *J. Chem. Soc., Faraday Trans.* **1995**, *91*, 3311.
23. S. Trasatti, *Electrochim. Acta* **1991**, *36*, 1659.
24. A. Hamelin, in *Modern Aspects of Electrochemistry* (Eds.: B. E. Conway, R. E. White, J. O. M. Bockris), Plenum Press, New York, 1985, p. 1, Vol. 16.
25. M. A. Vorotyntsev, in *Modern Aspects of Electrochemistry* (Eds.: B. E. Conway, R. E. White, J. O. M. Bockris), Plenum Press, New York, 1986, p. 131, Vol. 17.
26. S. Trasatti, *Elektrokhimiya* **1995**, *31*, 777.
27. R. Adzic, in *Modern Aspects of Electrochemistry* (Eds.: R. E. White, J. O. M. Bockris, B. E. Conway), Plenum Press, New York, 1990, p. 163, Vol. 21.
28. M. Jurkiewicz-Herbich, M. Milkowska, *J. Solid State Electrochem.* **2001**, *5*, 36.
29. J. W. Zheng, X. W. Li, R. N. Gu et al., *J. Phys. Chem. B* **2002**, *106*, 1019.
30. N. Quaas, M. Wenderoth, R. G. Ulbrich, *Surf. Sci.* **2004**, *550*, 57.
31. M. Giesen, R. Randler, S. Baier et al., *Electrochim. Acta* **1999**, *45*, 527.
32. S. Baier, S. Dieluweit, M. Giesen, *Surf. Sci.* **2002**, *502*, 463.
33. S. Baier, M. Giesen, *Phys. Chem. Chem. Phys.* **2000**, *2*, 3675.
34. M. I. HafTEL, T. L. Einstein, *Appl. Surf. Sci.* **2001**, *175*, 49.
35. V. V. Emets, B. B. Damaskin, V. E. Kazarinov, *Russ. J. Electrochem.* **1996**, *32*, 1313.
36. J. T. Li, W. D. Schneider, R. Berndt et al., *Phys. Rev. Lett.* **1998**, *80*, 3332.
37. H. Winkes, D. Schumacher, A. Otto, *Surf. Sci.* **1998**, *400*, 44.
38. M. F. Toney, J. N. Howard, J. Richer et al., *Nature* **1994**, *368*, 444.
39. M. L. Berkowitz, In-Chul Yeh, E. Spohr, Structure of water at the water-metal interface: molecular dynamics computer simulations in *Interfacial Electrochemistry. Theory, Experiment and Applications* (Ed.: A. Więckowski), Marcel Dekker, New York-Basel, 1999, p. 33.
40. Z. H. Sun, Q. W. Liu, Y. F. Li et al., *Chin. Phys. Lett.* **2004**, *21*, 1604.
41. K. Itaya, Atomic-scale aspects of anodic dissolution of metals: studies by *In situ* scanning tunneling microscopy in *Interfacial Electrochemistry. Theory, Experiment and Applications* (Ed.: A. Więckowski), Marcel Dekker, New York-Basel, 1999, p. 187.
42. K. Koga, *App. Phys. A – Mater.* **1999**, *69*, 457.
43. C. Mottet, R. Ferrando, F. Hontinfinde et al., *Surf. Sci.* **1998**, *417*, 220.
44. L. Pedemonte, R. Tatarek, G. Bracco, *Phys. Rev. B* **2002**, *66*, art. no. 045414.
45. L. Savio, L. Vattuone, M. Rocca et al., *Surf. Sci.* **2001**, *486*, 65.
46. J. J. Simpson, T. E. Furtak, *J. Electroanal. Chem.* **2001**, *500*, 163.
47. L. Savio, L. Vattuone, M. Rocca, *Phys. Rev. B* **2003**, *67*, art. no. 045406.
48. J. Sobkowski, M. Jurkiewicz-Herbich, *Wiad. Chem. (Poland)* **2004**, *58*, 5.
49. S. Trasatti, *J. Electroanal. Chem.* **1984**, *172*, 27.
50. G. Valette, *J. Electroanal. Chem.* **1987**, *230*, 189.
51. B. N. Afanasjev, Yu. P. Aktslova, *Elektrokhimiya* **1994**, *30*, 1357.
52. M. Jurkiewicz-Herbich, M. Milkowska, R. Słojkowska, *Colloids Surf. A* **2002**, *197*, 235.
53. L. M. Doubova, A. De Battisti, S. Daolio et al., *J. Electroanal. Chem.* **2001**, *500*, 134.
54. T. Vitanov, A. Popov, E. S. Sevastyanov, *J. Electroanal. Chem.* **1982**, *142*, 289.
55. S. Smolinski, P. Zelenay, J. Sobkowski, *J. Electroanal. Chem.* **1998**, *442*, 41.
56. L. M. Doubova, S. Daolio, C. Pagura et al., *Russ. J. Electrochem.* **2003**, *39*, 164.
57. L. M. Doubova, S. Trasatti, *J. Electroanal. Chem.* **2003**, *550–551*, 33.
58. M. L. Foresti, M. Innocenti, A. Hamelin, *Langmuir* **1995**, *11*, 498.
59. M. L. Foresti, M. Innocenti, R. Guidelli, *J. Electroanal. Chem.* **1994**, *376*, 85.
60. L. M. Doubova, S. Trasatti, S. Valcher, *J. Electroanal. Chem.* **1993**, *349*, 187.
61. R. A. Gu, Y. H. Sun, P. G. Cao et al., *Acta Chim. Sinica* **2001**, *59*, 1522.
62. D. Hecht, H. H. Strehblow, *J. Electroanal. Chem.* **1997**, *436*, 109.
63. R. L. Sobociński, J. E. Pemberton, *Langmuir* **1990**, *6*, 43.

64. R. Truu, P. Kippasto, E. Lust, *Proceedings of the Baltic Conference on Interfacial Electrochemistry*, Dept. Phys. Chem. Tartu University, Tartu, 1996, p. 232.
65. S. L. Joa, J. E. Pemberton, *Langmuir* **1992**, *8*, 2301.
66. J. E. Pemberton, S. L. Joa, A. Shen et al., *J. Chem. Soc., Faraday Trans.* **1996**, *92*, 3683.
67. J. E. Pemberton, A. J. Shen, *Phys. Chem. Chem. Phys.* **1999**, *1*, 5671.
68. C. H. Shi, X. W. Cai, Y. A. Chen et al., *Appl. Surf. Sci.* **2000**, *158*, 11.
69. R. R. Nazmutdinov, T. T. Zinkicheva, *Russ. J. Electrochem.* **2005**, *41*, 206.
70. D. D. Sneddon, A. A. Gewirth, *Surf. Sci.* **1995**, *343*, 185.
71. C. C. Chang, C. H. Lung, *J. Chin. Chem. Soc.-Taip.* **1996**, *43*, 145.
72. B. V. Andryushechkin, K. N. Eltsov, V. M. Shevlyuga et al., *Surf. Sci.* **1999**, *421*, 27.
73. B. M. Ocko, J. X. Wang, T. Wandlowski, *Phys. Rev. Lett.* **1997**, *79*, 1511.
74. O. Endo, D. Matsumura, K. Kohdate et al., *J. Electroanal. Chem.* **2000**, *494*, 121.
75. G. Beltramo, E. Santos, W. Schmickler, *Langmuir* **2003**, *19*, 4723.
76. G. Beltramo, E. Santos, *J. Electroanal. Chem.* **2003**, *556*, 127.
77. E. Santos, C. Schürer, G. Beltramo et al., *J. Solid State Electr.* **2003**, *7*, 567.
78. M. Kawasaki, H. Ishii, H. Uchiki, *Microsc. Res. Tech.* **1998**, *42*, 100.
79. V. D. Jović, B. M. Jović, *J. Electroanal. Chem.* **2003**, *541*, 1.
80. O. Endo, M. Kiguchi, T. Yokoyama et al., *J. Electroanal. Chem.* **1999**, *473*, 19.
81. S. W. Wang, P. A. Rikvold, *Phys. Rev. B* **2002**, *65*, art. no. 155406.
82. T. Wandlowski, J. X. Wang, B. M. Ocko, *J. Electroanal. Chem.* **2001**, *500*, 418.
83. J. X. Wang, R. P. Adzic, B. M. Ocko, In situ surface X-ray scattering studies of electro sorption in *Interfacial Electrochemistry. Theory, Experiment and Applications* (Ed.: A. Więckowski), Marcel Dekker, New York-Basel, 1999, p. 175.
84. C. Hanewinkel, A. Otto, T. Wandlowski, *Surf. Sci.* **1999**, *429*, 255.
85. T. Shimooka, J. Inukai, K. Itaya, *J. Electroanal. Chem.* **2002**, *149*, E19.
86. P. A. Rikvold, I. Abou Hamad, G. Brown et al., *Abstr. Pap. Am. Chem. Soc.* **2003**, *225*, 444-COLL.
87. I. Abou Hamad, T. Wandlowski, G. Brown et al., *J. Electroanal. Chem.* **2003**, *554*, 211.
88. S. J. Mitchell, G. Brown, P. A. Rikvold, *J. Electroanal. Chem.* **2000**, *493*, 68.
89. S. J. Mitchell, G. Brown, P. A. Rikvold, *Surf. Sci.* **2001**, *471*, 125.
90. T. Yamada, K. Ogaki, S. Okubo et al., *Surf. Sci.* **1996**, *369*, 321.
91. Y. Wang, Q. Sun, K. N. Fan et al., *Acta Chim. Sinica.* **2000**, *58*, 931.
92. H. R. Tang, W. N. Wang, Z. H. Li et al., *Surf. Sci.* **2000**, *450*, 133.
93. Y. Wang, Q. Sun, K. N. Fan et al., *Chem. Phys. Lett.* **2001**, *334*, 411.
94. T. Teshima, K. Ogaki, K. Itaya, *J. Phys. Chem. B* **1997**, *101*, 2046.
95. N. A. Rogozhnikov, *Russ. J. Electrochem.* **1997**, *33*, 668.
96. G. Baltrunas, G. S. Popkirov, R. N. Schindler, *J. Electroanal. Chem.* **1997**, *435*, 95.
97. A. Tadjeddine, A. Peremans, P. Guyot-Sionnest, *Surf. Sci.* **1995**, *335*, 210.
98. G. A. Bowmaker, J. M. Leger, A. Le Rille et al., *J. Chem. Soc., Faraday Trans.* **1998**, *9*, 1309.
99. F. Tielens, M. Saeys, E. Tourwe et al., *J. Phys. Chem. A* **2002**, *106*, 1450.
100. D. Lutzenkirchen-Hecht, H. H. Strehblow, *Electrochim. Acta* **1998**, *43*, 2957.
101. M. Innocenti, M. L. Foresti, A. Fernandez et al., *J. Phys. Chem. B* **1998**, *102*, 9667.
102. M. L. Foresti, M. Innocenti, F. Forni et al., *Langmuir* **1998**, *14*, 7008.
103. A. R. Alemozafer, X. C. Guo, R. J. Madix et al., *Surf. Sci.* **2002**, *504*, 223.
104. P. Paredes Olivera, M. Patrito, H. Sellers, Electronic structure calculations of polyatomic oxyanions adsorbed on metal surfaces in *Interfacial Electrochemistry. Theory, Experiment and Applications* (Ed.: A. Więckowski), Marcel Dekker, New York-Basel, 1999, p. 63.
105. E. J. Sobkowski, S. Smoliński, P. Zelenay, *Abstr. Pap. Am. Chem. Soc.* **1996**, *212*, 49-COLL.
106. J. Sobkowski, S. Smolinski, P. Zelenay, *Colloids Surf. A* **1998**, *134*, 39.
107. M. Schweizer, D. M. Kolb, *Surf. Sci.* **2003**, *544*, 93.
108. N. S. Marinkovic, J. S. Marinkovic, R. R. Adzic, *J. Electroanal. Chem.* **1999**, *467*, 291.

109. J. Blomqvist, P. Salo, M. Alatalo, *Surf. Sci.* **2004**, *566*, 1067.
110. M. Kittel, D. I. Sayago, J. T. Hoeft et al., *Surf. Sci.* **2002**, *516*, 237.
111. E. Giudice, E. Magnano, S. Rusponi et al., *Surf. Sci.* **1998**, *405*, L561.
112. G. Costantini, S. Rusponi, E. Giudice et al., *Carbon* **1999**, *37*, 717.
113. A. Goldoni, G. Paolucci, *Surf. Sci.* **1999**, *437*, 353.
114. C. Cepek, L. Giovanelli, M. Sancrotti et al., *Surf. Sci.* **2000**, *454*, 766.
115. C. Cepek, M. Sancrotti, T. Greber et al., *Surf. Sci.* **2000**, *454*, 467.
116. C. Cepek, R. Fasel, M. Sancrotti et al., *Phys. Rev. B* **2001**, *63*, art. no. 125406.
117. M. Grobis, X. Lu, M. F. Crommie, *Phys. Rev. B* **2002**, *66*, art. no. 161408.
118. W. W. Pai, C. L. Hsu, C. R. Chiang et al., *Surf. Sci.* **2002**, *519*, L605.
119. G. Valette, *J. Electroanal. Chem.* **1981**, *122*, 285.
120. G. Pirug, H. P. Bonzel, Electrochemical double-layer modeling under ultrahigh vacuum conditions in *Interfacial Electrochemistry. Theory, Experiment and Applications* (Eds.: A. Więckowski), Marcel Dekker, New York-Basel, 1999, p. 269.
121. N. Kizhakevariam, R. Döhl-Oelze, E. M. Stuve, *J. Phys. Chem.* **1990**, *94*, 5934.
122. A. Krasnopoler, E. M. Stuve, *J. Vac. Sci. Technol. A* **1995**, *13*, 1681.
123. G. Valette, *J. Electroanal. Chem.* **1982**, *138*, 37.
124. G. Niaura, R. Jakubenas, *J. Electroanal. Chem.* **2001**, *510*, 50.
125. T. C. Girija, M. Sangaranarayanan, *J. Colloid Interface Sci.* **2005**, *282*, 92.
126. K. J. Stevenson, D. W. Hatchett, H. S. White, *Langmuir* **1997**, *13*, 6824.
127. A. Krasnopoler, N. Kizhakevariam, E. M. Stuve, *J. Chem. Soc., Faraday Trans.* **1996**, *92*, 2445.
128. X. C. Guo, R. J. Madix, *Surf. Sci.* **2002**, *501*, 37.
129. L. Lee, J. X. Wang, R. R. Adzic et al., *J. Am. Chem. Soc.* **2001**, *123*, 8838.
130. M. Jafarian, M. G. Mahjani, O. Azizi, *Indian J. Chem. A* **2003**, *42*, 516.
131. A. A. Gurten, K. Kayakirilmaz, B. Yazici et al., *Int. J. Hydrogen Energy* **2003**, *28*, 1083.
132. D. Welipitiya, P. A. Dowben, J. D. Zhang et al., *Surf. Sci.* **1996**, *367*, 20.
133. C. M. Woodbridge, D. L. Pugmire, R. C. Johnson et al., *J. Phys. Chem. B* **2000**, *104*, 3085.
134. M. A. Langell, C. M. Woodbridge, D. L. Pugmire et al., *Abstr. Pap. Am. Chem. Soc.* **2000**, *219*, 124-COLL.
135. D. L. Pugmire, C. M. Woodbridge, N. M. Boag et al., *Surf. Sci.* **2001**, *471*, 155.
136. D. L. Pugmire, C. M. Woodbridge, M. A. Langell, *Surf. Sci.* **1998**, *411*, L844.
137. M. Akita, N. Osaka, S. Hiramoto et al., *Surf. Sci.* **1999**, *428*, 374.
138. A. Kokalj, A. Dal Corso, S. de Gironcoli et al., *Surf. Sci.* **2002**, *507*, 62.
139. A. Kokalj, A. Dal Corso, S. de Gironcoli et al., *J. Phys. Chem. B* **2002**, *106*, 9839.
140. A. Kokalj, A. Dal Corso, S. de Gironcoli et al., *Surf. Sci.* **2003**, *532*, 191.
141. L. Vattuone, L. Savio, L. Valbusa et al., *Chem. Phys. Lett.* **2000**, *331*, 177.
142. L. Vattuone, L. Savio, M. Rocca, *Int. J. Mod. Phys. B* **2003**, *17*, 2497.
143. A. Kokalj, A. Dal Corso, S. de Gironcoli et al., *Surf. Sci.* **2004**, *566*, 1018.
144. J. PawelaCrew, R. J. Madix, *J. Chem. Phys.* **1996**, *104*, 1699.
145. F. J. Williams, D. P. C. Bird, E. C. H. Sykes et al., *J. Phys. Chem. B* **2003**, *107*, 3824.
146. N. Osaka, M. Akita, K. Itoh, *J. Phys. Chem. B* **1998**, *102*, 6817.
147. J. L. Gland, J. T. Ranney, S. R. Bare, *Abstr. Pap. Am. Chem. Soc.* **1999**, *217*, 024-CATL.
148. J. I. Pascual, J. J. Jackiw, K. F. Kelly et al., *Phys. Rev. B* **2000**, *62*, 12632.
149. J. I. Pascual, J. J. Jackiw, Z. Song et al., *Phys. Rev. Lett.* **2001**, *86*, 1050.
150. K. F. Kelly, J. J. Jackiw, J. I. Pascual, *Abstr. Pap. Am. Chem. Soc.* **2000**, *220*, 192-COLL Part1.
151. J. I. Pascual, J. J. Jackiw, Z. Song et al., *Surf. Sci.* **2002**, *502*, 1.
152. S. G. Ma, G. Z. Wu, *J. Mol. Struct.* **1995**, *372*, 127.
153. X. M. Yang, K. Ajito, D. A. Tryk et al., *J. Phys. Chem.* **1996**, *100*, 7293.
154. V. Tsionsky, L. Daikhin, G. Zilberman et al., *Faraday Discuss.* **1997**, *107*, 337.
155. M. A. Nicholson, J. F. Aust, H. S. Booksh et al., *Vib. Spectrosc.* **2000**, *24*, 157.
156. A. Hamelin, S. Morin, J. Richer et al., *J. Electroanal. Chem.* **1989**, *272*, 241.
157. A. Hamelin, S. Morin, J. Richer et al., *J. Electroanal. Chem.* **1990**, *285*, 249.

158. A. Hamelin, S. Morin, J. Richer et al., *J. Electroanal. Chem.* **1991**, *304*, 195.
159. C. T. Shi, W. Zhang, R. L. Birke et al., *J. Electroanal. Chem.* **1997**, *423*, 67.
160. W. H. Li, X. Y. Li, N. T. Yu, *Chem. Phys. Lett.* **1999**, *305*, 303.
161. I. Lopez-Tocon, S. P. Centeno, J. L. Castro, *Chem. Phys. Lett.* **2003**, *377*, 111.
162. J. F. Arenas, I. L. Tocon, M. S. Woolley et al., *J. Raman Spectrosc.* **1998**, *29*, 673.
163. J. Bukowska, M. Calvo, M. Jurkiewicz-Herbich et al., *Pol. J. Chem.* **2002**, *76*, 1151.
164. A. G. Brolo, D. E. Irish, *J. Electroanal. Chem.* **1996**, *414*, 183.
165. A. G. Brolo, D. E. Irish, *J. Chem. Soc., Faraday Trans.* **1997**, *93*, 419.
166. A. G. Brolo, D. E. Irish, *Can. J. Chem.* **1997**, *75*, 1643.
167. A. G. Brolo, D. E. Irish, *ACS Symp. Ser. N.* **656** ACS, Washington, DC, Ch. 22, p. 310.
168. J. F. Arenas, M. S. Woolley, I. López-Tocón et al., *J. Chem. Phys.* **2000**, *112*, 7669.
169. J. F. Arenas, S. P. Centeno, I. López-Tocón et al., *Vib. Spectrosc.* **2004**, *35*, 39.
170. A. Kudelski, J. Bukowska, *Surf. Sci.* **1996**, *368*, 396.
171. J. Cehn, W. T. Zhao, J. M. Hu et al., *Chem. J. Chinese Univ.-Chinese* **1995**, *16*, 1697.
172. N. Osaka, M. Akita, S. Hiramoto et al., *Surf. Sci.* **1999**, *428*, 381.
173. P. Waszczuk, P. Zelenay, J. Sobkowski, *Electrochim. Acta* **1998**, *43*, 1963.
174. B. Parker, B. Immaraporn, A. J. Gellman, *Langmuir* **2001**, *17*, 6638.
175. R. Guidelli, M. L. Foresti, *J. Electroanal. Chem.* **1986**, *197*, 103.
176. M. Jurkiewicz-Herbich, M. Milkowska, R. Słojkowska, *Colloids Surf., A* **2002**, *197*, 235.
177. G. Wu, D. Stacchiola, M. Kaltchev et al., *Surf. Sci.* **2000**, *463*, 81.
178. G. Wu, D. Stacchiola, M. Collins et al., *Surf. Rev. Lett.* **2000**, *7*, 271.
179. L. M. Doubova, S. Valcher, S. Trasatti, *J. Electroanal. Chem.* **1994**, *376*, 73.
180. A. L. Schwaner, J. M. White, *J. Phys. Chem. B* **1997**, *101*, 11119.
181. A. L. Schwaner, J. M. White, *J. Phys. Chem. B* **1997**, *101*, 10414.
182. M. L. Foresti, M. Innocenti, R. Guidelli et al., *J. Electroanal. Chem.* **1999**, *467*, 217.
183. E. Santos, C. Schurrer, A. Brunetti et al., *Langmuir* **2002**, *18*, 2771.
184. X. W. Li, J. W. Zheng, Y. G. Zhou et al., *Chinese J. Anal. Chem.* **2003**, *31*, 1333.
185. C. Tegenkamp, H. Pfnnur, *J. Chem. Phys.* **2003**, *118*, 7578.
186. Z. J. Liu, G. Z. Wu, *Chem. Phys. Lett.* **2004**, *389*, 298.
187. Q. L. Zhong, D. Q. Wang, F. M. Liu et al., *Acta Phys-Chim. Sin.* **1998**, *14*, 562.
188. A. Łukomska, J. Sobkowski, *Pol. J. Chem.* **2004**, *78*, 1135.
189. S. Smoliński, J. Sobkowski, *Pol. J. Chem.* **2001**, *75*, 1493.
190. S. Yagi, Y. Nakano, E. Ikenaga et al., *Surf. Sci.* **2004**, *566*, 746.
191. T. Kasahara, H. Shinohara, Y. Oshima et al., *Surf. Sci.* **2004**, *558*, 65.
192. M. Schweizer, D. M. Kolb, *J. Electroanal. Chem.* **2004**, *564*, 85.
193. D. W. Hatchett, K. J. Stevenson, W. B. Lacy et al., *J. Am. Chem. Soc.* **1997**, *119*, 6596.
194. K. J. Stevenson, X. P. Gao, D. W. Hatchett et al., *J. Electroanal. Chem.* **1998**, *447*, 43.
195. D. W. Hatchett, R. H. Uibel, K. J. Stevenson et al., *J. Am. Chem. Soc.* **1998**, *120*, 1062.
196. C. A. Widrig, C. Chung, M. D. Porter, *J. Electroanal. Chem.* **1991**, *310*, 335.
197. D. W. Hatchett, X. P. Gao, S. W. Catron et al., *J. Phys. Chem.* **1996**, *100*, 331.
198. N. Mohtat, M. Byloos, M. Soucy et al., *J. Electroanal. Chem.* **2000**, *484*, 120.
199. H. Rieley, G. K. Kendall, R. G. Jones et al., *Langmuir* **1999**, *15*, 8856.
200. M. Cavallini, M. Bracali, G. Aloisi et al., *Langmuir* **1999**, *15*, 3003.
201. E. E. Doomes, P. N. Floriano, R. W. Tittsworth et al., *J. Phys. Chem. B* **2003**, *107*, 10193.
202. R. H. Uibel, D. W. Hatchett, K. J. Stevenson et al., *Abstr. Pap. Am. Chem. Soc.* **1998**, *215*, 204-COLL.
203. J. G. Lee, J. Lee, J. T. Yates, *J. Am. Chem. Soc.* **2004**, *126*, 440.
204. J. G. Lee, J. Lee, J. T. Yates, *J. Phys. Chem. B* **2004**, *108*, 1686.
205. O. Azzaroni, M. E. Vela, G. Andreasen et al., *J. Phys. Chem. B* **2002**, *106*, 12267.
206. R. Heinz, J. P. Rabe, *Langmuir* **1995**, *11*, 506.
207. A. Vivoni, S. P. Chen, D. Ejeh et al., *Langmuir* **2000**, *16*, 3310.
208. F. Cunha, J. R. Garcia, F. C. Nart, *J. Solid State Electr.* **2003**, *7*, 576.

209. F. Wang, J. Zheng, X. Li et al., *J. Electroanal. Chem.* **2003**, *545*, 123.
210. W. H. Li, X. Y. Li, N. T. Yu, *Chem. Phys. Lett.* **1999**, *312*, 28.
211. S. P. Chen, Z. Qiao, A. Vivoni et al., *Spectrochim. Acta, Part A* **2003**, *59*, 2905.
212. A. G. Brolo, P. Germain, G. Hager, *J. Phys. Chem. B* **2002**, *106*, 5982.
213. S. P. Chen, C. M. Hosten, A. Vivoni et al., *Langmuir* **2002**, *18*, 9888.
214. P. G. Cao, R. A. Gu, Z. Q. Tian, *J. Phys. Chem. B* **2003**, *107*, 769.
215. P. G. Cao, R. N. Gu, L. Qiu et al., *Surf. Sci.* **2003**, *531*, 217.
216. D. A. Carter, J. E. Pemberton, K. J. Woelfel, *J. Phys. Chem. B* **1998**, *102*, 9870.
217. M. Miłkowska, M. Jurkiewicz-Herbich, *Pol. J. Chem.* **1998**, *72*, 1096.
218. D. Hobara, K. Niki, T. M. Cotton, *Biospectroscopy* **1998**, *4*, 161.
219. G. Niaura, A. K. Gaigalas, V. L. Vilker, *J. Electroanal. Chem.* **1996**, *416*, 167.
220. T. Wandlowski, *J. Electroanal. Chem.* **1995**, *395*, 83.
221. R. Guidelli, M. L. Foresti, M. Innocenti, *J. Phys. Chem.* **1996**, *100*, 18491.
222. M. Cavallini, G. Aloisi, M. Bracali et al., *J. Electroanal. Chem.* **1998**, *444*, 75.
223. L. A. Dick, A. J. Haes, R. P. Van Duyne, *J. Phys. Chem. B* **2000**, *104*, 11752.
224. H. Yang, Z. Zhang, G. Shen et al., *J. Raman Spectrosc.* **2004**, *35*, 190.
225. Y. Fang, C. L. Bai, Y. Wei et al., *Appl. Spectrosc.* **1996**, *50*, 48.
226. F. J. Williams, O. P. H. Vaughan, K. J. Knox et al., *Chem. Commun.* **2004**, *15*, 1688.
227. S. Bernad, T. Soulimane, S. Lecomte, *J. Raman Spectrosc.* **2004**, *35*, 47.
228. W. Grochala, A. Kudelski, J. Bukowska, *J. Raman Spectrosc.* **1998**, *29*, 681.
229. A. G. Brolo, A. C. Sanderson, A. P. Smith, *Phys. Rev. B* **2004**, *69*, art. No. 045424.
230. S. H. de Araujo Nicolai, P. R. P. Rodrigues, S. M. L. Agostinho et al., *J. Electroanal. Chem.* **2002**, *527*, 103.
231. S. H. A. Nicolai, J. C. Rubim, *Langmuir* **2003**, *19*, 4291.
232. K. Itaya, N. Batina, M. Kunitake et al., *ACS Symp. Ser.* **1997**, *656*, 171.
233. X. C. Guo, R. J. Madix, *Surf. Sci.* **2004**, *564*, 21.
234. F. S. Tautz, S. Sloboshanin, V. Shklover et al., *Appl. Surf. Sci.* **2000**, *166*, 363.
235. R. Nowakowski, C. Seidel, H. Fuchs, *Phys. Rev. B* **2001**, *63*, art. no. 195418.
236. M. Itagaki, H. Hasegawa, K. Watanabe et al., *Electrochemistry* **2003**, *71*, 536.
237. S. Zabarnick, P. Zelesnik, S. D. Whitacre, *Ind. Eng. Chem. Res.* **1996**, *35*, 2576.
238. S. L. Chen, B. L. Wu, C. S. Cha, *J. Electroanal. Chem.* **1996**, *416*, 53.
239. S. L. Chen, B. L. Wu, C. S. Cha, *J. Electroanal. Chem.* **1997**, *420*, 111.
240. D. Bughiu, M. Buda, L. Anicai, *Rev. Roum. Chem.* **1997**, *42*, 429.
241. L. C. Nagle, A. J. Ahern, L. D. Burke, *J. Solid State Electrochem.* **2002**, *6*, 320.
242. E. R. Savinova, S. Wasle, K. Doblhofer, *Electrochim. Acta* **1998**, *44*, 1341.
243. G. Flätgen, S. Wasle, M. Lübke et al., *Electrochim. Acta* **1999**, *44*, 4499.
244. A. Raukema, D. A. Butler, A. W. Kleyn, *J. Phys. – Condens. Mat.* **1996**, *8*, 2247.
245. D. M. Bird, P. A. Gravil, *Abstr. Pap. Am. Chem. Soc.* **1997**, *213*, 8–PETR.
246. G. Benedek, F. B. De Mongeot, U. Valbusa et al., *Europhys. Lett.* **2001**, *53*, 544.
247. G. Cipriani, D. Loffreda, A. Dal Corso et al., *Surf. Sci.* **2002**, *501*, 182.
248. S. Altieri, S. F. Contri, S. Agnoli et al., *Surf. Sci.* **2004**, *566*, 1071.
249. B. M. Jovic, V. D. Jovic, G. R. Stafford, *Electrochim. Commun.* **1999**, *1*, 247.
250. E. R. Savinova, P. Kraft, B. Pettinger, et al. *J. Electroanal. Chem.* **1997**, *430*, 47.
251. E. R. Savinova, D. Zemlyanov, A. Scheybal et al., *Langmuir* **1999**, *15*, 6546.
252. E. R. Savinova, D. Zemlyanov, A. Scheybal et al., *Langmuir* **1999**, *15*, 6552.
253. D. Y. Zemlyanov, E. Savinova, A. Scheybal et al., *Surf. Sci.* **1998**, *418*, 441.
254. E. R. Savinova, D. Zemlyanov, B. Pettinger et al., *Electrochim. Acta* **2000**, *46*, 175.
255. M. Danckwerts, E. Savinova, B. Pettinger, *Appl. Phys. B – Lasers Opt.* **2002**, *74*, 635.
256. M. Danckwerts, E. R. Savinova, S. L. Horsswell et al., *Z. phys. Chem.* **2003**, *217*, 557.
257. S. K. Shaikhutdinov, E. R. Savinova, A. Scheybal et al., *J. Electroanal. Chem.* **2001**, *500*, 208.
258. L. Li, J. C. Yang, *Mater. High Temp.* **2003**, *20*, 601.
259. C. I. Carlisle, D. A. King, M. L. Bouquet et al., *Phys. Rev. Lett.* **2000**, *84*, 3899.
260. J. Kunze, H. H. Strehblow, G. Staikov, *Electrochim. Commun.* **2004**, *6*, 132.

261. S. L. Horswell, A. L. N. Pinheiro, E. R. Savinova et al., *G. Ertl., Langmuir* **2004**, *20*, 10970.
262. A. Kokalj, N. Bonini, A. Dal Corso et al., *Surf. Sci.* **2004**, *566*, 1107.
263. J. L. Conyers, H. S. White, *J. Phys. Chem. B* **1999**, *103*, 1960.
264. G. Flätgen, K. Krischer, B. Pettinger et al., *G. Ertl., Abstr. Pap. Amer. Chem. Soc.* **1996**, *212*, 69-COLL.
265. G. Flätgen, K. Krischer, B. Pettinger et al., *Science* **1995**, *269*, 668.
266. M. A. M. Ibrahim, H. H. Hassan, S. S. Abd El Rehim et al., *J. Solid State Electr.* **1999**, *3*, 380.
267. S. S. Abd El Rehim, H. H. Hassan, M. A. M. Ibrahim et al., *Monatsh. Chem.* **1999**, *130*, 1207.
268. L. Constant, B. Krenzer, W. Stenzel et al., *Surf. Sci.* **1999**, *428*, 262.
269. X. C. Guo, R. J. Madix, *Surf. Sci.* **2001**, *489*, 37.
270. U. Burghaus, H. Conrad, *Surf. Sci.* **1996**, *352*, 253.
271. U. Burghaus, H. Conrad, *Surf. Sci.* **1996**, *352*, 201.
272. J. V. Barth, T. Zambelli, *Surf. Sci.* **2002**, *513*, 359.
273. U. Burghaus, A. Bottcher, H. Conrad, *Surf. Rev. Lett.* **2003**, *10*, 39.
274. X. C. Guo, R. J. Madix, *Surf. Sci.* **2004**, *550*, 81.
275. G. S. Jones, M. A. Bartea, *J. Vac. Sci. Technol. A* **1997**, *15*, 1667.
276. G. S. Jones, M. A. Bartea, J. M. Vohs, *J. Phys. Chem. B* **1999**, *103*, 1144.
277. Q. Sun, Y. Wang, K. N. Fan et al., *Surf. Sci.* **2000**, *459*, 213.
278. B. Z. Zeng, F. Y. Ma, W. C. Purdy, *Electroanalysis* **1998**, *10*, 677.
279. B. Z. Zeng, W. C. Purdy, *Electroanalysis* **1999**, *11*, 879.
280. S. Y. Dong, J. B. Zheng, Y. L. Ning et al., *Chem. J. Chinese Univ.-Chinese* **2003**, *24*, 428.
281. B. X. Ye, X. Y. Zhou, *Talanta* **1997**, *44*, 831.
282. B. X. Ye, X. Y. Zhou, *Chem. J. Chinese Univ.-Chinese* **1996**, *17*, 33.
283. W. B. Cai, I. C. Stefan, D. A. Scherson, *J. Electroanal. Chem.* **2002**, *254*, 36.
284. J. W. Zheng, X. W. Li, H. Y. Xu et al., *Spectrosc. Spectr. Anal.* **2003**, *23*, 294.
285. G. X. Li, J. J. Zhu, H. Q. Fang et al., *J. Electrochem. Soc.* **1996**, *143*, L141.
286. J. J. McMahon, T. J. Gergel, D. M. Otterson et al., *Surf. Sci.* **1999**, *440*, 357.
287. S. Sanchez-Cortes, J. V. Garcia-Ramos, *Langmuir* **2000**, *16*, 764.
288. W. H. Li, X. Y. Li, N. T. Yu, *Chem. Phys. Lett.* **2000**, *327*, 153.
289. G. X. Li, H. Y. Chen, D. X. Zhu, *Anal. Chim. Acta* **1996**, *319*, 275.
290. G. X. Lin, H. Y. Chen, D. X. Zhu, *Chem. J. Chinese Univ.-Chinese* **1996**, *17*, 553.
291. G. X. Li, H. Q. Fang, Y. Q. Qian et al., *Electroanalysis* **1996**, *8*, 465.
292. J. J. Zhu, Y. Gong, J. J. Zhang et al., *Electroanalysis* **1997**, *9*, 1030.
293. G. X. Li, H. Q. Fang, Y. T. Long et al., *Anal. Lett.* **1996**, *29*, 1273.
294. S. Zhang, W. L. Sun, W. Zhang et al., *Anal. Lett.* **1998**, *31*, 2159.
295. Y. T. Long, J. Zou, H. Y. Chen, *Anal. Lett.* **1997**, *30*, 2691.
296. Y. T. Long, H. Y. Chen, *J. Electroanal. Chem.* **1997**, *440*, 239.
297. L. Tian, W. Z. Wei, Y. A. Mao, *Anal. Sci.* **2004**, *20*, 623.
298. L. Trnkova, *Talanta* **2002**, *56*, 887.
299. K. Jüttner, W. J. Lorenz, *Z. phys. Chem. NF* **1980**, *122*, 163.
300. E. Herreño, L. J. Buller, H. D. Abruna, *Chem. Rev.* **2001**, *101*, 1897.
301. G. Pacchioni, *Electrochim. Acta* **1996**, *41*, 2285.
302. S. G. Garcia, C. E. Mayer, D. R. Salinas et al., *J. Brazil. Chem. Soc.* **2004**, *15*, 917.
303. C. A. Zell, F. Endres, W. Freyland, *Phys. Chem. Chem. Phys.* **1999**, *1*, 697.
304. S. Garcia, D. E. Salinas, C. E. Mayer, *An. Asoc. Quim. Argent.* **1996**, *84*, 597.
305. S. Garcia, D. Salinas, C. Mayer et al., *Electrochim. Acta* **1998**, *43*, 3007.
306. N. Ikemiya, K. Yamada, S. Hara, *Surf. Sci.* **1996**, *348*, 253.
307. M. C. Gimenez, M. G. Del Popolo, E. P. M. Leiva, *Electrochim. Acta* **1999**, *45*, 699.
308. M. C. Gimenez, M. G. Del Popolo, E. P. M. Leiva et al., *J. Electrochem. Soc.* **2002**, *149*, E109.
309. E. D. Chabala, T. Rayment, *J. Electroanal. Chem.* **1996**, *401*, 257.
310. E. D. Chabala, A. R. Ramadan, T. Brunt et al., *J. Electroanal. Chem.* **1996**, *412*, 67.
311. A. R. Ramadan, E. D. Chabala, T. Rayment, *Phys. Chem. Chem. Phys.* **1999**, *1*, 1591.
312. V. Rooryck, C. Buess-Herman, G. A. Attard et al., *J. Vac. Sci. Technol. A* **1999**, *17*, 1647.

313. V. Rooryck, F. Reniers, C. Buess-Herman et al., *J. Electroanal. Chem.* **2000**, *482*, 93.
314. T. Kondo, J. Morita, M. Okamura et al., *J. Electroanal. Chem.* **2002**, *532*, 201.
315. H. Cercellier, Y. Fagot-Revurat, B. Kierren et al., *Surf. Sci.* **2004**, *566*, 520.
316. M. Watanabe, H. Uchida, M. Hiei, *Abstr. Pap. Am. Chem. Soc.* **1996**, *212*, 171-COLL.
317. S. Takami, G. K. Jennings, P. E. Laibinis, *Langmuir* **2001**, *17*, 441.
318. J. X. Wang, B. M. Ocko, R. R. Adzic, *Surf. Sci.* **2003**, *540*, 230.
319. D. Oyamatsu, M. Nishizawa, S. Kubawata et al., *Abstr. Pap. Am. Chem. Soc.* **1998**, *215*, 071-COLL.
320. X. Y. Hu, G. Xia, R. Guo, *Bull. Electrochem.* **2002**, *18*, 481.
321. D. G. Frank, O. M. R. Chyan, T. Golden et al., *J. Phys. Chem.* **1994**, *98*, 1896.
322. S. Ogura, K. Fukutani, M. Wilde et al., *Surf. Sci.* **2004**, *566*, 755.
323. E. Leiva, W. Schmickler, *Electrochim. Acta* **1994**, *39*, 1015.
324. K. J. Stevenson, D. W. Hatchett, H. S. White, *Langmuir* **1996**, *12*, 494.
325. J. Sackmann, A. Bunk, R. T. Potschke et al., *Electrochim. Acta* **1998**, *43*, 2863.
326. R. Widmer, H. Siegenthaler, *J. Electrochem. Soc.* **2004**, *151*, E238.
327. W. Obretenov, N. Dimitrov, A. Popov, *J. Cryst. Growth* **1996**, *167*, 253.
328. U. Schmidt, S. Vinzelberg, G. Staikov, *Surf. Sci.* **1996**, *348*, 261.
329. P. Waszczuk, A. Wnuk, J. Sobkowski, *Electrochim. Acta* **1999**, *44*, 1789.
330. J. X. Wang, R. R. Adzic, O. M. Magnussen, *Surf. Sci.* **1995**, *344*, 111.
331. S. Morin, A. Lachenwitzer, O. M. Magnussen et al., *Phys. Rev. Lett.* **1999**, *83*, 5066.
332. S. Morin, A. Lachenwitzer, F. A. Moller et al., *J. Electrochem. Soc.* **1999**, *146*, 1013.
333. A. Lachenwitzer, S. Morin, O. M. Magnussen et al., *Phys. Chem. Chem. Phys.* **2001**, *3*, 3351.
334. K. Sztyler, A. Budniok, *Bull. Electrochem.* **1997**, *13*, 223.
335. P. Luches, S. Altieri, C. Giovanardi et al., *Thin Solid Films* **2001**, *400*, 139.
336. M. Caffio, B. Cortigiani, G. Rovida et al., *J. Phys. Chem. B* **2004**, *108*, 9919.
337. G. D. Aloisi, M. Cavallini, M. Innocenti et al., *J. Phys. Chem. B* **1997**, *101*, 4774.
338. R. Z. Chen, D. S. Xu, G. L. Guo et al., *J. Mater. Chem.* **2002**, *12*, 1437.
339. R. Z. Chen, D. S. Xu, G. L. Guo et al., *Electrochim. Acta* **2004**, *49*, 2243.
340. R. Z. Chen, D. S. Xu, G. L. Guo et al., *J. Electrochem. Soc.* **2003**, *150*, G183.
341. M. Innocenti, G. Pezzatini, F. Forni et al., *J. Electrochem. Soc.* **2001**, *148*, C357.
342. M. Innocenti, S. Cattarin, M. Cavallini et al., *J. Electroanal. Chem.* **2002**, *532*, 219.
343. M. L. Foresti, G. Pezzatini, M. Cavallini et al., *J. Phys. Chem. B* **1998**, *102*, 7413.
344. T. Cecconi, A. Atrei, U. Bardi et al., *J. Electron Spectrosc. Relat. Phenom.* **2001**, *114*, 563.
345. G. Pezzatini, S. Caporali, M. Innocenti et al., *J. Electroanal. Chem.* **1999**, *475*, 164.
346. M. Cavallini, G. Aloisi, R. Guidelli, *Langmuir* **1999**, *15*, 2993.
347. S. Jayakrishnan, *Trans. Inst. Met. Finish.* **2000**, *16*, 124.
348. J. M. Zen, C. C. Yang, A. S. Kumar, *Electrochim. Acta* **2001**, *47*, 899.
349. M. Del Popolo, E. Leiva, *J. Electroanal. Chem.* **1997**, *440*, 271.
350. M. Dietterle, T. Will, D. M. Kolb, *Surf. Sci.* **1998**, *396*, 189.
351. R. Vidu, N. Hirai, S. Hara, *Phys. Chem. Chem. Phys.* **2001**, *3*, 3320.
352. P. Schieffer, C. Krembel, M. C. Hanf et al., *Solid State Commun.* **1996**, *97*, 757.
353. R. Abt, S. Blugel, *Philos. Mag. B* **1998**, *78*, 659.
354. O. Elmouhssine, G. Moraitis, J. C. Parlebas et al., *J. Appl. Phys.* **1998**, *83*, 7013.
355. A. J. Quinn, J. F. Lawler, R. Schad et al., *Surf. Sci.* **1997**, *385*, 395.
356. P. Steadman, C. Norris, C. L. Nicklin et al., *Phys. Rev. B* **2001**, *64*, art. no. 245412.
357. M. C. Hanf, C. Krembel, D. Bolmont, G. Gewinner, *Phys. Rev. B* **2003**, *68*, art. no. 144419.
358. M. H. Langelaar, D. O. Boerma, *Surf. Sci.* **1998**, *395*, 131.
359. S. Terreni, A. Cossaro, G. Gonella et al., *Phys. Rev. B* **2004**, *70*, art. no. 115420.
360. J. Dekoster, B. Degroote, H. Pattyn et al., *Appl. Phys. Lett.* **1999**, *75*, 938.
361. B. Degroote, H. Pattyn, S. Degroote et al., *Thin Solid Films* **2000**, *380*, 111.
362. F. Amitouche, S. Bouarab, C. Demangeat, *Catal. Today* **2004**, *89*, 375.
363. C. Leandri, H. Saifi, O. Guillermet et al., *Appl. Surf. Sci.* **2001**, *177*, 303.

364. J. A. Sprague, F. Montalenti, B. P. Uberuaga et al., *Phys. Rev. B* **2002**, *66*, art. no. 205415.
365. S. Sawaya, J. Goniakowski, G. Treglia, *Phys. Rev. B* **1999**, *59*, 15337.
366. U. Hasse, K. Wagner, F. Scholz, *J. Solid State Electrochem.* **2004**, *8*, 842.
367. U. Hasse, F. Scholz, *Electrochim. Commun.* **2005**, *7*, 173.
368. W. Simons, D. Gonnissen, A. Hubin, *J. Electroanal. Chem.* **1997**, *433*, 141.
369. D. Gonnissen, W. Simons, A. Hubin, *J. Electroanal. Chem.* **1997**, *435*, 149.
370. A. I. Dimitrov, S. H. Jordanov, K. I. Popov et al., *J. Appl. Electrochem.* **1998**, *28*, 791.
371. G. Baltrunas, E. Pakalniene, G. S. Popkirov et al., *Z. phys. Chem.* **2002**, *216*, 791.
372. G. Baltrunas, *Electrochim. Acta* **2003**, *48*, 3659.
373. V. Daujotis, D. Jasaitis, R. Raudonis, *Electrochim. Acta* **1997**, *42*, 1337.
374. V. Daujotis, V. Kairys, *Electrochim. Acta* **1997**, *42*, 1345.
375. A. Saito, T. Shibata, H. Ohura et al., *Denki Kagaku* **1998**, *66*, 1128.
376. J. V. Macpherson, P. R. Unwin, *J. Phys. Chem.* **1996**, *100*, 19475.
377. F. Scholz, U. Hasse, *Electrochim. Commun.* **2005**, *7*, 541.
378. R. Y. Bek, L. I. Shuraeva, A. F. Zherebilov et al., *Russ. J. Electrochem.* **1996**, *32*, 834.
379. R. Y. Bek, N. A. Rogozhnikov, *Russ. J. Electrochem.* **1995**, *31*, 1125.
380. R. Y. Bek, L. Shuraeva, S. N. Ovchinnikova, *Russ. J. Electrochem.* **2004**, *40*, 1079.
381. N. A. Rogozhnikov, *Russ. J. Electrochem.* **1998**, *34*, 61.
382. X. W. Sun, Y. C. Guan, K. N. Han, *Metall. Mater. Trans. B* **1996**, *27*, 355.
383. V. T. Yavors'kyi, O. I. Kuntyi, S. I. Kozak et al., *Mater. Sci.* **1999**, *35*, 893.
384. S. G. Garcia, D. R. Salinas, C. E. Mayer et al., *Electrochim. Acta* **2003**, *48*, 1279.
385. G. A. Hope, R. Woods, K. Watling, *J. Appl. Electrochem.* **2001**, *31*, 1285.
386. G. A. Hope, K. Watling, R. Woods, *J. Appl. Electrochem.* **2001**, *31*, 703.
387. X. W. Sun, Y. C. Guan, K. N. Han, *Metall. Mater. Trans. B* **1996**, *27*, 355.
388. M. E. Vela, G. Andreasen, R. C. Salvarezza et al., *Phys. Rev. B* **1996**, *53*, 10217.
389. M. Dolata, P. Kędzierzawski, *Pol. J. Chem.* **2003**, *77*, 1199.
390. J. A. Garcia-Vázquez, J. Romero, A. Souza, *Coord. Chem. Rev.* **1999**, *195*, 691.
391. V. E. Marquez, J. R. Anacona, *Polyhedron* **1997**, *16*, 2375.
392. A. Lewandowski, A. Szukalska, M. Galiński, *New J. Chem.* **1995**, *19*, 1259.
393. N. N. Greenwood, A. Earnshaw, *Chemistry of the Elements*, 2nd ed., Elsevier-Butterworth-Heinemann, Amsterdam, Boston, Heidelberg, 1997.
394. W. Grochala, R. Hoffmann, *Angew. Chem. Int. Ed. Engl.* **2001**, *40*, 2742.
395. N. R. Walker, R. R. Wright, A. J. Stace, *J. Am. Chem. Soc.* **1999**, *121*, 4837.
396. C. Brückner, *J. Chem. Educ.* **2004**, *81*, 1665.
397. F. A. Cotton, G. Wilkinson, *Advanced Inorganic Chemistry*, Wiley, New York, 1988.
398. B. E. Breyfogle, C. J. Hung, M. G. Shumsky et al., *J. Electrochem. Soc.* **1996**, *143*, 2741.
399. L. J. Kirschenbaum, J. D. Rush, *Inorg. Chem.* **1983**, *22*, 3304.
400. L. J. Kirschenbaum, J. D. Rush, *J. Am. Chem. Soc.* **1984**, *106*, 1003.
401. E. T. Borish, L. J. Kirschenbaum, *Inorg. Chem.* **1984**, *23*, 2355.
402. J. D. Rush, L. J. Kirschenbaum, *Inorg. Chem.* **1985**, *24*, 744.
403. R. Eujen, B. Hoge, D. J. Brauer, *Inorg. Chem.* **1997**, *36*, 3160.
404. R. Eujen, B. Hoge, D. J. Brauer, *Inorg. Chem.* **1997**, *36*, 1464.
405. E. K. Barefield, M. T. Mocella, *Inorg. Chem.* **1973**, *12*, 2829.
406. W. R. Scheidt, J. U. Mondal, C. W. Eigenbrot et al., *Inorg. Chem.* **1986**, *25*, 795.
407. H. Furuta, T. Ogawa, Y. Uwatoko et al., *Inorg. Chem.* **1999**, *38*, 2676.
408. H. Furuta, H. Maeda, A. Osuka, *J. Am. Chem. Soc.* **2000**, *122*, 803.
409. M. A. Muckey, L. F. Szczepura, G. M. Ferrence et al., *Inorg. Chem.* **2002**, *41*, 4840.
410. C. Brückner, C. A. Barta, R. P. Briñas et al., *Inorg. Chem.* **2003**, *42*, 1673.
411. M. Ali, A. I. Shames, S. Gangopadhyay et al., *Transition Met. Chem.* **2004**, *29*, 463.
412. K. M. Kadish, X. Q. Lin, J. Q. Ding et al., *Inorg. Chem.* **1986**, *25*, 3236.
413. A. Kahani, M. Abedini, M. Farnia, *Transition Met. Chem.* **2000**, *25*, 711.
414. D. Naumann, W. Tyrra, F. Trinias et al., *J. Fluor. Chem.* **2000**, *101*, 131.
415. B. X. Li, Z. J. Zhang, M. L. Wu, *Microchem. J.* **2001**, *70*, 85.

416. B. X. Li, Z. J. Zhang, M. L. Wu, *Anal. Chim. Acta* **2001**, *432*, 311.
417. A. Lehmani, P. Turq, J. P. Simonin, *J. Electrochem. Soc.* **1996**, *143*, 1860.
418. J. L. Hunting, M. Weiss, H. N. Po, *Abstr. Pap. Amer. Chem. Soc.* **1999**, *217*, 306-INOR.
419. D. Sroczyński, A. Grzejdziak, *J. Incl. Phenom. Macrocycl. Chem.* **2002**, *42*, 99.
420. M. Panizza, I. Duo, P. A. Michaud et al., *Electrochem. Solid State Lett.* **2000**, *3*, 550.
421. A. Paire, D. Espinoux, M. Masson et al., *Radiochim. Acta* **1997**, *78*, 137.
422. J. E. Graves, M. T. Goosey, D. Hirst et al., *Trans. Inst. Met. Finish.* **2001**, *79*, 90.
423. M. Ravera, C. Ciccarelli, V. Gianotti et al., *Chemosphere* **2004**, *57*, 587.
424. A. Kumar, Vaishali, P. Ramamurthy, *J. Chem. Soc., Perkin Trans.* **2001**, *27*, 1174.
425. I. Zilberman, J. Hayon, E. Maimon et al., *Electrochem. Commun.* **2002**, *4*, 862.
426. F. Mousset, F. Bediouï, C. Eysseric, *Electrochem. Commun.* **2004**, *6*, 351.

24.6**Electrochemistry of Mercury**

24.6.1	Double-layer Properties of Hg/Water Interface	959
24.6.1.1	Potential of Zero Charge	959
24.6.1.2	Surface Charge Density and Capacitive Current	959
24.6.1.3	Experimental and Theoretical Studies of the Hg/Water Interface	960
24.6.2	Double-layer Properties of Hg/Nonaqueous Media Interface	961
24.6.3	Adsorption and Electrode Reactions at Hg Surface	962
24.6.3.1	Deposition and Underpotential Deposition of Hg on Various Electrodes	962
24.6.3.1.1	Underpotential Deposition of Mercury on Gold Electrodes	962
24.6.3.1.2	Film Electrodes and Related Hg Electrodes	966
24.6.3.2	Adsorption and Electrode Reactions of Inorganic Ions and Coordination Compounds of Metal Ions	968
24.6.3.2.1	Analytical Applications	970
24.6.3.3	Adsorption and Electrode Reactions Involving Organic Compounds	971
24.6.3.3.1	Organic Compounds Containing Sulfur, Selenium, and Tellurium	972
	Anodization of Hg electrode	972
	Amino acids	973
	Proteins, enzymes	973
	Nucleic bases, nucleotides, and thiolipids	975
	Other sulfur-containing compounds	976
	Organic selenides and tellurides	977
24.6.3.3.2	Organic Nitrogen Compounds	977
24.6.3.3.3	Indicators and Dyes	980
24.6.3.3.4	Vitamins and Antibiotics	980
24.6.3.3.5	Enzymes and Coenzymes	981
24.6.3.3.6	Other Organic Compounds	981
	Mixed adsorption	983
24.6.3.3.7	Analytical Aspects of Adsorption of Organic Compounds	983
24.6.4	Ammonium and Quaternary-substituted Ammonium Amalgams	984
	References	986

The chapter on the electrochemistry of mercury was published in the IX-A volume of the *Encyclopedia of Electrochemistry of the Elements* [1] in 1982. At that time, mercury was probably the most often used electrode material. Hence the relevant chapter contained numerous data on standard and formal potentials in aqueous and nonaqueous solutions, voltammetric characteristics of mercury and double-layer properties of mercury/solution interface, electrochemical studies involving anodic dissolution and cathodic deposition of mercury, as well as examples of use of mercury and its compounds in applied electrochemistry. At present, however, it is clear that since the time that elapsed from publishing of that chapter, mercury as an electrode material partially lost its importance compared to solid (particularly single-crystal) noble metals or carbon (in electroanalysis) electrodes. The number of papers on the electrochemistry of this element is therefore also appropriately smaller than for other electrode materials, such as gold. However, a literature survey shows that a number of papers dealing with analytical studies of various compounds at mercury electrodes is still significant. Discussion of all these analytical papers is beyond the scope of this review, which is essentially focused on physicochemical aspects of electrochemistry of mercury published in the last decade. In some cases, the papers presenting analytical aspects of electrochemical processes at Hg electrodes are also briefly discussed.

24.6.1

Double-layer Properties of Hg/Water Interface

24.6.1.1 Potential of Zero Charge

Undoubtedly, the mercury/aqueous solution interface, was in the past, the most intensively studied interface, which was reflected in a large number of original and review papers devoted to its description, for example, Ref. 1, and in the more recent work by Trasatti and Lust [2] on the potentials of zero charge. It is noteworthy that in view of numerous measurements of the double-layer capacitance at mercury brought in contact with NaF and Na₂SO₄ solutions, the classical theory of Grahame [3] still holds [2]. According to Trasatti [4], the most reliable PZC value for Hg/H₂O interface in the absence of specific adsorption equals to -0.433 ± 0.001 V versus saturated calomel electrode, (SCE); residual uncertainty arises mainly from the unknown liquid junction potential at the electrolyte solution/SCE reference electrode boundary.

24.6.1.2 Surface Charge Density and Capacitive Current

R. A. Osteryoung and coworkers [5] have performed chronocoulometric measurements of surface charge density at a controlled-growth mercury electrode. After initial formation and equilibration of the mercury drop, it was expanded by further addition of mercury and the charge corresponding to the new area was directly measured. The obtained value

was used to estimate the surface charge density. Experimental studies were associated with numerical modeling, assuming stepwise spherical expansion of mercury drop. Spectral analysis of the noise was also performed. More recently, Brito et al. [6] have published a paper on accurate determination of surface charge density at mercury electrode by extrusion of mercury drops. The proposed method was free from the faradaic component contribution, originating from traces of electroactive species. This procedure involved the newly designed hanging mercury drop electrode (HMDE).

A novel method for the determination of surface charge density at a HMDE coated with a self-assembled phospholipid monolayer mimicking a biological membrane has been described by Becucci et al. [7]. Charge density was calculated by integrating the capacitance current, which flows at the constant potential as a consequence of slight contraction of mercury drop.

Although the charging of the mercury surface seems to be a well-understood process, it has appeared recently that the impedance characteristics of the capacitance current at the *streaming* mercury electrode are not fully recognized yet. Jurczakowski and Orlik [8] have found in pure supporting electrolyte solutions that the capacitive current, which permanently charges fresh portions of the flowing mercury even under potentiostatic conditions, causes the impedance response qualitatively equivalent to that of the faradaic process with charge transfer as the rate-controlling step. The corresponding equivalent circuit for pure capacitive response included parallel connection of differential double-layer capacitance C_d , and virtual resistor $R_d = (2\pi r C_d v)^{-1}$, where r and v denote the radius of the mercury stream, and the flow rate of mercury, respectively.

24.6.1.3 Experimental and Theoretical Studies of the Hg/Water Interface

Arihara et al. [9] have monitored *in situ* the Hg–Au electrode surface in HClO_4 solutions applying infrared reflection/absorption spectroscopy (IRAS). It has been found that the adsorption state of water molecules on Hg changes depending on the applied potential. The Hg–water interaction was considered stronger than the Au–water interaction. The structure of water within the dense part of electrical double layer at mercury electrode, in a wide range of surface charges, has also been analyzed theoretically by Nazmutdinov and Borisevich [10]. They used classical Monte Carlo method and ab initio quantum-chemical approach to calculate the potential for the interactions with the metal. It has been found that to theoretically explain earlier experimental data, it is sufficient to invoke dipole reorientation and the behavior of hydrogen bonds between H_2O molecules in a monolayer; any additional hypotheses on phase transitions are not necessary.

Damaskin and Grafov [11] have compared the Gonzalez-Sanz theory of the diffuse layer with the experimental data concerning mercury electrode capacitance in aqueous solutions of Na_2SO_4 and $\text{La}_2(\text{SO}_4)_3$. It has been shown that the Gonzalez-Sanz theory is rigorously consistent with the Gibbs adsorption equation, if the thickness of the inner part of the double layer (in the surface-inactive electrolyte solution) is independent of the electrode charge and the solvent concentration in the diffuse layer remains invariant. Furthermore, the experimental dependence of the capacitance of an uncharged mercury electrode on the concentration of aqueous solutions of Na_2SO_4 and $\text{La}_2(\text{SO}_4)_3$ was found to be in better agreement with the Gonzalez-Sanz theory than with the

classical Gouy-Chapman-Grahame theory. Eck and Spohr [12] have summarized earlier calculations and performed their own computer modeling of hydrated Li^+ , F^- , and Cl^- ions in the proximity of a mercury electrode. In most simulations, a simple rigid crystal model of mercury was assumed (it was also shown that the water structure is not strongly affected if a more realistic liquid model is used). The differences between the ions were explained in terms of solvation and steric interactions.

Cecchi et al. [13] have studied the influence of alkali halide compounds on photocurrent accompanying emission of electrons from dropping mercury electrode into water. Cathodic photocurrent was observed when the electrode was irradiated with UV light in nonfaradaic region of the polarographic curve in ultrapure water deaerated with pure hydrogen and in the absence of scavengers of hydrated electrons. After small additions of alkali metal halide compounds, the photocurrent was increased to an extent depending on the nature of alkali metal cations. In contrast, the current was decreased at concentrations exceeding 10^{-4} M.

24.6.2

Double-layer Properties of Hg/Nonaqueous Media Interface

An increasing interest in nonaqueous media, which began in the seventies of the XXth century, also resulted in the extended studies on the properties of the relevant Hg|solvent interface. Most of the papers discussing the dependence of E_{pzc} of Hg on the solvent used were published in the eighties [2]. The pzc values for selected solvents, including water for comparison, are collected in Table 1. They are expressed versus standard hydrogen electrode (SHE) and, in order to eliminate the unknown liquid junction potential, also versus the bis(biphenyl)chromium(I)/(0) standard potential, that was assumed to be solvent independent.

Systematic thermodynamic studies on the Hg|solvent interface led to the conclusion that entropy of its formation is always positive and lower than in the solution bulk, what suggests certain “structure making” effect of Hg for these solvents [2].

The Hg|solvent interface was intensively studied in, for example, various alcohols. For example, in EtOH and MeOH, similar data for double layer were obtained;

Tab. 1 Selected E_{pzc} values for Hg|solvent interface [2], expressed versus standard hydrogen electrode and bis(biphenyl)chromium(I)/(0) (BBCr) reference electrode

Solvent	Electrolyte	E_{pzc}/V versus aqueous SHE	$E_{\text{pzc}} (\pm 0.01 \text{ V})/\text{V}$ versus BBCr ($\pm 0.01 \text{ V}$)
H_2O	NaF	-0.192 ± 0.001	0.458 ± 0.001
Acetonitrile	LiClO_4	-0.03	0.56
Dimethylsulfoxide	LiClO_4	-0.08	0.52
<i>N,N</i> -Dimethylformamide	LiClO_4	0.00	0.51
Propylene carbonate	NaClO_4	-0.08	0.59
Methanol	KF	-0.05	0.51
Ethanol	LiClO_4	-0.05	
<i>n</i> -Propanol	LiClO_4	-0.07	

explanation for the small differences obtained (including higher capacitance at pzc in EtOH compared to MeOH) was the subject of controversy. Although some of them could be attributed to the difference in the size of EtOH and MeOH molecules, one should emphasize that the double-layer thickness was not equal to the real cross section of the solvent molecules. For EtOH, the following sequence of the surface activity of anions has been proposed: $\text{BF}_4^- < \text{ClO}_4^- < \text{Cl}^- < \text{Br}^- < \text{I}^-$ [2].

Systematic studies on double-layer properties of mercury in contact with various nonaqueous solvents were being carried out up to the beginning of the nineties of the twentieth century. A comprehensive survey of the obtained data and of the concepts used for their description is given in Ref. 2. At present, such studies are being undertaken rather occasionally. Adsorption of dimethylsulfoxide (DMSO) on mercury electrodes has been studied by Motheo and Gonzalez [14]. The Hg|0.15 M Na_2SO_4 (DMSO) interface was studied using the electrode charge density as the independent electrical variable. The observed adsorption behavior was governed by the Frumkin isotherm. Furthermore, it has been found that DMSO molecules, upon adsorption under the applied conditions, undergo partial reorientation.

Recently, Fuchs et al. [15], using the streaming mercury electrode and applying the Henderson equation, have determined the pzc value in the solutions of tetraethylammonium perchlorate in DMSO as -0.515 ± 0.001 V (versus Ag/0.01 M Ag^+ (DMSO) reference electrode). This value was corrected for the liquid junction potential and was independent of tetraethyl ammonium perchlorate (TEAP) concentration within the range: 0.02 to 0.75 M. Using the same methodology, Kišova et al.

[16] have determined pzc for 0.1–1.0 M sodium perchlorate solutions in DMSO as -0.527 ± 0.002 V (versus Ag/0.01 M Ag^+ (DMSO)).

24.6.3

Adsorption and Electrode Reactions at Hg Surface

24.6.3.1 Deposition and Underpotential Deposition of Hg on Various Electrodes

One of the subjects that is still quite intensively developed (using electrochemical methods frequently combined with nonelectrochemical techniques) concerns reduction of Hg compounds at various surfaces (e.g. Pt or Au), with the emphasis laid on underpotential deposition (UPD) of mercury. Deposition of mercury on other metals is generally important for better understanding of the mechanism of the formation of amalgams. Moreover, underpotential Hg deposition characteristics constitute a significant source of information on Hg–metal interactions. In turn, mercury film electrodes obtained by such deposition have a significant application in electrochemical analysis of various species.

24.6.3.1.1 Underpotential Deposition of Mercury on Gold Electrodes

Earlier studies of UPD of mercury were carried out applying only classical electrochemical methods and polycrystalline electrodes. The results have shown that UPD of Hg is accompanied by adsorption of mercury ions.

Salié and Bartels [17–20] have considered the process of Hg UPD from Hg(I) and Hg(II) perchloric acid solutions as proceeding in partial charge-transfer steps. The authors, in order to explain different experimental results, have assumed two-step process. In the first step, an intermediate is adsorbed at the gold surface and

the accompanying charge transfer is about 0.53e per mercury atom. At this stage, there is an interaction with Au atoms and with the species present in the solution. In the second step, full discharge of the intermediate species and formation of a full monolayer of mercury atoms occur.

Shay and Bruckenstein [21] have made an attempt to determine Hg(I) adsorption, which accompanies coulostatic UPD of mercury on gold, using electrochemical quartz crystal microbalance (EQCM). It has been found from ex situ EQCM that the mass change accompanying coulostatic deposition of mercury corresponds to the formation of one monolayer of Hg (1.7×10^{-9} mol cm $^{-2}$), with the additional adsorbed layer of Hg₂SO₄ (2.9×10^{-10} mol cm $^{-2}$). Hg₂SO₄ remained adsorbed on Hg even after rinsing the electrode with water.

In the recent years, single-crystal electrodes and new techniques, such as

scanning tunnelling microscopy (STM) and atomic force microscopy (AFM), and others, have been utilized in the studies of UPD of mercury, for example, on Au(111) [22–26]. In these papers, Abruña and coworkers have used, apart from electrochemical methods, X-ray diffraction and scattering techniques also. Cyclic voltammograms recorded using Au(111) in 0.1 M H₂SO₄ containing 1 mM Hg²⁺ are shown in Fig. 1.

Two pairs of sharp peaks around +0.93 V (see inset) correspond to adsorption of preadsorbed sulfate ions and deposition of Hg₂SO₄. The shape of these spikes suggests that these processes are fast. An ordered coadsorbed structure of Hg₂SO₄ was observed at potentials $+0.80 \leq E \leq +0.88$ V. Broad peak at +0.60 V corresponds to the deposition of the first Hg monolayer, which is completed at +0.52 V and reflected as sharp spikes, together with the onset of amalgam

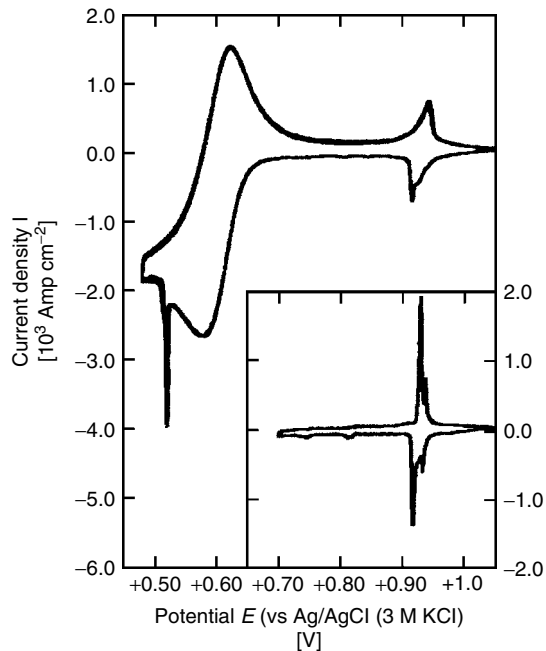
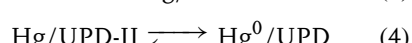
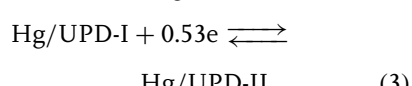
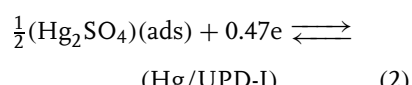
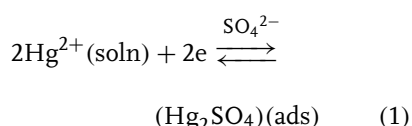


Fig. 1 Cyclic voltammogram of Au(111) electrode in 0.10 M sulfuric acid containing 1.0 mM Hg²⁺; scan rate: 2 mV s $^{-1}$. Inset: voltammetric profile over the potential range: +1.05 to +0.70 V versus Ag/AgCl (3 M KCl) (from Ref. 23).

formation. Broad shape of peaks in the potential range +0.50 to 0.70 V may suggest that these processes are slow, possibly due to the existence of intermediate states during reduction of Hg(I) to Hg(0) [17–20]. The authors have observed three UPD phases in 0.1 M H₂SO₄, at potentials preceding bulk mercury deposition. These phases consisted of two well-ordered intermediate states, which appeared to be either a fully discharged two-dimensional liquid Hg layer, or an amorphous Hg–Au monolayer [23]. Both intermediate phases had hexagonal structures with the lattice vectors rotated 30° with respect to those of the Au(111) substrate. The first phase occurred at the potential of +0.68 V (versus Ag/AgCl with 3 M KCl); it was metastable and underwent transition to the second ordered phase either at +0.68 V after longer waiting, or by moving the potential to less positive value (+0.63 V). Similar to the first phase, the second one was also metastable and might be transformed to the final, fully discharged state, being either a two-dimensional liquid Hg layer, or an amorphous Hg–Au layer. This process agreed well with the mechanism found by Salié and Bartels for polycrystalline Au electrode. The mechanism for the studied process can be represented by the following reactions:



Earlier, the first stage of Hg UPD on Au(111) in 0.10 M H₂SO₄ with 1 mM Hg²⁺ was studied by the same authors [22], who used synchrotron, X-ray scattering techniques, including grazing incidence X-ray diffraction and specular crystal-truncation rod measurements. An ordered coadsorbed structure of sulfate/bisulfate anions and mercury cations was found at the potentials between the first and the second Hg UPD peaks. The charge corresponding to the first UPD peak suggested that the coadsorbed structure is probably Hg₂SO₄. These results were consistent with those obtained for the chloride and acetate solutions [24]. Also, the voltammetric results were compared to the recent results from *in situ* AFM, STM, and surface X-ray scattering, in order to look for a correlation between the found voltammetric data and the surface structures and their transformations. The authors [22, 24] have proposed the following explanation for the observed processes. At potentials more positive than the first UPD peak, an ordered sulfate adlayer exists. The onset of mercury deposition triggers an order/disorder transition that, in turn, gives rise to the formation of the first set of UPD peaks. As the monolayer deposition is completed, again a disorder/order transition occurs and the second set of peaks appear. The adlayer is composed of Hg₂SO₄ with coadsorbed H₃O⁺ ions. A further voltammetric characteristic is the disappearance of the ordered coadsorbed structure. The final process is the completion of the mercury monolayer, followed by the formation of a mercury–gold amalgam.

The same group of researchers [25] has performed studies of Hg UPD on Au(111) in the presence and absence of strongly interacting anions, such as bisulfate, chloride, and acetate.

Abruña et al. [26] have carried out *in situ* surface X-ray diffraction studies in the following solutions: 0.1 M H₂SO₄, 0.1 M HClO₄, 0.1 M HClO₄ with 1 mM NaCl, and acetic buffer (0.1 M acetic acid +0.1 M sodium acetate). They have found that anions strongly determine the structure of Hg overlayer. As before, three ordered structures were found in sulfuric acid solutions. The overlayer structure in 0.10 M HClO₄ was dominated by trace amounts of Cl⁻ ions and was similar to that observed in the solution containing 1.0 mM chloride ions. In acetate solutions, an incommensurate hexagonal lattice was found for a bilayer structure, which was likely formed by HgCH₃COO complexes. The lattice constant varied dramatically in a wide range of electrode potentials, which suggests that the charge of the deposited Hg atoms changed with the potential. In all four used electrolytes containing different anions, Hg UPD appeared to follow a common mechanism with desorption of preadsorbed anions at the initial step and a subsequent deposition of a coadsorbed layer comprising mercury-anion neutral species.

Hg UPD on Au(111) electrodes in the presence of bisulfate anions has been studied by Abruña et al. [27] in order to illustrate the effects of the partial charge, retained by the metal, on the interactions between the adsorbed metal and the anion. In order to obtain structural information on the adsorbed species, the authors have carried out grazing incident X-ray diffraction measurements at several potentials. Three ordered structures were observed depending on the applied potentials, which were adjusted from cyclic voltammograms. At the early stages of Hg UPD, when mercury was still partially charged, an ordered mercurous-sulfate bilayer structure was formed at the electrode

surface. At more negative potentials, two additional ordered hexagonal mercury adlayers were formed, which interacted with the anions only slightly.

Herrero and Abruña [25] have also studied the kinetics and mechanism of Hg UPD on Au(111) electrodes in the presence and absence of bisulfate, chloride, and acetate ions. In the absence of the interacting anions (in perchloric acid), the Hg UPD was significantly controlled by gold–mercury surface interactions. In sulfuric acid solutions, the kinetics of the initial and final stages of mercury deposition/dissolution was altered. The presence of two well-ordered structures at potentials below and above mercury deposition led to the formation of two pairs of sharp spikes in cyclic voltammograms. In the chloride medium, the voltammetric profile exhibited two sharp peaks and thus it was very similar to that obtained in sulfuric acid solution. Neither nucleation, nor growth kinetics mechanism was found to be linked to the process of formation/disruption of the mercury chloride adlayer. The transients obviously deviated from the ideal Langmuir behavior.

The kinetics of Hg UPD in acetate media is clearly slower than in the previous media, as voltammetric and chronoamperometric measurements have revealed [26]. A delicate interplay between the presence of the strongly interacting anions and kinetics and structure of electrochemically induced phase transitions has been shown.

One should add that Abruña and coworkers have described UPD of Hg on various Au(*h,k,l*) electrodes in a review paper [28]. They have also studied UPD of other metals at various single-crystal metal surfaces.

Inukai et al. [29] have carried out UPD of mercury also on Au(111) and have investigated this process by *in situ* STM in sulfuric and perchloric acid solutions.

In sulfuric acid solution, the structure observed at potentials more positive than the first UPD peak was assigned to the adsorbed bisulfate ions. After the first UPD peak, two domains: $\begin{bmatrix} 2 & 0 \\ 3 & 3/2 \end{bmatrix}$ and $\begin{bmatrix} 1 & 1 \\ 4 & 4 \end{bmatrix}$, were located always on the same terrace. In HClO_4 solution, a different structure of $\begin{bmatrix} 0 & 2 \\ 2 & 1 \end{bmatrix}$ was found after the first UPD peak. These findings have proved again that there is a large influence of anions on the UPD structure.

Abaci et al. [30] have studied the influence of temperature on Hg UPD at Au(111) electrodes. Deposition was carried out in various solutions containing anions differently interacting with the studied system: ClO_4^- ions (HClO_4) were practically inert, SO_4^{2-} (H_2SO_4) interacted with the Au(111) substrate, and $\text{C}_2\text{H}_3\text{O}_2^-$ ($\text{HC}_2\text{H}_3\text{O}_2$) interacted with the dissolved Hg^{2+} ions. At the constant Γ_{Hg} , the temperature dependence of cyclic voltammetric potentials was constructed. From the obtained plot, entropy ($\Delta S_{\text{rc}}^0(\text{upd})$) and enthalpy ($\Delta H_{\text{rc}}^0(\text{upd})$) for Hg UPD were found to be: entropies -30.9 and $-18.3 \text{ J mol}^{-1} \text{ k}^{-1}$, and enthalpies -182 and -184 kJ mol^{-1} in perchloric acid and sulfuric acids, respectively. In acetic media, these thermodynamic parameters were strongly pH dependent.

Finally, one should mention that Hg UPD on Au(111) proceeds differently on the neighboring metals in the periodic table, such as Tl, Pb, and Bi. UPD layers of Tl and Pb, just prior to the bulk deposition on Au(111), were found to be compressed by only about 3% as compared to the bulk values, and decreased with the decreasing electrode potential. At the same time, two ordered Hg UPD phases had expanded structures compared to the frozen bulk Hg [23].

24.6.3.1.2 Film Electrodes and Related Hg Electrodes

Mercury films were prepared on reticulated vitreous carbon flow-through electrodes by Hg deposition from Hg^{2+} solutions in acetic buffer [31]. Such an electrode was designed for the purposes of trace metal analysis. Mercury film deposition/oxidation on reticulated vitreous carbon and glassy carbon electrodes were compared.

Daujotis et al. [32] have described the use of electrochemical quartz microbalance for the quantitative studies on monolayer adsorption on working mercury electrodes. Mercury was deposited on Pt at negative potentials (-0.4 to -0.5 V versus $\text{Ag}|\text{AgCl}|\text{KCl}_{\text{sat}}$). In order to avoid undesirable transformation of mercury into, for example, larger droplets, the thickness of mercury film could not exceed 20 nm . Then, the linear dependence of the frequency change on the added mass was achieved. Applicability of such an electrode for EQCM measurements has been demonstrated by performing electroreduction of $\text{Pb}(\text{II})$ and $\text{Tl}(\text{I})$, as an example.

Deposition of mercury at boron-doped diamond (BDD) and platinum electrodes has also been studied [33]. Deposition and oxidation of mercury was performed by cyclic voltammetry from the solution of $1 \text{ mM } \text{Hg}_2(\text{ClO}_4)_2$ in 1 M NaClO_4 . In order to learn more about this deposition, it was carried out also under chronoamperometric conditions. The results obtained are shown in Fig. 2 in the form of dimensionless current-time transients. Experimental curves obtained at two different overpotentials were compared with the theoretical curves calculated for instantaneous and progressive nucleation. A good agreement of experimental plots with the instantaneous nucleation mechanism was

Fig. 2 Comparison of the experimental dimensionless current-time transients for electrodeposition of mercury onto boron-doped diamond electrode with the theoretical transients for instantaneous (upper curve) and progressive (lower curve) nucleation; overpotentials: (\times) 0.862 V and (\blacklozenge) 0.903 V (from Ref. 33).

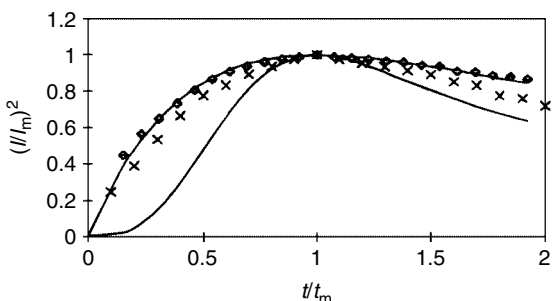
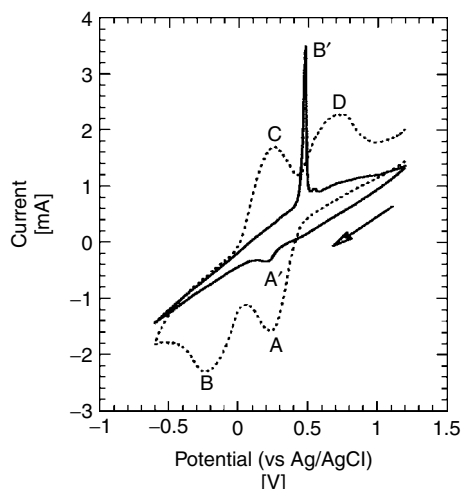


Fig. 3 A comparison of cyclic voltammograms obtained at the scan rate of 20 mV s^{-1} for reduction of Hg(II) –mesoporous silica (dotted line, $\text{Hg(II)} = 4\%$) and $1.0 \times 10^{-3} \text{ M Hg(II)}$ solution at a carbon paste electrode without mesoporous silica (solid line, current axis $\times 3$) in aqueous $0.1 \text{ M NaClO}_4 + 1.5 \text{ M HClO}_4$ (from Ref. 38).



found. One failed to describe deposition of Hg from Hg^{2+} solution either by instantaneous or progressive nucleation mechanism [33].

Wang et al. [34] have introduced a new heated mercury film electrode based on a screen printed carbon substrate. It was used in anodic stripping and exhibited a significantly improved signal-to-noise ratio. A directly heated mercury film electrode for anodic stripping voltammetry has been described by Jasinski [35]. Different factors influencing the quality of analytical determination have been investigated. Renewed mercury electrodes and examples of their various applications have been reviewed in Ref. 36. Lovric and Scholz [37] have discussed the conditions

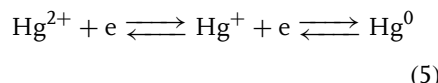
and the reasons that make anodic stripping voltammetry of mercury possible at the trace level also.

Bond et al. [38] have described a composite carbon paste electrode with mesoporous silica and Hg^{2+} metal ions adsorbed on the surface. The peak current recorded under cyclic voltammetric conditions was proportional to the amount of cation adsorbed on silica up to the surface saturation level, and also to the hydrogen ion concentration. Typical curve recorded using such electrodes is shown in Fig. 3 (dotted line).

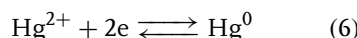
For a comparison, a cyclic voltammogram recorded at carbon paste electrode without mesoporous silica is also shown. In this case, $10^{-3} \text{ M Hg}^{2+}$ was present

in the aqueous solution containing 0.1 M NaClO₄ and 1.5 M HClO₄ as background electrolytes.

In case of Hg²⁺ adsorbed on silica, electroreduction was quasi-reversible and proceeded in two well-defined one-electron steps, according to the equation below:



For the conventional carbon paste and Hg²⁺ in the solution, reaction occurs in one step:



This can be seen in the cyclic curve in Fig. 3. In this voltammogram, relatively large anodic peak of mercury stripped from the paste electrode surface is observed. The presence of relatively stable Hg(I) at mesoporous silica carbon paste electrode may be due to adsorption.

The improvement in the preparation of renewable and reproducible mercury film-covered carbon paste electrode for use in anodic stripping voltammetry has been reported in Ref. 39. Mercury salts (mercuric oxalate) distributed in the electrode bulk served as a source of mercury.

Wang and Tsai [40] have described voltammetric behavior of chlorhexidine at film mercury electrodes in the aqueous medium.

Camarero et al. [41] have prepared graded cadmium–mercury–telluride thin films (Cd_xHg_{1-x}Te) applying cathodic electrodeposition at variable deposition voltage. Atomic proportions of mercury in the range 0.05–0.15 were considered.

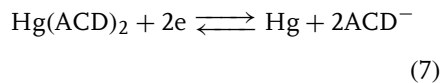
It is noteworthy that Scholz and coworkers [42] have studied electrochemical reduction of submicrometer size Hg₂Cl₂ and Hg₂Br₂ crystals immobilized on the surface of gold and platinum electrodes. The

process started at the three-phase junction, where the three phases: metal, mercury(I) halide, and electrolyte solution met. During deposition on gold electrodes, liquid mercury was transformed into a solid crystalline gold amalgam electrode. In case of Pt, liquid mercury wet the platinum surface.

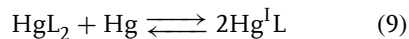
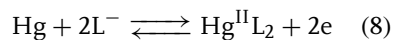
A Hg|Hg₂C₂O₄ secondary electrode has been proposed [43] for the potentiometric determination of the oxalate ion concentration.

24.6.3.2 Adsorption and Electrode Reactions of Inorganic Ions and Coordination Compounds of Metal Ions

Safavi and Gholivand [44] have studied electrochemical reduction of mercury complexes with 2-aminocyclopentene-1-dithiocarboxylic acid (ACD ≡ L) and its selected derivatives at mercury electrodes in DMSO. Reduction of Hg(ACD)₂ proceeded in a single 2-e step:



Hg(I) possibly participated as an intermediate. As a complementary study, redox behavior of the ligands themselves was investigated in DMSO solutions at Hg electrodes. 2-e oxidation of mercury proceeded according to the EC mechanism i.e. involving electrochemical step followed by chemical process:



Also, electroreduction of such complexes was studied at mercury electrodes.

The effect of the condensed adsorption layer on hydrogen evolution at mercury electrode has been studied by Ponomarev et al. [45].

Andrade and Molina [46] have performed electrochemical impedance studies of mercury electrodes with hematite particles adhered at different electrode potentials. Adhesion of such particles was strong and the decrease in the impedance was accompanied by an increase in the number of attached particles. Experimental results were analyzed in terms of an equivalent circuit including the constant phase element (CPE), the magnitude of which appeared to be directly related to the electrode coverage. A pore model for the metal/hematite particles interface has been proposed.

Anastopoulos et al. [47] have analyzed interfacial rearrangements of triphenylbismuth and triphenylantimony at mercury electrode in nonaqueous solvents of high dielectric constant. These phenomena were detected as the peaks in the capacitance-potential curves at intermediate negative potentials for triphenylbismuth and triphenylantimony in *N*-methylformamide, *N,N*-dimethylformamide, dimethyl sulfoxide, propylene carbonate, and methanol solutions.

Ramirez et al. [48] have studied adsorption of Ni(II)–dimethylglyoxime complex on mercury in ammonia and borate buffers using voltammetry and differential capacity measurements. Adsorption was found reversible and was governed by the Frumkin adsorption isotherm. The value of interaction parameter pointed toward the presence of attractive forces between the adsorbed molecules. The value of standard Gibbs energy of adsorption was close to those found for pentanol and hexanol. Later, Ramirez et al. [49] have investigated adsorption of Ni(II)–dimethylglyoxime complex on mercury in the same buffers. Electroreduction of the complex proceeded via reduction of Ni(II) to Ni with the simultaneous decomposition of the ligand.

Sander and Henze [50] have performed ac investigations of the adsorption potential of metal complexes at Hg electrode. Later, Sander et al. [51] have studied electrosorption of chromium–diethylenetriaminepentaacetic acid (DTPA) on mercury in 0.1 M acetate buffer at pH 6.2 using a drop-time method. The changes in the interfacial activity of the Cr(III)–DTPA complex with the bulk concentration obeyed the Frumkin adsorption isotherm.

Lobacz et al. [52] have described partial adsorption of Tl^+ –cryptand (2,2,2) complex on mercury electrode. From voltocoulometry, cyclic voltammetry, and chronocoulometry, it has been deduced that electroreduction of this complex proceeds via two parallel pathways: from the solution and from the adsorbed states, which are energetically close. Also, Damaskin and coworkers [53] have studied adsorption of the complexes of alkali metal cations with cryptand (2,2,2) using differential capacity measurements and a stationary drop electrode. It has been found that these complexes exhibit strong adsorption properties. Novotny et al. [54] have studied interfacial activity and adsorptive accumulation of UO_2^{2+} –cupferron and UO_2^{2+} –chloranilic acid complexes on mercury electrodes at various potentials in 0.1 M acetate buffer of pH 4.6 and 0.1 M NaClO_4 , respectively.

Kariuki and Dewald [55] have studied current oscillations accompanying reduction of indium(III) and gallium(III) in diluted chloride and nitrate solutions at a dropping mercury electrode.

Oscillations have also been reported for O_2/O_2^- redox reaction in quinoline media on HMDE, liquid Hg, and solid Hg-coated electrodes [56].

Acceleration and the associated oscillatory behavior of electroreduction of

H_2O_2 on Hg-adatom-modified polycrystalline Au electrodes have been described [57, 58].

Concerning more general application of mercury electrode in the studies on complexation equilibria, one should mention the paper by Jaworski et al. [59], who have investigated oxidation of mercury microelectrode in solutions with thiocyanates without any background electrolyte added. In the experiments, normal pulse voltammetry and staircase voltammetry were used. The authors have developed a general procedure for the determination of the stability constants, based on the data taken from the voltammograms. They have applied it to the analysis of $\text{Hg}(\text{II})-\text{SCN}^-$ complexes.

Bell et al. [60] have generated two complexes by anodic oxidation of mercury in the presence of a saturated acetonitrile solution of 1-methylimidazoline-2(3*H*)-thione. Their crystalline structure has been analyzed.

Stepnicka et al. [61] have synthesized mercury(II) complexes with 1'-(diphenylphosphino)ferrocenecarboxylic acid and studied their structure and electrochemical properties.

Also, Yam and Cheung [62] have carried out the synthesis of a series of novel polynuclear mercury(II) diimine complexes with bridging chalcogenate ligands and studied their luminescence and electrochemical properties.

Complex formation of Hg^{2+} , Zn^{2+} , and Pb^{2+} with polyacrylic and polymethacrylic acids has been studied [63] voltammetrically, using mercury drop and glassy carbon rotating disk electrodes. The formation constants of these complexes were calculated.

Electrochemical synthesis and structural characterization of zinc, cadmium, and mercury complexes of heterocyclic

bidentate ligands (N, S) have been described by Sousa-Pedrares et al. [64].

24.6.3.2.1 Analytical Applications In addition to the above-mentioned analytical aspects of the processes at Hg electrodes, in this section, we briefly review the papers focused on the subject of the affinity of various compounds to the mercury electrode surface, which allowed one to elaborate stripping techniques for the analysis of inorganic ions. Complexes of some metal ions with surface-active ligands were adsorptively accumulated at the mercury surface. After accumulation, the ions were determined, usually applying cathodic stripping voltammetry (CSV). Representative examples of such an analytical approach are summarized as follows.

Wang et al. [65] have described adsorptive stripping determination of uranium and chromium complexes with, for example, propyl gallate, after their adsorptive accumulation. Sensitive voltammetric determination of $\text{S}_2\text{O}_3^{2-}$ was performed, based on its electrosorption properties and utilizing the CSV analytical signal [66]. Also, Novotny and Krista [67] accumulated $\text{S}_2\text{O}_3^{2-}$ on mercury electrodes by applying a potential of $E_{\text{ac}} = 275$ mV (versus Ag/AgCl). Reduction peak of the deposit was formed at -0.38 V. Strong adsorption of $\text{S}_2\text{O}_3^{2-}$ was reflected in electrocapillary curves at potentials more positive than -0.4 V (SCE) in 0.1 M acetate buffer of pH 4.4 up to approximately -50 mV (SCE), where faradaic processes affected the γ versus E dependence. The potential of maximum adsorption was found to be -60 mV (SCE). After differentiation of the surface pressure π versus $\log c$ dependence, the adsorption isotherms obeying the Frumkin relation were obtained. At E_{max} , adsorption coefficient β equaled $105 \text{ m}^3 \text{ mol}^{-1}$.

Safavi et al. [68] have described an indirect method for the determination of CN^- ions and HCN. The method utilized the effect of cyanide on cathodic adsorptive stripping peak height of Cu-adenine.

The Co(II)-phenylthiourea-borax buffer system has been studied applying CSV at HMDE [69]. An irreversible peak observed at -1.5 V was attributed to the catalytic hydrogen evolution. The first reduction step, combined with the adsorptive accumulation of herbicide metribuzin at mercury electrode, has been used for its determination by adsorptive stripping voltammetry [70].

Fraga et al. [71] have proposed a new stripping voltammetric method for the determination of titanium and Co(II) [72] based on the adsorptive accumulation of its hydroxynaphthol blue complex on a static mercury drop electrode.

Traces of sulfides were determined by CSV at pH 10 in the presence of cobalt(II) ions. Cobalt sulfide was accumulated at -0.5 V (versus SCE), probably in the form of colloidal particles occluded into the mercury sulfide layer [73]. In the cathodic scan, CoS catalyzed evolution of hydrogen, which was reflected in the current peak at about -1.6 V .

Accumulation of Cu(II) complexes with xanthine and xanthosine has also been utilized in stripping analysis [74]. Copper(II) indapamide complex was adsorptively accumulated at a HMDE and used for the determination of the ligand in the cathodic stripping step [75].

Ivanov and Kaplun [76] used catechol in the determination of vanadium by adsorptive stripping voltammetry. It has been shown that the studied electrode process comprised one-electron reversible reduction of vanadium(IV) triscatecholate, previously accumulated at the electrode. It has also been found that the reduced

species, vanadium(III) complexes, were not accumulated.

Trace mercury determination by differential pulse (dp) anodic stripping voltammetry on polythiophene-quinoline/glassy carbon modified electrode has been reported [77].

Mercury electrodes were also polarized anodically in the solutions containing NaOH , HClO_4 , NaCl , NaI , NaF , Na_2SO_4 , NaHCO_3 , Na_2CO_3 , and tartaric and citric acids [78]. The solutions contained only one species, or the mixture of species, and no supporting electrolyte was added. For many of the above salts, linear calibration plots were obtained and, therefore, analytical possibilities were discovered. Anodization of mercury was also carried out in the real samples (wine, rain, tap and mineral water).

The construction and behavior of a mixed binder carbon paste electrode containing dimethylglyoxime have been described [79]. Such an electrode was used for CSV determination of mercury(II) and other metal ions. They were accumulated at the electrode surface during preconcentration step and later reduced from their complexes in the cathodic step.

Also, sodium montmorillonite-modified carbon paste electrode has been used for the determination of trace concentrations of mercury [80]. Hg^{2+} was preconcentrated at the electrode, reduced, and then stripped from the electrode surface in the positive potential scan. At a glassy carbon electrode modified with dithizone, mercury has been determined, applying anodic stripping voltammetry [81].

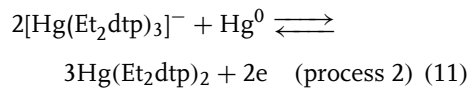
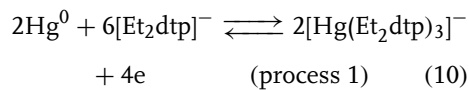
24.6.3.3 Adsorption and Electrode Reactions Involving Organic Compounds

Recently published studies on adsorption of organic compounds on mercury

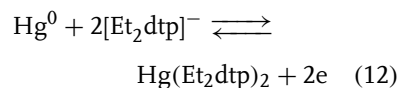
electrodes cover a relatively wide spectrum of substances, ranging from simple molecules to more complex compounds, and also of biochemical and/or pharmaceutical importance. Investigations of these compounds were performed either in the aqueous or nonaqueous media. It is noteworthy that a significant number of studies have been devoted to the sulfur-containing compounds. Typically, sulfur compounds or the products of their electrode processes adsorb or even form solid deposits at the mercury surface. For example, Mirceski et al. [82], applying polarography and cyclic and square-wave voltammetry at mercury electrodes, have described electrochemical behavior of three sulfur-containing drugs of different molecular structures. Adsorption and formation of insoluble salt at the electrode surface in this respect have been discussed.

24.6.3.3.1 Organic Compounds Containing Sulfur, Selenium, and Tellurium

Anodization of Hg electrode Polarographic studies [83, 84] have revealed that in the presence of Et_2dtp^- ($\text{Et}_2\text{dtp}^- = \text{S}_2\text{P}(\text{OEt})_2$, *o,o*-diethyldithiophosphate) in acetone mercury is oxidized in two consecutive steps:



Overall:



These processes were fast (reversible). Cathodic reduction of $\text{Hg}(\text{Et}_2\text{dtp})_2$ exhibited analogous behavior.

Bond and coworkers [85] have extended earlier [83] polarographic studies over a wider temperature range from 20 to -60°C . Assuming reversibility (processes 1 and 2), and considering the case of mercury oxidation in the presence of Et_2dtp^- , half-wave potentials depended on Et_2dtp^- concentration:

$$(E_{1/2}^r)_{\text{process 1}} = c_1 - \frac{RT}{F} \ln [(\text{Et}_2\text{dtp})^-] \quad (13)$$

$$(E_{1/2}^r)_{\text{process 2}} = c_2 + \frac{RT}{2F} \ln [(\text{Et}_2\text{dtp})^-] \quad (14)$$

where c_1 and c_2 are constants. The shapes of the waves were different. The corresponding I versus E dependencies were described by the expressions:

$$(E)_{\text{process 1}} = c'_1 + \frac{RT}{2F} \ln \left[\frac{I}{(I_d - I)^3} \right] \quad (15)$$

$$(E)_{\text{process 2}} = c'_2 + \frac{RT}{2F} \ln \left[\frac{I^3}{(I_d - I)^2} \right] \quad (16)$$

Additionally, the wave height ratio (process 1 : process 2) was predicted to be 2 : 1. $E_{1/2}^r$ values for the process 1 were almost independent of temperature (versus ferrocene electrode), and for the process 2, shifted to negative potentials as the temperature was lowered. Adsorption was enhanced significantly at lower temperatures, as noted previously for the room temperature [83, 84]. The third wave was observed close to the mercury electrode oxidation process. It was attributed to the formation of cationic mercury-rich dithiophosphate compounds, formed by oxidation of the mercury electrode and analogous to those characterized

for mercury dithiocarbamates [86–88]. There was no abrupt change in either the role or the nature of the electron transfer step at mercury electrode at the freezing point of mercury in both noninteracting (ferrocene) and interacting systems. $\text{Hg}(\text{Et}_2\text{dtp})_3^-$ was thermodynamically stable from 25 to -80°C . Optical studies of mercury microelectrodes have shown that their passivation, enhanced at low temperatures, is accompanied by the changes in the appearance of the surface.

Amino acids Cystine and cysteine are the amino acids, which have been the most extensively studied. Cathodic stripping of several sulfur compounds, including cysteine, cystine, and methionine has been described [89]. Voltammetric peaks were formed after accumulation at the constant potential. In case of cystine and cysteine in buffer of pH = 8.5, the potential of accumulation was 0.0 V versus SCE, while cathodic peaks were observed at about -0.55 V . The most important works on cystine reduction at mercury have been published by M. Heyrovsky et al. [90, 91]. They have found that cystine reacts chemically with mercury to give an adsorbed mercuric cysteine thiolate. Later, Heyrovsky and coworkers [92] have studied anodic reactions of cysteine at mercury electrodes, using several electrochemical methods. Two separate steps of mercury oxidation to cysteine mercurous and mercuric thiolates were distinguished. Both these compounds appeared to be strongly adsorbed at mercury electrodes. At low coverages of the electrode with the mercury-containing product, mercuric thiolate was formed by disproportionation of the adsorbed mercurous thiolate at the potentials of the second step. Under such conditions, only one electrode reaction

was observed. The authors have found that during the first step in acidic solutions, the molecules of mercurous cysteine thiolate in the compact film are perpendicularly oriented on the electrode, exhibiting strong lateral interactions. In alkaline solutions, S and N atoms of cysteine bind monomeric mercury(I). At the potential close to that of total mercury oxidation, the formation of cysteine mercuric thiolate occurs in the solution, followed by its adsorption at the electrode surface. Heyrovsky and Vavricka [93] have shown that adsorption and anodic reactions of homocysteine with mercury differ from those involving cysteine, due to slight differences in its hydrophilic properties and the structure of complexes with metal ions.

Proteins, enzymes Adsorption and electroreduction of proteins at mercury electrodes have been reviewed by several workers. Our short summary is partly based on the paper by Honeychurch [94]. Kuznetsov et al. [95] have suggested that the segments of the protein that interact with the surface, belong to relatively hydrophobic regions and they either denature or unfold following irreversible adsorption on mercury surface. Proteins spread on mercury electrodes [96] and form a layer of 8–10 Å in thickness, corresponding to the single polypeptide chain. This phenomenon is known as *surface denaturation*. Adsorption area and, consequently, the extent of denaturation are decreased with an increasing specific adsorption of the anion. The dependence of the molecular weight versus adsorption area shows that the proteins of large molecular weight (above 15 kD) behave differently from the smaller proteins [94], as they possibly do not denature and spread on mercury to the same extent as

smaller proteins do. It has also been suggested [94] that for adsorption of larger proteins, only the subunit attached to the surface denature. This makes the available adsorption area smaller than that predicted from the molecular weight versus adsorption area relation for smaller proteins.

Proteins can adopt several conformations at the electrode following adsorption, depending on which part of the molecules is initially bound to the electrode surface. In consequence, the number of electroactive disulfide bonds is a mean of the number of electroactive bonds corresponding to all possible conformations. Conformational variations of the adsorbed disulfide-containing proteins make the accessibility of disulfide bonds to the electrode surface to vary and may produce noninteger n values for the reduction process.

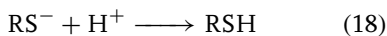
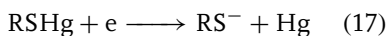
Honeychurch and Ridd [97] used chronopotentiometry to study reduction of five disulfide-containing proteins (bovine serum albumin, insulin, ribonuclease A, transferrin, and trypsin) adsorbed on HMDE. All studied proteins exhibited a reduction step at -0.6 V (versus SCE), due to reduction of disulfide groups.

The same authors [98] have presented a method for the estimation of the number of electroactive disulfide bonds in proteins adsorbed on mercury. The developed approach was based on the assumption that electroactive disulfides are located in more hydrophobic regions of the protein molecule.

Analogous to the electrode behavior of cystine and cysteine, one may expect chemical reaction occurring between mercury and protein disulfide bonds. Honeychurch and Ridd [99] have proved the correctness of such reaction pathway, applying potentiometric stripping analysis to investigate

chemical oxidation of electrolytically reduced disulfide bonds.

Electroreduction of iron-free apoferrodoxins has been studied by Ikeda et al. [100]. They have proposed the following pathway for the reaction occurring at -0.6 V versus SCE:

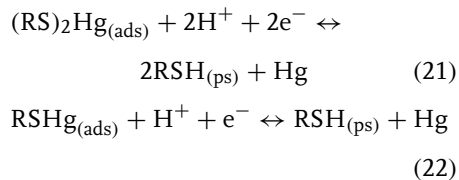
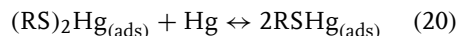
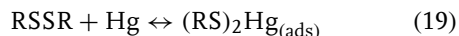


Also, different metallothioneins, a group of peptides and proteins, which play an important role in metabolism of metals in living organisms, have been studied [101, 102]. In the range of more anodic potentials, cyclic voltammograms recorded in the absence of metal ions were similar to those obtained for disulfide-containing proteins. The presence of metal ions in the solution shifted the voltammetric peaks, depending on the stability of the formed complex.

Egodage et al. [103] have described a novel application of monoclonal antibodies for the probing of conformation and orientation of the adsorbed protein using cytochrome $c(3)$ films on mercury electrode. Antibodies were utilized to confirm the presence of three conformationally distinct electrochemical forms of cytochrome dependent on the applied potential.

Chen and Abruña [104] have studied, using ac and dc cyclic voltammetry, interfacial interaction between the adsorbed porcine pancreatic phospholipase A_2 and mercury. The authors have proposed reaction mechanism based on the interaction of cystine residues (disulfide) with mercury. They have found that surface reactions are complex and that several factors influence their mechanism. Their results and observations agree with the reaction pathway postulated for the

cystine/cysteine system at mercury electrodes:



Subscript (ads) denotes adsorption via a thiolate linkage, while (ps) stands for a physisorbed and/or adsorbed state via different interactions. However, large dimensions of the studied molecules and their amphiphilic nature make the surface reaction mechanism more complex than in case of cystine/cysteine. Interfacial microstructure plays an important role in the determination of the surface behavior of the adsorbed molecules. From the study on the charge-transfer kinetics, the transfer coefficient α was calculated as slightly less than 0.50, while the rate constant (based on Laviron's derivations [105]) was of the order of 10^{-3} s^{-1} . The same authors [106] have shown earlier that the adsorption rate constant of porcine pancreatic phospholipase A₂ at mercury via one of its disulfide groups is of the order of 10^4 s^{-1} .

Yang and Zhu [107] have studied, applying several electrochemical methods and mercury electrodes, electrochemical behavior of pharmaceutically important dipeptide *captopril*. In acidic solution, one-electron transfer led to the formation of a univalent mercury–sulfur compound, which was strongly adsorbed at the electrode surface and gradually transformed into the divalent mercury–sulfur compound.

Nucleic bases, nucleotides, and thiolipids

Self-assembled surface layers of 6-thioguanine (6TG) on mercury electrode have been described and electrochemically characterized by Arias et al. [108, 109]. Several condensed phases of chemically adsorbed 6TG have been described. It has been found that under conditions of complete coverage, the films of chemisorbed molecules significantly inhibit mercury oxide formation at the electrode [108]. The self-assembled monolayer had no influence on the rate of outer-sphere processes, but strongly inhibited inner-sphere processes [109]. Arias et al. [110] have also given an electrochemical characterization of the mixed self-assembled monolayer comprising chemisorbed 6TG and physisorbed guanine molecules at a HMDE. The mixed monolayer was investigated, applying chronoamperometry, cyclic voltammetry, and phase-sensitive ac voltammetry. Compact packing of the molecules within the film was found. Ex situ measurements in the presence of dissolved oxygen have proved that the mixed monolayer was stable in the solution free of 6TG and guanine. Madueno et al. [111] have also studied adsorption and phase formation of 6TG on mercury electrode. At high potentials, the molecules were chemisorbed and were able to form a self-assembled monolayer. When the potential was scanned to more negative values, reductive desorption of the monolayer was observed. Cathodic voltammetric peaks, which are typical of a 2D condensed phase transition, divided the potential window into two regions: one, in which self-assembled monolayer was stable, and the second, in which a physisorbed state existed.

Some bioelectrochemical applications of self-assembled films on mercury (including among others, chlorophyll and

channel-forming gramicidin) have been described by Guidelli et al. [112].

Recently, Moncelli et al. [113] have described tethered bilayer lipid membranes self-assembled on Hg surface. In order to incorporate integral proteins in their functionally active state, metal-supported lipid bilayers must have a hydrophilic region interposed between the bilayer and the metal. An appropriate hydrophilic molecule must be terminated at one end with either sulfhydryl or disulfide group that anchors this hydrophilic spacer to the metal surface. The other end of the hydrophilic spacer may be covalently linked to the polar head of a phospholipid molecule, giving rise to a supramolecular “thiolipid”. Compared to gold, mercury has an advantage of providing a defect-free and fluid surface for the self-assembling spacer. The use of thiolipids allowed one to obtain particularly stable mercury-supported lipid bilayers.

Heyrovsky et al. [114] have shown that voltammetric behavior of isomeric end-labeled-SH deoxyoligonucleotides on HMDE depends on the dislocation of the electroactive components along the strand, as well as on their adsorptivity compared to the adsorptivity of other parts of the molecule.

Other sulfur-containing compounds Pardo et al. [115] have studied electrochemical oxidation of 2-mercaptopuridine N-oxide on Hg electrodes in aqueous solutions. It has been found that anionic form of this compound was oxidized to yield a radical. At low concentration, oxidation was reversible and the radical was strongly adsorbed. At high concentrations, this process was accompanied by diffusive reversible oxidation. Reorientation of the adsorbed 2-mercaptopuridine N-oxide molecules on Hg electrodes in the presence of Triton X-100 has been studied

by Mellado and Galvin [116]. Safavi and Gholivand [117] have shown that reduction of di(2-iminocyclopentylidine mercapto methyl) disulfide to its monomer in DMSO is not a simple two-electron transfer process, but it occurs via mercury complex formation. Calvente et al. [118] performed voltammetric study of the oxidation of 2-mercaptoethyl ether adsorbed on mercury. They have shown that the process involves one electron and is followed by fast reversible dimerization. Later, Gil et al. [119] (the same research group) performed voltammetric studies on surface redox processes perturbed by dimerization and adsorption of the products. They have theoretically predicted voltammetric behavior of 3-mercaptopropanol on mercury as a function of the solution pH. Mandler and coworkers [120] have studied the formation and organization of *self-assembled* monolayers of alkanethiols and omega-mercaptopcarboxylic acids on mercury. The measured charging currents and the observed charge-transfer process for the $\text{Ru}(\text{NH}_3)_5^{2+/3+}$ redox system have shown that adsorption of acids on mercury was followed by the formation of a densely packed array. Finally, Muskal and Mandler [121] have described the formation of self-assembled monolayers of omega-mercaptopalkanoic acids on a mercury electrode. It has been suggested that thiols are either physisorbed or chemisorbed, depending on the applied potential. The transition between these two states occurred via a faradaic process.

Specific conditions of the electron transfer reactions on Hg surfaces covered with sulfur compounds have been intensively investigated by Majda, Bilewicz, Słowiński, and coworkers [122–129]. The studies on electron tunneling involving Hg–Hg junction and mono- or bilayers of alkanethiolate trapped between small mercury

drops, were carried out. For example, in paper [123], it has been described that alkanethiol molecules of the chain length C-8–C-18 form densely packed, perpendicularly oriented monolayers on Hg in the course of a two-electron oxidation of Hg to mercuric thiolate. Exponential increase of the electron tunneling rate with the electrode potential, as well as exponential decay with the monolayer thickness was observed. For *n*-alkane-3-thiopropanamide bilayer junctions, tunneling currents were larger than those measured for the alkanethiolate junctions involving the same number of atoms [125]. This fact suggested that the presence of amide groups increases the electronic coupling in this type of systems. More recently, asymmetric electron transmission across the Hg–Au junction containing bilayers of alkanethiols of different chain lengths has been studied both experimentally and theoretically by Majda and coworkers [130]. Also, Sek et al. [131] have investigated electrochemically controlled Ag/Hg tunneling junction, with an Ag electrode covered with a self-assembled monolayer of *n*-alkanethiol.

Finally, Gugala et al. [132] have analyzed the effect of the concentration of the base electrolyte on adsorption of 1,1,3,3-tetramethyl-2-thiourea at mercury electrode. The Flory-Huggins and the Frumkin models were utilized for the quantitative analysis of the adsorption data.

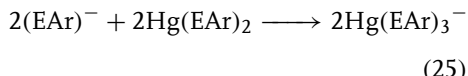
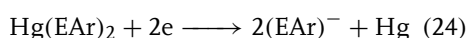
Organic selenides and tellurides Ludvik and Nygård et al. [133, 134] have studied electroreduction of aromatic diselenides and ditellurides (ArEEAr) at mercury electrodes. They have found that the charge-transfer process is preceded by a spontaneous heterogeneous reaction between these compounds and mercury,

according to the equation:

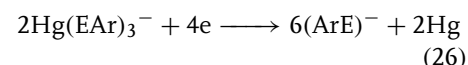


where E = Se or Te. $\text{Hg}(\text{ArE})_2$ is an analog of mercury thiophenolate, which is formed in case of the corresponding sulfur-containing compounds. On the basis of electrochemical and other experiments, the following mechanism has been proposed:

First wave:



Second wave:



This mechanism is analogous to that of mercury thiophenolate [135], but different from the reduction mechanism of aromatic disulfide(I).

Recently, Alvarez et al. [136] have studied interfacial and electrochemical behavior of diphenylselenide on HMDE in DMF-water mixture (3:7, v:v). Applying ac voltammetry and chronocoulometry, it has been shown that a multilayer film of chemisorbed diselenide of the progressively increasing thickness is formed.

24.6.3.3.2 Organic Nitrogen Compounds

Theoretical quantum-chemical study of pyridine adsorption at Hg electrode (including its charged surface) has been described by Man'ko et al. [137, 138]. An ab initio Hartree-Fock-Roothaan method has been employed. The electrode was modeled as a planar seven-atomic Hg-7 cluster. The deepest minimum of the total energy of the adsorption system was found for positive charge density and Py interacting with the metal through the lone electron

pair at the nitrogen atom. For a positive surface charge, vertical orientation of the adsorbate molecule was energetically favorable, whereas for the negatively charged surface, adsorption did not occur.

Formation of 2D phase accompanying electrochemical reduction of 4,4'-pyridine on mercury in the presence of iodide ions occurred via adsorption–nucleation and reorientation–nucleation mechanisms [139]. The first reduction step of Bpy on Hg in the presence of iodide as counterion in acidic medium at 15 °C involved the $\text{BpyH}_2^{2+}/\text{BpyH}^+$ couple and led to the formation of a 2D phase. The increased contribution of the reorientation term in the formation of the condensed phase was consistent with the increased adsorption strength of the anion to the electrode surface.

Afanasev et al. [140] have analyzed the literature data concerning adsorption of N-derivatives of morpholine and cyclohexylamine at the uncharged mercury electrode. They have also determined free energy of adsorption intrinsic to the interactions of organic molecules with mercury.

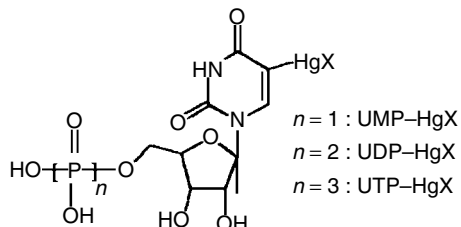
Higuera et al. [141] have studied reduction of 4-chloro-2,6-diisopropylamino-s-triazine in acidic media up to pH 5, applying dc differential pulse polarography. In the recorded voltammograms, two main reduction peaks were observed, with a prepeak at less negative potentials, and a postpeak at more negative potentials, what points to adsorption of the compound at the electrode. Two main peaks corresponded to two-electron reduction process.

Adsorption of L-histidine (His) has been studied [142] in aqueous KF and LiClO_4 solutions on mercury electrode and at air/solution interface. The strongest adsorption of His on Hg electrode was observed in solutions of $\text{pH} \geq 8$.

There are also several papers describing adsorption of quinoline. Sawamoto [143] have studied adsorption and reorientation of quinoline molecules at Hg electrodes by recording differential capacity-potential and differential capacity-time plots using the flow-injection method. Adsorption of quinoline was found reversible at any potential, with the possibility of reorientation of the molecules at the interface. Ozeki et al. [144] have studied adsorption, condensation, orientation, and reduction of quinoline molecules at pure Hg electrode from neutral and alkaline solutions, applying electrochemistry and Raman microprobe spectroscopy. The adsorbed quinoline molecules changed their orientation from the flat at $-0.1 \text{ V} > E > -0.3 \text{ V}$, to the upright at $E < -0.5 \text{ V}$. At potentials $-0.3 \text{ V} > E > -0.5 \text{ V}$, both orientations were observed. Later, Ozeki et al. [145] have extended the studies on reorientation of quinolinium ions at the Hg|acidic aqueous solution interface. For these conditions, the specific adsorption of quinoline was not observed.

Xanthine and xanthosine were investigated on HMDE, applying out-of-phase ac and dc voltammetries [74]. It has been shown that both compounds are strongly adsorbed and interact chemically. In the cathodic stripping process, one could determine both compounds at trace level. Naidu et al. [146] have performed polarographic studies to show that the product of anodic reaction (prewave) of potassium isobutyl xanthate is strongly adsorbed at the mercury electrode.

Cyclic voltammetry and in situ IRAS have been utilized in the studies on adsorption of heptyl viologen (HV) at mercury electrode [147]. A set of very sharp cathodic and anodic peaks formed at potentials more positive than the

Scheme 1

reduction wave was ascribed to the one-electron reaction in the adsorbed state. The areas corresponding to a single molecule adsorbed on the surface were estimated and equaled to 83 and 71 square Å for Ox and Red forms, respectively. In the potential region at the negative side of the spikelike peaks, the HV cation radicals formed a bilayer with bipirydine planes positioned parallel to the surface.

McGarvey et al. [148] have studied electrochemical and adsorption properties of lumiflavin (LF) (*7,8,10-trimethylbenzo[g]pteridine-2,4(3*H*,10*H*)-dione, C₁₃H₁₂N₄O₂)* at Hg electrode in buffer solution of pH 6, 7, and 8, applying cyclic voltammetry. It has been suggested that at low-coverage, LF molecules are adsorbed in the orientation parallel to the electrode surface, independently of the potential, while at higher coverage, concerted reorientations of LF monolayer occur as the potential is changed. For the extreme potentials: positive of ca –0.35 V and negative of –1.0 V, parallel configuration has been proposed. Between these two limits, two perpendicular orientations existed, ensuring the respective increase in attainable coverage. LF exhibited striking differences from flavin adenine dinucleotides (FAD), in spite of the presence of an isoalloxazine ring system – a common electrochemically active moiety present in both compounds.

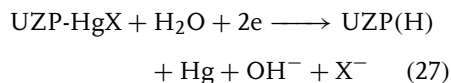
Komorsky-Lovric [149] has investigated adsorption and reduction of the plant

alkaloid berberine in electrolytes of various pH at mercury electrodes, applying ac polarography and square-wave voltammetry. Reduction of berberine appeared irreversible and occurred between –0.95 and –1.35 V, depending on the pH of the solution. The reduction product was canadine, which could not be oxidized at Hg electrodes. Both berberine and canadine formed condensed films at mercury electrodes, which limited the possibilities of analytical determination of berberine by adsorptive accumulation at the electrode. Since the condensed film of canadine was very stable, even at –0.5 V, it might prevent adsorption of berberine.

Wagner and Chambers [150] have published a study on electrochemical reduction of mono, di-, and triphosphate uridines (see Scheme 1) mercurated in 5-position of the pyrimidine ring in aqueous solutions. In 0.1 M KCl, these compounds exhibited two main electroreduction peaks in cyclic voltammograms in potential ranges –0.5 to –0.6 V and –0.8 to –0.9 V (versus SCE), respectively.

Voltammetric peaks, especially those of UDP and UTP, were sharper than those of the third compound, as they were adsorbed at the electrode surface. Coulometric studies (at –1.0 V, electroreduction) at mercury pool electrode (also glassy carbon) and analysis of the obtained products have shown that for all three compounds, the two-electron reductive cleavage of the carbon–mercury bond occurs. The electrode

process in the region of -1.0 V may be represented by the following reaction scheme:



where Z = M, D, or T signifies mono-, di-, or triphosphate nucleotide, respectively.

Philipp and Retter [151] have studied the formation of the first monolayer of adenine on mercury electrode in borate solutions. Applying potential-step method, they have proposed to explain the observed transients in terms of two-dimensional (2D) truncated progressive nucleation and constant growth of monolayer islands.

Fojta and Palecek [152] have described a supercoiled DNA-modified electrode as a highly sensitive tool for detection of DNA damage. The method is based on the measurement of an ac voltammetric peak, resulting from the scission of the single-strand in the covalently closed circular (supercoiled) DNA molecule. The method was found to be faster than gel electrophoresis. Recently, Fojta [153] has published a paper (including 188 references) reviewing applications of mercury electrodes in nucleic acid electrochemistry, emphasizing their role as sensitive analytical tools and probes of DNA structure. Generally, at mercury electrodes, nucleic acids produce (1) faradaic signals corresponding to redox processes of adenine, cytosine, and guanine residues, and (2) tensammetric signals referring to adsorption/desorption of polynucleotide chains at the electrode surface. Some of these signals appear to be highly sensitive to DNA structure. Mercury film and solid amalgam electrodes possess similar features as mercury drop electrodes in the analysis of nucleic acids.

24.6.3.3.3 Indicators and Dyes Abdel-Hamid [154] has studied adsorption of phenolphthalein at a HMDE in aqueous buffer solutions containing 10% v/v ethanol, applying cyclic voltammetry and double potential-step chronocoulometry. At $\text{pH} = 3.4$ and concentration at $5.1\text{ }\mu\text{mol dm}^{-3}$, phenolphthalein was adsorbed irreversibly and weakly, with triphenylmethane moiety positioned perpendicular to the electrode surface. For the solutions of $\text{pH} < 3.4$, adsorption of a neutral lactone form has been suggested. In alkaline solutions of $\text{pH} = 10.58$, no adsorption was reported. The formation and organization of a self-assembled monolayer of bromopyrogallol red in aqueous media at $\text{pH} 2.16$ at HMDE have been studied by El-Sagher [155]. Electroreduction process proceeded via an ECEC mechanism.

Constant current chronopotentiometry has been utilized by Honeychurch [156] to study reduction of methylene blue adsorbed at HMDE. The obtained results were interpreted in terms of a two consecutive electron transfers (EE) mechanism and the interfacial potential distribution model.

Adsorption and kinetics of electroreduction of safranine T in self-assembled phospholipid monolayer deposited on mercury have also been studied [157].

24.6.3.3.4 Vitamins and Antibiotics Gao et al. [158] have studied adsorptive voltammetric behavior of riboflavin tetrabutyrate (RT) on mercury electrodes and determined the rate constant of this process. In the presence of NaOH as the supporting electrolyte, riboflavin produced one pair of cathodic and anodic peaks, separated by 0.64 V . The adsorbed species was most probably a neutral molecule of RT of the maximum surface concentration of $5.42 \times 10^{-11}\text{ mol cm}^{-2}$. Adsorption of RT

was governed by the Frumkin model: adsorption constant was 4.6×10^5 ; attractive interaction parameter equaled 1.10; and standard Gibbs free energy of adsorption was $-32.30 \text{ kJ mol}^{-1}$. Sawamoto [159] has investigated the adsorption–desorption phenomena of vitamins at a mercury electrode by recording differential capacity versus time plots, applying flow-injection method and other techniques. Adsorption of vitamins was found to be irreversible.

Gomez et al. [160] have studied specific adsorption of potassium penicillin G (salt K) on Hg electrode from electrocapillary and capacity measurements. The Frumkin isotherm has been found applicable to the quantitative description of the data; repulsive interaction parameter equaled -3.5 and standard free Gibbs energy of adsorption at the zero charge was $-38.6 \text{ kJ mol}^{-1}$. ΔG_{ads}^0 depended linearly on the surface charge. Possible orientations of antibiotic molecules on the electrode surface were also discussed. Novotny [161] has studied adsorption of polyether-antibiotic monensin applying voltammetry at new miniaturized and compressible mercury electrodes. Hason et al. [162] have used several electrochemical methods to study electrochemical behavior of echinomycin and its interaction with single-stranded (ss) and double-stranded (ds) DNA at HMDE. It has been found from the capacity measurements that echinomycin gives a pseudocapacitance peak at -0.53 V . However, this peak was observed only for ds-DNA complex with echinomycin. Accordingly, by performing capacity measurements, one could distinguish both forms of DNA.

24.6.3.3.5 Enzymes and Coenzymes Electrochemical behavior of bovine erythrocyte superoxide dismutase adsorbed on Hg electrode has been studied by Qian

et al. [163]. Adsorption of this compound was described in terms of the Langmuir model; adsorption constant equaled 8.96×10^4 and Gibbs free energy was $-28.2 \text{ kJ mol}^{-1}$. Mei et al. [164] have studied adsorption of copper-zinc superoxide dismutase on mercury electrodes. Applying double potential-step chronocoulometry, it was found that dismutase formed a monolayer at the electrode. Wittstock and Emons [165] have carried out voltammetric studies on ubiquinone adsorption at mercury electrodes. Adsorption isotherms of ubiquinones UQ(4), UQ(6), UQ(9), and UQ(10) were determined using two independent voltammetric techniques at the stationary mercury/solution interface. While the redox behavior was essentially the same for all homologs investigated, the molar Gibbs free energy of adsorption increased steadily with the number of isoprenic units in the series from UQ(4) to UQ(10).

24.6.3.3.6 Other Organic Compounds

Turowska et al. [166] have studied adsorption of *m*-hydroxybenzoic acid in aqueous solutions on the dropping mercury electrode and determined the surface tension, differential capacity, and the potential of zero charge for this system.

Gugala et al. [167] have studied adsorption of butyl acetate at mercury electrode in 1, 0.5, and 0.1 M NaClO₄. The zero charge potential values at the streaming mercury electrode were found to shift to positive values with the increasing ester concentration, which indicated the hydrophilic part of the molecules to be directed toward the solution.

Muszalska et al. [168] have performed a comparative study on adsorption of dodecanol and cholesterol in ethylene glycol at Hg electrode and at the free surface of ethylene glycol phase. In

terms of the Frumkin model, significant differences in the quantitative adsorption characteristics of these two compounds were found and discussed.

In Ref. 169, some peculiarities associated with adsorption of alkyne peroxides from DMF–water solutions onto the mercury electrode in the presence of tetraethylammonium cations have been described. Polarography and electrocapillary measurements were employed as the experimental techniques. It has been shown that interfacial activity of these peroxides was determined by the species generated as a result of associative interactions between peroxides and DMF and tetraethylammonium cations.

Recently, Japaridze et al. [170] have investigated adsorption of some aromatic compounds, including naphthalene, naphthonitrile, naphthylamine, anthracene, and phenanthrene at the mercury electrode|ethylene glycol solution interface. The analysis of the differential capacity data obtained at the HMDE has revealed that adsorption of the above-mentioned compounds obeys the Frumkin model, with attractive interactions of the particles in the adsorption layer. The results for ethylene glycol were compared with those for other nonaqueous solvents and their role in determining the adsorption mode was discussed.

Damaskin and Baturina [171] have studied unstable states during coumarin adsorption on mercury electrode. These instabilities were attributed to the nonequilibrium phase transitions in the adsorption layer, during which the orientation of coumarin molecules changed at the electrode surface.

Adsorption of glycosidic surfactants at Hg electrode was studied by means of differential capacitance measurements

(tensammetry) [172, 173]. Monosaccharidic surfactants formed a hemimicelle monolayer, while for disaccharidic compounds, the formation of a micellar multilayer throughout the electrical double layer was suggested.

Adsorption of a condensed 1-hydroxyadamantane layer at the Hg electrode/(Na₂SO₄ or NaF) solution interface has been studied as a function of temperature by Stenina et al. [174]. Later, Stenina et al. [175] have determined adsorption parameters and their temperature dependence for a two-dimensional condensation of adamantanol-1 at a mercury electrode in Na₂SO₄ solutions. They have also studied coadsorption of halide (F[−], Cl[−], Br[−]) anions and 1-adamantanone molecules on Hg electrode [176]. More recently, Stenina et al. [177] have described a new type of an adsorption layer comprising organic molecules of a cage structure condensed at the electrode/solution interface. This phenomenon was discovered for adsorption of cubane derivatives at mercury electrode.

Moncelli et al. [178] have investigated monolayers and multilayers of chlorophyll on Hg electrode and described a novel experimental technique to investigate such thin films. Upon irradiation of the chlorophyll α -coated Hg electrode with an appropriate light, photocurrents generated by the chlorophyll aggregates were measured under short-circuit conditions. Electrochemical behavior of chlorophyll α films adsorbed at HMDE applying two different procedures has been investigated later in darkness by the same research group, who applied double potential-step chronocoulometry and cyclic voltammetry [179].

Lindholm-Sethson et al. [180] have investigated dioleyl phosphatidylcholine

(DOPC) monolayer-coated mercury electrodes in contact with different electrolytes, using electrochemical impedance spectroscopy and a multivariate analysis of impedance data. Rueda et al. [181] have analyzed impedance spectra of DOPC-coated mercury electrodes.

Mixed adsorption Saba [182] has described the properties of the mixed adsorption layer of *m*-toluidyne/polyethyleneglycols at Hg electrode in 1 M NaClO₄. The virial and the Frumkin models were used for the quantitative analysis of the adsorption data. Mixed adsorption layer of *p*-toluidyne and polyethyleneglycol (of average molecular masses of 400 or 10⁴ u) at mercury electrode in 1 M NaClO₄ has also been studied by Saba [183]. The author determined, from the experimental data, the parameters of the Frumkin and the virial isotherms. Similar studies have been carried out [184] with thiourea instead of *p*-toluidine. Saba et al. [185] have studied further the properties of the mixed polyethylene glycals (molecular weights 400 and 10⁴ u) – iodide ions adsorption layers at mercury electrode in NaClO₄ solutions.

Formation of a mixed layer of butan-1-ol and *o*-toluidine on Hg electrode has also been studied by Sienko et al. [186].

24.6.3.3.7 Analytical Aspects of Adsorption of Organic Compounds This chapter briefly summarizes representative examples of adsorption of various organic compounds on Hg surface, which have analytical applications.

Duan et al. [187] have studied adsorptive and electrochemical behavior of estradiol valerate at a static mercury electrode using cyclic voltammetry and chronocoulometry. A sensitive and

selective adsorptive stripping square-wave voltammetric method for the determination of estradiol valerate has been developed, providing detection limit of 1.1 × 10⁻⁸ M.

Kamal et al. [188] have described adsorptive stripping voltammetric analysis of 2,3,6-tri(2'-pyridyl)-1,3,5-triazine at mercury electrode, based on preliminary adsorption and accumulation of the determined compound.

Ceftazidime was accumulated at HMDE at pH 9.5 and potential of +0.1 V in the form of the adsorbed mercury salt. The reduction peak potential at -0.7 V was used in cathodic stripping voltammetric determination of this compound [189].

Cathodic stripping voltammetric determination of nanomolar level of two anthraquinone-based chlorotriazine dyes at HMDE has also been described [190].

Kizek et al. [191] have involved catalytic reaction at mercury electrode to electrochemical determination of metallothioneins. This determination was based on catalytic processes occurring at very negative potentials and accompanied by catalytic evolution (SH group) of hydrogen.

Electrode mechanism and analytical determination of cocaine and its metabolites, such as benzoylecgonine, ecgonine, and ecgonine methyl ester have been studied [192] at HMDE. These compounds were adsorbed at the electrode. Adsorption of benzoylecgonine was stronger than that of cocaine. Consequently, adsorptive stripping voltammetric method for the determination of cocaine was based on reduction of benzoylecgonine.

Fogg et al. [193] have presented a preliminary study on the indirect cathodic stripping voltammetric determination of 2-mercaptopbenzothiazole based on the accumulation of its mercury, copper(I),

and nickel(II) salts or complexes. This method, utilizing mercury, was susceptible to the interference from copper(II) and large amounts of nickel(I), and thus determination of 2-mercaptopbenzothiazole was less reliable. The same group of workers [194] have developed an indirect cathodic-stripping voltammetric method for the determination of trimercapto-*s*-triazine at sub-ppb levels in standard solutions. The analyte was accumulated and determined at pH 9.0 in the form of a salt, which was reduced at -0.47 V .

Application of adsorptive stripping analysis to the determination of nucleic acids at mercury electrodes has also been reported [195]. Tomschik et al. [196] have studied reduction and oxidation of peptide nucleic acid and DNA at mercury and carbon electrodes. The authors have utilized cyclic and square-wave voltammetries to study reduction and oxidation signals of single-stranded peptide nucleic acid and DNA decamers and pentadecamers.

Farias et al. [197] have presented cathodic adsorptive stripping voltammetry of guanine in the presence of copper at static mercury electrode. Cyclic voltammetry was also employed to characterize the interfacial and redox mechanisms.

Finally, 6-benzylaminopurine has been determined [198] by applying adsorptive stripping voltammetry.

At the end of this section focused on analytical problems, it should be mentioned that Thoming et al. [199] have evidenced that electrodialysis allows one to remove heavy metals from soils. During this process, the metals, including mercury, are transferred under the applied electric field to the pore water in either dissolved form or attached to colloids. This method is especially appropriate for the purification of fine-grained soils.

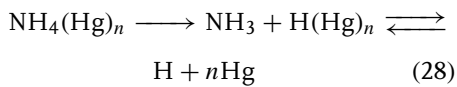
24.6.4

Ammonium and Quaternary-substituted Ammonium Amalgams

Although the properties of metal amalgams and intermetallic compounds in mercury have been investigating for many years and are already well recognized, the nature of ammonium amalgam, as well as quaternary ammonium amalgams, still remains a subject of controversy.

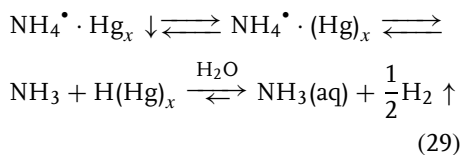
Ammonium amalgam was first reported in 1805 by Seebeck, who electrolyzed ammonium carbonate solution at mercury cathode. A concise review of the concepts on the structure of ammonium amalgam is given, for example, in Ref. 200.

Solubility of ammonium radical in Hg at 20°C reaches $1.55 \times 10^{-2}\text{ M}$ [201]. It has been found that redox behavior of ammonium amalgam is characterized by two equilibrium potential values, depending on the conditions of its preparation and aging [202, 203]. The more negative value of -1.7 V is typical of fresh ammonium amalgam and its concentration of $6 \times 10^{-4}\text{ M}$, which is below the solubility limit and is ascribed to the $\text{NH}_4^{\bullet}(\text{Hg})/\text{NH}_4^+$ (H_2O) couple. Saturated ammonium amalgam is characterized by less negative potential of -1.2 V , or with both values. This less negative value is associated with the $\text{H}(\text{Hg})/\text{H}_3\text{O}^+$ redox couple formed presumably in the decomposition reaction:



The studies on composition and instability of ammonium amalgam were continued later by the same group of researchers [204, 205].

Gumiński and Galus [206] critically evaluated the literature data concerning interaction of ammonium radical with mercury. It has been indicated [207] that NH_4^\bullet radical (as well as its alkyl derivatives) forms homogeneous amalgams. Significant inconsistencies of the literature data on NH_4^\bullet solubility in mercury have been emphasized. A possible role of impurities acting as decomposition catalysts has been suggested to explain these inconsistencies. The swelling phenomenon accompanying decomposition of ammonium amalgam has been described by the sequence of equilibria:



It is noteworthy that at 233 and 203 K, a $\text{NH}_4^\bullet\text{-Hg}$ solid phase has been identified [208].

Barański and Lu [209] have carried out, applying microelectrodes, voltammetric studies on ammonium amalgam in propylene carbonate solutions at room temperatures. The sweep rates up to 80 V s^{-1} were appropriate for the analysis of the formation kinetics of this compound. Experimental and numerical simulation results have shown that ammonium amalgam was formed via fast charge-transfer process and its first-order decomposition was characterized by the rate constant of about 0.6 s^{-1} . Diffusion coefficient of NH_4^\bullet radical in mercury was estimated to be about $1.8 \times 10^{-5} \text{ cm}^2 \text{ s}^{-1}$. The formal potential of $\text{NH}_4^+(\text{aq})/\text{NH}_4(\text{Hg})$ couple was determined as -1.723 V (SHE).

Kovaleva and Gladyshev [210] have proposed classification of hydrogen-containing amalgams. Ammonium amalgam ($\text{NH}_4^\bullet\text{-Hg}_n$) has been included in

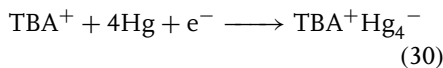
the group of binary amalgams of pseudometals (together with N_2H_5 , N_2H_6 , and $(\text{CH}_3)_n\text{NH}_4^{+n}; n = 1-4$ radicals). Formation of hydrogen amalgam has also been discussed.

Gumiński [211] has evaluated the equilibrium phase diagrams for the Hg-N system. For the ammonium amalgam, it has been indicated that Hg has the unique property of metallic alloying with the ammonium radical NH_4^\bullet . Lehman [212] has reported the formation of an ordered solid resulting from electroreduction of NH_4^+ on Hg, with the Hg-NH_4^\bullet layers seeming to be electrically conducting. Furthermore, Rich and Travers [213] have observed that the melting point of Hg was decreased to -45.61°C upon addition of 5.34 mol% NH_4^\bullet (a phenomenon that was analogous to the behavior of alkali metals in Hg). However, Gumiński [211] has found that this result disagrees with the solubility data of NH_4^\bullet in Hg at higher temperatures [206]. The formation of Hg-azide compound has also been discussed in this paper [211].

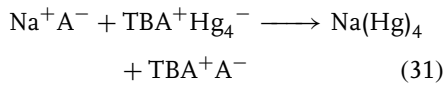
A more recent attempt to explain the structure of ammonium amalgam has been undertaken by Kariv-Miller et al. [200]. They have studied electrochemical reaction of NH_4^+ on mercury at temperatures below the freezing point of mercury, applying potential-step and linear sweep techniques. Under these conditions, "ammonium amalgam" was a solid phase stable for at least several minutes, the deposition of which at the mercury surface involved nucleation and growth steps. It has been concluded that such a phase belongs to the group of $\text{R}_4\text{N}^\bullet$ metals. Within this phase, electrons are bound by mercury in the form of negative clusters, and NH_4^+ ions act as counterions. The main role in the stability and electrochemical reversibility of ammonium amalgam has

been ascribed to the liquid–solid transition of mercury [200].

For *quaternary ammonium amalgams* it has been found that substitution of ammonium hydrogen atoms with alkyl groups increases amalgam stability [200, 214–216]. Already in 1986, Bard and coworkers [217] have suggested that “*quaternary ammonium amalgams*” are ammonium salts of anionic mercury species, of the type of Zintl ion salts and empirical formula $R_4N^+Hg_4^-$. These authors have studied the formation and stoichiometry of the compounds formed in the course of electroreduction of quaternary ammonium salts at mercury electrode, and also regeneration of R_4N^+ from the product upon chemical oxidation. Electrolysis of tetrabutylammonium hexafluorophosphate ($TBA^+PF_6^-$) solution in acetonitrile at $-20^\circ C$ was carried out at the potential of -4.5 V imposed on Hg (versus Ag wire quasi-reference electrode). Hg surface was covered with a black layer and finely divided particles of the product were dispersed in the solution. These phenomena have been ascribed to the reduction of tetrabutylammonium cation, which proceeded according to the equation:



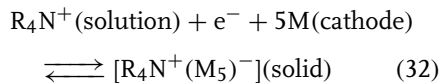
In the studies on the regeneration mechanism, addition of NaA (where $A = F^-$ or PF_6^-) caused black species to disappear, according to the reaction pathway:



The obtained product was identical (in the NMR spectrum) to the initial TBA^+ species. The latter reaction has

been suggested for easier synthesis of quaternary ammonium salts $R_4N^+A^-$.

Later, Kariv-Miller et al. have studied the properties of “tetraalkylammonium amalgams” both *in situ*, applying electrochemical techniques [218], and *ex situ*, applying solid-state techniques [219, 220]. It has been concluded that the solid products, which belong to R_4N metals, are formed in chemically and electrochemically reversible process:



Krasensky and Studnickova [221] have prepared quaternary ammonium amalgam via electroreduction of tetraethylammonium tetrafluoroborate in the aqueous medium at the room temperature. At the applied voltage of -2.8 to -2.4 V versus sodium saturated calomel electrode (SSCE) hydrogen evolution occurred simultaneously. Composition of the black precipitate formed was found to be $Et_4N \cdot Hg_x$, where $x = 2.9 \pm 0.8$.

Finally, Kovaleva and Gladyshev [222] have suggested that in the first step of electrolytic generation of either ammonium or quaternary ammonium amalgams, the amalgam of the corresponding hydride ($R^+[Hg_nH]^-$, $n = 10–12$) is formed, which is transformed to the RHg_n amalgam at more negative potentials.

To conclude, it should be said that in spite of numerous studies, the structure of ammonium amalgams has not yet been unequivocally established.

References

1. P. K. Wrona, Z. Galus, in *Encyclopedia of Electrochemistry of the Elements* (Ed.: A. J. Bard), Marcel Dekker, New York and Basel, 1982, Vol. IX-A, and references cited therein.

2. S. Trasatti, E.J. Lust, in *Modern Aspects of Electrochemistry* (Eds.: R.E. White, J.O.M. Bockris, B.E. Conway), Kluwer Academic/Plenum Publishers, New York, 1999, Vol. 33, and references cited therein.
3. D. C. Grahame, *J. Am. Chem. Soc.* **1954**, *76*, 4819.
4. S. Trasatti, *Pure Appl. Chem.* **1986**, *58*, 955.
5. J. J. O'Dea, M. Ciszkowska, R. A. Osteryoung, *Electroanalysis* **1996**, *8*, 742.
6. M. S. L. Brito, L. Angnes, C. M. A. Brett et al., *J. Electroanal. Chem.* **1999**, *468*, 150.
7. L. Becucci, M. R. Moncelli, R. Guidelli, *J. Electroanal. Chem.* **1996**, *413*, 187.
8. R. Jurczakowski, M. Orlik, *J. Electroanal. Chem.* **2004**, *562*, 205.
9. K. Arihara, F. Kitamura, T. Ohsaka et al., *J. Electroanal. Chem.* **2002**, *518*, 139.
10. R. R. Nazmutdinov, S. V. Borisevich, *Russ. J. Electrochem.* **1999**, *35*, 1091.
11. B. B. Damaskin, B. M. Grafov, *Russ. J. Electrochem.* **1998**, *34*, 967.
12. B. Eck, E. Spohr, *Electrochim. Acta* **1997**, *42*, 2779.
13. T. Cecchi, P. Passamonti, F. Pucciarelli, *Collect. Czech. Chem. Commun.* **2002**, *67*, 439.
14. A. J. Montheo, E. R. Gonzalez, *Electrochim. Acta* **1996**, *41*, 2631.
15. G. Fuchs, L. Kišova, J. Komenda et al., *J. Electroanal. Chem.* **1997**, *428*, 73.
16. L. L. Kišova, J. Komenda, I. Mayr et al., *J. Electroanal. Chem.* **2004**, *565*, 367.
17. G. Salié, K. Bartels, *J. Electroanal. Chem.* **1988**, *245*, 21.
18. G. Salié, *J. Electroanal. Chem.* **1989**, *259*, 315.
19. K. Bartels, G. Salié, *Z. Phys. Chem.* **1990**, *271*, 739.
20. G. Salié, K. Bartels, *Electrochim. Acta* **1994**, *39*, 1057.
21. M. Shay, S. Bruckenstein, *Langmuir* **1989**, *5*, 280.
22. J. Li, H. D. Abruña, *J. Phys. Chem. B* **1997**, *101*, 244.
23. J. Li, H. D. Abruña, *J. Phys. Chem. B* **1997**, *101*, 2907.
24. E. Herrero, H. D. Abruña, *Langmuir* **1997**, *13*, 4446.
25. E. Herrero, H. D. Abruña, *J. Phys. Chem. B* **1998**, *102*, 444.
26. J. Li, E. Herrero, H. D. Abruña, *Colloids Surf., A – Physicochem. Eng. Aspects* **1998**, *134*, 113.
27. H. D. Abruña, J. M. Feliu, J. D. Brock et al., *Electrochim. Acta* **1998**, *43*, 2899.
28. E. Herrero, L. J. Buller, H. D. Abruña, *Chem. Rev.* **2001**, *101*, 1897.
29. J. Inukai, S. Sugita, K. Itaya, *J. Electroanal. Chem.* **1996**, *403*, 159.
30. S. Abaci, L. Zhang, C. Shannon, *J. Electroanal. Chem.* **2004**, *571*, 169.
31. S. Armalis, E. Kubiliene, *Chem. Anal.* **2001**, *46*, 715.
32. V. Daujotis, C. Klingenberg, A. Teiserskiene, *Anal. Chim. Acta* **2000**, *419*, 243.
33. N. Vinokur, B. Miller, Y. Avyigal et al., *J. Electrochim. Soc.* **1999**, *146*, 125.
34. M. Jasinski, P. Grundler, G. U. Flechsig et al., *Electroanalysis* **2001**, *13*, 34.
35. M. Jasinski, A. Kirbs, M. Schmehl et al., *Electrochim. Commun.* **1999**, *1*, 26.
36. L. Novotny, M. Heyrovsky, *Croat. Chem. Acta* **1997**, *70*, 151.
37. M. Lovric, F. Scholz, *Electroanalysis* **1997**, *15*, 1189.
38. A. M. Bond, W. Miao, T. D. Smith et al., *Anal. Chim. Acta* **1999**, *396*, 203.
39. S. B. Khoo, S. X. Guo, *Electroanalysis* **2002**, *14*, 813.
40. L. H. Wang, S. J. Tsai, *Anal. Chim. Acta* **2001**, *441*, 107.
41. E. G. Camarero, J. Ramiro, E. Fatas, *Sol. Energy Mater. Sol. Cells* **1995**, *39*, 27.
42. U. Hasse, K. Wagner, F. Scholz, *Solid State Electrochem.* **2004**, *8*, 842.
43. E. Vasca, T. Caruso, M. Iuliano et al., *Ann. Chim.-Rome* **2000**, *90*, 181.
44. A. Safavi, M. B. Gholivand, *Can. J. Chem.* **1996**, *74*, 95.
45. E. A. Ponomarev, A. G. Krivenko, L. N. Sviridova et al., *Russ. J. Electrochem.* **2001**, *37*, 435.
46. E. M. Andrade, F. V. Molina, *J. Adhes. Sci. Technol.* **2001**, *15*, 1503.
47. A.G. Anastopoulos, P. Hadjiloizou, D. Nikoletou, *Langmuir* **2000**, *16*, 7789.
48. S. Ramirez, G. J. Gordillo, D. Posadas, *J. Electroanal. Chem.* **1996**, *407*, 219.
49. S. Ramirez, G. J. Gordillo, D. Posadas, *J. Electroanal. Chem.* **1997**, *431*, 171.
50. S. Sander, G. Henze, *Electroanalysis* **1996**, *8*, 253.
51. S. Sander, T. Navratil, P. Basova et al., *Electroanalysis* **2002**, *14*, 1133.
52. M. Łobacz, M. Orlik, J. Stroka et al., *Electroanalysis* **2002**, *14*, 583.

53. E. V. Stenina, O. A. Baturina, L. N. Sviridova et al., *Russ. J. Electrochem.* **2002**, *38*, 602.
54. L. Novotny, T. Navratil, S. Sander et al., *Electroanalysis* **2003**, *15*, 1687.
55. S. Kariuki, H. D. Dewald, *Electrochim. Acta* **1998**, *43*, 701.
56. J. F. Wu, T. Okajima, K. Tokuda et al., *Electrochemistry* **2000**, *68*, 277.
57. S. Uesugi, T. Katsumata, F. Matsumoto et al., *Electrochemistry* **2001**, *69*, 681.
58. F. Matsumoto, S. Uesugi, N. Koura et al., *J. Electroanal. Chem.* **2003**, *549*, 71.
59. A. Jaworski, Z. Stojek, J. G. Osteryoung, *J. Electroanal. Chem.* **2003**, *558*, 141.
60. N. A. Bell, W. Clegg, J. R. Creighton et al., *Inorg. Chim. Acta* **2000**, *303*, 12.
61. P. Stepnicka, I. Cisarova, J. Podlaha et al., *J. Organomet. Chem.* **1999**, *582*, 319.
62. V. W. W. Yam, K. K. Cheung, *J. Chem. Soc., Dalton Trans.* **2000**, 3658.
63. K. Siegel, Ü. Mauer, H. Keis, *Electrochim. Acta* **1997**, *42*, 2955.
64. A. Sousa-Pedrares, J. Romero, J. A. Garcia-Vazquez et al., *Dalton Trans.* **2003**, *7*, 1379.
65. J. Wang, J. Y. Wang, B. M. Tian et al., *Anal. Chem.* **1997**, *69*, 1657.
66. J. Krista, M. Kopanica, L. Novotny, *Anal. Chim. Acta* **1999**, *386*, 221.
67. L. Novotny, J. Krista, *Electroanalysis* **1998**, *10*, 965.
68. A. Safavi, N. Maleki, H. R. Shahbaazi, *Anal. Chim. Acta* **2004**, *503*, 213.
69. N. Spataru, F. G. Banica, *Analyst* **2001**, *126*, 1907.
70. J. Skopalova, K. Lemr, M. Kotoucek et al., *Fresenius' J. Anal. Chem.* **2001**, *370*, 963.
71. I. C. S. Fraga, A. K. Ohara, P. A. M. Farias, *Anal. Lett.* **2001**, *34*, 125.
72. I. C. S. Fraga, A. K. Ohara, P. A. M. Farias, *Anal. Lett.* **2000**, *33*, 905.
73. F. G. Banica, N. Spataru, T. Spataru, *Rev. Roum. Chim.* **1998**, *43*, 77.
74. Y. M. Temerk, M. M. Kamal, G. A. W. Ahmed et al., *Anal. Sci.* **2003**, *19*, 1115.
75. A. Radi, *Chem. Anal. (Warsaw)* **2003**, *48*, 273.
76. V. D. Ivanov, M. M. Kaplun, *J. Anal. Chem.* **1997**, *52*, 321.
77. K. S. Yoo, S. B. Woo, J. Y. Jyoung, *Bull. Korean Chem. Soc.* **2003**, *24*, 27.
78. M. A. Baldo, S. Daniele, G. A. Mazzocchin, *Anal. Chim. Acta* **1997**, *340*, 77.
79. Z. Q. Zhang, H. Liu, H. Zhang et al., *Anal. Chim. Acta* **1996**, *333*, 119.
80. W. S. Huang, C. H. Yang, S. H. Zhang, *Anal. Bioanal. Chem.* **2002**, *374*, 998.
81. W. S. Huang, S. H. Zhang, *Anal. Sci.* **2002**, *18*, 187.
82. V. Mirceski, B. Jordanoski, M. Avramov-Ivic, *J. Serb. Chem. Soc.* **1998**, *63*, 719.
83. A. M. Bond, A. T. Casey, J. R. Thackeray, *J. Electrochem. Soc.* **1973**, *120*, 1502.
84. A. M. Bond, A. T. Casey, J. R. Thackeray, *J. Electroanal. Chem.* **1973**, *48*, 71.
85. A. M. Bond, R. Colton, J. Harvey et al., *J. Electroanal. Chem.* **1997**, *426*, 145.
86. A. M. Bond, R. Colton, A. F. Hollenkamp et al., *J. Am. Chem. Soc.* **1987**, *109*, 1969.
87. A. M. Bond, A. F. Hollenkamp, R. Colton et al., *Inorg. Chim. Acta* **1990**, *168*, 233.
88. A. M. Bond, R. Colton, A. F. Hollenkamp et al., *Inorg. Chem.* **1991**, *30*, 192.
89. R. von Wandruska, X. Yuan, *Talanta* **1993**, *40*, 37.
90. M. Heyrovsky, P. Mader, V. Vesela et al., *J. Electroanal. Chem.* **1994**, *369*, 53.
91. S. Vavricka, M. Heyrovsky, *J. Electroanal. Chem.* **1994**, *375*, 371.
92. M. Heyrovsky, P. Mader, S. Vavricka et al., *J. Electroanal. Chem.* **1997**, *430*, 103.
93. M. Heyrovsky, S. Vavricka, *Bioelectrochem. Bioenerg.* **1999**, *48*, 43.
94. M. J. Honeychurch, *Bioelectrochem. Bioenerg.* **1997**, *44*, 13.
95. B. A. Kuznetsov, G. P. Shumakovich, N. M. Mestechkina, *J. Electroanal. Chem.* **1998**, *248*, 387.
96. F. Scheller, M. Jänen, H. J. Prümke, *Biopolymers* **1975**, *14*, 1553.
97. M. J. Honeychurch, M. J. Ridd, *J. Electroanal. Chem.* **1996**, *418*, 185.
98. M. J. Honeychurch, M. J. Ridd, *Bioelectrochem. Bioenerg.* **1996**, *41*, 115.
99. M. J. Honeychurch, M. J. Ridd, *Electroanalysis* **1996**, *8*, 654.
100. T. Ikeda, K. Toriyama, M. Senda, *Bull. Chem. Soc. Jpn.* **1979**, *52*, 1937.
101. R. W. Olafson, R. G. Sim, *Anal. Biochem.* **1979**, *100*, 343.
102. R. W. Olafson, *Bioelectrochem. Bioenerg.* **1988**, *19*, 111.
103. K. L. Egodage, B. S. da Silva, G. S. Wilson, *J. Am. Chem. Soc.* **1997**, *119*, 5295.
104. S. W. Chen, H. D. Abruña, *J. Phys. Chem. B* **1997**, *101*, 167.

105. E. Lavoron, *J. Electroanal. Chem.* **1979**, *101*, 19.
106. S. Chen, H. D. Abruña, *J. Phys. Chem.* **1995**, *99*, 17235.
107. Z. Yang, S. M. Zhu, *Chinese J. Anal. Chem.* **1999**, *27*, 1431.
108. Z. G. Arias, J. L. M. Alvarez, J. M. L. Fonseca, *J. Colloid Interf. Sci.* **2002**, *250*, 295.
109. Z. G. Arias, J. L. M. Alvarez, J. M. L. Fonseca, *Electroanalysis* **2004**, *16*, 1044.
110. Z. G. Arias, J. L. M. Alvarez, J. M. L. Fonseca, *J. Colloid Interf. Sci.* **2004**, *276*, 132.
111. R. Madueno, T. Pineda, J. M. Sevilla et al., *J. Electroanal. Chem.* **2004**, *565*, 301.
112. R. Guidelli, L. Becucci, A. Dolfi et al., *Solid State Ion* **2002**, *150*, 13.
113. M. R. Moncelli, L. Becucci, S. M. Schiller, *Bioelectrochem* **2004**, *63*, 161.
114. R. Kizek, L. Havran, T. Kubícarova et al., *Talanta* **2002**, *56*, 915.
115. I. Pardo, M. Angulo, R. M. Galvin et al., *Electrochim. Acta* **1996**, *41*, 133.
116. J. M. R. Mellado, R. M. Galvin, *Electrochim. Acta* **1996**, *41*, 1479.
117. A. Safavi, M. B. Gholivand, *Bull. Electrochem* **1998**, *14*, 218.
118. J. J. Calvete, M. L. Gil, R. Andreu et al., *Langmuir* **1999**, *15*, 1480.
119. M. L. Gil, R. Andreu, J. J. Calvete et al., *J. Electrochem. Soc.* **2002**, *149*, E45.
120. N. Muskal, I. Turyan, D. Mandler, *J. Electroanal. Chem.* **1996**, *409*, 131.
121. N. Muskal, D. Mandler, *Electrochim. Acta* **1999**, *45*, 537.
122. K. Słowiński, R.V. Chamberlain, R. Bilewicz et al., *J. Am. Chem. Soc.* **1996**, *118*, 4709.
123. K. Słowiński, R. V. Chamberlain, C. J. Miller et al., *J. Am. Chem. Soc.* **1997**, *119*, 11910.
124. S. Sek, R. Bilewicz, *J. Incl. Phenom. Macrocycl. Chem.* **1999**, *35*, 55.
125. K. Słowiński, H. K. Y. Fong, M. Majda, *J. Am. Chem. Soc.* **1999**, *121*, 7257.
126. K. Słowiński, K. U. Słowiński, M. Majda, *J. Phys. Chem. B* **1999**, *103*, 8544.
127. K. Słowiński, M. Majda, *J. Electroanal. Chem.* **2000**, *491*, 139.
128. R. L. York, P. T. Nguyen, K. Słowiński, *J. Am. Chem. Soc.* **2003**, *125*, 5948.
129. R. L. York, K. Słowiński, *J. Electroanal. Chem.* **2003**, *550–551*, 327.
130. M. Galperin, A. Nitza, S. Sek et al., *J. Electroanal. Chem.* **2003**, *550*, 37.
131. S. Sek, R. Bilewicz, K. Słowiński, *Chem. Commun.* **2004**, 404.
132. D. Gugala, Z. Fekner, D. Sienko et al., *Electrochim. Acta* **2004**, *49*, 2227.
133. J. Ludvik, B. Nygård, *Electrochim. Acta* **1996**, *41*, 1661.
134. J. Ludvik, *Phosphorus, Sulphur Silicon* **1998**, *136–138*, 413.
135. B. Person, B. Nygård, *J. Electroanal. Chem.* **1974**, *56*, 373.
136. J. L. M. Alvarez, A. G. Calzon, J. M. L. Fonseca, *Electrochim. Acta* **2004**, *49*, 1389.
137. L. Y. Man'ko, G. Y. Vyaseleva, V. P. Barabanov, *Russ. J. Electrochem.* **2000**, *36*, 916.
138. L. Y. Man'ko, V. P. Barabanov, *Russ. J. Phys. Chem.* **2001**, *75*, 943.
139. L. Gómez, J. J. Ruiz, L. Yamacho et al., *J. Electroanal. Chem.* **2004**, *564*, 17.
140. B. N. Afanasev, Y. P. Akulova, G. S. Aleksandrova et al., *Russ. J. Electrochem.* **1997**, *33*, 700.
141. M. J. Higuera, M. R. Montoya, J. M. R. Melaldo, *Electrochim. Commun.* **1999**, *1*, 184.
142. R. Słojkowska, M. Jurkiewicz-Herbich, *Polish J. Chem.* **1999**, *73*, 527.
143. H. Sawamoto, *J. Electroanal. Chem.* **1997**, *432*, 153.
144. T. Ozeki, M. Odziemkowski, D. E. Irish, *J. Solution Chem.* **2000**, *29*, 861.
145. T. Ozeki, K. Yokoi, M. Odziemkowski et al., *J. Electroanal. Chem.* **2001**, *505*, 142.
146. N. V. S. Naidu, G. Suresh, B. Prasad et al., *Anal. Sci.* **2004**, *20*, 399.
147. K. Arihara, F. Kitamura, T. Ohsaka et al., *J. Electroanal. Chem.* **2000**, *488*, 117.
148. C. McGarvey, S. Beck, S. Quach et al., *J. Electroanal. Chem.* **1998**, *456*, 71.
149. S. Komorsky-Lovric, *Electroanalysis* **2000**, *12*, 599.
150. G. J. Wagner, J. Q. Chambers, *Langmuir* **1997**, *13*, 3529.
151. R. Philipp, U. Retter, *Z. Phys. Chem.,-Int. J. Res. Phys. Chem. Chem. Phys.* **1996**, *196*, 125.
152. M. Fojta, E. Palecek, *Anal. Chim. Acta* **1997**, *342*, 1.
153. M. Fojta, *Collect. Czech. Chem. Commun.* **2004**, *69*, 715.
154. R. Abdel-Hamid, *Monatsh. Chem.* **1998**, *129*, 817.
155. H. M. El-Sagher, *Monatsh. Chem.* **1999**, *130*, 295.
156. M. J. Honeychurch, *J. Electroanal. Chem.* **1998**, *445*, 63.

157. R. Herrero, M. R. Moncelli, L. Becucci, R. Guidelli, *J. Electroanal. Chem.* **1997**, *425*, 87.
158. H. Y. Gao, Y. L. Zhou, Y. H. Zeng, *Chinese J. Anal. Chem.* **2001**, *29*, 667.
159. H. Sawamoto, *Bunseki Kagaku* **2002**, *51*, 1159.
160. M. M. Gomez, A. Arevalillo, J. M. Vara, *Electrochim. Acta* **1996**, *41*, 291.
161. L. Novotny, *Fresenius' J. Anal. Chem.* **1999**, *363*, 55.
162. S. Hason, J. Dvorak, F. Jelen et al., *Talanta* **2002**, *56*, 905.
163. W. Qian, Q. G. Meng, Q. H. Luo et al., *Chem. J. Chinese Univ-Chinese* **1996**, *17*, 687.
164. G. Q. Mei, W. Qian, Q. H. Luo et al., *Chinese J. Inorg. Chem.* **2003**, *19*, 774.
165. G. Wittstock, H. Emons, *Electroanalysis* **1997**, *9*, 449.
166. M. Turowska, D. Kaźmierczak, T. Błaszczyk, *Polish J. Chem.* **1997**, *71*, 221.
167. D. Gugala, D. Sienko, J. Saba, *Collect. Czech. Chem. Commun.* **2001**, *66*, 411.
168. A. Muszalska, M. Jurkiewicz-Herlich, J. Jasstrębska, *J. Chem. Soc., Faraday Trans.* **1996**, *92*, 3859.
169. K. R. Gorbachevska, N. L. Shvarchovska, M. M. Yatsyshyn et al., *Adsorpt. Sci. Technol.* **1996**, *14*, 229.
170. J. I. Japaridze, S. S. Japaridze, I. A. Gurgenidze, *J. Electroanal. Chem.* **2003**, *552*, 59.
171. B. B. Damaskin, O. A. Baturina, *Russ. J. Electrochem.* **2002**, *38*, 1141.
172. C. Mousty, C. Maurice, G. Mousset et al., *J. Colloid Interf. Sci.* **1996**, *184*, 671.
173. C. Mousty, C. Maurice, G. Mousset et al., *J. Colloid Interf. Sci.* **1997**, *188*, 238.
174. F. V. Stenina, L. N. Sviridova, L. O. Askinadze, *Russ. J. Electrochem.* **1997**, *33*, 1220.
175. F. V. Stenina, L. N. Sviridova, O. A. Baturina et al., *Russ. J. Electrochem.* **1999**, *35*, 1313.
176. E. V. Stenina, O. A. Baturina, L. N. Sviridova et al., *Russ. J. Electrochem.* **2001**, *37*, 931.
177. E. V. Stenina, L. N. Sviridova, A. G. Krivenko et al., *Russ. J. Electrochem.* **2003**, *39*, 1017.
178. M. R. Moncelli, L. Becucci, A. Dolfi et al., *Bioelectrochem* **2002**, *56*, 159.
179. F. T. Buoninsegni, L. Becucci, M. R. Moncelli et al., *J. Electroanal. Chem.* **2003**, *550–551*, 229.
180. B. Lindholm-Sethson, P. Geladi, A. Nelson, *Anal. Chim. Acta* **2001**, *446*, 121.
181. M. Rueda, I. Navarro, G. Ramirez et al., *J. Electroanal. Chem.* **1998**, *454*, 155.
182. J. Saba, *Gazz. Chim. Ital.* **1997**, *127*, 53.
183. J. Saba, *Monatsh. Chem.* **1997**, *128*, 1.
184. J. Saba, *Electrochim. Acta* **1996**, *41*, 297.
185. J. Saba, G. Dalmata, J. Nieszporek et al., *Croat. Chem. Acta* **2000**, *73*, 643.
186. D. Sienko, D. Gugala, J. Nieszporek et al., *Collect. Czech. Chem. Commun.* **2002**, *67*, 1579.
187. J. P. Duan, G. N. Chen, M. L. Chen et al., *Analyst* **1999**, *124*, 1651.
188. M. M. Kamal, A. Z. A. Zuhri, A. A. O. Nasser, *Fresenius Z. Anal. Chem.* **1996**, *356*, 500.
189. V. S. Ferreira, M. V. B. Zanoni, A. G. Fogg, *Anal. Chim. Acta* **1998**, *367*, 255.
190. M. V. B. Zanoni, A. G. Fogg, J. Barek et al., *Anal. Chim. Acta* **1997**, *349*, 101.
191. R. Kizek, J. Vacek, L. Trnkova et al., *Chem. Listy* **2004**, *98*, 166.
192. V. Pavlova, V. Mirceski, S. Komorsky-Lovric et al., *Anal. Chim. Acta* **2004**, *512*, 49.
193. A. G. Fogg, R. Ismail, R. Ahmad et al., *Analyst* **1996**, *121*, 1877.
194. A. G. Fogg, R. Ismail, A. R. H. M. Yusoff et al., *Talanta* **1997**, *44*, 497.
195. J. Wang, D. H. Grant, M. Ozsoz et al., *Anal. Chim. Acta* **1997**, *349*, 77.
196. M. Tomschik, F. Jelen, L. Havran et al., *J. Electroanal. Chem.* **1999**, *476*, 71.
197. P. A. M. Farias, A. D. R. Wagener, M. B. R. Bastos et al., *Talanta* **2003**, *61*, 829.
198. D. Tarkowska, M. Kotoucek, K. Dolezal, *Collect. Czech. Chem. Commun.* **2003**, *68*, 1076.
199. J. Thoming, B. K. Kliem, L. M. Ottosen, *Sci. Total Environ.* **2000**, *261*, 137.
200. E. Kariv-Miller, G. K. Lehman, V. Svetličić, *J. Electroanal. Chem.* **1997**, *423*, 87.
201. A. G. Stromberg, A. V. Konkova, *Zh. Fiz. Khim.* **1968**, *42*, 2063. (in Russian).
202. V. P. Gladyshev, T. V. Syroeshkina, *Sovr. Probl. Polar. z Nakapl* **1975**, *136*. (in Russian).
203. T. V. Syroeshkina, M. M. Raimzhanova, *Vsesoyuznoe Soveshchanie po Polarografi* **1978**, *196*. (in Russian).

204. T. V. Syroeshkina, M. M. Raimzhanova, V. P. Gladyshev, *Izv. Vyssh. Uchebn. Zav.* **1978**, 21, 933. (in Russian).
205. V. P. Gladyshev, A. I. Zebreva, T. V. Syroeshkina et al., *Izv. Vyssh. Uchebn. Zav., Khim. Khim. Tekhnol.* **1978**, 21, 1474. (in Russian).
206. C. Gumiński, Z. Galus, in *Solubility Data Series, Vol. 51 – Intermetallic Compounds in Mercury* (Eds.: J. G. Osteryoung, M. M. Schreiner, C. Gumiński et al.), Pergamon Press, Oxford, New York, Seoul, Tokyo, 1992.
207. *Gmelins Handbuch der Anorganischen Chemie*, 34, Tl. A, Lfg. 2, Verlag Chemie, Weinheim, 1962, p. 1006. (see also Ref. [206]).
208. N. C. Baenziger, J. W. Nielsen, E. J. Duwell, U.S. At. Ener. Comm. Rep., COO-126, 1957.
209. A. Barański, W. Lu, *J. Electroanal. Chem.* **1993**, 355, 205.
210. S. V. Kovaleva, V. P. Gladyshev, *Zh. Obshch. Khim.* **1996**, 66, 1761. (in Russian).
211. C. Gumiński, *J. Phase Equilib.* **1997**, 18, 101.
212. (a) G. K. Lehman, *Electroorganic Reductions at High Negative Potentials and NH₄-Hg Electroformation*, Ph. D. thesis, University of Minnesota, 1989, Minneapolis, MN; (b) *Dissert. Abstr. Intern.* **1990**, 50, 2930.
213. E. M. Rich, M. W. Travers, *J. Chem. Soc.* **1906**, 89, 872.
214. J. K. S. Wan, *J. Chem. Educ.* **1968**, 45, 40.
215. H. N. McCoy, W. C. Moore, *J. Am. Chem. Soc.* **1911**, 33, 273.
216. E. Kassab, E. M. Evleth, *J. Am. Chem. Soc.* **1987**, 109, 1653.
217. E. Garcia, A. H. Cowley, A. J. Bard, *J. Am. Chem. Soc.* **1986**, 108, 6082.
218. E. Kariv-Miller, V. V. Svetličić, P. D. Christian, *J. Electrochem. Soc.* **1995**, 142, 3386.
219. E. Kariv-Miller, P. D. Christian, V. V. Svetličić, *Langmuir* **1994**, 10, 3338.
220. E. Kariv-Miller, P. D. Christian, V. V. Svetličić, *Langmuir* **1995**, 11, 1817.
221. S. Krasensky, M. Studnickova, *Collect. Czech. Chem. Commun.* **1994**, 59, 2375.
222. S. V. Kovaleva, V. P. Gladyshev, *Zh. Obshch. Khim.* **1997**, 67, 342. (in Russian).

Part C:
Electrochemistry of Copper

*David B. Rorabacher and Ronald R. Schroeder
 Department of Chemistry, Wayne State University, Detroit, Minnesota, USA*

24.7
Electrochemistry of Copper

24.7.1	Introduction	993
24.7.1.1	Oxidation States of Copper	993
24.7.1.2	Reference Standards for Potential Values in Nonaqueous Solvent Studies	993
24.7.1.3	Methods Used for Potential Measurements	996
24.7.1.4	Potentials Involving Solvated Copper Species	996
24.7.2	Electrochemical Considerations for Copper(II/I) Complexes Involving Multidentate Ligands	997
24.7.2.1	Trends in Potentials of Copper(II/I) Complexes with Multidentate Ligands	998
24.7.2.2	Dependence of Copper(II/I) Potentials on Ligand Properties	999
24.7.2.3	Correlation of Potentials to Copper(II) Complex Stability Constants	1022
24.7.3	Mechanistic Aspects of Copper(II/I) Electron Transfer	1023
24.7.3.1	Ligand Conformational Change	1025
24.7.3.2	Complex Dissociation/Formation	1027
24.7.3.3	Interconversion of Ternary and Binary Complexes	1028
24.7.3.4	Interconversion of 1 : 2 and 1 : 1 Complexes	1029
24.7.3.5	Dimeric/Monomeric Species	1031
24.7.3.6	Other Phenomena Affecting Electrochemical Behavior	1031
24.7.3.6.1	Ligand Oxidation or Reduction	1031
24.7.3.6.2	Electroplating of Copper	1032
24.7.4	Biological Copper Systems	1032
24.7.5	Other Copper(II/I) Systems	1034
24.7.5.1	Unidentate Ligand Complexes	1035
24.7.5.1.1	Hydroxide Complexes	1035
24.7.5.1.2	Halide Complexes	1036
24.7.5.1.3	Cyanide and Thiocyanate Complexes	1036

24.7.5.1.4	Ammonia Complexes	1037
24.7.5.1.5	Complexes with Acetate and Other Common Brønsted Bases	1037
24.7.5.1.6	Noncomplexing Buffer Systems	1037
24.7.5.2	Binuclear Complexes	1038
24.7.6	Copper(III/II) Systems	1039
	References	1041

24.7.1 Introduction

Elemental copper is the least easily oxidized of the first-row transition metals. This largely accounts for the extensive use of copper electrodeposition for both industrial applications and analytical purposes. Since the electrochemistry of elemental copper, including electrodeposition, electroplating, and electrowinning, was treated extensively in the previous edition of this encyclopedia [1] and detailed descriptions are to be found elsewhere [2–4], it is not covered in this treatise.

The current chapter focuses on the electrochemistry of the ionic forms of copper in solution, starting with the potentials of various copper species. This includes the effect of coordination geometry, donor atoms, and solvent upon the electrochemical potentials of copper redox couples, specifically Cu(II/I). This is followed by a discussion of the various types of coupled chemical reactions that may contribute to the observed Cu(II/I) electrochemical behavior and the characteristics that may be used to distinguish the presence of each of these mechanisms. The chapter concludes with brief discussions of the electrochemical properties of copper proteins, unidentate and binuclear complexes,

and Cu(III/II) systems. A recent review on the kinetics and mechanisms of homogeneous electron transfer involving copper can be consulted as a supplement to this chapter [5].

24.7.1.1 Oxidation States of Copper

Copper is one of the few elements for which four successive oxidation states are accessible: 0, +1, +2, and +3. As a result, copper is an important redox catalyst, having the ability to catalyze many reactions in which one reacting partner undergoes a one-electron transfer while the other reactant undergoes a two- or three-electron transfer. Among metal ions that exhibit several stable oxidation states, copper is unique in that each successive state prefers a different coordination geometry. The change in geometry that accompanies electron transfer in copper systems has a significant impact upon the electrochemistry in terms of both thermodynamics and kinetics as noted in the sections that follow.

24.7.1.2 Reference Standards for Potential Values in Nonaqueous Solvent Studies

Electrochemical studies on copper systems are frequently conducted in nonaqueous solvents, principally for the purpose of improving the solubility of complexing ligands of interest. The largest number of such studies have been reported in

acetonitrile, not only because of its ability to solubilize organic ligands, but also because of its reasonably high dielectric constant (38.8 at 20 °C) and its ability to stabilize Cu(I).

Both in acetonitrile and in other non-aqueous solvents, a major problem arises in terms of the manner in which the potential values are reported by various investigators. Koepp, Wendt, and Strehlow [6] noted that hydrogen ion is the poorest reference material on which to base nonaqueous potentials because of the extreme differences in its solvation in various solvents. On the basis of an investigation of the solvent dependence of 18 redox couples, these investigators concluded that ferrocene/ferrocenium ion (i.e. bis(cyclopentadienyl)iron(III/II), abbreviated as Fc^+/Fc^0) and/or cobaltocene/cobalticenium ion represented optimal potential reference materials for nonaqueous studies. On the basis of their minimal charge (+1, 0) and their symmetry (treated as though they were roughly spherical), the potentials of these two redox couples are presumed to be relatively independent of solvent properties.

In recognition of the work of Strehlow and coworkers, Gagne, Koval, and Lisenksy [7] recommended that ferrocene be used as an internal standard for all potential measurements in nonaqueous solvents and that its aqueous potential of +0.400 V relative to the standard hydrogen electrode (SHE) could be considered to represent a consistent correction factor in referencing all nonaqueous potential measurements to aqueous SHE. This recommendation is somewhat in disagreement with the conclusion of Strehlow and coworkers who, on the basis of theoretical considerations, suggested that the potential of the ferrocene couple in acetonitrile should be

about +0.34 V relative to the aqueous SHE [8].

Subsequently, the International Union of Pure and Applied Chemistry (IUPAC) has recommended that all potential values in nonaqueous solvents be referenced directly to the potential of the ferrocene/ferrocenium couple or the bis(biphenyl)chromium(1/0) couple (as either an internal or external reference) without attempting to "correct" such potentials to aqueous SHE [9]. Despite this recommendation, many investigators continue to reference their nonaqueous potential measurements to the reference electrode used in their measurements such as Ag/AgCl, Ag/Ag⁺ (0.01 M), or the saturated calomel electrode (SCE). Even those workers who utilize ferrocene as a reference standard frequently report their result only in terms of values that are "corrected" to SHE without explaining the magnitude of the correction applied. This latter approach would not present a serious problem if the size of this "correction" were consistent. However, as noted above, Strehlow's and Gagne's recommendations are in disagreement as to whether the appropriate potential for ferrocene in acetonitrile should be +0.34 V or +0.40 V relative to SHE. And this disagreement pales in comparison with the subsequent conclusions of three other research groups that the potential of ferrocene in acetonitrile is +0.38 to +0.40 V relative to SCE, depending upon the anion present, which suggests that the appropriate correction for converting ferrocene potentials in acetonitrile to values referenced to aqueous SHE should be +0.62 to +0.64 V. (The magnitude of the correction cited here is based on the conclusion that the potential of ferrocene in acetonitrile relative to aqueous SCE is 0.38–0.40 V. Since the recognized potential of SCE is +0.241 V versus SHE,

the overall “corrected” potential of ferrocene is +0.64 V versus SHE) [10].

Pavlishchuk and Addison [11] have discussed the foregoing discrepancies and made careful measurements of the reference electrodes commonly utilized by investigators in measuring potentials in acetonitrile. The correction to be applied for converting a potential measured against a reference electrode, E_{ref} , to the ferrocene standard, E_{Fc} , can be expressed as:

$$E_{\text{Fc}} = E_{\text{ref}} - \delta \quad (1)$$

The δ values applicable in acetonitrile, as determined by Pavlishchuk and Addison, are as follows (TEAP = tetraethylammonium perchlorate):

Ag/0.1 M AgNO ₃ ,	0.1 M TEAP ("ANE1"):	$\delta = 0.037$ V
Ag/0.01 M AgNO ₃ ,	0.1 M TEAP ("ANE2"):	$\delta = 0.087$ V
Ag/0.001 M AgNO ₃ ,	0.1 M TEAP ("ANE3"):	$\delta = 0.133$ V
Ag/0.01 M AgClO ₄ ,	0.1 M TEAP ("APE"):	$\delta = 0.083$ V
Saturated calomel, aqueous (SCE):	$\delta = 0.380$ V	
Saturated sodium chloride, aqueous (SSCE):	$\delta = 0.384$ V	
Standard hydrogen, aqueous:	$\delta = 0.624$ V	

It should be noted that Lay and coworkers [12] have made a comparative study of the electrochemical behavior of ferrocene, 1,2,3,4,5-pentamethylferrocene and decamethylferrocene in 29 solvents and have concluded that increasing substitution on ferrocene reduces the solvent dependence of the ferrocene potential. Accordingly, they recommend that decamethylferrocene be adopted as a preferred reference standard for electrochemical measurements in nonaqueous

solvents. Although this recommendation has not yet been officially adopted, their data show that the redox potential of decamethylferrocene is −506 mV relative to ferrocene in acetonitrile so that potentials referenced to either one of these standards can be readily interconverted. The relative potentials for the latter two compounds in 28 other solvents are also included in their paper.

In the current treatise, we have adopted the IUPAC recommendation in citing nonaqueous potentials relative to the value obtained for ferrocene under identical conditions wherever possible. In those instances where investigators have utilized ferrocene as a reference material but have only reported the potential values after “correction” to SHE, we have “uncorrected” the values back to the ferrocene standard whenever the magnitude of the correction applied was evident in the pertinent publication. In those cases where the magnitude of the correction is not indicated or where values are reported only with respect to the reference electrode used, we have tabulated the potential values as reported by the specific investigators and have indicated in parentheses the reference standard to which these values purportedly apply. The corrections suggested by Pavlishchuk and Addison (above) may be applied by the reader, although it is not always clear whether the conditions used warrant this. However, values for related systems reported by the same workers against a common standard can at least be compared with each other.

In the accompanying tables, all potentials are given to the same number of decimal places as were reported in the original publications. The third decimal place, when reported, is often of questionable value as is evident when potential

values for a system have been determined by more than one set of workers.

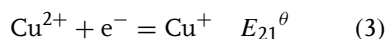
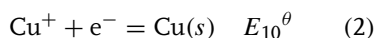
24.7.1.3 Methods Used for Potential Measurements

Redox potentials for copper systems have been based on a variety of approaches including (i) redox titrations, (ii) potentiostatic methods involving spectral monitoring, (iii) cyclic voltammetry (CV), and (iv) pulsed methods. Of these, CV measurements are by far the most prevalent. No effort has been made in this treatise to identify the method used for a specific reported potential value unless the method itself appeared to be pertinent.

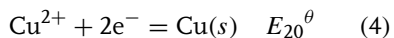
24.7.1.4 Potentials Involving Solvated Copper Species

No information is available on the solvated Cu^{3+} ion since the known solution chemistry for this oxidation state is limited

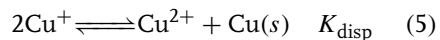
to complexes involving hard donor atoms. Thus, in the absence of complexing agents, the electrochemistry of solvated copper can be expressed by two one-electron processes:



The values of E_{10}^θ and E_{21}^θ for the solvated metal ion and the overall value of E_{20}^θ for a two-electron transfer,



have been determined in water, methanol, 80% methanol–20% water (w/w) and acetonitrile as listed in Table 1. It will be noted that, in water, methanol, and their mixtures, $E_{10}^\theta > E_{21}^\theta$, so that solvated Cu(I) is unstable with respect to disproportionation:



Tab. 1 Potential values for solvated copper ion in various solvents (all values in V versus aqueous SHE)

Solvent	E_{10}^θ	E_{21}^θ	E_{20}^θ	K_{disp}	References
Water	0.520	0.159	0.340	1.7×10^6	13
Methanol	0.64	0.40	0.513	1.1×10^4	14
80% methanol ^a	0.58	0.20	0.390 ^b	2×10^6	15
Acetonitrile	-0.344	0.133	-0.11	8.7×10^{-9}	16
Propylene carbonate ^c			0.157 ^c		17

^a Values are intended to be representative for the mixed solvent containing 80% methanol–20% water (by weight).

^b S. Minc, J. Jastrzebska, *Roczn. Chem.* **1954**, *28*, 519–520. In reporting the E_{20}^θ value for copper in various methanol–water mixtures, these authors did not specify whether percent methanol referred to weight, volume, or mole per cent. Although the potential values are claimed to be referenced to aqueous SHE, the actual internal reference electrode used was not specified and no mention was made of a correction for the liquid junction potential. Since the actual liquid junction potential for aqueous reference electrodes in methanol–water mixtures was not made until a later date [$E_j \approx -0.152$ V for 80% methanol (w/w): M. Alfenaar, C. L. deLigny, *Recl. Trav. Chim. Pays-Bas* **1967**, *86*, 1185–1190], it is presumed, in fact, that no correction was made for the liquid junction.

^c For propylene carbonate, the E_{20}^θ value was measured against a saturated calomel electrode for which a value of 0.2375 V versus SHE was assumed in correcting the measured value to an SHE standard.

Although the values of K_{disp} are relatively large in water and in methanol, a finite amount of Cu(I) exists in any Cu(II) solution that is in contact with metallic copper. In fact, the molecularity associated with K_{disp} dictates that the fraction of copper in solution in the form of Cu(I) increases as the total concentration of solvated copper ion decreases. Thus, at micromolar levels in water, for example, the two oxidation states can be maintained in essentially equal amounts. In acetonitrile, the equilibrium for reaction 5 lies far to the left so that solvated Cu(I) is readily generated by placing copper metal in contact with a Cu(II) solution (conproportionation). As a consequence, the Cu(I) salt, $[\text{Cu}(\text{CH}_3\text{CN})_4]\text{ClO}_4$, is easily prepared [18] and is temporally stable.

Due to the elongation of bonds arising from Jahn-Teller distortion, the aquated Cu(II) ion, $\text{Cu}(\text{H}_2\text{O})_6^{2+}$ is exceptionally labile with regard to inner-sphere substitution [20, 21] (A more recent neutron diffraction study has indicated that hydrated Cu(II) ion may be five coordinate. However, this latter conclusion may simply result from the asymmetric stretch of the axial waters such that, on average, the copper appears to have only five solvent bonds despite the fact that six waters may be interacting with the central copper atom.) [19] The d^{10} Cu^+ ion is also expected to be substitutionally labile in parallel to the lability of isoelectronic $\text{Zn}(\text{H}_2\text{O})_6^{2+}$ [21, 22]. Thus, other ligands can rapidly substitute into the inner-coordination sphere of both $\text{Cu}^{\text{I}}(\text{H}_2\text{O})_4^+$ and $\text{Cu}^{\text{II}}(\text{H}_2\text{O})_6^{2+}$. As a result, potential μ -bridging ligands such as Cl^- , Br^- , and I^- (at even very low concentrations) may affect the transfer of electrons between copper ions and the electrode surface in solution. For this reason, such potentially

bridging ligands should be rigorously excluded from solution when making careful potential measurements.

24.7.2

Electrochemical Considerations for Copper(II/I) Complexes Involving Multidentate Ligands

Most of the electrochemical studies currently appearing in the literature involve copper complexes with multidentate ligands. (Unidentate ligands will be considered later.) As noted earlier, each oxidation state of copper prefers a different coordination geometry. Like Ni(II), the d^8 Cu(III) state prefers a regular octahedral geometry, which generally reverts to a square planar complex, since this oxidation state is encountered in complexes exhibiting a strong ligand field. Because of the fact that definitive data on this oxidation state are relatively sparse, Cu(III) is discussed only briefly at the end of this treatise. The d^9 Cu(II) ion tends to form six-coordinate complexes that are subject to Jahn-Teller distortion in which the coordinate bonds along one axis (usually designated as the z -axis) elongate to form a distorted octahedral (tetragonal) complex. Several cases of six-coordinate Cu(II) complexes have been reported in which one of the coordinate axes appears to be shorter than the other two, resulting in a “compressed” Jahn-Teller distortion. However, such complexes actually represent a situation where two of the axes are participating in Jahn-Teller inversion, whereas the third axis is not, so that the latter axis appears to be shorter on average. The only Cu(II) compound for which Jahn-Teller compression has been rigorously established is KAlCuF_6 . [23, 24]. This is a fluxional effect, however, and, if all donor atoms are

identical, all three axes rapidly interconvert (dynamic Jahn-Teller effect) [25, 26].

In many Cu(II) complexes, one of the axial donor atoms is missing, resulting in a square pyramidal coordination geometry in which the copper atom is slightly displaced above the xy plane in the direction of the remaining axial donor atom [27–32]. Distortions arising from ligand constraints may result in complexes that are more nearly trigonal bipyramidal. The d^{10} Cu(I) ion, having no net crystal field stabilization energy, does not exhibit an electronic preference for a specific coordination geometry. In fact, several different geometries have been observed in crystal structures, including linear, trigonal, and tetrahedral [33]; even five-coordinate Cu(I) complexes have been reported [34, 35]. However, the balance between the energy gained from coordinate bond formation and the repulsion between the coordinated donor atoms commonly results in a tetrahedral geometry for Cu(I) complexes [23].

The influence of geometric constraints imposed by coordinated ligands in combination with the differences in donor atom preferences among the various oxidation states makes it possible to exert a considerable amount of control over copper redox potentials. In fact, the influence of ligand structure upon the electrochemical properties of copper is one of the most common themes in copper studies.

24.7.2.1 Trends in Potentials of Copper(II/I) Complexes with Multidentate Ligands

The standard potential values for solvated copper, as cited in Table 1, represent thermodynamic values in terms of activities. In practice, relatively high ionic strengths (≥ 0.01 M) are used in most electrochemical measurements so that the

experimental values are generally obtained as concentration potentials:

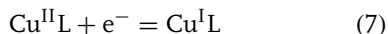
$$E = E_{21(\text{solv})}^{\theta'} - \frac{RT}{nF} \ln \frac{[\text{Cu}^+]}{[\text{Cu}^{2+}]}$$

where

$$E_{21(\text{solv})}^{\theta'} = E_{21}^{\theta} - \frac{RT}{nF} \ln \frac{\gamma_{\text{Cu}}^+}{\gamma_{\text{Cu}}^{2+}} \quad (6)$$

where γ_{Cu}^+ and γ_{Cu}^{2+} represent the relevant activity coefficients. For aquated Cu(II/I) at 25 °C and an ionic strength of 0.10 M, $E_{21(\text{solv})}^{\theta'} \approx 0.13$ V (versus SHE) [51].

In the presence of complexing agents, the potential values are usually reported in terms of the concentrations of the complexed species rather than the concentrations of the solvated copper ions:



$$E = E_{21}^{\theta'} - \frac{RT}{nF} \ln \frac{[\text{Cu}^{\text{I}}\text{L}]}{[\text{Cu}^{\text{II}}\text{L}]} \quad (8)$$

If the fraction of uncomplexed copper ion is relatively small in both oxidation states, the relationship between the concentration potential, $E_{21}^{\theta'}$, for any Cu(II/I) complex system and that for the solvated Cu(II/I) couple, can be represented as:

$$E_{21}^{\theta'} = E_{21(\text{solv})}^{\theta'} + \frac{RT}{nF} \ln \frac{K_{\text{Cu}^{\text{I}}\text{L}}}{K_{\text{Cu}^{\text{II}}\text{L}}} \quad (9)$$

Equation (9) is frequently used to estimate the value of one of the stability constants, $K_{\text{Cu}^{\text{II}}\text{L}}$ or $K_{\text{Cu}^{\text{I}}\text{L}}$, when the other stability constant has been determined experimentally.

Reported values of $E_{21}^{\theta'}$ for various Cu(II/I) complexes in aqueous solution range from approximately –0.6 to +0.9 V (versus SHE). Most of the potential values for Cu(II/I) currently reported in

the literature were obtained from CV determinations. The average potential of the cathodic (E_{pc}) and anodic (E_{pa}) peaks, designated as $E_{1/2}$, is assumed to approximate the value of $E_{21}^{\theta'}$ if the CV's are reasonably reversible (i.e. $\Delta E_p = E_{pa} - E_{pc} \approx 0.057$ V) [94]. The reported potential values for approximately 200 Cu^{II/I}/L complexes are listed in Table 2. The systems included in this compilation are those for which $\Delta E_p \leq 0.090$ V [94]. The complexes are grouped according to the nature of the ligand, starting with polypyridyl ligands (2,2'-bipyridine; 1,10-phenanthroline; and substituted derivatives), followed by cyclic, acyclic, tripodal, and branched ligands.

To aid in identifying the significant features of the ligands listed in Table 2, trivial names have been assigned using the following conventions:

Cyclic ligands: Square brackets designate that the ligand is cyclic and the number within the brackets is the number of atoms in the macrocyclic ring. Saturated macrocycles are designated by “ane”, while, for unsaturated ligands, “ene” is used preceded by a prefix to identify the number of double bonds (e.g. diene or tetraene). The donor atoms are then identified. Substituents attached to the macrocycle are indicated by either a prefix or suffix.

Acyclic ligands: Attached substituents are generally indicated by a prefix followed by a series of numbers representing the sequential number of carbon atoms connecting the donor atoms followed by the sequential identities of the donor atoms.

Tripodal ligands: A Greek “ τ ” is used to identify a tripodal ligand having a nitrogen bridgehead. This is followed by a series of three numbers that identify the number of atoms (generally carbons) connecting the

bridgehead nitrogen to the coordinating donor atoms in the three legs. Finally, abbreviations are used to indicate the nature of the appended groups.

The abbreviated prefixes and suffixes used in the foregoing trivial names are as follows:

bpy = bipyridine

bzim = benzimidazole

cyhx = cyclohexane

cypt = cyclopentane

Et = ethyl

en = ethylenediamine

imid = imidazole

Me = methyl

phen = phenanthroline

prz = pyrazine

py = pyridine

quin = quinoline

tmen = trimethylenediamine

Φ = phenyl

The structures of all ligands listed in Table 2 are illustrated in Fig. 1.

In selecting complexes for inclusion in Table 2, preference has been given to those systems that involve a series of related compounds since these serve to show the effects of changes in structure and donor atoms upon the resulting Cu(II/I) potential values. Systems in which the separation of the peak potentials (ΔE_p) exceeded 100 mV are not included.

24.7.2.2 Dependence of Copper(II/I) Potentials on Ligand Properties

For complexing agents containing several amine nitrogen donor atoms, the Cu(II/I) potential tends to be so negative in aqueous solution that accurate measurements are difficult to obtain. Such measurements are generally more accessible when using acetonitrile as the solvent. For example,

Tab. 2 Potential values for mononuclear copper(II/I) redox couples involving various multidentate ligands in commonly used solvents (all values are presumed to be for 25 °C, $\mu = 0.1 \text{ M}$, except as noted)

Complexed ligand ^a	Potential (V versus references indicated) ^b			References
	H ₂ O V versus SHE	CH ₃ CN V versus reference cited	Other, solvent V versus reference cited	
<i>Polypyridyl and polyimino ligands (unsaturated nitrogen donor atoms)</i>				
1:2 (<i>Bis</i>) complexes				
LAA = bipy	0.120	-0.20 (A1) ^c		36, 37 ^k
LAB = 6, 6'-Me ₂ bipy		0.38 (A1)		36 ^k
LAC = 6, 6'-Φ ₂ bipy		0.61 (A1)		36 ^k
LAD = phen	0.170		0.08 (SCE), DMF	37, 38
LAE = 2, 9-Me ₂ phen	0.603	0.28 (Fc)	0.58 (SCE), DMF	37–39
LAF = 4, 7-Me ₂ phen			0.01 (SCE), DMF	38
LAG = 5, 6-Me ₂ phen			0.05 (SCE), DMF	38
LAH = 3, 4, 7, 8-Me ₄ phen			0.02 (SCE), DMF	38
LAJ = 4, 7-Φ ₂ phen	0.62		0.08 (SCE), DMF	38
LAJ = Me ₂ Φ ₂ phen	0.62	0.27 (Fc)	0.59 (SCE), DMF	41
LAJa = Me ₂ (ΦSO ₃) ₂ phen			0.08 (SCE), DMF	38
LAK = 5-Mephen			0.15 (SCE), DMF	37, 38
LAL = 5-NO ₂ phen	0.257		0.14 (SCE), DMF	38
LAM = 5-Clphen				42
LAMA = bib		0.27 (Ag/AgCl)		
1:1 (Mono) complexes				
LAN = Me ₄ -dioxine		-0.64 (SCE), DMF		43

<i>Macrocyclic polyamine ligands</i>		
LAO = [1]2janeN ₄ (cyclen)	44	
LAP = Me ₄ ·[1]2janeN ₄	44, 45	
LAQ = bz ₄ ·[1]2janeN ₄	44	
LAR = [1]3janeN ₄	46	
LAS = Me,NO ₂ ·[1]3janeN ₄	47	
LAT = [1]4janeN ₄ (cyclam)	46	
LAU = Me,NO ₂ ·[1]4janeN ₄	47	
LAV = [1]4janeN ₄ -b (isocyclam)	46	
LAW = [1]5janeN ₄	46	
LAX = Me,NO ₂ ·[1]5janeN ₄	47	
LAY = [1]6janeN ₄	46	
LAZ = Me,NO ₂ ·[1]6janeN ₄	47	
LBA = [1]5janeN ₅	46	
LBB = [1]6janeN ₅	46	
LBC = [1]7janeN ₅	46	
LBD = Me-[14]dieneN ₃ PY	43	
<i>Macrocyclic polythioether ligands</i>		
1:1 (Mono) complexes		
LBE = [9]janeS ₃	0.72	0.54 (Fc)
		48

(continued overleaf)

Tab. 2 (continued)

Complexed ligand ^a	Potential (V versus references indicated) ^b			References
	H ₂ O V versus SHE	CH ₂ CN V versus reference cited	Other, solvent V versus reference cited	
LBF = [12]aneS ₄	0.69?	0.68 (SHE), 80% CH ₃ OH	49	
LBG = oxathiane-[12]aneS ₄	0.72		50	
LBH = [13]aneS ₄	0.52		49	
LBI = [14]aneS ₄ -a	0.58	0.21 (Fc)	49, 51, 52	
LBI = [14]aneS ₄ -b	0.69		53	
LBK = bz-[14]aneS ₄	0.84	0.46 (Fc)	31, 54	
LBL = <i>cis</i> -cyhx-[14]aneS ₄	0.54	0.17 (Fc)	54	
LBM = <i>cis</i> -crypt-[14]aneS ₄	0.56	0.20 (Fc)	55	
LBN = <i>trans</i> -cyhx-[14]aneS ₄	0.60	0.20 (Fc)	54	
LBO = <i>trans</i> -crypt-[14]aneS ₄	0.67	0.32 (Fc)	55	
LBP = bz- <i>cis</i> -cyhx-[14]aneS ₄	0.89	0.39 (Fc)	54	
LBQ = bz- <i>trans</i> -cyhx-[14]aneS ₄	0.78	0.38 (Fc)	54	
LBR = <i>syn</i> - <i>cis</i> , <i>cis</i> -dicicyhx-[14]aneS ₄	0.57	0.08 (Fc)	54	
LBS = <i>syn</i> - <i>cis</i> , <i>cis</i> -dicrypt-[14]aneS ₄	0.57	0.17 (Fc)	55	
LBT = <i>anti</i> - <i>cis</i> , <i>cis</i> -dicicyhx-[14]aneS ₄	0.67	0.21 (Fc)	54	
LBU = <i>anti</i> - <i>cis</i> , <i>cis</i> -dicrypt-[14]aneS ₄		0.28 (Fc)	55	
LBV = <i>meso</i> - <i>trans</i> , <i>trans</i> -dicicyhx-[14]aneS ₄	0.58	0.10 (Fc)	54	
LBW = <i>meso</i> - <i>trans</i> , <i>trans</i> -dicrypt-[14]aneS ₄		0.34 (Fc)	55	
LBX = <i>dl</i> - <i>trans</i> , <i>trans</i> -dicicyhx-[14]aneS ₄	0.69	0.26 (Fc)	54	
LBY = <i>dl</i> - <i>trans</i> , <i>trans</i> -dicrypt-[14]aneS ₄		0.39 (Fc)	55	
LBZ = <i>cis</i> , <i>trans</i> -dicicyhx-[14]aneS ₄		0.14 (Fc)	54	
LCA = <i>cis</i> , <i>trans</i> -dicrypt-[14]aneS ₄	0.60	0.65 (SHE), 80% CH ₃ OH	55	
LCD = <i>syn</i> -[14]aneS ₄ -diol	0.63	0.26 (Fc)	52	
LCE = <i>anti</i> -[14]aneS ₄ -diol	0.54		52	
	≈0.49			

$\text{LCC} = [1 5]\text{janeS}_4$	0.64	0.74 (SHE), 80% CH_3OH	49
$\text{LCH} = [1 6]\text{janeS}_4$	0.71	0.78 (SHE), 80% CH_3OH	49
$\text{LCI} = [1 5]\text{janeS}_5$	0.69	0.82 (SHE), 80% CH_3OH	49
$\text{LCJ} = [1 8]\text{janeS}_6$			56
$\text{LCK} = [2 9]\text{janeS}_6$			57
$\text{LCL} = [2 1]\text{janeS}_6$		0.805 (SHE), 80% CH_3OH	57
1:2 (<i>Bis</i>) complex		0.852 (SHE), 80% CH_3OH	57
$\text{LBE} = [9]\text{janeS}_3$	0.65	0.29 (Fc)	48
<i>Other macrocyclic complexes</i>			
$\text{LCM} = [1 2]\text{janeN}_2\text{S}_2$	0.12		58, 59 ^m
$\text{LCN} = \text{Me, NEt-[1 2]janeN}_2\text{S}_2$	0.15		59
$\text{LCO} = [1 4]\text{janeNS}_3\text{-}a$	0.38		51
$\text{LCP} = [1 4]\text{janeNS}_3\text{-}b$	0.41		53
$\text{LCQ} = [1 4]\text{janeNSNS}_2\text{-}b$	0.26		58 ^m
$\text{LCR} = [1 4]\text{janeN}_2\text{S}_2$	0.04, 0.08		51, 58, 59 ^m
$\text{LCS} = \text{Me-[1 4]janeN}_2\text{S}_2$	0.11		59
$\text{LCT} = \text{Me}_2\text{-[1 4]janeN}_2\text{S}_2$	0.18		59
$\text{LCU} = \text{Me, NEt-[1 4]janeN}_2\text{S}_2$	0.03		59
$\text{LCV} = \text{Me, NPr-[1 4]janeN}_2\text{S}_2$	0.12		59

(continued overleaf)

Tab. 2 (continued)

Complexed ligand ^a	Potential (V versus references indicated) ^b			References
	H ₂ O V versus SHE	CH ₃ CN V versus reference cited	Other, solvent V versus reference cited	
LCW = [14]aneN ₂ NN	-0.01			51
LCX = Me ₂ NO ₂ ·[14]aneN ₂ NN	-0.025			60
LCY = [14]aneN ₃ S	≈ -0.24			51
LCZ = [16]aneN ₂ S ₂	0.42			58 ^m
LDA = [16]aneNNSNS	0.40			58 ^m
LDB = [15]aneNS ₄	0.46			51
LDC = [15]aneN ₂ S ₃	0.10			51
LDD = [15]bpyS ₃		-0.13 (Fc)	-0.15 (A1)	35
LDDa = [16]S ₃ dioxime-BF ₂ (TtioxBF ₂)			-0.17 (A1)	61
LDDb = [16]SO ₃ dioxime-BF ₂ (OdtioxBF ₂)				61
LDE = [17]ipyS ₄ bz		≈0.65(A2)	-0.04 (A1)	62
LDF = dibz-[14]dieneneN ₂ S ₂			0.21 (A1)	63
LDG = dibz-[15]dieneneN ₂ S ₂			0.29 (A1)	63
LDH = dibz-[16]dieneneN ₂ S ₂			0.13 (SCE)	63
LDHa = bz ₂ ·[16]tetraeneN ₄ (TAAAB)	0.30		-0.31 (Fc)	64, 65
LDI = [18]aneN ₂ S ₄			0.05 (SCE), DMF	66
LDJ = Me ₂ ·[18]aneN ₂ S ₄			0.06 (Fc)	66
<i>Note:</i> The difference in the potentials of the foregoing two complexes is attributed to the fact that Cu ^{II} ([18]aneN ₂ S ₄) is racemic while Cu ^{II} (Me ₂ [18]aneN ₂ S ₄) is meso – both Cu(II) complexes having tetrahedral configurations in which Cu(II) is coordinated to one nitrogen and three sulfurs.				
LDK = bz ₂ ·[18]aneN ₂ S ₄	≈ -0.27 (SCE)			67
LDL = [18]aneS ₄ O ₂	0.37 (Fc)			68
1:2 (<i>Bis</i>) complex				
LDM = [9]aneS ₂ O	≈0.36(Fc)			68

<i>Bicyclic ligands</i>	
LDN = Me ₄ -bicycloN ₆ O	-0.06
LDO = Me ₅ -bicycloN ₇	-0.05
<i>Acyclic polyamine ligands</i>	
<i>Bis complexes</i>	44
LDP = en	-0.114
LDQ = Me ₂ en	-0.065
LDR = ten	-0.135
LDS = tmen	-0.042
LDT = Me ₂ -tmen	-0.044
LDU = <i>trans</i> -cyhx-(NH ₂) ₂	-0.250
<i>Mono complexes</i>	
LDV = 2, 2, 2-N ₄ (trien)	-0.28 (80% CH ₃ OH)
LDW = 2, 3, 2-N ₄ (2,3,2-tet)	-0.300
LDX = 3, 2, 3-N ₄	-0.270
LDY = Me-NH ₂ -2,3,2-N ₄	-0.310
LDZ = Me-NO ₂ -2,3,2-N ₄	-0.250
<i>Acyclic polythioether ligands</i>	
LEA = Me ₂ -2,3,2-S ₄	0.79

(continued overleaf)

Tab. 2 (continued)

Complexed ligand ^a	Potential (V versus references indicated) ^b			References
	H ₂ O V versus SHE	CH ₃ CN V versus reference cited	Other, solvent V versus reference cited	
LEB = Et ₂ 2,3,2-S ₄	0.79			49
LEC = Me ₂ 3,2,3-S ₄	0.83			70
LED = cis-cyhx-3,2,3-S ₄	0.75			70
LEE = trans-cyhx-3,2,3-S ₄	0.77			70
<i>Acyclic polyaminopyridyl ligands</i>				
LEF = 2, 2, 2-N ₂ P(2-(pdahx))	-0.20	-0.56 (Fc)	-0.73 (Fc), DMSO	44, 71
LEG = 2, 3, 2-N ₂ P(2-(pdahp))	-0.12	-0.55 (Fc)	-0.73 (Fc), DMSO	71, 72
LEH = 3, 2, 3-N ₂ PY ₂		-0.53 (Fc)	-0.70 (Fc), DMSO	71
LEI = Me ₂ 3,2,3-N ₂ PY ₂ (pdao)	0.10	-0.31 (Fc)		72
LEJ = Me ₂ 3,3,3-N ₂ PY ₂ (pdan)	0.28	-0.09 (Fc)		72
LEK = 2, 2, 2-N ₂ bzim ₂		-0.40 (A1) ^d		73
LEKa = (py) ₂ DAP		-0.136 (SCE)		34
LEKb = (imidH) ₂ DAP		-0.269 (SCE)		34
LEKc = (imidR) ₂ DAP		-0.256 (SCE)		34
LEL = N ₄ -mpy		0.21 (SCE)		74
<i>Bis complex</i>				
LELa = (MeimidΦ ₂) ₂ CO	0.59 (SCE)	0.80 (SCE) CH ₂ Cl ₂		75
<i>Acyclic polyaminothioether ligands</i>				
LEM = 2, 2, 2-N ₂ SN		0.36 (SHE) 80% CH ₃ OH		57
LEN = 2, 2, 2-NSSN		0.36 (SHE, 80% CH ₃ OH		57
LEO = Me ₂ 2,2,2-SNNS	0.28			76
LEP = 2, 3, 2-NSSN		0.31 (SHE), 80% CH ₃ OH		57
LEQ = Me ₂ 2,3,2-SNNS	0.23			76

LER = Et ₂ -2,3,2-SNNS		0.26	0.34 (SHE), 80% CH ₃ OH	57
LES = Me ₂ -3,2,3-SNNS				76
Other acyclic mixed-donor ligands				
1:2 (<i>Bis</i>) complexes				
LET = bzMe-S-py	0.53 (SCE)			74
LEU = Me-imine-imid (<i>p</i> -me)			-0.61 (SCE), DMF	43
LEV = <i>i</i> Pr-imine-imid (<i>p</i> - <i>i</i> -C ₃ H ₇)			-0.53 (SCE), DMF	43
LEW = <i>i</i> Pr-imine-phenoxy (sal- <i>i</i> -C ₃ H ₇)			-0.74 (SCE), DMF	43
LEX = <i>t</i> Bu-imine-phenoxy (sal- <i>t</i> -Bu)			-0.66 (SCE), DMF	43
Mono complexes				
LEY = 2,3,2-S ₄			≈0.84 (SHE), 80% CH ₃ OH	57
LEZ = bz ₂ -3,2,3-ONNO (salen)			-1.21 (SCE), DMF	43
LFA = Ac ₂ -3,2,3-ONNO (J-en)			-1.09 (SCE), DMF	43
LFB = bz ₂ -3,3,3,3-ON ₃ O (saldpf)			-1.08 (SCE), DMF	43
LFC = N ₂ S ₂ -mpy	0.77 (SCE)			74
LFD = 3,3-bzimSpy (Bipip)			0.28 (A1)	77
LFE = 3,2-bzimSpy (Bipth)			0.22 (A1)	77
LFF = 2,2,2-pyS ₂ Py	0.40		0.11 (Fc)	72
LFG = 2,3,2-pyS ₂ Py	0.47		0.15 (Fc)	72
LFH = 3,2,3-pyS ₂ Py (pdto)	0.59		0.21 (Fc)	72, 78
LFHa = 3,2,3-quinS ₂ quin (qdto)			0.60 (A1)	79

(continued overleaf)

Tab. 2 (continued)

Complexed ligand ^a	Potential (V versus references indicated) ^b			References
	H ₂ O V versus SHE	CH ₃ CN V versus reference cited	V versus solvent V versus reference cited	
LFI = 3, 3', 3-pyS ₂ Py (pdtn)	0.59	0.26 (Fc)		72
LFJ = 2, 2, 2, 2-pyS ₂ Py (pttn)	0.73 ^h	0.092, ⁱ 0.069 (Fc)		80, 81
LFJ _a = 2, 2, 2, 2-MePyS ₂ MePy (Mptn)		0.40 (A1)		79
LFJ _b = 3, 2, 2, 3-quinS ₃ quin (ttu)		0.62 (A1)		79
LFK = 2, 2, 2, 2-pySO ₂ Py		0.054, ⁱ 0.072 (Fc)		81
LFL = 2, 2, 2-bzimS ₃ bzim				80
LFM = Me ₄ -1,2,2,1-przS ₃ prz	0.95 ^h			80
LFN = 2, 2, 2-S ₃ dioxime (TioxH ⁻)		-1.10 (A1)		61
LFO = 2, 2, 2-SO ₂ dioxime (OdtioxH ⁻)		-1.15 (A1)		61
LFQa = 2, 2-OsO ₂ dicarboxylate (ta)	0.190			37
LFQb = 2, 1, 2-Os ₂ O-dicarboxylate (1dta)	0.266			37
LFQc = 2, 2, 2-Os ₂ O-dicarboxylate (2dta)	0.300			37
LFQd = 2, 3, 2-Os ₂ O-dicarboxylate (3dta)	0.310			37
LFQe = 3, 2, 2, 3-Os ₃ O-dicarboxylate (4ta)	0.439			37
<i>Tripodal ligands</i>				
LFP = <i>t</i> -2,2,2-MeS ₃ (TMMEA)	0.69	0.34 (SCE) ^g , DMF		43, 82
LFQ = <i>t</i> -2,2,2-EtS ₃ (TEMEA)	0.67			82
LFR = <i>t</i> -2,2,2-py(MeS) ₂ (PMMEA)	0.38	0.13 (SCE) ^g , DMF		43, 82
LFS = <i>t</i> -2,2,2-py(EtS) ₂ (PMAS)	0.40	0.30 (SCE), 80% CH ₃ OH -0.16 (Fc), DMF		78, 82, 83
LFT = <i>t</i> -3,2,2-py(MeS) ₂ (PEMEA)				84
LFU = <i>t</i> -3,2,2-py(EtS) ₂ (PEAS)	0.60			82
LFV = <i>t</i> -2,2,2-py(MeS) (BPMMEA)	0.60	0.11 (Fc), DMF		78, 82
LFW = <i>t</i> -2,2,2-py ₂ (EtS) (BPMEEA)	0.06			82
	0.08			

$\text{LFX} = \tau\text{-}3,3,2\text{-py}_2(\text{MeS})\text{ (BPMEA)}$	0.46	82
$\text{LFY} = \tau\text{-}3,3,2\text{-py}_2(\text{EtS})\text{ (BPFEFA)}$	0.47	82
$\text{LFZ} = \tau\text{-}2,2,2\text{-py}_3\text{ (TMPA)}_2$	-0.11 to -0.2	82, 85, 86
$\text{LGA} = \tau\text{-}3,3,3\text{-py}_3\text{ (TPEA, tpea)}$	0.17 to 0.51	82, 86, 87
$\text{LGB} = \tau\text{-}2,2,2\text{-py}_2\text{ (quin)}$		
$\text{LGC} = \tau\text{-}2,2,2\text{-py(quin)}_2$		
$\text{LGD} = \tau\text{-}2,2,2\text{-quin}_3$		
$\text{LGH} = \text{Me-}\tau\text{-}2,2,2\text{-quin}_3$		
$\text{LGJ} = \tau\text{-}2,2,2\text{-py}_2\text{ (Meimid)}$	-0.10 (Fc)	89
$\text{LGJ} = \tau\text{-}2,2,2\text{-py(Meimid)}_2$		
$\text{LGK} = \tau\text{-}2,2,2\text{-}(Meimid)}_3$	-0.19 (A2)	90 ^j
$\text{LGL} = \tau\text{-}2,2,2\text{-OH(bzim)}_2$		
$\text{LGM} = \tau\text{-}2,2,2\text{-}(bzim)}_3$	-0.15 (A1)	90 ^j
$\text{LGN} = \tau\text{-}1,1,1\text{-}(pyrz)}_3$		
$\text{LGO} = \tau\text{-}1,1,1\text{-}(\text{Me}_2\text{prz)}_3$	0.26	91
$\text{LGP} = \tau\text{-}1,1,1\text{-}(t\text{-Bu}_2\text{prz)}_3$		
$\text{LGQ} = \tau\text{-}2,2,2\text{-}(\text{Me}_2\text{prz)}_3$	0.41	92
$\text{LGR} = \tau\text{-}2,2,2\text{-}(S\text{-Meimid)}_3$		
<i>Branched ligands</i>		
$\text{LGS} = \text{en-}2,2,2\text{-OH(bzim)}_3$	-0.38 (A1) ^d	93
		93
		86
		84
		73

(continued overleaf)

Tab. 2 (continued)

Complexed ligand ^a	Potential (V versus references indicated) ^b			References
	H ₂ O V versus SHE	CH ₃ CN V versus reference cited	Other, solvent V versus reference cited	
LGT = en-2,2,2,2-OH(Mebzim) ₃		-0.43 (A1) ^d		73
LGU = en-2,2,2,2-(bzim) ₄		-0.43 (A1) ^d		73
LGV = en-2,2,2,2-(Mebzim) ₄		-0.45 (A1) ^d		73
LGW = cyhx-n-2,2,2,2-(bzim) ₄		-0.48 (A1) ^{d,e}		73
LGX = cyhx-n-2,2,2,2-(Mebzim) ₄		-0.57 (A1) ^{d,e}		73

^a Ligand structures are illustrated in Fig. 1.^b All aqueous potential values are referenced to the standard hydrogen electrode. Nonaqueous potential values are referenced to ferrocene (Fc) if possible. Other references are indicated in parentheses where SCE represents the standard calomel electrode, A1 represents the Ag/Ag⁺ reference electrode ([Ag⁺] = 0.01 M unless otherwise indicated), and A2 represents the Ag/AgCl reference electrode. In acetonitrile, potential values referenced to SCE may be corrected to the ferrocene reference standard by subtracting 0.380 V, depending upon the anion present: (a) Ref. 11, (b) Ref. 10c.^c [Ag⁺] = 0.1 M.^d In Ref. 73, text states that potentials were determined in CH₃CN, but table of values indicates that solvent was CH₃OH. It is presumed that CH₃CN was the solvent used.^e The reference does not indicate whether the cyclohexane moiety is *cis* or *trans*.^f Chloride ion occupies the fifth coordination site in Cu^{II}L.^g Bromide ion occupies the fifth coordination site in Cu^{II}L.^h Solvent used is not clearly specified.ⁱ ClO₄⁻ ion present.^j CF₃SO₃⁻ ion present.^k The reference Ag/Ag⁺ electrode used is reported to have a potential value of +0.31 V versus SCE in acetonitrile.^l These investigators have noted that the potential of ferrocene in DMF versus their Ag/Ag⁺ (0.01 M) reference electrode was +20 mV.^m Values in this study were determined at 20 °C, $\mu = 0.2$ and are slightly different from those shown in Table 4.

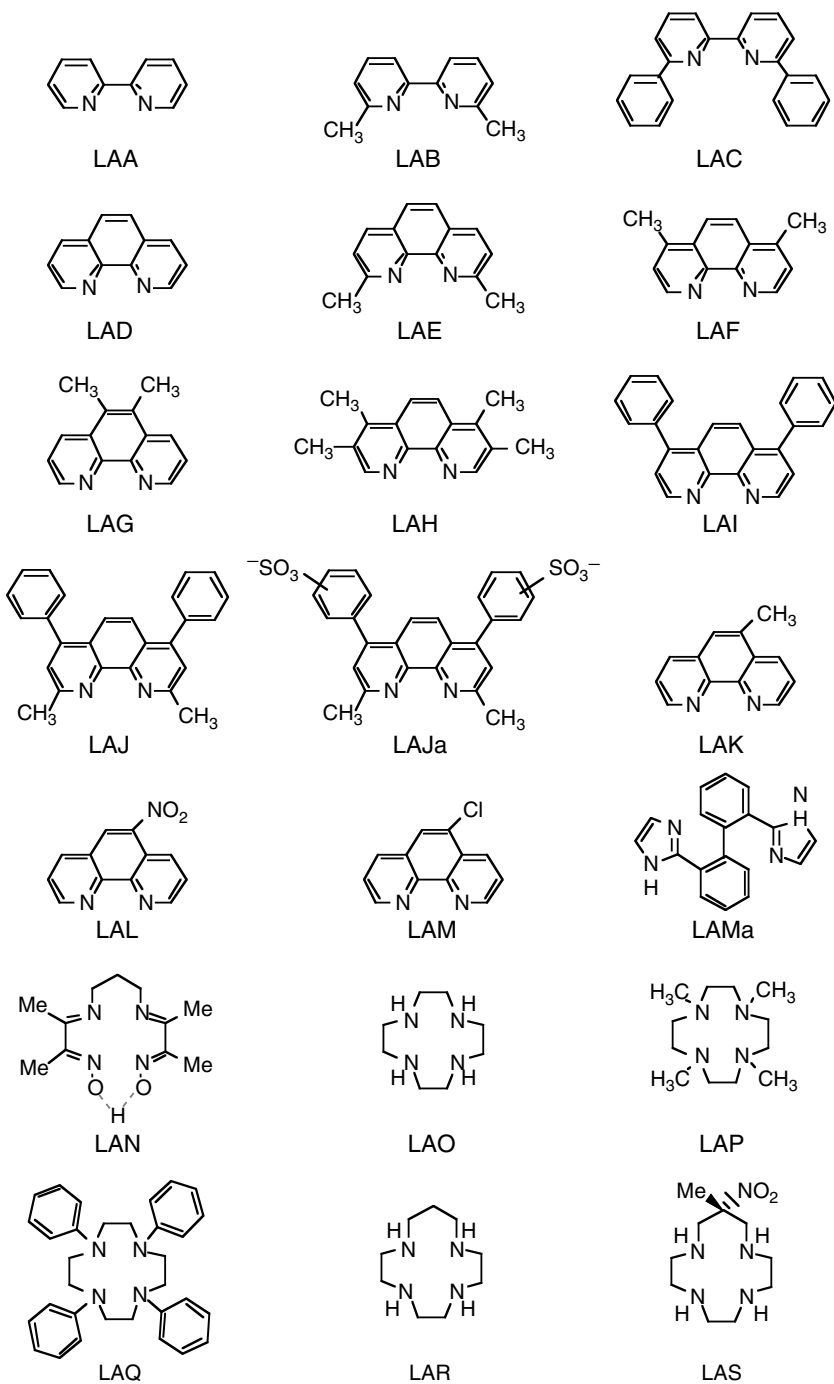
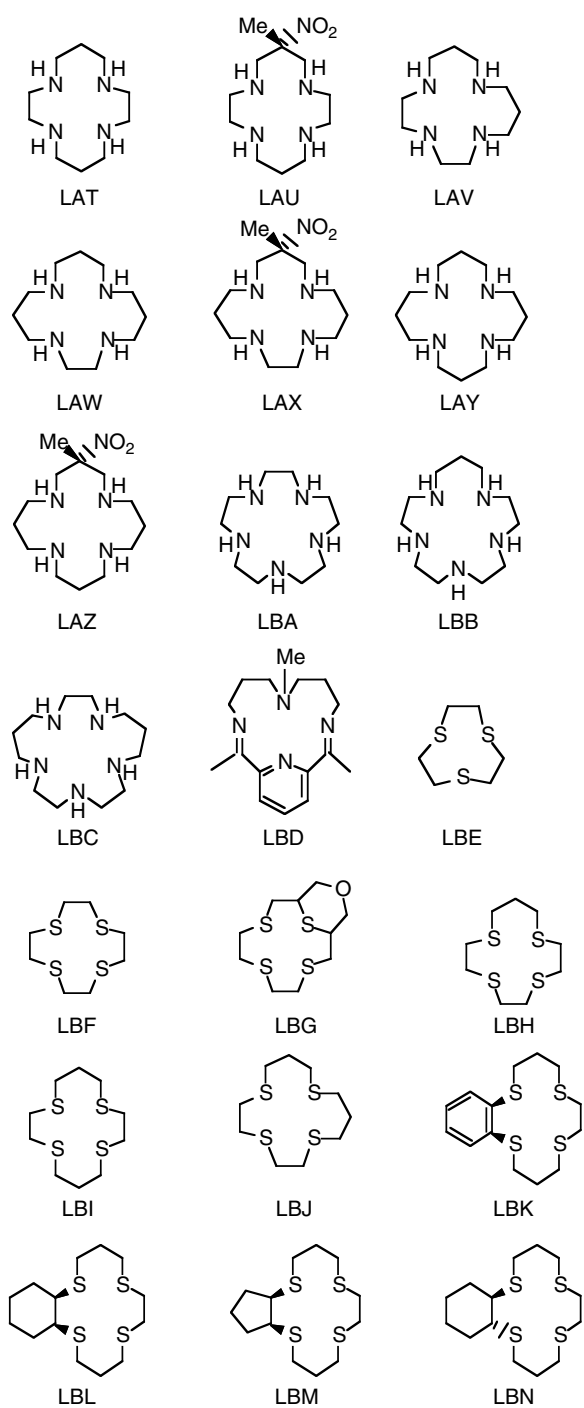


Fig. 1 Identification of ligands for which $\text{Cu}^{II}/\text{I}^{\text{L}}$ potentials are listed in Table 2.

**Fig. 1** (continued).

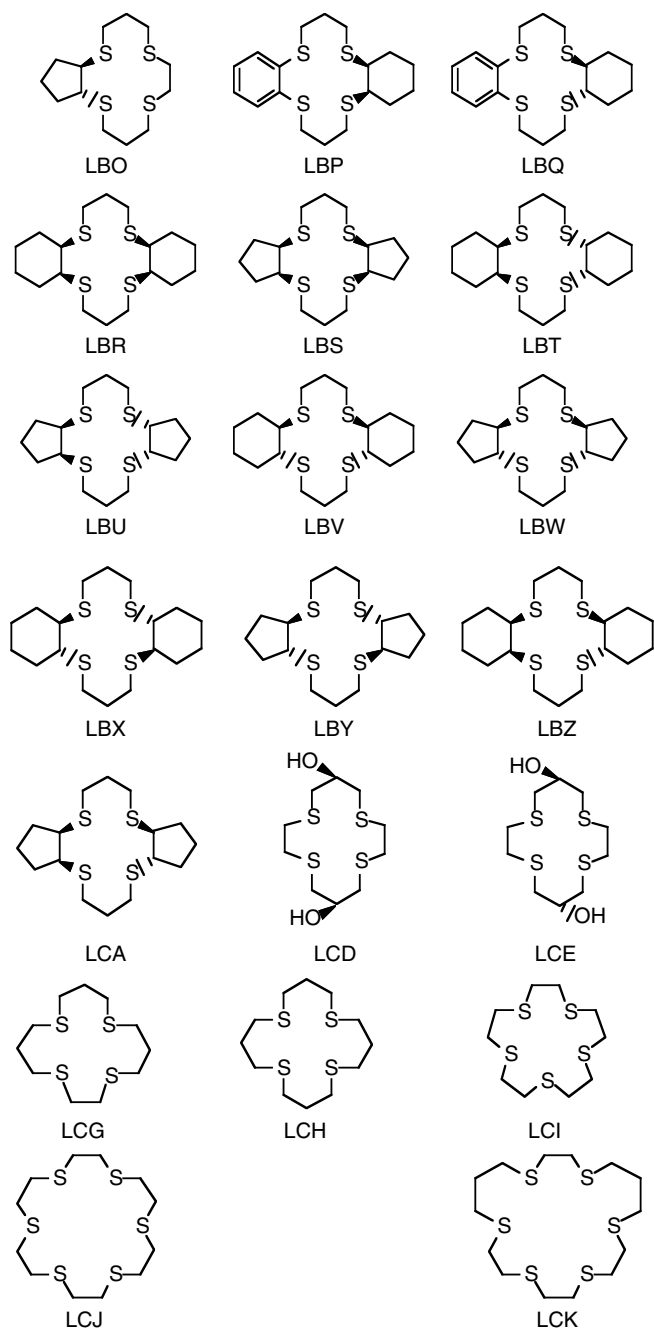
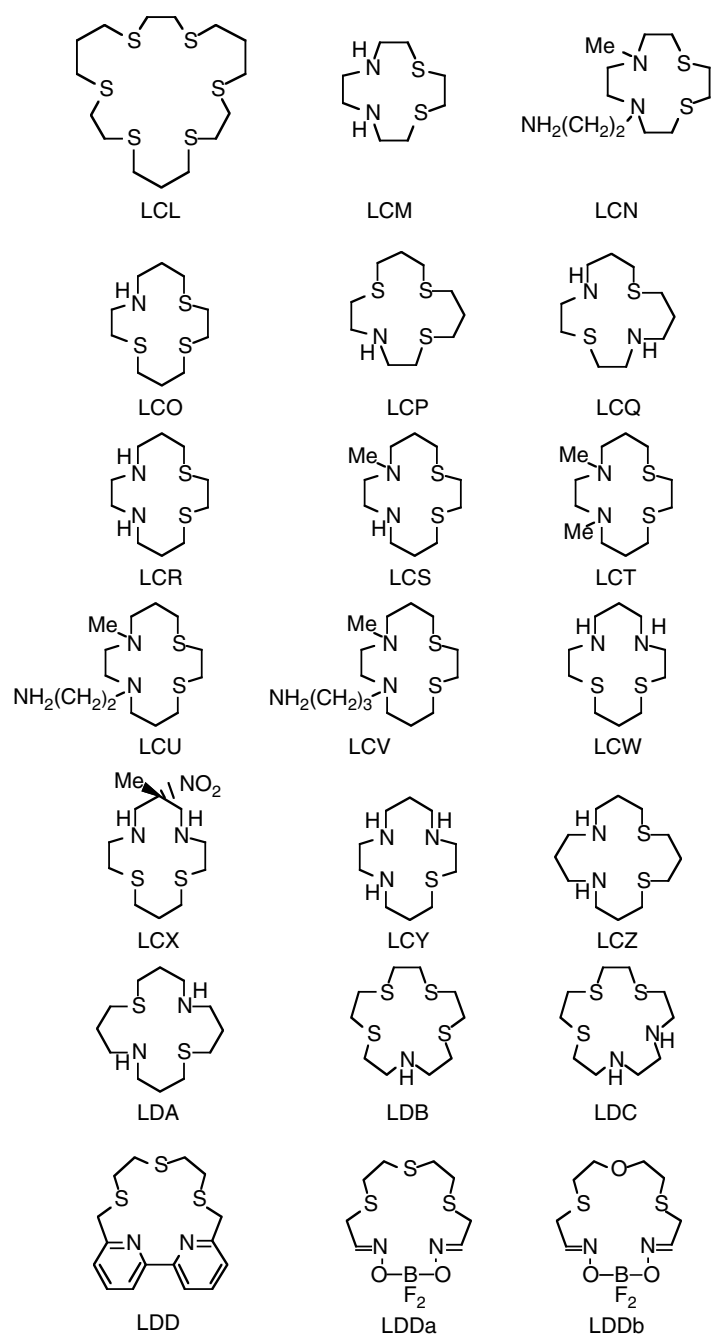


Fig. 1 (continued).

**Fig. 1** (continued).

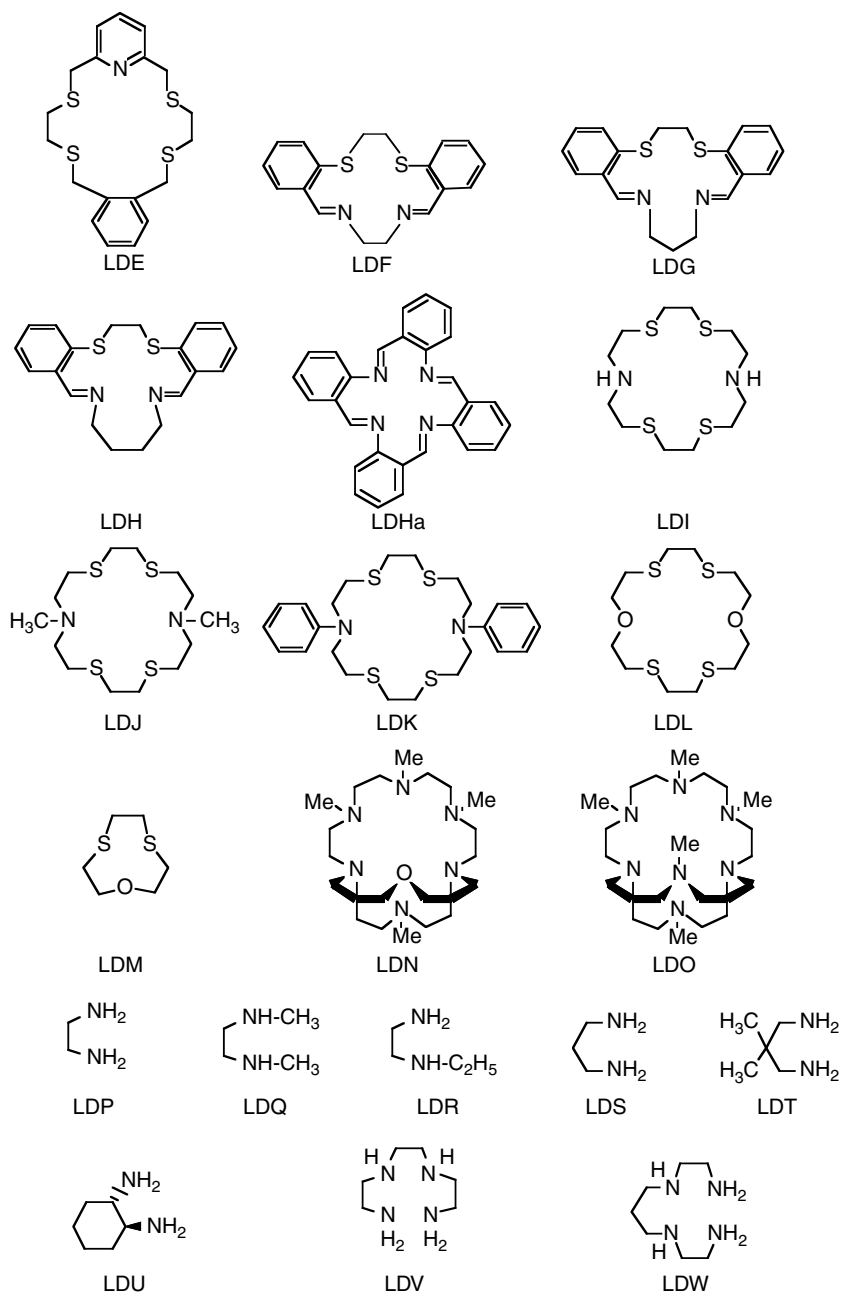
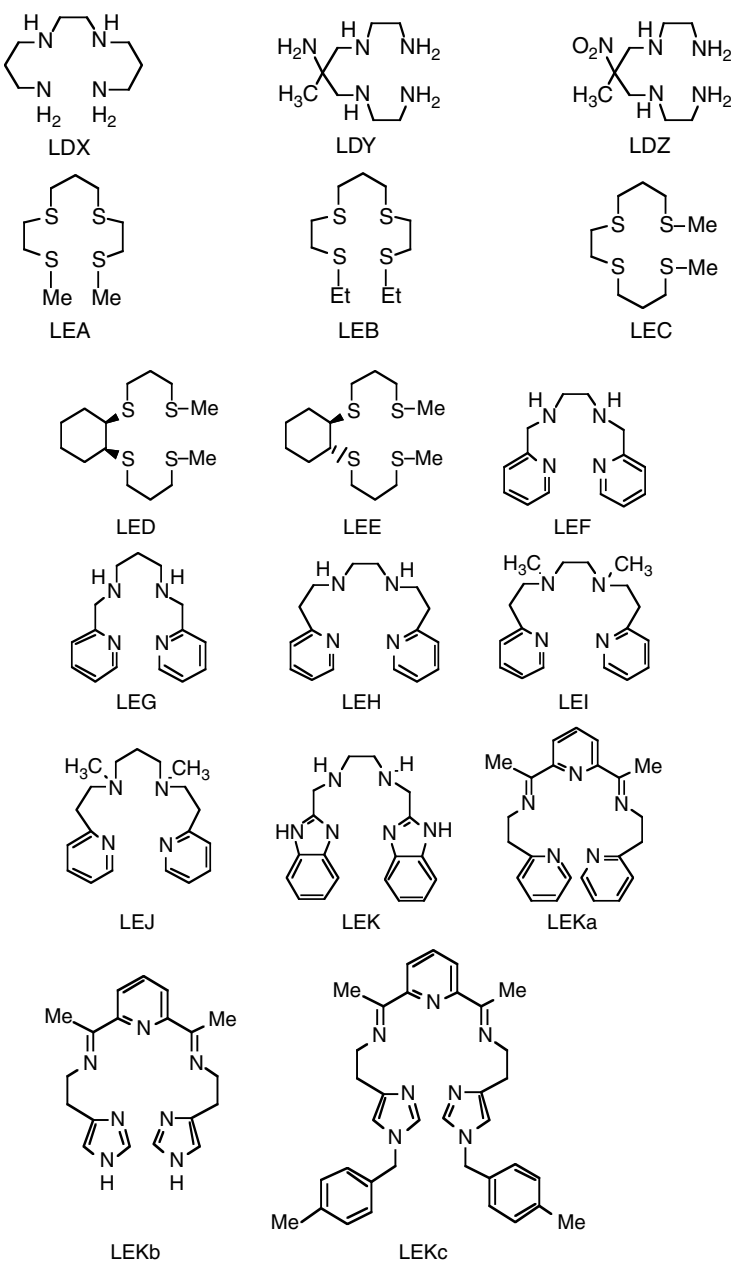
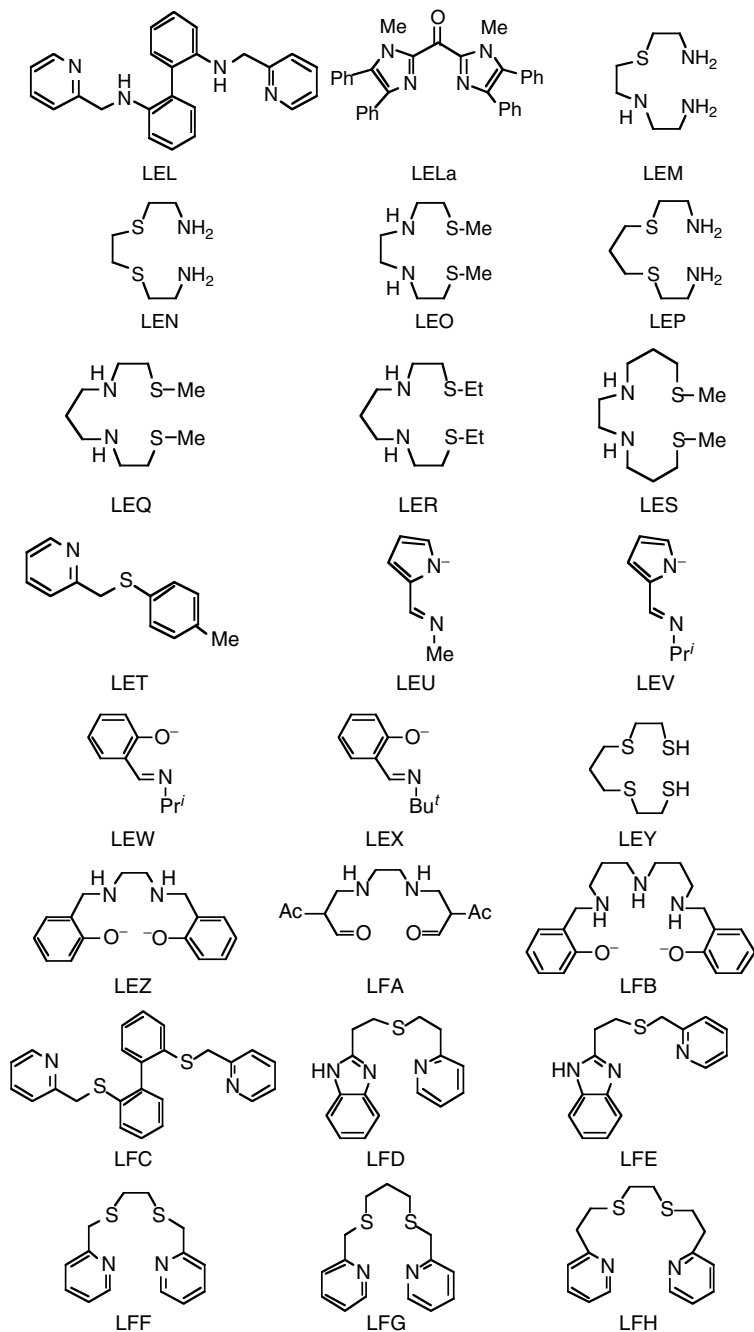
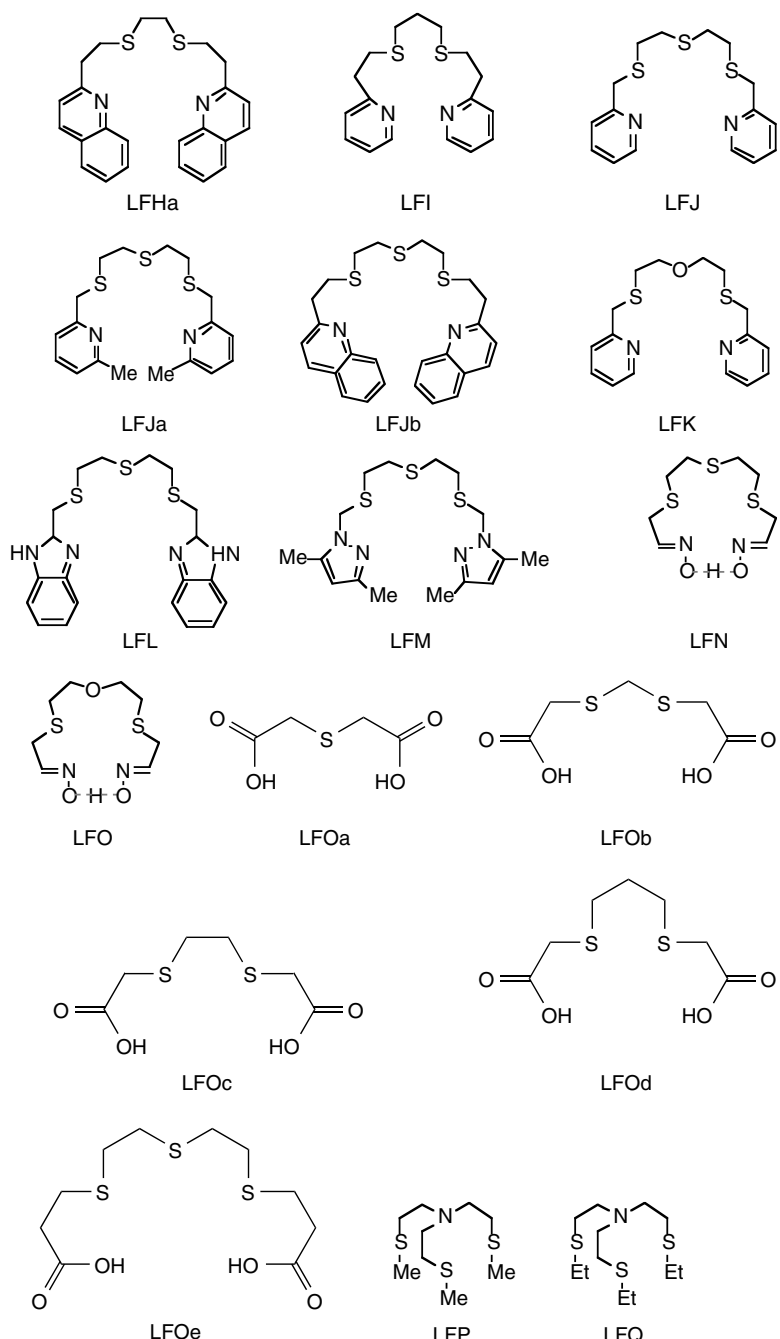
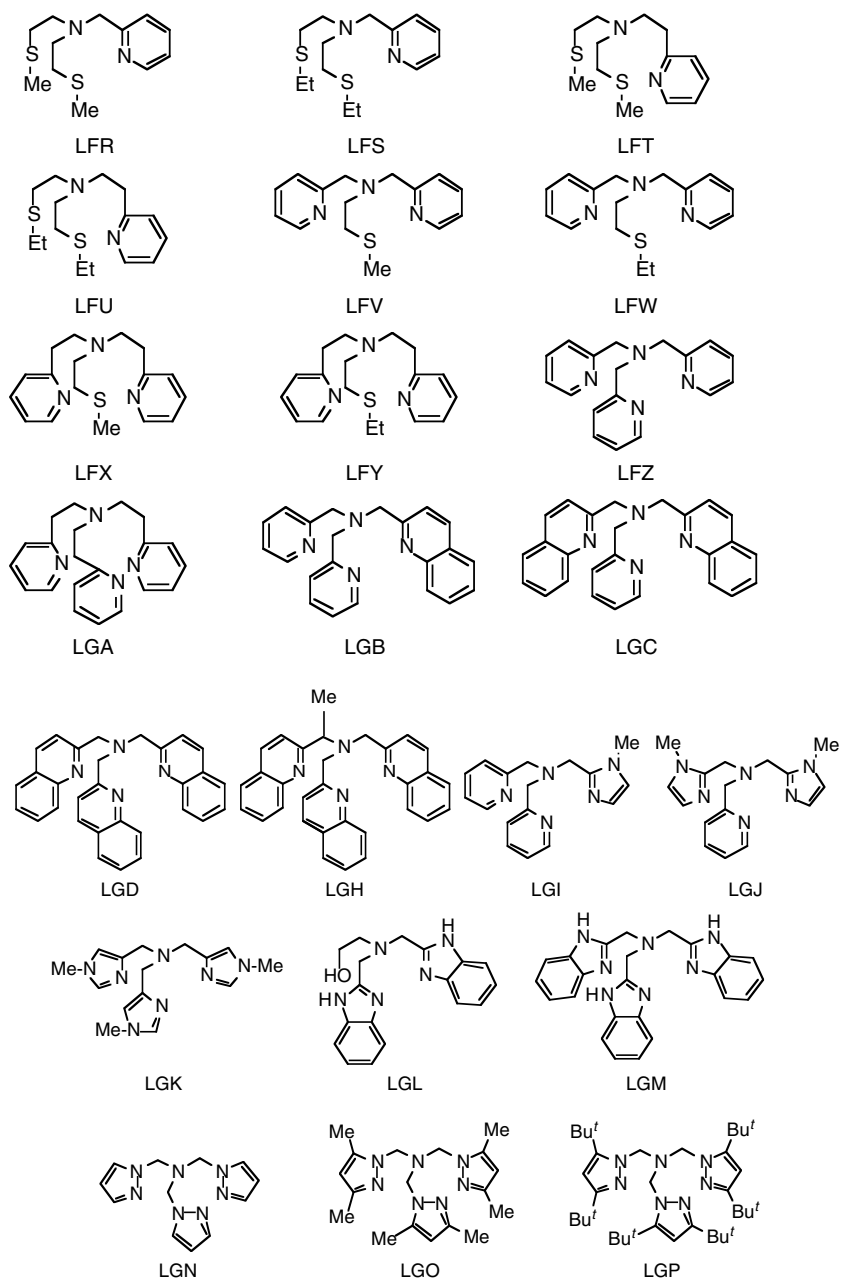


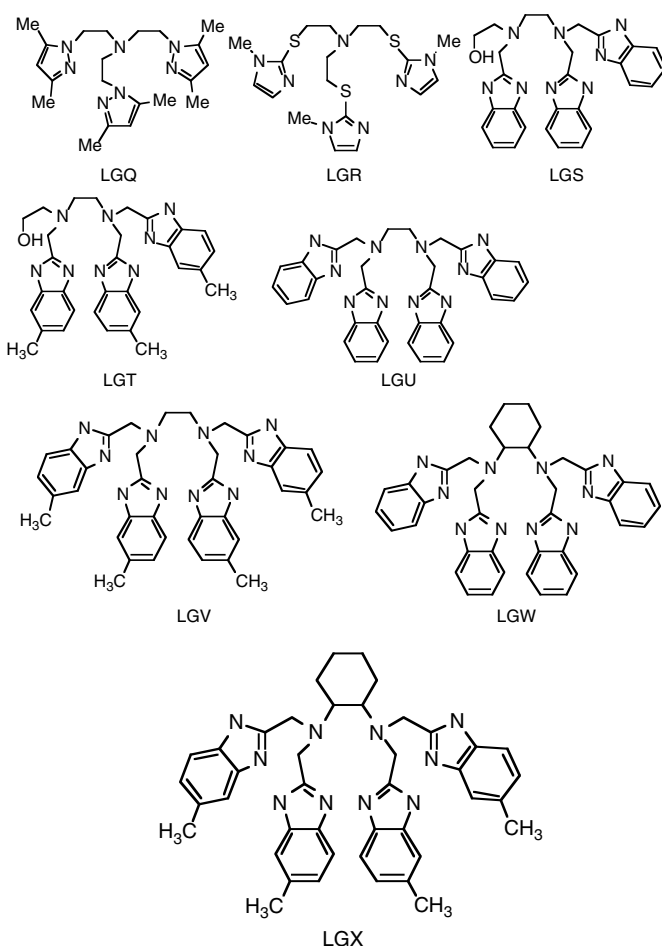
Fig. 1 (continued).

**Fig. 1** (continued).

**Fig. 1** (continued).

**Fig. 1** (continued).

**Fig. 1** (continued).

**Fig. 1** (continued).

Fabbrizzi, Poggi, and Zanello[46] used the latter solvent to measure the potential values of Cu(II/I) compounds involving 13- to 16-membered macrocyclic tetramines and 15- to 17-membered macrocyclic pentamines (Table 2).

As shown by Eq. (9), the relative affinity of specific ligands for the Cu(II) and Cu(I) oxidation states, as indicated by the magnitude of the stability constants, $K_{\text{Cu}^{\text{II}}\text{L}}$ and $K_{\text{Cu}^{\text{I}}\text{L}}$, respectively, is directly reflected in the Cu(II/I) redox potentials. Thus, an increase in the value of $E_{21}^{\theta'}$ is generally

interpreted to reflect either an increase in the stabilization of the Cu(I) state or the destabilization of the Cu(II) state (or both) by the complexing ligand. Because of the different geometric preferences exhibited by these two oxidation states, the influence of ligand structure upon Cu(II/I) potential values has been considered to be a matter of prime interest for more than four decades.

Patterson and Holm [95] carried out the first systematic investigation on the influence of the structure of coordinated

ligands upon Cu(II/I) potentials. Utilizing dimethylformamide (DMF) as the solvent, they made polarographic measurements on the Cu(II/I) complexes formed with 36 quadridentate and bis-bidentate ligands consisting primarily of salicylaldimine, β -ketoamine, β -iminoamine, and pyrrole-2-aldimine systems. These ligands were chosen to reveal the effect of stereochemical and donor atom variations on the resultant Cu(II/I) half-wave potentials.

One of the primary observations made by Patterson and Holm was that nonplanar bis-chelate complexes were easier to reduce than their planar counterparts. In particular, the $\text{Cu}^{\text{II}/\text{I}}(2,9\text{-Me}_2\text{phen})_2$ redox couple (2,9-Me₂phen = 2,9-dimethyl-1,10-phenanthroline) exhibits a potential in DMF that is more than 1 V larger than the potentials of nearly all other complex systems they studied. Molecular models readily show that, because of steric hindrance of the methyl groups in the 2,9-positions, the four nitrogen donor atoms in the Cu(II) complex are distorted out of plane. The Cu(II) presumably adopts a trigonal bipyramidal geometry by retaining an inner-sphere solvent molecule as shown in the crystal structure of a closely related bis-bipyridyl complex [96]. On the basis of the assumption that the potentials primarily reflect changes in the stabilities of the Cu(II) complexes (*vide infra*), the first observation reflects the preference of Cu(II) for four donor atoms in the *xy* plane.

Patterson and Holm also observed that rigid planar quadridentate or related planar bis-chelate complexes, and complexes differing only in donor atoms, are more readily reduced in the order $\text{N}_4 < \text{N}_2\text{O}_2 < \text{N}_2\text{S}_2$. This observation reflects the relative preference of Cu(II) for these donor atoms in the order N > O > S. Patterson and Holm noted that binuclear complexes were

reduced in one two-electron or two resolvable one-electron steps depending upon the ligand structure, a point that will be discussed later in this treatise.

Dockal et al. [57] used slow-scan CV to determine the $E_{21}^{\theta'}$ values for 17 Cu(II/I) complexes in 80% methanol – 20% water (w/w) – including nine complexes with macrocyclic terdentate, quadridentate, quinquedentate, and sexadentate thioethers and eight complexes with acyclic quadridentate ligands containing thioether sulfur and/or amine nitrogen donor atoms. (In naming the denticity of multidentate ligands, Dwyer, Lions, and coworkers have pointed out that “dentate” is a Latin root and proper nomenclature requires that Latin prefixes be used. Thus, ter-, quadri-, quinque-, and sexa- are preferred over the Greek prefixes tri-, tetra-, penta-, and hexa-. The lone exception appears to be for ligands with two donor atoms where bidentate is universally utilized rather than the more proper didentate) [97]. The macrocyclic quadridentate tetrathioether complexes exhibit slightly lower potentials than their acyclic counterparts, but the potentials increase for larger cavity sizes. Macroyclic ligands containing five or six thioether sulfurs exhibit the highest potential values observed. As noted by Patterson and Holm, a sharp decrease in potential was also observed by Dockal et al. when amine nitrogens were substituted for thioether sulfurs in the acyclic ligand series.

Addison [98] correlated a broad spectrum of published potential data on aqueous Cu(II/I) complexes – including those with N, S, and O donor atoms – to generate an empirical relationship between the various characteristic ligand features and the observed Cu(II/I) potentials. He concluded that closed (macrocyclic) ligand topology had little effect on the $E_{21}^{\theta'}$ values, but

certain tripodal ligands show a marked influence on the redox potentials, generally raising $E_{21}^{\theta'}$ by a few hundred millivolts. Based on 47 Cu(II/I) potential values from the literature, Addison generated the following empirical expression:

$$E_{21}^{\theta'} = E_{21(\text{solv})}^{\theta'} + \Sigma(n\Delta E_L) \quad (10)$$

In Eq. (10), ΔE_L represents the change in the Cu(II/I) potential brought about by various ligand features (such as donor atom type, number of five-membered chelate rings, etc.) and n represents the number of times that specific feature appears in a specific coordinated ligand. A tabulation of the values generated by Addison for the various ligand features is given in Table 3.

Bernardo et al. [51] subsequently determined the potentials of a series of copper(II/I) complexes formed with 14-membered macrocyclic quadridentate ligands involving amine nitrogen and thioether sulfur donor atoms and found that the substitution of each sulfur donor atom by an amine nitrogen resulted in an average decrease of 0.3 V in the Cu(II/I) potential. Since the $K_{\text{Cu}^{II}\text{L}}$ values had been determined previously for these systems [99], Bernardo et al. were able to calculate the $K_{\text{Cu}^{II}\text{L}}$ values using Eq. (9). The latter values proved to be nearly constant, indicating that Cu(I) does not discriminate

significantly between amine nitrogen and thioether sulfur donor atoms. Thus, the steady decrease in potential values as each nitrogen is substituted for a sulfur donor is almost entirely due to the *increase* in the stabilization of the Cu(II) complexes.

As noted by Addison, tripodal ligands appear to have the largest impact upon the Cu(II/I) potential values. Ambundo et al. [82] measured both the Cu(II) complex stability constants and the Cu(II/I) complex potential values for 12 different tripodal ligands containing amine nitrogen bridge-heads and thioether sulfur or aromatic nitrogen donor atoms on the three “legs”. Despite the differences in chelate ring size and donor atom type, all 12 compounds exhibit nearly constant $K_{\text{Cu}^{II}\text{L}}$ values as calculated using Eq. (9). Thus, the trend in Cu(II/I) potentials again parallels the stability of the Cu(II) complexes.

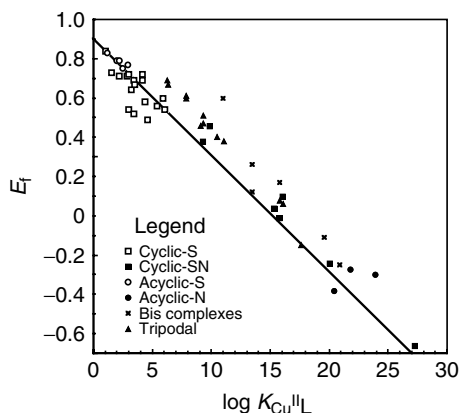
24.7.2.3 Correlation of Potentials to Copper(II) Complex Stability Constants

Based on the observations noted above, Ambundo et al. [82] plotted the aqueous $E_{21}^{\theta'}$ values for 35 Cu(II/I) systems involving neutral ligands against the corresponding $\log K_{\text{Cu}^{II}\text{L}}$ values. Their original data have been expanded in Fig. 2 to include 50 Cu(II/I) complexes, all involving uncharged ligands. The stability constant data for the systems included in

Tab. 3 Empirical parameters affecting copper(II/I) potential values (Ref. 98)

Ligand feature	$\Delta E_L [\text{mV}]$	Error [mV]	Significance level [%]
Thioether donor	+141	±12	>99.99
Aromatic N donor	+52	±13	>99.9
Aliphatic N donor	-75	±12	>99.99
Carboxylate O donor	-26	±23	70
Macrocyclic ligand	+24	±44	40
Five-membered chelate rings	-46	±10	>99.99
Tripodal ligand	+291	±52	>99.99

Fig. 2 Plot illustrating the relatively linear relationship between the Cu^{II}/I redox potential and logarithmic value of the Cu^{II}L stability constant, $K_{\text{Cu}^{\text{II}}\text{L}}$. The line drawn has the Nernstian slope (0.059) and represents a Cu^IL stability constant value of 10^{13} M⁻¹. All complexes represented involve uncharged ligands (see Table 4).



this plot are given in Table 4. The resulting plot is seen to be essentially linear for $K_{\text{Cu}^{\text{II}}\text{L}}$ values differing by 26 orders of magnitude with potentials covering nearly a 1.5 V range. The line drawn in this plot is based on an average $K_{\text{Cu}^{\text{I}}\text{L}}$ value of 10^{13} (Eq. 9) and has the Nernstian slope. The close clustering of nearly all points about this line indicates that, despite the wide variety of Cu(II/I) systems involved, the stability of the Cu(I) complexes is only slightly affected by the geometry of the ligands – whether macrocyclic, acyclic or tripodal – and by the donor atoms involved. Thus, it is presumed that nearly all statements in the literature (including past comments by the current authors) are *incorrect* when they conclude that observed increases in the Cu(II/I) redox potentials are attributable to a *stabilization* of the Cu(I) complexes.

On the basis of the trend illustrated in Fig. 2, it is evident that the measured value of $E_{21}^{\theta'}$ for any aqueous Cu(II/I) system can be used to estimate the stability constant of the Cu^{II}L complex within about 2 orders of magnitude. This is a useful tool since only a limited number of Cu^{II}L stability constants have been determined in aqueous solution, whereas a large array

of Cu(II/I) potential values have been reported.

A similar linear relationship between Cu(II/I) potential values and logarithmic Cu^{II}L stability constants may exist in non-aqueous solvents, but such a relationship has not been adequately established. Measurements conducted in our laboratories on a variety of polythioether complexes have shown that the Cu^{II}L stability constants tend to increase by approximately 10^6 on going from water to acetonitrile, whereas the Cu^IL stability constants tend to decrease by a similar order of magnitude [54]. These values obviously reflect the preference of Cu(II) to be solvated by water and the corresponding preference of Cu(I) to be coordinated to acetonitrile [111].

24.7.3

Mechanistic Aspects of Copper(II/I) Electron Transfer

Many electrochemical studies on Cu(II/I) systems exhibit irreversible or quasi-reversible behavior or involve coupled chemical reactions. There are no known examples of Cu(II/I) systems where irreversibility can be definitively attributed to slow electron transfer. However, many

Tab. 4 Correlation of Cu(II/I) redox potentials and stability constants of copper complexes in aqueous solution at 25 °C, $\mu = 0.1$

<i>Complexed ligand</i>	<i>LogK_{Cu^{II}L}</i>	<i>LogK_{Cu^IL}</i>	<i>E^f, V versus SHE</i>	<i>References</i>
<i>Macrocyclic ligands</i>				
[9]aneS ₃	4.14	≈14	0.72	48
[12]aneS ₄	3.39	12.0	<0.69	49, 100
Oxathiane[12]aneS ₄	3.02	12.0	0.72	101
[13]aneS ₄	3.44	10.0	≈0.52	49, 100
[13]aneS ₄ -ol	3.0	10.7	0.54	101
[14]aneS ₄	4.34	11.9	0.58	49, 100
[14]aneS ₄ -ol	4.59	10.7	0.49	101
bz[14]aneS ₄	≈1		≈0.84	31
cis-cyhx[14]aneS ₄	6.04		0.54	31
trans-cyhx[14]aneS ₄	5.90		0.60	31
cis-crypt[14]aneS ₄	5.36		0.56	31
trans-crypt[14]aneS ₄	3.48		0.67	31
[15]aneS ₄	3.17		0.64	49, 100
[15]aneS ₄ -ol	2.84	11.8	0.71	101
[16]aneS ₄	2.20		0.71	49, 100
[16]aneS ₄ -ol	1.51	11.6	0.73	101
[15]aneS ₅	4.18		0.69	49, 100
[14]aneNS ₃	9.25	13.6	0.38	51, 99
[14]aneN ₂ S ₂	15.26	13.9	0.04	51, 58, 99 ^b
[14]aneNSSN	15.72	13.5	-0.01	51, 99
[14]aneN ₃ S	≥20		≤ -0.24 (est)	51, 99
[14]aneN ₄ (cyclam)	27.20		-0.66 (est)	102
[15]aneNS ₄	9.80	15.6	0.46	51, 99
[15]aneN ₂ S ₃	16.02	15.7	0.10	51, 99
<i>Acyclic ligands</i>				
Me ₂ -2,3,2-S ₄	1.97		≈0.79	49, 100
Et ₂ -2,3,2-S ₄	2.18		0.79	49, 100
Me ₂ -3,2,3-S ₄	1.18		0.83	103
trans-cyhx-Me ₂ -3,2,3-S ₄	2.94		0.77	103
cis-cyhx-Me ₂ -3,2,3-S ₄	2.45		0.75	103
bis-en	19.60		-0.11	44, 104
bis-nncyhxn (nncyhxn = <i>trans</i> -1,2-diaminocyclohexane)	20.93		-0.25	44, 104
bis-phen	15.8		0.17	105, 106
bis-bpy	13.5	14.2	0.12	105, 106
bis-5-nitrophen	13.5		0.26	107, 108
bis-2,9-Me ₂ phen	11.0	19.2 ^a	0.60	108, 109
2,2,2-tet (trien)	20.4		≈ -0.38	110, 57 ^c
2,3,2-tet			-0.30	44
3,2,3-tet			-0.27	44
<i>Tripodal ligands</i>				
TMMEA	6.29	15.8	0.69	82
TEMEA	6.35	15.5	0.67	82
PMMEA	11.06	15.4	0.38	82

Tab. 4 (continued)

Complexed ligand	$\log K_{\text{Cu}^{\text{II}}\text{L}}$	$\log K_{\text{Cu}^{\text{I}}\text{L}}$	$E^{\text{f}}, \text{V versus SHE}$	References
PMAS	10.48	15.0	0.40	82
PEMEA	7.89	15.8	0.60	82
PEAS	7.87	15.9	0.61	82
BPMMEA	16.10	15.0	0.06	82
BPMEEA	15.82	15.0	0.08	82
BPEMEA	9.10	14.6	0.46	82
BPEEEA	9.29	15.0	0.47	82
TPMA	17.6	12.9	-0.15	82
TPEA	9.35	15.8	0.51	82

^aValue for $\log \beta_2$ value for $\text{Cu}^{\text{l}}(2,9\text{-Me}_2\text{phen})_2$ was determined directly.

^bValues in this study were determined at 20 °C, $\mu = 0.2$ and are slightly different from those shown in Table 4.

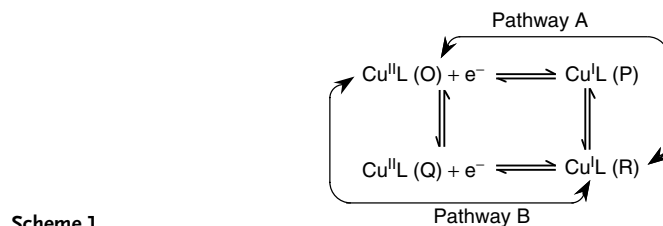
^cIn approximating the aqueous potential value, 0.10 V was subtracted from the potential value measured in 80% CH_3OH (w/w).

types of chemical processes have been proposed to account for the appearance of irreversibility in such systems. Several of the more credible reaction processes are described in the following paragraphs.

24.7.3.1 Ligand Conformational Change

The difference in the geometric preferences exhibited by Cu(II) and Cu(I) has been noted above. In the absence of complete ligand rigidity, this implies that, upon transferring an electron to or from the copper center, the ligand must undergo a change in conformation. If conformational change is rapid relative to the timescale of the experiment, the two processes will appear to

be concerted and will show no irregular behavior. In studying the homogeneous electron-transfer kinetics for a series of Cu(II/I) systems involving macrocyclic and acyclic polythioethers, Martin et al. [112] observed kinetic behavior that was strongly suggestive of a slow change in the ligand conformation. The CV behavior for such a mechanism was first theoretically described as a general phenomenon by Laviron and Roullier [113]. This behavior was first confirmed in the electrochemical behavior of Cu(II/I) systems by Bernardo et al. [114]. Their mechanism is illustrated in Scheme 1. In this mechanism, $\text{Cu}^{\text{II}}\text{L(O)}$ and $\text{Cu}^{\text{I}}\text{L(R)}$ represent the most stable conformational species, while $\text{Cu}^{\text{II}}\text{L(Q)}$ and $\text{Cu}^{\text{I}}\text{L(P)}$ represent



Scheme 1

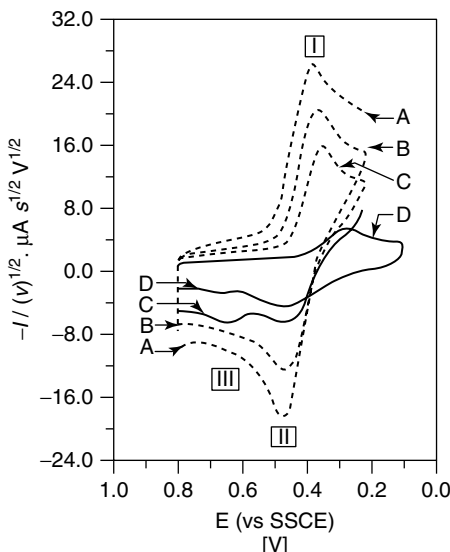


Fig. 3 Cyclic voltammetric behavior of the Cu(II) complex with [14]aneS₄ (LBI) as a function of temperature in 80% methanol (by weight) illustrating the effect of Scheme 1 upon the electron-transfer behavior. At 25 °C (curve A) and at 0 °C (curve B) a reversible voltammogram is observed in which the cathodic peak (I) represents the reduction of equilibrated O and Q and the anodic peak (II) represents the oxidation of equilibrated P and R. As the temperature is lowered to -23 °C (curve C), a second oxidation peak (III) appears at a more positive potential representing the direct oxidation of R to Q. As the temperature is decreased to -77 °C (curve D), peak III diminishes and a new peak II appears, representing the reoxidation of newly created P before it has time to convert to the more stable R. Similar behavior is observed using very fast sweep rates at ambient temperature. Reproduced with permission from Ref. 114. Copyright 1989 American Chemical Society.

metastable intermediates for which the ligand conformations are presumed to more closely approximate the stable conformations of the other oxidation state.

Since the molecularity for both reaction pathways is identical, this type of mechanism cannot be diagnosed by changes in concentration ratios. However, at sufficiently rapid-scan rates or low temperatures, the conformational changes designated by the vertical reactions in Scheme 1 can become rate limiting.

Based on CV studies carried out at low temperature (-77 °C) in 80% methanol/20% water (w/w), Bernardo et al. [114] demonstrated that Cu^{II/I}([14]aneS₄) (LBI) showed electrochemical behavior identical to that predicted by the Laviron and Roullier square scheme (Scheme 1). Subsequent CV studies by Robandt et al. [115], involving scan rates up to 80 000 V s⁻¹, made it possible to

determine the rate constants associated with all eight reaction arrows in Scheme 1 for a specific Cu(II/I) complex. Villeneuve et al. [116] later conducted a series of rapid-scan CV studies to evaluate the corresponding rate constants for seven additional related complexes that appear to conform to Scheme 1. As illustrated in Fig. 3, the primary features noted for Cu(II/I) systems corresponding to Scheme 1 is that, at sufficiently slow sweep rates, the CV's appear to be reasonably reversible with equilibrated O and Q being reduced on the cathodic sweep (peak I) and equilibrated R and P being oxidized (peak II) on the anodic sweep (Fig. 3, curves A and B). As the temperature is lowered (or as the sweep rate is increased at a constant temperature) for solutions initially containing only the oxidized complex, however, the rate of conversion of R to P becomes rate limiting and the anodic peak (III) at higher

potential – representing direct oxidation of R to Q – increases in magnitude for both $\text{Cu}^{\text{II}}\text{L}$ and $\text{Cu}^{\text{I}}\text{L}$ solutions (curve C in Fig. 3). At sufficiently low temperatures (or at sufficiently high sweep rates) for Cu(II) solutions, the higher potential anodic peak diminishes in magnitude and eventually disappears as a new peak grows at slightly lower potential than the original equilibrated peak (curve D in Fig. 3). This new peak represents the direct oxidation of P to O, since the P intermediate produced during the cathodic sweep no longer has time to convert to the stable R conformation prior to reoxidation. For solutions containing initially only the reduced complex, $\text{Cu}^{\text{I}}\text{L}$, the initial anodic sweep shows evidence of a second peak at higher potentials, even when slow-scan rates are used, representative of the oxidation of R directly to Q. This anodic peak becomes totally dominant as the sweep rate increases (or the temperature decreases) since R, which is the dominant species present in the initial reduced solution, does not have time to convert to P before oxidation occurs.

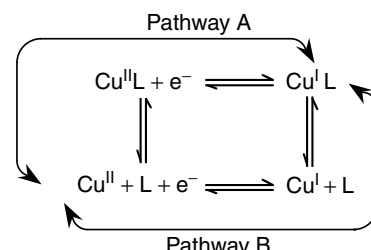
Homogeneous cross-reaction electron-transfer kinetic studies suggest that many other Cu(II/I) systems obey Scheme 1. However, few Cu(II/I) systems have been subjected to sufficiently low temperature or rapid-scan CV measurements to demonstrate the presence of rate-limiting conformational changes.

24.7.3.2 Complex Dissociation/Formation

One of the simplest mechanisms that has been considered for Cu(II/I) electrochemistry involves the dissociation of either the $\text{Cu}^{\text{II}}\text{L}$ or $\text{Cu}^{\text{I}}\text{L}$ complex species to the solvated species (designated in Scheme 2 as Cu^{II} and Cu^{I}), preceding or following the electron-transfer step [117].

Since both Cu(II) and Cu(I) tend to undergo rapid inner-sphere substitution, this mechanism would appear to be viable for Cu(II/I) redox couples containing weakly coordinated ligands. As noted above, most Cu(I) complexes have reasonably high stabilities in aqueous solution while Cu(II) complexes cover a wide range of stabilities. This suggests that, at least in aqueous solution, some $\text{Cu}^{\text{II}}\text{L}$ complexes will be largely dissociated so that only an anodic peak may be observed. (The reverse may occur in acetonitrile solutions where $\text{Cu}^{\text{II}}\text{L}$ complexes tend to be much more stable while $\text{Cu}^{\text{I}}\text{L}$ complexes are much less stable due to the stability of $\text{Cu}^{\text{I}}(\text{CH}_3\text{CN})_4^+$). [54] The presence of such a phenomenon can be probed by increasing the concentration of free ligand and observing whether the cathodic (or anodic) peak begins to appear and grow in magnitude in proportion to the concentration of excess ligand in solution. The possibility of observing the direct transfer of electrons via Pathway B in Scheme 2 is less likely in view of the fact that solvated copper tends to be extremely slow in undergoing

Scheme 2

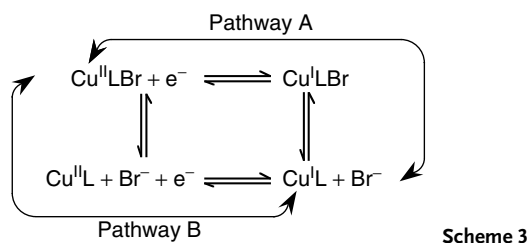


electron transfer in the absence of bridging ligands [118, 119]. For ligands that protonate readily, the extent of complex formation is generally pH dependent and a study of the electrochemical behavior as a function of pH should then be diagnostic.

24.7.3.3 Interconversion of Ternary and Binary Complexes

Even when a strongly complexing multidentate ligand is coordinated to the copper ion, the differences in the preferred coordination number for Cu(II) and Cu(I) imply that one or two copper–donor atom bonds will rupture during the reduction process. Water molecules tend to

undergo rapid inner-sphere substitution with both Cu(II) and Cu(I) so that the dissociation or formation of Cu–OH₂ bonds may have no observable impact on the reversibility of the cyclic voltammograms, even at rapid sweep rates. In the case of a ternary Cu(II) complex in which Cu(II) is coordinated to a tridentate or quadridentate ligand plus a bidentate or unidentate ligand, respectively, the dissociation of the latter species upon reduction has been observed in the cyclic voltammograms for a few systems. A typical example is that postulated by Conan and coworkers as illustrated in Scheme 3 [120].



Scheme 3

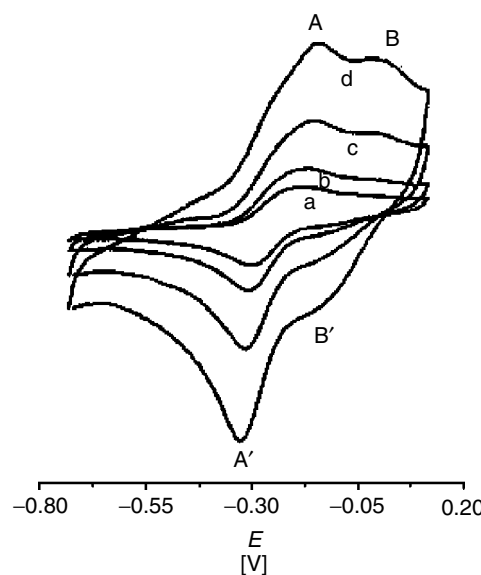


Fig. 4 Cyclic voltammetric behavior of $[\text{CuBrL}]_2[\text{Cu}_2\text{Br}_4]$ (L = 2, 6-bis[1-(2,6-diisopropylphenylimino)ethyl]pyridine as a function of scan rate: (a) $\nu = 0.1$, (b) $\nu = 0.2$, (c) $\nu = 0.5$, and (d) $\nu = 1.0$ V s^{-1} . Peaks A and A' are attributed to the $\text{Cu}^{\text{II}}/\text{BrL}$ moiety while peaks B and B' are assigned to the $\text{Cu}^{\text{II}}/\text{L}$ redox couple in which the $\text{Cu}-\text{Br}$ bond is dissociated. Reproduced with permission from Ref. 120. Copyright 2001 Elsevier Publishing Company.

The presence of such a mechanism was probed by varying the sweep rate as illustrated in Fig. 4. Caution must be exercised in drawing conclusions from such a study because, with halide ions (and with some other unidentate species), bridging by the halide between the copper ion and the electrode surface may accelerate the rate of electron transfer and lead to erroneous conclusions. This type of mechanism has also been proposed by Palaniandavar and coworkers [121] for the Cu(II/I) complex with deprotonated salicylideneglycine in the presence of cytosine or cytidine in which the latter species tends to be coordinated only to the oxidized complex.

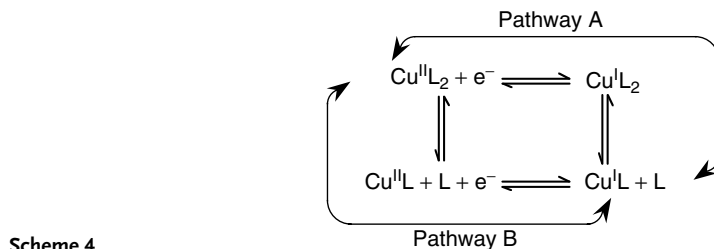
24.7.3.4 Interconversion of 1:2 and 1:1 Complexes

A similar mechanism may occur for systems involving Cu(II) coordinated to terdentate or bidentate ligands in which the oxidized complex exists primarily as a 1:2 complex while, upon reduction, the 1:1 complex predominates. Kandegedara et al. [48] reported that the system involving copper and the terdentate ligand [9]aneS₃ (LBE) appears to involve such a mechanism as illustrated in Scheme 4:

For the [9]aneS₃ system, Pathway B was not observed in homogeneous cross-reaction electron-transfer reactions [48] even when a huge excess of Cu(II) was added (up to 0.1 M) to force Cu^{II}L (the 1:1 complex) to become the dominant

oxidized form. However, the direct oxidation and reduction of the 1:1 complex can be observed electrochemically as shown by the CV trends in acetonitrile solution as a function of increasing ligand concentration (Fig. 5) [68]. In the presence of a 1:1 ratio of Cu(II) to ligand at low concentrations ($\approx 20 \mu\text{M}$), reversible peaks are observed representing the Cu^{II}/I_L redox couple with a second reduction peak, representative of the 1:2 complex, Cu^{II}L₂, occurring at lower potential. As the ligand concentration is increased, the Cu^{II}L reduction peak disappears and the anodic peak representative of Cu^IL₂ begins to emerge. At sufficiently high ligand concentrations, only the reversible peaks for the Cu^{II}/I_L₂ redox couple are observed. This latter ligand dependence emphasizes the necessity for utilizing a wide range of ligand concentrations to observe the changes in electrochemical behavior as a means of determining whether Scheme 4 applies (In the absence of such variations in concentrations, an earlier study mistakenly attributed the CV behavior for the Cu(II/I)-[9]aneS₄ system to Scheme 1, rather than Scheme 4.) [122].

The Scheme 4 mechanism is likely to apply to other Cu(II/I) systems involving terdentate ligands that are not sterically hindered. For example, it is suspected that the apparent irreversibility of the CV's observed by Neves and coworkers [123] for the Cu(II/I) system involving (2-hydroxybenzyl-2-pyridylmethyl) amine



Scheme 4

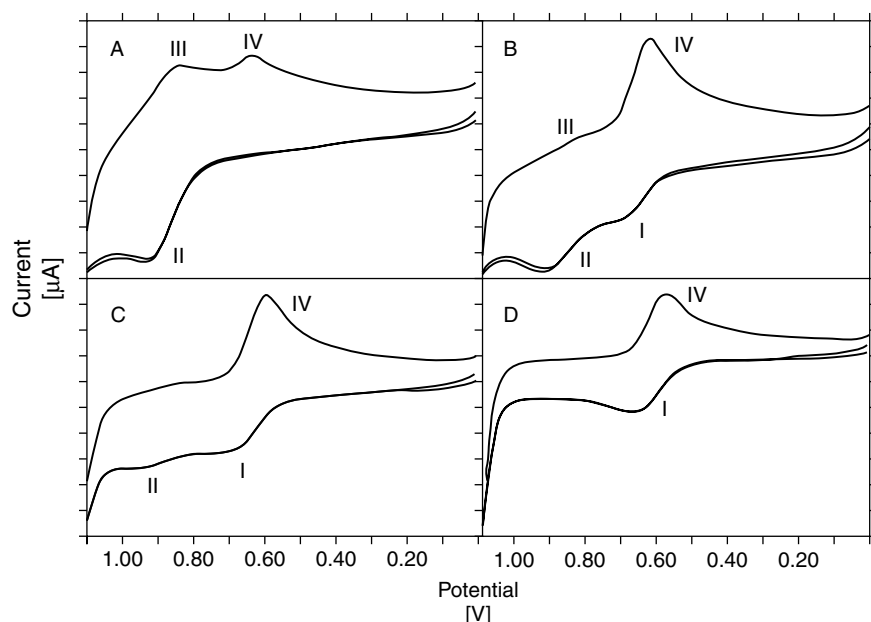
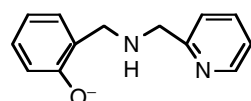


Fig. 5 Cyclic voltammograms for $\text{Cu}^{\text{I}}([9]\text{aneS}_3)_n$ in acetonitrile as a function of ligand concentration at 25°C , $\mu = 0.10 \text{ M}$ (NaClO_4). The concentration of the $\text{Cu}(\text{I})$ is $26 \mu\text{M}$ for all voltammograms. The total ligand concentration (C_L) varies as follows: (a, $C_L = 0.0228 \text{ mM}$; b, $C_L = 0.052 \text{ mM}$; c, $C_L = 0.52 \text{ mM}$; d, $C_L = 1.13 \text{ mM}$). Peaks II and III represent the 1:1 complex, $\text{Cu}^{\text{II}/\text{I}}([9]\text{aneS}_3)_1^{2+/+}$, while I and IV represent the 1:2 complex, $\text{Cu}^{\text{II}/\text{I}}([9]\text{aneS}_3)_2^{2+/+}$. Potentials shown are versus a Ag/AgCl reference electrode. The current scale differs slightly for each voltammogram but the peaks generally range from about -5 to $+5 \mu\text{A}$ (data from Ref. 68).

may be attributable to a mechanism of this same type.



Even more complicated behavior can be exhibited by bidentate ligand systems. For example, in acetonitrile, both $\text{Cu}(\text{I})$ and $\text{Cu}(\text{II})$ form 1:1 and 1:2 complexes with phenanthroline and bipyridine, while $\text{Cu}(\text{II})$ also forms a 1:3 complex. In the presence of relatively low ligand concentrations, the oxidized complex tends to be 1:2, while the reduced complex is 1:1 owing to the differing preference of the two

oxidation states for coordination to the acetonitrile solvent molecules. As the ligand concentration is increased, the oxidized species tends to convert to a 1:3 complex as the reduced complex becomes predominantly 1:2. Thus, at any specific ligand concentration, electron transfer may involve the loss of a coordinated bidentate ligand either before or following reduction. Since the dominant species for both oxidation states changes as a function of ligand concentration, the observed electrochemical behavior can be confusing and requires a comprehensive variation in ligand concentration if the contributions of the various species present are to be resolved [124, 125].

24.7.3.5 Dimeric/Monomeric Species

A number of Cu(II/I) systems have been reported where the oxidized complex tends to exist predominantly as a monomeric species while the reduced form is predominantly dimeric. This type of mechanism is illustrated in Scheme 5.

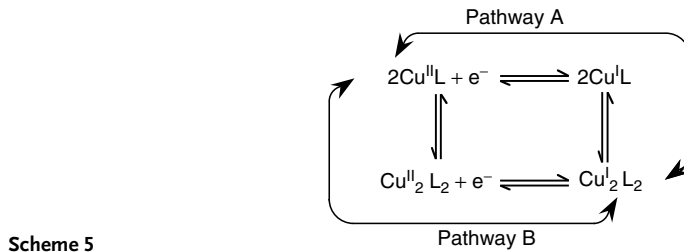
Such a dimeric/monomeric system has been proposed by Fabbrizzi and coworkers [126] for a series of acyclic ligand systems containing four unsaturated nitrogen donor atoms. As illustrated in Fig. 6, two irreversible peaks were observed, the lone reduction peak being ascribed to monomeric $\text{Cu}^{\text{II}}\text{L}$ and the lone oxidation peak to dimeric $[\text{Cu}^{\text{I}}\text{L}]_2$, indicating that the vertical reactions are slow on the CV timescale. Takagi and coworkers [127] have proposed similar behavior for a ligand involving two covalently linked phenanthrolines where,

again, the reduced complex exists preferentially in the dimeric form. For a single scan of the $\text{Cu}^{\text{I}}_2\text{L}_2$ dimer in acetonitrile at 1.0 V s^{-1} , they observed peaks representative of only the dimeric redox couple. However, in repetitive scans, a second cathodic peak emerged at lower potential representative of the $\text{Cu}^{\text{II}}\text{L}$ monomer. Since dimers tend to be favored at higher concentrations, diagnostic studies as a function of total complex concentration are recommended for systems suspected of conforming to Scheme 5.

24.7.3.6 Other Phenomena Affecting Electrochemical Behavior

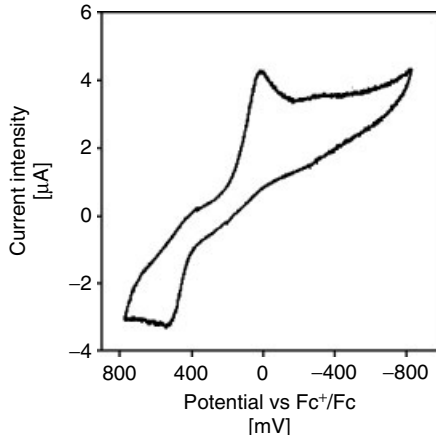
24.7.3.6.1 Ligand Oxidation or Reduction

When the CV potential range of Cu(II/I) complexes is extended to very high or



Scheme 5

Fig. 6 Cyclic voltammogram for an acetonitrile solution initially containing a dimeric $\text{Cu}^{\text{I}}_2(\text{L})_2^{2+}$ complex involving a tetramine ligand that favors the monomeric $\text{Cu}^{\text{II}}\text{L}^{2+}$ upon oxidation. The second cycle, which features both pairs of oxidation and reductions waves, is depicted here. The peaks at lower potential represent the monomeric redox couple while those at the more positive potential are for the dimer. Reproduced with permission from Ref. 126. Copyright 2001 American Chemical Society.



low values, the complexed ligand itself may be oxidized or reduced. Owing to entropy considerations, such ligand redox reactions are not readily reversible and, thus, irreversible voltammograms are almost inevitably produced as indicated by the lack of a corresponding peak on the return scan. Studies of the electrochemical behavior of the free ligand are generally helpful in identifying such behavior.

24.7.3.6.2 Electroplating of Copper

A limiting factor in cyclic voltammograms of all copper systems is the fact that copper may be deposited on the cathode at higher potentials than for any other first-row transition element. Therefore, a large deposition peak will be observed if the cathodic sweep is extended to sufficiently low potentials. This phenomenon places severe limitations on the accessible potential range if excess uncomplexed copper is present. In the absence of excess copper, the potential at which electroplating occurs depends directly upon the concentration of excess ligand and the conditional stability constant of the copper complex. The onset of copper plating is most readily identified by the presence of a sharp anodic stripping peak during the return (anodic) scan. This

interference can be eliminated by limiting the scan range so that copper plating is avoided.

24.7.4

Biological Copper Systems

Since copper is second only to iron in its prevalence in redox-active metalloproteins, an understanding of the electron-transfer properties of copper proteins has been recognized as a matter of prime interest. However, protein systems tend to present many problems when attempting to make meaningful electrochemical measurements. The most thoroughly studied redox-active copper proteins are the cupredoxins (the simplest class of the so-called “blue” copper proteins) that contain a single copper site designated as type 1 copper. In these proteins, the copper has an elongated trigonal pyramidal coordination geometry in which the copper coordination sphere consists of a thiolate sulfur from cysteine and two histidine nitrogens forming the triangular base with an elongated bond to an apical methionine sulfur (Fig. 7) [128, 129]. In stellacyanin and related phytocyanins, the apical methionine is replaced by a glutamine [130, 131]. In some cupredoxins, such as azurin, a glycine oxygen occupies an axial site

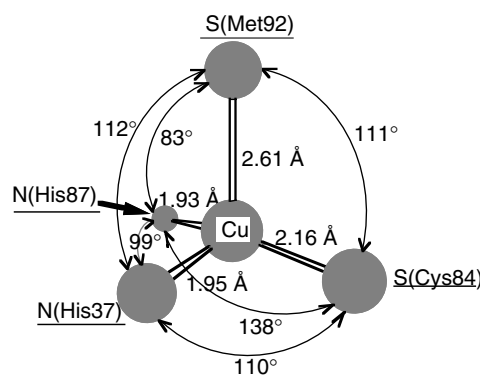


Fig. 7 Geometry of a typical type I copper site in plastocyanin. Bond lengths and bond angles are relatively constant upon reduction or oxidation of the copper site (J. M. Guss, P. R. Harrowell, M. Murata et al., *J. Mol. Biol.* **1986**, 192, 361–387).

opposite to the methionine sulfur to produce a trigonal bipyramidal coordination geometry [132, 133]. A primary focus of the electrochemical measurements has been the determination of the electron-transfer thermodynamics and kinetics and the correlation of these properties to the coordination geometry, particularly by generating mutant species [134, 135].

Unlike heme units, the coordination unit of the blue copper proteins does not exist outside the protein so that attempts to generate representative model compounds have been relatively unsuccessful. Electrochemical studies have been conducted directly on the native proteins, either by utilizing potentiostatic spectroelectrochemical methods [136] or by adsorbing the proteins on modified

gold, pyrolytic carbon or bare glassy carbon electrodes and conducting cyclic or square-wave voltammetric scans [137, 138]. In general, well-resolved cyclic voltammograms have been obtained with peak separations in the range of 55–100 mV. As illustrated by the values in Table 5, such measurements have yielded aqueous redox potentials that are predominantly in the region of 0.3 V (versus SHE), although the total range of potentials is 0.18–0.8 V [139–142].

The ability to obtain accurate redox potentials has played a key role in the investigation of copper proteins since it has provided investigators with data from which to generate an understanding of the factors giving rise to the unusually high potentials exhibited by some

Tab. 5 Potential values for copper(II/I) proteins (principally cupredoxins) in aqueous solution (all values are presumed to be for 25 °C, $\mu \approx 0.1$ M)

Protein type	Source	$E_{12}^{\theta'}, \text{ V versus SHE}$	References
Amicyanin	<i>Paracoccus versutus</i>	0.255	143
Auracyanin A	<i>Chloroflexus aurantiacus</i>	0.205	138
Auracyanin B	<i>Chloroflexus aurantiacus</i>	0.215	138
Azurin	<i>Pseudomonas aeruginosa</i>	0.307	144, 145
Azurin	<i>Alcaligenes denitrificans</i>	0.276	146
Azurin	<i>Alcaligenes faecalis</i>	0.266	146
CBP	<i>Cucumis sativus</i>	0.317, 0.321	147, 148
Fungal laccase	<i>Polyporus versicolor</i>	0.780	149
Mavicyanin	Zucchini	0.215	150
Plantacyanin	Spinach	0.345	151
Plastocyanin	<i>Spinacea oleracea</i>	0.366	144
Plastocyanin	<i>Phaseolus vulgaris</i>	0.360	145
Plastocyanin	<i>Cucumis sativus</i>	0.374	144
Plastocyanin	<i>Populus nigra, var. italic</i>	0.375	152
Pseudoazurin	<i>Alcaligenes faecalis S-6</i>	0.275	143
Rusticyanin	<i>Thiobacillus ferrooxidans</i>	0.680	153–155
Rusticyanin	Mutant Met148Lys	0.363	135
Rusticyanin	Mutant Met148Gln	0.563	135
Rusticyanin	Mutant Met148Leu	0.798	135
SBP	<i>Spinacea oleracea</i>	0.345	151
Stellacyanin	<i>Rhus vernicifera</i>	0.1870.191	144, 145
Stellacyanin	<i>Cucumis sativus</i>	0.265	144
Umecyanin	<i>Armoracia laphatifolia</i>	0.290	144

species. For example, a large number of mutant species of azurin have been examined to determine the effect of various alterations in the copper coordination sphere upon the resulting potential trends. The observed potentials span a range of about 0.3 V, although most were little changed from the wild-type protein [134]. Sola and coworkers [143, 156, 157] have evaluated the enthalpic and entropic contributions to the redox potentials of such mutants and concluded that entropic effects were notably influenced by the exposure of the copper site to the solvent.

As shown by the potential values in Table 5, stellacyanin exhibits one of the lowest potentials among known copper proteins. Since this protein has a glutamine amide in the axial position [130, 158] rather than the methionine thioether sulfur that commonly occupies this site in other cupredoxins, it was suspected that the Cu–S(Met) bond might be largely responsible for the high potential values of other cupredoxins. To investigate this possibility, Hasnain and coworkers prepared rusticyanin mutants in which the apical methionine was substituted by glutamine, lysine, and leucine. These mutants exhibited potentials that spanned the range from 0.37 to 0.80 V[135] (see Table 5), illustrating that the structure clearly had an effect upon the potential but that an apical sulfur was not a necessity. Olsson and Ryde [142] carried out density functional calculations and concluded that the axial ligands themselves have a small influence on the reduction potentials of the blue copper proteins. Instead, they suggested that the large variation in the reduction potentials seems to arise mainly from variations in the solvent accessibility to the copper site and in the orientation of protein dipoles around

the copper site. Subsequent theoretical calculations by Olsson and coworkers [155] led them to conclude that the reduction potential of plastocyanin is “tuned down” by the protein permanent dipole compared to the active site in regular water while in rusticyanin it is “tuned up”. They further concluded that this electrostatic environment is a property of the entire protein and solvent system and cannot be ascribed to any single interaction.

Armstrong and coworkers found that, even at scan rates up to 3000 V s^{-1} on cupredoxins adsorbed on pyrolytic graphite “edge” electrodes, the peak separation increases only slightly, indicating that electron transfer is relatively rapid [159]. These workers have also applied square-wave voltammetry to the blue copper protein azurin adsorbed on both pyrolytic graphite electrodes and gold electrodes modified with self-assembled monolayers of alkanethiols [160]. The standard electron-transfer “exchange” rate constant at zero driving force was shown to depend on the nature of the electrode. However, at high driving potential, a constant rate constant of $(6 \pm 3) \times 10^3\text{ s}^{-1}$ was reached, regardless of the electrode material, indicating that the rate of electron transfer had become “gated” by a rate-limiting conformational change in accordance with Scheme 1.

24.7.5

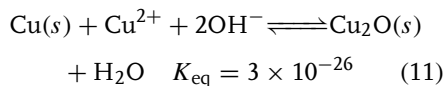
Other Copper(II/I) Systems

A large number of copper complexes involving unidentate ligands have been identified. The electrochemistry of such systems tend to be complicated by the fact that mixtures of the 1:1, 1:2, 1:3, and 1:4 complexes may be present,

each involving a different redox potential. In the case of anionic ligands with unit negative charge, the Cu^IL complex species (i.e. the 1:1 complex) is often found to be insoluble. Unidentate ligands that can form more than one coordinate bond may act as bridging species, either to form dimers or to bridge to the electrode surface, thereby altering the observed electrochemical behavior. A number of multidentate ligands can form binuclear complexes incorporating two or more metal ions. A brief summary of the more common unidentate ligand systems and selected examples of binuclear complexes are included in the following sections.

24.7.5.1 Unidentate Ligand Complexes

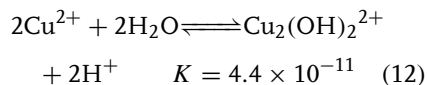
24.7.5.1.1 Hydroxide Complexes The hydrolysis of Cu(I) is too small to measure accurately in aqueous solution. However, the low solubility of Cu₂O limits the useful range of Cu(II) concentrations when in contact with elemental copper because of the following equilibrium [161]:



Since this phenomenon severely limits the concentration of Cu²⁺ that can remain in contact with the metal, the usefulness of the Cu²⁺/Cu(s) electrode is severely restricted.

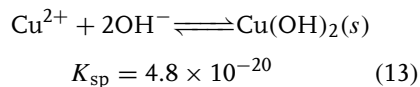
The stability of Cu^{II}OH⁺ has been reported by several investigators, but the value is uncertain. The principal hydrolysis product is, in fact, the dimeric species, Cu₂(OH)₂²⁺ [161]. Higher-order species with the general formula Cu_{n+1}(OH)_{2n}²⁺ have been reported by many investigators, but Baes and Mesmer [161] note that these data may reflect the presence of a colloidal

or active precipitate of Cu(OH)₂ in addition to Cu₂(OH)₂²⁺ at higher pH values. The formation constant for Cu₂(OH)₂²⁺ may be written in the following form [161]:



The introduction of hydroxide as a unique ligand into the inner-coordination sphere of solvated Cu(II) should diminish Jahn-Teller distortion and notably decrease the rate of inner-sphere substitution. This presumably accounts for the fact that no evidence has been found for a unique contribution of the Cu₂(OH)₂²⁺ ion in reactions involving solvated Cu(II) up to pH 5.8 [162]. (At higher pH, Cu(OH)₂ precipitates.)

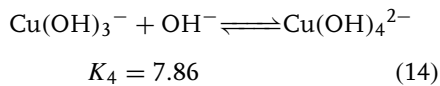
Among the divalent first-row transition metal ions, Cu(OH)₂ (or CuO) is the least soluble hydroxide (or oxide) species [163]:



For concentrated solutions, Cu(OH)₂ (or CuO) may begin to precipitate at pH values slightly above 4.0, thereby severely limiting the pH range in which solution electrochemical data involving Cu(II) can be obtained. For more dilute solutions of Cu(II) (e.g. $\leq 10^{-4}$ M), pH values approaching 6 may be attained before the onset of precipitate formation. A number of basic salts of Cu(II) are particularly insoluble, and this can further limit the range of conditions accessible for electrochemical studies involving solvated Cu(II). For example, nitrate ion should generally be excluded from electrochemical measurements on aqueous Cu(II) solutions to prevent precipitation of copper(II) trihydroxynitrate (also known as *basic copper*

nitrate), $\text{Cu}(\text{NO}_3)_2 \cdot 3\text{Cu}(\text{OH})_2$, which precipitates at pH values as low as 3 for Cu(II) solutions of intermediate concentration [164].

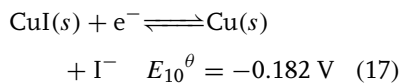
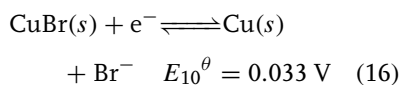
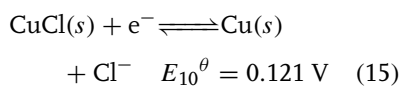
The high affinity of Cu(II) for hydroxide results in the formation of higher hydroxy species so that Cu(II) redissolves at very high pH (i.e. it is amphoteric). This permits electrochemical studies to be conducted on solvated Cu(II) in aqueous solution under high pH conditions that are not feasible for most other divalent transition metal ions [165]. McDowell and Johnston [166] measured the increasing solubility of CuO in KOH solutions and interpreted their data in terms of the formation of both $\text{Cu}(\text{OH})_3^-$ and $\text{Cu}(\text{OH})_4^{2-}$ for which they report the following equilibrium constant:



Baes and Mesmer [161] have suggested that McDowell and Johnston's data can be satisfactorily explained in terms of only the tetrahydroxy species if one allows for the probable effect of increasing ionic strength. However, this statement is presumably incorrect as McDowell and Johnston reported their equilibrium constant in terms of activities, and kinetic measurements on the complexation reactions of Cu(II) at $\text{pH} \geq 13$ indicate that two different hydroxy species exist [165].

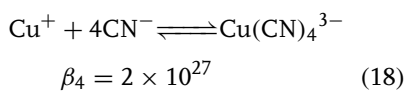
24.7.5.1.2 Halide Complexes Chloride, bromide, and iodide ions form complexes with both Cu(I) and Cu(II). Although the Cu(II) complexes are very weak (for chloride: $K_1 = 1.3$, $K_2 = 0.23$ at 25°C , $\mu = 1.0$) [167], the Cu(I) complexes are of appreciable stability (for chloride: $K_1 = 5 \times 10^2$, $K_2 = 2 \times 10^3$ at 25°C , $\mu = 5.0$) [168]. As with Ag(I), the 1:1 complexes

between Cu(I) and these halide ions are relatively insoluble (for chloride, bromide, and iodide: $K_{\text{sp}} = 4 \times 10^{-7}$, 5×10^{-9} , and $5 \times 10^{-13} \text{ M}^{-2}$, respectively) [168]. The electrochemical potentials reported for the insoluble halide salts of Cu(I) are as follows [13]:

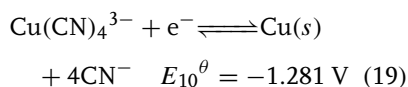


The insolubility of the Cu(I) halide salts, as well as the possibility of μ -halo-bridge formation between two copper atoms (as discussed later) or between the copper complex and the electrode surface, suggests that the presence of halides may alter the electrochemical properties observed for copper-containing solutions.

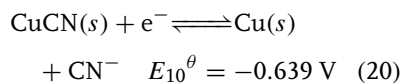
24.7.5.1.3 Cyanide and Thiocyanate Complexes Among other unidentate anionic ligands commonly encountered, cyanide forms stable complexes with both Cu(II) and Cu(I); however, the CuCN salt is so insoluble ($\text{p}K_{\text{sp}} = 19.5$) [169] that only the reduced complex has been characterized, that is, the addition of cyanide to an aqueous solution initially containing Cu(II) results in autoreduction to Cu(I). The overall equilibrium constant (β_4) for the reaction of Cu(I) with four cyanide ions was determined as early as 1904 by Kunschert [170] and subsequent measurements have yielded virtually identical values:



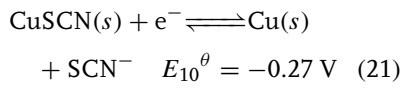
This value does not include activity corrections. The potential value reported in the literature for the electrodeposition of Cu from a solution containing high concentrations of cyanide [169, 171]



implies that $\beta_4 = 2.8 \times 10^{30}$ when expressed in terms of activities. The potential value for the reduction of solid CuCN has been determined [169]:

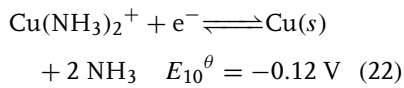


Although thiocyanate also forms an insoluble complex with Cu(I) ($\text{p}K_{\text{sp}}$ for $\text{CuSCN} = 12.7$) [172], the compound is more soluble than CuCN as reflected by the less negative standard potential for electrodeposition [173]:

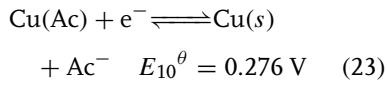


24.7.5.1.4 Ammonia Complexes Ammonia forms stronger complexes with Cu(II) than with any other divalent first-row transition metal ion. In practice, ammonia is often utilized as a masking agent to permit the study of Cu(II) at high pH by preventing the precipitation of Cu(II) hydroxide. The stepwise formation constants for Cu(II) with ammonia in aqueous solution are $K_1 = 1.3 \times 10^4$, $K_2 = 3 \times 10^3$, $K_3 = 7 \times 10^2$ and $K_4 = 1 \times 10^2$ [174]. Even stronger complexes have been reported for the addition of two NH_3 ligands to Cu(I): $K_1 = 8 \times 10^5$ and $K_2 = 8 \times 10^4$. A potential value for the reduction of the 1:2 Cu(I) complex with ammonia has been

reported as follows [175]:

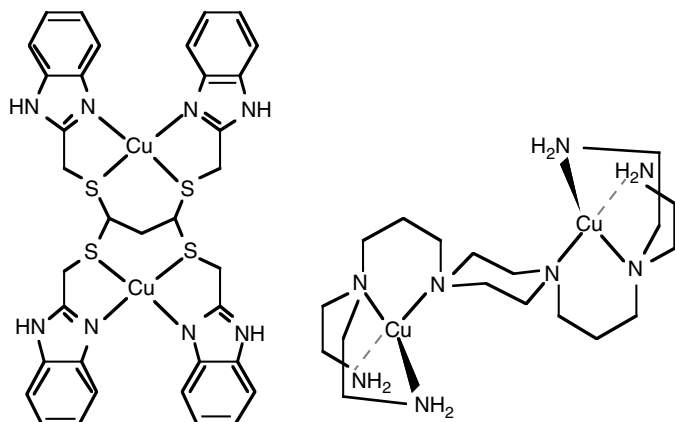


24.7.5.1.5 Complexes with Acetate and Other Common Brønsted Bases Many reactions of copper tend to be conducted in the range of pH 4.0–5.5 to avoid possible formation of hydroxycopper species. This is a range in which acetate is the most commonly used buffer. Unfortunately, acetate (Ac^-) is a very poor choice as it forms stronger complexes with Cu(II) than with any other divalent metal ion except Hg(II). The stepwise equilibrium constants for the formation of $\text{Cu}(\text{Ac})^+$, $\text{Cu}(\text{Ac})_2$, $\text{Cu}(\text{Ac})_3^-$, and $\text{Cu}(\text{Ac})_4^{2-}$ are 50, 10, 2.5, and 0.6, respectively [176]. This indicates that the apparent potential for Cu^{2+} reduction will be significantly decreased by the presence of acetate ion. Although no experimental data have been located for the reduction of Cu(II)–acetate complexes, a value has been reported for the reduction of the 1:1 Cu(I) complex with acetate [177]:



(By comparison to the aqueous E_{10}^θ value for solvated Cu^+ reduction in Table 1, this potential indicates that the K_{sp} value for $\text{Cu}(\text{Ac})$ is about 7.5×10^{-5} .) Thus, any electrochemical studies on copper that are conducted in the presence of acetate buffer will presumably be affected by the formation of acetate complexes.

24.7.5.1.6 Noncomplexing Buffer Systems Acetate is not the only buffer that causes difficulties when used in studies on copper systems. All Brønsted bases are also



Lewis bases and, therefore, potential complexing agents. Some investigators have attempted to avoid the problem by utilizing one of the series of buffers devised by Good and coworkers [178–180] (the so-called Good's buffers) on the basis of the assumption that these buffer compounds do not form metal complexes and are, therefore, suitable for pH control in Cu(II/I) studies. However, several studies have shown that Cu(II) is complexed by 17 of the 20 Good's buffers to a significant extent [181–186]. To prevent buffer interference when making electrochemical measurements on Cu(II)-containing solutions, noncomplexing buffers are recommended. A series of 10 sterically hindered tertiary amine compounds have recently been generated that cover the entire range of pH 3–11 and have been specifically demonstrated to provide interference-free buffering of Cu(II) solutions [181, 182].

24.7.5.2 Binuclear Complexes

A large number of binuclear complexes of copper have been reported in the literature. As first noted by Patterson and Holm [95], these systems may exhibit either two one-electron steps or a single two-electron

step. Ligands that tend to promote the formation of binuclear complexes consist of several types. The simplest systems are those in which the two copper atoms are coordinated to donor atoms that are well separated from each other, particularly within a large branched or macrocyclic ligand. Typical examples of such systems are illustrated above [187, 188].

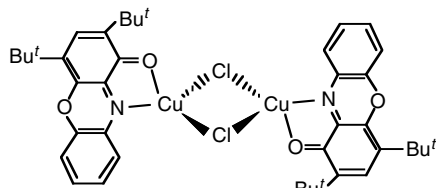
Cyclic voltammograms conducted in DMSO on the compound at left revealed two one-electron steps, both of which appear to be quasi-reversible with the differences in the potentials of the cathodic and anodic peaks for the two-electron-transfer processes being 210 and 310 mV when starting with the NO_3^- salt of the oxidized complex. In the presence of chloride ion, spontaneous reduction occurred upon sitting. Subsequent analysis of the resulting product revealed that the thioether functions were partially oxidized to sulfoxide. For the compound at the right, a single two-electron-transfer step was observed in acetonitrile. Variation of the concentration ratio of copper to ligand resulted in the generation of a 3:1 complex in which the two piperazine nitrogens were coordinated to a third copper atom, the coordination sphere of all three coppers

presumably being completed by solvent molecules or anions. The latter complex showed a single three-electron transfer step.

Other binuclear complexes can be formed by ligands in which at least one of the donor atoms serves as a bridge between the two copper atoms. Two such examples are illustrated below [189, 190]:

In both cases, the two copper atoms occupy identical sites but the electronic communication between them is much more intimate. In the example at left, the two copper atoms appeared to reduce at the same potential and the cyclic voltamograms were essentially reversible.

Bridged binuclear compounds are also frequently formed by smaller ligands, particularly in the presence of chloride ions that can act as μ -bridging ligands. A typical example is illustrated below [191]:



In this compound, two separate electron-transfer peaks were observed in acetonitrile, each of which was highly irreversible. In all of the foregoing examples, each Cu(II) ion is presumably coordinated to a

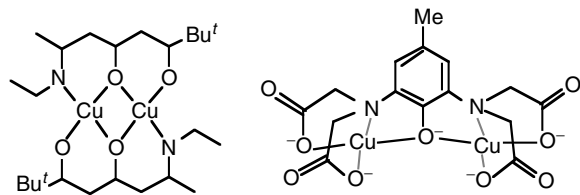
fifth donor atom to complete a square pyramidal or trigonal bipyramidal coordination sphere.

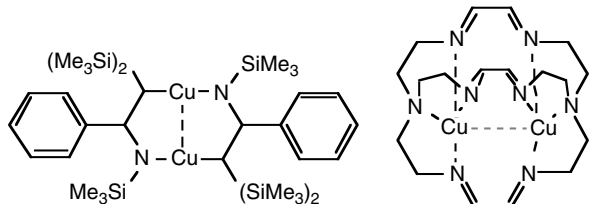
In a few instances, binuclear complexes have been reported in which the two copper atoms interact directly through a metal–metal bond. Two examples of such complexes are illustrated below [192, 193]. CV's run on the compound at left in both tetrahydrofuran and CH₂Cl₂ indicated the presence of two separate electron-transfer steps that were quasi-reversible.

24.7.6 Copper(III/II) Systems

Copper(III)-aquo and – amine species have been generated by pulse radiolysis [194] but these are transient species that undergo rapid decay. Electrochemical generation of Cu(III) complexes of macrocyclic amines have been reported in acetonitrile [195] but they are also unstable and undergo spontaneous reduction to Cu(II). Nonetheless, it is presumed that copper(III) intermediates are generated as transients in a number of reactions, particularly those involving copper catalysis of multielectron transfer reactions.

Endicott and coworkers have measured the Cu(III/II) potentials of a few macrocyclic tetramine complexes in acetonitrile [196–198]. These values are very positive, suggesting that the Cu(III) complexes tend to undergo spontaneous reduction. Margerum and coworkers were the first to demonstrate that Cu(II) complexes with





Tab. 6 Potential values for copper(III/II) complexes in aqueous solution at 25 °C, $\mu = 0.10$ M (NaClO_4) (tetramines from Refs 196 and 197; peptides from Ref. 201)

Coordinated ligand ^a	$E_{12}^{\theta'}$	Coordinated ligand ^a	$E_{12}^{\theta'}$
<i>Tetramines in CH₃CN (V versus reference shown)</i>			
α -trans-[14]dieneN ₄	1.56 (SCE)	β -trans-[14]dieneN ₄	1.57 (SCE)
Me ₆ -[14]aneN ₄ (tet-a)	1.54, 1.62 (SCE)	Me ₂ -[14]aneN ₄	0.63 (Ag/AgCl)
<i>Tripeptides, pH 7.7 in H₂O (V versus SHE)</i>			
GGG	0.92	AGG	0.89
GAG	0.88	GGA	0.88
GGA	0.85	GAA	0.85
AAA	0.81	LGG	0.88
GGL	0.87	GLG	0.87
LGL	0.83	LLL	0.77
VGG	0.88	GGV	0.87
IGG	0.88	GGI	0.86
GGF	0.89	GGβA	0.94
<i>Dipeptide amides (hydroxide complexes) in H₂O (V versus SHE)</i>			
Gga	0.85	Gaa	0.82
Aaa	0.78		
<i>Histidine-containing peptides, pH 7.5 in H₂O (V versus SHE)</i>			
Gghis	0.98	GghisG	1.02
Asp-Ala-His-Lys	0.96		
<i>Tripeptide amides pH 9.5 in H₂O (V versus SHE)</i>			
G ₃ A	0.64	GGAA	0.60
VGGa	0.61		
<i>Higher-order peptides and peptide amides, pH 9.5 in H₂O (V versus SHE)</i>			
G ₄	0.63	AG ₃	0.61
G ₄ a	0.68	G ₅	0.66
G ₄ A	0.66	G ₆	0.67
A ₄	0.60	V ₄	0.51
<i>N-Formyl tripeptides, pH 10.0 in H₂O (V versus SHE)</i>			
NfG ₃	0.75	NfA ₃	0.66
<i>N-Formyl peptides and peptide amides, pH 11.5 in H₂O (V versus SHE)</i>			
NfG ₄	0.55	NfG ₅	0.63
NfG ₃ a	0.49	NfGGA ₃	0.45

^a G: glycyl; A: alanyl; β A: beta-alanyl; V: valyl; L: leucyl-; I: isoleucyl; F: phenylalanyl; his: histidyl; asp: aspartyl; lys: lysyl; Gga: glycylglycylamide; Nf: N-formyl.

Tab. 7 Individual contributions to the electrode potentials of Cu(III/II)–peptide couples (from Ref. 201)

Ligand property	ΔE^θ [V] ^a
1. Replacement of an equatorially bound carboxylate group by a deprotonated-peptide group	−0.28
2. Replacement of an amine group by a deprotonated N-formylamine group	−0.15
3. Replacement of an equatorially bound carboxylate group by a hydroxide group	−0.07
4. Leucyl, valyl, isoleucyl C substituents (per substituent)	−0.05
5. Alanyl or phenylalanyl C substituents (per substituent)	−0.04
6. A 5,5,6-membered ring system	+0.06
7. Replacement of an equatorially bound carboxylate group by an Imidazole group	+0.04
8. Axially coordinated carboxylate groups in the Cu(II) complex	+0.04

^a Relative to $[\text{Cu}^{\text{III}/\text{II}}(\text{H}_2\text{GGG})]^{0,-}$ for which $E^\theta = 0.92$ V.

deprotonated tri- and tetrapeptides can readily be oxidized to form stable Cu(III) complexes [199, 200]. These workers used CV to determine the redox potentials of 40 Cu(III/II)–peptide complexes and confirmed these values by potentiometric titrations against $\text{IrCl}_6^{4-/3-}$ [201]. The CV's were nearly reversible with peak separations in the range of 72–89 mV. As shown in Table 6, the resultant Cu(III/II) potentials covered the range of 0.4 to 1.0 V with the di- and tripeptide complexes generally in the range of 0.77–0.99 V and the tetrapeptides at lower potentials of approximately 0.65 V (versus SHE). The potential of the Cu(III/II) complex with the quadruply deprotonated tetrapeptide C (*cyclo-(β-alanylglucyl-β-alanylglucyl)*) was subsequently shown to have an aqueous potential of only 0.48 V [202].

The coordination geometry of these Cu(III) complexes is presumed to be square planar, indicative of high field d⁸ complexes. This has been demonstrated in the crystal structure of deprotonated tri-α-amino butyric acid, $\text{Cu}^{\text{III}}(\text{H}-\text{Aib}_3)$, in which the copper–donor atom bonds were found to be 0.12–0.17 Å shorter than for the corresponding Cu(II) complex

[203]. Since the geometries of all peptide complexes studied by Margerum and coworkers are presumed to be essentially the same, these workers were able to generate an empirical set of factors that affect the Cu(III/II) redox potentials for the peptide complexes, analogous to the empirical factors generated by Addison for Cu(II/I) redox potentials (Table 3). These empirical additivity effects for Cu(III/II)–peptide complexes are listed in Table 7 [201].

References

- U. Bertocci, D. R. Turner, in *Encyclopedia of Electrochemistry of the Elements* (Ed.: A. J. Bard), Dekker, New York, 1973, pp. 383–497, Vol. II.
- A. M. Alfantazi, D. Valic, *J. Appl. Electrochem.* **2003**, *33*, 217–225.
- G. K. K. Poon, D. J. Williams, *J. Electron. Manuf.* **1998**, *8*, 15–37.
- C. Leger, L. Servant, J. L. Bruneel et al., *Physica A* **1999**, *263*, 305–314.
- D. B. Rorabacher, *Chem. Rev.* **2004**, *104*, 651–697.
- H.-M. Koepp, H. Wendt, H. Strehlow, *Z. Elektrochem.* **1960**, *64*, 483–491.
- R. R. Gagne, C. A. Koval, G. C. Lisensky, *Inorg. Chem.* **1980**, *19*, 2854–2855.
- H. M. Koepp, H. Wendt, H. Strehlow, *Z. Elektrochem.* **1960**, *64*, 483–491; Table 4.

9. G. Gritzner, J. Kuta, *Pure Appl. Chem.* **1984**, *56*, 461–466.
10. (a) J. P. Chang, E. Y. Fung, J. C. Curtis *Inorg. Chem.* **1986**, *25*, 4233–4241.
 (b) D. Chang, T. Malinski, A. Ulman, K. M. Kadish *Inorg. Chem.* **1984**, *23*, 817–824.
 (c) N. G. Connelly, W. E. Geiger *Chem. Rev.* **1996**, *96*, 877–910; Table 1.
11. V. V. Pavlishchuk, A. W. Addison, *Inorg. Chim. Acta* **2000**, *298*, 97–102.
12. I. Noviandri, K. N. Brown, D. S. Fleming et al., *J. Phys. Chem. B* **1999**, *103*, 6713–6722.
13. A. J. Bard, R. Parsons, J. Jordan, *Standard Potentials in Aqueous Solution*, Dekker, New York, 1985, pp. 287–293.
14. J. P. Demarquet, C. Trinh-Dinh, O. Bolck, *J. Electroanal. Chem.* **1970**, *27*, 101–108.
15. L. Aronne, B. C. Dunn, J. R. Vyvyan et al., *Inorg. Chem.* **1995**, *34*, 357–369 See p. 365, col. 2.
16. J. K. Senne, B. Kratochvil, *Anal. Chem.* **1971**, *43*, 79–82.
17. (a) R. N. Pandey, A. K. Srivastava, M. G. Bapat *J. Electroanal. Chem.* **1988**, *245*, 123–130. Cf., (b) R. A. Samant, V. S. Ijeri, A. K. Srivastava *J. Electroanal. Chem.* **2002**, *534*, 115–121.
18. B. J. Hathaway, D. G. Holah, J. D. Postlethwaite, *J. Chem. Soc.* **1961**, 3215–3218.
19. (a) D. H. Powell, L. Helm, A. E. Merbach, *J. Chem. Phys.* **1991**, *95*, 9258–9265.
 (b) A. Pasquarello, I. Petri, P. S. Salmon et al., *Science* **2001**, *291*, 856–859.
20. L. S. W. L. Sokol, T. D. Fink, D. B. Rorabacher, *Inorg. Chem.* **1980**, *19*, 1263–1266.
21. A. E. Merbach, *Pure Appl. Chem.* **1987**, *59*, 161–172.
22. D. B. Rorabacher, *Inorg. Chem.* **1966**, *5*, 1891–1899.
23. B. J. Hathaway, *Coord. Chem. Rev.* **1981**, *35*, 211–252.
24. V. M. Masters, M. J. Riley, M. A. Hitchman, *J. Synchrotron Rad.* **1999**, *6*, 242–243.
25. The dynamic nature of the Jahn-Teller effect is inhibited if the inner-coordination sphere is inhomogeneous.
26. N. W. Alcock, M. Duggan, A. Murray et al., *J. Chem. Soc., Dalton Trans.* **1984**, 7–14.
27. O. P. Anderson, A. B. Packard, *Inorg. Chem.* **1979**, *18*, 1940–1947.
28. M. J. Maroney, N. J. Rose, *Inorg. Chem.* **1984**, *23*, 2252–2261.
29. G. Patrick, M. P. Ngwenya, S. M. Dobson et al., *J. Chem. Soc., Dalton Trans.* **1991**, 1295–1299.
30. C. A. Salhi, Q. Yu, M. J. Heeg et al., *Inorg. Chem.* **1995**, *34*, 6053–6064.
31. P. Wijetunge, C. P. Kulatilleke, L. T. Dressel et al., *Inorg. Chem.* **2000**, *39*, 2897–2905.
32. B. J. Hathaway, *Struct. Bonding (Berlin)* **1984**, *57*, 55–118.
33. F. A. Cotton, G. Wilkinson, *Advanced Inorganic Chemistry*, 2nd ed., Interscience, New York, 1962.
34. J. A. Goodwin, D. M. Stanbury, L. J. Wilson et al., *J. Am. Chem. Soc.* **1987**, *109*, 2979–2991.
35. G. Chaka, M. J. Heeg, L. A. Ochrymowycz, D. B. Rorabacher, to be submitted for publication.
36. T. Maruyama, T. Yamamoto, *Inorg. Chim. Acta* **1995**, *238*, 9–13.
37. J. K. Yandell, in *Copper Coordination Chemistry: Biochemical and Inorganic Perspectives*, (Eds.: K. D. Karlin, J. Zubietra), Adenine Press, Guilderland, NY, 1983, pp. 157–166.
38. (a) G. Sanna, M. I. Pilo, M. A. Zoroddu, R. Seeber *Inorg. Chim. Acta* **1993**, *208*, 153–158. Cf., (b) M. I. Pilo, G. Manca, M. A. Zoroddu, R. Seeber *Inorg. Chim. Acta* **1991**, *180*, 225–230.
39. N. Koshino, Y. Kuchiyama, H. Ozaki et al., *Inorg. Chem.* **1999**, *38*, 3352–3360.
40. Y. Kuchiyama, N. Kobayashi, H. D. Takagi, *Inorg. Chim. Acta* **1998**, *277*, 31–36.
41. A. G. Lappin, M. P. Youngblood, D. W. Margerum, *Inorg. Chem.* **1980**, *19*, 407–413.
42. B. Xie, T. Elder, L. J. Wilson et al., *Inorg. Chem.* **1999**, *38*, 12–19.
43. Y. Nishida, M. Takeuchi, N. Oishi et al., *Inorg. Chim. Acta* **1985**, *96*, 81–85.
44. P. Comba, H. Jakob, *Helv. Chim. Acta* **1997**, *80*, 1983–1991.
45. R. L. Webb, M. L. Mino, E. L. Blinn et al., *Inorg. Chem.* **1993**, *32*, 1396–1402.
46. (a) L. Fabbrizzi, A. Poggi, P. Zanello *J. Chem. Soc., Dalton Trans.* **1983**, 2191–2195. Cf., (b) P. Zanello, R. Seeber, A. Cinquantini, G. Mazzocchin, L. Fabbrizzi, *J. Chem. Soc., Dalton Trans.* **1982**, 893–897 [for original data for CuII/I([14]aneN₄) and -(u-[14]aneN₄].
47. P. Comba, N. F. Curtis, G. A. Lawrence et al., *J. Chem. Soc., Dalton Trans.* **1988**, 2145–2152.

48. A. Kandegedara, K. Krylova, T. J. Nelson et al., *J. Chem. Soc., Dalton Trans.* **2002**, 792–801.
49. M. M. Bernardo, R. R. Schroeder, D. B. Rorabacher, *Inorg. Chem.* **1991**, *30*, 1241–1247.
50. K. Krylova, C. P. Kulatilleke, M. J. Heeg, C. A. Salhi, L. A. Ochrymowycz, D. B. Rorabacher, *Inorg. Chem.* **1999**, *38*, 4322–4328.
51. M. M. Bernardo, M. J. Heeg, R. R. Schroeder et al., *Inorg. Chem.* **1992**, *31*, 191–198.
52. N. E. Meagher, K. L. Juntunen, M. J. Heeg et al., *Inorg. Chem.* **1994**, *33*, 670–679.
53. S. Galijasevic, K. Krylova, M. J. Koenigbauer et al., *Dalton Trans.* **2003**, 1577–1586.
54. L. Aronne, B. C. Dunn, J. R. Vyvyan et al., *Inorg. Chem.* **1995**, *34*, 357–369.
55. P. Wijetunge, Ph.D. Dissertation, “The Effect of Sterically Restricting Cyclopentane Bridges on the Electron-Transfer Behavior of Copper(II/I) Macroyclic Tetrathiaether Complexes,” Wayne State University, 2002.
56. G. Chaka, L. A. Ochrymowycz, D. B. Rorabacher, *Inorg. Chem.* **2005**, *44*, 9105–9111.
57. E. R. Dockal, T. E. Jones, W. F. Sokol et al., *J. Am. Chem. Soc.* **1976**, *98*, 4322–4324.
58. K. P. Balakrishnan, T. A. Kaden, L. Siegfried et al., *Helv. Chim. Acta* **1984**, *67*, 1060–1069.
59. E. Hörmann, P. C. Riesen, M. Neuberger et al., *Helv. Chim. Acta* **1996**, *79*, 235–243.
60. P. Comba, G. A. Lawrence, M. Rossignoli et al., *Aust. J. Chem.* **1988**, *41*, 773–781.
61. M. J. Prushan, A. W. Addison, R. J. Butcher, *Inorg. Chim. Acta* **2000**, *300*–302, 992–1003.
62. M. Vetricelvan, Y.-H. Lai, K. F. Mok, *Dalton Trans.* **2003**, 295–303.
63. K. K. Nanda, A. W. Addison, R. J. Butcher et al., *Inorg. Chem.* **1997**, *36*, 134–135.
64. N. E. Tokel, V. Katovic, K. Farmery et al., *J. Am. Chem. Soc.* **1970**, *92*, 400–402.
65. J. Labuda, V. Plaskon, V. V. Pavlishchuk, *Inorg. Chim. Acta* **1988**, *146*, 13–18.
66. N. Atkinson, A. J. Blake, M. G. B. Drew et al., *J. Chem. Soc., Dalton Trans.* **1992**, 2993–3001.
67. P. D. Beer, J. E. Nation, S. L. W. McWhinnie et al., *J. Chem. Soc., Dalton Trans.* **1991**, 2485–2492.
68. A. Kandegedara, Ph.D. Dissertation, “Electron-Transfer Kinetics of Copper Complexes with Macroyclic Terdentate Ligands,” Wayne State University, 2001.
69. C. Bazzicalupi, A. Bencini, A. Bianchi et al., *J. Chem. Soc., Dalton Trans.* **1995**, 2377–2384.
70. B. C. Dunn, P. Wijetunge, J. R. Vyvyan et al., *Inorg. Chem.* **1997**, *36*, 4484–4489.
71. E. V. Rybak-Akimova, A. Y. Nazarenko, L. Chen et al., *Inorg. Chim. Acta* **2001**, *324*, 1–15.
72. D. E. Nikles, M. J. Powers, F. L. Urbach, *Inorg. Chem.* **1983**, *22*, 3210–3217.
73. M. Murali, M. Palaniandavar, T. Pandiyan, *Inorg. Chim. Acta* **1994**, *224*, 19–25.
74. M. R. Malachowski, M. Adams, N. Elia et al., *J. Chem. Soc., Dalton Trans.* **1999**, 2177–2182.
75. J. McMaster, R. L. Beddoes, D. Collison et al., *Chem.–Eur. J.* **1996**, *2*, 685–693.
76. T. A. Kaden, S. Kaderli, W. Sager et al., *Helv. Chim. Acta* **1986**, *69*, 1216–1223.
77. J. G. Gilbert, A. W. Addison, A. Y. Nazarenko et al., *Inorg. Chim. Acta* **2001**, *324*, 123–130.
78. K. D. Karlin, J. K. Yandell, *Inorg. Chem.* **1984**, *23*, 1184–1188.
79. R. P. F. Kanters, R. Yu, A. W. Addison, *Inorg. Chim. Acta* **1992**, *196*, 97–103.
80. B. Adhikary, C. R. Lucas, *Inorg. Chem.* **1994**, *33*, 1376–1381.
81. S. Liu, C. R. Lucas, R. C. Hynes et al., *Can. J. Chem.* **1992**, *70*, 1773–1783.
82. E. A. Ambundo, M.-V. Deydier, A. J. Grall et al., *Inorg. Chem.* **1999**, *38*, 4233–4242.
83. K. D. Karlin, P. L. Dahlstrom, J. R. Hyde et al., *J. Chem. Soc., Chem. Commun.* **1980**, 906–908.
84. K. D. Karlin, S. E. Sherman, *Inorg. Chim. Acta* **1982**, *65*, L39–L40.
85. H. K. Baek, R. A. Holwerda, *Inorg. Chem.* **1983**, *22*, 3452–3456.
86. M. R. Malachowski, H. B. Huynh, L. J. Tomlinson et al., *J. Chem. Soc., Dalton Trans.* **1995**, *31*–36.
87. H. K. Baek, K. D. Karlin, R. A. Holwerda, *Inorg. Chem.* **1986**, *25*, 2347–2379.
88. N. Wei, N. N. Murthy, K. D. Karlin, *Inorg. Chem.* **1994**, *33*, 6093–6100.
89. S. Zahn, J. W. Canary, *Angew. Chem., Int. Ed. Engl.* **1998**, *37*, 305–307.
90. N. Wei, N. N. Murthy, Z. Tyeklar et al., *Inorg. Chem.* **1994**, *33*, 1177–1183.
91. S. Chen, J. F. Richardson, R. M. Buchanan, *Inorg. Chem.* **1994**, *33*, 2376–2382.
92. A. W. Addison, H. J. Hendriks, J. Reedijk et al., *Inorg. Chem.* **1981**, *20*, 103–110.

93. T. N. Sorrell, D. L. Jameson, *Inorg. Chem.* **1982**, *21*, 1014–1019.
94. A. J. Bard, L. R. Faulkner, *Electrochemical Methods*, 2nd ed. Wiley: New York, 2001, p. 242, Table 6.5.1; p. 243, Table 6.5.2.
95. G. S. Patterson, R. H. Holm, *Bioinorg. Chem.* **1975**, *4*, 257–275.
96. P. J. Burke, K. Hendrick, D. R. McMillin, *Inorg. Chem.* **1982**, *21*, 1881–1886.
97. F. P. Dwyer, N. S. Gill, E. C. Gyarfas et al., *J. Am. Chem. Soc.* **1957**, *79*, 1269–1273; see footnote 2.
98. A. W. Addison, *Inorg. Chim. Acta* **1989**, *162*, 217–220.
99. B. C. Westerby, K. L. Juntunen, G. H. Leggett et al., *Inorg. Chem.* **1991**, *30*, 2109–2120.
100. L. S. W. L. Sokol, L. A. Ochrymowycz, D. B. Rorabacher, *Inorg. Chem.* **1981**, *20*, 3189–3195.
101. K. Krylova, K. D. Jackson, J. A. Vroman et al., *Inorg. Chem.* **1997**, *36*, 6216–6233.
102. M. Kodama, E. Kimura, *J. Chem. Soc., Dalton Trans.* **1977**, 1473–1478.
103. B. C. Dunn, P. Wijetunge, J. R. Vyvyan et al., *Inorg. Chem.* **1997**, *36*, 4484–4489.
104. G. A. Carlson, J. P. McReynolds, F. H. Verhoek, *J. Am. Chem. Soc.* **1945**, *67*, 1334–1339.
105. G. Anderegg, *Helv. Chim. Acta* **1959**, *42*, 344–349.
106. M. A. Augustin, J. K. Yandell, *Inorg. Chim. Acta* **1979**, *37*, 11–18.
107. C. V. Banks, R. C. Bystroff, *J. Am. Chem. Soc.* **1959**, *81*, 6153–6158.
108. M. A. Augustin, J. K. Yandell, *Inorg. Chem.* **1979**, *18*, 577–583.
109. B. R. James, R. J. P. Williams, *J. Chem. Soc.* **1961**, 2007–2019.
110. G. Schwarzenbach, *Helv. Chim. Acta* **1950**, *33*, 974–985.
111. M. Chaudhry, I. Persson, *J. Chem. Soc., Faraday Trans.* **1994**, *90*, 2243–2248.
112. M. J. Martin, J. F. Endicott, L. A. Ochrymowycz et al., *Inorg. Chem.* **1987**, *26*, 3012–3022.
113. E. Laviron, L. Roullier, *J. Electroanal. Chem. Interfacial Electrochem.* **1985**, *186*, 1–15.
114. M. M. Bernardo, P. V. Robandt, R. R. Schroeder et al., *J. Am. Chem. Soc.* **1989**, *111*, 1224–1231.
115. P. V. Robandt, R. R. Schroeder, D. B. Rorabacher, *Inorg. Chem.* **1993**, *32*, 3957–3963.
116. N. M. Villeneuve, R. R. Schroeder, L. A. Ochrymowycz et al., *Inorg. Chem.* **1997**, *36*, 4475–4483.
117. D. B. Rorabacher, M. J. Martin, M. J. Koenigbauer, et al., in *Copper Coordination Chemistry: Biochemical and Inorganic Perspectives*, (Eds.: K. D. Karlin, J. Zubietta), Adenine Press: Guilderland, NY, 1983; pp. 167–202, see p 184, eq 24.
118. M. J. Sisley, R. B. Jordan, *Inorg. Chem.* **1992**, *31*, 2880–2884.
119. J. Irangu, M. J. Ferguson, R. B. Jordan, *Inorg. Chem.* **2005**, *44*, 1619–1625.
120. B. Le Gall, F. Conan, N. Cosquer et al., *Inorg. Chim. Acta* **2001**, *324*, 300–308.
121. I. Samasundaram, M. K. Kommiya, M. Palaniandavar, *J. Chem. Soc., Dalton Trans.* **1991**, 2083–2089.
122. Sanaullah, H. Hungerbühler, C. Schöneich et al., *J. Am. Chem. Soc.* **1997**, *119*, 2134–2145.
123. A. Neves, C. N. Verani, M. A. de Brito et al., *Inorg. Chim. Acta* **1999**, *290*, 207–212.
124. M. P. McGillivray, Ph.D. Dissertation, “Electron-Transfer Kinetics of Copper(II/I) Complexes with 1,10-Phenanthroline and 2,2'-Bipyridine and Their Derivatives in Acetonitrile,” Wayne State University, 2005
125. M. P. McGillivray, D. B. Rorabacher, to be published.
126. V. Amendola, L. Fabbrizzi, L. Gianelli et al., *Inorg. Chem.* **2001**, *40*, 3579–3587.
127. S. Itoh, S. Funahashi, H. D. Takagi, *Chem. Phys. Lett.* **2001**, *344*, 441–449.
128. J. M. Guss, H. C. Freeman, *J. Mol. Biol.* **1983**, *169*, 521–563.
129. E. T. Adman, *Adv. Protein Chem.* **1991**, *42*, 145–197.
130. P. J. Hart, A. M. Nersessian, R. G. Herrmann et al., *Protein Sci.* **1996**, *5*, 2175–2183.
131. C. Dennison, M. D. Harrison, A. T. Lawler, *Biochem. J.* **2003**, *371*, 377–383.
132. G. E. Norris, B. F. Anderson, E. N. Baker, *J. Am. Chem. Soc.* **1986**, *108*, 2784–2785.
133. E. N. Baker, *J. Mol. Biol.* **1988**, *203*, 1071–1095.
134. T. Pascher, B. G. Karlsson, M. Nordling et al., *Eur. J. Biochem.* **1993**, *212*, 289–296.
135. J. F. Hall, L. D. Kanbi, R. W. Strange et al., *Biochemistry* **1999**, *38*, 12675–12680.
136. C. S. St. Clair, W. R. Ellis, H. B. Gray, *Inorg. Chim. Acta* **1992**, *191*, 149–155.

137. T. Sakurai, F. Nose, T. Fujiki et al., *Bull. Chem. Soc. Jpn.* **1996**, *69*, 2855–2862.
138. M. B. Rooney, M. J. Honeychurch, F. M. Selvaraj et al., *J. Biol. Inorg. Chem.* **2003**, *8*, 306–317.
139. F. A. Armstrong, N. L. Barlow, P. L. Burn et al., *Chem. Commun.* **2004**, 316–317.
140. L. J. C. Jeuken, F. A. Armstrong, *J. Phys. Chem. B* **2001**, *105*, 5271–5282.
141. T. Kohzuma, C. Dennison, W. McFarlane et al., *J. Biol. Chem.* **1995**, *270*, 25733–25738, and references therein.
142. M. H. M. Olsson, U. Ryde, *J. Biol. Inorg. Chem.* **1999**, *4*, 654–663. and references therein.
143. G. Battistuzzi, M. Bellei, M. Borsari et al., *Biochemistry* **2003**, *42*, 9214–9220.
144. G. Battistuzzi, M. Borsari, L. Loschi et al., *J. Am. Chem. Soc.* **1999**, *121*, 501–506.
145. V. T. Taniguchi, N. Sailasuta-Scott, F. C. Anson et al., *Pure Appl. Chem.* **1980**, *52*, 2275–2281.
146. E. W. Ainscough, A. G. Bingham, A. M. Brodie et al., *Biochemistry* **1987**, *26*, 71–82.
147. J. M. Guss, E. A. Merritt, R. P. Phizackerley et al., *Science* **1988**, *241*, 806–811.
148. G. Battistuzzi, M. Borsari, L. Loschi et al., *J. Biol. Inorg. Chem.* **1997**, *2*, 350–359.
149. V. T. Taniguchi, B. G. Malmström, F. C. Anson et al., *Proc. Natl. Acad. Sci. U.S.A.* **1982**, *79*, 3387–3389.
150. G. Battistuzzi, M. Borsari, L. Loschi et al., *J. Inorg. Biochem.* **2001**, *83*, 223–227.
151. G. Battistuzzi, M. Borsari, L. Loschi et al., *J. Inorg. Biochem.* **1998**, *69*, 97–100.
152. J. M. Guss, P. R. Harrowell, M. Murata et al., *J. Mol. Biol.* **1986**, *192*, 361–387.
153. R. L. Walter, S. E. Ealick, A. M. Friedman et al., *J. Mol. Biol.* **1996**, *263*, 730–751.
154. L. Harvey, Q. Hao, E. M. H. Duke et al., *Acta Crystallogr.* **1998**, *D54* 629–635.
155. M. H. M. Olsson, G. Y. Hong, A. Warshel, *J. Am. Chem. Soc.* **2003**, *125*, 5025–5039.
156. G. Battistuzzi, M. Borsari, G. W. Canters et al., *Biochemistry* **2001**, *40*, 6707–6712.
157. G. Battistuzzi, M. Borsari, L. Loschi et al., *Biochemistry* **2001**, *40*, 6422–6430.
158. S. DeBeer, D. W. Randall, A. M. Nersessian et al., *J. Phys. Chem. B* **2000**, *104*, 10814–10819.
159. J. Hirst, F. A. Armstrong, *Anal. Chem.* **1998**, *70*, 5062–5071.
160. L. J. C. Jeuken, J. P. McEvoy, F. A. Armstrong, *J. Phys. Chem. B* **2002**, *106*, 2304–2313.
161. C. F. Baes, R. E. Mesmer, Jr. *The Hydrolysis of Cations*, Wiley-Interscience, New York, 1976 Chapter 12.
162. V. B. Pett, G. H. Leggett, T. H. Cooper et al., *Inorg. Chem.* **1988**, *27*, 2164–2169.
163. D. C. Harris, *Quantitative Chemical Analysis*, 4th ed., Freeman, New York, 1995 Appendix F.
164. *CRC Handbook of Chemistry and Physics*. 64th ed., (Eds.: R. C. Weast), CRC Press, Boca Raton, FL, 1983–1984, p. B90.
165. C.-T. Lin, D. B. Rorabacher, G. R. Cayley et al., *Inorg. Chem.* **1975**, *14*, 919–925.
166. L. A. McDowell, H. L. Johnston, *J. Am. Chem. Soc.* **1936**, *58*, 2009–2014.
167. H. McConnell, N. Davidson, *J. Am. Chem. Soc.* **1950**, *72*, 3164–3167.
168. R. M. Smith, A. E. Martell, *Critical Stability Constants, Inorganic Complexes*, Plenum, New York, 1976, Vol. 4.
169. (a) M. G. Vladimirova, I. A. Kakovskii *Zh. Priklad. Khim.* **1950**, *23*, 580; as cited in (b) L. G. Sillen, A. E. Martell, *Stability Constants of Metal-Ion Complexes*; Special Publication No. 17; The Chemical Society, London, 1964
170. F. Kunschert, *Z. Anorg. Chem.* **1904**, *41*, 359–376.
171. R. A. Penneman, L. H. Jones, *J. Chem. Phys.* **1956**, *24*, 293–296.
172. (a) A. M. Golub, *Zh. Neorg. Khim.* **1956**, *1*, 2517; as cited in (b) L. G. Sillen, A. E. Martell, *Stability Constants of Metal-Ion Complexes*; Special Publication No. 17; The Chemical Society, London, 1964
173. G. Milazzo, S. Caroli, *Tables of Standard Electrode Potentials*, Wiley, New York, 1978
174. J. Bjerrum, *Metal Ammine Formation in Aqueous Solution*, P. Haase and Son, Copenhagen, 1957
175. R. Näsänen, *Suomen Kem.* **1944**, *17B*, 31–33.
176. (a) S. Fronaeus, Ph.D. Dissertation, Lund University, 1948; as cited in (b) A. Ringbom, *Complexation in Analytical Chemistry*; Interscience, New York, 1963, p 320.
177. M. Lloyd, V. Wycherley, C. B. Monk, *J. Chem. Soc.* **1951**, 1786–1789.
178. N. E. Good, G. D. Winget, W. Winter et al., *Biochemistry* **1966**, *5*, 467–477.

179. N. E. Good, S. Izawa, *Methods Enzymol.* **1972**, *24*, 53–68.
180. W. J. Ferguson, K. I. Braunschweiger, W. R. Braunschweiger et al., *Anal. Biochem.* **1980**, *104*, 300–310.
181. Q. Yu, A. Kandegedara, Y. Xu et al., *Anal. Biochem.* **1997**, *253*, 50–56.
182. A. Kandegedara, D. B. Rorabacher, *Anal. Chem.* **1999**, *71*, 3140–3144.
183. J. D. Gregory, S. W. Sajdera, *Science* **1970**, *169*, 97–98.
184. P. L. Lleu, G. Rebel, *Anal. Biochem.* **1991**, *192*, 215–218.
185. V. Kaushal, L. D. Barnes, *Anal. Biochem.* **1986**, *157*, 291–294.
186. L. Sigg, R. Hari, H. Xue, *Anal. Chem.* **2003**, *75*, 615–677.
187. A. Benzekri, C. Cartier, J.-M. Latour et al., *Inorg. Chim. Acta* **1996**, *252*, 413–420.
188. E. Monzani, L. Casella, G. Zoppellaro et al., *Inorg. Chim. Acta* **1998**, *282*, 180–192.
189. R. L. Lintvedt, K. A. Rupp, M. J. Heeg, *Inorg. Chem.* **1988**, *27*, 331–339.
190. L. Cai, W. Xie, H. Mahmoud et al., *Inorg. Chim. Acta* **1997**, *263*, 231–245.
191. G. Speier, J. Csihony, A. M. Whalen et al., *Inorg. Chim. Acta* **1996**, *245*, 1–5.
192. R. B. Hitchcock, M. F. Lappert, M. Layh et al., *J. Chem. Soc., Dalton Trans.* **1999**, 1455–1459.
193. J. A. Farrar, V. McKee, A. H. R. Al-Obaidi et al., *Inorg. Chem.* **1995**, *34*, 1302–1303.
194. D. Meyerstein, *Inorg. Chem.* **1971**, *10*, 2244–2249.
195. D. C. Olson, J. Vasilevskis, *Inorg. Chem.* **1971**, *10*, 463–470.
196. D. P. Rillema, J. F. Endicott, E. Papaconstantinou, *Inorg. Chem.* **1971**, *10*, 1739–1746.
197. M. Y. Udugala-Ganehege, M. J. Heeg, L. M. Hryhorczuk et al., *Inorg. Chem.* **2001**, *40*, 1614–1625.
198. J. F. Endicott, B. Durham, in *Coordination Chemistry of Macroyclic Compounds*, (Eds.: G. A. Melson), Plenum, New York, 1979, pp. 393–460. Chapter. 6.
199. G. L. Burce, E. B. Paniago, D. W. Margerum, *J. Chem. Soc., Chem. Commun.* **1975**, 261–262.
200. D. W. Margerum, K. L. Chellappa, F. P. Bossu et al., *J. Am. Chem. Soc.* **1975**, *97*, 6894–6896.
201. F. P. Bossu, K. L. Chellappa, D. W. Margerum, *J. Am. Chem. Soc.* **1977**, *99*, 2195–2203.
202. J. S. Rybka, D. W. Margerum, *Inorg. Chem.* **1981**, *20*, 1453–1458.
203. L. L. Diaddario, W. R. Robinson, D. W. Margerum, *Inorg. Chem.* **1983**, *22*, 1021–1025.

25

The Actinides

*Michael E. Stoll
Los Alamos National Laboratory, Los Alamos, New Mexico, USA*

25.1	Introduction	1049
25.2	Actinium	1049
25.2.1	Aqueous Solutions	1049
25.2.2	Electrodeposition	1050
25.3	Thorium	1050
25.3.1	Aqueous Solutions	1050
25.3.2	Nonaqueous Solutions	1051
25.3.3	Molten-salt Solutions	1051
25.3.4	Electrodeposition	1052
25.3.5	Organometallic and Coordination Compounds	1053
25.4	Protactinium	1054
25.4.1	Aqueous Solutions	1054
25.4.2	Electrodeposition	1054
25.4.3	Nonaqueous Solutions	1055
25.5	Uranium	1055
25.5.1	Aqueous Solutions	1056
25.5.2	Electrodeposition	1061
25.5.3	Molten-salt Solutions	1062
25.5.4	Nonaqueous Solutions	1063
25.6	Neptunium	1066
25.6.1	Aqueous Solutions	1066
25.6.2	Electrodeposition	1068
25.6.3	Nonaqueous Solutions	1068
25.6.4	Molten-salt Solutions	1069

25.7	Plutonium	1069
25.7.1	Aqueous Solutions	1070
25.7.2	Electrodeposition	1071
25.7.3	Molten-salt Solutions	1072
25.8	Americium	1073
25.8.1	Aqueous Solutions	1073
25.8.2	Molten-salt Solutions	1074
25.8.3	Nonaqueous Solutions	1075
25.8.4	Electrodeposition	1075
25.9	Curium	1075
25.9.1	Electrodeposition	1076
25.10	Berkelium	1076
25.11	Californium	1077
25.12	Einsteinium	1078
25.13	Fermium	1078
25.14	Mendelevium	1078
25.15	Nobelium	1079
	References	1079

25.1 Introduction

A concise review of the electrochemical behavior for the actinide elements is presented in this chapter. The material covered mainly focuses on the pertinent aspects of actinide electrochemistry covered in the latest literature reviews. For the elements for which the literature is sparse because of difficulties in handling and/or acquiring sufficient quantities of the elements owing to their radioactivity, a more general overview of their electrochemical behavior is covered. Covering the entire actinide series in a single chapter dictates a rather descriptive text, which is not possible because of space limitations. Sufficient leading references have been provided in each section to direct the interested reader to the original works. The electrochemistry of lawrencium has been omitted because of the lack of any published data.

25.2 Actinium

25.2.1 Aqueous Solutions

There is a relatively small volume of published electrochemical data on

actinium, mainly limited to aqueous electrodeposition studies. This stems in part from the intense gamma activity of the decay products from naturally occurring ^{227}Ac , making experimental work somewhat difficult. There were conclusions reached in some of the earlier literature proclaiming the existence of $\text{Ac}(\text{II})$ in aqueous solution on the basis of radiopolarography studies [1], a technique first described by Love [2], and a study employing 18-crown-6 to facilitate the $\text{Ac}(\text{III})/\text{Ac}(\text{II})$ electron-transfer process [3]. However, the more recent literature concerning this topic contradicts the earlier reports and now suggests an irreversible $\text{Ac}(\text{III})/\text{Ac}(0)$ electrodeposition process at -1.96 V versus standard hydrogen electrode (SHE) in aqueous 0.1 M LiClO_4 at pH 2.5–3.2 [4]. Although not an electrochemical study, the chemical reduction of $\text{Ac}(\text{III})$ with bivalent Sm in aqueous–ethanolic solution through a cocrystallization process was observed by Mikheev et al. [5], who found no evidence for its reduction to $\text{Ac}(\text{II})$. This method had been employed successfully for the production of bivalent Es and Fm in a previous study [6]. In addition, theoretical calculations predict the reduction potential for the $\text{Ac}(\text{III})/\text{Ac}(\text{II})$ couple (-3.3 V) to be more negative than the $\text{Ac}(\text{III})/\text{Ac}(0)$ couple (-2.12 V), which is already beyond the breakdown potential of the aqueous

solvent medium [7]. It is clear from the more recent results that the existence of Ac(II) as a stable species in aqueous media is very unlikely.

25.2.2 Electrodeposition

Although the theoretical studies predict solvent medium breakdown before the onset of actinium electrodeposition, there have been reports of Ac(0) electrodeposition from aqueous solutions utilizing several different methods [8, 9]. One set of studies [8] describes the electrodeposition of actinium from nitric acid solutions, with varying pH values (1.0–4.0) being set to the appropriate level by the addition of sodium hydroxide. The anode and cathode in these studies were platinum metal, and the current density was varied from 50 to 200 mA cm⁻². The authors found that quantitative electrodeposition of actinium could be achieved under various conditions, with the shortest electrolysis time of 1 h being obtained with a current density of 200 mA cm⁻² and a pH of 2.0. A second study employed a saturated aqueous solution of urea oxalate (ca 6.6% at 30 °C) as an electrolyte for the electrodeposition of Ac onto a nickel foil cathode [9]. The authors of this study found that the yield of electrodeposited Ac increased with time and reached a near quantitative maximum yield of 97% at a current density of 53 mA cm⁻² after 2 h. The Ac electrodeposits were suitable for further study using nuclear spectroscopy.

25.3 Thorium

The previous reviews regarding the electrochemical properties of thorium and

its complexes have been covered in the literature up to approximately the mid-1980s [10, 11]. Our intent in the current volume is to just summarize, for completeness, the main findings from the earlier literature and reviews, thereby providing a focus on the more recent results of thorium electrochemistry.

25.3.1 Aqueous Solutions

In aqueous solution, thorium exists as Th(IV), and no definitive data have been presented for the presence of lower-valent thorium ions in this medium. The standard potential for the Th(IV)/Th(0) couple has not been determined from experimental electrochemical data. The values presented thus far for the standard reduction potential have been calculated from thermodynamic data or estimated from spectroscopic measurements. The standard potential for the four-electron reduction of Th(IV) ions has been estimated as -1.9 V in two separate references [12]. The reduction of Th(OH)₄ to Th metal was estimated at -2.48 V in the same two publications. Nugent et al. calculated the standard potential for the oxidation of Th(III) to Th(IV) as +3.7 V versus SHE, while Miles provides a value of +2.4 V [13]. The standard potential measurements from studies in molten-salt media have been the subject of some controversy. The interested reader is encouraged to look at the summary from Martinot [10] and the original references for additional information [14].

Polarography studies of Th(IV) in aqueous solution have been investigated by several authors under various conditions. The results from these studies generally show an irreversible and nonreproducible reduction process. In 1 M LiCl solution, the $E_{1/2}$ value for the reduction

of $\text{Th}(\text{NO}_3)_4$ was reported as -1.27 V versus saturated calomel electrode (SCE), and the authors concluded that the reduction process is catalytic in nature [15]. For the reduction of $\text{Th}(\text{NO}_3)_4$ in $1\text{ M Li}_2\text{SO}_4$, the data were inconclusive and, for that in 0.1 M KNO_3 , a Th(IV) catalytic wave at approximately -1.2 V versus SCE was observed [16]. Better results were obtained when an organic solvent was mixed with the aqueous solutions. For example, Saxena and Chaturvedi found an irreversible diffusion-controlled reduction process in 0.5 M NaClO_4 , 0.002% Triton X, 0.4 mM Th(IV) , and 50% acetonitrile ($E_{1/2} = -1.440\text{ V}$ versus SCE) or 50% methanol ($E_{1/2} = -1.404\text{ V}$ versus SCE) [17].

25.3.2

Nonaqueous Solutions

In nonaqueous media, the polarography of Th(IV) tends to display more defined and reproducible reduction wave(s). Astheimer and Schwochau proposed a two-step reduction of ThCl_4 in dimethylsulfoxide according to the equations $\text{Th(IV)} + 2e^- \rightarrow \text{Th(II)}$ and $\text{Th(II)} + 2e^- \rightarrow \text{Th(0)}$ [18]. The interpretation of these results has subsequently been called into question by Duyckaerts and Degueldre after they performed polarography and chronoamperometry studies in dimethylsulfoxide and propylene carbonate [19]. They suggested that the reduction of Th(IV) proceeds through a one-step, four-electron reduction process, with $E_{1/2} = -1.65\text{ V}$ versus SCE. Additionally, to account for the observed electrochemical behavior, Duyckaerts et al. proposed the formation of an autoinhibiting layer of thorium on the surface of the mercury working electrode following initial reduction. Kolthoff and Ikeda studied the polarography of

$\text{Th}(\text{ClO}_4)_4$ in acetonitrile solvent (with 0.1 M tetraethylammonium perchlorate as the supporting electrolyte) and concluded that the reduction waves in the polarograms were due to the evolution of hydrogen and not the formation of an amalgam at the mercury surface [20]. More recently, Martinot et al. studied the reduction of ThCl_4 at 400 K in dimethylsulfone, $(\text{CH}_3)_2\text{SO}_2$, with LiCl as the supporting electrolyte [21]. As shown in Fig. 1, the cyclic voltammograms display an ill-defined reduction peak, with a characteristic oxidative stripping peak and a small pre-wave on the reverse scan. These results are attributed to the four-electron reduction of Th(IV) to Th(0) at the electrode with subsequent stripping of the metal from the working electrode surface on the return scan.

25.3.3

Molten-salt Solutions

Small quantities of Th metal can be electrodeposited as dendrites from molten NaCl at $\sim 800\text{ }^\circ\text{C}$ by cathodic electrolysis of a ThF_4 solution at a molybdenum cathode [22]. Martinot has published several papers describing the electrodeposition of Th metal in an $\text{LiCl}-\text{KCl}$ eutectic. Voltammetry experiments show that ThCl_4 can be reduced to Th(0) in $\text{LiCl}-\text{KCl}$ at 400 K at a tungsten working electrode (cathode) surface in a single four-electron step with no evidence for an intermediate Th(II) species [23]. More recently, a procedure was described for converting ThO_2 to Th metal [24]. The first step was the dissolution and conversion of ThO_2 into ThCl_4 in a vitreous carbon crucible by allowing HCl gas to flow through the $\text{LiCl}-\text{KCl}$ eutectic/ ThO_2 mixture at $400\text{ }^\circ\text{C}$. The carbon crucible served as the anode and a tungsten rod as the cathode during the

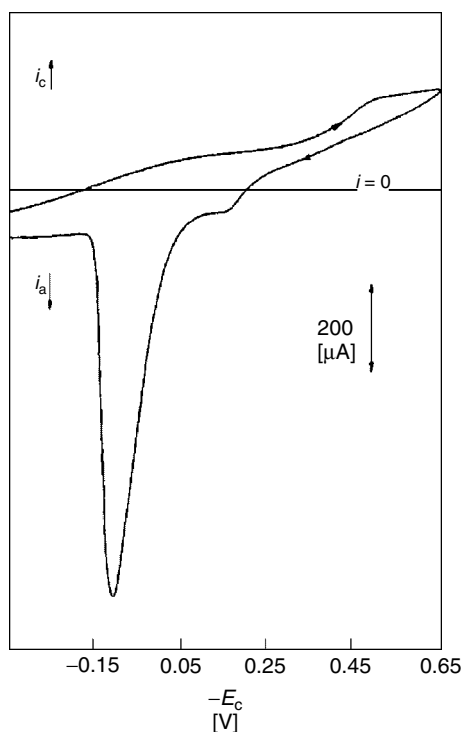


Fig. 1 Voltammetric reduction of ThCl_4 (2.6×10^{-2} M) in molten dimethylsulfone at 400 K (Pt cathode, scan rate = 0.1 V s^{-1} , 0.25 M LiCl) (reprinted from *Journal of Alloys and Compounds*, Vol. 228, L. Martinot, C. Licour, L. Lopes, Contribution to the Knowledge of the Electrochemical Properties of Actinides in Non-Aqueous Media III. The Reduction of Tetravalent Thorium and Tetravalent Neptunium in Various Organic Solvents, Pages 6–12, 1995, with permission from Elsevier).

electrolysis, with a potential difference of between 2.38 and 2.7 V.

25.3.4 Electrodeposition

The electrodeposition of thorium, typically as hydrous oxide, has been used as an efficient means of preparing samples for alpha spectrometric determination. Talvitie described a procedure at a 304 stainless steel cathode using 1 M $(\text{NH}_4)_2\text{SO}_4$ at pH 2 for 120 min, with a current density of 520 mA cm^{-2} [25]. Recently, Lee et al. compared Talvitie's method with a modified version employing the following conditions: stainless steel cathode, 300 mA cm^{-2} current density, 2 h electrolysis, pH of 1.8, and an electrolyte solution containing 0.3 M ammonium oxalate, 0.4 M ammonium sulfate, 0.1 M

hydroxyl ammonium sulfate, and 0.005 M diethyldiaminopentaacetic acid (DTPA) as chelating agents [26]. The modified procedure resulted in slightly higher deposition yields for thorium, $89.4 \pm 2.9\%$ versus $85.5 \pm 4.7\%$, and in the case of plutonium, and likely for the other actinides studied, a more uniformly electroplated analyte resulted. Glover et al. have described an optimized electrodeposition method for thorium and other actinides in which an $\text{NaHSO}_4-\text{H}_2\text{SO}_4-\text{NH}_4$ buffer was utilized [27]. The authors found close to quantitative yields (>90%) for thorium recovery with a 1-h electrodeposition time at pH 1.5–2 and a constant current of 0.75 A. The thorium was plated on a 1.59-cm stainless steel planchet. For thorium determination from soil and sediment samples with sulfate electrolytes, it was recently discovered that the poor thorium recoveries

(~1%) were associated with interfering aluminum in the electrolytic solution during the electrodeposition step [28]. Higher yields were obtained when the aluminum was complexed by fluoride ions. An ammonium acetate electrolyte can be used to efficiently plate (95% recovery) thorium from solution in 2 h under the following conditions: 0.35 M $[\text{NH}_4]\text{[CH}_3\text{COO}]$, pH of 1, approximately 12 V, and 400 mA stainless steel cathode [29]. Zarki et al. have employed a thorium electrodeposition step as part of their procedure for the analysis of thorium by alpha spectrometry [30]. Their method utilizes a solution of 70% ethanol, 0.45 M HCl, and 0.06 M HNO_3 for 1 h at a constant potential of 30 V and a resulting starting current of 0.95 A cm^{-2} .

25.3.5

Organometallic and Coordination Compounds

Cyclic voltammetry experiments have been performed on the complex (*tren'*) $\text{Th}(\text{Bu}'_2\text{DAB})$, where *tren'* = amino-tris[ethyl(trimethylsilyl)amido] and DAB = 1,4-diazabutadiene [31]. The voltammetry was performed in dry tetrahydrofuran (THF) with 0.2 M tetrabutylammonium hexafluorophosphate supporting electrolyte at a Pt disc working electrode. The voltammograms were consistent with a Nernstian and chemically irreversible oxidation of the coordinated DAB ligand at $E_p = 0.20 \text{ V}$ versus Fc/Fc^+ and an electrochemically irreversible reduction process at $E_p = -1.09 \text{ V}$ versus Fc/Fc^+ . Several bent metallocene complexes of thorium were studied by polarography in a nonaqueous medium of dimethylformamide (DMF) or THF solvent with $[(n\text{-C}_4\text{H}_9)_4\text{N}][\text{PF}_6]$ as the supporting electrolyte at a dropping mercury

electrode [32]. In DMF, $(\text{C}_5\text{Me}_5)_2\text{ThCl}_2$ was reduced at -2.45 V versus SCE, while its more stable cyclohexyl isocyanide derivative $(\text{C}_5\text{Me}_5)_2\text{ThCl}_2 \cdot \text{CNC}_6\text{H}_{11}$ was reduced at -2.32 V versus SCE. In THF, $(\text{C}_5\text{Me}_5)_3\text{ThCl}$ is reduced at -2.8 V versus SCE at a Hg electrode and at -2.5 V versus SCE at a Pt working electrode surface. Through correlation with the results from pulse radiolysis experiments of $\text{Th(IV)}-\text{THF}$ solutions, the authors conclude that the reduction process can be attributed to the production of Th(III) derivatives in solution. It should be pointed out that these results contradict an earlier report by Finke et al. in which they did not observe a faradaic electrode process during voltammetry experiments on $(\text{C}_5\text{Me}_5)_2\text{ThCl}_2$ in THF up to -2.7 V versus SCE [33]. In a recent account, Morris et al. commented on the lack of metal-based reductions in " $(\text{C}_5\text{Me}_5)_2\text{Th}$ " derivatives [34]. Indeed, their voltammetry studies on hydrazonato ($\eta^2(N, N')-\text{RNN=CPh}_2$; R=CH₂Ph, Ph) and ketimido ($-\text{N=C(Ph)(R)}$; R=CH₂Ph, Ph) complexes of " $(\text{C}_5\text{Me}_5)_2\text{Th}$ " show an absence of a metal-based $\text{Th(IV)}/\text{Th(III)}$ reduction process in contrast to the $\text{U(IV)}/\text{U(III)}$ reduction that is observed in uranium derivatives.

The reduction of $\text{Th}(\text{acac})_4$, where acac = acetylacetone, in THF at a platinum disc working electrode with $[(n\text{-C}_4\text{H}_9)_4\text{N}][\text{PF}_6]$ as supporting electrolyte shows two cathodic processes [35]. The first reduction at $E_p = -2.68 \text{ V}$ versus Ag/AgClO_4 is ascribed to the $\text{Th(IV)}/\text{Th(III)}$ couple to give $\text{Th}^{\text{III}}(\text{acac})_4$, which slowly liberates acac^- to produce the final product $\text{Th}(\text{acac})_3$. Full chemical reversibility for the $\text{Th(IV)}/\text{Th(III)}$ couple is evidenced only at sweep rates higher than 50 V s^{-1} in the cyclic voltammograms. The authors conclude from their

data that the second reduction process is associated with coordinated and uncoordinated acac/acac⁻ ligand reductions. The electrochemical and spectroelectrochemical behavior for several porphyrin and phthalocyanine complexes containing thorium have been investigated [36]. These complexes show oxidation and reduction processes that are associated with the macrocyclic ring as opposed to the Th(IV) metal center.

25.4 Protactinium

The most stable oxidation states for protactinium are Pa(V) and Pa(IV). The chemical behavior of Pa(V) closely mimics that of Nb(V) and Ta(V), and experimental data are consistent with a 5f(1) rather than a 6d(1) electron configuration for the Pa(IV) species [37]. The electrochemical literature for Pa is mainly focused on the characteristics of the Pa(V)/Pa(IV) couple and the electrodeposition of Pa metal films from aqueous and nonaqueous electrolyte solutions. In aqueous solutions, only Pa(V) and Pa(IV) ions are known to exist, and the standard potential for the Pa(V)/Pa(IV) redox couple is in the range of -0.1 to -0.32 V [38].

25.4.1 Aqueous Solutions

As mentioned in previous reviews, the polarography of Pa(V) has been studied in aqueous fluoride, sulfate, citrate, and oxalate media [39]. The results in [NH₄]F at pH 7.2 gave the most useful electrochemical data and will be discussed here briefly [40]. At a constant fluoride concentration of 3.84 M, two waves are observed in the polarogram. The first wave is the

larger of the two, is proportional to the concentration of protactinium, and has been ascribed to the Pa(V)/Pa(IV) redox couple with $E_{1/2} = -1.29$ V versus SCE. This couple approaches polarographic reversibility at low protactinium concentrations and displays a dependence on the concentration of fluoride in subsequent studies (lower fluoride concentrations give more negative $E_{1/2}$ values). The electrochemically active analyte species in the fluoride solution is thought to be [PaF₈]³⁻, with the Pa(IV) electrode product likely being [PaF₈]⁴⁻ or PaF₄. The nature of the second reduction process ($E_{1/2} \approx -1.57$ V versus SCE) is difficult to determine and not likely because of the further reduction of Pa(IV) to Pa(III).

25.4.2 Electrodeposition

Electrodeposition of Pa metal has been performed from both aqueous and nonaqueous solutions. An isopropanol solution of 10–20 µg mL⁻¹ Pa from 8 M HCl/0.01 M HF/Pa stock was employed for quantitative electrodeposition [41]. The cell consisted of a gold-plated Al cathode and a Pt wire anode. During deposition the current was maintained at 1 mA, which produced a potential of 400–600 V during the 90-min electrolysis. The progress of the electrolysis was externally monitored by alpha-counting of the electrolysis solution before and during the electrodeposition. Deposition studies of metal from aqueous solutions are more common. Pa was electrodeposited on platinum in 95% yield at tracer concentrations from an electrolyte of [NH₄]Cl/HCl [42]. Electrochemical and chemical conditions of the plating process were described for Pu solutions, which served as a model for the other actinide elements studied. Another tracer

concentration study found quantitative recovery of Pa on a stainless steel cathode from a variety of electrolyte solutions: 0.015 M $[\text{NH}_4]\text{F}$ /0.25 M $[\text{NH}_4]\text{Cl}$, 0.2 M $[\text{NH}_4]\text{F}$, and 0.02 M oxalic acid/0.06 M nitric acid [43]. The conditions for the electrolysis consisted of a controlled potential of 7–12 V for 4 h, with a resulting current density of approximately 160 mA cm^{-2} . Natural uranium was utilized in these experiments as a carrier, with its major influence likely associated with the evaporation and transfer steps preceding the electrodeposition. Lower deposition yields (maximum 80%) at a platinum cathode were obtained from a 0.1 N ammonium formate/0.1 N sulfuric acid electrolyte at 80 mA cm^{-2} for 8 h [44].

25.4.3

Nonaqueous Solutions

Concerning the reduction of Pa(IV), theoretical calculations have predicted a standard potential of ca –2.0 V for the Pa(IV)/Pa(III) couple [7, 45]. These results have been substantiated through a study using Tm(II) [$E^\ominus(\text{Tm}^{3+}/\text{Tm}^{2+}) = -2.22 \text{ V}$] as a reducing agent for the reduction of Pa(IV) to Pa(III) in chloride melts [2]. Due to the cathodic limit of the solvent at approximately –1.6 V the production of Pa(III) is thereby prohibited in aqueous solution. Therefore, it is likely that an error was made in the interpretation of earlier polarography data in which the authors claim to reduce Pa(IV) to Pa(III) in aqueous solution [46]. In a solution of acetonitrile with 0.1 M $[(\text{C}_2\text{H}_5)_4\text{N}][\text{ClO}_4]$ as supporting electrolyte, Schwochau and Astheimer observed a single electrochemically irreversible polarographic reduction wave for PaCl_5 ($E_{1/2} = -0.22 \text{ V}$ versus SCE), which they attribute to the two-electron reduction

of Pa(V) to Pa(III) on the basis of comparisons of limiting current values associated with NbCl_5 and TaCl_5 reductions [47]. Subsequent coulometry studies from –0.3 to –0.4 V were unable to confirm the Pa(V) to Pa(III) process in acetonitrile as reduction to the Pa(IV) species was observed [48]. The same authors studied the reduction of $\text{Pa(IV)}\text{Cl}_4$ in dimethylsulfoxide and identified a single electron–transfer process ($E_{1/2} = -1.49 \text{ V}$ versus SCE) consuming four electrons to give Pa(0) metal [48]. There was no evidence of the generation of a Pa(III) species in the polarograms.

25.5

Uranium

The volume of electrochemical data on uranium ions and complex compounds is substantially larger than that on the other actinides. Indeed a separate chapter just on the electrochemistry of uranium could be written without a struggle to find enough data. Our intention here is to cover the more recent literature on uranium electrochemistry and include a brief overview of the most pertinent information from earlier accounts. We have included in Table 1 the potentials for the various uranium redox couples. These potentials were obtained from the recent review by Kihara et al. in which the authors evaluated the standard redox potentials for the various uranium couples by extrapolating experimental formal potentials to the state of zero ionic strength [49]. Most of the electrochemical data in the review were obtained from the published works of Riglet et al. [50]. Additional reviews are contained within the *Gmelin Handbook of Inorganic and Organometallic Chemistry on Uranium* [51]. The earlier review covers

Tab. 1 Standard potentials for selected uranium couples

Electrode couple	E^\ominus (V versus SHE)	References
$\text{UO}_2^{2+}/\text{UO}_2^+$	0.089	50a
$\text{U}^{4+}/\text{U}^{3+}$	-0.573	49, 50b
$\text{UO}_2^{2+}/\text{U}^{4+}$	0.195	49, 54

the electrochemical properties of uranium in aqueous solutions [51a] and molten salts [51b]. The initial section contains information on the standard and formal potentials for the various uranium redox couples, a longer more detailed section follows on the polarographic and voltammetric behavior of uranium ions and complexes, and a separate chapter is included on electrochemistry of uranium in molten salts. The second, more recent review [51c] covers the electrochemistry of uranium in nonaqueous solvents and nonaqueous/aqueous mixtures. Electrochemical studies in nonaqueous solvents is oftentimes warranted because of the propensity for complex compounds of uranium that undergo hydrolysis. For a detailed and thorough analysis of the earlier literature on the electrochemistry of uranium, the interested reader is referred to the reviews mentioned above and the references contained therein.

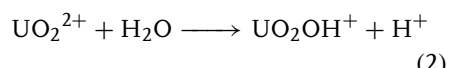
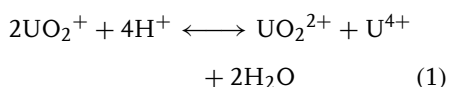
25.5.1 Aqueous Solutions

The general electrochemical behavior of uranium in aqueous solutions is dominated by the reduction of the hexavalent uranyl moiety, UO_2^{2+} . As shown in Table 1, the potential for the $\text{UO}_2^{2+}/\text{UO}_2^+$ couple is 0.089 ± 0.002 V versus SHE, as determined from formal potential data in ClO_4^- solutions (0.5–3.0 M) [49, 50a]. The electrochemical reduction of uranyl compounds has been a thoroughly studied

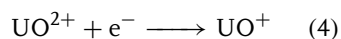
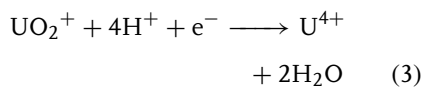
process under a range of solution conditions and typically at a mercury working electrode surface. A detailed overview of electrochemical UO_2^{2+} reduction chemistry can be found in the review by Franz and Schmitt [51a].

For most solution conditions, the initial reduction reaction is the one electron-transfer process mentioned above where the electrode product is the UO_2^+ species. The pentavalent uranyl moiety is rather unstable, although, as Morris has recently shown, it can be stabilized by the appropriate choice of ligand about the metal center [52]. The disproportionation of UO_2^+ into U(IV) and U(VI) ions is the well-known primary decomposition pathway, the specifics of which constitute a series of homogeneous chemical reactions (See Ref. 49 and references therein). A simplified overall disproportionation reaction is shown in Eq. (1). The pH of the electrolyte solutions can have a large influence on the reduction chemistry of the uranyl ion. This issue is discussed in more detail in a study by Sylva and Davidson [53]. The hydrolysis of UO_2^{2+} is more prominent in weakly acidic solutions and leads to the uranium product in Eq. (2). The UO_2OH^+ species is reduced at the electrode surface, and this further complicates the overall reductive electrochemical behavior of the uranyl ion. The electrogenerated UO_2^+ ion is most stable in a pH range of approximately 2–3 and in the absence of oxygen, whereas in strongly

acidic solutions the disproportionation reaction is facile.

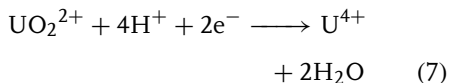


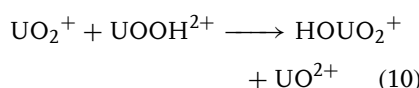
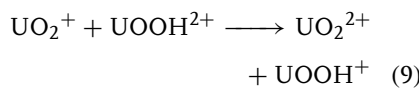
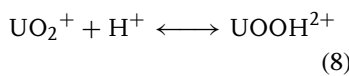
At more cathodic potentials during the reduction of UO_2^{2+} , the polarograms display a second reduction wave that is typically larger than the first wave. Depending on the solution conditions, the second wave can appear as a “composite wave” consisting of two closely spaced reduction processes usually ascribed to the U(V)/U(IV) and U(IV)/U(III) couples. Equations (3–6) outline the possible species involved in the reactions, in which UOOH^+ is generated during the disproportionation reactions of UO_2^+ (see Eqns (8) and (9)). Under solution conditions that produce a second reduction process displaying a wave of height equal to that of the $\text{UO}_2^{2+}/\text{UO}_2^+$ reduction, the reaction in Eq. (5) is thought to be responsible. A single two-electron wave associated with the $\text{UO}_2^{2+}/\text{U}^{4+}$ couple can be obtained in strongly acidic solutions, such as 0.5 M H_2SO_4 , 0.5 M H_3PO_4 , and 6 M HCl [54]. Experimental formal potential measurements for the $\text{UO}_2^{2+}/\text{U}^{4+}$ couple are scarce owing to the irreversibility of the electrode reaction. Sobkowsky and Minc [55] performed electromotive force measurements at a Pt electrode to obtain a formal potential for the couple, from which Kihara and coauthors calculated a standard potential of 0.195 V in their recent review [49].



The recent literature in this area is focused on the electrochemistry of uranyl ions and complexes in mixtures of aqueous and organic solvents, the influence of different electrode surfaces and compositions, and the impact of the ligands surrounding the central uranyl moiety. The influence of different electrode surfaces is being investigated because of interest in using U(IV) as a reducing agent in the treatment of spent nuclear fuel. The source of U(IV) is typically from electrolytic reduction of U(VI) in nitric acid. An overview of recent literature reports is included in the following pages.

Flow coulometry experiments were performed to study the reduction of UO_2^{2+} in nitric, perchloric, and sulfuric acid solutions [56]. The results of these studies show a single two-electron reduction wave attributed to the $\text{UO}_2^{2+}/\text{U}^{4+}$ couple. The direct two-electron process is observed without evidence for the intermediate UO_2^+ species because of the relatively long residence time of the uranium ion solution at the electrode surface in comparison to the residence time typically experienced at a dropping mercury working electrode. The implication here is that as the UO_2^+ is produced at the electrode surface, it is immediately reduced to the U^{4+} ion. As the authors note a simplified equation for this process can be written, Eq. (7), but the process is more complicated. Once the UO_2^+ species is produced it experiences homogeneous reactions comprising Eqns (8) and (9) or (8) and (10) followed by chemical decomposition of UOOH^+ or UO^{2+} to U^{4+} [49].





Dueber et al. studied the voltammetric behavior of the uranyl ion at a solid graphite working electrode, Pt mesh auxiliary, and SCE reference 57. The electrolyte was magnesium chloride in deionized water and the pH of the solutions was adjusted from 2.4 to 6.6 with appropriate quantities of HCl and NaOH. The authors observed a chemically reversible reduction process at pH of 2.4 corresponding to the $\text{UO}_2^{2+}/\text{UO}_2^+$ couple at potentials between 0 and -0.3 V versus SCE. On the return scan in the cyclic voltammograms, the wave shape is indicative of a surface confined species likely because of the adsorption of UO_2^+ . At higher pH values of approximately 4 and 6, the hydrolysis of UO_2^{2+} is greater and the resulting voltammograms show a decrease in the current for the $\text{UO}_2^{2+}/\text{UO}_2^+$ couple and the growth of a new process at more negative potentials, from -0.6 to -0.8 V versus SCE. The new process is due to the reduction of hydrolyzed uranyl complexes, likely $[(\text{UO}_2)_3(\text{OH})_5]^+$ and $[(\text{UO}_2)_4(\text{OH})_7]^+$. This second reduction process is chemically reversible and is due to the $\text{U(VI)}/\text{U(V)}$ couple for the hydrolyzed species. Studies on uranium oxides mechanically attached to the graphite electrode show similar behavior to that obtained for the second reduction process associated with the hydrolyzed species. The authors conclude from their studies that the reductive voltammetric behavior for uranyl in magnesium chloride

electrolyte at a solid graphite electrode is simpler than the results reported for other electrodes.

Wei et al. studied the reduction of UO_2^{2+} in different concentrations of nitric acid (0.1 – 6 M) with added hydrazine at a glassy carbon electrode [58]. The hydrazine was added to help suppress the reduction of the concentrated nitric acid solutions. In the 0.1 M HNO_3 solutions with no hydrazine added, the reduction of UO_2^{2+} results in two ill-defined reduction features and a single anodic wave on the reverse scan at substantially more positive potentials than either cathodic reductions. The authors assign the cathodic features as the reduction of U(VI) to U(V) and the reduction of U(V) to U(IV). The anodic feature is likely the reoxidation of U(V) to U(VI). In 3 M nitric acid, only a single reduction wave was observed with no oxidation wave on the return scan. The authors suggest the single two-electron reduction of U(VI) to U(IV), $\text{UO}_2^{2+}/\text{U}^{4+}$ couple, due to the increase in the H^+ concentration in solution. Since the authors' motivation for this study is related to the processing of spent nuclear fuel and separation of uranium from plutonium, solutions with high nitric acid concentrations are advantageous for the bulk oxidation of U(VI) to the desired U(IV) product. Maximum yield of U(IV) was obtained in constant-flow bulk electrolysis experiments with 6 M HNO_3 , at an applied potential of -0.3 V versus Ag/AgCl, with 0.075 – 0.125 M hydrazine added as suppressor, and flow rate of 3.5 – 5 mL min $^{-1}$.

The electrochemical reduction behavior of UO_2^{2+} was also studied in a nitric acid–hydrazine solution at a titanium electrode because of its resistance to corrosion in nitric acid [59]. It was necessary to pretreat the titanium electrode, to remove surface oxide, through cathodic

polarization at a potential of -0.9 V versus Ag/AgCl for about 25 min prior to obtaining meaningful data for UO_2^{2+} reduction. The voltammograms obtained at the oxide-free titanium electrode correspond to the irreversible $\text{UO}_2^{2+}/\text{U}^{4+}$ couple. The results from this study are intended to help understand the most desirable of conditions during operation of a U(VI)/U(IV) electrolysis process in a production facility utilizing nitric acid solutions with a titanium cathode electrode configuration.

Best and coauthors utilized IR spectroelectrochemistry to study the electrochemical reduction of UO_2^{2+} in aqueous solutions with KNO_3 as supporting electrolyte [60]. The pH of the solutions was set with appropriate quantities of HNO_3 and KOH . The optimal pH range for the study was 2.8–3.4, since within this range speciation of U(VI) is limited to UO_2^{2+} and $(\text{UO}_2)_2(\text{OH})_2^{2+}$, disproportionation of the electrogenerated U(V) species is minimized, and the U–O stretches for U(VI) are observable in the IR spectrum. The results from the study indicate that initial reduction of UO_2^{2+} at a platinum electrode surface leads to decomposition of the electrogenerated U(V) species into a film of uranium oxides on the platinum surface. After the surface is conditioned with the uranium oxides, further reduction of UO_2^{2+} produces UO_2^+ . The IR spectra show stretches associated with UO_2^{2+} and $(\text{UO}_2)_2(\text{OH})_2^{2+}$ at 954 and 938 cm^{-1} , respectively, and diminish as the electrolysis proceeds, and a new feature assigned to the asymmetric O–U–O stretch for UO_2^+ grows in at 914 cm^{-1} . The authors were unable to determine the exact nature of the electrogenerated UO_2^+ , as it could be incorporated within the uranium oxide film or dissolved in the electrolyte solution.

Ugo et al. studied the application of ion exchange voltammetry to the reduction of UO_2^{2+} at a Nafion-coated glassy carbon electrode as a possible means of detecting trace quantities of uranium in aqueous solutions [61]. The Nafion coating was employed to preconcentrate the uranyl ions within the polymeric material at the working electrode surface. Data obtained at bare glassy carbon electrodes were included in the study for comparison purposes. The reduction of UO_2^{2+} at the uncoated glassy carbon surface shows an initial reduction process associated with the $\text{UO}_2^{2+}/\text{UO}_2^+$ couple exhibiting limited chemical reversibility at pH 2.4 in 0.1 M NaCl with added HCl. As the scan is continued to more negative potentials, a second reduction process is evidenced with larger peak currents assigned to the production of U(III). This reduction process has an associated oxidation wave on the return scan with a smaller current value than its forward counterpart, again indicating limited chemical reversibility. On the return scan at potentials more anodic than the original reduction wave for the $\text{UO}_2^{2+}/\text{UO}_2^+$ couple a new anodic wave appears. The authors conclude that this wave is associated with the $\text{U}^{4+}/\text{UO}_2^{2+}$ couple, where the U^{4+} is generated from a comproportionation reaction between the two electrogenerated reduction products U(III) and U(V). Voltammetry at a Nafion-coated glassy carbon electrode in a solution identical to that described for the uncoated electrode shows different behavior. There is an increase in the current levels of approximately an order of magnitude, indicating incorporation of UO_2^{2+} into the Nafion coating. The initial reduction process is now considered to be the UO_2^{2+} to U^{4+} reduction because of the increase in H^+ activity within the Nafion coating even though the pH

of the contacting solution is identical to that employed with the uncoated electrode. This drives the disproportionation reaction of the initial electrode product UO_2^+ according to Eq. (1) and in the limiting case produces a two-electron wave. The second reduction process, which shows full chemical reversibility, is the $\text{U}^{4+}/\text{U}^{3+}$ couple.

Mizuguchi et al. performed cyclic voltammetry and UV/vis spectroelectrochemical experiments at Pt working electrodes on the reduction behavior of UO_2^{2+} in carbonate and acidic perchlorate solutions to learn about the redox behavior of uranium in groundwater environments [62]. The combined results for $\text{Na}_4[\text{UO}_2(\text{CO}_3)_3]$ reduction in 1 M Na_2CO_3 indicate a single-electron reduction (cathodic peak potential E_{pc} of -0.86 V versus Ag/AgCl) to a stable U(V) species, which the authors conclude is likely $[\text{UO}_2(\text{CO}_3)_3]^{5-}$. The potential of deep groundwater containing excess carbonate is typically about -0.3 V versus SHE and would not be adequate to reduce UO_2^{2+} complexes. In the 0.1 M $\text{HClO}_4/0.1$ M LiClO_4 medium reduction of UO_2^{2+} proceeds through two reduction processes, the first being a quasi-reversible reduction at $E_{pc} = -0.2$ V versus Ag/AgCl to UO_2^+ . The second irreversible reduction at $E_{pc} = -0.4$ V versus Ag/AgCl is attributed to the reduction of UO_2^+ to U(IV). The authors' conclusion is that in a reducing acidic groundwater environment the reduction of UO_2^{2+} ultimately produces U(IV).

Gopinath et al. describe the reduction of U(VI) to U(IV) at an activated platinum electrode in 1 M H_2SO_4 for the coulometric determination of uranium [63]. The platinum working electrode is chemically and electrochemically oxidized and then electrochemically reduced to produce a surface that is more active toward uranium

reduction. Quantitative conversion of U(VI) to U(IV) with 100% current efficiency was achieved at -0.150 V versus SCE within 15–18 min. Precision and accuracy were better than 0.2% at uranium levels of 5–10 mg. The results from the study confirm the adequacy of utilizing primary coulometry at an activated platinum electrode for the determination of uranium.

In recent years, reports have appeared concerning the reduction behavior of uranyl in the presence of complexing ligand molecules that may subsequently adsorb onto the working electrode surface. These studies are aimed at developing electrochemical methods for determining the concentration of uranium in dilute solutions. As an example, Mlakar and Branica studied the voltammetric behavior of the uranyl-salicylate-tri-*n*-butyl phosphate complex at a mercury drop electrode in sodium perchlorate solution [64]. The method developed allowed for the determination of $(2.2 \pm 0.08) \times 10^{-8}$ M UO_2^{2+} in natural seawater through peak current measurements from normal pulse voltammograms. The optimized conditions consisted of an accumulation potential of -0.1 V versus Ag/AgCl , a pH of 3.6, 2×10^{-4} M tri-*n*-butyl phosphate, and 1.4×10^{-3} M salicylic acid, which yielded a peak current maximum at -0.35 V versus Ag/AgCl . Other studies of interest include the reduction behavior of UO_2^{2+} as an EDTA complex in perchlorate solutions [65] and as a cupferron complex in acetate buffer solutions [66].

Morris studied the aqueous solution voltammetric behavior of some uranyl coordination complexes to learn how changes in the ligand environment influence the redox potentials and heterogeneous electron-transfer kinetic parameters for the single-electron transfer

of the $\text{UO}_2^{2+}/\text{UO}_2^+$ couple [52]. The specific complexes studied include aquo-, hydroxo-, acetato-, carbonato-, and chloro-ligated UO_2^{2+} . The acetato complex, $[\text{UO}_2(\text{C}_2\text{H}_3\text{O}_2)_3]^-$, displays electrochemically reversible behavior at a Hg surface in 1.0 M $\text{Na}(\text{C}_2\text{H}_3\text{O}_2)/0.1 \text{ NaNO}_3$ at pH 5.9, while the carbonato complex displays electrochemically irreversible electron transfer at a Hg surface in 0.1 M $\text{Na}_2\text{CO}_3/0.1 \text{ M NaNO}_3$ at pH 11.3. The remaining complexes display kinetic behavior that is intermediate between fully reversible and irreversible. Digital simulations of the voltammetric data were employed to quantify some of the kinetic parameters. The large spread in $E_{1/2}$ potentials, $[\text{UO}_2\text{Cl}_4]^{2-/3-} E_{1/2} = -0.065 \text{ V}$ and $[\text{UO}_2(\text{OH})_5]^{3-/4-} E_{1/2} = -0.927 \text{ V}$ versus Ag/AgCl, was ascribed to the differences in sigma-donor ability of the ligands.

Compared to studies in acidic media, studies on the electrochemical behavior of UO_2^{2+} in basic media are more limited. The report from Morris [52] describing voltammetry results for hydroxo and carbonato uranyl complexes is a recent example. Previous studies have been performed mostly in carbonate and bicarbonate solutions. Wester and Sullivan have studied the reduction of UO_2^{2+} in these solutions to find an electrochemically irreversible process but disproportionation of U(V)O_2^+ was evidenced only in the bicarbonate solutions [67].

25.5.2 Electrodeposition

The electrodeposition of uranium as an oxide is routinely employed as a means of preparing sources for quantitative analytical measurement through alpha spectroscopy. Recently dos Santos et al. studied the electrodeposition of uranium with

a focus on the characterization of the deposited film employing IR spectroscopy, Raman spectroscopy, X-ray diffraction, and thermoanalysis [68]. The optimum electrolysis conditions from a saturated NH_4Cl solution containing uranium nitrate consisted of a pH of 1, current density of 0.6 A cm^{-2} , electrolysis time of 60 min, and a distance between cathode and anode of 5 mm. The cathode was a 304 stainless steel disc coupled with a Pt wire anode. The electrodeposition is thought to proceed by precipitation of uranyl ions at the cathode surface due to the localized increased alkalinity in this area as the electrolysis progresses. The authors conclude that the deposited uranium is in the form of a polymeric hydrated uranium oxide in which some of the waters of hydration are replaced by ammonium ions. The monomeric formula of the deposit is likely $\text{UO}_2(\text{OH})_2 \cdot x\text{NH}_3 \cdot y\text{H}_2\text{O}$ and/or $\text{UO}_2(\text{OH})_{2-x} \cdot (\text{ONH}_4)_x \cdot y\text{H}_2\text{O}$. Similar electrodeposition results were obtained by Maya et al. onto stainless steel and nickel cathodes from a 0.2 M $(\text{NH}_4)_2\text{SO}_4$ electrolyte at pH of 2.5 [69]. A hydrated uranium oxide film is also advanced in this study as the composition of the electroplated uranium. The electrodeposition of uranium has been performed at aluminum cylinder cathodes from uranyl nitrate/isopropyl alcohol solutions [70].

Uranium metal can be prepared from a combination electrodeposition/thermal decomposition process by first forming a mercury amalgam and subsequently heating the amalgam to produce pure uranium metal. Hasegawa et al. utilized this methodology to prepare uranium metal with purity higher than a commercial grade of approximately 99.95% [71]. The electrochemical cell consisted of anode and cathode compartments separated by a proton-specific cation

exchange membrane. The platinum anode compartment was filled with 1 M sulfuric acid, while the cathode compartment contained 0.5–1.0 M HCl solution. The initial step in the process was reduction of U(VI) to U(IV) at -0.6 V versus SCE, followed by pH adjustment with an acetic acid/sodium acetate solution, and finally amalgamation from -2.0 to -2.3 V versus SCE. Most of the mercury was removed from the amalgam at 250 °C in a vacuum ($<1 \times 10^{-6}$ torr) before heating to 1200 – 1300 °C for 1 h. Martinot and coauthors have reported the electrodeposition of uranium metal from an organic solvent medium [72]. The report mostly focuses on La metal electrodeposition, but the conclusion with regard to uranium is that macroscopic quantities of metal can be deposited from γ -butyrolactone/tetrahydrofuran (60/40 vol %) solutions. The current density at the tungsten working electrode surface must be set between 20 and 40 mA cm $^{-2}$ for plating to occur. Since reduction of the solvent is a competing process, setting the current density too high results in the inhibition of the plating of uranium. Results from Inductively Coupled Plasma (ICP) analyses of the dissolved metal were used to calculate the faradaic yield (about 39% at 20 mA cm $^{-2}$).

25.5.3

Molten-salt Solutions

Molten salt-based uranium electrochemistry continues to be an important area of research because of the use of pyrochemical processes within the nuclear industry. Previous reviews have covered a large portion of the literature but recent reports have added to the body of knowledge. The recent review by Willit et al. on the electrorefining of uranium and plutonium offers comprehensive literature coverage from

1943 to 1991 [73]. The majority of literature data on the electrochemical behavior of uranium in molten salts is based upon chloride melts. The typical melts are combinations of several chloride species such as NaCl–KCl, LiCl–NaCl–CaCl $_2$ –BaCl $_2$, MgCl $_2$ –NaCl–KCl, and LiCl–KCl eutectic. There have also been uranium electrochemistry results obtained in fluoride melts on the basis of the fluoride salts BaF $_2$, CaF $_2$, LiF, and UF $_4$ [74].

Masset and coworkers studied the electrochemistry of UCl $_3$ at a tungsten working electrode in LiCl–KCl eutectic through the use of cyclic voltammetry and chronopotentiometry [75]. The study was performed as part of their attempt to build an updated and accurate database on the behavior of actinides in chloride melts. The results confirm a reversible single electron–transfer process for the U(III)/U(IV) couple up to 0.3 V s $^{-1}$ and independent of temperature from 400 to 550 °C. The three electron–transfer process U(III)/U(0) is reversible up to 0.2 V s $^{-1}$ at 550 °C after which a quasi-reversible electrode process ensues. The apparent standard potentials for the U(III)/U(IV) and U(III)/U(0) couples are -1.902 V + $0.0006104 \times T$ (K) and $-3.099 + 0.0007689 \times T$ (K) versus Cl $_2$ /Cl $^-$, respectively. The diffusion coefficients for U(IV) and U(III) at 430 °C were 2.7 and 1.9×10^{-6} cm 2 s $^{-1}$, respectively. A similar study was recently performed by Kuznetsov et al., and the results were very much in line with those presented in Refs 27, 76. The potentials for the two electrode processes differ slightly in each report, with Kuznetsov et al. reporting a slightly more negative value for the U(IV)/U(III) couple (-1.517 and -1.461 V versus Cl $_2$ /Cl $^-$ at 723 K) and a more positive value for the U(III)/U(0) electrodeposition step (-2.283 and -2.543 V versus

Cl_2/Cl^-). A third recent report from Reddy et al. again confirms the main findings discussed above [77].

Iizuka et al. studied the applicability of differentiated normal pulse and square-wave voltammetry to the on-line monitoring of actinide concentrations in $\text{LiCl}-\text{KCl}$ molten salt [78]. Most of the study was focused on uranium and plutonium analysis. The results indicate that for uranium the concentration dependence of peak current from the square-wave voltammograms was not linear at higher concentration ranges. The differentiated normal pulse voltammograms yielded linear concentration/peak current responses but lacked the high sensitivity and discrimination between closely spaced peaks afforded by the square-wave method. The authors conclude that an optimized procedure could be developed for application to the on-line monitoring of actinide concentrations during molten-salt electrorefining. The electrodeposition of uranium in molten $\text{NaCl}-\text{KCl}-\text{UCl}_3$ from 670 to 710 °C was studied by Serrano et al. to learn more about the factors influencing the morphology of the deposited uranium [79]. As previous studies have concluded, dendrite formation is unavoidable, and the initial step in the electrodeposition is the formation of a thin layer of deposited metal on the substrate surface followed by attachment of the dendrites to the thin layer. The dendritic deposits that are formed are not influenced to any large extent by uranium ion content or current density, however, temperature does play a more dominant role on the density of the coatings.

25.5.4 Nonaqueous Solutions

In comparison to the other actinides the electrochemical behavior of uranium

in nonaqueous solutions has received considerably more attention, although in comparison to most transition metals the number of studies is limited. Coordination and organometallic complexes of uranium have been a focus of inorganic chemists because of their fundamentally interesting and unique bonding arrangements. This leads to the inevitable studies with electrochemical techniques to probe the consequence of electron transfer since the uranium metal center can exist in a number of oxidation states. Morris et al. have studied the electrochemical behavior for a series of U(IV) “ $(\text{C}_5\text{Me}_5)_2\text{U}$ ” complexes ligated by either σ -donor ligands (Cl , SO_3CF_3 , CH_3 , CH_2Ph) or ligands containing at least a single nitrogen-donor (imido, hydrazone, ketimido) [34]. The electrochemistry was performed in THF solvent with $[(n\text{-C}_4\text{H}_9)_4\text{N}][\text{B}(\text{C}_6\text{F}_5)_4]$ as the supporting electrolyte at platinum and graphite working electrodes. The advantageous use of the perfluoro-phenyl borate anion in low dielectric constant solvents has received considerable attention recently, [80] and in the present study the use of this anion had the added advantage of not being susceptible to fluoride abstraction by the uranium organometallics. The complexes containing the σ -donor ligands display a chemically reversible U(IV)/U(III) couple between –1.8 and –2.6 V versus Fc/Fc^+ . The specific reduction potential tracks with the σ -donor ability of the coordinated ligands. The electrochemical reversibility of the couple varies because of slow electron-transfer kinetics. A metal-based oxidation process for complexes containing a σ -donor ligand is not observed. The voltammetry of the complexes containing at least one nitrogen-donor ligand show reduction behavior similar to that of the σ -donor complexes with reduction potentials from

~ -2 to -2.8 V versus Fc/Fc^+ . However, these nitrogen-donor ligand complexes also display a reversible oxidation process attributed to the metal-based $\text{U(IV)}/\text{U(V)}$ couple. The U(V) electrode product is stable on the voltammetric timescale in contrast to the typical behavior of U(V) organometallic complexes. This stability is likely because of the ability of the nitrogen ligands to engage in pi-bonding with the uranium metal center increasing the electron density at the metal to stabilize the U(V) oxidation state. The nitrogen-donor complexes contain additional oxidation processes associated with ligand-based oxidations at more positive potentials than the $\text{U(IV)}/\text{U(V)}$ couple. The U(VI) bis(imido) complex, $(\text{C}_5\text{Me}_5)_2\text{U}(=\text{NPh})_2$, shows a single electrochemically reversible $\text{U(VI)}/\text{U(V)}$ wave at -1.7 V versus Fc/Fc^+ .

Clappe et al. have studied the electrochemical behavior of $(\text{RC}_5\text{H}_4)_3\text{UCl}$ complexes ($\text{R}=\text{H}, \text{CH}_3, (\text{CH}_3)_3\text{C}, (\text{CH}_3)_3\text{Si}$) in THF with $[(n\text{-C}_4\text{H}_9)_4\text{N}][\text{PF}_6]$ as supporting electrolyte at platinum working electrodes [81]. The results for $(\text{MeC}_5\text{H}_4)\text{UCl}$ were described in detail and for the remaining complexes the general electrochemical oxidation and reduction processes were essentially identical. The authors observe a chemically and electrochemically reversible one-electron $\text{U(IV)}/\text{U(III)}$ reduction process from 0.05 to 2.0 V s $^{-1}$ for $(\text{MeC}_5\text{H}_4)\text{UCl}$ at -1.948 ± 0.004 V versus Fc/Fc^+ , which substantiates previous studies on the electrochemistry of Cp_3UCl in THF [82]. The oxidation wave associated with the $\text{U(IV)}/\text{U(V)}$ couple is chemically irreversible and shows an anodic peak current at slow sweep rates that is larger than anticipated for a simple one electron–transfer process. These results are explained by a disproportionation mechanism for the electrogenerated U(V) species, with an

approximate rate constant, $k_d = 6.3 \times 10^6$ mol $^{-1}$ L s $^{-1}$. An electrochemical study of $\text{Cp}_2\text{U}(\text{BH}_4)_2$ ($E_{1/2} = -1.62$ V versus Fc/Fc^+) and $\text{Cp}_3\text{U}(\text{BH}_4)$ ($E_{1/2} = -1.92$ V versus Fc/Fc^+) in THF with $[(n\text{-C}_4\text{H}_9)_4\text{N}][\text{PF}_6]$ as supporting electrolyte shows a reversible one-electron reduction process for both complexes at slow sweep rates, 0.05 V s $^{-1}$ [83]. Chemical reduction of both neutral complexes with Na/Hg amalgam yielded the stable anions $[\text{Cp}_2\text{U}(\text{BH}_4)_2]^-$ and $[\text{Cp}_3\text{U}(\text{BH}_4)]^-$. Voltammetry results from ultramicroelectrode studies in the absence of supporting electrolyte showed that the supporting electrolyte reacted with $\text{Cp}_2\text{U}(\text{BH}_4)_2$ giving $\text{Cp}_3\text{U}(\text{BH}_4)$ and $\text{Cp}\text{U}(\text{BH}_4)_3$. The latter species further decomposed to an electrochemically inactive product(s). The electrochemical reduction of bis(dicarbollide)uranium dibromide, $[(\eta^5\text{-C}_2\text{B}_9\text{H}_{11})_2\text{UBr}_2]\cdot 2[\text{Li}(\text{THF})_4]$, has been studied in THF with $[(n\text{-C}_4\text{H}_9)_4\text{N}][\text{PF}_6]$ supporting electrolyte at a platinum electrode [84]. The voltammograms show an electrochemically irreversible reduction with an onset potential of about -1.56 V versus Fc/Fc^+ . There is a return oxidation wave on the reverse scan well separated from the reduction process likely associated with a new species. Subsequent chemical reductions with Na/Hg amalgam in THF allowed isolation of the U(III) species $[(\eta^5\text{-C}_2\text{B}_9\text{H}_{11})_2\text{UBr}(\text{THF})]\cdot 2[\text{Li}(\text{THF})_2]$, resulting from loss of bromide from the parent U(IV) system.

The electrochemical behavior of UCl_4 in THF with $[(n\text{-C}_4\text{H}_9)_4\text{N}][\text{B}(\text{Ph})_4]$ as supporting electrolyte was studied to determine the fate of the electrogenerated U(III) species [85]. The voltammograms are not straightforward and a number of additional U(IV) chloride species

were synthesized and studied to uncover the mechanism of UCl_4 reduction. The reduction of UCl_4 displaying three cathodic waves is dominated by subsequent chloride ion transfer yielding anionic U(IV) chloride complexes, which are reduced at more negative potentials than the starting UCl_4 and its equilibrium U_2Cl_8 species. The U(IV) anions formed have been described as $[\text{U}_2\text{Cl}_9]^-$ and $[\text{UCl}_5]^-$. In recent years a number of reports have appeared concerning the one-electron reduction of uranyl complexes in dimethylsulfoxide (dmso) solvent with $[(n\text{-C}_4\text{H}_9)_4\text{N}][\text{ClO}_4]$ as supporting electrolyte [86–89]. The specific complexes reported contain mono-, bi-, tri-, and tetradeятate ancillary ligands coordinated to the central uranyl moiety in addition to a dmso solvent ligand. Most of the results have been summarized in a paper by Kim, Asakura, and coworkers, in which a clear trend toward more negative reduction potentials is presented as the denticity of the coordinated ligand(s) increases [90]. Additionally the authors have demonstrated the ability of certain ligands to stabilize the typically reactive U(V) oxidation state, allowing characterization of changes to the UO_2^{2+} moiety upon one-electron reduction. A common theme in the studies is weakened U=O bonds in the U(V) derivatives in comparison to the parent U(VI) starting compounds. Some of the complexes do show evidence of limited chemical stability for the electrogenerated U(V)O_2^+ , and these results are discussed in further detail in the referenced works.

Cyclic voltammetric studies were employed to determine the stability of electrogenerated U(V) derivatives for several bis(alkoxido)-uranium-triamidoamine complexes of the general formula $\text{U}(\text{NN}_3)(\text{OR})(\text{OR}')\text{Li}(\text{THF})_n$, in which $\text{NN}_3 = \text{N}(\text{CH}_2\text{CH}_2\text{NSiMe}_3)_3$ and R, R' =

Bu' or Ph [91]. The voltammetry was performed in THF with $[(n\text{-C}_4\text{H}_9)_4\text{N}][\text{PF}_6]$ as supporting electrolyte at a platinum disk working electrode. The three complexes studied, corresponding to the bis(butoxide), bis(phenoxide), and mixed butoxide/phenoxide derivatives, show a quasi-reversible, chemically reversible oxidation to the U(V) species and a second chemically irreversible oxidation that appears to be one electron in nature. The $E_{1/2}$ values for the U(IV)/U(V) couples are -1.04 V, -1.155 V, and -0.97 V versus Fc/Fc^+ for bis(butoxide), bis(phenoxide), and the mixed species. The subsequent irreversible second oxidation processes occur at E_p values of 0.86 V, 0.445 V, and 0.745 V versus Fc/Fc^+ . The stability of the U(V) derivatives evidenced in the voltammetry experiments allowed isolation and characterization from chemical oxidation experiments with the chemical oxidant $[\text{Cp}_2\text{Fe}][\text{PF}_6]$. Cathodic voltammetry scans conducted to observe the U(IV)U(III) couple in these complexes did not produce any voltammetric waves before breakdown of the solvent window. Avens et al. reported the chemically reversible oxidation of the U(III) complex U(OAr)_3 , in which OAr = 2,6-di-*tert*-butylphenoxide, at -1.22 V versus Fc/Fc^+ [92]. The quasi-reversible cyclic voltammograms were recorded in THF with $[(n\text{-C}_4\text{H}_9)_4\text{N}][\text{BPh}_4]$ as the supporting electrolyte at a gold disk working electrode. Martinot et al. studied the electrochemical behavior of Cs_2UCl_6 in a series of organic solvents (dimethylsulfone -400 K, hexamethylphosphoramide -298 and 400 K, dimethylsulfoxide -298 K, propylene carbonate -298 K, 1,2-dimethoxyethane -298 K) with $\text{Li}[\text{ClO}_4]$ as the supporting electrolyte [93]. The general results in all solvents consist of two reductive electrode processes corresponding first to the one-electron reduction to a

U(III) species and a second three-electron reduction to give U(0) metal. The first reduction, U(IV)/U(III) couple, is electrochemically and chemically irreversible except in hexamethylphosphoramide at 298 K where the authors report full chemical reversibility on the voltammetric timescale. The second reduction process is electrochemically irreversible in all solvents and only in dimethylsulfone at 400 K was an anodic return wave associated with uranium metal stripping noted. Electrodeposition of uranium metal as small dendrites from Cs₂UCl₆ starting material was achieved from molten dimethylsulfone at 400 K with 0.1 M LiCl as supporting electrolyte at a platinum cathode. The deposits of uranium and the absence of UCl₃, UCl₄, UO₂, and UO₃ were determined by X-ray diffraction. Faradaic yield was low at 17.8%, but the yield can be increased (55.7%) through use of a mercury pool cathode.

25.6 Neptunium

25.6.1 Aqueous Solutions

Neptunium has been characterized from the +3 to +7 oxidation states in aqueous solution. The standard potentials for various Np ions have been determined from measured formal potentials of the various redox couples. These data have been thoroughly reviewed by Martinot [94] and Fahay [95]. Recently the standard potentials for the redox couples NpO₂²⁺/NpO₂⁺, Np⁴⁺/Np³⁺, and NpO₂⁺/Np⁴⁺ in acidic aqueous solution have been reevaluated with more detailed consideration of activity coefficients [49, 50]. The standard potential accepted here for the NpO₂²⁺/NpO₂⁺ couple is 1.161 ± 0.011 V as determined from

formal potential measurements during voltammetry experiments at a Pt electrode in 1 M HClO₄ and 1 M HClO₄/1 M, 2 M NaClO₄ mixtures [50a]. For the Np⁴⁺/Np³⁺ couple a standard potential of 0.218 ± 0.005 V is presented under similar experimental conditions.

Kihara et al. employed flow coulometry to study the electrode reactions for Np ions in various acidic media [49]. Flow coulometry has an inherent advantage over the conventional bulk coulometry methods in that the electrolysis can be achieved rapidly to aid in the characterization of unstable electrode products. The resulting coulopotentiograms for the NpO₂²⁺/NpO₂⁺ and Np⁴⁺/Np³⁺ couples indicate reversible processes in nitric, perchloric, and sulfuric acids. The differences in potentials between the various acids are attributed to the associated stability constants of the electrode products with the anion of the acid in each case. Table 2 contains the half-wave potentials for each couple in the various acids.

Kim and coworkers recently studied the reduction of NpO₂²⁺ in 3 M HNO₃ by cyclic voltammetry and UV/vis spectroelectrochemistry [96]. The authors found a quasi-reversible process for the NpO₂²⁺/NpO₂⁺ couple at Pt and glassy carbon (GC) working electrodes with almost identical formal potentials of 0.907 V and 0.909 V versus Ag/AgCl, respectively. Digital simulations of the cyclic voltammetry data confirmed the quasi-reversibility of the electrode couple with experimental and calculated standard heterogeneous rate constants, k° , on the order of ca 2 × 10⁻³ cm s⁻¹. The UV/vis spectroelectrochemistry results confirm the stability and identity of the electrogenerated NpO₂⁺ species.

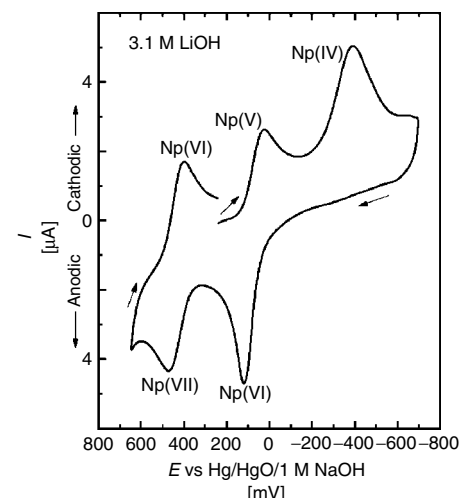
Tab. 2 Half-wave potentials (V versus Ag/AgCl) in acidic solution from flow coulometry studies [49]

Electrode couple	1 M HNO_3	1 M $HClO_4$	0.5 M H_2SO_4
NpO_2^{2+}/NpO_2^+	0.91	0.94	0.88
Np^{4+}/Np^{3+}	-0.13	-0.06	-0.21

The electrochemical behavior of Np ions in basic aqueous solutions has been studied by several different groups. In a recent study, cyclic voltammetry experiments were performed in alkali ($[OH^-] = 0.9 - 6.5$ M) and mixed hydroxo-carbonate solutions to determine the redox potentials of Np(V, VI, VII) complexes [97]. As shown in Fig. 2, in 3.1 M LiOH at a Pt electrode Np(VI) displays electrode processes associated with the Np(VI)/Np(V) and Np(VII)/Np(VI) couples, in addition to a single cathodic peak corresponding to the reduction of Np(V) to Np(IV). This latter process at $E_p \approx -400$ mV (versus Hg/HgO/1 M NaOH) is chemically irreversible in this medium. Analysis of the voltammetric data revealed an electrochemically reversible Np(VI)/Np(V)

couple at $E_c^{\theta'} = 0.148(9)$ V versus SCE and a quasi-reversible Np(VII)/Np(VI) couple at $E_{1/2} \approx 0.450$ V versus Hg/HgO/1 M NaOH. The voltammetry of Np is independent of base concentration above 1.8 M LiOH, but below this value the Np(VI)/Np(V) couple tends toward a system with reduced electrochemical reversibility. Voltammetric behavior in NaOH solutions is very similar to the voltammograms in LiOH, with a shift in potential for the Np(VI)/Np(V) couple to $E_c^{\theta'} = 0.106(6)$ V versus SHE in 3 M NaOH. In the mixed hydroxo-carbonate solutions (0.8 M NaOH/0.4 M Na_2CO_3 and 1.8 M NaOH/0.1 M Na_2CO_3) the Np(VII)/Np(VI) becomes chemically irreversible and the Np(VI)/Np(V) couple is quasi-reversible. This behavior is

Fig. 2 Cyclic voltammogram of Np(VI) in 3.1 M LiOH on a Pt electrode (area ~ 0.5 cm 2), first scan, 20 mV s $^{-1}$ (reprinted from *Radiochimica Acta*, Vol. 89, A. V. Gelis, P. Vanysek, M. P. Jensen, K. L. Nash, Electrochemical and Spectrophotometric Investigations of Neptunium in Alkaline Media, Pages 565–571, 2001, with permission from Oldenbourg Wissenschaftsverlag GmbH).



similar to that previously reported in pure carbonate and bicarbonate solutions [98]. At stronger hydroxide concentrations in the mixed media (6.2 M NaOH/0.3 M Na₂CO₃) the voltammetric behavior more closely resembles the behavior described in dilute base with no carbonate present: Np(VI)/Np(V) couple is electrochemically reversible and the Np(VII)/Np(VI) couple is quasi-reversible. The neptunium species in solution in the absence of carbonate are believed to be [NpO₂(OH)₄]^{3-/2-} for Np(V) and Np(VI), and [NpO₄(OH)₂]³⁻ for Np(VII).

25.6.2

Electrodeposition

Neptunium has been electrodeposited from aqueous and nonaqueous solutions for the preparation of pure sources of this element for various investigations. Ramaniah et al. electroplated Np as NpO₂(OH)₂ · 2H₂O from an isopropanol solution containing Np(V) ions [99]. The deposition was performed on an aluminum disc coated with a thin layer of gold at 600 V and a current density of 1–3 mA cm⁻². From an aqueous HCl solution at pH 2.7 containing an unspecified amount of NH₄Cl, a deposition yield of 95% or better was obtained for Np in a minimum of 15 min at 2 A cm⁻² with an applied potential between 8 and 12 V on a Ti metal foil cathode [100]. Np metal can be obtained through electrodeposition at a mercury cathode and subsequent thermal decomposition of the amalgam to yield a button of pure Np metal [101]. The electrochemical step is performed in acetate buffer solutions (acetic acid/sodium acetate) of pH 3.4–3.7 with current densities varying during the experiment from ca 50 to 200 mA cm⁻². A rotating disc electrode (RDE) method was developed

for the preparation of high-quality Np α -sources [102]. The advantages of this method are high deposition yields from large volumes (>10 mL) of aqueous solutions in 1–2 h and the use of low current densities for more homogeneous deposits. A 90% deposition yield of Np is obtained in approximately 60 min at 1.4 mA cm⁻² from a pH 4.3, 0.3 M sodium sulfate solution on a stainless steel cathode rotating at 1000 rpm.

25.6.3

Nonaqueous Solutions

There are a limited number of studies for Np complexes in nonaqueous organic solvent media. Sonnenberger and Gaudiello performed voltammetry studies on several organometallic Np complexes (Cp₄Np, Cp₃NpCl, and Cp*₂NpCl₂ in which Cp = C₅H₅ and Cp* = C₅Me₅) in THF solvent to observe the influence of ligand environment on the Np(IV)/Np(III) couple [103]. At a Pt working electrode with 0.2 M [(n-C₄H₉)₄N][BF₄] as supporting electrolyte the measured $E_{1/2}$ potentials versus the Fc/Fc⁺ couple were –1.27 V for Cp₄Np, –1.29 V for Cp₃NpCl, and –1.38 V for Cp*₂NpCl₂. While substitution of a chloride ligand for Cp did not have a large influence on the reduction potential, the more electron donating Cp* ligand shifts the reduction to a more negative potential. Detailed voltammetric data were not provided, but the electrode reaction appears to be chemically and electrochemically reversible over the sweep rates studied. The coordination compound Cs₂NpCl₆ was studied in several organic solvents with various electrochemical techniques [104]. In four of the solvents studied (hexamethylphosphoramide, dimethylsulfone, DMF, and acetonitrile) the nonideal voltammetric behavior is similar in that

two irreversible reduction waves are observed. The authors assign the first reduction to the $\text{Np}^{4+}/\text{Np}^{3+}$ couple and the second reduction to the three-electron process $\text{Np}^{3+}/\text{Np(s)}$. Controlled potential electrolyses at potentials more cathodic than the $\text{Np}^{3+}/\text{Np(s)}$ couple did not yield Np metal at a solid cathode in any solvent. In acetonitrile and dimethylsulfone small yields (7 and 0.4% current yield, respectively) of neptunium metal were obtained as amalgams at a mercury pool cathode. With formamide as a solvent only a single wave is observed during the voltammetry experiment, and no further elaboration is available from the authors.

25.6.4 Molten-salt Solutions

The electrochemistry of Np(III) has been studied in LiCl–KCl eutectic molten-salt mixtures by several research groups. The interest in the molten-salt studies stems from their use in the pyrometallurgical partitioning of actinide elements from radioactive wastes and the necessity to understand the redox behavior of the various elements in solution [78]. The general voltammetric behavior of Np(III) in the LiCl–KCl melt is that of a reversible single step three-electron transfer process in which Np metal is deposited at the working electrode surface during the cathodic sweep and stripped during the return anodic sweep. Standard potentials for the $\text{Np(III)}/\text{Np(0)}$ couple have been determined by several authors with good agreement among the different values in recent years. Sakamura et al. reported a standard potential of -1.484 V versus Ag/AgCl at 450°C with a tantalum wire working electrode [105]. Reports from Kreuger et al. [106] and Roy et al. [107] are in very good agreement with these results. At 450°C they report a standard potential

of -1.489 V versus Ag/AgCl at a tantalum surface. A slightly more negative potential of -1.519 V versus Ag/AgCl at 450°C was reported by Shirai et al. from electromotive force measurements [108]. However, in an earlier paper coauthor Shirai et al. [109] reported a potential of -1.496 V versus Ag/AgCl at 450°C , which is more consistent with the values of Roy and Kreuger.

In additional applied studies Martinot [110] and Shirai et al. [111] researched the electrodeposition of Np metal from NpO_2 and NpN, respectively. With methodology similar to that employed with ThO_2 , Martinot achieved 99.95% pure Np metal on the gram scale through dissolution of NpO_2 at 450°C in LiCl–KCl eutectic with HCl gas, followed by reduction of the resulting Np(IV) to Np(III) with H_2 , and finally electroreduction at a tungsten cathode (2.55 – 3.0 V potential difference) to collect Np metal. Shirai and coauthors utilized anodic electrodissolution (-0.773 V versus Ag/AgCl at 500°C) of NpN within a tungsten basket electrode in a molten solution of LiCl–KCl– NpCl_3 to produce Np(III) ions in solution. The Np(III) was then electrodeposited on a solid Mo working electrode at a potential of -1.800 V versus Ag/AgCl in approximately 90% overall yield based on the quantity of starting NpN. The redox potential for the $\text{Np(III)}/\text{Np(0)}$ couple was found to be -1.568 V versus Ag/AgCl.

25.7 Plutonium

The majority of literature concerning the electrochemical behavior of plutonium is focused on results obtained in acidic aqueous or molten salts solutions. Several reviews have appeared on the redox properties of plutonium in

solution and most include some data in relation to electrode reactions [112–114]. The redox properties of plutonium in acidic aqueous solution can be complex because of the possibility of four oxidation [$\text{Pu(III)}-\text{Pu}^{3+}$, $\text{Pu(IV)}-\text{Pu}^{4+}$, $\text{Pu(V)}-\text{PuO}_2^+$, $\text{Pu(VI)}-\text{PuO}_2^{2+}$] states to exist simultaneously. A thorough analysis of disproportionation and equilibrium reactions for plutonium ions is provided in the *Plutonium Handbook*, [115] and a brief overview of electrochemical methods for plutonium research has recently been reviewed by Peretrushkin and Maslen-nikov [112]. The prevalence of reported data in molten-salt solutions is due to the use of these solutions in the nuclear industry for separation and purification of plutonium metal. The recent review by Willit et al. provides a thorough coverage of the earlier literature in relation to plutonium electrorefining [73]. The more recent results (post-1991) will be covered in the present review.

25.7.1

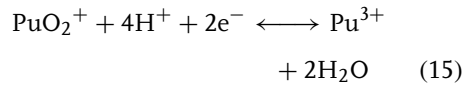
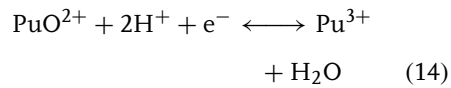
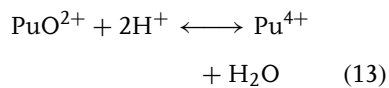
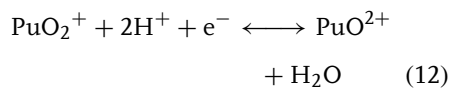
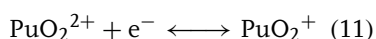
Aqueous Solutions

In acidic aqueous solution the $\text{PuO}_2^{2+}/\text{PuO}_2^+$ and $\text{Pu}^{4+}/\text{Pu}^{3+}$ couples are electrochemically reversible, while the $\text{PuO}_2^{2+}/\text{Pu}^{4+}$, $\text{PuO}_2^+/\text{Pu}^{4+}$, and $\text{PuO}_2^+/\text{Pu}^{3+}$ couples are electrochemically irreversible because of the breaking of the Pu–O bonds during the electron-transfer reactions. The earlier electrochemical data on plutonium ions were typically obtained at a single, relatively high ionic strength, thereby inhibiting the accurate extrapolation to zero ionic strength, which is needed for standard potential calculations. More recently the E^\ominus for the $\text{PuO}_2^{2+}/\text{PuO}_2^+$ and $\text{Pu}^{4+}/\text{Pu}^{3+}$ couples have been redetermined through application of the Specific Interaction

Theory (SIT) for more accurate consideration of activity coefficients [5, 49, 50b]. Kihara et al. [49] calculated values of 0.956 ± 0.010 V for $\text{PuO}_2^{2+}/\text{PuO}_2^+$ and 1.026 ± 0.010 V for $\text{Pu}^{4+}/\text{Pu}^{3+}$ from the cyclic voltammetry data of Riglet et al. [50] in perchlorate solutions. In an earlier study Capdevila and Vitorge determined E^\ominus of 0.938 ± 0.010 V for $\text{PuO}_2^{2+}/\text{PuO}_2^+$ and 1.044 ± 0.010 V for $\text{Pu}^{4+}/\text{Pu}^{3+}$ also from voltammetric data in perchlorate solutions [116]. Because of the irreversibility of the $\text{PuO}_2^{2+}/\text{Pu}^{4+}$ electrode reaction limited formal potential data exist in the literature for calculation of the standard potential. However, a value of 0.867 V has been calculated from the existing data and appropriate correction factors [49].

To learn more about the reduction of the electrogenerated pentavalent plutonyl species, PuO_2^+ , Kihara et al. studied the voltammetry of Pu ions in nitric and phosphoric acid mixtures at stationary and rotated glassy carbon working electrodes [49]. During the reduction of PuO_2^{2+} two waves were observed at the stationary electrode and three waves were observed when the electrode was rotated. From the rotating electrode data the three waves are thought to arise from the electrode reactions shown in Eqns (11–13), where the reaction in Eq. (11) is reversible ($E_{1/2} = 0.65$ V versus Ag/AgCl) and the reactions in Eqns (12) and (13) deviate from reversibility ($E_{1/2s} = 0.36$ V and -0.01 V versus Ag/AgCl). The $E_{1/2}$ potentials quoted here are from a mixed 1.0 M HNO_3 and 1.4 M H_3PO_4 solution. The authors believe that the Pu(IV) produced during the reduction of electro-generated PuO_2^+ is not Pu^{4+} , but rather PuO_2^+ that is stabilized by the presence of the phosphate anions. The PuO_2^+ decomposes to Pu^{4+} according to Eq. (14), and then reduces to Pu^{3+} at a potential similar

to that for PuO_2^+ described by Eq. (12). This leads to a two-electron wave during the stationary electrode experiments as the residence time of electrogenerated PuO^{2+} is increased compared to that in the rotating electrode experiments. The overall two-electron reduction of PuO_2^+ is outlined in Eq. (15).



As with U and Np ions, flow coulometry experiments were conducted to further study the electrode reactions of Pu ions in acidic aqueous solutions [49]. The results from these studies confirm the reversibility of the one-electron couples $\text{PuO}_2^{2+}/\text{PuO}_2^+$ and $\text{Pu}^{4+}/\text{Pu}^{3+}$ in nitric, perchloric, and sulfuric acid solutions. The further reduction of PuO_2^+ resulted in an irreversible two-electron transfer yielding Pu^{3+} . The flow coulometry results in the mixed phosphoric–nitric acid solutions confirm the overall conclusions that have been reached from the stationary and rotated working electrode experiments described previously, in which PuO^{2+} is the primary Pu(IV) product from PuO_2^+ reduction.

The technique of differential pulse stripping voltammetry has been developed for the determination of plutonium in nitric acid solutions [117]. The successful determination of plutonium was demonstrated

for sample solutions containing silver ions as a possible interfering species. The procedure consisted of electrodeposition for 20 s at -0.7 V versus Ag/AgCl (Pt working electrode) followed by an anodic sweep to 0.4 V at 4 mV s^{-1} with active background subtraction of the electrochemical solvent medium. This procedure provided data applicable for construction of a Pu calibration curve from concentrations of 50–1000 ppm with an relative standard deviation (RSD) of approximately $\pm 2\%$.

The $\text{Pu}^{4+}/\text{Pu}^{3+}$ couple for a series of Pu(IV)/(EDTA⁴⁻) based complexes, where EDTA = ethylenediaminetetraacetate, has been studied as a function of pH and EDTA concentration [118]. The voltammetry was also studied with citrate and carbonate ions present in solution. At a relatively low pH of 2.3 and equimolar Pu^{4+} /EDTA concentrations a quasi-reversible one-electron reduction is observed for Pu(EDTA) at $E_{1/2} = 0.342$ V versus SHE. The quasi-reversibility of this process remains as the pH is raised to 4.6. Additional voltammetry studies are discussed in the paper for the higher coordinate Pu^{4+} species, $\text{Pu}(\text{EDTA})\text{-L}$ (where L = EDTA, carbonato, citrato), all of which show irreversible electron-transfer behavior.

The electrochemical behavior of plutonium ions in alkaline media has received substantially less literature coverage in comparison to results in acidic solutions. Most of the literature has been reviewed by Martinot [113], and only minimal attention has been given to the topic since this previous review [119, 120].

25.7.2

Electrodeposition

The electrodeposition of plutonium is routinely employed as a means of preparing

plutonium samples for alpha spectrometric measurements. The modification of Talvities's method by Lee and Lee [26] described in Sect. 25.3.4 for thorium electrodeposition has been applied for Pu deposition. The modified method gave a yield of $98.6 \pm 3.1\%$ compared to $92.4 \pm 2.8\%$ in the previous method in addition to slightly enhanced peak resolution in the alpha spectra. The application of this method for Pu determination in environmental samples has been reported [121]. Luskus has recently compared electrodeposition of Pu from environmental air filter samples with that of the technique of microprecipitation of Pu for preparation of alpha spectrometric sources [122]. The Pu recovered from the air filter samples was consistently higher with the microprecipitation method than that recovered by the electrodeposition procedure. In addition, microprecipitation decreases the amount of equipment and equipment maintenance time needed to perform the analyses. A rotating disc cathode cell has been developed for the electrodeposition of plutonium with resulting high-quality and thin, uniform deposits [123]. The cathode is a stainless steel disc rotated at 1200 rpm in a 0.3 M sodium sulfate solution at pH 5 with an applied current density of 1 mA cm^{-2} for 35 min. The method gave a Pu yield of $97.5 \pm 2.5\%$.

25.7.3

Molten-salt Solutions

Recent studies on the electrochemical behavior of plutonium in molten salts have mainly been performed in LiCl–KCl based melts. The electrorefining step in a pyroprocessing procedure for the recycling of nuclear fuel from the Integral Fast Reactor (IFR) Program has been

described by Laidler and coauthors [124]. The process utilizes LiCl–KCl eutectic as solvent and is based on the electrodisolution of spent metal and subsequent selective electrodeposition of uranium, plutonium, and other transuranic (TRU) elements at a solid steel (U) or liquid cadmium (Pu, U, TRU) cathode. Nishimura et al. have described a similar electrorefining/pyroprocessing procedure [125], and have also described the pyrometallurgical partitioning of actinides from rare-earth elements [126]. The foundation of these processes is related to the fundamental electrochemical behavior and thermodynamic properties of Pu and the other metals in the LiCl–KCl molten salt. Because of the importance of Pu electrorefining, researchers continue to study the details of Pu electrochemistry in molten salts. Serp et al. studied the electrochemistry of trivalent PuCl_3 reduction in LiCl–KCl eutectic from 733 to 823 K [127]. The $\text{Pu}^{3+}/\text{Pu}^0$ couple was electrochemically reversible up to 200 mV s^{-1} with quasi-reversible behavior observed at higher sweep rates. From the cyclic voltammetry and chronopotentiometry data standard potentials for the $\text{Pu}^{3+}/\text{Pu}^0$ couple were calculated at 733, 773, and 823 K. At 733 K the calculations yield an average apparent E^\ddagger of -2.796 V versus Cl_2/Cl^- , which is similar to a previously reported value [107].

Uozumi, Iizuka, and coauthors have published several studies on the electrochemical behavior of Pu at liquid cadmium cathodes in LiCl–KCl eutectic melts [128–130]. In one account [130] the authors studied the reduction of Pu^{3+} to Pu^0 at the LiCl–KCl melt and liquid Cd interface and compared the results to those obtained at a solid Mo cathode surface. The electrode reaction at liquid Cd was found to be close to fully reversible with rapid,

diffusion-controlled electron transfer. At 723 K the $E_{1/2}$ value for the Pu^{3+}/Pu couple was -1.387 ± 0.002 V versus Ag/AgCl. The data reveal that the cathodic reduction peak potential for the Pu^{3+}/Pu couple is shifted to more negative potentials by about 0.340 V at a Mo electrode compared to that at the liquid Cd electrode. This difference was attributed to a lowering of the activity of Pu in the Cd phase and is similar to the Gibbs energy of formation of the intermetallic compound PuCd_6 in the liquid Cd phase. As mentioned in Sect. 25.5.3 on uranium molten-salt electrochemistry, Iizuka et al. [78] looked into the applicability of square-wave and normal pulse voltammetries for the on-line monitoring of Pu concentrations in $\text{LiCl}-\text{KCl}$ eutectic molten salt. The results for Pu were similar to those for U in which a nonlinear relationship was found between peak current and Pu concentration from the square-wave data. Additionally, while the normal pulse method shows more promise the authors point out that there is still a problem discriminating between closely spaced redox processes.

Electrochemical studies of plutonium in NaCl-based melts are less common than that in $\text{LiCl}-\text{KCl}$ mixtures. In a recent paper by Lambertin et al. the standard potentials for the $\text{Pu}(\text{III})/\text{Pu}(0)$ couple were determined from cyclic voltammetry data in equimolar $\text{NaCl}-\text{KCl}$ and CaCl_2

at 1073 K [131]. The E^\ominus in equimolar $\text{NaCl}-\text{KCl}$ was calculated as -2.54 ± 0.01 V versus Cl_2/Cl^- and -2.51 ± 0.01 V versus Cl_2/Cl^- in CaCl_2 . This result in $\text{NaCl}-\text{KCl}$ is similar to a previously published value of -2.585 V versus Cl_2/Cl^- [132].

25.8 Americium

25.8.1 Aqueous Solutions

The vast majority of electrochemical data on americium ions has been obtained in aqueous solutions. Americium can exist in aqueous solutions in the oxidation states III, IV, V, and VI. The divalent state is difficult to attain in aqueous solutions because of the proximity of the standard potential of the $\text{Am}(\text{III})/\text{Am}(\text{II})$ couple to the solvent/supporting electrolyte breakdown potential. Previous reviews have presented the formal and standard potentials for the various americium couples and these reviews should be consulted by the interested reader for more detailed discussion [133, 134]. Table 3 contains a summary of selected formal potentials E_c^\oplus from these reviews in 1 M HClO_4 for convenience. All values are calculated from various measurement techniques except for the $\text{Am}(\text{VI})/\text{Am}(\text{V})$ couple ($\text{AmO}_2^{2+}/\text{AmO}_2^+$), which was determined directly.

More recent experimental reports have focused on detailed electrochemical studies to characterize the different americium ions in solution in relation to their stability and molecular composition. The electrochemical behavior of americium in carbonate media has been studied by several different authors because of the tendency

Tab. 3 Formal Potentials E_c^\oplus for Am ions in 1 M HClO_4 [133, 134]

Electrode couple	Potential [V]
$\text{AmO}_2^{2+}/\text{AmO}_2^+$	+1.60
$\text{AmO}_2^{2+}/\text{Am}^{3+}$	+1.68
$\text{Am}^{4+}/\text{Am}^{3+}$	+2.6
$\text{Am}^{3+}/\text{Am}^{2+}$	-2.3
$\text{Am}^{3+}/\text{Am(s)}$	-2.07

of strong complexing agents such as carbonates to stabilize the Am(IV) oxidation state [135–138]. A common theme among these studies is the existence of four different oxidation states of americium including Am(III)/(IV)/(V)/(VI), which are dependent on the pH of the solution, the anode potential for oxidation of Am(III), and the concentration of $\text{MHC}\text{O}_3/\text{M}_2\text{CO}_3$ (where M = K or Na). As an example of americium behavior in carbonate media the results from Myasoedov et al. indicate 100% production of Am(IV) at pH 8.2–9.7, 100% Am(VI) at pH 11–12.5, and 100% Am(V) at pH > 13.5 [135]. These results were obtained within 3 M $\text{KHCO}_3-\text{K}_2\text{CO}_3$ solutions at a potential of 1.25 V versus SHE. Similar results were obtained from the other referenced reports. In acetate solutions (0.05–0.4 M sodium acetate and 0.1 M acetic acid) Fedoseev and Krot found that oxidation of Am(III) led to the production of Am(VI) in solution [139]. The characterization of the different americium ions in solution was performed by absorption spectra. Kulyako et al. found that mixtures of acetonitrile with low concentrations of H_3PO_4 (0.3–2.0 M) were suitable for the oxidation of Am(III) to Am(IV) at 1.4 V versus $\text{Hg}/\text{Hg}_2\text{SO}_4$ in essentially quantitative yields [140]. This is in contrast to results obtained in H_3PO_4 solutions where a concentration ≥ 10 M is required for the production of pure Am(IV) [141].

Another strong complexing agent sodium tripolyphosphate, $\text{Na}_5\text{P}_3\text{O}_{10}$, was employed during the electrolysis of Am(III) in a dilute (2 mM) H_2SO_4 solution to attempt stabilization of Am(IV) [142]. The concentration of $\text{Na}_5\text{P}_3\text{O}_{10}$ was 0.17–0.8 M at pH 1–3 with 0.9 mM Am(III). The reported results indicate that a mixture of Am(IV) and Am(VI) was produced in solution during the electrolysis at 1.9 V versus SHE.

Additional strong complexing agents such as alkali metal tungstophosphate and tungstosilicate heteropolyanions ($[\text{P}_2\text{W}_{17}\text{O}_{61}]^{10-}$ and $[\text{SiW}_{11}\text{O}_{39}]^{8-}$) have been used to stabilize the Am(IV) oxidation state upon electrolysis of Am(III) ions in acidic aqueous media [143]. The electrogenerated Am(IV) ions form 1:1 and/or 1:2 complexes, $[\text{Am}]:[\text{anion}]$, depending on the total concentration of Am and the anion in solution.

25.8.2

Molten-salt Solutions

There is a relatively large volume of electrochemical data on americium in molten-salt media, specifically $\text{LiCl}-\text{KCl}$ eutectic at solid (W, Mo, Ta) and liquid (Cd, Bi) electrodes. Lambertin et al. studied the electrochemical reduction of AmCl_3 in $\text{LiCl}-\text{KCl}$ at 470 °C at a tungsten working electrode [144]. It was determined from the cyclic voltammetric data that Am(III) is first reduced to Am(II) and subsequently reduced in a second step to Am(0). The voltammetry data were used to estimate the standard potential for the Am(III)/Am(II) couple as –2.84 V versus Cl^-/Cl_2 and –2.945 V versus Cl^-/Cl_2 for Am(II)/Am(0). These results are in very good agreement with an earlier study by Fusselman and coauthors [105, 145]. They determined standard potentials for the Am(III)/Am(II) couple as –2.83 V versus Cl^-/Cl_2 and –2.852 V versus Cl^-/Cl_2 for the Am(II)/Am(0) couple at 450 °C. More recently Lambertin et al. extended their studies with a report on the stability of Am ions in molten $\text{LiCl}-\text{KCl}$ in the presence of fluoride ions [146]. They found that Am(III) undergoes a direct three-electron reduction to Am(0) in the presence of fluoride at –2.91 V versus Cl^-/Cl_2 without voltammetric evidence

for Am(II). At more cathodic potentials the authors believe that the data are indicative of Li_xAm_y alloy formation. Serp et al. have confirmed the previously published two-step [Am(III)/Am(II) and Am(II)/Am(0)] voltammetric behavior of Am(III) in LiCl–KCl at a W working electrode and extended the work by studying the behavior at an Al working electrode [147]. At an Al surface the reduction of Am(III) proceeds in a single step, Am(III) to Am(0), and occurs at more positive potentials than the corresponding values at a W surface. The shift in reduction potential is attributed to the formation of Al–Am alloys.

25.8.3 Nonaqueous Solutions

Electrochemical studies in nonaqueous media with organic solvents are limited with the published reports being relegated to experiments in acetonitrile solvent. Myasoedov and coauthors concluded from their studies of $\text{Am}(\text{ClO}_4)_3$ reduction in acetonitrile/0.1 M $[(\text{C}_2\text{H}_5)_4\text{N}][\text{ClO}_4]$ that americium can be reduced to the divalent state with a formal potential of -1.55 V versus SCE, but small amounts of water in the acetonitrile react with Am(II) to give basic precipitates of the formula $\text{Am}(\text{OH})_x^{(3-x)+}$ [148]. The stabilization of the Am(IV) oxidation state through the use of a neutral oxygen donor ligand (Ph_3AsO) was noted by Payne and Peterson from voltammetry studies in acetonitrile in the presence of the ligand [149]. The Am(IV)/Am(III) oxidation potential was reported as 0.3 V versus Ag/AgCl, although the published cyclic voltammogram appears nonideal for the determination of this potential. From an earlier study in acetonitrile/0.1 M $[(\text{C}_2\text{H}_5)_4\text{N}][\text{ClO}_4]$ a standard potential of -1.4 V versus SHE

was determined for the Am(III)/Am(II) couple [150].

25.8.4 Electrodeposition

A common method for the electrodeposition of Am is from isopropanol solutions containing small quantities of dilute acid stock solutions of Am ions. Aqueous deposition methods have also been employed, but the organic electrolyte medium is more advantageous in that it tends to produce more uniform coatings [151]. Zhi et al. prepared relatively thick targets of Am from a mixture of isopropanol and dilute (0.1 N) nitric acid stock solutions of $^{241,243}\text{Am}(\text{NO}_3)_3$ [152]. The electrolysis was typically carried out at 5 mA cm^{-2} with a resulting potential of approximately 500 V between the platinum wire anode and aluminum foil cathode. Total plating efficiencies of 98% for ^{241}Am and 94% for ^{243}Am were ultimately obtained in about 1 h of electrolysis. The thickness of the films ranged from 622 to $910 \mu\text{g cm}^{-2}$ for ^{241}Am and from 1.0 to $1.2 \mu\text{g cm}^{-2}$ for ^{243}Am . Becerril-Vilchis and coauthors performed an in-depth study on the electrodeposition of Am and physicochemical behavior of the aqueous electrolyte solutions containing Na_2SO_4 at different pH values adjusted with H_2SO_4 and NaOH [153]. The electroplating method described for thorium in Sect. 25.3.4 utilizing DTPA as a chelating agent was also employed by Lee and Lee for the preparation of ^{243}Am targets [26]. With this method a deposition yield of $93.8 \pm 3.4\%$ was achieved in 2 h.

25.9 Curium

Electrochemical studies of curium are mostly limited to radiopolarography

measurements in aqueous solution and electrodeposition from aqueous and nonaqueous media for the preparation of curium targets and sources. However, Martinot et al. have performed a chronopotentiometric study on the reduction of Cm(III) in molten LiCl–KCl in which they observe a single wave attributed to the direct reduction of Cm(III) to Cm(0) at a Pt foil cathode [154]. The radiopolarography results are well summarized in a recent paper by Yamana and Moriyama [155]. A value of -1.77 V versus SHE is presented for the $E_{1/2}$ value of the Cm(III)/Cm(0) couple at pH 3.0 in 0.10 M LiCl from the work of Shiokawa et al. [156]. Frenkel and coauthors presented results for the oxidation of Cm(III) to Cm(IV) in 2 M K_2CO_3 solution at pH 13 [157]. They concluded from their electrochemical and spectroscopic data that 20% of the Cm(III) was oxidized to a stable Cm(IV) species after a 90 min electrolysis at 1.25 V versus Hg/HgO.

25.9.1 Electrodeposition

Lobanov et al. electroplated curium (ultimately converted to CmO_2) in a series of electrodeposition steps from solutions of curium nitrate in isobutanol [158]. The electrochemical setup consisted of a Ti foil cathode, Ti or Al foil anode, potential difference of 600 V, and a plating time of 10–15 min for each plating step. Between each deposition step the deposited curium was converted to CmO_2 . The multistep procedure allowed targets of curium with the desired thickness ($300\text{--}400\text{ }\mu\text{g cm}^{-2}$) to be obtained with a deposition yield of no less than 90%. Ramaswami and coauthors electroplated curium from isopropanol solution [159]. A $100\text{ }\mu\text{L}$ aliquot

of curium nitrate was added to 10 mL of isopropanol and plating was conducted in an electrochemical cell containing a gold-coated aluminum foil cathode, platinum wire anode, at an applied potential of 600 V. Within 2 h quantitative electrodeposition of curium was achieved at a density of $1\text{--}50\text{ }\mu\text{g cm}^{-2}$. Martinot [160] has previously mentioned the electroplating of curium from a solution of 50 : 45 : 5 by volume ethanol/acetone/water at pH 2–3 obtained by the addition of 0.1 N HNO_3 [161]. The electrodeposition is carried out at a stainless steel cathode, with a platinum wire anode, and a current density of 15 mA cm^{-2} . Curium is deposited by this method at 96% efficiency within 4 h with a density of $15\text{ }\mu\text{g cm}^{-2}$. Hallstadius described a method for curium electrodeposition at 90% yield from a $\text{Na}_2\text{SO}_4/\text{H}_2\text{SO}_4$ medium at a stainless steel cathode [162].

25.10 Berkelium

Electrochemical studies of berkelium in aqueous media show a reversible $\text{Bk(IV)}/\text{Bk(III)}$ couple. Indeed the Bk(IV) species is stable in aqueous media and the chemical behavior of Bk is often compared to that of Ce. The formal potential for the $\text{Bk(IV)}/\text{Bk(III)}$ couple has been studied in a number of weakly and strongly coordinating mineral acids and carbonate solutions. The general findings from these studies indicate a shift in the oxidation potential of Bk(III) ions, with the shift correlating with the complexing ability of the anions present in the electrochemical solution: strongly complexing anions ($\text{SO}_4^{2-} < \text{PO}_4^{3-} < \text{CO}_3^{2-}$) shift the oxidation to more negative potentials [163]. This shift implies stabilization of the electrochemically generated Bk(IV)

species with strongly complexing anions. In a noncomplexing perchlorate solution (1 M HClO₄) the formal potential for the Bk(IV)/Bk(III) couple was recently determined by Atonio et al. [164] from X-ray absorption near edge structure (XANES) spectroelectrochemistry and Nernst analysis as $E^\ominus = 1.584$ V versus SHE. This result is in good agreement with previously published data from Stokely [165] and Simakin [166]. In basic solution Bk(III) is unstable and undergoes auto-oxidation from oxygen and radiolytically produced peroxide to give Bk(IV) [167].

Detailed cyclic voltammetric and bulk electrolysis studies have been performed on the Bk(IV)/Bk(III) couple in concentrated aqueous carbonate solutions (2 M and ca 5 M K₂CO₃; pH range from 9.5 to 13.5) [168]. The results from these studies show that solution-composition changes impart large influences on the nature of the voltammetric response for the Bk(IV)/Bk(III) couple. A quasi-reversible process is evidenced in 2 M carbonate solutions at pH 10 and 13.5 with $E_{1/2} = -0.021$ and 0.20 V versus SCE, respectively. Characterization of the heterogeneous electron-transfer parameters was performed through digital simulation of the voltammetric data. In 2 M carbonate at an intermediate pH value of 11.7 the voltammetry becomes more complicated as two electroactive Bk(IV) species are present in similar concentration in the solvent medium. The authors have invoked a square scheme involving electrochemical and chemical reactions to account for the voltammetric behavior. For a more detailed discussion the reader is referred to the original paper [168a]. In 2.5 M carbonate at pH 9.5 and 4.8 M carbonate at pH 10.4 the voltammetry exhibits behavior characteristic of a nondiffusive species that interacts strongly with the electrode surface.

Radiopolarography measurements for the cathodic reduction of Bk(III) to Bk(0) at a dropping mercury electrode in 0.1 M LiCl at pH ~ 2 give an amalgamation half-wave potential value of 1.63 V versus SHE and an estimated E^\oplus of 2.18 V [169]. Analysis of the electrochemical data leads the authors to conclude that the Bk(III)/Bk(0) electrode process is irreversible.

25.11 Californium

There is a fairly limited set of electrochemical data on Cf with previous reviews covering the most pertinent electrochemical results [170]. The oxidation of Cf(III) to Cf(IV) in aqueous media is very difficult because of the relatively positive potential of the couple, ca 3.2 V as calculated by Nugent et al. [46]. As with Am, strongly complexing anions can shift the potential of the Cf(IV)/Cf(III) couple to facilitate the electron-transfer process. Indeed it has been demonstrated that in aqueous potassium phosphotungstate solutions Cf(III) can be chemically oxidized to Cf(IV) with persulfate dianion (S₂O₈²⁻) [171]. The results in carbonate solution are more ambiguous as Hobart et al. [172] were not able to oxidize Cf(III) to Cf(IV) in carbonate, but Myasoedov and coauthors [135] claim 20% oxidation of Cf(III) presumably to Cf(IV) in 2 M K₂CO₃ at pH 13.2.

Samhoun and David [169] have studied the reduction of Cf(III) by radiopolarography in 0.1 M LiCl at pH ~ 2 and found a reversible electrode process attributed to the Cf(III)/Cf(0) couple at $E_{1/2} = -1.508$ V versus SHE with an estimated standard potential of -2.030 V. These results were called into question in a subsequent paper by Musikas et al. [173] in which they determined

through voltammetry and polarography studies on larger quantities of Cf(III) that the reduction proceeds in two steps, Cf(III)/Cf(II) and Cf(II)/Cf(0), with measured $E_{1/2}$ values of -1.47 and -1.68 V versus SHE, respectively. The measurements were performed in dilute H_2SO_4 solutions ($\text{pH } 2.9\text{--}3.0$) with $[(\text{CH}_3)_4\text{N}]I$ as supporting electrolyte. Definitive evidence for the existence of Cf(II) in solution, albeit nonaqueous, was also noted by Friedman et al. [174] during polarography experiments on $\text{Cf}(\text{ClO}_4)_3$ in anhydrous acetonitrile at a dropping mercury electrode with $0.1\text{ M }[(\text{C}_2\text{H}_5)_4\text{N}][\text{ClO}_4]$ as supporting electrolyte. The $E_{1/2}$ values for the Cf(III)/Cf(II) and Cf(II)/Cf(0) were -1.00 and -1.43 V versus SCE, respectively. The results for californium were substantiated by comparison with the polarographic behavior of $\text{Sm}(\text{ClO}_4)_3$, which displays an intermediate Sm(II) species, and also with $\text{Nd}(\text{ClO}_4)_3$, which displays a direct three-electron reduction to the Nd(0).

Trautmann [100] obtained better than 90% electrodeposition of Cf-nitrate from a 5-mL isopropanol solution containing $100\text{ }\mu\text{L}$ of 0.1 M HNO_3 . Electrodeposition was performed at 1000 V for 30 min onto Ti, Ta, and C cathode foils. The electrodeposition procedure can also be performed from an aqueous HCl solution at $\text{pH } 2.7$ with added NH_4Cl as electrolyte. With an applied potential of $8\text{--}12\text{ V}$ and a resulting current density of $1.6\text{--}2\text{ A cm}^{-2}$, 98% of Cf can be deposited on Ti or Ta cathode foils in 15 min .

25.12 Einsteinium

The electrochemical behavior of einsteinium has received only minimal literature coverage. Nugent et al. [175] employed

electron-transfer band and f-d absorption band measurements to determine the standard potential for the Es(III)/Es(II) couple as -1.2 ± 0.2 V. As with some of the other actinides covered in this review radiopolarography measurements on Es(III) were obtained by Samhoun and David [170]. They found a reversible electrode process for the Es(III)/Es(0) couple in 0.1 M LiCl at $\text{pH } \sim 2$ with $E_{1/2} = -1.460$ V versus SHE and an estimated E^θ of -1.98 V. Electrodeposition of Es can be performed from aqueous and nonaqueous solutions. A relatively recent paper from Fowler et al. describes the preparation of ^{254}Es targets from isopropanol for subsequent use in accelerator bombardment studies [176]. The electrodeposition was performed on a Pd coated Be foil cathode from a 1-mL isopropanol solution with $50\text{ }\mu\text{L}$ of 0.1 M HNO_3 as electrolyte.

25.13 Fermium

The calculated standard potential for the Fm(III)/Fm(II) couple is -1.1 V as determined by Nugent and coauthors [175, 177]. Radiopolarography measurements gave an $E_{1/2}$ value of -1.47 ± 0.01 V versus SHE for the Fm(II)/Fm(0) amalgamation in 0.1 M LiCl at $\text{pH } \sim 2$ [169].

25.14 Mendelevium

The standard potential for the Md(III)/Md(II) couple as proposed by Nugent et al. is -0.15 ± 0.05 V [175]. This value is similar to the estimated value of -0.1 V reported by Maly and Cunningham [178]. Samhoun et al. have

studied the electrochemical behavior of Md at a mercury cathode in aqueous solution in the presence of acetate and the more strongly complexing citrate ions [179]. They determined $E_{1/2}$ potentials of -1.49 ± 0.01 and -1.60 ± 0.01 V versus SCE for the Md(II)/Md(0) couple in 0.1 M acetate and citrate solutions, respectively. The results were similar to the behavior of Fm, which is known to proceed through a two-step reduction, Fm(III)/Fm(II) and Fm(II)/Fm(0), during its amalgamation with mercury.

25.15 Nobelium

In aqueous solution nobelium ions are most stable in the +2 oxidation state. In this oxidation state nobelium has a filled f-electron shell, $5f^{14}$, which is likely a major factor for its stability. The potential for the No(III)/No(II) couple has been calculated by Nugent et al. as 1.45 ± 0.05 V [177]. A value of -1.4 to -1.5 V was determined by Silva and coauthors from experimental measurements [180]. David et al. have performed electrochemical amalgamation experiments for the reduction of No(II) to No(0) in aqueous acetate and citrate solutions [181]. They determined half-wave potentials of -1.709 ± 0.006 V versus SCE in acetate and -1.780 ± 0.004 V versus SCE in citrate. Their data was consistent with a reversible two-electron reduction process for which the data in acetate solution was taken as representative of a noncomplexing medium. The $E_{1/2}$ value in acetate was converted to a value of -1.47 ± 0.01 V versus SHE and subsequently used to derive a standard potential value of -2.49 ± 0.06 V for the No(II)/No(0) couple.

References

1. F. David, *Compt. Rend. Acad. Sci. Paris, Ser. C* **1970**, *271*, 440–442.
2. D. L. Love, *Anal. Chim. Acta* **1958**, *18*, 72–80.
3. H. Yamana, T. Mitsugashira, Y. Shiokawa et al., *J. Radioanal. Chem.* **1983**, *76*, 19–26.
4. (a) F. David, A. G. Maslennikov, V. P. Peretrushkin, *J. Radioanal. Nucl. Chem. Radioanal. Nucl. Ch.* **1990**, *143*, 415–426. (b) S. H. Eberle, *Gmelin Handbook of Inorganic Chemistry-Actinium*, 8th ed. (Eds.: H. K. Kugler, C. Keller), Springer-Verlag, Berlin, 1981, pp. 205–238, Vol. 1, Chap. 12.
5. N. B. Mikheev, I. E. Veleshko, A. N. Kamenskaya et al., *Radiochemistry* **1995**, *37*, 297–299.
6. N. B. Mikheev, A. N. Kamenskaya, I. A. Rumer et al., *Radiokhimiya* **1983**, *25*, 143–157.
7. S. G. Bratsch, J. J. Lagowski, *J. Phys. Chem.* **1986**, *90*, 307–312, and references therein.
8. (a) M. Rajagopalan, M. Ramaniah, *Radiochim. Acta* **1966**, *3*, 236. (b) R. H. Iyer, H. C. Jain, M. V. Ramaniah, C. L. Rao, *Radiochim. Acta* **1964**, *3*, 225.
9. A. T. Rane, K. S. Bhatki, *Int. J. Radiat. Isot.* **1973**, *24*, 385–389.
10. L. Martinot, in *Encyclopedia of Electrochemistry of the Elements* (Eds.: A. J. Bard, H. Lund), Marcel Dekker, New York, 1978, pp. 153–159, Vol. VIII.
11. G. Marx, in *Gmelin Handbook of Inorganic Chemistry – Thorium* (Eds.: R. Keim, C. Keller), Springer-Verlag, Berlin, 1988, pp. 13–21, Vol. D1.
12. (a) W. M. Latimer, *Oxidation Potentials*, 2nd ed., Prentice-Hall, Englewood Cliffs, NJ, 1961, p. 299. (b) S. Ahrland, J. O. Liljenzin, J. Rydberg, in *Comprehensive Inorganic Chemistry, The Actinides, Solution Chemistry* (Eds.: J. C. Bailar, H. J. Emeléus, Sir. R. Nyholm et al.), Pergamon Press, New York, 1973, pp. 465–635.
13. (a) L. J. Nugent, R. D. Baybarz, J. L. Burnett et al., *J. Phys. Chem.* **1973**, *77*, 1528–1539. (b) J. H. Miles, *J. Inorg. Nucl. Chem.* **1965**, *27*, 1595–1600.
14. (a) M. V. Smirnov, L. Ivanovskii, *Zh. Fiz. Khim.* **1957**, *31*, 801–806. (b) R. Srinivasan, S. Flengas, *Can. J. Chem.* **1964**, *42*, 1315–1322. (c) S. Yoshida, R. Oyamada,

- T. Kuroda, *J. Electrochem. Soc.* **1967**, *35*, 183–188. (d) D. Inman, G. Hills, L. Young et al., *Ann. N.Y. Acad. Sci.* **1960**, *79*, 803–829. (e) M. V. Smirnov, V. Ya. Kudjakov, Yu. V. Posokhin et al., *Sov. At. Energy* **1970**, *28*, 419.
15. R. Saxena, M. Mittal, *Indian J. Chem.* **1964**, *2*, 333–335.
16. (a) R. Kapoor, O. Agrawal, *Proc. Nat. Acad. Sci. India, Sect. A* **1960**, *29*, 273–276. (b) R. Kapoor, O. Agrawal, *Vijnana Parishad Ahusandhan Patrika* **1960**, *3*, 185–187.
17. R. S. Saxena, U. S. Chaturvedi, *J. Indian Chem. Soc.* **1972**, *49*, 621–624.
18. L. Astheimer, K. Schwochau, *J. Inorg. Nucl. Chem.* **1973**, *35*, 223–230.
19. G. Duyckaerts, Cl. Degueldre, *J. Electroanal. Chem.* **1981**, *119*, 347–354.
20. I. M. Kolthoff, S. Ikeda, *J. Phys. Chem.* **1961**, *65*, 1020–1026.
21. L. Martinot, C. Licour, L. Lopes, *J. Alloys Compd.* **1995**, *228*, 6.
22. J. G. Reavis, D. F. Bowersox, D. C. Christensen et al., *Radiochim. Acta* **1985**, *38*, 135.
23. L. Martinot, *J. Radioanal. Nucl. Chem. Lett.* **1986**, *103*, 357–363.
24. L. Martinot, *J. Less-Common Met.* **1989**, *147*, 73–77.
25. N. A. Talvitie, *Anal. Chem.* **1972**, *44*, 280–283.
26. M. H. Lee, C. W. Lee, *Nucl. Instrum. Methods Phys. Res., Sect. A* **2000**, *447*, 593–600.
27. S. E. Glover, R. H. Filby, S. B. Clark et al., *J. Radioanal. Nucl. Chem.* **1998**, *234*, 213–218.
28. P. Blanco Rodríguez, F. Vera Tomé, J. C. Lozano, *Appl. Radiat. Isot.* **2001**, *54*, 29–33.
29. S. C. Lee, J. G. Choi, V. F. Hodge, *J. Alloys Compd.* **1994**, *213*, 465–466.
30. R. Zarki, A. Elyahaoui, A. Chiadli, *Radiochim. Acta* **2004**, *92*, 161–169. and references therein.
31. P. Scott, P. B. Hitchcock, *J. Chem. Soc. Chem. Commun.* **1995**, 579–580.
32. A. M. Koulkès-Pujo, J. F. Le Maréchal, A. Dormond et al., *Inorg. Chem.* **1987**, *26*, 3171–3175.
33. R. G. Finke, G. Gaughan, R. Voegeli, *J. Organomet. Chem.* **1982**, *229*, 179–184.
34. D. E. Morris, R. E. Da Re, K. C. Jantunen et al., *Organometallics* **2004**, *23*, 5142–5153.
35. A. Vallet, E. Lavoron, A. Dormond, *J. Chem. Soc., Dalton Trans.* **1990**, 921–924.
36. K. M. Kadish, Y. H. Liu, J. E. Anderson et al., *Inorg. Chim. Acta* **1989**, *163*, 201–205. and references therein.
37. S. Fried, J. C. Hindman, *J. Am. Chem. Soc.* **1954**, *76*, 4863–4864.
38. M. Haissinsky, E. Pluchet, *J. Chim. Phys.* **1962**, *10*, 608–610.
39. (a) N. B. Mikheev, S. A. Kulyukhin, N. A. Konovalova, *Radiokhimiya* **1992**, *34*, 23–26, and references therein. (b) R. Guillaumont, G. Ionova, J. C. Krupa, F. David, *Radiochim. Acta* **1996**, *75*, 97–103.
40. (a) L. Martinot, in *Encyclopedia of Electrochemistry of the Elements* (Eds.: A. J. Bard, H. Lund), Marcel Dekker, New York, 1978, pp. 151–153, Vol. VIII. (b) F. Baumgartner, D. Brown, S. H. Eberle, et al., *Gmelin Handbook of Inorganic Chemistry – Protactinium Main Series*, 8th ed., (Ed.: K.-C. Buschbeck), Springer-Verlag, Berlin, 1977, pp. 128–131–323–332, Vol. 2.
41. C. Ferriera de Miranda, A. G. Maddock, *J. Inorg. Nucl. Chem.* **1962**, *24*, 1623–1633.
42. S. Prakash, R. J. Singh, M. V. Ramaniah, *Inorg. Nucl. Chem. Lett.* **1972**, *8*, 113–117.
43. R. F. Mitchell, *Anal. Chem.* **1960**, *32*, 326–328.
44. G. Smith, G. A. Barnett, *J. Inorg. Nucl. Chem.* **1965**, *27*, 975–978.
45. H. Shimojima, J. Takagi, *J. Inorg. Nucl. Chem.* **1964**, *26*, 253–255.
46. L. J. Nugent, R. D. Baybarz, J. L. Burnett et al., *J. Inorg. Nucl. Chem.* **1971**, *33*, 2503–2530.
47. A. N. Nesmeyanov, *Radiochemistry* **1978**, *20*, 312.
48. K. Schwochau, L. Astheimer, *J. Inorg. Nucl. Chem.* **1970**, *32*, 119–126.
49. S. Kihara, Z. Yoshida, H. Aoyagi et al., *Pure Appl. Chem.* **1999**, *71*, 1771–1807.
50. (a) Ch. Riglet, P. Vitorge, I. Grenthe, *Inorg. Chim. Acta* **1987**, *133*, 323–329. (b) Ch. Riglet, P. Robouch, P. Vitorge, *Radiochim. Acta* **1989**, *46*, 85–94.
51. (a) Ch. Franz, R.-E. Schmitt, in *Gmelin Handbook of Inorganic Chemistry – Uranium*, 8th ed., (Eds.: V. Haase, R. Keim), Springer-Verlag, Berlin, 1984, pp. 36–78, Vol. D1. (b) L. Martinot, in *Gmelin Handbook of Inorganic Chemistry – Uranium*, 8th ed., (Eds.: V. Haase, R. Keim), Springer-Verlag, Berlin, 1984, pp. 336–378, Vol. D1. (c) Z. Kolarik, in *Gmelin Handbook of Inorganic Chemistry – Uranium*, (Ed.: R. Keim),

- Springer-Verlag, Berlin, 1996, pp. 184–235 Vol. D6.
52. D. E. Morris, *Inorg. Chem.* **2002**, *41*, 3542–3547.
 53. R. N. Silva, M. R. Davidson, *J. Chem. Soc., Dalton Trans.* **1979**, 465–471.
 54. G. L. Booman, J. E. Rein, in *Treatise on Analytical Chemistry, Part 2, Analytical Chemistry of the Elements*, (Eds.: I. M. Kolthoff, P. J. Elving), John Wiley and Sons, New York, 1962, pp. 1–188, Vol. 9.
 55. J. B. Sobkowski, S. Minc, *J. Inorg. Nucl. Chem.* **1961**, *19*, 101–106.
 56. (a) H. Aoyagi, Z. Yoshida, S. Kihara, *Anal. Chem.* **1987**, *59*, 400–405. (b) S. Kihara, Z. Yoshida, H. Muto et al., *Anal. Chem.* **1980**, *52*, 1601–1606. (c) S. Kihara, *J. Electroanal. Chem.* **1973**, *45*, 45–58.
 57. R. E. Dueber, A. M. Bond, P. G. Dickens, *J. Electrochem. Soc.* **1994**, *141*, 311–316.
 58. Y.-Z. Wei, B. Fang, T. Arai et al., *J. Radioanal. Nucl. Chem.* **2004**, *262*, 409–415.
 59. K.-W. Kim, J.-D. Kim, H. Aoyagi et al., *J. Nucl. Sci. Technol.* **1993**, *30*, 554–559.
 60. S. P. Best, R. J. H. Clark, R. P. Cooney, *Inorg. Chim. Acta* **1988**, *145*, 141–147.
 61. P. Ugo, B. Ballarin, S. Daniele et al., *J. Electroanal. Chem.* **1992**, *324*, 145–159.
 62. K. Mizuguchi, Y.-Y. Park, H. Tomiyasu et al., *J. Nucl. Sci. Technol.* **1993**, *30*, 542–548.
 63. N. Gopinath, N. N. Mirashi, K. Chander et al., *J. Appl. Electrochem.* **2004**, *34*, 617–622.
 64. M. Mlakar, M. Branica, *J. Electroanal. Chem.* **1988**, *256*, 269–279.
 65. M. Paneli, H. Ouguenuone, F. David et al., *Anal. Chim. Acta* **1995**, *304*, 177–186.
 66. K.-S. Jung, S. C. Sohn, Y. H. Ha et al., *J. Electroanal. Chem.* **1991**, *315*, 113–124.
 67. D. W. Wester, J. C. Sullivan, *Inorg. Chem.* **1980**, *19*, 2838–2840.
 68. L. R. dos Santos, M. E. Sbampato, A. M. dos Santos, *J. Radioanal. Nucl. Chem.* **2004**, *261*, 203–209.
 69. L. Maya, B. D. Gonzalez, M. J. Lance et al., *J. Radioanal. Nucl. Chem.* **2004**, *261*, 605–607.
 70. D. Luna-Zaragoza, J. Serrano, *Appl. Radiat. Isot.* **1999**, *51*, 499–503.
 71. (a) K. Hasegawa, Y. Shiokawa, M. Akabori et al., *J. Alloys Compd.* **1998**, *271–273*, 680–684. (b) Y. Shiokawa, K. Hasegawa, K. Konashi et al., *J. Alloys Compd.* **1996**, *255*, 98–101.
 72. L. Martinot, L. Lopes, J. Marien et al., *J. Radioanal. Nucl. Chem.* **2002**, *253*, 407–412.
 73. J. L. Willit, W. E. Miller, J. E. Battles, *J. Nucl. Mater.* **1992**, *195*, 229–249.
 74. (a) T. Shimada, N. Tedzuka, Y. Shimizu et al., *J. Alloys Compd.* **1994**, *204*, 1–4. (b) P. A. Haas, S. P. Cooper, *J. Chem. Eng. Data Chem. Eng. Data* **1993**, *38*, 26–30.
 75. P. Masset, D. Bottomley, R. Konings et al., *J. Electrochem. Soc.* **2005**, *152*, A1109–A1115.
 76. S. A. Kuznetsov, H. Hayashi, K. Minato et al., *J. Electrochem. Soc.* **2005**, *152*, C203–C212.
 77. B. Prabhakara Reddy, S. Vandarkuzhali, T. Subramanian et al., *Electrochim. Acta* **2004**, *49*, 2471–2478.
 78. M. Iizuka, T. Inoue, O. Shirai et al., *J. Nucl. Mater.* **2001**, *297*, 43–51.
 79. K. Serrano, P. Taxil, O. Dugne et al., *J. Nucl. Mater.* **2000**, *282*, 137–145.
 80. (a) R. J. LeSuer, C. Buttolph, W. E. Geiger, *Anal. Chem.* **2004**, *76*, 6395–6401. (b) N. Camire, U. T. Mueller-Westerhoff, W. E. Geiger, *J. Organomet. Chem.* **2001**, *637*, 823–826. (c) R. J. LeSuer, W. E. Geiger, *Angew. Chem., Int. Ed. Engl.* **2000**, *39*, 248–250.
 81. C. Clappe, D. Leveugle, D. Hauchard et al., *J. Electroanal. Chem.* **1998**, *448*, 95–103.
 82. (a) D. Hauchard, M. Cassir, J. Chivot et al., *J. Electroanal. Chem.* **1991**, *313*, 227–241. (b) D. C. Sonnenberger, J. G. Gaudiello, *Inorg. Chem.* **1998**, *27*, 2747–2748.
 83. D. Hauchard, M. Cassir, J. Chivot et al., *J. Electroanal. Chem.* **1993**, *347*, 399–407.
 84. F. M. de Rege, W. H. Smith, B. L. Scott et al., *Inorg. Chem.* **1998**, *37*, 3664–3666.
 85. O. Maury, M. Ephritikhine, M. Nierlich et al., *Inorg. Chim. Acta* **1998**, *279*, 210–216.
 86. K. Mizouka, Y. Ikeda, *Radiochim. Acta* **2004**, *92*, 631–635.
 87. K. Mizouka, S.-Y. Kim, M. Hasegawa et al., *Inorg. Chem.* **2003**, *42*, 1031–1038.
 88. S.-Y. Kim, H. Tomiyasu, Y. Ikeda, *J. Nucl. Sci. Technol.* **2002**, *39*, 160–165.
 89. S. H. Lee, K. Mizuguchi, H. Tomiyasu et al., *J. Nucl. Sci. Technol.* **1996**, *33*, 190–192.
 90. S.-Y. Kim, T. Asakura, Y. Morita et al., *Radiochim. Acta* **2005**, *93*, 75–81.
 91. P. Roussel, P. B. Hitchcock, N. D. Tinker et al., *Inorg. Chem.* **1997**, *36*, 5716–5721.

92. L. R. Avens, D. M. Barnhart, C. J. Burns et al., *Inorg. Chem.* **1994**, *33*, 4245–4254.
93. L. Martinot, D. Laeckmann, T. Materne et al., *J. Less-Common Met.* **1990**, *163*, 185–197.
94. L. Martinot, in *Encyclopedia of Electrochemistry of the Elements*, (Eds.: A. J. Bard, H. Lund), Marcel Dekker, New York, 1978, pp. 159–171, Vol. VIII.
95. J. A. Fahey, in *The Chemistry of the Actinide Elements*, 2nd ed. (Eds.: J. J. Katz, G. T. Seaborg, L. R. Morss), Chapman and Hall, New York, 1986, pp. 469–481, 487, Vol. 1, Chap. 6.
96. S.-Y. Kim, T. Asakura, Y. Morita et al., *J. Radioanal. Nucl. Chem.* **2004**, *262*, 311–315.
97. A. V. Gelis, P. Vanysek, M. P. Jensen et al., *Radiochim. Acta* **2001**, *89*, 565–571.
98. (a) D. W. Wester, J. C. Sullivan, *J. Inorg. Nucl. Chem.* **1981**, *43*, 2919–2923. (b) P. G. Varlashkin, D. E. Hobart, G. M. Begun et al., *Radiochim. Acta* **1984**, *35*, 91–96.
99. M. V. Ramaniah, R. J. Singh, S. K. Awasthi et al., *Int. J. Appl. Radiat. Isot.* **1975**, *26*, 648–650.
100. N. Trautmann, H. Folger, *Nucl. Instrum. Methods Phys. Res., Sect. A* **1989**, *282*, 102–106.
101. K. Hasegawa, Y. Shiokawa, M. Akabori et al., *J. Alloys Compd.* **1998**, *271–273*, 680–684.
102. V. Tsoupko-Sitnikov, F. Dayras, J. de Sanoit et al., *Appl. Radiat. Isot.* **2000**, *52*, 357–364.
103. D. C. Sonnenberger, J. G. Gaudiello, *Inorg. Chem.* **1988**, *27*, 2747–2748.
104. L. Martinot, C. Licour, L. Lopes, *J. Alloys Compd.* **1995**, *228*, 6–12.
105. Y. Sakamura, T. Hijikata, K. Kinoshita et al., *J. Alloys Compd.* **1998**, *271–273*, 592–596.
106. C. L. Kreuger, T. S. Storwick, J. J. Roy et al., *J. Electrochem. Soc.* **1991**, *138*, 1186–1187.
107. J. J. Roy, L. F. Grantham, D. L. Grimmett et al., *J. Electrochem. Soc.* **1996**, *143*, 2487–2492.
108. O. Shirai, M. Iizuka, T. Iwai et al., *J. Appl. Electrochem.* **2001**, *31*, 1055–1060.
109. Y. Sakamura, O. Shirai, T. Iwa et al., *J. Electrochem. Soc.* **2000**, *147*, 642–649.
110. L. Martinot, *J. Less-Common Met.* **1991**, *170*, 121–126.
111. O. Shirai, M. Iizuka, T. Iwai et al., *J. Nucl. Sci. Technol.* **2000**, *37*, 676–681.
112. V. F. Peretrukhin, A. G. Maslennikov, in *Transuranium Elements A Half Century*, (Eds.: L. R. Morss, J. Fuger), American Chemical Society, Washington, 1992, pp. 515–523, Chap. 50.
113. L. Martinot, in *Encyclopedia of Electrochemistry of the Elements*, (Eds.: A. J. Bard, H. Lund), Marcel Dekker, New York, 1978, pp. 171–187, Vol. VIII.
114. F. Weigel, J. J. Katz, G. T. Seaborg, in *The Chemistry of the Actinide Elements*, 2nd ed. (Eds.: J. J. Katz, G. T. Seaborg, L. R. Morss), Chapman and Hall, New York, 1986, 499–886, Vol. 1, Chap. 7.
115. J. M. Cleveland, in *Plutonium Handbook-A Guide to the Technology*, (Ed.: O. J. Wick), American Nuclear Society, Illinois, 1980, pp. 403–520, Vol. 1 and 2, Chap. 13.
116. H. Capdevila, P. Vitorge, *Radiochim. Acta* **1995**, *68*, 51–62.
117. A. C. Almon, *Anal. Lett.* **1992**, *25*, 119–124.
118. H. Boulhalfa, S. D. Reilly, W. H. Smith et al., *Inorg. Chem.* **2004**, *43*, 5816–5823.
119. N. A. Budantseva, I. G. Tananaev, A. M. Fedoseev et al., *J. Alloys Compd.* **1998**, *271–273*, 813–816.
120. M. A. Abuzwida, A. G. Maslennikov, V. F. Peretrukhin, *J. Radioanal. Nucl. Chem.* **1991**, *147*, 41–50.
121. M. H. Lee, M. Pimpl, *Appl. Radiat. Isot.* **1999**, *50*, 851–857.
122. C. A. Luskus, *J. Radioanal. Nucl. Chem.* **1998**, *234*, 287–292.
123. V. A. Becerril, V. Y. Meas, R. A. Tejera et al., *Nucl. Instrum. Methods Phys. Res., Sect. A* **1993**, *328*, 512–516.
124. J. J. Laidler, J. E. Battles, W. E. Miller et al., *Prog. Nucl. Energ.* **1997**, *31*, 131–140.
125. T. Nishimura, T. Koyama, M. Iizuka et al., *Prog. Nucl. Energ.* **1998**, *32*, 381–387.
126. (a) K. Kinoshita, T. Inoue, S. P. Fusselman et al., *J. Nucl. Sci. Technol.* **2003**, *40*, 524–530. (b) Y. Sakamura, T. Hijikata, K. Kinoshita et al., *J. Nucl. Sci. Technol.* **1998**, *35*, 49–59.
127. J. Serp, R. J. M. Konings, R. Malmbeck et al., *J. Electroanal. Chem.* **2004**, *561*, 143–148.
128. K. Uozumi, M. Iizuka, T. Kato et al., *J. Nucl. Mater.* **2004**, *325*, 34–43.
129. M. Iizuka, K. Uozumi, T. Inoue et al., *J. Nucl. Mater.* **2001**, *299*, 32–42.
130. O. Shirai, M. Iizuka, T. Iwai et al., *J. Electroanal. Chem.* **2000**, *490*, 31–36.

131. D. Lambertin, S. Ched'homme, G. Bourgès et al., *J. Nucl. Mater.* **2005**, *341*, 124–130.
132. V. I. Silin, O. V. Skiba, M. V. Smirnov et al., *At. Energ.* **1968**, *25*, 26–29.
133. L. Martinot, in *Encyclopedia of Electrochemistry of the Elements*, (Eds.: A. J. Bard, H. Lund), Marcel Dekker, New York, 1978, pp. 188–193, Vol. VIII.
134. W. W. Schulz, R. A. Penneman, in *The Chemistry of the Actinide Elements*, 2nd ed., (Eds.: J. J. Katz, G. T. Seaborg, L. R. Morss), Springer-Verlag, New York, 1986, pp. 910–919, Vol 1. Chap. 8.
135. B. F. Myasoedov, I. A. Lebedev, P. L. Khizhnyak et al., *J. Less-Common Met.* **1986**, *122*, 189–193.
136. J. Y. Bourges, B. Guillaume, G. Koehly et al., *Inorg. Chem.* **1983**, *22*, 1179–1184.
137. P. Berger, P. Blanc, J. Bourges, *Radiochim. Acta* **1988**, *43*, 217–222.
138. V. Ya. Frenkel, P. L. Khizhnyak, I. A. Lebedev et al., *Radiokhimiya* **1985**, *27*, 576–581.
139. A. M. Fedoseev, N. N. Krot, *Radiokhimiya* **1982**, *24*, 176–178.
140. M. Yu. S. S. Kulyako, V. Perevalov et al., *Radiokhimiya* **1986**, *28*, 256–261.
141. (a) I. A. Lebedev, Va. Frenkel', B. F. Myasoedov, *Radiokhimiya* **1977**, *19*, 570–578.
(b) B. F. Myasoedov, M. S. Milyukova, I. A. Lebedev et al., *J. Inorg. Nucl. Chem.* **1975**, *37*, 1475–1478. (c) B. F. Myasoedov, V. M. Mikhailov, I. A. Lebedev et al., *Radiochim. Radioanal. Lett.* **1973**, *14*, 17–24.
142. Yu. M. Kulyako, S. A. Perevalov, I. A. Lebedev et al., *Radiokhimiya* **1984**, *26*, 140–142.
143. (a) D. Chartier, L. Donnet, J. M. Adnet, *Radiochim. Acta* **1999**, *85*, 25–31.
(b) D. Chartier, L. Donnet, J. M. Adnet, *Radiochim. Acta* **1999**, *83*, 129–134.
144. D. Lambertin, J. Lacquement, S. Sanchez et al., *Plasmas & Ions* **2000**, *3*, 65–72.
145. S. P. Fusselman, J. J. Roy, D. L. Grimmett et al., *J. Electrochem. Soc.* **1999**, *146*, 2573–2580.
146. D. Lambertin, J. Lacquement, S. Sanchez et al., *Electrochim. Comm.* **2001**, *3*, 519–523.
147. J. Serp, M. Allibert, A. Le Terrier et al., *J. Electrochem. Soc.* **2005**, *152*, C167–C172.
148. B. F. Myasoedov, Y. M. Kulyako, I. S. Sklyarenko, *J. Inorg. Nucl. Chem.* **1976**, *38*, 827–830.
149. G. F. Payne, J. R. Peterson, *Radiochim. Acta* **1986**, *39*, 155–158.
150. C. Musikas, B. Myasoedov, *Radiochim. Radioanal. Lett.* **1969**, *2*, 21.
151. C. Ingelbrecht, A. Moens, R. Eykens et al., *Nucl. Instrum. Methods Phys. Res., Sect. A* **1997**, *397*, 34–38.
152. Q. Zhi, G. Junsheng, G. Zaiguo, *Appl. Radiat. Isot.* **2001**, *54*, 741–744.
153. A. Becerril-Vilchis, Y. Meas, A. Rojas-Hernández, *Radiochim. Acta* **1994**, *64*, 99–105.
154. L. Martinot, J. Reul, G. Duyckaerts, *Anal. Lett.* **1975**, *8*, 233–239.
155. H. Yamana, H. Moriyama, *J. Nucl. Sci. Technol.* **1997**, *34*, 288–297.
156. Y. Shiokawa, S. Suzuki, in *Americium and Curium Chemistry and Technology*, (Eds.: N. M. Edelstein, J. D. Navratil, W. W. Schulz), D. Reidel, Boston, 1985, pp. 105–114.
157. V. Ya. Frenkel, V. M. Chistyakov, Yu. M. Kulyako et al., *J. Radioanal. Nucl. Chem. Lett.* **1986**, *107*, 159–163.
158. Yu. V. Lobanov, G. V. Buklanov, F. Sh. Abdullin et al., *Nucl. Instrum. Methods Phys. Res., Sect. A* **1997**, *397*, 26–29.
159. S. P. Ramaswami, S. P. Dange, S. Prakash, *Radiochim. Acta* **1973**, *19*, 46–47.
160. L. Martinot, in *Encyclopedia of Electrochemistry of the Elements*, (Eds.: A. J. Bard, H. Lund), Marcel Dekker, New York, 1978, pp. 194–196, Vol. VIII.
161. J. E. Hardcastle, N. E. Levine, *Radiochim. Acta* **1972**, *18*, 59.
162. L. Hallstadius, *Nucl. Instr. Meth. Phys. Res.* **1984**, *223*, 266–267.
163. (a) L. Martinot, in *Encyclopedia of Electrochemistry of the Elements*, (Eds.: A. J. Bard, H. Lund), Marcel Dekker, New York, 1978, pp. 196–198, Vol. VIII. (b) D. E. Hobart, J. R. Peterson in *Chemistry of the Actinide Elements*, 2nd ed., (Eds.: J. J. Katz, G. T. Seaborg, L. R. Morss), Chapman and Hall, New York, 1986, pp. 989–1024, Vol. 2, Chap. 10.
164. M. R. Antonio, C. W. Williams, L. Soderholm, *Radiochim. Acta* **2002**, *90*, 851–856.
165. J. R. Stokely, R. D. Baybarz, J. R. Peterson, *J. Inorg. Nucl. Chem.* **1972**, *34*, 392–393.
166. G. A. Simakin, V. N. Kosyakov, A. A. Baranov et al., *Soviet Radiochem.* **1977**, *19*, 302.
167. G. A. Timofeev, E. A. Erin, V. M. Chistyakov et al., *Soviet Radiochem.* **1987**, *29*, 296–300.
168. (a) D. E. Morris, D. E. Hobart, P. D. Palmer et al., *Radiochim. Acta* **1990**, *49*, 125–134.

- (b) D. E. Hobart, D. E. Morris, P. D. Palmer et al., *Radiochim. Acta* **1990**, *49*, 119–124.
169. K. Samhoun, F. David, *J. Inorg. Nucl. Chem.* **1979**, *41*, 357–363.
170. (a) L. Martinot, in *Encyclopedia of Electrochemistry of the Elements*, (Eds.: A. J. Bard, H. Lund), Marcel Dekker, New York, 1978, p. 198, Vol. VIII. (b) G. Haire, in *Chemistry of the Actinide Elements*, 2nd ed., (Eds.: J. J. Katz, G. T. Seaborg, L. R. Morss), Chapman and Hall, New York, 1986, pp. 1025–1070, Vol. 2, Chap. 11.
171. (a) B. F. Myasoedov, in *Actinides in Perspective* (Ed.: N. M. Edelstein), Pergamon Press, New York, 1982, pp. 509–540. (b) V. N. Kosyakov, G. A. Timofeev, E. A. Erin et al., *Radiokhimiya* **1977**, *19*, 82–84.
172. D. E. Hobart, P. G. Varlashkin, K. Samhoun et al., *Rev. Chim. Miner.* **1983**, *20*, 817–827.
173. C. Musikas, R. G. Haire, J. R. Peterson, *J. Inorg. Nucl. Chem.* **1981**, *43*, 2935–2940.
174. H. A. Friedman, J. R. Stokely, R. D. Baybarz, *Inorg. Nucl. Chem. Lett.* **1972**, *8*, 433–441.
175. L. J. Nugent, R. D. Baybarz, J. L. Burnett et al., *J. Phys. Chem.* **1973**, *77*, 1528–1539.
176. M. M. Fowler, J. C. Gursky, J. B. Wilhelm, *Nucl. Instrum. Methods Phys. Res., Sect. A* **1991**, *303*, 99–101.
177. L. J. Nugent, R. D. Baybarz, J. L. Burnett, *J. Phys. Chem.* **1969**, *73*, 1177–1178.
178. J. Maly, B. B. Cunningham, *Inorg. Nucl. Chem. Lett.* **1967**, *3*, 445.
179. K. Samhoun, F. David, R. L. Hahn et al., *J. Inorg. Nucl. Chem.* **1979**, *41*, 1749.
180. R. J. Silva, T. Sikkeland, M. Nurmia et al., *J. Inorg. Nucl. Chem.* **1969**, *31*, 3405.
181. F. David, K. Samhoun, R. W. Lougheed et al., *Radiochim. Acta* **1990**, *51*, 65–70.